HC 38789-1-MS-CF

MRS
MATERIALS RESEARCH SOCIETY
SYMPOSIUM PROCEEDINGS

Volume 517

High-Density Magnetic Recording and Integrated Magneto-Optics: Materials and Devices

EDITORS
James Bain
Miguel Levy
Joseph Lorenzo
Tom Nolan
Yasuyuki Okamura
Kurt Rubin
Bethanie Stadler
Raymond Wolfe

REPORT DOCUMENTATION PAGE

Form Approved
OMB NO. 0704-0188

Public reporting burden for this collection of information is estimated to average 1 hour per response, including the time for reviewing instructions, searching existing data sources, gathering and maintaining the data needed, and completing and reviewing the collection of information. Send comment regarding this burden estimates or any other aspect of this collection of information, including suggestions for reducing this burden, to Washington Headquarters Services, Directorate for information Operations and Reports, 1215 Jefferson Davis Highway, Suite 1204, Arlington, VA 22202-4302, and to the Office of Management and Budget, Paperwork Reduction Project (0704-0188), Washington, DC 20503.

1. AGENCY USE ONLY *(Leave blank)*	2. REPORT DATE	3. REPORT TYPE AND DATES COVERED
		Final Report

4. TITLE AND SUBTITLE

High-Density Magnetic Recording and Integrated Magneto-Optics: Materials and Devices

5. FUNDING NUMBERS

DAAG55-98-1-0223

6. AUTHOR(S)

Dr. Robert H. Pachavis, principal investigator

7. PERFORMING ORGANIZATION NAMES(S) AND ADDRESS(ES)

Materials Research Society
506 Keystone Drive
Warrendale, PA 15086

8. PERFORMING ORGANIZATION REPORT NUMBER

9. SPONSORING / MONITORING AGENCY NAME(S) AND ADDRESS(ES)

U.S. Army Research Office
P.O. Box 12211
Research Triangle Park, NC 27709-2211

10. SPONSORING / MONITORING AGENCY REPORT NUMBER

ARO 38789.1-MS-CF

11. SUPPLEMENTARY NOTES

The views, opinions and/or findings contained in this report are those of the author(s) and should not be construed as an official Department of the Army position, policy or decision, unless so designated by other documentation.

12a. DISTRIBUTION / AVAILABILITY STATEMENT

Approved for public release; distribution unlimited.

12 b. DISTRIBUTION CODE

13. ABSTRACT *(Maximum 200 words)*

14. SUBJECT TERMS			15. NUMBER IF PAGES
			16. PRICE CODE
17. SECURITY CLASSIFICATION OR REPORT	18. SECURITY CLASSIFICATION OF THIS PAGE	19. SECURITY CLASSIFICATION OF ABSTRACT	20. LIMITATION OF ABSTRACT

High-Density Magnetic Recording and Integrated Magneto-Optics: Materials and Devices

19990316 008

DTIC QUALITY INSPECTED 1

MATERIALS RESEARCH SOCIETY
SYMPOSIUM PROCEEDINGS VOLUME 517

High-Density Magnetic Recording and Integrated Magneto-Optics: Materials and Devices

Symposium held April 12–16, 1998, San Francisco, California, U.S.A.

EDITORS:

James Bain
Carnegie Mellon University
Pittsburgh, Pennsylvania, U.S.A.

Miguel Levy
Columbia University
New York, New York, U.S.A.

Joseph Lorenzo
USAF Rome Laboratory
Hanscom AFB, Massachusetts, U.S.A.

Tom Nolan
Komag Incorporated
San Jose, California, U.S.A.

Yasuyuki Okamura
Osaka/Wakayama University
Toyonaka, Osaka, Japan

Kurt Rubin
IBM Almaden Research Center
San Jose, California, U.S.A.

Bethanie Stadler
University of Minnesota
Minneapolis, Minnesota, U.S.A.

Raymond Wolfe
Lucent Technologies, Bell Laboratories
Murray Hill, New Jersey, U.S.A.

Materials Research Society
Warrendale, Pennsylvania

Support for Symposium M proceedings was furnished by the U.S. Army Research Office, Contract #DAAG55-98-1-9223. The views, opinions, and/or findings contained in this report are those of the authors and should not be construed as an official Department of the Army position, policy, or decision, unless so designated by other documentation.

Single article reprints from this publication are available through
University Microfilms Inc., 300 North Zeeb Road, Ann Arbor, Michigan 48106

CODEN: MRSPDH

Copyright 1998 by Materials Research Society.
All rights reserved.

This book has been registered with Copyright Clearance Center, Inc. For further information, please contact the Copyright Clearance Center, Salem, Massachusetts.

Published by:

Materials Research Society
506 Keystone Drive
Warrendale, PA 15086
Telephone (724) 779-3003
Fax (724) 779-8313
Website: http://www.mrs.org/

Library of Congress Cataloging in Publication Data

High-density magnetic recording and integrated mageto-optics: materials and devices : symposium held April 12-16, 1998, San Francisco, California, U.S.A. / editors, James Bain, Miguel Levy, Joseph Lorenzo, Tom Nolan, Yasuyuki Okamura, Kurt Rubin, Bethanie Stadler, and Raymond Wolfe
p. cm. -- (Materials Research Society symposium proceedings ; v. 517)
Includes bibliographical references and index.
ISSN 0272-9172
ISBN 1-55899-423-8
1. Computer storage devices---Congresses. 2. Magnetic recorders and recording--Materials---Congresses. 3. Magnetoresistance--Congresses. 4. Integrated optics--Congresses. I. Bain, James, II. Levy, Miguel, III. Lorenzo, Joseph, IV. Nolan, Tom, V. Okamura, Yasuyuki, VI. Rubin, Kurt, VII. Stadler, Bethanie, VIII. Wolfe, Raymond, IX. Series : Materials Research Society symposium proceedings ; v. 517.

TK7895.M3H54 1998 98-29133
621.39'7--dc21 CIP

Manufactured in the United States of America

CONTENTS

Preface (Symposium L) xv

Preface (Symposium M) xvii

Materials Research Society Symposium Proceedings xviii

SYMPOSIUM L

MATERIALS FOR HIGH-DENSITY MAGNETIC RECORDING

Head Materials for Write Transducers and Readback Sensors

PART I: HIGH MOMENT POLE MATERIALS

*Microstructures and Properties of High-Saturation Soft Magnetic Materials for Advanced Recording Heads 5
S.X. Wang, J. Hong, and K. Sin

PART II: ANISOTROPIC MAGNETORESISTANCE (AMR), GIANT MAGNETORESISTANCE (GMR), AND EXCHANGE MATERIALS

*Surface Effects in the Growth of Giant Magnetoresistance Spin Valves 9
W.F. Egelhoff, Jr., P.J. Chen, C.J. Powell, D. Parks, R.D. McMichael, J.H. Judy, D. Martien, A.E. Berkowitz, and J.M. Daughton

Thermal Instability of the Cu-Ni Interface Above 200°C 13
T.H. Westmore, J.E.E. Baglin, V.R. Deline, A.J. Kellock, M.A. Parker, R. Beyers, and E.L. Allen

Magnetic Stability of Spin Valves Exchange-Biased by a Synthetic Antiferromagnet 19
J.L. Leal and M.H. Kryder

Exchange Coupling Properties Between Ordered Antiferromagnetic PdPtMn and NiFe Films 25
A. Tanaka, Y. Shimizu, H. Kishi, K. Nagasaka, C. Hou, and H. Fujiwara

Spin-Valve Sensors with $Mn_{1-x}Rh_x$ Exchange Films 31
A. Veloso, P.P. Freitas, J. Fernandes, and M. Ferreira

Magnetization Process of F/AF Systems 37
C. Hou, H. Fujiwara, F. Ueda, and H.S. Cho

Influence of Crystal Lattice Defects on Domain-Wall Nucleation and Motion in Exchange-Bias Films 43
V.I. Nikitenko, V.S. Gornakov, L.M. Dedukh, A.J. Shapiro, R.D. Shull, and A. Chaiken

*Invited paper

Exchange Property Correlation on Deposition Gas Species and Interface Structure of Ion-Beam-Deposited Ta(50Å)/NiFe(xÅ)/FeMn(yÅ)/Ta(50Å) Layers 49
H. Hegde, J. Wang, and S.B. Sant

Heat Dissipation Material Application for Magnetoresistive Head 55
Xiao-feng Zhang, X. Yan, R.F. Xiao, Ji-bin Geng, and Jie Xhie

Structural and Magnetic Anisotropy of Electrodeposited Co/Cu Multilayers 61
M. Shima, L. Salamanca-Riba, T.P. Moffat, and R.D. McMichael

The Magneto-Transport Properties of Sandwich Films of Permalloy/Cu/Co 67
C.K. Lo, C.H. Ho, I. Klik, Y.D. Yao, S.F. Lee, H.H. Huang, Y.C. Chen, C.Y. Wu, D.Y. Chiang, C.A. Chang, M.T. Lin, and D.R. Huang

The GMR Effect of Permalloy/Cu Multilayers on Si(100) and Si(111) 73
C.H. Ho, C.K. Lo, Y.D. Yao, S.F. Lee, I. Klik, M.T. Lin, Y. Liou, D.Y. Chiang, and D.R. Huang

Inductively-Coupled Plasma Etching of NiFe and NiFeCo 79
K.B. Jung, J.R. Childress, S.J. Pearton, M. Jenson, A.T. Hurst, Jr., and D. Johnson

PART III: SPIN TUNNEL JUNCTIONS

*Magnetic Tunnel Junctions With Low Resistance, High Current Density, and Good Uniformity 87
H. Tsuge, T. Mitsuzuka, A. Kamijo, and K. Matsuda

Double-Barrier-Spin-Dependent Tunnel Junctions With an Intermediate Ferromagnetic Layer 97
R.C. Sousa, P.P. Freitas, T.T. Galvão, J.J. Sun, V. Soares, A. Kling, M.F. da Silva, and J.C. Soares

Spin-Dependent Tunneling Junctions With Ta_2O_5 Barrier 103
Manish Sharma, Janice H. Nickel, and Shan X. Wang

PART IV: COLOSSAL MAGNETORESISTANCE (CMR) MATERIALS

*Characterization of Doped CMR-Manganite Perovskites by Raman Spectrometry 111
B. Güttler, L. Skuja, O.Yu. Gorbenko, A.R. Kaul, M. Novozhilov, N.A. Babushkina, and L.M. Belova

Magnetoresistance Behavior in External, Internal, and Mixed-Doped Lanthanum Manganite Thin Films 123
Srinivas V. Pietambaram, D. Kumar, Rajiv K. Singh, and C.B. Lee

*Invited paper

Postannealing and Colossal Magnetoresistance in Epitaxial La-Nd-Ca-Mn-O and La-Y-Ca-Mn-O Films by dc Sputtering 129
L.H. Chen and J.L. Lin

Microstructure and Magnetoresistance of La-Sr-Mn-O Thin Films Grown by rf Sputtering 135
K.K. Choi, K. Nakano, M. Yamasaki, and Y. Yamazaki

Plasma Chemistries for Etching of $La_{0.41}Ca_{0.59}MnO_3$ and SmCo CMR Structures 141
J.J. Wang, K.B. Jung, J.R. Childress, S.J. Pearton, F. Sharifi, K.H. Dahmen, E.S. Gillman, F.J. Cadieu, R. Rani, X.R. Qian, and Li Chen

Effects of Closed d-Shell (Sn) and Partially Filled d-Shell (Ru) Elements on the GMR Properties of $La_{0.7}Ca_{0.3}Mn_{1-x}M_xO_3$ (M = Sn, Ru, and □) and $Pr_{0.7}Ca_{0.3}Mn_{1-x}M_xO_3$ (M = Sn and Ru) 147
K. Chandrasekaran, R. Vijayaraghavan, M.S. Ramachandra Rao, and U.V. Varadaraju

Effect of the Cationic Size Variation in the GMR Compound $Pr_{0.7-x}Ho_xSr_{0.3}MnO_3$ and in the Charge Ordered Compounds $Pr_{0.5-x}Ho_xSr_{0.5}MnO_3$ 153
Sirisha K, A. Narayanasamy, and U.V. Varadaraju

Phase Relations in the System La_2O_3-SrO-CaO-Mn_2O_3 With Emphasis on $LaMnO_3$ 159
P. Majewski and F. Aldinger

Microstructure and Magnetoresistance in La-Y-Sr-Mn-O Thick Films 165
L.H. Chen, D.H. Wu, and C.S. Hsi

Magnetoresistance in $Pr_{0.65}Ba_{0.05}Ca_{0.3}MnO_{3-\delta}$ Thin Films 171
D. Kumar, Srinivas V. Pietambaram, Rajiv K. Singh, and C.B. Lee

High-Density Magnetic Recording Media

PART V: MICROSTRUCTURAL ISSUES IN LONGITUDINAL RECORDING MEDIA

*Magnetic Media Performance: Control Methods for Crystalline Texture and Orientation 181
David N. Lambeth, Wei Yang, Heng Gong, David E. Laughlin, Bin Lu, Li-Lien Lee, Jie Zou, and Peter S. Harllee

In-Plane Anisotropy in CoCr(Ta,Pt)/Cr Films Deposited Onto Substrates With Controlled Topography 193
D.J. Twisselmann, B.T. Adekor, M. Farhoud, Henry I. Smith, P.C. Dorsey, and C.A. Ross

*Invited paper

Effects of Sputtering Conditions on Texture, Microstructure, and Magnetic Properties of the CoCrPt/NiAl Thin Films 199
Y-N. Hsu, D.E. Laughlin, and D.N. Lambeth

Quantitative Measurements of Segregation in Co-Cr-X Magnetic Recording Media by Energy-Filtered Transmission Electron Microscopy 205
J. Bentley, J.E. Wittig, and T.P. Nolan

Chromium Distribution in CoCrTa/Cr Longitudinal Recording Media 211
J.E. Wittig, T.P. Nolan, R. Sinclair, and J. Bentley

The Effects of Substrate Preheating and Postdeposition Annealing on CrMn/CoCrPt/CrMn/NiAl Films 217
Jie Zou, David E. Laughlin, and David N. Lambeth

Intergranular Coupling and Grain Isolation of Thin Co Films 223
Heng Gong, Wei Yang, David N. Lambeth, and David E. Laughlin

PART VI: THERMAL STABILITY OF MAGNETIC RECORDING MEDIA

*Determination of Critical Volumes in Recording Media 231
K. O'Grady, P. Dova, and H. Laidler

*Compositional Microstructure and Micromagnetics of Co-Based Thin-Film Media 243
M. Futamoto, N. Inaba, Y. Hirayama, K. Ito, and Y. Honda

Magnetic-Force-Microscopy Analysis of Thermal Stability in Longitudinal Media 255
E.N. Abarra, I. Okamoto, and T. Suzuki

Dynamic Coercivity and Thermal Decay of Magnetic Media 261
Kurt Rubin, Jason Goldberg, Hal Rosen, Ernesto Marinero, Mary Doerner, and Manfred Schabes

Effect of Grain Size and Magnetic Switching Volume on Media Noise Due to Intergranular Coupling in CoCrTaPt/Cr Thin-Film Media 267
Sudhir S. Malhotra, Brij B. Lal, and Michael A. Russak

Effects of dc Bias on the Thermal Stability of dc Inline Sputtered CoCrTa/Cr Thin-Film Media 273
J.P. Wang, L.P. Tan, T.Y.F. Liew, T.S. Low, H.L. Wong, and Y.K. Lee

Computer Simulations of Thermal Switching in Small-Grain Ferromagnets 279
M.A. Novotny, G. Brown, and P.A. Rikvold

*Invited paper

A Simulation of Rotational Hysteresis Energy Loss in Longitudinal Thin-Film Media 285
Wei Yang and David N. Lambeth

Modeling Complex Aftereffect Behavior in Recording Materials Using a Preisach-Arrhenius Approach 291
E. Della Torre, L.H. Bennett, and L.J. Swartzendruber

PART VII: PERPENDICULAR MAGNETIC MEDIA AND NOVEL STRUCTURES

*Large Magnetic Anisotropy in Co_3Pt Ordered Phase Thin Films 299
Yoshiyasu Yamada and Takao Suzuki

Magnetic Order of $Co_{0.1}Pt_{0.9}$ in Proximity of $CoPt_3$ 311
A.L. Shapiro, F. Hellman, and M.R. Fitzsimmons

Thickness-Dependent Perpendicular Magnetic-Domain Patterns in Sputtered Epitaxial FePt(001) $L1_0$ Films 319
J-U. Thiele, L. Folks, M.F. Toney, and D.K. Weller

Structural and Magnetic Properties of $Co_{50 \pm x}Pt_{50 \mp x}$ Thin Films Prepared by MBE Coevaporation on (001)MgO Substrate at Various Temperatures 325
V. Parasote, M-C. Cadeville, V. Pierron-Bohnes, and W. Grange

Disturbed Array Formation of Electrochemically Grown Self-Organized Nanostructures 331
D.D. Dierickx, J.P. Celis, and V.V. Moshchalkov

Structure and Magnetic Properties of Co, Ni, Mn, Cr, and Cu Substituted Magnetites 337
M. Sorescu, D. Mihaila-Tarabasanu, and L. Diamandescu

Macroscopic Probing of the Joint Between Metals in MR Heads 343
Ji-bin Geng, X. Yan, X.X. Zhang, Xiao-feng Zhang, N. Wang, and K.K. Fung

Interparticle Interaction Effects in Nonmiscible CoAg Thin Films With High Co Concentration 349
A. Butera and J.A. Barnard

Behavior of Magnetic Aftereffect Along a Magnetization Reversal Curve in a Metal Particle Recording Material 355
L.J. Swartzendruber, L.H. Bennett, E. Della Torre, H.J. Brown, and J.H. Judy

Compensation Temperature of a Mixed Ising Ferrimagnetic Model in the Presence of External Magnetic Fields 361
G.M. Buendia, E. Machado, and M.A. Novotny

*Invited paper

Tribology, Lubrication, and Head/Disk Interface Materials

PART VIII: NANOTRIBOLOGY OF WEAR LAYERS FOR RECORDING MEDIA

*Application of Cathodic Arc-Deposited Amorphous Hard Carbon Films to the Head/Disk Tribology 371
Simone Anders, C. Singh Bhatia, Walton Fong, Roger Yu Lo, and David B. Bogy

Characterization of Thin DLC Films Using Film Stress and Raman Techniques 383
J.E. Turlo, Danny Gan, and Niranjan Gopinathan

Observations of Depth-Sensing Reciprocating Scratch Tests of DLC and Nitrogenated-DLC Overcoats on Magnetic Disks 389
T.W. Scharf, R.D. Ott, D. Yang, and J.A. Barnard

AFM Nanoindentation as a Method to Determine Microhardness of Hard Thin Films 395
T. Bao, P.W. Morrison, Jr., and W. Woyczynski

PART IX: TRIBOLOGY, LUBRICANTS, AND CORROSION

*Structure of Molecularly-Thin Perfluoropolyether Films on Amorphous Carbon Surfaces 403
G.W. Tyndall and R.J. Waltman

Study of Hard Disk and Slider Surfaces Using X-ray Photoemission Electron Microscopy and Near-Edge X-ray Absorption Fine Structure Spectroscopy 415
Simone Anders, Thomas Stammler, C. Singh Bhatia, Joachim Stöhr, Walton Fong, Chao-Yuan Chen, and David B. Bogy

Corrosion Protection of Cu, Fe, Mn, and Co Surfaces 421
J.E.E. Baglin, A.J. Kellock, T.T. Bardin, T. Karis, and D. Keck

A Method for Laser Zone Texturing of Glass-Based Magnetic Media Using Nd:YAG Lasers 427
M.P. Rosenblum and C.A. Ross

The 1280 CM^{-1} Absorption Line in Amorphous Hydrogenated Boron Carbide 433
Shu-Han Lin and Bernard J. Feldman

The Application of Amine-Quinone Polymers in High- Density Recording Media for Improved Corrosion Protection 439
Rahul Sharma, G.W. Warren, D. Nikles, Y. Hu, and S. Street

*Invited paper

SYMPOSIUM M
INTEGRATED MAGNETO-OPTICS—MATERIALS AND DEVICES

PART I : GARNET MATERIALS FOR INTEGRATED PHOTONICS: FABRICATION AND PROCESSING

*Metalorganic Chemical Vapor Deposition of Magneto-Optical Ce: YIG Thin Films 449
Yi-Qun Li, Mondher Cherif, Jankang Huang, Wayne Liu, and Qiushui Chen

Optimized Nonreciprocal Rib Waveguides for Integrated Magneto-Optic Isolators 463
M. Wallenhorst, V. Backherms, A. Josef, N. Bahlmann, M. Lohmeyer, H. Dötsch, and P. Hertel

Integrated Optical Isolator Employing Nonreciprocal Phase Shift by Wafer Direct Bonding 469
H. Yokoi and T. Mizumoto

Crystal Ion Slicing of Magnetic and Ferroelectric Oxide Films 475
M. Levy, R.M. Osgood, Jr., A. Kumar, H. Bakhru, R. Liu, and E. Cross

Integration of Yttrium Iron Garnet Films Via Reactive rf Sputtering 481
Bethanie J.H. Stadler and Anand Gopinath

Patterned Garnet Films on Substrates With Ion-Beam-Bombarded Micropatterns 487
Yasuyuki Okamura and Sadahiko Yamamoto

Magneto-Optical Properties of Co Doped $Bi_3Fe_5O_{12}$ Garnet Film 493
T. Okuda, T. Mima, K. Ando, N. Ohmori, N. Adachi, and H. Ohsato

PART II: GARNET MATERIALS: DEVICES FOR INTEGRATED PHOTONICS

*Integrated Nonreciprocal Devices for Application in Optical Communication Systems 501
T. Shintaku, N. Sugimoto, A. Tate, E. Kubota, H. Kozawaguchi, and Y. Katoh

A Comparison of an Improved Design for Two Integrated Optical Isolators Based on Nonreciprocal Mach-Zehnder Interferometry 513
N. Bahlmann, M. Lohmeyer, M. Wallenhorst, H. Dötsch, and P. Hertel

*Invited paper

Radiatively-Coupled Waveguide Concept for an Integrated Magneto-Optic Circulator 519
M. Lohmeyer, M. Shamonin, N. Bahlmann, P. Hertel, and H. Dötsch

*Recent Advances in Magneto-Static Waves-Based Integrated Magneto-Optic Bragg Cell Modulators in YIG-GGG Waveguides 525
Chen S. Tsai

Magneto-Static Wave Oscillator-Based Integrated Magneto-Optic Bragg Cell Modulator 535
Jun Su and Chen S. Tsai

*Faraday Effect Devices, Optical Isolators 541
Donald K. Wilson

A Lens-Free and Mirror-Free Fiber-Integrated Optical Magnetic-Field Sensor Using Bi-Substituted Garnet 547
H. Minemoto, N. Itoh, D. Ishiko, and S. Ishizuka

PART III: MAGNETO-OPTIC RECORDING MEDIA: MATERIALS AND DEVICES

*Amorphous Rare-Earth-Transition-Metal Alloys for Magneto-Optical Storage 555
Richard J. Gambino

*Characterizing the Magneto-Optic Properties of Amorphous Rare-Earth-Transition-Metal Thin Films 565
W.A. Challener

Magnetic and Magneto-Optical Properties of Al Substituted Bi-RIG Particles Dispersed in a Plastic Binder 577
T. Hirano, K. Yoshida, Y. Yamazaki, T. Namikawa, and M. Kishi

Colloidal Particles: Spherical Yttrium Iron Garnet 583
R.H.M. Godoi, M. Jafelicci, Jr., R.F.C. Marques, and L.C. Varanda

*High-Density Recording of Conventionally Structured Magneto-Optical Disk by Magnetic-Field Modulation 589
M. Kaneko and A. Fukumoto

Near-Field Magneto-Optic Fiber Probe 599
M.A. Seigler and D.N. Lambeth

Readout of Magnetic Film-Based Memories by Nonlinear Optical Magnetic Kerr Effect 605
T.V. Murzina, N.V. Didenko, A.A. Fedyanin, A.V. Melnikov, T.V. Misuryaev, and O.A. Aktsipetrov

*Invited paper

PART IV: DILUTED MAGNETIC SEMICONDUCTORS AND OTHER MATERIALS

*Diluted Magnetic Semiconductor Thin Films and Multilayers 613
J.K. Furdyna

*Diluted Magnetic Semiconductor Magneto-Optic Waveguides for Monolithic Integration With Semiconductor Optic Devices 625
K. Ando, W. Zaets, and K. Watanabe

Magnetization Process in Cr Substituted Diluted Magnetic Semiconductor Films 633
N. Adachi, J. Hirano, T. Yamazaki, T. Okuda, H. Kitazawa, and G. Kido

*Solution Flow System for Hydrothermal-Electrochemical Synthesis: New Opportunities for Multilayered Oxide Films 639
W. Suchanek, T. Watanabe, B. Sakurai, and M. Yoshimura

Magnetic Second-Harmonic-Generation Studies of Co-Cu Granular Films 651
T.V. Misuryaev, T.V. Murzina, E.A. Ganshina, V.S. Gushin, D.V. Kazantsev, and O.A. Aktsipetrov

Nonlinear Magneto-Optical Kerr Effect in Gd-Containing Langmuir-Blodgett Films 657
N.V. Didenko, A.A. Fedyanin, G.B. Khomutov, T.V. Murzina, and O.A. Aktsipetrov

Author Index 663

Subject Index 667

*Invited paper

PREFACE

This book contains the proceedings of two symposia held at the 1998 MRS Spring Meeting in San Francisco, California. The editors of each symposium have provided individual prefaces below. The decision for joint publication of the proceedings was based on a commonality of interest in the audiences of the two symposia, as well as some logistical considerations.

Preface for Symposium L
Materials for High-Density Magnetic Recording

High-density magnetic recording continues to be one of the fastest growing and most rapidly improving technologies in the computer industry. Information storage density has doubled every two years for the past two decades. Nevertheless, recent materials advances in several areas have allowed an even faster rate of improvement during the past six years. Completely new areas of materials science are moving rapidly from basic theory to practical application in commercial products in a few short years.

Symposium L, "Materials for High-Density Magnetic Recording," occupied a full four days of meetings, including an evening poster session, and covered a range of materials topics relevant to magnetic recording applications. Approximately two-thirds of the symposium focused on materials which have found commercial application within the longitudinal magnetic recording industry (or are likely to in the near term). Longitudinal magnetic recording, the format of most commercial disk and tape drives, is the mainstay of commercial information storage. In the sessions on near-term head materials, the focus was on improved high-moment pole materials for magnetic write heads and improved magnetic sensor materials for read heads (magnetoresistive: MR, and giant magnetoresistive: GMR). Within the sessions on longitudinal media, discussions centered on small-grain, magnetically anisotropic media for low noise, as well as issues of thermal stability of very small magnetic grains. The tribology sessions addressed protective head/media interface tribological materials for low flying heights, and included a joint session on nanotribology.

The remainder of the symposium focused on materials with an application horizon beyond five years, or with applications to technologies which have not yet found widespread commercial viability. These included a number of papers on colossal magnetoresistive (CMR) materials and spin-dependent tunneling sensors for read heads. These technologies require a new level of understanding and control of interface structure and properties, at the quantum mechanical as well as physical levels. Also examined within this context was a series of papers on perpendicular media, which continues to be a possible alternative to the longitudinal format.

The great success of this symposium is due in no small part to the help of many people and companies. The conference organizers thank them all. General financial support was provided by:

Commonwealth Scientific Corporation
Headway Technologies
IBM Corporation
Intevac
Komag Inc.
Seagate Corporation
Stor-Media

The staff of the Materials Research Society provided guidance and help from the planning throughout the execution phase of the symposium. An excellent opening tutorial was presented by Professor Mark Kryder of Carnegie Mellon University. The invited speakers provided a consistently high standard of presentation. The session chairs all worked hard to keep the sessions lively and run on time. And finally, the organizers thank Dr. John Baglin, Professor David Bogy, Professor Caroline Ross, and Dr. Dieter Weller for their advice during the formative stages of organizing Symposium L.

Jim Bain
Tom Nolan
Kurt Rubin

Editors, Symposium L

Preface for Symposium M
Integrated Magneto-Optics—Materials and Devices

"Integrated Magneto-Optics—Materials and Devices" (Symposium M of the 1998 MRS Spring Meeting) drew international researchers with approximately one-third each coming from Japan and the U.S., and the remaining one-third coming from Europe, Russia and South America. Symposium topics included fabrication and processing of garnet materials for integrated photonics, devices for integrated photonics, magneto-optic (MO) recording media, diluted magnetic semiconductors, and other materials.

Integration of the garnets with semiconductor platforms was achieved by monolithic techniques, such as MOCVD and rf sputtering including selective-area growth, and by hybrid techniques such as crystal ion slicing and wafer direct bonding. Other processing techniques of interest included laser annealing and growth via a hydrothermal-electrochemical flow cell. Diluted magnetic semiconductors were also discussed, as they have an excellent potential for integrated MO applications due to their inherent semiconductor compatibility.

Devices of interest included integrated isolators, circulators, Bragg cell modulators, and optical magnetic field sensors for applications in optical communications, photonic integrated circuits, microwave devices, and sensors. Technologies behind the devices were based on a range of magneto-optical effects, from the well-known Kerr and Faraday effects to Mach-Zehnder interferometry in a magnetic field, radiatively coupled waveguides, and magnetostatic waves.

Two magneto-optic recording media were discussed: amorphous rare-earth-transition metal alloys and colloidal garnet particles. New recording technologies such as magnetic field modulation, fiber probes, nonlinear Kerr effect, and second harmonic generation promise higher densities of recording and improved readout of memories.

This symposium and its proceedings provide a forum for materials scientists, chemists and physicists interested in the development of magneto-optics for integrated applications.

The success of this symposium was the result of contributions from various participants and support from the U.S. Army Research Office. The editors are also indebted to Andrew Davis and Helen Dauplaise of the Air Force Research Laboratory for their assistance in reviewing manuscripts and to Andrew Davis for filling in as session chair.

Bethanie Stadler
Miguel Levy
Joseph Lorenzo
Yasuyuki Okamura
Raymond Wolfe

Editors, Symposium M

MATERIALS RESEARCH SOCIETY SYMPOSIUM PROCEEDINGS

Volume 481— Phase Transformation and Systems Driven Far From Equilibrium, E. Ma, P. Bellon, M. Atzmon, R. Trivedi, 1998, ISBN: 1-55899-386-X
Volume 482— Nitride Semiconductors, F.A. Ponce, S.P. DenBaars, B.K. Meyer, S. Nakamura, S. Strite, 1998, ISBN: 1-55899-387-8
Volume 483— Power Semiconductor Materials and Devices, S.J. Pearton, R.J. Shul, E. Wolfgang, F. Ren, S. Tenconi, 1998, ISBN: 1-55899-388-6
Volume 484— Infrared Applications of Semiconductors II, S. Sivananthan, M.O. Manasreh, R.H. Miles, D.L. McDaniel, Jr., 1998, ISBN: 1-55899-389-4
Volume 485— Thin-Film Structures for Photovoltaics, E.D. Jones, R. Noufi, B.L. Sopori, J. Kalejs, 1998, ISBN: 1-55899-390-8
Volume 486— Materials and Devices for Silicon-Based Optoelectronics, J.E. Cunningham, S. Coffa, A. Polman, R. Soref, 1998, ISBN: 1-55899-391-6
Volume 487— Semiconductors for Room-Temperature Radiation Detector Applications II, R.B. James, T.E. Schlesinger, P. Siffert, M. Cuzin, M. Squillante, W. Dusi, 1998, ISBN: 1-55899-392-4
Volume 488— Electrical, Optical, and Magnetic Properties of Organic Solid-State Materials IV, J.R. Reynolds, A.K-Y. Jen, L.R. Dalton, M.F. Rubner, L.Y. Chiang, 1998, ISBN: 1-55899-393-2
Volume 489— Materials Science of the Cell, B. Mulder, V. Vogel, C. Schmidt, 1998, ISBN: 1-55899-394-0
Volume 490— Semiconductor Process and Device Performance Modeling, J.S. Nelson, C.D. Wilson, S.T. Dunham, 1998, ISBN: 1-55899-395-9
Volume 491— Tight-Binding Approach to Computational Materials Science, P.E.A. Turchi, A. Gonis, L. Colombo, 1998, ISBN: 1-55899-396-7
Volume 492— Microscopic Simulation of Interfacial Phenomena in Solids and Liquids, S.R. Phillpot, P.D. Bristowe, D.G. Stroud, J.R. Smith, 1998, ISBN: 1-55899-397-5
Volume 493— Ferroelectric Thin Films VI, R.E. Treece, R.E. Jones, S.B. Desu, C.M. Foster, I.K. Yoo, 1998, ISBN: 1-55899-398-3
Volume 494— Science and Technology of Magnetic Oxides, M. Hundley, J. Nickel, R. Ramesh, Y. Tokura, 1998, ISBN: 1-55899-399-1
Volume 495— Chemical Aspects of Electronic Ceramics Processing, P.N. Kumta, A.F. Hepp, D.B. Beach, J.J. Sullivan, B. Arkles, 1998, ISBN: 1-55899-400-9
Volume 496— Materials for Electrochemical Energy Storage and Conversion II—Batteries, Capacitors and Fuel Cells, D.S. Ginley, D.H. Doughty, T. Takamura, Z. Zhang, B. Scrosati, 1998, ISBN: 1-55899-401-7
Volume 497— Recent Advances in Catalytic Materials, N.M. Rodriguez, S.L. Soled, J. Hrbek, 1998, ISBN: 1-55899-402-5
Volume 498— Covalently Bonded Disordered Thin-Film Materials, M.P. Siegal, J.E. Jaskie, W. Milne, D. McKenzie, 1998, ISBN: 1-55899-403-3
Volume 499— High-Pressure Materials Research, R.M. Wentzocovitch, R.J. Hemley, W.J. Nellis, P.Y. Yu, 1998, ISBN: 1-55899-404-1
Volume 500— Electrically Based Microstructural Characterization II, R.A. Gerhardt, M.A. Alim, S.R. Taylor, 1998, ISBN: 1-55899-405-X
Volume 501— Surface-Controlled Nanoscale Materials for High-Added-Value Applications, K.E. Gonsalves, M-I. Baraton, J.X. Chen, J.A. Akkara, 1998, ISBN: 1-55899-406-8
Volume 502— *In Situ* Process Diagnostics and Intelligent Materials Processing, P.A. Rosenthal, W.M. Duncan, J.A. Woollam, 1998, ISBN: 1-55899-407-6
Volume 503— Nondestructive Characterization of Materials in Aging Systems, R.L. Crane, S.P. Shah, R. Gilmore, J.D. Achenbach, P.T. Khuri-Yakub, T.E. Matikas, 1998, ISBN: 1-55899-408-4
Volume 504— Atomistic Mechanisms in Beam Synthesis and Irradiation of Materials, J.C. Barbour, S. Roorda, D. Ila, 1998, ISBN: 1-55899-409-2
Volume 505— Thin-Films—Stresses and Mechanical Properties VII, R.C. Cammarata, E.P. Busso, M. Nastasi, W.C. Oliver, 1998, ISBN: 1-55899-410-6
Volume 506— Scientific Basis for Nuclear Waste Management XX, I.G. McKinley, C. McCombie, 1998, ISBN: 1-55899-411-4
Volume 507— Amorphous and Microcrystalline Silicon Technology—1998, S. Wagner, M. Hack, H.M. Branz, R. Schropp, I. Shimizu, 1998, ISBN: 1-55899-413-0

MATERIALS RESEARCH SOCIETY SYMPOSIUM PROCEEDINGS

Volume 508— Flat-Panel Display Materials—1998, G. Parsons, T.S. Fahlen, S. Morozumi, C. Seager, C-C. Tsai, 1998, ISBN: 1-55899-414-9
Volume 509— Materials Issues in Vacuum Microelectronics, W. Zhu, L.S. Pan, T.E. Felter, C. Holland, 1998, ISBN: 1-55899-415-7
Volume 510— Defect and Impurity Engineered Semiconductors and Devices II, S. Ashok, J. Chevallier, K. Sumino, B.L. Sopori, W. Goetz, 1998, ISBN: 1-55899-416-5
Volume 511— Low-Dielectric Constant Materials IV, C. Chiang, J.T. Wetzel, T-M. Lu, P.S. Ho, 1998, ISBN: 1-55899-417-3
Volume 512— Wide-Bandgap Semiconductors for High Power, High Frequency and High Temperature, S. DenBaars, M.S. Shur, J. Palmour, M. Spencer, 1998, ISBN: 1-55899-418-1
Volume 513— Hydrogen in Semiconductors and Metals, N.H. Nickel, W.B. Jackson, R.C. Bowman, 1998, ISBN: 1-55899-419-X
Volume 514— Advanced Interconnects and Contact Materials and Processes for Future Integrated Circuits, S.P. Murarka, D.B. Fraser, M. Eizenberg, R. Tung, R. Madar, 1998, ISBN: 1-55899-420-3
Volume 515— Electronic Packaging Materials Science X, D.J. Belton, R. Pearson, M. Gaynes, E.G. Jacobs, 1998, ISBN: 1-55899-421-1
Volume 516— Materials Reliability in Microelectronics VIII, T. Marieb, J. Bravman, M.A. Korhonen, J.R. Lloyd, 1998, ISBN: 1-55899-422-X
Volume 517— High-Density Magnetic Recording and Integrated Magneto-Optics: Materials and Devices, K. Rubin, J.A. Bain, T. Nolan, D. Bogy, B.J.H. Stadler, M. Levy, J.P. Lorenzo, M. Mansuripur, Y. Okamura, R. Wolfe, 1998, ISBN: 1-55899-423-8
Volume 518— Microelectromechanical Structures for Materials Research, S.B. Brown, C. Muhlstein, P. Krulevitch, G.C. Johnston, R.T. Howe, J.R. Gilbert, 1998, ISBN: 1-55899-424-6
Volume 519— Organic/Inorganic Hybrid Materials, R.M. Laine, C. Sanchez, E. Giannelis, C.J. Brinker, 1998, ISBN: 1-55899-425-4
Volume 520— Nanostructured Powders and Their Industrial Application, G. Beaucage, J.E. Mark, G. Burns, H. Duen-Wu, 1998, ISBN: 1-55899-426-2
Volume 521— Porous and Cellular Materials for Structural Applications, D.S. Schwartz, D.S. Shih, H.N.G. Wadley, A.G. Evans, 1998, ISBN: 1-55899-427-0
Volume 522— Fundamentals of Nanoindentation and Nanotribology, N.R. Moody, W.W. Gerberich, S.P. Baker, N. Burnham, 1998, ISBN: 1-55899-428-9
Volume 523— Electron Microscopy of Semiconducting Materials and ULSI Devices, C. Hayzelden, F.M. Ross, C.J.D. Hetherington, 1998, ISBN: 1-55899-429-7
Volume 524— Application of Synchrotron Radiation Techniques to Materials Science IV, S.M. Mini, D.L. Perry, S.R. Stock, L.J. Terminello, ISBN: 1-55899-430-0
Volume 525— Rapid Thermal and Integrated Processing VII, M.C. Öztürk, F. Roozeboom, P.J. Timans, S.H. Pas, 1998, ISBN: 1-55899-431-9
Volume 526— Advances in Laser Ablation of Materials, R.K. Singh, D.H. Lowndes, D.B. Chrisey, J. Narayan, T. Kawai, E. Fogarassy, 1998, ISBN: 1-55899-432-7
Volume 527— Diffusion Mechanisms in Crystalline Materials, Y. Mishin, N.E.B. Cowern, C.R.A. Catlow, D. Farkas, G. Vogl, 1998, ISBN: 1-55899-433-5
Volume 528— Mechanisms and Principles of Epitaxial Growth in Metallic Systems, L.T. Wille, C.P. Burmester, K. Terakura, G. Comsa, E.D. Williams, 1998, ISBN: 1-55899-434-3
Volume 529— Computational and Mathematical Models of Microstructural Evolution, J.W. Bullard, R. Kalia, M. Stoneham, L-Q. Chen, 1998, ISBN: 1-55899-435-1
Volume 530— Biomaterials Regulating Cell Function and Tissue Development, D. Mooney, A.G. Mikos, K.E. Healy, Y. Ikada, R.C. Thomson, 1998, ISBN: 1-55899-436-X
Volume 531— Reliability of Photonics Materials and Structures, E. Suhir, M. Fukuda, C.R. Kurkjian 1998, ISBN: 1-55899-437-8
Volume 532— Silicon Front-End Technology—Materials Processing and Modelling, N.E.B. Cowern, D. Jacobson, P. Griffin, P. Packan, R. Webb, 1998, ISBN: 1-55899-438-6
Volume 533— Epitaxy and Applications of Si-Based Heterostructures, E.A. Fitzgerald, P.M. Mooney, D.C. Houghton, 1998, ISBN: 1-55899-439-4

Prior Materials Research Society Symposium Proceedings available by contacting Materials Research Society

Symposium L

Materials For High-Density Magnetic Recording

Head Materials for Write Transducers and Readback Sensors

Part I

High Moment Pole Materials

MICROSTRUCTURES AND PROPERTIES OF HIGH SATURATION SOFT MAGNETIC MATERIALS FOR ADVANCED RECORDING HEADS

S. X. WANG [1,2], J. HONG [1], and K. SIN [1]
[1] Dept. of Materials Science and Engineering, Stanford University, CA 94305-2205, sxwang@ee.stanford.edu
[2] Dept. of Electrical Engineering, Stanford University, CA 94305-2205

ABSTRACT

This paper presents recent development on sputtered FeXN-based (X=Ta, Rh, Mo, Al, etc.) high saturation materials [1,2] and compare them with amorphous CoZr-based materials and electroplated NiFe- and CoFe-based materials [3,4] in the context of advanced high density magnetic recording. In particular, correlations among processing, microstructure and magnetic properties under oblique incidence and in laminated structures are discussed. Due to the extrinsic nature of coercivity, the mechanisms of soft magnetism are very complex and difficult to characterize. With the help of synchrotron radiation, pole figure analysis, transmission electron microscopy (TEM), torque magnetometry, and magnetic force microscopy (MFM), we can identify that (110) fiber texture plays a key role in the soft magnetism of FeXN films, in addition to the effects of film composition, stress, grain size and shape, and lattice spacing [5]. Soft films, both single and laminated, usually display well defined bcc (110) textures even on sloping surfaces. In contrast, films with poor (110) textures and asymmetric pole figures tend to have relatively large coercivities, and in certain cases possess perpendicular anisotropy and stripe domains. Processing conditions promoting (110) texture, including substrate bias, lamination with AlN, and appropriate base layer, lead to soft magnetism in FeXN films [6]. The addition of N and a third element, and lamination with insulating layers, result in significant increases in electrical resistivity, important to high frequency applications. The addition of N and X can also lead to enhanced pitting corrosion resistance [7].

REFERENCES

1. K. Sin, C-T. Wang, S. X. Wang, and B. M. Clemens, J. Appl. Phys., **81(8)**, 4507, 1997.
2. J. Hong, K. Sin, L. Nguyentran, and S. X. Wang, IEEE Trans. Magn., **33**, 2845, 1997.
3. N. Robertson, B. Hu, C. Tsang, IEEE Trans. Magn., **33**, 2818, 1997.
4. K. Ohashi, et. al., Paper DQ-09, the 7th Joint MMM-Intermag Conference, San Francisco, 1998.
5. S. X. Wang and J. Hong, to be published.
6. J. Hong, S. X. Wang, and K. Rook, IEEE Trans. Magn., **34**, 1998 (in press).
7. L. Nguyentran, K. Sin, J. Hong, P. Pizzo, and S. X. Wang, IEEE Trans. Magn., **33**, 2848, 1997.

Mat. Res. Soc. Symp. Proc. Vol. 517 © 1998 Materials Research Society

Part II

Anisotropic Magnetoresistance (AMR), Giant Magnetoresistance (GMR), and Exchange Materials

SURFACE EFFECTS IN THE GROWTH OF GIANT MAGNETORESISTANCE SPIN VALVES

W. F. EGELHOFF, JR., P. J. CHEN, C. J. POWELL, D. PARKS, AND R. D. McMICHAEL
National Institute of Standards and Technology
Gaithersburg, MD 20899

J. H. JUDY
University of Minnesota
Minneapolis, MN 55455

D. MARTIEN AND A. E. BERKOWITZ
University of California at San Diego
La Jolla, CA 92093

J. M. DAUGHTON
Nonvolatile Electronics, Inc.
Eden Prairie, MN 55344

EXTENDED ABSTRACT

A class of magnetic multilayers known as spin valves, which exhibit the giant magnetoresistance (GMR) effect, are likely to play two key roles in ultrahigh density data-storage technologies of the coming decade.[1] One is as the read-head element in hard disk drives and the other is as the storage element in a non-volatile version of dynamic random access memory chips. We have investigated the deposition (by dc magnetron sputtering) and processing of a variety of spin valve structures with the aim of optimizing their properties. We have found that many of the magnetic and magnetoresistive properties of spin valves are strongly influenced by surface and interface effects occurring during growth.[2,3] These effects include the balance of surface and interface free energies, surface diffusion, interdiffusion at interface, low temperature deposition, the use of surfactants to modify growth, and specular electron scattering at surfaces. In some cases, it is possible to control these factors or to use them to manipulate the growth or improve post-growth processing of spin valves to improve their magnetic and magnetoresistive properties.

The balance of surface and interface free energies is crucial to the growth morphology of spin valves. Scanning tunneling microscopy of spin valves typically reveals polycrystalline grains ~10 nm in diameter separated by grain boundary valleys or grooves which appear to have a depth of ~0.5 to 1 nm (and perhaps deeper if the STM tip is not sharp enough).[4] Our studies suggest the this type of roughness is primarily responsible for the "orange peel" ferromagnetic coupling commonly observed in spin valves. A large interfacial free energy favors deep grooves. A large surface free energy favors shallow grooves. In principle, drastic changes in either surface or interfacial free energy may be brought about by the presence of surfactant atoms. We have investigated Pb, In, Hg, Au, Ag, C, N, and O as surfactants. All species might be expected to lower the surface free energy as adsorbates and to lower the interfacial energy if incorporated in

Mat. Res. Soc. Symp. Proc. Vol. 517 © 1998 Materials Research Society

the grain boundaries, but it is not clear which effect should dominate. In practice, we have found that some types of surfactant atoms deposited early in spin valve growth tend to float out to the growing surface with little incorporation inside the crystalline grains. However, there is some loss of surfactant atoms to grain boundaries. It appears that this effect dominates the balance of surface and interface energies because major reductions in "orange peel" coupling can be achieved by the use of surfactants, with Ag and O being particularly effective. There are some indications that an additional effect may reduce the coupling when Pb is used as a surfactant. Transmission electron micrographs seem to suggest that Pb suppresses the conformal character of the roughness, an effect which is important for "orange peel" coupling.[5]

Without surfactants it appears that the grain boundary grooves in typical spin valves are not at their equilibrium depth when the films are deposited at room temperature. As a result we observe that increasing the diffusivity of surface atoms during growth, for example by negative substrate bias or by elevated substrate temperature, can produce major increases in the "orange peel" coupling. However, such increases seem to depend on the cleanliness of the growing surface. The presence of surfactant atoms, such as O, tends to suppress such increases.

Since low temperatures tend to suppress surface diffusion, one way to reduce the coupling is to carry out the deposition on cooled substrates.[6] Note that diffusion of atoms away from grain boundary sites is the likely mechanism by which grain boundary grooves develop.

It is very important to note that in most spin valve deposition systems contamination (especially oxygen) is present on the growing surface and probably acts as a surfactant. However, since the impurity concentration on the surface is generally unknown in most deposition systems, it is not clear whether there is too much or too little oxygen present.

Recently, it has become clear that surfactants, especially oxygen atoms, can play two other very important roles in spin valve growth.[2] One is to suppress the interdiffusion that occurs when a magnetic metal is deposited on Cu. The interdiffusion is mediated by the segregation of Cu atoms onto the magnetic metal during deposition as well as by place exchange between deposited magnetic metal atoms and Cu surface atoms.[7] Though once thought controversial,[8] it is now a generally accepted consensus that interdiffusion at the interface is the rule rather than the exception when magnetic metals such as Ni, Co, or Fe are deposited on Cu surfaces.[7] The use of oxygen as a surfactant can dramatically suppress this interdiffusion. Two consequences of the sharper interface are a lower resistivity of the spin valve and a larger GMR. We have found that, for metal deposition rates of ~0.02 nm/s, the best method of spin valves growth is to have $5x10^{-9}$ Torr ($7x10^{-7}$ Pa) of O_2 present in the chamber for the entire deposition.[2]

The other important role that oxygen can play as a surfactant in spin valve growth is to increase the degree of specular electron scattering at the top surface.[2] This effect is especially important in so-called bottom spin valves in which the pinning layer is at the bottom or is the substrate. The contribution of specular scattering to the performance of bottom spin valves has been investigated by roughening the surface and suppressing specular scattering by the deposition of ~2 monolayers (ML) of Ta. The data suggest that the oxygen produces a flatter surface. The mechanism for this effect is very likely to be the same as one commonly found in the epitaxial growth of metal single crystals using surfactants. The surfactant lowers the barrier for descent of an atom on an upper layer terrace to a lower layer terrace, thus yielding a smoother surface.[9] Figure 1 presents a schematic illustration of the mechanism.

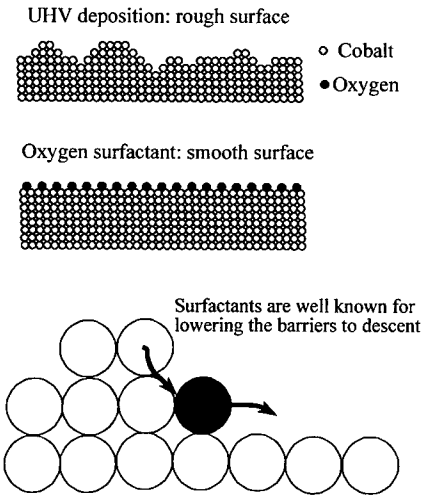

Figure 1 A schematic illustration of how surfactant atoms such as oxygen can lower the activation energy barrier for descent allowing upper terrace atoms to descend to a lower terrace more readily and thus yield a flatter surface.

A further indication that surfactants can yield flatter surfaces is the observation that they permit the use of thinner Cu layers. Using surfactants such as Pb, Ag, or oxygen, measurable values of GMR can be observed for spin valves with Cu layers as thin as 1.1 nm, whereas under very clean conditions it is rare to find any GMR when the Cu is thinner than 1.8 nm. However, so far these unusually thin Cu layers have not yielded any record-setting values of GMR.

A different method for increasing the extent of specular electron scattering at the top surface of bottom spin valves is to deposit ~2 ML Au on the top Co film. The Au increases the GMR typically from ~14% to ~16%. This result would seem to indicate that the Au-terminated surface is flatter than the Co-terminated surface. However, the Au-terminated surface must be far from perfectly specular because no significant reduction in thickness of the top Co film is possible without a loss of GMR in the structure.[3]

Surfactants clearly will have an important role to play in the future of spin valves. Using $5x10^{-9}$ Torr ($7x10^{-7}$ Pa) of O_2 during spin valve growth, we have been able to fabricate spin valves with some of the best properties ever observed. For example, in symmetric (or dual) spin valves, GMR values as large as 24.8% have been achieved, and for simple spin valves (containing only one Cu layer) GMR values as large as 19% have been achieved.[2]

Oxygen is the most successful surfactant we have investigated. The least successful was carbon. The incorporation of even a few atomic percent carbon in a spin valve sharply reduces the GMR. Unfortunately, some carbon contamination is to be expected in most deposition systems.

One of the insights derived from this work is that best hope for someday achieving GMR

values in simple spin valves as large as those found for GMR superlattices (110%)[10] is to increase the degree of specular electron scattering at the top and bottom surfaces and to reduce the bulk defect scattering.

REFERENCES

[1] See, for example, IBM J. Res. Devel. Vol. 42, No. 1, Jan. 1998 (entire issue).
[2] W. F. Egelhoff, Jr., P. J. Chen, C. J. Powell, M. D. Stiles, and R. D. McMichael, J. H. Judy, K. Takano, and A. E. Berkowitz, J. Appl. Phys. 82, 6142 (1997).
[3] W. F. Egelhoff, Jr., P. J. Chen, C. J. Powell, M. D. Stiles, and R. D. McMichael, J. H. Judy, K. Takano , A. E. Berkowitz, and J. M. Daughton, IEEE Trans. Mag., 33, 3580 (1997).
[4] R. D. K. Misra, T. Ha, Y. Kadmon, C. J. Powell, M. D. Stiles, R. D. McMichael, and W. F. Egelhoff, Jr., Mat. Res. Soc. Symp. Proc. 384, 373 (1995).
[5] H. D. Chopra, B. J. Hockey, P. J. Chen, R. D. McMichael, and W. F. Egelhoff, Jr., J. Appl. Phys. 81, 4017 (1997).
[6] W. F. Egelhoff, Jr., T. Ha, R.D.K. Misra, C. J. Powell, M. D. Stiles, R. D. McMichael, C.-L. Lin, J. M. Sivertsen,and J. H. Judy, J. Appl. Phys. 79, 282 (1996).
[7] C. Tölkes, R. Struck, R. David, P. Zeppenfeld, and G. Comsa, Phys. Rev. Lett. 80, 2877 (1998); S. Mróz, H. Otop, and Z. Jankowski, Surf. Rev. Lett. 4, 1273 (1997); S. T.Coyle, G. G. Hembree, and M. R. Scheinfein, J. Vac. Sci. Technol. A15, 1785 (1997); J. Camarero, J. J. de Miguel, T. Graf, R. Miranda, W. Kuch, M. Zharnikov, A. Dittschar, C. M. Schneider, and J. Kirschner, Surf. Sci., in press.
[8] D. A. Steigerwald and W. F. Egelhoff, Jr., Phys. Rev. Lett. 60, 2558 (1988); D. Pescia, M. Stampanoni, G. L. Bona, A. Vaterlaus, F. Feier, G. Jennings, and R. Willis, Phys. Rev. Lett. 60, 2559 (1988).
[9] S. Esch, M. Hohage T. Michely, and G. Comsa, Phys. Rev. Lett. 72, 518 (1994); P. J. Feibelman, Phys. Rev. Lett., in press.
[10] S. S. P. Parkin, to be published.

THERMAL INSTABILITY OF THE Cu-Ni INTERFACE ABOVE 200°C

T.H. WESTMORE[1,2], J.E.E. BAGLIN[1], V.R. DELINE[1], A.J. KELLOCK[1], M.A. PARKER[3], R. BEYERS[1] AND E.L. ALLEN[2].
[1]IBM Almaden Research Center, 650 Harry Road, San Jose, CA 95120;
[2]Department of Materials Engineering, San Jose State University, San Jose, CA 95192;
[3]IBM Storage Systems Division, 5600 Cottle Road, San Jose, CA 95193.

ABSTRACT

Interdiffusion kinetics between Cu and Ni polycrystalline films have been studied in the temperature range 200-300°C, in order to understand degradation paths for spin valve sensors at device processing temperatures. Fast grain boundary diffusion is found to cause extensive change for films of device dimensions.

INTRODUCTION

In the development of GMR sensors, it is important to assure that their constituent assembly of thin (typically few nm) metal layers will be physically stable at device processing temperatures (e.g., photoresist curing at 240°C). Severe degradation of spin valve magnetoresistance $\Delta R/R$ in the range 200-350°C was noted by Huang *et al.*[1], and interpreted as a loss of effective thickness of the magnetic layer ($Ni_{80}Fe_{20}$), by as much as 20%. They attributed this to interdiffusion at the $Ni_{80}Fe_{20}$/Cu interface, and supported the model with x-ray diffraction measurements made on the assembly. Although Ni and Cu can form solid solutions, their lattice diffusivities would be inconsistent with even 1Å of intermixing at 225°C after many hours[2]. In order to develop a more realistic understanding of the origin of thermal degradation, we have made a new study of diffusion dynamics for the Ni-Cu thin film system, in the range from 225°C to 300°C. The low temperature results are presented in this report. In view of the complete immiscibility of Fe and Cu at these temperatures, it is expected that the behavior of $Ni_{80}Fe_{20}$-Cu will be similar to that found for the Ni-Cu system. However, future experiments will be done to test this assumption.

EXPERIMENT

Polycrystalline film samples of Cu(800Å)/Ni(800Å) were sputter deposited on oxidized silicon substrates. X-ray diffraction (θ - 2θ) data showed a typical grain size (normal to the film) of approximately 250Å, with both Ni and Cu showing marked (111) texture. Such relatively thick films were chosen to enable measurement of standard diffusion kinetics data, which could then be scaled appropriately to predict diffusion effects for the case of much thinner spin valve layers.

Samples were heat treated in a flowing helium furnace for a variety of times and temperatures. The elemental depth profiles for Ni and Cu in each sample were then obtained by sputter-profiling Auger Electron Spectrometry (AES) and, for selected samples, image-filtered XTEM was used to obtain images of elemental distributions in the films after heat treatment. In order to separate the Ni AES peak at 848 eV from the interfering Cu AES peak at 845 eV, a new algorithm was developed. A standard Cu integral spectrum between 833 and 853 eV, referenced to the intensity of the primary Cu AES peak at 920 eV, was subtracted from the total integral

Mat. Res. Soc. Symp. Proc. Vol. 517 © 1998 Materials Research Society

spectrum within the same energy range, leaving the residual Ni component for quantitation. Consequently, in the resulting analyses, we estimate the uncertainty due to signal crosstalk to be less than 1 at.%. Typical resulting concentration profiles are shown in Fig.1.

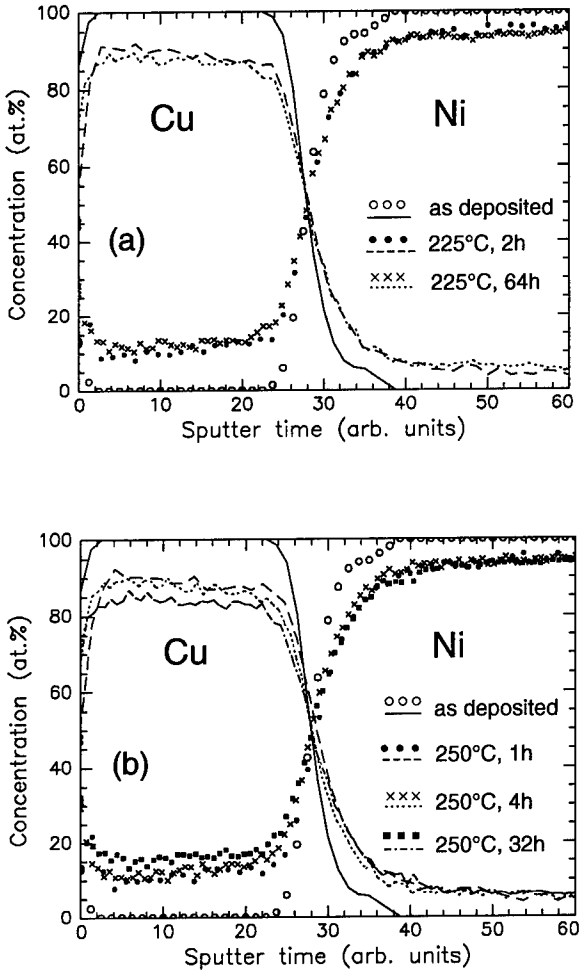

Fig.1 : Concentration profiles for Cu(800Å) / Ni(800Å) / SiO_2 / Si, as-deposited, and (a) after 225°C heat treatment for 2h and 64h, and (b) after 250°C heat treatment for 1h, 4h and 32h.

RESULTS

Fig. 1(a) shows AES profiles for Cu/Ni/substrate samples, before and after 225°C heat treatments. We immediately note the plateaus, indicating that, after only 2 hours at 225°C, Ni has migrated throughout the Cu layer, presumably spreading over the free surface, and has populated the Cu layer to the extent of approx. 12 atomic percent. Similarly, Cu has permeated the Ni layer, to an average concentration of 6 at.%. The interface profiles show slight penetration of Cu into the Ni region, but little movement of Ni into the Cu layer. A saturation state has evidently been reached in less than 2 hours, after which longer heating produced little change, up to 64 h. A similar result for heating at 250°C is shown in Fig. 1(b). In this case, the plateau representing Cu in Ni is established in less than 1 h, and remains unchanged up to 32 h; for Ni in Cu, the plateau is formed in less than 1 h, but its level rises slightly after 32 h.

The development of the surface layer of Ni on Cu is evident in the XTEM image from the 8-h, 225°C sample (Fig. 2), in which Ni regions appear bright. The profile of Ni intensity (inset) along the line shown qualitatively supports the AES depth profile data. No microscopic evidence of pinholes or pores in the films was found.

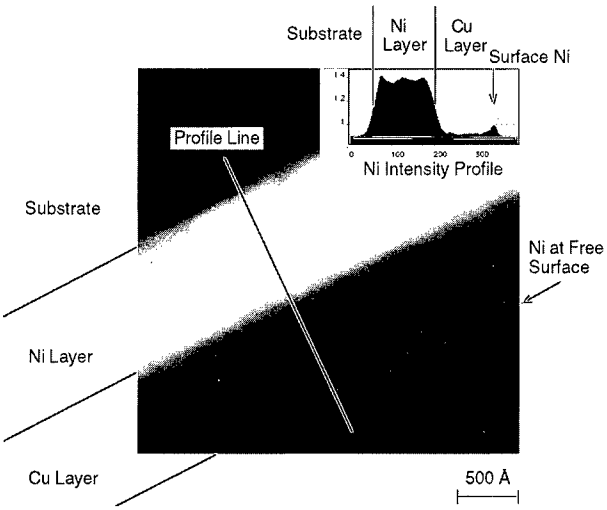

Fig. 2: XTEM image for Cu/Ni (225°C, 8 h), using energy filtering to image Ni (bright) in contrast to Cu. Inset: Profile of Ni intensity across the map, along the line shown; note the surface peak and the resident Ni concentration within the Cu film.

Fig. 3 shows the AES mean concentration of diffusant at the center plane of each host layer, as a function of heating time, at temperatures of 225, 250, 300 and 350°C, for (a) Ni in the Cu layer and (b) Cu in the Ni layer. For each temperature, the data are distinguished by an extremely fast rise to a "saturation" level, which this experiment does not claim to delineate. For Ni moving into Cu, a further, slower diffusion process apparently follows, being significant even at 250°C, and leading to 40% intermixing at 350°C. Although not displayed in this paper, the concentration plateau remained flat even after this large change at 350°C. For Cu moving into Ni, the plateau at ~ 6 at.% appears to prevail between 225 and 300°C, although it takes longer to establish saturation at the lower temperatures. At 350°C, the abrupt change reflects a drastic change in the depth profile shape for Cu in Ni. Further measurements made at 350 and 400°C indicated the onset of a different regime of rapid, inhomogeneous transport of Cu into the Ni layer. This regime will be discussed in a future publication.

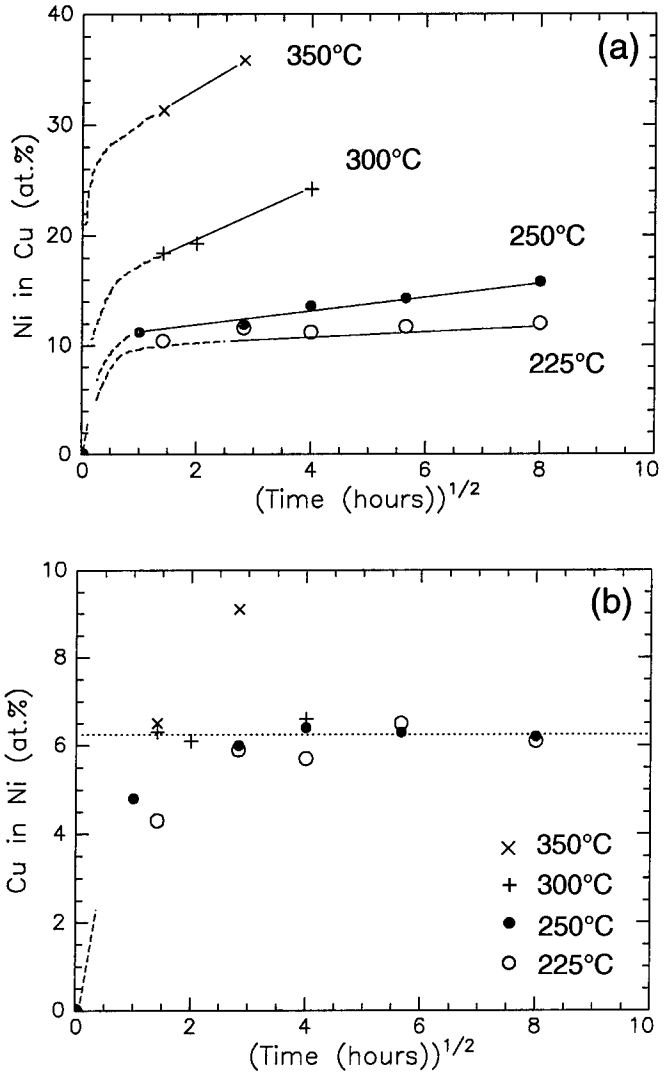

Fig.3 : Mean (plateau) concentrations of diffusant in the center plane of the host film, after heat treatments for various times and temperatures (a) Ni in Cu (b) Cu in Ni. (Lines connecting data points are drawn to guide the eye. Note that the rise from the initial point at the origin must be steep, but was not determined in this experiment.)

DISCUSSION

The data are consistent with a model of grain boundary (gb) diffusion rapidly populating the network of grain boundaries in each host film (including the free surface), and thereafter remaining stable for T<300°C. Since the experiment displays permeation of 800Å of each host layer in less than 2 h at 225°C, the gb diffusivity for each couple must exceed $9x10^{-15}$ cm^2/s (c.f. $\sim 10^{-16}$ cm^2/s of Ref. 3). A geometrical model[4] of uniform 250Å grains, with grain boundaries of effective width 5Å, filled with a diffusant, yields an average diffusant concentration in the film of ~6 at.%. This would be consistent with the observed saturation of Cu in the Ni film. If the Cu grain structure were rather columnar, with in-plane grain dimensions of 150Å (plausible, but not measured), then the Ni resident in the Cu film would amount to ~12%, as observed. Lattice in-diffusion from grain boundaries may be estimated from single-crystal data[2] to amount to much less than 1Å at 225°C after 64 h – a negligible effect. Only new mechanisms, like grain growth and nucleation, occurring apparently at higher temperatures, will cause further changes after gb saturation.

CONSEQUENCES FOR SPIN VALVE STABILITY

Scaling the observed gb filling to the dimension of layers and grains of a spin valve sensor implies dramatic consequences. Fig. 4 shows the layer structure of Ref. 1, where the magnetic NiFe layer (50Å) faces a 20Å Cu layer that also contacts another NiFe layer. If we simplistically assume that diffusion observed for Ni will be similar to that for NiFe, then our results imply that gb saturation is reached in less than 1 minute at 225°C. At that point, all gb's will be populated by diffusant, which may affect the sensor signal ΔR/R. Of perhaps greater concern, assuming that metal grain sizes scale with film thickness, ~3% of the Ni(Fe) sensor layer will have been lost into the gb's of the Cu layer, while over 30% of the Cu layer will have departed to fill gb's in Ni(Fe). This closely corresponds to the "loss of effective thickness" of active layer invoked in Ref. 1 to account for the degradation of device response.

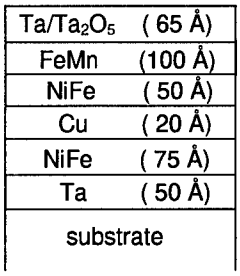

Fig. 4: Schematic of the spin-valve sensor used in Ref. 1.

It is thus perhaps more important than previously recognized to control the structure of the adjacent Cu layer, in order to reduce and limit its capacity as a sink for the depletion of NiFe. Its net gb capacity can be controlled by film thickness and grain size, and also by strong texture, with small-angle grain boundaries.

ACKNOWLEDGEMENTS

The authors wish to thank T.T. Bardin for many helpful discussions in the course of this work.

REFERENCES

1. T.C. Huang, J.-P. Nozieres, V.S. Speriosu, B.A. Gurney and H. Lefakis, Appl. Phys. Lett. **62,** 1478 (1993).
2. C.A. McCliet, Phys. Rev. **109,** 1964 (1958).
3. H. Lefakis, J.F. Cain and P.S. Ho, Thin Solid Films **101,** 207 (1983).
4. T.H. Westmore, M.S. Thesis, Department of Materials Engineering, San Jose State University, San Jose, CA , (1997).

MAGNETIC STABILITY OF SPIN VALVES EXCHANGE BIASED BY A SYNTHETIC ANTIFERROMAGNET

J. L. LEAL, M. H. KRYDER
Data Storage Systems Center, Department of Electrical and Computer Engineering,
Carnegie Mellon University, Pittsburgh, PA 15213

ABSTRACT

Spin valves (SV) with generic configuration glass\ Cr\ Co\ Ru\ Co\ Cu\ Co\ NiFe, where the Co\ Ru\ Co trilayer is a synthetic antiferromagnet (SyAF), were fabricated and characterized. Room temperature measurements show giant-magnetoresistance ratios above 5%, and that fields in excess of 6000 Oe are needed to saturate the SyAF. The in-plane stabilization of the SyAF is determined by the material and thickness of the buffer layer. It is shown that a 25 Å Cr buffer layer induces an increase in the effective in-plane anisotropy of the SyAF by increasing the intrinsic anisotropy of the Co layers, contributing consequently to the overall stability of the SV system. It is also shown that low intrinsic anisotropies or a pronounced layer asymmetry in the SyAF can lead to a strong reduction of the SyAF effective anisotropy (H_{eff}). The saturation field (H_{SAT}) of the SyAF is higher than 3000 Oe at 250 °C, which yields the possibility of observing the spin valve effect at very high temperatures. Long annealings at temperatures as high as 233 °C do not affect the stability of the SyAF nor the magnitude of the indirect exchange interaction.

INTRODUCTION

Spin valves [1] are now widely accepted as being the front runner candidate for the read sensor in the 10 Gbit/in^2 disk drive generation, because of their attractive magnetoresistive (MR) signal and sensitivity at low fields. The standard SV structure consists of two ferromagnetic (FM) transition metal layers separated by a nonmagnetic noble-metal layer, with the magnetization of one of the magnetic layers pinned along the perpendicular to the air bearing surface. A change of resistivity is observed whenever there is a variation in the relative angle between the magnetization of the two FM layers, with the resistivity maximum occurring in the antiparallel configuration and the minimum in the parallel configuration. This change of resistivity is due to the giant magnetoresistive effect [2].

One of the most important aspects to take in consideration when making a SV based sensor is the magnetic configuration of the two FM layers. To obtain a linear output, a 90° configuration is necessary at zero applied field [3]. Until recently, this was obtained by pinning the magnetization of one of the FM layers to an antiferromagnet by means of the direct exchange interaction, and by using crystalline or shape anisotropy to set the preferential magnetization direction of the other FM layer.

The use of the antiferromagnet/ FM pair has, however, some negative consequences. The direct exchange field is highly sensitive to temperature. Although relatively high values can be observed at room temperature, blocking temperatures between 150 and 200 °C may reduce the pinning effectiveness in small size devices working at temperatures between 100 and 150 °C [4]. Another disadvantage of the traditional pinning technique is the strong magnetostatic coupling between the two FM layers in patterned structures near or under 1 μm. This coupling causes the SV device to be biased far from zero applied field and demands the use of high current densities in order to achieve a suitable bias state.

The use of a Co/Ru/Co synthetic antiferromagnet [5, 6] has been recently shown to improve the thermal and magnetic properties of a SV when the traditional exchange layer is replaced by the SyAF. It was shown [6] that this new kind of SV can endure very high temperatures without loss of pinning, and that, when patterned, their particular magnetic configuration promotes an almost vanishing magnetostatic coupling.

In this paper we discuss the magnetic stabilization of the SyAF, a critical aspect for the fabrication of these devices. The stability of the SyAF is studied in terms of its in-plane magnetic anisotropy and its dependence on the buffer layer material and thickness, as well as on the SyAF

Mat. Res. Soc. Symp. Proc. Vol. 517 © 1998 Materials Research Society

layer asymmetry (Co t_{Co1}/ Ru/ Co t_{Co2}, with t_{Co1} not necessarily equal to t_{Co2}). The thermal stability of the system is also discussed.

SAMPLE PREPARATION AND MEASUREMENTS

SV's with a generic configuration substrate\ Cr t_{Cr}\ Co t_{Co1}\ Ru 7 Å\ Co t_{Co2}\ Cu 21 Å\ Co 12 Å\ NiFe 45 Å \ Ru 15 Å, were deposited by dc magnetron sputtering on water cooled glass substrates (≈15 °C). Magnetization and resistivity measurements in the ±100 Oe field range were made using a commercial B-H loop tracer (SHB BHL 108). Magnetization measurements in the ±10 kOe range were performed using a vibrating sample magnetometer (VSM). Transport measurements in the ±600 Oe range were done using a standard dc four-point probe technique ($2x10^4$ A/cm^2 applied current density). The annealings were done in a N_2 environment (500 mTorr pressure).

RESULTS

The magnetization curve, measured at room temperature, for a SV with t_{Cr} = 25 Å and t_{Co1} = t_{Co2} = 30 Å, is shown in Fig. 1(a). A field in excess of 6000 Oe has to be applied in order to saturate the Co/Ru/Co SyAF. The magnitude of the interlayer coupling, which is due to the Ruderman-Kittel-Kasuya-Yosida (RKKY) indirect exchange interaction [7], depends on the thickness of the Ru spacer and reaches an antiferromagnetic maximum for a Ru thickness of 7 Å. The rotation of the Co/NiFe free layer is observed near zero field.

The change in the resistance, for the same sample, is shown in Fig. 1(b), within a ±600 Oe field range. A change over 5% is observed when the configuration between the two magnetic layers adjacent to the Cu spacer changes from parallel to antiparallel. This clearly shows that relatively small external fields, when compared with the magnitude of the SyAF saturation field, do not significantly affect the magnetic configuration of the SyAF. However, a small reduction of the MR signal is observed as the external field approaches +600 Oe.

The magnetization curve for a SV with a reduced buffer thickness (t_{Cr} = 17Å) and t_{Co1} = t_{Co2} = 30 Å, is shown in Fig. 2(a). The curve is almost identical to the one shown in Fig. 1(a), but a small reduction is observed in the field necessary to saturate the SyAF. The change in the resistance, for the same sample, is shown in Fig. 2(b). Unlike what was observed for a thicker buffer (Fig. 1(b)), a field between 200 and 300 Oe is enough to change the angle between the free layer and the pinned layer (t_{Co2}) from the antiparallel to the parallel configuration.

The easy-axis coercivity of the glass\ Cr t_{Cr}\ Co 30 Å\ Ru 15 Å system, measured as a function of the Cr buffer thickness, is shown in Fig. 2(c). A dramatic increase in the coercivity is observed when the Cr thickness changes from 21 to 25 Å. The easy-axis coercivity of the glass\ Cr t_{Cr}\ Co t_{Co}\ Ru 15 Å system, measured as a function of the Co layer thickness, is shown in Fig. 2(d) for samples with no buffer and samples with a 25 Å Cr buffer. A decrease in the coercivity is observed when t_{Co} increases.

The change in the resistance, for a SV with t_{Cr} = 25 Å, t_{Co1} = 40 Å and t_{Co2} = 30 Å, is shown in Fig. 3(a). The small asymmetry between the two Co layers of the SyAF (t_{Co1} > t_{Co2}) seems to affect the system in a positive way since, within the ±600 Oe field range, the magnetic configuration of the SyAF remains unaffected. Contrary to what was shown in Fig. 1(b), the MR

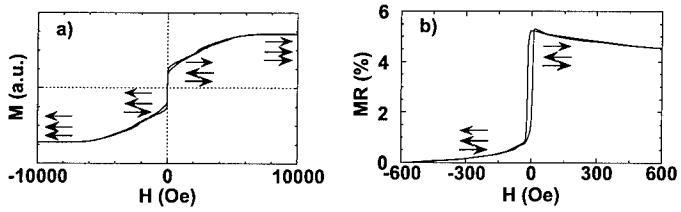

Fig. 1. Room temperature magnetization versus field (a) and MR hysteresis loop (b) for a SV with t_{Cr} = 25Å and t_{Co1} = t_{Co2} = 30 Å.

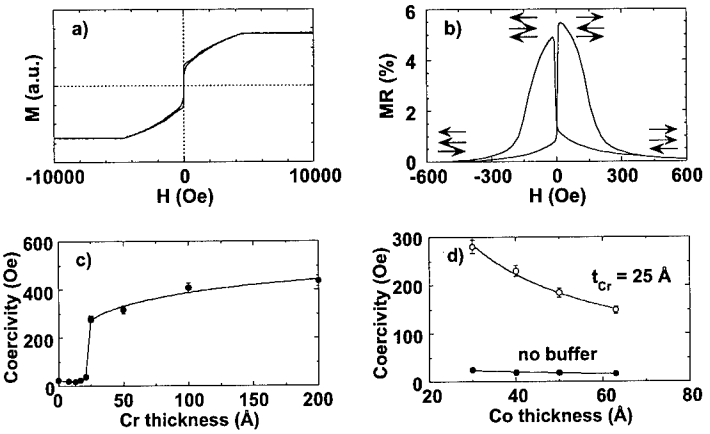

Fig. 2. Room temperature magnetization versus field (a) and MR hysteresis loop (b) for a SV with t_{Cr} = 17Å and t_{Co1} = t_{Co2} = 30 Å. (c) Easy-axis coercivity measured in glass\ Cr t_{Cr}\ Co 30 Å\ Ru 15 Å samples, as a function of the Cr buffer thickness; (d) Easy-axis coercivity, measured as a function of the Co layer thickness, for two different buffer thicknesses.

curve is a perfect step and, besides the rotation of the free layer near the zero external field, the application of fields as high as 600 Oe do not change the angle between the free and the pinned layer (flat plateaus). The magnetization curve, for the same sample, is shown in Fig. 3(b). A small decrease in H_{SAT} is observed.

The change in the resistance, for a SV with t_{Cr} = 25 Å, t_{Co1} = 63 Å and t_{Co2} = 30 Å, is shown in Fig. 3(c). Due to the greater thickness asymmetry, the SyAF behaves like a ferrimagnet. In applied fields greater than 300 Oe, the Co t_{Co1} / Ru/ Co t_{Co2} ferrimagnet rotates in the plane of the sample, so that its net magnetization is aligned with the direction of the applied field (the field necessary to promote this rotation is defined as the SyAF effective anisotropy field, H_{eff}). This results in the antiparallel configuration between the free and the pinned layer (t_{Co2}) and,

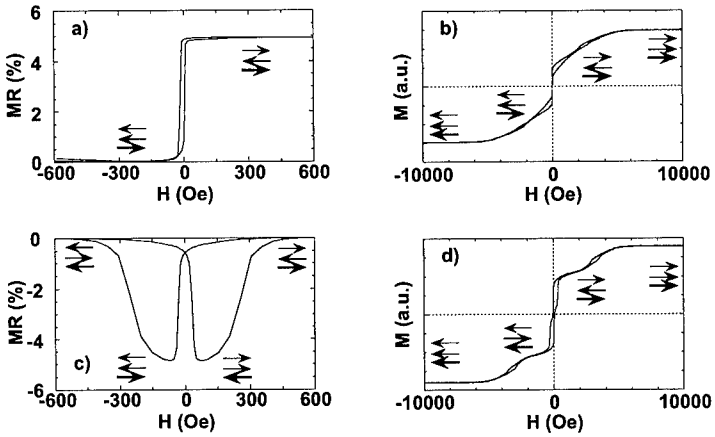

Fig. 3. Room temperature magnetization versus field (a) and MR hysteresis loop (b) for a SV with t_{Cr} = 25Å, t_{Co1} =40 Å and t_{Co2} = 30 Å. Magnetization versus field (c) and MR hysteresis loop (d) for a SV with t_{Cr} = 25Å, t_{Co1} =63 Å and t_{Co2} = 30 Å.

consequently, to a maximum in the magnetoresistance. When the external field inverts its sign, it leads to the rotation of the free layer, and a parallel configuration between the free and the pinned layer is achieved. The magnetization curve, for the same sample, is shown in Fig. 3(d). Values of H_{SAT} over 5000 Oe are observed, confirming that the angle between the two constitutive Co layers of the Co t_{Co1} / Ru/ Co t_{Co2} SyAF remains constant.

The change in the resistance, for a SV with t_{Cr} = 25 Å, t_{Co1} = 30 Å and t_{Co2} = 40 Å, is shown in Fig. 4(a). Due to the thickness asymmetry the SyAF behaves again like a ferrimagnet. Since $t_{Co1} < t_{Co2}$, the resistance reaches a minimum when a field greater than H_{eff} (>500 Oe) is applied. When the external field changes sign, and the free layer rotates in accordance, an antiparallel configuration is obtained and a maximum in the resistance is observed. The magnetization curve, for the same sample, is shown in Fig. 4(b). As before, a high H_{SAT} (≈4000 Oe) confirms that the angle between the two Co layers of the SyAF remains constant for small applied fields.

The change in the resistance, for a SV with t_{Cr} = 25 Å, t_{Co1} = 30 Å and t_{Co2} = 63 Å, is shown in Fig. 4(c). A dramatic decrease of H_{eff} is observed due to the pronounced layer asymmetry. The magnetization curve, for the same sample, is shown in Fig. 4(d). A value of H_{SAT} slightly smaller than 4000 Oe is observed.

The field necessary to saturate a SV with t_{Cr} = 25 Å and $t_{Co1} = t_{Co2}$ = 30 Å, as a function of temperature, is shown in Fig. 5(a). Although a decrease in H_{SAT} is observed as the temperature increases, a field higher than 3000 Oe is still needed to saturate the SV at 250 °C. In the same figure, the maximum change in the resistance (MR_{MAX}) is also shown as a function of temperature. A decrease of (MR_{MAX}), as the temperature increases, is observed. However, even at high temperatures, the pinned layer continues to have its magnetization well pinned in a particular direction. Thus, the SV effect can be observed at temperatures as high as 275 °C, as shown in Fig. 5(b).

The maximum change in the resistance, measured after annealing a SV with t_{Cr} = 25 Å and $t_{Co1} = t_{Co2}$ = 30 Å for 6 hours, is shown in Fig. 5(c), as a function of the annealing temperature. The transport properties of these SV's are not affected for annealings performed under 215 °C. For annealing temperatures above 215 °C, we observe a decrease in the value of $(MR)_{MAX}$. The magnetization curve, measured after annealing the SV at 233 °C, is shown in Fig. 5(d). H_{SAT} has not changed from its preannealing value (6000 Oe). Thus, long high temperature anneals do not degrade the magnetic properties of the SyAF.

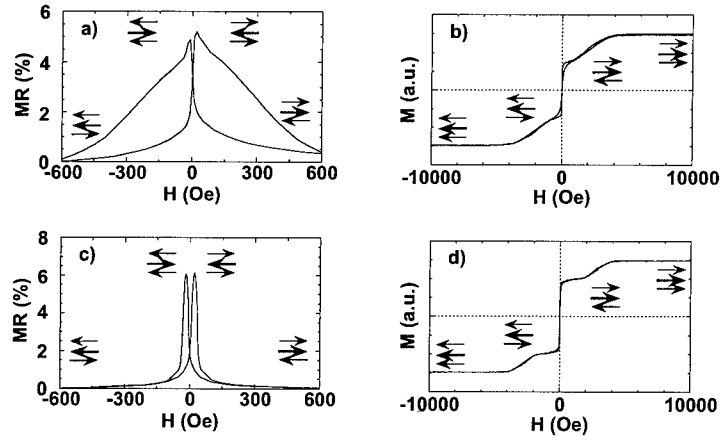

Fig. 4. Room temperature magnetization versus field (a) and MR hysteresis loop (b) for a SV with t_{Cr} = 25Å, t_{Co1} =30 Å and t_{Co2} = 40 Å. Magnetization versus field (c) and MR hysteresis loop (d) for a SV with t_{Cr} = 25Å, t_{Co1} =30 Å and t_{Co2} = 63 Å.

DISCUSSION

The stability of the SyAF biased SV depends on the magnetic and thermal stability of the Co t_{Co1} / Ru/ Co t_{Co2} trilayer. The thickness of the Ru spacer defines the strength of the coupling between the two FM layers of the SyAF, but the RKKY interaction has no intrinsic in-plane preferential orientation. The in-plane stabilization depends on the effective anisotropy of the SyAF. For moderate external magnetic fields (H_{EXT} « H_{SAT}), the antiparallel configuration of the SyAF is not significantly affected. The effective net anisotropy of the SyAF is then given approximately by:

$$H_{eff} = (H_1 t_{Co1} + H_2 t_{Co2}) / (t_{Co1} - t_{Co2}) \quad (1)$$

where H_1 and H_2 are the intrinsic uniaxial anisotropies of the two Co layers. If $t_{Co1} = t_{Co2}$, then H_{eff} is infinite, independently of the magnitude of the intrinsic anisotropies, and the SyAF does not react to small fields. However, if the two layers do not exactly match, then H_{eff} is finite. In particular, for $H_1 = H_2 = 20$ Oe, a 4 Å (≈ 2ML) difference (assume $t_{Co1} = 26$ Å) leads to a decrease of H_{eff} to values between 200 and 300 Oe. The results shown in Fig. 2(b) can then be explained by the presence of a slight layer asymmetry together with a reduced intrinsic coercivity (see Fig. 2(c)). The layer asymmetry problem can be solved by increasing the coercivity of one of the Co layers of the SyAF. If H_1 is increased to values of the order of 300 Oe, then H_{eff} increases to values over 2000 Oe, for the same layer asymmetry. Consequently, within a ± 600 Oe minor loop, the SyAF is not expected to alter significantly its magnetic configuration, as shown in Fig. 1(b).

Although a high intrinsic anisotropy can compensate for slight layer asymmetries, it does not assure a good in-plane stabilization once the layer asymmetry becomes too pronounced. This is observed in Figs. 3(c) and 4, where, due to the large denominator in eq. (1), H_{eff} becomes smaller than 600 Oe. A comparison between Figs. 3 and 4 also suggests that, when the layer asymmetry is reversed (e.g. from $t_{Co1} = 40$ Å and $t_{Co2} = 30$ Å to $t_{Co1} = 30$ Å and $t_{Co2} = 40$ Å) the value of H_{eff} is not kept constant and, moreover, the case $t_{Co1} < t_{Co2}$ leads systematically to a small value of H_{eff}. There are two reasons for this behavior: the first one is the dependence of the intrinsic anisotropies on the Co layer thickness. The second reason is the possible presence of a dead layer, which reduces the effective thickness of the first Co layer ,t_{Co1} . This last effect tends to reduce the effect of the layer asymmetry in the case $t_{Co1} < t_{Co2}$, and to increase it in the case $t_{Co1} > t_{Co2}$.

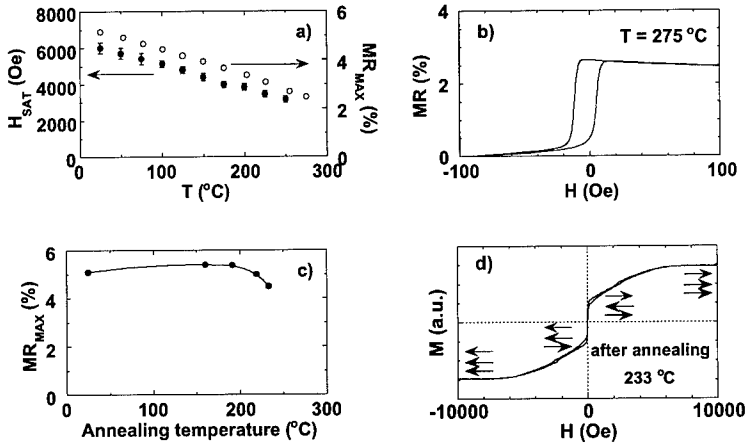

Fig. 5. (a) Field necessary to saturate the SyAF for a SV with $t_{Cr} = 25$Å and $t_{Co1} = t_{Co2} = 30$ Å (solid dots) and maximum change in the magnetoresistance, (open dots), as a function of temperature; (b) MR hysteresis loop measured at 275 °C; (c) Annealing temperature dependence of the MR ratio (annealing time: 6 hours) for SVs with $t_{Cr} = 25$Å and $t_{Co1} = t_{Co2} = 30$ Å; (d) Room temperature magnetization versus field measured after annealing at 233 °C for 6 hours.

Two aspects should be considered when discussing the thermal stability of a SV. The first one is the temperature dependence of the magnetic interaction that is used to pin the magnetization of the pinned layer. The second one is the capability of the SV to thermally resist induced structural degradation. For the case of the SyAF biased SV, the two relevant questions are: (i) what is the temperature dependence of the RKKY interaction responsible for the antiparallel configuration in the SyAF? (ii) Is the SyAF structure affected by long exposures to high temperatures? The data shown in Fig. 5 may be used to answer both questions. The thermal dependence of H_{SAT} (shown in Fig. 5(a)) is very smooth, and values above 3000 Oe can still be observed for temperatures as high as 250 °C. The existence of a very strong pinning mechanism even at high temperatures makes it possible to operate a SV sensor in a very wide temperature range. In Fig. 5(b), the SyAF biased SV is magnetically stable at temperatures as high as 275 °C and maintains its step-like characteristics.

The question of the structural stability can be divided into two parts: one concerns its effect on the transport properties. The data shown in Fig. 5(c) suggests that no relevant effects occur between room temperature and 215 °C. The decay of the MR signal for temperatures above 215 °C is generally attributed to partial alloying of the sense layer and/or to changes in the morphology of the Co/Cu interfaces [8]. The second aspect to be considered is the effect of a long thermal exposure in the SyAF, and consequently its effect on the RKKY indirect exchange interaction. The magnetization curve displayed in Fig. 5(d) clearly shows that a long high temperature anneal (233 °C) does not affect the RKKY coupling strength, which retains its initial magnitude (6000 Oe).

CONCLUSIONS

The magnetic and thermal stability of SyAF biased SV's were studied. It was shown that the effective in-plane anisotropy of the SyAF depends on the thickness of the Cr buffer and on the thickness asymmetry between the two constitutive Co layers. It was shown that a thin Cr layer (25 Å) can induce an effective anisotropy higher than 600 Oe, for SyAF SV's with nominally equal Co layer thicknesses, and that relatively small layer asymmetries ($\leq$ 10 Å) do not significantly affect the stability of the SyAF within a $\pm$ 600 Oe field range.

It was also shown that this kind of SV can sustain temperatures as high as 275 °C without loosing the pinning direction and that exposure to long anneals at temperatures as high as 233 °C do not induce any relevant degradation in the magnitude of the RKKY indirect exchange interaction.

ACKNOWLEDGMENTS

J.L.L. thanks JNICT for a stipend under the Praxis XXI program. This work was supported in part by the National Science Foundation under grant number ECD-8907068.

REFERENCES

1. B. Dieny et al., Phys. Rev. B **43**, 1297 (1991).

2. M. Baibich et al., Phys. Rev. Lett. **61**, 2472 (1988).

3. C. Tsang et al., IEEE Trans. Magn. **30**, 3801 (1994).

4. A. Kos et al., IEEE Trans. Magn. **33**, 3541 (1997).

5. K. Coffey et al., U.S. Patent No. 5 583 725 (10 December 1996).

6. J. Leal, and M. Kryder, J. Appl. Phys. **83**, 3720 (1998).

7. S. Parkin, N. More, and K. Roche, Phys. Rev. Lett. **64**, 2304 (1990).

8. X. Portier et al., Appl. Phys. Lett. **72**, 118 (1998).

EXCHANGE COUPLING PROPERTIES BETWEEN ORDERED ANTIFERROMAGNETIC PdPtMn AND NiFe FILMS

A. Tanaka*, Y. Shimizu*, H. Kishi*, K. Nagasaka*
C. Hou**, H. Fujiwara**
*File memory lab. Fujitsu LTD. Morinosato-Wakamiya, Atsugi, Japan 243-0197
** Center for Materials for Information Technology, University of Alabama, Tuscaloosa, AL 35487-0209

ABSTRACT

The exchange coupling between ordered PdPtMn and NiFe films was studied to understand the pinning mechanism of this system. It was found that the exchange bias field, H_{ua}, appeared when the PdPtMn was thicker than 10 nm and at this thickness the coercivity, H_c, had a peak. The critical thickness for exchange coupling was estimated to be approximately 10 nm which is almost twice than the critical thickness of FeMn in the NiFe/FeMn system. The temperature dependence of the H_{ua} and H_c in PdPtMn(25 nm)/NiFe(5-20 nm) bilayer films was measured between 5 K and 613 K. The exchange bias field was zero above 550 K, and it appeared and increased as the temperature decreased to 420 K. In the same temperature range the H_c showed a broad peak. Both phenomena are in agreement with a thermal fluctuation model[1] and a simple model introduced by Mauri et al.[2]. In the temperature range between 50 K and 420 K the H_{ua} remained constant and H_c increased monotonously. The coercivity was also found to be proportional to $1/t_F^{1.8}$, where t_F is the NiFe film thickness. This and the behavior of H_c and H_{ua} below 420 K can not be explained by the simple exchange coupling between PdPtMn and NiFe. An interfacial lattice distortion may lead to this characteristic behavior of PdPtMn/NiFe system.

INTRODUCTION

The exchange coupling between antiferromagnetic (AF) and ferromagnetic (FM) films has been extensively studied[3-6] partially because of its key importance in MR heads and spin-valve read heads. Disordered FeMn is a well-known AF material and its characteristics have been reported by others[3]. However, FeMn/FM bilayer films exhibit relatively low blocking temperature and FeMn has poor corrosion resistance. Therefore, a ternary AF material, PdPtMn, was developed to replace the FeMn in spin valve structures[7]. The PdPtMn/FM bilayer films show sufficiently large H_{ua}, high blocking temperature (550 K), and superior corrosion resistance for practical use in read heads. On the other hand, its minimum thickness for exchange bias field is greater than 10 nm and the coercivity of the pinned ferromagnetic layer, H_c, is larger than that of FeMn/FM bilayer films. In order to understand and to improve the pinning properties of PdPtMn/FM system we investigated its behavior in the temperature range between 5 K and 613 K.

EXPERIMENT

The $Pd_{29.0}Pt_{17.5}Mn_{53.5}$ and $Ni_{81}Fe_{19}$ bilayer films were prepared using DC magnetron sputtering. The deposition conditions were reported elsewhere[7]. In order to estimate the critical thickness of PdPtMn for producing exchange coupling Ta (10 nm) / NiFe(20

Mat. Res. Soc. Symp. Proc. Vol. 517 © 1998 Materials Research Society

nm) / PdPtMn films with different PdPtMn thicknesses (5-25nm) were prepared on Si substrates. Top type films of Si/Ta(10 nm)/ NiFe (5-20 nm) / PdPtMn(25 nm) and bottom type films of Si / Ta (10 nm) / NiFe (5 nm)/ PdPtMn (25 nm) /NiFe(20 nm) were also deposited for comparison. A buffer layer of Ta/NiFe was introduced for the bottom type films to enhance the (111) crystalline orientation of PdPtMn and to increase the exchange bias field[8]. In the as-deposited PdPtMn films the atoms are randomly distributed in a cubic structure. A high temperature annealing is required to convert the PdPtMn into $L1_0$ type ordered phase in which the atoms are antiferromagnetically aligned. In this study the annealing was carried out at 553 K for 3 hours in a magnetic field of 2.5 kOe. After annealing, the magnetization curves parallel and perpendicular to the pinning direction were measured as a function of temperature using VSM (300 K-613 K) and SQUID magnetometers (5 K-250 K).

RESULTS

Critical Thickness of PdPtMn

The H_{ua} and H_c of Si/Ta/NiFe(20 nm)/PdPtMn(5-50 nm) samples as a function of PdPtMn thickness are shown in Fig. 1. The exchange coupling field, H_{ua}, is zero below PdPtMn thickness of 5 nm, and it increases rapidly as the thickness increases to 10 nm, where the H_c has a peak. This 10 nm thickness may well be regarded as the critical thickness, t_{cr}, of PdPtMn. The exchange coupling constant, J_k, and the magnetic anisotropy constant, K_u, of PdPtMn can be calculated from the following equations[9]:

$$H_{ua} = J_k / M t_F \quad (1)$$

$$K_u = H_{ua} M (t_F / t_{cr}) \quad , \quad (2)$$

where M is the saturation magnetization and t_F is the ferromagnetic film thickness. The obtained exchange coupling constant, J_k, and the anisotropy constant, K_u, of the NiFe/PdPtMn system were 0.167 erg/cm^2 and 2.2x10^5 erg/cm^3, respectively. This value of J_k is 60% and K_u is 250% larger than the corresponding values of the NiFe/FeMn system[9].

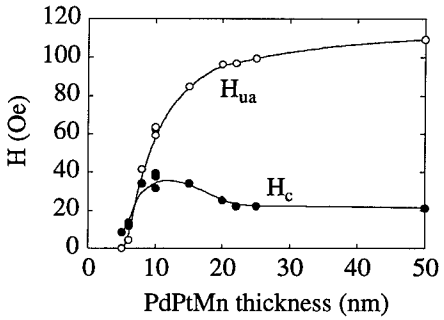

Fig. 1. Hua and Hc as a function of PdPtMn thickness. The sample structure was Si/Ta/NiFe(20 nm)/PdPtMn(X nm), and all samples were annealed at 553 K for 3 hours in magnetic field for crystalline ordering.

Temperature Dependence of H_{ua} and H_c

Figure 2 shows the temperature dependence of H_{ua} and H_c of NiFe/PdPtMn films for various PdPtMn thicknesses. Compared to the disordered NiFe/FeMn system, where H_{ua} increases monotonously with decreasing temperature, and where H_c is almost constant around room temperature, the PdPtMn system shows rather different behavior. The exchange bias field is constant

for all the samples between 300K and 420K and above 420K H_{ua} decreases and eventually disappears around 550K. This is the blocking temperature of NiFe/PdPtMn system. Regardless of the PdPtMn thickness, the behavior of H_c is similar and its value is almost the same for all samples.

The value of H_c decreases slightly above 300 K and has a broad peak around 510K. The thermal fluctuation model proposed by Fulcomer et al. [1] can explain the rapid decrease of H_{ua} and the broad peak of H_c just below the blocking temperature. These two phenomena are also in qualitative agreement with the simple model by Mauri et al.[10]. According to their model, as the normalized exchange coupling, λ, increases from zero, the normalized exchange field increases rapidly and normalized coercivity force gradually decreases. λ is the normalized interface exchange coupling defined as $J_k/2\sqrt{(AK_u)}$, where A is the exchange stiffness of the AF material, and K_u is the anisotropy constant. At the blocking temperature, $\lambda = 0$, that is, $J_k = 0$. At 300K, λ is estimated to be 0.28 from $J_k \sim 0.167$ erg/cm^2 and $K_u \sim 2.2 \times 10^5$ erg/cm^3, assuming A 4×10^{-7} erg/cm.

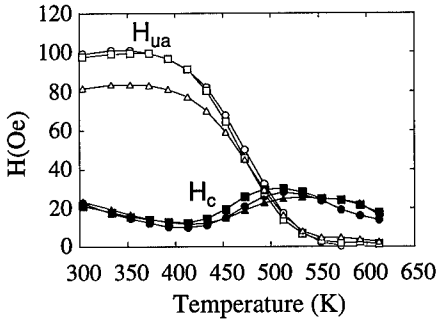

Fig. 2. Temperature dependence of Hua and Hc for Si/Ta/NiFe(20 nm)/PdPtMn(x nm) films. PdPtMn thickness is 15 nm for △,▲, 25 nm for □, ■, 50 nm for ○, ●.

Top and Bottom Type Bilayer Films

We prepared NiFe/PdPtMn (top type) and PdPtMn/NiFe (bottom type) films to investigate the FM/AF and AF/FM interfaces. A buffer structure of Ta (10 nm) /NiFe (5 nm) was introduced for the bottom type samples to enhance the (111) orientation of PdPtMn. The measured H_{ua} and H_c of the top and bottom type

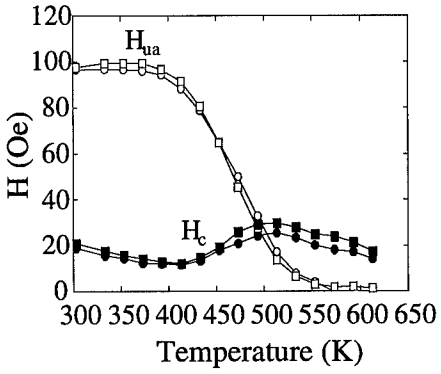

Fig. 3. Temperature dependence of Hua and Hc for top and bottom type samples. The top type is Si/Ta(10 nm)/NiFe(20 nm)/PdPtMn(25 nm) represented by □ and ■. The bottom type is Si/Ta(10 nm)/ NiFe(5 nm) /PdPtMn (25 nm)/ NiFe(20 nm) indicated by ○ and ●.

samples with 20 nm NiFe layers are plotted as a function of temperature in Fig. 3. Both samples show almost the same value of H_{ua} and H_c over the whole temperature range. This means that the exchange coupling constant, J_k, is almost the same for both FM/AF and AF/FM interfaces in spite of the fact that the coupling originates from atomic scale interactions. This is useful for practical applications, because it allows the fabrication of top and bottom-type spin valves with same exchange properties.

The PdPtMn exchange-couples with both the buffer layer and the top layer of NiFe in the bottom type sample. The H_{ua} of the buffer layer is 320 Oe at 300 K which is close to the expected value[2]. Therefore, the 25 nm-thick PdPtMn has independent exchange coupling with the two different NiFe layers. The estimated critical thickness of our system is 10 nm and so the independent exchange is reasonable.

Low Temperature Behavior

Figure 4 shows the temperature dependence of H_{ua} and H_c of the top type sample between 613K and 5K. The dc transverse susceptibility was also measured below 300K, where an external magnetic field ($\pm$20 Oe) was applied perpendicular to the pinned direction. The plotted H_{p0} is defined as M_s (saturation magnetization) divided by the susceptibility (Fig. 4). The H_{ua} was found to decrease slightly as the temperature decreased below 400K and increased again as the temperature further decreased below 50 K. On the other hand, H_{p0} and H_c increased monotonously with decreasing temperature. This behavior is different from NiFe/FeMn[11]. In principle, H_{p0} is the best parameter to evaluate exchange coupling[12]. In our case, the increase of H_{p0} with decreasing temperature is thought to come from the increase of J_k and the product of A and K_u. H_c is showing stronger temperature dependence than H_{p0}, which suggests that J_k increases more rapidly than A and/or K_u with decreasing temperature. H_{ua} and H_c of NiFe may not be simply determined by exchange coupling at very low temperatures.

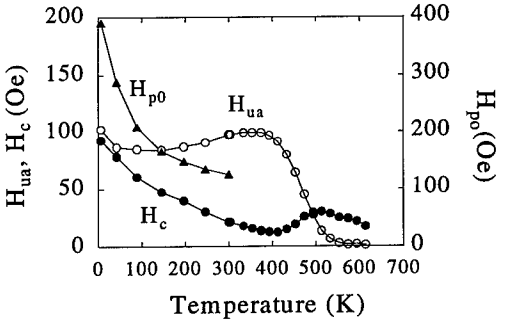

Fig. 4. Temperature dependence of H_{ua}, H_c and H_{p0} between 5K and 613K. The film structure was Si/Ta/NiFe(20 nm)/PdPtMn(25 nm). The H_{p0} was calculated from saturated NiFe moment and susceptibility.

NiFe Thickness Dependence

In order to investigate the behavior of H_{ua} and H_c we prepared top type samples with different (5, 10, and 20 nm) NiFe thicknesses. Figure 5 shows the temperature dependence of H_{ua} and H_c for these films above 300 K.

Here, $H_c \cdot t_F$ and $H_{ua} \cdot t_F$ (t_F : the thickness of the NiFe layer) are plotted. If H_{ua} and H_c are proportional to the exchange coupling strength, they should be inversely proportional to the thickness of FM layer [2]. The 10 nm and 20 nm thick NiFe samples obey this rule, but the 5 nm sample had smaller value of H_{ua} than expected. The H_c of all the three samples deviates far from the expected values. At 300 K, the H_c is proportional to $1/t_F^{1.8}$ (Fig. 6).

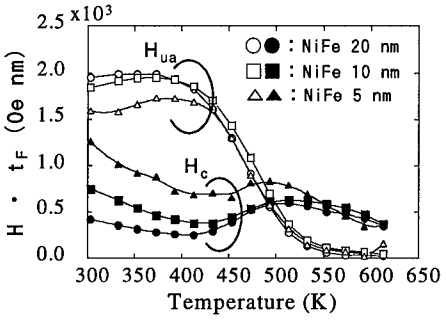

Fig. 5. The temperature dependence of H_{ua} and H_c for top type bilayer films with the structure of NiFe(5, 10 or 20 nm)/ PdPtMn(25 nm).

One of the conceivable origins of this deviation may be an interfacial lattice mismatch. In the ordered AF/FM system, the bilayer films require annealing for crystalline ordering. The AF films convert from cubic to the $L1_0$ type structure during the heat treatment. The d-spacing of the (111) planes was observed to change from 0.227 nm to 0.224 nm. The lattice parameter of the fcc NiFe is 0.204 nm, therefore, a mismatch of 9% is present between the AF and the FM layers. In the NiFe/FeMn system partial epitaxial growth was reported [13]. In our case, the interface of the as-deposited AF and FM layers completely disappears and a new interface is formed during the annealing process [14]. This misfit at the interface can strongly affect H_{ua} and H_c. In lower temperature region the difference of thermal expansions may enhance this tendency.

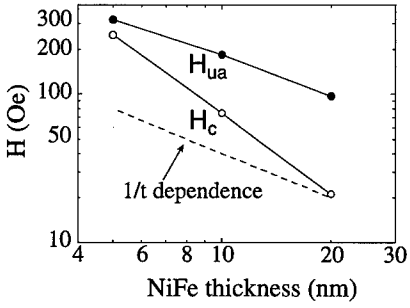

Fig. 6. The Hua and Hc as a function of NiFe thickness (5, 10, 20 nm) at 300 K.

CONCLUSIONS

The critical thickness of ordered antiferromagnetic materials of PdPtMn for exchange coupling is estimated to be 10 nm and the exchange coupling and anisotropy constants were found to be 60% and 250% larger than that of FeMn at 300K. The blocking temperature for the NiFe/PdPtMn system was 550K, and below this temperature the H_{ua} increased rapidly and the H_c had a broad peak. This behavior can be

explained qualitatively by either the thermal fluctuation model of Fulcomer and Charap or the simple exchange coupling model proposed by Mauri et al. The temperature dependence of H_{ua} and H_c can not be explained by simple exchange coupling phenomena in the temperature region below 400 K. As the temperature decreases, the H_c increases monotonously, and the increase of H_c was stronger than that of H_{p0}, whereas the H_{ua} stayed almost constant. At 300K, H_c strongly depended on the NiFe thickness. Interfacial lattice distortion may lead to this characteristic behavior of the PdPtMn/NiFe system.

ACKNOWLEDGMENTS

The authors are greatly indebted to Prof. Metzger who kindly spared precious time and offered the SQUID measurements system for our use. The authors would like to thank Prof. W. D. Doyle for encouragement of this work and valuable discussions. A part of this work was performed under the management of Association of Super-Advanced Electronics Technology (ASET) in the MITI's R&D Program supported by NEDO.

REFERENCES

1. E. Fulcomer and S. H. Charap, J. Appl. Phys. 43, p.4190 (1972).
2. D. Mauri, H.C. Siegmann P. S. Bagus and E. Kay, J. Appl. Phys. 62, p. 3047(1987).
3. C. Tsang, N. Heiman and K. Lee, J. Appl. Phys. 52, p. 2471(1981).
4. A. P. Malozemoff, Phys. Rev. B 35, p. 3679(1987).
5. T. Lin, C. Tsang, R. E. Fontana and J. K. Howard, IEEE Trans. Magn. 31, p. 2585(1995).
6. N. C. Koon, Phys. Rev. Lett. 78, p. 4865 (1997).
7. H. Kishi, Y. Shimizu, Y. Miyake, A. Tanaka and K. Kobayashi, IEEE Trans. Magn. 32, p. 3380 (1996).
8. A. Tanaka, Y. Shimizu, H. Kishi, K. Nagasaka and M. Oshiki, IEEE Trans. Magn. 33, p. 3592 (1997).
9. D. Mauri, E. Kay, D. Scholl and J. K. Howard, J. Appl. Phys. 62, p. 2929 (1987).
10. D. Mauri, H. C. Siegmann, P. S. Bagus and E. Kay, J. Appl. Phys. 62, p. 3047 (1987).
11. H. Fujiwara, K. Nishioka, C. Hou, M. R. Parker, S. Gangopadhyay and R. Metzger, J. Appl. Phys. 79, p. 6286(1996).
12. C. Hou, H. Fujiwara, F. Ueda and H.S. Cho, to be presented at the 1998 MRS Spring Meeting, San Francisco, CA, 1998.
13. C. Hwang, R. H. Geiss and J. K. Howard, J. Appl. Phys. 64, p. 6115(1988).
14. A. Tanaka, Y. Shimizu, H. Kishi, K. Nagasaka and M. Oshiki, to be presented at the 4th International Symposium on Physics of Magnetic Materials, Sendai, Japan, 1998.

Spin valve sensors with $Mn_{1-x}Rh_x$ exchange films

A. Veloso[1,2], P. P. Freitas[1,2], J. Fernandes[3], M. Ferreira[3]
[1]Instituto de Engenharia de Sistemas e Computadores (INESC), R. Alves Redol 9, 1000 Lisboa, Portugal
[2]Instituto Superior Técnico (IST), Physics Dept., Av. Rovisco Pais, 1000 Lisboa, Portugal
[3]Instituto Superior Técnico (IST), Chemical Engineering Dept., Av. Rovisco Pais, 1000 Lisboa, Portugal

Abstract- $Mn_{1-x}Rh_x$ alloys were investigated as exchange layers for spin valve sensors. It was found that deposition pressure affects the final composition of the deposited MnRh film. For x=22 at.%, the exchange coupling constant for a MnRh/CoFe bilayer is 0.20 erg/cm^2. The blocking temperature is 235 °C. The approximately linear temperature dependence of the unidirectional exchange field obtained in as-deposited $Mn_{1-x}Rh_x$ biased spin valves was improved through short post deposition anneals. A comparative study with MnRhIr and MnIr alloys shows that the MnIr/Co interface has a slightly higher blocking temperature (260 °C) and a narrower distribution of local blocking temperatures, but lower exchange constant. Potentiodynamic polarization scans performed in a sodium sulfate electrolyte show that MnRh films exhibit a good corrosion behavior and the highest free corrosion potential of all the materials tested (MnRh, MnNi, MnIr, NiFe, Co and CoFe). Spin valve sensors with MnRh exchange layers were fabricated and show good thermal stability up to 225 °C.

INTRODUCTION

Spin valve sensors are being actively pursued as read heads for very high density recording[1]. For safe and reliable head performance, spin valve heads should have a thermally stable, corrosion resistant, exchange film to keep the magnetization of the pinned ferromagnetic layer fixed in the transverse orientation. The films must maintain their exchange properties after high temperature processing steps (200-250 °C), and survive any thermal excursions occurring during the life of the head. The thermal stability of the head is controlled by the blocking temperature (T_B) at which the unidirectional exchange field (H_{ex}) vanishes, as well as by interdiffusion.

In a previous study [2], we have proposed $Mn_{78}Rh_{22}$ films as a new exchange material since it requires no post deposition anneal to obtain the antiferromagnetic phase and it leads to sensors with good corrosion properties and good exchange coupling characteristics. The as-deposited $Mn_{78}Rh_{22}$ biased spin valve coupon samples were observed to exhibit an approximately linear temperature dependence of the unidirectional exchange field and a blocking temperature of 235 °C. Tsang *et al.* showed that this type of $H_{ex}(T)$ dependence is representative of a broad distribution of local blocking temperatures (T_{Bi}) and that it can be improved by narrowing the T_{Bi} distribution [3].

In this paper, the effect of post deposition anneal and of substrate bias applied during the exchange film deposition on the $H_{ex}(T)$ dependence is investigated. The effect of the deposition pressure on the composition of the MnRh alloy and its effect on the exchange properties is described. A comparative study with MnIr and MnRhIr biased spin valves is also made. The corrosion behavior of MnRh, MnIr, MnNi, NiFe, Co and CoFe thin films is investigated. The thermal stability of spin valve sensors with MnRh exchange layers is discussed.

Mat. Res. Soc. Symp. Proc. Vol. 517 © 1998 Materials Research Society

EXPERIMENT

The following spin valves were prepared in a load-locked magnetron sputtering system (Nordiko 2000) with a base pressure of $5x10^{-8}$ Torr, onto Si <100> substrates:

A) Ta(78 Å)/NiFe(60 Å)/CoFe(5 Å)/Cu(20 Å)/CoFe(23 Å)/$Mn_{78}Rh_{22}$ (170 Å)/Ta(50 Å),
B) Ta(70 Å)/NiFe(40 Å)/CoFe(5 Å)/Cu(20 Å)/CoFe(23 Å)/$Mn_{77}Rh_{19}Ir_4$(150 Å)/Ta(50 Å),
C) Ta(70 Å)/NiFe(40 Å)/CoFe(5 Å)/Cu(23 Å)/CoFe(22 Å)/$Mn_{80}Rh_{20}$ (150 Å)/Ta(50 Å),
D) Ta(70 Å)/NiFe(40 Å)/Co (5 Å)/Cu(25 Å)/Co (22 Å)/$Mn_{80}Rh_{20}$ (199 Å)/Ta(50 Å),
E) Ta(70 Å)/NiFe(40 Å)/Co (5 Å)/Cu(25 Å)/Co (17 Å)/$Mn_{81}Ir_{19}$ (192 Å)/Ta(50 Å).

Here, CoFe and NiFe stand for $Co_{90}Fe_{10}$(at.%) and $Ni_{81}Fe_{19}$(at.%). The free and pinned spin valve layers have parallel easy axis induced by a 20 Oe field applied in the film plane during deposition. The starting MnRh and MnIr targets (20 at.% Rh, 20 at.% Ir) were obtained from MITSUI-Japan. Iridium chips were added to the MnRh target to obtain the MnRhIr films. For corrosion tests, MnNi(50 at.% Ni) exchange bilayers were also prepared. In this case, the samples were subject to a 6 hour anneal at 260 °C in a magnetic field after deposition to induce the antiferromagnetic ordered fct phase. Fig.1 shows the $Mn_{1-x}Rh_x$ film stoichiometry (Rutherford Backscattering analysis) as a function of sputtering Ar pressure. The composition of the sputtered alloy is sensitive to the deposition pressure. The percentage x of Rh in the sputtered $Mn_{1-x}Rh_x$ films was seen to increase from 19.5 to 22 at.% by lowering the pressure from 4.2 to 3.0 mTorr. A RBS analysis of $Mn_{1-x}Ir_x$ films sputtered at 4.5 mTorr from a starting $Mn_{80}Ir_{20}$(at. %) target indicates that x=19 at.%.

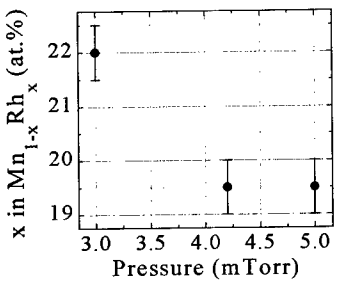

Figure 1. Dependence of x on $Mn_{1-x}Rh_x$ with deposition pressure.

To check the thermal stability of the spin valve sensor, MnRh/CoFe biased spin valve coupon samples were annealed for different periods of time in a high-vacuum furnace (10^{-6} Torr) at a temperature T_A. After anneal, the samples were furnace cooled to room temperature (RT) in 2 hours. A 500 Oe field was applied parallel to the pinned layer easy axis during the annealing and the cooling. H_{ex} vs temperature was measured in the samples in an Ar flow with a vibrating sample magnetometer (VSM).

Unshielded sensors were fabricated with the sensor element defined by soft sputter etch and the Al contact leads patterned by lift off. Consecutive 5 hours anneals were done under the same conditions as described before. During the magnetoresistance (MR) measurements, the easy axis of both the pinned and free layers as well as the direction of the applied field is kept parallel to the sensor and the coupon samples height.

The corrosion resistance of several exchange materials, MnRh, MnIr and $Mn_{50}Ni_{50}$, when coupled with NiFe, Co and CoFe was studied by potentiodynamic polarization experiments carried out in a 0.1 N Na_2SO_4 electrolyte (PH=7), at a scan rate of 500 μV/s, separately for each of the films. All the exchange materials were tested as deposited except MnNi. The coupon samples used for these experiments had the structure glass/Ta(80 Å)/X(100 Å), X=NiFe, MnNi, MnIr, MnRh, and glass/Y (500 Å), Y= Co, CoFe. After deposition, their surfaces were protected by photoresist which was removed shortly before introducing the film in the sodium sulfate solution.

RESULTS

The exchange coupling properties of $Mn_{80}Rh_{20}$ and $Mn_{81}Ir_{19}$ were studied for Ta(80 Å)/NiFe(200 Å)/X(170 Å) (X=$Mn_{80}Rh_{20}$, $Mn_{81}Ir_{19}$) bilayers. The $Mn_{80}Rh_{20}$/NiFe and $Mn_{81}Ir_{19}$/NiFe interfaces show an exchange coupling strength (J_{ex}) of 0.14 erg/cm^2 and 0.12 erg/cm^2, respectively. Here J_{ex} is calculated from $J_{ex}=H_{ex}.M_F.t_F$, where M_F and t_F are the saturation magnetization and the thickness of the pinned ferromagnetic layer.

Magnetic and transport properties for the five types of spin valves previously described are summarized on table I. The value for the exchange coupling strength at the $Mn_{1-x}Rh_x$/CoFe interface is higher for x=22 at.% than for x=20 at.%. The ferromagnetic coupling field (H_f) was also seen to be smaller for the $Mn_{1-x}Rh_x$/CoFe biased spin valves with the higher concentration of Rh. In the phase diagrams of bulk $Mn_{1-x}Y_x$ alloys (Y=Rh, Ir) ordered phases develop near 25 at.% Rh or Ir in Mn [4], which leads us to conclude that the better coupling properties obtained for x=22 at.% may be due to a higher degree of order.

Spin valve type	H_{ex} (Oe)	H_c^f (Oe)	H_c^p (Oe)	H_f (Oe)	MR (%)	T_B (°C)	J_{ex} (erg/cm^2)
A	546	3.5	77	10	7.45	235	0.20
B	490	2	69	16	7.51	225	0.18
C	442	1.5	81	15	7.55	230	0.15
D	436	2.5	55	12.5	6.93	225	0.14
E	349	1	56	14	5.80	260	0.11

Table I. Spin valve properties. H_c^f and H_c^p are the coercivities of the free and the pinned ferromagnetic layers, respectively.

Figure 2 shows the temperature dependence of the unidirectional exchange field for the $Mn_{78}Rh_{22}$/CoFe, $Mn_{80}Rh_{20}$/CoFe, $Mn_{80}Rh_{20}$/Co, $Mn_{77}Rh_{19}Ir_4$/CoFe and $Mn_{81}Ir_{19}$/Co biased spin valve structures, measured in coupon samples. The dashed lines correspond to cycling back the samples to room temperature in the absence of an applied field. For all samples, H_{ex} decreases with increasing temperature, vanishing at a blocking temperature T_B ranging from 225 to 260 °C. The highest T_B is observed for the $Mn_{81}Ir_{19}$/Co spin valve. All the samples exhibit an approximately linear $H_{ex}(T)$ dependence suggesting that, for all the cases under study, the unidirectional exchange field is the average of contributions from exchange components with various blocking temperatures T_{Bi} below T_B [3][5]. The H_{ex} decreases slower with the temperature for the $Mn_{81}Ir_{19}$/Co biased spin valves. This feature suggests a smaller contribution to the T_B distribution from the exchange paths with lower T_{Bi} at the $Mn_{81}Ir_{19}$/Co interface, compared to the T_B distribution for the $Mn_{80}Rh_{20}$, $Mn_{78}Rh_{22}$ and $Mn_{77}Rh_{19}Ir_4$ spin valve samples. This narrower distribution of T_{Bi} is associated with a sharper, less interdiffused interface [3][5].

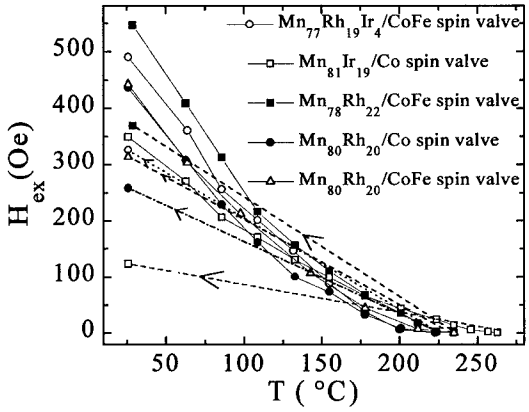

Figure2. $H_{ex}(T)$ dependence of spin valves with $Mn_{78}Rh_{22}$, $Mn_{80}Rh_{20}$, $Mn_{81}Ir_{19}$ and $Mn_{77}Rh_{19}Ir_4$ as exchange layers.

Similarly, the slight difference in the $H_{ex}(T)$ found for the two $Mn_{80}Rh_{20}$/(Co or CoFe) biased spin valve structures can also be attributed to the existence of a sharper, less interdiffused, $Mn_{80}Rh_{20}$/CoFe interface. Notice, however, that $Mn_{81}Ir_{19}$/Co spin valves lose the most of their initial exchange when heated above T_B and cooled to RT without a field, while for $Mn_{78}Rh_{22}$/CoFe biased spin valves most of the initial exchange is still recovered.

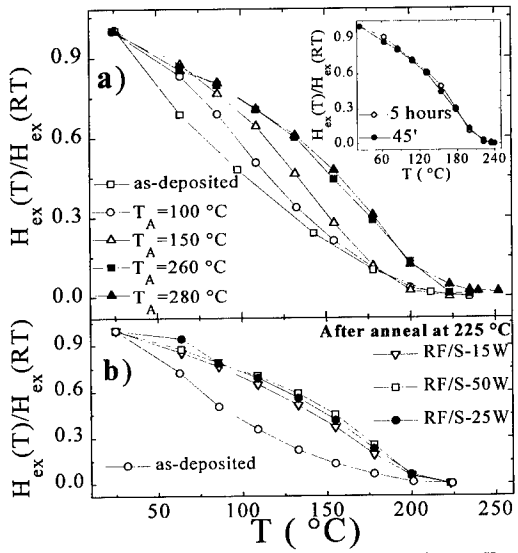

Figure3. a) $H_{ex}(T)$ improvement through anneal. b) H_{ex}-T curves for spin valve coupon samples as-deposited and after anneal at 225 °C. A bias was applied to the substrate during the exchange layer deposition

Fig.3a shows the effect of short time anneals on $H_{ex}(T)$ for $Mn_{80}Rh_{20}$/CoFe spin valve coupon samples (45 minutes, field applied parallel to pinned layer easy axis). No observable difference was seen after doing longer anneals of 5 hours (in the inset). With increasing T_A the local blocking temperatures distribution was narrowed, as observed by the more rounded H_{ex} vs T curve. Although no direct proof is presented here, unmixing and/or anneal out of defects at the $Mn_{80}Rh_{20}$/CoFe interface after cooling back to room temperature appears to be the most plausible explanation for the improvement of the $H_{ex}(T)$ dependence with the anneals. By weakening the interdiffusion processes and hence acquiring a sharper $Mn_{80}Rh_{20}$/CoFe interface, the exchange components with lower ordering temperatures are reduced, resulting in a slower temperature decrease of the unidirectional exchange field.

Thin film interfacial interdiffusion is reported to be usually enhanced by application of a substrate bias during the sputter deposition of the exchange layer [6]. Accordingly, one expects to have more exchange components with lower ordering temperatures. This fact seems to be confirmed by our experimental data since by applying bias to the substrate during the deposition of the antiferromagnetic $Mn_{80}Rh_{20}$ layer we observe a reduction in the value of the unidirectional exchange field with increasing bias voltage as well as a reduction in the value of the T_B (~10 °C). However, after anneal, the $H_{ex}(T)$ dependence is improved in an identical way as for the samples deposited without a bias applied to the substrate (Fig.3b).

The thermal stability for $Mn_{1-x}Rh_x$ /CoFe biased spin valve unshielded sensors and coupon samples is now analyzed. Fig. 4a shows the MR thermal stability for $Mn_{78}Rh_{22}$ biased spin valve sensors after consecutive 5 hours vacuum anneals at a temperature T_A. Sensor trackwidth is 6 μm and sensor hight is 2 μm. The sensors keep an MR signal greater than 90 % of the initial RT value after vacuum anneals up to 225 °C. The exchange field dependence on annealing temperature for coupon samples (fig. 4b) reveals that after cooling from 280 °C to room temperature we still recover an exchange field of 335 Oe (75% of the initial H_{ex} value). Therefore, the MR decrease after anneals above 225 °C can not be attributed to a loss of exchange since the exchange field is high enough for the pinned layer to remain in its transverse

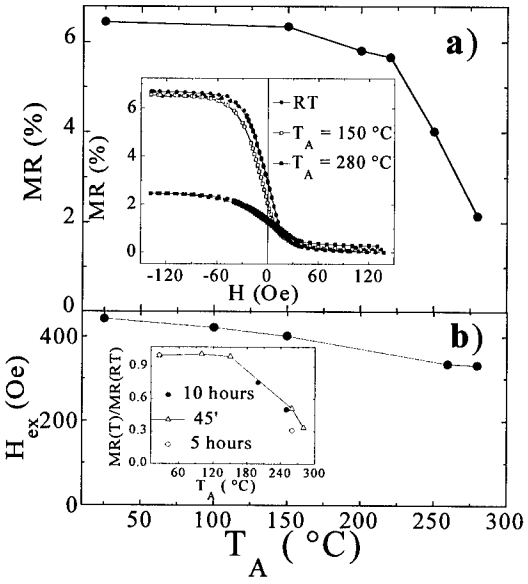

Figure 4.a) MR signal of the $Mn_{78}Rh_{22}$ biased unshielded spin valve sensors as a function of anneal temperature T_A. The inset shows the MR transfer curves after different anneals. b) Exchange field dependence on annealing temperature. The inset displays the relative MR signal measured at room temperature after annealings of 10 hours for $Mn_{78}Rh_{22}$ spin valve coupon samples. For $Mn_{80}Rh_{20}$ spin valve coupon samples the values obtained after anneals of 45 minutes and 5 hours are also shown.

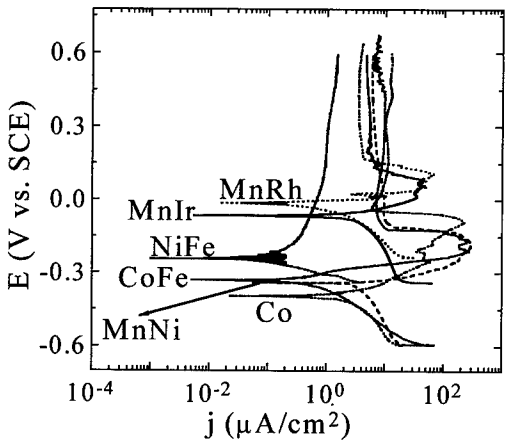

Figure 5. Potentiodynamic polarization plots for MnRh, MnIr, MnNi, NiFe, CoFe and Co done in a 0.1 N Na_2SO_4 solution.

orientation. This can be seen by the linearity of the sensors transfer curves measured at room temperature after cooling from an annealing temperature T_A as high as 280 °C (inset of fig. 4a). The irreversible MR decrease appears to be related to interdiffusion between NiFe and Cu through the 5Å thick CoFe layer which may not constitute a good diffusion barrier [7][8].The inset of fig. 4b displays the relative MR signal for $Mn_{78}Rh_{22}$/CoFe and $Mn_{80}Rh_{20}$/CoFe biased spin valve coupon samples after being vacuum annealed at different temperatures and during different periods of time. For $Mn_{80}Rh_{20}$ spin valves, a significant difference was observed in the MR value after 45' and 5 hours anneal at 260 °C, which appears to be related to an increase, with time, of the interdiffusion processes that occur at the NiFe/CoFe/Cu interfaces. It was also observed that $Mn_{1-x}Rh_x$/CoFe biased spin valves exhibit a better MR(T_A) dependence for x=22 at.%.

Fig. 5 shows the potentiodynamic polarization plots obtained for MnRh, MnIr, MnNi, NiFe, Co and CoFe in a 0.1 N Na_2SO_4 solution. In the spin valve structure, the exchange films are associated with other materials forming galvanic couples. Since MnRh exhibits the highest free corrosion potential when compared to the other materials present in the spin valve, it is expected a sacrificial effect of the other materials in favor

of a cathodic protection of the MnRh. At the same time, from the three exchange materials tested, MnRh is the one with the highest free corrosion potential. This places this alloy in a better position when compared to the other exchange alloys as far as corrosion is concerned.

CONCLUSIONS

The composition of the exchange material, $Mn_{1-x}Rh_x$, obtained from a starting $Mn_{80}Rh_{20}$ (at.%) target is sensitive to the deposition pressure: the concentration x of Rh in the sputtered films increases by lowering the pressure. $Mn_{1-x}Rh_x$ biased spin valves exhibit a thermal stability and an exchange coupling strength better for x=22 at.% than for 20 at.%, which could be due to a better ordered structure for x=22 at.%. The $H_{ex}(T)$ dependence can be improved through a short annealing under a field applied along the spin valve easy axis. $Mn_{81}Ir_{19}$ spin valves were seen to have a narrower T_B distribution related to a sharper $Mn_{81}Ir_{19}$/Co interface, but a smaller J_{ex}, when compared to the $Mn_{1-x}Rh_x$/Co, $Mn_{1-x}Rh_x$/CoFe (x=20-22 at.%) or $Mn_{77}Rh_{19}Ir_4$/CoFe interfaces. $Mn_{1-x}Rh_x$ (x=20-22 at.%) exhibits the highest free corrosion potential among $Mn_{81}Ir_{19}$, $Mn_{50}Ni_{50}$, NiFe, Co and CoFe films which places this alloy in a better position as far as corrosion is concerned when coupled with a ferromagnetic material in a spin valve structure.

ACKNOWLEDGEMENTS

This work was partially supported by a PRAXIS project (PRAXIS/3/3.1/TIT/11/94) and the author A. Veloso was supported by the PRAXIS grant PRAXIS XXI/BD/9420/96.

We acknowledge E. Alves, M. F. da Silva and J. C. Soares at Instituto Tecnológico Nuclear, Lisboa, Portugal for the Rutherford Backscattering analysis of the $Mn_{1-x}Rh_x$ and $Mn_{81}Ir_{19}$ alloys and the Marabun Corporation Japan for supplying the $Mn_{80}Rh_{20}$ and $Mn_{80}Ir_{20}$ targets.

REFERENCES

[1] D. E. Heim, R. E. Fontana Jr., C. Tsang, V. S. Speriosu, B. A. Gurney, and M. L. Williams, IEEE Trans. Magn. **30**, 316 (1994).

[2] A. Veloso, P. P. Freitas, N. J. Oliveira, J. Fernandes, and M. Ferreira (accepted for publication on IEEE Trans. Magn.).

[3] C. Tsang and K. Lee, J. Appl. Phys. **53**(3), 2605 (1982).

[4] M. Hansen and K. Anderko, Constitution of Binary Alloys (McGraw-Hill, New York, 1958).

[5] S. Soeya, T Imagawa, K. Mitsuoka, and S. Narishige, J. Appl. Phys. **76**(9), 5356 (1994).

[6] A. H. Eltoukhy and J. E. Greene, J. Appl. Phys. **51**(8), 4444 (1980).

[7] T. C. Huang, J. P. Nozieres, V. S. Speriosu, B. A. Gurney, and H. Lefakis, Appl. Phys. Lett. **62**(13), 1478 (1993).

[8] V. S. Speriosu, J. P. Nozieres, B. A. Gurney, B. Dieny, T. C. Huang, and H. Lefakis, Phys.Rev. B **47**(17), 11579 (1993).

MAGNETIZATION PROCESS OF F/AF SYSTEMS

C. Hou, H. Fujiwara, F. Ueda*, H. S. Cho
MINT Center and Department of Physics, University of Alabama, Tuscaloosa, Alabama
* Data Storage and Retrieval System Div., Hitachi. Ltd. Kozu, Odawara, Japan.

ABSTRACT

We have studied the relationship between the hysteresis loop shift H_p, the coercivity H_c and the effective pinning field H_{p0} in the F/AF (Ferromagnet/Antiferromagnet) system. H_{p0} is an effective field exerted on the magnetization of the F layer through the exchange coupling with the AF layer after saturation in the original pinned direction. It is found in NiFe/FeMn systems that $H_p + H_c \cong H_{p0}$ no matter how H_p and H_c behave individually. H_{p0} may well be called *intrinsic pinning field.* Here, we show that, assuming the rotation mechanism for the magnetization process in both F and AF layers, it is generally verified that the switching field at which the magnetization of the F layer starts to rotate $|H_{sw}| = H_{p0}$ by means of multiple variable energy minimization for arbitrary mirror symmetric anisotropy distribution both in direction and in strength in the AF layer, and for arbitrary F-AF coupling strength. Thus, for samples with M-H curve of large squarness, we should have $H_p + H_c \cong H_{p0}$. This implies that the rotation magnetization process dominates in the samples following this $H_{p0} \cong H_p + H_c$ relationship, contrary to the fact that domain wall motion dominates in single F layers.

INTRODUCTION

Recently, extensive studies on ferromagnetic-antiferromagnetic (F-AF) exchange coupling have been carried out [1-6] because of its high potential for the applications in both MR and GMR heads. Much attention has been paid to the loop shift H_p in the pinning direction which is also called exchange bias field H_{eb}, fewer studies have been carried out about the coercivity H_c, and very few studies on the H_{p0} which we call *intrinsic pinning field.* H_{p0} is the effective pinning field in the pinned direction which is defined as the field at which the extrapolation of the initial transverse magnetization curve crosses the saturation magnetization M_s, that is, $H_{p0} = M_s/\chi_\perp$, where $\chi_\perp$ is the initial susceptibility in the direction transverse to the pinning direction. Very recently, Qian et al[6] pointed out $H_p + H_c \cong H_{p0}$ for the NiFe/NiO system and proposed a model in which the existence of a uniaxial interfacial anisotropy was assumed. We found a similar phenomenon independently. We studied the hysteresis loop shift H_p and the coercivity H_c in a NiFe/FeMn(F/AF) system as a function of both AF layer thickness and the coupling strength which is controlled by inserting thin Cu spacer or by changing the degree of contamination of the interface between F and AF layers. The degree of contamination was controlled by varying the waiting time between the depositions of the F and AF layers. We also measured the *intrinsic pinning field* H_{p0}. Our results show that $H_p + H_c \cong H_{p0}$ no matter how H_p and H_c behave individually with the thickness of the AF layer or the coupling strength between the F and AF layer, provided that the hysteresis is small in the transverse direction. We investigated this problem assuming various models for the AF layer: i) single crystal with a single domain with a uniaxial anisotropy; ii) a single crystal with a uniaxial anisotropy forming a planar wall; iii) poly-crystalline with arbitrary anisotropies whose easy axes are randomly distributed with mirror symmetry with respect to the easy axis of the F layer. The F layer was assumed to be of a single domain with rotational magnetization process in all cases. For the calculation, multiple variable energy minimization method was employed. The interfacial uniaxial anisotropy assumed by Qian et al[6] is thought to result from the switching of some interfacial spins of the AF layer accompanying the switching of the magnetization of the F layer.

Mat. Res. Soc. Symp. Proc. Vol. 517 © 1998 Materials Research Society

EXPERIMENT

Samples of glass/Ta(10nm)/NiFe(8nm)/FeMn(t_{FeMn}nm)/Ta(5nm) and Glass/Ta(10nm)/NiFe(8 nm)/Cu(t_{Cu})/FeMn(8nm)/Ta(5nm) and Glass/Ta(10nm)/NiFe(8nm)/impurity/FeMn(8nm)/Ta(5nm) were prepared by sputter deposition in Argon pressure of 5 mTorr with a base pressure of about .3 μTorr. The applied field during the depositions of the films was about 80 Oe. The as-deposited films were measured in the pinning direction to determine their loop shift H_p, and coercivity H_c. Just following the measurement in the pinning direction, the initial susceptibility $\chi_\perp$ in the transverse direction as well as the saturation moment M_s was measured to determine the intrinsic pinning field H_{p0} which is $M_s/\chi_\perp$. All the measurements were carried out with a vibrating sample magnetometer(VSM). A typical hysteresis loop in the pinning direction is shown in Fig. 1. H_p is the shift of the loop from the origin, H_c is the half width of the loop. A typical hysteresis loop in the transverse direction is shown in Fig. 2. We also prepared some samples of Co/NiO system to see if the above relationship would hold or not.

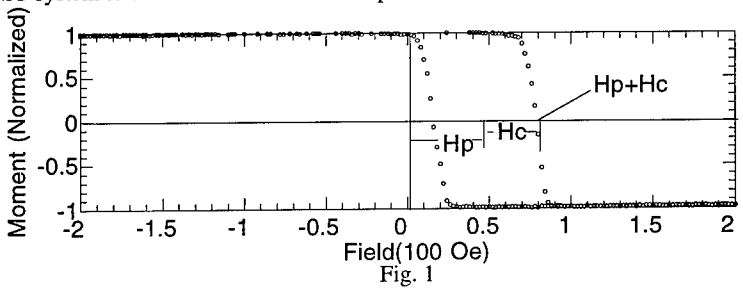

Fig. 1

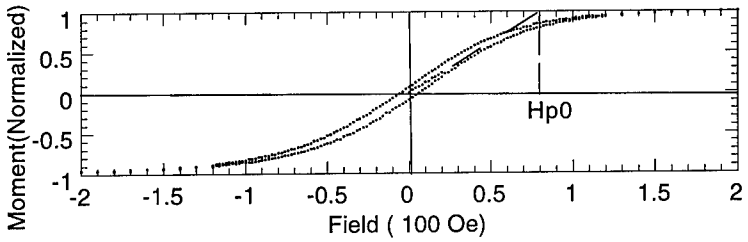

Fig. 2

RESULTS

Fig. 3, Fig. 4 and Fig. 5 show the H_p, H_c as a function of H_{p0} for the samples of Glass/Ta(10nm)/NiFe(8nm)/FeMn(t_{FMn}nm)/ Ta(5nm), and Glass/Ta(10nm)/NiFe(8nm) /Cu(t_{Cu})FeMn(8nm)/Ta(5nm) and Glass/Ta (10nm)/NiFe(8nm)/impurity/FeMn(8nm)/Ta(5n m), respectively. All the data show that no matter how H_p and H_c vary independently, their summation H_p+ H_c comes close to the diagonal, showing the relationship $H_p + H_c \cong H_{p0}$ as seen in the graphs.

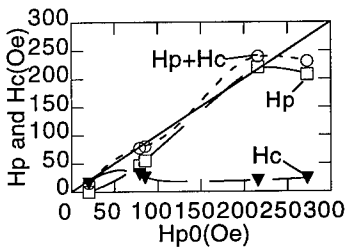

Fig. 3

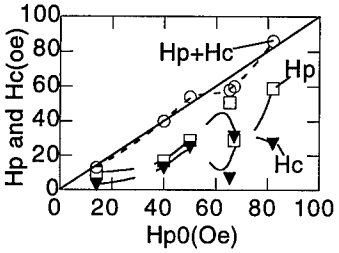

Fig. 4

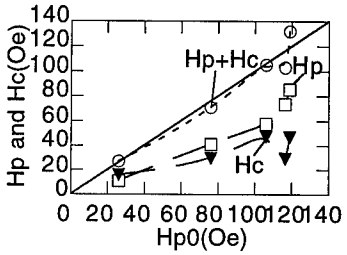

Fig. 5

MODELING AND CALCULATION

Model I. Single Domain Model for Both F and AF Layers

First, we assume that both F and AF layers behave as single domain particles, and that both layers have uniaxial anisotropies with their easy axes parallel to each other.

When a field is applied to measure the hysteresis loop as shown in Fig. 6, the energy can be expressed as:

$$E = K_F V_F \sin^2\theta - HM_s V\cos(\varphi-\theta) + K_{AF}V_{AF}\sin^2\beta - JA\cos(\theta-\beta), \quad (1)$$

where H is the applied field, M_s the saturation magnetization of the F layer, K_F and K_{AF} the uniaxial anisotropy constant of the F and AF layers, V_F and V_{AF} their volume, J exchange coupling constant and A the area of the sample. The angles θ and β are the angles of the moments of the F layer and the surface spin of the AF layers making with the easy axis, and φ is the angle of the applied field to the pinning direction as shown in Fig. 6.

When $\varphi = 0$, which means that the applied field is in the pinning direction, the first and second derivatives of the energy with respect to the angles θ and β are:

$$\frac{\partial E}{\partial\theta} = K_F V_F \sin 2\theta + HM_s V_F \sin\theta + JA\sin(\theta-\beta) = 0, \quad (2)$$

$$\frac{\partial E}{\partial\beta} = K_{AF}V_{AF}\sin 2\beta - JA\sin(\theta-\beta) = 0, \quad (3)$$

$$\frac{\partial^2 E}{\partial^2\theta} = 2K_F V_F\cos 2\theta + HM_s V_F\cos\theta + JA\cos(\theta-\beta), \quad (4)$$

$$\frac{\partial^2 E}{\partial^2\beta} = 2K_{AF}V_{AF}\cos 2\beta + JA\cos(\theta-\beta), \quad (5)$$

$$\frac{\partial^2 E}{\partial\theta\partial\beta} = -JA\cos(\theta-\beta). \quad (6)$$

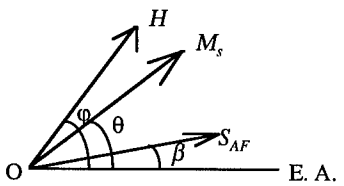

Fig. 6

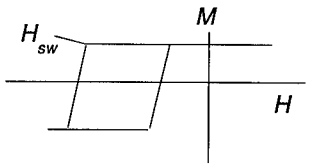

Fig. 7

The switching field H_{sw} is defined as the field when the magnetization starts to rotate as shown in Fig. 7.

The stable conditions are:

$$\left(\frac{\partial^2 E}{\partial\theta^2}\right) > 0 \quad , \quad \left(\frac{\partial^2 E}{\partial\beta^2}\right) > 0 \quad \text{and}$$

$$\left(\frac{\partial^2 E}{\partial\theta^2}\right)\left(\frac{\partial^2 E}{\partial\beta^2}\right) - \left(\frac{\partial^2 E}{\partial\theta\partial\beta}\right)^2 > 0. \quad (7)$$

For $\theta = 0, \beta = 0$, we get:

$$H > H_{sw} = -\frac{2K_F}{M_s}\left[1 + \frac{1}{2K_F t_F}\left(\frac{1}{2K_{AF}t_{AF}} + \frac{1}{J}\right)^{-1}\right], \quad (8)$$

or $H_{sw} = -H_k - \frac{J}{M_s t_F}\left(\frac{1}{1+r}\right)$. (9)

where $H_k = 2K_F/M_s$, $r = J/2K_{AF}t_{AF}$ with t_F and t_{AF} denoting the thickness of the F and AF layers, respectively.

For, $\theta = \pi$, $\beta = 0$ stable if $r<1$ and $H < H_k - \frac{J}{M_s t_F}\left(\frac{1}{1-r}\right)$. For $r>1$, with the switching of the magnetization, the AF spins also switch, making $\theta = \pi$ and $\beta = \pi$ for which the stable condition is $H < H_k + \frac{J}{M_s t_F}\left(\frac{1}{1+r}\right)$ which will results in the coercivity enhancement as will be discussed later.

When $\varphi = \pi/2$, which means that the applied field is in the transverse direction, the first derivatives with respect to the angles θ and β should be zero:

$$\frac{\partial E}{\partial \theta} = K_F V_F \sin 2\theta - HM_s V_F \cos\theta + JA\sin(\theta-\beta) = 0, \quad (10)$$

$$\frac{\partial E}{\partial \beta} = K_{AF} V_{AF} \sin 2\beta - JA\sin(\theta-\beta) = 0. \quad (11)$$

For infinitesimal changes of H, θ and β:

$$2K_F V_F \cos 2\theta\delta\theta + HM_s V_F \sin\theta\delta\theta - HM_s V_F \cos\theta\delta H + JA\cos(\theta-\beta)(\delta\theta-\delta\beta) = 0, \quad (12)$$

$$2K_{AF} V_{AF} \cos 2\beta\delta\beta - JA\cos(\theta-\beta)(\delta\theta-\delta\beta) = 0. \quad (13)$$

From the above two equations, we obtain:

$$\delta H = \frac{1}{M_s V_F \cos\theta}\left(2K_F V_F + HM_s V_F \sin\theta + \frac{JA\cos(\theta-\beta)\cdot 2K_{AF}V_{AF}\cos 2\beta}{JA\cos(\theta-\beta) + 2K_{AF}V_{AF}\cos 2\beta}\right)\delta\theta \ . \quad (14)$$

By definition:

$$H_{p0} = \left(\frac{\delta H}{\delta\theta}\right) \text{ at } \theta = 0,\ \beta = 0.$$

Thus $H_{p0} = \frac{2K_F}{M_s}\left[1 + \frac{1}{2K_F t_F}\left(\frac{1}{2K_{AF}t_{AF}} + \frac{1}{J}\right)^{-1}\right]$, or $H_{p0} = H_k + \frac{J}{M_s t_F}\left(\frac{1}{1+r}\right)$. (15)

It is seen that H_{p0} shown in equation (15) has the same formula as the H_{sw} shown in equation (9).

Model II. AF Layer with planar wall

In this case, spins at the top surface of the AF layer are assumed frozen, while spin fanning exists inside the AF layer when the spins at the bottom surface of the AF layer rotate along with the rotation of the magnetization of the F layer under an applied field as shown in Fig. 8.

Following Mauri [2], when the applied field H is in the direction with an angle φ to the pinning direction, the energy per unit area of this F-AF coupled system is:

$$E = 2\sqrt{A_{AF}K_{AF}}(1-\cos\alpha) + J[1-\cos(\theta-\alpha)] + K_F t_F \sin^2\theta + HMt_F[1-\cos(\varphi-\theta)]. \quad (16)$$

where A_{AF} and α are the exchange stiffness and the bottom surface spin angle of the AF layer.

Following all the same procedures described above, H_{p0} and the switching field H_{sw} can be found for $\varphi = \pi/2$ and $\varphi = \pi$ as:

$$H_{p0} = -H_{sw} = \frac{2K_F}{M_s}\left[1 + \frac{1}{2K_F t_F}\left(\frac{1}{2\sqrt{A_{AF}K_{AF}}} + \frac{1}{J}\right)^{-1}\right], \quad (17)$$

or $H_{p0} = -H_{sw} = H_k + \frac{J}{M_s t_F}\left(\frac{1}{1+r'}\right)$. (18)

where $H_k = 2K_F/M_s$, $r' = J/2\sqrt{A_{AF}K_{AF}}$.

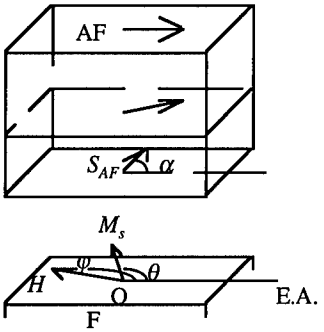

Fig. 8

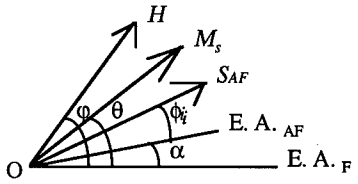

Fig. 9

Model III. Mirror Symmetric Random Distribution of Anisotropy in AF Layer

In the above two special cases, the easy axis of the AF layer is assumed to be parallel to the easy axis of the F layer. For a general case, the AF layer is thought to be composed of particles with their easy axes randomly distributed. Here, we impose a mirror symmetricity with respect to the easy axis of the F layer which is still fairly general. The anisotropy energy of each AF particle is assumed to be a general function of the angle its bottom spin makes with its easy axis.

When the applied field H is in the direction with an angle φ to the pinning direction as shown in Fig. 9, the total energy of the system is:

$$E = K_F V_F \sin^2\theta - HM_s V_F \cos(\varphi - \theta) - \sum_i J_i A_i \cos(\theta - \alpha_i - \phi_i) + \sum_i K_{AFi} V_{AFi} f(\phi_i), \quad (19)$$

where K_{AFi} and V_{AFi} are the anisotropy constants of the i th AF particles.

Making use of the multiple variable minimization technique, the stable condition for $\varphi = 0$ can be proven to be:

$$\frac{\partial^2 E}{\partial\theta^2} > \sum_i \frac{\left(\partial^2 E/\partial\theta\partial\phi_i\right)^2}{\partial^2 E/\partial{\phi_i}^2} \quad \text{and} \quad \frac{\partial^2 E}{\partial{\phi^2}_i} > 0. \qquad (20)$$

Making use of the above conditions and following the same procedures described earlier, we can find

$$H_{p0} = -H_{sw} = \frac{2K_F}{M_s}\left[1 + \frac{1}{2K_F V_F}\sum_i \left(\frac{1}{K_{AFi}V_{AFi}f''(\phi_i)} + \frac{1}{J_i A_i \cos(\alpha_i - \phi_i)}\right)^{-1}\right], \qquad (21)$$

where $f''(\phi_i)$ denotes the second derivative of $f(\phi_i)$ to ϕ_i. The angle ϕ_i is determined by the conditions that all the first derivatives with respect to all the angles θ and ϕ_i are zero.

DISCUSSION

As is shown above, if we assume that the magnetization of the F layer switches by coherent rotation, any F/AF coupled system should hold the relationship $|H_{sw}| = H_{p0}$. Therefore, the observed relationship implies that when a reverse field is applied to the system, the magnetization switches its direction from positive to negative soon after the magnetization starts to rotate. More

detailed analysis [7] assuming a uniaxial anisotropy for the AF layer showed that this situation occurs when there exists distribution in the easy axis direction, especially when the distribution is random, which is very likely to occur in the structures of actual samples.

As seen from the analysis of model I, the AF spins do not switch with the switch of the magnetization if $r<1$. Therefore the coupling does not result in any coercivity enhancement. For $r>1$, however, the AF spins switch with the switch of the magnetization, resulting in the coercivity enhancement of $J/M_s t_F(1+r)$ without giving any pinning effect. Therefore, if we have a distribution in r value, some of the AF spins switch and some remain with the switching of the magnetization of the F layer. Thus it is thought that this $J/M_s t_F(1+r)$ part is responsible for the surface uniaxial anisotropy effect introduced by Qian, et al.[6].

It was reported that NiFe/NiO system also abide by the relationship[6]. We have confirmed that some samples of NiFe/NiMn system also follow this relationship too[5]. However, the samples of Co/NiO system did not show the relationship as shown in Fig. 9. Clearly, H_{p0} is much greater than $H_p + H_c$. It is observed in Co/NiO system that H_c in the pinning direction and in transverse direction are much higher than H_p. This implies that the coherent rotation model for the F layer will no longer valid. The domain wall motion may still dominate in the Co/NiO system or that significant local anisotropies exist in the Co/NiO system which will greatly reduce the initial susceptibility in the transverse direction, although thorough investigation is still necessary to make it clear.

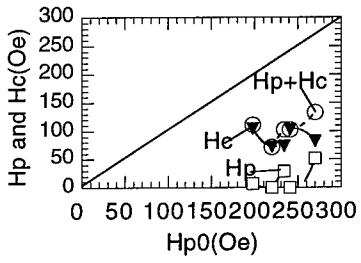

Fig. 9

CONCLUSIONS

We have measured H_{p0}, H_p and H_c of the samples of structures Glass/Ta(10 nm)/NiFe(8nm)/FeMn(t_{FeMn}nm)/Ta(5nm), Glass/Ta(10nm)/NiFe(8nm)/Cu(t_{Cu})/FeMn(8nm)/Ta (5nm) and Glass/Ta(10nm)/NiFe(8nm)/impurity/FeMn(8nm)/Ta(5 nm). It was found that $H_{p0} \cong H_p + H_c$ no matter how H_p and H_c vary individually with the change of H_{p0}. Assuming a coherent rotation for the magnetization of the F layer, we have proven that $|H_{sw}| = H_{p0}$ holds for any F/AF coupled system. Exactly speaking $|H_{sw}| \leq H_p + H_c$. However, detailed numerical analysis showed $|H_{sw}| \cong H_p + H_c$ if AF layer is assumed to be composed of particles having uniaxial anisotropies with their easy axes randomly distributed as will be the case in actual samples. The observed relationship $H_{p0} \cong H_p + H_c$ for actual samples of NiFe/FeMn system is thought to be explained along this line. But this relationship does not hold for the systems with large coercivity in the transverse direction such as NiO/Co, for which the coherent rotation model for the F layer will no longer be valid. No definite answer has been found and further investigations are needed.

REFERENCES

1. C. Tsang, Kenneth Lee, J. Appl. Phys. **53**, 1982 (2605).
2. D. Mauri, et al., J. Appl. Phys. **62**, 3047 (1987).
3. A . P. Malozemoff, Phys. Rev. B, **35**, 3679 (1987).
4. H. Fujiwara, et al., J. Appl. Phys. **79**, 6286 (1996).
5. T. Lin, D. Mauri, N. Staud, C. Hwang, Appl. Phys. Lett. **65**(9), 1183(1994).
6. Z. Qian, et al., presented at 7th joint MMM-INTERMAG Conference.
7. To be published elsewhere.

INFLUENCE OF CRYSTAL LATTICE DEFECTS ON DOMAIN WALL NUCLEATION AND MOTION IN EXCHANGE-BIAS FILMS

V.I. Nikitenko*, V.S. Gornakov*, L.M Dedukh*, A.J. Shapiro**, R.D. Shull**, A. Chaiken***,
*Institute of Solid State Physics, Russian Academy of Sciences, 142432, Chernogolovka, Moscow District, Russia, nikiten@issp.ac.ru
**National Institute of Standards and Technology, Gaithersburg, MD 20899
***Hewlett-Packard Laboratory, Palo Alto, CA 94304,

ABSTRACT

The affect of dislocations on the elementary events of the magnetization reversal processes in exchange-biased NiFe/NiO bilayer films and in free NiFe films grown on MgO substrates were investigated using the magneto-optic indicator film technique and vibrating sample magnetometry. It was revealed that dislocations not only influence the spatial distribution of spins, resulting in their inhomogeneous rotations during remagnetization, but also stipulate the formation of unusual quasi-one-dimensional domains localized on dislocation slip planes. Asymmetry in the dislocation activity as domain wall nucleation centers was investigated, and possible reasons for the revealed phenomena are discussed.

INTRODUCTION

As is well known, the processes of magnetization reversal in traditional bulk ferromagnetic materials cannot be described without taking into account the influence of crystal lattice defects. It has been shown that the characteristics of magnetization curves of real crystals significantly depend on the magnetoelastic energy, which is determined by the change of the relativistic and exchange interactions under the influence of spatially inhomogeneous internal stresses. Dislocations are the most important sources of internal stresses, since each of them produces a slowly-decreasing long-range stress field. Consequently, theories are being developed in ferromagnets [1,2] to explain the effect of dislocations on the processes of magnetization rotation and of domain-wall motion. Direct experimental study of the influence of individual dislocations on these processes has shown [3 - 5] that the dislocation induces an inhomogeneous distribution of the magnetization vectors around it, affects the rotation of these vectors under the action of an external magnetic field, determines the kinetics of spin reorientation phase transformations, and acts as a pinning center for domain wall motion.

Until now, the influence of dislocations (and other crystal defects) on the properties of modern magnetic nanostructured materials has not been studied. In exchange-bias films, for example, most attention in the past has been focussed on interface roughness [6] effects in order to explain the difference between theory and experiment of the exchange anisotropy field, H_E. In the present report, we show experimental data that crystal lattice defects and, in particular, dislocations dramatically influence the magnetization reversal processes in thin NiO/NiFe bilayers.

EXPERIMENTAL METHODS

NiO (50 nm)/NiFe (10 nm) bilayers were grown by ion beam sputtering onto single crystal (001) MgO and onto polycrystalline Si substrates [7]. NiFe (50 nm) films grown onto (001) MgO or onto Si without NiO buffers were also prepared. Both uniaxial (in NiFe films) and unidirectional (in NiO/NiFe films) anisotropy was induced during deposition by means of

Mat. Res. Soc. Symp. Proc. Vol. 517 © 1998 Materials Research Society

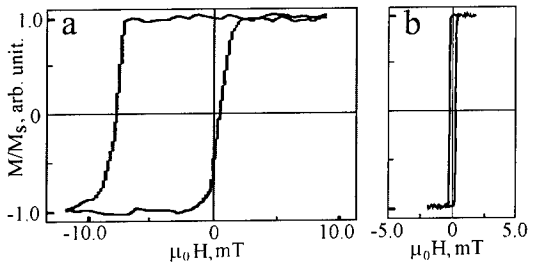

Fig.1. Reduced magnetization (M/M_S) vs. applied field (H) along the [110] direction for (a) biased NiO/NiFe bilayer and (b) a free NiFe thin film.

permanent magnets producing a uniform bias field, $\mu_0 H = 30$ mT in the plane of the substrate. In this paper we will examine films where this bias field was along either the <110> or <100> sample direction.

Macroscopic hysteresis loops of the films were measured at room temperature with a vibrating sample magnetometer (Fig.1). Optical reflecting microscopy and a photoelasticity method [8] were used to reveal the crystal lattice defects in the films. The magnetization reversal processes in the samples were studied using the magneto-optical indicator film (MOIF) technique [9]. This latter technique utilizes a Bi-substituted iron garnet film with in-plane anisotropy, which is placed on the sample. Polarized light passes through the indicator film and is reflected back by an Al underlayer covering the bottom surface of the film. The polarization of the passed light experiences a Faraday rotation through an angle proportional to the component of the local magnetic field parallel to the light propagation direction. When the polarizing prisms in the microscope are slightly uncrossed the bright or dark variations of the image represent the variations of the stray field component pointed up or down. The resulting Faraday portrait contains information about the domain structure as well as about defects in the crystal structure, which affect the spin distribution in the sample.

RESULTS AND DISCUSSIONS

Fig.2a shows NiFe surface steps revealed in reflected light on the NiO/NiFe bilayer epitaxially deposited onto MgO (001). They are created by the intersection of screw dislocation slip planes with the top NiFe surface. Fig.2b shows a birefringence picture of the same area due to effective internal microstresses caused by edge dislocations aligned along (110) and (1$\underline{1}$0) slip planes. Both screw and edge dislocations were introduced into the MgO substrate while cleaving the substrate prior to the bilayer deposition. The steps on the top NiFe surface indicate that these MgO dislocations propagated during the deposition through the NiO and NiFe layers and, hence, these screw dislocations also introduced steps into the interface of the bilayer.

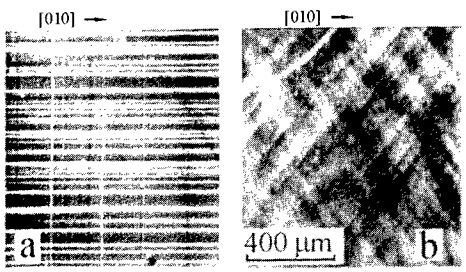

Fig.2. (a) Surface steps revealed in reflected light on MgO/NiO/NiFe and (b) a birefringence picture of the same sample region.

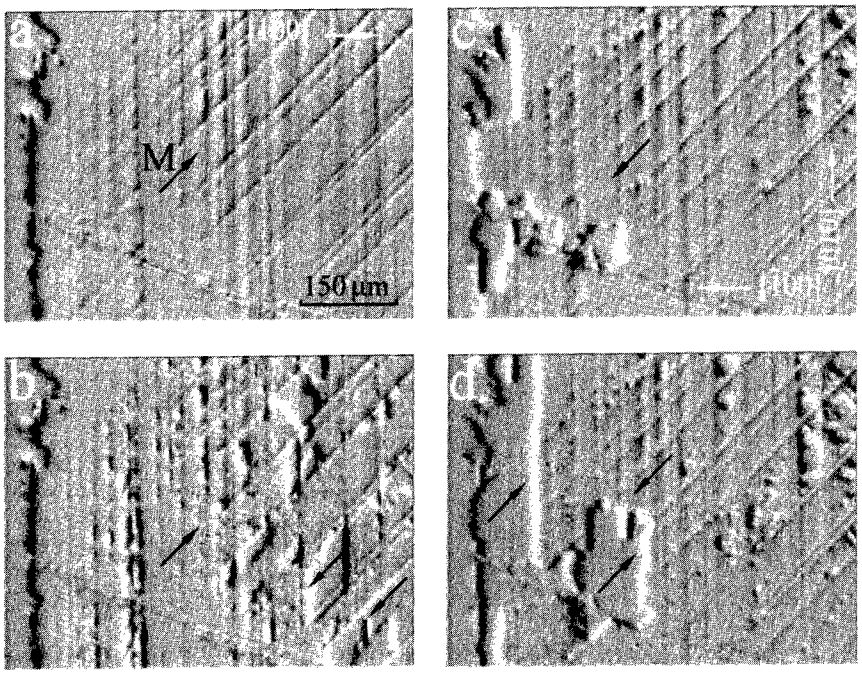

Fig.3. MOIF images of the same sample region during the [110] unidirectional-axis remagnetization in the MgO(001)/NiO/NiFe sample. Applied field $\mu_0 H$ = -3.0 (a), +1.6 (b), -6.2 (c), and -6.4 mT (d). Arrows (here and in the following Figures) indicate the local magnetization directions.

The MOIF images shown in Fig.3 illustrate the behavior of the domain structure in the biased MgO(001)/NiO/NiFe sample during reversal of its magnetization along the [110] unidirectional axis. The sample was first magnetized to saturation with the field $\mu_0 H$ = -30 mT aligned opposite the direction of the unidirectional anisotropy. The MOIF image of the saturated sample (not shown) was homogeneous and only stray magnetic fields at the sample edge were revealed (as a black band). As the applied field was decreased, incoherent rotation of the magnetization occurs (Fig.3a), resulting in an inhomogeneous distribution of spins which is entirely associated with the dislocation structure of the sample (compare with Fig.2). Upon increasing the applied field in the reverse sense, a large amount of domain nucleation occurs at the dislocation slip planes and at their intersections (Fig.3b). These new domains grow slightly until domain wall annihilation occurs. At this point, the domains disappear, and an inhomogeneous distribution of magnetization similar to that shown in Fig.3a appears.

At the last stage of the remagnetization, an unexpected effect of dislocations on the magnetization near saturation of the bilayer is revealed. Fig. 4 shows for this case, that specific quasi-one-dimensional domains exists at the ($1\underline{1}0$) edge dislocation slip planes. Moreover, remagnetization is accompanied by the vertical motion of domain walls along the band domains. Their magneto-optical contrast is changed, indicating reversal of the magnetization in the domains. These dislocation microdomains remain up to higher fields.

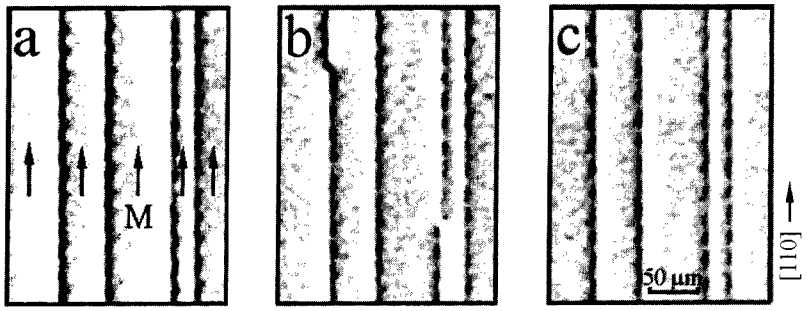

Fig.4. MOIF images of microdomans localized on the edge dislocation slip planes in the same region of the MgO(001)/NiO/NiFe sample. Applied field $\mu_0 H$ = +3 mT (a), +4.2 (b), and +6.9 (c).

For magnetization reversal in the opposite direction, the domain structure changes in a similar fashion to the above picture. However, nucleation of reversed-phase domains occurs at different local centers (Fig.3c, d). In addition, nucleation starts at a larger absolute value of the reversed applied field because the applied field in this direction must overcome the unidirectional anisotropy. Consistent with this behavior, an asymmetric hysteresis loop is observed (Fig.1a). This loop exhibits an exchange shift $\mu_0 H_E$ = 3.5 mT and coercive field $\mu_0 H_C$ = 4 mT.

In the NiO/NiFe bilayer having a [110] unidirectional anisotropy axis the most significant feature of the remagnetization process is the complicated domain structure resulting from the strong influence of edge and screw dislocations on both spin rotation and domain nucleation and growth. In fact, it is observed that the dislocations pin these domain walls so effectively that the domain sizes do not exceed the spacing between neighboring dislocation slip planes. It should be emphasized that while the screw dislocations introduce inhomogeneous internal stresses and additionally create steps at the NiO/NiFe interface (which can frustrate the interface NiO/NiFe magnetization vectors), the edge dislocations introduce only inhomogeneous internal stresses. This difference suggests that the induced inhomogeneous magnetic anisotropy due to magnetoelastic interactions plays an important role in the remagnetization of the bilayer. Similar domain behavior was observed for in-plane remagnetization in any other direction. For remagnetization along a hard-axis no shift in the hysteresis loop was observed, and the coercivity was very small.

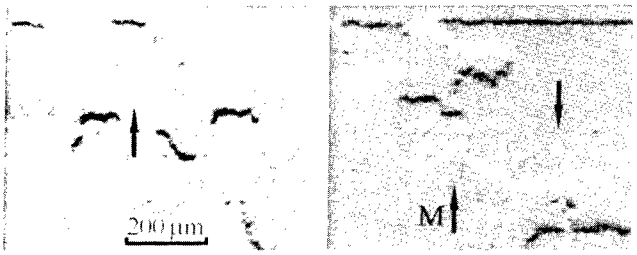

Fig.5. MOIF images of the [100] unidirectional axis magnetization reversal in the MgO(001)/NiO/NiFe sample: (a) $\mu_0 H$ = -4.2 mT and (b) $\mu_0 H$ = +1.5 mT.

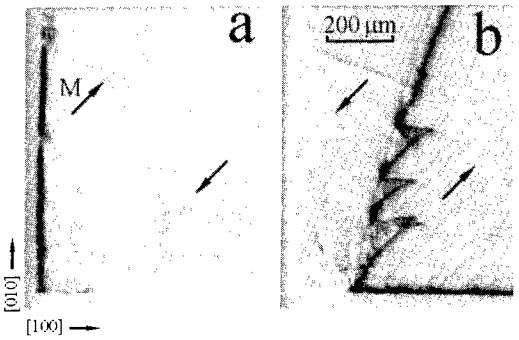

Fig.6. MOIF images of the [110] easy-axis magnetization reversal in the MgO(001)/NiFe sample. (a) and (b) correspond to the opposite remagnetization directions.

When an unidirectional anisotropy was induced along the [100] direction in the NiO/NiFe bilayer, the dislocations also stimulate domain nucleation and impede domain wall motion. However, in this case the domain walls can more easily overcome the dislocations barriers, and therefore, the domain sizes are larger (Fig.5). Compare, for example, Figs.2 and 5. It is obvious from Fig.5 that the domains in the [100] biased bilayer can grow to sizes much larger than the dislocation slip planes spacing. The measured unidirectional exchange field ($\mu_0 H_E$ = 2 mT) and coercivity ($\mu_0 H_C$ = 2.6 mT) of this bilayer are smaller than that in the NiO/NiFe bilayer with a [110] unidirectional biased axis. This means that the reversal process depends on the relationship between the unidirectional and an induced anisotropies.

The MOIF images of the domain structure taken during the [110] easy-axis magnetization reversal of a free NiFe layer (grown on MgO (001) without a NiO buffer) in two opposite directions are shown in Fig.6. The dislocation structure of this sample is also similar to the one shown in Fig.2. As is obvious, there is no strong dislocation influence on the domain structure of the free NiFe layer. This is due to an almost zero magnetostriction in the NiFe. Domains nucleate and disappear, as a rule, at film edges for both field directions due to a minimization of stray fields at edges. Remagnetization proceeds by the growth of domains over the whole sample. Though these particular patterns were obtained for the 50 nm thickness NiFe, such a behavior is typical for free ferromagnetic films with different thicknesses [10].

Comparison of the domain structure behavior in the free ferromagnetic film (Fig.6) with that in the exchange-biased film (Fig.3) led us to propose that dislocations in the NiO/NiFe bilayer influence primarily the spin configurations in the antiferromagnetic layer. This antiferromagnetic layer, however, affects the behavior of spins in the ferromagnetic layer. To confirm this proposition, we show in Fig.7 the domain patterns taken during remagnetization of a

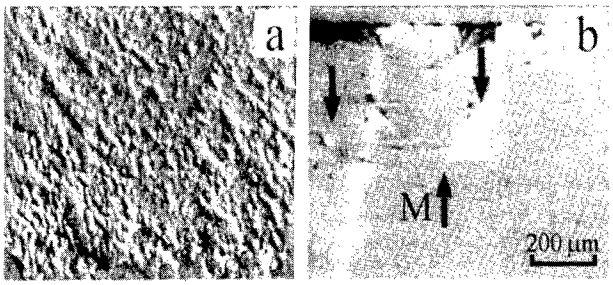

Fig.7. MOIF images of the magnetization reversal in (a) polycrystalline Si/NiO/NiFe and (b) polycrystalline Si/NiFe films.

polycrystalline NiO/NiFe bilayer (Fig.7a) and a free NiFe layer (Fig.7b) deposited on Si substrates. It is obvious that the domain structure in the polycrystalline NiO/NiFe bilayer is complicated and fine-scaled. On the contrary, in the polycrystalline NiFe layer, the remagnetization proceeds by the motion of almost rectilinear domain walls with cross ties over large distances. It does indicate that the polycrystalline structure in the NiO affects the magnetization reversal process in the bilayer.

CONCLUSION

The processes of incoherent spin rotation and of domain nucleation and growth are strongly governed by the dislocation structure of the NiO/NiFe bilayer. It was found that this dislocation influence is effective even for ferromagnetic films with almost zero magnetostriction because the influence on the bilayer reversal is realized through the antiferromagnetic layer. Therefore, in order to describe the reversal of the exchange-biased film it is necessary to take into account the details of the crystalline and spin structures of the antiferromagnetic layer.

ACKNOWLEDGMENTS

The Russian co-workers gratefully acknowledge a research grant from the Russian Foundation for Basic Research No. 97-02-16879.

REFERENCES

1. W. F. Brown, Phys. Rev. **58**, p. 736 (1940); **60**, p. 139 (1941).

2. Seeger, H. Kronmuller, H. Rieger, and H. Trauble, J. Appl. Phys. 35, p. 740 (1964); F. Vicena, Czech. J. Phys. **4**, p. 419 (1954); **5**, pp. 11, 480.(1955).

3. V. K. Vlasko-Vlasov, L. M. Dedukh, and V. I. Nikitenko, Sov. Phys.-JETP **38**, p. 184 (1974).

4. V. K. Vlasko-Vlasov, L. M. Dedukh, M. V. Indenbom, and V. I. Nikitenko, Sov. Phys.-JETP **57**, p. 159 (1983).

5. L. M. Dedukh and V. I. Nikitenko, Sov. Phys.-JETP **49**, p. 696 (1979); . L. M. Dedukh, M. V. Indenbom, and V. I. Nikitenko, **53**, p. 194 (1981).

6. P. Malozemoff, Phys. Rev. B **35**, p. 3679 (1987); J. Appl. Phys. **63**, p. 3874 (1988).

7. R. P Michel, A. Chaiken, C. T. Wang, and L. E. Johnson, IEEE Trans. Magn. **32**, p. 4651 (1996).

8. V. I. Nikitenko and L. M. Dedukh, Phys. Stat. Sol. (a) **3**, p. 383 (1970).

9. V. S. Gornakov, V. I. Nikitenko, L. H. Bennett, H. J. Brown, M. J. Donahue, W. F. Egelhoff, R. D. McMichael, and A. J. Shapiro, J. Appl. Phys. **81**, p. 5215 (1997).

10. T. Miyazaki, T. Aljima, and F. Sato, J. Magn. Magn. Mater. **81**, p. 86 (1989).

Exchange property correlation on deposition gas species and interface structure of Ion Beam Deposited Ta (50Å) / NiFe (xÅ) / FeMn (yÅ) / Ta (50Å) layers

H. Hegde [*], J. Wang [*], and S.B. Sant [**]

[*] Veeco Instruments Inc., Terminal Drive, Plainview, NY 11803
[**] Veeco Technology Center, 80 Las Colinas Lane, San Jose, CA 95119

ABSTRACT

In the quest for giant magnetoresistance exchange biased spin valves, the exchange coupling at the interface between the ferromagnetic layer and the antiferromagnetic layer is critical. We have correlated the exchange property, in ion beam deposited Ta (50Å) / NiFe (xÅ) / FeMn (yÅ) / Ta (50Å) layers, as a function of the deposition gas species, beam energy, deposition angle and resultant interface structures. High-resolution transmission electron microscopy was employed to understand the role of interface roughness, grain size of individual layers, towards optimization of the exchange behavior. Under certain conditions, exchange fields >300 Oe were consistently obtained for NiFe and FeMn thickness of 50Å and 100Å respectively. To the best of our knowledge, exchange-coupling strength of 0.25 ergs/cm^2 so obtained is the highest for such structures.

INTRODUCTION

For high-density magnetic recording, magnetoresistive heads are replacing inductive heads as the read back transducer [1]. The associated domain wall movement gives rise to Barkhausen noise that can be suppressed using a longitudinal bias field. The use of an antiferromagnetic layer which exchange couples with the ferromagnetic layer is capable of providing this longitudinal bias field [2,3]. It has also been demonstrated that the future of high-density recording will be giant magnetoresistance (GMR) exchange biased spin valves in which the exchange biasing material also pins the pinned layer [4]. Of the exchange biasing materials, FeMn and NiO are the most common [5]. NiO suffers from its low interfacial exchange energy of 0.059 ergs/cm^2 that makes it unfavorable to narrow track applications. IrMn is showing promising properties with good exchange fields when coupled with $Co_{90}Fe_{10}$ as also good corrosion resistance and thermal stability [6]. In spite of its poor corrosion resistance and poor thermal stability with a blocking temperature of 150°C, FeMn is by far the best because of the large exchange field (H_{ex}), the low coercivity (H_c) of the pinned layer and the ease of deposition of thin films. It has been reported that FeMn has to be grown on a suitable face-centered-cubic (fcc) NiFe layer for achieving exchange coupling with an increased easy-axis H_c and H_{ex} in the pinned layer [7]. Various methods have been used to stabilize the fcc γ phase of FeMn needed for the high H_{ex} [8]. Studies have shown that promotion of (111) texture of NiFe in ion beam sputtered NiFe/FeMn films have decreased the pinned layer H_c [9]. The mechanism and conditions that produce strong exchange bias is not clearly understood, although it has been known that extrinsic properties of the antiferromagnetic layer such as grain size, domain size and interface roughness are likely to influence the response of the ferromagnetic layer.

As part of a broad investigation on ion beam deposited GMR films, the present study focuses on the effect of different gas species, beam energy and deposition angle on exchange property and its correlation with the microstructure of the multilayer, especially high-resolution transmission electron microscopy (HRTEM). The advantages of ion beam deposition include ultra-high

Mat. Res. Soc. Symp. Proc. Vol. 517 © 1998 Materials Research Society

vacuum conditions, process control flexibility, minimized contamination and hence excellent film quality.

EXPERIMENTAL PROCEDURE

The different films were grown on a Veeco IBD 210 three-target tool without exposing the individual layers to atmosphere. The base pressure of the system was better than 1.0×10^{-7} torr while the process pressure was $3.0\text{-}5.0 \times 10^{-5}$ torr. Figure 1 shows schematically, the geometry of the chamber layout.

The primary ion source is the RF 210, which is a three-grid source such that a low beam divergence provides optimized beam focus for deposition without grid sputtering from charge exchange ions and for optimal beam confinement on the target. The RF 210 allows operation of the source with ultra low grid intercept current at less than 1% of the beam current to form high purity films. The Ta, NiFe and FeMn targets, 7.5 inch x 8 inch in size, were bombarded with a focused ion beam extracted from the deposition source at energy up to 1000 eV and sputtered material was deposited on silicon substrates which were pre-cleaned by ion beam generated from the assist source. Different gas species (Ar and Xe), ion beam parameters (500 to 1000 eV) and source-target-substrate geometry were used to investigate the correlation between film properties and process conditions. In this study the effect of fixture angle was examined, in particular 15° and 45°. The fixture angle is defined as shown in the schematic drawing of figure 1.

In all cases films were grown in a magnetic field of 50 Oe.

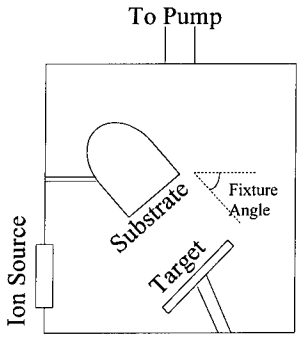

Figure 1: Schematic of IBD chamber

Magnetic measurements were made with a vibrating sample magnetometer. High-resolution cross-sectional transmission electron microscopy samples were prepared by making slices, dimpling and ion milling. A Philips CM20 TEM was used to record images in high-resolution mode.

RESULTS AND DISCUSSION

Figures 2 through 4 show cross-sectional HRTEM images of Si/ Ta 50 Å/ NiFe 50 Å/ FeMn 100 Å/ Ta 50 Å deposited at a fixture angle of 15° under different process conditions. The sample shown in Figure 2 was grown using Ar as the process gas at 1000 eV beam voltage and it can be seen that the NiFe layer is highly crystalline showing the presence of large columnar grains. Figures 3 and 4 shows similar TEM images in which the films were deposited using Xe as the process gas at beam voltages of 1000 eV and 500 eV respectively. In figures 3 and 4, the NiFe layer is thinner than with Ar and is highly crystalline showing the presence of smaller columnar

grains. The thickness of the NiFe film using Argon is much higher than with Xenon as can be seen in the cross-sectional images while that of Ta is remarkably the same for both gas species. The samples in figures 3 and 4 are very similar, e.g., NiFe layers show strong horizontal fringes, except that the NiFe/FeMn interface appears smoother at 1000 eV beam voltage than at 500 eV.

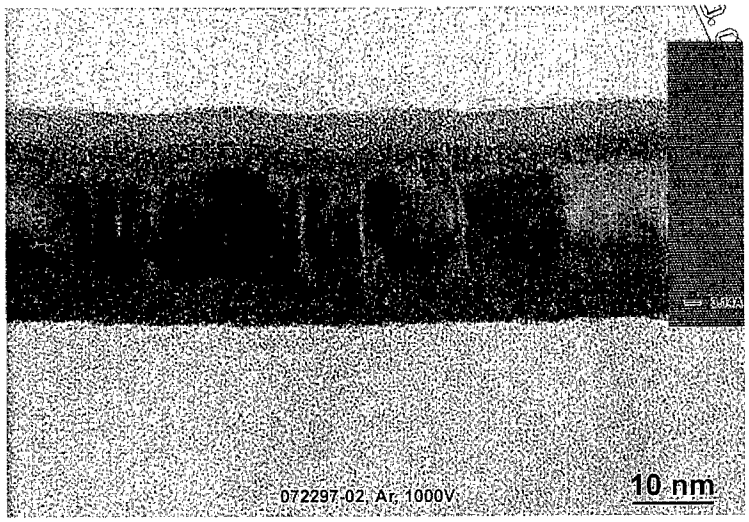

Figure 2:TEM Micrograph of 072297-02, Ar, 1000 eV

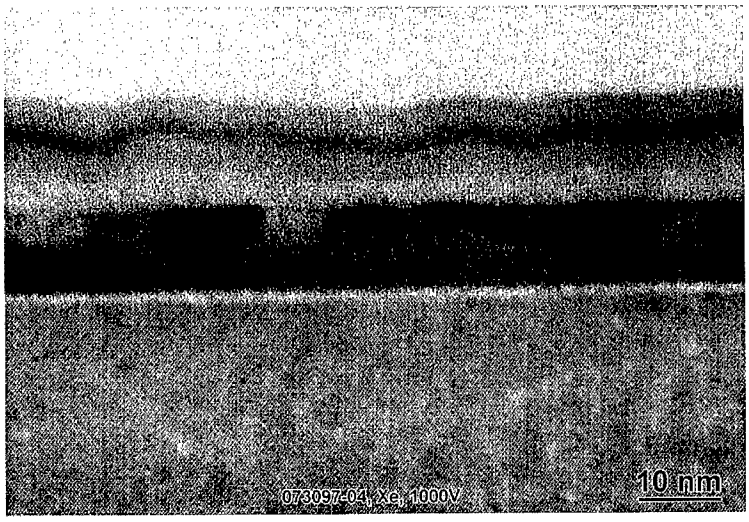

Figure 3:TEM Micrograph of 073097-04, Xe, 1000 eV

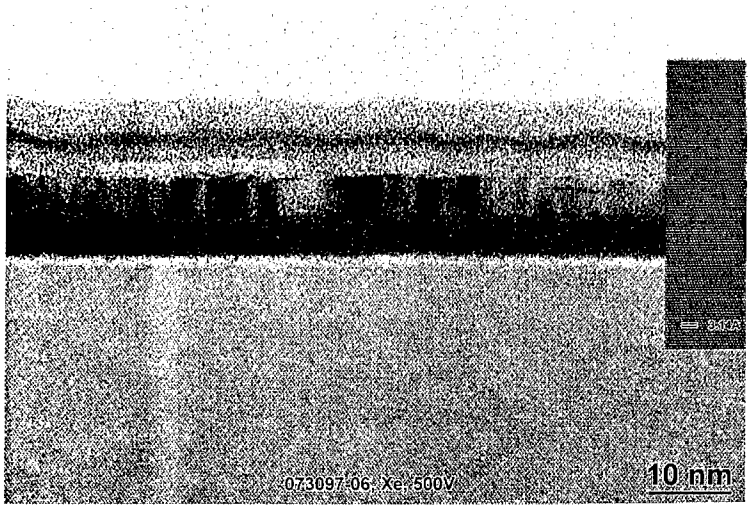

Figure 4:TEM Micrograph of 073097-06, Xe, 500 eV

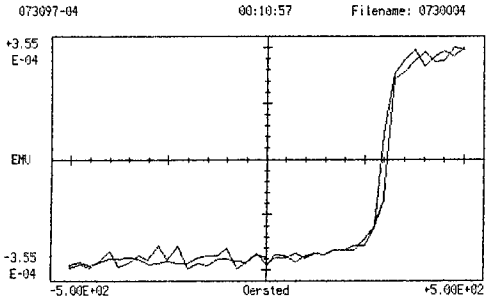

Figure 5: Vibrating Sample Magnetometer plot of Ta 50Å / NiFe 50Å / FeMn 100Å / Ta 50Å

Figure 5 shows a vibrating sample magnetometer plot of Ta 50Å/NiFe 50Å/FeMn 100Å/Ta 50Å. The exchange field, H_{ex} is over 300 Oe while the coercivity, H_c, is less than 10 Oe. The H_{ex} reported in this study is more than twice that reported in films grown by magnetron sputtering [10].

Figures 6 and 7 shows the change in exchange field as a function of the NiFe thickness (FeMn constant at 100 Å) and the FeMn thickness (NiFe constant at 50 Å) respectively. It is clear that an increase in the ferromagnetic layer thickness causes the exchange field to decrease monotonically, while a change in the antiferromagnetic layer thickness has only a minor effect, it

appears that this peaks at a FeMn thickness of 100 Å. The reason for this peak is not well understood.

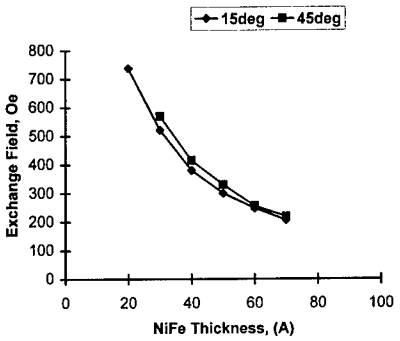

Figure 6: Exchange Field vs. NiFe thickness, FeMn 100 Å, Xe, 1000 eV

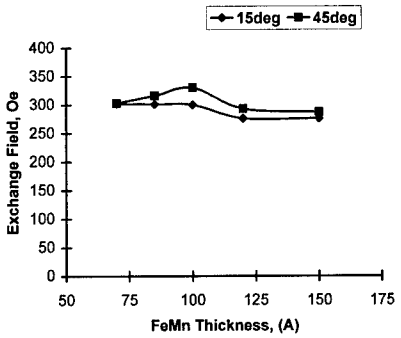

Figure 7: Exchange Field vs. FeMn thickness, NiFe 50 Å, Xe, 1000 eV

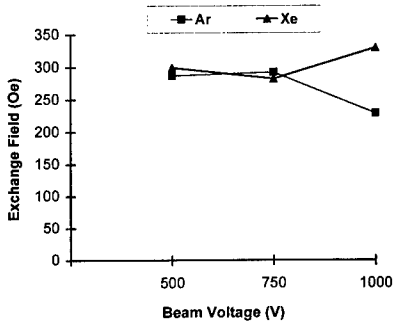

Figure 8: Exchange Field of NiFe 50 Å/ FeMn 100 Å, 45 degrees.

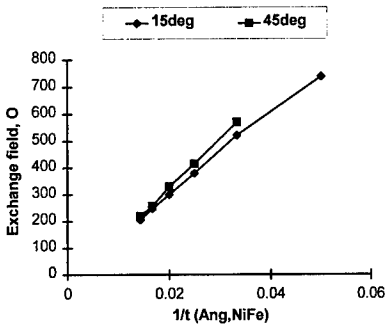

Figure 9: 1/t (NiFe) vs. Exchange Field, FeMn 100 Å, Xe 1000 eV. Exchange Coupling Strength is 0.25 ergs/ cm^2.

Figure 8 shows the change in exchange field as a function of beam voltage for both Ar and Xe gas species in samples with a constant NiFe thickness of 50 Å and FeMn thickness of 100 Å.

For beam energies of 500 eV and 750 eV, the exchange fields are similar using Ar and Xe. However, at a beam voltage of 1000 eV we notice a rather large difference for the two gas species with higher exchange fields using Xe. If we correlate this with the HRTEM images we can see that the drop in exchange field with Ar may be related to the larger thickness of the NiFe layer, work is in progress to fully understand the reasons for this difference. Figure 9 shows a plot of the exchange field as a function of the inverse thickness of NiFe at a FeMn thickness of 100 Å, using Xe as the process gas and a beam voltage of 1000eV. The slope of the graph gives the exchange coupling strength to be 0.25 ergs/ cm^2 that is the largest value to the best of our knowledge.

CONCLUSION

The process gas species used for ion beam deposition of exchanged biased layers has an influence on the magnetic properties of the thin films formed. We have successfully demonstrated the ability to produce exchange fields of more than 300 Oe in a multilayer consisting of Ta 50 Å /NiFe 50 Å /FeMn 100 Å /Ta 50 Å, using Xe as the process gas and a beam energy of 1000 eV. These conditions also gave rise to an exchange coupling strength of 0.25 ergs/ cm^2 that is the largest value to the best of our knowledge. The exchange field decreases with increase of beam energy over 750 eV using Ar as the process gas. HRTEM has shown that the use of Xe gives smoother, well-defined interfaces in the multilayer.

ACKNOWLEDGEMENTS

The authors would like to thanks the guidance of Jim Weldon, the assistance with Ion Sources provided by Alan Hayes, Viktor Kanarov and Rustam Yevtukhov as well as the constant encouragement by Emanuel Lakios.

REFERENCES

1. R. P. Hunt, IEEE Trans. Magn, MAG-7, (1971), 150
2. C. Tsang, IEEE Trans. Magn, MAG-25, (1989), 3692
3. T. Lin, C. Tsang, R. E. Fontana and J. K. Howard, IEEE Trans. Magn, MAG-31, (1995), 2585
4. R. L. White, IEEE Trans. Magn, MAG-28, (1992), 2482
5. M. F. Toney, C. Tsang and J. K. Howard, J. Appl. Phys. 70 (1991), 6227,
6. H. N. Fuke, K. Saito, Y. Kamiguchi, H. Iwasaki and M. Sahashi, J. Appl. Phys. 81 (1997), 4004
7. R. D. Hempstead, S. Krongelb and D. A. Thompson, IEEE Trans. Magn, MAG-14, (1978), 521
8. C. Tsang, N. Heiman and K. Lee, J. Appl. Phys. 52 (1981), 2471
9. W. E. Bailey, N. Zhu, R. Sinclair and S. Wang, J. Appl. Phys. 79 (1996), 6393
10. G. Choe and S. Gupta, Appl. Phys. Lett. 70 (1997), 1766.

HEAT DISSIPATION MATERIAL APPLICATION FOR MAGNETO-RESISTIVE HEAD

Xiao-feng Zhang*, X Yan,* R.F. Xiao*, Ji-bin Geng*, Jie Xhie**
* Physics department, Hong Kong University of Science and Technology, Clear Water Bay, Kowloon, Hong Kong. xfzhang@usthk.ust.hk
**Materials Characterisation and Preparation Facility, Hong Kong University of Science and Technology, Clear Water Bay, Kowloon, Hong Kong.

ABSTRACT

The requirement that a magneto-resistive(MR) head dissipate the heat produced by a resistive heating in the sensing element without excessive temperature rise is one of the factors limiting the electric current density in the head [1]. This, in turn, limits the signal to noise ratio attainable for a particular head design. Moreover, unreleased local heating will deteriorate high sensitive MR head unless a careful thermal management is included in the design process. The purpose of this investigation is to determine thermal conductivity of heat dissipation material AlN by using a new technique, which has been demonstrated to be useful for measuring thermal conductivity coefficient for a variety of insulator thin film layers. In this experiment AlN material was shown to have a better heat dissipation performance than that of Al_2O_3 which is currently used in the MR head industry.

INTRODUCTION

In MR recording heads, in addition to the field sensing layer, there are many other layers with different functionality. The dissipation layer is critically required to reduce excessive temperature rise generated by resistive heating. Therefore the requirement of dissipation layer must satisfy both isolating MR sensor from metallic heat-sink and spreading heat from sensor to shield effectively [2]. The applicable approaches could be to use a high heat conductivity material AlN layer for replacing present Al_2O_3 layer. AlN is well known for its high thermal conductivity and dielectric strength(see table-I), sintered AlN has been used in the semiconductor industry as substrates for integrated circuits [3]. It can become a potential candidate of dissipation layer for replacing Al_2O_3 in MR recording heads due to its several characteristics, such as good heat conduction, high dielectric strength and controllable deposition process.

Table-I Properties of selected materials with large thermal conductivity[3-5]

Name	BN	AlN	$Al_2O_3(\alpha)$	Diamond	BeO
Thermal conductivity W/m.K(25 °C)	1300	320	35	2000	380
Dielectric Strength kV/cm(25 °C)	2000	170	100	40000	100
Thermal expansion $x10^{-6}$/°C(25-400°C)	1.2	2.6	5.6	0.8	8.0
Hardness (kG/mm^2) Knoop-type	4500	1200	1370	5700~10400	1250
Crystal structure	h:a=2.5	h:a=3.1	h:a=4.8	c:a=3.6	h:a=2.7
Lattice constant(Å)	c=4.2	c=4.98	c=13.0		c=4.4
metastable phase	c:a=3.6	c:a=4.3			

Mat. Res. Soc. Symp. Proc. Vol. 517 © 1998 Materials Research Society

A special technique was developed for nitride thin film thermal conductivity measurement. Basically we can utilise thin metallic wire as a heater as well as a temperature sensor to perform heat conductivity measurement due to the fact that the metal resistivity change $\Delta\rho$ varies linearly with its changed temperature ΔT, i.e., $\Delta\rho \propto \alpha\Delta T$. The thin metallic wire can be heated up by resistive heating. Heat generated by the metallic wire is conducted through the thin AlN film to a large substrate, which acts as a ideal heat sink. With this model, the thermal conductivity of AlN could be measured with equation (1) by using testing device as shown in figure-1[12].

$$K = \frac{I_1^2 R_1 - I_2^2 R_2}{(R_1 - R_2)} \left(\frac{R_0 \alpha \delta}{A}\right) \qquad (1)$$

Where R_0 is metal wire resistance at room temperature, R_1 and R_2 are resistance corresponding to different temperature T_1 and T_2, and $\Delta T = T_1 - T_2$. A is total area of top heating wire, δ is nitride film thickness(~1000Å) and thermal coefficient of metal α can be obtained through an independent R~T characterisation[12]. With this technique, essential experimental data will be obtained to demonstrate that AlN insulating layer performs higher thermal conductivity than Al_2O_3.

EXPERIMENT

In this experiment, the film was deposited by reactive magnetron sputtering[6~10]. Reactive magnetron sputtering can use a pure Aluminium ingot (99.999%) as target and N_2 with Ar as sputtering gas to achieve amorphous like AlN film without heating up the substrate. The pressure of Ar and N_2 mixture was 40mTorr. Deposition rate of AlN and metallic NiFe layer is around 2.5Å/sec and 1.2Å/sec, respectively. Patterning of the film was performed using ion-milling etching at 1.5~2Å/sec removing rate. Ultrasonic wire bonder was employed to bond wire to metallic film for electrical measurement.

We have performed material characterisation on AlN film. The surface roughness of AlN film was analysed by AFM and the composition was studied by XPS. We first deposited a 1000Å thick AlN film on the top of Si(100) substrate and another 1000Å metallic was deposited on the top of AlN film with $Ni_{80}Fe_{15}Mo_5$ target. Afterwards, a micro metallic film was patterned by ion beam etching as shown in Figure-1.

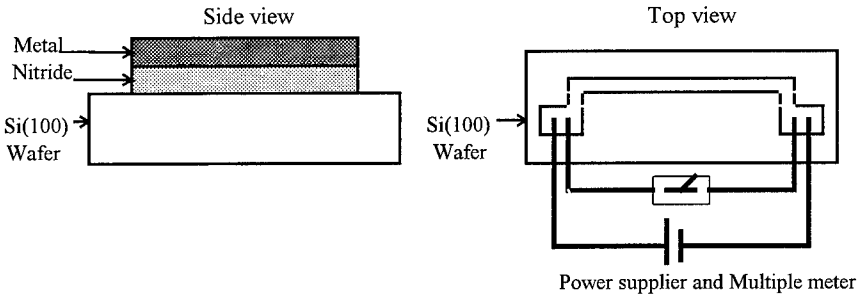

Fig.1. Heat thermal conductivity measurement device.

By measuring the wire resistance R1 and R2 at two different current I_1 and I_2, thermal conductivity K of insulator nitrides film can be obtained by equation(1). Because voltage and current followed through the metallic patterned film can be measured by multi-meter, a heat conductivity comparison of AlN and Al_2O_3 layers would be obtained by comparing the micro wire local temperature rise under the different heat dissipation material AlN and Al_2O_3.

We can ignore the heat stored in the wire due to its negligible heat capacity. Furthermore we are assuming that the substrate temperature was constant when small heating current was applied. The following assumptions are made:

- The current density in the wire was uniform, resulting in a uniform generation of heat[11].
- The temperature distribution along wire length direction was uniform.
- The heat lost through air was negligible due to its small thermal conductivity compared to the nitride film.
- The heat radiation through air could be ignored because of its relative low temperature(~60°C).
- The heat conduction through lead and edge was also negligible due to its large ratio of length to width, resulting in a rather uniform temperature distribution along with wire length.

RESULTS

The nitride film x-diffraction(XRD) result shows that the nitride film was amorphous like structure. Atomic Force Microscopy(AFM) was used for the nitride film surface morphology analysis. The result shows that the surface of nitride film was smooth and the roughness was ~2nm. The composition of the nitrides film was analysed by XPS technique. Figure-2 shows that a small amount of oxygen was observed inside nitride film which probably caused by oxygen inside the base sputtering gas.

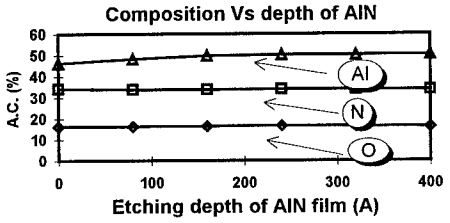

Fig.2. With different sputtering etching depth, a small amount of oxygen was observed inside AlN film.

In temperature coefficient measurement, we observed that the metallic wire's electrical resistance change ΔR linearly changes with its local temperature change ΔT, the temperature coefficient α is around $0.00077k^{-1}$. The temperature change of the metallic wire would be measured by measuring resistance change of the metallic wire. When two different current I_1 and I_2 was sent into metallic wire, the thermal conductivity coefficient of both AlN and Al_2O_3 layers would be measured by equation(1). A thermal conductivity comparison between AlN and Al_2O_3 layer was shown in Figure-3. At the same metallic wire temperature, around 20%

current density increment would be obtained if AlN layer is used, which, in turn, will improve signal significantly.

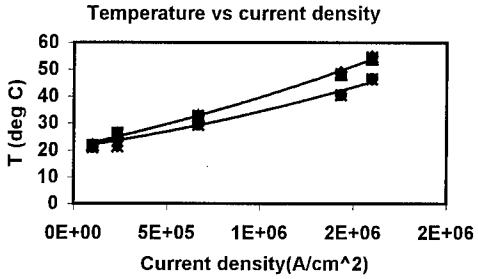

Fig.3. With different dissipation layers Al_2O_3 and AlN, current density can be gained by around 20% at same temperature.

The thermal conductivity experimental data of AlN and Al_2O_3 layer was shown in Table-II, which demonstrated that the thermal conductivity of AlN is twice of Al_2O_3 layer's. The thermal conductivity value of Al_2O_3 layer is around 0.45 W/m.K, which is close to results published[5]. Notice that only an improvement of 20% in current density is obtained since Joule heating is quadratic in current density.

Table-II Experimental thermal conductivity of AlN and Al_2O_3 layers.

Material	AlN thin film	Al_2O_3 thin film
Thermal conductivity, W/m.K(25 °C)	0.95W/m.K	0.45W/m.K

CONCLUSIONS

In this study, the AlN thin film was found having better thermal conductivity than Al_2O_3. At the same metallic layer temperature constraint, around 20% more current density will be obtained with AlN thin film layer, which, in turn, will improve signal significantly in the MR heads. So, AlN material may be a good candidate as a replacement for Al_2O_3 in MR head industry. Additionally, a new thermal conductivity measurement technique for thin film was demonstrated in this study. The model employed in above study is based on various assumptions in which the heat loss through lead and air was not taken in consideration. However, it is OK for comparison between two materials like Al_2O_3 and AlN. A more accurate model would be developed in future work.

ACKNOWLEDGEMENTS

The authors thank Dr. Po-Kang Wang for helpful discussion and explanation, and also thank Prof. M Yu, Dr. Catherine Wong and Dr. L.T. Weng for material characterisation.

REFERENCES

[1]J.Brug, K. Tran, M.Bhattachayya, A. Jander, J. Nickel, and T. Anthony, Impact of new magnetoresistive materials on magnetic recording heads, in press.

[2]Mallinson, John C, Magneto-resistive heads, (San Diego, Calif, 1996).

[3]F.Miyashiro, N.Iwase, A. Tsuge, F. Ueno, M. Nakahashi, and T. Takahashi, IEEE Trans. On Component, Hybrid, and Manufacture Technol. 13, 313 (1990).

[4]P. Klocek, Handbook of Infrared Optical Materials, (Marcel Dekker, New York, 1991).

[5]Union Carbide, Advanced Ceramics catalog, (Cleveland, OH).

[6]A.J. Chuskus, T.M. Reeder, and E.L. Paradis, Appl. Phys. Lett. 24, 155(1974); C.R. Aita, J. Appl. Phys. 53, 167(1982); J.S. Morgan, W.A. Bryden, T.J. Kistenmacher, S.A. Ecelberger, and T.O. Poehler, J. Mat. Res. 5, 2677(1990); W.J. Meng, J. Heremans, and Y.T. Cheng, Appl. Phys. Lett. 59, 2097(1991); F.F. Stedile, I.J.R. Baumvol, W.H. Schreiner, and F.L. Freire, Jr, J. Vac. Sci. Technol. A10, 3272(1992); W.J. Meng, and G.L. Doll J. Appl. Phys. 79, 1788(1996).

[7]M.Penza, M.F. De Riccardis, L. Mirenghi, M.A. Tagliente, and E. Verona, Thin Solid Films 259, 154(1995); H. Okana, Y. Takahashi, T.Tanaka, K.Shibata, and S. Nakano, Jpn. J. Appl. Phys. 31, 31, 3446(1992).

[8]I. Ivanov, L. Hultman, K. Jarrendahl, P. Matensson, J.E. Sundgren, B. Hjorvarrsson, and J.E. Greene, J. Appl. Phys. 78, 5721(1995).

[9]M.Mieno, and T.Yoshida, Jpn, J. of Appl. Phys. 29, L1175(1990); K. Bewilogua, J. Buth, H.Hubsch and M.Grichke, Diamond Related Mater. 2, 1206(1993); H.Luthie, K. Bewilogua, S. Daaud, M.Johansson, K. Hultman, Thin Solid Films 257,40(1995).

[10]K.Tominaga, H. Imai, and M.Shirai, Jpn. J. Appl. Phys. 30, 2574(1991).

[11]K. Young, IBM J. Res. Develop., vol. 34, p. 706, September 1990.

[12]Appendix of thermal calculation model:

According to the facts that the resistance change is proportional to the temperature change in the metal, which can be interpreted as equation(2):

$$\frac{R-R_0}{R_0} = \alpha \bullet (T - T_0) ----(2)$$

Where R is the metallic wire resistance at temperature T, R_0 is the metallic wire resistance at room temperature T_0. α is metal temperature coefficient. Referring to figure-1, consider to send two current I_1 and I_2 flow through metallic layer, we have two heat transfer equations (3) and (4):

$$\frac{dQ_1}{dt} = -kA.\frac{\Delta T_1}{\delta} + \frac{q_1}{\Delta t} = I_1^2 R_1 -----(3)$$
$$\frac{dQ_2}{dt} = -kA.\frac{\Delta T_2}{\delta} + \frac{q_2}{\Delta t} = I_2^2 R_2 -----(4)$$

Where the Q_1 and Q_2 are the heat flow through AlN layer from metallic layer to the substrate which acts as a perfect heat sink in perpendicular direction in the case of I_1 and I_2. The δ is heat dissipation layer thickness and A is total area of patterned metallic wire. The Δt is the decay time of heat stored in the wire. The q_1 and q_2 are heat stored in metallic patterned wire. The R_1 and R_2 are resistance corresponding to different temperature T_1 and T_2. $\Delta T_1 = T_1 - T_s$ and $\Delta T_2 = T_2 - T_s$ are defined as temperature difference between patterned metallic wire and heat sink (substrate) when it arrives at steady state. T_s is defined as substrate constant temperature. K is thermal conductivity of insulator layer. Since heat stored in wire is very small since its small heat capacity and small volume comparing to huge substrate. We can substrate q_1 and q_2 from (3) and (4) then we can got (5):

$$I_1^2 R_1 - I_2^2 R_2 = -kA.\frac{\Delta T_2 - \Delta T_1}{\delta} = -kA.\frac{(T_2 - T_1)}{\delta} ----(5)$$

Combining (5) with (2), AlN insulator layer thermal conductivity could be interpreted as (6):

$$K = \frac{I_1^2 R_1 - I_2^2 R_2}{(R_1 - R_2)} (\frac{R_0 \alpha \delta}{A}) -----(6)$$

STRUCTURAL AND MAGNETIC ANISOTROPY OF ELECTRODEPOSITED Co/Cu MULTILAYERS

M. Shima *, L. Salamanca-Riba *, T. P. Moffat ** and R. D. McMichael **

* Department of Materials and Nuclear Engineering, University of Maryland, College Park, MD 20742
** Materials Science and Engineering Laboratory, National Institute of Standards and Technology, Gaithersburg, MD 20899

ABSTRACT

A variety of Co/Cu multilayers were grown by electrodeposition on Si(001) substrates covered with a Cu seed layer. High-angle X-ray diffraction shows that the Co/Cu multilayers have a strong (001) texture. Φ-scan X-ray diffraction and TEM reveal that the multilayers have fourfold symmetry in the plane with a 45 degree rotation with respect to the Si substrates. Superparamagnetic behavior is observed in the electrodeposited Co/Cu multilayers with Co layer thickness below 2 monolayers(ML). The superparamagnetic behavior could be due to discontinuity of the very thin Co layers, which follows from the nucleation and growth process. In-plane fourfold symmetry of the magnetization and magnetoresistance is observed when the Co layer thickness is above 4 ML. The fourfold symmetry correlates with the in-plane crystalline structure of the multilayers.

INTRODUCTION

There has been considerable interest in recent years in artificially layered materials which exhibit novel physical properties. Particular attention has been given to magnetic multilayers which exhibit the giant magnetoresistance(GMR) effect[1]. Films showing the GMR effect are potential candidates for future applications in magnetic field sensors, magnetic data recording and position sensors. A variety of fabrication techniques have been used to produce GMR multilayers. Electrodeposition has several advantages: low cost, ease of operation, capability of producing extremely fine laminated structures, and sustained epitaxial growth at low deposition temperatures[2]. While the growth of well-defined strained-layer superlattices by electrodeposition has been reported, these studies have largely focused on using thick polycrystalline or single crystal metallic substrates[2, 3]. Unfortunately, the conductivity of the substrate hampers an assessment of the magnetoresistance of the multilayers. In prior experiments the shunting substrates were removed by chemical etching[2]. However, this process leads to ill-defined changes in the stress-state of the film. As an alternative we have begun exploring the use of highly oriented thin metal seed layers which allow the magnetotransport properties to be evaluated while taking advantage of the microstructural dependence of growth on different crystallographic orientations[3, 4]. Recently, electrodeposition of Co/Cu multilayers on Si(001) surfaces was also reported, though no examination of the in-plane structure was presented[5].

In this paper, we explore the dependence of the GMR on in-plane crystallography as well as the influence of ferromagnetic layer thickness on the magnetic behavior of Co/Cu multilayers.

Mat. Res. Soc. Symp. Proc. Vol. 517 © 1998 Materials Research Society

EXPERIMENTAL DETAILS

Co/Cu multilayers were electrochemically deposited onto Si(001) substrates which had a 20-40 nm copper seed layer deposited using electron beam evaporation. Immediately prior to loading into the evaporator the Si wafers were hydrogen terminated by immersion in 10% HF. The copper seed layer serves as a buffer layer that determines the orientation, or texture, of the multilayer. Symmetric X-ray diffraction indicated that the copper seed layer was highly (001)-textured and a rocking curve analysis indicates a mosaicity of 5.9~6.7 °(FWHM) about the (002) pole. An ohmic contact was made by contacting the backside of the Si wafers with InGa eutectic. The electrodeposition cell has been described previously[3].The Co/Cu multilayers were grown in a single electrolyte with a pH of 3.5 containing 1.5 mol/L $CoSO_4$, 0.008 mol/L $CuSO_4$ and 0.5 mol/L H_3BO_3. The films were grown under potentiostatic control with a programmable coulometer used to toggle the potential between appropriate values. The nominal Co layer thickness was varied in the range from 1 ML to 12 ML while the thickness of Cu was fixed at 17 ML. Chronoamperometry and atomic absorption were used to determine the current efficiency of Co and Cu deposition. For Co, the current efficiency was a function of the thickness ranging between 70-82 % while that of Cu lies between 95-100 %. The thickness values cited in this paper have been normalized reflecting the current efficiency. The structure of the multilayers was characterized by x-ray diffraction and TEM. Magnetic hysteresis loops and in-plane vector magnetization curves were obtained using a vibrating sample magnetometer (VSM) at room temperature. The magnetoresistance was measured using a conventional four-point probe technique.

RESULTS AND DISCUSSION

The superlattice structure of a $[Co(9.5\ ML)/Cu(17\ ML)]_{100}$ multilayer was examined by symmetric X-ray diffraction measurement. The X-ray spectrum from the film is shown in Fig. 1. A strong Bragg peak associated with the fcc (002) reflection of the multilayer was observed, which suggests that the multilayer has a strong (001)-texture and is pseudomorphic with the Cu seed layer. The first order satellite peaks observed in the vicinity of the (002) Bragg peak indicate that the multilayer structure is reasonably well-defined. The modulation period of the multilayer structure calculated from the position of the satellite peaks is 4.98 nm, which is in good agreement with the designed value of 5.0 nm. A rocking curve analysis indicates that the multilayer has a mosaicity of ~1.8°(FWHM) about the (002) pole.

The in-plane structure of the multilayers was examined by X-ray ϕ-scan measurements. Φ-scans for a $[Co(9.5\ ML)/Cu(17\ ML)]_{100}$ multilayer are presented in Fig. 2. The data were obtained with the detector at the Bragg angle for the multilayer (111) (Fig. 2a) and Si (111) (Fig. 2b) reflections. In both cases four peaks are observed at intervals of 90°, indicating in-plane fourfold symmetry. However, the peak positions for the multilayer are shifted by 45° from those for the Si substrate. Thus, the epitaxial relationship between the Si substrate, the Cu seed layer and the multilayer is Si(001)//Cu-seed(001)//multilayer(001), and Si[100]//Cu-seed[110]//multilayer[110] in the plane of the film. The variation of the peak intensities of the multilayer(111) reflections may be due to a slight misorientation of the multilayer relative to the Si substrate. The average lattice constant of the strained Co/Cu superlattice calculated from the (002) Bragg peak position is 0.357 nm. The misfit between the Si substrate and the multilayer is ≈34 % without rotation, while it is reduced to 7 % with 45° rotation. Hence the in-plane relationship is a result of minimization of the in-plane strain.

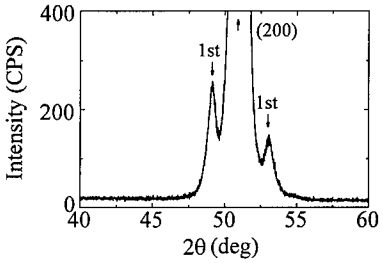

Fig. 1 High angle X-ray spectrum from a $[Co(9.5\ ML)/\ Cu(17\ ML)]_{100}$ multilayer.

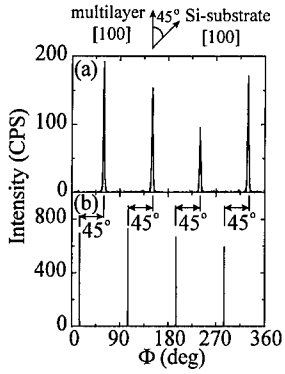

Fig.2 In-plane ϕ-scans for (111) reflections for a) Co/Cu multilayer and b) Si substrate.

A TEM image and associated diffraction patterns from a $[Co(9.5\ ML)/Cu(17\ ML)]_{100}$ multilayer are shown in Fig. 3. The cross-section image in Fig. 3(a) shows the layered structure of the Co/Cu electrodeposited film. The gray band between the multilayer and the Si substrate is the Cu seed layer. Figs. 3(b) and (c) show the (110) and (100) diffraction patterns taken from the Si substrate and the Co/ Cu multilayer, respectively, which reveals the epitaxial in-plane relationship of Si[110]//Cu-seed[100]//multilayer[100] in agreement with the result obtained from the X-ray ϕ-scans. The TEM image shows that the multilayer is reasonably well defined within grains. However significant curvature was also observed at the edges of the grains. This curvature could potentially give rise to an orange peel effect in the magnetization[6].

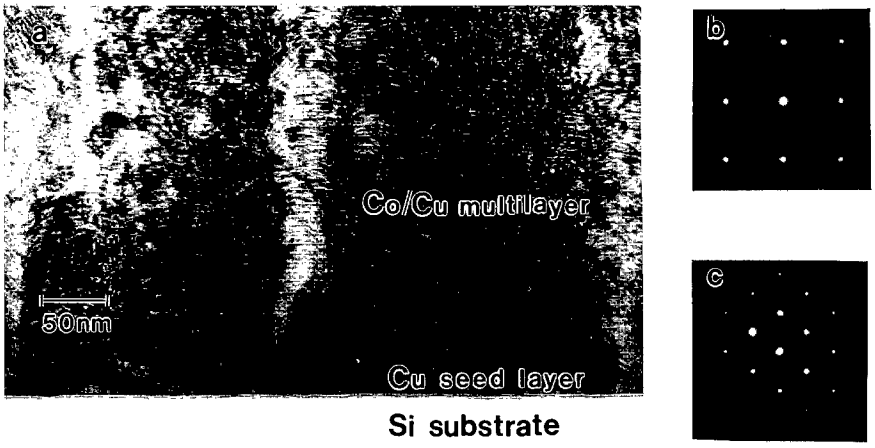

Fig. 3 (a) Cross-section TEM image, (b) (100) diffraction pattern from the Co/Cu multilayer and (c) (110) diffraction pattern from the Si substrate of a $[Co(9.5\ ML)/Cu(17\ ML)]_{100}$ multilayer.

The in-plane vector magnetization curves from a $[Co(9.5\ ML)/Cu(17\ ML)]_{100}$ multilayer are shown in Fig. 4. The VSM sample was prepared by cleaving the sample into a square, 5 mm × 5 mm, with the cleaved edge corresponding to the <100> direction of the multilayer. The longitudinal magnetization, M_l, and transverse magnetization, M_t, were measured as the sample was rotated about its normal axis from 0° to 360° and back to 0° in an applied field of 0.1 T. Both M_l and M_t exhibit oscillations congruent with the structural fourfold symmetry and reflect the magnetocrystalline anisotropy of the cubic structure. The minima of the M_l curve correspond to the <100> directions of the Co/Cu multilayer, which is the magnetically hard direction. This is consistent with the result of Co/Cu multilayers electrodeposited onto a (001) Cu single crystal substrate[7]. The maxima of the M_l curve correspond to the in-plane <110> directions. Therefore, in the absence of a magnetic field the residual magnetization M_r lies along one of the <110> directions in the plane. Using the M_t curve in Fig. 4 the values of $M_t/\delta\phi_H$, which is the slope of the M_t curve near $M_t = 0$, and M are 5.2×10^6 A/m and 1.0×10^7 A/m, respectively[8]. From the values and the applied field $\mu_0 H = 0.1$ T one obtains the value of (98 ± 9) mT for the anisotropy field $2K_1/M$. The anisotropy constant K_1 is then found to be $(-4.1 \pm 0.4)\times10^4$ J/m^3 in fair agreement with the values between -4.1×10^4 J/m^3 and -6.2×10^4 J/m^3 measured on fcc single crystal Co films[9].

The dependence of the magnetoresistance on in-plane direction was examined as shown in Fig. 5. M-H hysteresis loops and magnetoresistance curves were obtained from a $[Co(9.5\ ML)/Cu(17\ ML)]_{100}$ multilayer along both <100> and <110> directions of the multilayer in an applied field of up to 0.7 T, where the magnetization was measured along the in-plane orientation. Comparing the hysteresis loops measured along the two directions, the remanent magnetization in the <100> direction is slightly smaller than that of the <110> direction. This difference reflects the fact that the <100> directions are magnetically harder than the <110> directions. This result is consistent with the result obtained by Bean[10]. The hysteresis loop for $M_{||}$ obtained in the <110> direction has a fairly rectangular shape in the vicinity of zero field, which may indicate that the Co layers consist of nearly single domains and that the magnetization reversal takes place by a nucleation and growth process of domains. On the other hand, the hysteresis loop obtained in the <100> direction has a slightly more complex shape, which may be a result of the rotation of magnetization from the easy axes of <110> to the hard axes of <100> after domain wall motion[11].

The magnetoresistance measured as a function of the in-plane direction is shown in Fig. 5. GMR effects are readily observed along both <100> and <110> directions, indicating that different fractions of antiferromagnetic coupling between the Co layers are present even though the effect is not very strong. Such fractional antiferromagnetic coupling states are probably due to the four-fold magnetocrystalline anisotropy. The GMR effects were 7.5 % and 5.0 % in the <100> and <110> directions, respectively. As clearly seen in these figures, the slopes of the magnetoresistance curves in the <100> and <110> directions are different. The slope of the curves at higher fields indicates that the magnetic coupling state between the Co layers is still in transition and saturation has not been achieved at a magnetic field of 0.7 T. The slope of the $\Delta R/R$ vs. H curve is larger in the <100> direction than the <110> direction presumably because <100> is a magnetically hard direction compared to the <110> direction. As explained above, the in-plane vector magnetization curves clearly show the existence of the magnetocrystalline anisotropy in the multilayer and the anisotropy constant of the multilayer is nearly as high as that of a single crystal Co film[8]. Therefore, such in-plane anisotropy of the GMR effect must be associated with the magnetocrystalline anisotropy of the Co/Cu multilayer.

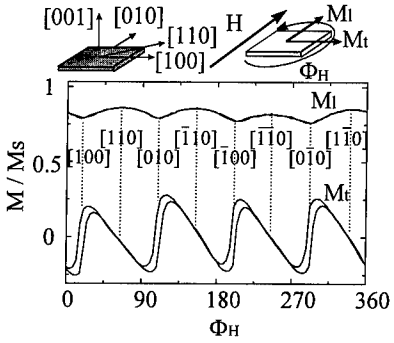

Fig. 4 Longitudinal and transverse vector magnetization curves of the [Co(9.5 ML)/ Cu(17 ML)]$_{100}$ sample at 0.1 T.

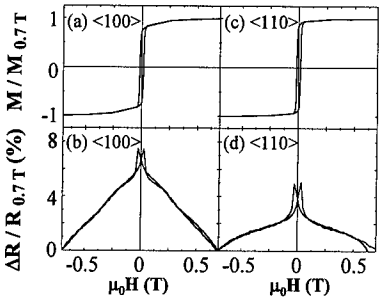

Fig. 5 (a) Magnetic hysteresis loops for a [Co(9.5 ML)/Cu(17 ML)]$_{100}$ sample measured with the applied field in-plane and parallel to (a) <100> and (c) <110> directions. (b) and (d) show the corresponding GMR plots.

The magnetic properties of the multilayers were studied as a function of Co layer thickness. Values ranging from 0.7 ML to 10 ML were examined. The dependence of the coercive field, the squareness of the magnetic hysteresis loops, $Mr/M_{0.9T}$, and the average magnetic moment of Co on the Co layer thickness are shown in Fig. 6(a), (b) and (c), respectively. As the Co layer thickness decreases, the coercive field decreases from Hc = 19.4 mT for x = 9.5 ML to Hc = 5.0 mT for x = 0.7 ML. The ratio of the remanent magnetization to the magnetization at H = 0.9 T

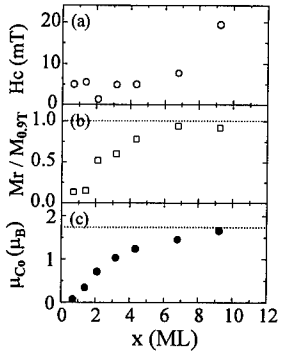

Fig. 6 Dependence of (a) the coercive field (b) the squareness of the magnetic hysteresis loops and (c) the average magnetic moment of Co on the Co layer thickness, x, in the [Co(x ML)/Cu(17 ML)]$_{100}$ multilayers. The dotted lines in (b) and (c) indicate the values of $Mr / M_{0.9T} = 1$ and the magnetic moment of pure Co, i.e., 1.7 μ_B, respectively.

decreases gradually as the Co layer thickness decreases from x = 9.5 ML to 2 ML and approaches zero below x = 2 ML. The average magnetic moment of Co in the multilayer decreases as the Co layer thickness decreases below x = 9.5 ML, deviating gradually from the value for pure Co. The multilayers with the Co layer thickness below 2 ML show hysteresis loops with sigmoidal shapes, while those with more than 4 ML exhibit rectangular shape. The reduced magnetization in very thin Co layers could be due to a superparamagnetic behavior that results from discontinuities in the Co layer as well as Co alloying with Cu at the interface. A similar decrease in the magnitude of the saturation magnetization has been reported for thin Co layers deposited on Cu(001)[12].

CONCLUSIONS

A variety of Co/Cu multilayers were grown by electrodeposition on Si(001) substrates covered with a Cu seed layer. High-angle X-ray diffraction shows that the Co/Cu multilayers have a strong (001) texture. Φ-scan X-ray diffraction and TEM reveal that the multilayers have fourfold symmetry in the plane with a 45 degree rotation with respect to the Si substrate. The giant magnetoresistance appears to depend on the in-plane orientation of the multilayer due to the magnetocrystalline anisotropy. In-plane fourfold symmetry of the magnetization and magnetoresistance is observed when the Co thickness is above 4 ML. The fourfold symmetry correlates with the in-plane crystal structure of the multilayers. We have observed evidence for a superparamagnetic behavior in multilayers with Co layer thickness of less than 2 ML. This effect is believed to result from the discontinuous Co layers.

ACKNOWLEDGMENTS

This work was supported by NSF Contract No. DMR91-11516 and the NIST Metallurgy Division. The authors would like to thank J. Dura, M. Vaudin and L. J. Swartzendruber for helpful discussions, J. Cline for the use of the X-ray diffractometer and J. Bonevich for the use of the transmission electron microscope.

REFERENCES

1. S. S. P. Parkin, Ann. Rev. Mater. Sci. **25**, 357(1995).
2. W. Schwarzacher and D. S. Lashmore, IEEE Trans. Magn. **32**, 3133(1996).
3. T. P. Moffat, Mater. Res. Soc. Proc. **451**, 413(1997).
4. C. Chang, Appl. Phys. Lett. **57**, 297(1990).
5. S. K. J. Lenczowski, C. Schonenberger, M. A. M. Gijs and W. J. M. de Jonge, J. Magn. Magn. Mater. **148**, 455(1995).
6. L. Néel, C. R. Acad. Sci. 255, 1545(1962).
7. R. D. McMichael, U. Atzmony, C. Beauchamp, L. H. Bennett, L. J. Swartzendruber, D. S. Lashmore and L. T. Romankiw, J. Magn. Magn. Mater. **113**, 149(1992).
8. M. Shima, L. Salamanca-Riba, T. P. Moffat, R. D. McMichael and L. J. Swartzendruber, J. Appl. Phys. (in press).
9. W. Doyle, J. Appl. Phys. **35**, 929(1964).
10. C. P. Bean, J. D. Livingston and D. S. Rodbell, J. Physique Rad. **20**, 298(1959).
11. J. J. de Miguel, A. Cebollada, J. M. Gallego, R. Miranda, C. M. Schneider, P. Schuster and J. Kirschner, J. Magn. Magn. Mater. **93**, 1(1993).
12. W. Schindler and J. Kirschner, Phys. Rev. B 55, R1989(1997).

THE MAGNETO-TRANSPORT PROPERTIES OF SANDWICH FILMS OF PERMALLOY/Cu/Co

C.K. Lo[a], C.H. Ho[b], I. Klik[c], Y.D. Yao[c], S.F. Lee[c], H.H. Huang[d], Y.C. Chen[a], C.Y. Wu[a], D.Y. Chiang[a], C.A. Chang[a], M.T. Lin[b], and D.R. Huang[a]

[a]Opto-Electronics & System Lab., Industrial Technology Research Institute, Hsinchu, Taiwan, ROC.

[b]Department of Physics, National Taiwan University, Taipei, Taiwan, ROC.

[c]Institute of Physics, Academia Sinica, Taipei, Taiwan

ABSTRACT

The magnetic behaviour of sputtered $Py_{5nm}/Cu_t/Co_{5nm}$ films on glass, Si(100), and Si(111) was studied by measurements of the transverse, longitudinal, polar magneto-resistance, and the magneto-optical Kerr effect (MOKE). The sample can be rotated about its surface normal to obtain angular dependent information during the MOKE measurement. All specimens have non-vanishing normal component of magnetization as revealed by MR with field applied normal to the film and confirmed by polar MOKE. Spin valve MR with very small coercivity is observed as t is increased. The minor R-H curve shows two states at zero magnetic field, which is desirable for MRAM application. An increase in the periodicity number increases the MR ratio, but also, significantly, the coercivity.

INTRODUCTION

Spin valves and layered structures consist of alternating ferromagnetic and non-magnetic layers. They exhibit giant magneto-resistance (GMR) effect and have been widely studied for over a decade. In applications this effect was also used for sensing of magnetic field [1] and in magnetic storage [2]. Recently, the usa of GMR effect is regarded as a potential technology for fabricating high-density and fast access time permanent memory [3]. In particular with magneto-resistive random access memory (MRAM) device among the various digital MR its applications have many advantages such as non-volatile, non-destructive read out, radiation hardness, and simple manufacturing base in mirco-electronic technology [3]. GMR multilayers with low coercivity are essential to magnetic industry, and therefore, search for and characterization of these kinds of magnetic materials are the first step for their application. Different modulations of Permalloy (Py) and Co films have drawn attention for a long time due to their low coercivity, and possibly a high GMR value [4]. The combination of these hard and soft magnetic layers with a non-magnetic metallic spacer also gives rise the so-called spin valve (SV) effect and hence the

Mat. Res. Soc. Symp. Proc. Vol. 517 © 1998 Materials Research Society

SV GMR. In this proceeding we report on the studies of Py/Cu/Co sandwich films which show AMR, GMR and SV GMR depending on the thickness of the Cu spacer.

EXPERIMENT

$Py_{5nm}/Cu_t/Co_{5nm}$ sandwich films were sputtered at room temperature respectively on glass, Si(100), and Si(111) in a high vacuum system with a base pressure better than 3×10^{-7} torr. The Ar pressure was kept at about 5 mtorr for all films during deposition. The growth rate of each layer was set at about 0.1~0.2nm/s. The thickness of Cu, t, was varied from 2 to 7nm, while the Py and Co films were fixed at 5nm. Transverse and longitudinal MR ($MR_\perp$, $MR_\parallel$) were used to examine the magneto-transport properties, while longitudinal magneto-optical Kerr effect (LMOKE) was employed for magnetic hysteresis measurement. The sample was about 5mm$\times$ 3mm and the voltage terminals were separated by 2mm. A constant current of 10mA was passed into the sample during the MR measurement. For checking the possibility of canted magnetization, external field can be applied normal to the sample surface during the MR (PMR) and MOKE (PMOKE) measurement. Furthermore, sample can be rotated about its surface normal during the LMOKE measurement and the anisotropic behavior can then be studied.

RESULTS AND DISCUSSIONS

Fig.1a shows the coercivity of the sandwich films as a function of t on different substrates as extracted from MR and LMOKE measurement. According to angularly resolved LMOKE data (not shown here) the sample with t=3nm on Si(111) shows strong uniaxial anisotropy. Uniaxial behavior is not present in films on glass and Si(100), apparently due to the superposition of cubic and induced unaxial anisotropy [5]. Angular LMOKE revealed that samples on Si(111) tend to become isotropic as the Cu thickness is increased, on the other two substrates, however, the shape of the loop does not change too much. Intriguingly, AMR was observed for films on glass and Si(100) but not very clear on Si(111). Fig.1b-1d plots the MR measurements as a function of Cu thickness on different substrates.

Selected MR loops for t = 3 and 7nm are shown in Fig.2 and Fig.3. For films on glass, the MR increases gradually as t is increased. AMR was detected for films on glass with x below 3nm (Fig.2a and 2b), and the films show GMR for x beyond 4nm. The maximum values of transverse and longitudinal MR of this system are 1.6% at x=6nm and 1.75% at 7nm, respectively. Films on Si(100) also exhibit AMR at t = 2nm. The maximum values of $MR_\perp$ and $MR_\parallel$ in this series are 2.3% at x=3nm, and 2.2% at x=6nm, respectively. For samples on Si(111), a maximum change of 2.2% appears at 5nm in $MR_\perp$ and 1.7% in $MR_\parallel$ at the same thickness of Cu. It should be noted that all samples exhibit SV GMR for a thick Cu spacer. This is because the coupling between

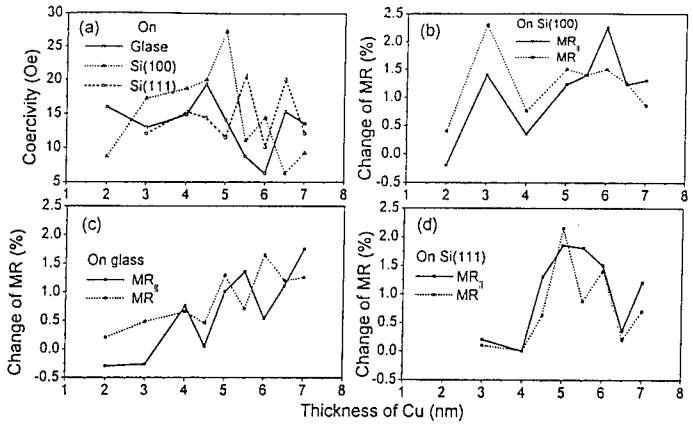

Fig.1

(a) The coercivity of samples on different substrates

(b), (c), and (d) show the change of Transverse and longitudinal MR on indicated substrates. Lines are guides for eyes only.

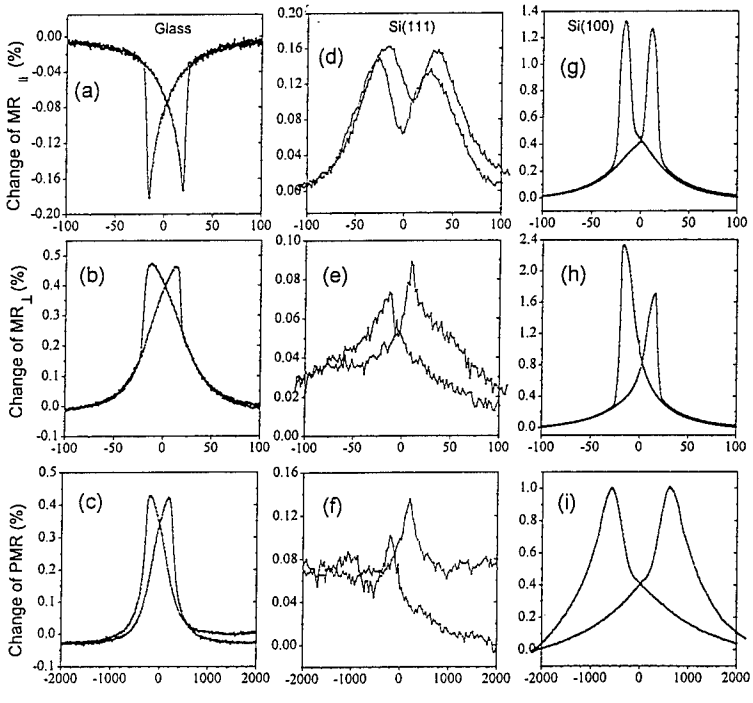

Fig.2, MR for sample of $Py_{5nm}/Cu_{3nm}/Co_{5nm}$ on:

glass- the first colum, on Si(111)- the second colum, and on Si(100)-the last colum.

The last row of this figure shows PMR which indicates for canted magnetisation.

these two ferromagnetic layers is reduced as t is increased.

The non-vanishing MR with applied field normal to the film was also observed, as seen in Fig.2c, 2f, 2i, and Fig.3c, 3f, 2i. This indicates the presence of canted magnetization, as was also confirmed by polar MOKE (PMOKE). Perpendicular or canted magnetization of permalloy film has been reported elsewhere [5] and is not surprising in these samples. However, the MR curves for some samples are complicated as seen in Fig.2d, and Fig.3a. This could be due to a superposition of the GMR and AMR, and also due to a contribution of the normal component of magnetization.

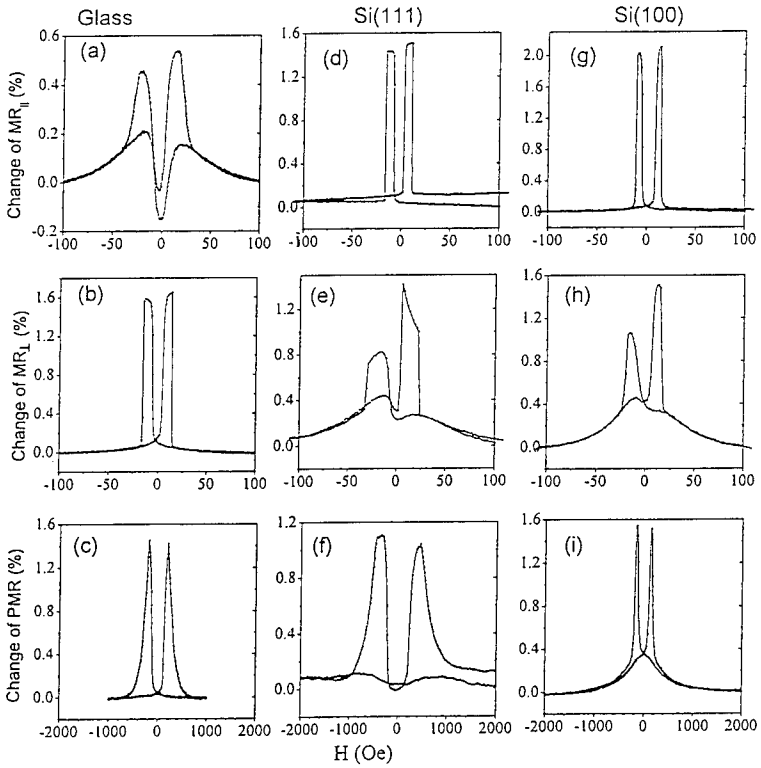

Fig.3, MR for sample of $Py_{5nm}Cu_{7nm}/Co_{5nm}$ on:
Glass-first column, Si(111)-second column, and Si(100)- last column.
The last row shows PMR.

Fig.4a and 4b shows a major and minor MR loops for the sample of $Py_{5nm}/Cu_{7nm}/Co_{5nm}$ on Si(100). Clearly, two magnetic states exist at zero field, as is desirable for permanent storage. The Py layer is softer and easier to rotate with external field, and this results in SV GMR. It is noted in Fig.4 that the MR state of minor loop in the negative field traces the major loop on the same side exactly, however, the loop goes back on different way. This is because an additional field is needed to overcome the bias from the Co layer on the negative side, and therefore, asymmetric R-H curve about the origin is resulted. All samples with t thicker than 5nm exhibit this SV GMR.

We have also increased the periodicity n to study whether the MR would be enhanced further. Our results show that MR is increased to about 3% for n=2 on Si(100), however, the coercivity is also raised up from 5Oe to 100Oe. This research still continues.

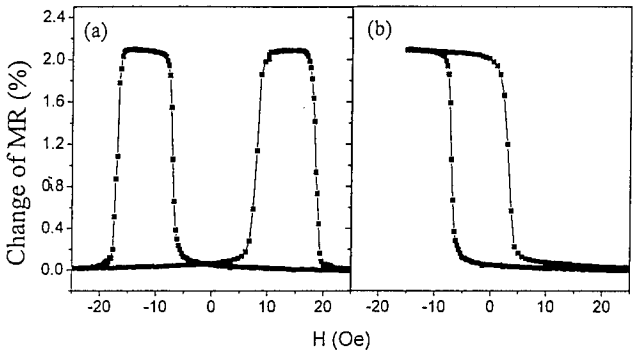

Fig.4 MR of $Py_{5nm}/Cu_{7nm}/Co_{5nm}/Si(100)$
(a) major loop, and (b) minor loop
It should be noted that there are two magnetic sates at zero field.

CONCLUSIONS:

The magnetic behavior of $Py_{5nm}/Cu_t/Co_{5nm}$ sandwich films on glass, Si(111), and Si(100) have been studied. The magnetization of these systems is canted out-of-plane. The strength of the coupling between two ferromagnetic layers is reduced as the thickness of the Cu space is increased, and SV GMR is resulted for Cu spacer thicker than 5nm. We also demonstrate possible magnetic memory states. The asymmetry of the R-H minor loop about the origin comes from the bias of the Co layer. MR will be enhanced further as n is increased; these results will be analyzed and reported later.

ACKNOWLEDGMENTS

This work is supported by Ministry of Economic Affair, ROC under the grant of 87-EC2-A-17-0212

REFERENCES

1. Magnetic field sensor, for example, products from Honeywell Inc.
2. J.J. Fernandez-de-Castro, C.S. Mowry, J. Ding, J. Giusti, D. Saunders, J. Appl. Phys. **81** (8) p.4887 (1997)
3. J.L. Brown and A.V. Pohm, IEEE Trans. Comp. Pack. Manu. Tech. Part A, Vol.17, No.3, p.373 (1994)
4. L.H. Bennett and R.E. Watson (Editors), "Magnetic Multilayers", p.360, World Scientific Publising Co. Pte. Ltd. (1994)
5. C.K. Lo, I. Klik, C.H. Ho, C.J. Chang, Y. Liou, Y.D. Yao, IEEE Trans. Magn. Vol.33, No.5, p3526 (1997)

THE GMR EFFECT OF PERMALLOY/CU MULTILAYERS ON Si(100) AND Si(111)

C. H. Ho[a], C. K. Lo[b], Y. D. Yao[c], S. F. Lee[c], I. Klik[c], M. T. Lin[a], Y. Liou[c], D. Y. Chiang[b], and D.R.Huang[b]

[a]Department of Physics, National Taiwan University, Taipei, Taiwan.

[b]Magnetic Tech.Dept., Opto-Electronics & System Laboratories, Industrial Technology Research Institute, Hsinchu, Taiwan.

[c]Institute of Physics, Academia Sinica, Taipei, Taiwan.

ABSTRACT

[Permalloy$_{1.5nm}$/Cu(t)]n multilayers with a 5 nm thick Fe buffer layer were sputtered on Si(100) and Si(111). Under the same preparation condition, the giant magnetoresistance (GMR) ratio of the multilayers on Si(100) is always larger than that on Si(111). The GMR ratio is very sensitive to the Ar gas pressure during sputtering. We found that 2 m Torr is the optimum discharge gas pressure. Electrical and magnetic properties of permalloy/Cu multilayers with a Cu layer thickness (t) near its second oscillatory peak were reported. We conclude that the GMR ratio of the [permalloy/Cu(t)]n multilayers was strongly dependent on the Cu layer thickness t, on the periodicity number n, and on the (100) crystalline orientation of the Si substrate.

INTRODUCTION

Permalloy(Py)/Cu multilayers with giant magnetoresistance (GMR) effect have been intensively studied recently due to their potential applications in magnetic recording [1-6]. However, many conflicting results between these studies have been reported. According to these previous studies, it seems that the GMR effect is significantly changed with deposition techniques, such as ion beam, DC and RF magnetron sputtering. The preparation conditions, base and sputtering pressures, for examples, also have effect on the GMR ratio [5,6]. In general, the GMR amplitude can be modified by inserting spin dependent scatterers at the interfaces [7] or by roughening the interfaces [8,9]. It was also reported that the GMR ratio at room temperature near the second antiferromagnetic (AF) coupling peak was very sensitive to the sample preparation condition. This motivates us to study the physical properties of magnetic multilayers under different preparation conditions. In this paper we report the GMR response at room temperature for DC magnetron sputtered permalloy/Cu multilayers with a Cu layer thickness near the second oscillatory peak [1].

Mat. Res. Soc. Symp. Proc. Vol. 517 © 1998 Materials Research Society

EXPERIMENT

Prior to the growth of permalloy/Cu multilayers, a 5 nm thick Fe buffer layer was deposited on Si(100) and Si(111) wafers. All films were grown by DC magnetron sputtering in a high vacuum system with a base pressure of 5×10^{-7} torr. The high purity Ar gas pressure was kept at 2 or 5 m Torr during the deposition. The distance between the target and the substrate was about 15cm, while the samples were grown at an oblique angle of about 10°. The film thickness was controlled by a quartz thickness monitoring system calibrated by Rutherford back scattering. The MR was measured at room temperature by using a standard 4-point-probe. The magnetic hysteresis loops was examined by longitudinal magneto-optical Kerr effect (LMOKE). In additions, the samples were rotated about their surface normal during the measurement to characterize the anisotropic behavior of GMR effect and magnetic hysteresis.

RESULT AND DISCUSSIONS

Fig. 1a shows the GMR ratio of the multilayers $(NiFe_{1.5nm}/Cu_t)_{30}$ with Fe buffer layer of 5nm on Si(111) [circles] and on Fe_{5nm}/Si(100) [dots] as a function of the Cu thickness, t. These samples were prepared with the Ar pressure of 5 mTorr. It is found that a maximum MR ratio of about 1.5% for sample on Si(100) and of about 0.6% for sample on Si(100) appears at t=1.9nm. Typical MR-H loops of $(Py_{1.5nm}/Cu_{2nm})_{30}$ multilayers on Fe_{5nm}/Si(111) [top curve] and on Fe_{5nm} /Si(100) [bottom curve] are selected and shown in Fig.1b. Clearly, the GMR ratio of the multilayers on Si(100) is always larger than that on Si(111) under the same preparation condition.

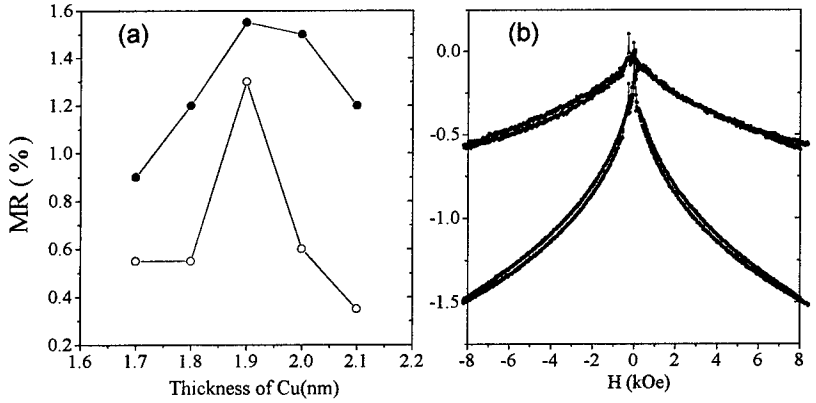

Fig.1
(a) The MR ratio of $(Py_{1.5nm}/Cu_t)_{30}$ on Si(100) [upper curve] and on Si(111) [lower curve.
(b) MR of $(Py_{1.5nm}/Cu_{19nm})_{30}$ [upper curve] and on Si(111) [lower curve].

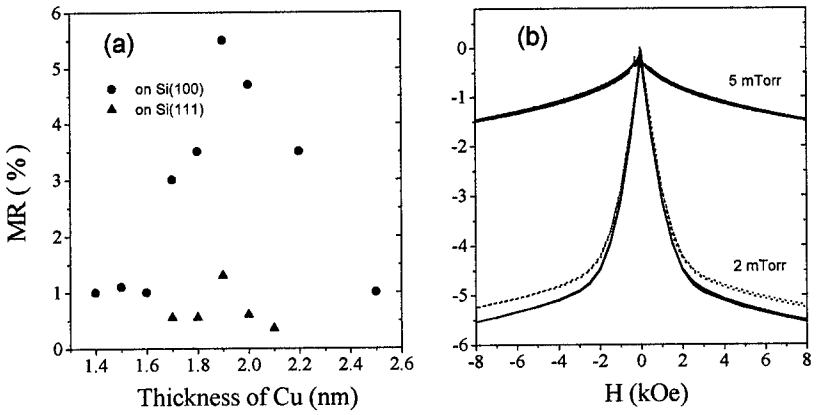

Fig.2
(a) The MR ratio of $[Py_{1.5nm}/Cu_t]_{30}$ on Fe_{5nm}/Si(100) as a function of copper thickness, t, prepared at 2 mTorr (circle) and 5 mTorr (triangle).
(b) Sample with t=1.9nm at different Ar pressures as indicated.

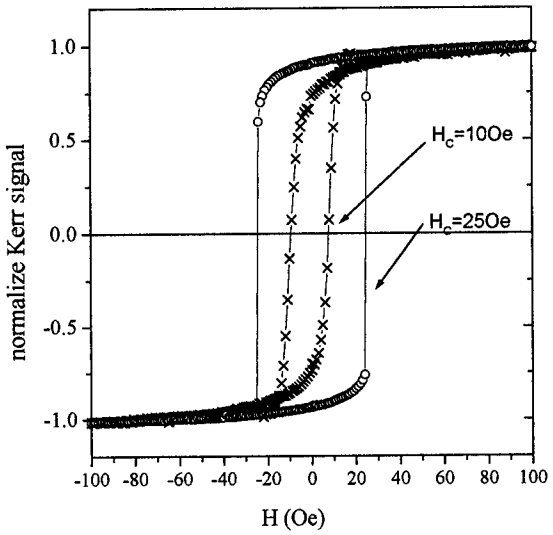

Fig.3
The normalised LMOKE signal of $(Py_{1.5nm}/Cu_t)_{30}$ on Fe_{5nm}/Si(100) with t=1.9nm (cross) and t=1.4nm (circle).

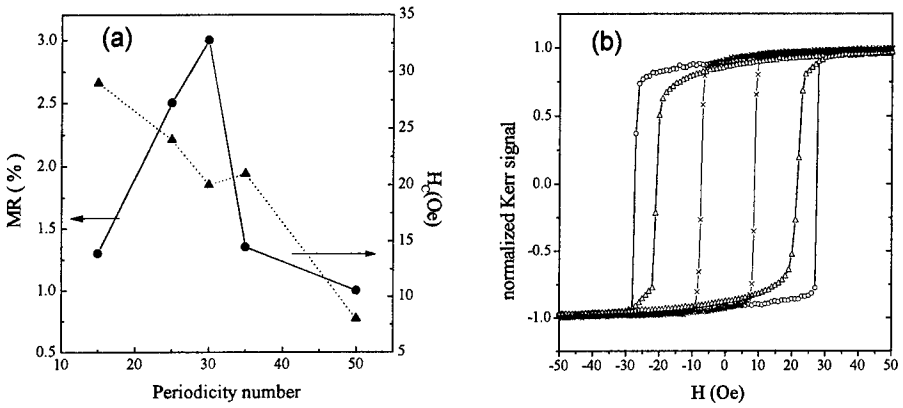

Fig.4
(a) The GMR ratio and the coercivity for the sample of$(Py_{1.5nm}/Cu_{1.7nm})n/Fe_{5nm}/Si(100)$
(b) LMOKE signal of $(Py_{1.5nm}/Cu_{1.7nm})_n/Fe_{5nm}/Si(100)$ for n=15 (circles) and, 30 (triangles), and 50 (crosses).

In order to study the influence of discharge Ar pressure, $Fe_{5nm}(Py_{1.5nm}/Cu_t)_{30}$ was prepared on $Fe_{5nm}/Si(100)$ with Ar pressure of 2 mTorr and 5 mTorr, respectively as seen in Fig.2a for different thickness of Cu spacer. The maximum value of MR was found at t = 1.9nm even at different sputtering . Their MR-H loops are shown in Fig.2b that the top curve with GMR ratio of roughly 1.5% represent the sample prepared under a discharge gas pressure of 5 m Torr, and the bottom curves with GMR ratio of roughly 5.5% represent the sample prepared under a discharge gas pressure of 2 m torr. Interestingly, samples prepared at different Ar pressures have remarkable effect on the GMR ratio. The GMR effect is also sensitive to the thickness of the spacer between two ferromagnetic layers as have seen in Fig.1a and Fig.2a. It is clear that the GMR ratio is not only sensitive to the discharge gas pressure, but also the spacer thickness.

Fig. 3 plots the normalized MOKE signal for the multilayer of $(Py_{.5nm}/Cu_t)_{30}/Fe_{5nm}/Si(100)$ with t = 1.9 nm [crosses] and t = 1.4 nm [circles]. The coercivity and normalized remanance drop down from 25 Oe and 0.95 at t = 1.9nm to 10 Oe and 0.75 at t = 1.4nm, respectively. The coercivity and the normalized remanance are significantly reduced. Since the multilayer with Cu spacer thickness of 1.9nm is very close to the second oscillatory peak, and hence a comparable increment of antiferromagnetic coupling between magnetic layers.

The influence of periodicity number n on magnetic hysteresis and GMR effect is also studied. Fig.7 plots the GMR ratio and the coercivity for the sample of $(NiFe_{1.5nm}/Cu_{1.7nm})_n/Fe_{5nm}/Si(100)$ as functions of n. The maximum MR ratio of ~3% was found for sample with n equals 30. Fig.6 shows the LMOKE signal of $(NiFe_{1.5nm}/Cu_{1.7nm})_n/Fe_{5nm}$ /Si(100)

with n = 15[circles], 30[triangles], and 50[crosses], respectively. The coercivity decreases as n is increased. This is because the permalloy is dominant the whole magnetic behavior as n is increased.

CONCLUSION

In summary, we have reported the studies of GMR and the magnetic hysteresis at room temperature for [permalloy/Cu(t)]n multilayers with a 5 nm thick Fe buffer layer on Si(100) and Si(111) near its second antiferromagnetic oscillatory peak. Under the same preparation conditions, the GMR ratio of the multilayers on Si(100) is always larger than that on Si(111). The GMR ratio of the [permalloy/Cu(t)]n multilayers was strongly dependent on the crystalline orientation of the Si substrate, on the Ar pressure, on the Cu spacer thickness t, on the periodicity number n. We also found that 2 m torr was the optimum discharge gas pressure.

REFERENCES

1. S. S. P. Parkin, Appl. Phys. Lett. **60**, 512 (1992).
2. M. Sato, S. Ishio and T. Miyazaki, J. Magn. Magn. Mater. **126**, 460 (1993).
3. T. Dei, R. Nakatani and Y. Sugita, Jpn. J. Appl. Phys. **32**, 1097 (1993).
4. M. Naoe, Y. Miyamoto and S. Nakagawa, J. Appl. Phys. **75**, 6525 (1994).
5. M. Mao, C. Cerjan, M. Gibbons, B. Law, F. Grabner, S. P. Vernon and M. Wall, Intermag '97 CP-11; to be published.
6. Y. Huai, M. Tan and R. Rottmayer, Intermag '97 CP-12; to be published.
7. B. A. Gurney, P. Baumgart, D. R. Wilhoit, B. Dieny and V. S. Speriosu, J. Appl. Phys. **70**, 5867 (1991).
8. E. F. Fullerton, D. M. Kelly, J. Guimpel, I. K. Schuller and Y. Bruynseraede, Phys. Rev. Lett. **68**, 859 (1992).
9. Y. D. Yao, Y. Liou, J. C. A. Huang, S. Y. Liao, I. Klik, W. T. Yang, C. P. Chang and C. K. Lo, J. Appl. Phys., **79**, 6533 (1996).

Inductively Coupled Plasma Etching of NiFe and NiFeCo

K.B.Jung*, J.R.Childress*, S.J.Pearton*, M.Jenson**, A.T.Hurst,Jr.** and D.Johnson***
*Dept. Materials Science and Engineering, University of Florida, Gainesville FL 32611
**Solid State Electronics Center, Honeywell, Inc., Plymouth MN 55441
***Plasma Therm, St. Petersburg FL 33716

ABSTRACT

The etch yield and rates of $Ni_{0.8}Fe_{0.2}$ and $Ni_{0.8}Fe_{0.13}Co_{0.07}$ in ICP Cl_2-based plasma has been measured as a function of both ion flux and ion energy. At low ion energies ≤100eV, the etch rates peak at 700Å·min^{-1} for Cl_2/Ar plasma chemistry, with somewhat lower rates (~400Å·min^{-1}) for N_2 or H_2 addition. The etch mechanism is formation of $NiCl_X$, $FeCl_X$ and $CoCl_X$ species, which are desorbed by ion-assistance. If the ion-to-neutral ratio is not optimized then the etching reverts to either a pure sputtering regime, or to net deposition through formation of a thick chlorinated selvedge layer on both NiFe and NiFeCo. Under ICP conditions other materials comprising a GMR stack, including Cu, TaN and CrSi, can also be etched. Each selectivities over SiO_2 and SiN_X masks are low and are typically under unity.

INTRODUCTION

The push to higher bit densities in magnetic storage devices requires the development of methods for producing large numbers of sub-micron metallic multilayer structures.[1-4] Since most of the materials used in magnetic multilayers (e.g. NiFe, NiFeCo, Cu) are relatively involatile in normal dry etching techniques (see for example Table I) such as reactive ion etching, then it is usual to employ ion milling.[5-10] A problem often encountered with this technique is redeposition onto the sidewall of the features being patterned, which may degrade the magnetic performance of the device. This redeposition occurs because there is no formation of a volatile etch product in ion milling. Magnetic read/write heads based on giant magnetoresistance (GMR) and radiation hard, non-volatile memory such as Magnetoresistive Random Access Memory (MRAM) are two of the key areas requiring advanced pattern transfer processes.[11] In this paper we investigated etch yields and rates of NiFe and NiFeCo in ICP Cl_2-based discharge with addition of Ar, H_2 and N_2. Selectivities over SiO_2 and SiN_X and feature anisotropy were also examined.

EXPERIMENTAL

Layers of $Ni_{0.8}Fe_{0.2}$ or $Ni_{0.8}Fe_{0.13}Co_{0.07}$ ~5,000Å thick were deposited on Si substrates by dc magnetron sputtering. For measurement of etch selectivity with respect to common mask materials. We also deposited 3,000Å thick layers of plasma enhanced, chemical vapor deposited SiO_2 or SiN_X on Si substrates. All samples were lithographically patterned with AZ5209E resist. Etching was performed in a Plasma Therm 790 ICP system. Samples were thermally bonded to a Si carrier wafer which was mechanically clamped to a rf-powered (13.56MHz, 0-450W), He backside cooled chuck. The power on this chuck controls the incident ion energy. A 3-turn coil ICP source operating at 2MHz and powers up to 1000W was used to generate the plasmas. The

Mat. Res. Soc. Symp. Proc. Vol. 517 © 1998 Materials Research Society

process pressure was held constant at 2mTorr for Cl_2/Ar, Cl_2/H_2 and Cl_2/N_2 with a total gas flow rate of 15 standard cubic centimeters per minute (sccm).

Stylus profilometry of the etched features after removal of the resist was used to obtain etch rates, while etch yields were obtained using the model of Lee et al.[12] to calculate ion fluxes at different plasma conditions.

Table I. Boiling points of potential etch products in ICP etching of metals.

Products	Boiling point (°C)	Products	Boiling point (°C)
$TaCl_5$	239.35	$NiCl_2$	subl 973
NCl_3	71	$FeCl_3$	316
$CrCl_4$	dec>600	$FeCl_2$	1023
$CrCl_3$	dec 1300	$CoCl_3$	.....
$CrCl_2$	1300	$CoCl_2$	1049
O_2Cl_2	3.8 exp	$SiCl_4$	57.65
OCl_2	9.9 exp	O_2	-183

RESULTS AND DISCUSSION

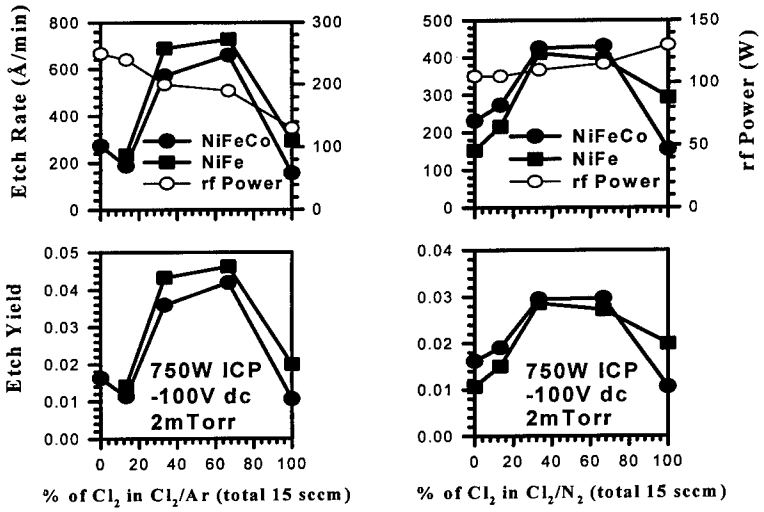

Figure 1. Etch rates and etch yields of NiFeCo and NiFe as a function of plasma composition in ICP Cl_2/Ar discharges (left) and Cl_2/N_2 discharges (right)

Figure 1 (left) shows the etch rates and etch yields for NiFe and NiFeCo as a function of Cl_2 percentage in Cl_2/Ar discharges at fixed ICP source power (750W) and dc self-bias (-100V). To maintain the fixed self-bias, the rf chuck power was adjusted , as shown in the top part of the figure. The etch rates initially increase as Cl_2 is added to the discharge, indicating there is a chemical enhancement present in the etch mechanism. We have previously interpreted such behavior as indicating the $NiCl_X$, $FeCl_X$ and $CoCl_X$ etch

products are being efficiently removed by ion-assistance, provided the ion/neutral ratio does not become too small.[13] Beyond ~66% Cl_2, the etch rates and yields begin to decrease and this is likely a result of formation of a thick chlorinated selvedge layer that limits the removal rate of the etch products. Note from the etch yield data that ≥20 ions are needed to remove one atom of the magnetic layers. This shows why conventional reactive ion etching cannot achieve practical etch rates for these materials, because the ion densities are more than two orders of magnitude lower than in an ICP tool.

Similar data is shown in Figure 1 (right) for the Cl_2/N_2 plasma chemistry. The same basic trends are evident as were seen with Cl_2/Ar, but the overall etch rates and etch yields are lower, probably because N_2^+ and N^+ ions are less efficient at helping desorb the chloride etch products than are the heavier Ar^+ ions. Cl_2/N_2 discharges have previously been reported to produce more atomic chlorine neutrals than Cl_2/Ar, but if that indeed is the case it does not assist the etch rate in our case because product desorption is the limiting step, not chlorine supply.

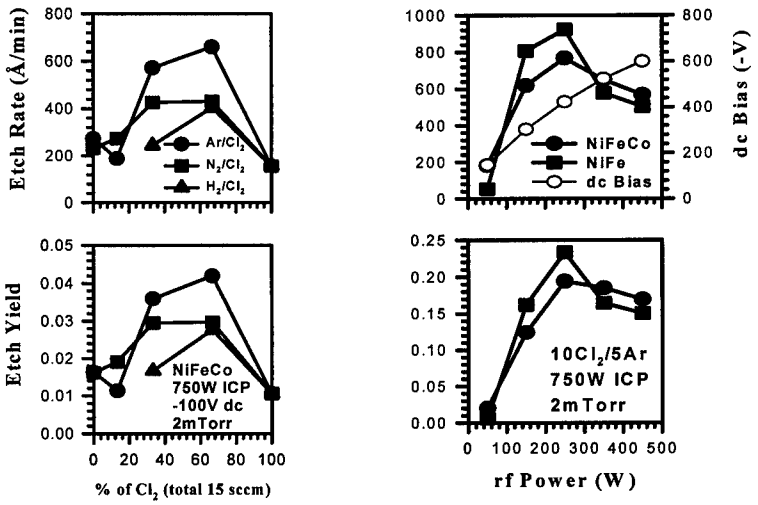

Figure 2. Etch rates and etch yields of NiFeCo as a function of plasma composition in ICP Cl_2/Ar, Cl_2/N_2 and Cl_2/H_2 discharges (left) and NiFe and NiFeCo as a function of rf chuck power in $10Cl_2/5Ar$, 750W source power discharges (right)

Figure 2 (left) shows results for NiFeCo etching in the three different plasma chemistries investigated, namely Cl_2/Ar, Cl_2/N_2 and Cl_2/H_2, as a function of plasma composition. The results show quite clearly that in terms of etch rates and etch yields, Ar addition produces the highest values, and this is most likely due to its better sputtering efficiencies.

Apart from plasma composition, another key parameter is ion energy, which is controlled by rf chuck power. Figure 2 (right) shows etch rates and etch yields for NiFe and NiFeCo in $10Cl_2/5Ar$ discharges at fixed ICP source power (750W). The etch rates initially rise rapidly with rf chuck power, consistent with enhanced removal of the etch products by the more energetic ions. However, above a bias of ~-400V, the rates

decrease. This is often observed in high density plasma etching,[14] and is generally ascribed to sputter-enhanced removal of the neutral chlorine atoms before they can react with the magnetic films.

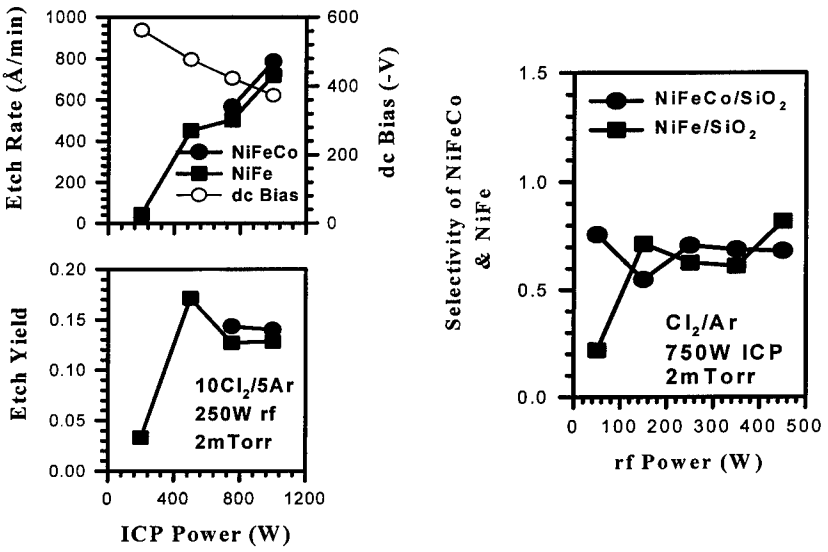

Figure 3. Etch rates and etch yields of NiFeCo and NiFe as a function of ICP source power in $10Cl_2/5Ar$, 250W rf chuck power discharges (left) and selectivity of NiFeCo and NiFe over SiO_2 in 750W ICP source power discharges of Cl_2/Ar as a function of rf power (right)

The previous results have shown that the etch rates of the magnetic material are a strong function of both ion-to-neutral ratio and ion energy. The third parameter of interest is the ion flux, which is controlled by the ICP source power. Figure 3 (left) shows the influence of this source power on NiFe and NiFeCo etch rates and yields in $10Cl_2/5Ar$ discharges at fixed rf chuck power (250W). Since ion density increases under these conditions, the dc self-bias decreases with source power. The etch rates continue to increase with ion flux, while yield saturates or decreases. This is expected since at some point we would expect that the etching would become reactant-limited and that too high an ion flux might desorb chlorine neutrals before they can react with the magnetic materials. A final thing to note is the very low etch rates measured at low ICP source powers, which shows why reactive ion etching does not produce sufficient removal rates for these materials.

The final area of interest when considering a process for the patterning of magnetic thin films is the availability of suitable masks. A typical MRAM stack is only ~1500Å thick, and therefore etch selectivity of NiFe and NiFeCo with respect to mask materials is not that important, though in read/write heads there are some applications requiring deeper etches. The chlorinated products for SiO_2 and SiN_X are quite volatile, and we might expect that they will not provide much etch resistance under high density

plasma conditions. Figure 3 (right) shows the selectivities of NiFe and NiFeCo in Cl_2/Ar discharges at fixed source power(750W), as a function of rf chuck power. The selectivities are low, as expected, and are typically under unity for Cl_2/Ar plasma chemistry. We have found that when careful attention is paid to avoiding sample heating effects during etching, by use of He backside cooling, that photoresist can be a suitable mask for relatively deep etching(>1μm) of NiFe and NiFeCo in the halogen chemistries investigated here.

We found that photoresist was generally not suitable as an etch mask for MRAM. Figure 4 shows SEM micrographs of features etched into NiFe using a $10Cl_2/5Ar$, 1000W ICP plasma and a SiO_2 mask (left). SiO_2 was forced to provide superior masking characteristic. The resist is severely degraded by exposure to the high ion flux, Figure 4 (right), we can observe rough edges in the NiFe feature due to the irregular flow of the resist.

15KV ×8600 1μm UFMSE

15KV ×8600 1μm UFMSE

Figure 4. SEM micrographs of features etched with NiFe using $10Cl_2/5Ar$, 200W rf, 2mTorr, 750W ICP source power discharge, using either SiO_2 (left) or photoresist (right) as the masking materials

SUMMARY AND DISCUSSION

Cl_2/Ar, Cl_2/N_2 and Cl_2/H_2 plasma chemistries for high density plasma etching of NiFe and NiFeCo were investigated. The etch rates are a strong function of ion-to-neutral ratio, ion flux and ion energy. The data are consistent with efficient ion-assisted desorption of the fully- or partially-chlorinated etch products, thus overcoming their inherent low volatilities. We do not observe redeposition on feature sidewalls, suggesting that the mean free paths of these desorbed products is reasonably long. We have also found that poor selectivities over SiO_2 and SiN_X masks are obtained when using Cl_2-based plasma chemistries. The low etch yield obtained with Cl_2-based plasma chemistry emphasize the need for high density conditions in order to achieve practical etch rates.

ACKNOWLEDGMENTS

The work at UF and Honeywell is partially supported by ONR contract N00014-96-C-2114 and at UF by a DOD MURI (contract F49620-96-1-0026) monitored by Air Force Office of Scientific Research (H. C. DeLong).

REFERENCES

1. G. A. Prinz, in Ultra-Thin Magnetic Structures II, ed. B. Heinrich and J. A. C. Bland (Springer-Verlag, Berlin, 1994).
2. R. Giridhar, Jpn. J. Appl. Phys. 35 6347 (1996).
3. C. Tsang, M. Chen, T. Yogi and K. Ju, IEEE Trans. Magn. 30 281 (1994).
4. F. C. M. J. van Delft, J. Magn. Mag. Mat. 140-144 2203 (1995).
5. K. Kinoshita, K. Yamada and H. Matutera, IEEE Trans. Magn. 27 4888 (1991).
6. H. Gokan and S. Eho, J. Vac. Sci. Technol. 18 23 (1981).
7. M. Balooch, D. S. Fischl, D. R. Olander and W. J. Siekhaus, J. Electrochem. Soc. 135 2090 (1988).
8. D. S. Fischl and D. W. Hess, J. Vac. Sci. Technol. A4 1841 (1986).
9. D. W. Hess, Plasma Chem. Plasma Proc. 2 141 (1982).
10. M. J. Vasile and C. J. Mogab, J. Vac. Sci. Technol. A4 1841 (1986).
11. see for example, Physics Today, April 1995, ed G. A. Prinz and K. Hathaway.
12. J. W. Lee, C. R. Abernathy, S.J. Pearton, C. Constantine, R. J. Shul and W. S. Hobson, Plasma Source Sci. Technol. 6 499 (1997).
13. K. B. Jung, E. S. Lambers, J. R. Childress, S. J. Pearton, M. Jenson and A. T. Hurst, Jr., J. Vac. Sci. Technol. A16 May/June (1998).
14. S. J. Pearton, J. W. Lee, E. S. Lambers, J. R. Mileham, C. R. Abernathy, F. Ren, W. S. Hobson and R. J. Shul, J. Vac. Sci. Technol. B14 188 (1996).

Part III

Spin Tunnel Junctions

MAGNETIC TUNNEL JUNCTIONS WITH LOW RESISTANCE, HIGH CURRENT DENSITY AND GOOD UNIFORMITY

H. TSUGE, T. MITSUZUKA, A. KAMIJO AND K. MATSUDA
Fundamental Research Labs., NEC Corporation, 4-1-1 Miyazaki, Miyamae-ku, Kawasaki 216, Japan

ABSTRACT

We have demonstrated a controllable fabrication process for magnetic tunnel junctions, including *in situ* deposition of a junction trilayer and tunnel barrier formation with *in situ* natural oxidation of an Al metal layer. The trilayer was patterned into junction structures with dimensions as small as 2x2 μm^2 using photolithography and ion milling. The resultant junction resistance scaled linearly with the junction area over all dimensions used. The normalized resistance values of about $2.4x10^{-6}\ \Omega\ cm^2$ were obtained in maintaining magnetoresistance (MR) ratios of 10 % to 12 % at room temperature. The resistance values are much smaller than ever reported for junctions with tunnel barriers formed using thermal oxidation in air or plasma oxidation. The maximum variation of the resistance was ± 6.5 % for 10x10 μm^2 over a 2-inch wafer. The MR ratios showed no significant change up to at least $1x10^4$ A/cm^2 as junction current density was increased. The process used in this work can be expected to satisfy many device applications such as an MR head and magnetic random access memory (MRAM).

INTRODUCTION

Study on magnetic tunneling effect has become active since large MR ratios were observed in relatively low magnetic fields at room temperature. The observation has attracted much interest from the viewpoint of device applications as well as physics studies. Magnetic tunnel junctions comprise the basic structure, with ferromagnetic electrodes separated by an insulating tunnel barrier. The tunneling electrons strongly depend on the density of states of the majority and minority energy bands at Fermi level in the ferromagnetic electrodes [1-3]. Therefore, when the relative orientation of magnetization in the two electrodes is changed through applying an external magnetic field, the tunneling current or junction resistance can be modulated [3,4]. The junction resistance becomes minimum in the parallel orientation, and maximum in the antiparallel orientation.

The magnetic tunneling effect was first demonstrated between two ferromagnetic electrodes by Julliere in 1975 [2]. For some time, MR ratios as large as predicted theoretically could not be obtained. However, recently, several groups have reported significantly high MR ratios at room temperature [5-8]. Miyazaki and Tezuka [5] found an 18 % value in an Fe/Al_2O_3/Fe junction with a junction area of 1x1mm^2, while Moodera *et al.* [7] reported 22 % in CoFe/Al_2O_3/Co junctions, 0.2x0.3mm^2 in area. Sato and Kobayashi [8] also reported a value as large as 24 % in an exchange-biased type junction with a NiFe/Co/Al_2O_3/Co/NiFe/FeMn multilayer. In this paper, MR ratios are defined as the change in resistance divided by the saturated resistance in order to provide consistency for the reported data. These groups used contact shadow masks to make the junctions. On the other hand, Gallagher *et al.* [9] applied electron-beam lithography and optical lithography in producing NiFe/FeMn/NiFe/Al_2O_3/Co and NiFe/FeMn/NiFe/Co/Al_2O_3/NiFe structures with micron-to-submicron dimensions and obtained MR ratios of up to 22 %. All of the junctions reported have Al_2O_3 tunnel barriers formed by thermal oxidation in air [5,8] or plasma oxidation [6,7,9] of thin Al metal layers. In the conventional methods applied to tunnel

Mat. Res. Soc. Symp. Proc. Vol. 517 © 1998 Materials Research Society

barrier formation, it seems to be difficult to achieve the low junction resistance required for many device applications. This paper reports a junction fabrication technique suitable for obtaining the low resistance and high critical current density in a controllable and reproducible manner. The distinctive feature of the technique is *in situ* deposition of junction layers and tunnel barrier formation with natural oxidation under a controlled oxygen pressure [10].

DEVICE STRUCTURE AND FABRICATION

Figure 1 is a schematic drawing of the magnetic tunnel junctions fabricated in this work. The junctions have the structure of an $Fe/Al_2O_3/Co_{50}Fe_{50}$ trilayer sandwiched with bottom and top Al lead layers in cross-strip geometry. Fe and CoFe were selected as base and counter electrodes simply because they possess different coercivities and have relatively large spin polarizations for ferromagnetic transition metals. Al lead layers were used in order to reduce the junction electrode resistance. If the electrode resistance is not substantially lower than the junction resistance, the electrical properties of the junctions can not be measured accurately because of spatially nonuniform current distribution in the junction electrodes [11-13]. The Al lead layers play an especially important role in our devices with lower resistance values. Figure 1 also shows two different layered structures of type A and type B. The junction area is defined only by the counter electrode in type A, but by both the base and counter electrodes in type B. Both types have very similar electrical properties and uniformity in the properties, primarily, the data for type A are shown in this paper.

The junctions were fabricated using photolithography and ion milling compatible with the process usually employed for commercially available magnetic devices such as MR heads and sensors. A schematic diagram of the fabrication process is illustrated in Fig. 2. First, as shown in Fig. 2(a), an Al(50nm)/Fe(50nm for type A, 10nm for type B)/Al(2nm) multilayer was deposited *in situ* on a 2-inch diameter Si wafer with thermally oxidized SiO_2 on the surface. The Al and Fe layers were deposited under a background pressure of about around $2x10^{-8}$ Torr at room temperature by electron-beam evaporation and rf magnetron sputtering, respectively. Layer thickness was controlled using a quartz-crystal oscillator for evaporation and time-controlled for

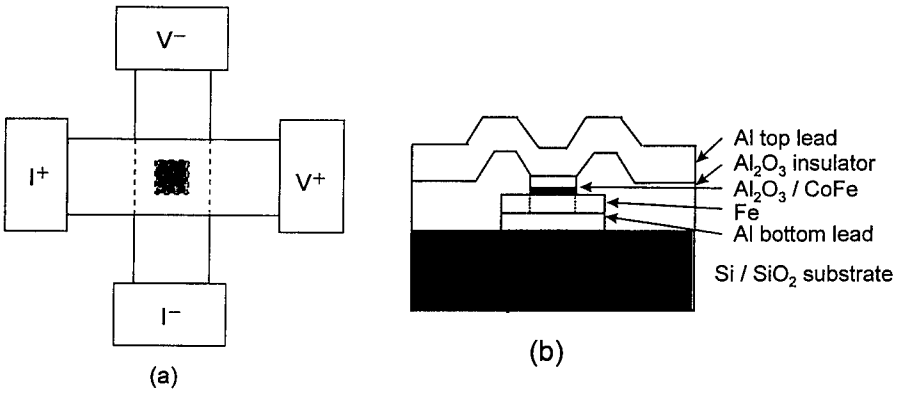

Fig. 1. Schematic top view (a) and cross-sectional view (b) of magnetic tunnel junctions with two different configurations of type A (solid line) and type B (dotted line) for the Fe base electrode. In the top view, the current and voltage leads are labeled with I^+, I^-,V^+ and V^-.

sputtering. The top Al layer was then oxidized normally in pure O_2 of 20 Torr at room temperature for 20 min without breaking vacuum to form an Al_2O_3 tunnel barrier. After pumping down to the background pressure, a $Co_{50}Fe_{50}$ layer of 20 to 30 nm in thickness was evaporated. The multilayer was patterned into the bottom lead shape using a photoresist mask by ion milling [Fig. 2(b)]. The junction areas were then defined by doing ion milling in resist to the surface of the Fe base electrode in type A [Fig. 2(c)], and to the surface of the bottom Al lead layer in type B. Retaining the resist mask, a 300-nm-thick Al_2O_3 layer for insulation was evaporated and lifted off [Fig. 2(d)]. The junctions were completed with the evaporation and lift off of a 200-nm-thick Al layer for the top lead after sputter cleaning the CoFe counter electrode to remove any surface contaminants [Fig. 2(e)]. Sixteen 10x10 mm^2 chips were designed in a 2-inch Si wafer. One chip contains five junctions with junction areas ranging from 2x2 to 40x40 μm^2.

Scanning electron micrographs of a fabricated junction are shown in Fig. 3. The junction area seems to be well defined by the self-aligned process though a little Al_2O_3 residue is observed at the junction edge. The junction interface was characterized by

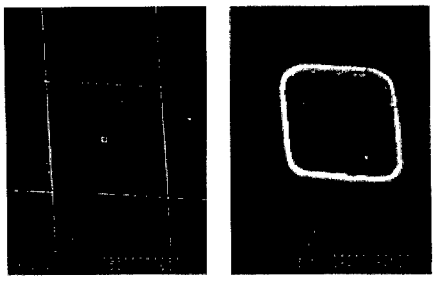

Fig. 3. Scanning electron micrographs of a fabricated junction, 4x4 μm^2 in area. In the left picture, a junction area is visible near the center, which is magnified in the right picture.

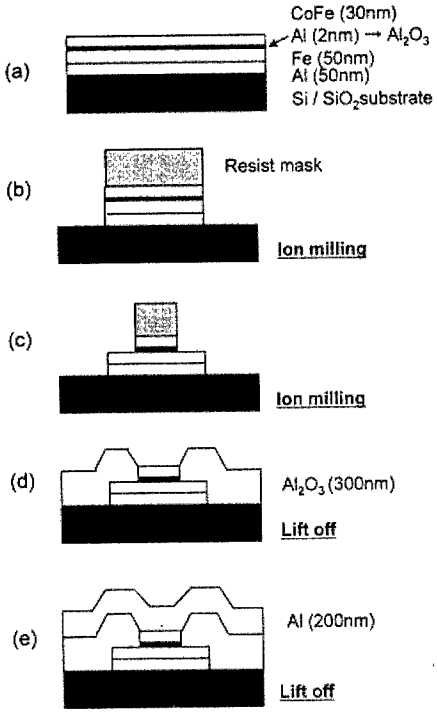

Fig. 2 Schematic of the fabrication process for a tunnel junctions with an Fe/Al_2O_3/CoFe trilayer sandwiched with the bottom and top Al lead layers. The tunnel barrier consisting of Al_2O_3 is formed by *in situ* natural oxidation of a 2-nm-thick Al layer.

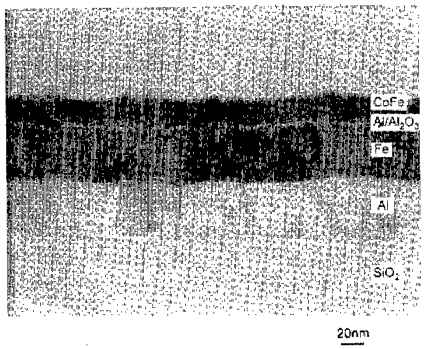

Fig. 4. Cross-sectional transmission electron micrograph of the multilayer structure in the junction area.

using cross-sectional transmission electron microscopy (TEM), atomic force microscopy (AFM) and X-ray photoelectron spectroscopy (XPS). Figure 4 shows the layered structure observed by TEM. The surface of the Fe layer is rather rough, presumably due to the marked growth of its columnar texture. The roughness was evaluated to be about 10 nm in maximum by AFM. This value corresponds to 5 times the thickness of the Al overlayer. Judging from this picture alone, it is not clear if the barrier layer completely covers the Fe underlayer surface, although the barrier layer appears to be continuous.

An XPS study was performed in order to supplement the data obtained from the TEM observation. Figure 5 shows the XPS spectra of Al *2p* and Fe *2p* from the surface of the tunnel barrier. After the sample was prepared in the same way as the device, up to the process of the tunnel barrier in a vacuum chamber, it was transferred *in situ* to the XPS chamber and analyzed. The background pressure was maintained below $4x10^{-9}$ Torr during the analysis. Mg Kα radiation of energy of 1253.6 eV was used as a source of excitation. In the Al *2p* region, both AlO_X and Al metal peaks are observed. The peak position of AlO_X is located at binding energy of 75.4 eV, which is 0.7 eV higher than the expected position of 74.7 eV for Al_2O_3 . These results suggest that some unoxidized Al metal is left after the oxidation process for a 2-nm-thick Al layer and that AlO_X deviates slightly from the stoichiometry of Al_2O_3. On the other hand, in the Fe *2p* region, only Fe metal peaks are identified with the expected binding energies of 706.8 eV for Fe $2p_{3/2}$ and 720.0 eV for Fe $2p_{1/2}$. FeO_X peaks are not observed in the limit of our XPS resolution. The Fe layer seems to be reasonably covered by the Al overlayer in spite of the roughness (up to 10 nm) of the Fe underlayer.

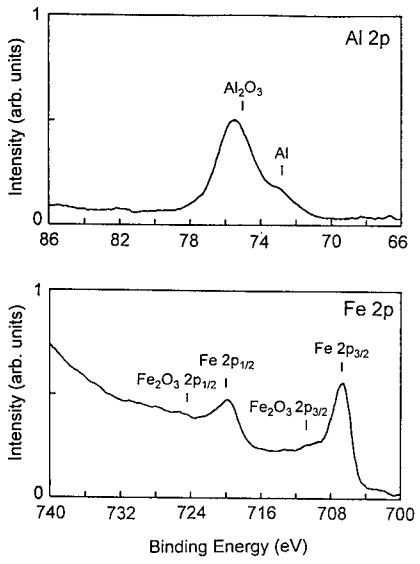

Fig. 5 *In situ* XPS spectra of Al *2p* and Fe *2p* detected from the tunnel barrier, which was formed by *in situ* naturally oxidizing the surface of Al(50nm)/Fe(50nm)/Al(2nm) trilayer.

RESULTS AND DISCUSSION

The electrical properties of the fabricated junctions were measured using a four-probe dc method in ambient atmosphere. A magnetic field was applied to the longer direction of the bottom lead layer for MR measurements. In addition to the low-resistance leads consisting of Al, the smaller junction configuration defined by photolithography was advantageous to obtain accurate electrical properties.

Prior to measuring MR, the differential conductance of the junctions was measured as a function of voltage to confirm that the transport was dominated by electron tunneling, as shown in Fig. 6. The characteristics exhibited a parabolic dependence at voltages of less than about 60mV. This means that the transport mechanism is primarily based on tunneling. From the fitting of the experimental data to Simmons' theory of tunneling [14], the mean barrier height

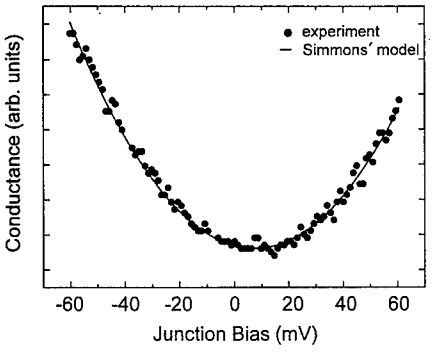

Fig. 6. Differential conductance as a function of dc bias for an $Fe/Al_2O_3/CoFe$ junction at room temperature.

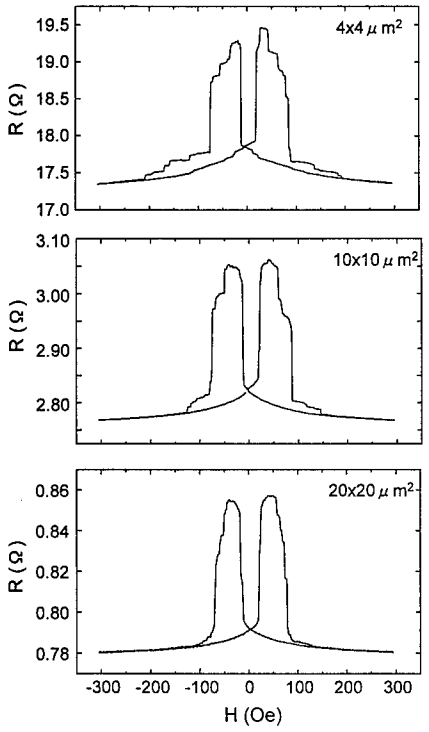

Fig. 7. Magnetoresistance curves for the junctions with the different junction areas.

and thickness were derived to be in the range of 0.6 to 0.7 eV and 1.1 to 1.2 nm for several junctions. These values are relatively small compared with those reported for thermal oxidation in air [8] and plasma oxidation [6,7]. This results in lower resistances in our junctions. The offset voltage of about 7 mV seen in Fig.6 is probably due to the barrier height difference between both interfaces.

Figure 7 shows the MR curves for the junctions with various junction areas. The marked changes in resistance at around 20 Oe and 80 Oe correspond to the coercivities for the Fe base and CoFe counter electrodes, respectively. Numerous random resistance steps are also observed for small junctions as shown in Fig. 7. The steps become clearly discernible with decreasing junction area. Such phenomena were not visible for large junctions with millimeter-order dimensions, which were prepared previously using a metal mask. This suggests that the resistance steps reflect magnetic domain-wall motion in the junction electrodes. Moreover, for junctions with type B structures, another phenomenon was viewed, i.e. the resistance in zero field was much higher than that expected for the parallel orientation of the magnetizations and the slope of the curve in the lower field range was very broad. This tendency became distinct when junction area was decreased to 2x2 μm^2. This is apparently due to the antiferromagnetic coupling of both electrodes caused by the magnetostatic fields generated at the junction edges.

Figure 8 shows junction resistance as a function of junction area for junctions in a wafer. Data for a line of three chips traversing the center of the wafer are plotted. The slope of the solid line, fitted using a least square technique, is a minus unit (-1) with a deviation of less than 1% in logarithmic coordinates. This means that the resistance scales linearly with the junction area over all dimensions used. From the slope in Fig.8, the resistance normalized with the junction area is evaluated to be $2.4x10^{-6}\ \Omega cm^2$. This value is much smaller than ever reported for thermal oxidation in air and plasma oxidation. The maximum variation of the resistance is ± 6.5 % for

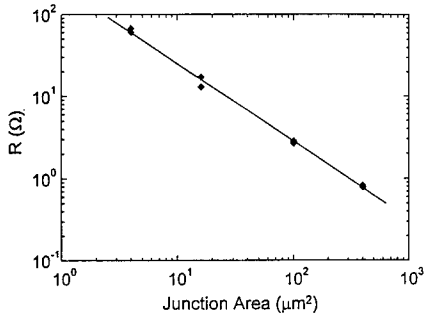

Fig. 8. Tunneling resistance vs junction area for junctions with the area of 10x10 μm^2 in a 2-inch Si wafer. The experimental data are fitted with a least square method (solid line). The slope is -0.997.

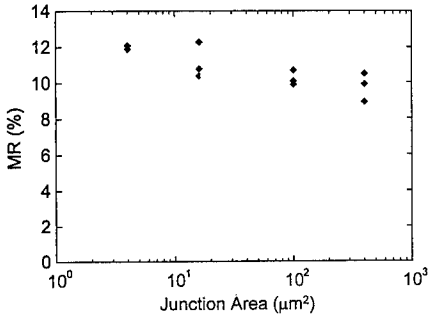

Fig. 9. MR ratio vs junction area for the same samples as in Fig. 8.

junctions with the area of 10x10 μm^2 over a wafer. This variation is presumably related to the quality of each junction because the value is too large to be attributed to the microfabrication process used. MR ratios are in the range from 9.0 % to 12.3 % for the junction areas defined in this experiment and exhibit no significant dependence on the area, as shown in Fig. 9. Although these values are approximately 50 % of the best data reported for junctions with much higher resistance values, the scatter of the values is reasonably small.

As described above, low resistance junctions were successively fabricated with good uniformity in junction resistance and MR ratio. This result is strongly associated with the junction fabrication process, which includes *in situ* junction trilayer deposition and tunnel barrier formation using natural oxidation in vacuum. In such a well-controlled atmosphere, oxidation reaction proceeds uniformly over the entire surface, resulting in the uniform junction characteristics. Moreover, low resistance was easily achieved because tunnel barriers grow slowly and steadily at an O_2 pressure below atmospheric pressure.

When our samples were cooled down to 4.2 K, the MR ratios increased by about 70 %. However, the values were still small compared with the 61 % evaluated based on Julliere's model [2], assuming spin polarizations of 44 % for Fe [15] and 53 % for $Co_{50}Fe_{50}$ [16]. The lower MR ratios are probably due to the smaller values of barrier height and thickness in our junctions, which were estimated using Simmons' theory [14]. Small barrier height can cause the decrease in spin polarization of the tunneling current because of the increase in the tunneling probability for minority spins, as discussed in Slonczewski's theory [3]. On the other hand, a thin barrier is likely to cause ferromagnetic coupling like the so-called "orange peel" effect between the base and counter electrodes. The rough surface of the Fe base electrode (see Fig. 4) may enhance such phenomena. The existence of unoxidized Al metal left after the oxidation can decrease the spin polarization of the tunneling electrons at the surface of the base electrode by causing spin flip scattering.

The dependence of normalized resistance and MR ratio on oxygen pressure (P_{O2}) was studied for junctions with type B structures. The main parameters for varying tunnel resistance in natural oxidation are oxygen pressure, oxidation time and temperature. The experiment was performed at a constant oxidation time of 20 min at room temperature. The resistance decreases monotonically as P_{O2} decreases in the range measured. The relationship between the resistance

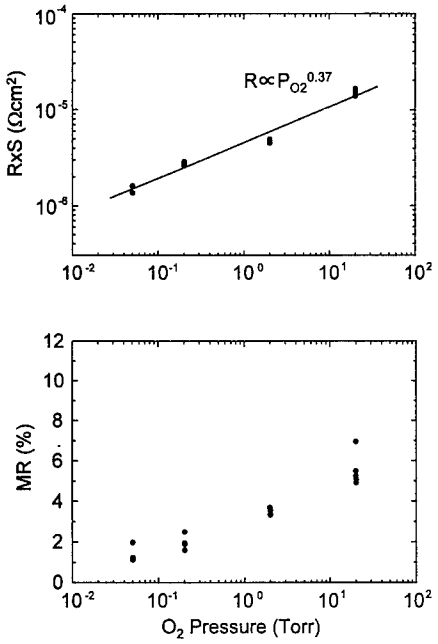

Fig. 10. Normalized resistance and MR ratio as a function of oxygen pressure during tunnel barrier formation for junctions with the structure of type B. The resistance data are fitted with a least square method (solid line).

and P_{O2} can be expressed by a simple power law. The exponent obtained by the least square fitting was 0.37. This sort of relationship agrees reasonably with that for the naturally oxidized Al reported [17]. The MR ratio also tends to decrease with decreasing P_{O2}.

Fugure 11 shows barrier height and thickness as a function of P_{O2}. The calculated values using Simmons' theory for several junctions in Fig.11 are plotted against P_{O2}. In addition to the slight decrease in barrier thickness, the mean barrier height exhibits a significant decrease with decreasing P_{O2}. These facts seem to correspond well with XPS data. The intensity ratio of the Al *2p*

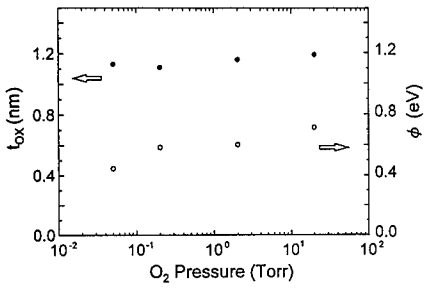

Fig. 11. Barrier height (ϕ) and thickness (t_{OX}) vs oxygen pressure for several junctions in Fig. 10.

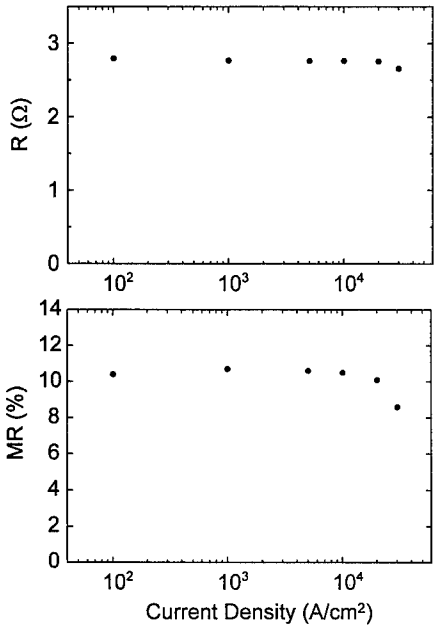

Fig. 12. Tunnel resistance and MR ratio as a function of junction current density for an $Fe/Al_2O_3/CoFe$ junction of type A, 10x10 μm^2 in area.

peak to AlO_X *2p* peak increased with decreasing P_{O2}, while the peak of AlO_X *2p* indicated a continuous chemical shift to higher energy. This latter result can reflect the change in the quality of the tunnel barrier. In order to obtain higher MR ratios, it seems to be important to improve the quality of the barrier as well as the smoothness in the Fe base electrode surface, in other words, the coverage of the Al overlayer to the base electrode surface.

In order to apply magnetic tunnel junctions to various devices, sufficient output signal voltage is needed in the actual device configurations. Since the output signal voltage is given by the product of relative resistance change and junction current, it is effective to increase not only the MR ratio but also the critical current density. The junction resistance and MR ratio are plotted as a function of current density in Fig. 12. The junction area is 10x10 μm^2. As junction current density increases, both of the values remain constant up to about $1x10^4$ A/cm^2, but decrease between $1x10^4$ A/cm^2 and $3x10^4$ A/cm^2. The decrease in MR ratio was about 20 %. These decreases can be reversed by decreasing current density. The values of $1x10^4$ A/cm^2 and $3x10^4$ A/cm^2 correspond to output signal voltages of about 3 mV and 7 mV, respectively. These voltage values plus the lower resistance values obtained in this work suggest that magnetic tunnel junctions have good potential for use in device applications such as MR heads, sensors and MRAMs.

CONCLUSIONS

We have proposed a junction fabrication technique, consisting of *in situ* deposition of an $Fe/Al_2O_3/Co_{50}Fe_{50}$ trilayer and tunnel barrier formation with natural oxidation under a controlled oxygen pressure. Normalized resistance values of about $2.4x10^{-6}$ Ωcm^2 were consistently obtained with the spatial variation of ± 6.5 % for junctions with an area of 10x10 μm^2 over a 2-inch wafer. MR ratios were in the range of 10 % to 12 % at room temperature even at the low resistance values obtained. The MR ratios remained constant up to $1x10^4$ A/cm^2. The fact that the MR ratios obtained were smaller than the best values reported for junctions with much higher resistance values is presumably due to the smaller values of barrier height and thickness in our junctions, which can cause a decrease in spin polarization of the tunneling electrons.

ACKNOWLEGMENTS

The authors would like to thank N. Shohata, M. Nakada, H. Matsutera and M. Hidaka for useful discussions and J. Nakajima, H. Tamegai and T. Yonezawa for helping with the TEM observation. A part of this work was performed under the management of Association of Super-Advanced Electronics Technologies (ASET) in the Ministry of International Trade and Industry (MITI) Program of Super-Advanced Electronic Technologies supported by New Energy and Industrial Technology Development Organization (NEDO).

REFERENCES

1. R. Merservey and P. M. Tedrow, Phys. Rep. 239, 174 (1994).
2. M. Julliere, Phys. Lett. 54A, 225 (1975).
3. J. C. Slonczewski, Phys. Rev. B39, 6995 (1989).
4. S. Maekawa and U. Gafvert, IEEE Trans. Magn. 18, 707 (1982).
5. T. Miyazaki and N. Tezuka, J. Magn. Magn. Mater. 139, L231 (1995).
6. J. S. Moodera, L.R.Kinder, T. M. Wong, and R. Meservey, Phys. Rev. Lett. 74, 3273 (1995).
7. J. S. Moodera and L. R. Kinder, J. Appl. Phys. 79, 4724 (1996).

8. M. Sato and K. Kobayashi, IEEE Trans. Magn. 33, 3553 (1997).
9. W. J. Gallagher, S. S. P. Parkin, Yu Lu, X. P. Bian, A. Marley, K. P. Roche, R. A. Altman, S. A. Rishton, C. Jahnes, T. M. Shaw, and Gang Xiao, J. Appl. Phys. 81, 3741 (1997).
10. H. Tsuge and T. Mitsuzuka, Appl. Phys. Lett. 71, 3296 (1997).
11. R. J. Petersen and F. L. Vernon, Jr., Appl. Phys. Lett. 10, 29 (1967).
12. J. S. Moodera, L. R. Kinder, J. Nowak, P. LeClair, and R. Meservey, Appl. Phys. Lett. 69, 708 (1996).
13. R. J. M. van de Veedonk, J. Nowak, R. Meservey J. S. Moodera and W. J. M. de Jonge, Appl. Phys. Lett. 71, 2839 (1997).
14. J. G. Simmons, J. Appl. Phys. 34, 1793 (1963).
15. P. M. Tedrow and R. Meservey, Phys. Rev. B7, 318 (1973).
16. J. S. Moodera, E. F. Gallagher, K. Robinson and J. Nowak, Appl. Phys. Lett. 70, 3050 (1997).
17. A. W. Keinsasser, R. E. Miller and W. H. Mallison, IEEE Trans. Appl. Supercond. 5, 26 (1995).

DOUBLE BARRIER SPIN DEPENDENT TUNNEL JUNCTIONS WITH AN INTERMEDIATE FERROMAGNETIC LAYER

R.C. Sousa[a], P.P. Freitas[a,b], T.T. Galvão[a,b], J.J. Sun[a], V. Soares[a], A. Kling[c,d], M.F. da Silva[c], and J.C. Soares[c,d]
[a]Instituto de Engenharia de Sistemas e Computadores (INESC), R. Alves Redol 9, 1000 Lisboa, Portugal.
[b]Instituto Superior Técnico (IST) Dept. of Physics, Av. Rovisco Pais, 1096 Lisboa, Portugal.
[c]Instituto Tecnologico e Nuclear (ITN), Estrada Nacional 10, 2685 Sacavém, Portugal.
[d]Centro de Fisica Nuclear da Universidade de Lisboa (CFNUL), Av. Prof. Gama Pinto 2, 1699 Lisboa, Portugal.

ABSTRACT

A new spin dependent tunnel junction configuration using two insulator barriers with an intermediate ferromagnetic layer is described. The junction structure is bottom electrode/insulator/intermediate ferromagnet/insulator/top electrode. The electrodes are CoFe layers pinned by TbCo or MnRh exchange films. The insulator is Al_2O_3 obtained by RF plasma oxidation of a thin Al film. Co, NiFe and CoFe intermediate ferromagnetic layers were used. In one of the three types of fabricated structures spin dependent tunneling is observed through the two Al_2O_3 insulating barriers. The measured tunneling magnetoresistance (TMR) was 7%. For most double junctions studied however, only one of the barriers seems to be active, either the top or bottom one, with TMR values up to 18%. Rutherford Backscattering (RBS) analysis is used to check the oxidation level of the two barriers. For the case where double tunneling was observed, the TMR falls to half its value for a bias above 500 mV and an asymmetry in the forward and reverse bias behavior was found. Conductance measurements at room temperature (RT) exhibit the usual parabolic curve as for single barrier junctions.

INTRODUCTION

Recent work done in spin polarized tunneling junctions has demonstrated TMR signals of 20% to 30% at RT[1,2,3]. For device applications (MRAMS, sensors), free layers must switch in few Oe and the resistance area product has to be in the order of few $k\Omega\times\mu m^2$, to provide ns switching times. Obtaining large TMR with low resistance area products is still an open problem, since junction resistance increases exponentially with barrier thickness, and reducing deposited Al thickness below 10 to 12 Å often results in pinholes. The most commonly used technique for insulator layer fabrication is Al deposition (10 to 20 Å thick) followed by DC or RF plasma oxidation (up to 3 min). Control of electrode switching has been obtained with spin-valve like geometries, where exchange layers pin one of the electrodes. Fig 1 shows the MR curve for a $Co_{90}Fe_{10}$ / Al_2O_3 / $Co_{90}Fe_{10}$ junction ($12\times2\mu m^2$) with pinned top electrode, fabricated by lithography. The TMR signal is 27.1% at RT, for a 123 kΩ resistance. TMR drops 50% at 430 mV. This junction has an effective barrier height of

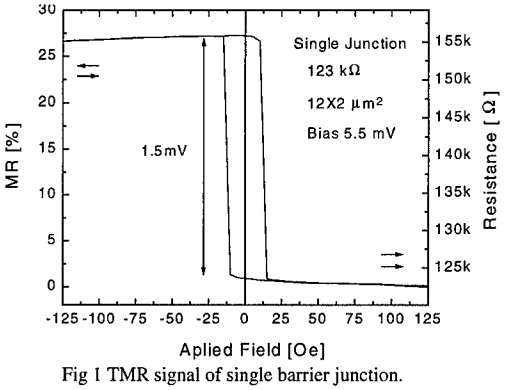

Fig 1 TMR signal of single barrier junction.

Mat. Res. Soc. Symp. Proc. Vol. 517 © 1998 Materials Research Society

2.6eV and an effective thickness of 11.6 Å (deposited Al thickness is 18 Å, 2 min oxidation), values obtained from fitting to Simmon's theory[4]. The easy axis is parallel to the longer dimension of the top electrode and the field is applied parallel to the easy axis.
In this paper, spin dependent tunneling in double barrier junctions is evaluated. Recently theoretical predictions were made for double junction structures of the type, ferromagnet (FM) / insulator (I) / ferromagnet (FM) / insulator (I) / ferromagnet (FM). Theoretically[5], TMR enhancement and anomalies in conductance were predicted. First results obtained on double junctions are presented and discussed. Junction fabrication, magnetic layer switching, TMR signal, conductance and TMR bias voltage dependence are described.

EXPERIMENTAL METHOD - DOUBLE JUNCTION FABRICATION

Samples using CoFe for both external FM electrodes were deposited with the FM / I / FM /I / FM structure, using a Nordiko 2000 sputtering system. All the samples have a Ta / Cu / Ta / NiFe buffer with a total thickness under 300 Å and are passivated with a Ta / $TiW(N_2)$ top protective layer. To pin the magnetization of the electrodes TbCo or MnRh exchange layers were used . The insulating barrier is Al_2O_3 fabricated depositing a 18Å Al layer (DC magnetron) and oxidizing it in an O_2 plasma for 1-2 minutes. The oxidation conditions used were a 50 sccm O_2 flux at 2.7 mTorr and a power density of 7 mW/cm^2 resulting in a substrate voltage of –35 V. The Al layer deposition and RF plasma oxidation are done in a different system with vacuum break between electrode and barrier deposition. RBS measurements of the fabricated junction show Al:O ratios of 1:1.6(± 0.3). Assuming the Al_2O_3 density the thickness of the insulator barrier is found to be 30% higher than the deposited Al.

Three types of double barrier structures were fabricated, and are shown in Fig 2:

Type I: substrate/ pinned layer (H_{ex1})/ barrier/ free layer/ barrier/ pinned layer (H_{ex2}).

Type II: substrate/ free layer/ barrier/ pinned layer (H_{ex1})/ barrier/ pinned layer (H_{ex2}).

Type III: substrate/ free layer (H_{c1})/ barrier/ free layer (H_{c2})/ barrier/ pinned layer(H_{ex}).

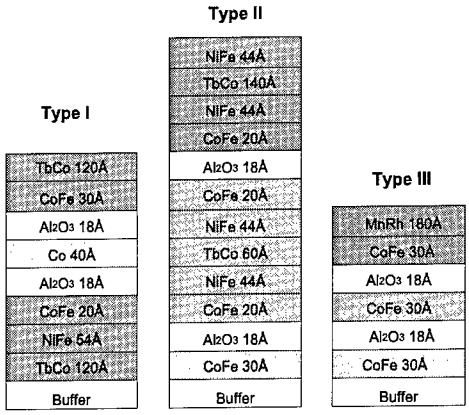

Fig 2 Detailed layer description of fabricated double junction types.

The structure of the two ferromagnetic electrodes and of the intermediate ferromagnetic layer is chosen to allow independent switching of the three magnetic layers. After junction deposition on 25×25mm^2 glass substrates, the samples are submitted to a self-aligned microlithographic process to define junction areas ranging from 18 to 10 000 μm^2. The fabrication process starts with 2 etching steps, in which the areas of the sample not protected with photoresist are removed in the sputter-etching

module of a Nordiko 7000 sputtering system. The self-aligned process described in Fig 3, allows defining the junction area and opening the contact via in the same lithographic step.

First, the material around the junction pillar is etched away. Then the top electrode is defined setting the dimensions of the junction area. A SiO_2 passivation layer is then deposited, without removing the photoresist. The vias then opened by a lift-off process have the exact dimensions of the top electrode. Al contact leads are made using a lift-off process.

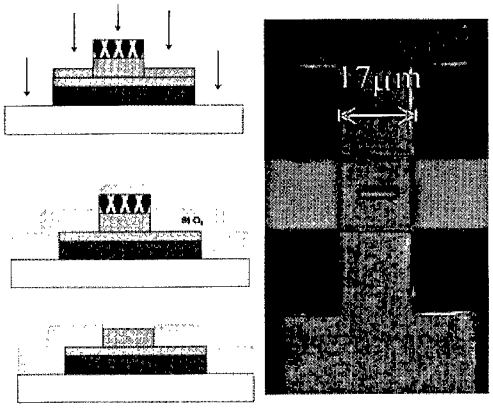

Fig 3 Self-aligned process steps and close view of the junction area.

RESULTS AND DISCUSSION

Fig 4 shows TMR behavior for a type I double junction with an intermediate "free" Co layer 40Å thick. Junction area is $9x5\mu m^2$. The inset shows the magnetization hysteresis loop measured in an unpatterned portion of the sample, confirming the individual switching of the three layers. The arrows and letters indicate the magnetization switching of the individual layers. The slower switching of the free layer observed in the small junction when compared with the bulk sample is probably related to demagnetizing effects. 18% TMR is observed when the free middle layer switches (A to B) giving rise to an antiparallel alignment of the three ferromagnetic layers. When the bottom pinned layer switches (B to C), the MR falls to zero, despite the antiparallel alignment between the middle layer and top electrode. The fact that the MR falls back to zero, and not to an intermediate value between 0% and 18%, indicates that the observed 18% TMR occurs only in the bottom barrier of the double junction. The conclusion from this study of type I double junctions is that only one barrier is working.

Fig 5a and 5b show the TMR behavior for a type II double junction. VSM measurements prove that the 5 layers used as the intermediate electrode, have a coherent behavior showing uniaxial anisotropy and switching at +-120 Oe. The free layer switches at +-10 Oe, and the top pinned layer has unidirectional exchange switching only for fields higher than 250 Oe. Analysis of the magnetization and MR loops, for this double junction type,

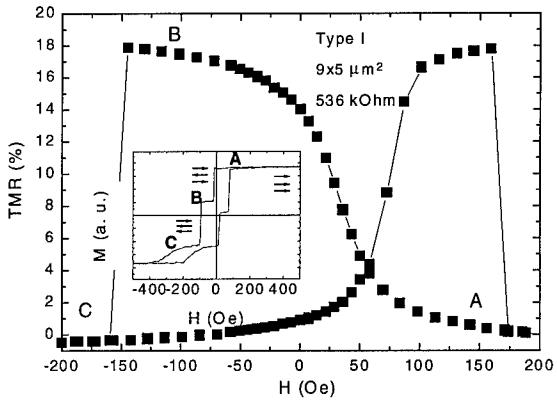

Fig 4 Type I, TMR signal and magnetization loop result.

shows again that only one of the barriers seems active. Fig 5a shows 18% TMR observed for the top junction, between the middle and the top layer. Fig 5b shows 4% TMR measured between the bottom free layer and the middle layer for a different double junction on the same substrate. In the type II junctions fabricated no combined double barrier effect was observed and only one barrier, either the top or bottom, seems active.

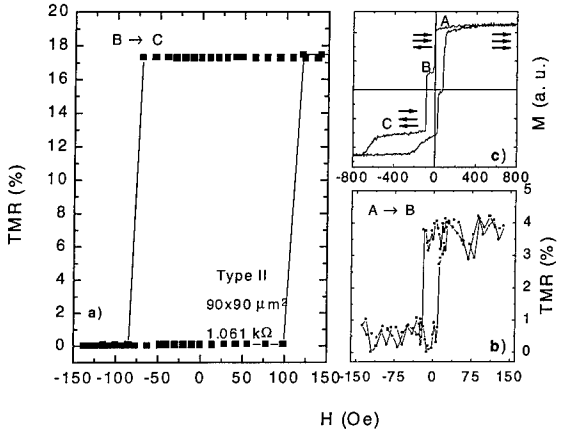

Fig 5 Type II, TMR signal of top **a)** and bottom **b)** barrier tunneling VSM measurement **c)**.

Fig 6 shows TMR data for type III double junctions. In this case, the free layer is on the bottom, and the middle layer is free but has different coercivity. For this type of junctions, two jumps in the TMR cycle are observed. One corresponding to the switching of the bottom free layer (near +-10 Oe), and another gradual switch of the middle layer (between −20 and −75 Oe). The separate switching of the two free layers was confirmed by the magnetization loop. In this case, switching of the individual bottom and middle layers is observed and both bottom and top barriers seem to be active. However their specific contribution to the total signal is different, as indicated by the two distinct TMR jumps. Following the first 1.5% increase in TMR, as the bottom free layer switches, the magnetization of the middle free layer starts changing resulting in two opposite contributions to the total signal. The reduction of the antiparallel alignment in the lower barrier decreases the resistance, with the exact inverse situation occurring in the top barrier. The inset shows one junction where the signal decreases slightly after the first rise, demonstrating the lower barrier contribution. At −100 Oe the full signal is reached with the higher TMR contribution of the top barrier. For this type of junctions it was possible to demonstrate double barrier tunneling, each one with distinct contributions.

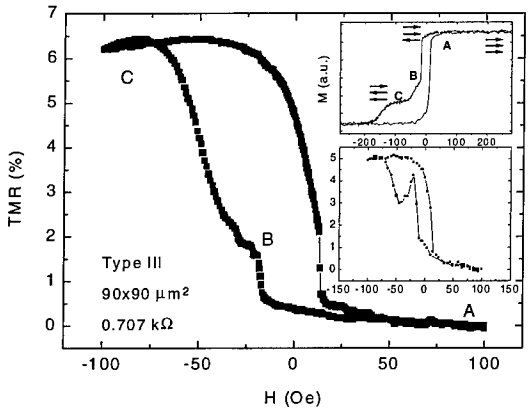

Fig 6 Type III, TMR signal showing tunneling in both barriers.

The conductance-voltage curves measured at room temperature are shown in Fig 7 for the three types of double junctions studied, and compared with single barrier ones. The dI/dV values were obtained by numerical differentiation of the experimental I–V curve. The studied samples show a parabolic-like characteristic as for single junctions. No anomalies, as predicted by Zhang *et al*[4] for double junctions, are observed. Thermal excitation could be preventing the observation of the predicted conductance anomalies. Low temperature measurements, in junctions where both barriers are active will be made in the near future.

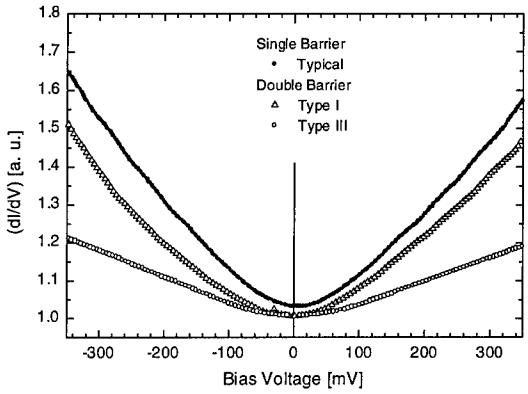

Fig 7 Conductance at room temperature.

Fig 8 shows the TMR dependence on bias for single and double barrier junctions. An asymmetry on the TMR dependence for forward and reverse voltage bias is observed in all the double junctions where indication of double barrier tunneling exists. The TMR drops to half its maximum value for a bias voltage of 0.5V. The other double junctions where only one barrier is active, and single barrier junctions show a symmetric bias dependence, with TMR dropping to half its zero bias value between 300 to 350 mV.

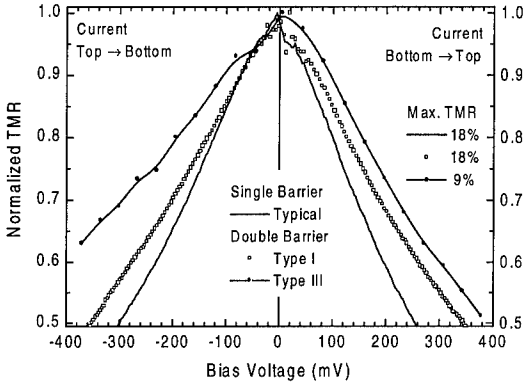

Fig 8 TMR dependence on bias voltage.

In all the three junction types, the two barriers behave differently. In most cases the total or major part of the signal originating in the top barrier. This may probably be related to some processing difficulty when patterning the bottom junction, or some irreproducibility in the oxidation of the Al layer in the two barriers. In the first case, re-deposition of material, while defining the junction area, shorting the two sides of the barrier renders it inoperative. The complete etch of the top and intermediate electrode is controlled using calibration samples. Ideally the etch should stop in the lower barrier. This being difficult to accomplish, the over-etch time may not be enough to prevent some shorting. The occurrence of a short in the top barrier is less probable, because the actual over-etch time is increased by the time needed to remove the intermediate electrode.

The oxidation process reliability for the dual junction fabrication was checked by RBS analysis. Samples deposited, simultaneously with type II junctions, on Si substrates were

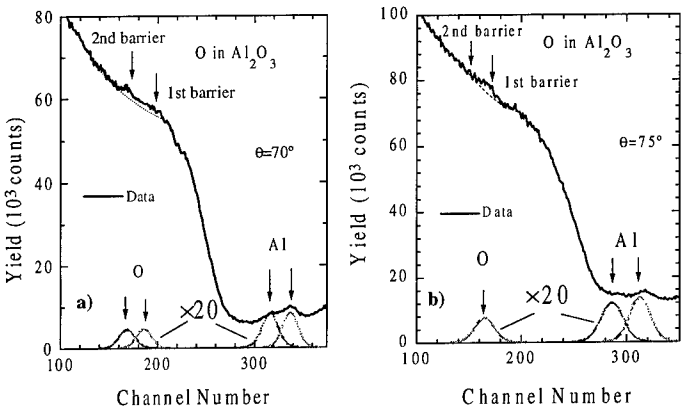

Fig 9 a) b) Insulating barrier oxidation measured by RBS.

measured by RBS. The results are shown in Fig 9a and b. In Fig 9a both Al layers are oxidized, as seen by the individual Al and O peaks. In Fig 9b, only the top barrier is oxidized. The bottom Al layer is present, but for some unforeseen reason, it is not completely oxidized.

CONCLUSIONS

Double junction structures were fabricated. Tunneling through one of the barriers is always observed, with different TMR for bottom or top barriers. Top and bottom barrier TMR reaches 18%. Tunneling through both barriers is observed only for one type of double junction strucures. In this case, 7% TMR is observed through the double structure. No conductance anomalies are observed in these double junctions at room temperature. However, for junctions where both barriers are active, the TMR bias dependence is different for reverse and forward bias. RBS analysis was used to check the oxidation level of the two Al_2O_3 layers. RBS indicates that in some junctions one of the barriers is not properly oxidized.

REFERENCES

1. J.S. Moodera, L.R. Kinder, T.M. Wong, and R. Meservey, Phys. Rev, Lett. **74,** 3273 (1995); J.S. Moodera and L.R. Kinder, J. Appl. Phys. **79,** 4724 (1996).
2. W.J. Gallager, S.S.P. Parkin, Yu Lu, X.P. Bian, A. Marley, R.A. Altman, S.A Rishton, K.P. Roche, C. Jahnes, T.M. Shaw, and Gang Xiao, to be published J. Appl. Phys. April 1997.
3. J.J.Sun, R.C.Sousa, T.T.P.Galvao, V.Soares, T.S.Plaskett, and P.P.Freitas, J.Appl.Phys., June(1998)
4. J.C. Simmons, J. Appl. Phys. **34**, 1793 (1963).
5. Xiangdong Zhang, Bo-Zang Li, Gang Sun, Fu-Cho Pu, Phys. Rev. B **56**, 5484 (1997)

SPIN-DEPENDENT TUNNELING JUNCTIONS WITH Ta_2O_5 BARRIER

Manish Sharma**, Janice H. Nickel†, Shan X. Wang**, ‡, §
**Electrical Engineering, Stanford University, Stanford, CA 94305-2205
†Hewlett-Packard Laboratories, 1501 Page Mill Rd 5L-D, Palo Alto, CA 94304-1126
‡Materials Science and Engineering, Stanford University, Bldg 550, Rm 550J, Stanford, CA 94305-2205

ABSTRACT

Spin-dependent tunneling junctions with the NiFe/oxide/NiFe structure have been fabricated with oxide barriers of Ta_2O_5, Al_2O_3 and composite Ta_2O_5/Al_2O_3 films. The barriers were formed by plasma oxidation of sputter-deposited Ta/Al films. Room-temperature tunneling magnetoresistance (TMR) effects observed are up to 4% in junctions with Ta_2O_5 and composite Ta_2O_5/Al_2O_3 barriers, significantly lower than the typical 15% effects seen in junctions with comparable Al_2O_3 barriers and having similar electrodes.

X-ray Photoelectron Spectroscopy (XPS) was used to study the oxidation profile of the barrier. Depth-profiles in the barrier regions show Al is fully oxidized while some unoxidized Ta remains. Increasing the oxidation time yields fully oxidized barriers, and increases junction resistance and TMR. At increased oxidation times, however, slight oxidation of the underlying electrode was observed, pointing towards a tradeoff between full oxidation of the barrier and likelihood of damage to the underlying electrode. Lower TMR ratios in Ta oxide junctions may be due to spin-flip scattering of electrons by residual unoxidized Ta and/or a lower tunneling probability in Ta_2O_5.

INTRODUCTION

Spin-dependent tunneling (SDT) between two ferromagnetic electrodes of Fe and Co separated by a barrier layer of Ge was first observed by Julliere [1]. More recently, tunneling magnetoresistance has been reported in several device structures, such as $NiFe/Al_2O_3/Co$ [2, 3] Ni/NiO/Co [4], $Fe/Al_2O_3/Fe$ [5], and $Fe/MgO/Co$ [6, 7], and $Fe/HfO_2/Co$ [6]. The properties of the tunneling barrier are quite important in an SDT device. Not all known barrier materials exhibit spin-polarised tunneling effects, the reason for this being still not clear. The highest observed TMR ratios and the best junction properties have been achieved with Al_2O_3 as the barrier material [2, 5, 8, 9]. Other materials tried have been MgO and HfO_2 [6], and NiO and GdO_x [4]. Reactively sputtered Ta_2O_5 for the barrier was previously attempted without success by Platt et al [6].

We report the use of plasma-oxidized Ta to form the SDT barrier. Following a description of the experimental techniques used, observed transport properties of the devices are described. Results of preliminary studies using X-ray Photoelectron Spectroscopy (XPS) to study the oxide barrier are also presented.

§Email: sxwang@ee.stanford.edu

Mat. Res. Soc. Symp. Proc. Vol. 517 © 1998 Materials Research Society

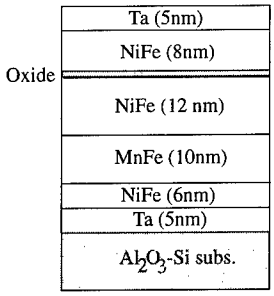

Figure 1: Typical SDT stack used. Samples were made with oxide layers $0.5 - 1.5nm$ thick.

EXPERIMENT

A Sputtered Films Shamrock deposition system was used to deposit SDT junctions with a NiFe/oxide/NiFe SDT structure on Si wafers with $4nm$ of Al_2O_3. The bottom electrode was exchange-biased using an adjacent FeMn layer. The barrier was formed by plasma-oxidation of sputter-deposited $0.5 - 1nm$ thick Ta, Al and composite Ta/Al layers. Dimensions of a typical structure are shown in Figure 1. The junction was defined and the electrodes patterned using photolithography.

Samples were tested with a Keithley S110 Hall Effect measurement system. Measurements of TMR ratio and I-V Curves were done for the samples from room ($296K$) down to low temperatures ($20K$). X-ray Photoelectron Spectroscopy (XPS) measurements were done on the samples using a Surface Science Instruments S-Probe system. Depth-profiling was performed by slow Ar sputter-etching with XPS measurements repeated at each etch step. Detail's of these experiments are being reported elsewhere [10, 11].

RESULTS

In Figure 2(a) is shown a typical TMR versus applied bias curve obtained for Sample A (Ta 1 nm, 1.5 min oxidation). TMR is found to decrease with increasing bias, and a slight asymmetry in the curve is seen. Interesting features in TMR versus bias curves possibly

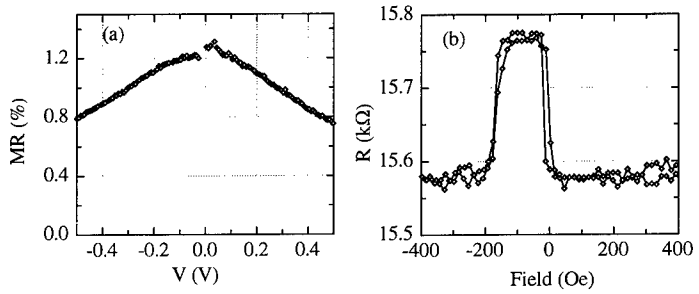

Figure 2: Results for Sample A (Ta $1nm$, $1.5min$ oxidation) at $297K$. (a) MR versus applied voltage, and (b) R-H loop.

Table I: TMR and R results for samples with different barriers. Values are for $5\mu m \times 10\mu m$ sized junctions with a bias of $10mV$ (top electrode positive) measured at room ($297K$) and low ($20 - 30K$) temperatures.

Sample	A	B	C	D	E	F
Barrier (nm)	Ta 1.0	Ta 1.0	Ta 0.75/ Al 0.75	Al 0.75/ Ta 0.75	Ta 0.5/ Al 0.5	Al 1.25
Oxidation Time (min)	1.5	2.5	4	4	1	2.5
R, room ($M\Omega \cdot \mu m^2$)	0.8	5.5	107	61	0.05	0.2
R, low ($M\Omega \cdot \mu m^2$)	1.2	13	140	135	0.06	-
$\Delta R/R$, room (%)	1.3	1.4	1.25	2.0	2.2	15
$\Delta R/R$, low (%)	1.4	3.5	2.26	4.0	2.7	-

due to variations in spin polarization with bias voltage have been observed in devices with composite Ta/Al oxide barriers. These have been investigated and are being reported elsewhere [11]. Fits to I-V curve data suggest barrier heights of $1 - 2eV$ for Ta_2O_5 barriers. In Figure 2(b) is shown a typical R-H loop obtained for Sample A at room temperature. Exchange biases of about $200Oe$ at 297K and $300Oe$ at $20 - 30K$ were observed.

A summary of the TMR results obtained is given in Table I. Both the resistance and TMR of the devices are higher at low temperatures. The increase in TMR at low temperatures is not that significant for samples A and E, which had thinner barriers and/or were oxidized for shorter times. For these two samples, there is a decrease in TMR with increase in junction size, as can be seen from Table II. Both these observations suggest the possibility of incomplete oxidation in samples A and E.

In Figure 3 are shown depth profiles obtained for Samples A and B in the barrier region. The relative proportions of Ta_2O_5, TaO and unoxidized Ta were calculated from fits to shifted peaks of the Ta $4f_{7/2}/4f_{5/2}$ doublet. As can be seen, the two samples show different profiles. A significant amount of residual Ta is present in both the samples albeit to a lesser extent in Sample B, which had an increased oxidation time. The peak in residual Ta in Sample A occurs at a higher depth than the Ta_2O_5 peak. This suggests oxidation of the Ta layer is occuring from bottom to top. Slight oxidation of the underlying NiFe electrode could also be identified in Sample B (cf. Figure 4). There is thus a tradeoff

Table II: Variation of TMR (in %) with junction size. Values are for room temperature ($297K$).

Size (μm^2)	A	B	C	D	E
50	1.3	1.4	1.25	2.0	2.2
200	0.66	1.4	1.04	1.9	0.68
1800	0.6	1.2	1.16	1.9	0.5

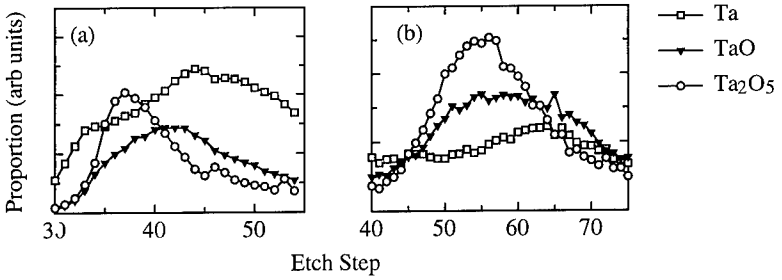

Figure 3: XPS profiles in the barrier region for (a) Sample A (Ta $1nm$, $1.5min$ oxidation), and (b) Sample B (Ta $1nm$, $2.5min$ oxidation).

between full oxidation of the barrier and possible damage to the underlying electrode when oxidation time is increased. It is to be noted that even though the escape depth in these measurements was about $2.5nm$, and thus comparable to the film thicknesses of the SDT multilayers, quite good profiles could be obtained. The utility of XPS as a tool for characterizing SDT junctions is clearly evident from these experiments.

CONCLUSIONS

Tunneling magnetoresistance is observed in SDT junctions with Ta_2O_5 barrier. On the whole, the resistances of the Ta_2O_5 ($1 - 6.25M\Omega{\cdot}\mu m^2$) and composite Ta_2O_5/Al_2O_3 ($50 - 100M\Omega{\cdot}\mu m^2$) junctions are found to be significantly higher than comparable Al_2O_3 ($0.2M\Omega{\cdot}\mu m^2$) junctions. With a thin composite Ta/Al film and a small oxidation time (cf. Sample E in Table I), it is possible to get resistances comparable to those of junctions with Al_2O_3 barrier. MR effects of $1-4\%$ are observed, markedly lower than the 15% observed in samples with Al_2O_3 barriers. It is believed that the lower TMR in the case of Ta_2O_5 is due to (a) scattering from residual unoxidized Ta, as revealed bydepth profiling done with Xray Photoelectron Spectroscopy, and (b) a lower probability of tunneling of spin-polarised electrons in Ta_2O_5 in comparison with Al_2O_3 [11].

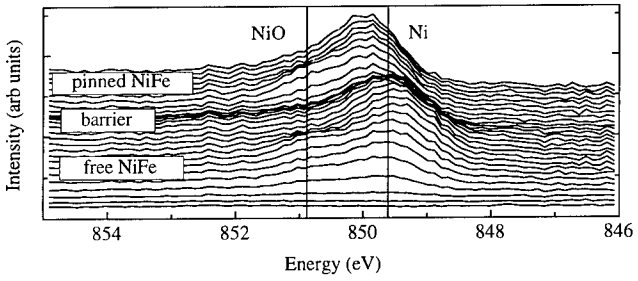

Figure 4: XPS profile of the Ni peak for Sample B (Ta $1nm$, $2.5min$ oxidation). The presence of the satellite NiO peak indicates that there is some oxidation of the underlying Ni close to the barrier. A $0.2eV$ shift in the Ni peak due to sample charging is discernible.

In addition to detecting the amount of residual Ta in the barrier region, XPS profiles also suggest that proportions of Ta_2O_5, TaO and unoxidized Ta in the barrier change with oxidation time. Slight oxidation of the surface of the underlying NiFe electrode is observed for samples with higher oxidation times. Oxygen profiles are dependent on the order of deposition of Ta and Al, this being most likely due to differing mechanisms of oxide formation and diffusion in Ta and Al.

ACKNOWLEDGMENTS

The authors would like to thank Tom Anthony and Mary West for help with depositions of the SDT junctions. MS would like to thank Prof Michael Kelly for help with setting up the XPS experiments and also Kyusik Sin for assistance in low-temperature measurements. This work is supported in part by the NSF MRSEC program through the Center for Materials Research at Stanford University.

REFERENCES

1. M. Julliere, Phys. Lett. **A54**, 225 (1975).

2. J.S. Moodera, L.R. Kinder, T.M. Wong, and R. Meservey, Phys. Rev. Lett. **74**, 3273 (1995).

3. T. Miyazaki, T. Yaoi, and S. Ishio, J. Magn. Magn. Mater. **98** (1-2), L7 (1991).

4. J. Nowak and J. Rauluszkiewicz, J. Magn. Magn. Mater. **109**, 79 (1992).

5. T. Miyazaki and N. Tezuka, J. Magn. Magn. Mater. **139** (3), L231 (1995).

6. C.L. Platt, B. Dieny, and A.E. Berkowitz, J. Appl. Phys. **81** (8), 5523 (1997).

7. J.S. Moodera and L.R. Kinder, J. Appl. Phys. **79** (8), 4724 (1996).

8. R. Meservey and P.M. Tedrow, Phys. Rep. **238** (4), 173 (1994).

9. T.S. Plaskett, P.P. Freitas, J.J. Sun, R.C. Sousa, F.F. da Silva, T.T.P. Galvao, N.M. Pinho, S. Cardoso, and J.C. Soares, MRS Proc, Spring 1997.

10. M. Sharma, S.X. Wang, and J.H. Nickel, *to be published.*

11. M. Sharma, S.X. Wang, and J.H. Nickel, *to be published.*

Part IV

Colossal Magnetoresistance (CMR) Materials

CHARACTERIZATION OF DOPED CMR-MANGANITE PEROVSKITES BY RAMAN SPECTROMETRY

B. GÜTTLER*, L. SKUJA*+, O.YU. GORBENKO**, A.R. KAUL**, M. NOVOZHILOV**, N.A. BABUSHKINA***, L. M.BELOVA***
*Physikalisch-Technische Bundesanstalt, Bundesallee 100, 38116 Braunschweig, Germany
**Chemistry Department, Moscow State University, 119899 Moscow, Russia
*** RRC Kurchatov Institute, 123182 Moscow, Russia
+Permanent address: University of Latvia, Kengaraga 8, LV 1063 Riga, Latvia

ABSTRACT

Colossal magnetoresistive manganites of the solid solution series $(La_{1-x}Pr_x)_{0.7}Ca_{0.3}MnO_3$ show first order Raman active phonon bands with A_g symmetry near 80 cm^{-1}, a doublet structure between 220 cm^{-1} - 290 cm^{-1} and a further band near 439 cm^{-1}. Similar bands were found in ceramics and films of similar composition and with a thickness of down to 60 nm. The bands are superimposed by a strong background scattering with broad maxima near 490 cm^{-1} and 610 cm^{-1}. The bands between 220 cm^{-1} - 290 cm^{-1} and 439 cm^{-1} were unambiguously identified as oxygen bands by isotope exchange experiments. The background maxima were related to second-order Raman phonon scattering in the same way. The variations of the double band structure between 220 cm^{-1} - 290 cm^{-1} can be quantitatively correlated with the orthorhombic distortion of the lattice, and provide a measure for the average ionic size of the A cation site, or the tolerance factor which describes the distortion of the octahedral network and determines the electronic properties of the system. Shifts of the Raman phonon bands related to an oxygen isotope exchange process can be quantitatively explained by the isotope mass ratio. Colossal oxygen isotope effects found in $(La_{1-x}Pr_x)_{0.7}Ca_{0.3}MnO_3$ ceramics and films can be quantitatively related to the changing isotope composition. Significant contributions from lattice effects or impurities can be excluded from the Raman data in this case.

INTRODUCTION

The electrical resistivity of manganite perovskites can be changed by more than seven orders of magnitude when the material is exposed to external magnetic fields [1,2].The term colossal magnetoresistance (CMR) has been proposed for the phenomenon [3] and makes this class of material a prime candidate for technical applications as sensors, for example as reading heads for magnetic storage devices. The size of the effect must be compared with magnetoresistance (MR), which does not exceed the order of 1-2 % ($\rho(H) - \rho(0)/\rho(0)$) in most metals and some 50 % in case of the so called giant magnetoresistance (GMR) observed in magnetic multilayers and nanoscale composite [4,5].

CMR is observed in bulk material in conjunction with a ferro-to-paramagnetic phase transition [4,5]. Here, a double exchange transport mechanism occurs in the spin aligned low temperature phase. Charge transport requires parallel spins on both sites during a hopping process [6]. Electronic conduction is hindered in the vicinity of the phase transition as a result of magnetic fluctuations at higher temperatures. Close to the transition temperature, an external magnetic field causes a spin alignment on all sites. Disorder is removed and the electrical resistance strongly decreases. For a quantitative understanding of CMR, however, simultaneous charge ordering effects and electron-phonon coupling must also be considered [7].

Technical problems are the large external fields required to produce CMR and the low temperatures where the maximal CMR occurs. The advantage of the manganite family of materials stems, however, from the possibility to chemically tune the electronic properties over a wide range by changing the composition in various solid solution series [4,5,8]. This may eventually allow the design of materials with optimized properties for technical applications and superior performances compared to other MR materials. The complex system requires, on the other hand, sophisticated analytical tools which can cope with small structural and chemical changes which might cause large variations of the electronic properties. It was, therefore, our aim

Mat. Res. Soc. Symp. Proc. Vol. 517 © 1998 Materials Research Society

to see, whether Raman spectrometry is able to detect the changing properties in the critical compositional ranges of the materials.

Optimizing the CMR properties in manganite perovskites requires doping and controlled structural deformation. Perovskites have the general formula ABO_3. They consist of a network of corner sharing oxygen octahedra with the B-type metal ion in its centre while the octahedra themselves are located in the edges of a cube with an A-type cation in a twelvefold coordination in its centre. Manganese occupies the B-site, the A-site is filled with a trivalent metal, for example a rare earth cation R such as La^{3+} or Pr^{3+}. Stoichiometric $LaMnO_3$ is an antiferromagnetic insulator at room temperature and doping is required in this system in order to establish the paramagnetic-to-ferromagnetic transition which is the prerequisite for CMR. This can be achieved by replacing the trivalent atom R by a doubly charged cation M such as alkaline earth elements. This leads to the general formula $R_{1-x}M_xMnO_3$. Although the end-members of such series are all antiferromagnetic insulators at low temperatures [9], they become ferromagnetic and metallic at intermediate x-values and have a pronounced Curie temperature.
A maximum CMR is established at a doping level of x= 0.3 in case of divalent doping. The magnetic transition occurs at a temperature of approx. 260 K in case of Ca doping and is accompanied by a metal- insulator transition at the same temperature. The low-temperature phase is a ferromagnetic metal, the para-phase a disordered insulator. CMR occurs near the transition temperature and reaches at least approx. 80 %. T_c and MR greatly depend, however, on the real structure of material: variations of the synthesis procedure can result in T_c's in the range of 100-300 K and a MR higher than 500% (even with $T_c \sim 260$ K) for $La_{0.7}Ca_{0.3}MnO_3$ films [3,10]. Doping is accompanied by the partial removal of the orthorhombic distortion in the stoichiometric $LaMnO_3$ parent material. The cooperative elongation of the octahedra caused by the Jahn-Teller effect of Mn^{3+} vanishes [11] and the octahedral buckling induced by the steric conditions decreases due to the increase of Mn^{4+}/Mn^{3+} ratio [12].

The critical electronic properties of the system can be further largely enhanced even without a variation of the charge carrier concentration. Exchanging the A-site cation with an ion of similar charge but different size results in variations of the internal pressure which are compensated for by a rotation (buckling) of the MnO_6 octahedra. This changes the Mn-O-Mn bond angle and, hence, also the angle between the B-site *d* orbitals and oxygen *p* orbitals which form the conduction band in the system. Deviations from the ideal 180° Mn-O-Mn bond angle result in a decreasing bandwidth. Decreasing the average atomic radius $\langle r_a \rangle$ results, therefore, in a decreasing maximum resistivity temperature T_P and a drastically increasing magnetoresistance [13]. Eventually the Mn-O-Mn overlap becomes insufficient. The ferromagnetic state is replaced by antiferromagnetic ordering at low temperatures and localised holes form a charge ordered insulator.

The study of solid solution series of this kind are, therefore, of twofold interest: They can be used to optimize the desired magnetoresistive properties and also serve as a workbench for experiments towards a better understanding of the underlying physical principles. It seems sensible, therefore, to keep the dopant and doping level at its optimum (x=0.3 in $R_{1-x}M_xMnO_3$) and to change the size of the trivalent cation in $(A_{1-x}A'_x)_{0.7}M_{0.3}MnO_3$, where A and A' are trivalent rare earth metals of different size. The La-to-Pr series was studied mainly for two reasons: Firstly, because the oxygen stoichiometry is rather insensitive to heat-treatment in this case yet again stabilising the Mn^{3+}/Mn^{4+} ratio, and secondly because the series is in the regime where magnetic and charge ordering coexist [1]. The magnetic transition temperatures T_c and T_p change drastically and simultaneously in the series starting from 260 K in the La endmember to 0 K in the Pr endmember. Decreasing resistivity in an applied field is interpreted as the magnetically induced breakdown of the charge ordered state. A ferromagnetic metal is replaced by an antiferromagnetic insulator at constant temperature between the endmembers [13]. This means that the series passes through a critical range which can be used to demonstrate the importance of electron-phonon coupling in the system. It has been proposed that the transfer of holes between Mn^{3+} and Mn^{4+} is accompanied by a large dynamic Jahn-Teller induced lattice distortion leading to small polaron formation. This should result in an increasing resistance and largely enhances MR to true CMR.
In the transition range octahedral vibrations may lead to a situation where the material is at the

breakdown to the insulating state but still metallic because the critical bond angle varies periodically between states in the metallic and non-metallic regime. Slight changes of the vibrational self energy should then lead to a drastic variation of the electrical properties. Isotope exchange experiments are a clear-cut path to check such a model. $^{16}O/^{18}O$ exchange experiments in $La_{0.175}Pr_{0.525}Ca_{0.3}MnO_3$ have indeed confirmed the existence of a dramatic isotope effect. Replacing ^{16}O by ^{18}O drives manganites into the non-metallic regime. The resistivity vs. temperature curves diverge below the phase transition temperature near 110 K and the resistivity of the ^{18}O enriched material increases drastically. At low temperatures the conductivity differs by no less than ten orders of magnitude and provides a most impressive proof for the importance of electron-phonon coupling in the system.

CMR appears as the result of a concerted interaction of magnetic, Coulomb and electron-phonon forces controlled by a complex chemical environment. Optimizing the magnetoresistive properties requires a wide range of analytical information covering not only chemistry but also physical and crystallographic properties. The real structure of the material significantly influences the desired properties. Detailed knowledge about phase purity, lattice distortions, charge carrier concentration, the oxygen stoichiometry and the isotope ratio is needed. Particularly in case of industrial applications measurements should be quick, carried out on-site, and non-destructive. Furthermore, technological products such as thin films require a control of the epitaxial growth process. Layer structures with a thickness of less than 100 nm must be analysed and electronic microstructures ultimately require a tool with a spatial resolution in the micrometer range.

The situation resembles that in high temperature superconductors, where Raman spectrometry is a key analytical tool and technological developments benefit considerably from the application of this method. It has been argued recently that Raman spectrometry is not applicable in case of manganites because of crystallographic and electronic constraints which massively reduce Raman scattering efficiencies [14]. It is shown here, however, that Raman spectra of manganite solid solution series which exhibit critical variations of the electronic properties can indeed provide information of similar importance as in case of superconductors in spite of these difficulties.

EXPERIMENT

Aerosol MOCVD was used to prepare thin films. The procedure includes deposition from precursor vapour produced by the evaporation of their organic solution nebulized in the carrier gas flow [15]. Single crystalline (001) $LaAlO_3$ (pseudocubic cell) and (001) $SrTiO_3$ were used as substrates. The films prepared were about 350 nm thick, two films of the composition $La_{0.35}Pr_{0.35}Ca_{0.3}MnO_3$ were prepared with lower thickness (60 nm). SEM was accomplished by CAMSCAN equipped with EDAX system for quantitative analysis of the films. The metallic component ratio in the precursor solution was adjusted to provide proper stoichiometry in the film. The films are twinned and oriented with the c-axis perpendicular to the film plane. The ceramic samples were prepared from water solution of the metal nitrates: ash-free paper filters were soaked with the solution, dried and burned. Ashes of the precursors were pressed into pellets and sintered in air at 1200°C. XRD did not reveal impurity phases in either films or ceramics.

For isotope exchange pairs of 1x8 mm^2 strips were cut from the samples and put into alumina boats which were placed in two quartz tubes mounted in a furnace. The quartz tubes formed parts of two identical closed loops to which an enforced gas circulation was applied. One part of the each sample was heated in $^{16}O_2$ atmosphere, the other part of the each sample was heated in $^{18}O_2$ (molar fraction of $^{18}O_2$ 85%). The diffusion annealing was carried out for 4h at a temperature 800°C (thin films) and for 48 h at the temperature 950°C (ceramic pellets) under an oxygen pressure 1 bar.

Raman spectrometric measurements were performed with a triple monochromator system (Jobin-Yvon T64 000) in a subtractive arrangement and in a backscattering geometry of the incident laser light. The samples were placed under an Olympus BH2 microscope with an 80x objective so that the spatial resolution is of the order of 1.5 micrometer. The 514.5 nm line of an

Ar^+-ion laser was used as the exciting laser line in most cases. An LN_2-cooled CCD camera was used as a detector and allowed the simultaneous measurement of the frequency range from 15 to 720 cm^{-1} at an excitation wavelength of 514.5 nm.

Raman spectra of both ceramics and films were measured with a laser power of up to 50 kW/cm^2, which corresponds to an output power of 100 mW of our Ar^+ - ion laser system. Higher laser power leads to a shift of the Raman bands as a result of laser heating.

RESULTS

Mode Assignment

In the solid solution series $(La_{1-x}Pr_x)_{0.7}Ca_{0.3}MnO_3$ first order Raman active phonon bands can be detected near approx. 80 cm^{-1}, a doublet between 220-290 cm^{-1} and a mode near 439 cm^{-1} (Fig. 1). They are superimposed by a strong background scattering which exhibits maxima near 490 cm^{-1} and 610 cm^{-1}. Isotope exchange experiments unambiguously identify the doublet between 220-290 cm^{-1} and the mode near 439 cm^{-1} as oxygen vibrations while the band near 80 cm^{-1} remains unshifted in such experiments within the experimental accuracy so that this band must be related to cation vibrations. The line positions are listed in Table I. The features near 490 cm^{-1} and 610 cm^{-1} are also of phononic origin as they also show an oxygen isotope shift. They are, thus, assigned to second order Raman scattering mainly due to oxygen vibrational modes. Polarized measurements reveal a B_g-like character for the mode near 439 cm^{-1} and an A_g-like character for the modes near approx. 80 cm^{-1} and the doublet between 220 cm^{-1} - 290 cm^{-1}. The bands exhibited a fairly weak and broad character in character, which corresponds to the close similarity of the structure to its Raman-inactive cubic parent structure.

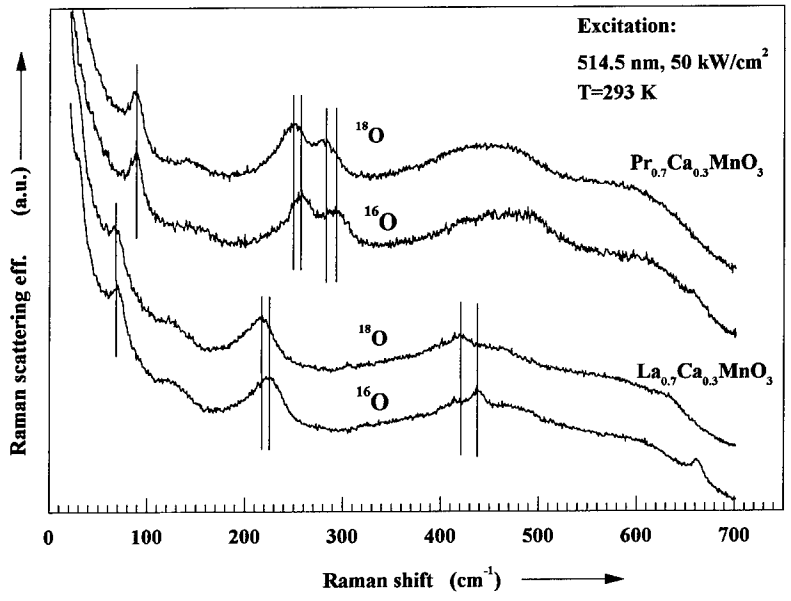

Fig. 1. Raman spectra of $La_{0.7}Ca_{0.3}MnO_3$ and $Pr_{0.7}Ca_{0.3}MnO_3$, films subjected in parallel to an oxygen isotope exchange in $^{16}O_2$ and $^{18}O_2$ (molar fraction of $^{18}O_2$: 85%).

TABLE I. First order Raman phonon frequencies (cm^{-1}) in $La_{0.7}Ca_{0.3}MnO_3$ and $Pr_{0.7}Ca_{0.3}MnO_3$ subjected in parallel to an oxygen isotope exchange in $^{16}O_2$ and $^{18}O_2$ (molar fraction of $^{18}O_2$:85%).

	mode	$cm^{-1}(^{16}O)$	$cm^{-1}(^{18}O)$	$\Delta\omega$	$-\Delta\omega/\omega$	$^{18}O/(^{16}O+^{18}O)$
$La_{0.7}Ca_{0.3}MnO_3$	B_g	439	419	20	0.046	0.78
	A_g	-	-	-	-	-
	A_g	227	217	10	0.044	0.75
	A_g	72	72	0	0	-
$Pr_{0.7}Ca_{0.3}MnO_3$	B_g	-	-	-	-	-
	A_g	293	280	13	0.044	0.76
	A_g	260	249	11	0.042	0.73
	A_g	90	90	0	0	-

$(La_{1-x}Pr_x)_{0.7}Ca_{0.3}MnO_3$ are orthorhombic perovskites with space group *Pnma* (D_{2h}^{16}). Raman spectra have been measured in case of the structurally related $LaMnO_3$ and the rhombohedral $La_{0.7}Sr_{0.3}MnO_3$ [16, 17]. The band near 227 cm^{-1} in the $La_{0.7}Ca_{0.3}MnO_3$ endmember of our series seems to be comparable with the band near 190 cm^{-1} in $La_{0.7}Sr_{0.3}MnO_3$, both having an A_g character. This band was correlated with the band near 284 cm^{-1} in the undoped $LaMnO_3$ parent system. This also has an A_g character and was assigned as an out-of-phase x-rotation vibration of the MnO_6-octahedra by lattice dynamical calculations [17]. The band near 290 cm^{-1} in $(La_{1-x}Pr_x)_{0.7}Ca_{0.3}MnO_3$ is absent in $La_{0.7}Sr_{0.3}MnO_3$. The mode near 435 cm^{-1} in $La_{0.7}Sr_{0.3}MnO_3$ is obviously similar to the mode near 439 cm^{-1} in $La_{0.7}Ca_{0.3}MnO_3$ both showing a B_g-character. It has been correlated with the out-of-phase oxygen bending mode near 481 cm^{-1} in $LaMnO_3$ [17,18]. No data are available for doped $La_{1-x}M_xMnO_3$ or $LaMnO_3$ below 100 cm^{-1}.

Doping by replacing a trivalent metal with a divalent one drives the structure further towards the cubic phase mainly because of a vanishing static Jahn-Teller distortion.This leads to an extremely small Raman scattering efficiency and is the reason for the difficulties in measuring the phonon Raman scattering observed earlier [14]. Only 5 out of 24 symmetry allowed Raman modes in the orthorhombic *Pnma* symmetry of the perovskite structure can be detected as first order phonon bands.

Remarkable is the absence of the strong phonon lines near 490 cm^{-1} and 612 cm^{-1} in the doped material. These bands dominate the $LaMnO_3$ parent structure [17]. It is in sharp contrast to the preserved scattering of the modes below 350 cm^{-1}. Only second-order scattering with broad maxima can be observed in the vicinity of the former 490 cm^{-1} and 612 cm^{-1} bands in the $(La_{1-x}Pr_x)_{0.7}Ca_{0.3}MnO_3$ series. The bands have been related to octahedral stretching and bending vibrations [17] and may be stronger affected by the influence of the static Jahn-Teller distortion of the octahedra in the parent structure which relaxes on doping.

Heating Effects

As well as the close similarity to the ideal cubic structure a further problem is the large absorbance of the material in the visible frequency range [19] which results in a black appearance of the samples and significantly reduced Raman scattering cross sections because of the small penetration depth of the laser beam. It also results in a local heating process in the sample which might obscure a correct measurement of various features in the spectra such as the line positions. This puts an upper limit to the applicable excitation laser power and, thereby, further reduces the observable Raman scattering efficiency.

A low energy shift of the Raman bands is observed in all samples as a result of laser heating when exceeding 150 kW/cm^2 (Fig. 2). The system is driven towards the cubic phase as evidenced by the low energy shift of the mode near 260 cm^{-1} and the smaller scattering efficiency of the

mode near 290 cm^{-1}. The effect is, however, purely dynamical in films and ceramics at excitation powers of at least up to 500 kW/cm^2. Repeated measurements at 50 kW/cm^2 after intermediate exposure to a laser power of up to 500 kW/cm^2 show that the induced line shifts are fully reversible and leave the sample unaffected. This is in sharp contrast to the case of orthorhombic $LaMnO_3$, which irreversibly transforms into its rhombohedral state as a result comparable laser heating [17] most probably due to the variation of the oxygen stoichiometry. The higher thermodynamic stability of the ternary oxides corresponds to the more stable oxygen content of these samples [20].

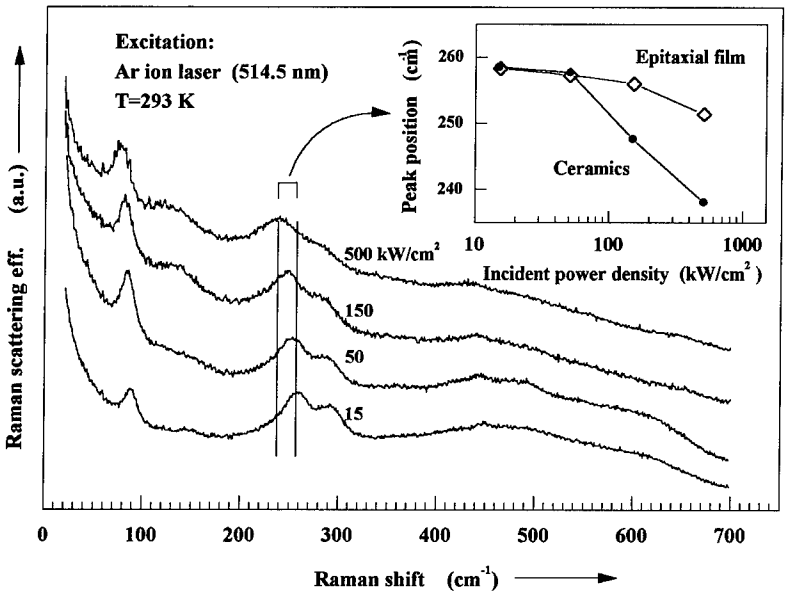

Fig. 2. Laser heating effect in the Raman spectrum of a $Pr_{0.7}Ca_{0.3}MnO_3$ ceramic. The inset shows the line shifts of the mode near 260 cm^{-1} as observed in films and ceramics.

The $(La_{1-x}Pr_x)_{0.7}Ca_{0.3}MnO_3$ Solid Solution Series

Exchanging Pr for La does not change the charge carrier concentration but drives the structure further towards the cubic symmetry. The cation exchange process results in a variation of the lattice constant in response to the changing average atomic radius on the A lattice site. This is achieved by a tilting of the octahedral network so that the size of voids between the octahedra is reduced. The structural change is measured by the tolerance factor $t = d(\text{A-O})/\sqrt{2}d(\text{Mn-O})$ where d denotes the average interatomic distances.The process is reflected in the spectra by large line shifts of the modes near 260 cm^{-1} moving to 227 cm^{-1} and the mode near 90 cm^{-1} which shifts to 72 cm^{-1}. The mode near 290 cm^{-1} in $Pr_{0.7}Ca_{0.3}MnO_3$ vanishes in $La_{0.7}Ca_{0.3}MnO_3$ (Fig. 3). The line positions are listed in Table II.

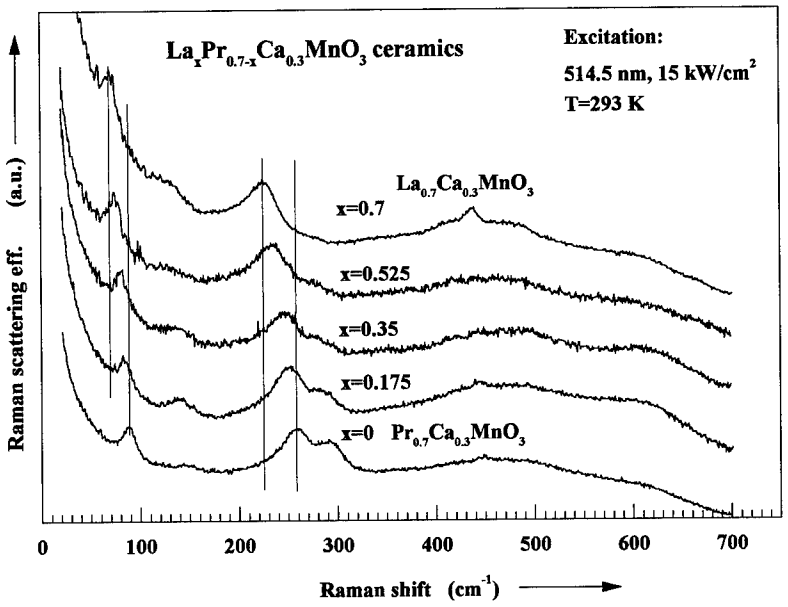

Fig. 3. Raman spectra of the $La_{0.7}Ca_{0.3}MnO_3$ to $Pr_{0.7}Ca_{0.3}MnO_3$ series. Line shifts are shown in the inset.

TABLE II. First order Raman phonon frequencies (cm^{-1}) in the $La_{0.7}Ca_{0.3}MnO_3$ to $Pr_{0.7}Ca_{0.3}MnO_3$ series

$La_{0.7-x}Pr_xCa_{0.3}MnO_3$	mode	x=0	x=0.125	x=0.35	x=0.525	x=0.7
	A_g	72	76	82	87.5	90
	A_g	227	236	248	252	260
	A_g	-	275	279	287	293
	B_g	439	-	-	-	-

The modes near 260 cm^{-1} and 90 cm^{-1} in the Pr-rich endmember change linearly with the changing average cationic size and, hence, with the tolerance factor t, because the average Mn-O bond distance is almost constant throughout the series (Fig. 4). The position of the bands decreases by 33 cm^{-1} and 18 cm^{-1}, respectively, on replacing Pr by La. This corresponds to an increase of the average cationic radius from 1.179 Å in $Pr_{0.7}Ca_{0.3}MnO_3$ to 1.205 Å in $La_{0.7}Ca_{0.3}MnO_3$ and a shift of the tolerance factor by 0.01, i.e. from 0.907 to 0.917 [13]. The effect can be related solely to the structural changes because the change of mass on replacing La by Pr is very small (m_{La}/m_{Pr}=0.99). The tolerance factor can be further increased by exchanging the divalent atoms instead of the trivalent ones. A value of 0.93 is found in case of $La_{0.7}Sr_{0.3}MnO_3$ [13]. When extrapolating the results from our series to this value a further low-frequency shift to some 180 cm^{-1} is expected, which is near the observed frequency of 190 cm^{-1} (Fig. 4). Considering the large mass difference between the exchanged cations (m_{Sr}/m_{Ca}=2.18) and also differences in their electronic properties, this is a reasonable agreement. It clearly confirms that factors other than the structure itself are of secondary importance to Raman mode frequency. It also confirms the assignment of the mode as an oxygen vibration which is practically not affected by the mass change of the cation.

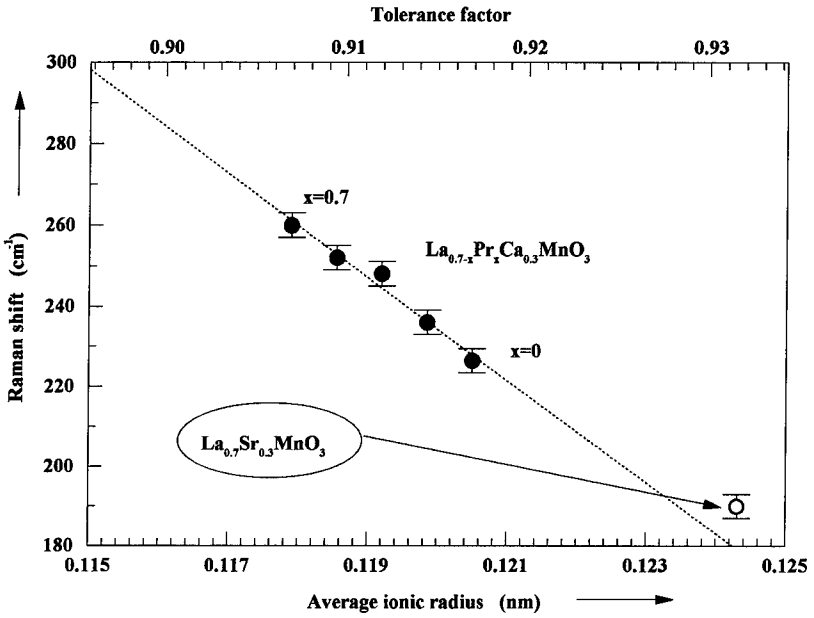

Fig. 4. Line shift of the mode near 227 cm^{-1} in $La_{0.7}Ca_{0.3}MnO_3$ in the $(La_{1-x}Pr_x)_{0.7}Ca_{0.3}MnO_3$ solid solution series as a function of the atomic radius ($La_{0.7}Sr_{0.3}MnO_3$ from [16]).

Based on this evidence the A cation atomic radius and also the tolerance factor can be directly deduced from the line shift of this mode in the Raman spectrum. The mode frequency can be quantitatively correlated with the structural state, at least if the Raman-spectra of the end-members of the solid solution series are known. But the correlation seems to be more general and a further extension towards a more universal measure of the tolerance factor in the manganite system seems possible as long as the charge carrier concentration is kept constant. The method is obviously also valid beyond the series studied here, namely in case of a substitution of the divalent cation, although the accuracy is not quite the same.

Measuring the tolerance factor over a wide range is of critical importance for the further development of improved CMR materials. As described above, it critically determines the electronic properties of the system. This interpretation is supported by a comparison with $CaTiO_3$, which undergoes an isostructural orthorhombic-to-cubic (*Pnma-Pm3m*) phase transition on heating. Here, the structural variation is solely due to the vanishing buckling of the octahedra on increasing the temperature; no further physical or chemical effects are relevant. Similar changes of the tolerance factor lead to similar shifts of the Raman active bands in both the manganite solid solution series and in $CaTiO_3$ [21].

It has been argued [16] that the doping level in $LaMnO_3$ can be studied in a similar way by the line shift of the mode near 284 cm^{-1} in $LaMnO_3$ on doping with Sr. The low energy shift was explained by the increasing average cation radius on the A lattice site. Compared to the line positions observed for the Ca doped samples with a smaller average A cation radius we would, however, expect a lower energy for a similar mode in undoped $LaMnO_3$ rather than a higher one. We can see here that the situation is more complex when doping accompanies the cation exchange process, and the shift is obviously also strongly dependent on other factors such as the charge carrier concentration. For instance, the growth of the Mn^{4+}/Mn^{3+} ratio with the increase of

Ca-doping results in the decrease of the mean Mn-O bond length. The variation has a similar effect on the lattice deformation as doping with a larger trivalent A cation.

Comparison of films and ceramics

Technical applications often require epitaxial films as the basis for microelectronic structures. Intuitively, the low Raman scattering efficiencies of the manganites seem to be a severe burden in the investigation of thin samples with a supposedly small scattering volumes. Because of the small penetration depth of the material, however, even thin films are not transparent if the sample thickness is exceeding some 250 nm. As a result, there is no significant difference in the Raman experiment between bulk and film material in this case, and they exhibit the same scattering cross section. Further, thin films have significantly better heat transport properties than bulk material, most probably due to grain boundary effects and voids in the latter case. They can, therefore, be exposed to higher laser power without heating.This is particularly important when it comes to the comparison of the results obtained from thin films and ceramics, because the sensitivity to local heating differs considerably in both systems. Spectra measured under similar conditions then show different line positions in films and ceramics which, however, do not reflect physical differences between the samples. (Fig. 2).The Raman band near 260 cm^{-1} in $Pr_{0.7}Ca_{0.3}MnO_3$ is shown as an example of this effect (Fig. 2, inset). It is shifted by 21 cm^{-1} to 234 cm^{-1} at an incident laser power of 500 kW/cm^2 in the case of ceramic samples. A shift of only 7 cm^{-1} is observed in case of thin films. Comparing the size of the line shift with that observed in low temperature data for $La_{0.7}Sr_{0.3}MnO_3$ [16] allows a rough estimate of the temperature of the exposed sample spot. We can expect the temperature to increase by 300 K when there is a line shift of 20 cm^{-1}. This corresponds to a temperature of some 580 K at the ceramic surface in case of an incident laser power of 500 kW/cm^2 while it is only 400 K in case of thin films. No significant variations are found up to an incident laser power of 50 kW/cm^2 as used in all our experiments.

Spectra of films show the same first order Raman active phonon bands near approx. 80 cm^{-1}, between 220 cm^{-1} - 290 cm^{-1} and near 439 cm^{-1} as those of ceramics (Figs. 1, 2, 3). An additional line near 660 cm^{-1} was found in many, but not all ^{16}O films. It has also been found in films by Malde et al. [18]. The band near 660 cm^{-1} is, however, absent in ceramics and has varying scattering efficiencies in films with similar chemical composition. It is, therefore, believed to be an impurity band most probably caused by a manganese oxide. Electrical measurements show similar results for films and ceramics of similar chemical composition and no impurities are found in XRD measurements. This sets an upper limit to the impurity level of some 2-3 %. Evidently, even small amounts of impurities lead to comparatively strong Raman bands in this case. This is also a signature of the weak Raman scattering of CMR-manganites because of their small deviation from the non-Raman-active cubic structure.

Epitaxy

Raman spectrometry can also be used to detect the epitaxial growth of the films. This feature is best detected by depolarized spectra parallel to the film edges (X'Y') and rotated by 45° (XY) (Fig. 5). The band near 439 cm^{-1} in $La_{0.7}Ca_{0.3}MnO_3$ almost vanishes in X'Y'. In $Pr_{0.7}Ca_{0.3}MnO_3$, the comparatively strong background scattering near 490 cm^{-1} and 610 cm^{-1} in X'Y' is weaker in XY. Epitaxial films require lattice-matching substrate materials. Lattice matching is, however, never perfect and the strain at the film-substrate interface is compensated by a different buckling of the octahedral chains in and out of the film plane, producing an effect on T_p comparable with the effect of chemical pressure near the critical value $t \sim 0.91$. T_p values actually become divergent on approaching the critical t value. In this region, T_p varies from the highest value for the film on $SrTiO_3$ to the lowest value for the film on $LaAlO_3$. In the films on $SrTiO_3$ the bending of the Mn-O-Mn chains is decreased in the plane of the film whereas it is increased in the plane of the film on $LaAlO_3$.

This process is not reflected in the Raman phonon bands between 220 cm^{-1} - 290 cm^{-1} and the

band near 439 cm^{-1} in spite of their sensitivity to the octahedral buckling produced in the solid solution series: The mode frequencies of epitaxial films on $SrTiO_3$ and $LaAlO_3$ were found to be identical within the measurement accuracy.

The tetragonal distortion has opposite direction for the films on $LaAlO_3$ and $SrTiO_3$ in agreement with the difference of the mismatch between the lattice constants of the substrates and films. The lattice constant of $SrTiO_3$ is larger, consequently the tensile strain in the film demands an in-plane expansion of the perovskite cube. The deformation of the lattice normal to the substrate (ε_3) is proportional to the in-plane strain components (σ_1,σ_2): $\varepsilon_3 = -(\sigma_1+\sigma_2)\eta/E$, where η is the Poisson coefficient, E the elastic modulus[22]. Thus, the films on $SrTiO_3$ are contracted along the normal. The opposite is true for the films on $LaAlO_3$. As a result, the average length of the A - O bond cation remains unchanged in this case and this is obviously the reason for the absence of an effect in the Raman spectrum.

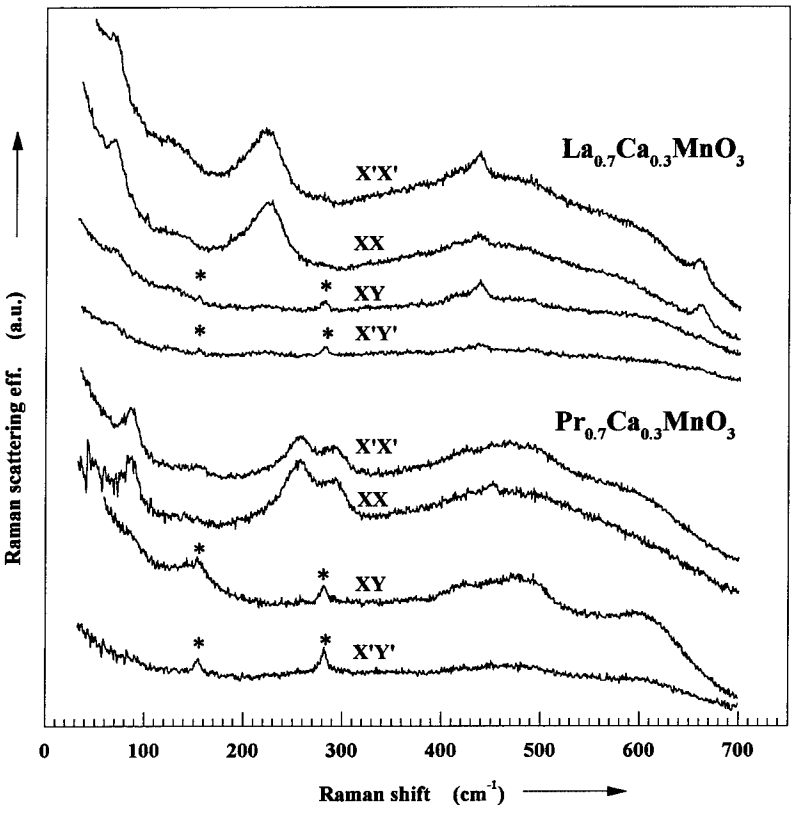

Fig. 5. Polarized Raman spectra of the $La_{0.7}Ca_{0.3}MnO_3$ and $Pr_{0.7}Ca_{0.3}MnO_3$ films. X and Y denote the crystallographic axes. They are rotated by 45° relative to the film edges X' and Y'. Lines marked by asterisks are artefacts of the polarizer.

Oxygen isotope shift

An isotope shift is found in films and ceramics. The $^{18}O/^{16}O$ exchange process causes a line shift of Raman phonon bands generated by lattice vibrations dominated by the mass of these isotopes. The line shift follows the isotope mass ratio according to

$$\omega_1/\omega_2 = \sqrt{m_2/m_1}$$

In films, a significant isotope effect was found for the doublet between 220-290 cm^{-1} and the modes near 439 cm^{-1} and 660 cm^{-1} (Fig. 1). It corresponds to an $^{18}O/^{16}O$ ratio of approx. 0.8±0.1. This is in good agreement with an $^{18}O/^{16}O$ ratio of 0.85 in the exchange gas used in our experiments. It identifies the shifting bands as oxygen phonon lines and indicates a complete gas exchange process of the atoms involved in the vibrations. Also, there are no significant contributions from other potential factors resulting from the isotope exchange process, such as impurities. This result provides the evidence that is needed to correlate the enormous variation of the electrical properties of films and ceramics with the isotope exchange process. The variation of the Raman spectrum is solely due to the changing isotope mass. This information is difficult to provide by other methods, particularly in case of films and demonstrates the analytical power of Raman spectrometry in this case. The effect has even been observed in films as thin as 60 nm.

CONCLUSIONS

Raman spectrometry is suitable for studying key structural processes in manganites. The atomic origin of the Raman bands was unambiguously identified in several cases. The tilting of the octahedral network can be quantified by phonon line shifts. The method seems to be extendible to a wider tolerance factor range than studied here. Even the case of a variation of the divalent cation can be included provided that the charge carrier concentration is kept constant. Further information is required in this respect and the evidence provided here may serve as the starting point for more comprehensive studies in the field.

Considerable care is required in Raman studies of manganite films and ceramics in order to achieve comparable results because of varying laser heating effects in both systems.
The colossal oxygen isotope effect can be unambiguously and quantitatively identified with the oxygen isotope exchange process, a conclusion which is difficult to obtain with other experimental tools particularly in case of thin films.

REFERENCES

1. O.Yu. Gorbenko, A.R. Kaul, N.A. Babushkina and L.M. Belova, J. Mat. Chem. **7**, p. 747 (1997).

2. F.Damay, N.Nguyen, A.Maignan, M.Hervieu and B.Raveau, Solid St. Comm. **98**, p. 997 (1996).

3. S. Jin, T.H. Tiefel, M. McCormack, R.A. Fastnacht, R. Ramesh and J.H. Chen, Science **264**, p. 413 (1994).

4. C.N.R. Rao, A.K. Cheetham and R. Mahesh, Chem.Mat.**8**, p. 2421 (1996).

5. A.P. Ramirez, J. Phys. Condens. Matter **9**, p. 8171 (1997).

6 . C.Zener, Phys. Rev. **82**, p. 403 (1951).

7. A.J. Millis, Phys. Rev. B **53**, p. 8434 (1996).

8. Y. Tomioka, A. Asamitsu, Y. Moritomo, H. Kuwahara and Y. Tokura Phys. Rev. Lett. **74**, p. 5108 (1995).

9. P. Schiffer, A.P. Ramirez, W. Bao and S.W. Cheong, Phys. Rev. Lett. **75**, p. 3336 (1995).

10. Y.Q. Li, J. Zhang, S. Pombrik, S. DiMascio, W. Stevens, Y.F.Yan and N.P.Ong, J. Mater. Res. 10, p. 2166 (1995).

11. J.L. Garcia-Munos, M. Suaaidi, J. Fontcuberta and J. Rodriguez-Carvajal, Phys. Rev. B **55**, p. 34 (1997).

12. A.M. Glazer, Acta. Cryst. B **28**, p. 3384 (1972).

13. H.Y. Hwang, S.W. Cheong, P.G. Radaelli, M. Marezio and B. Batlogg, Phys. Rev. Lett. **75**, p. 914 (1995).

14 R. Gupta, A.K. Sood, R. Mahesh and C.N.R. Rao, Phys. Rev. B **54**, p. 14899 (1996).

15. O.Yu. Gorbenko, V.N. Fuflyigin, Y.Y. Erokhin, I.E. Graboy, A.R. Kaul, Yu.D. Tretyakov, G.Wahl and L.Klippe, J. Mater. Chem. **4**, p. 1585 (1994).

16. V.B. Podopedov, A. Weber, D.B. Romero, J.P. Price and H.D. Drew Sol. State Commun. **105**, p. 589 (1998).

17. M.N. Iliev, M.V. Abrashev, H.-G. Lee, V.N. Popov, Y.Y. Sun, C. Thomsen and R.L. Meng, C.W. Chu Phys. Rev. **B57**, p. 2872 (1998).

18. N. Malde, P.S.I.P.N. de Silva, A.K.M. Akther Hossain, L.F. Cohen, K.A. Thomas, J.L. MacManus-Driscoll, N.D. Mathur, and M.G. Blamire, Solid State Communications. **105**, p. 643 (1998).

19. J.F.Lawler, J.G.Lunney and J.M.Coey, Appl. Phys. Lett. 65, p. 3017 (1994).

20. N.A. Babushkina, L.M. Belova, O.Yu. Gorbenko, A.R. Kaul, A.A. Bosak, V.I. Ozhogin and K.I. Kugel, Nature **391**, p. 159 (1997).

21. P. Gillet, F. Guyot, G. Price, B. Tournerie, and A. Le Cleach, Phys. Chem. Minerals **20**, p. 159 (1993).

22 H.J. Bunge, in Texture Analysis in Material Science, Butterworths, London, p. 321 (1982).

MAGNETORESISTANCE BEHAVIOR IN EXTERNAL, INTERNAL AND MIXED DOPED LANTHANUM MANGANITE THIN FILMS

SRINIVAS V. PIETAMBARAM*, D. KUMAR*, RAJIV K. SINGH*, and C. B. LEE**,
*Department of Materials Science and Engineering, University of Florida, Gainesville, Florida 32611-6400. **Department of Electrical Engineering, North Carolina A&T State University, Greensboro, North Carolina 27411.

ABSTRACT

A systematic investigation focused on the magnetoresistance behavior of $La_{0.7}Ca_{0.3}MnO_3$, $La_{0.7}MnO_3$ and $La_{0.7}Ca_{0.2}MnO_3$ thin films has been carried out. Thin films of these materials have been grown *in situ* on (100) $LaAlO_3$ substrates using a pulsed laser deposition technique. Microstructural characterization carried out on these films has shown that the films are smooth, free from impurities, and highly textured. As indicated by their unit chemical formulae, these films represent external, internal and mixed (external and internal) doped lanthanum manganite systems, respectively. Electrical resistance and magnetoresistance have been measured in the 10-300 K range in magnetic field up to 5T using SQUID magnetometer. The MR ratios of $La_{0.7}Ca_{0.3}MnO_3$, $La_{0.7}MnO_3$, and $La_{0.7}Ca_{0.2}MnO_3$ films are found to be 825%, 700% and 750% at 200 K, 240 K and 220 K, respectively. The variation in the insulator to metal transition and the MR ratio is attributed to internal chemical pressure and vacancy localization effects.

INTRODUCTION

$LaMnO_3$ is the basic compound among lanthanum based manganite systems, the transport properties of which can be varied dramatically by means of partial substitution of trivalent lanthanum ions with divalent cations [1-9]. This sparked off a tremendous interest in studying the magnetotransport properties of the doped perovskite manganites $La_{1-x}M_xMnO_3$ (M=Ba, Ca, Sr, Pb) because of their potential in technological applications such as magnetic read-write heads and magnetic sensors. In numerous papers [1-9], it has been shown that over an appreciable range of doping these materials exhibit a very large magnetoresistance effect at temperatures close to those where they undergo a ferromagnetic-paramagnetic transition. The presence of divalent alkaline earth cations on the La sites of the perovskite induces a Mn^{3+}/Mn^{4+} mixed valence state which is responsible for both metallic conductivity and ferromagnetism in accordance with the double exchange (DE) interaction [10].

Although the magnetoresistance effects brought about by the partial doping of lanthanum sites with divalent cations have been studied extensively [1-9], there are very few papers in the literature reporting the transport and magnetic properties of self-doped lanthanum manganites [11-13]. Self-doped lanthanum manganites can be synthesized using lanthanum deficiency at lanthanum sites. According to neutron diffraction and x-ray diffraction studies carried out on $LaMnO_3$, this compound does exist as a single phase defect perovskite with a range of vacancies principally on the lanthanum sites [14]. The chemical composition of the lanthanum deficient compounds can be represented by a general formula, $La_{1-x}MnO_3$. The electronic doping in lanthanum deficient $La_{1-x}MnO_3$ should be similar to that in other lanthanum manganites obtained by divalent substitution. In other words, the nonstoichiometric $La_{1-x}MnO_3$ compound will have mixed Mn^{3+}/Mn^{4+} valence

Mat. Res. Soc. Symp. Proc. Vol. 517 © 1998 Materials Research Society

in a manner similar to that in the divalent substituted compounds $La_{1-x}M_xMnO_3$.

In the present paper, we report the growth and characterization of $La_{0.7}Ca_{0.3}MnO_3$,$La_{0.7}MnO_3$, $La_{0.7}Ca_{0.2}MnO_3$ systems in thin film form. The selection of these systems has been inspired by an intention to understand the effects of external, internal and a combination of external and internal (mixed) doping on transport and magnetic properties of lanthanum manganites with same ratio of Mn^{3+} and Mn^{4+} ions. If M substitution is equivalent to hole doping, $La_{0.7}Ca_{0.3}MnO_3$, $La_{0.7}MnO_3$, and $La_{0.7}Ca_{0.2}MnO_3$ represent external, internal, and mixed doped systems with the same Mn^{3+}/Mn^{4+} ratio respectively.

EXPERIMENT

The bulk samples of nominal composition $La_{0.7}MnO_3$, $La_{0.7}Ca_{0.2}MnO_3$ and $La_{0.7}Ca_{0.3}MnO_3$ were prepared by a ceramic method. The required quantities of respective oxide or carbonate powders were mixed and sintered at 1400°C for 24 hours. The films of these materials were grown *in situ* using a pulsed laser ablation system. A detailed description of the deposition system is mentioned elsewhere [15]. In brief, a 248 nm KrF pulsed laser with 5 Hz repetition rate and 1.6 J/cm^2 energy density was used. A substrate temperature of 700 - 800°C and oxygen pressure of 250 mTorr were used during the deposition of the films. The films deposited were characterized using scanning electron microscopy (SEM), energy dispersive x-ray analysis (EDX), and x-ray diffraction (XRD measurements. The temperature dependence of resistance of the films were examined in zero and applied field using four-probe technique and the quantum design superconducting quantum interference device (SQUID) magnetometer. Both the transport current and applied field were in the film plane. The MR ratio, $\Delta R/R(H)$, was calculated using $\Delta R/R(H) = [R(H)-R(0)]/R(H)]$, where R(H) and R(0) are resistances in applied and zero field.

RESULTS AND DISCUSSION

XRD patterns of $La_{0.7}Ca_{0.3}MnO_3$, $La_{0.7}Ca_{0.2}MnO_3$ and $La_{0.7}MnO_3$ grown on (100) $LaAlO_3$ substrate at 700°C are shown in figure.1. From the figure it is clear that all the films are single phase with (00*l*) peaks with l = 1 and 2. The presence of only (00*l*) peaks implies the highly textured growth of all the films on (100) $LaAlO_3$ substrate with lattice parameters of 3.87, 3.91 and 3.90 Å, for $La_{0.7}Ca_{0.3}MnO_3$, $La_{0.7}Ca_{0.2}MnO_3$ and $La_{0.7}MnO_3$ films, respectively.

The variation of electrical resistance in zero and applied field (5T) as a function of temperature for $La_{0.7}Ca_{0.3}MnO_3$, $La_{0.7}Ca_{0.2}MnO_3$ and $La_{0.7}MnO_3$ films are shown in Fig. 2. All the three films were grown under identical conditions so that film

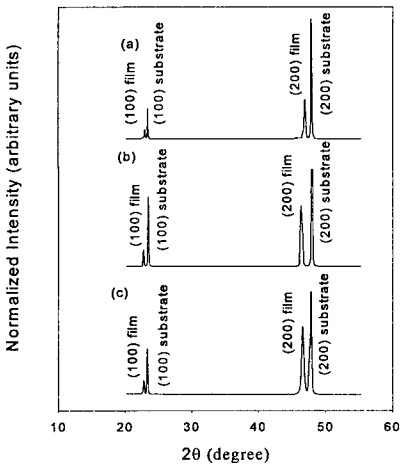

Fig.1. X-ray diffraction patterns of (a)$La_{0.7}Ca_{0.3}MnO_3$, (b) $La_{0.7}Ca_{0.2}MnO_3$ and (c) $La_{0.7}MnO_3$ films grown at 700^0 C on (100) $LaAlO_3$ substrates

thickness and oxygen contents of all the films could be kept identical. It is important to keep these two parameters (thickness and oxygen content) identical in order to resolve the effects of the nature of doping on magnetotransport properties in these films. According to the variation of resistance shown in Fig.2, all the three films have similar qualitative magnetotransport behavior. That is, all the films undergo an insulator to metal (I-M) transition as the temperature is lowered down and the resistance of all the films is suppressed significantly with the application of magnetic field. As observed frequently by others in several manganite systems [1-8], here also the suppression in film resistance in each case is maximum near the resistivity peak in zero field. However, the temperature at which I-M transition takes place in each system is different from each other. The internal doped system ($La_{0.7}MnO_3$) attains the metallic state earliest (240 K) followed by the mixed doped system ($La_{0.7}Ca_{0.2}MnO_3$), and external doped ($La_{0.7}Ca_{0.3}MnO_3$) system with I-M transitions around 220 and 200 K, respectively. Thus, it appears that the electronic doping in self-doped compounds is similar to that of the compounds with external doping.

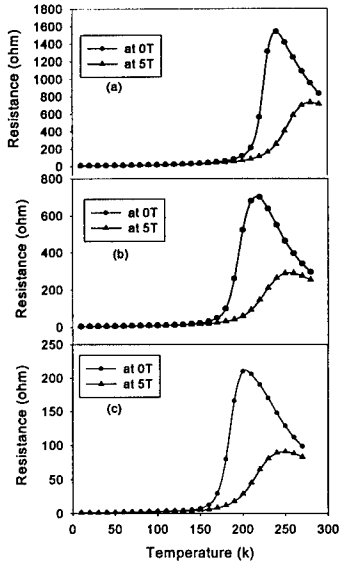

Fig.2. Resistance versus temperature plots for (a) $La_{0.7}MnO_3$, (b) $La_{0.7}Ca_{0.2}MnO_3$ and (c) $La_{0.7}Ca_{0.3}MnO_3$ films in 0 and 5T magnetic fields

The difference in the values of I-M transition temperature in the systems we have studied here may be explained on the basis of tolerance factor (t). The tolerance factor essentially determines the Mn-O-Mn bond angle, which in turn, controls the effective electron transfer between Mn^{3+} and Mn^{4+} within the framework of double exchange mechanism[16]. The deviation in *t* from unity is a measure of the mismatch between the equilibrium bond lengths La-O and Mn-O in a perovskite structured lanthanum manganite system [17]. The room-temperature, ambient-pressure value of *t* is calculated from the sums of the empirical ionic radii given in tables, e.g., those of Shannon and Prewitt [18]. A $t<1$ places the Mn-O bonds under compression and La-O bonds under tension. If these internal stresses are not

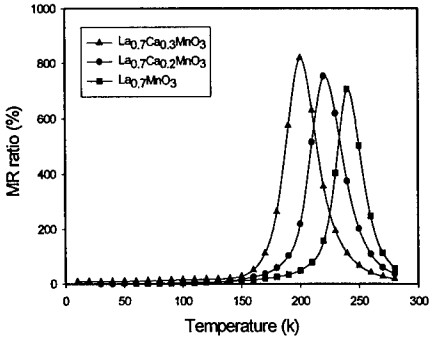

Fig.3. Variation of MR ratio with temperature for $La_{0.7}MnO_3$ (filled square), $La_{0.7}Ca_{0.2}MnO_3$ (filled circle) and $La_{0.7}Ca_{0.3}MnO_3$ (filled triangle) films

relieved due to structural hindrance in rotation of MnO_6 octahedra[27], the lattice will be in the state of internal pressure [19,20]. The tolerance factors of the compounds investigated in the present study, $La_{0.7}Ca_{0.3}MnO_3$, $La_{0.7}Ca_{0.2}MnO_3$ and $La_{0.7}MnO_3$, were calculated to be 0.90, 0.85, and 0.80, respectively. Therefore, in accordance with previous reports by Yoshizawa et al. [19],and Raveau et al.[20], these compounds with varying tolerance factors are likely to experience different internal stresses, and hence, different chemical pressures. As a result of difference in chemical pressure, the insulator to metal transition in each system occurs at different temperature: $La_{0.7}MnO_3$ films which has largest deviation of *t* from unity, and hence, highest internal chemical pressure undergoes an I-M transition at higher temperature (240 K) compared to I-M transitions of $La_{0.7}Ca_{0.2}MnO_3$ (I-M transition: 220 K) and $La_{0.7}Ca_{0.3}MnO_3$ (I-M transition: 200K) films.

The MR ratios of $La_{0.7}Ca_{0.3}MnO_3$, $La_{0.7}Ca_{0.2}MnO_3$ and $La_{0.7}MnO_3$ films were calculated using the data in Fig. 2. The MR ratios obtained are plotted in Fig. 3 as a function of temperature at 5 T. The figure shows that $La_{0.7}Ca_{0.3}MnO_3$ has the highest MR ratio (~825%) which is followed by $La_{0.7}Ca_{0.2}MnO_3$ (MR ratio~750 %) and $La_{0.7}MnO_3$ (MR ratio ~700%) systems. The variation in MR ratios of these compounds are explained as follows. The occupancy of e_g band is expected to be similar for all the three systems assuming that oxygen remains divalent and Mn^{3+}/Mn^{4+} ratio is the same in all the systems. However, due to difference in vacancies at La-sites (arising from lanthanum deficiency), the localization effects, and hence, the mobility of charge carriers are different in different systems. Since the density of lanthanum deficiency is more in $La_{0.7}MnO_3$ system (internal doped), the localizing effect of random vacancies is stronger in $La_{0.7}MnO_3$ films than that in $La_{0.7}Ca_{0.2}MnO_3$ (mixed doped) film. Therefore, the random potential fluctuations due to missing La^{3+} ions will favor the Anderson localization more strongly in the former system than in the later system [21]. As a result of this, the MR ratio obtained for $La_{0.7}MnO_3$ film is less than that of $La_{0.7}Ca_{0.2}MnO_3$ film. There is no such localization effect in stoichiometric $La_{0.7}Ca_{0.3}MnO_3$ films due to absence of vacancies which is manifested with the realization of highest MR ratio among the three systems discussed here.

CONCLUSIONS

In summary, we have presented the studies of magnetoresistance behavior in $La_{0.7}Ca_{0.3}MnO_3$, $La_{0.7}MnO_3$, and $La_{0.7}Ca_{0.2}MnO_3$ which are external, internal, and mixed doped systems with the same Mn^{3+}/Mn^{4+} ratio. The results obtained have shown that the electronic doping in non-stoichiometric compounds is similar to that of the compounds with divalent substitution. The variation in insulator to metal transition and MR ratio in these systems have been explained using the concept of internal chemical pressure and localization effects.

ACKNOWLEDGMENTS

The authors would like to thank the U.S. Department of Energy (Grant No. DE-FG 05-95ER45533) for funding this research.

REFERENCES

1. S. Jin, T. H. Tiefel, M. McCormack, R.A. Fastnatch, R. Ramesh, and L. H. Chen, Science **264**, 413 (1994).

2. S. S. Manoharan, K. M. Satyalakshmi, M. S. Hegde, V. Prasad, and S. V. Subramanyam, J. Appl. Phys. **76**, 3923 (1994).

3. H. L. Ju, C. Kwon, Qi Li, R. L. Greene, and T. Venkatesan, Appl. Phys. Lett. **65**, 2108 (1994).

4. M. F. Hundley, M. Hawley, R. H. Helfner, Q. X. Jai, J. J. Neumeir, J. Tesmer, J. D. Thomson, and X. D. Wu, Appl. Phys. Lett. **67**, 860 (1995).

5. X. T. Zeng and H. K. Wong, Appl. Phys. Lett. **66**, 3371 (1995).

6. R. Mahendiran, S. K. Tiwary, A. K. Raychauduri, T. V. Ramakrishnan, R. Mahesh, N. Rangavittal, and C. N. R. Rao, Phys. Rev. B **53**, 3348 (1996).

7. D. Kumar, R. Kalyanaraman, J. Narayan, and D. K. Christen, Mater. Res. Soc. Symp. Proc. **397**, 241 (1996).

8.. F. Damay, A. Maignan, C. Martin, and B. Raveau, J. Appl. Phys. **81**, 1372 (1997).

9. J. M. D. Coey, M. Viret, and K. Ounadjela, Phys. Rev. Lett. **75**, 3910 (1995).

10. C. Zener, Phys. Rev. **82**, 403 (1951).

11. S. S. Manoharan, D. Kumar, M. S. Hegde, K. M. Satyalakshmi, V. Prasad, and S. V. Subramanyam, J. Solid State Chem. **117**, 420 (1995).

12. A. Gupta, T. R. McGuire, P. R. Duncombe, M. Rupp, J. Z. Sun, W. J. Gallagher, and G. Xiao, Appl. Phys. Lett. **67**, 3494 (1995).

13. P. S. I. P. N. de Silva, F. M. Richards, L. F. Cohen, J. A. Alonso, M. J. Martinez-Lope, M.T. Casais, K. A. Thomas and J. L. MacManus-Driscoll, J. Appl. Phys. **83**, 394 (1998).

14. B. C. Tofield and W. R. Scott, J. Solid State Chem. **10**, 183 (1974).

15. D. Kumar, Rajiv K. Singh, C. B. Lee, Physical Review B **56**, 13 666 (1997).

16. H. Y. Hwang, S.-W. Cheong, P. G. Radaelli, M. Marezio, and B. Batlogg, Phys. Rev. Lett. **51**, 914 (1995).

17. W. Archibald, J.-S. Zhou, and J. B. Goodenough, Phys. Rev. B **53**, 14 445 (1996).

18. R. D. Shannon and C. T. Prewitt, Acta Crystallogr. B **25**, 725 (1969); 26, (1970).

19. H. Yoshizawa, R. Kajimoto, H. Kawano, Y. Tamioka and Y. Tokura, Phys. Rev. B **55**, 2729 (1997).

20. B. Raveau, A. Maignan, and V. Caignaert, J. Solid State Chem. **117**, 424 (1995).

21. L. Ranno, M. Viret, A. Mari, R. M. Thomas, and J. M. D. Coey, J. Phys.: Condens. Matter **8**, L33 (1996).

POST ANNEALING AND COLOSSAL MAGNETORESISTANCE IN EPITAXIAL La-Nd-Ca-Mn-O AND La-Y-Ca-Mn-O FILMS BY D.C. SPUTTERING

L.H. Chen and J.L. Lin
Department of Materials Engineering, I-Shou University, Kaohsiung, Taiwan, ROC

ABSTRACT

The strongly textured $La_{0.67}Ca_{0.33}MnO_{3-x}$, $La_{0.60}Nd_{0.07}Ca_{0.33}MnO_{3-x}$ and $La_{0.60}Y_{0.07}Ca_{0.33}MnO_{3-x}$ films have been grown on the (100)$LaAlO_3$ substrates at temperatures between 650 °C-750 °C in an atmosphere of Ar/O_2 by a d.c. magnetron sputtering process. All of the as-deposited films exhibit small MR values and monotonously increasing tendency of resistivity and magnetoresistance value, as temperature decreases from room temperature to 30 K. However, upon annealing at temperatures between 900 °C-950 °C for 4 hr, the MR ratios increase and show the maximum values of about 32%, 600% and 5300% at lower temperatures for La-Ca-Mn-O, La-Nd-Ca-Mn-O and La-Y-Ca-Mn-O films, respectively. The temperature dependence of zero-field resistivity of annealed La-Ca-Mn-O film show a metal-insulator transition centered at ~180 °K, which is decreased to ~100 °K and ~70 °K for the annealed La-Nd-Ca-Mn-O and La-Y-Ca-Mn-O films, respectively. Such a significant influence of post annealing on the MR and electric transport behavior is believed to be correlated to the change in the concentration of oxygen ions, as well as the modification of microstructure and the change in residual stress.

INTRODUCTION

The recent discovery of anomalous reductions in electrical resistivity of La-Ca-Mn-O under the applied magnetic field has sparked much interest in its mechanisms and the potential applications in magnetic sensors and read heads in magnetic information systems[1]. More than 3 orders of magnitude greater than were previously reported for the GMR type multilayers, the colossal magnetoresistance values of 1,000,000% have been reported for epitaxial thin films of La-Ca-Mn-O[2].

It is well known that the magnetoresistance behavior of manganites depends on the sample composition and preparation process. As reported in our previous papers[1,2], a high quality epitaxial growth of films is one of the key points to obtain high magnetoresistance, as evidenced by that the bulk and polycrystalline materials and non-epitaxial films do not give impressive magnetoresistance values. The chemical doping of materials, for example by a partial substitution of lanthanum with a smaller yttrium ion, is another way to obtain the colossal magnetoresistance even in bulk, polycrystalline La-Y-Ca-Mn-O without using the epitaxial growth at all[3].

Lanthanum manganites films were mainly prepared by the pulsed laser deposition method under stringent conditions[4-7]. In this work, we prepared the epitaxial grown $La_{0.67}Ca_{0.33}MnO_{3-x}$ $La_{0.60}Nd_{0.07}Ca_{0.33}MnO_{3-x}$ and $La_{0.60}Y_{0.07}Ca_{0.33}MnO_{3-x}$ films on $LaAlO_3$ substrates by using a simple d.c. magnetron sputtering technique. The influence of annealing and Nd/Y doping on the electric transport and magnetoresistance behavior of films will be discussed.

Mat. Res. Soc. Symp. Proc. Vol. 517 © 1998 Materials Research Society

EXPERIMENTS

The 2-inch sputtering targets were prepared by the mixing of high-purity components of oxides or carbonates, grinding, calcining at 1200 °C and sintering at ~ 1400 °C in an O_2 atmosphere. The ~ 4000 A thick La-Nd-Ca-Mn-O, La-Nd-Ca-Mn-O and La-Y-Ca-Mn-O films were grown on (100) $LaAlO_3$ by d.c. magnetron sputtering in an Ar/O_2 mixed atmosphere with a volumn ratio of 7:3. The deposition was carried out under a pressure of 50 mTorr. The substrate temperature was maintained at ~650-750 °C. The films were post-annealed in an oxygen atmosphere of 3 atm at ~ 900-950 °C for several hours.

The crystal structures of films were investigated by x-ray diffraction (XRD) using K_α (Cu) radiation. The resistivity and magnetoresistance were measured as functions of both temperature and magnetic field by the four-point technique in a magnet with the maximum applied field of 2 T. A constant dc current ranging from 1nA to 10μA was used in the magnetoresistance measurement. The MR effect was always negative and isotropic in this study. The MR value is defined here as $\triangle R/R_H = (R_o-R_H)/R_H$, where R_o and R_H are resistance under fields of 0 and 2 T, respectively.

RESULTS AND DISCUSSION

Figure 1a shows the typical θ /2θ pattern of XRD for the La-Ca-Mn-O film deposited on the (100)$LaAlO_3$ substrate at 700 °C in an atmosphere of $70Ar/30O_2$ (in vol%). The XRD pattern exhibits only two sets of diffraction peaks of {100} planes for the La-Nd-Ca-Mn-O film and $LaAlO_3$ substrate, respectively. This suggests that the as-deposited film has a perovskite-type cubic structure with a lattice parameter a of ~3.96A and shows a strong texture on the $LaAlO_3$ substrate (a = ~3.79 A).

The XRD pattern for the La-Ca-Mn-O film annealed at 950 °C for 2 hr in O_2 atmosphere is displayed as curve b in Figure 1. A similar XRD pattern as that for the as-deposited film is found for the post-annealed film, except that the diffraction peaks become sharper and

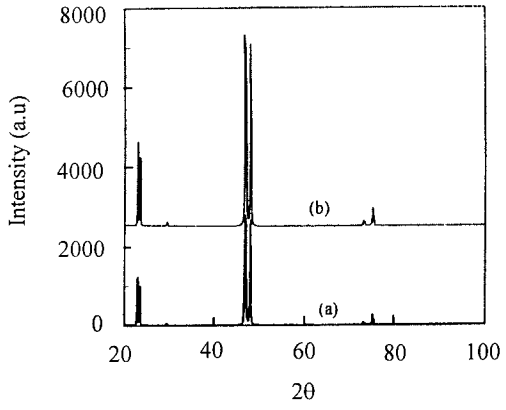

Figure 1.The typical θ/2θpatterns of XRD for the as-deposited (curve a) and post-annealed (curve b) La-Ca-Mn-O films, respectively.

the peak positions for both film and substrate come closer. This suggests that a post annealing decreased the lattice parameter of films, which is believed to be caused by the higher ratio of Mn^{4+} to Mn^{3+}, as a result of the incorporation of O_2 into film. Besides, the effect of improvement of crystal quality of the film by a post-annealing is also responsible, for the elimination of part of defects and stress in the film as a result of high temperature diffusion of atoms during annealing.

The resistivity of the as-deposited and annealed La-Ca-Mn-O films on (100)$LaAlO_3$ substrate is measured as a function of temperature and magnetic field. As shown in Figure 2, the resistivity of as-deposited film gradually increases as the temperature decreases from room temperature (~300 °K) to near 140 °K, and then abruptly increases at temperatures below. Due to the measurement limit of resistance in our laboratory, the resistivity at temperature below 80 °K is not measured. Upon annealing, the resistivity of La-Ca-Mn-O film significantly decreases. The resistivity of annealed film also increases as temperature drops from room temperature and a semiconducting behavior is displayed. However, there is a metal-insulator transition observed at ~ 180 °K, and the resistivity of film decreases as temperature is further lowered.

The resistivity of both as-deposited and annealed La-Ca-Mn-O films shows an decreasing tendency under applied magnetic fields up to 2 T. As no saturation is observed, it is thus believed that the resistivity of films will be further decreased, when the applied field further increases. The room temperature magnetoresistance value of film under a field of 2T is about 0.3%, which also increases to 1.3% as the temperature decreases to 100 °K, as shown in Figure 3 (curve a). As reported in previous study[1], the MR values of the Lanthanum manganites shows a similar temperature dependence as that of resistivity, except that a maximum MR value appears at slightly lower temperature than that in the resistivity versus temperature curve. This indicates that the MR values of this as-deposited film will be higher than 1.3% at temperatures below 100 °K.

Upon annealing at 950 °C for 4 hr, the La-Ca-Mn-O film shows an obvious magnetoresistance behavior at room temperature, which shows a MR value of ~2.0%. The MR value of film increase as temperature decreases and reaches a maximum value of ~32% at 200 °K, as curve b in Figure 3. Although the exact reasons for the improvement

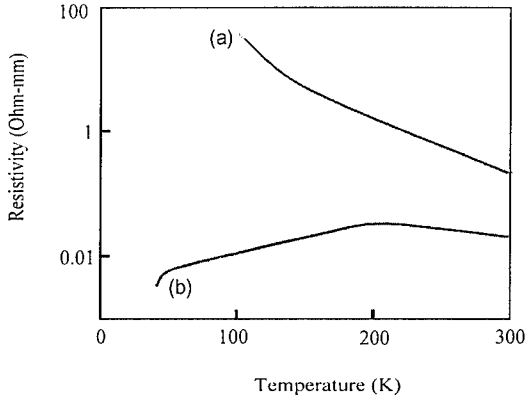

Figure 2. The resistivity versus temperature curves for the as-deposited (curve a) and post-annealed (curve b) La-Ca-Mn-O films, respectively.

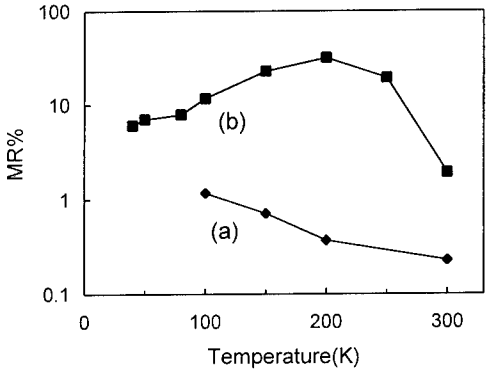

Figure 3. The temperature dependence of MR value for the as-deposited (curve a) and post-annealed (curve b) La-Ca-Mn-O films, respectively.

of MR behavior are not known at this moment, they are believed to be correlated to the incorporation of more O_2 into the film, as well as the modification of film microstructure, for examples the decreasing of defect concentration and residual stress, during the high temperature annealing treatment.

The influence of partial substitution of La^{3+} by smaller Nd^{3+} and Y^{3+} on the MR behavior of La-Ca-Mn-O films is displayed in Figures 4 and 5. The as-deposited La-Nd-Ca-Mn-O and La-Y-Ca-Mn-O film exhibit the similar MR behavior as that of La-Ca-Mn-O film. The room temperature MR value of as-deposited La-Nd-Ca-Mn-O film is small, which monotonously increases to ~2.2% as temperature decreases to 65 ^{o}K. Upon annealing at 900 ^{o}C for 4 hr, the La-Nd-Ca-Mn-O film also exhibits a small MR value of 0.7 % at room temperature. However, the MR value of annealed film significantly increases as temperature decreases and reaches a maximum value of ~600 % at 85 ^{o}K, shown as curve b in Figure 4. Similarly, the as-deposited La-Y-Ca-Mn-O film only shows

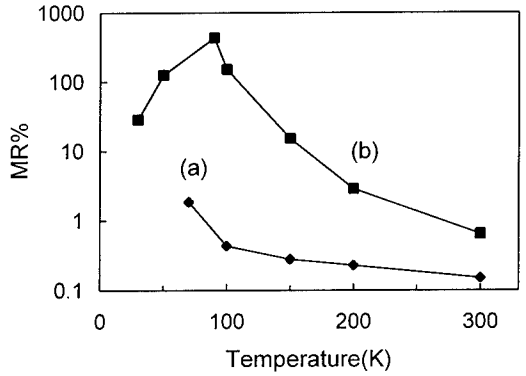

Figure 4. The temperature dependence of MR value for the as-deposited (curve a) and post-annealed (curve b) La-Nd-Ca-Mn-O films, respectively.

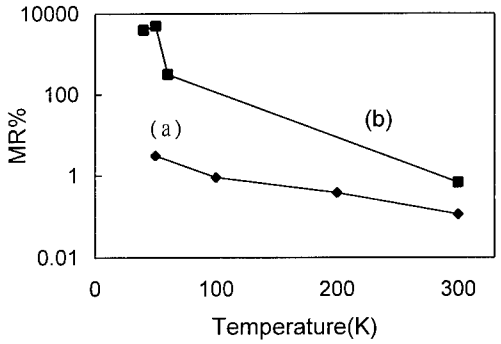

Figure 5. The temperature dependence of MR value for the as-deposited (curve a) and post-annealed (curve b) La-Y-Ca-Mn-O films, respectively.

a MR value of 0.15 % at room temperature, which increases to ~3.1% at 50 ^{o}K. The MR value of annealed La-Y-Ca-Mn-O film is ~0.7% at room temperature, which increases to a maximum of 5300% as temperature decreases to 50 ^{o}K.

Inspection of the magnetoresistance behavior of films reveals that partial substitution of La3+ by smaller Nd3+ and Y3+ in La-Ca-Mn-O film improve the MR behavior, especially at lower temperature, and decreases the temperature of metal-insulator transition to ~100 ^{o}K and ~70 ^{o}K for the annealed La-Nd-Ca-Mn-O and La-Y-Ca-Mn-O films, respectively. Such modification of MR behavior is believed to be correlated to the change in length and angle of Mn-O-Mn bonds in these perovskite-like La-manganite films, as a result of smaller ions doping.

CONCLUSIONS

We have grown the strongly textured La-manganite films on (100)$LaAlO_3$ substrates by using a d.c. magnetron sputtering process. The resistivity and magnetoresistance value of the as-deposited films increases as the temperature decreases from room temperature to 40 ^{o}K, and no metal-insulator transition is observed in this temperature range. A post-annealing at 900/950 ^{o}C for 4 hr shifts the temperature of metal-insulator transition to a higher temperature and significantly enhances the MR values, as a result of modification of film microstructure as well as the incorporation of O_2. The partial substitution of La^{3+} by Nd^{3+} and Y^{3+} in La-Ca-Mn-O film improves the MR behavior, especially at lower temperatures, which is correlated to the change in length and angle of Mn-O-Mn bonds in these films.

ACKNOWLEDGMENTS

This work is supported by the National Science Council at Taiwan under the contract number of NSC87-2216-E-214-004.

REFERENCES

1.S. Jin, T.H. Tiefel, M. McCormack, R.A. Fastnacht, R. Ramesh, and L.H. Chen, Science **264**, 413(1994)

2.L.H. Chen, S. Jin, T.H. Tiefel, R. Ramesh, and D. Schurig, IEEE Trans on Magn. **31**, 3912(1995)

3.S. Jin, H.M. O'Bryan, T.H. Tiefel, M. McCormack, and W.W. Rhodes, Appl. Phys. Lett.**66**,382(1995)

4.H. C. Ju, C. Kwen, Q.Li, R.L. Greene, and T. Venkatesan, Appl. Phys. Lett. **65**, 2108(1994).

5.B. Ravean, A. Maignan, and V. Caignaert, J. of Solid State Chemistry **117**., 424(1995)

6.Y. Moritomo, A. Asamitsu, and Y. Tokura, Phys. Rev. B **51**, 16491(1995)

7.J. Z. Liu, I. C. Chang, S. Irons, P. Klavins, R. N. Shelton, K. Song, and S. R. Wasserman, Appl. Phys. Lett. **66**., 3218(1995)

MICROSTRUCTURE AND MAGNETORESISTANCE OF La-Sr-Mn-O THIN FILMS GROWN BY rf SPUTTERING

K.K. Choi, K. Nakano, M. Yamasaki, and Y. Yamazaki
Dept. of Innovative and Engineered Materials, Tokyo Institute of Technology,
Yokohama 226-8502, JAPAN

ABSTRACT

The relationship between the microstructure and the magnetoresistive properties of La-Sr-Mn-O thin films was investigated. $La_{0.76}Sr_{0.24}Mn_{0.98}O_{3-\delta}$ films were deposited onto (100) $SrTiO_3$, (100) $LaAlO_3$, (110) sapphire and polycrystalline YSZ substrates by rf sputtering. The films grew epitaxilly on $SrTiO_3$ and $LaAlO_3$ substrates with a large number of defects, whereas in-plane oriented and non-oriented polycrystalline films of 50～100 nm grains grew on the sapphire and the polycrystalline YSZ substrates, respectively. The magnetoresistance ratio (H=8 kOe) of epitaxial films has a peak at a temperature slightly below the maximum resistance temperature. The polycrystalline films exhibited substantial magnetoresistance over a wide temperature range. The resistivity of the epitaxial films was ten times less than that of the polycrystalline films. As the film thickness decreased, the resistivity decreased in the epitaxial films, however, increased in the polycrystalline films. The existence of grain boundaries was found to be correlated to the resistivity and the temperature dependence of the magnetoresistance.

INTRODUCTION

Perovskite manganese oxide thin films showing colossal magnetoresistance (CMR) with magnetic field-dependent electrical resistivity changes more than six orders of magnitude have been reported[1]. The magnetic and electronic properties of lanthanum-based manganites, $La_{1-x}D_xMnO_{3-\delta}$ where D is a divalent metal ion, have been examined due to their many potential applications including magnetoresistive read heads and bolometer-type uncooled infrared detectors[1, 2]. In polycrystalline bulk and thin films, spin-polarized tunneling and spin-dependent scattering at grain boundary make a significant contribution to the magnetoresistance (MR) at low magnetic fields[3, 4]. Substrate material is an important factor in manganite thin films, because lattice strain influences the Curie temperature shift, and strain is a function of lattice and thermal expansion mismatch between the film and the substrate[5, 6].

In this work, we present the effects of microstructure and crystallinity on the MR properties of rf sputtered La-Sr-Mn-O thin films. Epitaxial films were prepared on (100) $SrTiO_3$ and (100) $LaAlO_3$. In-plane oriented and non-oriented films grown on (110) sapphire and polycrystalline YSZ substrates were studied. The substrate dependent microstructures were compared. We also investigated the relationship between transport properties and crystalline structure.

EXPERIMENTAL

The sputtering target with nominal composition, $La_{0.7}Sr_{0.3}Mn_{1.2}O_{3-\delta}$, having a diameter of 100 mm was prepared using a solid reaction technique. Using this target thin films were prepared by rf sputtering at 650℃ onto single crystals of (100) $SrTiO_3$, (100) $LaAlO_3$, (110) sapphire and polycrystalline YSZ (average grain size : 5 ㎛) substrates with a sputtering atmosphere of 60 % Ar and 40 % O_2. The lattice parameter and the thermal expansion coefficient

Mat. Res. Soc. Symp. Proc. Vol. 517 © 1998 Materials Research Society

of La-Sr-Mn-O and the substrate materials used in this work are summarized in Table 1. During the deposition process, the total pressure was maintained at 8.0 Pa, and rf power was 2.5 W/cm^2. The thickness of all films studied here was 20~400 nm depending on the deposition time. After deposition, all films were annealed at 900℃ for 1.5 hours in oxygen. The chemical composition of the deposited films was established by inductively coupled plasma emission spectrometry (ICP). The crystallinity and the microstructures of the films were examined by x-ray diffraction (XRD) and transmission electron microscope (TEM). The DC electric resistivity was measured over temperature region from 100 K to 350 K by a 2-point method. The MR was measured using a constant current of 1 mA and an applied magnetic field of 8 kOe. The measurements were performed with the applied magnetic field parallel to the plane of the film and in the direction of the current flow. The MR ratio is defined as $\Delta R/R_{8kOe}$, where $\Delta R=(R_{8kOe}-R_0)$ and R_0 is the zero-field resistance.

Table 1. Lattice parameter and thermal expansion coefficient of La-Sr-Mn-O and the substrate materials.

	La-Sr-Mn-O	$SrTiO_3$	$LaAlO_3$	Sapphire	YSZ
Lattice Parameter (Å)	a=3.87*	a=3.90	a=3.79*	a=4.76 c=12.3	a=5.14
Thermal Expansion Coefficient (/K)	$\sim 11\times10^{-6}$	$\sim 9\times10^{-6}$	$\sim 10\times10^{-6}$	c ∥ $\sim 8.5\times10^{-6}$ c⊥ $\sim 7.7\times10^{-6}$	$\sim 10\times10^{-6}$

* La-Sr-Mn-O and $LaAlO_3$ are considered as pseudo-cubic crystals

RESULTS AND DISCUSSION

Fig. 1 shows the XRD spectra for each of the $La_{0.76}Sr_{0.24}Mn_{0.98}O_{3-\delta}$ (LSMO) thin films deposited on the various substrates as indicated. The XRD patterns of the films deposited on (100) $SrTiO_3$ and (100) $LaAlO_3$ substrates are shown in Figs. 1 (a) and (b), respectively. These films showed preferential [100] orientation. On the other hand, the XRD patterns of the films deposited on (110) sapphire and polycrystalline YSZ substrates showed a (110) peak as well as several (h00) peaks as seen in Figs. 1 (c) and (d).

Plan-view TEM observations indicate that LSMO thin films have substrate dependent grain size and orientation. TEM bright field images and transmission high energy electron diffraction (THEED) patterns indicate that the films grown on $SrTiO_3$ and $LaAlO_3$ substrates have similar microstructures as seen in Fig. 2 and Fig. 3, respectively. However, in both substrate cases lower magnification images reveal many inhomogeneities and defects. In particular these films are composed of large areas (~5 μm) which have well crystallized features (A regions of Figs. 2 and 3) separated by regions containing mixtures of triangle-shaped crystals and amorphous structure (B regions of Figs. 2 and 3). The high-magnification image of a C region, seen in Fig. 3 C is consistent with amorphous structure. Since, this region is composed of crystallites of less than 3 nm size. The inhomogenous morphology and the many defects seen in these films appear to be associated with either a Mn deficiency and/or the presence of substrate surface defects. It is important to note that the films made here are quite different from the epitaxial thin films made by the pulsed laser deposition (PLD) method reported by Gommert et al. [7] in which columnar grains of ~ 20 nm diameter were observed.

Fig. 4 and Fig. 5 show the TEM images and corresponding THEED patterns of the LSMO films deposited on (110) sapphire and polycrystalline YSZ substrates, respectively. As clearly seen, polycrystalline films with grain size ranging from 50 nm to 100 nm were grown on both

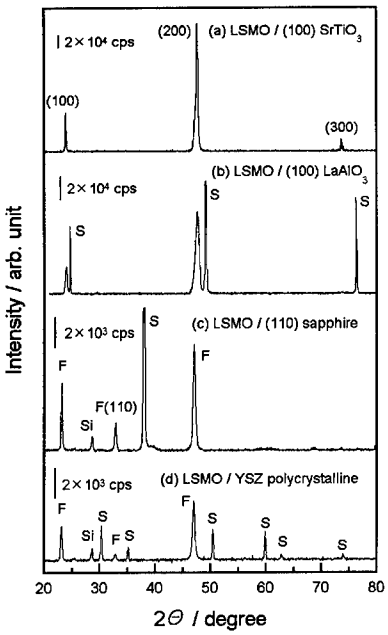

Fig. 1 X-ray diffraction patterns of LSMO thin films deposited on (100) $SrTiO_3$ (a), (100) $LaAlO_3$ (b), (110) sapphire (c) and YSZ polycrystalline (d) substrates. The notation F, S and Si represents the patterns for film, substrate and Si for internal standard, respectively.

substrates. The THEED patterns of the films on sapphire substrate indicate an in-plane oriented structure, while the ring-shaped THEED patterns for the films on the polycrystalline YSZ substrate indicate that non-oriented polycrystalline film was grown in this case. The replicated grain boundary of the underlying polycrystalline YSZ substrate can also be observed. Unlike the PLD films reported by Gupta et al. [8], the rf sputtered polycrystalline films exhibited no epitaxial growth regions. These observations suggest that the growth and the microstructure of rf sputtered LSMO films are highly dependent on the substrate materials.

Fig. 6 shows the zero-field resistivity of the LSOM films deposited on various substrates as a function of temperature. The resistivity of the epitaxial films is one order of magnitude smaller than that of the polycrystalline films. The resistivity increases with increasing temperature until reaching its peak value, T_p, after which the resistivity decreases with further increasing temperature as indicated in Fig. 6. The epitaxial film has a T_p of 286 K which is ~90 K higher than that of the polycrystalline films (190 K for LSMO/(110) sapphire, 199 K for LSMO/YSZ polycrystalline). It can also be seen in Fig. 6 that the resistivity as a function of temperature has a steeper slope in the epitaxial film cases in the low temperature (or metallic) region.

The MR-T plots shown in Fig. 7, also show substrate dependent features. For the epitaxial films, the MR ratio has a peak at a temperature slightly below T_p and MR disappears at low temperatures ($T \leq 100$ K). On the other hand, the polycrystalline films have significant MR over a wide temperature range including T=100 K (the lowest temperature measured in this work). No MR maximum could be observed in the case of film with an in-plane preferential orientation (on sapphire substrate), however, the non-oriented polycrystalline film (on polycrystalline YSZ substrate) showed a broad MR peak at ~156 K as indicated in Fig. 7. The low temperature, low field MR in polycrystalline films have been previously explained in terms of spin-dependent grain boundary scattering or spin-polarized tunneling between the grains[3, 4]. Our results demonstrate that preferential in-plane grain orientation can also affect the transport properties of these polycrystalline films.

The temperature and thickness dependence of the resistivity, shown in Figs. 8 and 9, offers an interesting insight into the transport mechanisms of these films. For the epitaxial films (on $LaAlO_3$ substrates), the resistivity decreases and T_p increases as the film thickness decreases. These results suggest that the lattice strain increases with increasing the film thickness, and therefore the lattice polaron conduction mechanism is affected. The large resistivity of the thinnest polycrystalline film case (on sapphire substrates) is due to an island like initial growth with well separated grains which coalesce in the thicker films to form a continuous network[9].

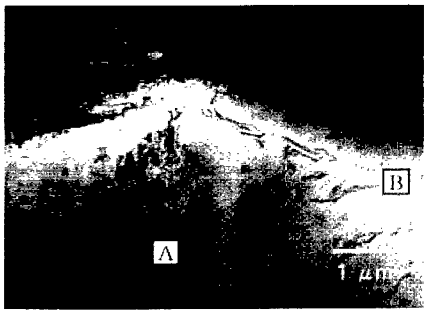

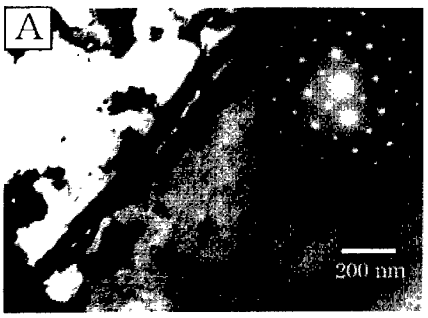

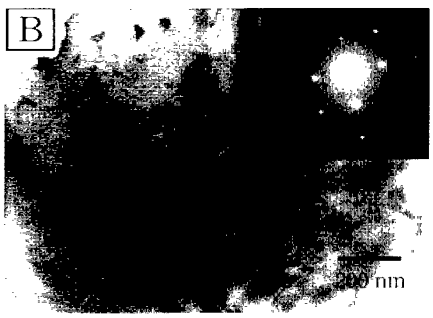

Fig. 2. TEM bright field images of 400 nm-thick LSMO film grown on (100) $SrTiO_3$ substrate. The areas marked by A and B are enlarged and the corresponding THEED patterns are shown in the insets.

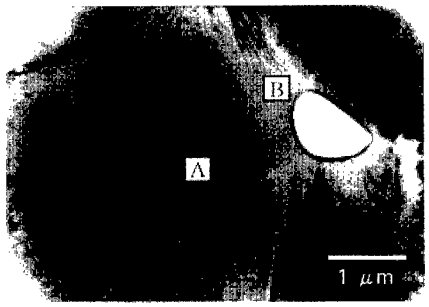

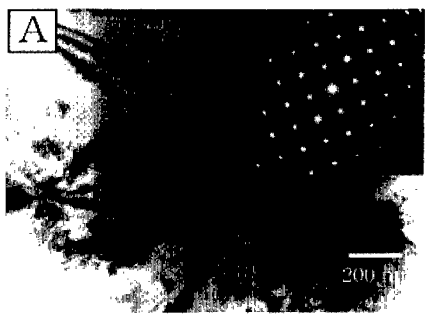

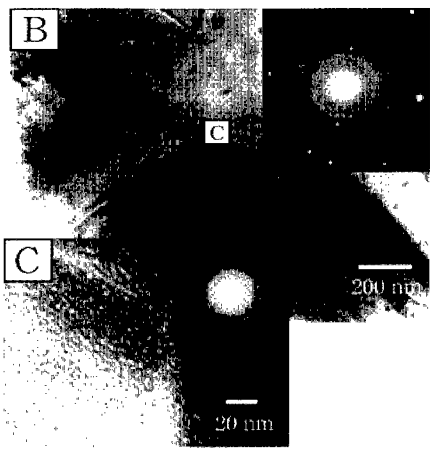

Fig. 3. TEM bright field images of 400 nm-thick LSMO film on (100) $LaAlO_3$ substrate. The areas marked by A, B and C are enlarged and the corresponding THEED patterns are shown in the insets.

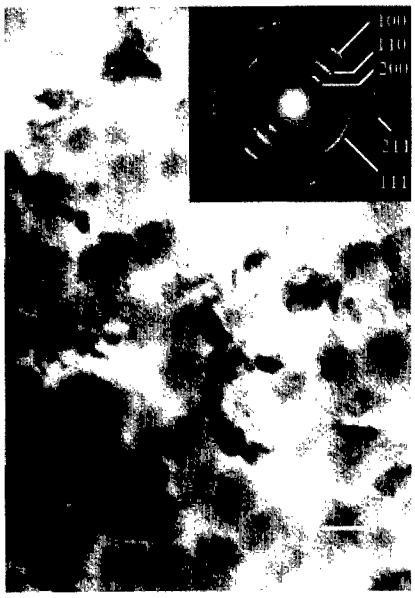

Fig. 4. TEM bright field image of 400 nm- thick LSMO film grown on (110) sapphire substrate. The THEED pattern is shown in the inset.

Fig. 5. TEM bright field image of 400 nm- thick LSMO film grown on YSZ polycrystalline substrate. The THEED pattern is shown in the inset.

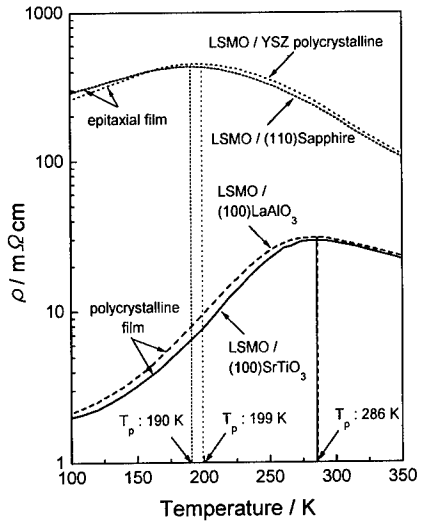

Fig. 6. Temperature dependence of the resistivity ρ for 400 nm-thick LSMO thin films deposited on various substrates.

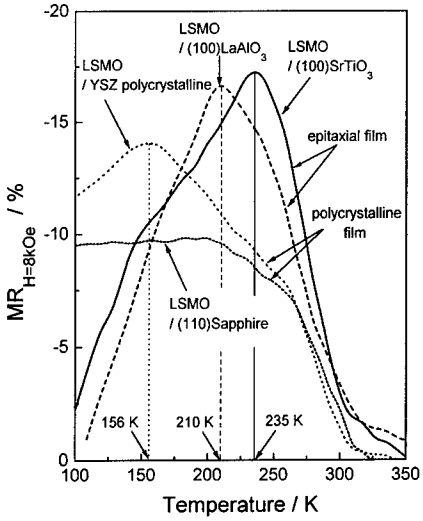

Fig. 7. Temperature dependence of the MR ratio at H=8 kOe for 400 nm-thick LSMO thin films deposited on various substrates.

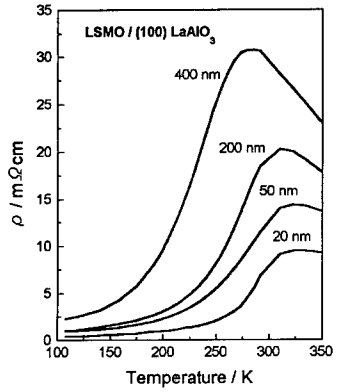

Fig. 8. Temperature dependence of the resistivity ρ as a function of the thickness of LSMO thin films deposited on (100) $LaAlO_3$ substrate.

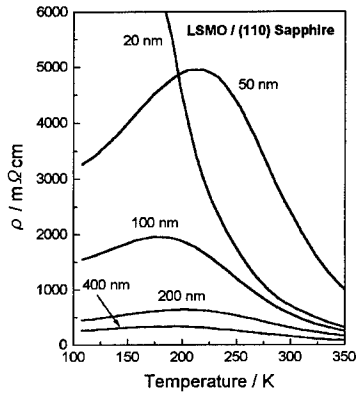

Fig. 9. Temperature dependence of the resistivity ρ as a function of the thickness of LSMO thin films deposited on (110) sapphire substrate.

CONCLUSION

Effects of the substrate dependent microstructures and crystallinity on the transport properties of rf sputtered LSMO thin films were investigated. Local epitaxial growth with numerous defects and inhomogeneous phases were observed in the films deposited on lattice matched substrates. On the lattice mismatched and polycrystalline substrates, polycrystalline films with small grains were formed. The existence of grain boundaries was found to be correlated to the resistivity and the temperature dependence of MR. The transport properties in the polycrystalline films were also affected by preferential in-plane grain orientation. The results of the thickness dependence of the resistivity suggest the importance of lattice strain generated during the LSMO thin film growth.

ACKNOWLEDGMENTS

This work is supported in part by the Storage Research Consortium (SRC).

REFERENCES

1. S. Jin, T. H. Tiefel, M. McComack, R. A. Fastnacht, R. Ramesh, and L. H. Chen, Science, **264**, p. 413 (1994).
2. A. Goyal, M. Rajeswari, R. Shreekala, S. E. Lofland, S. M. Bhagat, T. Boettcher, C. Kwon, Ramesh, and T. Venkatesan, Appl. Phys. Lett., **71**, 2535 (1997).
3. H. Y. Hwang, S. W. Cheong, N. P. Ong, and B. Batlogg, Phys. Rev. Lett., **77**, 2041 (1996).
4. X. W. Li, A. Gupta, G. Xiao, and G. Q. Gang, Appl. Phys. Lett., **71**, 1123 (1997).
5. M. Kitagawa, and Y. Yamazaki, J. Mag. Soc. Jpn., **20**, 925 (1996).
6. T. Y. Koo, S. H. Park, K. B. Lee, and Y. H. Jeong, Appl. Phys. Lett., **71**, 977 (1997).
7. E. Gommert, H. Cerva, A. Rucki, R. v. Helmolt, J. Wecker, C. Kuhrt, and K. Samwer, J. Appl. Phys., **81**, 5496 (1997).
8. A. Gupta, C. Q. Gong, Gang Xiao, P. R. Duncombe, P. Lecoeur, P. Trouilloud, Y. Y. Wang, V. P. Dravid, J. Z. Sun, Phys. Rev. B, **54**, R15629 (1996).
9. K. K. Choi, M. Yamasaki, T. Namikawa and Y. Yamazaki, to be published.

Plasma Chemistries for Etching of $La_{0.41}Ca_{0.59}MnO_3$ and SmCo CMR Structures

J.J. Wang*, K.B. Jung*, J.R. Childress*, S.J. Pearton*, F. Sharifi**, K.H. Dahmen***, E.S. Gillman***, F.J. Cadieu****, R. Rani****, X.R. Qian**** and Li Chen****
*Dept. Materials Science and Engineering, University of Florida, Gainesville FL 32611
**Dept. Physics, University of Florida, Gainesville FL 32611
***MARTECH, Florida State University, Tallahassee FL 32306
****Dept. Physics, Queens College of CUNY, Flushing, NY 11367

ABSTRACT

A number of different plasma chemistries have been employed for patterning of $La_{0.41}Ca_{0.59}MnO_3$ and SmCo thin films for application in magnetic field-biased structures based on the colossal magneto-resistive effect. For $La_{0.41}Ca_{0.59}MnO_3$ there was no chemical enhancement in etch rate over simple Ar sputtering for Cl_2, SF_6 and CH_4/H_2 plasmas under high ion density conditions except BI_3 and BBr_3 plasmas. This is expected based on the vapor pressures of the prospective etch products. For SmCo however, etch rates up to 7,000 Å/min were obtained in Cl_2/Ar plasmas, which is an order of magnitude faster than Ar sputtering under the same experimental conditions. Smooth etched surface morphologies and anistropic sidewalls were obtained for both materials over a wide range of plasma source and chuck powers.

INTRODUCTION

Renewed interest in the design of magnetic sensors, magnetic memories, and other devices based on magnetic and magneto-resistive materials has been initiated by the study of La-manganite perovskite "colossal magnetoresistive"(CMR) materials.[1] In this case the implementation of practical microelectronic devices requires the development and control of etching and patterning procedures which do not degrade the magnetic properties of the materials. In the case of La-manganite materials, another limitation at present is that the observed field-induced resistivity transition is most sensitive above magnetic fields of about 1 Tesla. Consequently it may be necessary to provide a fixed, built-in bias field within the device, from a hard magnet materials such as SmCo. In that case etch and patterning recipies must also be developed for such materials. In this paper we report on the Ar-based plasma etching of $La_{0.41}Ca_{0.59}MnO_3$ and SmCo-based materials which may be used as the basis for CMR-device structures, and on the effect of different plasma chemistries, namely SF_6, CH_4/H_2, Cl_2, BI_3 and BBr_3 additions, on the etch characteristics.

EXPERIMENTAL

Liquid delivery metalorganic chemical vapor deposition using 2,2,6,6-tetramethyl-3,5-heptanedionato (TMHD) precursors (i.e. $La(TMHD)_3$, $Sr(TMHD)_2$, $Mn(TMHD)_3$ and $Ca(TMHD)_2$) was employed to deposit films of $La_{0.41}Ca_{0.59}MnO_3$ on Al_2O_3 (0001) single crystal substrates at 700°C. The precursors were transported by N_2 carrier gas, with direct injection of O_2 and N_2O as oxidants.[2]

The SmCo-based films were directly crystallized by RF diode sputtering (100 mTorr Ar) onto moderately heated (375-425°C) polycrystalline aluminum oxide substrates. The samples had

Mat. Res. Soc. Symp. Proc. Vol. 517 © 1998 Materials Research Society

a nominal composition of Sm 13%, Co 58%, Fe 20%, Cu 7%, Zr 2% and were directly crystallized upon deposition into the disordered TbCu7 type crystal structure.

Samples of $La_{0.41}Ca_{0.59}MnO_3$ and SmCo were masked with either photoresist, SiN_x or apiezon wax for etching experiments. The dry etching was performed either in a Plasma-Therm SLR 770 reactor with an ASTEX 4400 low-profile ECR source[3] or a Plasma-Therm 790 reactor in which the plasma is generated by a 3-turn inductive coil operated with up to 1000W of 2MHz power. For the ECR system, the ECR cavity was formed with an upper magnet (170 A) and collimated with a lower magnet (40 A). The process pressure was held constant at 1.5mTorr. The rf power (13.56 MHz) varied between 50 and 350 W and the microwave power was held constant at 1000 W. The plasma chemistries used were 15 standard cubic centimeter per minute (sccm) Ar, $10SF_6/5Ar$, $2.5CH_4/7.5H_2/5Ar$ or $10Cl_2/5Ar$. For the I-C-P system, the sample position was separately powered with 0-450W of 13.56MHz power and the chuck is He backside-cooled to hold the sample temperature to $\leq$ 40°C. Process pressure was held constant at 5mTorr for all experiments. The BI_3 (melting point 40°C) and BBr_3 (boiling point 91°C) were held at ~ 45°C within a stainless steel vacuum vessel- total gas loads of 10 sccm were injected into the I-C-P source through electronic mass flow controllers. Etch rates were determined by stylus profilometry measurements using a Tencor system after removal of the mask material. Surface morphologies were examined with Scanning Electron Microscopy (SEM) and Atomic Force Microscope (AFM) using a Si tip in tapping mode, while the near surface stoichiometry was obtained from Auger Electron Spectroscopy (AES) experiments.

Table 1 lists boiling points of some potential etch products in the plasma chemistries investigated here.[4] To achieve smooth etched surfaces, it is obviously necessary to remove the etch products at equal rates for all of the elemental constituents.

Table 1. Boiling points of potential etch products of $La_{0.41}Ca_{0.59}MnO_3$ and SmCo

Etch Products	Boiling Point (°C)	Etch Products	Boiling Point (°C)	Etch Products	Boiling Point (°C)
$LaCl_3$	>1000	MnI_2	subl vac500	SmF_2	>2400
LaF_3	.....	$MnBr_2$	858	SmF_3	2323
La_2S_3	2100 vac.	$(CH_3)_2Mn$	.....	SmH_2	.....
LaI_3	>1000	Cl_2O	2.2	$(CH_3)_2Sm$	.....
$LaBr_3{\cdot}7H_2O$	1577	ClO_2	11	$CoCl_2$	1049
$(CH_3)_3La$	.....	Cl_2O_3	.....	$CoCl_3$	.....
$CaCl_2$	1935.5	Cl_2O_6	≈200	CoF_2	≈1400
CaF_2	2533.4	O_2	-183	CoF_3	.....
CaH_2	d 816	Cl_2O_7	82	CoH_2	.....
CaI_2	ca1100	F_2O	-144.75	$(CH_3)_2Co$	.....
$CaBr_2$	806-812	F_2O_2	-57	$FeCl_3$	316
CaI_2	ca1100	H_2O	100	$FeCl_2$	1023
$CaBr_2$	806-812	$(CH_3)_2O$	-23.6	FeF_3	726
$(CH_3)_2Ca$	.....	BrO_2	9	FeF_2	1837
CaS	d	Br_2O	4.5	CuCl	1490
$MnCl_2$	1190	Br_3O_8	.....	CuF	s 1100
$MnCl_3$	d	IO_2	13	$ZrCl_2$	d 350
MnF_2	> 856	I_2O_4	.....	$ZrCl_3$	s 331
MnF_3	d	I_2O_5	.....	ZrF_4	s 600
MnH_2	.....	I_4O_9	d75	ZrH_2	.....
MnI_2	subl vac500	$SmCl_2$	> 740	ZrS_2	>1550
$MnBr_2$	858	$SmCl_3$	.....		

RESULTS AND DISCUSSION

Figure 1(left) shows the dependence of $La_{0.41}Ca_{0.59}MnO_3$ etch rate on dc self- bias on the

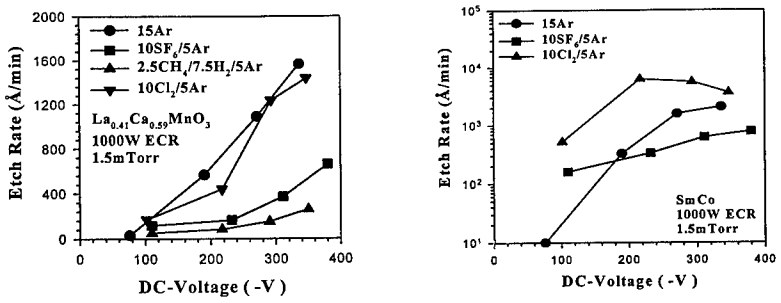

Figure 1. Etch rate of $La_{0.41}Ca_{0.59}MnO_3$ (left) & SmCo (right) in various plasma chemistries as a function of chuck self-bias. The ECR source power was held constant at 1000W.

sample chuck for the four different plasma chemistries. Note that the results for Cl_2/Ar basically follow those for pure sputtering (Ar), indicating that the La, Ca and Mn chlorines are not particularly volatile even at the high ion fluxes (~10^{15} ions/cm^2 ·sec) available in the ECR tool. This is generally not an attractive option from a practical viewpoint because of the limitation it places on mask materials and the requirement for reproducible thermal contact for each sample.[5,6] The results for the SF_6/Ar and CH_4/H_2/Ar plasma chemistries show that the etch products for these are even less volatile and the etching is most likely retarded by formation of a selvedge or reaction layer with these chemistries.

There was a substantial degree of chemical enhancement observed from the etching of SmCo in Cl_2/Ar chemistries, as shown in Figure 1(right). The etch rate is approximately a factor of 10 to 12 higher than for pure Ar up to dc self-biases of ~ -217V, at higher biases the etch rate with Cl_2/Ar saturates and then decreases. The self-bias corresponds fairly close to the acceleration voltage experienced by ions impinging on the sample.[7] Up to a particular energy, the etch rate is increased by the higher sputtering efficiency that more effectively desorbs the etch products. However above this energy (in these experiments ~ 250eV) the ions are able to desorb the chlorine radicals before they are able to react with the SmCo and hence the etch rate decreases. The SF_6/Ar plasma chemistry provides etch rates faster than pure sputtering at biases up to ~ -200V, but show a dependence on bias that is less than that for Ar at higher values.

Figure 2 shows SEM micrographs of features etched into both materials using a Cl_2/Ar plasma at -200V dc self-bias and an SiO_2 mask which was subsequently removed. The etched

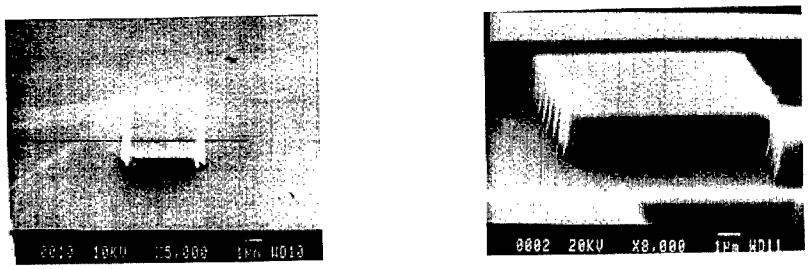

Figure 2. SEM micrographs of features etched into $La_{0.41}Ca_{0.59}MnO_3$ (left) and SmCo-based film (right) using a Cl_2/Ar plasma. The SiO_2 masks have been removed.

surfaces under these conditions are essentially as smooth as the unetched regions and the sidewalls are reasonably vertical. The striations on the sidewall are typically observed on dry etched features and originate from roughness on the edges of the original photoresist mask that was used to transfer the pattern into the SiO_2.[8,9]

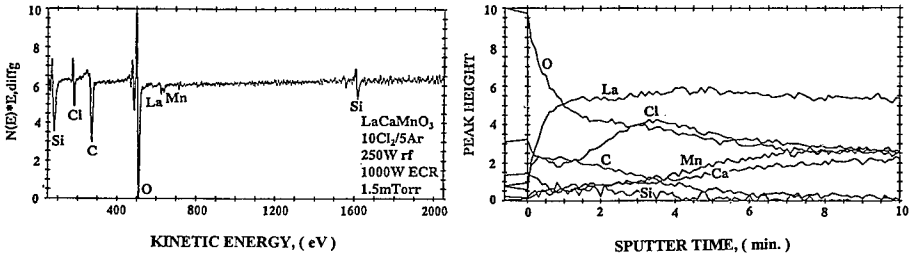

Figure 3. AES surface scan (left) and depth profile (right) from $La_{0.41}Ca_{0.59}MnO_3$ after etching in a Cl_2/Ar ECR plasma.

To better understand the role of plasma chemistry and ion energy in the surface roughening, AES surface scans and near-surface depth profiles were measured on the samples in Figure 3. By sharp contrast in the sample etched in Cl_2/Ar at higher bias (-293V), the near-surface is deficient in the lighter elements O, Ca and Mn (atomic weights of 16,40 and 55, respectively compared to 139 for La). The surface roughness also leads to non-abrupt depth profiles, which explains the prolonged Cl signal. The Cl originates from the presence of remnant etch products that were not completely desorbed because of their low volatility.

An additional important consideration is selection of a mask material for the etching process. Photoresist is typically not suitable for high density plasma processes because the high ion currents lead to reticulation and loss of dimensional stability.[10] Figure 4 shows Cl_2/Ar etch selectivity for both SmCo and $La_{0.41}Ca_{0.59}MnO_3$ over the dielectrics SiO_2 and SiN_x. Since there is basically no chemical enhancement for etching $La_{0.41}Ca_{0.59}MnO_3$, there is also no selectivity over the dielectrics. This is a severe limitation if one needed to pattern deep features into $La_{0.41}Ca_{0.59}MnO_3$ because the mask thickness would need to be at least as thick as the required etch depth. For SmCo however, the etch selectivity is ~ 4 at low rf chuck powers and increases initially as this power is increased because the etch rate of the magnetic material rises faster than that of the dielectrics. At higher powers the selectivity decreases because of the fall-off in etch rate of the SmCo (Figure 1, right), and the fact that the dielectric etch rate continues on to increase as ion energy is increased. Therefore, the modest chuck self-bias region is advantageous from the viewpoint of higher etch rates and selectivity with respect to the mask materials.

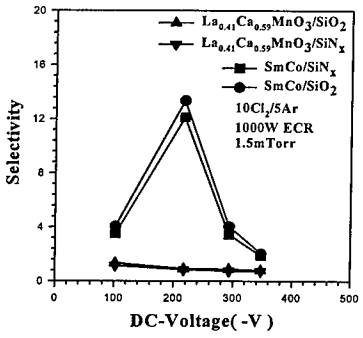

Figure 4. Selectivity for etching SmCo-based films or $La_{0.41}Ca_{0.59}MnO_3$ over either SiO_2 or SiN_x mask material, as a function of chuck self-bias.

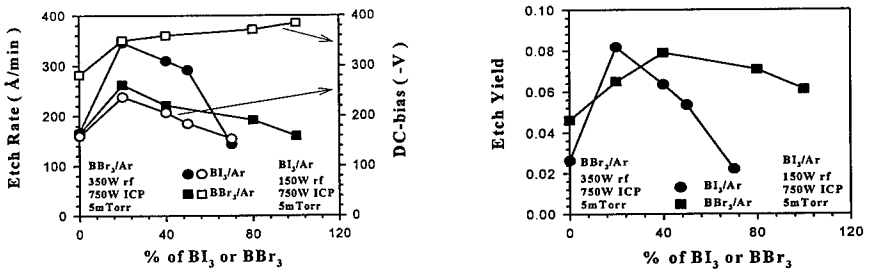

Figure 5. Etch rate (left) and etch yield (right) for $La_{0.41}Ca_{0.59}MnO_3$ in 750W I-C-P source power discharges of either BI_3/Ar or BBr_3/Ar, as a function of halide gas percentage. The rf chuck power was 150W for the BI_3/Ar and 350W for BBr_3/Ar.

Figure 5 shows the dependence of $La_{0.41}Ca_{0.59}MnO_3$ etch rate (left) on BI_3 or BBr_3 percentage in 750W source power, 350W rf chuck power halide/Ar discharges. For both chemistries the etch rate initially increases as halide is added, indicating the presence of some chemical enhancement in the etch mechanism, but beyond ~20% by flow the rate decreases forward the value obtained by pure Ar sputtering. The same trends are reflected in the etch yields (right) calculated from a simple model for ion current in this I-C-P tool.[11] Note that these yields are low, with up to 50 ions required to remove one atom of each of the lattice constituents. The fact that both etch rate and yield decrease at higher halide contents in the discharge is consistent with adsorbed iodine or bromine neutrals blocking the surface to ion-assisted desorption of the etch products, the same mechanism that limits NiFe etching in Cl_2/Ar discharges.[12] The important parameter is thus the ion-to-neutral ratio at the sample surface. If this is too high then there will be predominantly physical sputtering, and if it is too low a selvedge layer will form that retards etching.

Since the chemical component of the etching is relatively small, we would expect anisotropic pattern transfer. Figure 6 shows SEM micrographs of features etched into $La_{0.41}Ca_{0.59}MnO_3$ using either BI_3/Ar (left) or BBr_3/Ar (right) discharges and SiO_2 masks that were subsequently removed. The etched surface morphologies are again similar to those of the unetched regions, with slightly sloped sidewalls due to mask erosion. We have found that photoresist is typically not suitable as a mask material for high density plasma processes because the high ion currents lead to reticulation and loss of dimensional stability.[13]

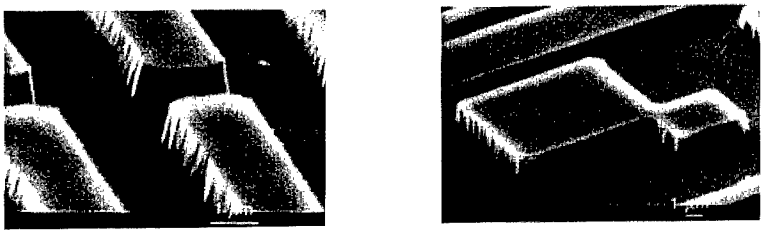

Figure 6. SEM micrographs of features etched into $La_{0.41}Ca_{0.59}MnO_3$ using either $4BI_3$/6Ar (left) or $4BBr_3$/6Ar (right) discharges with 750W of source power. The rf chuck power was 150W for the BI_3/Ar and 350W for the BBr_3/Ar. The SiO_2 masks have been removed from both samples.

SUMMARY AND CONCLUSIONS

Plasma chemistries based on Cl_2, F_2 or CH_4/H_2 did not show any degree of chemical enhancement for etching of $La_{0.41}Ca_{0.59}MnO_3$. Use of I_2- or Br_2-based mixtures provides a small degree of chemical enhancement relative to pure Ar sputtering, and enables smooth, anisotropic pattern transfer. The etch rates are a strong function of plasma composition, ion flux and ion energy. Ion-to-neutral ratios on order 0.02 are available under I-C-P conditions (much higher than in conventional RIE tools, $\sim 10^{-6}$)[9], and provide the ability to enhance the desorption of otherwise involatile etch products. However it is still problematic as to whether there is sufficient advantage gained by using BI_3 and BBr_3 relative to pure Ar sputtering to justify the extra precautions needed in handling these corrosive materials. For SmCo, chemical etch enhancements relative to pure Ar sputtering were obtained with Cl_2/Ar over the whole range of dc self-biases examined and with SF_6/Ar at low biases (up to approximately -200V). The sidewalls on etched features were again vertical, and the etched field quite smooth. Selectivities as high as ~ 12 were obtained for SmCo with respect to SiO_2 and SiN_x in Cl_2/Ar discharges.

ACKNOWLEDGMENTS

This work is supported by a DARPA grant monitored by S.Wolf, No.N00014-961-0767 and is further supported at UF by a DOD Multidisciplinary Research Initiative monitored by AFOSR (H.C.DeLong), No. F49620-96-1-0026.

REFERENCES

1. R. von Helmolt, J. Wecker, B. Holzapfel, L. Schultz and K. Samwer, Phys. Rev. Lett. **71**, 2331 (1993).
2. E.S.Gillman, K.H. Dahmen, S. Watts, X. Yu, S. Wirth and J.J. Heremans, presented at 1997 Fall MRS Meeting, Boston MA Dec 1 1997 (to be published).
3. S.J. Pearton, C.R. Abernathy and F. Ren, Appl. Phys. Lett. **64** 2294 (1994).
4. CRC Handbook of Chemistry and Physics, 70th Edition (CRC Press, Boca Raton FL 1990).
5. R.J. Shul, G.B. McClellan, R.D. Briggs, D.J. Rieger, S.J. Pearton, C.R. Abernathy, J.W. Lee, C. Constantine and C. Barratt, J. Val. Sci. Technol. A **15** 633 (1997).
6. S. Thomas III , K.K. Ko and S.W. Pang, J. Vac. Sci. Technol. A **13** 894 (1995).
7. High Density Plasma Sources, ed. O.A. Popov (Noyes Publications, Park Ridge, NJ 1996).
8. U.K. Chakrabarti, S.J. Pearton and F. Ren, Semicond. Sci. Technol, **6** 408 (1991).
9. D.T.C. Hou, M.F. Yan and J.D. Wynn, J. Electrochem. Soc. **137** 3639 (1990).
10. J.W. Lee and S.J. Pearton, Semicond. Sci. Technol. **11** 812 (1996).
11. J.W. Lee, D. Hays, C.R. Abernathy, S.J. Pearton, W.S.Hobton and C. Constantine, J. Electrochem. Soc. 144 L245 (1997); J.W. Lee, C.R. Abernathy, S.J. Pearton, C. Constantine, R.J. Shul and W.S. Hobton, Plasma Sources Sci. Technol. **6** 499 (1997).
12. K.B. Jung, E.S. Lambers, J.R. Childress, S.J. Pearton, M. Jenson and A.T. Hurst, Jr., Appl. Phys. Lett. **71** 1255 (1997).
13. J.W. Lee and S.J. Pearton, Semicond. Sci. Technol. **11** 812 (1996).

Effects of closed d-Shell (Sn) and partially filled d-shell (Ru) elements on the GMR properties of $La_{0.7}Ca_{0.3}Mn_{1-x}M_xO_3$ (M = Sn, Ru & □) and $Pr_{0.7}Ca_{0.3}Mn_{1-x}M_xO_3$ (M = Sn & Ru)

K. Chandrasekaran, R. Vijayaraghavan, M.S. Ramachandra Rao and U.V. Varadaraju.
Materials Science Research Centre, Indian Institute of Technology, Chennai
600 036, India.

Abstract:

The dependence of GMR properties on the magnetic (partially filled d-shell) and non-magnetic (closed d-shell) dopant elements in $La_{0.7}Ca_{0.3}MnO_3$ and $Pr_{0.7}Ca_{0.3}MnO_3$ has been studied. It is found that non-magnetic element substitution drastically affects the ferromagnetic transition temperature.

Introduction:

$LaMnO_3$ is an antiferromagnetic insulator. Suitable doping by substitution at La- site with alkaline earth metals (Ca,Sr, Ba) or by self doping through La and Mn vacancies leads to ferromagnetic ordering and Giant Magneto Resistance (GMR) effects [1]. Through the above dopings mixed valency of Mn is created. Depending on the ratio of Mn^{3+}/Mn^{4+} the structural, electrical and magnetic properties of these manganites vary [2]. The size of A-site ion is important in controlling the GMR properties [3]. Zener double exchange interaction is considered to be the cause of the strong ferromagnetic exchange interaction between Mn^{3+} and Mn^{4+} [4]. Altering the B-ion character (Mn- site) would affect the double exchange mechanism and bring about significant changes in the magnetoresistance properties [5]. The B-O-B bond angle is also crucial in determining the GMR properties and any substitution at B-site would affect the angle. In order to understand the interplay between the nature of the B-site substituted ion and the magneto resistive properties, we have investigated the substitution of manganese by various trivalent (Fe,Cr) and tetra valent(Ru,Sn) elements in $La_{0.7}Ca_{0.3}MnO_3$ and $Pr_{0.7}Ca_{0.3}MnO_3$. In the latter, the A-site ionic size is on the border line in the phase diagram showing the dependence of magnetic states on the size. We have attempted to increase the B- site ionc size by doping with bigger Ru^{4+} and Sn^{4+} ions and look for GMR. We have compared the results of the substitution of magnetic (Ru^{4+}, partially filled d shell) and non-magnetic (Sn^{4+}, closed d- shell) elements. In order to account for the volatility, if any, of Ru during the preparation, we have prepared compounds by intentionally creating vacancies at the Mn-site.

Experimental:

All the compositions were prepared from stochiometric mixtures of respective oxides and carbonates. The mixtures were first heated at 900°C for 12h, then at 1200°C for 24h with intermittent grindings. The product was pressed into bar shaped pellets and sintered at 1200°C for 24h. In the case of Ruthenium containing compositions, the reactant mixtures were initially heated at 600°C for 24h (pre-reaction step) in order to avoid Ru volatalization. The phase purity was established by powder X-ray diffraction. Resistivity measurements were carried out on sintered bars in the temperature range 300-40K in the absence and presence of magnetic field (1.2 Tesla). The samples were first zero field cooled and then the magnetic field was applied. Ac susceptibility measurements (SUMITOMO, Japan) were carried out in the temperature range 300-15K.

Mat. Res. Soc. Symp. Proc. Vol. 517 © 1998 Materials Research Society

Results and discussion:

All the compositions crystallize in cubic structure with a ≈7.7Å (see table1). The a-parameter (7.73Å) of the parent compound $La_{0.7}Ca_{0.3}MnO_3$ agrees well with that reported in the literature [2].

Table I Structural, Electrical and Magnetic properties of $La_{0.7}Ca_{0.3}Mn_{1-x}M_xO_3$

M	'x'	Lattice parameter a (Å)	Tc(ρ)	$T_c(\chi)$	ρ_{300K} Ohm cm	MR ratio (%)
Cr	0.0	7.730	260	260	0.01	-
	0.02	7.726	250	255	0.03	18
	0.04	7.731	235	240	0.02	23
	0.06	7.725	225	240	0.04	21
	0.08	7.715	215(155)*	230	0.03	20(12)*
	0.10	7.731	120	210	0.03	13
Fe	0.02	7.726	220	220	0.05	25
	0.04	7.646	185	195	0.07	36
	0.06	7.720	135	165	0.08	50
	0.08	7.725	80	125	0.18	60
	0.10	7.729	-	125	0.07	-
Ru	0.02	7.728	260	260	0.01	18
	0.04	7.741	260	255	0.01	15
	0.06	7.734	250	255	0.02	17
	0.08	7.742	245(165)*	250	0.02	19(16)*
	0.10	7.748	235(115)*	250	0.03	20(18)*
Sn	0.02	7.739	205	200	0.06	25
	0.04	7.749	150	160	0.11	43
	0.06	7.762	-	160	0.17	-
	0.08	7.763	-	155	0.11	-
	0.10	7.758	-	150	0.17	-
□	0.02	7.733	255	260	0.02	-
	0.04	7.744	230	255	0.09	-
	0.06	7.746	175	245	0.19	-
	0.08	7.743	125	245	0.13	-
	0.10	7.748	100	235	0.14	-

* Corresponds to second peak.

In general, the room temperature resistivity (ρ_{300K}) values tend to increase with dopant concentration in all the substitutions (Table 1) . In the $La_{0.7}Ca_{0.3}Mn_{1-x}Cr_xO_3$ system, the ferromagnetic transition temperatures (T_c) obtained from resistivity measurements decrease marginally in the initial composition ($0.02 \leq x \leq 0.06$). The decrease is more drastic for $x > 0.06$. The ac susceptibility measurement show only marginal decrease in the ferromagnetic transition temperatures (Table 1). The MR ratios are around 20%. In the $La_{0.7}Ca_{0.3}Mn_{1-x}Fe_xO_3$ system, the

T_c (ρ) decreases continuously which is supported by ac susceptibility measurement,T_c (χ) . The MR ratio increases systematically and a highest ratio (60%) is obtained for x=0.08 composition. A typical GMR curve is shown in Fig.1 .The composition x=0.10 is insulating. In the $La_{0.7}Ca_{0.3}Mn_{1-x}Ru_xO_3$ system, the $T_c(\rho)$ decreases only marginally with composition and the ac susceptibility measurements (Fig.2) support this observation. Interestingly resistivity measurements exhibit a double hump behaviour for $0.06 \leq x \leq 0.10$. However, the second peak at low tempearture is suppressed by oxygen annealing.

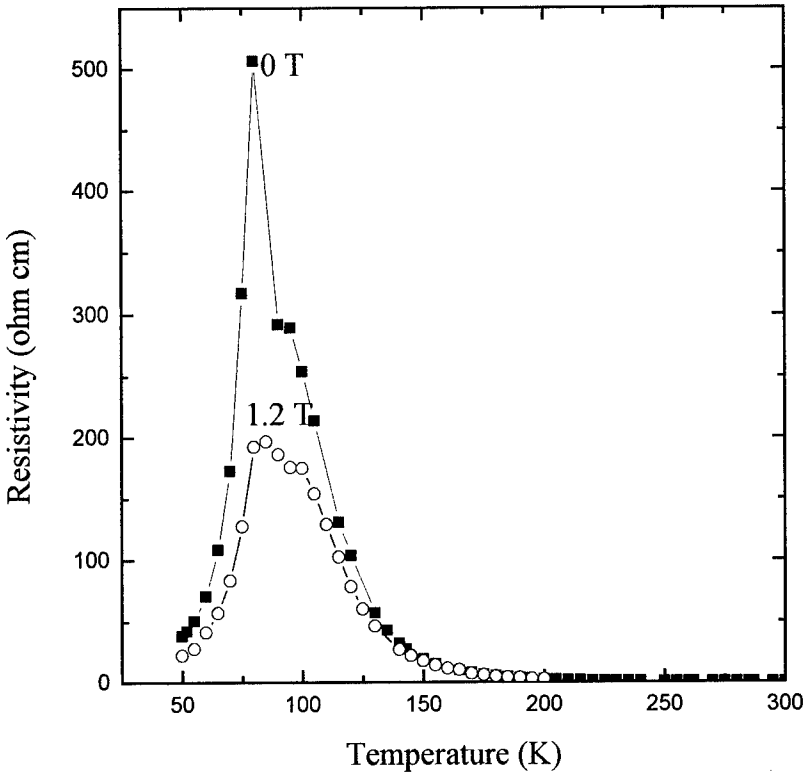

Fig.1 Resistivity Vs Temperature plot of $La_{0.7}Ca_{0.3}Mn_{0.92}Fe_{0.08}O_3$ (H=0 and 1.2 T)

For compositions in the range $0.00 \leq x \leq 0.04$ only a single transition is observed. The MR ratios are small compared to Fe substitution and are around 20%. In the $La_{0.7}Ca_{0.3}Mn_{1-x}Sn_xO_3$ system, ac susceptibility measurements (Fig.3) show that non- magnetic, filled d-shell Sn^{4+} dopant decreases the T_c (χ) drastically. Resistivity measurements reveal that a single transition is observed in the compositional range $0.00 \leq x \leq 0.04$, whereas between $0.06 \leq x \leq 0.10$, it is insulating. The MR ratios are in the range 25-40%. In the $La_{0.7}Ca_{0.3}Mn_{1-x}\square_xO_3$ system, the $T_c(\rho)$ values decrease continously, where as the $T_c(\chi)$ values decrease marginally. In the $Pr_{0.7}Ca_{0.3}Mn_{1-x}M_xO_3$ system (M = Ru and Sn), all the compositions are insulating. A plot of $T_c(\rho)$ vs x in $La_{0.7}Ca_{0.3}Mn_{1-x}M_xO_3$ is shown in Fig.4.

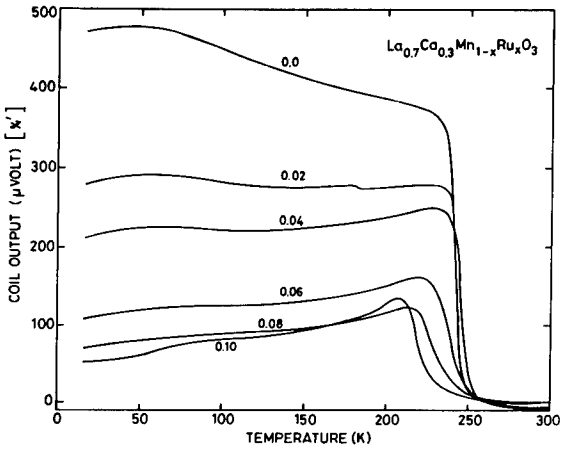

Fig.2. Ac susceptibility Vs Temperature plot of $La_{0.7}Ca_{0.3}Mn_{1-x}Ru_xO_3$

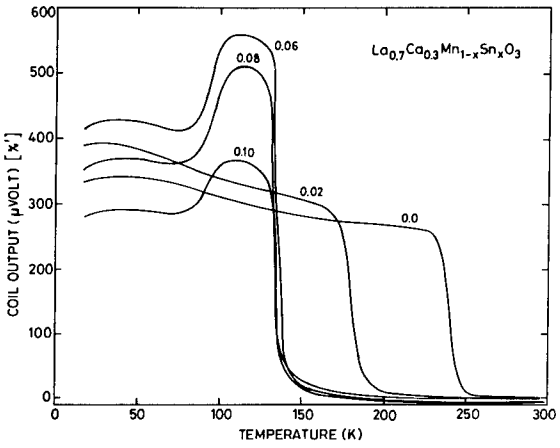

Fig.3. Ac susceptibility Vs temperature plot of $La_{0.7}Ca_{0.3}Mn_{1-x}Sn_xO_3$

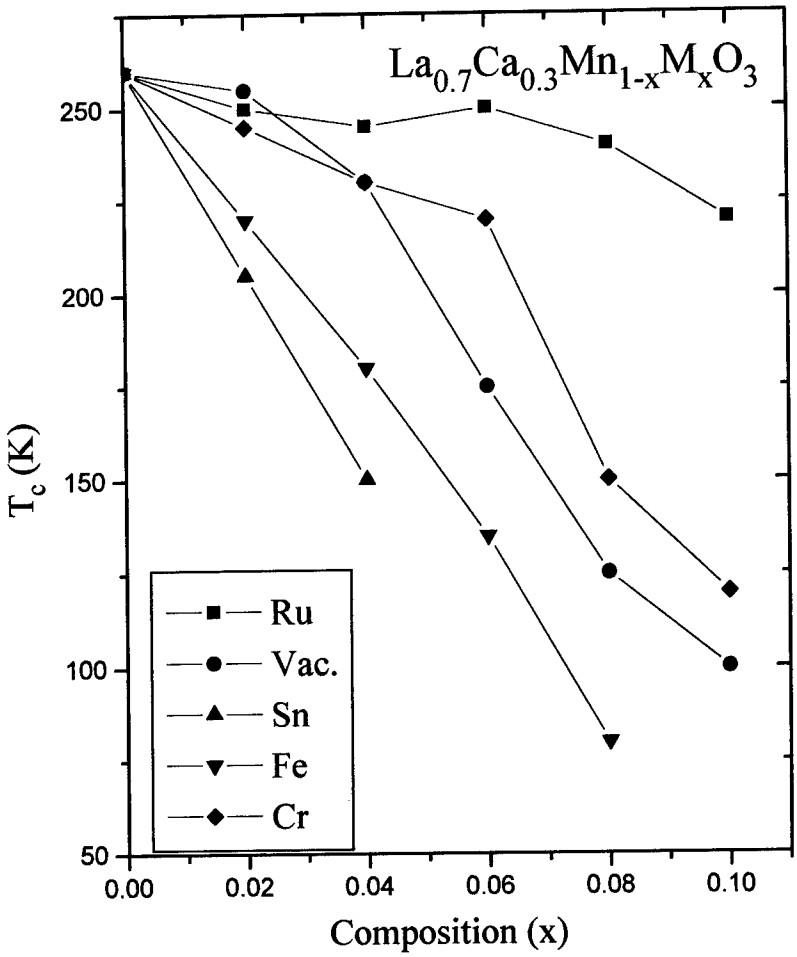

Fig.4. Variation of ferromagnetic transition temperature with composition.

A drastic decrease in T_c is found for non-magnetic Sn. The marked differences observed in the case of non-magnetic Sn and magnetic Ru substituted compunds could be discussed by drawing the analogy of T_c suppression caused by the non-magnetic Zn doping in $YBa_2Cu_3O_{7-\delta}$ superconductor.

Conclusions

The non-magnetic Sn^{4+} doping suppresses the ferromagnetic transition temperature drastically compared to magnetic Ru^{4+} doping. The marked differences observed could be discussed by drawing the analogy of T_C suppression caused by the non-magnetic Zn doping in $YBa_2Cu_3O_7$ superconductor.

References

1.K.Chanara, T.Ohno, M.Kasai and Y.Kozono, Appl. Phys. Lett. **63**, p1990 (1993).
2.R.Mahendiran, S.K.Tiwary, A.K.Raychaudhuri, T.V.Ramakrishnan, R.Mahesh, N.Rangavittal and C.N.R.Rao, Phys.Rev.B. **53**, p3348 (1996).
3.A.Maignan, Ch.Simon, V.Caignaert and B.Raveau, Z.Phys.B.**99**, p305 (1996).
4.C.Zener, Phys.Rev. **82**, p403 (1951).
5.H.Yoshizawa, H.Kawano, Y.Tomioka and Y.Tokura, J.Phys.Society of japan, **65**, p1043 (1996).

EFFECT OF THE CATIONIC SIZE VARIATION IN THE GMR COMPOUND $Pr_{0.7-X}Ho_XSr_{0.3}MnO_3$ AND IN THE CHARGE ORDERED COMPOUNDS $Pr_{0.5-X}Ho_XSr_{0.5}MnO_3$

Sirisha K[a] , A.Narayanasamy[a], U.V.Varadaraju[b]
[b]Materials Science Research Centre, Indian Institute of Technology, Madras 600 036, INDIA.
[a]Dept. of Nuclear Physics, University of Madras, Guindy Campus, Madras 600 025, INDIA.

Abstract

Praseodymium manganites doped with holmium $Pr_{1-x-y}Ho_xSr_yMnO_3$ (x=0-0.1 in steps of 0.2 and y = 0.3, 0.5) have been prepared and characterized by powder X-ray diffraction, ac magnetic susceptibility, dc magnetic susceptibility, dc electrical resistivity ($\rho_{H=0}$ and $\rho_{H=1.2T}$) and electron microscopy studies. Both series have a pseudotetragonal distorted perovskite like structure (Pbnm space group). Magnetic and electrical properties of the manganites have been investigated and the compositions are ferromagnetic insulators which exhibit small values of negative magnetoresistance. The highest MR ratio ($MR=(R_O-R_H)/R_O$) of 48% at 152 K for a field of 1.2T for $Pr_{0.6}Ho_{0.1}Sr_{0.3}MnO_3$. The results emphasize the role played by the dopant holmium. SEM studies show well structured grains which vary with concentration of the dopant. The compounds were found to favour antiferromagnetism with increasing x.

Introduction

There are two types of GMR compounds, type I ($Ln_{1-X}A_XMnO_3$, $0.2<x<0.5$) and type II ($Ln_{0.5}A_{0.5}MnO_3$ i.e. $Ln_{1-X}A_XMnO_3$, x=0.5). The type I compounds show a maximum GMR effect for x=0.3 because the Mn^{3+}:Mn^{4+} ratio is 7:3 and the type II compounds are charge ordered because the Mn^{3+}:Mn^{4+} ratio is 1:1. Zener's double exchange model explains the metallic to insulator transition seen in the type I compounds. It also gives the relation between T_C, conductivity and the average size of the A-site cation $\langle r_A \rangle$ (in ABO_3) explained by Zener [1] and C.N.R.Rao [2]. The Zener's double exchange model is based on the hopping of electrons from site to site which induces metallicity and ferromagnetism in the compound. However, in the charge ordered state the electrons are localized which gives rise to the insulating antiferromagnetic state. The electrical and magnetic properties of $PrMnO_3$ on the substitution of dopants in the A-site are of current interest. Different perovskite systems with different dopants have been studied in detail [3,4,]. Detailed studies on the $Pr_{1-X}Y_XSr_{0.5}MnO_3$ were carried out by Raveau et al [5] in which Yttrium does not carry magnetic moment. The aim of the present study is to study the effect of substitution of Ho which has a very high magnetic moment in place of non-magnetic Y. Ho has a high magnetic moment. In $La_{1-X}Ca_XMnO_3$ reported by Schiffer et al [6] at less T_C and high resitivity, larger MR have been observed. The MR is enhanced by small grain size as is observed. The above reported MR ratio of 48% is the highest at 1.2T. Studies on the series $Pr_{1-X}Y_XSr_{0.3}MnO_3$ have not been carried out as yet. The present study is conducted on two types of GMR compounds namely type I and type II. The compounds $Pr_{0.7-X}Ho_XSr_{0.3}MnO_3$ exhibit type I behavior and the compounds $Pr_{0.5-X}Ho_XSr_{0.5}MnO_3$ exhibit type II behavior (wherein x=0-0.1 in steps of 0.02). The aim is to find the effect $\langle r_A \rangle$ and the Mn^{3+}:Mn^{4+} ratio on the T_C and MR ratio of the compounds.

Mat. Res. Soc. Symp. Proc. Vol. 517 © 1998 Materials Research Society

Experimental

The samples $Pr_{0.7-X}Ho_XSr_{0.3}MnO_3$ and $Pr_{0.5-X}Ho_XSr_{0.5}MnO_3$ were prepared using the high temperature solid state reaction method. High purity oxides Pr_6O_{11} (preheated at 950°C), Ho_2O_3, MnO_2 and carbonate $SrCo_3$ were used as starting materials in stoichiometric amounts. The samples were heated at 1000°C for 12 hours for decarbonation. They were cooled to room temperature and ground and heated at 1200°C for 12 hours for calcination. They were then cooled, ground and pelletised into 8mm or 12mm diameter and 1-2mm thick pellets for sintering. The sintering was carried out at 1500°C for 12 hours. The powder X-ray diffraction patterns were taken using CuK_α radiation.

The magnetic transitions were determined using ac susceptibility measurements in the temperature range 300-13K.(H= 0.1-4Oe at 313 Hz). The dc susceptibility measurements were done using a Vibrating Sample Magnetometer (H=1.2 T) in the temperature range 300-13K. The resistivity vs field (1.2 T) measurements were done with a closed cycle He refrigerator in the temperature range 300-13K. The resistivity measurements were done using the four probe van der Pauw method. The SEM measurements on the compounds were carried out using a scanning electron microscope. Since the samples are not conducting in the normal state, they were coated with gold and then examined by SEM.

Results and Discussion

Powder X-ray diffraction shows that all the compounds are formed in single phase. In the case of type I compounds viz. $Pr_{0.7-X}Ho_XSr_{0.3}MnO_3$, all reflections were indexed on the basis of an orthorhombic unit cell (Pbnm space group). The orthorhombic distortion could be very small and the corresponding characteristic splitting of the (202) and (312) reflections could not be seen in the XRD patterns. Such a situation is encountered in other perovskite systems (e.g. $BaPbO_3$) as well.

In the case of type II compounds viz. $Pr_{0.5-X}Ho_XSr_{0.5}MnO_3$, the corresponding characteristic splitting of the (202), (220) and (312) reflections can be seen as x increases which yields pseudo tetragonal structure. For x >0.04, the orthorhombic distortion is more predominant. Ho^{3+} has a smaller ionic radius (1.12Å in 12 fold coordination) compared to Pr^{3+} (1.179Å). This should result in systematic decrease in lattice parameters with increase in Ho content 'x'. However, the variation in lattice parameters is very small due to the low concentration of dopants.

Fig.1 shows the ac magnetic susceptibility curves in the temperature range 300-13 K. It shows type I behavior. The transition from paramagnetic state to ferromagnetic state is seen in all the compositions characterized by a sudden increase in susceptibility as temperature decreases. The transition is sharp for $Pr_{0.7}Sr_{0.3}MnO_3$. Ho doping leads to broadening of the transition. The onset temperature (T_C) for ferromagnetism decreases systematically with increase in x. This is explained by Zener's double exchange model. It is also observed that there is an increased tendency towards a second transition from the ferromagnetic state to an antiferromagnetic state at low temperature with increase in x. Decrease in $\langle r_A \rangle$ does induce the charge ordered state.

Charge ordering in manganites depends on the width of the e_g band which is governed by $\langle r_A \rangle$ or the tolerance factor, as distortion in the Mn-O-Mn bond angle affects the transfer interaction of the e_g electrons. When $\langle r_A \rangle$ is large, ferromagnetism and the insulator to metallic transition are observed but charge ordering is not observed. When $\langle r_A \rangle$ is small, the reverse is observed.

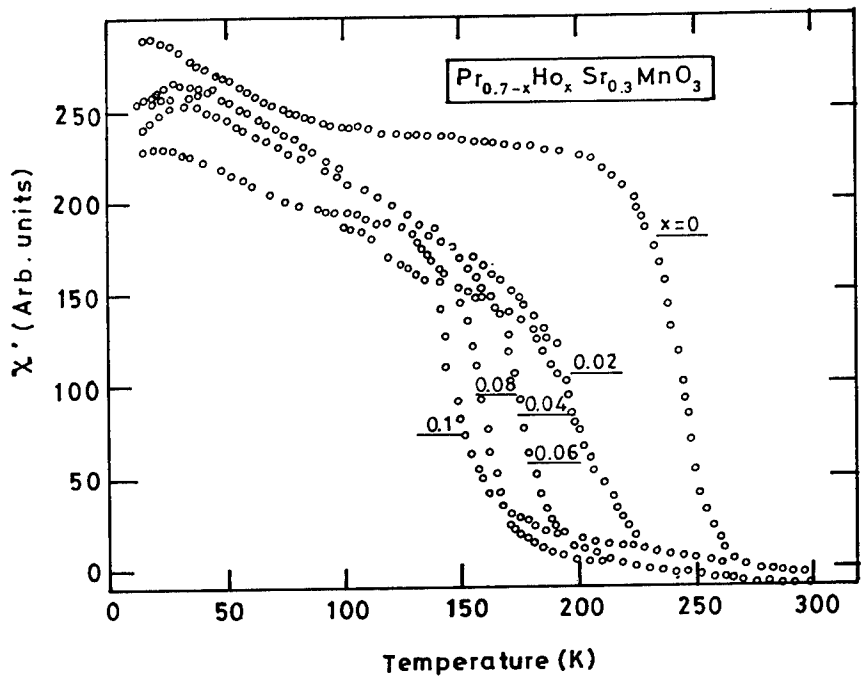

Fig. 1 ac magnetic susceptibility vs temperature curves of $Pr_{0.7-x}Ho_xSr_{0.3}MnO_3$ compounds

Fig.2 shows the ac magnetic susceptibility of type II compounds $Pr_{0.5-x}Ho_xSr_{0.5}MnO_3$ The transition from the paramagnetic state to the ferromagnetic state can be seen in the $Pr_{0.5-x}Ho_xSr_{0.5}MnO_3$ series. The transition is sharp for $Pr_{0.5}Sr_{0.5}MnO_3$. The transition broadens as x increases. The ferromagnetic onset temperature (T_C) decreases as with increasing x in a systematic order. A second transition from the ferromagnetic to the antiferromagnetic state is observed in all the compounds by a decrease in the susceptibility as temperature decreases. The onset of antiferromagnetism becomes sharp as x increases. The antiferromagnetism onset temperature (T_{CO}) increases with increasing x. The charge ordering of the compounds can be seen and it is observed that as the temperature increases, the charge ordering state collapses and spin ordering sets in. This is explained by Zener's double exchange model. As is known, the double exchange model opposes charge ordering phenomeneon.

The dc-susceptibility measurements of the compounds are given in Fig.3. The magnetization vs temperature plot and the transition temperatures observed in the ac susceptibility measurements were reproduced.

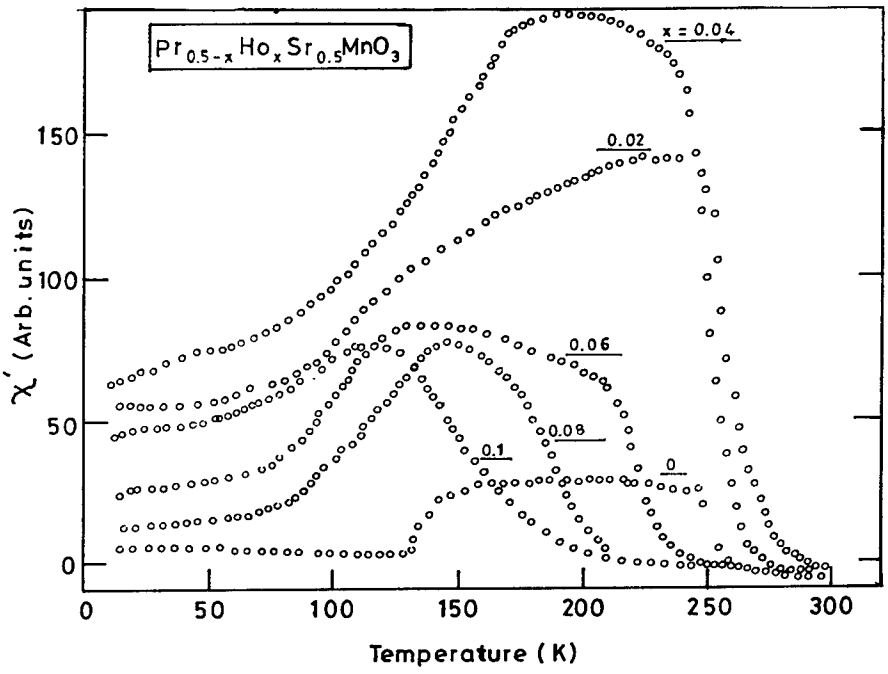

Fig. 2 ac magnetic susceptibility vs temperature curves of $Pr_{0.5-X}Ho_XSr_{0.3}MnO_3$ compounds

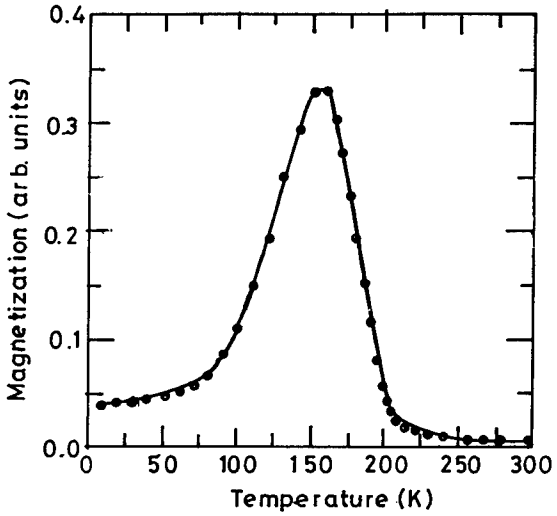

Fig.3 The dc magnetic susceptibility vs temperature plots

In the resistivity vs temperature plots (Fig.4) of the type I compounds T_{max} is defined as the temperature at which the maximum resistivity is observed i.e. the transition from the paramagnetic state to ferromagnetic state. T_{max} is found to decrease systematically with increasing x. It is also found that the resistivity values at any given temperature, increases as x increases. The maximum resistivity is observed for $Pr_{0.6}Ho_{0.1}Sr_{0.3}MnO_3$ and the highest T_{max} for $Pr_{0.7}Sr_{0.3}MnO_3$. Since Ho^{3+} has a smaller radius than Pr^{3+}, $<r_A>$ decreases. It is observed that T_{max} decreases as $<r_A>$ decreases. It implies that to obtain a higher transition temperature, $<r_A>$ should be increased. This is explained by the double exchange model.

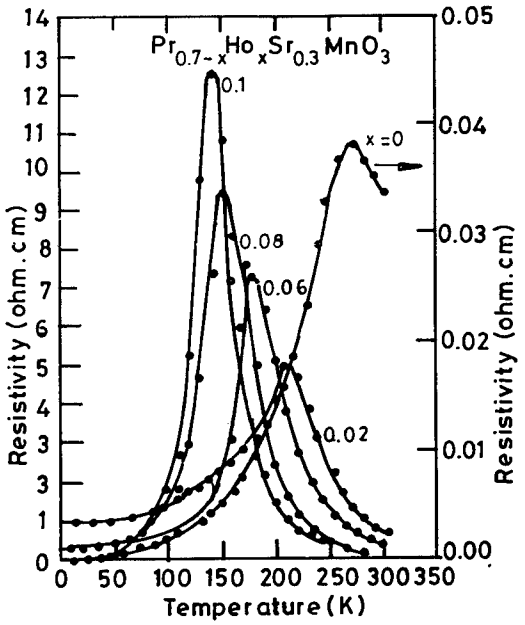

Fig.4 The resistivity vs temperature plots of $Pr_{0.7-x}Ho_xSr_{0.3}MnO_3$ compounds

The resistivity was measured as a function of temperature in the presence of a magnetic field on the compound $Pr_{0.6}Ho_{0.1}Sr_{0.3}MnO_3$ under fields varying from 0-1.2T. Under a field of 1.2 T, a MR ratio of 48% at 152K was observed. The resistivity was found to decrease systematically with increasing H. T_{max} was found to increase with increasing H.

In the type II compounds, the transitions from the semiconducting to the metallic to the insulating state are observed. The compounds are polycrystalline and due to grain boundary effects the transition temperatures are not clearly defined.

The micrographs in Fig.5 show well structured grains which vary with the concentration of the dopant. The grain size decreases with increasing x. The grains show a tendency towards a hexagonal structure and the grain boundaries are clearly defined showing the crystalline nature of the sample.

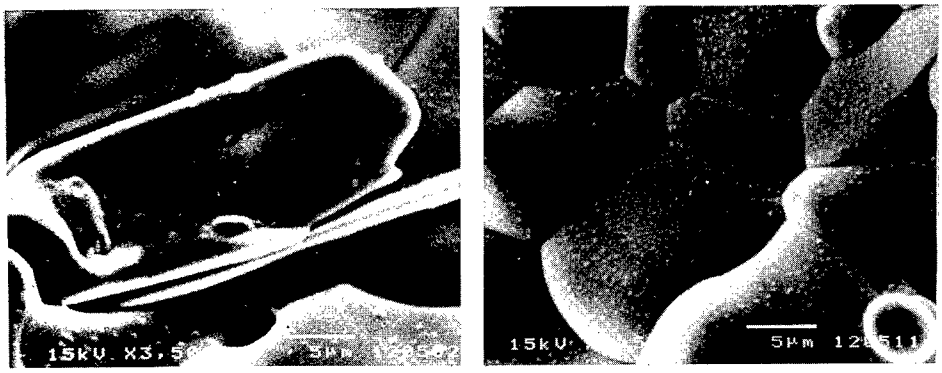

$Pr_{0.7}Sr_{0.3}MnO_3$ $Pr_{0.6}Ho_{0.1}Sr_{0.3}MnO_3$

Fig.5 SEM micrographs of $Pr_{0.7}Sr_{0.3}MnO_3$ and $Pr_{0.6}Ho_{0.1}Sr_{0.3}MnO_3$

The grain sizes are about 15-5 microns. Higher MR is observed for smaller grain size as reported by Schiffer et al [6].

References

1. C.Zener, Phys. Rev. **82** , 403 (1951).
2. C.N.R.Rao, Chem. Eur. J. **2** , 1499 (1996).
3. K. Chahara, T. Ohno, M. Kasai, Y. Kozono, Appl. Phys. Lett. 63, 1990 (1993).
4. A. Urishibara, Y. Morimoto, T. Arima, A. Asamatsu, G. Kido, Y. Tokura, Phys. Rev. *B*, **51**, 14103 (1995).
5. A. Maignan, Ch. Simon. V. Caignaert and B. Raveau, Z. Phys. B **99**, 305 (1996).
6. P.Schiffer, A.P.Ramirez, W.Bao, S.W.Cheong, Phys. Rev. Lett. **75,** 3336 (1995).

PHASE RELATIONS IN THE SYSTEM La_2O_3-SrO-CaO-Mn_2O_3 WITH EMPHASIS ON $LaMnO_3$

P. MAJEWSKI, F. ALDINGER
Max-Planck-Institut für Metallforschung, Pulvermetallurgisches Laboratorium,
Heisenbergstraße 5, 70569 Stuttgart, Germany

Abstract

At 1200 °C in air (La,Sr,Ca)MnO_3 do not form a complete solid solution. An extended miscibility gap exists between Sr and Ca containing $LaMnO_3$ and $SrMnO_3$ and $CaMnO_3$, respectively. Therefore, for the preparation of single phase (La,Sr,Ca)MnO_3 with intermediate Sr or Ca contents annealing temperatures of above 1400 °C are required.

Introduction

Phase diagrams representing the fundamental thermodynamic phase equilibrium of multi component systems are the basis for the preparation of single phase or controlled multi phase materials. The system La_2O_3-SrO-CaO-Mn_2O_3 (LSCM) involves the technological important compound (La,Sr,Ca)MnO_3 (LM). Due to its significant magneto resistive properties the phase is of great importance for the GMR technology. In addition, high temperature oxygen and electron conductivity as well as catalytic properties qualifies the compound for cathode material of solid oxide fuel cells. The binary systems of LSCM are already known. The system La_2O_3-MnO_3 [1], CaO-Mn_2O_3 [2] and SrO-Mn_3O_4 [3] contain the perovskite structured phase ABO_3 with A = Sr, Ca or La and B = Mn (Figure 1-3).

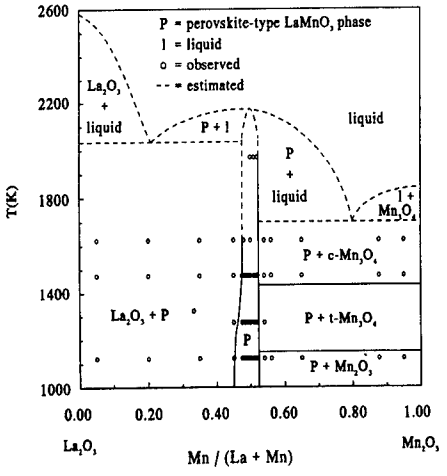

Figure1: The system La_2O_3-Mn_2O_3 [1].

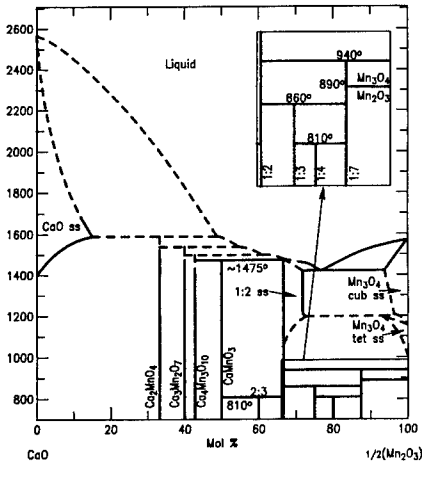

Figure 2: The system CaO-Mn_2O_3 [2, temperature in °C]

Mat. Res. Soc. Symp. Proc. Vol. 517 © 1998 Materials Research Society

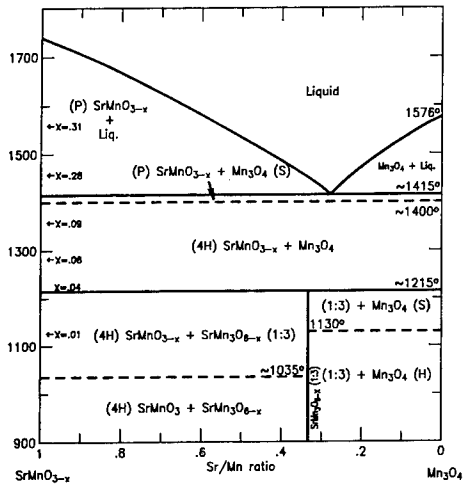

Figure 3: The system and $SrO\text{-}Mn_3O_4$ [3, temperature in °C].

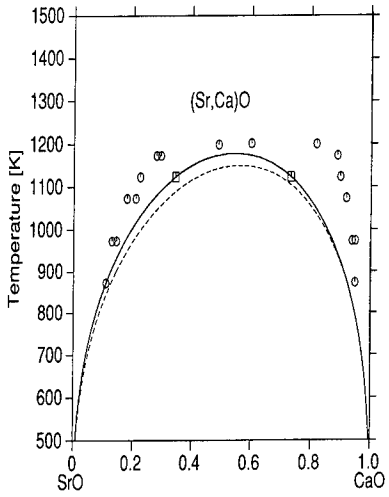

Figure 4: The system SrO-CaO [6].

In the systems La_2O_3-SrO and La_2O_3-CaO no binary phases were observed below about 1500 °C [4,5]. The system SrO-CaO forms the almost complete solid solution (Sr,Ca)O above 900 °C (Figure 4) [6].Ternary phases are only known in the system La_2O_3-SrO-Mn_2O_3 the compositions of which are $La_{1-x}Sr_{1+x}MnO_4$ and $La_{2-x}Sr_{1+x}Mn_2O_7$ [7].

Experiment

Samples with different compositions were powdermetallurgically prepared using La_2O_3, $SrCO_3$, $CaCO_3$ and MnO_2 (purity > 99 %). The homogenized powders were calcined at 1200 °C in for 12 h, ground, cold isostatically pressed, sintered at 1200 °C in air for 48 h with intermediate regrinding and pressing and finally furnace cooled. Samples with the composition $La_{0.5}Sr_{0.5}MnO_3$ were sintered at 1500 °C in air and subsequently annealed at 1400, 1350, 1300, 1200, 1000 and 800 °C in air for up to 500 h and furnace cooled (batch 1). In addition, samples with the same composition were sintered at 1000, 1300, 1350 and 1400 ° C in air for 48 h with intermediate regrinding and pressing (batch 2). Phase identifications were performed using scanning electron microscopy with EDX (Zeiss DSM 982 Gemini) and x-ray diffraction (Siemens D-5000).

Results

Figure 5 shows the quasiternary system $LaMnO_3$ (LM) - $SrMnO_3$ (SM) - $CaMnO_3$ (CM). It is emphasized that the phases do not form a complete solid solution, but separate phases with extended solubilities of La, Sr and Ca, respectively.

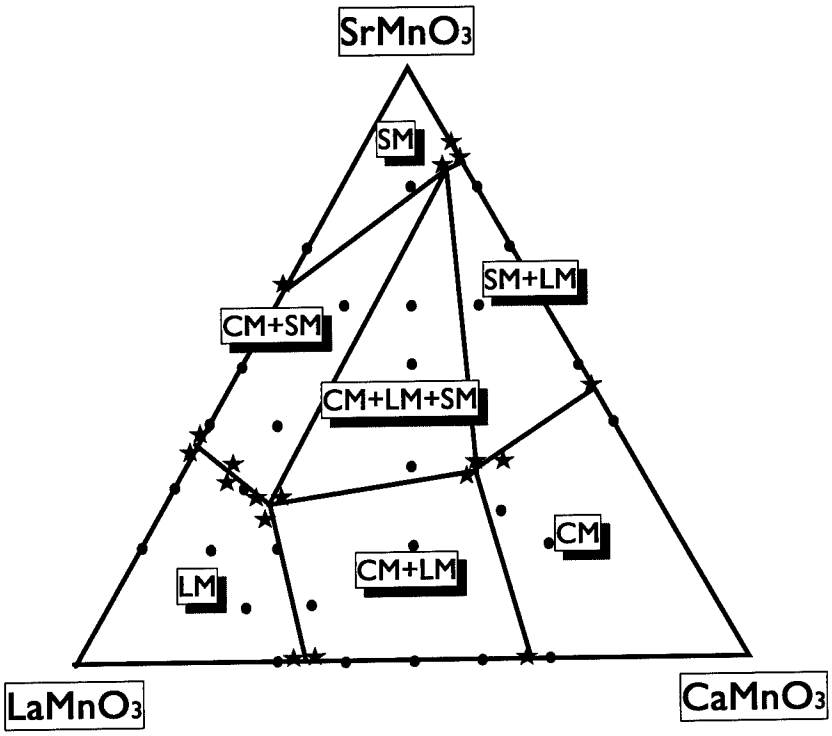

Figure 5: The quasiternary system $LaMnO_3$-$SrMnO_3$-$CaMnO_3$ at 1200 °C in air. Dots: samples; stars: microprobe analysis of the phases of multi phase samples.

Figure 6 shows a micrograph of the sample of batch 2 with the composition $La_{0.5}Sr_{0.5}MnO_3$ sintered at 1200 °C. Sr containing LM and La containing SM can easily identified with the scanning electron microscope using EDX indicating that both phases are separated phases and do not form a complete solid solution at that temperature. The decomposition of single phase $La_{0.5}Sr_{0.5}MnO_3$ (batch 1) prepared at 1500 °C in air into LM and SM at 1200 °C is shown in Figure 7. The XRD plot clearly shows the occurrence of reflections of SM beside LM at 1200 °C. Figure 8 shows the temperature concentration diagram for the quasibinary system $SrMnO_3$-$LaMnO_3$ depicting the miscibility gap between SM and LM below 1400 °C in air.

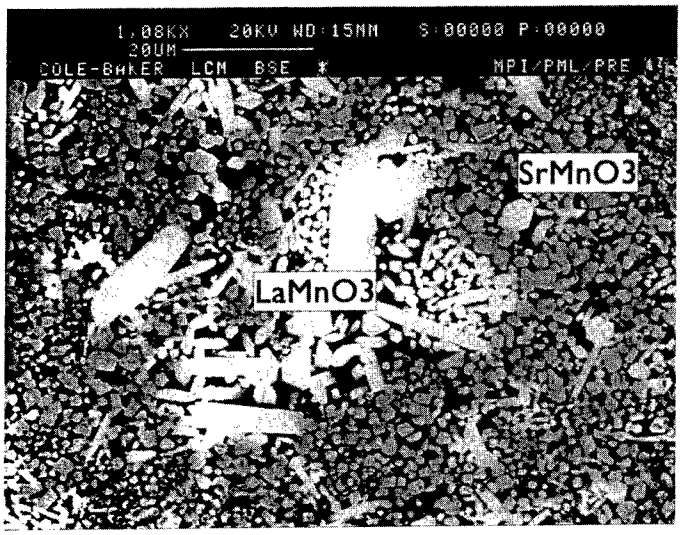

Figure 6: Micrograph of a sample with the composition $La_{0.5}Sr_{0.5}MnO_3$ at 1200 °C in air (batch 2).

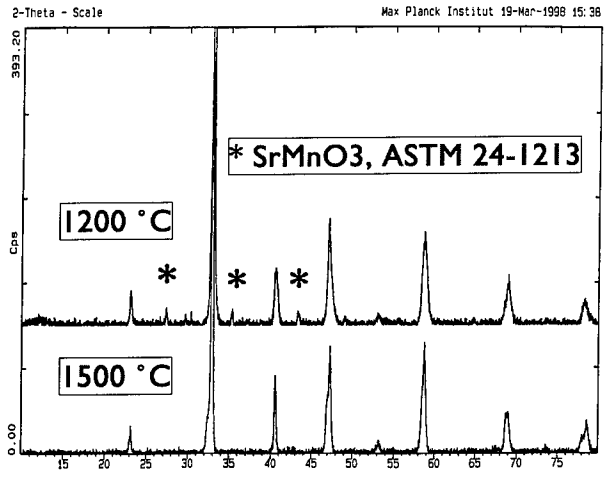

Figure 7: XRD plot of a sample with the composition $La_{0.5}Sr_{0.5}MnO_3$ sintered at 1500 °C and subsequently annealed at 1200 ° in air (batch 1). The stars mark reflections of $SrMnO_3$. All other reflections can be attributed to $(La,Sr)MnO_3$.

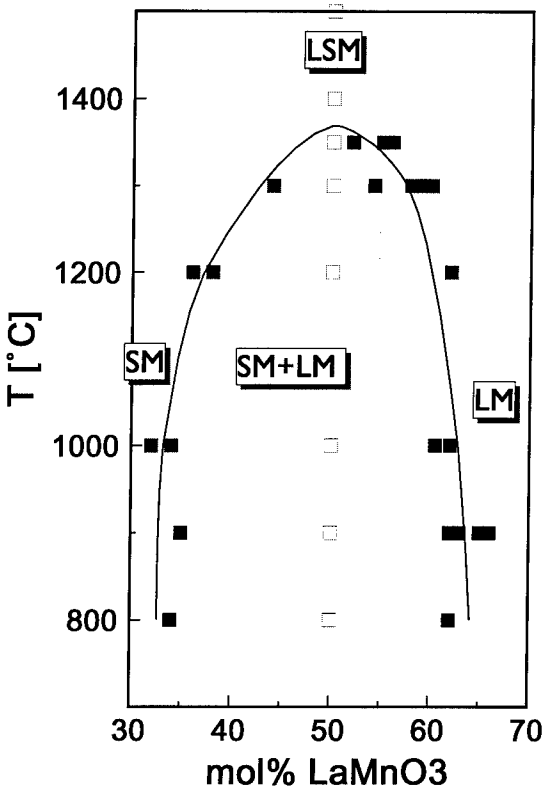

Figure 8: Temperature concentration diagram of the quasibinary system $SrMnO_3$-$LaMnO_3$. Open squares: prepared samples; filled squares: results of EDX analysis of SM and LM of the samples of batch 1 and 2.

Discussion

The preparation of single phase LM with intermediate Sr contents requires temperatures of above 1400 °C in air. Below that temperature a miscibility gap exits in which Sr containing LM is stable beside La containing SM. The fact that the samples of batch 1 and 2 give identical results indicate that the samples are in equilibrium. The solid solution $(La,Ca)MnO_3$ were not studied in detail, yet. However, the phase diagram studies of the quasiternary system LM-SM-CM indicate that a miscibility gap exists even between LM and CM at temperatures of about 1200 °C in air. However, a decomposition of LM with intermediate Sr contents during furnace cooling was not observed. Annealing times of above 100 h are

necessary to decompose single phase $La_{0.5}Sr_{0.5}MnO_3$ into LM and SM at 1200 °C in air. Nevertheless, considering that solid oxide fuel cells are applied at 800-1000 °C for very long times, e.g. 50,000 h, decomposition of LM could be important for the reliability of the cathode material.

Conclusion

For the controlled preparation of single phase samples of the $(La,Sr,Ca)MnO_3$ solid solution with intermediate Sr or Ca contents annealing temperatures of above 1400 °C are required. Below that temperature the solid solution decomposes forming $LaMnO_3$ and $SrMnO_3$ and $CaMnO_3$, respectively. However, the decomposition reaction is slow and therefore, it does not affect the material during furnace cooling.

Reference

1] J.A.M. van Roosmalen, P. van Vlaanderen, E.H.P. Cordfunke, W.L. Ijdo, D.J.W. Ijdo, J. Solid State Chem., **114** (1995) 516.
2] H.S. Horowitz, J.M. Longo, Mater. Res. Bull., **13** (1978) 1359.
3] T. Negas, J. Solid State Chem., **7** (1973) 85.
4] Phase Diagrams for Ceramists, Annual '93, A.E. McHale (ed.), The Am. Ceram. Soc., Westerville, Ohio, USA.
5] L.M. Lopato, L.I. Lugin, G.I. Gerasimyuk, A.V. Shevchenko, Sov. Prog. Chem., **38** (1972) 32.
6] D. Risold, B. Hallstedt, L.J. Gauckler, J. Am. Ceram. Soc., 80 (1997) 537.
7] Y. Moritomo, A. Asamitsu, H. Kuwahara, Y. Tokura, Nature, 380 (1996), 141.

MICROSTRUCTURE AND MAGNETORESISTANCE IN La-Y-Sr-Mn-O THICK FILMS

L.H. Chen, D.H. Wu and C.S. Hsi
Department of Materials Engineering, I-Shou University, Kaohsiung, Taiwan, ROC

ABSTRACT

The microstructure and magnetoresistance behavior of $La_{0.67}Sr_{0.33}MnO_{3-x}$ and $La_{0.60}Y_{0.07}Sr_{0.33}MnO_{3-x}$ thick films, prepared by a doctor-blade process, has been studied in this work. A MR ratio of 6.5% in a field of 2 T is found at room temperature for the $La_{0.67}Sr_{0.33}MnO_{3-x}$ thick film, which monotonously increases to a value of 23.5% as temperature decreases to 40 K and is presumably higher at even lower temperatures. On the other side, the MR ratio of the $La_{0.60}Y_{0.07}Sr_{0.33}MnO_{3-x}$ thick film is as high as 18.2% at room temperature and decreases as the temperature is lowered. Such an variance in MR behavior of both thick films is probably related to their microstructure, which is denser and more continuous as a result of the enhanced sintering by Y-doping. Besides, the modification of Mn-O-Mn bonding and lattice parameter may be also responsible.

INTRODUCTION

Due to the colossal magnetoresistance (CMR) with many orders of magnitude change in resistivity, perovskite-like manganites, such as L-A-Mn-O (L=La, Pr, Nd...., A=Ca, Sr, Ba.....), have received extraordinary attention in recent years[1-5]. However, the pratical applications of CMR manganites have been limited by the fact that the huge changes in resistivity are only observed at very low temperatures (< 150 K) and under fields of the 10^4 Oe range.

It is well-known that the maximum MR ratio and higher field sensitivity are expected to occur around the magnetic Curie temperature. Thus, the manganite systems with T_c temperature close to room temperature will be the first candidates for the MR device materials. The La-Sr-Mn-O is one of the systems with T_c temperature near room temperature and has been extensively studied[6-8]. In addition, perovskite-like La-Sr-Mn-O manganites have also received lots of attention due to their application potentials to anode and interconnector materials for solid-oxide fuel cells.

In general, materials are mostly used in thin film form in order to be easily manufactured and to be well-controlled in size. On the other hand, thick films offers considerable advantages in reduction of cost. In this paper, we prepare thick films of La-Sr-Mn-O and La-Y-Sr-Mn-O by a doctor-blade technique. The microstructure, magnetoresistance and magnetization behavior of films are discussed. The influence of Y3+ doping on the magnetoresistance behavior is also described.

EXPERIMENTS

The $La_{0.67}Sr_{0.33}MnO_{3-x}$(La-Sr-Mn-O) and $La_{0.60}Y_{0.07}Sr_{0.33}MnO_{3-x}$(La-Y-Sr-Mn-O) powders have been prepared by standard solid-state reaction techniques. The starting materials of oxides and carbonates, such as La_2O_3, Y_2O_3, $SrCO_3$, and $MnCO_3$, is mixed, grounded and calcined at 1200 C for 4 hr in an O_2 atmosphere.

Mat. Res. Soc. Symp. Proc. Vol. 517 © 1998 Materials Research Society

In order to form a tape by using a doctor-blade method, the ceramic powders have been mixed with an organic carrier (Ferro, B73305), which is composed of binders, dispersants and plasticizers. The ratio of ceramic powders to organic carrier of 60:40 in wt is checked to be appropriate in this study. The subsequent sintering involves three steps. In the first one, the thick films are slowly heated (1 C/min) up to a temperature at which the organic carrier is allowed to decompose. Thermogravimetry analysis (TGA) is used to determine the decomposition temperature of the organic carrier. A temperature of 350 C has been determined in this study. In the second step, the films are heated up to 1400 C at 3 C/min and sintered for 4 hr. Finally, the films are furnace cooled down to the room temperature. All thermal treatments are processed under flowing O_2.

Structure characterization of the films have been carried out by using a Scintag Xgen-4000 X-ray diffractometer with k-α(Cu) radiation and Scanning Electron Microscopy. The electrical transport and magnetoresistance behavior have been measured by a four-probes technique under fields up to 2 T. The MR ratio in this study is defined as $(\rho - \rho_{2T})/\rho_{2T}$. Here ρ_{2T} is the resistivity of film under a field of 2 T. The magnetization curve is obtained at room temperature by an alternating gradient magnetometer (AGM) under a maximum field of 8 kOe.

RESULTS AND DISCUSSION

Figure 1 shows the X-ray diffraction patterns of La-Sr-Mn-O and La-Y-Sr-Mn-O thick films. The sintered La-Sr-Mn-O thick films exhibit the polycrystalline and perovskite-like structure with a series diffraction peaks of (100), (110), (111), (200), (102), (112), (202), (300), (103), (113), (222), (203), and (213). It is identical to the precursor calcined ceramic powders. The refined lattice parameter a of La-Sr-Mn-O thick film is ~3.882 A. The La-Y-Sr-Mn-O thick film also has a similar perovskite-like structure, except of the smaller lattice parameter of ~3.876 A, which is due to the partial substitution of La^{3+} by a smaller ion of Y^{3+}.

The microstructure of La-Sr-Mn-O thick film is characterized by using the SEM. As shown in the Figure 2, the La-Sr-Mn-O film, sintered at 1400 C for 4 hr, have a porous structure with a average grain size of ~ 4 μm in diameter. The bulk density of film is ~5.81 g/cm3, which is ~90 % of theoretical density(T.D.). When incorporated with minor Y_2O_3 addition, the La-Y-Sr-

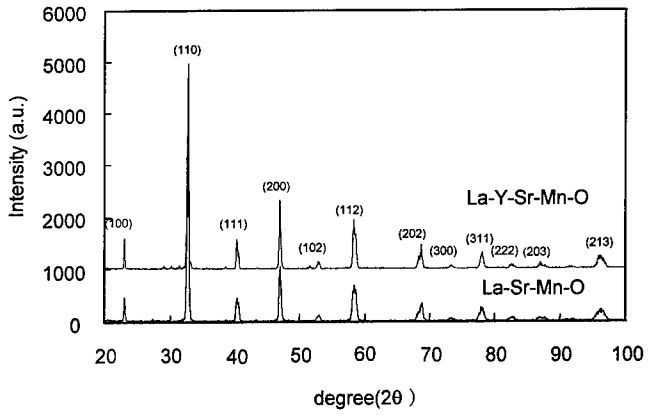

Figure1.The typical θ/2θ XRD patterns of La-Sr-Mn-O and La-Y-Sr-Mn-O thick films.

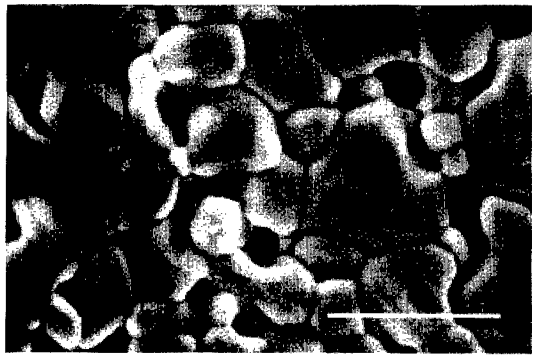

Figure 2. The microstructure of La-Sr-Mn-O thick film sintered at 1400 C for 4 hr. The scale bar equals 15 μm.

Mn-O film is found to have a microstructure with well grown and connected grains of ~8 μm in average diameter and almost no pore inside. The bulk density of La-Y-Sr-Mn-O film is ~ 95% of T.D, which is much higher than that of La-Sr-Mn-O film. Such an enhanced sintering and grain growth of thick film is probably related to the addition of Y_2O_3.

Figure 3 shows the room temperature magnetization behavior of La-Sr-Mn-O and La-Y-Sr-Mn-O thick films. The magnetization of La-Sr-Mn-O film rapidly increases in the low field region and almost saturates in a field of 1 KOe. Inspection of this curve reveals that the La-Sr-Mn-O film exhibits a ferromagnetic behavior at room temperature with a coercivity of less than 30 Oe and a saturation moment of ~9.0emu/g. Similar as that of La-Sr-Mn-O film, the La-Y-Sr-Mn-O film also displays a ferromagnetic behavior at room temperature. However, the magnetization of La-Y-Sr-Mn-O film does not saturate and still shows an increasing tendency in fields up to 8 kOe.

The field dependence of resistivity has been measured by using the four-probes method under fields up to 2 T. It is revealed that the resistivity of both La-Sr-Mn-O and La-Y-Sr-Mn-O thick films have similar field dependence. In Figure 4, we show the results for La-Y-Sr-Mn-O film measured at temperatures of 298 K, 200 K and 100 K, respectively. At all temperatures, the

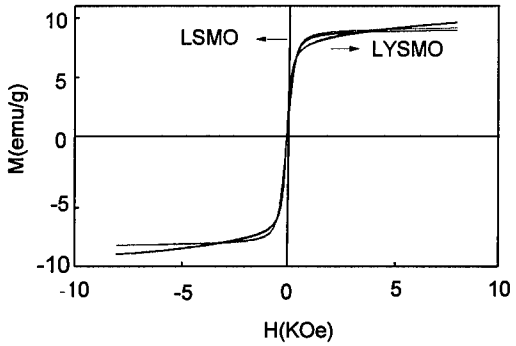

Figure 3 The room temperature magnetization curves of La-Sr-Mn-O and La-Y-Sr-Mn-O thick films, respectively.

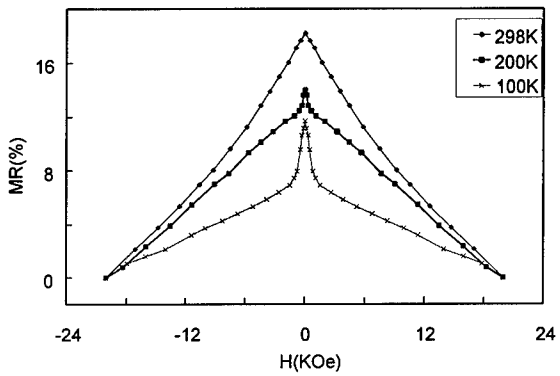

Figure 4 The field dependence of resistivity of La-Y-Sr-Mn-O thick film at room temperature , 200 K and 100 K, respectively.

resistivity of film always decreases in an applied field, and does not saturate in the maximum applied field of 2 T. It is worth noting that there exists a sharp drop of resistivity in low field region (< 1 kOe) in the MR curve, as shown in Figure 4, which becomes more significantly as temperature is decreased. In fact, the low field MR has been selected for many sensor applications because permanent magnets are going to be used in that field region.

Figure 5 displays the temperature dependence of resistivity for thick films. The absolute values of measured resistivity can only be taken as approximate, due to the porosity of film. The zero-field resistivity of La-Sr-Mn-O film is found to increase as temperature decreases from room temperature and almost reach a maximum at a lower temperature of ~ 65 K, which is designated the temperature (T_{MI}) of metal-insulator transition. As shown in Figure 6, the overall MR ratio of La-Sr-Mn-O film in the 2 T field region is ~ 6.5 % at room temperature, which increases as temperature decreases from room temperature and reaches a maximum of 23.5 % at ~ 55 K. However, the La-Sr-Mn-O film has been found to be ferromagnetic at room

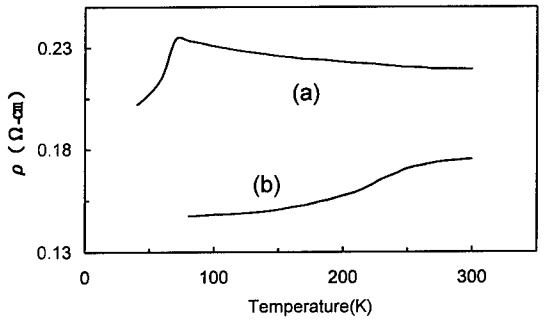

Figure 5. The temperature dependence of resistivity for La-Sr-Mn-O (curve a) and La-Y-Sr-Mn-O (curve b) thick films, respectively.

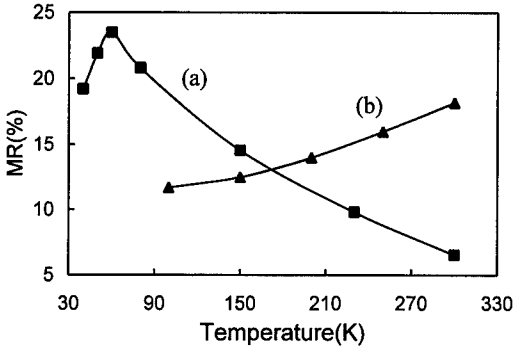

Figure 6. The temperature dependence of MR ratio for La-Sr-Mn-O (curve a) and La-Y-Sr-Mn-O (curve b) thick films, respectively.

temperature, suggesting that the temperature (T_c) of magnetic transition is higher than room temperature. It is quite unusual to find that metal-insulator transition occurred at temperature much lower than that for magnetic ordering change for the La-Sr-Mn-O thick film prepared in this study. Most of the experimental studies assert that T_{MI} coincides with the Tc for the onset of ferromagnetism. Only a few papers reported that T_{MI} may not be the same as T_c[9,10]. Although the exact reasons for the discrepancy between T_{MI} and T_c in this work are not known at this moment, it is believed that such difference may arise from a distinct effect that can be related to the porosity in the microstructure of the thick film and/or to the reduction effect associated to the decomposition of the organic carrier.

The Y^{3+} doping of La-Sr-Mn-O film on the electric transport and magmetoresistance behavior is also shown in Figures 5 and 6. Compared to the La-Sr-Mn-O film, the resistivity of La-Y-Sr-Mn-O film is always lower and decreases as temperature decreases from room temperature to 30 K. The MR ratio of La-Y-Sr-Mn-O film is ~ 18.2 % at room temperature, which also decreases as temperature decreases. As revealed in Figure 5, the temperature T_{MI} of La-Y-Sr-Mn-O film is above room temperature, which is comparable to that obtained for the common studied bulk samples. Such shift of temperature of metal-insulator transition to be above room temperature may be related to the much denser microstructure, as a result of enhanced sintering by the doping of Y^{3+} which is supported by the microstructural characterizaton. However, the influence of Y^{3+} doping on the lattice pameter *a* and the length and angle of Mn-O-Mn bonds can not be ruled out.

CONCLUSIONS

We have discussed the microstructure and magnetoresistance behavior of La-Sr-Mn-O and La-Y-Sr-Mn-O thick films, prepared by a doctor-blade technique. The sintered La-Sr-Mn-O film has a porous microstructure and shows a MR ratio of ~6.5 % at room temperature, which increases as temperature decreases and reaches a maximum at ~55 K. On the other hand, the MR ratio of La-Y-Sr-Mn-O film is as high as 18.5% at room temperature and monotonously decreases as temperature decreases. Such influence of Y^{3+} doping on the electrical transport and magnetoresistance beahavior of La-Sr-Mn-O film is believed to be related to the enhancement of the microstructure densification during sintering, as well as the change in lattice parameter of unit cell and in length and angle of Mn-O-Mn bonds.

ACKNOLEDGMENTS

This work was support by the National Science Council of Republic of China under the contract number of NSC87-2216-E-214-004.

REFERENCES

1.S. Jin, T.H. Tiefel, M. McCormack, R.A. Fastnacht, R. Ramesh and L.H. Chen, Science, **264**, 413(1994)

2.H.Y. Hwang, S.-W. Cheong, P.G. Radaelli, M.Marezio and B. Batlogg, Phys. Rev. Lett., **75**, 914(1995)

3.L.H. Chen, T.H. Tiefel, S. Jin, T.T.M. Pastra, R. Ramesh and C. Kwon, IEEE Trans. On Magn., **32**, 4692(1996)

4.J. Fontcuberta, B. Martinez, A. Seffar, S. Pinol, J.L. Garcia-Munoz and X. Obradors, Phys. Rev. Lett., **76**, 1122(1996)

5.Y. Kwon, E. Chi, J. Kang and N.H. Hur, J. Appl. Phys., **82**, 3072(1997)

6.H.L. Ju, C. Kwon, Q. Li, R.L. Greene and T. Venkatesen, Appl. Phys. Lett., **65**, 108(1994)

7.M.C. Martin, G. Shirane, Y. Endoh, K. Hirota, Y. Moritomo and Y. Tokura, Phys. Rev. B, **53**, 14825(1996)

8.T. Manabe, I. Yamaguchi, W. Knodo, S. Mizuta and T. Kumagai, J. Mater. Res., **12**, 541(1997)

9.S. Zhang, J. Appl. Phys., **79**, 4542(1996)

10.S.E. Lofland, S.M. Bhagat, K. Ghosh, R.L. Greene, S.G. Karabashev, D.A. Shulyatev, A.A. Arenov and Y. Mukovskii, Phys. Rev. B, **56**, 13705(1997)

MAGNETORESISTANCE IN $Pr_{0.65}Ba_{0.05}Ca_{0.3}MnO_{3-\delta}$ THIN FILMS

D. KUMAR*, SRINIVAS V. PIETAMBARAM*, RAJIV K. SINGH* & C.B.LEE**, *DEPARTMENT OF MATERIALS SCIENCE & ENGINEERING, UNIVERSITY OF FLORIDA, GAINESVILLE, FLORIDA 32611-6400.**DEPARTMENT OF ELECTRICAL ENGINEERING, NORTH CAROLINA A & T STATE UNIVERSITY, GREENSBORO, NC 27411.

ABSTRACT

Interesting magnetotransport behavior has been observed in $Pr_{0.65}Ba_{0.05}Ca_{0.3}MnO_{3-\delta}$ films (PBCMO or Ba-doped PCMO). The films are grown in-situ on (100) $LaAlO_3$ substrates using a pulsed laser deposition technique. Microstructural characterization carried out on these films has shown that the films are smooth, free from impurity phases, and highly textured. The electrical resistance and magnetoresistance (MR) have been measured in the 10-300 K range in magnetic field up to 5 T using the SQUID magnetometer. With the application of magnetic fields of 0.5 T and 5 T, the resistance of the films has been found to drop spectacularly, resulting in the realization of MR ratio (at ~60 K) as high as 5.3 X 10^3 and 5.6 X 10^8, respectively.

INTRODUCTION

Hole doped manganites $La_{1-x}M_xMnO_3$ (M=Ba, Sr, Ca, Pb) with pervoskite structures are known since long as an interesting class of materials [1-5]. Searle et al. [6] were the first to report in 1969 a large magnetoresistance (MR) in $La_{1-x}Pb_xMnO_3$ (x=0.31) system. However, with the recent observation of colossal MR ratio by Jin et al.[7] in $La_{0.67}Ca_{0.33}MnO_3$ thin films, a renaissance of manganites has taken place [8-21]. The basic manganite is $LaMn(III)O_3$ which is antiferromagnetic and insulating. After doping La partially by divalent metal in $LaMnO_3$, a corresponding number of formerly triply charged Mn becomes quadruply charged and the displacement of these holes increases the conductivity and provides a mechanism for ferromagnetic interaction in $La_{1-x}Mn_x(III)Mn_{1-x}(IV)O_3$ [8, 9, 11,13]. Presently most of the efforts to improve the MR ratio at lower fields and higher temperatures, which are very important for the practical application of these materials in devices, are focused on La-based manganites [22]. Since the MR behavior in manganites is closely related to magnetic-exchange interactions between two magnetic cations separated by an anion, which in turn is determined by interatomic distance, and hence by lattice parameter, Nd-and Pr-based (ionic radii of Nd^{3+}, Pr^{3+} are nearly 6% smaller than the ionic radius of La^{3+}) manganites are anticipated to show improved MR behavior in comparison to their La-based counterparts [23,24]. In this report , we present our studies on the effect of Ba-doping on the magnetotransport behavior of Pr-based manganite thin films. The selection of Ba as a dopant was inspired by an intention to induce chemical pressure inside the lattice to favor the effective electron (or hole) transfer between the neighboring Mn sites.

EXPERIMENT

Ba-doped PCMO pellets with nominal composition $Pr_{0.65}Ba_{0.05}Ca_{0.3}MnO_{3-\delta}$ were prepared by mixing required quantities of respective oxide or carbonate powders and sintering them at 1200 ^oC for 24 hours. The final targets (25mm diam, 4mm thickness) were obtained by

Mat. Res. Soc. Symp. Proc. Vol. 517 © 1998 Materials Research Society

regrinding the pellets followed by repelletizing and sintering in open air at 1400 ^{o}C for 30 hours. In-situ film deposition on (100) $LaAlO_3$ substrates were carried out in a pulsed laser ablation system. A 248 nm KrF laser with a 10Hz repetition rate and 2.5 J cm^{-2} energy density was used. A substrate temperature of 700 ^{o}C and oxygen pressure of 250 m Torr were used during film deposition. After termination of film-deposition, films were cooled to room temperature in approximately half-an-hour in 500 Torr of oxygen in the growth chamber. The films deposited were characterized using scanning electron microscopy (SEM), energy dispersive x-ray (EDX) analysis and x-ray diffraction (XRD) measurements.The temperature dependance of resistance of Ba-doped PCMO films were examined in zero and applied field using four-probe technique and the quantum design SQUID magnetometer. The transport current was in the film plane. The applied field was also in the film plane and was parallel to current direction. The MR ratios, $\Delta R/R(H)$, were calculated using $\Delta R/R(H) = [R(H)-R(0)]/R(H)$, where R(H) and R(0) are resistances in applied and zero field.

RESULTS AND DISCUSSION

An x-ray diffraction pattern of a Ba-doped PCMO film grown on (100) a $LaAlO_3$ substrate at 700 ^{o}C is shown in Fig. 1. Only (00l; l=1 and 2) lines are seen indicating the highly textured growth of Ba-doped PCMO film on the $LaAlO_3$ substrate. The variation of electrical resistance of Ba-doped PCMO film as a function of temperature in zero and applied field (H=5 T) are shown in Fig. 2. For these measurements, the film dimension was: thickness=2000 Å ,width=3mm, length=1mm (distance between voltage probes). The figure shows that application of the external magnetic field suppresses the resistance of the film throughout the temperature range we have studied. However, the suppression in resistance is maximum (~10^7 times) near the resistivity peak in zero field. The temperature dependence of the magnetoresistance ratio for the same film is also shown in this figure. As seen, the maximum value of the MR ratio for Ba-doped PCMO film in the magnetic field of 5 T is as high as 5.3 X 10^8 % at 77 K. Although the phenomenon observed is in a field much larger than currently used in magnetic read-head devices, it is worthy to note that a magnetic field can alter the transport resistance of a solid in such a remarkable fashion.

The magnetoresistance behavior of Ba-doped PCMO can be understood as follows: According to the most of the literature

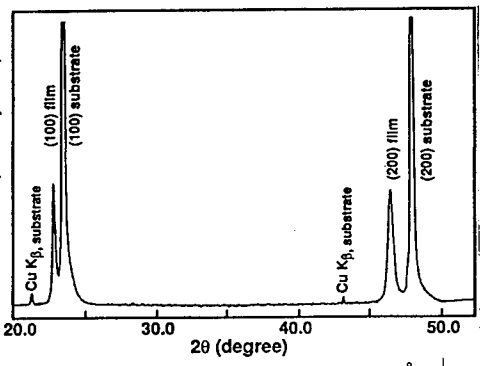

Fig.1. X-ray diffraction patterns of2000 Å thick Ba-doped PCMO filmgrown on (100) $LaAlO_3$ substrate at 700^{0} C.

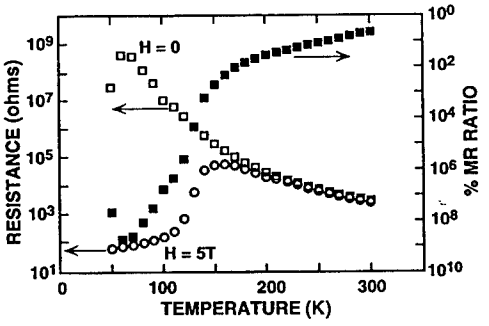

Fig.2. Resistance vs temperature plots for Ba-doped PCMO film in zero and 5 T magnetic field. Magnetoresistance ratio dependence on temperature is also shown.

$Pr_{1-x}Ca_xMnO_3$ system remains insulating against Ca doping [25-28]. Its resistivity shows insulating behavior over the whole Ca ion concentration. This is partly because the charge-transport in $Pr_{1-x}Ca_xMnO_3$ is amenable to the charge ordering of Mn^{3+} and Mn^{4+}. Similar charge-ordering phenomena in other distorted pervoskite manganites have been reported in $La_{1-x}Ca_xMnO_3$ ($x \sim 0.5$), $Pr_{1/2}Sr_{1/2}MnO_3$ and $Nd_{1/2}Sr_{1/2}MnO_3$. In general, the cations with smaller ionic radii in (R,A) sites of $R_{1-x}A_xMnO_3$ cause a larger alternating tilting of MnO_6 octahedra in a pseudoperovskite $GdFeO_3$-type structure, and leads to a distortion-dependent reduction of a one-electron bandwidth in these manganites causing a charged-ordered state, and simultaneous stabilization of an antiferromagentic (AFM) spin structure [25].

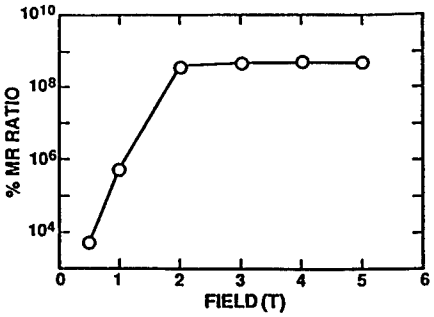

Fig.3. Magnetoresistance ratio variation with magnetic field for a Ba doped PCMO film at 60 K.

However, the Ba-doping of PCMO results in a reduction of lattice distortion, which in turn, may not permit appreciable reduction in one-electron bandwidth. At the same time, the Ba-doping induces sufficient chemical-pressure inside the PCMO lattice to cause insulator-metal transition as shown in Fig. 2. This is consistent with the double exchange (DE) model [1-3] according to which, the effective electron (or hole) transfer interaction t_{ij} between the neighboring Mn sites is given by $t_{ij} = t_o \cos(\theta_{ij}/2)$ where $\Delta\theta_{ij}$ is the relative angle between the local sins (t^3_{2g}) of the Mn sites and t_o is the transfer in the full spin-polarized state. The chemical pressure, in essence, change the Mn-O bond in such manner that results in increase in transfer interaction between the neighboring Mn sites.

The suppression in electrical resistance of Ba-doped PCMO films in presence of magnetic field is also within the framework of DE model. The resistivity in the absence of magnetic field is higher due to the decreased transfer interaction ($\Delta\theta_{ij} \neq 0$) while the spins are perfectly aligned ($\Delta\theta_{ij} = 0$) along the direction of applied magnetic field resulting in the improvement in transfer interaction and thereby decrease in electrical resistance in the presence of magnetic field. Figure 3 shows the variation in MR ratio of a Ba-doped PCMO film as a function of field applied at the temperature (~60 K) where the maximum MR is observed. Two important features of the film are evident from this figure. The first feature is the beginning of saturation (around H=2 T) of MR at field smaller than mostly reported and second is the realization of MR ratio of ~5 X 10^3 at 0.5 T (5000 Oe). This value of MR ratio at such a low field is much higher than previously reported. Both these features are very advantageous for fabrication of devices based on manganite thin films. The start in trend of MR ratio to saturate suggests that the most of the spins on Mn ions are lined-up in the field direction at ~ 2 T. The realization of large MR ratio at relatively low magnetic field may be associated with the hybridization of the more extended Pr 4f orbitals with the oxygen 2p orbitals in praseodymium based manganites favoring the double exchange [29].

CONCLUSIONS

In summary, we have investigated the insulator to metal transition in Ba-doped PCMO thin

films which was grown using a pulsed laser deposition technique. The insulator to metal transition in the Ba-doped films is believed to be caused by chemical pressure induced in the lattice due to the presence of Ba ions. The results presented in this paper have shown that a magnificent magnetoresistance ratios can be obtained in Ba-doped PCMO films even at lower magnetic fields.

ACKNOWLEDGMENTS

The authors would like to thank the Department of Energy (grant # DE-FG 05-95ER45533) for funding this research.

References:

1. P.-G. De Gennes, Phys. Rev. , **118**, 141 (1959).

2. C. Zenner, Phys. Rev., **82**, 403 (1951).

3. G.H. Jonker and J.H. Van Santen, Physica, **17**, 337 (1950).

4. J.B. Goodenough, Prog. Solid State Chem., **5**, 145 (1971).

5. E.O. Wollan and W.C. Koehler, Phys. Rev., 100, 545 (1955).

6. C.W. Searle and S.T. Wang, Can. J. Phys. , **47**, 2703 (1969).

7. S. Jin, T.H. Tiefel, M. McCormack, R.A. Fastnatch, R. Ramesh, and L.H. Chen, Science, **264**, 413 (1994).

8. R. Von Helmolt, J. Wecker, B. Hlozapfel, L. Schultz, and K. Samwer, Phys. Rev. Lett. **71**,2331 (1993).

9. M.F. Hundley, M. Hawley, R.H. Helfner, Q.X. Jai, J.J. Neumeir, J. Tesmer, J.D. Thompson, and X.D. Wu, Appl. Phys. Lett., **67**, 860 (1995).

10. Y.Tokura, A. Urushibara, Y. Moritomo, T. Arima, A. Asamitsu, G. Kido, and N. Furukawa, J. Phys. Soc. Jpn., **63**, 3931 (1994).

11. E.L. Nagaev, Phys. Rev. B, **54**, 16608 (1996).

12. K. Chahara, T. Ohno, M. Kasai, and Y. Kozono, Appl. Phys. Lett., **63**, 990 (1993).

13. R. Mahendiran, S. K. Tiwary, A.K. Raychaudhuri, T.V. Ramakrishnan, R. Mahesh, N. Rangavittal, and C.N. R. Rao, Phys. Rev. B, **53**, 3348 (1996).

14. A. Gupta, T.R. McGuitre, P.R. Duncombe, M. Rupp, J.Z. Sun, W.J. Gallagher, and G. Xiao, Appl. Phys. Lett., **67**, 3494 (1995).

15. J. Fontcuberta, A. Seffar, X. Granados, J.L. Gaarcia-Munoz, X. Obradors, and S. Pinol, Appl.Phys. Lett., **68**, 2288 (1996).

16. X.T. Zeng and H.K. Wong, Appl. Phys. Lett., **66**, 3371 (1995).

17. S.S. Manoharan, D. Kumar, M.S. Hegde, K.M. Satyalakshmi, V. Prasad, and S.V. Subramanyam, J.Solid State Chem., **117**, 420 (1995).

18. D. Kumar, R. Kalyanaraman, J. Narayan, and D. K. Christen, Mat. Res. Soc. Symp. Proc., **397**, 241 (1996).

19. S.S. Manoharan, K.M. Satyalakshami, M.S. Hegde,V. Prasad, and S.V. Subramanyam, J. Appl. Phys., **76**, 3923 (1994).

20. H.L. Ju, C. Kwon, Qi Li, R.L. Greene, and T. Venkatesan, Appl. Phys. Lett., **65**, 2108 (1994).

21. F. Damay, A. Maignan, C. Martin, and B. Raveau, J. Appl. Phys., **81**, 1372 (1997).

22. G. Gong, C. Canedy,G. Xiao, J.Z. Sun, A. Gupta, and W.J. Gallagher, Appl. Phys. Lett.

23. G.C. Xiong, Q.Li, H.L. Ju, S.N. Mao, L. Senapati, X.X.Xi, R.L. Greene, and T. Venkatesan, Appl. Phys. Lett, **66**, 1427 (1995).

24. B. Raveau, A. Maignan, and V. Caignaert, J. Solid State Chem., **117**, 424 (1995).

25. H. Yoshizawa, H. Kawano, Y. Tomioka, T. Tokura, Phys. Rev.B, **52**, R 13 145 (1995).

26. Z. Jirak, S. Krupicka, V. Nekvasil, E. Pollert, G. Villeneuve, and F. Zounova, J. Magn. Magn. Mater. **15-18**, 519 (1980).

27. E. Pollert, S. Krupicka, and E. Kuzmicova, J. Phys. Chem. Solids, **43**, 1137 (1982).

28. Z. Jirak, S. Krupicka, Z. Simsa, M. Dlouha, and S. Vratislav, J. Magn. Magn. Meter., **53**, 153 (1985).

29. A. Zibold, H.L. Liu, D.B. Tanner, J.Y. Wang, M. Gruninger, H.P. Geserich, T. Kopp, Th. Wolf, W. Widder, and H.F. Braun, Phys. Rev. Lett. (in press).

High-Density Magnetic Recording Media

Part V

Microstructural Issues in Longitudinal Recording Media

MAGNETIC MEDIA PERFORMANCE: CONTROL METHODS FOR CRYSTALLINE TEXTURE AND ORIENTATION

DAVID N. LAMBETH, WEI YANG, HENG GONG, DAVID E. LAUGHLIN, BIN LU, LI-LIEN LEE, JIE ZOU, and PETER S. HARLLEE

ECE and MSE Departments, Data Storage Systems Center, Carnegie Mellon University, Pittsburgh, PA 15213, lambeth@ece.cmu.edu

ABSTRACT

Currently, and during the past few years, areal recording densities have doubled approximately every 18 months. This has resulted in the recent introduction of products exceeding 4 Gigabit/in^2. Furthermore, there have been recent laboratory demonstrations of over 11 Gigabit/in^2. This rapid technological pace is forcing media producers to seek new methods to control the media magnetic properties. It has recently been pointed out that due to the required signal to noise ratio and the resulting continued reduction in grain size the industry will soon be faced with the onset of thermal instabilities to data retention. Since the medium properties could limit the areal density of most recording systems, a systematic design approach toward media invention is necessary. Very small magnetic grains of near crystalline perfection will be required in order to achieve the coercivities and noise requirements for the next doubling of areal density (25 Gigabit/in^2). Following this not only will crystalline perfection be required, but extremely uniformly sized and singly oriented grains will be required to approach 50 Gigabit/in^2. Over the past few years we have taken an approach of controlled growth of the magnetic microstructure of thin film media to accomplish this. Here we provide an overview of the guiding media design philosophy and discuss materials issues, multi-layered thin film material structures and processing techniques which are used to control the microstructure and magnetic properties of Co-alloy films. Efforts toward epitaxial growth of multiple thin film layers on single crystalline Si is discussed as a method of achieving perfect crystallites of various highly oriented thin films. In the case of non-cubic materials, such as magnetic hcp Co-alloys, these films have well defined axial directions determined by the substrate and multiple thin film epitaxial relationships.

INTRODUCTION AND MOTIVATION

The continuing market force driven need for improved hard disk data storage is evident by the sudden change in the compound annual growth rate of areal densities in the early 1990's from 20 to 60%. This rate is still approximately 60% and there are no signs of abatement. The single largest, obvious, technical factor making this possible was the change from particulate disk media to sputtered thin film media. This smoother media surface has allowed continual decreases in the head to disk fly height to the present 50 nm and less. During the mid 1990's, even as trackwidths were shrinking, head disk interface technologies such as robust 15 nm thin CNx or CHx overcoats, laser produced mechanical texture and quasi-contact slider operation enabled reduced head to disk spacing and enabled the ubiquitous inductive head transducer to continue to perform adequately. With the advance to the more sensitive, low noise, magnetoresistive, and recently the spin valve device, record-playback transducer technology is returning media noise to being the limiting factor to further increases in areal density. While various laboratory demonstrations, such as IBM's recent announcement of 11 Gigabit/in^2 recording, have been used to herald the next generation of recording densities a more accurate measure of progress is provided by monitoring

Mat. Res. Soc. Symp. Proc. Vol. 517 © 1998 Materials Research Society

actual product performance. As of early 1998, the highest areal density of a commercial product fell very close to the 60% growth curve at 4.1 Giga bit/in^2. Concurrent with the progression of areal density has been a remarkable increase in data transfer rate and disk rotational frequency to decrease access times. This bandwidth increase, along with the introduction of the spin valve transducer, and the higher areal densities conspire to require even lower noise media.

These recent commercial improvements in longitudinal recording could not have been possible without the significant improvements already made in the recording media magnetic and microstructural properties. Ultimately, the achievable areal recording density should be determined by the media signal to noise ratio, which if the recording system is designed properly, is largely determined by the media thin film microstructure. For ideal media where the magnetic particles are totally non-interacting one might roughly estimate the media signal power to noise power ratio, SNR_{op}, (zero to peak signal to rms noise ratio) to be proportional to the average number of particles, N, sensed by the recording transducer. This assumption is based upon the concept that the large number of particles in a given volume is described by a Gaussian probability distribution and to determine the noise one merely estimates the variance to the average number of particles sensed. The signal power then goes as N^2 while the noise power goes as N. Hence, for a differentiating transducer system, 1000 particles would imply a SNR_{op} of 27db, a value that is sometimes viewed as necessary for an acceptable error rate. Therefore, assuming sufficient transducer sensitivity, in order to maintain an adequate SNR as the areal density is doubled, N would remain constant and, the number of particles per unit area would need to double. For thin film media, in which the particle extends through the thickness of the thin film, the particle or grain surface diameter would have to decrease by the square root of two.

Charap and Lu [1] recently modeled the limits of areal recording density based upon the concept that if a magnetic particle's anisotropy energy density-volume product is made too small it will spontaneously reverse due to thermal fluctuations. Their estimate of the limit of this product divided by the Boltzman energy is $K_uV/k_BT > 60$. At the same time since the media coercivity is proportional to the anisotropy field, $H_c \propto H_k = 2M_s/K_u$ the anisotropy energy density cannot be increased to a point where Hc would be greater than the maximum available transducer record fields. These field levels are determined as a fraction of the Ms of available head transducer materials. Based upon these boundary conditions: a maximum K_u to allow recording, a minimum thermally stable grain volume and a fixed number of grains to provide the required SNR, they estimated that a limit to long term data stability may occur around 40 Gigabit/in^2. We would like to suggest, however, that the statistical arguments concerning the number of particles required may be somewhat flawed. Unlike particulate tape media, thin film media is essentially volume filling. That is, there are no intentional voids in the media and the total magnetic moment sensed by the transducer would be essentially constant if the magnetic easy axes of all of the grains were in the same direction. In traditional rotating thin film hard disk media the easy axis is designed to be random in the plane of the disk to avoid modulation of the signal as the disk turns. Hence, at any position on the disk a large fraction of the grains have their easy axes either perpendicular or considerably off axis from the transducer recording direction. In the extreme case of totally non-interacting particles these grains contribute little or no output flux to the transducer and appear as magnetic voids. Hence, even if all particles were the same size and regularly spaced, mis-orientation would still provide a mechanism for fluctuation in the signal. Clearly these mis-orientations along with the distribution of grain sizes limits the SNR. By narrowing the size distribution or, better still, restricting it to a singly uniform size the SNR would improve. However, by orienting all the easy axes to a single direction, comparable to the transducers' sensitive direction, the noise would become dependent only upon the size distribution and would be further reduced. A smaller number of grains would be required to achieve the same

SNR and recording densities could be extended beyond the current suggested thermal stability limit. Since grain size distributions are typically skewed and the smaller particles are thermally unstable they should be eliminated. By eliminating these and the variance in particle number due to random orientation distribution it would seem to be reasonable to expect that the noise could be reduced by at least a square root of two and perhaps considerably more. A factor of two reduction would lift the predicted areal recording density limit to well over 50 Gigabit/in^2.

The above arguments assume non-interacting particles and it would seem to be naive to ignore magnetostatic or intergranular exchange interactions in a discussion of noise. However, it is the goal in the media design to eliminate the intergranular exchange by isolating each grain. Hence, noise induced by magnetostatic interactions can be limited if the media and recording system are designed correctly, as discussed next.

MAGNETIC RECORDING PHYSICS ISSUES

While the playback signal is extremely dependent upon the head to medium spacing and transducer resolution (gap length), it is also proportional to the magnetic medium film thickness and the spatial gradient of the magnetization along the recording track. Hence, one would be inclined to argue that the larger the remnant-film thickness product ($M_r\delta$) the better. This is not the case however, as the recorded transition length increases with this quantity and magneto-resistive playback transducers are easily driven into a non-linear regime of operation if the sensed field is too large. Hence, there is a maximum, and optimal $M_r\delta$, for the media determined by the head sensitivity function and the head to media spacing. For currently commercial high performance media $M_r\delta$ has been reduced to less than 0.5 milli-emu/cm^2. This is beneficial to media design for two reasons: One is that, for exchange coupled media or for a system with a poor record head field gradient, the apparent media transition noise can be directly correlated to the demagnetization fields at the transition. The second reason is that the down-track (linear) recording density is limited by the finite flux reversal length. This length is measured by the transition parameter, a_x, which is determined either via transition demagnetization forces or by the finite record head field gradient. The media noise is always lower if the coercivity is greater than the demagnetization field (Hc > Hd). In the ideal limit where the head is in contact with an zero thickness media and has a zero gap length the recorded magnetization profile would be a step function provided that Hc > Hd and that the media were homogenous. For the more realistic media microstructure the transition length would be determined by the characteristics of the set of grains that lie at the immediate location where the ideal transtion would have been. The transition length is then nominally the average grain size and the transition location variance (noise) is determined by the grain location, size and orientation distributions. In other words, even if media microstructure were made ideal, it would still be easy to incorrectly design a recording system to induce apparent media noise.

As an example for disussion consider Figure 1 which shows the media noise power spectra of several differing media determined by the noise power spectral integration technique. These datum were obtained using a Read Rite Tripad head with a .22 micron gap and flying just above medium contact at approximately 25 nm (at 7.1 m/sec.). In each case it is noted that the noise power initially increases linearly with density as the noise power is dominated by the flux transition location jitter and increases linearly with recording frequency as transition density increases. The fact that there is noise even at zero frequency indicates the discrete non-zero size of the randomly oriented magnetic switching units or grains. The initial slopes of these curves are determined by the grain size, intergranular exchange coupling, the maximum demagnetization field (determined by $M_r\delta$), and the finite head field gradient. At higher recording densities it is

common that the noise increases supra-linearly as the individual flux transitions interact during the recording process and begin to interpercolate. The onset of this supra-linearly noise behavior typically occurs as the flux transition density approaches the transition length, a_x. From a practical standpoint, but to some extent dependent upon the signal processing encoding technique, this noise limits the data transition spacing to approximately πa_x. At extremely high flux transition densities the noise again decreases as the media appears to be AC erased. A media with highly exchange coupled grains will show little DC frequency noise as the magnetization of all grains tend to align, while when AC erased the percolation effect is large. This DC result is a clear example that thin film media is volume filling and that this noise is not simply controlled by particle counting statistics. For a media with little exchange coupling the DC noise will correlate to the number density and orientation of the grains. When the media is designed with very small grain sizes and such that the Hd < Hc the head field gradient during the record process determines a_x and not the demagnetization fields associated with the media. The lowest noise curves of Figure 1 indicate that these media have sufficiently small grains (low slope) and a small enough $4\pi M_s$ /Hc that the supra-linear increase in noise does not occur until well after the maximum measured kfci. Hence, the grain size (isolated magnetic switching unit size) in combination with the random in-plane orientation determines the slope of this curve, as well as, the DC erased noise power shown at low frequencies. Whereas, media with large grains will show a large low flux density noise slope and if the Hd > Hc the supra-linear noise behavior will set on early. The higher noise curves represent this type of media. The lowest noise media of this set is comparable to today's best commercial media. If a medium noise is not head field gradient limited, but limited

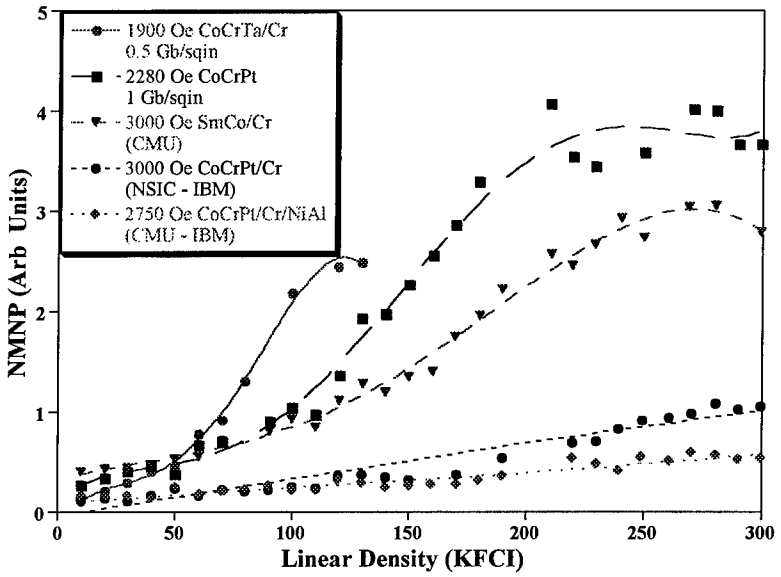

Figure 1. Normalized media noise vs. flux reversal density for media with various degrees of exchange coupling, Mrδ, and head field gradient induced noise.

by the statistical nature of the medium grains, then the required average grain size, assuming random size and orientation distributions, for 10 Gigabit/in^2 technology is estimated to be about 15-20 nm.

MEDIA CONSTRUCTION AND THE ROLE OF CRYSTALLINE TEXTURE

To attain the highest recording densities the coercivity should be maximized. In order to accomplish this the media designer could choose a magnetic alloy to achieve a higher anisotropy constant, lower the $4\pi M_S$ which also decreases the flux transition demagnetization effects, or gain better control of the microstructure to achieve the maximum potential anisotropy energy density of a given alloy. While studies have been performed on other alloys, in modern hard disk media hcp Co alloys are almost exclusively chosen due to their corrosion resistance and high anisotropy constants. Second and third elements such as Ni, Cr, Ta, Nb, B or Pt are chosen to promote diffusion of non-magnetic elements to the grain boundaries during film processing. In current products Cr and Ta are widely used and have proven to be especially useful at providing magnetic grain to grain isolation, while Pt appears to increase the anisotropy constant, but is not as effective at providing isolation. Likewise, these non-ferromagnetic elements usually lower the magnetization by dilution. The Co alloy is typically deposited onto a thin film underlayer structure which induces both an hcp Co phase and orients the crystalline c-axis by epitaxial growth. Perfect, defect free and isolated, hcp crystalline grains of appropriate size insure that domain walls do not nucleate at grain boundaries, crystalline flaws or stacking faults to lower the coercivity, while the orientation of the c-axis determines the maximum achievable coherent rotation coercivity. Via modeling, Yang [2] has predicted the hystersis loop dependence upon the orientation of the c-axis with respect to the film plane. For ideal Stoner-Wohlfarth particles with easy axes (c-axes) parallel to the applied record field the coercivity would be equal to the anisotropy field, $H_k = 2K_u/M_S$, while for a random ensemble of particles with c-axes in the film plane the predicted coercivity is reduced to 0.51 of H_K. However, if the c-axes are randomly oriented in all three dimensions the grains with axes out of plane, (or even only somewhat dispersed about the plane) have their magnetization forced back into the plane via demagnetization fields and these additional fields further reduce the coercivity. For the rotating longitudinal recording hard disk media format the singly directed ensemble is currently impractical and so the random two-dimensional structure is the most desirable. Hence, the choice of the underlayer texture upon which to perform epitaxial growth is critical in determining the Co alloy c-axis orientation. In addition these underlayer structures are critical in determining Co alloy crystalline quality and the grain size. Historically [3], and even though a number of other elements have been investigated, bcc Cr and Cr alloys have been used almost exclusively for this purpose.

Most current hard disk thin film magnetic media are constructed upon a highly polished NiP electrolessly plated AlMg, glass, or glass ceramic substrate by sputter deposition of a sequence of metallic layers. The exact structure depends upon the substrate, but usually consists of sequential depositions of a non-magnetic seed layer and underlayer followed by a magnetic Co-alloy, followed by a ceramic-like protective coating (principally carbon, CH_x or CN_x), and finally a very thin lubricant. The seed layers that have been used include both oxides and metals depending upon the substrate and the manufacturer. The purpose of the seed and the underlayers are to buffer the substrate surface and to initiate the crystalline growth and texture of the very thin magnetic layer. Hence, their composition, interaction with the substrate, and the processing conditions are important in determining the microstructural interface to the magnetic layer. In addition, the objective of the seed and underlayer is to establish a controlled grain size for the growth of other epitaxial layers.

If the atoms of a metallic thin film have sufficient surface mobility during the deposition process they arrange into a minimum surface energy configuration. For most simple lattice structures this implies a close packed atomic surface configuration. For fcc or hcp lattices the thin film surface will have a (111) or (0002) texture, respectively, while for the bcc lattices a (110) texture results. Hence, for bcc Cr alloys the (110) texture is commonly observed. As an example of this process consider Figure 2 which shows a series of x-ray diffraction θ-2θ scans of a CoCrPt film sputter deposited upon very thin, but varying thicknesses of sputter deposited Cr on a glass substrate. The glass substrate represents a high energy oxidized surface upon which arriving Co atoms would have limited mobility. By first placing a very thin Cr layer on this oxidized surface the mobility of the Co atoms can be significantly increased. However, below 5 nm the Cr is so thin that little or no crystalline texture has evolved and so it could, perhaps, be thought of as amorphous or very conducive to strain relaxation. Nevertheless, its presence alters the interfacial energy between the glass substrate and the Co alloy sufficiently to allow the thicker Co alloy film to seek its lowest energy close packed arrangement. Hence, while the (0002) texture is initially

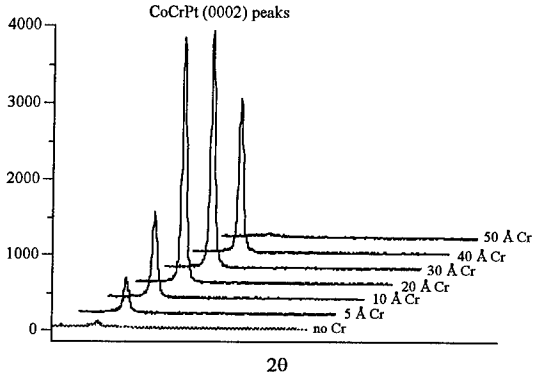

Figure 2. Close packed (0002) texture evolution of 40 nm thick CoCrPt grown on very thin Cr.

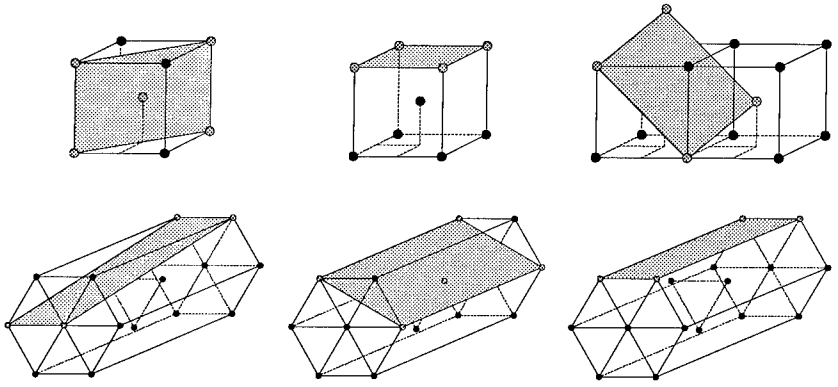

Figure 3. Epitaxial orientational relationships between bcc Cr and hcp Co.

not present when little or no Cr is deposited, it appears quite strong as the Cr thickness becomes sufficient to allow the Co to wet the substrate, then again disappears as the Cr becomes thick enough to develop and maintain a texture upon which the Co alloy is forced to epitaxially grow in different directions. The fact that the Cr has not developed a strong texture of its own at 5 nm thickness results in the Co texture being random. A similar effect, of this natural Co texture evolution, would occur if the underlayer allowed wetting of the Co to the surface or did not present a crystalline structure suitable for any epitaxial growth. Ta films, which appear amorphous when very thin, are known to perform a similar function for (111) fcc Ni alloys and are typically used as initializing seed layers for spin valve transducers. Other crystalline metals will perform this task if the lattice spacing or crystalline symmetry is largely different from that of the following layer. Likewise, if the atomic mobility is limited by substrate to film interfacial energy or by competition between the deposition rate and the atomic surface relaxation, or by impinging atomic kinetic energy, then other textures may appear. Consequentially, if the film nucleation process produces island like growth with high aspect ratios then the sides of the islands can represent a large fraction of a nucleating grain surface area and the lowest surface energy {110} planes of a bcc will not be parallel to the substrate surface, but to the island sides. This results in a (002) texture in addition to the common (110) texture. Historically the most commonly sought Cr texture has been the (002). To a limited extent this texture can be induced by deposition at elevated temperatures and at high deposition rates which induce a high aspect ratio island growth [4]. On occasion, especially for very thick films, as a powder diffraction pattern might begin to appear, the (112) texture would even be observed. Hence, the epitaxial growth relationships between Co alloys and the various Cr textures have been discussed in depth [5 and references therein]. The more relevant texture and orientation relationships are summarized as:

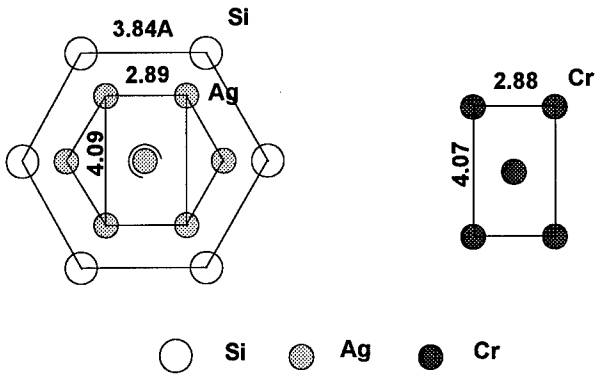

Figure 4. Orientational relationships for Cr(110)/Ag(111)/Si(111).

Bi-crystal:	Co(11$\underline{2}$0)[0001] \|\| Cr(002)[110] or Co(11$\underline{2}$0)[0001] \|\| Cr(002)[1$\underline{1}$0]
Quad-crystal:	Co(10$\underline{1}$1)[$\underline{1}$2$\underline{1}$0] \|\| Cr(110)[1$\underline{1}$0] or Co(10$\underline{1}$1)[$\underline{1}$2$\underline{1}$0] \|\| Cr(110)[$\underline{1}$10]
Uni-crystal:	Co(10$\underline{1}$0)[0001] \|\| Cr(112)[1$\underline{1}$0]

Figure 3 illustrates these three Co textures. While the Cr (002) and Cr (112) textures induce the Co c-axis into the film plane the most easily formed Cr (110) texture results in the c-axis being inclined at ±28 degrees with respect to the surface. Hence, a lower coercivity would be anticipated from the Co grown on the Cr (110) texture as the c-axis is not parallel to the recording plane. Also we see that there are multiple directions that the Co c-axis can be placed upon the Cr (002) and the Cr (110) textures. Hence, upon a single (002) textured Cr grain two possible c-axis orientations can grow (bi-crystal) while upon a single (110) textured Cr grain four

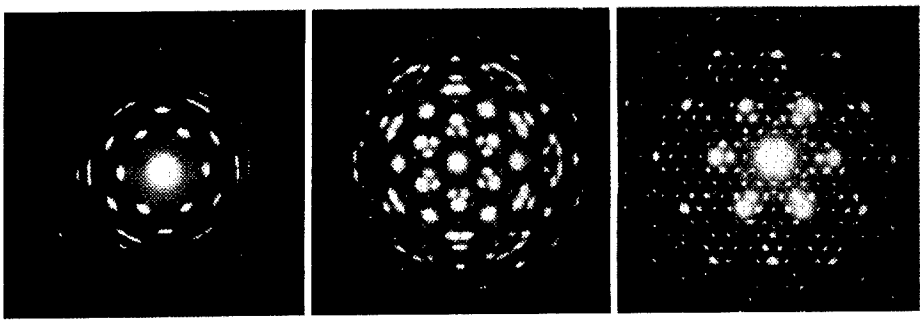

Cr(110) Cr(110)/Ag(111) Ag(111)/Si(111)

Figure 5. TEM diffraction patterns for Cr(110) and Ag(111) epitaxially grown on Si(111).

possible c-axis orientations of Cr can grow (quad-crystal). These bi-crystals and quad-crystals can never have both c-axes parallel to the applied field simultaneously. Hence, by the Stoner-Wolhfarth model one would anticipate the coercivity to be compromised. Likewise, when two or more Co variants do appear on a single Cr grain it is less likely that they will be isolated from one another by grain boundary diffusion as when compared to two Co grains located on two separate Cr grains. Hence, the boundary between the two variants can be thought of as a crystalline defect at which the magnetic spin orientation must be twisted and this provides for wall nucleation or an incoherent spin rotation center to initiate the switching process. This also compromises the maximum achievable particle anisotropy and hence, coercivity. Even worse, the four possible directions of the Co(10$\underline{1}$1)//Cr(110) texture relation places the Co c-axes ±28 degrees from the film plane and this in combination with the perpendicular demagnetization field always lowers the coercivity to an in-plane field. On the other hand, in the absence of severe Co alloy compositional flaws, the uni-crystal Co(10$\underline{1}$0)//Cr(112) texture relationship only allows a single orientation upon a Cr grain and conceivably could result in a higher coercivity if aligned to the recording field. In addition, the surface atomic spacings (a/sqrt(3) = 2.50; sqrt(2) x a = 4.07A) of this Cr texture closely matches both the c (~4.07A) and a (~2.50A) axes lattice spacing of the Co alloy simultaneously while the other Cr textures only match well in one of the two directions. Since only an uni-crystal can grow on an individual underlayer grain the anisotropy energy is not compromised by multiple growth variants. Unfortunately, this Cr texture is seldom seen, as processing at low temperatures or with an applied substrate bias results in Cr (110) texture while high temperatures and deposition rates can partially induce the Cr (002) texture. It is believed that the (112) texture of the bcc derivative, NiAl, provides a high coercivity template while the strong intermetallic Ni-Al bonding provids a small uniform grain size template [6,7].

In addition, it should be mentioned that extended Co alloy stacking faults, caused by compositional inhomogeneity or epitaxial lattice mis-match, could appear as small regions of the Co fcc phase. This cubic phase has a considerably lower anisotropy than the hcp phase and since it is in intimate exchange contact with the remaining hcp portion of the crystallite it may locally reduce the anisotropy energy and, hence, the coercivity. Processing at an elevated temperature and possibly with substrate bias during the Co deposition helps to provide the atomic mobility to minimize this crystalline disorder. The first criterion for the selection of Cr as an underlayer for Co was the close atomic lattice spacing match. Hence, these stacking flaws are exaggerated, or epitaxial growth does not even result, if the Co-alloy additives create too great a lattice mis-match. Due to its large atomic size Pt solutes significantly increase the Co lattice constant and to

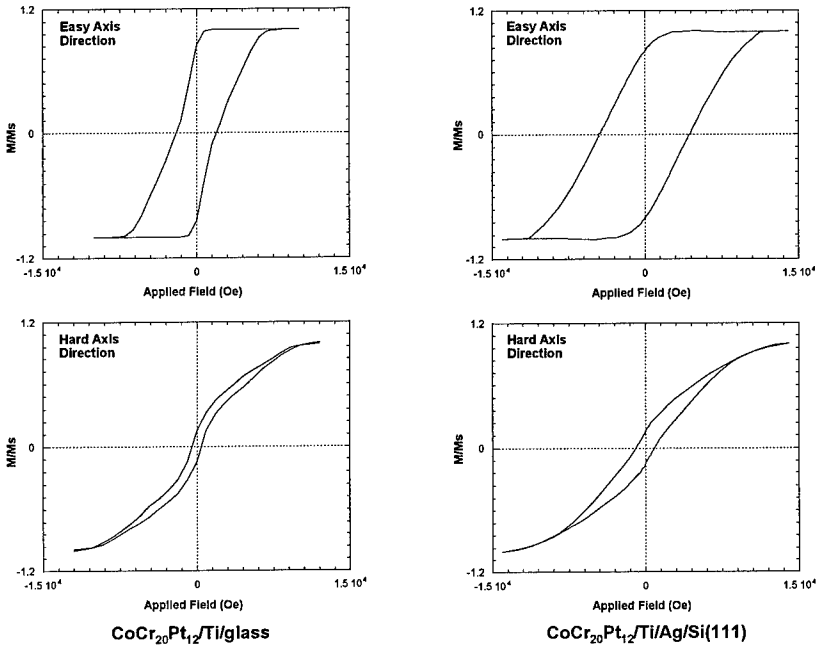

Figure 6. Comparison of easy and hard axes hystersis loops for CoCrPt (0002) films.

correct for this V, Ti, and Mo have been alloyed into Cr to expand its lattice constant appropriately.

HIGHLY ORIENTED MAGNETIC THIN FILMS

From the previous discussions, we see that it is desirable to grow Co-alloy and underlayer crystalline grains of considerable perfection and appropriate texture to avoid compromising the crystalline anisotropy. Likewise, to maximize the coercivity and to minimize the media noise it is desirable to control the easy axes orientations. By utilizing single crystal Si as a substrate we have developed a model system to approach these goals. Silicon is reasonably inexpensive and could conceivably be used as a media substrate. By first removing the SiO_2 surface layers a metallic epitaxial layer growth can be obtained. In particular we have found that fcc metals such as Ag, Au, Cu, and Al can grow on various Si surface orientations with a very high degree of epitaxy. Furthermore, these fcc metallic quasi-single crystal thin films can then easily be used to epitaxially grow other quasi-single crystal films of similar or differing crystalline structure. By proper choice of lattice constants various textures can be achieved with limited induced lattice strain. Multiple layers allow a transition from what would be thought of as an impossible lattice strain situation to one of little strain, a high degree of texture and orientation results as determined by the substrate [8]. As examples consider a few of the texture relationships we have obtained:

Bi-crystal: Co(11$\underline{2}$0)/Cr(100)/Ag(100)/Si(100)

Quad-crystal: Co(10$\underline{1}$1)/Cr(110)/Ag(111)/Si(111)

Perpendicular: Co(0002)/Ti(0001)/Ag(111)/Si(111)

Soft cubic: NiFe(111)/Cu(111)/Ag(111)/Si(111)

Uni-crystal: Co(10$\underline{1}$0)/Cr(112)/Ag(110)/Si(110).

In each of these the Ag to Si lattice match occurs at a unit cell ratio of 4 to 3, respectively. The very long range order of the single crystal Si is believed to promote the order of the metal contacting layer. The following metal layers' crystalline axes may then either align to the principle Si axes or be rotated through fixed angles depending upon the lattice parameter relationships. In the case of Co growth on the quasi-single crystal Cr thin films the orientational relationships listed in the earlier discussion of texture apply. The excellent epitaxial relationships between the single crystal substrate and the bi-crystal Co(11$\underline{2}$0) were described earlier[8], however, it was not clear from that work that the extensive array of other epitaxial relationships would exist.

Consider Figure 4 showing one of the three orientational relationships of bcc Cr(110) on fcc Ag(111) used to promote the quad-crystal structure. It is worth noting that these are the close packed lattice planes and since the atomic spacings of the Cr and the Ag match reasonably well the high energy Cr(111) would not be anticipated to grow. Since there are three possible orientations for the Cr(110) on the Ag(111) surface and since there are four possible orientations (quad-crystal) for the Co(10$\underline{1}$1) growth on Cr(110) there are actually twelve possible Co orientations on the Si substrate. This represents enough orientations that it is tempting to advocate that a quad-crystal rotating disk made from a Si(111) substrate would have little rotational signal modulation. However, this would be far from the uni-orientational structure

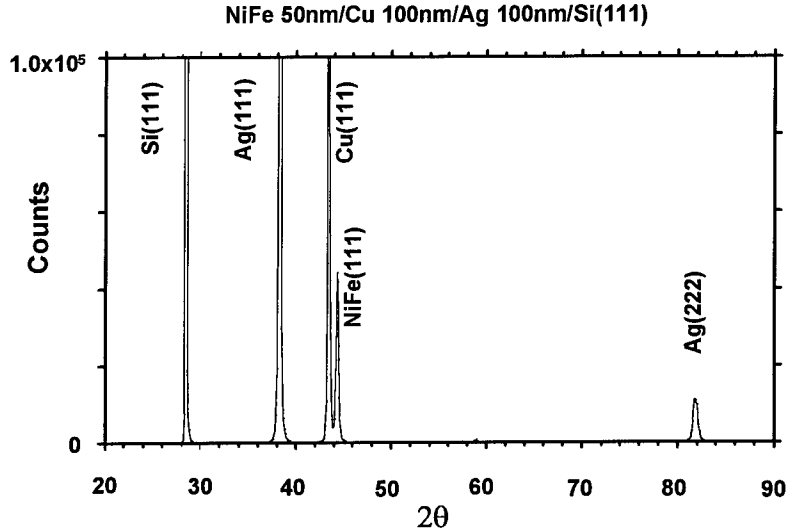

Figure 7. X-ray diffraction scans of NiFe(111)/Cu(111)/Ag(111)/Si(111).

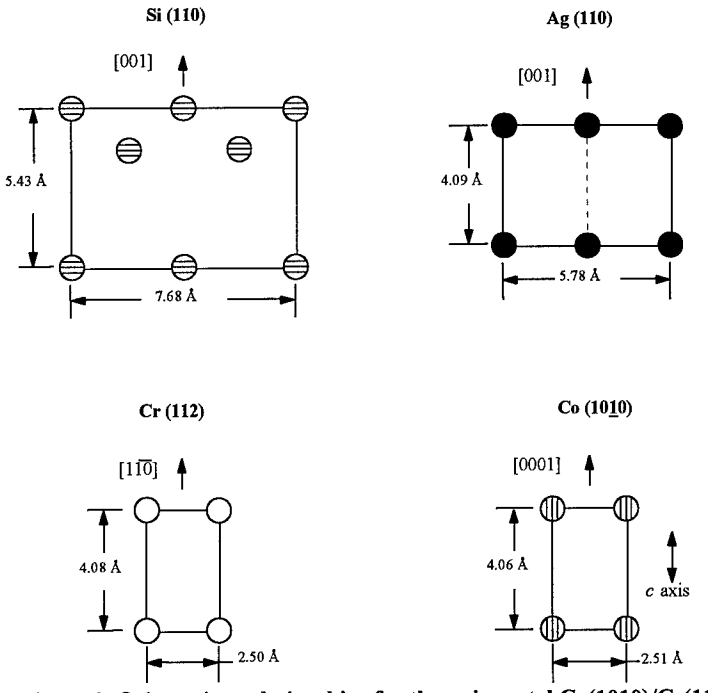

Figure 8. Orientation relationships for the uni-crystal Co(10$\underline{1}$0)/Cr(112)/Ag(110)/Si(110).

advocated earlier. Figure 5 shows TEM electron diffraction patterns to demonstrate the alignment between the Si substrate and the metal underlayers for the quad-crystal structure.

In conventional perpendicular recording media Ti is commonly used as an underlayer to induce the Co-alloy (0002) texture. However, the Co-alloy(0002) texture that develops on Ti usually requires that the Co-alloy be grown rather thick. Since Ti(0001) (a = 2.95A) is well lattice matched to Ag (a/sqrt(2) = 2.89A) highly textured Ti(0001) films were grown on quasi-crystal Ag(111)/Si(111) templates. Unfortunately, the Ti(0001) does not provide a good lattice match for Co(0002) (a = 2.50A). Nevertheless as an example of the effect of providing a long

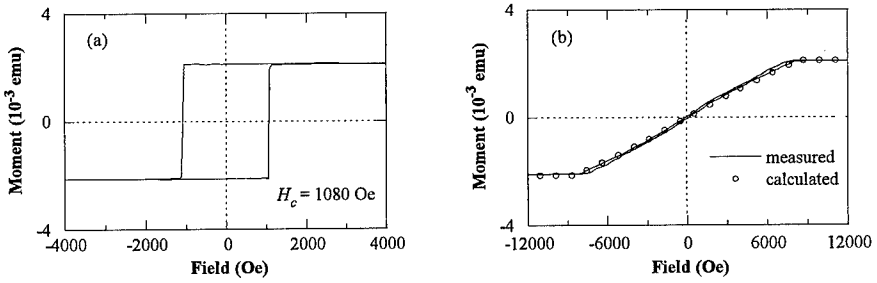

Figure 9. Easy and hard axes hystersis loops for uni-crystal Co-alloy films.

range ordered underlayer Co/Ti was grown on Ag(111)/Si(111) and for comparison to a conventionally prepared perpendicular media it was simultaneously deposited on glass. Hystersis loops for both the easy and hard axes of both samples are shown in Figure 6. Clearly the magnetic characteristics are much improved when the Si substrate is used.

For perpendicular media a soft magnetic underlayer is commonly advocated. Figure 7 shows the θ–2θ x-ray diffraction scans for an epitaxial (111) textured soft NiFe layer. The diffraction peak heights are extremely large, especially for the Cu and Ag, which are buried under the NiFe, when compared to films which would be grown without the single crystal Si substrate. Peak heights of thousands of counts are common for most of the films grown on Si, whereas a typical Cr(110) film grown on glass and measured in the same manner would have peak heights of only tens of counts. Rocking curve measurements of each of the Ag(111), Cu(111) and NiFe(111) film layers indicate a very small dispersion ($\Delta\theta_{50} \leq 0.7°$), while preliminary TEM data indicates epitaxial orientation of each layer. The hard axis coercivity of approximately an oersted and is believed to be due to the influence the earth's field during deposition.

For the often sought after uni-crystal structure Cr(112) develops nicely on the Ag(110)/Si(110) surface. TEM diffraction patterns show a clear epitaxial relationship as detailed in Figure 8. By calculation, one would predict that Cr(110) would grow on Ag(110) because a good lattice match is found in two directions. However, while Cr(112) only matches in one direction, it is suspected that extra energy due to the lack of a bond for the body-centered atom dominates and forces the (112) texture. The resulting Co films are highly oriented and represent a wonderful opportunity for the study of anisotropy energy. Figure 9 shows the nearly ideal easy and hard axes loops where the calculated data points were derived from measured torque curves.

CONCLUSIONS

In this paper we have presented a brief summary of the magnetic recording physics issues that motivate better crystalline quality, texture, and orientation of thin film hard disk media of the future. Arguments concerning the postponement of reaching thermal stability limits to magnetic data retention were given to justify the need for achieving a singly oriented media. We then gave a summary of new methods of achieving highly oriented magnetic materials via epitaxial growth on single crystal silicon.

The results presented represent knowledge accumulated from many years of effort by students, staff, and faculty involved with media development at Carnegie Mellon University, as well as discussions with many other friends and colleagues. Much of the work described was supported in part by the Department of Energy (DE-FG02-90ER45423), the National Science Foundation (ECD 89-07068), or via grants from IBM, Intevac, and Seagate.

REFERENCES:

1. P. Lu and S. H. Charap, IEEE Trans. Magn. **30**, 4230 (1994).
2. W. Yang and D. N. Lambeth, IEEE Trans. Magn. **33** (5), 2965 (1997).
3. J. Daval and D. Randet, IEEE Trans. Magn., **6** 768 (1970).
4. Y. C. Feng, D. E. Laughlin and D. N. Lambeth, J. Appl. Phys., **76** (11), 7311-7316 (1994).
5. D. E. Laughlin, B.-K. Cheong, Y. C. Feng, D. N. Lambeth, L.-L. Lee and B. Wong, Scripta Metallurgica et Materialia, **33** (10/11), 1525-1536 (1995).
6. L.-L. Lee, D. E. Laughlin, L. Fang, and D. N. Lambeth, IEEE Trans. Magn., **30**, 3951 (1994).
7. L.-L. Lee, D. E. Laughlin, L. Fang, and D. N. Lambeth, IEEE Trans. Magn., **31**, 2728 (1995).
8. W. Yang, D. N. Lambeth, L. Tang, and D. E. Laughlin, J. Appl. Phys., **81** 4370 (1997).

IN-PLANE ANISOTROPY IN CoCr(Ta,Pt)/Cr FILMS DEPOSITED ONTO SUBSTRATES WITH CONTROLLED TOPOGRAPHY

D.J. Twisselmann[1], B.T. Adekor[1], M. Farhoud[2], Henry I. Smith[2], P.C. Dorsey[3] and C.A. Ross[1]*
[1]Department of Materials Science and Engineering, Massachusetts Institute of Technology, Cambridge, MA 02139 (*caross@mit.edu)
[2]Department of Electrical Engineering and Computer Science, Massachusetts Institute of Technology, Cambridge, MA 02139
[3]Komag Inc, 1704 Automation Parkway, San Jose, CA 95131

ABSTRACT

In-plane magnetic anisotropy can be induced in Cr-underlayer/Co-alloy thin films by grooves or scratches in the substrate. To quantify this effect, silica substrates have been prepared with large areas of submicron grooves using interferometric lithography. The growth of Cr films and Cr/Co-alloy bilayer films on these substrates has been investigated, and in-plane magnetic anisotropy has been observed.

INTRODUCTION

Magnetic hard disks are commonly made by depositing a Cr underlayer and a Co-alloy magnetic layer onto a substrate made from nickel-phosphorus (NiP)-plated aluminum. The substrate is often roughened by mechanical abrasion to form a set of circumferential grooves or scratches, in order to reduce stiction between the recording head and the disk. The scratches are typically 20–50 nm deep and 100–500 nm apart. The presence of these scratches can create in-plane magnetic anisotropy in which the coercivity, squareness and remanence of the magnetic film are higher parallel to the scratches [1-18]. This effect can be significant. For example, the coercivity can be higher by a factor of 1.3–1.5 parallel to the scratches compared to the perpendicular direction.

The enhancement of squareness and coercivity parallel to the scratches can be useful, but its origin is not fully understood. It could be due to elongation [1-2] of the magnetic grains, to growth of chains of grains [3] parallel to the scratches, to in-plane strain differences [4-10], to preferential alignment of the cobalt c-axes along the scratches [10-14], or to differences in magnetic interactions between the two in-plane directions [14-16]. One difficulty in analysing how these scratches can create such a large magnetic effect is that hard-disk substrates contain a range of surface features with various heights and surface profiles. This makes it difficult to ascertain which features of the film microstructure contribute to the magnetic anisotropy.

The object of this research is to deposit magnetic films onto substrates with controlled topographic features in order to quantify the variation of the magnetic film properties as a function of surface profile, peak-to-valley height and spatial frequency. To measure magnetic properties such as hysteresis loops or magnetic anisotropy, relatively large areas of thin film are required, of the order of 0.5 cm^2. These areas need to be patterned with uniform features on a 100–200 nm scale. To pattern an area of this size using electron-beam lithography would be prohibitively slow and expensive. However, interferometric lithography provides a rapid, economical method of patterning wafer-sized areas with periodic structures on a scale of 100–200 nm and above.

Topographically-induced magnetic anisotropy has been observed in films in which the Cr layer has a (200) preferred orientation (crystallographic texture), so that the subsequent Co alloy layer grows epitaxially with $(11\bar{2}\ 0)$ texture [18]. This puts the Co-alloy c-axis, the magnetic easy axis, parallel to the film plane. This epitaxial relationship occurs when the Cr film is deposited at temperatures over about 200°C on an Al/NiP substrate. There is evidence [19-20] that the Cr (200) texture can also be obtained on silicon substrates at elevated temperatures, so oxidized silicon was chosen as a suitable substrate for these experiments. In this article, we will describe the fabrication

Mat. Res. Soc. Symp. Proc. Vol. 517 © 1998 Materials Research Society

of oxidized silicon substrates with periodic grooves, compare the growth of Cr/Co-alloy films on oxidized silicon with growth on Al/NiP hard-disk substrates, and describe topographically-induced magnetic anisotropy on grooved silica substrates.

EXPERIMENTAL METHODS

Fabrication of grooved substrates

Substrates were made from 10 cm-diameter (100) silicon wafers initially coated with 100 nm thick thermal oxide. The substrates were patterned using interferometric lithography, in which the standing wave formed by the intersection of two laser beams is used to expose a resist layer on a substrate with a periodic pattern of fringes [21-24]. Fig. 1 illustrates the interferometric lithography apparatus. The 351-nm argon-ion laser wavelength interferometric lithography (IL) system, Fig. 1(a), was used to produce structures with a 200 nm-period and greater. The period of the fringes is equal to $\lambda/(2\sin\theta)$, where λ is the laser wavelength and 2θ the angle of intersection of the laser beams. For this system, the thermally oxidized wafers were coated with a trilayer stack [21] consisting of 250 nm Brewer anti-reflective coating (ARC), a 40 nm electron-beam evaporated silica etch mask, then 200 nm of a positive resist, Sumitomo PFI-34. Substrates were exposed for periods of typically 30 s using a 1W laser beam that diverged from the spatial filters shown in Fig. 1(a) to illuminate the substrate. After development, the pattern was transferred through the silica and the ARC by using reactive ion etching. This produced a grating of silica/ARC on the substrate which is used as an etch mask. These steps are shown in Fig. 2.

For making finer structures, an achromatic interferometric lithography (AIL) system was used, Fig. 1(b). In this system the period of the exposed pattern is given by half the period of the parent phase gratings. The phase gratings were made using the IL system and have periods of 200 nm, hence the AIL system produced 100 nm period structures. A 193 nm pulsed ArF excimer laser was used with exposure times of a few minutes or less, resulting in an exposed area on the substrate of 3 x 3 cm. The trilayer stack in these samples consisted of 240 nm ARC/ 50 nm silica/ 100 nm PMMA (polymethyl methacrylate) resist. The AIL system has been used to produce the finest interferometric lithography structures reported to date [22].

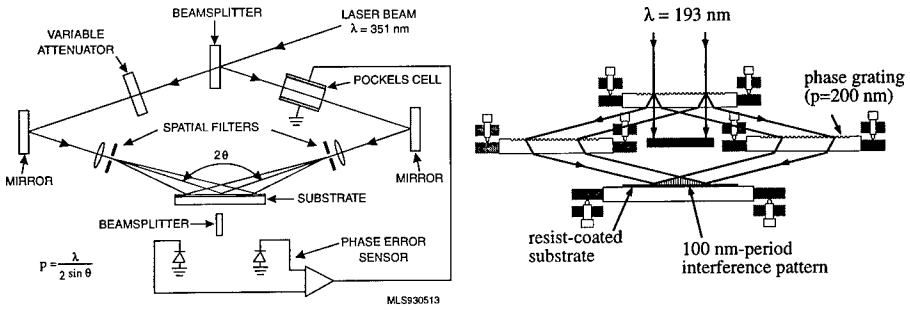

Fig. 1. (a) left: Interferometric lithography system. A 351 nm laser beam is split, reflected at two mirrors, and allowed to interfere at a substrate to create a set of fringes that expose the photoresist with a grating pattern of period p, typically set to 200 nm. The Pockels cell ensures stable fringe positioning during the exposure, and the attenuator is used to obtain identical intensity in the two beams. (b) right: Achromatic interferometric lithography system. A 193 nm laser beam is passed through a grating, and the first order diffracted beams are subsequently diffracted by a pair of phase gratings, and recombined on the substrate to form a fringe pattern. The period of the fringe pattern is half the period of the parent phase gratings. This system is used to produce 100 nm-period patterns from 200 nm-period phase gratings.

To etch grooves into the silica, reactive ion etching in CHF_3 was used. This also removed the silica etch mask above the ARC. The final process step was removal of the mask using an "RCA" ($H_2O_2/NH_4OH/H_2O$) cleaning process. Groove depths in the range of 10–40 nm have been made. The profile of the grooves as etched resembled a square-wave. Smoother profiles were produced by immersion of the grating in NaOH (10% by weight in H_2O at 59°C for 30 min).

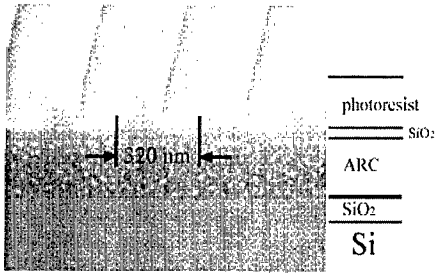

(a) Expose/develop resist

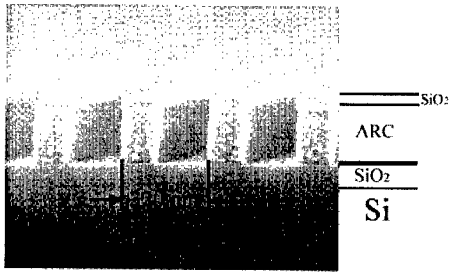

(b) Reactive ion etch with CHF_3 then O_2/He

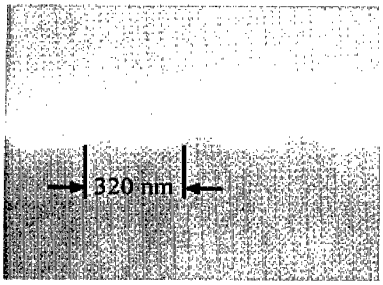

(c) Reactive ion etch CHF_3 then RCA clean

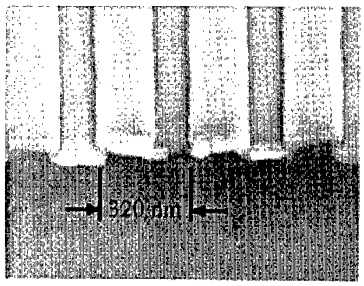

(d) Substrate in (c) with Cr/CoCrPt sputtered film

Fig. 2. (a-c) SEM images of the fabrication method for patterned substrates and (d) a substrate with 40 nm-high steps, after sputtering

As an illustration of this capability, Fig. 3 shows a comparison between a commercial hard-disk substrate and a substrate patterned with 100 nm-period grooves made by AIL.

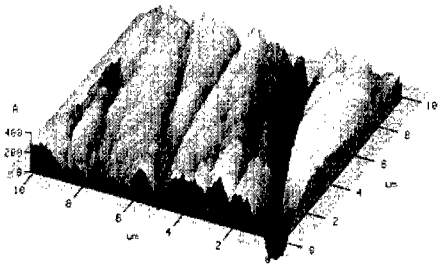

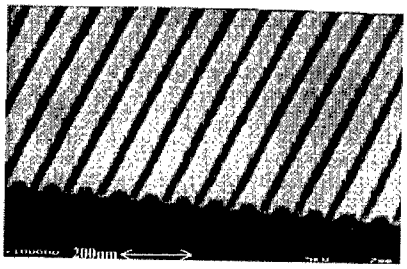

Fig. 3. (a) left: Atomic force micrograph of a commercial hard-disk substrate showing scratches with a distribution of heights, depths and surface profiles. Note that the vertical scale is exaggerated. (b) right: Electron micrograph of a silicon substrate showing 100-nm period grooves with 40 nm depth.

Growth of magnetic films

The substrates used in these experiments included commercial Al/NiP hard disk substrates, both superpolished and mechanically grooved, smooth silicon with a native oxide layer, thermally oxidized silicon with lithographically-defined grooves, and silicon with grooves formed by abrasion with a fine grit sandpaper. Films were deposited by r.f. magnetron and d.c. magnetron sputtering in two separate sputter systems. The r.f. system had three 5 cm-diameter targets, and operated with a base pressure of 10^{-7} torr and deposition rates of up to 0.5 nm/s. Substrates were mounted onto a copper block facing downwards towards the sputter sources, and heated by conduction. The sputter flux was controlled by shutters, so bilayer films could be deposited with less than 1 s time delay between the two layers. Targets were pure Cr (99.999%), Co-10at%Cr-6at%Ta and Co-22at%Cr-12at%Pt. The d.c. system was a commercial hard-disk sputter system with a base pressure of at best 10^{-8} torr. Substrates were heated using quartz lamps, and sputter rates were 5–10 nm/s. Each pair of 13 cm-diameter sputter targets occupied its own process chamber with independently controlled gas pressure, sputter power and substrate bias. Hard-disk substrates were held at the edges and placed vertically between the pair of parallel targets, so that both sides of the substrate were sputtered simultaneously. Because the substrates were held vertically, the silicon pieces had to be attached to the hard disk substrates using adhesive in order to sputter them. A Co-20at%Cr-8at%Pt alloy target was used in this system.

Crystallographic textures of the films were determined using θ–2θ x-ray diffraction (XRD) with copper Kα radiation. The (100)-silicon substrates produced a strong peak at 69° 2θ as well as smaller peaks from other wavelengths such as tungsten Lα. Magnetic hysteresis loops were measured using a vibrating sample magnetometer (VSM).

RESULTS AND DISCUSSION

Comparison of film growth on oxidized silicon and NiP

Films of Cr were grown on oxidized silicon and Al/NiP hard-disk substrates at a range of substrate temperatures and sputter conditions to determine the conditions under which the (200) Cr texture could be obtained. The texture was characterized by the peak ratios of the Cr (110) and (200) peaks. The Powder Diffraction File (PDF) predicts a value of 16% for the (200)/(110) intensity ratio for a random polycrystal sample of Cr. Fig. 4(a) shows x-ray data from Cr films grown on smooth Si and smooth NiP by r.f. magnetron sputtering at 3 mTorr and 0.5 nm/s. On the NiP substrate, the Cr grew with a (110) texture at ambient temperature but a strong (200) texture was observed above 200°C. For the oxidized Si substrate, a similar trend was observed but the (200) texture was less pronounced than on the NiP substrate.

The CoCrPt films grew on (200) Cr with a (11$\bar{2}$0) texture. The Co (11$\bar{2}$0) peak intensity was found to correlate with the Cr (200) intensity as shown in Fig. 4(b) for r.f. magnetron films sputtered at 3 mTorr and 0.5 nm/s. From atomic force microscope images, grain size was similar on the two substrates for both Cr film samples and Cr/Co-alloy film samples.

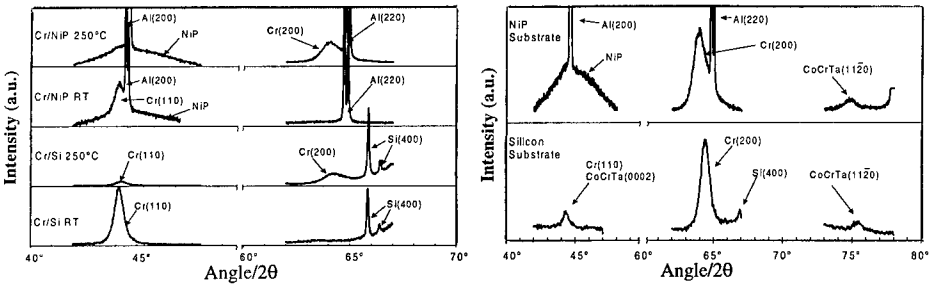

Fig. 4 (a) left: x-ray scans from Cr films grown on smooth NiP and Si. (b) right: x-ray data from Cr/CoCrTa bilayers at 250°C on smooth NiP and silicon. (RT = room temperature)

Magnetic Properties

DC Magnetron sputtered films

Figure 5 shows hysteresis loops for $CoCr_{20}Pt_8/Cr$ grown at 260°C on two grooved Si substrates with periods of 320 nm and step heights of 20 nm and 40 nm, compared to the hysteresis loops for films deposited onto smooth NiP under the same conditions. The grooved Si clearly shows in-plane anisotropy. Magnetic data are given in Table 1. An electron micrograph of the sample with 40 nm groove heights is shown in Figure 2(d).

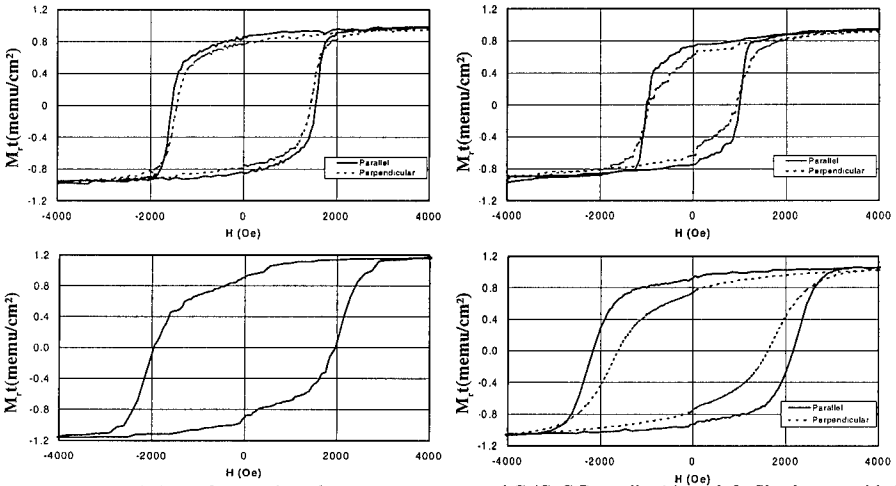

Fig. 5. Hysteresis loops from various d.c. magnetron sputtered Cr/CoCrPt media. (a) top left: Si substrate with 320 nm period, 20 nm high steps, (b) top right: Si substrate with 320 nm period, 40nm high steps, (c) bottom left: smooth NiP, (d) bottom right: textured NiP. For (a,b,d), loops are shown parallel (solid) and perpendicular (dotted) to the grooves.

	Parallel to grooves				Perpendicular to grooves				OR	
Substrate	H_c	M_rt	Sq	S*	H_c	M_rt	Sq	S*	H_c	M_rt
Si 20nm	1542	0.862	0.763	0.881	1432	0.762	0.685	0.856	1.08	1.13
Si 40nm	998	0.740	0.690	0.834	939	0.612	0.508	0.773	1.06	1.21
NiP smooth	1963	0.904	0.775	0.727						
NiP textured	2151	0.916	0.796	0.773	1604	0.739	0.638	0.612	1.34	1.24

Table 1. Coercivity H_c (Oe), Remanence-thickness product M_rt (memu/cm^2), Squareness (M_r/M_s), and S* values for d.c. magnetron sputtered CoCrPt on various substrates. The last two columns show orientation ratio (OR) which is the ratio of coercivity or M_rt parallel vs. perpendicular to the grooves.

Although all samples were deposited under similar conditions, the absolute coercivities for the silicon pieces were lower than for the NiP. We believe this was partly due to outgassing by the adhesive used to bond the silicon to a disk substrate in order to transport it through the sputter system.

RF Magnetron sputtered films

Hysteresis loops from CoCrTa films sputtered by r.f. magnetron onto silicon and NiP substrates were similar to those shown in Fig 5, but with lower coercivity. In these experiments, Si and NiP were each grooved by abrasion with fine sandpaper. The coercivity orientation ratios were 1.19 for the grooved Si and 1.44 for grooved NiP, for films sputtered at 250°C, 3 mTorr, and 0.5 nm/s. Work is underway with lithographically-defined substrates in this system. Samples

were mechanically clamped during sputtering, avoiding contamination from adhesive, and it was found that films grown on silica and NiP have similar coercivities.

CONCLUSIONS

A method has been demonstrated for making oxidized silica substrates with controlled grooved topographies over large areas using interferometric lithography. The structures can be made with periods of 100–300 nm and peak-to-valley heights of 10–40 nm, and the profiles can be controlled between sharply and smoothly varying. These substrates provide model structures for the study of the topographically-induced in-plane magnetic anisotropy observed in Cr(200)/Co-alloy $(11\bar{2}\,0)$ bilayer films. (200)-textured Cr films can be grown on silica above 200°C, and $(11\bar{2}0)$ Co-alloy grows on the (200) Cr. CoCrTa/Cr and CoCrPt/Cr films deposited by both d.c. magnetron sputtering in a production hard disk system and r.f. magnetron sputtering in a smaller, batch system demonstrate in-plane magnetic anisotropy on grooved silica substrates. Work is underway to quantify the microstructural contributions to this anisotropy.

ACKNOWLEDGEMENTS

The support of MIT's Department of Materials Science and Engineering is acknowledged. We thank Steven Spector of Komag for d.c. magnetron sputter deposition. B.T. Adekore was supported through the MIT Materials Processing Center Summer Scholars Program.

REFERENCES

1 W.G. Haines, J. Appl. Phys. 61 p3497 (1987).
2 E.M. Simpson, P.B.Narayan, G.T.K.Swami and J.L.Chao, IEEE Trans. Magn. 23 p3405 (1987).
3 M.R. Kim, S. Guruswamy and K.E. Johnson, J. Appl. Phys. 74 p4643 (1993).
4 R. Nishikawa, T. Hikosaka, K. Igarashi and M. Kanamaru, IEEE Trans. Magn. 25 p890 (1989).
5 M.F. Doerner, P.W. Wang, S.M. Mirzamaani, D.S. Parker and A.C. Wall, Proc. Mater. Res. Soc. 232 p27 (1991).
6 A. Kawamoto and F. Hikami, J. Appl. Phys. 69 p5151 (1991).
7 J.A. Bain, B.M. Clemens, S.M. Brennan and H. Kataoka, IEEE Trans. Magn. 29 p300 (1993).
8 K.E. Johnson, M. Mirzamaani and M.F. Doerner, IEEE Trans. Magn. 31 p2721 (1995).
9 C.A. Ross, M.E. Schabes, R. Ranjan, G. Bertero and T. Chen, J. Appl. Phys. 79 p5342 (1996).
10 T. Hirose, H. Teranishi, M. Ohsawa, A. Ueda, O. Ishiwata, T. Ataka, K. Ozawa, S. Komiya and A. Iida, IEEE Trans. Magn. 33 p2971 (1997).
11 T. Ohno, Y. Shiroishi, S. Hishiyama and Y. Matsuda, IEEE. Trans. Magn. 23 p2809 (1987).
12 H. Kataoka, J.A. Bain, S.M. Brennan and B.M. Clemens, J. Appl. Phys. 73 p7591 (1993).
13 T.P. Nolan, Ph.D. thesis, Dept. Materials Science and Engineering, Stanford University (1994).
14 Y. Zhao and H.N. Bertram, J. Appl. Phys. 77 p6411 (1995).
15 J. Miles and J. Middleton, IEEE Trans. Magn. 31 p2770 (1995).
16 M.P. Morales, K. O'Grady, B. Zhang, W.R. Bennett and G.C. Rauch, IEEE Trans. Magn. 32 p3595 (1996).
17 E. Teng and N. Ballard, IEEE Trans. Magn. 22 p579 (1986).
18 M. Mirzamaani, K.E. Johnson, D. Edmonson, P. Ivett and M. Russak, J. Appl. Phys. 67 p4695 (1990).
19 T. Kawanabe, J.G. Park and M. Naoe, Mat. Sci. Eng. A134 p1305 (1991).
20 T. Kawanabe, J.G. Park and M. Naoe, IEEE Trans. Magn. 27 p5031 (1991).
21 M.L. Schattenburg, R.J. Aucoin and R.C. Fleming. J. Vac. Sci. Tech. B13 p3007 (1995).
22 T.A. Savas, M.L. Schattenburg, J.M. Carter and H.I. Smith, J. Vac. Sci. Tec. B14 p4167 (1996).
23 H.I. Smith, "Submicron and Nanometer Structures Technology", Nanostructures Press, Sudbury MA (1994).
24 M. Farhoud, M. Hwang, H.I. Smith, J.M. Bae, K. Youcef-Toumi and C.A. Ross, *in press, IEEE Trans. Magn. (1998).*

EFFECTS OF SPUTTERING CONDITIONS ON TEXTURE , MICROSTRUCTURE AND MAGNETIC PROPERTIES OF THE CoCrPt / NiAl THIN FILMS

Y.-N. HSU*, D. E. LAUGHLIN* and D. N. LAMBETH**
*Department of Materials Science and Engineering, Data Storage Systems Center,
**Department of Electrical and Computer Engineering, Data Storage Systems Center,
Carnegie Mellon University, Pittsburgh, PA 15213

ABSTRACT

The effects of sputtering argon pressures and sputtering power on the microstructure, texture and magnetic properties of NiAl underlayers on CoCrPt films were investigated. In this paper, the relationship between the sputtering conditions, microstructure, crystallographic texture and magnetic properties of these thin films will be discussed. By controlling the sputtering pressure and sputtering power, the texture and microstructure of NiAl underlayers were found to vary. This in turn was found to influence the magnetic properties of CoCrPt thin films. It was found that 10 mtorr is the optimum pressure to deposit the NiAl thin films to obtain the best magnetic properties for our system. At this argon pressure, the coercivity reached a maximum value because of the strongest CoCrPt ($10\bar{1}0$) texture and smallest grain size. At lower argon pressures (< 10 mtorr), NiAl tended to have a (110) texture reducing the CoCrPt ($10\bar{1}0$) texture, which in turn reduced the CoCrPt coercivity and S*. Also, high NiAl deposition pressures (>30 mtorr) yielded larger grains and a weaker CoCrPt ($10\bar{1}0$) texture, thereby decreasing the coercivity of the CoCrPt films. Increasing the sputtering power has been found to increase the CoCrPt coercivity and S* value. However, the grain sizes of the CoCrPt/NiAl thin films deposited at higher sputtering power were larger than those obtained at lower sputtering power.

INTRODUCTION

To achieve high density longitudinal recording, hcp Co-based thin films with their c-axis lying in the plane of the film are needed as well as small and magnetically isolated grains[1-5]. Compared to the traditional Cr underlayer, the new B2 underlayer was found to possess not only the unique (112) texture but also very small grains (15 nm) [6,7]. The B2 (112) texture can induce the CoCrPt ($10\bar{1}0$) texture with the c-axis to lie in the plane of the thin film. This unicrystalline CoCrPt caused by the ($10\bar{1}0$) texture is believed to have higher coercivity than the bicrystal resulting from the CoCrPt ($11\bar{2}0$) texture. At the same time, the smaller grain size of the B2 underlayer can effectively reduce the media noise. Also, these textures and microstructural features, that strongly affect the magnetic properties, can be further improved by changes in the deposition process. In this paper, we will focus on the effects of the deposition conditions on one of the B2 underlayer samples, NiAl underlayers. The emphasises of this research are to investigate (1) the effects of the argon pressure and sputtering power of the NiAl underlayers on the crystallography texture and microstructure (2) the correlation of the magnetic properties of the CoCrPt films with the crystallographic texture and microstructure (3) optimization of the magnetic properties by controlling the argon pressure and sputtering power of the NiAl underlayers.

Mat. Res. Soc. Symp. Proc. Vol. 517 © 1998 Materials Research Society

EXPERIMENT

The CoCrPt / NiAl thin films were deposited on glass substrates by RF diode sputtering in an LH Z-400 system. The base pressure was $5x10^{-7}$ mtorr. The target diameter is about 75 mm. The NiAl underlayers were deposited at various pressures and sputtering powers at room temperature without applying substrate bias voltage. The CoCrPt films were deposited at room temperature with a fixed argon pressure of 10 mtorr, RF power of 2.3 W/cm^2 and -100 V substrate bias voltage. The thickness of the NiAl and CoCrPt films were fixed at 100 nm and 40 nm, respectively. However, because the B2 (112) texture was more observable only in the x-ray spectrum of the thicker B2 films, NiAl films were also deposited to thicknesses of 400nm while varying the same sputtering parameters, i.e., argon pressures and sputtering powers. Characterization of CoCrPt / NiAl thin films was carried out using the Rigaku X-ray diffractometer with Cu Kα radiation to determine texture, Philips EM 420T transmission electron microscope (TEM) to observe microstructure and VSM with fields up to 10 kOe to measure magnetic properties.

RESULTS AND DISCUSSION

I. ARGON PRESSURE EFFECTS

The TEM plane-view bright field images and diffraction patterns of 100-nm thick NiAl deposited at 5 mtorr, 10 mtorr and 30 mtorr are shown in Fig. 1a, Fig. 1b and Fig. 1c, respectively. All figures show that the NiAl films have the B2 structure in spite of the different argon pressures. At 30 mtorr, the 100-nm thick NiAl film grain size is 17 nm, which is larger than that obtained when the pressures were 10 and 5 mtorr (13 nm). The TEM bright field images of 30 mtorr sample show voids are present at the grain boundaries. From Fig. 1a and Fig. 1b, it can be seen that NiAl films deposited at 5 and 10 mtorr have a more uniform and dense microstructure.

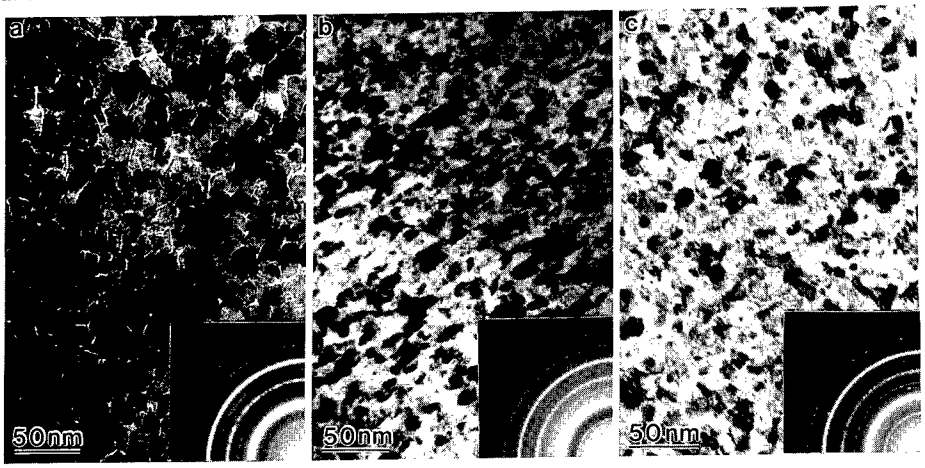

Fig. 1 TEM bright field images and the corresponding electron diffraction patterns of the 100 nm NiAl films deposited at (a) 30 mtorr (b) 10 mtorr (c) 5 mtorr.

The x-ray diffraction spectra shown in Fig. 2a reveal the texture evolution of the 100-nm thick NiAl films deposited at varying argon pressures. The peak intensity of the NiAl (110) reflection decreases with the argon pressure. No obvious NiAl (112) peak is observed at the 100 nm thickness. Fig. 2b shows the x-ray spectra of the 400-nm thick NiAl thin films. The NiAl (112) texture is strongest at the argon pressure of 10 mtorr. The NiAl thin films were (110) and (112) oriented at lower pressures. However, the NiAl texture changed to (001) at argon pressures higher than 20 mtorr. Fig. 2c is the x-ray diffraction spectra of the CoCrPt/NiAl thin films. The intensity of the CoCrPt $(10\bar{1}0)$ peak is strongest at 10 mtorr. At pressures lower than 10 mtorr, the NiAl (110) texture dominates, so that the CoCrPt $(10\bar{1}0)$ peak is very weak. Due to the NiAl (001) texture, no CoCrPt $(10\bar{1}0)$ texture is induced at higher argon pressures. Thus, our optimum argon pressure for the NiAl / CoCrPt films is 10 mtorr.

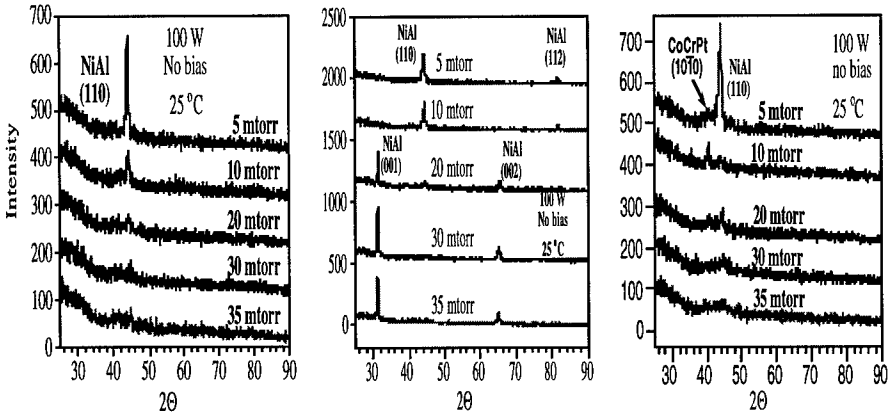

Fig. 2 X-ray diffraction spectra of (a) 100 nm NiAl films(b) 400 nm NiAl films (c) (40nm) CoCrPt / (100nm) NiAl films on glass substrates deposited at various argon pressures.

Fig. 3 shows the coercivity and coercive squareness of the CoCrPt films on the NiAl underlayer deposited at various argon pressures. The coercivity and squareness are also the highest at 10 mtorr. This appears to be because the CoCrPt $(10\bar{1}0)$ texture is the strongest at 10 mtorr where the CoCrPt has the smallest and most uniform grains.

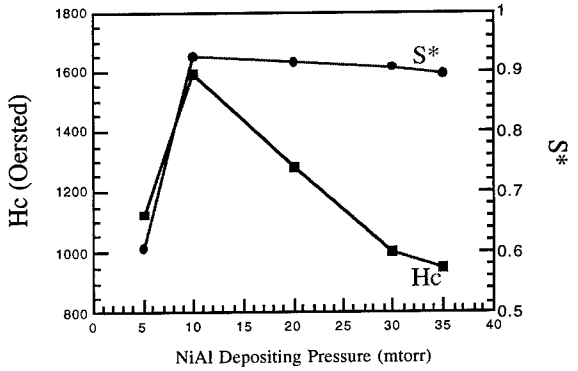

Fig. 3 In-plane coercivity and squareness of the 40 nm CoCrPt films on the 100 nm NiAl underlayers deposited at various argon pressures.

II. SPUTTERING POWER EFFECTS

The TEM bright field image (Fig. 4) shows that the NiAl deposited at 300 W has a larger grain size (16 nm) than those deposited at 100 W and 25 W (13 nm). The NiAl thin films deposited at 300 W and 25 W both have uniform and dense microstructure.

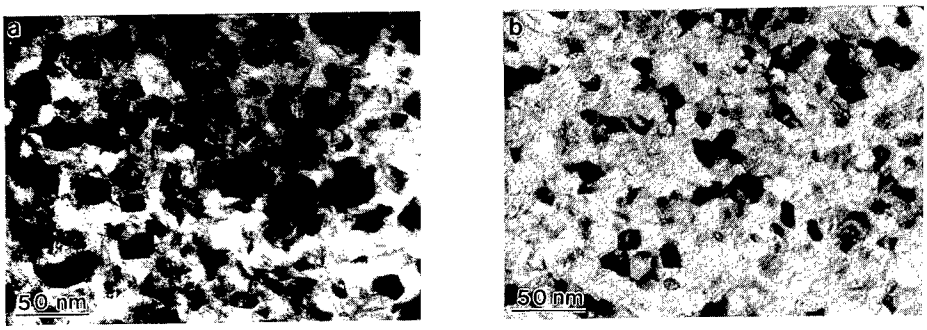

Fig. 4 TEM bright field image and the corresponding electron diffraction pattern of the 100 nm NiAl films deposited at (a) 300 W (b) 25 W.

The X-ray spectra of the 100 nm NiAl films in Fig. 5a shows a weakening NiAl (110) texture with decreasing sputtering powers. No NiAl (112) peak was observed at the thickness of 100 nm. The NiAl (112) peak intensity is seen unchanged as a function of deposition pressure in the 400 nm NiAl films (Fig. 5b). The intensity ratio of the NiAl (112) peak over the (110) peak is 0.3. The NiAl thin films at 25 W is (112) textured as the ratio is approximately 1. On the other hand, at 300 W the NiAl is more (110) textured as the ratio is approximately 0.1. The CoCrPt $(10\bar{1}0)$ peak intensity is shown to slightly increases with the sputtering powers in Fig 5c.

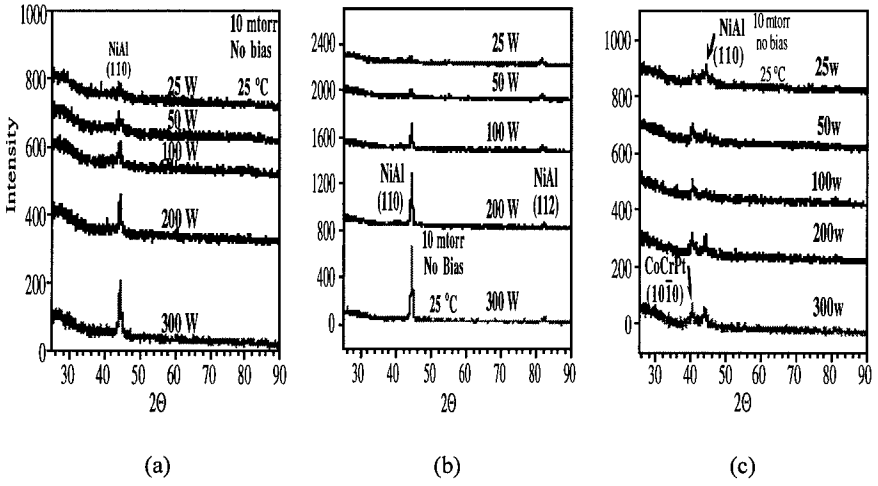

Fig. 5 X-ray diffraction spectra of the (a) 100 nm NiAl film (b) 400 nm NiAl films (c) (40 nm) CoCrPt / (100 nm) NiAl films on glass substrates deposited at various sputtering powers.

The coercivity of the CoCrPt thin films appears to increase with the sputtering power in Fig. 6. This can be explained since the CoCrPt (10$\bar{1}$0) peak intensity increases with the sputtering power. From Fig. 6, it is seen that the coercive squareness (S*) has a maximum value at the sputtering power of 100 W.

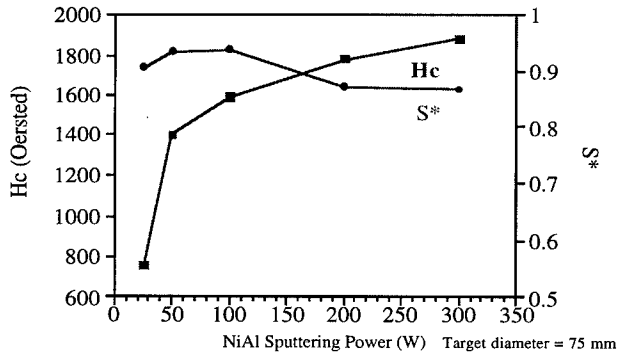

Fig. 6 In-plane coercivity and squareness of the 40 nm CoCrPt films on the 100 nm NiAl underlayers deposited at various sputtering powers.

CONCLUSION

From this study, it can be concluded that the texture and microstructure are strongly affected by the deposition conditions. The magnetic properties can be significantly influenced by controlling the deposition conditions. The coercivity of the CoCrPt films increases with the sputtering power. The coercivity is also optimized when the intensity of the CoCrPt $(10\bar{1}0)$ peak is the strongest. For our system the optimum argon deposition pressure is 10 mtorr for the CoCrPt / NiAl films. This is because the coercivity and squareness are the highest when not only the best CoCrPt $(10\bar{1}0)$ texture but also the smallest and most uniform grains are obtained at this pressure.

ACKNOWLEDGMENTS

The government has certain rights to this materials. This research is supported by the Data Storage Systems Center at CMU under a grant from NSF (ECD-89-07068).

REFERENCES

1. S.Iwasaki, K. Ouchi and H. Honda, IEEE Trans. Mag. 16, p.1111 (1987).
2. D. J. Rogers, J. N. Chapman, J.P.C. Bemards and S. B. Luitjens, IEEE Trans. Mag. 25, p.4180 (1989)
3. K. E. Johnson, Proceedings of the Second International Symposium on Magnetic Materials, Process, and Devices of the Electrochemical Society 92-10, p.27 (1991)
4. T. Lin and t. Yamashita, IEEE Trans. Mag. 24, p.2700 (1988)
5. T. Yogi, C. Tsang, T. A. Nguyen, K. Ju, G. L. Gorman and G. Castillo, IEEE Trans. Mag. 26, p.2271 (1990)
6. L.-L. Lee, D. E. Laughlin and D. N. Lambeth, IEEE Trans. Mag. 30, p.3951-3953 (1994)
7. L.-L.Lee, D. E. Laughlin and D. N. Lambeth, J. Appl. Phys. 81, p.4366-4368 (1997)

QUANTITATIVE MEASUREMENTS OF SEGREGATION IN Co-Cr-X MAGNETIC RECORDING MEDIA BY ENERGY-FILTERED TRANSMISSION ELECTRON MICROSCOPY

J. BENTLEY,* J.E. WITTIG,† and T.P. NOLAN‡
*Metals and Ceramics Division, Oak Ridge National Laboratory, PO Box 2008, Oak Ridge, TN 37831-6376, bentleyj@ornl.gov
†Vanderbilt University, Nashville, TN 37235
‡Komag Inc., 1704 Automation Parkway, San Jose, CA 95131

ABSTRACT

Reliable core-loss spectroscopic methods have been developed for mapping elemental segregation in Co-Cr-X magnetic recording media by energy-filtered transmission electron microscopy. Extraction of quantitative compositions at a spatial resolution approaching 1 nm involves sophisticated treatments for diffraction contrast, variations in specimen thickness, and closely-spaced oxygen K and chromium L_{23} ionization edges. These methods reveal that intergranular chromium levels are ~25 at.% for random-angle boundaries and ~15 at.% for 90° boundaries in films of $Co_{84}Cr_{12}Ta_4$ d.c. magnetron sputtered at 250°C.

INTRODUCTION

Microstructure-property-processing correlations can provide invaluable insight for the development of magnetic recording media with improved performance. High-resolution elemental distribution maps can be routinely produced from energy-filtered core-loss images obtained with commercial imaging energy-filters and slow-scan charge-coupled device (CCD) cameras on transmission electron microscopes (TEMs).[1] Following the early demonstration of Kimoto et al.[2] such energy-filtered transmission electron microscopy (EFTEM) methods have recently been used to characterize segregation effects, particularly Cr enrichment and Co depletion at grain boundaries and other defects, in CoCrTa/Cr magnetic recording media.[3] Thin-film Co-Cr-X media provide many challenges for EFTEM elemental mapping methods, including diffraction contrast, thickness gradients, and closely-spaced oxygen K and chromium L_{23} edges. Reliable methods for quantitative elemental mapping by EFTEM at ~1nm spatial resolution have been developed only recently and continue to be refined.[4] The goal of this work is to provide robust methods for measuring compositions of statistically significant numbers of grain boundaries for correlation with magnetic properties and materials processing.

EXPERIMENTAL

Results presented here are for a model material of ~60 nm of $Co_{84}Cr_{12}Ta_4$ on a 75 nm Cr underlayer which were d.c. magnetron sputtered onto a NiP-plated Al substrate pre-heated to 250°C. Specimens of other compositions and thinner layers (~30 nm) have also been studied. The Cr and $Co_{84}Cr_{12}Ta_4$ have <100> and <1120> textures, respectively, with edge-on (0001)//{011} giving the possibility of 90° grain boundaries in the media from the two variants on a single Cr grain. Back-thinned plan-view TEM specimens were prepared by standard dimpling and ion milling techniques.

Experiments were performed with a Gatan Imaging Filter (GIF™)[5] interfaced to a Philips CM30T TEM operated at 300 kV with a LaB_6 emitter, and DigitalMicrograph™ software on Macintosh computers, including some plug-in scripts developed at ORNL.[6] After extensive experimentation to optimize acquisition conditions (which involve trade-offs among chromatic-aberration-limited resolution, specimen drift, signal strength, and signal-to-background), gain-normalized images with 512 x 512 pixels (2× on-chip binning) were recorded under the following conditions: incident beam divergence α=2.9 mrad, collection half-angle β=4.8mrad, probe current >100 nA, TEM magnification ~4000×, CCD image pixel size ~0.6 nm, exposure times ~10 or 15s, and slit-widths (energy windows) Δ=30eV (for pre- and post-edge images). Zero-loss I_0 (Δ=10eV) and "total" intensity I_T (unfiltered, i.e., no slit) images were used to produce maps of t/λ

Mat. Res. Soc. Symp. Proc. Vol. 517 © 1998 Materials Research Society

$= \ln(I_T / I_0)$, where t is specimen thickness and λ is the total inelastic mean free path. Core-loss maps were produced by AE^{-r} background extrapolation from two pre-edge windows.[1,5] Jump-ratio images (post-edge divided by pre-edge) were also produced.[1,5] Specimens were carefully tilted to avoid strong diffraction contrast in as many grains as possible while keeping the grain boundaries as close to edge-on as possible.

RESULTS

The basic steps in generating elemental maps are illustrated in Fig. 1 for the Co L_{23} edge. The two pre-edge images are used to calculate fitting parameters for an AE^{-r} inverse power-law background at each pixel. The extrapolated background at the post-edge energy is subtracted from the post-edge image to yield the Co L_{23} net core-loss intensity (also known as Co signal or Co map). The post-edge image divided by a pre-edge image yields a jump-ratio image. Diffraction contrast, similar to that seen in low-loss images, is present in the pre- and post-edge images and persists in the net core-loss intensity image. The effects of diffraction contrast and thickness variations are largely cancelled out by the division process used to form jump-ratio images. For this reason jump-ratio images are useful for qualitative assessments of segregation effects. They are also useful for measuring grain size distributions. The intergranular Co depletion is clearly visible in the Co map and jump-ratio images. The width of the intergranular segregation is typically 3 to 4 nm. Even in these basic image processing operations, accurate image alignment is critical. Misregistry of only one pixel can cause severe black-white contrast effects, especially at steep contrast gradients, and can cause especially misleading contrast for thin layers of segregant when auto-scaling contrast is used to display images.

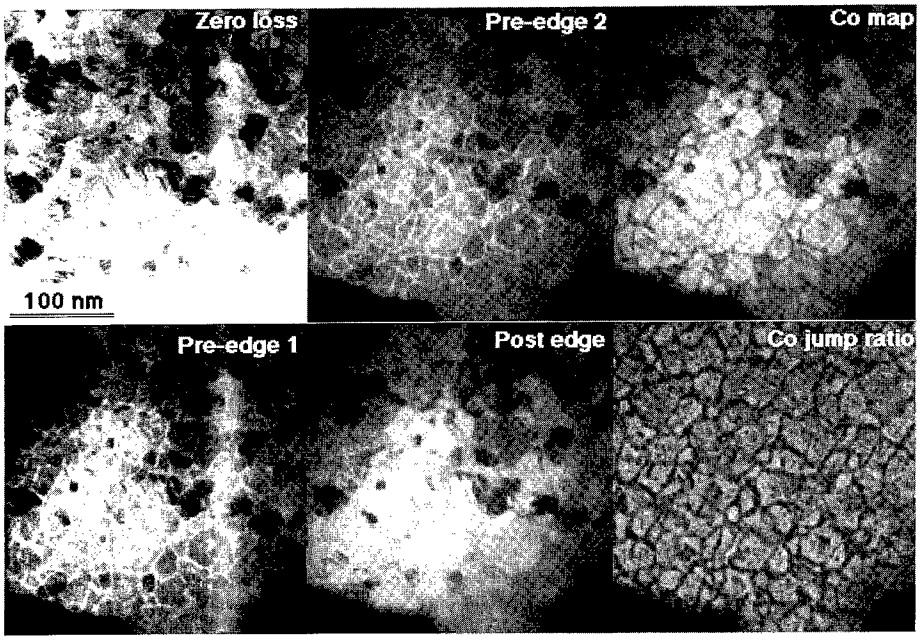

FIG. 1 Basic steps in generating CoL_{23} elemental maps. Subtraction from post-edge (794eV) of AE^{-r} background extrapolated from pre-edge 1 (730eV) and pre-edge 2 (760eV) yields the Co map. Note persistence of diffraction contrast (seen most clearly in the zero-loss image) in edge and map images. Post-edge divided by pre-edge 2 yields the Co jump-ratio image, where effects of thickness, diffraction contrast, and non-uniform incident intensity are largely cancelled out.

A complicating factor for the specimens in this work is the presence of a strong oxygen K edge, as shown in the electron energy-loss spectrum of Fig. 2, recorded from a ~200nm diameter region. The major source of the oxygen signal is a surface oxide film, not unexpectedly formed during specimen preparation. The O-K net core-loss intensity map is shown in Fig. 3, along with a map of oxygen atoms/area (see below). There is clearly enhanced oxygen at grain boundaries; whether this is oxygen segregated with Cr in the bulk of the film or just enhanced surface oxidation of the Cr-enriched regions is unknown at this time.

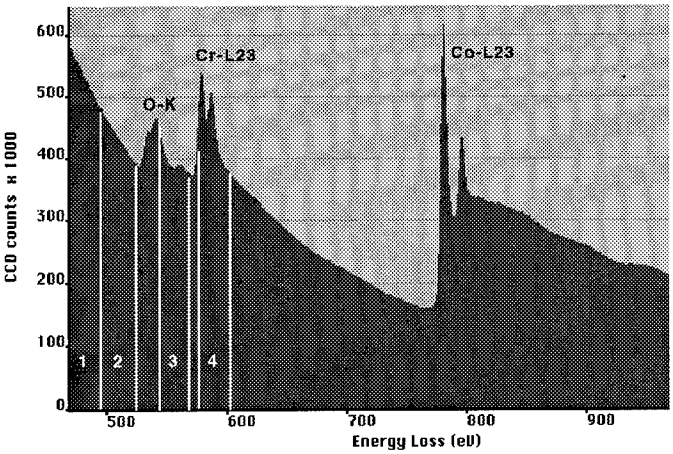

FIG.2 Electron energy-loss spectrum recorded from a ~200nm diameter region of Fig. 1 showing the presence of a strong oxygen K edge, due primarily to a surface oxide film. The approximate positions of the windows 1 to 4 for the 4-window mapping of Cr L_{23} are indicated.

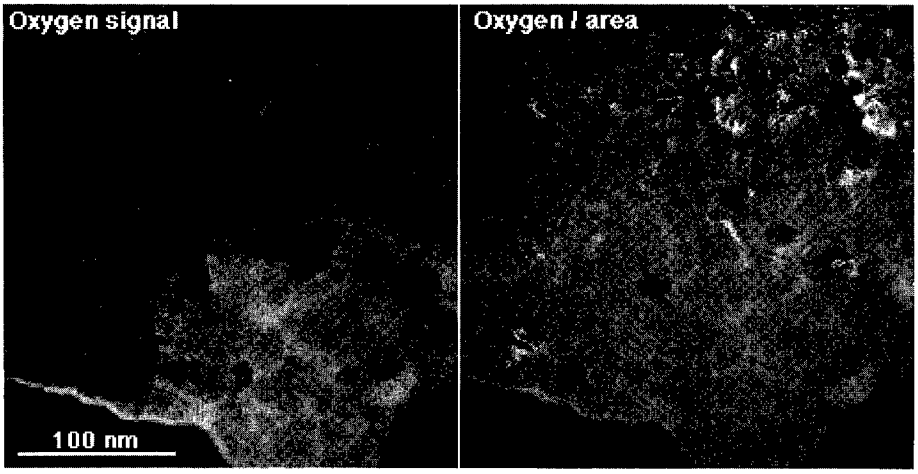

FIG. 3 Oxygen signal (net core-loss intensity) and oxygen areal density (oxygen atoms/area) images showing enhanced levels at grain boundaries. Strong contrast at top right is artifact from slight differences in diffraction contrast between low-loss image and core-loss image series.

The presence of oxygen is particularly troublesome for mapping the Cr L_{23} signal. Ignoring the presence of oxygen in conventional 3-window mapping with ~30eV windows will lead to an overestimate of the extrapolated background under the Cr L_{23} edge, and thus to an underestimate of the net Cr L_{23} intensity, to the extent that in regions of high oxygen signal and low Cr signal, negative Cr L_{23} intensities result. A 4-window method has been developed by Anderson et al.[7] for the similar situation with austenitic stainless steels. This method uses 2 pre-oxygen-edge windows to determine the exponent r for an AE^{-r} background, and the oxygen post-edge window to determine the value of the pre-exponential A for calculating the extrapolated background intensity for the Cr L_{23} post-edge window. The method assumes constant r over the limited energy-loss range of ~460 to 610 eV, which is easily verified from ln(I)-ln(E) plots. Constant r is found to be a good approximation for $t/\lambda<0.5$, but breaks down by $t/\lambda\sim1$. A DigitalMicrograph™ plug-in script has been written for the image processing procedure. Fig. 4 compares results from the inadequate 3-window method with the reliable 4-window method.

As mentioned above, the effects of diffraction contrast and thickness variations are largely cancelled out by the division process used to form jump-ratio images, but unfortunately persist in net core-loss intensity images that must be used for quantitative compositional information. Corrections for these effects may be necessary for a quantitative interpretation and can be implemented following the scheme used for energy-loss spectra.[8] Dividing the net core-loss intensity map by a low-loss image recorded with identical Δ and β (but inevitably much smaller exposure), yields an image with intensities proportional to atoms per unit area. Further normalization by t/λ compensates for variations in specimen thickness (assuming λ does not vary much with composition - a good approximation in this work) and yields an image with intensities proportional to concentration of atoms per unit volume. This scheme is illustrated in Fig. 5 for the Cr L_{23} map. Image alignment can be difficult but is again critical and can be helped by the use of custom scripts.[5] Strong diffraction contrast for some grains is difficult to avoid and can cause severe problems such as artifacts in t/λ maps. Worse still are changes in diffraction contrast in the low-loss images caused by foil buckling when the beam is spread to achieve managable exposure times.

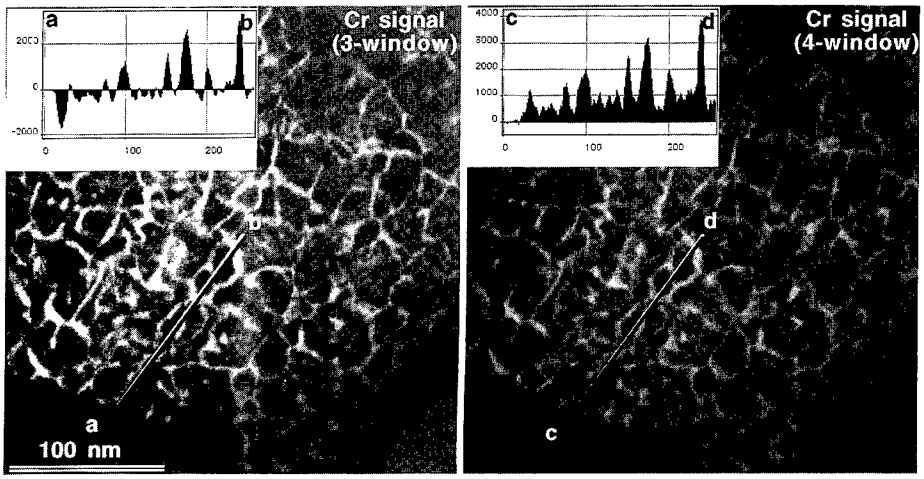

FIG. 4 Cr L_{23} signal (net core-loss intensity) images generated by conventional 3-window and improved 4-window method. The image intensities scale from -1500 (black) to 2500 (white) and from 0 (black) to 4000 (white), respectively. Inset profiles show inadequacy of 3-window method for Cr L_{23} in presence of oxygen edge.

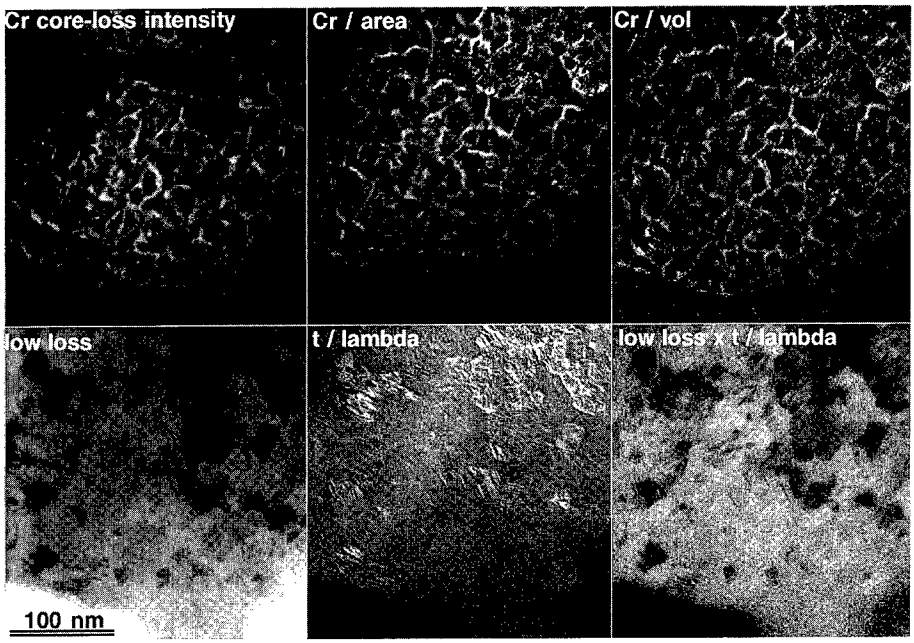

FIG. 5 Basic steps in generating Cr concentration maps. Cr L_{23} net core-loss intensity image divided by the low-loss image yields an image with intensities $\propto$ Cr atoms/area. Further division by t/λ map yields an image with intensities $\propto$ Cr atoms/volume. The correction function (low-loss $\times$ t/λ) is dominated by diffraction contrast.

The final processing step is to scale the mean intensities of an atoms/volume image to the mean composition determined by x-ray microanalysis or PEELS or, as in this work, to the nominal film composition (see Fig. 6). The local compositions of inter- or intragranular regions can then simply be read off such a map or profiles of it. Statistically significant numbers of grain boundaries may be measured from a single map. By also performing high-resolution lattice imaging of the same areas (possible in the same TEM) correlations between grain boundary character and segregation levels can be made. For example in Fig. 6, the boundaries marked x are 90° boundaries and show Cr levels ~15 at.%, whereas random high-angle boundaries marked y show Cr levels ~25 at.%. These results agree very well with nanoprobe x-ray microanalysis data from the same material.[9]

Extension of the EFTEM quantitative elemental mapping procedures to Ta and Pt, the distributions of which are also of interest for these media, is troublesome at the moment. The O_{23} edges have delayed maxima and occur at only 36 eV (Ta) and 52 eV (Pt) where there is overlap with multiple plasmon peaks and AE^{-r} background fits are invalid. The M_{45} edges at 1735 eV (Ta) and 2122 eV (Pt) give signals that are so weak that S/N (or drift) limits the spatial resolution.

CONCLUSIONS

Elemental mapping of Co-Cr-X based magnetic recording media at resolutions approaching 1 nm by energy-filtered transmission electron microscopy provides unmatched microstructural characterization information for correlation with magnetic properties and materials processing. Depletion of Co and enrichment of Cr at grain boundaries and intragranular defects has been measured quantitatively. Although the electron microscopy and subsequent image processing are demanding, quantitative segregation levels at a large number of boundaries are generated.

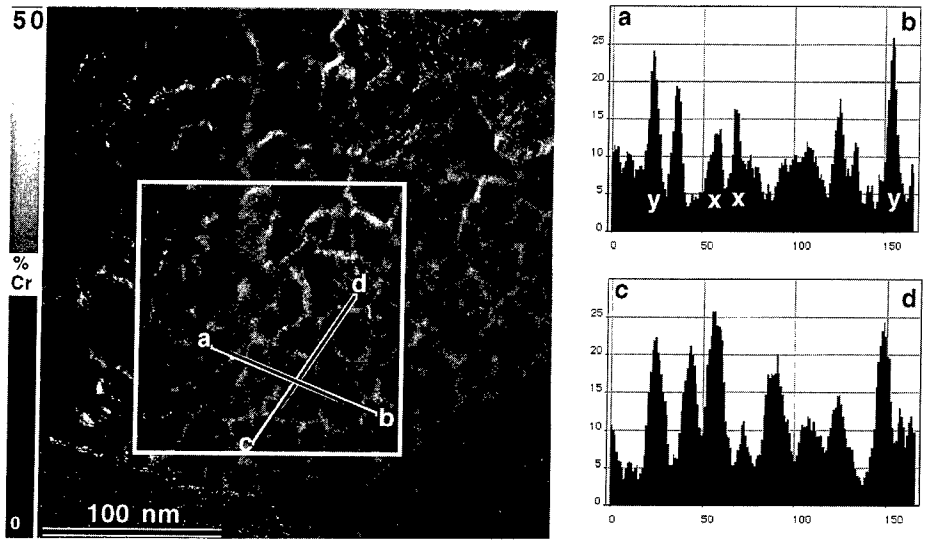

FIG. 6 Cr concentration map where intensities scale from 0 (black) to 50 at.% Cr (white), generated by scaling the mean intensity of boxed area to the nominal film composition of 12 at.%. In the profile along a-b, the maxima marked x correspond to 90° boundaries with 15 ± 2 at.% Cr, and the maxima marked y correspond to random high-angle boundaries with 25 ± 2 at.% Cr.

ACKNOWLEDGEMENTS

Research at the Oak Ridge National Laboratory (ORNL) SHaRE User Facility sponsored by the Division of Materials Sciences, U.S. Department of Energy, under contract DE-AC05-96OR22464 with Lockheed Martin Energy Research Corp., and and through the SHaRE Program under contract DE-AC05-76OR00033 with Oak Ridge Associated Universities. Support from the Vanderbilt University Research Council and Komag Inc. is gratefully acknowledged. Thanks to Drs. Ian Anderson and Neal Evans (ORNL) for useful discussions and help with image processing.

REFERENCES

1. A.J. Gubbens and O.L. Krivanek, *Ultramicroscopy* **51** (1993) 146.
2. K. Kimoto, Y. Yahisa, T. Hirano, K. Usami, and S. Narishige, *Jpn. J. Appl. Phys.* **34**, L352 (1995).
3. J.E. Wittig, T.P. Nolan, C.A. Ross, M.E. Schabes, K. Tang, R. Sinclair and J. Bentley, *IEEE Trans. Magn.*, in press.
4. J. Bentley, E.A. Kenik, K. Siangchaew and M. Libera, in *Proc. Microscopy & Microanalysis '96*, edited by G.W. Bailey et al. (San Francisco Press, San Francisco, 1996) p. 542.
5. O.L. Krivanek, A.J. Gubbens and N. Dellby, *Microsc. Microanal. Microstruct.* **2**, 315 (1991); O.L. Krivanek, A.J. Gubbens, N. Dellby and C.E. Meyer, *Microsc. Microanal. Microstruct.*. **3**, 187 (1992).
6. N.D. Evans and M.K. Kundmann, in *Proc. Microscopy & Microanalysis '96*, edited by G.W. Bailey et al. (San Francisco Press, San Francisco, 1996) p. 546.
7. I.M. Anderson, J. Bentley and J.R. Busby, submitted to *J. Microscopy*
8. J. Bentley, E.A. Kenik, N.D. Evans, E.L. Hall and S.J. Zinkle, in *Proc. EMAG95, Inst. Phys. Conf. Ser. No. **147***, edited by D. Cherns (IOP Publ., Bristol, 1995) p. 187.
9. J.E. Wittig, T.P. Nolan, R. Sinclair and J. Bentley, these proceedings.

CHROMIUM DISTRIBUTION IN CoCrTa/Cr LONGITUDINAL RECORDING MEDIA

J.E. Wittig*, T.P. Nolan**, R. Sinclair*** and J. Bentley****
*Vanderbilt University, Nashville TN 37235
**Komag Inc., 1704 Automation Parkway, San Jose CA 95131
***Stanford University, Palo Alto CA 94305
****ORNL, Oak Ridge TN 37831

ABSTRACT

The current study of $CoCr_{12}Ta_4$/Cr longitudinal recording media combines high resolution electron microscopy (HRTEM) with nanoprobe energy dispersive spectroscopy (EDS) and energy-filtered imaging (EFTEM) to correlate the Cr distribution with specific microstructural features. EFTEM images show Cr enrichment at grain boundaries, both random angle boundaries and 90° bicrystal boundaries. Cr segregation within grains is also observed in the elemental maps. This intragrain segregation often occurs at a series of defects that may define separately nucleated grains having 0° misorientation. Nanoprobe EDS measurements indicate that these defects contain localized concentrations of 25 to 30 % Cr. The random angle grain boundary Cr concentration occurs with a wide range, 19 to 36 at% (mean 22%) whereas the more crystallographically related 90° boundaries contain less Cr with less variation, 15 to 21 at% (mean 17% Cr). Composition profiles across grain boundaries using both nanoprobe EDS and EFTEM images show the full-width-half-maximum of the segregation to be approximately 4 nm, with Cr depleted regions next to the grain boundary having less than 7 at% Cr. The Ta concentration revealed no statistical evidence of segregation.

INTRODUCTION

Low noise longitudinal recording media must have small ferromagnetic grains isolated by nonmagnetic regions to block the magnetic exchange interaction. Cr segregation to grain boundaries is the most common mechanism for decoupling magnetic exchange between grains in the prevalent CoCrX/Cr thin film media. However, the actual Cr compositional microstructure and the diffusion mechanisms that produce it are not well understood. Correspondingly, the sputter deposition parameters and alloy compositions that give the desired amount of segregation to the desired places are not well known. Computer modeling and theoretical analysis of media magnetic properties and recording performance are similarly limited by lack of an appropriate structural model.

Reliable, better than 2 nm resolution analysis of chemical composition by transmission electron microscopy (TEM) is now available.[1,2] This allows compositional mapping, including quantitative assessments of composition in specific regions within ~10 nm grains, as well as at grain boundaries. Recent papers have demonstrated the application of this capability to study composition effects of sputtering parameters such as substrate temperature[3-5], target alloy composition[6-8] and vacuum condition.[9] These results are repeatable and are consistent with each other and with expected corresponding magnetic performance trends. More detailed analyses of the compositional microstructure are now possible. This capability can be used to further study the effects of these and other parameters such as substrate bias, and to test mechanisms for enhancing or hindering diffusion pathways. Development of improved structural models for simulation based upon this type of result is already underway.[8,10] Media models having grains with nonuniform magnetic anisotropy K_u[8] and different exchange interaction at bicrystal and random mis-orientation grain boundaries[10] have already been simulated. There is evidence that these structures are producing more realistic simulated magnetic properties.

This paper presents the most detailed analysis to date of the chemical composition at different types of grain boundaries and defects in a Cr segregated CoCrTa/Cr thin-film longitudinal recording medium.

Mat. Res. Soc. Symp. Proc. Vol. 517 © 1998 Materials Research Society

EXPERIMENT

Oriented media of $Co_{84}Cr_{12}Ta_4$ with a 75 nm Cr underlayer were d.c. magnetron sputtered onto a NiP-plated Al substrate preheated to 250°C. Both back-thinned plan-view samples and cross-section samples were prepared for TEM by standard dimpling and ion milling methods. These samples were analyzed in detail for their structure, crystallography, and chemical composition by high resolution TEM (HRTEM), nanoprobe energy dispersive spectroscopy (EDS), and energy filtered imaging (EFTEM). The nanoprobe (EDS) was performed with a field emission Philips CM20ST – FEG operating at 200 keV. Thin film analysis methods with experimental standards quantified the Co, Cr, and Ta distribution. An advantage of nanoprobe EDS is that microstructural details imaged at lattice resolution can be directly analyzed for their chemical composition with spatial resolution of ~1.5 nm. In addition to individual spot analysis, a beam control program can accurately position and move the nanoprobe in 1 nm steps to provide composition profiles across grain boundaries. Manual drift correction after each 10 sec. counting interval and a liquid nitrogen cold stage for contamination control were used to achieve the highest spatial resolution. EFTEM was performed at 300 keV with a Philips CM30T equipped with a LaB_6 cathode and a Gatan Image Filter (GIF). This imaging method is based on the electron energy loss spectroscopy technique. Jump ratio images (the post edge energy window divided by the pre-edge window) for the Co (779 eV) and Cr (574 eV) $L_{2,3}$ edges reveal qualitative information concerning the chemical composition. Elemental maps using appropriate background subtraction methods, compensation for diffraction effects, and foil thickness correction provide quantitative composition information for Co and Cr with spatial resolution of ~1 nm.[11] The Ta (1735 eV) $M_{4,5}$ edge did not allow for analysis owing to insufficient signal at this energy loss region in the spectra.

RESULTS

Figure 1 is a cross section TEM bright field image of the $CoCr_{12}Ta_4$/Cr longitudinal media. This 60 nm magnetic layer exhibited relatively low media noise with a signal/noise ratio measured at 20kfci of approximately 5 dB less than a similarly processed CoCrPt alloy. Although the film thickness limits the magnetic properties (intrinsic coercivity ~1700 Oe), it provided an ideal sample to develop a three dimensional picture of the Cr grain boundary distribution. Both the Cr underlayer and Co alloy have a columnar structure with highly vertical grain boundaries. The Cr underlayer grains (~ 40 nm grain size) grew with a strong preferred <200> orientation and resulted in epitaxial <11.0> CoCrTa with a smaller grain size of 15-30 nm.

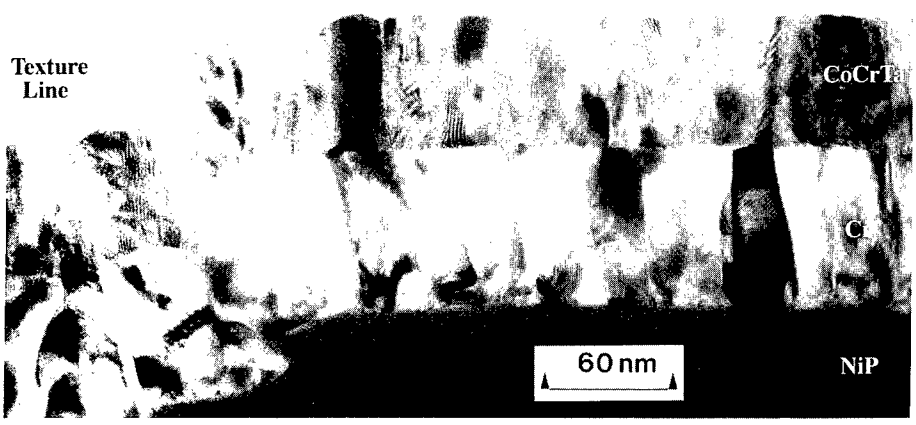

Figure 1: Cross-section TEM image of CoCrTa/Cr media.

The plan view HRTEM image in Figure 2 reveals the strong c-axis in-plane texture, consistent with <11.0> growth. Both random angle grain boundaries and the 90° grain boundaries from the bicrystal cluster structure are apparent.[12] In addition, vertical planar defects, which appear at the termination of stacking faults, are located within the grains. These intragrain defects often are located similarly to grain boundaries, but with 0° crystallographic mis-orientation.

Jump ratio images in Figure 3 qualitatively show the Cr and Co distribution in the magnetic layer. In the plan view images, Figures 3 a&b, a large variation in the grain boundary image intensity implies that a wide range of Cr segregation exists in the film. Correlation of the EFTEM image to the corresponding HRTEM image reveals Cr segregation to both the random angle and 90° grain boundaries, although the 90° bicrystal boundaries appear to have less segregated Cr. Another observation is the presence of intragrain Cr segregation. Regions with Cr concentration similar to that observed at grain boundaries are isolated within the grains.

The nanoprobe EDS data confirm these observations. A summary of the spot analysis of 36 different grain boundaries shows that the random angle boundaries have a large range in Cr enrichment (19 to 36 at%) with an average of 22 at%. The 90° bicrystal boundaries have less Cr content (mean 17 at%) and a smaller variation (15 to 21 at%) compared to the random angle boundaries. This result is expected if the grain boundary mis-orientation controls the Cr segregation level. Random angle boundaries have a large range in mis-orientation whereas the 90° boundaries all have essentially the same mis-orientation. Greater mis-match at some of the random angle grain boundaries could be responsible for the larger amounts of Cr segregation. Finally, it is important to recognize that these spot EDS measurements from a ~1 nm diameter electron probe come from an interaction volume of material dependent upon the foil thickness. Despite sample thicknesses of 60 nm or less, beam broadening creates some x-rays from regions greater than 2 nm. Therefore, the actual maximum local Cr levels are probably larger than those reported here.

As shown in Figure 4, the nanoprobe also located the intragrain segregation that appeared in the EFTEM images. The average Cr composition over the entire region of the image, measured using a large defocused beam, was 13 at%. However, at two regions inside of the grain, the local Cr level was 26 and 30 at%. This Cr level is similar to the 34% at the adjacent grain boundary. These regions of intragrain segregation are easily identified since they correspond to the bright regions at the end of stacking faults in the high resolution image as described in Figure 2. However, a spot EDS scan on the stacking fault line shows only 9% Cr. The origin of these defects is unknown. It may be that two Co grains nucleate on a Cr underlayer grain with the same orientation of the c-axis. During columnar growth, the two grains impinge with a "0° grain boundary". The stacking faults may contribute to the intragrain segregation via a fast diffusion path. Conversely, the Cr depleted stacking fault may be the result of Cr segregation during growth, along the basal plane toward the defect at the end.

Figure 5a is a typical nanoprobe EDS grain boundary composition profile created by moving the electron probe across a grain boundary in 1 nm steps. Within the statistical accuracy of the EDS data, the Ta concentration remains constant. However, the Cr level shows strong grain boundary enrichment and a depletion region in the adjacent area. The full width at half maximum of the Cr composition is approximately 4 nm, which indicates that the actual width of the Cr segregation is less than this owing to an interaction volume of approximately 1.5 to 2 nm. Comparison with a composition profile made from an EFTEM Cr map using a 4 pixel wide line scan in Figure 5b shows a similar distribution. Since each pixel point represents 0.6 nm, the FWHM of this example is 3.6 nm. The quantitative grain boundary Cr levels from the Cr maps also corresponds with the EDS data; the random angle grain boundaries range from 20 to 30 at% Cr.

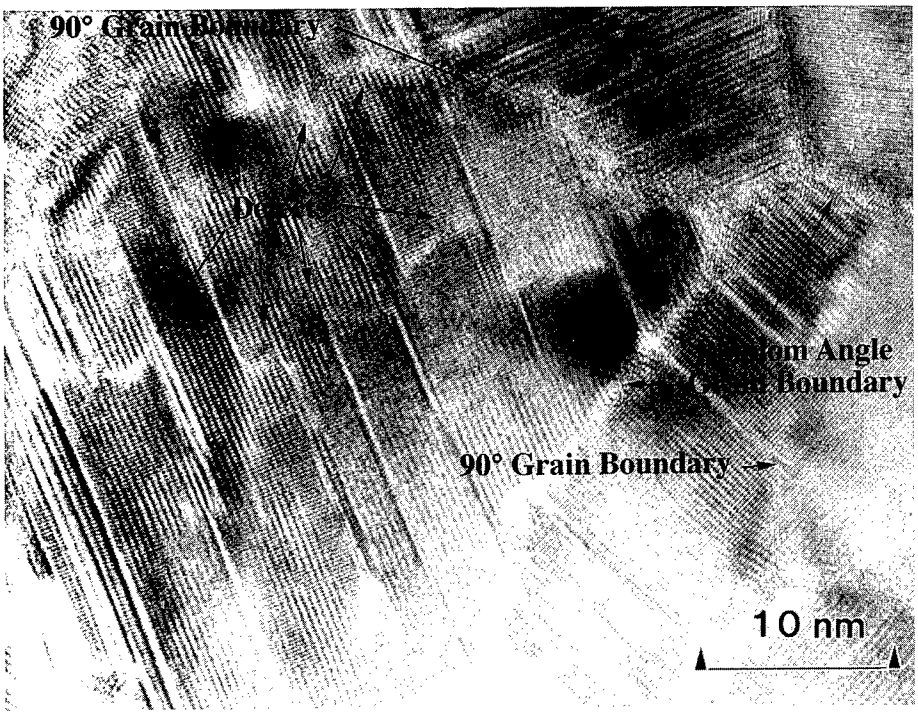

Figure 2: Plan-view TEM image showing random angle and 90° grain boundaries, and a series of defects suggesting a boundary between separately nucleated particles with the same orientation.

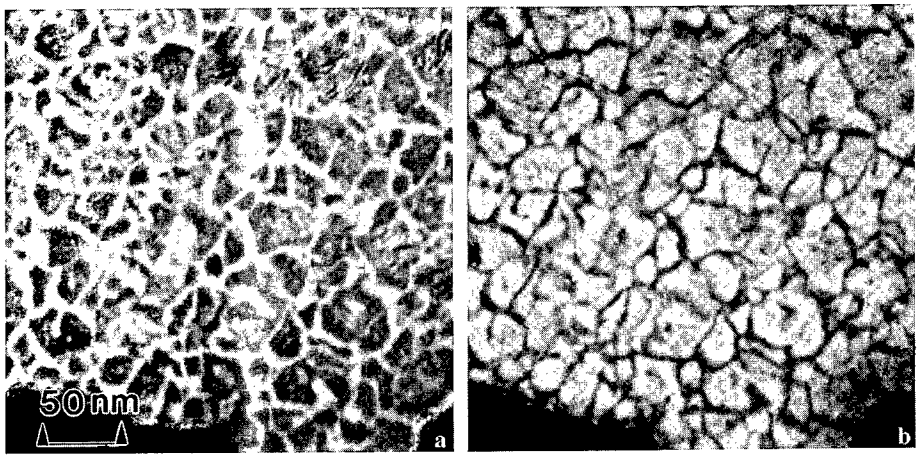

Figure 3: Energy filtered TEM images of a) Cr and b) Co composition.

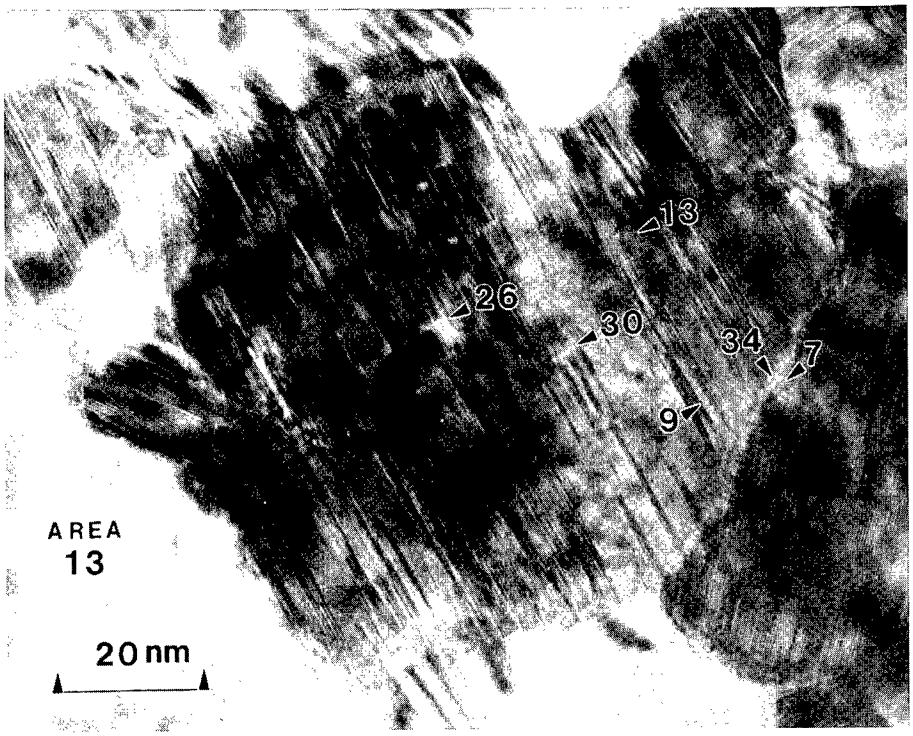

Figure 4: Plan-view TEM image showing representative nanoprobe EDS composition measurements at different types of defects. Numbers represent local Cr concentration in at%.

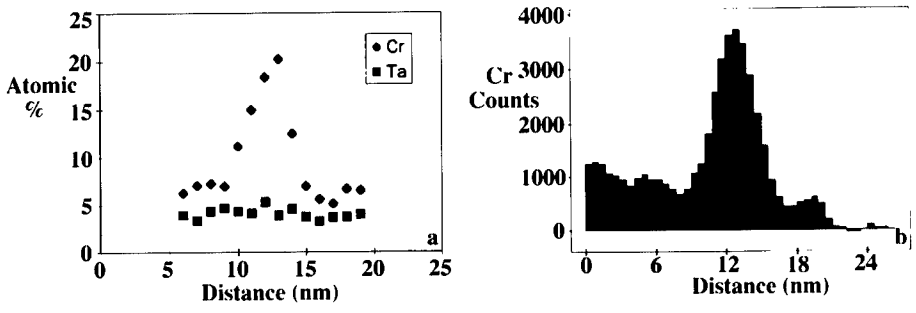

Figure 5: Line profiles of compositional structure by a) nanoprobe EDS and b) energy filtered TEM, showing similar segregation to grain boundaries.

CONCLUSIONS

Cr enrichment is observed at both random angle grain boundaries and 90° bicrystal boundaries. Cr segregation is also observed within the grains, at defects that appear to define boundaries between distinct CoCrTa particles that nucleated separately, but with the same crystallographic orientation. Localized intra-grain concentrations of 25 to 30 % Cr are comparable to those observed at grain boundaries. The Cr concentration at random angle grain boundaries has a wide distribution, from 19 to 36 at% (mean 22%); whereas the more crystallographically related 90° boundaries contain less Cr and less variation, 15 to 21 at% (mean 17% Cr). Composition profiles across grain boundaries using both nanoprobe EDS and EFTEM images show the full-width-half-maximum of the segregation to be approximately 4 nm, with Cr depletion regions next to the grain boundary having less than 7 at% Cr. No statistically significant evidence of Ta segregation was observed.

ACKNOWLEDGMENTS

Support from the Vanderbilt University Research Council and Komag Inc. is gratefully acknowledged. The research at the ORNL SHaRE User Facility was sponsored by the Division of Materials Sciences, U.S. Department of Energy, under contract DE-AC05-96OR22464 with Lockheed Martin Energy Research Corp., and through the SHaRE Program under contract DE-AC05-76OR00033 with Oak Ridge Associated Universities.

REFERENCES

1. J. Bentley Proc. Microscopy and Microanalysis, 533 (1997).
2. M. R. Kim, S. Guruswamy and K. E. Johnson, IEEE Trans. Magn, **29**, 3673 (1993).
3. Y. Yahisa, K. Kimoto, K. Usami, Y. Matsuda, J. Inagaki, K. Furusawa and S. Narishige, IEEE Trans. Magn **31**, 2836 (1995).
4. K. Kimoto, Y. Hirayama, and M. Futamoto, J. Magn. Magn. Mater. **159**, 401 (1996).
5. K. Tang, M. E. Schabes, C. A. Ross, L. He, R. Ranjan, T. Yamashita and R. Sinclair, IEEE Trans. Magn. **33**, 4074 (1997).
6. N. Inaba, T. Yamamoto, Y. Hosoe and M. Futamoto, J. Magn. Magn. Mater. **168**, 222 (1997).
7. J. E. Wittig, T. P. Nolan, C. A. Ross, M. E. Schabes, K. Tang , R. Sinclair and J. Bentley, IEEE Trans. Magn., in press.
8. M. Futamoto, N. Inaba, Y. Hirayama, K. Ito and Y. Honda, Mat. Res. Soc. Proc., this proceedings.
9. M Takahashi, A. Kikuchi and S. Kawakita, IEEE Trans. Magn. **33** 2938 (1997).
10. T. P. Nolan, M. Hara, K. Yoshida and M. Futamoto, J. Appl. Phys., **81**, 3922 (1997).
11. J. Bentley, J. E. Wittig and T. P. Nolan, Mat. Res. Soc. Proc., this proceedings.
12. T. P. Nolan, R. Sinclair, R. Ranjan, and T. Yamashita, J. Appl. Phys., **73**, 5566 (1993).

THE EFFECTS OF SUBSTRATE PREHEATING AND POST-DEPOSITION ANNEALING ON CrMn/CoCrPt/CrMn/NiAl FILMS

JIE ZOU *, DAVID E. LAUGHLIN **, and DAVID N. LAMBETH*
*Department of Electrical and Computer Engineering, **Department of Materials Science and Engineering, Data Storage Systems Center, Carnegie Mellon University, Pittsburgh, PA 15213, jzou@henry.ece.cmu.edu

ABSTRACT

In this study, we examine the effects of introducing CrMn as an intermediate layer between the NiAl underlayer and the CoCrPt magnetic layer, and as an overlayer on top of the Co-alloy film. The effects of deposition temperature and post-deposition annealing on the texture and magnetic properties were studied. Post-deposition annealing effectively lowered the exchange coupling between grains, increased the coercivity by 38%, up to 4600 Oe, and moderately decreased the Ms by 15%. Interlayer diffusion of CrMn into the CoCrPt grain boundaries is believed to cause the change in magnetic properties. It was also found that granular exchange coupling seems to be correlated to the Co-alloy in-plane texture.

INTRODUCTION

High Pt content CoCrPt alloys have relatively large Ku values [1], thus these are good candidates for high coercivity and thermally stable magnetic media. However, they exhibit larger noise than CoCrTa alloys because the granular exchange coupling is higher [2]. One approach to solving this problem is to increase the Cr concentration and the deposition temperature to isolate the grains by Cr segregation at the grain boundaries [3]. However, the Curie temperature and the Ms of the alloy decreases rapidly for higher Cr content. Another method proposed has been to surround the Co-alloy grains with non-magnetic materials to form granular media [4]. However, this kind of media suffers from relatively low Ms. Interdiffusion of Cr from the underlayer into the magnetic layer by post-deposition annealing was also investigated [5,6]. The coercivity increased, grain isolation improved but Ms decreased after annealing. Recently, L. L. Lee et al. found that CrMn underlayers induce higher coercivity in CoCrPt films than pure Cr underlayers when deposited at elevated temperatures [7]. Interdiffusion of Mn to the grain boundaries of the magnetic layer was proposed as being responsible for altering the magnetic properties.

In this study, we have investigated multilayer-structured media including a NiAl underlayer, a CrMn intermediate layer, a CoCrPt magnetic layer, and a CrMn overlayer. The effects of substrate preheating and post-deposition annealing on grain isolation and magnetic properties were studied.

EXPERIMENT

CoCrPt films on CrMn, NiAl or combined CrMn/NiAl underlayers were studied. CrMn overlayers on top of CoCrPt films were also investigated. All films were deposited onto glass substrates by RF diode sputtering either with or without substrate preheating. The Ar sputtering pressure was 10 mTorr and the base pressure was about $5x10^{-7}$ Torr. Deposition was performed at a fixed AC power density of 2.3 W/cm^2. All CoCrPt and NiAl layers were 300 and 1000 Å thick, respectively. The CrMn layer thickness was varied. Post-deposition annealings were performed under Ar gas flow.

Mat. Res. Soc. Symp. Proc. Vol. 517 © 1998 Materials Research Society

The compositions of the CoCrPt films determined by energy dispersive x-ray spectroscopy (EDX) were 78 at% Co, 6 at% Cr, and 16 at% Pt. The Mn concentration of the CrMn alloy films deposited in this study was 22 at%.

The in-plane magnetic properties of the samples were measured using a vibrating-sample magnetometer (VSM) and an alternating-gradient magnetometer (AGM) with a maximum applied field of 10 kOe. Film textures were examined by θ-2θ scan x-ray diffractometry with Cu-Kα radiation.

RESULTS AND DISCUSSION

The in-plane coercivities, Ms, ΔM/Mr peak values, and S* for CoCrPt/CrMn/NiAl films are plotted against the CrMn intermediate layer thickness in Fig. 1 (a)-(d), respectively. Data for samples deposited with substrate preheating to 260 °C and without preheating are shown. Selected x-ray θ-2θ scans of the above films are shown in Figs. 2 and 3 for comparison.

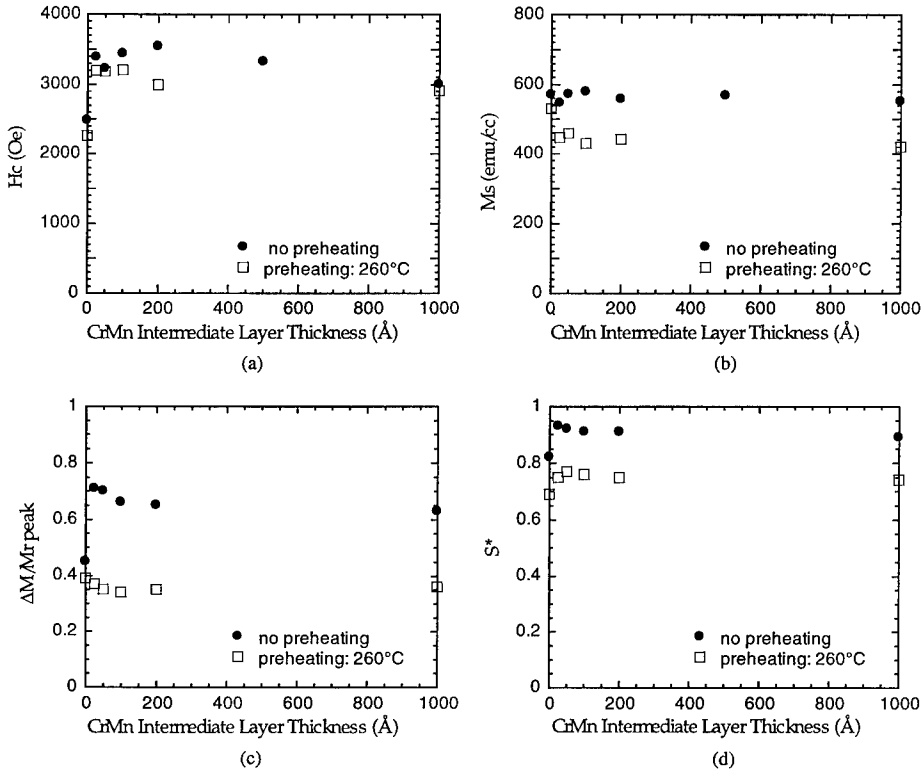

Fig. 1 In-plane magnetic properties (a) coercivity, (b) Ms, (c) ΔM/Mr peak, and (d) S* as functions of CrMn thickness for CoCrPt(300Å)/CrMn(x)/NiAl(1000Å) films deposited with or without substrate preheating.

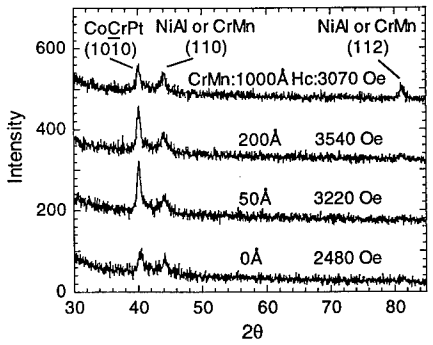

Fig. 2 X-ray diffraction spectra of 300 Å CoCrPt films on various thickness of CrMn intermediate layers on top of 1000 Å NiAl underlayers. No substrate preheating .

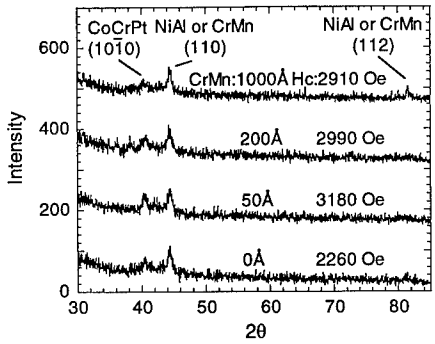

Fig. 3 X-ray diffraction spectra of 300 Å CoCrPt films on various thickness of CrMn intermediate layers on top of 1000 Å NiAl underlayers. Substrate preheating: 260 °C .

Without substrate heating, adding a CrMn intermediate layer as thin as 25 Å between the CoCrPt magnetic layer and the NiAl underlayer increased the coercivity by 900 Oe and improved the CoCrPt (10$\bar{1}$0) texture. No further improvement in the coercivity or the Co-alloy texture was obtained by increasing the CrMn thickness. This is similar to the effect reported for Cr and CoCrTa intermediate layers [8,9]. Contrary to the results reported for CrMn underlayers [7], we have found that for the combined CrMn/NiAl underlayers, applying substrate heating degraded the CoCrPt texture and the coercivity decreased.

The Ms values for samples prepared with no preheating are essentially independent of CrMn thickness and are around 560 emu/cc. When substrate preheating was applied, the Ms of the films with CrMn intermediate layers decreased about 20%, while for the sample with no CrMn layer, no significant decrease in Ms was observed. This is probably due to the diffusion of CrMn into the CoCrPt magnetic layer.

For the CoCrPt/CrMn/NiAl structure, elevation of the deposition temperature lowered the ΔM/Mr peak by about half. Further increases in the thickness of the CrMn intermediate layer from 25 Å to 1000 Å resulted in no significant change in the ΔM/Mr curves. This implies that only small amounts of CrMn need to diffuse into the magnetic layer to cause the decrease in the granular exchange coupling. This is consistent with the hypothesis that the grain boundary diffusion is the dominant transport mechanism at this relatively low temperature, since grain boundary diffusion is known to have a lower activation energy than bulk lattice diffusion and generally dominate in polycrystalline films at temperatures of less than one half of the melting temperature [10].

The S* behavior is consistent with that of the ΔM/Mr peak, and follows the concept that clusters of strongly exchange-coupled grains tend to switch together, causing a sharp M-H transition at the coercivity.

It should be noted that the CoCrPt/NiAl sample shows a significantly smaller ΔM/Mr peak than the better-textured CoCrPt/CrMn/NiAl sample when deposited without substrate preheating. To possibly exploit the relationship between Co-alloy texture and the intergranular exchange coupling, the magnetic properties of samples with different in-plane CoCrPt texture were examined and the results are summarized in Table I. With no substrate heating, the (10$\bar{1}$0)

textured CoCrPt film on the NiAl underlayer has a higher positive ΔM/Mr peak than the $(10\bar{1}1)$ textured CoCrPt film on the CrMn underlayer. The CoCrPt/CrMn/NiAl sample that has a stronger CoCrPt $(10\bar{1}0)$ texture shows an even higher ΔM/Mr peak. The stronger intergranular exchange coupling seems to be correlated with the better in-plane c-axis orientation.

Table I In-plane magnetic properties of samples with different CoCrPt texture.

Sample	Heating	Texture	Hc (Oe)	Ms (emu/cc)	S*	ΔM/Mr peak
CoCrPt(300Å)/CrMn(1000Å)	No	$(10\bar{1}1)$	1810	541	0.73	0.21
	260 °C	$(11\bar{2}0)$	3510	433	0.71	0.16
CoCrPt(300Å)/NiAl(1000Å)	No	$(10\bar{1}0)$	2480	571	0.82	0.45
	260 °C	$(10\bar{1}0)$	2260	530	0.69	0.39
CoCrPt(300Å)/CrMn(1000Å) /NiAl(1000Å)	No	$(10\bar{1}0)$	3000	550	0.89	0.63
	260 °C	$(10\bar{1}0)$	2910	419	0.74	0.36

As shown in Table II, adding a CrMn overlayer on top of the CoCrPt magnetic films increases the coercivity and further decreases the ΔM/Mr peak when substrate preheating is applied. This is further evidence that CrMn interlayer diffusion into the CoCrPt grain boundaries might be responsible for the change in the magnetic properties. As anticipated the CoCrPt texture does not change with the addition of an overlayer.

Table II In-plane magnetic properties of CoCrPt(300Å)/CrMn(1000Å)/NiAl(1000Å) films with and without a 200Å thick CrMn overlayer.

Heating	no		260 °C	
CrMn Overlayer	no	yes	no	yes
Hc (Oe)	3000	3290	2910	3300
Ms (emu/cc)	550	524	419	428
S*	0.89	0.87	0.74	0.72
ΔM/Mr peak	0.63	0.60	0.36	0.22

Deposition at elevated temperatures can lower the intergranular exchange coupling but it also appears to cause the Co-alloy texture to degrade. Post-deposition annealing may be a better solution. Annealing was performed on the samples with a CrMn overlayer prepared without substrate heating. The overlayer has the function of preventing the CoCrPt film from being oxidized during the annealing and it should be more efficient for CrMn to diffuse from both sides into the magnetic layer. Starting from 250 °C, the sample was annealed at the series of temperatures, 250 + 50N °C (where N = 0, 1, 2, 3, 4) for 1 minute. The in-plane magnetic properties are plotted vs. the annealing temperature in Fig. 4. The ΔM/Mr peaks and Ms decrease, and the coercivity increases for the higher annealing temperatures. At the annealing temperature of 450 °C, the ΔM/Mr peak drops to about 0.1, the coercivity increases by 40% to 4700 Oe, while the Ms decreases about 30%. The decrease in Ms, as the processing temperature is increased, is most likely a Co bulk alloy dilution effect due to the incorporation of Cr or Mn. However, it is not known how, if at all, the anisotropy energy density, Ku, changes with these dilutions. Since Hc is usually viewed as being proportional to Hk, and since Hk = 2Ku/Ms, only a portion of the Hc increase is due to the 30% Ms decrease. To account for the full 40% increase in Hc, either the Ku must have increased or more likely, the increase in Hc is reflecting a decrease in magnetic reversal via domain wall motion across grain boundaries due to a decrease in the granular exchange coupling [11].

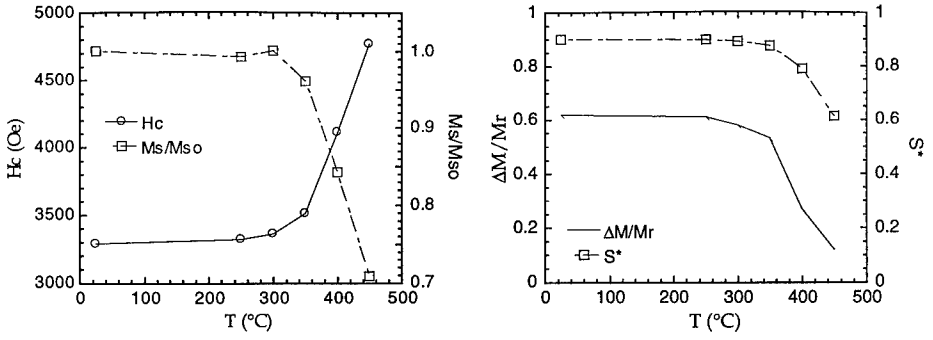

(a) (b)

Fig. 4 (a) coercivity and normalized Ms to Mso, the value before annealing (b) ΔM/Mr peak and S* as functions of the annealing temperature for the CrMn(200Å)/CoCrPt(300Å) /CrMn(1000Å)/NiAl(1000Å) films deposited with no heating.

Another series of annealings were performed, in which the temperature was held constant at 400 °C and the sequence of annealing times were 1, 2, 4, and 8 minutes. The M-H loops and ΔM curves are shown in Fig. 5 and Fig. 6, respectively. The ΔM/Mr peak and Ms decrease, and the coercivity increases for the longer annealing times. At the annealing time of 8 minutes, the ΔM curve is significantly flatter and the coercivity increases by 38%, to about 4600 Oe. The decrease in the Ms is about 15%. The difference in the percentage of the increase in the coercivity from the decrease in the Ms is larger than the above case. The improvement in grain isolation apparently contributes even more to the coercivity increase. These annealing conditions appears to be sufficient to drive the CrMn diffusion along the CoCrPt grain boundaries but not quite enough to overcome the energy barrier to enter the bulk of the CoCrPt grains. The post-deposition annealing of samples prepared without substrate preheating yields better properties than depositing films at elevated temperatures. This approach significantly lowers the granular exchange coupling, dramatically increases the coercivity, but causes a smaller decrease in Ms.

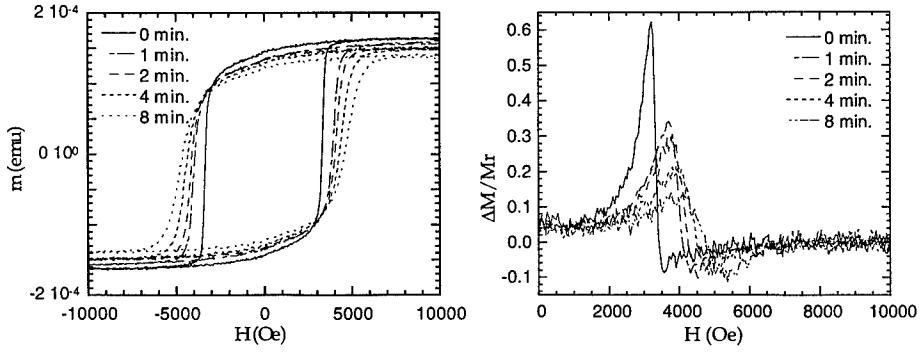

(a) (b)

Fig. 5 (a) hysteresis loop (b) ΔM/Mr curve as functions of the annealing time at the temperature of 400 °C for the CrMn(200Å)/CoCrPt(300Å)/CrMn(1000Å)/NiAl(1000Å) films deposited without substrate preheating.

CONCLUSIONS

Inserting a CrMn intermediate layer between the CoCrPt magnetic layer and the NiAl underlayer improves the CoCrPt ($10\bar{1}0$) texture and increases the coercivity. Applying substrate preheating to 260 °C lowers the granular exchange coupling but degrades the Co-alloy texture. Post-deposition annealing was found to be an even better method for lowering the intergranular exchange coupling. Under the optimal annealing conditions found in this study, the $\Delta M/Mr$ peak dropped to almost zero and the coercivity increased by 38%, to 4600 Oe, while the Ms moderately decreased by 15%. CrMn interdiffusion into CoCrPt grain boundaries is believed to increase the grain to grain isolation. The exchange coupling between grains seems to be correlated with the Co-alloy in-plane texture. The better the texture, the stronger the exchange coupling.

ACKNOWLEDGMENTS

This material is based upon work supported in part by Seagate Technology, Inc. and by the Data Storage Systems Center of Carnegie Mellon University under a grant from the National Science Foundation # ECD-8907068. The government has certain rights to this material.

REFERENCES

1. M. Futamoto, N. Inaba, and A. Nakamura, Inst. Elect. Infor. Comm. Eng. (Japan) **MR96-43**, pp 47 (1996).
2. J. Nakai, E. Kusumoto, M. Kuwabara, T. Miyamoto, M. R. Visokay, K. Yoshikawa, and K. Itayama, IEEE Trans. Magn. **30**, pp 3969 (1994).
3. M. F. Doerner, T. Yogi, D. S. Parker, S. Lambert, B. Hermsmeier, O. C. Allegranza, T. Nguyen, IEEE Trans. Magn. **29**, pp 3667 (1993).
4. A. Murayama, S. Kondoh, and M. Miyamura, J. Appl. Phys. **75**, pp 6147 (1994).
5. T. Kawanabe, et al, IEEE Trans. Magn. **26**, pp 42 (1990).
6. Y. C. Feng, D. E. Laughlin, and D. N. Lambeth, IEEE Trans. Magn. **30**, pp 3948 (1994).
7. L.-L. Lee, D. E. Laughlin, and D. N. Lambeth, to be published by IEEE Trans. Magn.
8. L.-L. Lee, D. E. Laughlin, L. Fang, and D. N. Lambeth, IEEE Trans. Magn. **31**, pp 2728 (1995).
9. J. Zou, D. E. Laughlin, and D. N. Lambeth, to be published by IEEE Trans. Magn.
10. D. Gupta in Diffusion Phenomena in Thin Films and Microelectronic Materials, edited by D. Gupta and P. S. Ho, Noyes Publications, Park Ridge, New Jersey, 1988, pp 33-51.
11. J.-G. Zhu and H. N. Bertram, J. Appl. Phys. **69**, pp 6084 (1991).

INTERGRANULAR COUPLING AND GRAIN ISOLATION OF THIN CO FILMS

Heng Gong, Wei Yang, David N. Lambeth and David E. Laughlin*
Department of Electrical and Computer Eng., *Department of Materials Science and Eng.
Data Storage Systems Center, Carnegie Mellon University, Pittsburgh, PA 15213-3890

ABSTRACT

The effects of rapid oxidation and overcoat diffusion processes on the intergranular coupling and grain isolation in thin Co films were studied. The oxidation process was found to be strongly temperature dependent. The optimal coercivities can only be achieved within a narrow range of temperatures, while further increasing the temperature incurs significant thermal instability. CrMn underlayers were confirmed to be more effective in enhancing the grain isolation by the grain boundary diffusion during the oxidation process. The oxidation process does not change the Co anisotropy, and hence the coercivity increase is appears to be a result of better grain isolation. The in-situ diffusion of Ag and Cr overcoats were also found to have siginificant effects on the grain isolation in Co and CoCr films.

INTRODUCTION

For current magnetic recording, well isolated, high coercivity thin-film media with small grain sizes are desired [1]. As the grain size decreases, intergranular interaction becomes one of the key factors determining the medium thermal stability, which is a critical concern for future ultra-high density recording [2, 3]. Hence it is important to understand the role of intergranular coupling in very small grain size media. In our previous work, we have found that when thin Co films are exposed to the atmosphere at elevated temperatures immediately after deposition, the oxidation of the film results in better grain isolation, a significant coercivity increases and thermal decay effects. We also showed that $Cr_{78}Mn_{22}$ underlayers were more effective in Co grain isolation during this oxidation process [3]. In this paper we report our latest investigation on the temperature dependence of the oxidation process. The effects of $Cr_{78}Mn_{22}$ and Cr underlayers will also be compared in greater detail. Meanwhile, we have prepared uni-crystal thin Co films on single crystal silicon to study the effect of the oxidation on the magnetocrystalline anisotropy. In these uni-crystal films the easy axes of the Co grains are almost perfectly aligned along a single direction, hence, by measuring the hysteresis loops along the hard axis, the anisotropy field can be conveniently determined. In this work, we also prepared thin Co films with various overcoats deposited immediately after the Co layer. This in-situ overcoat diffusion process was found to have significant effect on the intergranular coupling of Co grains.

EXPERIMENTAL

Film Deposition

Thin films were deposited by RF diode sputtering in a Leybold-Haereus Z-400 sputtering system. The sputtering power density and Ar gas pressure were set to 2.25W/cm^2 and

Mat. Res. Soc. Symp. Proc. Vol. 517 © 1998 Materials Research Society

Fig.1 Sample film structures for the study on the oxidation process. (a) samples grown on glass substrates with Cr or CrMn underlayers, and (b) on single crystal Si(110) wafers.

10mTorr, respectively. The base vacuum pressure was below $5x10^{-7}$ Torr. Corning 7059 glass substrates were used for all samples except the uni-crystal Co films. The details of the preparation of uni-crystal films will be discussed elsewhere [4]. In order to study the temperature dependence of the oxidation process, substrates were heated to various temperatures before film deposition.

Characterization of Magnetic Properties

Magnetic properties were investigated by a vibrating sample magnetometer (VSM) and an alternating gradient magnetometer (AGM). Intergranular interactions were characterized by measuring the ΔM curves. The $\Delta M(H)$ curve is defined as

$$\Delta M(H) = I_d(H) - [1-2\, I_r(H)]\,, \qquad (1)$$

where $I_r(H)$ is the normalized isothermal remanence (ISR) curve, obtained through progressive magnetization of an initially AC demagnetized sample, and $I_d(H)$ is the normalized DC demagnetization remanence (DCR) curve, obtained through progressive demagnetization from a previous saturated state.

RESULTS AND DISCUSSION

Rapid Oxidation Process

In order to study the temperature dependence of the oxidation process and the underlayer effects, we prepared two series of samples, one with Cr underlayers and the other with $Cr_{78}Mn_{22}$ underlayers, and exposed them to atmosphere at various temperatures. The thickness of the Cr or $Cr_{78}Mn_{22}$ underlayers was 45nm and the Co layers were 8 nm in all samples. Uni-crystal thin Co films were also prepared to study the anisotropy of the Co films during the oxidation process. The film structures are shown schematically in Fig. 1.

Shown in Fig. 2 are the measured ΔM peak values for the two series of samples oxidized at different exposure temperatures. At low temperatures, the ΔM curves show positive peaks, implying strong exchange interactions in the films. When the samples are exposed at higher

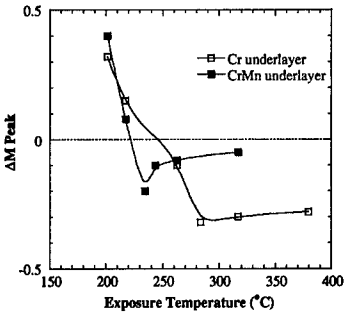

Fig. 2. Measured peak values of ΔM curves for samples oxidized at various temperatures.

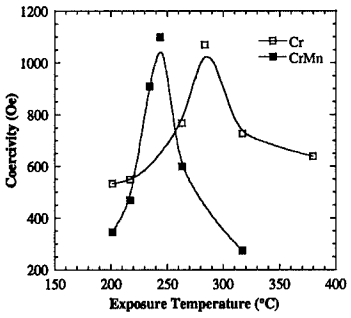

Fig. 3. The coercivities of the samples oxidized at different exposure temperature.

temperatures, the ΔM peaks decrease and become negative, indicating a predominant magnetostatic coupling. In our previous work [3], we have shown by electron diffraction that Co oxide was formed during the oxidation process. The oxide shells on the grain boundaries are believed to provide isolation between Co grains, while it is not believed that significant oxygen diffuse into the bulk of the Co grains occurs. At relatively low exposure temperatures, oxide formation is insufficient to effectively decouple the Co grains. When the exposure temperature is increased, the oxide shells grow thicker, resulting in better grain isolation. Hence the exchange coupling is suppressed, and finally the magnetostatic interactions become dominant.

Comparing the samples with Cr and CrMn underlayers, one finds that the ΔM peaks of the samples grown on CrMn drop to negative values at a relatively lower exposure temperature than those with Cr underlayers. The diffusion of Mn along with the Cr into the grain boundaries is believed to have helped further isolate the Co grains during the oxidation.

The coercivities of the two series of samples are plotted in Fig. 3. The small coercivities at low exposure temperatures are due to strong exchange coupling among Co grains resulting in domain wall activity. At higher exposure temperatures the coercivities are increased as a result of better grain isolation. After reaching the maximum values at certain temperatures, however, the coercivities start to drop with a further increase in exposure temperature. Hence, in order to achieve the optimal coercivities, the temperature must be well controlled within a narrow range for this sensitive process. The negative ΔM peaks indicate that the grains are still well isolated. Significant thermal instability is the main reason for these small coercivity values. As the oxide shells become thicker at higher exposure temperatures, the effective Co grain size in these thin, 8nm thick films keeps decreasing, and the thermal effects become more and more detrimental. This interpretation is further confirmed in Fig. 4 and Fig. 5, which show, respectively, the measured saturation magnetization and the remanence squareness of the samples oxidized at different temperatures. In Fig. 4, the saturation magnetization is normalized by the value of a non-oxidized film, and it is found to decrease monotonically with an increasing temperature. It is also noted that the Ms drops much faster for samples with CrMn underlayers. The diffusion of Mn into the Co films along with the oxidation probably makes the growth of non-magnetic grain boundary regions much easier, so better grain isolation can be achieved in the samples with CrMn underlayers at relatively low temperatures. Meanwhile, the effective Co grain size also decreases faster in these films grown on CrMn, and a significant thermal instability shows up at a lower exposure temperature when compared to the films with Cr underlayers.

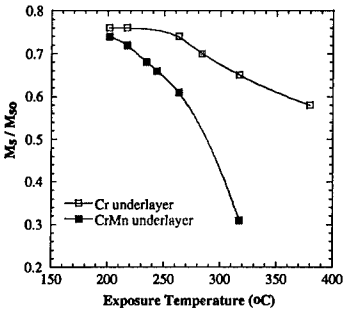

Fig. 4. Normalized M_S of samples oxidized at various exposure temperatures.

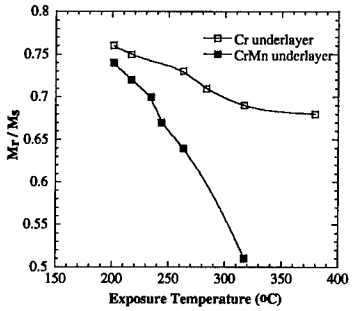

Fig. 5. Remanent squareness of samples oxidized at various temperatures.

As further evidence, the remanence squareness is plotted in Fig. 5 for the samples oxidized at various temperatures. It also decreases monotonically with increasing exposure temperature, due to the elimination of exchange coupling by grain isolation, followed by the growing aggravation of thermal instability as a result of the small grain size.

To further understand the mechanism of the oxidation process, we investigated its effect on the anisotropy of the Co films. Two uni-crystal thin Co films, with the same 8nm thickness, were prepared; one was not oxidized while the other was oxidized at about 260°C. From the hard axis hysteresis loops (Figs. 6 and 7) of the two samples, the same anisotropy field value was found (H_K = 2600 Oe), leading support to the perception that no significant diffusion of the oxygen into the bulk of the Co grains occurs. The easy axis loop of the non-oxidized sample shows a coercivity of 763 Oe, while for the oxidized sample the coercivity is 2003 Oe, not far from H_K. These results reveal that the oxidation process does not change the anisotropy constants of the films. The much smaller easy axis coercivity of the non-oxidized film indicates

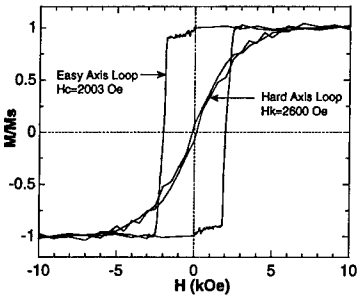

Fig. 6. Easy and hard axis loops for a 8 nm thick uni-crystal pure Co film oxidized at 260°C.

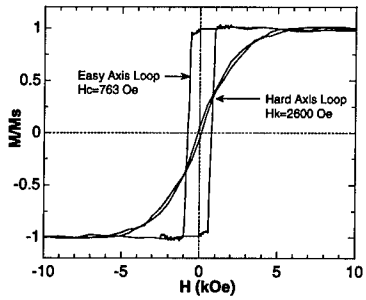

Fig. 7. Easy and hard axis loops for a 8 nm uni-crystal non-oxidized pure Co film deposited at 260°C.

domain wall activity and is due to the strong exchange coupling, while the grain isolation dramatically improved the coercivity of the oxidized sample.

OVERCOAT EFFECTS

In this work we also studied an overcoat diffusion approach to influence the intergranular coupling in thin Co and Co-alloy films. These overcoats are sputtered in-situ immediately after the deposition of Co layers. The diffusion of overcoat material into the Co grain boundaries is found to have significant effects on the intergranular interactions in the Co layers.

The magnetic properties of the samples with different overcoats are compared in Table I. Significant changes are observed after overcoats were deposited. Compared to the properties of sample A, which has no overcoat (also not oxidized), the lower H_c and higher positive ΔM peak of sample B indicates a stronger exchange coupling. The diffusion of Cr into the Co grain boundaries has enhanced the exchange interactions between the Co grains in sample B. It is also noted that the M_s of sample B is almost the same as that of sample A, hence the diffusion of Cr does not form a non-magnetic CoCr grain boundary material at this temperature.

TABLE I
COMPARISON OF MAGNETIC PROPERTIES OF SAMPLES WITH Cr AND Ag OVERCOATS

Sample	Film Structure	Substrate Temperature	Hc (Oe)	ΔM peak	Ms (emu/cc)
A	Co 8 nm / Cr 45 nm	260 °C	470	+0.72	1390
B	Cr 15 nm / Co 8 nm / Cr 45 nm	260 °C	360	+0.95	1375
C	Ag 15 nm/ Co 8 nm / Cr 45 nm	260 °C	980	-0.35	750

In contrast to the effect of Cr, a 15 nm Ag overcoat in sample C greatly increased the coercivity of the film, and changed the ΔM peak to negative. The Ag overcoat has effectively eliminated the intergranular exchange coupling. The M_s of sample C also dropped significantly to 750 emu/cc. Although Ag is immiscible with Co, it seems that the diffusion of Ag atoms leads to the formation of non-magnetic grain boundary region, resulting in the better grain-to-grain isolation and the decreased M_s.

Table II.
COMPARISON OF MAGNETIC PROPERTIES OF SAMPLES WITH Cr AND Ag OVERCOATS

Sample	Overcoat	Film Structure	Substrate Temperature	Hc (Oe)	ΔM Peak	Ms (emu/cc)
D	none	$CoCr_{20}$ 8 nm/ Cr 45 nm	260 °C	233	0.30	550
E	Cr 15 nm	$CoCr_{20}$ 8 nm/ Cr 45 nm	260 °C	276	0.25	535
F	Ag 15 nm	$CoCr_{20}$ 8 nm/ Cr 45 nm	260 °C	380	0.23	540
G	none	$CoCr_{20}$ 8 nm/ Cr 45 nm	320 °C	252	0.30	550
H	Cr 15 nm	$CoCr_{20}$ 8 nm/ Cr 45 nm	320 °C	630	0.18	540
I	Ag 15 nm	$CoCr_{20}$ 8 nm/ Cr 45 nm	320 °C	750	0.15	540

Shown in Table II are the overcoat effects on $CoCr_{20}$ films. In contrast to the pure Co films, for which only Ag helps with the grain isolation, both Cr and Ag overcoats were found to

enhance the coercivity. In CoCr films the Cr segregation results in a more Cr-rich, probably already non-magnetic, grain boundary regions [5], which help to weaken, yet not completely eliminate the exchange coupling. Hence the additional overcoat diffusion into these boundaries still cause the coercivity to increase.

The overcoat diffusion effect is found to be very sensitive to the deposition temperature. At 260°C only a slight increase in coercivity due to the overcoats were resulted. When the temperature was increased to 320°C, however, the coercivity almost tripled after the overcoats were deposited. This also confirms that better grain isolation and the resulting coercivity increase is due to the overcoat diffusion. At both temperatures, the diffusion of Ag overcoats showed a more significant effect on increasing the coercivity. No obvious change in M_s was observed during these in-situ diffusion processes. ΔM peaks decreased after overcoat diffusion, but remained positive. It seems that with the already existing CoCr grain boundaries, the diffusion effects are not as strong as they are in the pure Co films.

CONCLUSIONS

In this work we have extended our study on the rapid oxidization process, and it was found to be an effective method to achieve grain isolation in strongly exchange coupled Co films. This process was found to be very sensitive to the exposure temperature. The optimal coercivities can only be achieved within narrow ranges of temperature. Further increasing the temperature decreases the effective grain size, and the coercivity drops due to thermal instability. It is also confirmed that the CrMn underlayers can help further isolate Co grains during the oxidation process. With the uni-crystal films we have been able to show that this oxidation process does not change the Co anisotropy, and hence the oxidation induced coercivity increase is indeed a result of better grain isolation. Overcoat diffusion effects have also been explored. For thin Co films, Ag overcoats can help eliminate the exchange coupling and increase the coercivity, while the diffusion of Cr overcoats is found to enhance the exchange coupling and decrease the coercivity of the film. For CoCr films, both Ag and Cr overcoats can help to increase the coercivity, but Ag overcoats are more effective. The overcoat diffusion process was also found to be strongly temperature dependent.

ACKNOWLEDGMENT

This work was supported by the National Storage Industry Consortium (NSIC) and in part by the National Science Foundation under grant #ECD-8907068.

REFERENCES

1. D.N. Lambeth, E.M.T. Velu, G.H. Bellesis, L.L. Lee and D.E. Laughlin, J. Appl. Phys. **79**, 4496(1996).
2. P.-L. Lu and S.H. Charap, IEEE Trans. Magn. **30**, 4230(1994).
3. H. Gong, W. Yang, D.N. Lambeth, M. Rao and D.E. Laughlin, Paper ES-07, the 7th joint MMM-Intermag Conference 1998, IEEE Trans. Magn., in press.
4. W. Yang, D.N. Lambeth, and D.E.Laughlin, to be published.
5. Y. Hirayama, M. Futamoto, K. Kimoto, and K. Usami, IEEE Trans. Magn. **32**, 3807(1996).

Part VI

Thermal Stability of Magnetic Recording Media

DETERMINATION OF CRITICAL VOLUMES IN RECORDING MEDIA

K.O'Grady, P. Dova and H. Laidler

School of Electronic Engineering and Computer Systems
University of Wales, Dean Street, Bangor LL57 1UT, UK

ABSTRACT

In this overview paper the concept of thermal activation of magnetisation reversal is reviewed in terms of the Wohlfarth-Gaunt formalism. This formalism gave rise to the concept of an activation volume of reversal. Other techniques have been developed for the determination of activation or critical volumes of reversal and these are reviewed. It is found that these methods give the same approximate value for the activation volume but the only method based on micromagnetism is the waiting time experiment which is consistent with Gaunt. Factors which affect the activation volume such as incoherent reversal and intergranular coupling are discussed together with measures that may be required in order to generate ultrahigh density recording media that are relatively free from thermal loss of signal.

Introduction

1. Basis of Thermal Activation

Magnetisation reversal in thin film media is governed by the Stoner-Wohlfarth theory which describes the behaviour of the magnetic moment of a single domain particle at 0°K[1]. In this theory it is shown that for a single domain particle with easy axis aligned parallel to an applied field, reversal occurs at a field $H = H_K$ which is the anisotropy field. For the case of the system with the easy axis aligned parallel to the applied field $H_K = 2K/M_s$ and for a randomly oriented system H_K is $0.96K/M_s$. Hence the anisotropy field is the coercivity at 0°K.

The second theory of great relevance in thin film media is the thermal activation model first formalised by Néel [2]. This model laid down the definition of the relaxation time τ for a system of fine particles undergoing coherent reversal under the influence of thermal activation

$$\tau^{-1} = f_o \exp-\left[KV\left(1-H/H_K\right)^2/kT\right] \qquad (1)$$

Mat. Res. Soc. Symp. Proc. Vol. 517 © 1998 Materials Research Society

where f_0 is a frequency factor taken to be 10^9 Hz and V is the particle volume. τ is the time taken for the magnetisation to fall to 37% of its original value. K is the anisotropy constant. Thus the magnetisation at other than 0°K exhibits time dependence according to equation 1. In real materials it is found that the decay of magnetisation follows an lnt law [3]. This arises due to the distribution of energy barriers present in the material and in some way represents a sum of relaxation times. This observation, first made by Street and Wooley, gives rise to

$$M(t) = M(0) \pm S \ln t \qquad (2)$$

where S is the magnetic viscosity coefficient, $S = dM/dlnt$ and $S(H)$ goes through a maximum at $H = H_c$. Equation 2 is found to hold experimentally over many decades of time. It has been shown [4] that the lnt law represents a first order approximation to a series expansion which accurately describes the variation of magnetisation with time for any system. In physical terms an lnt law is followed if the distribution of energy barriers $f(\Delta E)$ is constant during the time of measurement. Where $f(\Delta E)$ is narrow, non-linear forms of the variation of M with lnt result.

Figure 1(a) shows a schematic of an energy barrier distribution and marked on the diagram at point 1 is a hypothetical active region of the energy barrier distribution undergoing thermal activation. At this point a log t variation will be observed as long as $f(\Delta E)$ is constant. If the distribution is narrow then moments that are at a slightly higher energy barrier will also be relaxing, which will give rise to a higher value of S. Hence S is seen to accelerate with time and curvature in the M versus ln$t$ curve which is convace downwards is observed. At the peak in the energy barrier distribution (point 2) the distribution is in effect, constant and for an extremely narrow distribution an accelerating rate of time dependence will be observed initially, followed be a decelerating rate after the peak. This gives rise to a characteristic S shaped curve. At point 3 as time passes, the number of grains available to reverse decreases and hence a decelerating rate of logarlthmic decay is observed. These three forms of time dependence are often observed in thin film media and are shown schematically in figure 1b.

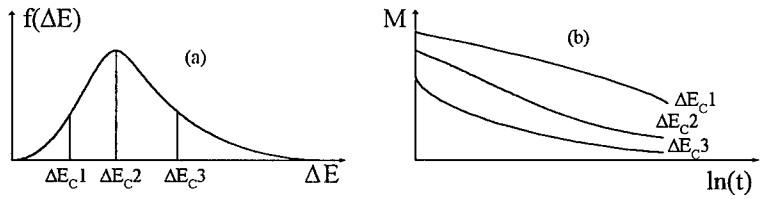

Figure 1. The origin of non-linear time dependence.

This formalism was first laid down in a seminal work by Gaunt [5] who showed that

$$S = 2M_2KTf(\Delta E_c(H)) \tag{3}$$

and hence the relationship between time dependence and the energy barrier distribution is clear.

2. Fluctuation Fields and Activation Volumes

Street *et al* [6] described time dependence of magnetisation in terms of thermal energy acting on the moment as would a fluctuating magnetic field (H_f) and showed that (H_f)

$$H_f(H) = S(H) / \chi_{irr}(H) \tag{4}$$

where $\chi_{irr}(H)$ is the irreversible susceptibility generally determined from the differential of an appropriate remanence curve. Arguing on dimensional grounds Wohlfarth [7] showed that the fluctuation field must be given by an equation of the form

$$H_f = kT / vM_s \tag{5}$$

where v is the activation volume. In Gaunt [5], a complete analysis of the activation volume of reversal in terms of the energy barrier distribution is presented. For a single domain particle undergoing coherent reversal the form of the fluctuation field was modified according to

$$H_f = \frac{kT}{vM_s\left(1 - H/H_K\right)} \text{ and } v = V\left(1 - H/H_K\right) \qquad (6)$$

where V is the physical volume of the grain. Hence, there is no correlation between the physical grain size and the activation volume at fields other than zero where little or no thermal activation is expected. In this work it was assumed that the variation of magnetisation with time follows the original Int law and hence there now remains the difficulty of determining H_f where this behaviour is not observed.

The first attempt to describe such a system was the work of Estrin et al [8] who described magnetic viscosity in terms of a phenomenological Equation of State model within which it was shown that it was possible to measure a fluctuation field termed Λ,

$$\Lambda = \left.\frac{\Delta H}{\ln(\dot{M}_{irr2} / \dot{M}_{irr1})}\right|_{\dot{M}_{irr}} \qquad (7)$$

In this relationship $\dot{M}_{irr}$ is the rate of change of the irreversible component of the magnetisation which for most materials exhibiting a large coercivity, is equivalent to the rate of change of the total magnetisation. This parameter is measured at two distinct fields but at a constant value of M_{irr} which is taken to be M_{tot}. The basis of this measurement is shown in Fig.2 where the parameters in equation 7 are defined. The activation volume is obtained as a function of field from equation 6.

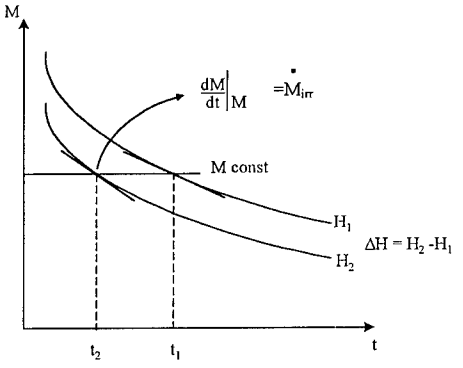

Figure 2 Techniques for the determination of H_f.

There are clear difficulties with this measurement technique since it involves the measurement of the slope of a tangent to the curves. Given that these curves are almost identical so as to ensure that ΔH is small, the requirements for accuracy of measurement for this technique are excessive and our experience is that these measurements often subject to large error.

el Hilo *et al* [9] used an alternative technique to determine the fluctuation field, again using the variation of magnetisation with time they showed that H_f was given by

$$H_f = \left.\frac{\Delta H}{\ln(t_2 / t_1)}\right|_M \tag{8}$$

where the difference in time between the achieving of a fixed value of magnetisation at two different fields is used to determine the fluctuation field, as shown in Fig.2. Further in a subsequent paper Lyberatos and Chantrell [10] showed that this expression was in fact equivalent to the Equation of State model. This formalism is a much easier approach for the experimentalists and is found by ourselves and others to give consistent and repeatable results.

3. The Sweep-rate Dependence of Coercivity and Critical Volumes

A further manifestation of thermal activation of magnetisation reversal is observed in the sweep-rate dependence of coercivity. This aspect of thermal activation gives rise to a significant increase in coercivity at high frequencies typically used to write data to media and to a significant reduction in the effective storage coercivity of such media once the bits are written. This subject was discussed extensively at a symposium at the recent 1998 Intermag conference and the interested reader is particularly referred to a review of this effect by Doyle [11].

The first substantive study of the sweep-rate dependence of coercivity was undertaken by Sharrock [12]. This can be used to obtain a particle volume by fitting for V in the equation

$$H_c(t) = H_K\left(1 - \left[\frac{kT}{KV}\left(\ln\frac{tf_o}{0.693}\right)\right]^{1/2}\right) \tag{9}$$

Sharrock and co-workers found that the volume given by equation (9) for elongated particles used in tape media was always smaller than the physical volume due to incoherent reversal mechanisms. This is in agreement with de Witte et al [13] who found for a particle of say, axial ratio 7 the activation volume was 1/7th of the particle volume.

el Hilo et al [14] derived equation (9) explicitly in terms of the sweep-rate R (= dH/dt)

$$H_c(R) = H_K\left(1-\left[\ \frac{kT}{KV_m}\ln\left(\frac{f_o H_K kT}{2KV_m}\frac{1}{R}\right)\ \right]^{1/2}\right) \qquad (10)$$

where V_m is the median volume of the particle size distribution. In this work on particulate media, the activation volume was substituted for V_m to obtain a good fit.

In a study of ultra-thin films Bruno et al [15] provided an analysis based on the sweep-rate dependence of coercivity which gave rise to the Barkhausen volume (V^*). From this analysis a plot of coercivity against the log of the sweep-rate $\dot{H}$ is predicted to be linear and of slope

$$dH_c / d\ln\dot{H} = kT / V^* M_s \qquad (11)$$

and hence V^* is simply obtained. These workers and studies by others, e.g.[16] have found this linear behaviour and hence this technique has achieved great popularity for the determination of a critical or Barkhausen volume. Unfortunately, this technique is somewhat flawed as acknowledged by Bruno et al in the original work. They state that the theory is based upon a single activation energy which relaxes exponentially and ... *"yields an order of magnitude of the characteristic volume involved in the activation process. It fails to give an accurate description of the observed activation phenomena."* The wide use of this technique has given conflicting results with more theoretically sound models of magnetisation reversal. It is clear that the activation energy in a thin film is not single valued and hence a single value of a critical volume is unhelpful even if it represents some kind of mean. The activation volume of importance in the case of thin film media is that applicable at the appropriate demagnetising field not the coercivity.

Experimental

In this work we describe magnetic measurements on a range of samples which have been supplied to us by a number of collaborators. These include the media division of Seagate in Fremont and IBM Storage System Division in San Jose. Where appropriate, reference is made to publications which describe their preparation hence no details of preparaton are provided here.

All the magnetic measurements described in this work were undertaken using a Princeton Measurement Systems model 2900 alternating gradiant force magnetometer. It is our view that this instrument is that most suitable for measurements of the magnetic properties of thin film media because of its high resolution and fast averaging time which enables a large number of

measurements to be made in a short period of time. In our studies we characterise the basic properties via measurements of coercivity, S^*, etc. and examine switching in terms of remanence curves [17]. We also characterise materials in terms of the ΔM parameter [17] where

$$\Delta M(H) = M_D(H) - \left(1 - 2M_R(H)\right) \tag{12}$$

ΔM is positive where exchange coupling dominates and negative for a dipolar coupled system. The maximum slope of the ΔM(H) curve gives an indication of the strength of the coupling.

Due to intergranular coupling the hysteresis loops of thin film media are usually fairly square which implies that the distribution of energy barriers is relatively narrow. This would imply that the variation of magnetisation with $\ln t$ is non-linear, which we observe, and S / χ_{irr} is not applicable. Thus, in order to determine the fluctuation field and hence the activation volume it is necessary to use either the Equation of State model or the waiting time formalism. It is clear that the simplest and most convenient measurement is that of the waiting time. Furthermore, a knowledge of the simple hysteresis loop means that the value of the fluctuation field and hence the activation volume can be probed as a function of field.

Experimental Results and Discussion

In this work we have measured time dependence and activation volumes together with details of the intergranular coupling. This is essential since as originally predicted by Wohlfarth [7], the activation volume is that volume of material which reverses in a single step and when grains are coupled this constitutes a volume bigger than that of a single grain.

The first set of samples we consider are an original set of CoNiCr films prepared by IBM [17]. These films were grown on Cr underlayers of thickness ranging from 100Å - 2000Å. This structure resulted in a systematic decrease in exchange coupling and for the sample grown on a 2000Å underlayer, a dipolar coupled structure resulted. The original ΔM curves are shown in Fig.3 and details of their general properties including noise performance are shown in Table1.

In Fig. 4 the variation of activation volume with field for these samples is shown. This data exhibits a broad maximum in the activation volume as a function of field. This maximum occurs around the remanent coercivity i.e. the peak of the energy barrier distribution. This is a confirmation of the theory of Gaunt [5].

Cr U/layer	H_C	M_r/M_s	S*	S_0/N
100 Å	549	1.59	0.94	0.074
500 Å	826	1.67	0.90	0.034
1000Å	1406	1.19	0.90	0.021
2000 Å	1431	1.50	0.88	0.021

Table 1. Properties of CoNiCr/Cr films.

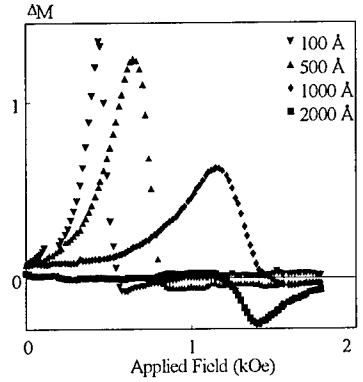

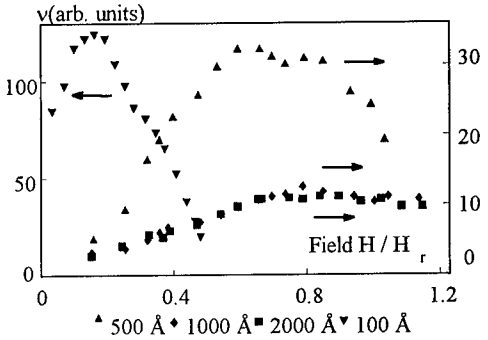

Figure 4. ΔM curves for the CoNiCr films. Figure 3. Activation volumes for the CoNiCr films.

The activation volume data presented here is in arbitrary units but given that the films were all produced from the same target the values quoted are relative and the grain size was maintained almost constant at between 260 and 300Å. Hence, from the data it is clear that for the 2 samples grown on the thickest underlayers where the coupling is minimised, the activation volume is only of the order of a half that for the sample grown on the 500Å underlayer. Furthermore, the sample grown on the 100Å underlayer has an activation volume which is more than a factor 2 greater again. Hence, it is clear that the predominant factor controlling activation volumes in thin film media is the intergranular exchange coupling between the grains entirely consistent with the original suggestion of Wohlfarth [7].

We have also studied films composed of CoPtCr grains grown on underlayers such that a controlled bicrystal or non-bicrystal structure results. These samples were grown at IBM in the group of Dr. M. F. Doerner. The basic parameters for this set of samples are shown in table 2. and the activation volumes in Fig.5, also marked on the right hand abscissa are the physical grain sizes for the films.

Sample	H_c (kOe)	S*	Grain Size (Å)	S_0/N (dB)
D	0.89	0.00	125	23.4
E*	1.66	0.63	200	24.4
F	1.28	0.61	115	34.1
G*	1.75	0.57	220	29.1

Table 2. Properties of CoPtCr films.

From this data it is clear that a correlation between the grain size and the physical volume is not present. The closest correlation found is for film G which in fact was the weakest coupled film as determined by a ΔM analysis. Films D and E were fairly strongly coupled films having a lower content of Cr. In this case we believe that the lower Cr content has resulted in stronger exchange coupling and hence in a higher activation volume. Films F and G having a higher Cr content are less strongly coupled and hence have a somewhat lower activation volume. In our original work on these systems [18] we concluded that the value of the activation volume was a potential predictor of noise in the system since samples having a large activation volume will generally have less smooth transitions than those where the activation volume is smaller.

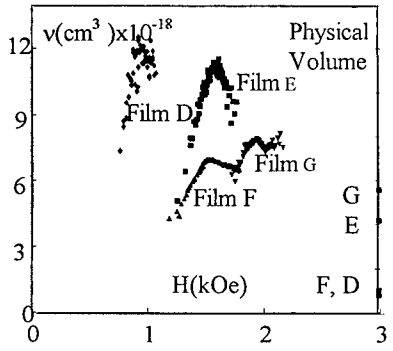

Figure 5. Activation volumes for CoPtCr films.

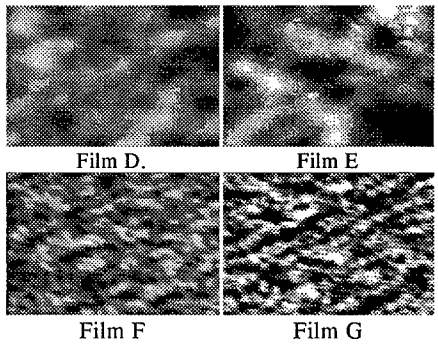

Figure 6. MFM images for CoPtCr films.

Further confirmation of the correlation between the activation volume and the noise sources can be seen in the MFM images in Fig. 6. These images are of the domain structure in the films in the AC erased state. From these images it is clear that samples D and E exhibit substantially larger domains than samples F and G. This is a real physical confirmation of the significance of the

activation volume and indeed it would be expected that the samples with a course grain structure would exhibit larger noise as was found to be the case for these materials.

The question then arises, is it ever the case that the activation volume agrees with the physical volume? This question will only at best ever have an approximate answer due to the inherent experimental errors associated with any technique to measure an activation volume. In an earlier work [19] we have established that the activation volume does agree with the physical volume for ultra-fine (100Å) particles dispersed at low packing fraction (5%) in a non-magnetic matrix.

The only instance where our studies have shown a close correlation between grain size and the activation volume were on films consisting of barium ferrite particles. In this case, due to the non-metallic nature of the films exchange coupling is not possible and such films exhibit exclusively dipolar coupled behaviour. This has been confirmed by measurements of ΔM. Measurements of the activation volume gave values of (280 - 300)Å compared with a physical grain size estimated to be of the order of 350Å. Hence, for an exclusively dipolar coupled film grain size and activation volume can agree.

It is also worth considering the role of thermal activation and the concept of the activation volume in providing and understanding of the phenomenon of thermal loss of magnetisation. It is generally found to be the case that thermal loss of data is observed to follow an lnt law. This is a further manifestation of a range of exponential barriers decaying in unison. A formalism similar to that developed by Gaunt [5] would be expected to explain this phenomenon. Of course, within thin film media there exists a distribution of energy barriers which can be measured by the differential of a remanence curve[17]. Such a distribution is shown in Fig.7.

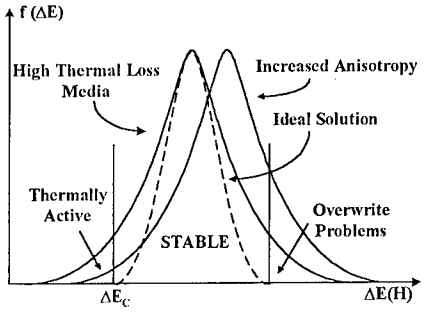

Figure 7. Thermal loss and the energy barrier distribution.

In the figure we have marked schematically those grains which will be expected to be thermally unstable and also those grains having larger energy barriers areas where difficulties with ovewrite would be expected. It is currently suggested that the solution to the thermal loss problem is to increase the overall anisotropy in the system and also shown in the figure is a schematic distribution of the effect of such a change. From this figure it is clear that whilst the thermal loss would be reduced, it would be expected that significant overwrite problems would result from the use of high anisotropy films. Also shown in the figure is the concept of reducing the overall width of the energy barrier distribution which would result in a reduction in overwrite problems whilst simultaneously removing thermal loss effects. This is clearly the ideal solution.

Possible mechanisms to reduce the width of the energy barrier distribution are:

1. A reduction in the width of the grain size distribution.
2. An improvement in the compositional uniformity of the grains within the film.
3. An improvement in the in-plane crystallographic orientation of the grains.
4. An improvement in the uniformity of intergranular exchange coupling.

Thus, it is clear that measurements of parameters such as the activation volume and the detailed characterisation of media including analysis of grain size, will be required in order to allow for improvements in materials and hence in thermal loss performance.

Acknowledgements

The authors wish to acknowledge the previous and ongoing financial support of Seagate Recording Media Division of Fremont, IBM Storage Systems Division of San Jose and the Engineering and Physical Sciences Research Council of the United Kingdom.

REFERENCES

[1] Stoner, E.C. and Wohlfarth, E.P., **240** p.599-642 (1948).

[2] Néel, L., Ann Geophys. **5** p.99 (1949).

[3] Street, R. and Woolley, J.C., Proc. Phys. Soc. p.562-572 (1949).

[4] el-Hilo M., K. O'Grady, R.W. Chantrell and D.P.E. Dickson, J.Mag. and Mag.Mater **123** p30-34 (1993).

[5] P. Gaunt, J.Appl.Phys. **59** (12) p4129-4132 (1986).

[6] Street, R. Wooley, J.C. and Smith P.B., Proc.Phys.Soc. **B65** p.679 (1952).

[7] Wohlfarth, E.P., Phys.Lett., **70A**,5 and 6, p.489.

[8] Estrin, Y. McCormick, P.G. Street, R., J.Phys:Condens. Matter **1** p.4845-4851 (1989).

[9] el-Hilo (submitted to J.Phys.D.).

[10] Lyberatos, A. and Chantrell, R.W., J.Phys:Condens.Matter **9** p.2623-2643 (1997).

[11] Doyle proceedings Intermag. 98 IEEE Trans.Mag. (in press)

[12] Sharrock, M.P. IEEE Trans.Mag. **26**(1) p193-197 (1990).

[13] A-M de Witte, O'Grady K, Coverdale, G.N. and Chantrell, R.W., J.Mag. and Mag. Mater **88** p.183-193 (1990).

[14] el-Hilo, M., deWitte A.M, O'Grady K, and Chantrell R.W., J. Mag.and Mag.Mater **117** p.307-310 (1992).

[15] Bruno, P., Bayreuther, G, Beauvillian, P., Chappert, C., Lugert, G., Renard, D., Renard, J.P. and Seiden, J. J.Appl.Phys. **68** (11) p.5759-57666 (1990).

[16] Sellmeyer, D.J., Shen, Z.S., Liu, Y., Lion, S.H., Malhotra, S.S. and Robertson, B.W., Scripta Metallurgica et Materialia **33** p.1545-1552 (1995).

[17] Mayo, P.I., O'Grady, K., Chantrell, R.W., Cambridge, J.A., Sanders, I.L., Yogi T., Howard, K.J.Mag. and Mag. Mater **95** p.109-117 (1991).

[18] Dova, P. O'Grady, K., Doerner, M.F., and Mirzamaami, M. IEEE Trans. Mag. **33**(5) p.2953-2955 (1997)

[19] de Witte, A-M. and O'Grady, K. IEEE Trans. Mag. **26**(5) p.1810-1812 (1990)

COMPOSITIONAL MICROSTRUCTURE AND MICROMAGNETICS OF Co-BASED THIN FILM MEDIA

M. FUTAMOTO, N. INABA, Y. HIRAYAMA, K. ITO, Y. HONDA
Central Research Laboratory, Hitachi Ltd.
Kokubunji, Tokyo 185, Japan, futamoto@crl.hitachi.co.jp

ABSTRACT

Elemental segregation of CoCrTa and CoCrPt thin films for longitudinal and perpendicular media is investigated using high spacial resolution transmission electron microscopes equipped with compositional analysis facilities. Strong Cr segregation exceeding 20 at% within 1.5-2 nm width is observed along the grain boundaries for both types of CoCrTa films prepared at elevated substrate temperatures. Weaker Cr segregation is observed along the grain boundaries of the longitudinal and the perpendicular CoCrPt films. The strong Cr segregation at grain boundaries is related with the small magnetic cluster size and the low media noise characteristics of CoCrTa thin film media. The Cr content inside the grain is several % lower than the average composition of the CoCrTa films. The magnetocrystalline anisotropy constants(Ku) for different Cr compositions are determined using single crystalline thin film technology to discuss the thermal stability of recorded information.

INTRODUCTION

CoCrTa and CoCrPt thin films are widely applied to longitudinal recording media. They show high coercivities and low noise characteristics which are required properties for high density magnetic recording. The media noise characteristics are interpreted to be associated with the structural and the compositional inhomogeneities of these films, especially non-magnetic Cr segregations. When Cr segregates at grain boundaries, the Cr-rich layer decreases the magnetic exchange coupling between grains, thus increasing the coercivity and reducing the media noise. The size reduction of magnetically isolated grains is an important technology to develop low noise recording media for high density magnetic recording. This is generally realized by reducing the magnetic layer thickness to get a smaller Br·t/Hc value which leads to a higher recording resolution. However, when the grain size becomes smaller than a certain value, thermal instability of recorded information arises[1]. Employment of perpendicular magnetic recording is an effective way to continuously increase the linear recording density because we can employ a thicker recording layer[2,3].

The microstructural Cr segregation in CoCr-based alloy films with both longitudinal and perpendicular easy magnetization axes has been investigated by electron microscopy studies on chemically etched samples[4,5], analytical electron microscopic studies using X-ray energy dispersive spectroscopies[6], and atom-probe field-ion microscopy[7,8]. The existence of ferromagnetic and paramagnetic phases in the CoCr-based alloy films prepared at elevated temperatures are confirmed through these investigations. These investigations also indicate that the compositional microstructure varies greatly depending on the film composition, thickness, deposition conditions, etc. Aanalytical electron microscopes equipped with a field emission electron source have been demonstrated to be very effective in the investigation of the film compositional microstructures[9-11]. Clear Cr segregations at grain boundaries are observed for longitudinal[12-14] and perpendicular CoCr-based alloy films[15,16].

In the present paper, we investigate the structural and the compositional microstructures of longitudinal and perpendicular CoCr-based thin films. From the results of microscopic compositional analysis, we consider it important to determine the magnetic properties of core-grains. Thus we used the single crystal magnetic thin film technology[17] to determine the magnetocrystalline anisotropy constants(Ku) of CoCr-alloy thin films to discuss the thermal stability of recorded bits at high areal densities.

Mat. Res. Soc. Symp. Proc. Vol. 517 © 1998 Materials Research Society

EXPERIMENTAL PROCEDURE

Thin film media preparation, structural and magnetic property measurements

CoCrTa and CoCrPt thin films were deposited by dc magnetron sputtering on heated substrates, with Ar pressures at 2-3mTorr. 10 nm thick carbon was sputter deposited as the protective layer for recording experiments. The structures and the magnetic properties of these samples are summarized in Table 1.

Thin film specimens for plan-view transmission electron microscopy(TEM) were prepared by mechanical polishing followed by ion-beam milling. The film thinning was carried out from the substrate side up to the magnetic layer. The removal of the underlayer of CrTi or Ti was confirmed through analytical TEM by monitoring the intensity of the Ti signal. Two analytical TEM techniques were employed in the present study. One is the electron microscopy with a field emission electron source operated at an acceleration voltage of 200 kV(Hitachi: HF2000) using energy dipersive spectroscopy of characteristic X-rays(EDAX). The electron beam probe diameter is estimated to be 1.5 nm. The other employs a similar field emission source TEM equipped with an imaging filter(Gatan: image filter model 678). The imaging filter was based on the electron energy loss spectroscopy(EELS). It was possible with this method to obtain energy-filtered two-dimensional images of compositional distributions with high spacial resolution of about 1 nm and energy loss spectra with a precision of 0.1 V when the electron microscope was operated at 200 kV[11]. This analysis was applied to map two dimensional compositional distributions.

The media noise characteristics were measured using an inductive write head and an MR read head. The magnetization microstructure images were observed by using a magnetic force microscope.

Table 1 Structures and magnetic properties of CoCrTa and CoCrPt thin films

	Longitudinal Thin Film Media		Perpendicular Thin Film Media	
Composition (Thickness)	$CrCr_{15.2}Ta_{4.3}$ (25nm)	$CrCr_{13.4}Pt_{13}$ (25nm)	$CrCr_{17}Ta_3$ (100nm)	$CrCr_{19}Pt_{10}$ (100nm)
Underlayer (Thickness)	$CrTi_{15}$ (50nm)	$CrTi_{15}$ (50nm)	Ti (30 nm)	Ti (30 nm)
Deposition Temperature	300 C	300 C	230 C	230 C
Ms	460 emu/cc	530 emu/cc	495 emu/cc	470 emu/cc
Hc(Longitudinal)	1.6 kOe	2.9 kOe	0.20 kOe	0.25 kOe
Hc(Perpendicular)	——	——	1.95 kOe	1.60 kOe

Preparation of single crystalline magnetic thin films

To investigate the basic magnetic properties of CoCr-based alloy thin films with uniform microscopic compositions, single crystalline magnetic thin films were prepared by employing an epitaxial thin film growth technique[17,18]. A conventional dc magnetron sputtering system was used to sequentially deposit an underlayer (Cr or CrTi, 50 nm), a Co-alloy thin film(25 nm), and a carbon overcoat (10nm) on a mirror polished MgO(110) single crystal substrate. Magnetocrystalline anisotropy constants(Ku) were determined using magnetic torque measurements carried out on single crystalline magnetic thin films. The structural and compositional properties were studied using a high resolution TEM equipped with an EDAX facility.

RESULTS AND DISCUSSION

Longitudinal CoCrTa and CoCrPt thin film media

(Recording noise characteristics)

The linear recording density dependence of media noise measured for $CoCr_{15}Ta_4$ and $CoCr_{13}Pt_{13}$ longitudinal media are compared in Fig.1. The noise is normalized by the output intensity S_0 recorded at 2 kFCI. The DC-erase noise levels are almost the same for both media, but with increasing linear density, the noise of the $CoCr_{13}Pt_{13}$ medium increases faster than that of $CoCr_{15}Ta_4$. The noise of the $CoCr_{13}Pt_{13}$ medium is 1.6 times that of the $CoCr_{15}Ta_4$ medium at 200 kFCI recording density.

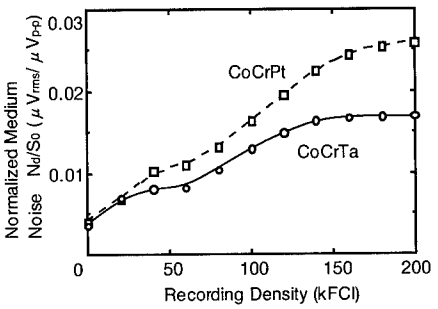

Fig.1 Linear recording density dependence of media noize for longitudinal $CoCr_{15}Ta_4$ and $CoCr_{13}Pt_{13}$ thin films

(Compositional Microstructures)

A plan-view TEM micrograph of the $CoCr_{15}Ta_4$ longitudinal thin film is shown in Fig.2. Electron diffraction analysis indicates that most of the magnetic grains are aligned with their c-axes parallel to the film plane. The parallel lines in the micrograph are the (0001) lattice planes which are perpendicular to the easy magnetization c-axis. It is possible using the EDAX data to determine the local compositions by referring to the average film composition ($CoCr_{15.2}Ta_{4.8}$) determined using a wide or scanned electron beam. The average film composition determined by EDAX was similar to that determined by induction coupled plasma spectroscopy(ICPS). EDAX spectra were obtained using a 1.5 nm diameter electron beam along the analysis line indicated in the TEM micrograph. Fig. 3 shows the local concentrations of Co, Cr, and Ta examined for the two crystalline grains including three grain boundaries. The boundary of the two grains seems to be very sharp with no physical separation nor with an amorphous layer. These two grains are selected for the compositional analysis because of the very sharp contrast of the grain boundaries, which proves that the grain boundaries in the specimen are almost parallel to the incident TEM electron beam. If the grain boundary is slanted with respect to the electron beam, it is not possible to determine accurately the grain boundary composition. The dashed lines in Fig.3 show the average compositions of Co, Cr, and Ta determined by ICPS. It is clear that the Cr concentration is increased at the grain boundaries and is decreased inside of the grains when compared with the average Cr composition. The Cr concentration at grain boundary is 23 - 26 at%, while inside the grain it fluctuates between 6 - 12 at%. The Co distribution shows the opposite profile to that of Cr. Namely, Co is depleted at the grain boundary and is enriched inside the grain though there exists compositional fluctuations within the grain. On the other hand, the Ta distribution seems to be scatted both sides of the average compositional line shown in Fig.3. More data are necessary to discuss the compositional segregation profile of Ta. Fig. 4 shows the compositional distributions measured for another $CoCr_{15}Ta_4$ sample. There is also strong segregation of Cr at grain boundaries though the increase of Cr near the boundaries are not so sharp as compared with the results shown in Fig.3. This could be due to slight slanting of the boundary with respect to the incident electron beam for micro-compositional analysis. The Ta intensity profile in Fig.4 resembles to that of Cr. This result indicates that Ta has a little tendency to segregate at grain boundaries[19]. The width of the Cr-enriched region at the grain boundary is estimated to be 1.5 - 2nm taking into account of the probe diameter and the incident angle towards the grain

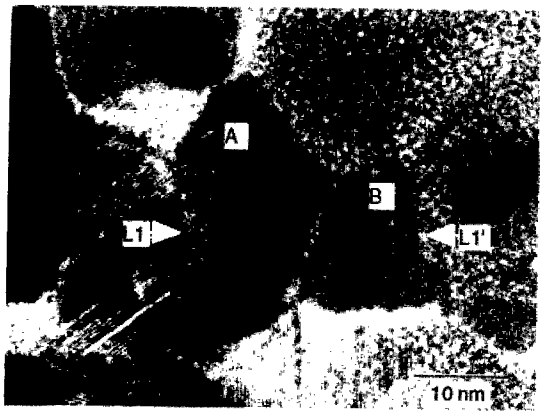

Fig. 2 Plan-view TEM micrograph of CoCr15Ta4 longitudinal thin film. Chemical composition is examined for the grain A and B along L1 - L1' line.

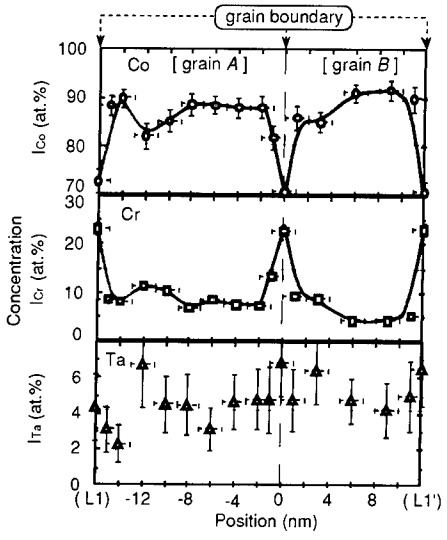

Fig.3 Chemical composition profiles of Co, Cr, and Ta measured for the CoCr15Ta4 longitudinal thin film along L1-L1' in TEM pictureshown in Fig.2.

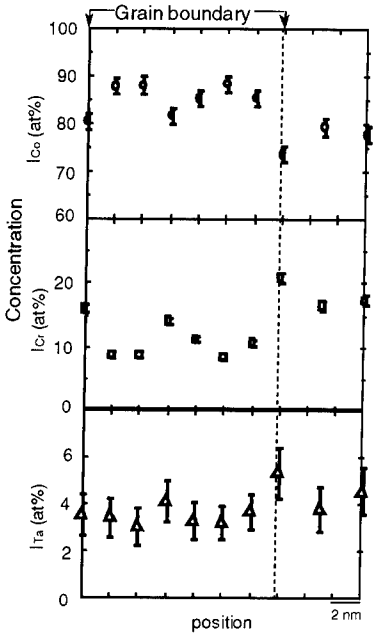

Fig.4 Compositional distributions examined another CoCr16Ta6 longitudinal thin film. Ta shows segregation profile similar to that of Cr.

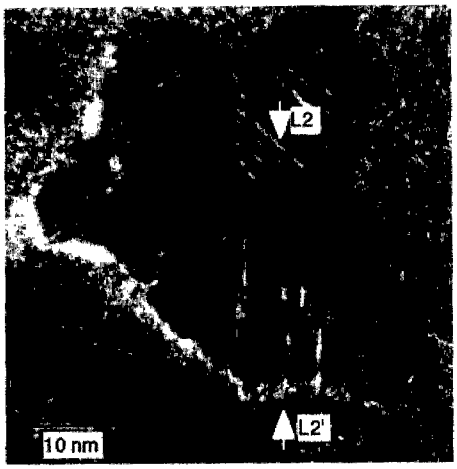

Fig.5 Plan-view TEM micrograph of $CoCr_{13}Pt_{13}$ longitudinal thin film.

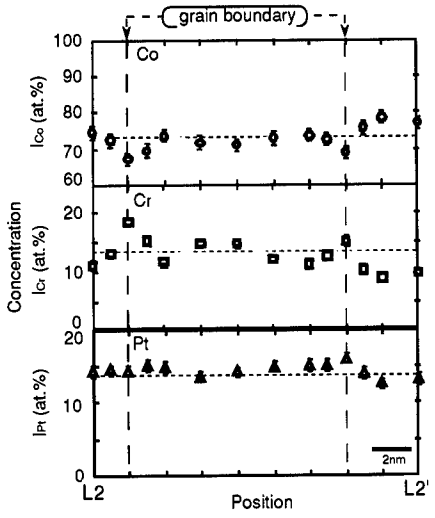

Fig.6 Chemical compositional profiles examined along L2-L2' in the corresponding TEM image of Fig.5.

boundary[14].

Fig. 5 shows a crystalline lattice image of the $CoCr_{13}Pt_{13}$ thin film, which indicates that the easy magnetization axes of the grains are lying parallel to the substrate. Local compositions were investigated along the L2-L2' line shown in the TEM micrograph. The result is shown in Fig.6. The $CoCr_{13}Pt_{13}$ thin film has also Cr segregated grain structure but the amount of Cr concentration at a grain boundary is lower than the previous $CoCr_{15}Ta_4$ thin film case. The Cr composition at the grain boundary is 16 - 18 at% which is only 2 - 4 at% greater than the average Cr composition. The width of the Cr segregated boundary is estimated to be 2-3 nm which is larger that that of the $CoCr_{15}Ta_4$ film. The chemical composition at a distance more than 2 nm inside from the boundary seems almost the same with the average compositon($CoCr_{13.4}Pt_{13.0}$). The Pt shows an almost flat distribution along the analysis line. These results together with repeated experiments using other parts of the sample show that the amount of Cr segregation at grain boundaries and the diffusion distance of Cr are far smaller than the case of the $CoCr_{15}Ta_4$ thin film though the films were deposited under a similar substrate temperature condition.

Perpendicular CoCrTa and CoCrPt thin film media

(Recording noise characteristics)

The linear recording density dependence of media noise measured for the $CoCr_{17}Ta_3$ and the $CoCr_{19}Pt_{10}$ perpendicular media is shown in Fig.7. In contrast to the case of longitudinal media, the perpendicular media noise does not increase much with increasing linear recording density. The DC-erase noise level of the $CoCr_{17}Ta_3$ medium is more than 60% lower than that of $CoCr_{19}Pt_{10}$ perpendicular medium and this difference is maintained almost up to 300 kFCI.

(Compositional Microstructures)

Scanning electron micrographs of the perpendicular $CoCr_{17}Ta_3$ and the $CoCr_{19}Pt_{10}$ thin films are compared in Fig.8. The compositions and the magnetic properties are shown in Table 1. The surface grain diameters of these samples are nearly the same at about 30 nm. Fig. 9 shows the plan-view TEMs and the local composition distributions of the $CoCr_{17}Ta_3$ and $CoCr_{19}Pt_{10}$ recording media. The electron diffraction analysis showed that the easy magnetization axes of the grains are perpendicular to the film planes. Compositional distributions examined by EELS across the grain boundaries are also shown in Fig.9. Strong Cr segregation of more than 30 at% is recognizable at grain boundaries for the $CoCr_{17}Ta_3$ perpendicular recording medium. On the contrary, the Cr content at most of the grain boundaries of the $CoCr_{19}Pt_{10}$ thin film is lower than 25 at%. When the Cr content exceeds 25 at% in the Co-Cr alloy binary system, the region becomes paramagnetic at room temperature[20]. The Cr segregation at the $CoCr_{19}Pt_{10}$ thin film grain boundaries seems insufficient to decouple the magnetic exchange between the neighboring magnetic grains. On the other hand, the magnetic exchange between neighboring grains seems to be decoupled for the perpendicular $CoCr_{17}Ta_3$ thin film, judging from the strong Cr segregation at grain boundaries. This magnetic behavior should be related with the magnetization structure. The magnetization microstructures of the DC-erase state are compared between the perpendicular $CoCr_{17}Ta_3$ and the $CoCr_{19}Pt_{10}$ thin films. The MFM images are shown in Fig. 10. The dark contrast regions in the MFM images correspond to the reversed magnetic domains or to the magnetization irregularities which are the major noise source in perpendicular recording media[21,22]. The average size of magnetization irregularities are estimated to be 75 and 130 nm for the $CoCr_{17}Ta_3$ and the $CoCr_{19}Pt_{10}$ perpendicular media, respectively. The size is 2 to 3 times greater than the average magnetic crystalline grain diameter of the $CoCr_{17}Ta_3$ medium. It is several times greater than the grain diameter of the high DC-erase noise $CoCr_{19}Pt_{10}$ perpendicular medium. The magnetization irregularity size is expected to depend on the magnetic interaction strength between the neighboring grains. It seems reasonable that the $CoCr_{17}Ta_3$ medium shows the smaller size magnetization irregularity where Cr segregation greater than 25 at% is observed at grain boundaries.

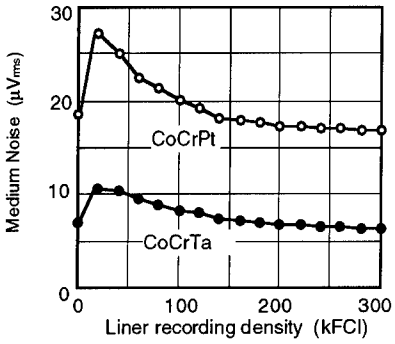

Fig.7 Linear recording density dependence of media noise for perpendicular $CoCr_{17}Ta_3$ and $CoCr_{19}Pt_{10}$ thin film media

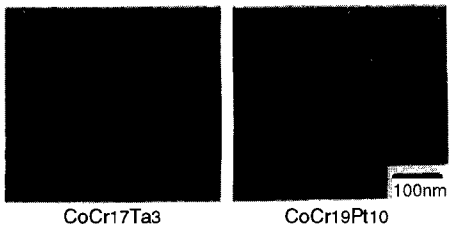

Fig.8 Surface morphorogies of perpendicular $CoCr_{17}Ta_3$ and $CoCr_{19}Pt_{10}$ perpendicular thin films.

In the case of the longitudinal medium, the major noise source is known to be the magnetization transitions. When the magnetic exchange interaction between grains is stronger while other properties including Hc, Br·t, Ms, etc. are assumed to be similar, the magnetization transition will broaden by forming wider zigzag transitions. It seems necessary to further

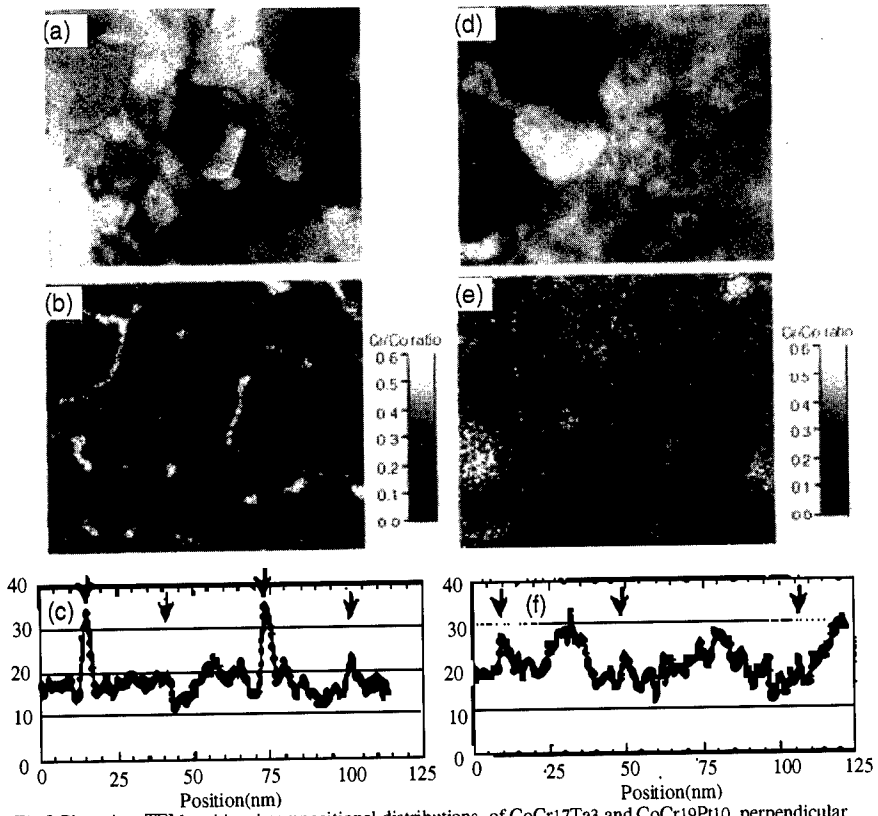

Fig.9 Plan-view TEM and local compositional distributions of CoCr17Ta3 and CoCr19Pt10 perpendicular recording media.

CoCrTa: (a) TEM image, (b) Two dimentional EELS image. Bright contrast shows high Cr concentration. (c) Line-scan Cr intensity distribution. Arrows show grain boundaries.

CoCrPt: (d) TEM, (e)Two dimentional EELS image, (f) Line-scan Cr intensity distributions.

enhance the nonmagnetic element(Cr) segregation at grain boundaries of $CoCr_{19}Pt_{10}$ thin films for both the longitudinal and the perpendicular recording media.

The CoCrTa thin films seem to be closer to ideal recording media in terms of magnetic exchange decoupled structure which is the necessary condition for a low noise medium. It is interesting to make a grain model for the low noise medium based on, for example, the experimental results obtained with the longitudinal CoCrTa medium.

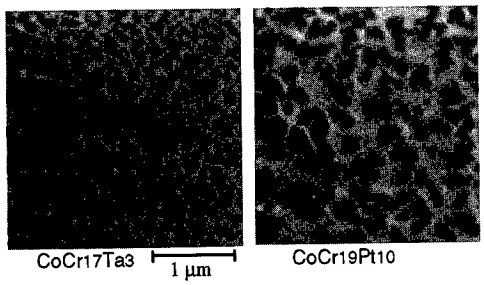

Fig. 10 DC-erased state MFM images of perpendicular CoCr17Ta3 and CoCr19Pt10 thin film media

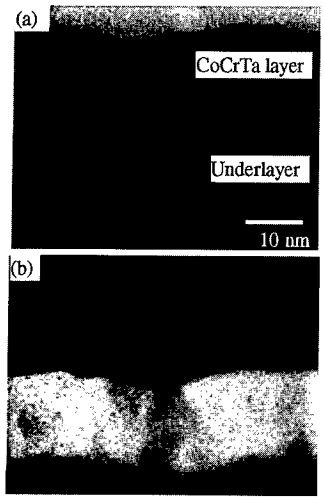

Fig.11 Cross-sectional TEM (a) and Cr intensity EELS image (b) of longitudinal $CoCr_{15}Ta_4$ film.

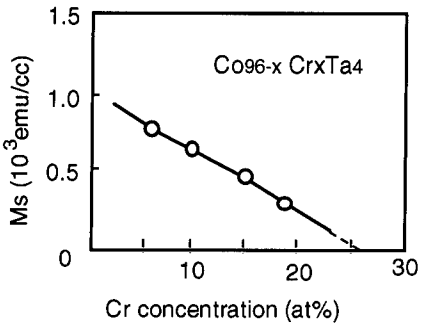

Fig. 12 Cr concentration dependence of saturation magnetization(Ms) for $Co_{96-x}Cr_xTa_4$ thin film system.

Such a model can be used for recording property and thermal stability considerations in computer simulations[23,24]. We take into account (1)plan-view Cr segregation structure, (2) cross-sectional Cr segregation structure, (3) average grain size, (4)number of nearest neighbor grains, (5)Ms value of CoCrTa with different Cr composition, (6)average Ms, and (7)magnetic layer thickness. Careful EDAX analysis using a finely focused electron beam while changing the incident beam angle with respect to the sample[14] indicates that the Cr enriched thickness is 1nm and the average Cr composition is 22.9 at%. The analysis also indicates that the average Cr concentration inside the grain core is 9.1 at%. The cross-sectional Cr intensity image observed by EELS-TEM is shown in Fig.11. The interface between the $CoCr_{15}Ta_4$ magnetic layer and the Cr-based underlayer is very sharp, indicating no strong Cr diffusion form the underlayer toward the magnetic layer. The Cr content inside the CoCrTa layer seems to be homogeneous along the film growth direction. It is not possible from the cross-sectional EELS-TEM data to profile the Cr concentration along one crystalline grain because of overlapping with the other grains along the thickness direction and the limited resolution(1 nm). It seems reasonable, when considering the Cr diffusion behavior from the interior to outside the grain, to assume a similar thickness of Cr enriched layer at the bottom and at the surface of the grain. The average grain diameter and the number of nearest neighbors are determined to be 13.2 nm and 5.4, respectively from the plan-view TEM analysis. The nearest neighbor grain value of 5.4 indicates that the grain can be approximated to be hexagonal with 6 nearest neighbor grains. To estimate the saturation magnetization values of the grain model and to compare the average Ms values measured for the sample, the Ms dependence on Cr concentration is determined using $Co_{96-x}Cr_xTa_4$ samples as shown in Fig.12. The threshold composition of Cr above which the material transforms to non-magnetic is estimated to be 27 at%. Fig. 13 shows the crystalline grain model of the $CoCr_{15}Ta_4$ longitudinal medium. From the data, the Ms value of the Cr enriched(22.9 at%) 1 nm thick shell around the hexagonal magnetic core shell is assumed to be 80 emu/cc, while the Ms of core(Cr:9.1 at%) is assumed to be 650 emu/cc, respectively. The average Ms value calculated from the model crystal grain is 500 emu/cc which is nearly equal to the experimentally determined Ms value of 460 emu/cc.

The amount of Cr segregation of the model still seems insufficient to decouple the magnetic exchange coupling. A similar model can be made for the perpendicular $CoCr_{17}Ta_3$

medium. We should also note that the composition of the grain core, which plays an important role in determining the magnetic properties including the thermal stability of recorded information, is different from that expected from the average composition. It is apparent that we should take into account the intrinsic magnetic properties of crystalline core materials, especially with magnetic exchange decoupled low noise medium.

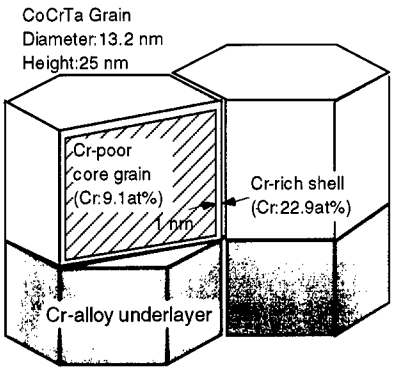

Fig. 13 Crystalline grain model of the CoCr15Ta4 longitudinal medium. Co-richi core grain is surounded by Cr-rich thin shell.

Fig.14 Plan-view TEM micrograph of single crystalline CoCr15Ta4 thin film.

Determination of magneto-crystalline anisotropy constants

In order to determine the intrinsic magnetic properties including Ku value, it is necessary to prepare a well defined Co-alloy thin film specimen with uniform composition and a similar stacking structure to that used in the recording medium. The lattice matching between the underlayer and the Co-alloy magnetic layer is known to give some influence to the magnetic properties[18]. Thus, we used single crystalline thin films with Cr or Cr-alloy underlayers formed on MgO(110) single crystal substrates with layer thicknesses similar to those used for the recording medium[25] to measure the Ku values of Co-alloy thin films. A plan-view TEM micrograph of a $CoCr_{15}Ta_4$ thin film prepared using the technique[26] is shown in Fig.14. X-ray and TEM diffraction analyses showed that the film is single crystalline. The local Cr composition examined by EDAX remained close to the average composition(15.2at%) with $\pm$ 3% fluctuation[26]. No strong segregation was observed for single crystalline Co-alloy thin films prepared on MgO(110) substrates.

Ku values of some Co-alloy thin films determined using single crystalline films are shown in Table 2. The Ku values determined for single crystalline thin films using the magnetic torque method are found to be higher than those determined using a rotational hysteresis loss method. The Ku value(1×10^6 erg/cc) of a polycrystalline $CoCr_{15}Ta_4$ longitudinal medium determined by rotational hysteresis loss method is nearly 30% lower than that(1.3×10^6 erg/cc) determined using the single crystalline $CoCr_{15}Ta_4$ thin film. It is pointed out by Uesaka et al. that the Ku value can change greatly depending on the determination method as well as the microstructure of the sample[27]. When Cr segregation is taken into account, the difference in Ku will be further enhanced. A higher Ku value(2.8×10^6 erg/cc) is observed for the single crystalline $CoCr_8Ta_4$ thin film whose composition is similar to the core grain of the Cr segregated $CoCr_{15}Ta_4$ polycrystalline film. It is clear that the Ku value of the core grain is

Table 2 Ku values determined using single crystalline magnetic thin films. KuV/kT values are calculated assuming several grain sizes for longitudinal and perpendicular recording media.

		KuV/kT				
	Ku (x 10^6 erg/cc)	Longitudinal media (h/d=1.0)			Perpendicular media (h/d=3.0)	
	Grain volume: $(8\ nm)^3$	$(10\ nm)^3$	$(15\ nm)^3$	24nmx$(8nm)^3$	30nmx$(10nm)^3$	
CoCr15Ta4	1.3	16	31	106	48	93
CoCr12Ta4	1.8	22	44	147	66	132
CoCr8Ta4	2.8	35	68	230	105	204
CoCr15Pt12	3.3	41	80	270	123	240
Co	4.5	56	109	368	168	327

more than twice that estimated by the rotational hysteresis method using the polycrystalline $CoCr_{15}Ta_4$ specimen. Details of the Ku determination will be published elsewhere.

In Table 2, the KuV/kT values of Co-alloy grains are calculated assuming some grain volumes for longitudinal and perpendicular recording modes. The grain aspect ratio h/d (h: height, d:diameter) is assumed to be 1.0 for longitudinal media and 3.0 for perpendicular media, respectively. When the KuV/kT values becomes smaller than a certain value, the recorded output intensity begins to decrease drastically. Several threshold KuV/kT values are reported based on the experiments [28,29] and computer simulations[24]. It should be pointed out that the KuV/kT value can change by more than 200% depending on the method of Ku determination. Here, for example, when the threshold value of 100[24,29] is assumed, it is clear from the Table 2 that Co-alloy recording media can be used down to 8 nm grain diameter by employing a perpendicular recording mode. On the contrary, it is necessary to keep the grain diameter greater than 15nm in the longitudinal recording mode. The maximum linear recording density where we can assure a reasonable thermal stability of recorded information seems to be limited around 300 - 400 kFCI (bit length:83 - 62nm) with a longitudinal recording mode, as it seems necessary to have at least several crystalline grains within the bit transitions to assure an acceptable media S/N ratio. More detailed studies considering other factors such as the crystalline grain distribution and the temperature dependence of magnetic properties are needed to estimate the attainable linear recording density with Co-based alloy recording media. The proposed crystalline grain model based on the experimental results and the Ku values determined using single crystalline thin films are believed to be useful to discuss the future media properties.

CONCLUSIONS

The compositional microstructures of Co-based longitudinal and perpendicular recording media is investigated using high-resolution analytical electron microscopies. Clear Cr segregation is observed for both types of media sputter deposited at elevated temperatures. The Cr concentration at grain boundaries of CoCrTa thin films is several % greater than the average Cr concentration for both type of the media. The thickness of the Cr-enriched region at grain boundaries is estimated to be 1.5 - 2 nm. The Co compositional distribution is opposite to the case of Cr, while that of Ta seems to show similar segregation profile to that of Cr. The amount of Cr segregation for the longitudinal and the perpendicular CoCrPt thin films are only 2 - 4 % greater than the average composition. The Cr distribution profiles inside of the grains are very similar between the longitudinal and perpendicular thin film media. The strong Cr segregation at grain boundaries is related with the small magnetic cluster size and the low media noise characteristics of CoCrTa thin film media.

A model grain structure for the longitudinal CoCrTa thin film media is proposed based on the experimental studies. It is pointed out that the alloy composition of the core magnetic grain is different from the average film composition. It is necessary to take into account the

core magnetic properties to discuss properties such as the thermal stability of recorded information.

Single crystalline thin films formed on MgO(110) substrates with similar layer stacking structures to those of recording media are used to determine the magnetocrystalline anisotropy constants. The Ku values thus determined are a useful base-data to discuss the thermal stability of recorded information.

ACKNOWLEDGMENTS

The authors would like to thank Drs. K. Kimoto and K. Usami of Hitachi Research Laboratory for discussions and cooperation of the EELS experiment. They also express gratitude to Prof. Y. Sugita of Tohoku University and Prof. Y. Uesaka of Nihon University for useful discussions.

A part of this work was carried out under the ASET program supported by NEDO, Japan.

REFERENCES

[1] P-L.Liu and S.H.Charap, IEEE Trans. Magn. 30, 4230(1994).

[2] S.Iwasaki, K.Ouchi, and N.Hondaa, IEEE Trans. Magn. 32, 3795(1996).

[3] M.Futamoto, Y.Honda, Y.Hirayma, K.Itoh, H.Ide, and Y.Maruyama, IEEE Trans. Magn. 32, 3789(1996).

[4] Y. Maeda, S. Hirono, and M. Asahi, Jpn. J. Appl. Phys.,24,L951(1985).

[5] D. Rogers, Y. Maeda, and K. Takei, J. Mag. Soc. Jpn. 18, Suppl.S1, p79(1994).

[6] J. N. Chapman, I. R. McFadyen, and J. P. C. Bernards, J. Mag.n. Magn. Mater. 62, p359(1986).

[7] K. Hono, S. Babu, Y. Maeda, N. Hasegawa, and T. Sakurai, Appl. Phys. Lett., 62,p2504(1993).

[8] K. Hono, K. Yeh, Y. Maeda, and T. Sakurai, Appl. Phys. Lett. 66, p1686(1995).

[9] N. Inaba, Y. Matsuda, M. Suzuki, A. Nakamura, and M. Futamoto, J. Appl. Phys. 75, p6126(1994).

[10] M. Futamoto, Y. Matsuda, N. Inaba, M. Suzuki, and Y. Honda, J. Magn. Magn. Mater. 134,p298(1994).

[11] K. Kimoto, T. Hirano, K. Usami, and H. Hoshiya, Jpn. J. Appl. Phys. 33, L1642(1994).

[12] M. Futamoto, Technical Report of IEICE, MR94-81, p53(1995-2).

[13] Y. Yahisa, K.Kimoto, K. Usami, Y.Matsuda, J.Inagaki, K.Furusawa, and S.Narishige,IEEE Trans. Magn. 31, 2836(1995).

[14] N.Inaba, T.Yamamoto, Y.Hosoe, and M.Futamoto, J. Mag. Magn. Mater. 168, 222(1997).

[15] K. Kimoto, Y. Hirayama, and M. Futamoto, Magn. Magn. Mater.159, 401(1996).

[16] Y.Hirayama, M.Futamoto, K.Kimoto, and K.Usami, IEEE Trans. Magn. 32, 3807(1996).

[17] A.Nakamura, M.Koguchi, and M.Futamoto, Jpn. J. Appl. Phys. 34, 2307(1993).

[18] N.Inaba, A.Nakamura, T.Yamamoto, Y.Hosoe, and M.Futamoto, J. Appl. Phys. 79, 5354(1996).

[19] K.M.Kemner, V.G.Harris, W.T.Elan, Y.C.Feng, D.E.Laughlin, and J.C.Woick,IEEE Trans. Magn. 31, 2806(1995).

[20] W.G.Haines, J. Appl. Phys. 55, 2263(1984).

[21] Y.Honda, Y.Hirayama, K.Ito, and M.Futamoto, J. Mag. Soc. Japan. Vol.19, Suppl. No.S2, 10 (1995).

[22] Y.Honda, Y.Hirayama, K.Ito, and M.Futamoto, The 7th Joint MMM-Intermag Conference, GT-03.

[23] J.G..Zhu,"Micromagnetics of Thin Film Media" in Magnetic Recording. edited by C.D.Mee and E.D.Daniel, McGraw-Hill(New York,1995).

[24] Y.Uesaka, Y.Takahashi, Y.Nakatani, N.Hayashi, and H.Fukushima, Technical Report of IEICE, MR96-37, 7 (1996.11).

[25] M.Futamoto, N.Inaba, A.Nakamura, and Y.Honda, to be published in Acta/Scripta Materialia.

[26] N.Inaba, M.Futamoto, and A.Nakamura, The 7th Joint MMM-Intermag Conference, AB-13.

[27] Y.Uesaka, K.Yoshida, Y.Nakatani, and N.Hayashi, J. Appl. Phys. 77, 5303 (1995).
[28] E.N.Abarra and T.Suzuki, IEEE Trans. Magn. 33, 2995 (1997).
[29] Y.Hosoe, I.Tamai, T.Tanahashi, Y.Takahashi, T.Yamamoto, T.Kanbe, and Y.Yajima, IEEE Trans. Magn. 33, 3208(1997).

MAGNETIC FORCE MICROSCOPY ANALYSIS OF THERMAL STABILITY IN LONGITUDINAL MEDIA

E. N. ABARRA*, I. OKAMOTO**, AND T. SUZUKI*
*Toyota Technological Institute, Nagoya 468, Japan, eabarra@toyota-ti.ac.jp
**FUJITSU Ltd., Atsugi 243-01, Japan

ABSTRACT

The thermal stability of written bits in high density longitudinal recording media is investigated using magnetic force microscopy (MFM). The time dependence of the MFM signal is examined for different linear densities on CoCrPt–based media of various thickness. At ambient temperature, lesser decay is observed using the MFM compared to spin stand measurements on the same CoCrPtTaNb media on Al which emphasizes the dependence of bit stability with writing conditions. Moderate anneals at 373 K reveal a rapid initial ~ 10% signal decay followed by stable behavior not observed in the magnetization time dependence measurements. 200 kfci tracks on a 20-nm thick CoCrPtTa medium on Si with a coercivity of 3 kOe displayed stable (~ 2%) behavior against a 105-hour anneal at 373 K in air. These results are correlated with media properties to obtain parameters that are good indicators of thermal stability performance.

INTRODUCTION

A significant issue in the increase of linear density in longitudinal magnetic recording is the adverse effect of thermal agitation due to the reduction in size and the magnetic isolation of the grains [1,2]. Many studies have been made especially by magnetometry and spin stand measurements [3,4]. However, correlation of the above measurements with other relevant magnetic properties and with changes in the magnetization patterns due to thermal decay is further needed, especially at elevated temperatures recording media may be subject to. We have recently reported magnetic force microscopy (MFM) investigations of magnetic domain pattern stability with annealing [5] and signal change with time [6]. Detection of signal changes for the latter was made possible by checking the MFM tip sensitivity against previously written tracks [6]. In this paper, we present annealing studies near 373 K on CoCrPtTaNb media on textured NiP/Al [6,7] and on high coercivity CoCrPtTa media on Si.

EXPERIMENT

Media

Two sets of CoCrPt-based media were investigated, one on Al and the other on Si substrates. The media on Al are made of CoCrPtTaNb (CCPTN hereafter), the same composition used for the 8 Gbit/in^2 demonstration [7]. The media on Si are made of CoCrPtTa (CCPT hereafter). For CCPTN, media of thickness δ = 10, 16, 25 nm were sputtered, by varying the deposition time, on a 25 nm-thick CrMo seed layer on NiP/Al substrates textured along the track direction. A detailed description of the structure and room temperature magnetic properties of the textured CCPTN media is given elsewhere [6,7]. Here, a summary of the magnetic properties and selected properties at elevated temperatures is provided. The CCPT media (δ = 20 nm) was also sputtered onto a CrMo underlayer. Moreover, a thin buffer layer was first deposited on the Si substrate to break the crystal epitaxy.

Mat. Res. Soc. Symp. Proc. Vol. 517 © 1998 Materials Research Society

Magnetic Force Microscopy

For the CCPTN media, tracks with linear recording densities up to 240 kfci were first written for spin stand measurements at ambient temperatures covering a period of 65 hours. The change in signal was determined by comparing with a newly written track as described in [3]. For the MFM study, bits were allowed to decay for a while and were later used to detect changes in the tip sensitivity when investigating new tracks [6]. These "calibration" tracks decay negligibly during the period over which newer patterns may be degrading. Written bits were imaged approximately 30 minutes after writing. The same bits were examined over a month. For the annealing studies, several chips were prepared from the disk and heated to ~ 373 K in vacuum ($<10^{-7}$ Torr). MFM scans of the *same* bits were made at room temperature before and after annealing. Locating the same bits on the CCPT media was much more difficult. Therefore, the average signal profile of many transitions in a test coupon was compared to those of annealed coupons from the same Si disk. For the media on Si, annealing was made at 373 ± 2 K in air over a hot plate.

Magnetic Characterization

A vibrating sample magnetometer (VSM) was used to measure the saturation magnetization M_s. Remanence curves, magnetization time dependence, and coercivity variation with sweeping field were obtained at room temperature using an alternating gradient force magnetometer (AGFM). Time dependence experiments at 373 K were made using a SQUID magnetometer. The grain anisotropy K_u was estimated using a 45-degree technique suggested by H. N. Bertram and J.-G. Zhu [8,9]. The extrapolated torque L_∞ at infinite magnetic field is given by

$$L_\infty = 2\pi M_s^2 + aK_u, \qquad (1)$$

where a = ½ for a 2-d random c-axis distribution. X-ray data indicate the c-axes to be in plane; a 2-d random orientation was assumed for both media on different substrates. Some anisotropy in the c-axis distribution is expected for the media on textured NiP/Al [10] but this does not change the factor a very much; the anisotropic contribution effect is estimated to be < 10%. For the CCPTN media, the rotational hysteresis loss W_r technique tended to underestimate K_u which could be due to the difficulty in determining when $W_r = 0$ in an inverse field H^{-1} scale [6].

RESULTS AND DISCUSSIONS

Magnetic Properties

Table I lists selected properties of the media at room temperature. The CCPT media on Si exhibits a large coercivity. The room temperature grain anisotropy is significant for this composition, $K_u = 2.2 \times 10^6$ erg/cm^3, compared to 1.6×10^6 erg/cm^3 (average of $\parallel$ and $\perp$ to track values) for CCPTN. Selected magnetic properties at 373 K and 423 K are shown in Table II.

Figure 1 shows the dependence of the coercivity with sweeping field for both media. The Barkhausen volume is estimated from the slope of the following relationship derived by P. Bruno *et al.* [11],

$$H^*_C = (\ln(dH/dt) + const.)\, k_B T/M_S V^*, \qquad (2)$$

where V^* is the Barkhausen volume which corresponds to the unit of switching magnetization at

TABLE I
STRUCTURAL AND ROOM TEMPERATURE MAGNETIC PROPERTIES

magnetic layer δ	20 nm	25 nm	16 nm	10 nm
Substrate	Si	NiP/Al	NiP/Al	NiP/Al
M_S (emu/cm^3)	340	265	270	~ 240
$M_r\delta$ (memu/cm^2)	0.56	0.61	0.35	0.2
S^*	0.82	0.70	0.62	< 0.5
H_C (Oe) [a]	3100	2760	2360	1315
K_u (10^6 erg/cm^3)	2.2	1.6	1.6	1.6
K_uV/k_BT [b]	142	130	83	52

(a) dH/dt = 50 Oe/s for CCPT and 1000 Oe/s for the CCPTN media (track direction).
(b) V is average grain size estimated from TEM measurements of 25 nm-thick medium on NiP/Al, K_u is also from 25 nm-thick medium value; for CCPT, V^* is taken as V.

TABLE II
MAGNETIC PROPERTIES AT VARIOUS TEMPERATURES

	25 nm CCPTN		20 nm CCPT	
	373 K	423 K	373 K	423 K
M_S (emu/cm^3)	~ 230	~205	333	~ 330
$M_r\delta$ (memu/cm^2)	0.45	-	0.49	-
H_C (Oe)	1530	-	2300	-
K_u (10^6 erg/cm^3)	1.3	1.25	1.45	1.26
K_uV/k_BT	84	71	87	57

least for fields near H_C. Assuming cylindrical grains, the estimated diameter is approximately 13 nm for all the media investigated. TEM observations of the 25 nm-thick CCPTN medium are consistent with the above estimation.

Various magnetic properties of CCPTN have been reported before [6]. Figure 2 shows the magnetization decay per decade seconds with reversing field H_r for various CCPTN media thickness along the track direction and for the 20 nm-thick CCPT medium. This was obtained from time dependence measurements where the media were first saturated followed by application of a H_r to mimic the effect of demagnetizing fields. The magnetization decayed with time

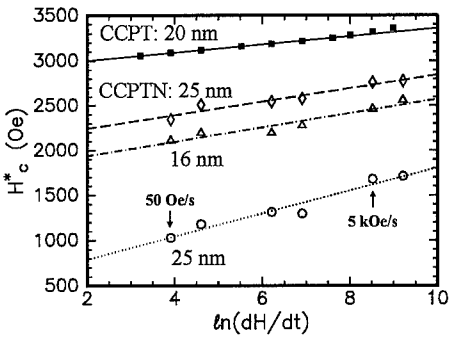

Fig. 1. Apparent coercivity with sweeping field for CCPT media (■) and for CCPTN media (open symbols).

at different rates indicating a range of activation energies. The data at 295 K were taken at $t = 10^1$ and 10^3 seconds while the data at 373 K were from $t = 10^2$ and 10^4 seconds. The K_uV / k_BT values are given in parentheses. Small decay rates (< 2%) are observed for all media at room temperature even for H_r = - 800 Oe. For the 16 nm-thick CCPTN media, the rate of decay dramatically increases at 373 K which is not a very high temperature compared to that inside an operating disk drive.

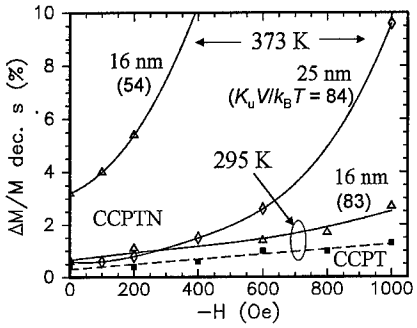

Fig. 2. Magnetization decay per decade seconds with reversing field for CCPT (■) and CCPTN media (open symbols). Lines are fits to the data. $\Delta M / M$ = 10.3 % for 16 nm-thick sample at 373 K and -600 Oe.

Dependence on the ratio K_uV / k_BT is not very clear in the rate of decay (compare, for example, K_uV / k_BT = 77 for the 16 nm-thick CCPTN medium at 295 K and 84 for 25 nm-thick medium at 373 K). $M_r\delta$ decreases with temperature which should lead to more stable behavior. The ratio $M_r\delta / H_C$ which is a measure of the transition length is ~ 18 nm for the 16 nm-thick sample at 295 K and increases to ~ 24 nm at 373 K. However, $M_r\delta / H_C$ ~ 37 nm for the 25 nm-thick medium such that no clear dependence on this ratio can be established. The instability behavior seems to be more correlated to the coercivity than the above-mentioned parameters. However, the coercivity itself is dependent on K_u and the intergranular interactions in the medium. The contribution of pinning due to structural inhomogeneity may be significant but is expected not to be strongly temperature dependent over the narrow temperature range under consideration compared to the grain magnetic anisotropy and intergranular interactions. A decrease in K_u and an increase in the intergranular interactions are consistent with a decrease in the coercivity. However, this leads to the unexpected conclusion that increased (exchange) interaction leads to more significant magnetization decay in a reversing field. This increase may, however, explain the subsequent stability observed in written bits as described below.

From a magnetization decay point of view, media with high coercivities at drive operating temperatures are needed. Therefore, media with sufficiently high Curie temperatures are essential.

MFM Signal Decay: CCPTN at 373 K

Magnetization measurements are relatively easy to obtain and it is of interest to determine the correlation with the actual bit signal decay. Figure 3 shows the decay in signal of written bits for different chips annealed at 373 K in vacuum up to 18 hours. The signal is normalized to the original signal before annealing. (The scatter in the data is likely due to the difficulty in controlling the temperature or in preventing overshoots.) There is a rapid decrease in the signal followed by a stable behavior; the chips annealed at 2 hours do not show any further decay after 16 hours of further anneal. No apparent correlation with the magnetization time dependence data is observed. Obviously, the magnetization configuration in a bit transition, acted on by time dependent demagnetizing fields, is quite different from that of a saturated state acted on by a constant applied reversing field. Direct measurement of the signal decay is therefore necessary to predict bit stability.

The rapid decrease in the MFM signal may correspond to small decoupled grains which

become superparamagnetic at 373 K. Small grains are expected to form near the magnetic layer/underlayer interface [3]. The rapid signal decay observed for both the 16 nm and 25 nm-thick media indicates similar proportion of small unstable particles. This suggests that small grains are not necessarily confined at the interface but may be distributed evenly throughout the film thickness. Alternatively, the initial decay may simply be due to the reduction in the coercivity and thus to a reduction in the stability of the magnetization against demagnetizing fields H_d. The relaxation of the transition length lowers H_d which may explain the subsequent stability. The enhance exchange interaction mentioned above may also have a significant effect.

MFM Signal Decay: CCPTN at 295 K

We have earlier reported room temperature MFM data for the CCPTN media [6]. Due to the time lag between writing and MFM imaging, it was difficult to establish the reference signal near $t = 0$. Figure 4 shows the change in signal over various times for different linear densities. Spin stand results for the 25 nm-thick medium reveal stable behavior but not for the 10 nm-thick medium. The > 5% difference between the MFM and GMR read head results cannot be explained by differences in the reference (t = 0) signal. The read head width was narrow enough not to be adversely affected by the track edges. The head was parked and not directly on top of the written tracks when the signal was not being monitored such that any small head field and or head permeability effects can be ruled out. However, different heads were used to write the data for the spin stand and the MFM experiments which suggests that the subsequent behavior of written bits can be significantly affected by write head parameters such as the head field and field gradient. However, this should be more significant for high linear densities. A more evident cause for the discrepancy may simply be the indirect second derivative sensitivity of the MFM to the stray field.

MFM Signal Decay: CCPT at 373 K

200 kfci tracks on the CCPT medium exhibited stable behavior (± 2%) for a 105-hour anneal at 373 K in air. The ratio $K_uV/k_BT = 87$ at 373 K compared to 84 for the 25 nm-thick CCPTN medium. No initial rapid signal decrease was observed. At 373 K, the CCPTN coercivity is much less than that of the CCPT medium (1530 Oe vs. 2300 Oe) which may account for the

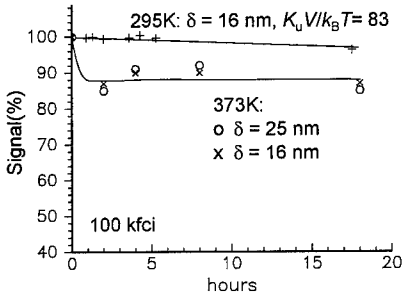

Fig. 3. Signal decay with time for 25 and 16 nm-thick CCPTN media at 373 K. Data for 16 nm-thick medium at 295 K is shown for comparison.

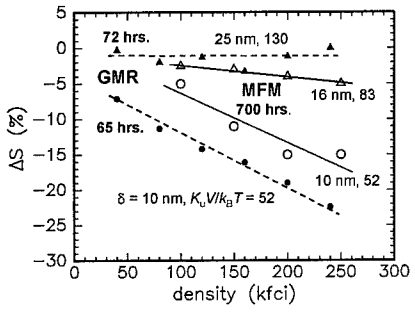

Fig. 4. Change in signal for 2 μm wide bits at ambient temperatures determined by a GMR head and a MFM for various recording densities and magnetic layer thickness.

difference in thermal stability behavior, consistent with the results shown in Fig. 2.

Annealing at 398 K for 1 hour resulted in dramatic changes: ~5% decrease in the signal for 100 kfci tracks and ~14% signal decrease for 200 kfci tracks. The grain anisotropy is still significant above 398 K. At 423 K, $K_u \sim 1.3 \times 10^6$ erg/cm^3 but $K_uV/k_BT = 57$. If the coercivity is assumed to be decreasing linearly with temperature, H_C is estimated to be ~ 2 kOe at 398 K. This is not an especially low coercivity. For this case, the significant degradation at 398 K (only 25 K above 373 K where the bits are thermally stable) may primarily be due to the decrease in the ratio K_uV/k_BT. This correlates with the exponential dependence of the relaxation time of magnetically isolated grains with the switching barrier K_uV/k_BT.

CONCLUSIONS

The time dependence of magnetization for CCPTN and CCPT media were found not to correlate with bit signal decay. This is attributed to the difference in magnetization configuration between a saturated state and that of a transition. Direct measurement of the written bit signal degradation is therefore essential. Media coercivity was shown to be a good indicator of thermal stability. Therefore, media with sufficiently high coercivities at drive operating temperatures are essential. A precipitous drop in the signal was observed for the CCPT medium for $K_uV/k_BT < 60$ which suggests the suitability of this parameter for this case.

ACKNOWLEDGMENTS

We would like to acknowledge G. N. Phillips for his contribution in the initial stages of this project. This work has been supported in part by the Storage Research Consortium in Japan.

REFERENCES

1. P.-L. Lu and S. H. Charap, IEEE Trans. Magn., vol. 30, 4230 (1994); vol. 31, 2767 (1995); J. Appl. Phys. **75**, 5768 (1994).
2. Y. Uesaka, Y. Takahashi, Y. Nakatani, N. Hayashi, and H. Fukushima, J. Mag. Mag. Mater. (1997).
3. Y. Hosoe, I. Tamai, K. Tanahashi, Y. Takahashi, T. Yamamoto, T. Kanbe, and Y. Yajima, IEEE Trans. Magn. vol. 33, 3028 (1997); Y. Hosoe, T. Kanbe, K. Tanahashi, I. Tamai, S. Matsunuma, Y. Takahashi, Y. Uesaka, K. Yoshida, and F. Akagi, IEEE Trans. Magn., vol. 34 (1998), in press.
4. J. H. Judy, J. Magn. Soc. Japan, vol. 21, No. S2, (1997), and references therein.
5. E. N. Abarra and T. Suzuki, IEEE Trans. Magn. vol. 33, 2995 (1997); J. Mag. Mag. Mater. 175, 148 (1997).
6. E. N. Abarra, G. N. Phillips, I. Okamoto, and T. Suzuki, J. Magn. Soc. Japan, vol. 21, No. S2, 291 (1997).
7. K. Shimoda, T. Sugawara, K. Kasai, T. Ohshima, and Y. Mizoshita, IEEE Trans. Magn., vol. 33, 2812 (1997).
8. H. N. Bertram and J.-G. Zhu, IEEE Trans. Magn., vol. 27, 5043 (1991).
9. J. J. K. Chang, Q. Peng, H. N. Bertram, and R. Sinclair, IEEE Trans. Magn., vol. 32, 4902 (1996).
10. G. Khanna, J. M. Freitag, and B. M. Clemens, this proceedings.
11. P. Bruno, G. Bayreuther, P. Beauvillain, C. Chappert, G. Lugert, D. Renard, J. P. Renard, and J. Seiden, J. Appl. Phys. **98**, 5759 (1990); T. Suzuki, Scripta. Met. Mat. **31**, 1609 (1995).

DYNAMIC COERCIVITY AND THERMAL DECAY OF MAGNETIC MEDIA

Kurt Rubin, Jason Goldberg*, Hal Rosen, Ernesto Marinero, Mary Doerner**, Manfred Schabes
IBM Research, 650 Harry Road, San Jose, Ca 95120, rubinka@ almaden.ibm.com
*presently at UCSD, San Diego, Ca, **IBM, 5600 Cottle Rd, San Jose, Ca.

ABSTRACT

Thermally induced decay of longitudinally recorded magnetic transitions is measured on a spin-stand. The decay rate increases with increased linear density and decreases with increased media coercivity. A new spin-stand experimental technique has been developed which allows measurements of the time dependence of the media coercivity as a function of write times spanning short times characteristic of write times in drives to long times associated with VSM measurements. The ratio of long to short write time coercivity was larger for media which are thermally unstable.

INTRODUCTION

The rapid increase of areal density of magnetic disk drives requires continued reduction of the crystalline grain size of the magnetic media in order to maintain adequate signal to noise ratio to read back the recorded data reliably. The grain sizes are becoming small enough that the thermal stability of the magnetic state of the grains is becoming an issue. This has caused a recent focus on understanding the conditions under which thermal decay becomes a problem [1,2]. Thermal stability can be increased by increasing the anisotropy, K_u, of the media. However, there is concern that write head fields will not be adequate to write low jitter magnetic transitions on the high K_u media, particularly since it is known that the coercivity, which depends strongly on K_u, increases with decreased write times. In this work, we first discuss measurements on thermal decay and then present a new technique to characterize the media coercivity at both short and long write times.

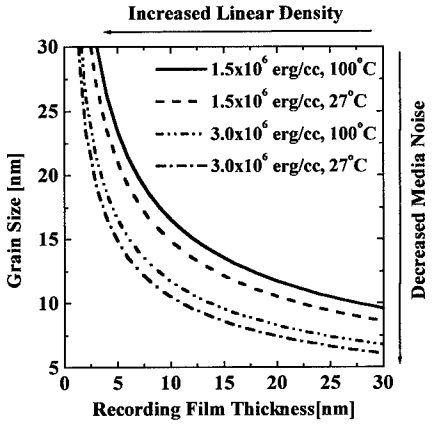

Figure 1. Contours of constant grain volume showing tradeoff of grain size versus film thickness (t) corresponding to constant stability factor of 80. Two anisotropy coefficients (K_u) and temperatures are plotted.

THERMAL DECAY

An intuitive understanding of the stability vs. grain geometry trade-offs can be obtained by treating the thermal stability according to a simple phenomenological model in which the magnetic clusters or "grains" are magnetically isolated from one another and have an activation energy against thermally induced reversal of E_a. Assuming uniform Stoner-Wohlfarth type rotation, the barrier height is proportional to the anisotropy, K_u, and the grain volume, V. To ensure stability of 10 years for media, we assume that the average barrier should be ~80 times the thermal energy at room temperature. Figure 1 illustrates this assuming the total grain volume is constant and the grain height is the same as the film thickness. The equation $K_uV/k_bT=80$ is plotted, for two values of K_u, $1.5x10^6$ and $3.0x10^6$ erg/cm^3, which for simplicity are assumed to be temperature independent, and two temperatures, 27°C and 100°C. The grains are assumed to have constant thickness t and

Mat. Res. Soc. Symp. Proc. Vol. 517 © 1998 Materials Research Society

constant thickness t and uniform cross-sectional area A.

Grains having higher anisotropy can have smaller volumes and still be stable. At elevated temperatures of drive operation, the grain volume must be larger to ensure adequate stability. From a drive perspective, ever-increasing areal density is desired, which means reducing the magnetic recording layer thickness to allow higher linear density and reducing the size of each individual grain to decrease media noise. However, the combination of the grain dimensions and anisotropy must be such that the grain volume

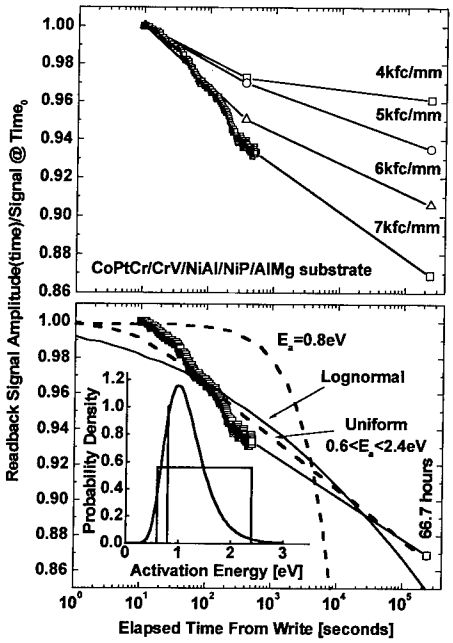

Figure 3. Top plot: Signal decay vs. time for 0.17Mrt film recorded at 4, 5, 6, and 7kfc/mm linear recording densities. Bottom plot: signal decay of most dense pattern (7kfc/mm) along with several fits to the decay assuming (I) single activation energy (II) uniform distribution of activation energies, (III) lognormal distribution of activation energies. Inset shows the three distribution functions used for the modeling.

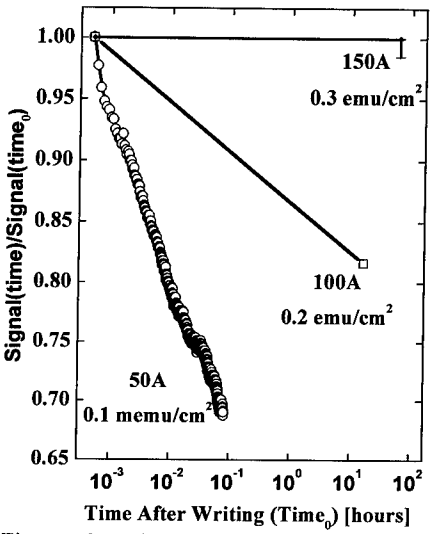

Figure 2. Thermal decay of magnetic transitions recorded at 7kfc/mm on quaternary alloy media. The data have been normalized to the signal obtained immediately after recording. The thinner media decayed much more rapidly.

lies at a point above the contour line of Figure 1. Grains volumes that lie below the contour lines are susceptible to significant thermal decay. This simple model indicates how thermal decay depends upon grain properties. In practice the situation is complicated by the presence of magnetic interactions between the grains. Micromagnetic models have been developed to describe thermally activated magnetization processes in thin film media by combining Monte Carlo methods with molecular dynamics calculations that integrate the Landau-Lifhsitz-Gilbert equations for arrays of coupled Stoner-Wohlfarth particles. Further complications arise from the fact that polycrystalline magnetic thin film media may have considerable dispersion in the size and magnetic properties of the grains. It is therefore imperative that experimental measurement of the decay be performed to allow quantitative prediction of the lifetime of recorded data.

Experimentally, thermal decay was

measured for two material systems. In both, the sputter conditions, compositions and thicknesses were all kept constant except for varying the deposition time, in order to produce magnetic layers which differed in film thickness. The goal was to reduce the volume of the magnetic "grains" to the sizes where thermal decay was observed. Thermal decay was measured on a spin-stand by first writing a set of uniformly spaced magnetic transitions, and then determining the amplitude of the readback signal vs. time for various spacings between transitions. Cross-track profiles were conducted to locate the peak amplitude for all except the 0.1 memu/cm^2 sample because that particular sample decayed so rapidly that thermal drift was found to be insignificant during the measurement. Concern that changes of read back amplitude might be due to other reasons than thermal decay, such as changes of fly height and head sensitivity was addressed by writing fresh tracks at the end of each decay experiment to ensure that the same amplitude as the initial amplitude before decay was obtained.

Measured thermal decay is plotted for three quaternary magnetic layers grown on Cr underlayers is shown in Figure 2. The Mrt was measured with a Remnant Moment Magnetometer (RMM) to be approximately 0.1, 0.2 and 0.3 memu/cm^2 remnant moment thickness product (M,T) and the corresponding film thickness were ~50A, ~100A and ~150A, respectively [3]. The readback amplitude decay of magnetic transitions recorded at a density of 7kfc/mm is shown in Figure 2. The read back signal from the 0.3 memu/cm^2 sample was essentially constant over the 66 hour time period, within experimental error. The 0.2 memu/cm^2 sample showed a drop of signal of 18% in 19 hours. The 0.1 memu/cm^2 sample was the most unstable with a significant drop of 30% occurring in just 5 minutes after writing the track. Although not shown, the rate of decay was dependent on the recording density with higher linear density producing a larger rate of decay.

Thermal decay measurements were also made on a ternary sample as shown in Figure 3. Again, a very thin magnetic layer was used in order to produce a disk that demonstrated significant thermal decay at room temperature. The thin-film disk used for the thermal decay measurements was prepared by magnetron sputtering on a NiP-plated Al-Mg substrate. An underlayer of 60 nm was first deposited followed by 20 nm of $Cr_{80}V_{20}$ and finally 5.5 nm of $Co_{64}Pt_{14}Cr_{22}$. The Mrt was measured with a RMM to be 0.17 memu/cm^2. TEM analysis of films deposited with the same structure except for larger magnetic layer thickness' of 10.2 and 17.5 nm both demonstrated a grain size of 15 nm[4].

The bottom plot shows how the decay rate varies with recording density. The top curve shows the highest density, 7kfc/mm data plotted. Overlaying that plot are three simulations of the thermal decay in which a distribution of activation barrier energies is assumed. If all the grains were the same size, had identical magnetic properties and were isolated from one another, then one might assume a thermal relaxation process dominated by a single activation energy. However, the data shows that it is not possible to fit the decay curve with a single activation energy. This is consistent with most TEM observations of magnetic media that invariably show a range of crystalline grain size and hence a likely distribution of magnetic cluster sizes. The experimental decay exhibits quite linear behavior vs. log time over many decades of time. This is consistent with a uniform distribution of energy barriers and a fit with such a distribution is also shown in the plot. The best fit was obtained with an energy distribution of FWHM 1.8eV centered at 1.5eV. Note that the low end of the distribution, 0.6eV, corresponds to a stability ratio of 0.6/.02=24, much less than the 80 referred to in the introduction. This is consistent with the large thermal decay of this sample, even at room temperature. In practice, it is unlikely that the distribution would be exactly uniform. We also show a fit to the decay assuming a log normal distribution that tails off gradually both at low and high activation energies. This also fits the data, although not quite as well as the uniform distribution. Further experiments are required to narrow down the choice of distribution function.

DYNAMIC COERCIVITY

A general approach to increase data stability for long times is to increase the anisotropy (K_u) of each grain, but this approach will be limited by the ability of the head to write high coercivity media at short times. It is important to know quantitatively how much the coercivity varies with write time. As the media becomes more thermally unstable, the coercivity at short times is expected to increase relative to the long time coercivity. Techniques such as VSM, AGFM or RMM all work with write times which are 1 or more seconds long. This is 8 to 9 orders of magnitude longer than the writing times. At very short write times, the relative trends of coercivity can be inferred from the DC erase current which causes maximum media noise and the general trend of the time dependence of the coercivity can be obtained by using multi-pass erase [5]. However, calibration of the write field and dwell time

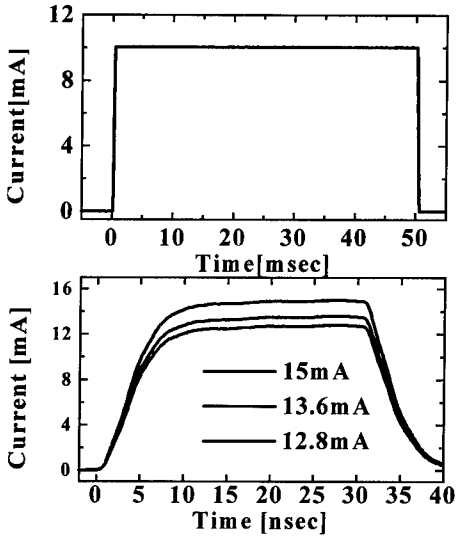

Figure 5. Write current profiles for 50ms (top) and 30ns (bottom) pulse widths.

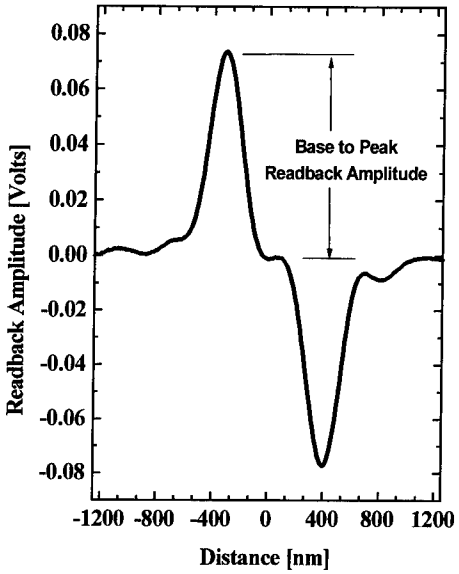

Figure 4. Readback signal from dipulse written on disk, after averaging out electronic noise.

are required and the short dwell time per pass limits the maximum practical write time to be many orders of magnitude less than 1 second, making it difficult to directly connect with RMM, VSM or other coercivity measurement techniques which employ long write times.

Here, we describe a new spin-stand based technique which allows the media coercivity to be determined as a function of write time continuously spanning the short times associated with writing with a head to the long write times intrinsic to VSM measurements. The procedure is to (1) erase a track while the disk is spinning, (2) stop the disk so the slider lands and is stationary, (3) reverse the polarity and write a current pulse of chosen amplitude and duration and (4) spin up the disk and read the signal from the di-pulse which was written. The readback signal is averaged to remove electronic noise. Figure 4 shows an example of the readback signal obtained while flying over such a di-bit which was written with the disk stationary. The

positive and negative pulses correspond to the two magnetic transitions on the disk which are separated approximately by the write gap of the head.

Since reversal rates depend strongly on applied field, in these experiments a special unipolar current driver was constructed which minimized any overshoot of the current pulse generating the write head field and kept the current constant as much as possible during the entire pulse. Figure 5 shows examples of both short and long time current pulses used for writing the di-bit. Efforts were made to minimize any overshoot of the current pulse and to keep the current constant as much as possible during the entire pulse.

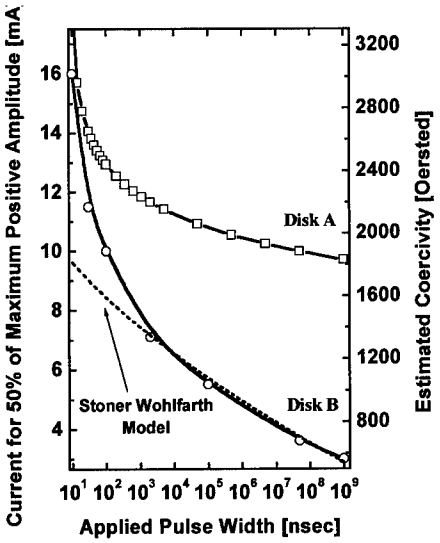

Figure 7. Current vs. pulse width (left axis) yielding constant readback amplitude of ½ the maximum signal. Right axis is estimated coercivity vs. write time. The dashed line shows a fit assuming uniform Stoner-Wohlfarth rotation with switching volume = $(10^{-6})^3$ cm^3, $K_u = 0.55 \times 10^6$erg/cm^3, M_s=250 emu/cm^3 where good agreement was required at long times. It was not possible to simultaneously get a good fit to the short time data which is consistent with head rise time effects existing at short times.

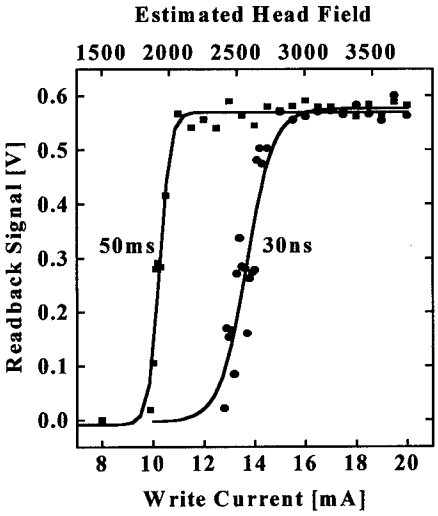

Figure 6. Readback signal vs. write current for short (30ns) and long (50ms) write pulse. Lines are only to guide eye.

Figure 6 shows the readback amplitude versus write current for two pulse widths of 30 ns and 50 ms. The base to peak amplitude, increases monotonically with increased current until it saturates. Figure 6 also illustrates the rather sharp threshold for writing on the disk. Each data point is media noise limited and illustrates the amount of scatter associated with using this technique. Part of the scatter is due to a slight non-uniformity of the disk properties around the disk circumference. The remainder of the scatter would encompass variations in height of the write gap after landing. Above that threshold, only a small variation of the current is necessary to go from threshold to full saturation.

Measurements were made for a range of pulse widths and currents and the results are summarized in Figure 7. In this figure, the plotted points correspond to the current necessary for the di-bit amplitude to be ½ the saturated readback amplitude. The left axis of the plot shows the current versus pulse time.

The current necessary to write a given amplitude di-bit is less when longer pulse widths are used. Disk A, which is has an Mrt of approximately 1 memu/cm^2 and is quite stable against thermal decay, exhibited a very gradual increase of coercivity with decreased write pulse width. In contrast, disk B, the NSIC 0.17 memu/cm^2 sample, exhibited a much stronger drop of coercivity with increased pulse width which is presumably due to a thermal effect since disk B showed substantial thermal decay at room temperature

The current increases with decreased pulse width. The increase is rather gradual, down to pulses of 1μs and then the required current increases rapidly. The cause of this increase is under investigation and will be reported on elsewhere. The right hand axis shows an estimated coercivity as a function of the write time. This is obtained by assigning a value of the disk coercivity for 1 second long write times to be the same value measured by an RMM, which also uses a 1 second write time. Figure 6 also shows measurements on disk B, the 0.17 memu/cm^2 disk described above. For shorter write times, this experiment determines not just the media response, but the total system response of the media, write head and write driver. Thus, while the media coercivity appears to increase rather dramatically when the pulse duration is less than ~1μs, it is likely that this increase is due to head rise time effects. Efforts are underway to deconvolute the head response from the media response.

SUMMARY

A new spin-stand based experimental technique has been developed which allows the time dependence of the magnetic media to be determined over many orders of magnitude of write time. This technique allow measurements in a VSM to be readily correlated to spin-stand performance. Thermally unstable materials showed the largest dependence of coercivity on write-time. The thermal decay of two material systems was examined. The decay was found to increase with increase linear density, consistent with demag field enhanced thermal instability. Media having thinner magnetic layers were much more prone to thermal decay.

ACKNOWLEDGMENTS

The authors thank Jim Lyerla for helpful discussions and Tony Juliana for technical assistance.

REFERENCES

[1] P. L. Lu, S. H. Charap, "High density magnetic recording media design and identification: susceptibility to thermal decay", IEEE Trans. Magn. Vol. 31, No. 6. (1995) 2767-2769.

[2] S. H. Charap, P. L. Lu, Y. He, "Thermal stability of recorded information at high densities", IEEE Trans. Magn. Vol.33, No.1 (1997) 978-983.

[3] L. Morellon et al., to be submitted.

[4] Mingjun Yu, Mary Doerner and David Sellmyer, Paper AB-03, MMM-Intermag '98.

[5] H. Richter et al, IEEE Trans. Magn. Vol.33, No.1 (1997) p2701.

EFFECT OF GRAIN SIZE AND MAGNETIC SWITCHING VOLUME ON MEDIA NOISE DUE TO INTERGRANULAR COUPLING IN CoCrTaPt/Cr THIN FILM MEDIA

Sudhir S. Malhotra, Brij B. Lal, Michael A. Russak
HMT Technology, Fremont, CA 94538

ABSTRACT

In this work the effect of grain size and magnetic switching volume on media noise due to intergranular coupling for CoCrTaPt/Cr thin film media deposited at substrate temperature of 160 and 260^{0}C are investigated. The film deposited at substrate temperature of 260^{0}C showed weaker intergranular interaction and lower media noise compared to the film deposited at 160^{0}C. The magnetic switching volume (V*) is an important consideration for thermal stability and media noise in high density recording media. The magnetic switching volume V* for the film deposited at 160 and 260^{0}C was calculated to be 3.7 x 10^{-18} and 3.2 x 10^{-18} cm^3 respectively. The magnetic switching volume is correlated to the average Co-alloy grain size, media noise and the interactions between the grains.

INTRODUCTION

High density recording media will require materials with high coercivity (Hc), low noise and magnetically de-coupled smaller grains. The magnetic switching volume will also become an issue for thermal stability due to the reduction in grain size [1,2]. The thermal stability requirement is that $KuV^*/k_BT \leq \approx 100$ where Ku, k_B, T are the anisotropy constant, Boltzmann's constant and temperature respectively. The magnetic switching volume can be obtained by measuring the coercivity as a function of the sweep rate of the applied field. As the substrate temperature increases from 160 to 260 ^{0}C the average Cr and Co-alloy grain size increases but the media noise reduces due to the weaker intergranular interaction.

Here we report the results of the dependence of physical Co-alloy grain size and magnetic grain size on media noise due to the intergranular coupling for the CoCrPtTa/Cr media deposited at a substrate temperature of 160 and 260^{0}C.

EXPERIMENT

The samples investigated in this study were CoCrPtTa/Cr thin film media deposited at substrate temperature of 160 and 260^{0}C on textured NiP/Al substrates with DC-magnetron sputtering. The magnetic properties and the intergranular interaction measured in terms of the ΔM curves for the films were determined using a vibrating sample magnetometer. The anisotropy constant (Ku) was determined using Torque Magnetometer. The magnetic switching volume was determined using a Alternating Gradient Force Magnetometer (AGFM). High Resolution Transmission Electron Microscopy (HRTEM) was used to determine the average Co-alloy and Cr underlayer grain size. Magnetic recording measurements were made with a dual element head consisting of thin film inductive head for writing and MR head for read back.

Mat. Res. Soc. Symp. Proc. Vol. 517 © 1998 Materials Research Society

RESULTS AND DISCUSSIONS

The coercivity (Hc), Mrt, coercivity squareness (S*) and the anisotropy constant (Ku) for the films deposited at 160 and 260^{0}C are given in Table 1. The film deposited at 160^{0}C has Hc = 1900 Oe, Mrt = 0.90 memu/cm^2 and higher S* value compared to the film deposited at 260^{0}C which has a coercivity of 2700 Oe and Mrt = 0.90 memu/cm^2. The magnetic interaction between the grains was measured in terms of the ΔM curves [3]. Fig. 1 shows the ΔM curves for the two samples, the film deposited at 160^{0}C has a positive peak value of ΔM = +0.55 while the film deposited at 260^{0}C has ΔM = +0.20. This is indicative of the weaker exchange interaction between the grains for the film deposited at higher substrate temperature. The media noise and SNR as a function of recording density for the two samples are shown in Fig. 2 and 3 respectively. The film deposited at 260^{0}C has 35% lower media noise and 5 dB higher SNR at 150 kfci recording density in comparison to the film deposited at 160^{0}C. The lower value of S*, ΔM and media noise is indicative of weaker intergranular interaction between the grains for the media deposited at higher substrate temperature. Similar media noise characteristics as a function of deposition temperature has been reported in case of CoCrTa/Cr media[4].

Table 1: Hc, Mrt, S* and Ku for the CoCrPtTa/Cr thin film media deposited at different substrate temperature.

Substrate Temperature (^{0}C)	Hc (Oe)	Mrt (memu/cm^2)	S*	Ku (ergs/cm^3)
160	1900	0.90	0.93	1.9 x 10^6
260	2700	0.90	0.76	2.1 x 10^6

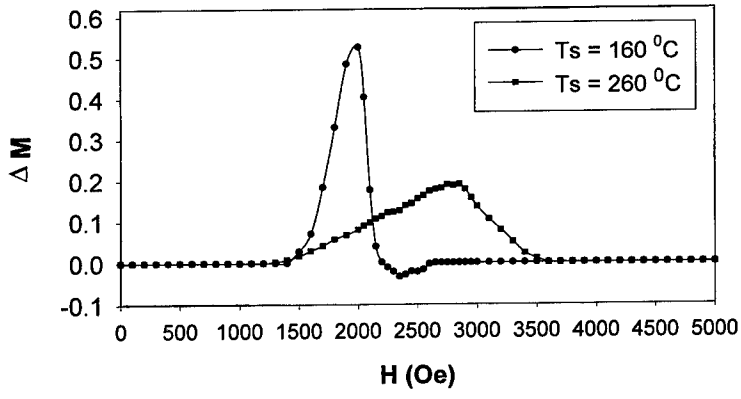

Fig. 1. ΔM curves for the CoCrPtTa/Cr films deposited at 160 ^{0}C and 260 ^{0}C.

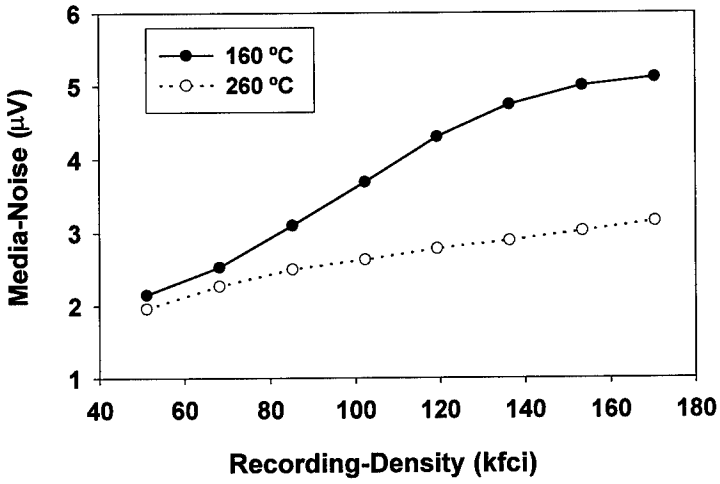

Fig. 2. Media Noise vs. Recording Density for CoCrPtTa/Cr media deposited at 160 ^{0}C and 260 ^{0}C.

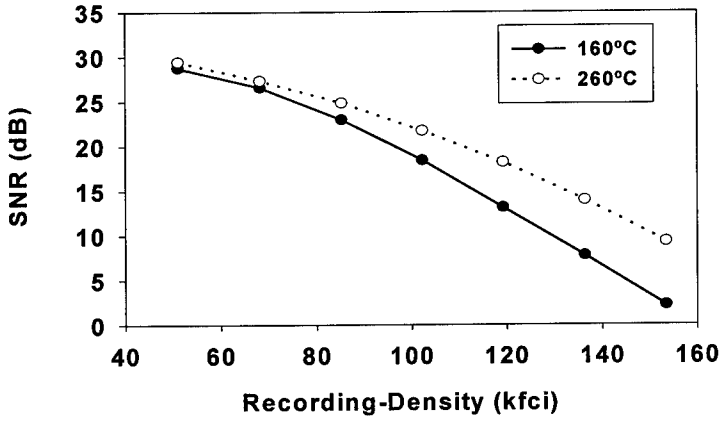

Fig. 3. SNR vs. Recording density for CoCrPtTa/Cr media deposited at 165 ^{0}C and 260 ^{0}C.

The magnetic switching volume for the two samples was measured by the dependence of the apparent coercivity on the sweep rate of the magnetic field using the AGFM. The coercivity as a function of the sweep rate of the magnetic field is given by [5,6]

$$Hc = C + \left[\frac{k_B T}{V^* Ms}\right] \ln\left[\frac{dH}{dt}\right] \qquad \text{..... (1)}$$

where C is a constant independent of the field-sweep rate. The magnetic switching volume can be obtained from the slope of Hc vs. ln(dH/dt) plot. Fig. 4 shows the dependence of Hc on ln(dH/dt) for the samples deposited at 165 ^{0}C and 260 ^{0}C. The sweep rate was varied from 50 Oe/s to 1000 Oe/s. Both the samples exhibit the approximate linear relation of Hc on ln(dH/dt). From the slope, one can estimate the magnetic switching volume from Eq. (1). The V* was estimated to be 3.7 x 10^{-18} and 3.2 x 10^{-18} cm^3 for the films deposited at 160 ^{0}C and 260 ^{0}C respectively. Using this value and the film thickness, the diameter of the magnetic grain can be estimated assuming that it is a cylindrical cell whose height is the thickness of the film[7]. The magnetic grain diameter is about 140 Å for the film deposited at 160 ^{0}C and ~130 Å for the film deposited at 260 ^{0}C.

Next we report the physical grain size determined using TEM. Fig. 5a and 5b shows the HRTEM micrographs of the magnetic layer for the films deposited at 160 ^{0}C and 260 ^{0}C respectively. As the substrate temperature increases the average Co-alloy and Cr grain size increases. The average Co-alloy grain size for the film deposited at 160 ^{0}C is about 109 Å and for the film deposited at 260 ^{0}C is about 150 Å. The Cr grain size increased from 170 to 250 Å with the increase in deposition temperature from 160 ^{0}C to 260 ^{0}C. Table 2 summarizes the average Co-alloy and Cr grain size, magnetic grain diameter, peak value of ΔM, and KuV^*/k_BT value for the films deposited at 160 ^{0}C and 260 ^{0}C.

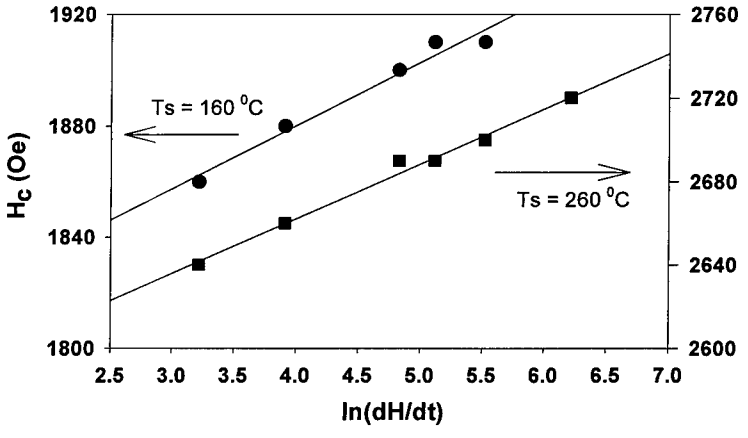

Fig. 4. Hc vs. ln(dH/dt) for the CoCrPtTa/Cr films deposited at 160 ^{0}C and 260 ^{0}C.

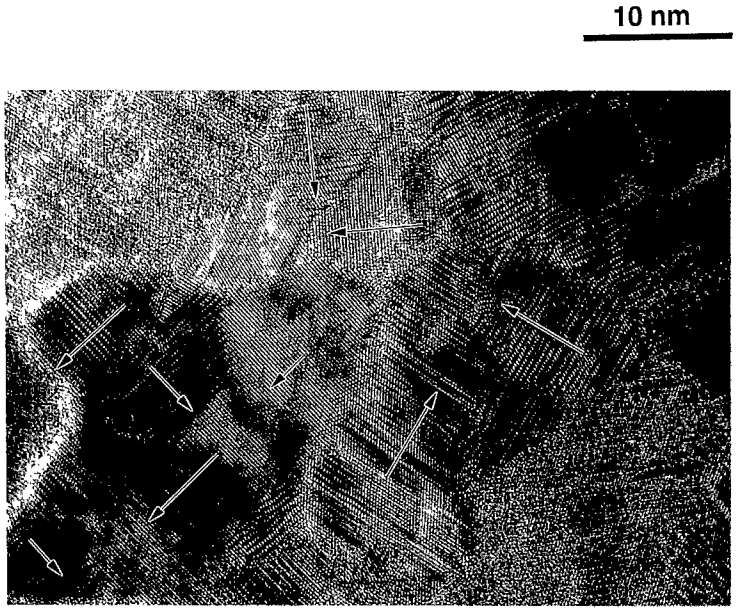

Fig. 5(a). HRTEM micrographs for CoCrPtTa/Cr thin film media deposited at 160 ^{0}C.

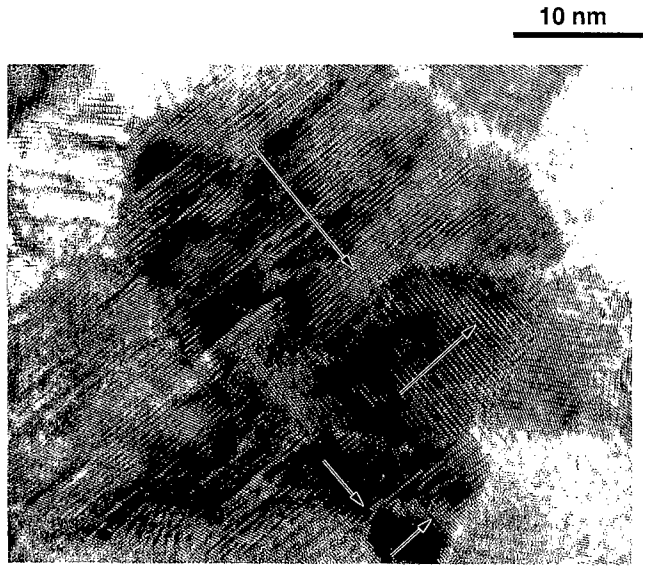

Fig. 5(b). HRTEM micrographs for CoCrPtTa/Cr thin film media deposited at 260 ^{0}C.

Table 2. Average Co-alloy and Cr grain size, V*, Magnetic grain size and KuV^*/k_BT for the CoCrPtTa/Cr films deposited at 160 ^{0}C and 260 ^{0}C.

Property	**Ts = 160 ^{0}C**	**Ts = 260 ^{0}C**
Average Co-alloy grain size	109 Å	150 Å
Average Cr grain size	170 Å	250 Å
V*	3.7×10^{-18} cm^3	3.2×10^{-18} cm^3
Magnetic grain size	140 Å	130 Å
KuV^*/k_BT	178	154

CONCLUSION

In this work we correlate the effect of Co-alloy grain size and magnetic grain size on media noise due to intergranular coupling for the CoCrPtTa/Cr thin film media. As the substrate temperature increases the average Cr underlayer and the Co-alloy grain size increases. The Hc appears to be correlated to the grain size. For the film deposited at 160 ^{0}C the average Co-alloy grain size is about 109 Å while the magnetic grain diameter is about 140 Å, and for the film deposited at 260 ^{0}C the average Co-alloy grain size is ~ 150 Å while the magnetic grain size is about 140 Å. The CoCrPtTa/Cr thin film deposited at lower substrate temperature (160 ^{0}C) has smaller Co-alloy grain size but larger magnetic grain diameter due to the strong intergranular interaction resulting in higher media noise. But for the film deposited at 260 ^{0}C the average Co-alloy grain size is roughly the same as the magnetic grain size due to the weaker exchange interaction between the grains as reflected by the lower positive peak value of ΔM and S*, resulting in lower media noise. Thus it is not only necessary for future low noise media to have small physical Co-alloy grain size but also exchange de-coupled grains so that the magnetization reversal roughly takes place in the unit of the magnetic grain size.

ACKNOWLEDGEMENTS

Authors would like to thank Donald Stafford, Varsha Patel and Z.S. Shan for their help with the sample preparation and measurements. Our thanks also go to Prof. D. J. Sellmyer at University of Nebraska for the AGFM, D.W. Park and Prof. R. Sinclair at Stanford University for the HRTEM work.

REFERENCES

1. M. P. Sharrock, IEEE Trans. Magn., vol. 26, pp. 193-197, (1990).
2. P. Lu and S.H. Charap, J. Appl. Phys., vol. 75, pp. 5768- 5770, (1994).
3. P. E. Kelly, K. O'Grady, P.I. Mayo and R.W. Chantrell, IEEE Trans. Magn., vol. 25, pp. 3881-3883, (1989).
4. J. H. Judy, IEEE Trans. Magn. vol. 29, pp. 209-211, (1993).
5. P. Bruno, G. Bayreuther, P. Beauvillian, C. Chappert, G. Lugert, D. Ranard, and J. Seiden, J. Appl. Phys., vol. 68, pp. 5759-5761, (1990).
6. E. W. Singleton, Z. S. Shan, Y.S. Jeong and D. J. Sellmyer, IEEE Trans. Magn., vol. 31, [[. 2743-2745, (1995).
7. S. S. Malhotra, Z. S Shan, D. C. Stafford, S. H. Liou and D. J. Sellmyer, IEEE Trans. Magn. vol. 32, pp. 4019-4021, (1996).

EFFECTS OF DC BIAS ON THE THERMAL STABILITY OF DC IN-LINE SPUTTERED CoCrTa/Cr THIN FILM MEDIA

J. P. Wang, L. P. Tan, T. Y. F. Liew, and T. S. Low
Data Storage Institute, National University of Singapore, 10 Kent Ridge Crescent, Singapore 119260
H. L. Wong and Y. K. Lee
StorMedia International Ltd (Singapore Branch), 9 Tuas Avenue 5, Singapore 639335

ABSTRACT

The effects of DC bias on the thermal stability and magnetic anisotropy of CoCrTa/Cr thin film media fabricated by using a DC in-line sputtering machine is presented in this paper. In sputtering, a negative DC bias voltage, varying from 0 to 400 V, was applied for the CoCrTa layer. The coercivity was observed to increase almost linearly from 1800 to 2300 Oe for negative bias voltage from 0 to 400V. The thermal stability of these media was studied by measuring the time decay of remanent magnetization under various reverse magnetic fields. The maximum value of the magnetic viscosity coefficient, which happens around remanent coercivity of each samples, decreases with increasing substrate bias voltage. This implies an improvement in the thermal stability of the CoCrTa/Cr thin film media. The magnetic anisotropy constants were measured using both a torque magnetometer and a vibrating sample magnetometer. The magnetic anisotropy measured using torque magnetometer decreases, while that measured using the method of the law of approach to saturation was found to be almost constant, with increasing bias voltage. The activation volumes decreased with increasing bias voltage. The magnetic hardness coefficient determined using the law of approach to saturation, indicating the number of in-depth defects in the CoCrTa layer, increased with increasing bias voltage. The internal stress in these films measured using X-ray diffractometer also supported the existence of in-depth defects. The pinning of the rotation of magnetization by these defects in the magnetic grains maybe responsible for the improvement of thermal stability.

INTRODUCTION

Substrate bias has been known to be a useful sputtering parameter for modifying film properties [1]. Both DC and RF bias technology have been used to increase the coercivity of sputtered hard disk media. Many groups have studied the effects of substrate bias on magnetic properties of sputtered films [2–6]. Glijer et al. reported RF substrate bias increases stress and possibly the amount of faulting in the films [7]. Deng et al. reported that the increase of coercivity of CoCrTa/Cr thin film media with increasing bias voltage resulted from the variation of the film composition [8]. Deng et al. also ruled out the effects of the increased substrate temperature induced by bias voltage on the magneic properties of the CoCrTa/Cr films [9]. Okumura et al. reported that the application of low negative bias voltage to a substrate during sputtering enhances Cr segregation in CoCr grains in CoCr/Cr films [10]. Hence, Ms and Hc were found to increase. They also found that the application of a high negative bias makes the distribution of Cr within grains homogeneous and hence enhances the diffusion of Cr from the Cr underlayer to grain boundaries, giving rise to a decrease in Ms and an increase in Hc. Lal et al. used the bias technique to develop a coercivity-gradient double magnetic layer thin film media [11] and recently reported that the bias only for Cr underlayer did not affect Hc. The application of bias during magnetic layer or during both Cr and magnetic layers deposition increased the in-plane Hc, reduced media noise and NLTS, and increased SNR [12].

Recently, thermal instability study for longitudinal thin film media has become very important as superparamagnetism will be the big obstacle for the recording areal density of longitudinal media to go beyond 40 Gbit/in^2 [13]. Han et al. found that RF bias can reduce the magnetic viscosity coefficient for CoCrTa/Cr thin film media [14]. However, no further explanation and investigation was given. In this paper, the influence of DC negative substrate bias on the thermal stability of

Mat. Res. Soc. Symp. Proc. Vol. 517 © 1998 Materials Research Society

CoCrTa/Cr thin film media was investigated by measuring the magnetic viscosity coefficient, magnetic anisotropy, activation volume and in-depth defects.

EXPERIMENT

CoCrTa/Cr thin film media were deposited on textured NiP/Al substrates using an in-line DC magnetron sputtering system. The thickness of the Cr underlayer is about 90 nm. The negative DC bias voltage was applied during the deposition of CoCrTa magnetic layer. No substrate bias was applied during Cr underlayer deposition. A set of CoCrTa/Cr samples were obtained by varying the substrate DC bias voltage from 0 to -400 V while keeping all the other sputtering condition at the same. The deposition pressure is 8m Torr and the substrate preheating temperature before Cr layer deposition is about 250 °C.

The bulk magnetic properties of the samples were measured using a vibrating sample magnetometer (VSM). The magnetic anisotropy was measured using a torque magnetometer. The law of approach to saturation was also used to determine the effective magnetic anisotropy [15]. In-depth defects were investigated by measuring the magnetic hardness coefficient using the law of approach to saturation [16].

The time decay of magnetization was measured for various reverse magnetic fields ranging from H_{rev}/H_c=0.9 to 1.10. The coefficient of magnetic viscosity S is obtained from the following relationship

$$M_r(H_{rev}, t) = M_0(H_{rev}, 0) + S \cdot \ln(t) \quad (1)$$

where $M_r(H_{rev},t)$ is the remanent magnetization of the thin film at the in situ reverse field H_{rev} and the decay time t following application and then removal of a saturation field (10 kOe). $M_0(H_{rev},0)$ is the initial (t=0) remanent magnetization of the thin film at the same reverse field H_{rev}. S is obtained by fitting the measured $M_r(H_{rev},t)$. The thermal activation volume V_{act} was determined from $V_{act}=k_BT/M_sH_f$. The fluctuation field $H_f=S/\chi_{irr}$ was derived from the irreversible susceptibility χ_{irr}, calculated from dc demagnetization remanence curves (DCD), and the magnetic viscosity coefficients [17]. The crystallographic texture and stress in the films was determined using an X-ray diffractometer (XRD). Rutherford back scattering (RBS) was used to measure the film composition and film thickness.

RESULTS

Table I summarizes the bulk magnetic properties for the samples deposited under various bias voltages. Listed are the coercivity (H_c), the remanent-magnetization thickness product (M_rt), the saturation magnetization (M_s), the coercivity squareness (S^*), and the remanent squareness (SQ). H_c shows an almost linear increase with increasing bias voltage. M_s also shows a decrease with increasing bias voltage.

Table 1. Magnetic properties of CoCrTa/Cr thin film media deposited under various DC bias voltages.

Substrate bias voltage (V)	Magnetic Properties				
	Hc(Oe)	S*	SQ	M_s (emu/cm^3)	M_rtx10^{-3} (emu/cc)
0	1856	0.8701	0.7577	759	2.07
-100	1919	0.8778	0.7445	703	1.98
-200	2145	0.8455	0.7232	689	1.89
-300	2175	0.8683	0.7024	686	1.78
-400	2287	0.8498	0.7224	669	1.69

The thickness and the composition, measured using RBS, for the CoCrTa/Cr samples are shown in Table II. The thickness of the CoCrTa layer is nearly constant for the different samples. The composition of CoCrTa layer also shows no significant variation with increasing bias voltage up to

–300V. The film deposited under –400V bias voltage has higher Cr content than those deposited under low bias voltage.

Table II. Thickness and composition of CoCrTa/Cr media deposited under various DC bias voltages.

Bias voltage (V)	Thickness (Co alloy)	Thickness (Cr underlayer.)	Co (%)	Cr (%)	Ta (%)
0	36 nm	93 nm	80	16	4
-100	38 nm	109 nm	80	15.8	4.2
-200	38 nm	94 nm	82	14	4
-300	37 nm	85 nm	80	16	4
-400	35 nm	94 nm	74	22	4

Fig.1 gives the atomic force microscope (AFM) images for samples deposited without bias voltage and with 300 V bias voltage. It shows smaller grains in the later. It was also found that the average grain size decreased with increasing bias voltage [5].

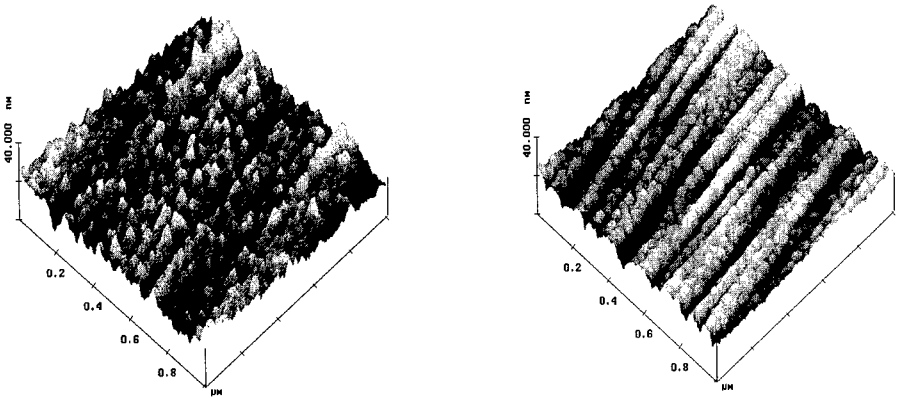

Fig.1 AFM images (1μm x 1μm) for CoCrTa/Cr samples with 0 (left) and –300 V (right) bias voltage.

The time decay of magnetization for samples deposited with different bias voltages were measured under various reverse magnetic fields. As an example, Fig.2 shows the magnetization decay in the range of 300 seconds at various reverse fields for CoCrTa/Cr sample deposited with 300 V bias voltage. The beginning of the time decay process for magnetization is more important for analyzing the problem of thermal stability [14]. In the following discussion, the magnetic viscosity coefficient S is calculated for the samples within the 300 seconds. Fig.3 shows the variation of the magnetic viscosity coefficient S with the reverse magnetic field normalized by the film remanent coercivity for CoCrTa/Cr samples deposited without bias voltage and with –300 V bias voltage. The magnetic viscosity exhibits a pronounced peak at the field values for H_{rev}/H_{cr}=0.97~1.0. The maximum peak values of the magnetic viscosity coefficient were obtained from these curves.

The variation of the maximum magnetic viscosity coefficient for samples with the bias voltage is shown in Fig.4. A very important observation was found that the peak values of the magnetic viscosity coefficient decreased by 100% with increasing negative bias voltage from 0 to 300 V and then increased for sample deposited with 400 V bias voltage. This result suggests an improvement in thermal stability for CoCrTa/Cr thin film media sputtered with increasing substrate bias voltage up to a certain value.

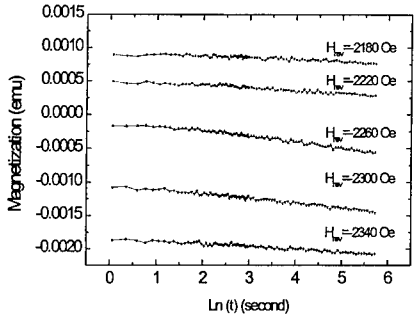

Fig. 2 Time decay of magnetization at various reverse field for CoCrTa/Cr under 300 V bias

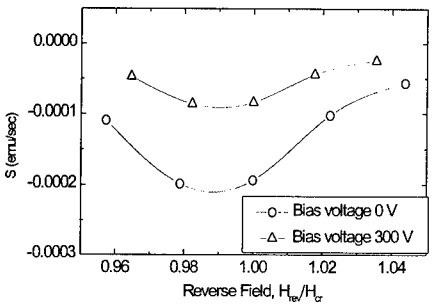

Fig. 3 Magnetic viscosity coefficient vs. reverse field for CoCrTa/Cr samples

So far, it is believed that the ratio of the anisotropy energy barrier to the thermal energy KV/k_BT is key to understanding the behavior of the thermal instability although this ratio was obtained based on a uniform rotation model without considering interaction between magnetic grains [16,18]. To determine the anisotropy energy barrier effect on magnetic viscosity coefficient, both the activation volume and the magnetic anisotropy were measured for the samples. The peak values of magnetic viscosity coefficient S and χ_{irr} obtained from the dc demagnetization remanent curves were used to calculate the magnetic fluctuation field H_f and thus the activation volume [17]. Fig.5 shows the variation of the activation volume with the bias voltage. The activation volume decreases with increasing bias voltage. If the thin film samples become thermally stable, one of the possibilities is the increase of the activation volume. However, the activation volume alone cannot account for the improvement of thermal stability for samples deposited under bias voltage. The magnetic anisotropy may be another factor to consider.

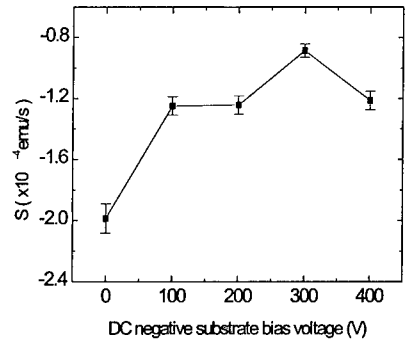

Fig. 4 Maximum magnetic viscosity coefficient vs. the substrate bias voltage for CoCrTa/Cr thin film media

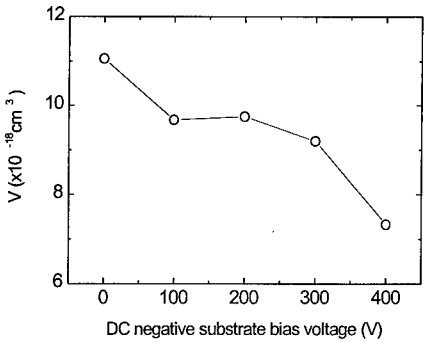

Fig. 5 Activation volume vs. substrate bias voltage for CoCrTa/Cr thin film media

Two methods were applied to measure the magnetic anisotropy constants for the CoCrTa/Cr thin film media samples. First, torque magnetometery was used to measure the magnetic anisotropy along the

circumferential direction for the samples. The magnetic field rotates in a plane defined by the sample's circumferential direction (L direction) and the sample normal, with the initial field along the L direction. The total net anisotropy (K) can be obtained from $K = 2\pi M_s^2 + K_u = L_{pp}/2V$, where $2\pi M_s^2$ is the shape anisotropy of the crystallites in the film, K_u the film uniaxial anisotropy, V sample volume and L_{pp} the peak-to-peak torque. The magnetic anisotropy constant K_u for the CoCrTa/Cr samples measured using torque magnetometer are shown in Fig.6. The magnetic anisotropy constant K_u decreased with increasing negative bias voltage up to 300 V and then increased a little at 400 V. The uniaxial magnetic anisotropy measured using the torque magnetometer is mainly contributed magnetocrystalline anisotropy. The drop in the magnetocrystalline anisotropy may result from the increase in the imperfection in magnetic grains with increasing bias voltage. The details will be discussed later. We also used the law of approach to saturation, as shown in Eq. (2), to measure the effective magnetic anisotropy. The law of approach to saturation can be expressed as

$$M_H = M_S(1 - \frac{a}{H} - \frac{b}{H^2} - \cdots) + \chi_p H \qquad (2)$$

where H is the applied magnetic field, M_S the saturation magnetization and M_H the magnetization. The paramagnetic term χ_p caused by an increase in the spontaneous magnetization by the high external magnetic field is small and negligible. The origin of the a/H term was attributed to dislocations and non-magnetic inclusions or voids [15, 16, 19]. a is called the magnetic hardness coefficient. The origin of the b/H^2 term is from the different types of magnetic anisotropies [16, 20]. It was shown that the coefficient b is equal to $4K_e^2/15M_s^2$ for uniaxial magnetic anisotropy [20], where K_e is the effective anisotropy. K_e was determined by fitting the process of approach to saturation. The magnetic anisotropies determined in this way is thus an average and covers all magnetic anisotropy energies including magnetocrystalline anisotropy, stress anisotropy, shape anisotropy and other anisotropy. The effective magnetic anisotropy constant K_e measured using Eq. (2) for the CoCrTa/Cr samples deposited with various bias voltage are shown in Fig.6. The measured K_e is almost constant with increasing bias voltage within measurement tolerance. This difference between K_u and K_e may come from stress. In these CoCrTa/Cr thin film samples, the magnetic shape anisotropy cannot contribute to the above difference as the the shape of the magnetic grains shows very little variation with bias voltage. Stress anisotropy may be the cause.

As discussed above, both the variation of the activation volume and magnetic anisotropy with the bias voltage cannot account for the improvement of thermal stability in CoCrTa/Cr thin film media. One possible contributor could be defects in the media.

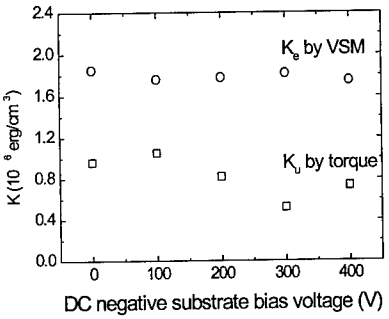

Fig.6 Magnetic anisotropy constant vs. bias voltage for CoCrTa/Cr thin film media

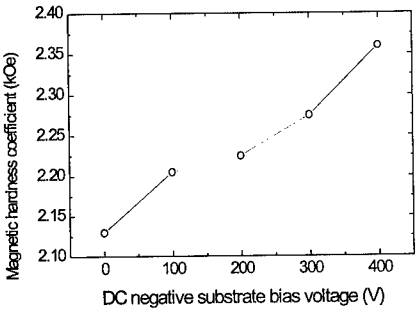

Fig. 7 Magnetic hardness coefficient vs. bias voltage for CoCrTa/Cr thin film media

The magnetic hardness coefficient was determined using Eq.(2) to characterize the in-depth defects in the CoCrTa/Cr thin film media. Néel studied the relationship between the magnetic hardness

coefficient and the density of iron powder and found that voids in sample increased the magnetic hardness coefficient [13, 18]. Brown found that the magnetic hardness coefficient increased with the number and the distribution of the dislocation in magnetic films [19]. Fig.7 shows the variation of the magnetic hardness coefficient with the bias voltage for CoCrTa/Cr samples. The magnetic hardness coefficient a shows a very clear linear increase for negative bias voltage from 0 to 400 V. This indicates an increase in in-depth defects. The in-depth defects here can be stacking faults, dislocation, and impurity in the film. These in-depth defects may pin the rotation of magnetization in the magnetic grain and thus improve the thermal stability. The increase of the number of in-depth defects is also consistent with the increase of the stress in films. X-ray diffraction shows that the in-plane stress for CoCrTa/Cr thin film media increases from 1.6 to 3.9 GPa with increasing bias voltage from 0 to 400 V. Further detailed analysis of the in-depth defects using high-resolution TEM is needed.

CONCLUSIONS

The effect of negative substrate bias voltage on the thermal stability was investigated by measuring the time decay of magnetization for CoCrTa/Cr thin film media. It was found that the CoCrTa/Cr thin film media became thermally more stable when deposited under higher bias voltage. Magnetic anisotropy was measured and analyzed using both torque magnetometer and the law of approach to saturation. The activation volume was measured using the Wohlfarth's equation. Both the variation of the magnetic anisotropy and the activation volume cannot explain the improvement in thermal stability of these films. It was found that the incorporation of in-depth defects induced by higher bias voltage during deposition, as evidenced from the increasing magnetic hardness coefficient, may be the cause for the improvement in thermal stability. These in-depth defects might have contributed to the pinning of the rotation of magnetization in films.

REFERENCES

1. S. Honda, H. Noguchi and T. Kusuda, J. Magn. Jpn. Vo.13, no. S1, p. 913 (1989).
2. Noriaki Tani, Masanori Hashimoto, Michio Ishikawa, Yoshifumi Ota, Kyuzo Nakamura and Akio Itoh, IEEE Trans. Magn. Vol. 26, p.1282 (1990).
3. T. Yogi, T. A. Nguyen, S. E. Lambert, G. L. Gorman, and G. Castillo, IEEE Trans. Magn. 26, p. 1578 (1990).
4. R. D. Fisher, H. R. Khan, N. Heiman and C. W. Nelson, IEEE Trans. Magn. Vol. 26, p.109 (1990).
5. Miaogen Lu, J. H. Judy and J. M. Siversten, IEEE Trans. Magn. Vol. 26, p.1581 (1990).
6. Jason Pressesky, Sany Y. Lee, Shanlin Duan, and Deborah Williams, J. Appl. Phys. 69, p. 5163 (1991).
7. Pawel Glijer, J. M. Siversten, and J. H. Judy, J. Appl. Phys. 73, p. 5563 (1993).
8. Y. Deng, D. N. Lambeth, X. Sui, L.-L. Lee and D. E. Laughlin, J. Appl. Phys. 73, p.5557 (1993).
9. Y. Deng, D. N. Lamberth and D. E. Laughlin, IEEE Trans. Magn., Vol.29, p. 3676 (1993).
10. Y.Okumura, H. Morita, H. Fujimori, X. B. Yang and I. Endo, IEEE Trans. Magn., Vol.29, p. 3144 (1993).
11. Brij B. La and T. Shinohara, IEEE Trans. Magn., Vol. 30, p. 3981 (1994).
12. Brij B. Lal and Michael A. Russak, J. Appl. Phys., 81, p. 3934 (1997).
13. Pu-Ling Lu, and S. H. Charap, IEEE Trans. Magn., Vol.30, p. 4230 (1994).
14. De-Hua Han, J. G. Zhu, J. H. Judy and J. M. Siversten, IEEE Trans. Magn., Vol.33, p. 3025 (1997).
15. L. Néel, C. R. Acad. Sci., Vol. 220, p. 738 (1945).
16. L. Néel, C. R. Acad. Sci., Vol. 220, p. 814 (1945).
17. E. P. Wohlfarth, J. Phys., F14, p. 1155 (1984).
18. Y. Hosoe, I. Tamai, K. Tanahashi, Y. Takahashi, T. Yamamoto, T. Kanbe, and Y. Yajima, IEEE Trans. Magn., Vol. 33, p. 3028 (1997).
19. W. F. Brown, J. Appl. Phys., Vol.30, Suppl., p. 130S (1959).
20. K. Y. Ho, X. Y. Xiong, J. Zhi, and L. –Z. Cheng, J. Appl. Phys., Vol.74, p.6788 (1997).

COMPUTER SIMULATIONS OF THERMAL SWITCHING IN SMALL-GRAIN FERROMAGNETS

M. A. NOVOTNY*, G. BROWN*,**, and P. A. RIKVOLD*,**
*Supercomputer Computations Research Institute, Florida State U., Tallahassee, FL 32306-4130, USA; novotny@scri.fsu.edu; browngrg@scri.fsu.edu; rikvold@scri.fsu.edu
**Center for Materials Research and Technology and Department of Physics, Florida State U., Tallahassee, FL 32306–4350

ABSTRACT

We present Monte Carlo and Langevin micromagnetic calculations to investigate thermal switching of single-domain ferromagnetic particles. For the Monte Carlo study we place particular emphasis on the probability that the magnetization does not switch by time t, $P_{\rm not}(t)$. We find that $P_{\rm not}(t)$ has different behaviors in different regimes of applied field, temperature, and system size, and we explain this in terms of different reversal mechanisms that dominate in the different regimes. In the micromagnetic study of an array of Ni pillars, we show that the reversal mode is an 'outside-in' mode starting at the perimeter of the array of pillars.

INTRODUCTION

All facets of the dynamics of nanoscale magnetic materials are currently active areas of research. The ability to construct single-domain nanoparticles via various methods and to measure the properties of individual nanoparticles and small arrays of nanoparticles [1 — 4] provides clean experiments compared with previous studies of mixtures of magnetic particles. One of the driving forces for applications is the rapid increase in density of magnetic recording devices, and the associated need to store each bit of information on a smaller number of grains [5]. On the theoretical and simulational side, a detailed understanding of nucleation and growth mechanisms that lead to the decay of a metastable state in finite systems has led to the identification of different decay modes in different parameter regimes [6 — 10]. In addition, new simulation algorithms are becoming available that may allow microscopic simulations at the inverse phonon frequency to extend to the technologically important time scales of years [11, 12].

In this brief paper we concentrate on using the thermal activation picture of nucleation and growth in simple metastable systems to better understand the reversal mechanisms for more realistic models of magnetism. We present Monte Carlo simulations for $P_{\rm not}(t)$, the probability that the metastable magnetization has not yet reversed at time t. We show how well this simulation of a heterogeneous system fits our theoretical description for $P_{\rm not}(t)$. We also present Langevin micromagnetic results for an array of Ni pillars. In the Langevin micromagnetic calculations the switching mechanism involves escape over a saddle point driven by random thermal fluctuations at constant field, rather than the deterministic disappearance of the metastable state as the field increases [13, 14]. Consequently, the Langevin micromagnetic calculations have the ability to measure $P_{\rm not}(t)$ directly.

MODELS AND METHODS

We have preformed two types of computer calculations. The first consists of Monte Carlo

Mat. Res. Soc. Symp. Proc. Vol. 517 © 1998 Materials Research Society

simulations [15] of the square-lattice Ising model with Hamiltonian

$$\mathcal{H} = -J \sum_{\langle i,j \rangle} s_i s_j - \sum_i H_i s_i \ , \tag{1}$$

where s_i=$\pm$1 and the local fields H_i are random numbers uniformly distributed between a maximum and a minimum value. This work uses periodic boundary conditions and a Glauber Monte Carlo update at randomly chosen sites. The initial state has all spins up, and at t=0 a negative field $\{H_i\}$ is applied. The unit of time is Monte Carlo Steps per Spin (MCSS). A rigorous derivation of the stochastic Glauber dynamic for Ising models from microscopic quantum Hamiltonians has been established under certain conditions in the thermodynamic limit [16], with the Monte Carlo time unit related to heat-bath phonon frequencies. This simulation has been performed to test our prediction for the forms of $P_{\rm not}(t)$ in a system with quenched bulk randomness.

In order to simulate models with realistic spin degrees of freedom, we have programmed a Langevin micromagnetics code similar to that reported in [17]. We have used a phenomenological damping parameter α, and classical spins of constant length given by the bulk saturation magnetization $M_{\rm s}$. Then at each lattice site i there is a scaled magnetization $\vec{m} = \vec{M}_{\rm s}/M_{\rm s}$. The standard Ginzburg-Landau-Lifshitz micromagnetic equation [13, 14] is

$$\frac{d\vec{m}_i}{dt} = -\frac{1}{1+\alpha^2}\vec{m}_i \times \left(\vec{h}_{i,\rm eff} + \alpha \vec{m}_i \times \vec{h}_{i,\rm eff}\right) \ . \tag{2}$$

The scaled effective field at each site, $\vec{h}_{i,\rm eff}$, contains contributions from terms including the exchange interaction, the dipole-dipole interaction, the interaction due to crystalline anisotropy, the applied field, and a scaled noise term proportional to the the Langevin fields $\zeta(t)$ [14, 17]. The Langevin noise term ζ and the integration time step Δt are related by $\zeta \propto \sqrt{\Delta t}$. Even though the set of equations used in this Langevin micromagnetics simulation are approximations to the actual equations [18], the approximation should be reasonable far below the critical temperature. We have used a fourth-order Runge-Kutta algorithm as the integration scheme in order to keep the length of the $\vec{m}_i$ constant.

RESULTS

In the Ising simulation, we used 100$\times$100 lattices at T=0.8$T_{\rm c}\approx$1.815J. As in the case of homogeneous nucleation [7], homogeneous nucleation for single-domain Ising particles with demagnetizing fields [8], and for single-domain Ising particles with different boundary conditions [9], we have identified different decay regimes [6 — 10]. The functional form for quantities such as $P_{\rm not}(t)$ are different in the different decay regimes. In particular, in the single-droplet (SD) regime of a single-domain magnetic particle, $P_{\rm not}(t) = \exp(-t/\tau)$. Here τ is the average lifetime for the decay of the metastable magnetic state due to thermal fluctuations. However, in the multi-droplet (MD) regime for single-domain particles the functional form for $P_{\rm not}(t)$ is given by

$$P_{\rm not}(t) = \frac{1}{2}{\rm erfc}\left(\frac{t-\tau}{\Delta}\right) \ , \tag{3}$$

where erfc is the complementary error function, and the width Δ depends on the system size. This form for $P_{\rm not}(t)$ results from the assumption that many independent droplets nucleate and grow in different parts of the system, collectively leading to the magnetization reversal.

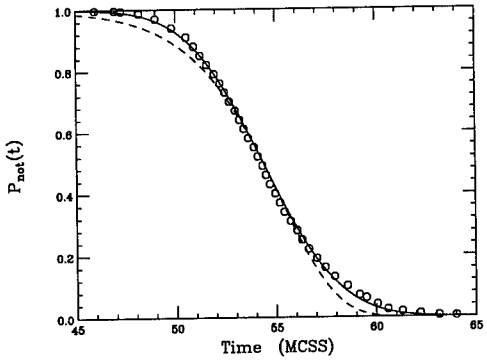

Figure 1: The probability $P_{\rm not}(t)$ in the multidroplet (MD) regime for a 100×100 Ising model with periodic boundary conditions at T=0.8T_c. The data (open circles) are for 1000 escapes from the metastable state. The random fields H_i are uniformly distributed, and centered on −0.34725 with a width of 0.34725. Two different one-parameter fits to the data are shown. The solid line is a fit to the complementary error function given by Eq. (3). The dashed curve is a one-parameter fit to a stretched exponential. In both of these fits the average lifetime was set at the measured value of τ=54.4 MCSS. (So that the solid line can be seen, only a small number of the 1000 data points are shown.)

Figure 1 shows data obtained from 1000 reversals with the fields H_i uniformly distributed with width 0.34725 J centered about −0.34725 J. This distribution for H_i ensures that the system is in the multi-droplet regime [7]. This figure should be compared with Fig. 3c of Ref. [7] which is for the Metropolis dynamic with a uniform field. The lifetime τ was measured to be τ=54.4 MCSS, where the time unit is Monte Carlo Steps per Spin (MCSS). Using the Mathematica nonlinear fit function to fit Eq. (3) to the data, gives the value Δ=4.26 MCSS, which is shown as a solid curve in Fig. 1. It is also possible to try other standard expressions for the sigmoidal curve for $P_{\rm not}(t)$ in the MD regime. Fig. 1 also shows a one-parameter fit to a stretched exponential, which gives $P_{\rm not}(t) = \exp(-bt^{20.7})$, shown as the dashed line. Here b is determined by requiring that the average of the distribution be τ. Clearly among these one-parameter fits, the one to Eq. (3) fits the data much better than does a stretched exponential.

Figure 2 shows an example of the type of thermal switching simulations [19] that can be performed using Langevin micromagnetic calculations. This figure represents a square array of magnetic Ni pillars. Similar arrays of Fe pillars have been built and measured experimentally [1, 2]. The simulation was started with all spins pointing up, and at t=0 a field parallel to the spins was applied for 1 nsec to allow the system to come to thermal equilibrium. Then the field was reversed to point opposite to the average magnetization, leaving the spins in a metastable state. However, the magnitude of the applied field would not have been sufficient to switch the system at zero temperature, and the switching event depicted in Fig. 2 is enabled by the thermal fluctuations included in Eq. (2). The random thermal field has its strongest effect at the edges of the array, where the demagnetizing field is

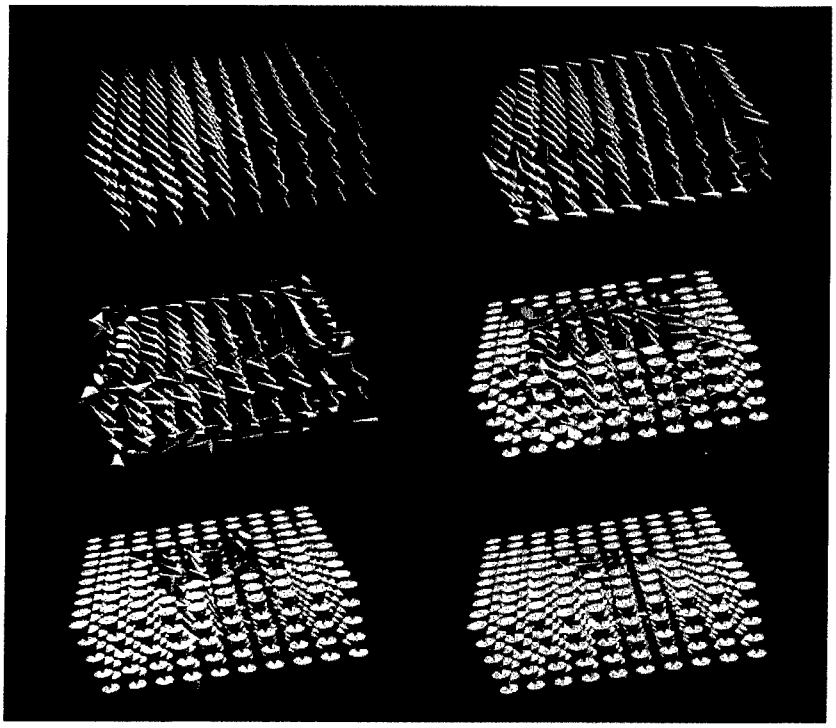

Figure 2: A series of snapshots of a Langevin micromagnetic calculation for magnetization reversal in a square array of Ni pillars that are 200 nm tall, 200 nm apart, and each have a diameter of 40 nm. Each pillar is discretized using 5 lattice points. (For clarity of presentation, the vertical scale of this figure is enhanced compared with the horizontal scale.) The temperature is 300 K, the spins are initially up, and the applied field is down with a magnitude of 1225 Oe. The integration time step is Δt=1 psec. The time sequence following field reversal, (reading line by line – left to right and top to bottom) is 4 nsec, 8 nsec, 12 nsec, 16 nsec, 20 nsec, and 24 nsec. This reversal mode is different from coherent rotation [5, 20].

weakest. In particular, an 'outside-in' switching mode is seen, in which the decay towards the stable magnetizaton direction starts from the pillars at the edge and subsequently propagates to the pillars in the interior of the array.

It is important to note that both the Monte Carlo and the Langevin micromagnetic simulations were conducted for applied fields sufficiently weak that a free-energy barrier against decay of the metastable state remained, and that this barrier had to be overcome by the thermal fluctuations in order for the magnetization switching to occur.

CONCLUSIONS

Realistic simulations of models for magnetic materials have been carried out. The form for the probability of not switching, $P_{\rm not}(t)$, is shown to fit the form of a complementary error function. The reversal mode for arrays of single-domain magnetic pillars has been identified as reversal of pillars on the boundary, followed by reversal of interior pillars.

ACKNOWLEDGMENTS

This research was supported in part by NSF Grant No. 9520325, FSU MARTECH, and FSU SCRI (DOE Contract No. DE-FC05-85ER25000). Supercomputer access was provided by the DOE at NERSC.

REFERENCES

1. A. D. Kent, S. von Molnár, S. Gider, and D. D. Awschalom, J. Appl. Phys. **76**, 6656 (1994).
2. S. Wirth, M. Field, D. D. Awschalom, and S. von Molnár, Phys. Rev. B, Rapid Communications, in press (1998).
3. W. Wernsdorfer et al., Phys. Rev. Lett. **77**, 1873 (1996); Phys. Rev. B **55**, 11552 (1997); Phys. Rev. Lett. **78**, 1791 (1997).
4. M. Lederman, S. Schultz, M. Ozaki, Phys. Rev. Lett. **73**, 1986 (1994).
5. J. C. Mallinson, The Foundations of Magnetic Recording (Academic, New York, 1993), Second Edition.
6. P. A. Rikvold, H. Tomita, S. Miyashita and S. W. Sides, Phys. Rev. E **49**, 5080 (1994).
7. H. L. Richards, et al., J. Magn. Magn. Mater. **150**, 37 (1995).
8. H. L. Richards, et al., Phys. Rev. B **54**, 4113 (1996).
9. H. L. Richards, et al., Phys. Rev. B **55**, 11521 (1997).
10. For a review see P. A. Rikvold, M. A. Novotny, M. Kolesik, and H. L. Richards, in Dynamical Properties of Unconventional Magnetic Systems, edited by A. T. Skjeltorp and D. Sherrington, NATO Science Series E: Applied Sciences, Vol. 349 (Kluwer, Dordrecht, 1998).
11. M. A. Novotny, Phys. Rev. Lett. **74**, 1 (1995), Erratum **75**, 1424 (1995); M. Kolesik, M. A. Novotny, and P. A. Rikvold, Phys. Rev. Lett. **80**, 3384 (1998).

12. A. F. Voter, Phys. Rev. Lett. **78**, 3908 (1997); J. Chem. Phys. **106**, 4665 (1997).

13. A. Aharoni, Introduction to the Theory of Ferromagnetism, (Clarendon Press, Oxford, 1996).

14. W. F. Brown, Phys. Rev. **130**, 1677 (1963).

15. K. Binder, in Monte Carlo Methods in Statistical Physics, edited by K. Binder, (Springer, Berlin, 1979).

16. P. A. Martin, J. Stat. Phys. **16**, 149 (1977).

17. E. D. Boerner and H. N. Bertram, IEEE Trans. Magn. **33**, 3052 (1997).

18. D. A. Garanin, Phys. Rev. B **55**, 3050 (1997).

19. G. Brown, M.A. Novotny, and P.A. Rikvold, in preparation.

20. L. Néel, Ann. Phys., Paris **3**, 137 (1948).

A SIMULATION OF ROTATIONAL HYSTERESIS ENERGY LOSS IN LONGITUDINAL THIN-FILM MEDIA

Wei Yang and David N. Lambeth
Data Storage Systems Center, Department of Electrical and Computer Engineering
Carnegie Mellon University, Pittsburgh, PA 15213

ABSTRACT

The field dependence of the rotational hysteresis energy loss was simulated for longitudinal thin-film media with the purpose of examining the validity of this method for measuring the anisotropy field. The field at which the rotational hysteresis vanishes, which is usually taken as the experimentally measured anisotropy field, was found to be smaller than the real anisotropy field when intergranular magnetostatic and exchange interactions are included in the simulations. Hence the rotational hysteresis method may result in an underestimation of the anisotropy field for the films with non-negligible grain interactions. To confirm this experimentally, two CoCrTa films, one with strong in-plane easy axis texture and the other with uniaxially aligned grain easy axes, were prepared under the same conditions. The anisotropy field determined by the rotational hysteresis of the first sample was found to be smaller than the more accurate value obtained from the hard axis hysteresis loop of the second sample.

INTRODUCTION

Co-based alloy polycrystalline thin films are currently the most popular longitudinal recording media. Achieving an increasing areal density in these media requires a higher coercivity to obtain high linear density, and a smaller Co grain size to reduce medium noise. Co alloys exhibit uniaxial anisotropy, and the anisotropy constant (K) is one of the important parameters governing the coercivity [1] and the thermal stability [2] of Co alloy thin-film media. Determined by the Stoner-Wohlfarth model [1] of rotation magnetization, the maximum coercivity that can be realized in an ideal Co-alloy thin film consisting of isolated, non-interacting single domain grains with an in-plane 2D random easy axis distribution is about half of the anisotropy field H_K (defined as $2K/M_s$, where M_s is the saturation magnetization). A large value of K, therefore, provides the greatest potential for achieving high coercivity. Meanwhile, with a decreasing grain volume V, the energy barrier of the order of KV against the thermally activated magnetization reversal becomes lower, and a large K is essential for the stability of high density recorded data. Hence, the knowledge on the anisotropy constants of Co alloy materials is important in order to envision the limits of this medium system for future high density recording.

If the easy axes of the Co grains are all made parallel to the same direction in the film plane, the anisotropy constants can be measured from the torque curves of the sample. Longitudinal media, however, are usually polycrystalline thin films with isotropic grain easy axes, and the field dependence of the rotational hysteresis energy loss has been employed to determine the anisotropy field for these media. Rotational hysteresis is defined as the net work required to rotate a sample slowly through 360° in a field. A non-zero rotational hysteresis is a

Mat. Res. Soc. Symp. Proc. Vol. 517 © 1998 Materials Research Society

result of irreversible rotation of magnetization. For a single domain particle or an assembly of non-interacting particles with uniaxial anisotropy, the range of field values that incur irreversible switching is between $0.5H_K$ and H_K, and thus the rotational hysteresis vanishes when the field is greater than H_K [3,4]. The use of rotational hysteresis as an experimental method of measuring the anisotropy field is mainly based upon this fact.

In real thin films, however, there possibly exist magnetostatic and exchange interactions between the Co grains. In this study we have performed simulation studies on the effect of these intergranular couplings on the field dependence of rotational hysteresis. Our objective is to examine the validity of this experimental method of determining the anisotropy field.

SIMULATION DETAILS

In our simulation, a longitudinal medium is modeled as a regular array of particles with 2D in-plane randomly oriented easy axes. The energy density of the medium, including the magnetostatic and exchange interaction energies, is

$$\frac{E}{K} = -\frac{1}{N}\left[\frac{2}{H_K}\sum_i \hat{\boldsymbol{m}}_i \cdot \boldsymbol{H} + \sum_i (\hat{\boldsymbol{m}}_i \cdot \hat{\boldsymbol{k}}_i)^2 + c_m \sum_{i,j} \hat{\boldsymbol{m}}_i \cdot \mathbf{D}_{ij} \cdot \hat{\boldsymbol{m}}_j + c_e \sum_{i,j=nn} \hat{\boldsymbol{m}}_i \cdot \hat{\boldsymbol{m}}_j\right], \qquad (1)$$

where

$$c_m = M_s / H_K \text{, and } c_e = JM_s / H_K .$$

Here $\boldsymbol{H}$ is the applied field, and $\hat{\boldsymbol{m}}_i$ and $\hat{\boldsymbol{k}}_i$ are unit vectors denoting the directions of the magnetization and the easy axis of each particle. $\mathbf{D}_{ij}$ is the matrix specifying the magnetostatic interaction between grains, which are approximated as dipolar energies between particle pairs. J is the phenomenological exchange constant. N is the number of particles in the simulations. When volume densities are evaluated the spacing between the grains is ignored.

The torque curves were calculated with the field rotating within the film plane in small angular steps. At each angle of the field, $\hat{\boldsymbol{m}}_i$ is determined by finding the minimum of Eq. (1) in the vicinity of the $\hat{\boldsymbol{m}}_i$ corresponding to the minimum obtained in the previous step. The torque density, normalized by K, is computed as

$$\frac{T}{K} = \frac{1}{N}\frac{2}{H_K}\sum_i \hat{\boldsymbol{m}}_i \times \boldsymbol{H} . \qquad (2)$$

The field is cycled until a steady state torque curve is obtained. The rotational hysteresis energy loss per unit volume (W_r) can be obtained as half the area between the clockwise and counter-clockwise torque curves. H_0, defined as the field at which W_r vanishes, is calculated by extrapolating W_r with respect to $1/H$. Unless otherwise specified, the simulations start with samples initially in AC demagnetized states.

RESULTS AND DISCUSSION

Without the intergranular interactions ($c_m = c_e = 0$), W_r are plotted in Fig. 1 as a function of the applied field H. At fields below $0.5H_K$, W_r remains zero. Then it rises abruptly to a peak at $H_p = 0.5H_K$. From H_p to H_K, W_r decreases and finally becomes zero again at and above $H_o = H_K$. This curve is the same as that for a single domain particle.

When the magnetostatic interactions are introduced in the simulation, both H_p and H_o decrease when compared with the case of non-interacting particles. Shown in Fig. 1 are the $W_r(H)$ curves for values of c_m ranging from 0.05 to 0.4 (with no exchange interaction, $c_e = 0$). With the magnetostatic interactions, W_r becomes non-zero at fields below $0.5H_K$ and rises slowly to the maximum at H_p. H_p are now smaller than $0.5H_K$, and the corresponding peak values of W_r are also lower than that for the medium with non-interacting particles. When the field is further increased, W_r is found to decrease; it becomes virtually zero when the field goes beyond H_o,

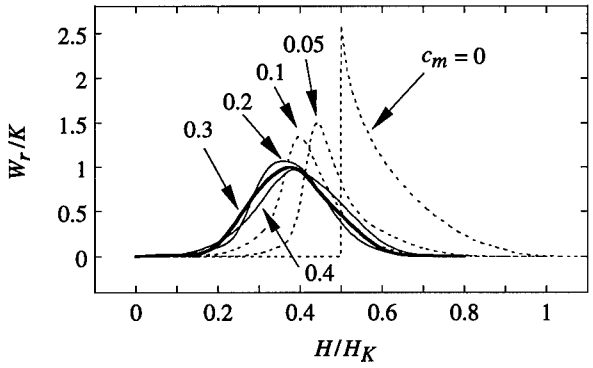

Fig. 1. The simulated field dependence of the rotational hysteresis for different magnetostatic interaction parameter c_m ($c_e = 0$).

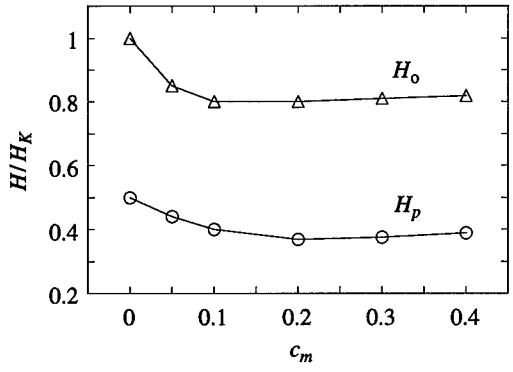

Fig. 2. H_p (the field at which W_r is maximum) and H_o (the field at which W_r vanishes) as functions of the magnetostatic interaction parameter c_m ($c_e = 0$).

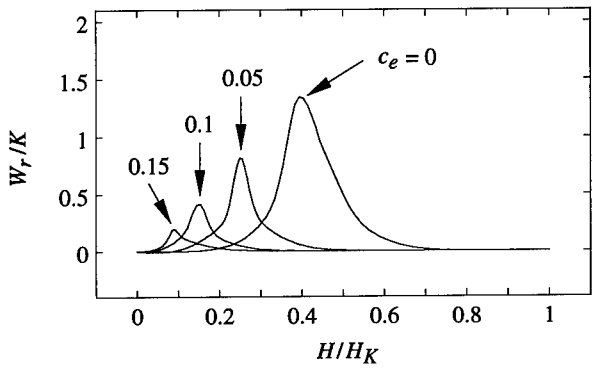

Fig. 3. The simulated field dependence of the rotational hysteresis for different exchange interaction parameter c_e ($c_m = 0.1$).

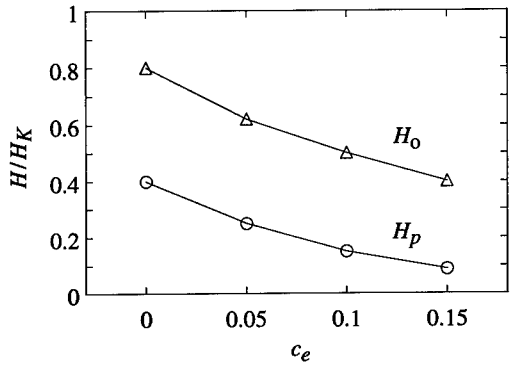

Fig. 4. H_p (the field at which W_r is maximum) and H_0 (the field at which W_r vanishes) as functions of the exchange interaction parameter c_e ($c_m = 0.1$).

whose value is smaller than H_K. H_p and H_0 are plotted in Fig. 2 as functions of the parameter c_m. Both are found to decrease at small values of c_m, yet start to flatten out and even increase slightly as c_m is further increased.

When both the magnetostatic and the exchange interactions are included, $W_r(H)$ curves peak at even smaller H_p ($< 0.5H_K$) with further decreased peak values, and H_0 is also further decreased. Shown in Fig. 3 are the $W_r(H)$ curves for $c_m = 0.1$ while c_e varies from 0 to 0.15. Again the values of H_p and H_0 are plotted in Fig. 4 as functions of the parameter c_e. Both are found to continuously decrease to smaller values when c_e increases.

If the simulations are performed on a sample starting at its remanent magnetized state, the $W_r(H)$ curve is slightly different from that for an initially AC demagnetized sample. The two cases are compared in Fig. 5 with the same interaction parameters, $c_m = 0.1$ and $c_e = 0.05$. The

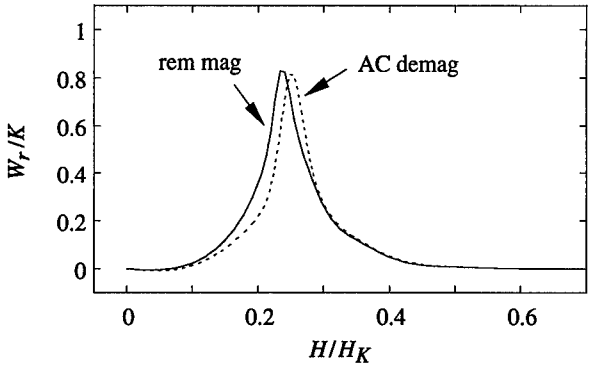

Fig. 5. The simulated field dependence of the rotational hysteresis for a sample with different initial states.

difference is most significant at fields below and about H_p, and the two curves overlap as the field approaches H_0. This is not totally unexpected since H_0 is much greater than the sample coercivity, the different initial states will bear little effect at fields around H_0. As a result, the same H_0 were found from both curves.

These simulation results have shown that W_r vanishes at fields well below H_K due to the intergranular coupling. Hence they predicate that the experimental $W_r(H)$ method underestimates the value of H_K for thin films in which the grain interactions are not negligible.

To verify this experimentally, we prepared a $Co_{84}Cr_{13}Ta_3$(200Å)/Cr(300Å) thin film on a glass substrate. The sample was sputter deposited with a substrate temperature about 250°C, and strong (002) Cr and (11$\bar{2}$0) CoCrTa in-plane easy axis textures were confirmed by x-ray diffraction. The coercivity of the sample is about 2.0 kOe. The field dependence of the rotational hysteresis was measured and shown in Fig. 6(a), from which H_0 is found to be 5.5 kOe. Meanwhile we also prepared a uni-crystal film with the same processing conditions and

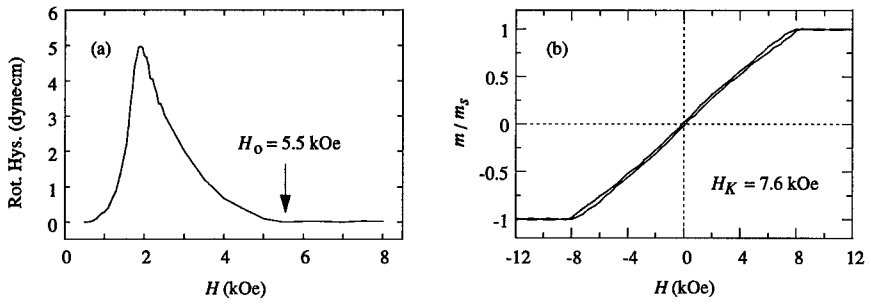

Fig. 6 (a) The measured field dependence of the rotational hysteresis for a (11$\bar{2}$0) textured CoCrTa/Cr film, and (b) the hard axis hysteresis loop of a uni-crystal CoCrTa/Cr film. Both films were prepared under the same conditions.

CoCrTa and Cr thicknesses [5]. In this uni-crystal sample all the grain easy axes are highly oriented along the same direction. Almost straight lines were observed in the hysteresis loop measured along the hard axis [Fig. 6(b)]. The anisotropy field was determined to be H_K = 7.6 kOe, which is obviously greater than H_0. It should be pointed out that this H_0 for the textured film is determined by the grains with in-plane easy axes, which exhibit the maximum critical fields [6]. The small portion of the grains with out-of-plane easy axes should have no, or a much less significant role.

CONCLUSIONS

In this study we have simulated the field dependence of the rotational hysteresis for thin films in which the particle-to-particle interactions are not negligible. The field at which the rotational hysteresis vanishes, which is usually taken as the measured anisotropy field, was found to be smaller than the real anisotropy field. Hence the rotational hysteresis method is likely to result in an underestimation of the anisotropy field. We have further confirmed this in our experiment. The torque curve or the hard axis hysteresis loop measured on a uni-crystal film are therefore more desirable methods for accurately determining the anisotropy constants of Co-alloy thin films.

ACKNOWLEDGMENTS

This work is supported by an IBM Partnership Award and in part by the National Science Foundation under Grant No. ECD-8907068. The U.S. government has certain rights in this material.

REFERENCES

[1] E.C. Stoner and E.P. Wohlfarth, Trans. Roy. Soc. (London) **A240**, 599(1948).
[2] S.H. Charap, P.-L. Lu, and Y. He, IEEE Trans. Magn. **33**, 978(1997).
[3] C.P. Bean and W.H. Meiklejohn, Bull. Am. Phys. Soc. Ser. II. **1**, 148(1956).
[4] I.S. Jacobs and F.E. Luborsky, J. Appl. Phys. **28**, 467(1957).
[5] W. Yang, D.N. Lambeth, and D.E. Laughlin, to be published.
[6] W. Yang and D.N. Lambeth, IEEE Trans. Magn. **33**, 2965(1997).

MODELING COMPLEX AFTEREFFECT BEHAVIOR IN RECORDING MATERIALS USING A PREISACH-ARRHENIUS APPROACH

E. DELLA TORRE,* L. H. BENNETT* AND L. J. SWARTZENDRUBER
National Institute of Standards and Technology, Gaithersburg, MD 20899
*Also with the Institute for Magnetics Research, George Washington University, Washington, DC 20052

ABSTRACT

A Preisach-Arrhenius aftereffect model, that accurately calculates the entire relaxation process, including the linear log-time region, is used to describe some other characteristics of the time decay. The location of the peak of the decay coefficient is shown to be less than the peak of the irreversible coercivity by an amount that is a function of the standard deviation of the critical field, the fluctuating field, and the moving parameter. The model computes a magnetization decay that includes nonmonotonic behavior under certain circumstances, depending upon the applied field history. A conclusion of this paper is that procedures for accelerated testing of magnetic media are suspect.

INTRODUCTION

A Preisach-Arrhenius model was previously presented to describe aftereffect [1]. In this model it assumed [2] that for a hysteron to cross an energy barrier to a lower energy state, the expected value of the time, τ, is given by the Arrhenius law

$$\tau = \tau_0 \exp(W/kT), \tag{1}$$

where W is the energy barrier, k is Boltzmann's constant, T is the absolute temperature, and τ_0^{-1} is the attempt frequency. A collection of hysterons, each of which has a different energy barrier, will have a normalized irreversible component of magnetization, m_i, that varies with time given by

$$m_i(t) = m_i(0) + \Delta m_i f(t), \tag{2}$$

where $f(0)$ is zero and m_i will eventually approach the anhysteretic magnetization. Here, we consider two cases of relaxation processes, each starting with a material saturated in the negative direction. In the first instance, which we will refer to as a *single-field process*, the field is rapidly switched to a field, H, which is maintained constant throughout the experiment. This is the usual method of measuring the decay coefficient. If a single number is reported for the decay coefficient, H should be chosen to optimize the speed of relaxation. In the second case, which we will refer to as a *double-field process*, the field is rapidly switched to a field, H_1, followed immediately by a second field, $H_2 < H_1$, which is then maintained constant throughout the experiment. The constant field, either H or H_2, at which the relaxation rate is measured, will be called the *holding field.*

SINGLE-FIELD PROCESSES

A Preisach function suitable for describing interaction in a magnetic medium, such as a recording medium, whether it is particulate or thin film and whether the interaction is magnetostatic only or includes exchange, was shown to be Gaussian [3]. This is given by

Mat. Res. Soc. Symp. Proc. Vol. 517 © 1998 Materials Research Society

$$p(H_i,H_k) = \frac{1}{2\pi\sigma_i\sigma_k}\exp\left[-\frac{(H_i+\alpha M)^2}{2\sigma_i^2}+\frac{(H_k-\bar{H}_k)^2}{2\sigma_k^2}\right], \quad (3)$$

where the interaction field, H_i, and the critical field, H_k, of a hysteron are describable in terms of the up and down critical fields by

$$H_x = (U+V)/2 \quad \text{and} \quad H_\varrho = (U-V)/2, \quad (4)$$

where U and V are the switching fields of a hysteron. The average critical field, $\bar{H}_k$, is equal to the remanent coercivity for single-quadrant media, but will be less than that for three-quadrant media [4]. We will describe the processes in terms of operative fields, $h = H + \alpha M$, so that the Preisach function does not depend upon the magnetization. With these definitions, it has been shown in [1] that $f(t)$ is given by

$$f(t) = 1 - \frac{h_\omega}{\sigma}\sqrt{\frac{2}{\pi}}\int_\eta^\infty dy\, \exp\left\{-\frac{te^{-\hat{}}}{\tau_\eta}-\frac{[h-\bar{h}_\varrho+h_\omega y]^\theta}{2\sigma^\theta}\right\}, \quad (5)$$

where $\bar{h}_k$ is the average critical field, and the standard deviation of the critical field, σ, in terms of σ_i and σ_k, the standard deviations of the interaction fields and the critical fields respectively, is given by

$$\sigma = \sqrt{\sigma_x^\theta + \sigma_\varrho^\theta}. \quad (6)$$

The fluctuating field, h_f, is defined as $kT/\mu_0 MV$, where V is the activation volume which can be obtained from a micromagnetic calculation such as in [5]. Is noted that all the parameters are a function of temperature , thus h_f is not a linear function of T. A particularly useful discussion of fluctuation fields and activation volumes is given by Lyberatos and Chantrell [6].

It was shown in [1] that $f(t)$, for a material saturated by a positive field that is subject to a negative holding field equal to $\bar{h}_k$, starts from zero, then increases linearly with log t for a considerable period, and finally saturates. If the holding field is equal to $\bar{h}_k$, then Δm_i is equal to one and $f(t)$ is the normalized aftereffect. If a material is first saturated in the negative direction, then $m_i(0)$ is given by

$$m_x(0) = \text{erf}\left[(h-\bar{h}_\varrho)/\sigma\right]. \quad (7)$$

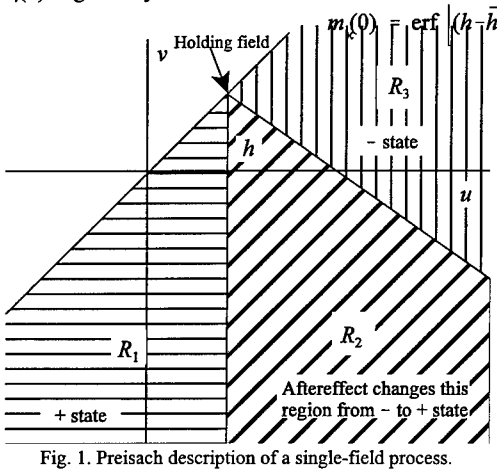

Fig. 1. Preisach description of a single-field process.

It was shown in [1] that the ground state magnetization in the presence of a holding magnetic field, h, is given by

$$m_x(\infty) = \text{erf}\left[h/\sigma_x\right]. \quad (8)$$

This process is illustrated in Fig. 1, where immediately after the application of the holding field, all hysterons in R_1 are positive and those in R_2 and R_3 are negative. During the relaxation process, the hysterons in R_2 go from negative to positive. Thus, in this case, Δm_i is given by

$$\Delta m_x = \text{erf}\left[h/\sigma_x\right] - \text{erf}\left[(h-\bar{h}_\varrho)/\sigma\right]. \quad (9)$$

A plot of Δm_i, the change in magnetization during the relaxation process, for various values of σ, when σ_k is equal to zero and h_k is equal to one, is shown in Fig. 2. It is seen that the field which maximizes Δm_i is half h_k, since this is the difference of two error functions, one centered at h_k and the other centered at zero. Since the maximum change in magnetization is limited to two, the curve saturates at that value for small σ. The curve is symmetrical with respect to the peak only in this case, since σ_i is equal to σ when σ_k is equal to zero. Since σ_i is always less than or equal to σ, the slope at the origin is usually steeper than at h_k, and the peak of this curve will occur at a value less than one-half.

The decay coefficient, $\hat{S}$, can be computed by taking the derivative of (2) with respect to log-time. It is noted that

$$\hat{S} = \frac{dm(t)}{d\ln t} = t\,\Delta m_\infty \frac{df(t)}{dt}. \tag{10}$$

Thus, $\hat{S}$ is given by

$$\hat{S} = \Delta m_\infty \frac{h_\omega t}{\tau_\eta \sigma}\sqrt{\frac{2}{\pi}}\int_\eta^\infty \exp\left[-y-\frac{te^{-y}}{\tau_\eta}-\frac{(h-\bar{h}_\varrho+h_\omega y)^\theta}{2\sigma^\theta}\right]dy = \Delta m_\infty g(t). \tag{11}$$

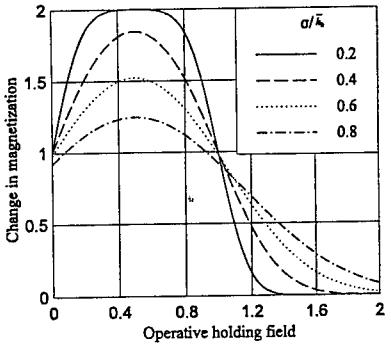

Fig. 2. Variation in the total change in magnetization, Δm_i, with normalized holding field, $h/\bar{h}_k$, for relaxation to the ground state.

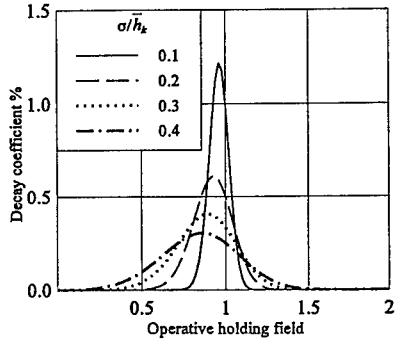

Fig. 3. Variation in decay coefficient with holding field for various critical field distributions for negligible h_f.

It was shown in [1], that for a sufficiently small fluctuating field, $g(t)$, is a constant over a wide range of times, and in this range it can be approximated by

$$g \approx \sqrt{\frac{2}{\pi}}\,\frac{h_f \exp[-(h-\bar{h}_k)^2/2\sigma^2]}{\sigma}. \tag{12}$$

Thus, g has a maximum for $h = \bar{h}_k$; however, at this value, Δm_i is a decreasing function of h, which shifts the location of the peak of $\hat{S}$ to a value smaller than $\bar{h}_k$. The amount of decrease in the location of the peak depends upon the slope of Δm_i versus h, which is roughly inversely proportional to σ. This variation in decay coefficient with holding field has a maximum that is inversely proportional to σ, as illustrated in Fig. 3 for four different values of σ.

In addition to the shift in the peak due to Δm_i, there is a shift due to the fluctuating field which can be computed by an alternate approach, that is, by solving the differential equation also derived in [1]. In particular, each hysteron on the Preisach plane obeys the following:

$$\frac{dQ}{dt} + Q\left(\frac{\tau_+ + \tau_-}{\tau_+\tau_-}\right) = \frac{\tau_+ - \tau_-}{\tau_+\tau_-}, \tag{13}$$

where

$$\tau_+ = \tau_\eta \exp[(u-h)/h_\omega] \qquad \text{and} \qquad \tau_- = \tau_\eta \exp[(h-v)/h_\omega]. \tag{14}$$

A calculation of the decay coefficient as a function of the applied field, for a material whose $\overline{h}_k$ is 100 mT and whose σ is 0.5, is shown in Fig. 4. It is seen that as the fluctuating field increases, the decay coefficient increases and the field which maximizes the decay coefficient decreases. For example, if the fluctuating field is 1.5 mT, the field at which $\hat{S}$ is a maximum is roughly half $\overline{h}_k$. Furthermore, the maximum decay coefficient is 20% larger at this field than it is at $\overline{h}_k$. The variation in the maximizing field and the largest value of the decay coefficient is illustrated in Fig. 5.

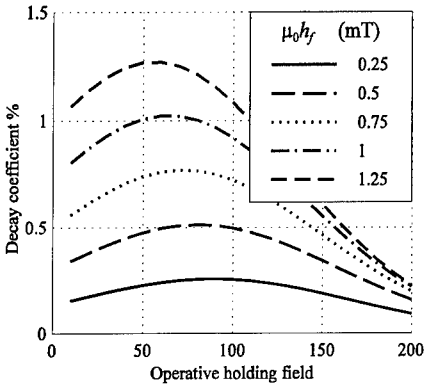

Fig. 4 Variation of decay coefficient with holding field for various fluctuation fields from (13).

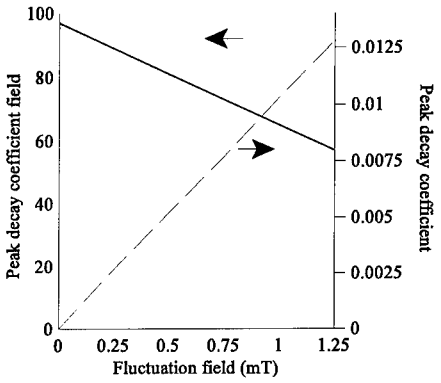

Fig. 5. Maximum decay coefficient and its location as a function of the fluctuation field from (13).

DOUBLE-FIELD PROCESSES

The initial conditions for the differential equation, (13), are determined by the conventions of the Preisach model. Thus, after applying a field, h_1, the initial state of the magnetization is given by

$$Q(u,v,0) = \begin{cases} 1 & \text{for } u<h_\theta \\ -1 & \text{for } u>h_\theta. \end{cases} \tag{15}$$

This state will not change immediately from this initial state when the field is changed to h_2, if h_2 is less than h_1. The hysteron density will decay to a steady state value, which is the ground state of the system for this holding field, with a time constant equal to

$$\tau(u,v) = \frac{\tau_+\tau_-}{\tau_+ + \tau_-} = \frac{\tau_\eta}{\exp\left(\dfrac{v-h_\theta}{h_\omega}\right)+\exp\left(\dfrac{h_\theta-u}{h_\omega}\right)}. \tag{16}$$

The final magnetic state of the hysterons under the holding field, h_2, is given by

$$Q(\infty) = (\tau_+-\tau_-)/(\tau_++\tau_-) = \tanh[(h_x-h_\theta)/h_\omega]. \tag{17}$$

This is consistent with Maxwell-Boltzmann statistics.

If h_f is small, then (16) can be approximated by

$$\tau(u,v) = \begin{cases} \tau_\eta \exp\left((h-v)/h_\varphi\right) & \text{for } u+v>2h \\ \tau_\eta \exp\left((u-h)/h_\varphi\right) & \text{for } u+v<2h, \end{cases} \tag{18}$$

and (17) can be approximated by

$$Q(\infty) = \begin{cases} 1 & \text{if } h_\Theta > h_\theta \\ -1 & \text{if } h_\Theta < h_\theta. \end{cases} \tag{19}$$

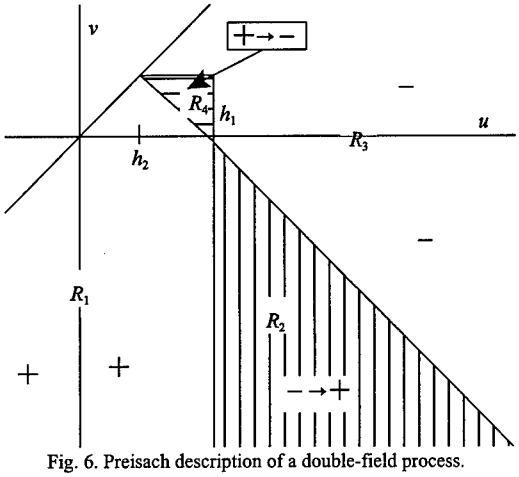

Fig. 6. Preisach description of a double-field process.

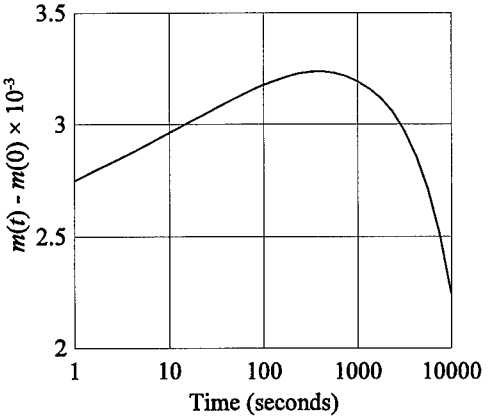

Fig. 7. Plot of the aftereffect due to a double-field process.

This can be described on the Preisach plane as shown in Fig. 6, showing that a double-field process divides the Preisach plane into four regions. The first region, R_1, is magnetized positively for the entire relaxation process by h_1; the second region, R_2, was initially magnetized negatively, but becomes magnetized positively during the relaxation process; the third region, R_3, is magnetized negatively for the entire relaxation process by h_1; and finally region R_4 is initially magnetized positively, but becomes magnetized negatively during the relaxation process.

From (18), we see that the time constants increase monotonically from h_2 with increasing u. Thus, the time constants of the different hysterons in R_4 are all shorter than the ones in R_2. Thus, R_4 will become negative faster than R_2 will become positive. This causes the magnetization to increase initially and then decrease as it approaches the final state. This nonmonotonic effect is similar to that observed by LoBue, et al. [7]. In particular, if h_1 is equal to $\overline{h}_k$, and h_2 is equal to zero, then both the initial and the final magnetizations are zero; however, in the process of relaxing, the magnetization will at first go negative due to hysterons in R_4 relaxing and then revert to zero as the hysterons in R_2 relax. On the other hand, if h_1 is equal to h_2, then the process is single-field and the magnetization will approach the equilibrium state monotonically.

The calculated magnetization as a

function of time for a typical process in which h_1 is slightly greater than $\overline{h}_k$ and h_2 is slightly less than $\overline{h}_k$ is shown in Fig. 7. The details of the parameters are discussed elsewhere [8]. The magnetization starts from a small positive value, then increases for a while, and then decreases towards a negative value. If h_1 is equal to $\overline{h}_k$ and h_2 is equal to zero, the magnetization would start from zero and then eventually return to zero; however, the time at which the magnetization would start to decrease is very large and impractical to measure for recording media.

CONCLUSIONS

Wohlfarth indicated [9] that the peak in the decay coefficient occurs at the peak of the irreversible coercivity. We have now shown that the location of the peak also depends upon the standard deviation of the critical fields and the size of the fluctuating field. Furthermore, the behavior of the magnetization in a holding field depends upon both the value of the holding field and upon the magnetic history. The latter can be explained satisfactorily by the Preisach-Arrhenius model [1]. It was shown that for single-field processes, the magnetization decays linearly with log-time for an appropriate time window, and the decay is a maximum value at fields less than the remanence coercivity. The decrease in the location of the peak depends upon both the standard deviation of critical fields and the fluctuating field. It is noted that measuring the decay coefficient at the peak of the irreversible susceptibility can drastically underestimate the lifetime of a recording. A dramatic example of this can be seen by examining Fig. 3; we see that the decay coefficient measured at the coercivity *increases* with decreasing σ. However, at fields less than half the coercivity, the decay coefficient *decreases* with decreasing σ, thus invalidating one of the procedures for accelerated testing of media.

For double-field processes, the magnetization decay, under certain circumstances, can change direction during the relaxation. For some situations the time at which this change in direction occurs can be very long. This paper presents a theory behind this decay behavior, and a companion paper [8] shows that these calculations agree with the results of extensive experiments on magnetic tape samples.

ACKNOWLEDGMENTS

We would like to thank Jie Lou and other members of the Institute for Magnetics Research at George Washington University for useful discussions.

REFERENCES

1. E. Della Torre and L. H. Bennett, *IEEE Trans. Mag.*, Sep. 1998, (in press).
2. L. Néel, *J. Phys. Rad.* **12**, 339 (1951).
3. E. Della Torre and F. Vajda, *J. Appl. Phys.*, **81** (8), 15 Apr. 1997, pp. 3815-3817.
4. J. Lou, L. H. Bennett and E. Della Torre, *IEEE Trans. Mag.*, Sep. 1998, (in press).
5. Y. D. Yan and E. Della Torre, *J. Appl. Phys.* **66**, 320 (1989).
6. A. Lyberatos and R. W. Chantrell, *J. Condens. Matter*, **9**, 2623 (1997).
7. M. LoBue, V. Basso, G. Bertotti, K.-H. Muller, *IEEE Trans. Mag.* **33**, 3862 (1997).
8. L. J. Swartzendruber, L. H. Bennett, E. Della Torre, H. J. Brown and J. H. Judy in these proceedings.
9. E. P. Wohlfarth, *J. Phys. F: Met. Phys.*, **14**, 1984, pp. L155-L159.

Part VII

Perpendicular Magnetic Media and Novel Structures

LARGE MAGNETIC ANISOTROPY IN Co_3Pt ORDERED PHASE THIN FILMS

Yoshiyasu Yamada and Takao Suzuki
Information Storage Materials Laboratory, Toyota Technological Institute, 2-12-1, Hisakata, Tempaku, Nagoya, JAPAN

ABSTRACT

The very large perpendicular magnetic anisotropy of the order of 2×10^7 erg/cm^3 at room temperature was found in $Co_{1-x}Pt_x(0<x<0.5)$ alloy thin films made by e-beam evaporation. The large magnetic anisotropy is likely related to the anisotropic Co-Co bonding distribution, which is similar to the cases of Co/Pt multilayers and FePt alloy thin films. The activation energy estimated for the ordering is approximately 0.3 eV, which is preferably compared to 0.2 eV for FePt. A model is proposed, for which both a short range and long range ordering are present, depending on substrate deposition temperature.

1 INTRODUCTION

Co-Pt and Fe-Pt alloys have been well known for its high anisotropy, and many researches have been carried out so far. Visokay[1] et al. reported that co-sputtered CoPt and FePt films, which were deposited at higher than 400 °C, form $L1_0$ type ordered phase and possess a high K_u value of more than 10^7 erg/cm^3. Lairson[2] et al. produced CoPt $L1_0$ ordered phase by annealing the Co/Pt artificial multilayers. The K_u of 1.9×10^7 erg/cm^3 was observed in the annealed sample. A significant enhancement in magneto-optical Kerr rotation is also observed in these systems[3,4]. The origin of this high magnetic anisotropy was discussed in many ways[5-7]. Harp et al.[8] suggested the existence of Co_3Pt ordered phase produced in a thin film deposited onto $Al_2O_3(0001)$ substrate with Pt underlayer and observed a specific peak for the ordered phase in magneto-optical Kerr rotation spectrum. Recently, Yamada, Suzuki, and Abarra[9] showed that electron beam evaporated Co_3Pt alloy thin films exhibit a large magnetic anisotropy constant in the order of 10^7 erg/cm^3. X-ray diffraction measurements confirmed that these films contain a superlattice structure of Co_3Pt, first reported by Harp et al.[8] In the present study, the magnetic and structural properties of Co_3Pt alloy ordered film in connection with the origin of the large K_u value is discussed.

2 EXPERIMENTAL

$Co_{1-x}Pt_x(0<x<0.5)$ alloy thin films were deposited using an electron beam co-evaporation system with two electron guns. The purity of metal sources was better than 99.9%. The compositions of the films were varied by changing each deposition rate. $Al_2O_3(0001)$ substrate was used. The substrates were rotated at 20 rpm during deposition. No underlayer was deposited onto the substrates. The pressure of the chamber was maintained better than 5×10^{-9} Torr prior to the deposition, and better than 5×10^{-7} Torr during the deposition. The substrates were heated from an ambient temperature to 550 °C by an electric heater installed inside the chamber. The thickness of the films is approximately 1000 Å. Magnetic properties were measured using VSM (Vibrating Sample Magnetometer), AGFM (Alternating Gradient Force Microscope), and Torque magnetometer in the field up to 20 kOe. Structural analyses were made using X-ray diffractometer (Cu-Kα, 40 kV, 60 mA), and Transmission Electron Microscope (Accelerating voltage: 400 kV). The chemical composition of the films was measured by Electron Probe Micro Analyzer.

Mat. Res. Soc. Symp. Proc. Vol. 517 © 1998 Materials Research Society

3 RESULTS AND DISCUSSIONS

3.1 Magnetic Properties

3.1.1 Dependence on Pt content

M_s and H_c were measured from M-H loops obtained using VSM. The dependence of M_s on Pt content for the samples deposited at R.T., 230 °C, and 400 °C is shown in Fig. 1. They are very close to that for bulk Co-Pt alloy within the accuracy of measurement. Similarly, the dependence of H_c on Pt content is plotted in Fig. 2. It is noted that the perpendicular coercivity for the samples deposited at 400 °C increases drastically to more than 2 kOe beyond 30 % Pt.

The intrinsic perpendicular anisotropy constant K_u (defined as $K_u = K_\infty + 2\pi M_s^2$, where K_∞ is the torque amplitude as $H \rightarrow \infty$) at different compositions of Co-Pt alloy films was measured using a torque magnetometer. Figure 3 shows K_u as a function of Pt content for the samples deposited onto $Al_2O_3(0001)$ at T_s = R.T., 230 °C, and 400 °C, respectively. One can see that K_u values of the films deposited at T_s = 230 °C and 400 °C exhibit a maximum at approximately 25 at % Pt. On the other hand, the very little change of K_u with film composition for the samples deposited at an ambient temperature was observed. The maximum values of K_u when T_s = 400 °C and 230 °C are 2.1×10^7 erg/cm^3 and 1.3×10^7 erg/cm^3, respectively. The value for 400 °C is more than 4 times bigger than that for bulk hcp Co. It is noted that the

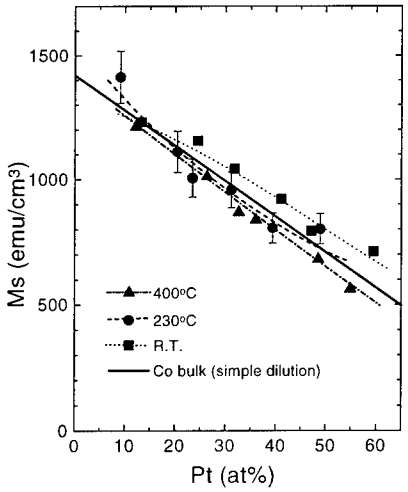

Fig. 1 Saturation magnetization as a function of Pt content.

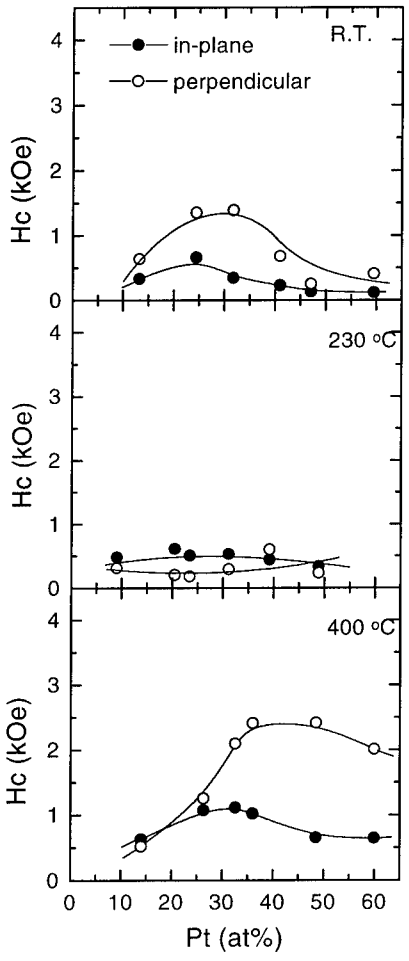

Fig. 2 In-plane and perpendicular coercivities as a function of Pt content.

samples deposited at 400 °C maintain high K_u values of more than 10^7 erg/cm^3 in a wide range from 10 at% Pt to 60 at% Pt.

3.1.2 Dependence of K_u on Substrate Deposition Temperature

Since Co-Pt alloy thin films showed an interesting behavior of K_u at about 25 at % Pt, the films of this composition has been intensively investigated. Figure 4 shows M_s and measured Pt content as a function of T_s for nominal $Co_{75}Pt_{25}$ samples. The change in M_s with T_s corresponds to that of Pt content, i.e. the higher the M_s, the lower the Pt content becomes. Figure 5 shows the dependence of both in-plane and perpendicular H_c on T_s. Interestingly, both in-plane and perpendicular H_c exhibit peaks at approximately 400 °C. The dependence of K_u on T_s in Fig. 6 for the samples deposited onto Al_2O_3(0001) substrate is shown. The K_u value increases when T_s increases, and reaches the maximum value at T_s = 400 °C, then decreases drastically beyond 430 °C. This rapid drop may be caused by the phase transition from hcp to fcc.

3.2 Structural Properties

In order to clarify the crystallographic structure of the films, several structural

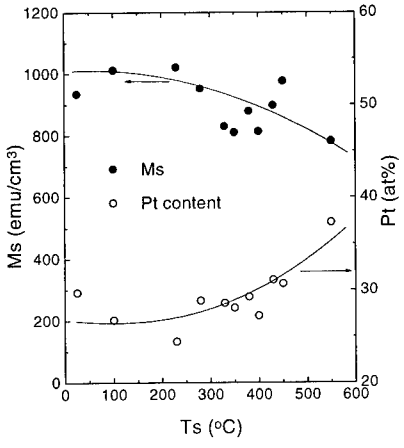

Fig. 4 Saturation magnetization as a function of substrate deposition temperature for nominal $Co_{75}Pt_{25}$

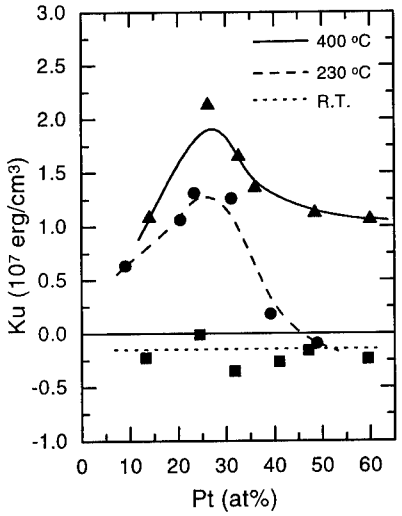

Fig. 3 Uniaxial anisotropy constant K_u as a function of Pt content.

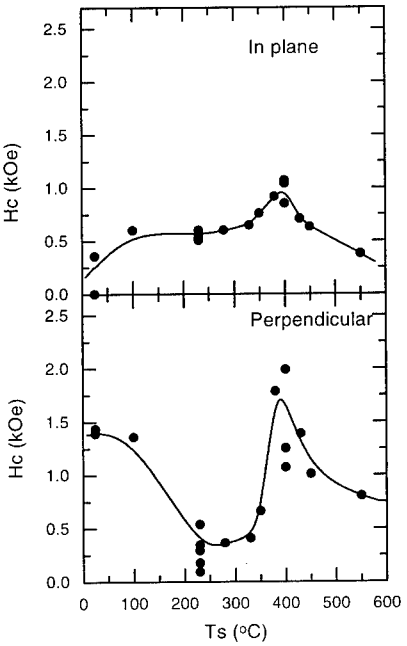

Fig. 5 Coercivities as a function of substrate deposition temperature for $Co_{75}Pt_{25}$

measurements have been carried out, such as x-ray diffraction (XRD), grazing angle incident x-ray diffraction (GIXD), electron diffraction, transmission electron microscopy, and so on.

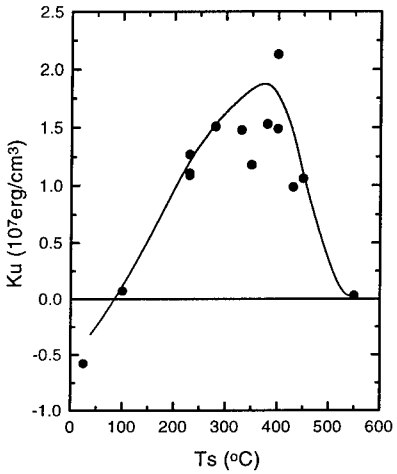

Fig. 6 Uniaxial anisotropy constant K_u as a function of substrate deposition temperature for $Co_{75}Pt_{25}$

First, the θ-2θ scan x-ray diffraction measurement shows that all the samples under investigation possess $\langle 00\cdot 1\rangle$ axis along the film normal. The so-called ϕ scan diffraction analysis was made, in which the sample was rotated along the film normal. The diffraction peaks of $(10\cdot 0)$ for the sample deposited at 400 °C were observed at every 60° (Fig. 7). This result indicates that the films possess a well-textured structure in the film plane. GIXD measurement was carried out to investigate the quality of the crystallographic property, that is to say, if the sample was epitaxially grown or not. This technique provides the information on the single crystallinity in the film plane. It does also the epitaxial relation between the film and the substrate. The measurement configuration is shown in Fig. 8. The lattice constant $d_{11\cdot 0}$ of hcp Co_3Pt structure is found to be approximately 2.6 Å. The epitaxial relation between the film and substrate is estimated by rotating the sample along the film normal. The obtained spectra explain that Co_3Pt $(10\cdot 0)$ plane and Al_2O_3 $(30\cdot 0)$ plane are tilted to each other by 30°, as shown in Fig. 9. That is, $Co_3Pt(11\cdot 0)$ plane is parallel to $Al_2O_3(10\cdot 0)$ plane, and the second neighbor atoms in Co_3Pt form hexagon whose one side (a'_{Co_3Pt}) is equal to 4.5 Å. The misfit parameter of this hexagon to basal plane of $Al_2O_3(0001)$ is calculated as 5.86 %. This value is smaller than that for the case without tilting, which is calculated as 8.79 %. Therefore, the 30° tilting is preferable.

X-ray diffraction spectra for the films were measured on the θ-2θ configuration. Figure 10 is an example obtained from the $Co_{75}Pt_{25}$ thin film deposited at 400 °C. The fundamental peaks $\{00\cdot 2\}$ and $\{00\cdot 4\}$ of Co-Pt alloy are seen in this spectrum. In addition, a superlattice peak $\{00\cdot 1\}$ is observed at approximately 2θ = 21.0°. This result implies that the film is partially ordered, which was first suggested by Harp et al.[8] This structure consists of two kinds of layers; one consists of the same amount of Co and Pt atoms and the other consists of only Co

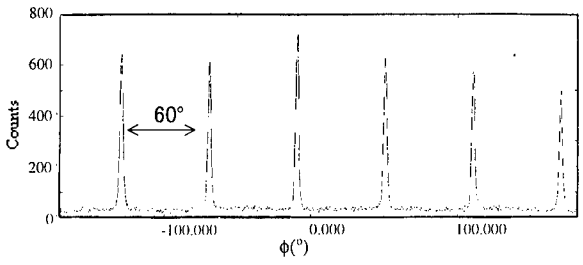

Fig. 7 A spectrum of ϕ scan for the sample deposited at 400 °C

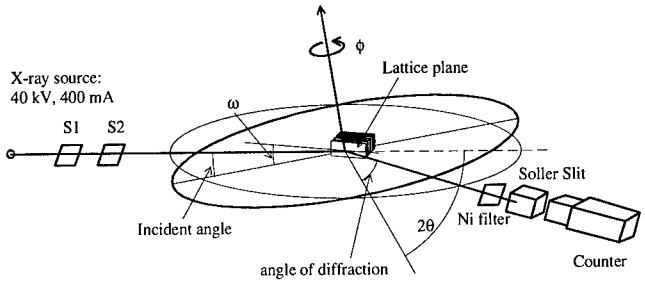

Fig. 8 Schematic diagram of GIXD

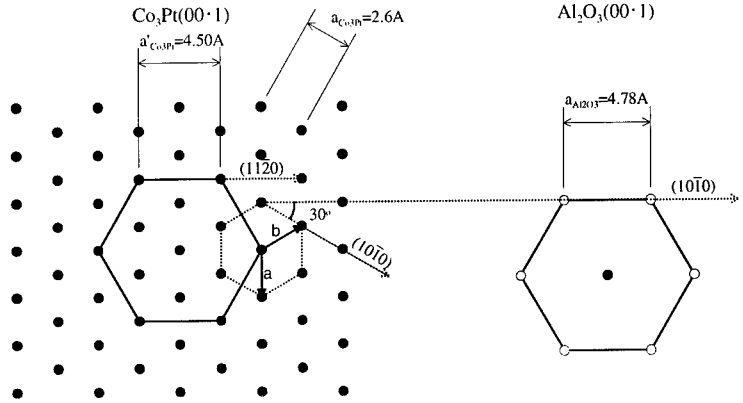

Fig. 9 Epitaxial relation between $Co_3Pt(00\cdot1)$ and $Al_2O_3(00\cdot1)$substrate

atoms, and they are stacking alternately. The superlattice peak corresponds to the layer distance of 4.2 Å. The order parameter *S*, which indicates the degree of ordering, can be calculated from the integrated intensity of the peaks as follows.

The structure factor *F* of hcp structure is estimated by an equation as,

$$F = \frac{f_{Co} + f_{Pt}}{2} + f_{Co} e^{2\pi i g} \left(g = \frac{h+2k}{3} + \frac{l}{2} \right) \cdots\cdots (1),$$

where f is an atomic scattering factor[10]. Therefore, the structure factors of $\{00\cdot1\}$ and $\{00\cdot2\}$ planes are described as

$$F_{(00\cdot1)} = (f_{Co} + f_{Pt})/2 - f_{Co} \cdots\cdots (2), \quad F_{(00\cdot2)} = (f_{Co} + f_{Pt})/2 + f_{Co} \cdots\cdots (3), \text{ respectively.}$$

The intensity *I* is

$$I = |F|^2 p \left(\frac{1+\cos^2 2\theta}{\sin^2\theta \cos\theta} \right) e^{-M(T)} \cdots\cdots (4),$$

where p is the multiplicity factor, $\left(\frac{1+\cos^2 2\theta}{\sin^2\theta \cos\theta} \right)$ is the Lorentz polarization factor, and $e^{-M(T)}$ is the temperature factor, where $M(T)$ is the Debye-Waller temperature factor, given by

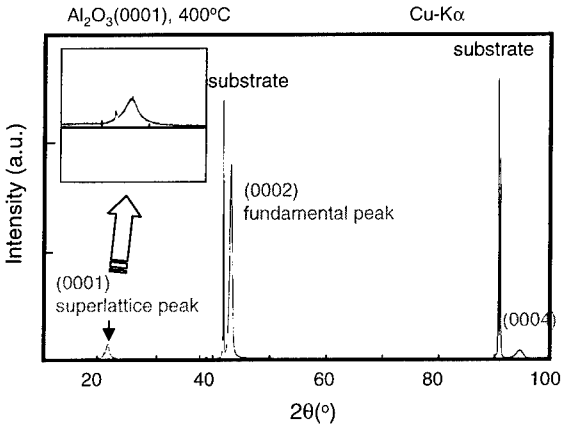

Fig. 10 An XRD spectrum for the sample deposited at 400 °C

$B(T)\left(\frac{\sin\theta}{\lambda}\right)^2\left(B(T)=\frac{6h^2T}{mk\Theta^2}\left[\phi(x)+\frac{1}{4}\right]\right)$. The p values for both $(00\cdot1)$ and $(00\cdot2)$ are 2. The ratio of $I_{(00\cdot1)}/I_{(00\cdot2)}$ is 0.796 for f_{Co}=23.23, f_{Pt}=70.78 and f_{Co}=18.5, f_{Pt}=61.07 for $\{00\cdot1\}$ and $\{00\cdot2\}$. The order parameter S is defined as,

$$S=\left(\frac{I_{(00\cdot1)}/I_{(00\cdot2)}}{0.796}\right)^{\frac{1}{2}}=1.12\cdot\left(I_{(00\cdot1)}/I_{(00\cdot2)}\right)^{\frac{1}{2}}\cdots\cdots(5)$$

This will be discussed later in connection with the model of the perfect ordered phase.

Figure 11 shows the dependence of S on T_s for the $Co_{75}Pt_{25}$ samples deposited onto Al_2O_3(0001). The value of S increases with T_s, showing a peak at ~ 400 °C. This result is consistent with the work by Harp *et al.*[8] Roughly speaking, the behavior of S is similar to that of K_u, but is not quite for the T_s range below 350 °C or so.

The dependence of S on Pt content is also investigated for T_s = 230 °C and 400 °C. Figure 12 is the dependence of S on Pt content. The S value shows the maximum at approximately 25 ~ 30 % for both the T_s cases. It is noted that even for high Pt contents, the S values remain relatively high (S ~ 0.35), where K_u of the order of 10^7 erg/cm^3 was observed.

A structural investigation has been carried out using a high resolution transmission electron microscope (TEM) operated at 400 kV (JEOL 4000FXII). The samples were prepared as follows. First, small pieces of 3 mm in diameter were cut from the samples using an ultrasonic disk cutter. Then, the substrates were ground down to 80 μm from 500 μm in thickness using a precise disk grinder and several kinds of grinding paper. Then, the center regime of them was dimpled, followed by an ion milling thinning process in Ar gas for final.

Figures 13(a) and 13(b) show the electron diffraction patterns with the zone axis $\langle 00\cdot1\rangle$ of the samples deposited at 380 °C (S = 0.32) and 230 °C (S < 0.001), respectively. Also shown is in Fig. 13(c) the calculated diffraction pattern based on the model of the ordered phase of Co_3Pt, which is shown in Fig. 14(a) and 14(b) (a plan view along $[00\cdot1]$). Here, it is emphasized that the ordered structure has a different unit cell from that of the disordered structure, as shown in Fig. 14(b). The lattice constant a, b for the ordered phase is twice the ones (a' and b') of the disordered phase. By comparing the diffraction pattern in Fig. 13(a) with Fig. 13(c), one can

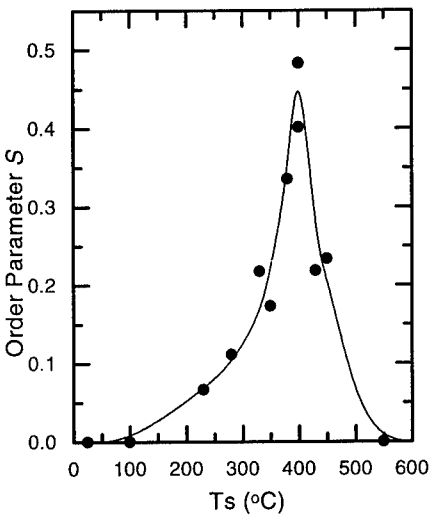

Fig. 11 Dependence of order parameter S on substrate deposition temperature for $Co_{75}Pt_{25}$

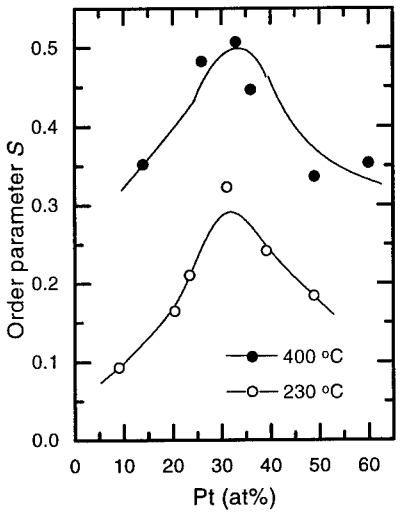

Fig. 12 Dependence of order parameter S on Pt content

clearly identify the spots $\{1/2\ 1/2\ 0\}$ (though weak in intensity) resulted from the ordered phase. This result provides the information that the sample does possess the ordering in the film plane. Based on the model, the intensity ratio $I_{(00\cdot1)}/I_{(00\,2)}$ was calculated to be 0.794. This simulation value is very close to the calculated on using eq. (4) within the accuracy of calculation.

Together with the result of x-ray diffraction, one can say that the sample made at 380 °C is indeed of the three-dimensional ordered (though partially) structure. The same statement can be made for the sample deposited at 230 °C (Fig. 13(c)) that though the intensity of $\{1/2\ 1/2\ 0\}$ is much weaker than that for 380 °C, this sample does consist of a three dimensional partially-ordered phase. From the calculated pattern, one would expect the two-fold symmetry of the $\{1/2\ 1/2\ 0\}$ spots. The pattern of Fig. 13(a) has the six-fold symmetry, instead of the two-fold symmetry. It is believed that the appearance of the six-fold symmetry results from the contribution of the mosaic structure, where fine grains (10 to 50 nm in size, based on the TEM photograph, shown in Fig. 15(b)) makes very small-angle grain-boundaries. It is further mentioned that the diffraction lines associated with spots $\{100\}$ and $\{110\}$ seen in both Figs. 13(a) and (b) are believed to evidence the mosaic structures. A more detailed study is needed, however, to clarify this matter.

Figure 15(a) shows a high resolution TEM image of the sample deposited at 380 °C onto $Al_2O_3(0001)$. Grains recognized with diffraction contrast are about 10 ~ 50 nm in size. Although some of grains are clearly observable, most of them are providing less contrast. This result indicates that the film morphology is rather uniform, whose crystallographic c-axis is along the film normal ($\Delta\theta_{00\cdot2} \approx 1°$) by x-ray diffraction. The structure is of the mosaic type as mentioned before. The image of the sample deposited at 230 °C shown in Fig. 15(b) has much less contrast. This means that the structure consists of very fine grains less than 10 nm or so.

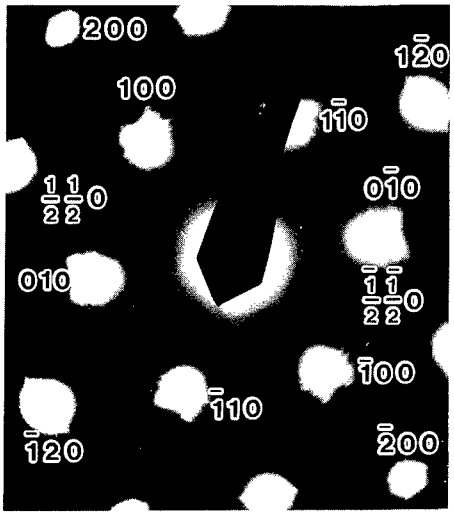

Fig. 13(a) Electron diffraction pattern for the sample deposited at 380 °C

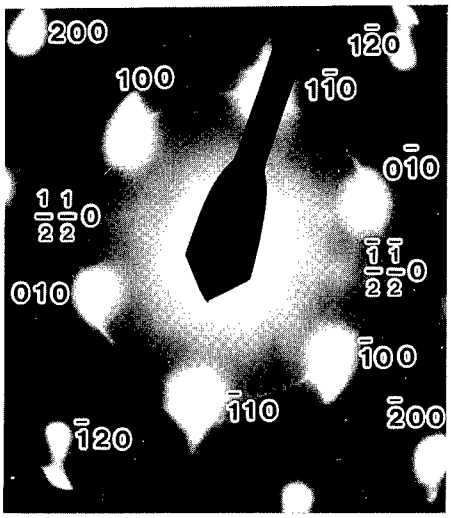

Fig. 13(b) Electron diffraction pattern for the sample deposited at 230 °C

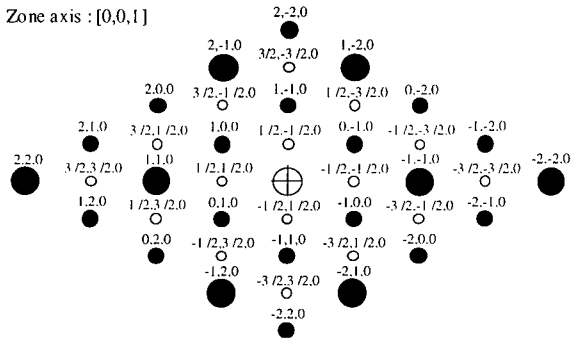

Fig. 13(c) Simulated diffraction spots obtained from the structure in Fig. 14

It should be emphasized that the film does have the mosaic structure according to the x-ray and electron diffraction. The above mentioned results suggest that these films made at T_s less than 350 °C or so possess the mosaic structure in which a short range ordering over less than 10 nm is present.

3.3 Relation between K_u and Order Parameter

The correlation between K_u and S is plotted in Fig. 16 for $Co_{75}Pt_{25}$ samples. The number, which is indicated beside each data point, is T_s for each sample. This graph shows an apparent correlation between them, i.e., K_u varies linearly with S for T_s between 380 °C and 450 °C. The behavior indicates that the ordering is a primary factor governing K_u in this temperature range. One can estimate the K_u value for the perfectly ordered state by extraporating the straight line, which gives us K_u of 4×10^7 erg/cm^3. On the other hand, there is no clear correlation between K_u and S in the T_s range from 230 °C to 380 °C. Yet, in this range, the large K_u values of more than 10^7 erg/cm^3 are obtained with very small S values. It is emphasized that the order

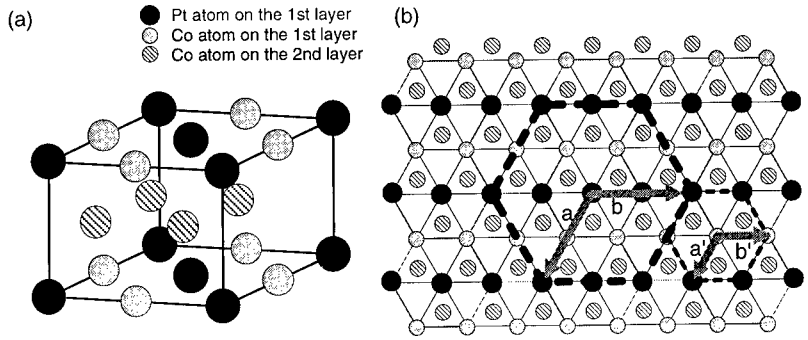

Fig. 14(a) A model of the Co_3Pt structure with in-plane and perpendicular ordering, (b) Plan view of the model along $\langle 00\cdot 1\rangle$

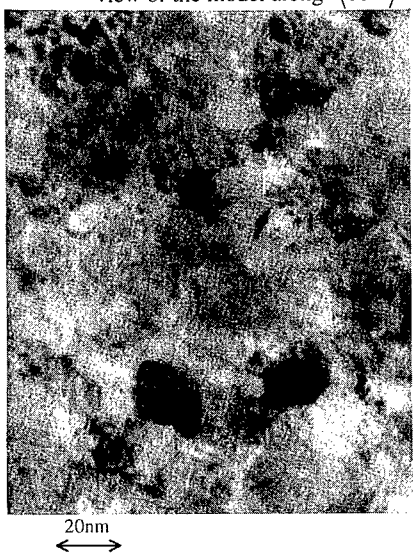

Fig. 15(a) High resolution TEM image of the sample deposited at 380 °C

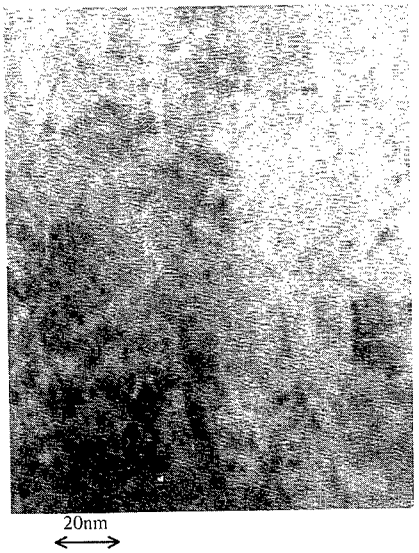

Fig. 15(b) High resolution TEM image of the sample deposited at 230 °C

parameter S is the quantity reflecting the "ordering" along the $\langle 00\cdot 1\rangle$ axis, which is a so-called one-dimensional order parameter. To discuss the correlation between K_u and S, one must take into account the three-dimensional order parameter. This issue remains for future study.

3.4 Mechanism for ordering

Nowick et al.[11] discussed the order parameter S as a function of temperature. Farrow et al.[12] assumed that the spontaneous ordering for FePt alloy is induced by surface diffusion, and calculated the diffusional barrier height from a plot of ln (S) vs $1/T$. They obtained approximately 0.2 eV as the barrier height for FePt films. The same analysis was made for the samples made at various T_s. Figure 17 shows ln (S) as a function of $1/T$ for the present samples. A linear correlation in the temperature range from 230 °C to 400 °C is found, The kinetic

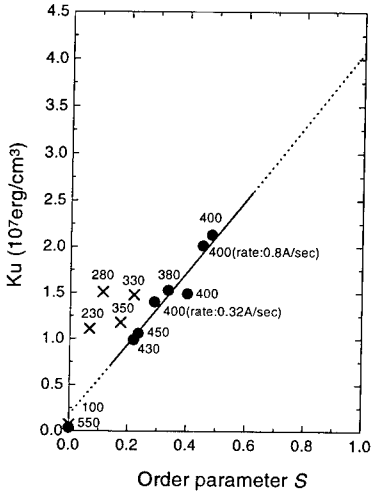

Fig. 16 Relation between order parameter S and K_u for $Co_{75}Pt_{25}$

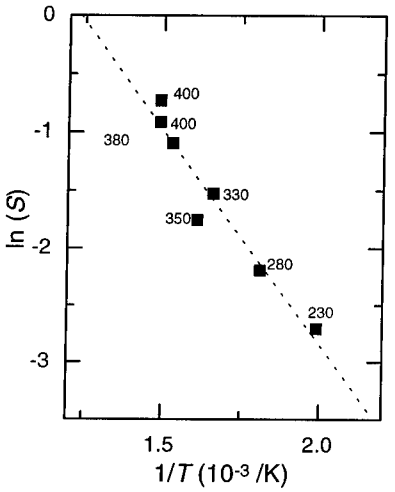

Fig. 17 Relation between ln (S) and 1/T for $Co_{75}Pt_{25}$

barrier height to ordering is about 0.32 eV. This value is close to that on $Co_{50}Pt_{50}$ by Pierron-Bohnes et al.[13], indicating that the rate limiting step for the ordering of Co_3Pt alloy films is also surface diffusion.

3.5 The origin of the Large K_u

As to the origin of the magnetic anisotropy, several models have been put forward. They include the magneto-striction[14], the bond-orientational anisotropy[15], the anisotropic pair correlations[16], the dipolar effects[17,18], and the growth induced structural anisotropy[19]. Harris et al.[20] reported that they found an evidence for a structural anisotropy in amorphous Tb-Fe films using extended x-ray-absorption fine structure (EXAFS), i.e. Fe-Fe and Tb-Tb pair correlations are greater in-plane and Tb-Fe correlations are greater perpendicular to the film plane. Regarding the Co-Pt alloy system, Tyson et al.[7] have claimed that there is an excess of Co-Co bonds in the film plane such that Co atoms are forming two-dimensional clusters in $Co_{28}Pt_{72}$ thin film, which is a plausible origin for the perpendicular anisotropy. This result means that internal interfaces between Co (rich) and Pt (rich) regions are formed, which are analogous to those of Co/Pt multilayers. MacLaren et al.[21] carried out the *ab initio* electronic structure calculations for Co/Pt superlattices and showed that the magnetic anisotropy energy was dependent on Co and Pt layer thickness. The largest value of magnetic anisotropy was given from 1 ML Co/1 ML Pt in each period. This result suggests that a large perpendicular magnetic anisotropy can be induced through the existence of interfaces. Concerning the present study, Co_3Pt ordered phase is analogous to 1ML $Co_{50}Pt_{50}$/1ML Pt multilayers where the interfaces between Co (rich) layer and Pt (relatively rich) layer are present. Therefore, the ordered phase can be responsible for the cause of the perpendicular magnetic anisotropy in the same way as Co/Pt multilayers case. However, in the present study, the films show a large K_u value of more than 10^7 erg/cm^3 with a much smaller order parameter when the film is deposited at ~ 230 °C as described in sec. 3.3. We propose a model for the structure, which could explain the behaviors of K_u and S. When T_s is high enough such as 400 °C, Co_3Pt ordered phase can be formed simultaneously in the entire film during deposition, where a

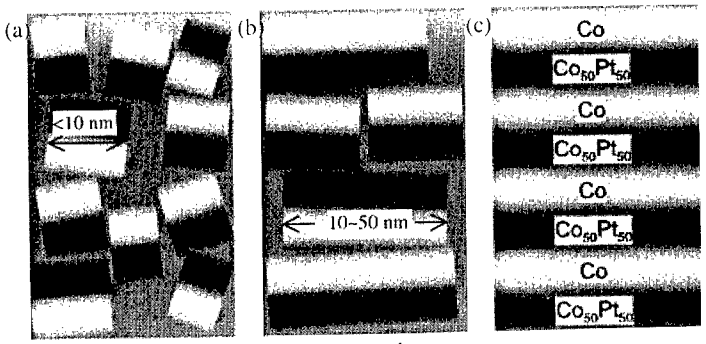

Fig. 18 (a) Schematic diagram for the structures of samples deposited at ~230 °C, (b) ~ 400 °C, (c) A perfect ordered Co_3Pt phase

superlattice peak can be observed by x-ray diffraction measurement (Fig. 18(b)). However, when T_s is not high enough, i.e. 230 °C, the activity of atomic diffusion is not sufficiently large enough to form the Co_3Pt ordered phase. Therefore, the order parameter is smaller. Although the films deposited at lower T_s do not have large *S*, they are still considered to contain a so-called short range ordered phase (Fig. 18(a)). This short range ordered phase consists of Co (rich) and Pt (rich) region, which is responsible for large K_u values with small *S* values. To support this model, an experiment was performed where samples were fabricated at a lower deposition rate. It may be possible that atoms can reach the proper atomic site to form the ordered phase at a lower deposition rate.

3.6 Relation between K_u and Deposition Rate

Figure 19 shows both K_u and *S* as functions of deposition rate for T_s = 230 °C and 400 °C. The normal deposition rate for Co_3Pt alloy thin film (sum of the rate for Co and that for Pt) was approximately 1.6 Å/sec. The total rate was lowered to 1/5 of the normal rate. K_u and *S* behave quite identically for both T_s. For 230 °C, the order parameter *S* increases, and also the K_u value increased. This result supports the model proposed in Fig. 18, where a fine mosaic structure (a) would be transformed to the one (b) with lowering deposition rate. On the other hand, for 400 °C, the change is opposite to the case of 230 °C. The reason for this difference is probably due to the phase transformation from hcp to fcc since the temperature 400 °C is the same as the

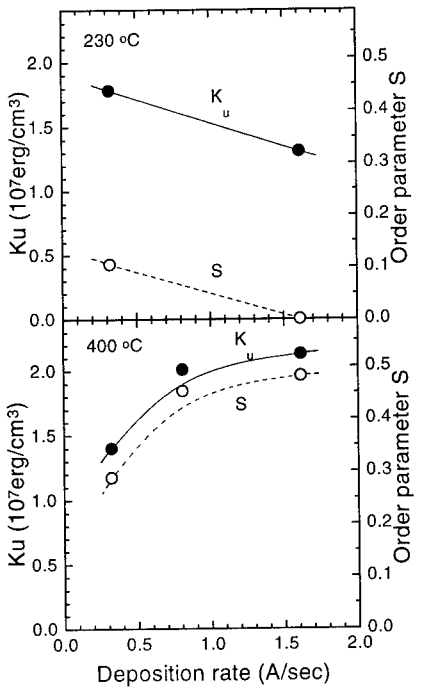

Fig. 19 K_u and order parameter as functions of deposition rate.

transition temperature.

4 CONCLUSIONS

The very large perpendicular magnetic anisotropy of the order of 2×10^7 erg/cm^3 at room temperature was found in $Co_{1-x}Pt_x(0<x<0.5)$ alloy thin films made by e-beam evaporation. The mechanism of the large magnetic anisotropy is likely related to the anisotropic Co-Co bonding distribution, which is similar to the cases of Co/Pt multilayers and FePt alloy thin films. The activation energy estimated for the ordering is approximately 0.3 eV, which is preferably compared to 0.2 eV for FePt. A model is proposed, for which both a short range and long range ordering are present, depending on substrate deposition temperature.

ACKNOWLEDGEMENTS

This work has been partially supported by the Storage Research Consortium and the Original Industrial Technology R & D Promotion Program from the New Energy and Industrial Technology Development Organization (NEDO) of Japan (Contract No. 8C-039-1). The authors gratefully acknowledge Mr. Usami at Hitachi Laboratories, Hitachi Ltd. for the GIXD measurement. They also acknowledge the support of DENSO CORPORATION.

REFERENCES

1. M. R. Visokay and R. Sinclair, Appl. Phys. Lett. **66**, 1692(1995).
2. B. M. Lairson, M. R. Visokay, E. E. Marinero, R. Sinclair, and B. M. Clemens, J. Appl. Phys. **74**, 1922(1993).
3. B. M. Lairson and B. M. Clemens, Appl. Phys. Lett. **63**, 1438(1993).
4. A. Cebollada, D. Weller, J. Sticht, G. R. Harp, R. F. C. Farrow, R. F. Marks, R. Savoy, and J. C. Scott, Phys. Rev. B, **50**, 3419(1994).
5. C. J. Lin and G. L. Gorman, Appl. Phys. Lett. **61**, 1600(1992).
6. S. E. Park, P. Y. Jung, and K. B. Kim, J. Appl. Phys. **77**, 2641(1995).
7. T. A. Tyson, S. D. Conradson, R. F. C. Farrow, and B. A. Jones, Phys. Rev. B, **54**, R3702(1996).
8. G. R. Harp, D. Weller, T. A. Rabedeau, R. F. C. Farrow, and M. F. Toney, Phys. Rev. Lett. **71**, 2493(1993).
9. Y. Yamada, T. Suzuki, and E. N. Abarra, IEEE Trans. Magn. **33**, 3622(1997).
10. B. D. Cullity, Elements of X-ray Diffraction, 2nd ed. (Addison-Wesley, Massachusetts, 1978), P. 383.
11. A. S. Nowick and L. R. Weisberg, Acta. Metall. **6**, 260(1958).
12. R. F. C. Farrow, D. Weller, R. F. Marks, M. F. Toney, S. Hom, G. R. Harp, and A. Cebollada, Appl. Phys. Lett. **69**, 116(1996).
13. Vronique Pierron-Bohnes, presented at the Spring Mtg. MRS (San Francisco, U. S. A., 1998).
14. S-C. N. Cheng, M. H. Kryder, and M. C. A. Mathur, IEEE Trans. Magn. **25**, 4018(1989).
15. X. Yan, M. Hirsher, T. Egami, and E. E. Marinero, Phys. Rev. **B43**, 9300(1991).
16. R. J. Gambino and J. J. Cuomo, J. Vac. Sci. Technol. **15**, 296(1978).
17. T. Mizoguchi and G. S. Cargill, III, J. Appl. Phys. **50**, 3570(1979).
18. H. Fu, M. Mansuripur, and P. Meystre, Phys. Rev. Lett. **66**, 1086(1991).
19. F. Hellman and E. M. Gyorgy, Phys. Rev. Lett. **68**, 1391(1992).
20. V. G. Harris, K. D. Aylesworth, B. N. Das, W. T. Elan, and N. C. Koon, Phys. Rev. Lett. **69**, 1939(1992).
21. J. M. MacLaren and R. H. Victora, Appl. Phys. Lett. **66**, 3377(1995).

MAGNETIC ORDER OF $CO_{0.1}PT_{0.9}$ IN PROXIMITY OF $COPT_3$

A.L. SHAPIRO*, F. HELLMAN* AND M.R. FITZSIMMONS**
*University of California—San Diego, La Jolla, CA 92093
**Los Alamos National Laboratory, Los Alamos, NM 87545

ABSTRACT

A polarized neutron reflectometry study of the magnetization density depth profile of a $Co_{0.1}Pt_{0.9}$-$CoPt_3$ bilayer film found evidence for an induced moment in the $Co_{0.1}Pt_{0.9}$ overlayer in close proximity to the $CoPt_3$ underlayer. If the moment of Co in these films is that of the bulk, then the $\mu_{Pt} = 0.09(1)\mu_B$ in the overlayer, and $\mu_{Pt} = 0.04(1)\mu_B$ in the underlayer. In addition, ferromagnetic order of the $Co_{0.1}Pt_{0.9}$ overlayer was observed 8K above T_c for the material in the bulk.

INTRODUCTION

A magnetic moment can be induced in a material not normally magnetic, but easily polarizable, or enhanced in a material, when in close proximity to a strongly magnetic material [1]. The polarization of the non-magnetic material by a magnetic material is called the proximity effect. Examples of the proximity effect include: enhancements of the magnetic moment of Fe in Fe-Co alloys, or an induced moment of Pd in Pd-Fe alloys. In these instances, the polarizable atom is spread uniformly in a dilute concentration throughout the alloy. Alternatively, the polarizable material can be a thin film in contact with a strongly magnetic material. In this case, the magnetic material can induce magnetization of the portion of the polarizable material close to the film interface.

The motivation for this work was to explore the proximity effect in alloys of Co and Pt— here, Pt would be the easily polarizable material. The particular system chosen for study was one composed of a low Curie temperature thin film, $Co_{0.1}Pt_{0.9}$, which was deposited onto a film of $CoPt_3$ with a high Curie temperature, to form a bilayer sample. There are two issues posed by this study. First, what is the magnetic moment of Pt in the two Co-Pt alloys? Secondly, could ferromagnetic ordering in the $Co_{0.1}Pt_{0.9}$ overlayer be induced above its Curie temperature in the bulk by the strongly ferromagnetic $CoPt_3$ underlayer? In order to address these questions, polarized neutron reflectometry— a technique well-suited to studies of ferromagnetism across interfaces and in thin films [2], was employed.

EXPERIMENT

Sample Preparation

The bilayer sample was manufactured by co-evaporating Co and Pt from separate targets using e^- beam guns onto an epitaxially polished (100) oriented MgO single crystal substrate [3]. The substrate measured 2.5 x 2.5 cm^2 by 1mm thick. The substrate was cleaned by heating to 900K and then cooled to 500K prior to deposition of the film. The deposition was made in an ultra-high-vacuum chamber with a base pressure of 10^{-7} Pa. The deposition consisted of two steps. During the first step, the deposition rates of Co and Pt were adjusted to produce a film with the stochiometry of $CoPt_3$. The film was grown to be 31nm thick. During growth, the Reflection High Energy Electron Diffraction (RHEED) pattern was observed. Streaks were observed in the RHEED pattern, which suggested the $CoPt_3$ film was single crystalline with the (001) orientation.

Following the deposition of the $CoPt_3$ film, the depositions rates were readjusted to produce a film with the stochiometry $Co_{0.1}Pt_{0.9}$. The readjustment took 20s, during which time the $CoPt_3$ surface was exposed to about 0.2 monolayers of gas atoms. A 12nm thick film of $Co_{0.1}Pt_{0.9}$ was deposited directly on the $CoPt_3$ crystal. During the growth of the $Co_{0.1}Pt_{0.9}$ film, the RHEED pattern indicated that the $Co_{0.1}Pt_{0.9}$ film grew as a single crystal with the (001) orientation. A schematic diagram of the bilayer sample is shown in the inset of Fig. 1.

Mat. Res. Soc. Symp. Proc. Vol. 517 © 1998 Materials Research Society

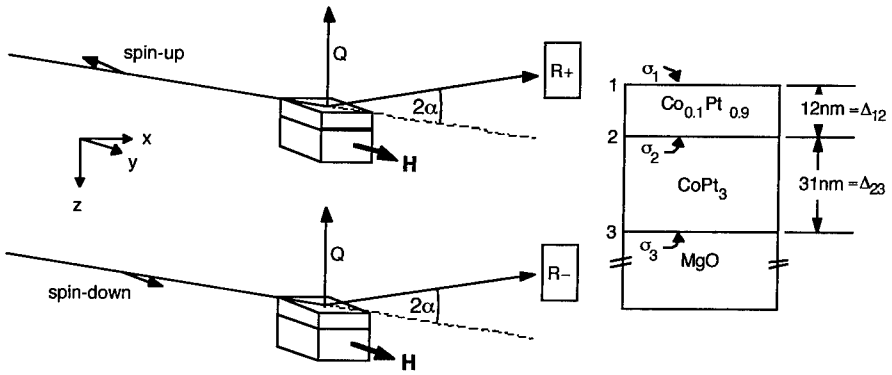

Fig. 1 Schematic diagram of a scattering experiment using a beam of (X-rays) neutrons with spins aligned anti-parallel (spin-up) or parallel (spin-down) to the field, **H**, applied to the sample. Inset: diagram of the $Co_{0.1}Pt_{0.9}$-$CoPt_3$ bilayer sample.

Sample Characterization

The susceptibility of a similarly prepared sample was measured with a vibrating sample magnetometer equipped with an liquid-N_2 flow cryostat. Kinks in the susceptibility curve measured as a function of temperature were observed at 540K and 240K. The kink at the higher of the two temperatures corresponded to the onset of ferromagnetic order in the $CoPt_3$ underlayer, i.e. its Curie temperature, T_C. The low temperature kink corresponded to the Curie temperature of the $Co_{0.1}Pt_{0.9}$ overlayer.

The thickness of the $Co_{0.1}Pt_{0.9}$ and $CoPt_3$ films, and the roughness of the air-film, $Co_{0.1}Pt_{0.9}$-$CoPt_3$ and film-substrate interfaces were measured with X-ray reflectometry. Reflectometry involves measuring the intensity of the radiation specularly reflected by a smooth sample through an angle, 2α (see Fig. 1), and comparing this intensity to the intensity of the radiation illuminating the sample. The ratio, called the reflectivity— R, is measured as a function of momentum transfer, $Q=4\pi\sin(\alpha)/\lambda$, where λ is the wavelength of the radiation.

The X-ray reflectivity of the sample was measured using X-rays with a wavelength λ=1.54178Å, selected from a spectrum with a graphite monochromator. X-rays were produced by an 18kW rotating anode X-ray generator at the Los Alamos Neutron Science Center (LANSCE). The X-ray beam was collimated with a pair of slits located between the monochromator and sample. The intensity of the incident X-ray beam was monitored using a scintillation detector and a Mylar sheet, which scattered a small portion of the X-ray beam into the detector. The intensity of the incident X-ray beam was needed in order to measure the exposure of the sample to the beam. The position and intensity of the reflected X-ray beam were measured with a Xe-filled position sensitive detector (PSD). The intensity profile measured as a function of angle off the sample surface by the PSD was a Gaussian-shaped peak on a smooth background. The integrated intensity of the peak after removal of the background was the reflectivity of the sample at Q, which was determined by selecting the angle of incidence— the angle, α, between the incident X-ray beam and its projection on the sample surface. The profile was assembled by incrementing α, and repeating the measurement and integration procedure. The reflectivity profile taken for the sample at 296K is shown in Fig. 2. X-ray reflectivity measurements were also taken at 81 and 248K with the aide of a Displex closed-cycle He cryostat equipped with Be-domes. The three X-ray reflectivity profiles were not statistically different.

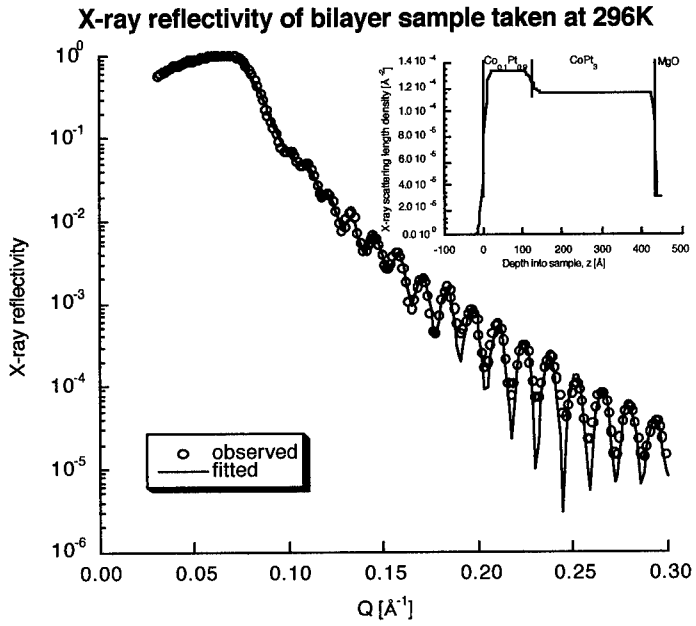

Fig. 2 Reflectivity of the bilayer sample measured with X-rays (O) at 296K. The solid curve is the profile calculated for a model structure whose X-ray scattering length density varies with depth into the sample (inset).

For extremely small values of $Q<Q_c\sim0.07Å^{-1}$, the X-radiation in the sample becomes evanescent, so the sample reflectivity was unity [4]. For larger values of Q, the radiation penetrated into the sample and was reflected by internal planar interfaces [5]. The radiation reflected from these interfaces interfered with the radiation reflected from the sample surface producing modulations in the reflectivity profile (Fig. 2). The modulation frequency of the reflectivity profile is related to the thicknesses of the $Co_{0.1}Pt_{0.9}$ and $CoPt_3$ layers. The amplitude of the modulation and the attenuation of the profile with Q are related to the change of electron density and roughness of the sample interfaces, respectively.

The reflectivity of the sample was also measured using the polarized neutron reflectometer at LANSCE. A detailed description of this instrument is found in ref. [6]. Briefly, a beam of neutrons with spins aligned anti-parallel (spin-up) to the magnetic field applied to the sample was produced using polarizing neutron supermirrors. Since LANSCE is a pulsed-neutron source, the time-of-flight technique was used to measure neutron wavelength, so the so-called spin-up sample reflectivity, R+, was measured as a function of Q by fixing α and varying λ (the latter was accomplished by the pulsed-source). The spin-down sample reflectivity, R-, was measured by reversing the field applied to the supermirrors; thus reversing the polarization of the neutron beam with respect to the field on the sample, **H** (Fig. 1). Normally, the reversal of the field applied to the polarizer would produce a zero-point in the field between the polarizer and sample, which was undesirable, since the neutron beam would become depolarized. This problem was avoided by using a YBCO-cryoflipper which isolated the fields applied to the sample and polarizer from each other; thus, preserving the polarization of the neutron beam [6].

The spin-up and spin-down sample-reflectivities were measured with neutrons after first cooling the sample to 81K in a strong magnetic field (H=6.5kOe). The field was applied to the sample during the entire neutron experiment. Neutron reflectivity measurements were made for sample temperatures of 81, 248 and 296K (Fig. 3). The interpretation of the neutron reflectivity profiles is

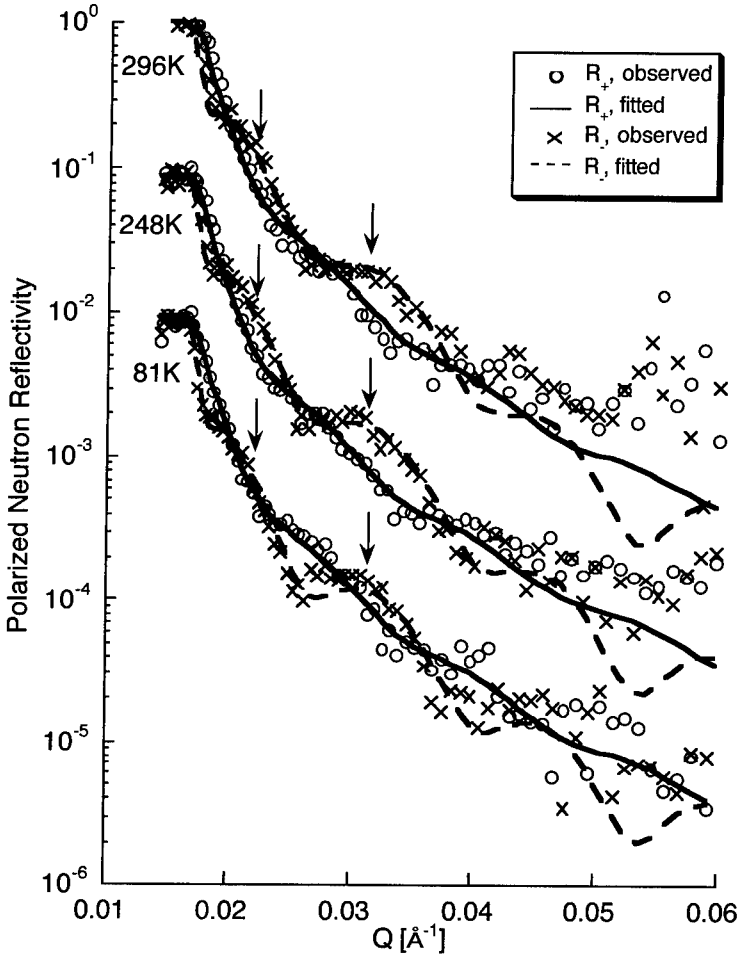

Fig. 3 Polarized neutron reflectivity profiles for the $Co_{0.1}Pt_{0.9}$-$CoPt_3$ sample measured at 81, 248 and 296K. Differences with temperature were most pronounced for the spin-down profile in the region $0.02Å^{-1}<Q<0.03Å^{-1}$ (arrows). The profiles have been displaced for the sake of clarity.

similar to that of the X-ray profile, i.e. the periodicity of the fringes is related to the film thickness, the amplitude of the modulation is related to the change in scattering length density across the interfaces, and the attenuation of the profile is related to the roughness of the interface. In contrast to the X-ray measurements, the scattering of the polarized neutron beam also depends upon the net magnetization of the sample parallel to **H** and perpendicular to **Q**. Information about ferromagnetism, e.g. the magnetic moment of Pt in the $Co_{0.1}Pt_{0.9}$ and $CoPt_3$ films, can be deduced from differences between R+ and R-. In the this study, a splitting of R+ and R- is seen at all

temperatures (since the $CoPt_3$ underlayer was always ferromagnetic), and a change in the splitting occurred with temperature, particularly in the region $0.02Å^{-1}<Q<0.03Å^{-1}$ for the spin-down profiles (arrows in Fig. 3).

RESULTS

The bilayer sample contained three reflecting interfaces— the air-film, $Co_{0.1}Pt_{0.9}$-$CoPt_3$, and film-substrate interfaces. These interfaces are denoted by the numerals 1, 2 and 3 (Fig. 1). In order to obtain information about interfaces, for example the distance, Δ_{12}, between interfaces 1 and 2, the sample was represented by the model in Fig. 1, from which the reflectivity of the model was computed and then compared to the measured reflectivity profiles. Perturbations to parameters of the model were made until the difference between the calculated and measured profiles weighted by the statistical precision of the data were minimized.

The attenuation of the profile beyond the usual Q^{-4} Porod decay [5], was attributed to roughness of the interfaces. Typically roughness is treated as if it were small random or Gaussian distributed fluctuations of the interface height in the z-direction (direction parallel to the interface normal) with variance of σ^2. The roughness of each interface was refined independently. Finally, the power of a material to scatter X-rays (or neutrons) is called the scattering length density of the material. Since the films have different compositions, and their components scatter X-rays and neutrons differently, three X-ray and six neutron (three nuclear and three magnetic) scattering length densities were required.

For X-ray scattering in the small-angle regime, the scattering length density β is the product of the Bohr radius, $r_e=2.82\bullet10^{-5}$ Å, and the density of electrons in the material (the scattering length density is related to the index of refraction for the material) [7]. For scattering with polarized neutrons, β has nuclear and magnetic components. The nuclear component is the product of the average neutron scattering length of the material, b, and the number density of atoms, N, so $\beta_n=bN$ [8]. The magnetic component is the product of a constant, $C=2.645\bullet10^{-5}$ $Å\mu_B^{-1}$, the magnetic moment of the material, μ [μ_B], and N, i.e. $\beta_m=\pm C\mu N$ [9]. The positive sign is used to compute the spin-up scattering length density and the negative sign— the spin-down scattering length density. It is the value of $\mu(z)$ which is desired for the $Co_{0.1}Pt_{0.9}$-$CoPt_3$ sample.

Of the fourteen model parameters, only two parameters, $\mu(Co_{0.1}Pt_{0.9})$ and $\mu(CoPt_3)$, will produce splitting of R+ and R- (Fig. 3). Indirectly, $\mu(Co_{0.1}Pt_{0.9})$ and $\mu(CoPt_3)$ can be influenced by correlation with the remaining 12 parameters— those that describe the nuclear structure of the sample, in a numerical refinement used to obtain the best-fitting model. Correlation with the nuclear parameters can be avoided if the latter are determined by X-ray reflectometry.

The X-ray fitting involved calculating the X-ray scattering length density profile of the sample as a function of depth into the sample, z, and then computing the reflectivity of such a profile using the Parratt formalism [5]. The scattering length density profile (inset Fig. 2) is composed of three plateaus which represent the scattering length densities of $\beta(Co_{0.1}Pt_{0.9})$, $\beta(CoPt_3)$ and $\beta(MgO)$. The widths of the $Co_{0.1}Pt_{0.9}$ and $Co_{0.1}Pt_{0.9}$ plateaus are Δ_{12} and Δ_{23}. The plateaus are connected to each other by error functions, whose derivative with z are Gaussian functions with root-mean-square widths $\sigma_{1,2,3}$ (Fig. 1). The reflectivity of a sample with the scattering length density profile shown in the inset of Fig. 2 is the solid curve in the larger figure and best-fits the X-ray data. From this analysis, the thickness of the $Co_{0.1}Pt_{0.9}$ overlayer was determined to be $\Delta_{12}=12.4(5)$nm and $\Delta_{23}=31.0(5)$nm for the $CoPt_3$ underlayer. The roughness of the air-film interface was $\sigma_1=0.8(1)$nm, the $Co_{0.1}Pt_{0.9}$-$CoPt_3$ interface was $\sigma_2=1.1(1)$nm, and the film-substrate interface was $\sigma_3=0.4(1)$nm.

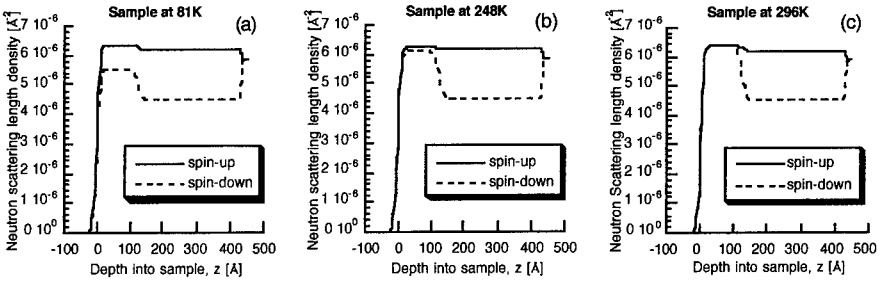

Fig. 4 Neutron scattering length density profiles deduced from model fitting to the data shown in Fig. 3. Splitting between the spin-up and spin-down profiles is indicative of the film magnetization corresponding to a particular depth into the sample.

A two-step fitting procedure was used to measure the magnetization of the overlayer. First, the structural parameters deduced from the X-ray fitting, were used in the fitting of a model to the neutron data taken at 81K. In this fit, only the neutron nuclear and magnetic scattering length densities were refined for the $Co_{0.1}Pt_{0.9}$ and $CoPt_3$ films. From this refinement, the average magnetic moment of $Co_{0.1}Pt_{0.9}$ and $CoPt_3$ in the fully saturated state were readily obtained, since the temperature, 81K, of the sample was well below the Curie temperatures of both films. For this temperature, the spin-up and spin-down neutron scattering length densities, whose reflectivities produced the best-fitting curves in Fig. 3, are shown in Fig. 4(a).

The second step in determining the magnetization of the $Co_{0.1}Pt_{0.9}$ overlayer above T_c, involved using the nuclear scattering length densities deduced for the $Co_{0.1}Pt_{0.9}$ and $CoPt_3$ films, and the magnetic scattering length density of $CoPt_3$ obtained from the first step, and refining only the magnetization of the $Co_{0.1}Pt_{0.9}$ overlayer. Since T_c for the $CoPt_3$ underlayer was much larger than room temperature, the magnetization of the underlayer was not expected to change as the sample temperature was increased from 81 to 296K. Only the magnetization of the $Co_{0.1}Pt_{0.9}$ overlayer was refined to accommodate the shift of the fringes for the spin-down neutron cross-section towards higher reflectivity and smaller values of Q (arrows in Fig. 3). The neutron scattering length density profiles for the sample at 248 and 296K are shown in Fig. 4(b) and (c), respectively.

CONCLUSIONS

Using the relationship $\mu(z) = \beta_m(z)/CN(z)$, and values of N for the films, $N(Co_{0.1}Pt_{0.9})=0.066$ Å^{-3}, and $N(CoPt_3)=0.070$ Å^{-3}, the average magnetic moment for the $Co_{0.1}Pt_{0.9}$ and $CoPt_3$ films were determined. At 81K, $\mu(Co_{0.1}Pt_{0.9})=0.25(2)\mu_B$, and $\mu(CoPt_3)=0.46(1)\mu_B$. At 248K, the mean moment for the $Co_{0.1}Pt_{0.9}$ overlayer decreased to $\mu(Co_{0.1}Pt_{0.9})=0.04(2)\mu_B$, and at 296K, the moment was $\mu(Co_{0.1}Pt_{0.9})=0.00(1)\mu_B$, i.e. the overlayer had no ferromagnetic component in the direction of the applied field at room temperature.

In contrast to magnetometry measurements, we find evidence for some ferromagnetic order of $Co_{0.1}Pt_{0.9}$ in a 12nm thick film 8K *above* T_c for $Co_{0.1}Pt_{0.9}$ in the bulk. While the magnetometry and neutron studies used different thermometers, both were calibrated thermometers and suitable for use in high magnetic fields; therefore, the discrepancy was not likely due to errors in thermometry. A more plausible explanation is one attributing the increase of T_c in $Co_{0.1}Pt_{0.9}$ to a higher degree of sensitivity for polarized neutron reflectometry to detect ferromagnetism in thin films than magnetometry. In other words, if the magnetometer could have measured moments as small as $0.04\mu_B$ from 12nm thick films, then the value of T_c deduced from magnetometry would have been higher.

Presently, the magnetization of the overlayer was treated as if it were uniform over its 12nm thickness. Alternatively, the overlayer may be largely paramagnetic at 248K except for a very thin region close to the $Co_{0.1}Pt_{0.9}$-$CoPt_3$ interface. For example, the magnetization of the overlayer may increase exponentially from zero at the $Co_{0.1}Pt_{0.9}$ surface to a non-zero value at the $Co_{0.1}Pt_{0.9}$-$CoPt_3$ interface. This possibility was examined by modifying the magnetization profile to assume the form $\mu_0 \exp(-\Lambda|z-\Delta_{12}|)$ in the overlayer; however, refinement of this model yielded the simpler uniform layer model, since $\mu_0 \rightarrow 0.04\mu_B$ and $\Lambda \rightarrow 0$. Either the magnetic correlation length, Λ^{-1}, was much larger than the 12nm thickness of the film, or the quality of the neutron data taken at 248K was not sufficient for an unique refinement of the more sophisticated model.

Finally, the magnetic moment induced in Pt when in close proximity to Co at 81K was calculated for the two film compositions. If the magnetic moment of Co in the films were that of Co in the bulk, $\mu_{Co} = 1.715\mu_B$ [10], and the moment of Co was parallel to the applied field, then lower limits for μ_{Pt} can be established. In the $Co_{0.1}Pt_{0.9}$ overlayer, μ_{Pt} is at least $0.09(1)\mu_B$, and in the $CoPt_3$ underlayer, μ_{Pt} is at least $0.04(1)\mu_B$, thus, we find evidence for an induced magnetic moment in Pt when in proximity of Co.

ACKNOWLEDGMENTS

This study was supported by the U.S. Department of Energy under Contract No. W-7405-ENG-36 with the University of California. The Manuel Lujan Jr., Neutron Scattering Center is a national user facility funded by the U.S. Department of Energy Office of Basic Energy Science. We acknowledge valuable discussions with Dr. F. Mezei and Dr. S. Trugman.

REFERENCES

1. L.M. Falicov, et al., J. Mater. Res., **5**(6), 1299(1990).
2. G.P. Felcher, R.O. Hilleke, R.K. Crawford, J. Hanmann, R. Kleb and G. Ostowski, Rev. Sci. Instrum. **58**, 609 (1987).
3. P.W. Rooney, A.L. Shapiro, M.Q. Tran and F. Hellman, Phys. Rev. Lett., **75**(9), 1843 (1995).
4. The roll-over of the X-ray reflectivity profile below Q_c is caused when the cross-section of the beam is larger than the cross-section of the sample. The reflectivity of the sample is still unity for $Q < Q_c$, and the roll-over can be accounted for with a simple geometrical factor.
5. L.G. Parratt, Phys. Rev., **95**, 359 (1954).
6. M.R. Fitzsimmons, M. Luett, H. Kinder and W. Prusseit, accepted for publication in Nucl. Instrum. and Methods.
7. H. Dosch, Phys. Rev. B, **35**(5), 2137 (1987).
8. G.L. Squires, Thermal Neutron Scattering, Dover Publications, New York, 1978, p. 7.
9. D.J. Hughes and M.T. Burgy, Phys. Rev., **81**(4), 498 (1951).
10. Chih-Wen Chen, Magnetism and Metallurgy of Soft Magnetic Materials, Dover Publications, New York, 1986, p. 38.

THICKNESS DEPENDENT PERPENDICULAR MAGNETIC DOMAIN PATTERNS IN SPUTTERED EPITAXIAL FePt (001) $L1_0$ FILMS

J.-U. Thiele, L. Folks, M. F. Toney, D. K. Weller
IBM Almaden Research Center, 650 Harry Rd., San Jose, CA 95120

ABSTRACT

The present paper discusses the magnetic anisotropy and magnetic domain structure of highly ordered epitaxial FePt(001) films grown on Pt seeded MgO(001) substrates. These films were grown by dc-magnetron sputtering from a $Fe_{50}Pt_{50}$ alloy target at a substrate temperature of 550 °C during deposition. Thicknesses were varied between 15 and 170 nm. The presence of the highly anisotropic face centered tetragonal $L1_0$ crystal structure with a maximum long range chemical ordering of 95% and a low degree of misorientations was confirmed by specular and grazing incidence X-ray diffraction measurements. For film thicknesses ≥ 50 nm in-plane and out-of-plane hysteresis measurements indicate large perpendicular magnetic anisotropy and at the same time low remanent magnetisation. Magnetic force microscopy reveals highly interconnected perpendicular stripe domain patterns. From their characteristic width, which is strongly dependent on the film thickness, a value of the dipolar length, D_0, of 50 ±5 nm is derived. Assuming an exchange constant of 10^{-6} erg/cm, this value is consistent with an anisotropy constant $K_U \sim 1 \cdot 10^8$ erg/cc.

INTRODUCTION

Among the thin film and superlattice systems exhibiting perpendicular magnetic anisotropy, the face centered tetragonal (fct) phase of binary alloy systems like CoPt, FePd and FePt, also referred to as CuAu(I) or $L1_0$ phase, has in recent years attracted great interest. This phase consists of a monatomic, chemically modulated superlattice of the two elements. When grown with the monatomic layers parallel to the film plane, i. e. with the c-axis of the fct unit cell in the film normal direction, this structure results in perpendicular magnetic anisotropy. Large polar magneto-optical Kerr effects of up to 0.8° at 2 eV photon energy in FePt [1], make these materials attractive candidates for media applications in magneto-optical recording. Furthermore, it is generally assumed that high anisotropy is a prerequisite to support large coercivities and thermal stability at ever smaller physical grain sizes in high density magnetic recording media [2]. The magneto-crystalline anisotropies of FePt and CoPt are among the highest reported in the literature [3], making them attractive base materials for future high density magnetic recording media [4].

Epitaxial growth of chemically ordered FePt thin films with the c-axis perpendicular to the film plane has previously been demonstrated by molecular beam epitaxy (MBE) [1] and magnetron sputtering [5, 6]. The temperature dependence of the chemical ordering shows that a markedly lower temperature is required for complete ordering in thin film growth [7] as opposed to bulk material [8] (i. e. 500 °C vs. 1300 °C, respectively). This has been attributed to the enhanced surface mobility during thin film growth [7].

Here we present a detailed investigation of the magnetisation behaviour and the magnetic domain structure of fully chemically ordered FePt epitaxial thin films grown by magnetron sputtering. A more detailed investigation of the structural properties of these films can be found in [9]. Here we focus on the film thickness dependence of the magnetic domain size and

Mat. Res. Soc. Symp. Proc. Vol. 517 © 1998 Materials Research Society

the magnetisation behaviour. We demonstrate that the magnetisation curves and the domain structure of the perpendicular magneto-crystalline anisotropy films depend primarily on the film thickness, in agreement with the derivations by Landau [10] and Kittel [11].

EXPERIMENT

Samples and seed/buffer layers were deposited in a high vacuum system (base pressure ~ $3 \cdot 10^{-8}$ mbar at 550 °C) using DC magnetron sputtering onto single crystalline MgO (001) substrates sourced from Commercial Crystal Inc. For a description of the substrate cleaning procedure see [1]. Seed layers consisting of about 3 nm Cr and 12 nm Pt were deposited first at a substrate temperature of ~ 550 °C. The FePt alloy was then immediately sputtered from a single alloy target of $Fe_{50}Pt_{50}$ composition, resulting in films of about equiatomic composition (±2 at.%) as determined by Rutherford back scattering (RBS). For all layers the sputtering power was kept at 10-15 W, yielding deposition rates of 0.01-0.03 nm/s. The thickness of the FePt films was varied between 15 nm and 170 nm. To protect them from oxidation the films were capped with a 2 nm thick Pt layer, deposited at room temperature.

Degree of epitaxy and chemical ordering of the films were determined from specular and grazing incidence X-ray diffraction (XRD) using Cu K_α radiation [9]. Here we restrict our discussion to films with a high degree of chemical ordering, i. e. with a long range order parameter $S \geq 0.9$, and a very low level of misorientation [9]. Room temperature values of saturation magnetisation and anisotropy of the alloys were determined with standard vibrating sample magnetometry (VSM) and torque magnetometry, respectively. Hysteresis properties were measured using the magneto-optical Kerr effect (MOKE) in polar (perpendicular) and transverse (in-plane) geometries at a fixed wavelength (HeNe laser: $h\nu = 2$ eV). The domain structure of the samples was explored in the thermally demagnetized, as-grown state, i. e. before exposing them to any magnetic field, and subsequently in an ac demagnetized state, using magnetic force microscopy (MFM). A Dimension 3000 Scanning Probe Microscope (Digital Instruments Inc.) was used with magnetically "hard" CoCr-coated Si tips magnetised along the tip axis (i. e. perpendicular to the film plane). The instrument was operated in a non-contact ac-mode with the cantilever oscillating at resonance (about 70 kHz) while scanning at a fixed distance above the sample surface. The tip was scanned at sufficiently large sample-tip distances (30 - 90 nm) to minimize the perturbation of the tip magnetization by the strong sample stray field. No indication of influence of the tip on the domain structure of the samples was observed. The MFM images obtained of the FePt samples exhibit strong domain contrast, similar to that described by Belliard *et al.* [12]. They may be interpreted by correlating dark areas with domains with magnetization parallel to the surface normal, and light areas with domains with magnetization antiparallel to the surface normal.

RESULTS

Hysteresis curves

Figures 2a and 2b show the hysteresis curves of a ~ 170 nm and a ~ 30 nm thick sample, measured in the perpendicular and in-plane geometries, respectively. The thicker film has a very low remanence; upon decreasing the applied field from 20 kOe the sample remains saturated, until at a certain value, H_N, the magnetisation begins to drop rapidly. This type of hysteresis behaviour was first observed by Kooy and Enz in single-crystalline $BaFe_{12}O_{19}$ samples [13]. They related the sudden drop in magnetisation to the spontaneous nucleation of stripe domains

opposing the external field, as predicted by Kittel [11]. The shape of the hysteresis loops is indicative of low resistance to the movement of the nucleated domain walls and, by implication, low number of pinning sites in films of high perpendicular magnetic anisotropy.

Interestingly, despite their high degree of epitaxy and chemical ordering, perpendicular magnetisation curves of films thinner than a critical thickness of about 50 nm exhibit almost 100% remanence, as illustrated in figure 2b. Figure 2c shows the nucleation fields, H_N (low remanence films: H_N positive; high remanence films: H_N negative), and coercivities, H_C, of a series of FePt films of varying thickness, grown under otherwise identical conditions. In perfect single-crystalline films H_N has been observed to be positive down to very thin film thicknesses, e. g. a few monolayers in Co films [14]. Here, the negative H_N and the increasing coercivity imply an increasing impedance for domain wall motion with decreasing film thickness. The likely origin of this lies in the structure of the films: despite their high degree of epitaxy, they are not single crystalline, but consist of individual epitaxial grains. The size of these grains is above the resolution limit of the XRD setup used for our studies, so only a lower limit of 30 nm can be given; the actual grain size may be considerably larger. However, it is plausible that the grain size increases, and thus the impedance for domain wall motion decreases, with increasing film thickness.

While the saturation magnetisation, Ms, measured with a vibrating sample magnetometer, for both films is 1100 ±50 emu/cc, the magneto-crystalline anisotropy is almost constant at $K_1 = 3.2 \cdot 10^7$ erg/cc for thicker films and decreases slightly to $K_1 = 2 \cdot 10^7$ erg/cc for a film thickness of 50 nm [9]. Interdiffusion at the interface between the FePt layer and the Pt buffer, promoted by the high growth temperatures and evident in RBS measurements, may be the origin of this decrease. Note however, that the presently measured K_1 values, even for the thicker films, are smaller by about a factor of 2 than the values obtained for the best MBE grown films [15].

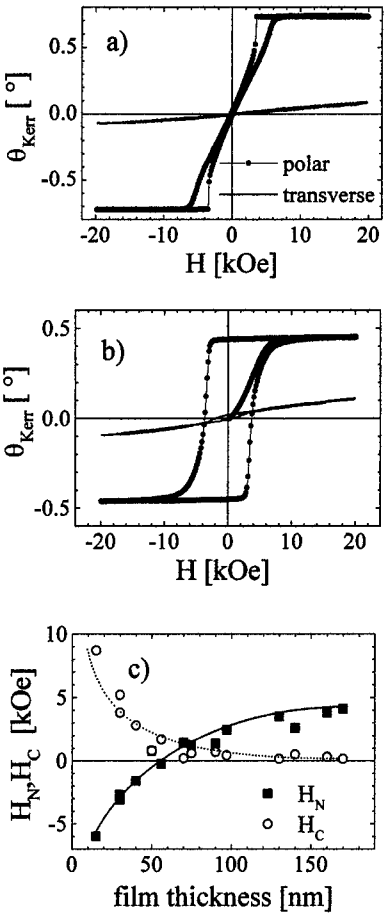

Figure 1: Kerr rotation as a function of applied field for a) a 170 nm thick FePt film and b) a 30 nm thick FePt film, measured in polar and transverse geometries, i. e. perpendicular to and in the plane of the film. c) Nucleation field H_N and coercivity H_C of a series of FePt films. The lines are guide lines to the eye. Note that no account has been taken of demagnetizing fields

Domain structure analysis by Magnetic Force Microscopy

Structure and width of magnetic domains in the series of FePt films with film thicknesses in the range of 18 nm to 170 nm were examined using magnetic force microscopy. Understanding the influence of film thickness on the equilibrium domain size in the framework of a simple theory is only possible for the case of samples with magnetisation strictly perpendicular to the plane of the film. Furthermore, MFM images can be most readily interpreted in this case. As seen in the previous section films with a thickness below about 50 nm always showed high remanence; their domain structure is dominated by bubbles of irregular sizes and shapes. In contrast, thicker films with large perpendicular anisotropy and low remanence show a domain pattern of highly interconnected stripes, similar to the ones observed in chemically ordered FePd (001) $L1_0$ films [16]. Therefore, we shall restrict our discussion here to film thicknesses $\geq$ 50 nm. In figure 2 MFM images of the as-grown domain structure of a 56 nm and a 170 nm thick film are shown. The width of the magnetic domains, measured perpendicular to the stripes, is larger for the thicker film. In figure 3a the domain size, measured from such MFM images, is plotted as a function of the film thickness. The steady decrease in domain width with decreasing film thickness resembles the behaviour found in FePd by Gehanno et al. [16]. Changes in this steady decrease, specifically a minimum and a subsequent steep increase in the domain width for very thin films, are expected at or below the dipolar length D_0 [16]. According to

$$D_0 = 2 \cdot \sqrt{A \cdot K_U} / \pi \cdot M_S^2 \qquad (1)$$

a dipolar length $D_{0,FePt} \approx 30$ nm can be calculated using values of $A = 1 \cdot 10^{-6}$ erg/cm for the exchange constant, $K_1 = 3.2 \cdot 10^7$ erg/cc for the anisotropy, and $M_S = 1100$ emu/cc for the saturation magnetisation of FePt. Due to the aforementioned constraints in film thickness, we are not able to verify this change in the variation of domain size with film thickness for $t \leq D_0$.

In the following we shall discuss the film thickness dependence in the accessible range using a simple continuum model developed by Landau *et al.* [10] and Kittel [11]. For the simple case of films with a high perpendicular anisotropy, resulting in purely up/down stripe domains, the domain size is determined by an equilibrium between domain wall energy and magnetostatic energy [11].

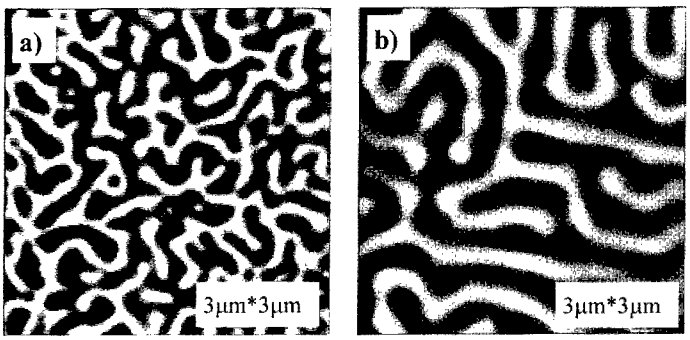

Figure 2: Magnetic Force Microscopy images (size: 3µmx3µm) of fully chemically ordered FePt films of thicknesses a) 70 nm and b) 170 nm

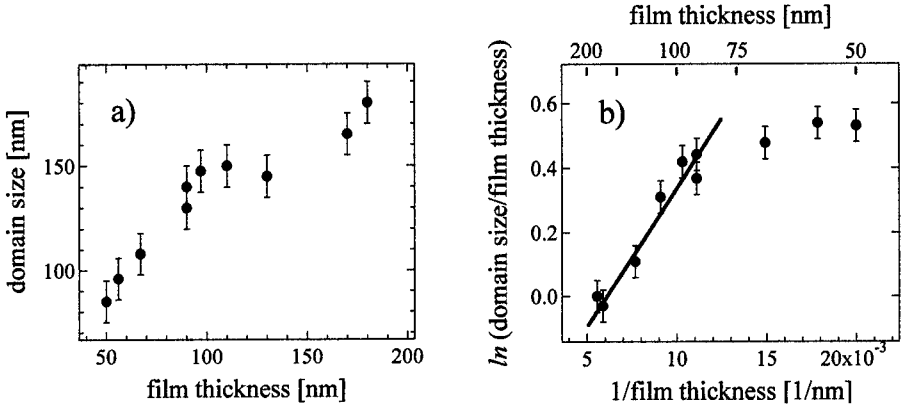

Figure 3: a) Magnetic domain stripe width, d, as a function of the thickness, t, of the FePt magnetic layer. b) Plot of ln (d/t) as a function of π/2t. The solid line is a linear fit for the indicated range of thicknesses.

Gehanno *et al.* [16] showed that the extension of Kittel's formalism to very thin films originally derived by Kaplan *et al.* [17] for thicknesses well below D_0,

$$d \propto t \cdot e^{\pi D_0/2t}, l_{ex} < t \ll D_0 \qquad (2)$$

where l_{ex} is the exchange length, is also valid for film thicknesses of about the dipolar length and above. Plotting our data according to this expression yields a good correlation with a linear fit from the thickest film down to thicknesses of about 70 nm. Below this thickness the domains are somewhat smaller than expected, as can be seen in figure 3b. Using only the values for films of thicknesses ≥ 70 nm a value for D_0 of about 50 ±5 nm is estimated from the slope of a linear fit (shown as solid line in figure 3b). From equation (1) and the measured saturation magnetisation M_S of 1100 emu/cc the product $A \cdot K_U$ can be calculated. With a value for the exchange constant of $A = 1 \cdot 10^{-6}$ ergs·cm a value of $K_U = 1 \pm 0.25 \cdot 10^8$ ergs/cc is obtained for the magneto-crystalline anisotropy. This is significantly higher than the value of $K_U = 3.2 \cdot 10^7$ ergs/cc measured with a 45° torque method with high field extrepolation. While this discrepancy may be due to the uncertainty in the value of the exchange constant, it remains an open question, how the Pt rich region near the interface to the seed layer influences the domain size as measured by magnetic force microscopy.

CONCLUSION

FePt films grown by sputter deposition on buffer layers consisting of 3 nm Cr/ 12 nm Pt on MgO (100) substrates at 550 °C reveal a high degree of epitaxy and chemical ordering. In films thicker than 65 nm, highly interconnected magnetic stripe domains with magnetisation perpendicular to the film plane were found. The width of the domains as well as the nucleation field depend on the film thickness. Comparing the domain structure of FePt to FePd [16] for identical film thicknesses we find that the domains in FePt are wider by a factor of 2.5-3, consistent with a higher magneto-crystalline anisotropy of FePt. The high temperatures required for the growth of

highly crystalline and chemically ordered FePt films cause interdiffusion at the interface between the Pt buffer and the FePt films. This Pt rich region at the interface causes a drop of the thickness averaged magneto-crystalline anisotropy as measured by torque magnetometry. It may also be the origin of the observed reduction of the magnetic domain size from that expected from theoretical considerations.

ACKNOWLEDGMENTS

We are indebted to Andrew Kellock for film thickness and composition analysis using Rhutherford back scattering and to Thaddeus Norman for XRD. J.-U. T. is grateful for funding by the Alexander-von-Humboldt-Stiftung (Bonn, Germany).

REFERENCES

[1] A. Cebollada, D. Weller, J. Sticht, G. R. Harp, R. F. C. Farrow, R. F. Marks, R. Savoy, J. C. Scott, Phys. Rev. B **50**, (1994) pp. 3419 -3422.

[2] S. H. Charap, P.-L. Lu, Y. He, IEEE Trans. Mag. **33** (1997) pp. 978-983.

[3] T. Klemmer, D. Hoydick, H. Okumura, B. Zhang, W. A. Soffa, Scripta Metallurgica et Materialia **33** (1995) pp. 1793-1805.

[4] K. R. Coffey, M. A. Parker, J. K. Howard, IEEE Trans. Mag. 31 (1995) pp. 2737-2739.

[5] B. M. Lairson, M. R. Visokay, R. Sinclair, B. M. Clemens, Appl. Phys. Lett. **62** (1993) pp. 639-641.

[6] M. Watanabe, M. Homma, Jpn. J. Appl. Phys. **35** (1996) L1264-L1267

[7] R F. C. Farrow, D Weller, R. F. Marks, M. F. Toney, J. Appl. Phys. **79** (1996) pp. 5967-5969.

[8] T. B. Massalski, *Binary alloy phase diagrams 2nd ed.*, ASM International (1990).

[9] J.-U. Thiele, L. Folks, M. F. Toney, D. K. Weller, J. Appl. Phys., submitted for publication (5/98).

[10] L. D. Landau, E. Lifshitz, Physik. Zeits. Sowjetunion **8** (1935) pp. 153-156.

[11] C. Kittel , Phys. Rev. **70** (1946) pp. 965-971.

[12] L. Belliard, A. Thiaville, S. Lemerle, A. Lagrange, J. Ferre, J. Miltat J. Appl. Phys. **81** (1997) pp. 3849-3851.

[13] C. Kooy, U. Enz, Philips Res. Rep. **15** (1960) pp. 7-29.

[14] R. Allenspach, M. Stampanoni, A. Bischof, Phys. Rev. Lett. **65** (1990) pp. 3344-3347.

[15] R. F. C. Farrow, D. Weller, R. F. Marks, M. F. Toney, S. Hom, G. R. Harp , A. Cebollada, Appl. Phys Lett. **69**, (1996) pp. 1166 -1168.

[16] V. Gehanno, Y. Samson, A. Marty, B. Gilles, A. Chamberod, J. Mag. Mag. Mat. **172** (1997) pp. 26-40.

[17] B. Kaplan, G. A. Gehring, J. Mag. Mag. Mat. **128** (1993) pp. 111-116.

STRUCTURAL AND MAGNETIC PROPERTIES OF $Co_{50 \pm x} Pt_{50 \mp x}$ THIN FILMS PREPARED BY MBE CO-EVAPORATION ON (001) MgO SUBSTRATE AT VARIOUS TEMPERATURES

V. PARASOTE, M.-C. CADEVILLE, V. PIERRON-BOHNES AND W. GRANGE
IPCMS-GEMM, CNRS-ULP, 23 Rue du Loess, F-67037 Strasbourg, FRANCE

ABSTRACT

Structural and magnetic properties of $Co_{50 \pm x} Pt_{50 \mp x}$ films 25-50 nm thick, prepared by molecular beam epitaxy onto a Pt buffer grown on MgO (001) substrate have been investigated. A series of 3 samples with different compositions (x = 6, 0, -6) was grown at 800 K on a 10 nm thick Pt buffer and another series of 5 samples of equiatomic composition was prepared at various growth temperatures (390 K$\leq T_G \leq$ 780 K) on a Pt buffer 4 nm thick. X-ray diffraction and TEM studies show the presence of grains with [111] and [002] orientations, the [002] grains being a mixture of the tetragonal $L1_0$ ordered phase and of the fcc disordered one. Both the thickness of the buffer layer and the deposition temperature are determinant parameters of the structural quality of the films and of the degree of long range order (LRO). An apparent LRO parameter (η_{app}) is deduced from the superstructure and main peak intensity ratio. Its increase with the growth temperature is described through a thermally activated model that yields a small activation energy of 0.28 eV, illustrating the role played by both surface diffusion and surface interactions in building the $L1_0$ compound in agreement with theoretical predictions. An average uniaxial magnetocrystalline anisotropy energy (K_u^{av}) is deduced from the magnetization curves measured by a SQUID. The anisotropy energy of the [002] grains (K_u^{002}) is deduced, assuming a linear relationship between the anisotropies and the phase percentages. One observes a continuous but not linear increase of K_u^{002} with η_{app}.

INTRODUCTION

Equiatomic CoPt alloy thin films have received significant attention as possible magneto-optic recording media. Many preparation methods have already been proposed in order to get the most ordered and well orientated $L1_0$ thin film compound with a magnetocrystalline anisotropy energy close to the high value (~ 4.10^7 ergs/cm^3) determined at RT by Eurin et al. [1] in a bulk monovariant ordered single crystal. Besides sputtering techniques [2, 3], the molecular beam epitaxy technique (MBE) was already used by Harp et al. [4] to prepare 100 nm thick $Co_{52}Pt_{48}$ films at 300°C and 500°C on (001) MgO substrate. Their work focus on the magneto optical Kerr spectroscopy as a probe of chemical ordering in CoPt, showing also the important role played by the growth temperature on both the texture and the degree of long range order in the films. In this paper we present a detailed investigation of the occurrence of the $L1_0$ long range ordering in CoPt films prepared by MBE as a function of the growth conditions and we investigate their magnetic properties, focusing on the uniaxial magnetic anisotropy and its link with the chemical ordering. After a brief review of the properties of the bulk CoPt that will be useful for the present study, the experiment is described. Then, results of structural and magnetic properties are successively presented and discussed.

PREVIOUS RESULTS

Structural, electronic, magnetic and thermodynamic properties of ordered and disordered bulk

Mat. Res. Soc. Symp. Proc. Vol. 517 © 1998 Materials Research Society

CoPt have been extensively investigated. For a general review see ref. [5]. For our purpose, let us just recall that the order-disorder transition is strongly of the first order, showing a large discontinuity of the long range order parameter η from 0.86 to 0 at the transition temperature T_C of 1110 K. This has, as a consequence a domain of η variation limited to 0.85-1, over a temperature range of 200 K below T_C, as confirmed by the *a* and *c* lattice constant temperature dependencies [6]. That means that any experimental determination giving η smaller than 0.85 would indicated that the alloy consists of a mixture of ordered and disordered phase.

Magnetic properties determined in both ordered and quenched disordered states [7, 8] show a weak dependence of the saturation magnetization (M_S) upon the degree of LRO ($M_S^O/M_S^D \sim 1.06$ at the stoichiometric composition) but a greater sensitivity of the Curie temperatures (T_M) which are clearly lower in the ordered state than in the disordered one ($T_M^O/T_M^D = 0.88$ for CoPt). In the ordered phase, the saturation field of a polycrystalline sample investigated at the LCMI of Grenoble has been found to be as high as 15 T [8], whereas the uniaxial magnetic anisotropy energy of a single crystal with 97% of a dominant variant, as deduced from magnetization curves measured in magnetic fields up to 7T, has been evaluated to be 4.10^7 erg/cm^3 [1].

EXPERIMENTAL

Two series of CoPt samples have been prepared by electron gun co-deposition in a UHV chamber on cleaned (001) MgO substrates covered by a Pt buffer layer deposited at 970 K. The first series consists of 3 samples with nominal compositions of 44, 50 and 56 % of Co and nominal thickness of 50 nm, grown at 800 K on a 10 nm thick Pt buffer. The second series of 5 samples at the equiatomic composition have been deposited at 780 K, 680 K, 570 K, 480 K and 390 K on a 4 nm thick Pt buffer. Their nominal thickness is 50 nm, except for that prepared at 780 K which is 25 nm. All the samples are covered by a cap layer of 4 nm thick Ru deposited at 270 K to prevent oxidation. Each series is prepared within a single run in the deposition chamber, using a rotating sample holder where six substrates can take place. This has, as a consequence, a different annealing time at the growth temperature for each sample, the longer for the first deposited sample (the sequence is : x = 0, +6, -6 for the first series, T_G decreasing for the second series) and proportionally decreasing as the preparation of the other samples advances. The average deposition rates are around 0.012 nm s^{-1} so that the total deposition time of a 50 nm thick alloy film is about one hour.

Structural characterizations were obtained through X-ray diffraction measurements performed on a D500 Siemens diffractometer equipped with the Co K_α incident beam. $\theta/2\theta$ reflection scans and rocking curves in symmetrical geometry were collected. Diffraction scans were also performed on the W22 instrument of the LURE laboratory on a $Co_{50}Pt_{50}$ prepared at 800 K using a small wavelength of 0.0698 nm, in order to get higher order diffraction peaks as necessary to determine the Debye-Waller attenuation factors. Preliminary plan view TEM studies were performed on a Topcon 200 kV microscope operating in both image and diffraction mode.

STRUCTURAL PROPERTIES

We present here the partial results of our X-ray investigations which are absolutely necessary for our purpose, complete results being found in [9] and in forthcoming papers. Figure 1 displays a typical specular X-ray diffraction spectrum set up on the CoPt film grown at 780 K. Diffraction peaks corresponding to the Pt buffer layer and to the alloy film are distinctly observed, as well as the presence of both [111] and [002] fundamental peaks and that of the [001] superstructure line

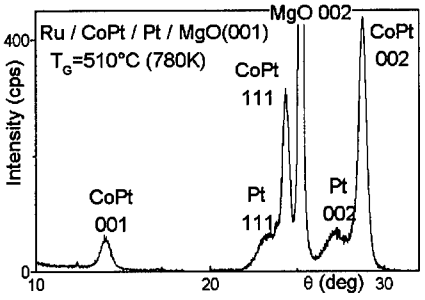

Fig. 1 : Typical θ / 2θ diffraction scan.

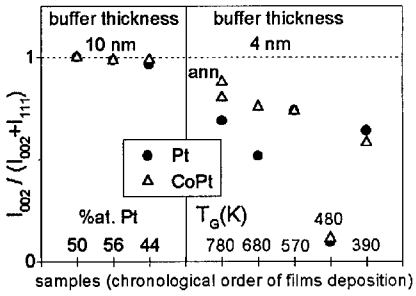

Fig. 2 : Platinum buffer and alloy film textures.

characteristic of the $L1_0$ ordered phase. In order to have a criteria to characterize the structural quality of these films, we define the texture by the integrated intensity ratio : $I^{002} / (I^{111} + I^{002})$, a ratio of the unity being the desired quality. The results are collected in Figure 2 for both the Pt buffer and the alloy films. In the first series of 3 samples prepared at 800 K, the alloy film and the buffer (10 nm thick) have strictly the same texture, which is dominantly the [002] orientation. In the second series of samples prepared at various temperatures, the texture of the alloy film still follows that of the buffer (4 nm thick) but they are not so much strongly correlated as in the first series. The [002] orientation is the dominant one in most samples, except for that grown at 480 K which is at 90 ± 5 % [111] orientated. We believe that this type of [111] growth, which is characteristic of non epitaxial films, is accidental, indicating non adherence to the substrate that was probably not perfectly cleaned. However this [111] orientated sample will be very useful for us in the following, to determine the magnetic anisotropy corresponding to that orientation. Figure 2 shows clearly that : i) roughly speaking, the alloy film adopts the texture of the buffer layer, ii) the texture of the buffer improves with its thickness (a minimum thickness of 10 nm is necessary to get the [002] orientation). As the buffers are deposited simultaneously at 970 K, an increase of the thickness corresponds to an increase of the deposition time, i.e. to an annealing time increase. This shows the important role played by both temperature and time of deposition on the structural quality of the thin films. It is probably the reason why we observe an improvement of the alloy film texture with respect to that of buffers, in films deposited at the higher temperatures (they are also the first prepared specimens, i.e. those which undergo the longer anneal times).

Determination of the LRO parameter : dependence upon T_G.

In order to determine the values of the LRO parameter η, the Debye-Waller (D-W) attenuation factors were determined in the 800 K CoPt sample using the method developed by Berg and Cohen [10]. η was deduced from the intensity ratios I^{001} / I^{002} and I^{003} / I^{004} after corrections by the polarization, Lorentz and D-W factors. Both ratios give the same values of η within the error bars. For all samples, η is smaller than 0.86, indicating a mixture of ordered and disordered phases. This is confirmed by both the values of the lattice constants and by TEM observations. For example, in the most ordered sample (η = 0.62) the *c* lattice parameter deduced from the position of the [001] peak is that of the totally ordered $L1_0$ compound, whereas that deduced from the position of the [002] peak is clearly higher, corresponding to a mixture of ordered and disordered states. In plane TEM dark field images built with the [110] diffraction spot clearly

reveal the coexistence of white (ordered) and dark (disordered) regions. The LRO parameter deduced from the diffraction line intensities is thus called an apparent LRO parameter (η_{app}). Both its temperature and concentration dependencies are shown in Figure 3. The value of η for the sample grown at 780 K is that obtained after an *ex situ* anneal of 25 min at the growth temperature, to take into account the thickness and the corresponding deposition time differences with respect to the other samples of the series.

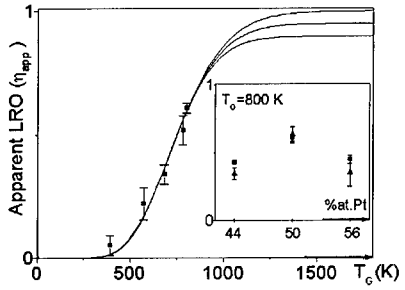

Fig. 3 : Growth temperature (T_G) dependence of the LRO parameter and its simulation with relation (1). In inset : LRO parameter as a function of the composition.

The $\eta(T_G)$ dependency is described using a thermal activation model previously developed to model the occurrence of metastable LRO along the growth direction in Co-Pt and Co-Ru alloy films [11]. Briefly said, it lies on a surface segregational or wetting effect which would lead to a some kind of bilayer-by-bilayer growth mode, an effect which would be amplified for the layered $L1_0$ structure. Such a growth mode, which has been theoretically predicted for the codeposition of a $L1_0$ compound [12], has been recently observed by Gehanno et al.[13], using RHEED oscillations during the MBE growth of $L1_0$ FePd alloys. This amounts to write that, in the two first surface layers, the surface order parameter (η_S) tends towards its equilibrium value $\eta_{S,eq}$ during t_0, the characteristic time for a bilayer deposition. The relaxation mechanism is similar to that describing the order relaxation in intermetallics [14], with a relaxation time τ_S that varies with temperature as an Arrhenius law :

$$\eta_S(T_G) = \eta_i + \eta_{S,eq}(1 - \exp - t_0/\tau_S) \text{ with } \tau_S = \tau_{0S} \exp E_S/k_B T_G \qquad (1)$$

with E_S the activation energy of the surface diffusion, k_B the Boltzmann constant and η_i the initial value of the surface order. Experimental data are very well reproduced through relation (1), giving an activation energy (E_A) of 0.28 eV, which is independent of the value imposed to $\eta_{S,eq}$ taken between 0.85 and 1. E_A really corresponds to a surface diffusion energy, being clearly lower than that corresponding either to diffusion or to ordering kinetics [11b, 14] in bulk alloys, but in agreement with theoretical values calculated by Treglia [15] for the interchange of Pt atoms between the surface plane and its underlayer. This result clearly shows that the ordering process in these CoPt films is really driven by surface effects, occurring at temperatures clearly lower than in bulk alloys. The concentration dependence of η normalized by the composition, shown in inset of Figure 3, is symmetric with respect to the stoechiometry, reflecting the symmetry of the phase diagram [6].

MAGNETIC ANISOTROPIES

The magnetic uniaxial anisotropies have been deduced from the magnetization curves measured at 298 K in a SQUID set up in both perpendicular and parallel configurations. The maximum

magnetic field was 7 T. An effective average anisotropy (K^{av}_{eff}) is deduced from the area difference between the parallel and perpendicular magnetization curves. In samples having a high anisotropy energy, where the saturation magnetization (M_S) is not attained in the maximum field of 7 T accessible in the SQUID instrument, a phenomenological extrapolation law ($M(H) = M_S(1 + a/H + b/H^2)$) was used to continue the experimental points as illustrated in Figure 4 for the CoPt 780K. Also shown in that figure are the magnetization curves set up: i) along the hard magnetization direction in an ordered single crystal up to 7 T, and ii) in an ordered polycrystalline sample up to 15 T. The ordered single crystal with 97 % of [001] variant orientation has the larger magnetic anisotropy, but measurements up to at least 15 T would be necessary to set up the total magnetization curve. In our measurements the magnetization curves were normalized to the saturation value determined along the easy magnetization axis. To calculate the anisotropy energy, the M_S values were taken as those of the ordered bulk samples determined at RT (M_S = 740 emu/cm^3 for the equiatomic CoPt [1], and M_S = 799 and 681 emu/cm^3 for respectively $Co_{56}Pt_{44}$ and $Co_{44}Pt_{56}$ [7]). After corrections by the magnetic energy term ($2\pi M_S^2$), the average magnetic anisotropy K_U^{Av} was obtained. In order to take into account the presence of both [111] and [002] grain orientations, a linear relationship between the anisotropies and the texture is assumed :

$$K_U^{Av} = A^{111} K_U^{111} + A^{002} K_U^{002} \qquad (2)$$

A^{111} and A^{002} are respectively the proportions of [111] and [002] grains. K_U^{111} is obtained from the measurement of the CoPt sample grown at 480 K which is 90 ± 5 % [111] orientated, the contribution of the [002] fraction being neglected as weakly ordered and anisotropic at such a low growth temperature. The values of K_U^{002} deduced from (2) are plotted in Figure 5 as a function of η^{app} and in the inset as a function of the composition.

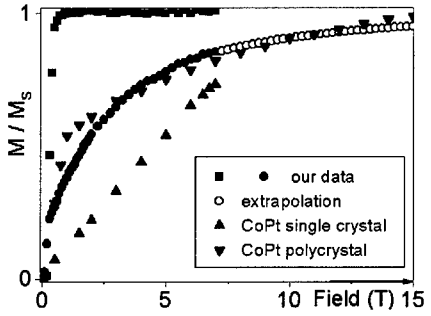

Fig. 4 : Normalized SQUID response (M / M_S) along easy (■) and hard (●) magnetization axes.

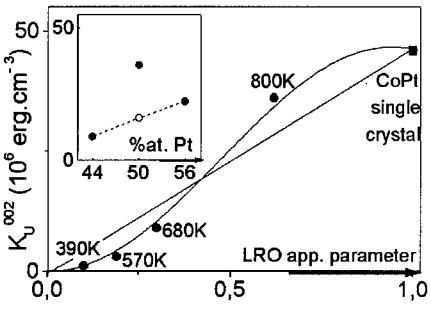

Fig. 5 : Dependence of the uniaxial anisotropy (K_U^{002}) upon apparent LRO parameter. In inset : composition dependence (O : estimated value for η=0.4 from the $K_U(\eta)$ curve).

The increase of K_U^{002} with η_{app} is not linear as expected in first approximation, which neglects the magnetic anisotropy of the disordered phase and assumes that the fraction of ordered phase is totally ordered (η = 1). In that case, both quantities would be proportional to the fraction of $L1_0$ phase. Really, the behavior of $K_U^{002}(\eta_{app})$ looks like a sigmoid curve typical of first order phase transformations that will be discussed in a forthcoming paper after more complete TEM investigations. The dependence of the magnetic anisotropy upon the Pt content, shown in inset of

the figure, is not really significant, as it corresponds to different phase mixtures. For the same value of η_{app} ($\eta \sim 0.4$), one observes an important increase of K_U with the Pt content. This increase has certainly its origin in the spin-orbit coupling effect which originates the magnetic anisotropy in these $L1_0$ CoPt phases through the hybridization of the Co-Pt electronic states along the c-axis [16]. In these partially ordered alloys, the effect of an platinum atoms excess with respect to stoechiometry is different in respectively the ordered and disordered phases. In the totally ordered $L1_0$ phases, a concentration of Pt (Co) beyond the stoechiometry is expected to decrease the anisotropy by decreasing the number of Co-Pt bonds along the c-axis. In the disordered phase, the inverse trend is expected : statistically, the number of c-oriented bonds with respect to that of equivalent Co-Co bonds increases with x_{Pt}. So we believe that the increase of K_u with x_{Pt} can be associated to the presence of anisotropic short range order in the disordered phases of the films. It is similar effect which has been shown to originate the perpendicular magnetic anisotropy of disordered CoPt3 alloy thin films[17].

CONCLUSION

The textures of Pt buffer grown at 970 K on (001) MgO substrate and that of CoPt films grown on this Pt buffer are strongly correlated : a Pt thickness of at least 10 nm is necessary to enhance the [002] orientation. X-ray diffraction data completed by TEM observations show that the [002] grains consist of a mixing of ordered $L1_0$ and disordered phases. The increase of the apparent LRO parameter with the growth temperature, described by a thermally activated model, emphasizes the dominant role played by the surface effects in driving the occurrence of the $L1_0$ structure. The uniaxial anisotropy of the [002] orientated grains follows the increase of the apparent LRO parameter.

REFERENCES

1. P. Eurin and J. Paulevé, IEEE Trans. on Magnetics **Mag.5**, 216 (1969).
2. B. M. Lairson et al., J. Appl. Phys. **74** (3) 1922 (1993).
3. M. R. Visokay and R. Sinclair, Appl. Phys. Lett. **66** (13) 1692 (1995).
4. G. R. Harp et al., Mat. Res. Soc. Symp. Proc. **313**, 493 (1993).
5. M.C. Cadeville et al., Physica Scripta, **T49** 364-372 (1993).
6. C. Leroux et al. J. Phys. F : Met. Phys. **18,** 2033 (1988).
7. C. E. Dahmani, PhD Thesis Université Louis Pasteur, Strasbourg, France (1985).
8. M. C. Cadeville, C.E. Dahmani and F. Kern, JMMM **54-57**, 1055 (1986).
9. V. Parasote, PhD thesis, Louis Pasteur University, Strasbourg, France (1998).
10. H. Berg and J. B. Cohen, Metal. Trans., **3**, 1797 (1972).
11. L. Bouzidi et al., Thin Solid Films, in press (1998) and V. Pierron-Bohnes et al., to be published in "Diffusion Mechanisms in Crystalline Materials " Mat. Res. Soc. Symp. Proc. (1998).
12. D. Stoeffler and F. Gautier, Surface Science, **249**, 265 (1991).
13. V. Gehanno, A. Marty, B. Gilles and Y. Samson, Phys. Rev. B, **55,** 12552 (1997).
14. C.E. Dahmani, M.C. Cadeville and V. Pierron-Bohnes, Acta Metall., **3,** 369 (1985).
15. G. Treglia, private communication.
16. A. Samuka, J. Phys. Soc. Jap., **63** 3053 (1994).
17. C. Meneghini et al., J. Phys. IV France 7 (suppl.), C2-1115 (1997).

DISTURBED ARRAY FORMATION OF ELECTROCHEMICALLY GROWN SELF-ORGANISED NANOSTRUCTURES.

D.D. DIERICKX*, J.P. CELIS** AND V.V. MOSHCHALKOV*

*K.U.Leuven, Dept. of Physics, Laboratory of Solid State Physics and Magnetism, Celestijnenlaan 200D, B3001 Heverlee, Belgium
**K.U.Leuven, Dept. of Metallurgy and Materials Engineering, de Croylaan 2, B3001 Heverlee, Belgium

ABSTRACT

The formation of electrochemically etched, self-organised nanostructures on aluminium enables the production of large area regular arrays in a fast and cost-effective way. These microstructures could form the basis to develop masks for subsequent materials deposition without the need for time consuming patterning techniques.

The desired regular arrays result from a steady state interaction between the electrolyte and samples' surface under the influence of a cell potential. The type of array formed depends on this cell potential and shows an evolution from lines to dots.

Although a gradual progress towards a regular lattice spanning large areas is expected, the presence of initial disturbances of the samples' surface or bulk distorts the final lattice considerably. In this work the modulation depth and type of the resultant nanostructures produced at different cell potentials are assessed in view of practical applications.

INTRODUCTION

The increasing miniaturisation of components and storage media in micro-electronics forces the existing processing techniques to their limits. Recent progress in the production of nanostructures opens new possibilities in a technological application area governed by quantum-effects[1]. The small characteristic dimensions of the individual components leads to special quantum effects which determine electrical and magnetic properties. Besides simple individual quantum structures (dots, lines and heterojunctions), research is now primarily focused on the development of very sophisticated ordered quantum arrays for application as new mass storage media and micro-electronic components[2]. The traditional production methods like e-beam lithography show their limitations under these extreme conditions: (1) long processing times due to the strictly serial patterning by writing each pixel individually, (2) presence of process induced defects due to the high energy e-beams and reactive etching, (3) decreased spatial accuracy when these methods are used to write large areas. Additionally, the equipment needed for these procedures is very sophisticated and expensive, especially taking into account parallel e-beam writers when high throughput speeds are aimed for. Especially in the production of large repetitive arrays of simple nanostructures the existing e-beam techniques will be replaced by a cheaper electrochemical process.

Billions of simple structures can be formed in a parallel way using electrochemical self-organising procedures[3,4], yielding large regular arrays of nanodots at the appropriate electrochemical cell conditions. This allows a fast and cheap alternative electrochemical production of large (up to cm scale) regular arrays of electrical or magnetic dot or line structures. Potential applications of such structures are in the field of high density magnetic storage media or microelectronic components. With a lateral period of the self-organised array

Mat. Res. Soc. Symp. Proc. Vol. 517 © 1998 Materials Research Society

of 200 nm this kind of patterning could yield a storage density of 30 Gbyte/cm² in the absence of magnetic interactions between neighbouring magnetic nanodots.

The self-organised electrochemical array formation is mainly governed by the metal/electrolyte couple, cell potential and processing time. The system tends to a stable regime of regular surface arrays of nanostructures

THEORY OF EXPERIMENT

Samples of 1.0x1.0 cm² were prepared from bulk Al with a purity of 99.99%. Sample surfaces were ground to 7 μm, polished using diamond to a 1 μm finish and subsequently degreased. The polishing procedure was performed just prior to electrochemical etching. The electrolyte consisted of ethanol, butylcellusolve and water, for details see ref. 3.

The electrochemical etching set-up consists of a vertical tubular cell with the sample mounted at the bottom and a tubular Pt counter electrode at 3 cm distance. The electrolyte was injected in the cell just prior to applying the cell potential. The electrolyte was removed form the cell within ten seconds after completion of the etching procedure.

The total cell diameter is limited to 8 mm to achieve a homogeneous distribution of the electric field lines across the samples surface. All samples have been electro-etched for 30 sec. No cooling was applied during the etching procedure. Due to the small cell dimensions in situ temperature measurements were not performed. Mounting of the samples was done using wax.

The resultant surfaces were observed using Atomic Force Microscopy (AFM, Digital Instrument Nanoscope III) and Scanning Electron Microscopy (SEM; Philips XL30 equipped with a field emission gun). The AFM data were left untreated as much as possible, only a first order plane fit correction was applied in order to allow image representation at 256 grey levels. Measurements of periods were obtained from sectioning analysis dispersed over the samples surfaces. SEM measurements were performed at 10 kV to assess the overall structure formation across the full area of the electropolished samples.

RESULTS

Figure 1 shows the development of self-organised structures on the surface of several Al samples produced at cell potentials ranging from 50 to 90 V. At lower cell potentials the surface structures largely consist of an irregular array of depressions. At 50 V the surface structure consists of lines with a period of 150 nm measured at 90 degrees to their long axis and a height amplitude of 7 to 9 nm. Completely straight and parallel lines were not observed over long distances. Line splitting and recombination are numerous throughout the complete surface area.

With increasing the cell potential to 60 V, the line segments break up into smaller parts and locally form arrays of hillocks. The break-up continues up to 80 V where the hillock array is completely formed. Increasing the cell potential to 90V results in a more regular array, but substantially reduces the amplitude of the surface structure below 5 nm.

In all samples the throughs are less regular than the crests, even at 90V the throughs show irregular small pits as expected following the proposed stabilisation process of the surface structures[3].

The distortion on the regular lattice introduces a large uncertainty on the period measurements. The typical period of the linestructures measured on several samples is situated around 150 nm. The intermediate curved line segments display the largest typical period in excess of 200 nm, while the transition to the dot array is accompanied by a decrease of the

typical period to 180-190 nm. As all samples consist of a mix of several structure types, the uncertainty on the period measurement is increased considerably.

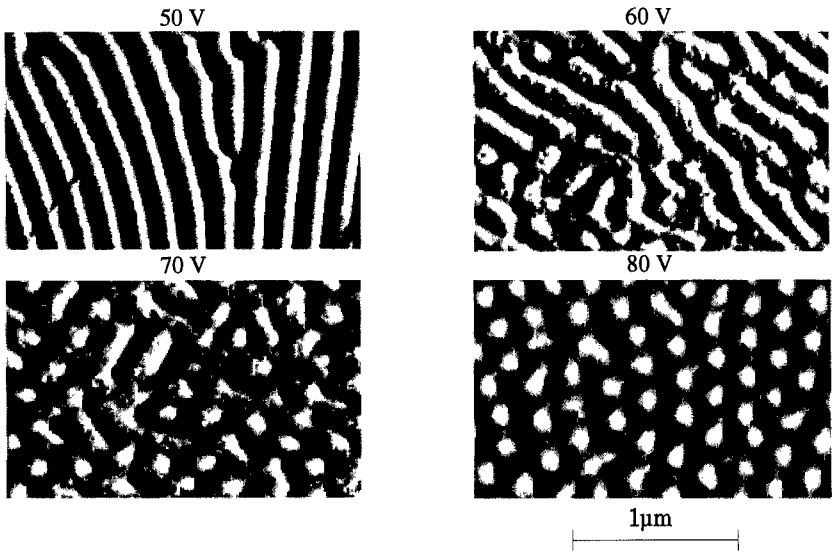

Figure 1 AFM measurements on electrochemically etched aluminium. Tip deflection is shown. General development of surface microstructure as a function of cell potential. At low voltage, line structures are observed which split into shorter line segments at higher potentials until finally the dot array is formed.

Figure 2A shows an array formed at a cell potential of 90 V, while Fig. 2B offers a more detailed AFM height map. For the generation of Fig. 2B a first order plane fit was performed on the original data.

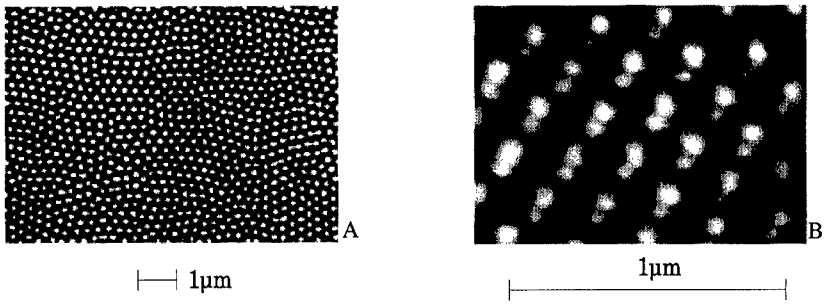

Figure 2. General view on the hillock array regularity adapted from an AFM height map of an electrochemically etched sample at 90 V cell potential. The hillock array shows ordered regions but at micrometer scale the arrays are clearly bent. The detailed view in figure B with an original z scale of 15 nm. shows the influence of a bent surface at µm scale superimposed on the hillock array. As a result the hillocks at the centre of the image appear to be more prominent.

At the centre of the image the hillocks appear to be more prominent than at the edges as a result of the curvature of the samples surface. The typical dimensions of these curved areas are approximately micrometer size and are comparable to the distortion of larger parts of the dot array.

Table 1 Overview of applied cell potential versus the observed microstructure. The typical period of the self-organised surface structures as well as their height are reported.

Cell potential (V)	observed structure	period (nm)	height (nm)
50	lines	150	7-9
60	curved line segments	200-230	8-11
70	randomly attached hillocks	210-230	9-15
80	distorted array	175-200	9-10
90	distorted array with twin peaks	200	<5
100	no structures observed	/	/

An overview of the measurements is presented in table 1. The transition between different types of surface structures in function of cell potential is clear. The change in typical period and amplitude is unfortunately not as evident. No clear increase in the typical period can be discerned comparable to the dependence described in ref. 3. The typical periods observed in these experiments are also 50% larger than cited in ref. 3. This indicates that the main parameter governing the period of the array was not under control in this set of experiments.

Figure 3 shows a graphic representation of the observed height versus cell potential dependence. Although the height values are the result of only twenty random observations, the graph shows a clear change of dependence around 70 V.

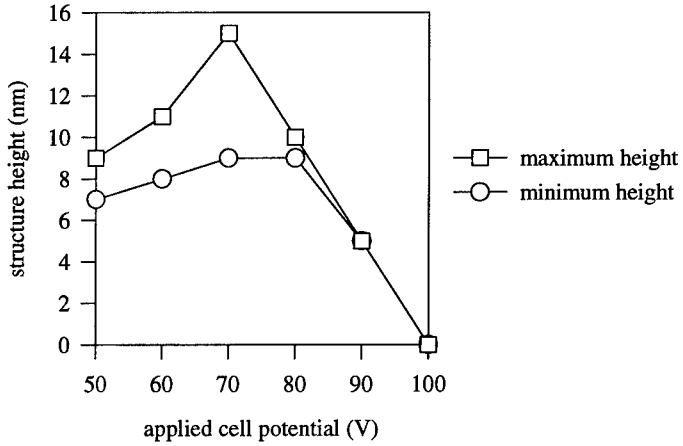

Figure 3. Minimum and maximum structure height versus applied cell potential. The height was measured at twenty random crest positions. Above 70 V the trend of an increasing height interval is changed into an almost linear decrease to zero height at 100 V. This overall dependency is an indication of the importance of heat generated at higher cell potentials.

The increasing typical structure height and height interval is curbed to a linear decrease to zero height at 100 V. The amplitude reduction for the 90 V and 100 V samples is attributed to excessive heat generation as the relative number of sample mount failures increased substantially with higher voltages.

The large scale (μm) flatness of the samples has to be increased drastically in order for mesa etching of large surfaces to become feasible. Laser profilometer measurements indicate that the electro-etched surfaces show micrometer roughness. The periodic arrays thus have an order of magnitude smaller height amplitudes. Extrapolating the increasing height dependency at low cell potentials to 100 V indicates a possible height amplitude of 50 nm, which is still considerably lower than the present surface roughness.

CONCLUSIONS

The polycrystalline structure of the bulk Al is responsible for the distortion of the arrays formed during electropolishing. Therefore single crystal material or thin film substrates are advisable. A gradual shift from lines over curved line segments, randomly attached, to hillock arrays is observed at increasing cell potentials. The discrepancy between observed and previously reported periods of the surface structures could be attributed to heat generated during electropolishing, but this remains to be proven by further experiments. In this case, the heat generated at higher cell potentials reduces the structure's height amplitude substantially. The present micrometer roughness of the Al samples has to be reduced substantially for large area mesa etching to become feasible.

ACKNOWLEDGEMENTS

This work has been financially supported by the Research Council of the KU.Leuven V.I.S. project 96/6, FWO-Vlaanderen, the Flemish GOA and Belgian IUAP Research Programmes. D. Dierickx is a post-doc of the K.U.Leuven Research Council.

REFERENCES

1. Stucky G.D., Dougall J.E., Science, **247**, 669 (1990).
2. Routkevitch D., Chan J., Xu J., Moskovits M., Growth of the Porous Anodic Alumina Templates for Advanced Nanofabrication, (ECRS Proc. 191,Montreal 1997), p. 178
3. Bandyopadhyay S., Miller A. E., Chang H-C., Banerjee G., Yuzhakov V., Yue D-F., Ricker R.E., Jones S., Eastman J.A., Baugher E., Chandrasekhar M., Nanotechnology, **7**, 360 (1996).
4. Ricker E., Miller A.E., Yue D-F., Banerjee G., Bandyopadhyay S., J. Electronic Materials, **25**, 1585 (1996).

STRUCTURE AND MAGNETIC PROPERTIES OF Co, Ni, Mn, Cr AND Cu SUBSTITUTED MAGNETITES

M. SORESCU*, D. MIHAILA-TARABASANU**, L. DIAMANDESCU**
*Duquesne University, Bayer School of Natural and Environmental Sciences, Physics Department, Pittsburgh, Pennsylvania 15282, U.S.A.
**Institute of Atomic Physics, National Institute of Materials Physics, R-76900 Bucharest-Magurele, Romania

ABSTRACT

Co, Ni, Mn, Cr and Cu substituted magnetites were prepared by the hydrothermal method at 300° C, with concentrations x ranging from 8.2 to 12.5%. Transmission electron microscopy determined the average particle diameter $<\Phi>$ to be in the hundred of nm range and the morphological modifications induced by the various substitutions employed. Hysteresis loop measurements were performed to determine the coercive field H_c and saturation magnetic moment m_s. While H_c decreased with increasing $<\Phi>$, the particle shape was found to play an important role in explaining the dependence of m_s on $<\Phi>$. Transmission Mössbauer spectroscopy was used to determine the site preference of the substitutions and their effect on the hyperfine magnetic fields. The room temperature Mössbauer spectra were analyzed assuming a random distribution of substitutents using the binomial distribution from the ionic crystal point of view. Superparamagnetic particles were observed at room temperature in the case of Cu and Cr substituted magnetites.

INTRODUCTION

Magnetite (Fe_3O_4) is an oxide with the inverse spinel structure, which has one Fe^{3+} ion on the tetrahedral (A) site and two Fe ions, with a total valence of 5+, on the octahedral [B] site.[1,2] Naturally occurring magnetites are frequently intergrown with other minerals, making their separation from rocks and soils very difficult. On the other hand, synthetic magnetites, free from other minerals, can be synthesized using the precipitation technique.[3] Sometimes, impurity elements have been added to these preparations, simulating natural materials. In most of these studies,[4-7] it has been assumed that the substitutions are distributed at random throughout the magnetite crystal.

Although the syntheses and transformations of various iron oxides and oxyhydroxides, such as haematite, maghemite and goethite have been studied in detail,[8-10] not much is known about the formation of synthetic magnetites and the incorporation of impurity elements into them. The present investigations are aimed at studying the formation of several synthetic magnetites under hydrothermal conditions and determine their structural and magnetic properties by the combined application of magnetic measurements and Mössbauer spectroscopy.

EXPERIMENTAL

Several substituted synthetic magnetites were prepared by the hydrothermal method at 300° C. The concentrations corresponding to each type of impurity have been determined by X-ray fluorescence and are given in Table I. The average particle size and morphology were determined by TEM. Hysteresis loop measurements were perfomed at 4.2 K in a magnetic field up to 1 T applied parallel to the sample plane. Room temperature transmission Mössbauer measurements were recorded with the γ rays perpendicular to the absorber plane using a constant acceleration spectrometer. The 35-mCi source was ^{57}Co diffused in a Rh matrix. Least squares fitting of the Mössbauer spectra was performed in the assumption of a random distribution of impurity ions, using the binomial formula. The relative areas of the outer : inner line pairs were correlated to be the same for all component sextets.

Mat. Res. Soc. Symp. Proc. Vol. 517 © 1998 Materials Research Society

RESULTS AND DISCUSSION

Table I shows the values of the average particle diameter <Φ> and morphology corresponding to the various types of substitutions employed. Both undoped and Ni-substituted magnetites consist of polyhedral particles, whereas Co and Mn-doped magnetites exhibit a spherical/polyhedral morphology, and the Cr and Cu-substituted magnetites have particles of all shapes. The average particle diameter, determined by TEM and confirmed by X-ray diffraction, is in the hundred nanometer range, except for Fe_3O_4:Cu^{2+}, which consists of particles in the tens of nanometer range.

TABLE I. Average particle size <Φ>, saturation magnetic moment m_s, coercive field H_c and particle shape of doped synthetic magnetites. All specimens have the same mass.

Composition	Concentration x (%)	<Φ> (μm)	m_S (emu)	H_c (kOe)	Particle shape
Fe_3O_4		0.340	0.156	0.49	polyhedral
Fe_3O_4:Co^{2+}	8.20	0.400	0.083	0.40	spherical/polyhedral
Fe_3O_4:Ni^{2+}	8.50	0.680	0.294	0.25	polyhedral
Fe_3O_4:Mn^{2+}	10.70	0.540	0.089	0.35	spherical/polyhedral
Fe_3O_4:Cu^{2+}	11.06	0.084	0.237	0.99	all shapes
Fe_3O_4:Cr^{3+}	12.50	0.580	0.396	0.33	all shapes
Errors:	+/-0.05	+/-0.005 to +/-0.030	+/-0.005	0.01	

Figure 1 shows the hysteresis loop measurements recorded at 4.2 K in an applied field up to 1 T. It can be seen that the saturation magnetic moment, coercive field and hysteresis phenomenon depend strongly on the type of substitution introduced in the magnetite structure. In particular, the coercive field decreases with increasing particle diameter, in agreement with results obtained on ball-milled nanocomposite materials.[11] As expected, the saturation magnetic moment was found to increase with increasing particle size in the case of Fe_3O_4:Ni^{2+}, which exhibits the same morphology as polyhedral Fe_3O_4. In all other cases, deviations from the expected proportionality between m_S and <Φ> were obtained and attributed to prevailing shape anisotropy factors.

The room-temperature transmission Mössbauer spectra of Fe_3O_4, Fe_3O_4:Co^{2+}, Fe_3O_4:Cr^{3+}, Fe_3O_4:Ni^{2+}, Fe_3O_4:Mn^{2+} and Fe_3O_4:Cu^{2+} are given in Fig. 2. The fitted Mössbauer parameters obtained from these spectra are listed in Table II. The Mössbauer spectrum of Fe_3O_4 was analyzed by considering two sextets, corresponding to the tetrahedral (A) and octahedral [B] magnetic sublattices, in a 1:2 areal intensity ratio, typical of stoichiometric magnetite. No matter what charge, the substitutions employed were found to prefer the B sites. The relaxation time for electron diffusion, which allows the Fe[B] charge to redistribute itself, is smaller than the time characteristic to the Mössbauer experiment, so that the measured hyperfine fields will not be those of the pure Fe^{2+} and Fe^{3+} states, but time-averaged values for the different local configurations and ratios of the Fe^{2+} and Fe^{3+} states. The statistical distribution of impurity ions makes it possible to derive the statistical weight of the different finite numbers of local distributions and ionic surroundings as a function of x, with the aid of the binomial distribution function.

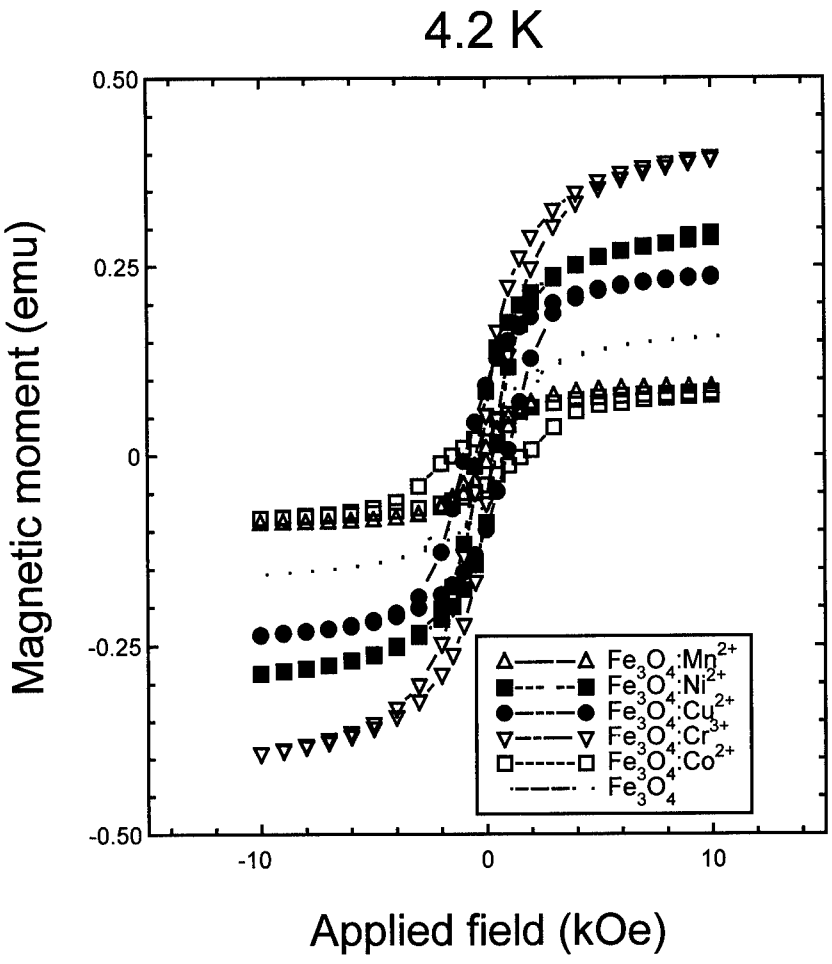

FIG. 1. Hysteresis loop measurements recorded at 4.2 K in applied magnetic fields up to 1 T, for undoped and substituted Fe_3O_4 samples.

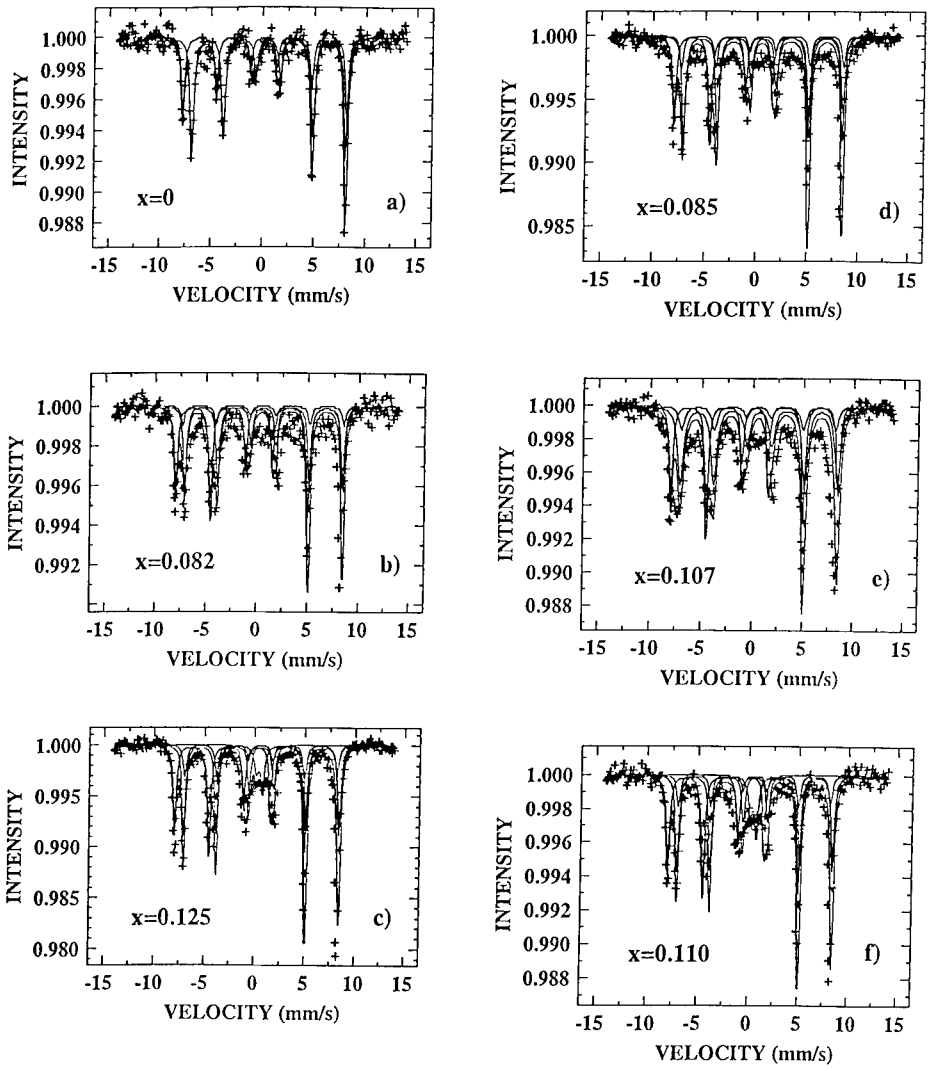

FIG. 2. Room-temperature transmission Mössbauer spectra of (a) Fe_3O_4, (b) Fe_3O_4:Co^{2+} and (c) Fe_3O_4:Cr^{3+}, (d) Fe_3O_4:Ni^{2+}, (e) Fe_3O_4:Mn^{2+} and (f) Fe_3O_4:Cu^{2+}. The substituent concentrations are also indicated on the figure.

TABLE II. Binomial distribution probability P_1, hyperfine magnetic field H_{hf}, quadrupole splitting ΔE_Q, isomer shift δ (relative to α-Fe at 300 K), and relative areas corresponding to the component patterns in the transmission Mössbauer spectra of substituted Fe_3O_4.

Composition	Concentration x (%)	P_1	H_{hf} (T)	δ (mm/s)	ΔE_Q (mm/s)	Relative areas (%)	Assignment of sites
Fe_3O_4			49.0	0.25		33.3	A (Fe^{3+})
			46.0	0.67		66.7	B (Fe^{3+}, Fe^{2+})
Fe_3O_4:Co^{2+}	8.20		51.0	0.25		50.0	A (Fe^{3+})
			48.0	0.67		40.6	B (Fe^{3+}, Fe^{2+})
		0.19	49.0	0.60		9.4	B (Fe^{3+}, Fe^{2+}, Co^{2+})
Fe_3O_4:Ni^{2+}	8.50		51.0	0.25		40.3	A (Fe^{3+})
			48.0	0.67		45.6	B (Fe^{3+}, Fe^{2+})
		0.20	49.0	0.60		14.1	B (Fe^{3+}, Fe^{2+}, Ni^{2+})
Fe_3O_4:Mn^{2+}	10.70		51.0	0.25		37.0	A (Fe^{3+})
			48.0	0.67		48.2	B (Fe^{3+}, Fe^{2+})
		0.24	47.0	0.60		14.8	B (Fe^{3+}, Fe^{2+}, Mn^{2+})
Fe_3O_4:Cu^{2+}	11.06		51.0	0.25		41.7	A (Fe^{3+})
			48.0	0.67		37.5	B (Fe^{3+}, Fe^{2+})
		0.25	47.0	0.60		12.5	B (Fe^{3+}, Fe^{2+}, Cu^{2+})
				0.20	0.6	8.3	superparamagnetic
Fe_3O_4:Cr^{3+}	12.50		51.0	0.25		41.1	A (Fe^{3+})
			48.0	0.67		38.4	B (Fe^{3+}, Fe^{2+})
		0.27	47.0	0.60		13.7	B (Fe^{3+}, Fe^{2+}, Cr^{3+})
				0.20	0.6	6.8	superparamagnetic
Errors:	+/-0.05		+/-0.1	+/-0.01		+/-0.1	

Consequently, the Co^{2+} and Ni^{2+} substitutions led to the additional appearance of a sextet with the hyperfine field of 49.0 T, which indicates a more pronounced Fe^{3+} character than the average Fe[B] line in the pure magnetite spectrum at room temperature. Conversely, the Mn^{2+}, Cu^{2+} and Cr^{3+} substitutions led to the occurrence of a different resonant surrounding, corresponding to a hyperfine magnetic field of 47.0 T, having a more pronounced Fe^{2+} character. The relative intensities of both Mössbauer Fe[B] subspectra are in excellent agreement with the predictions of the binomial distribution model.

The room-temperature Mössbauer spectra of Cu^{2+} and Cr^{3+} substituted magnetites exhibit the additional presence of a quadrupole-split doublet, with the hyperfine parameters typical of superparamagnetic magnetite particles. They represent 8.3 and 6.8% respectively, of the compositions of doped magnetites at room temperature. The occurrence of superparamagnetic particles is due to the small average particle diameter in the case of Fe_3O_4:Cu^{2+} and to a broader range of particle size distribution in the case of Fe_3O_4:Cr^{3+}.

CONCLUSIONS

Co, Ni, Mn, Cu and Cr-substituted magnetites were prepared by the hydrothermal method and studied by dc magnetic and Mössbauer spectroscopy measurements, complemented by TEM. The coercive fields were found to decrease with increasing particle size, whereas

morphology-related effects played an important role in explaining the dependence of the saturation magnetic moments on the average particle diameter. All substitutions employed were found to prefer the B sublattice of Fe_3O_4 and distribute at random within the magnetite structure, according to the binomial distribution function. Superparamagnetic particles were observed at room temperature in the case of Cu and Cr-substituted magnetites.

ACKNOWLEDGMENT

This work was supported by a Cottrell College Science Award of Research Corporation.

REFERENCES

1. M. Sorescu, J. Mat. Sci. Lett., in print.

2. A. Okamura, S. Nakamura, M. Tanaka and K. Siratori, J. Phys. Soc. Jpn. **64**, 3484 (1995).

3. P.S. Sidhu, R.J. Gilkes and A.M. Posner, J. Inorg. Nucl. Chem. **40**, 429 (1978).

4. H.N. Ok, L.S. Pan and B.J. Evans, Phys. Rev. B **17**, 85 (1978).

5. P.A. Dickof, P.J. Schurer and A.H. Morrish, Phys. Rev. B **22**, 115 (1980).

6. U. Schwertmann and E. Murad, Clay & Clay Minerals **38**, 196 (1990).

7. R.M. Persoons, E. DeGrave and R.E. Vandenberghe, Hyperfine Interact. **54**, 655 (1990).

8. P.H. Hsu, J. Soil Sci. **23**, 17 (1972).

9. S. Morup, M.B. Madsen, J. Franck, J. Villadsen and C.J.W. Koch, J. Magn. Magn. Mater. **40**, 163 (1983).

10. L. Diamandescu, D. Mihaila-Tarabasanu, S. Calogero, N. Popescu-Pogrion and M. Feder, Solid State Ionics, in press.

11. A.K. Giri, C. DeJulian and J.M. Gonzales, J. Appl. Phys. **76**, 6573 (1994).

MACROSCOPIC PROBING OF THE JOINT BETWEEN METALS IN MR HEADS

Jibin GENG, X. YAN, X.X. ZHANG, Xiaofeng ZHANG, N. Wang, K.K. Fung
Physics Department, Hong Kong University of Science And Technology, Clear Water Bay, Kowloon, Hong Kong

ABSTRACT

During the wafer manufacturing process of magnetoresistive (MR) heads which are widely used in Hard Disk Drives, the metal leads are deposited on both sides of the MR sensing element through the photoresist masks. Due to the shadowing effect of the photoresist, there may be some contamination at joint interfacial region even after ion etching. This introduces additional contact resistance and causes some region of the sensing element to be unpinned. As the geometry of the sensor element decreases, and the contamination, located in regions of few thousands of angstroms, is becoming more severe for MR head than ever. In this paper, we developed a systematic method to evaluate the contact resistance between the two metal layers. A comparison was made between the magnetic read width and the physical width. Finally TEM analysis successfully revealed the interfacial junction contamination.

INTRODUCTION

One typical MR head structure consists of the MR element tri-layer, the longitudinal biasing layer and the electric metal lead as shown in Fig. 1 [1-3]. The tri-layer are the MR layer, the spacing layer and the soft adjacent layer (SAL) with the typical thickness 20nm,10nm and 12nm. At both sides, ~30nm exchange layer is deposited for longitudinal biasing and ~50nm metal lead is deposited above the exchange layer. In this structure, there are some metal joints such as the joint between the MR tri-layer and the exchange layer, the joint between the exchange layer and the metal lead. In these joints, the contact between two metal layers may not be good, which will be called poor contact in this study. The electrical functions of the MR head were found to be influenced by this kind of poor contact.

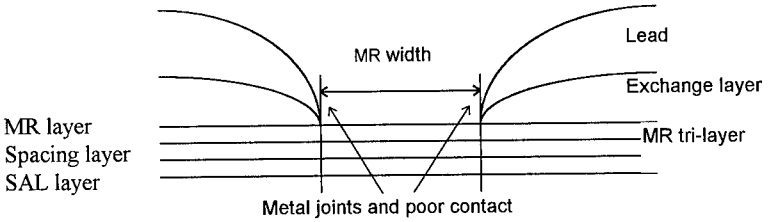

Fig.1 . MR head structure with exchange longitudinal biasing.

Basically the influences of poor contact on the MR head are in three aspects: the dynamic performance, the reliability and the read width defining. The poor contact causes additional dummy resistance in the MR head, which never contributes to the signal but causes the joule heating. Therefore, the MR element local temperature becomes high, which will result in a loss in reliability such as electro-migration or inter diffusion etc [7,8]. The poor contact will also cause the MR

Mat. Res. Soc. Symp. Proc. Vol. 517 © 1998 Materials Research Society

element to become partially unpinned under the exchange layer, which will lead to greater active width than the designed. This problem will become more severe as the recording density increases.

Although the poor contact affects MRE performance quite strongly, it has not been studied carefully. Recently, the poor contact was observed, and it was confirmed that it arose from the interfacial contamination in the TEM studies. Since the TEM study is a destructive, time consuming and very delicate experiment, it is very necessary to develop a new technique for detecting the poor contact in the industrial wafer production process. Here we will report a newly developed macroscopic resistance method to detect the poor contact. It has been found that the results obtained by this resistance measurement is in good agreement with the TEM analysis.

EXPRIMENT

Observation of Poor Contact

During the characterization of the MR heads, some phenomena were found to be related to the poor contact problem. The first is that the measured MR head resistance was always a few ohms larger than the designed, see Fig 2.

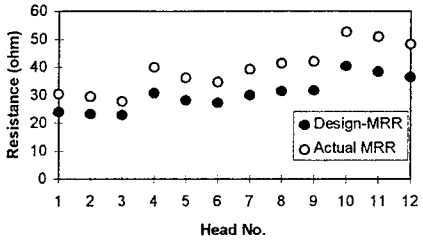

Fig. 2. The measured MR resistance is always larger than the designed MR resistance.

The second is that there was a width offset between magnetic read width and physical width as shown in Fig.3. The physical width can be measured by High Resolution Scanning Electron Microscope (HR SEM). The magnetic width can be measured through cross micro track profile by using Guzik 1701 tester[4,5]. The magnetic read width was found wider than the physical width. It is opposite to the usual thinking that the magnetic read width is narrower than the physical width due to the magnetic transition region at the both sides of the MR stripe [9]. Those phenomena indicate both the existence of poor contact and its influence to the functions of the MR head.

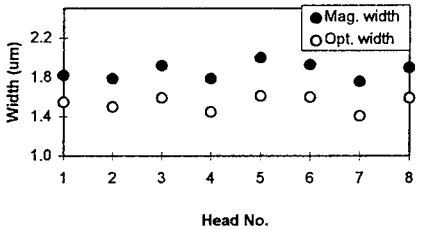

Fig.3. The magnetic read width is wider than physical width.

Resistance Model

It is understood that the poor contact causes the additional resistance. The simple resistance model is described by the following equations:

$$R = \frac{\rho \times W}{t \times H} + \frac{C}{H} + R_{lead} \qquad (1)$$

The total resistance of a MR head can be divided into three parts: the first part is MR stripe resistance. ρ is the averaged resistivity of the tri-layer, W, t and H stand for physical width, total thickness and height of the MR stripe respectively. The second part is the contact resistance term C/H, which is supposed to be reverse proportional to the stripe height. C is the coefficient of the contact resistance. The third part is the lead resistance which only depends on the lead structure. Normally, we use S in the equation instead of ρ/t, called sheet resistance in ohm. Then, Eq. (1) can be rewritten as.

$$R = \frac{SW}{H} + \frac{C}{H} + R_{lead} \qquad (2)$$

Measurement Of Contact Coefficient

According to above model, the following resistance method was developed to determine the C coefficient. Several specific MR sensors were designed neighbored to the standard MR sensor with same lead structure and deposited at the same process, so that the C, S and R_{lead} can be considered to be the same. Then, the resistance is only the function of width W and height H of the stripes. Three MR sensors with dimensions of W_1xH_1, W_2xH_2, W_3xH_3 have been chosen and their resistance R_i (i=1,2,3) has been measured by ohm meter. By solving Ri=f(Wi, Hi), (i=1,2,3), we obtained C, S, and R_{lead} respectively.

However, the C term obtained above is not accurate enough. To get a more accurate C term, another experiment was developed. Note that R_1, R_2, R_3 can be designed at the same zero height datum as the standard MR sensor. When a lapping is applied to the MR sensors from the bottom, the resistance of the sensor will increase as it's height is reduced due to lapping. The resistance of the sensors can be taken down as the height is changing continuously. By specific design of original Wi and Hi, using the resistance of R_1, R_2, R_3 after lapping, the height H of the sensor close to the standard sensor at each resistance can be calculated. The height H of the standard sensor can be thought as the same as the closest sensor. Then, by plotting the standard sensor resistance R vs 1/H, the slope can be got. This slope equals to SxW+C. As S is known already, W can be measured by SEM, hence, C value can be worked out. The C value by this method is more accurate due to two reasons. The first reason is that the slope is got by fitting many data points of MRR and 1/H. The second reason is due to using measured W by HRSEM instead of using design value.

RESULTS

Experimental Data Of Resistance Measurement Method

Fig.4. shows the typical plots of R as function of 1/H obtained on the two wafers. It is evident that MRR depends linearly on 1/H. By fitting the data to a straight line, the lope was accurately obtained, consequently the C value. The obtained C value are 12.04ohm.μm and 4.53 ohm.μm for wafer 1 and wafer 2 respectively. The result indicates that the wafer 2 has significantly better contact than wafers 1, which is confirmed by the direct observation on TEM.

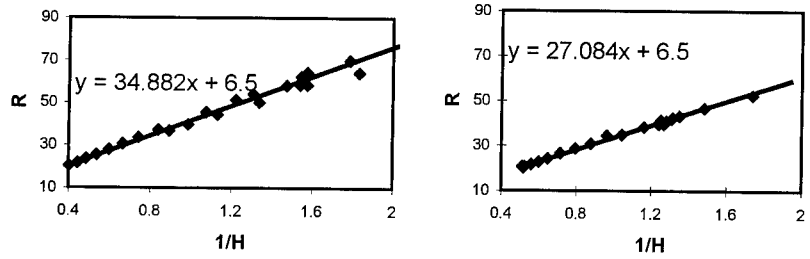

a. Wafer 1, S=15.33ohm, W=1.49um, C=12.04ohm.um.

b. Wafer 2, S=15.34ohm, W=1.47um, C= 4.53 ohm.um

c.

Fig.4. The plot of R vs 1/H. The slope equals to SxW+C. The S is calculated from the R_1, R_2, R_3, the W can be measured by SEM, then the C can be worked out.

Comparison With TEM And Width Offset Measurement

TEM analysis at the metal joints was performed on the two wafers. As observed from the TEM picture shown in Fig. 5, there are white lines, which indicate the poor contact between the MR layer and exchange layer, and also between the exchange layer and metal lead layer. The length of white line were measured as 280nm in wafer 1 and 180nm in the wafer 2.

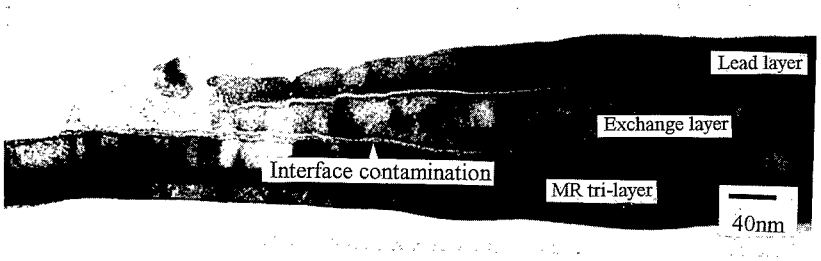

a. TEM picture of wafer 1(top), white line is around 280nm.

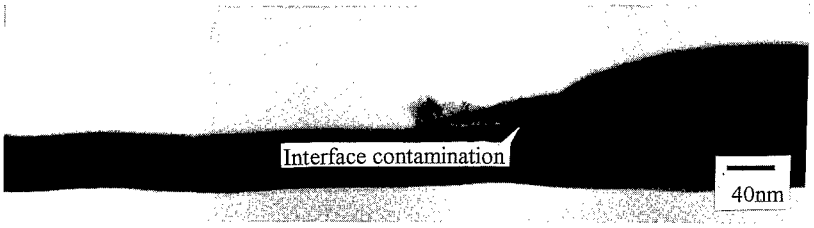

b. TEM picture of wafer 2(bottom), white line is around 180nm

Fig.5. TEM pictures of the joint area, the white lines indicate the poor contact at the interface.

The offset between the magnetic read width and physical width were measured for the two wafers. The offset between the two widths should be caused by the poor contact layer width. The wafer 1 and wafer 2 have offset around 500nm and 300nm respectively. The comparison between the three methods is listed in Table.1.

By comparing results obtained in different process, it is clear that the size of poor contact detected by microscopic method can be effectively determined by the macroscopic resistance measurements, which is non-destructive, fast and easy method.

Table.1. The comparison of three methods

	C-term ($\Omega.\mu m$)	width offset (nm)	width of one side by TEM (nm)
Wafer 1	12.04	500	280
Wafer 2	4.53	300	180

Discussion

The poor contact was demonstrated to be due to some interface contamination between the metallic layers as revealed by TEM. Normally, after the film deposition of the MRE tri-layers in vacuum, the wafer will be taken out for photo process. Consequently, the wafer will go through the exchange layer and the lead deposition processes [6]. The contamination could exist on the surface of the MR layer, so the ion etching process is needed before the deposition of the exchange layers and leads. However, the mountain like photo-resist on the MRE may cause shadow effect, then the ion can not reach the bottom region as indicated in Fig. 6. To reduce the poor contact, ion beam cleaning with certain angle can be applied so that the ions can reach and clean the bottom region of the photo resist. Also, thinner photoresist may have less shadow effect and may also be able to help reduce the poor contact.

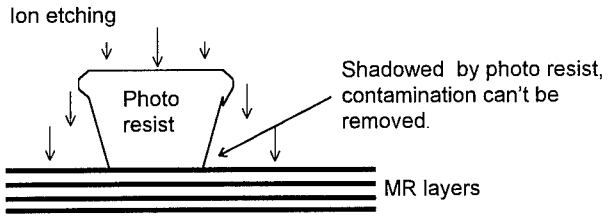

Fig.6. The photo resist shadow effect could be the reason of the interface contamination.

CONCLUSIONS

The poor contact problem between the metallic layers has been studied through TEM analysis. A simple macroscopic resistance measurement was developed. This technique can be used to detect the poor contact quantitatively. Compared with the TEM analysis, the resistance measurement is much simpler, easier in wafer process monitoring. This resistance measurement technique can also be used to detect the surface contact quality for general metallic joints.

ACKNOWLEDGMENTS

The authors would like to thank Dr. Po Kang Wang for very helpful discussions.

REFERENCES

1. Nouyuki Ishiwata, Tsutomu Ishi, Hisao Matsutera, and Kazuhiko Yamada, IEEE Trans. Magn., Vol.32, p.38. (1996).
2. John C. Mallinson, Magneto-Resistive Heads (ACADEMIC PRESS, 1996) p.52-53.
3. C.Tsang, IEEE Trans. Magn., Vol. 25, p. 3692.(1989).
4. WITE and GPTE User's Menu, Guzik Technical, Inc., 1995.
5. Internal program "MR TEST" for MR head characterization in GUZIK WITE environment.
6. Gunther Baubock, Huan Q. Dang, David C. Hinson, Luarence L.Rea, and Young K Kim, IEEE Trans. Magn, Vol.32., P.25 (1996).
7. Howard G. Zolla, INTERMAG'97 Article FP-13 (1997).
8. A. Gangulee and F.M. d'Heurle, Japan J. Appl. Phys. Suppl. Vol.2. p. 625 (1974).
9. Private discussions with Dr. Po Kang Wang.

INTERPARTICLE INTERACTION EFFECTS IN NONMISCIBLE CoAg THIN FILMS WITH HIGH Co CONCENTRATION

A. Butera and J. A. Barnard

Center for Materials for Information Technology and Department of Metallurgical and Materials Engineering, The University of Alabama, Tuscaloosa, Alabama 35487-0209

ABSTRACT

A series of Co-rich CoAg heterogeneous thin films, with Co concentrations greater than 65 % volume fraction and film thickness in the range 5 nm - 50 nm, was prepared by dc magnetron sputtering. Annealing in high vacuum ($P < 3\times10^{-7}$ Torr) above 400 °C was necessary to promote phase separation between the two elements. Maximum room temperature coercivities, $H_c \sim 900$ Oe, were obtained at a thickness of 20 nm for CoAg 70:30 vol % films. These coercivities are almost two orders of magnitude larger than the values observed in as-deposited films. The concentration of maximum coercivity, that is usually associated to the threshold for magnetic percolation, is much higher than the 40-50 vol % commonly observed in bulk granular materials. The shift in the magnetic percolation limit was related to the reduced dimensionality of the very thin films. Coercivity was found to vary both with film composition and with thickness. Delta M curves and time decay (magnetic viscosity) measurements were done to determine the interparticle interactions and the activation volumes. A maximum in the remanent coercivity (coincident with the maximum in H_c) was found for a film thickness $\phi \sim$ 15-20 nm in all the alloys. At this same thickness a negative minimum in the interparticle interaction parameter α (indicating that the particle interactions favor the demagnetized state) was observed. The absolute value of α increases for larger Co concentrations. The irreversible susceptibility is an increasing function of film thickness and the magnetic viscosity has a minimum for $\phi \sim$ 15-20 nm . The activation volume also increases with thickness, changing from $(15\text{ nm})^3$ to $(40\text{ nm})^3$ for the more diluted alloys, values similar to the average particle size determined by transmission electron microscopy.

INTRODUCTION

The nonmiscible alloys of ferromagnetic/nonmagnetic metals have recently attracted much attention[1-3] due to the presence of giant magnetoresistance (GMR) in granular or heterogeneous films where the nonmagnetic metal is the majority phase. However, comparatively little work[4-6] has been done in the ferromagnetic-rich systems that do not exhibit GMR, particularly in very thin films where the ferromagnetic material is expected to be the matrix and the nonmagnetic metal the isolated grains. Granular systems where the ferromagnetic (FM) material is Co or a high magnetocrystalline anisotropy Co-alloy are currently under extensive research because of their potential applications as low-noise ultra-high density magnetic recording media[7]. Chien[8] reviewed the magnetic properties of granular materials and showed that when the volume fraction, x_v, of the ferromagnetic metal is less than the percolation threshold, x_p, the FM grains are single domain and have relatively large coercivities. If $x_v > x_p$, the ferromagnet surrounds the nonmagnetic material forming a network-like structure and the film behaves as a soft FM, at least for films with a thickness on the order of 1 μm. The magnetic behavior of thick (several μm) FM/nonmagnetic-metallic films as a function of composition shows a maximum room temperature coercivity ($H_c \sim$ 500 Oe) for a concentration of the FM element, $x_v \sim 0.45$, coincident with the percolation limit[9,10]. The largest values of H_c are observed in films that are heat treated to obtain the desired grain size, either by heating the substrates during sputtering or by post-deposition thermal annealing. Very little work has been done on the thickness dependence of the magnetic properties of FM-rich thin granular films. However, it was recently

Mat. Res. Soc. Symp. Proc. Vol. 517 © 1998 Materials Research Society

shown[5,6] that the magnetic percolation threshold in CoAg heterogeneous alloys is thickness dependent, quite probably because of the reduced dimensionality of very thin films.

The comparison of the magnetic remanent state after different field cycles has been shown to be a very useful and powerful technique to study the magnetic interactions among particles in powder-like materials and thin films[11]. The δM curve is defined[12] as the difference of two zero-field remanence curves: $\delta M = 2M_r\text{-}1 - M_d$. M_r is the isothermal remanent magnetization (or IRM) and is obtained by starting from a demagnetized state and measuring the magnetization at zero field after applying fields of increasing amplitude. M_d is known as the dc demagnetization curve (or DCD) and can be obtained by applying a large negative saturating field, then a positive field (that is increased after each measurement) and then measuring the remanent magnetization. Although several different ways to quantify the interparticle interactions have been proposed, the most widely accepted is the one proposed by Che and Bertram[12] in which two parameters, α and β, can be derived from a phenomenological model considering magnetostatic and exchange interactions. An easy method to derive α and β from the experimental data was proposed by Harrell *et al.*[13], leading to

$$\alpha = \int_0^\infty \delta M dh, \quad \beta = \frac{\alpha}{3M_r^0 - 1}. \qquad (1)$$

In the expression above h is the incremental applied field normalized to the remanent coercivity, H_{rem} is the reverse negative field that, after saturation in the forward direction, produces a zero magnetization at zero field, and M_r^0 is the remanent magnetization at the point where the δM curve crosses zero. Positive values of the parameter α originate when the interparticle interactions favor a magnetized state and in thin film media are generally due to exchange coupling[14]. Negative values of α, on the other hand, are usually related to weakly interacting particles coupled via dipolar-type interactions. When the δM curve does not cross zero, the β parameter is defined as zero.

The time dependent effects are usually characterized through the magnetic viscosity S. If a magnetic sample is saturated in one direction and a magnetic field (close to H_c) is applied in the opposite direction, M changes with time, even if H is kept constant. The change in magnetization with time is due to thermally activated magnetization transitions over anisotropy barriers. $M(t)$ is generally[15] found to obey a logarithmic law[16],

$$M(t) = C + S\ln(t / t_0), \qquad (2)$$

where C and t_0 are constants and t is the time elapsed since the field was applied. Sometimes the magnetization decay is expressed in percent decay/decade, δ, that is simply related to S by $\delta = \ln(10)\ (S/M_s) \times 100$. The magnetic viscosity and the irreversible susceptibility, χ_{irr}, (obtained from the derivative of the dc demagnetization remanence curve) are used to obtain the fluctuation field, H_f, and the activation volume[17], V_{ac},

$$\frac{S}{\chi_{irr}} = H_f = -\frac{k_B T}{V_{ac} M_s}. \qquad (3)$$

The fluctuation field is an imaginary field equal to the effect of thermal agitation responsible for the magnetization reversal. The activation volume is the volume of a noninteracting single domain particle or the volume swept between pinning centers by a single jump of a moving domain wall. It is, in principle, a measure of the smallest domain that can be written in magnetic media.

EXPERIMENTS AND RESULTS

Sample Preparation

All films were prepared using dc magnetron sputtering techniques. A single 5 cm Co target was used. Two Ag rectangular pieces with a length equal to the target diameter and a width that was changed depending on the desired composition were placed, one perpendicular to the other, on top of the Co. We used the same deposition parameters for all films: base pressure < 3×10^{-7} Torr, Ar pressure 4 mTorr, sputtering power 1.4 W/cm^2, target to substrate distance 10 cm. With these conditions the sputtering rate changed from 0.1 nm/sec for pure Co to 0.2 nm/sec for the 65:35 vol% films. Samples for magnetic measurements were deposited on Corning 7059 glass. For TEM the films were deposited on carbon-coated copper grids and for composition determination via EDAX analysis they were deposited on Si <100>. We sputtered a series of four different Co-rich alloys; 65, 70, 80, and 90 Co vol % Co. Pure Co films were also grown as a reference. For each composition, samples with thickness in the range 5-50 nm were prepared in order to study the variation of magnetic properties in a region where dimensionality effects are expected to be important. Annealing experiments to study the influence of grain size were also made. Selected samples were annealed in high vacuum (P < 3×10^{-7} Torr) for 30 minutes at 420 °C.

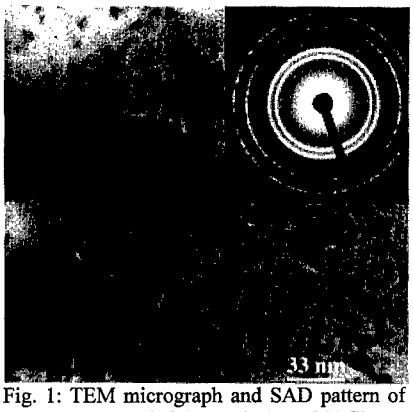

Fig. 1: TEM micrograph and SAD pattern of a 10 nm annealed CoAg 65:35 vol % film.

Microstructure

As deposited films of all compositions have an average grain size of less than 5 nm determined from TEM bright field images. The corresponding selected area diffraction (SAD) patterns present broad and diffuse rings that could be indexed as an fcc phase with a lattice parameter similar to that of Ag. Using high resolution EDAX techniques it was shown[18] that CoAg alloys are phase separated, even in the fast quenched as-deposited state. The absence of Co diffraction rings is possible due to the very small size of the Co grains. After annealing the samples at 420 °C for 30 minutes an increase in the grain size is observed. We show in Fig. 1 the TEM micrograph of a 10 nm thick CoAg 65:35 vol % film and the corresponding SAD pattern. Grain average size is now around 30 nm. Image contrast usually arises from grains with different crystallographic orientations with respect to the incident electron beam. However, evidence of image contrast due to different atomic species was observed in Ag-rich CoAg and FeAg[18, 19], where the bright regions corresponded to the lighter element. Our micrographs are quite similar to those of Ref. [18, 19] suggesting that the most important contribution to the contrast is composition rather than grain orientation. Note also that the majority phase corresponds to brighter grains as expected for Co (a lighter element than Ag). For this particular concentration complete percolation of the Co grains should be achieved. However, careful analysis of the micrograph reveals that they are weakly percolating or non-percolating at all for this particular thickness. Contrary to the as-deposited sample, the diffraction pattern now shows rings that can be indexed as fcc Ag and fcc Co. Evidence of the presence of hcp Co was found in films with a higher Co concentration[5]. X-ray photoemission spectroscopy experiments done on 15 nm thick annealed films revealed a small tendency of Ag to segregate towards the film surface.

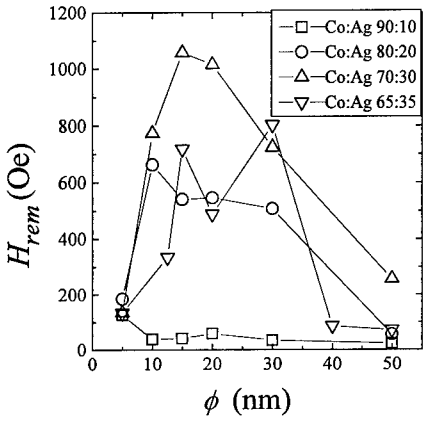

Fig. 2: Remanent coercivity as a function of film thickness for several Co concentrations.

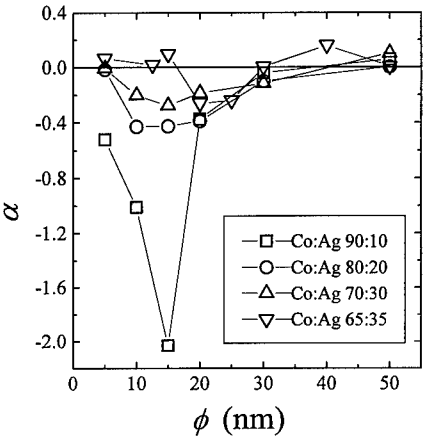

Fig. 3: Interparticle interaction parameter vs film thickness for various Co volume fractions.

Magnetic Properties

Almost all as-deposited films have coercivities below ~ 20 Oe, probably because of the very small grain size. High temperature annealing was necessary to promote grain growth and reach the critical single domain grain size where maximum coercivity is observed. As already discussed in Ref. [5], the largest value of coercivity for very thin films (that can be associated with the percolation threshold) depends on concentration and film thickness. As the film thickness is reduced, the maximum H_c is found for larger Co volume fractions. This same behavior is also observed for the remanent coercivity. In Fig. 2 we show H_{rem} vs film thickness for several different films. Values exceeding 1000 Oe are observed in the CoAg 70:30 vol % alloy. Note that, as the Co concentration increases, the thickness of maximum H_{rem}, above which the Co grains form a percolating network, shifts to lower values. The reduction in H_{rem} for very thin films is likely due to a decreasing particle volume leading to superparamagnetic effects.

The interparticle interaction parameter α is presented in Fig. 3. Almost all measured films have negative α and no zero crossing in the δM curves, indicating that the predominant interactions favor the demagnetizing state. Hence the β parameter, that accounts for first order field fluctuations from the mean field[12], is zero. As can be seen in the figure, α is both thickness and composition dependent. For CoAg 65:35 vol %, α is almost zero for all thicknesses, indicating small intergranular interactions. For films with higher Co concentrations, a minimum in α is observed around 15 nm. The absolute value of α increases strongly with the Co volume fraction. This is not unexpected since it was already observed in particle tape media[12] that the intergranular coupling is an increasing function of the packing fraction. The decrease in α for very thin films may be again attributed to superparamagnetic effects. For thicker films α tends to become positive. This means that the exchange coupling among particles becomes important and compensates (and even overcomes for 50 nm films) the demagnetizing interactions. The maxima of the irreversible susceptibility and the magnetic viscosity normalized to M_s are presented in Fig. 4 as a function of film thickness. It can be seen in Fig. 4(a) that χ_{irr} is larger for thicker films and, for a fixed ϕ, it is larger for alloys with higher Co concentrations.

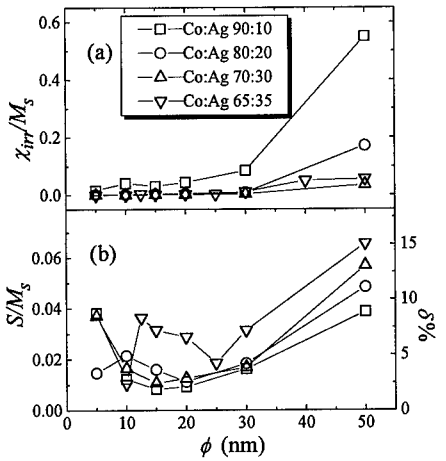

Fig. 4: Film thickness dependence of the normalized irreversible susceptibility (a) and magnetic viscosity (b) for several different alloys.

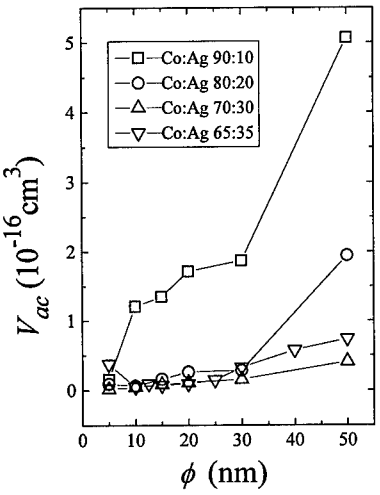

Fig. 5: Activation volume for films of different thickness and composition.

This is consistent with the fact that, in thick films and in high Co concentration alloys, the interactions favor predominantly the magnetized state. A similar behavior in the maximum value of χ_{irr} with increasing α was observed in CoNiCr thin film media with Cr underlayers of varying thicknesses[14] and was attributed to the majority exchange (dipolar) coupling interactions in films with thin (thick) Cr underlayers. The magnetic viscosity is shown in Fig. 4(b). All $M(t)$ vs $\ln(t)$ curves were found to be linear and the values presented correspond to the maximum S, normally obtained for a field close to H_{rem}. The viscosity seems to have a minimum around 15-20 nm. A possible explanation for this minimum may be due to the following: films used as magnetic media with very small grain volume were found to have high values of viscosity ($\delta >$ 10%/decade)[20], so that a decrease in S is expected as the film thickness increases, at least for very thin films. On the other hand an increase in S with film thickness for $\phi > 20$ nm was observed in Fe films sputtered on nanochannel alumina membranes[21]. This behavior is not unexpected since strong intergranular coupling can reduce the energy barrier for switching producing a more rapid decay of the magnetization. Note that samples with large coercivity (for example CoAg 70:30 vol %, $\phi = 15$ nm, has $H_c \sim 900$ Oe) have $\delta \sim 2.5$ %/decade. This value is very small compared to CoCrPtTa media[20] ($\delta \sim 10$ %/decade) and also smaller than values found in γ-Fe_2O_3 ($\delta \sim$ 3-4 %/decade)[20].

Finally the activation volume is shown in Fig. 5. It is observed that V_{ac} is larger for the thicker films. This is mainly due to the increasing particle volume of thicker films noting, however, that the activation volume is not always strictly related to the physical volume and may also increase if the intergranular interaction increases[21]. If we assume a plate-like shape for the grains and divide V_{ac} by ϕ an "activation diameter", D_{ac}, is obtained. For $\phi = 15$ nm $D_{ac} = 21$, 24, 33 and 95 nm for Co volume fractions of 65, 70, 80 and 90 respectively. The activation diameter for the first three concentrations is quite similar to the actual particle size determined with TEM measurements. For the CoAg 90:10 vol % film, which forms a fully percolating ferromagnetic network, the estimated activation diameter is much larger than the particle size. A similar behavior in very thin nickel films was attributed by Wohlfarth[22] to the very strong interactions existing among crystal grains.

CONCLUSIONS

The interparticle interactions, magnetization decay and activation volumes of phase separated CoAg thin films were investigated as a function of film thickness for Co-rich samples. It was found that films with a composition CoAg 70:30 vol % and ϕ = 15 nm exhibit properties that make them potentially interesting as thin film magnetic media; that is, high H_c, slow magnetization decay and small activation volumes. It is important to mention that these samples have not been optimized for applications and alloys with better properties can be expected if proper preparation conditions and materials (for example high crystalline anisotropy Co alloys) are used.

ACKNOWLEDGMENTS

We thank Dr. D. Yang and Dr. T. Klemmer for helping us with the XPS and TEM studies. This work is primarily supported by NSF-DMR-9713497 with supplemental support from NSF-PYI-9157402. It also made use of MRSEC Shared Facilities supported by NSF-DMR-9400399.

REFERENCES

[1]A. E. Berkowitz, J. R. Mitchell, M. J. Carey, A. P. Young, S. Zhang, F. E. Spada, F. T. Parker, A. Hutten, and G. Thomas, Phys. Rev. Lett. **68** (1992).

[2]J. Q. Xiao, J. S. Jiang, and C. L. Chien, Phys. Rev. Lett. **68**, 3749 (1992).

[3]J. A. Barnard, A. Waknis, M. Tan, E. Haftek, M. R. Parker, and M. L. Watson, J. Magn. Magn. Mater. **114**, L230 (1992).

[4]J. Q. Xiao, C. L. Chien, and A. Gavrin, J. Appl. Phys. **79**, 5309 (1996).

[5]A. Butera, T. J. Klemmer, and J. A. Barnard, J. Appl. Phys. (1998 in press).

[6]A. Butera, T. J. Klemmer, K. Minor, H. S. Cho, and J. A. Barnard, IEEE Trans. Magn. (1998 in press).

[7]J.-J. Delaunay, T. Hayashi, M. Tomita, S. Hirono, and S. Umemura, Appl. Phys. Lett. **71**, 3427 (1997).

[8]C. L. Chien, J. Appl. Phys. **69**, 5267 (1991).

[9]S. H. Liou, S. Malhotra, Z. S. Shan, D. J. Sellmyer, S. Nafis, J. A. Woollam, C. P. Reed, R. J. DeAngelis, and G. M. Chow, J. Appl. Phys. **70**, 5582 (1991).

[10]J. R. Childress and C. L. Chien, J. Appl. Phys. **70**, 5585 (1991).

[11]P. E. Kelly, K. O'Grady, P. I. Mayo, and R. W. Chantrell, IEEE Trans. Magn. **116**, 3881 (1989).

[12]X.-d. Che and H. N. Bertram, J. Magn. Magn. Mater. **116**, 121 (1992).

[13]J. W. Harrell, D. Richards, and M. R. Parker, J. Appl. Phys. **73**, 6722 (1993).

[14]K. O'Grady, R. W. Chantrell, and I. L. Sanders, IEEE Trans. Magn. **29**, 286 (1993).

[15]In materials where the magnetization reversal is governed by a narrow energy barrier distribution the time dependence may not be linear with ln(t). See for example P. Dova, K. O'Grady, M. P. Morales, and M. F. Doerner, J. Appl. Phys. **81**, 3949 (1997).

[16]R. Street and J. C. Wooley, Proc. Phys. Soc. London, Sec. A **62**, 562 (1949).

[17]E. P. Wohlfarth, J. Phys. F **14**, L155 (1984).

[18]H. Wan, A. Tsoukatos, G. C. Hadjipanayis, Z. G. Li, and J. Liu, Phys. Rev. B **49**, 1524 (1994).

[19]C. Yu, Y. Yang, Y. Zhou, S. Li, W. Lai, and Z. Wang, J. Appl. Phys. **76**, 6487 (1994).

[20]S. Stinnett, W. D. Doyle, P. J. Flanders, and C. Dawson, IEEE Trans. Magn. (1998 in press).

[21]A. Butera, J. L. Weston, and J. A. Barnard, J. Appl. Phys. **81**, 7432 (1997).

[22]E. P. Wohlfarth, J. Electr. Contr. **10**, 33 (1961).

BEHAVIOR OF MAGNETIC AFTEREFFECT ALONG A MAGNETIZATION REVERSAL CURVE IN A METAL PARTICLE RECORDING MATERIAL

L. J. SWARTZENDRUBER[a], L.H. BENNETT[a,b], E. DELLA TORRE[a,b], H.J. BROWN[a], J.H. JUDY[a,c]
[a]National Institute of Standards and Technology, Gaithersburg, MD 20899
[b]Institute for Magnetics Research, The George Washington University, Washington, D.C.
[c]Department of Electrical Engineering, University of Minnesota, Minneapolis, MN

ABSTRACT

Experimental measurements of the aftereffect along a magnetization reversal curve are compared with the predictions of a Preisach-Arrhenius model for a high density particulate recording medium. The Preisach parameters are determined from the measurement of the major hysteresis loop and the remanence loop. The Arrhenius parameters were determined from a single aftereffect curve. It was then found that the model gives good qualitative agreement with both the initial slope and, for the case in which the aftereffect is not monotonic, the peak value of the aftereffect.

INTRODUCTION

As recording densities and frequencies increase, loss of information due to aftereffect assumes greater importance and, in some cases, may be a limiting factor. This places increased importance on understanding and modeling of the magnetic aftereffect (also sometimes referred to as magnetic viscosity or time decay). To determine experimentally the aftereffect, accelerated testing is usually performed. This consists of first magnetically saturating the material in one direction, and then switching to a field of opposite sign near the coercive field. The field is then held constant and the rate of decay of the magnetization observed. We refer to this as a *single-field process*. Such a measurement is often used to compare the aftereffect in different materials. However, this comparison can be invalid because 1) the maximum aftereffect does not necessarily occur at the coercive field and 2) the long term aftereffect at zero field is not simply related to this measured value but depends on material properties. Further, because recording materials often undergo a variety of magnetic histories, knowledge of the aftereffect behavior in more complex situations would be useful. We discuss here a model which can provide estimates of the aftereffect for any magnetic history based on the results of a single aftereffect measurement.

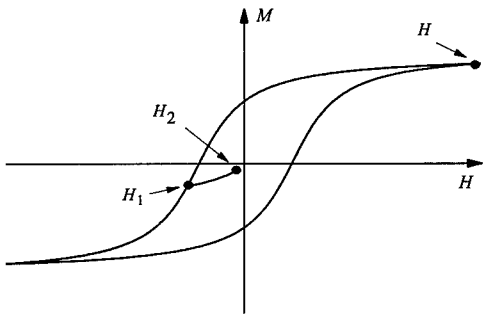

Fig. 1. Illustration of single-field (H to H_1) and double-field processes (H to H_1 to H_2). For a single-field process the aftereffect is measured with the field held constant at H_1, for a double-field while the field is held constant at H_2.

A single-field process is illustrated in Fig 1. The material is first saturated at field H. Then the field is directly

Mat. Res. Soc. Symp. Proc. Vol. 517 © 1998 Materials Research Society

moved to field H_1 where the field is held constant and the magnetization is recorded as a function of time. A process with a more complicated magnetic history is generated if the material is first saturated at field H, changed to field H_1, then immediately changed to field H_2, with $|H_2| < |H_1|$. We will refer to this sequence as a *double-field process*, which is also illustrated in Fig. 1. This can obviously be extended to multi-field processes. It has been previously shown [1] how a Preisach-Arrhenius approach can be used to model single-field processes. We will show here how such an approach also describes the aftereffect in a double-field process.

For a single-field process as illustrated in Fig. 1, the magnetization drifts monotonically to lower values. It is generally found that the aftereffect is linear in log-time for many orders of magnitude. For the double-field process, the magnetization would initially drift to higher values, then eventually turn around and drift to lower values. Deviation from log-linear behavior can be observed, often with a change in direction of the magnetization drift, on a time scale observable in the laboratory. In both cases, the magnetization will, given enough time, eventually reach equilibrium at a point on the anhysteretic curve associated with the holding field. Such non-monotonic behavior has been observed, for example, in Nd-Fe-B hard magnets exhibiting the spring effect by LoBue et al. [2] who used a thermodynamic generalization of the Preisach model [3]. This model utilized a time-dependent field moving in the Preisach plane similar to that used by Mitcheler et al. [4]

The current model uses a time-dependent Preisach state function $Q(u,v,t)$ which obeys the following differential equation

$$\frac{dQ(u,v,t)}{dt} + \left(\frac{\tau_+ + \tau_-}{\tau_+ \tau_-} \right) Q(u,v,t) = \frac{\tau_+ - \tau_-}{\tau_+ \tau_-}, \tag{1}$$

where

$$\tau_+ = \tau_0 \exp[(u-h)/h_f] \quad \text{and} \quad \tau_- = \tau_0 \exp[(h-v)/h_f]. \tag{2}$$

Here $1/\tau_0$ is an attempt frequency on the order of 10^{10} Hz and h_f is a fluctuation field which is equal to $kT/\mu_0 MV$. Here V is an activation volume which could be obtained from micromagnetic calculations [5,6]. The initial value of Q, when an operative field, h_1, is applied after saturation is

$$Q(u,v,0) = \begin{cases} 1 & \text{if } h_1 < u \\ -1 & \text{if } h_1 > u. \end{cases} \tag{3}$$

If the system is allowed to relax to the ground state in the presence of a field, h_2, where $|h_2|$ is less than $|h_1|$ then it is seen that

$$Q(u,v,\infty) = (\tau_+ - \tau_-)/(\tau_+ + \tau_-) = \tanh[(h_i - h_2)/h_f)], \tag{4}$$

and the magnetization as a function of time can be computed by

$$m(t) = \iint_{u>v} p(u,v)\, Q(u,v,t)\, du\, dv. \tag{5}$$

A computer program has been implemented to calculate the magnetization as a function of time using the above prescription for double-field processes. In this program the moving Preisach model is used with a Gaussian for the Preisach function $p(u,v)$. Details of this model are given in a paper in this volume [7]. To apply this model, the Preisach parameters which describe the static hysteresis loop are first obtained from the static hysteresis loop and the remanent loop using a

method such as described in [8]. These parameters are: α, the moving parameter, $\overline{h}_k$, the average critical field of the hysterons, σ_i, the standard deviation of the interaction fields, and σ_k, the standard deviation of the critical fields. For calculation of the time decays for both single-field and double-field processes two additional parameters are required. These are τ_0, the inverse of the attempt frequency for crossing an energy barrier, and h_f, the magnitude of the fluctuation field arising from magnetic domain interactions. Of these two additional parameters results are most sensitive to the value of h_f, and not very sensitive to the value of τ_0. Since we are dealing here only with room temperature measurements, we select h_f to give agreement with one experimentally determined single-field aftereffect. These values are then used to compute the aftereffect for other single-field and double-field processes and the results compared with experiment.

RESULTS AND DISCUSSION

The data were obtained on a sample of commercially obtained metal particle tape. Details concerning this tape and its accommodation and single-field aftereffect properties have been previously published [9]. This material is anisotropic with easy and hard directions. Fig. 2 shows the remanent values of the magnetization and the coercive field as a function of angle. Data presented here were taken for the applied field along the easy direction, i.e. the direction in which M_{rx} (the remanence along the field direction) has a maximum, M_{ry} (the remanence at right angles to the field) is zero, and the coercive field has a maximum. All data were taken at room temperature.

The hysteresis loop and the remanence loop as a function of applied field for the magnetic particle tape are shown in Fig. 3. To obtain the remanence loop, the sample was first saturated in the negative direction, then subject to a positive field, H, which was then reduced to zero. The resulting magnetization as a function of H is the remanence loop. The remanent coercive field, H_{RC}, is the field at which the remanence is zero. The Preisach parameters for use here were obtained from the data in Fig. 3. All parameters are normalized to a saturation magnetization of unity. In particular, as described in [8], the moving parameter α can be obtained using the remanence loop. The moving parameter α is used to determine operative fields, h, where $h=H+\alpha M$. For this material we find αM_s=76 mT, H_C = 144 mT, h_{RC} = 149 mT, $\overline{h}_k$ = 162 mT, σ_i = 81 mT, and σ_k = 73 mT.

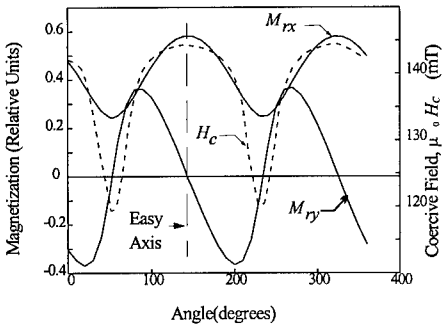

Fig. 2. Remanence M_{rx} (along the field direction) and M_{ry}, and coercive field H_c (right axis) as a function of orientation. Easy axis was used in all subsequent measurements.

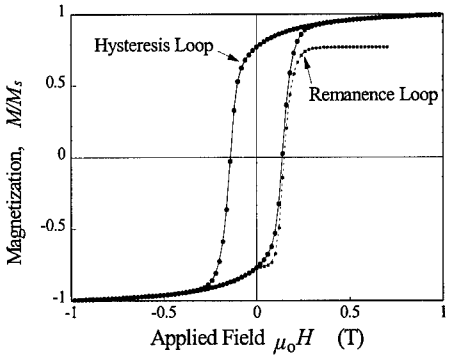

Fig. 3. Hysteresis and remanence loops (easy axis) used to determine the Preisach parameters.

The aftereffect was measured in a SQUID magnetometer. Results for a single-field process with H_1 = -160 mT are shown in Fig. 4. It can be seen that the magnetization decay is linear in log time over the length of the experiment. A dimensionless slope, S, is defined as

$$S=\frac{d(M/M_s)}{d\ \ln t}. \tag{6}$$

The value of S can also be expressed in percent as shown in Fig. 4 starts for $\ln(t-t_0) \approx 4$ due to the fact that the field cannot be switched at high speed. The value of t_0 was selected to make the plot linear for $\ln(t-t_0)$ less than about 5.5. The linearity and the slope for times greater than this were not sensitive to the value of t_0. This value of t_0 was used for all subsequent analysis. The data of Fig. 4 were used to determine an appropriate value for the fluctuation field. Over the range of time investigated here, the value of S is determined mainly by the value of the fluctuation field and changes little for large changes of the attempt frequency. To obtain an estimate for the attempt frequency, the decay at very short times after the field change would need to be observed. With an assumed value of 10^{10} for the attempt frequency, a fluctuation field of h_f = 85 mT gave the correct value for S. Using this value for the fluctuation field, the initial value of S along a reversal curve was calculated from the theory. The initial slope for this calculation was taken as the average slope between $\ln(t)$ = 4 and $\ln(t)$ = 6 for t in seconds. The slopes were also experimentally measured and the initial slopes determined by the same criterion.

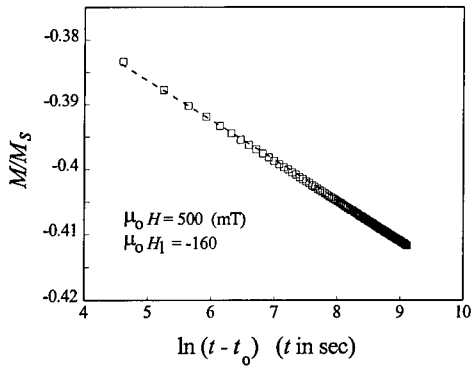

Fig. 4 Single-field process aftereffect for H switched from positive saturation to a negative holding field slightly larger than the remanent coercive field. The dashed line is used to chose h_f. t_o is the time at which the field was switched to the holding field.

The calculations are compared with measurements in Fig. 5. The dashed line represents the calculated values and the squares connected by lines are the experimental values. The theoretical prediction of a rapid change in S for small values of H_2-H_1, is corroborated by experiment. The theory also agrees closely with the experimental H_2 value at which the initial S crosses from a negative to a positive value. The few remaining quantitative differences between theory and experiment are undoubtedly due to the inability to switch from H_1 to H_2 sufficiently quickly.

When the value of S for the double-field process is near zero but positive, a slope reversal can be observed within the time scale of the experiment (approximately 5 days.) Some aftereffect curves obtained for such double-field processes are shown in Figs. 6-9. For H_2 less than -100 mT the observed initial slope was always negative. This is due to the fact that the initial positive slope occurs at times smaller than our available switching speed. For H_2 greater than about -80 mT, the time required for turn around was too long to be observed within the time scale used here. The aftereffect curve for H_2=0 is shown in Fig. 9. Although the observed drift will eventually change sign and the magnetization return to zero (the equilibrium value at H=0) this will take a very long time (many years.)

The data of Figs. 6-8 show that a reversal in the aftereffect can be observed for a double-field process with H_2 approximately -100 mT. The position of the peak in these curves could not be predicted with any precision using the theory as it now stands. One reason for this can be seen from the calculations displayed in Fig. 10. Here we see a reversal for a double-field process calculated for two different values of k, where k is the ratio of the interaction field standard deviation to the critical field standard deviation as used in the Gaussian Preisach function. A very small change in k (about 5%) shifts the position of the peak over nearly the entire

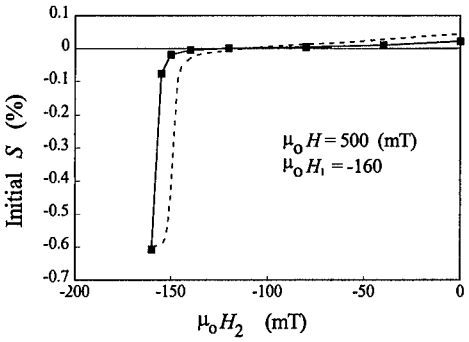

Fig. 5. Comparison of measured and calculated (dashed) initial slopes for a double-field process along a reversal curve. Good agreement is seen.

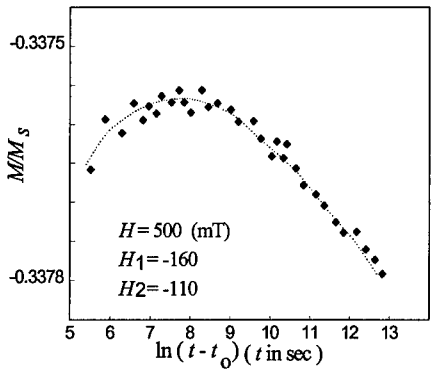

Fig. 6. Aftereffect for a double-field process. Dotted curve is drawn to show position of the peak.

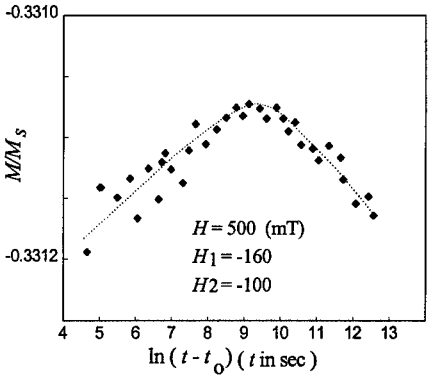

Fig. 7. Aftereffect for a double-field process. Dotted curve is drawn to show position of the peak.

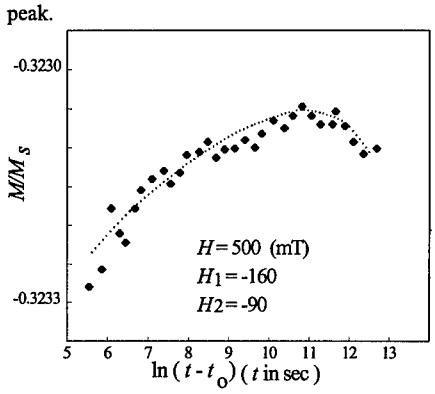

Fig. 8. Aftereffect for a double-field process. Dotted curve is drawn to show position of the peak.

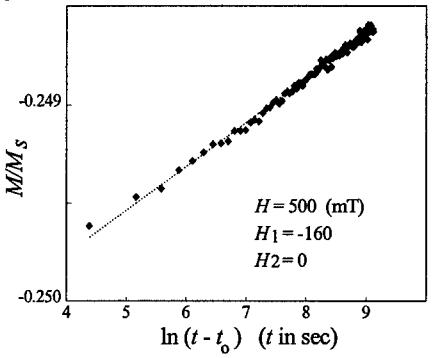

Fig. 9. Aftereffect for a double-field process. Dotted curve is a linear least squares fit to the data.

time that experimental data were taken. (The value of k determined from the data of Fig. 3 was 1.17.) Improvement in both theory and experiment are necessary. Better theoretical treatment, for example, of the reversible components of the magnetization is needed. Inclusion of minor loops would aid in better experimental measurement of the Preisach parameters. Faster experimental switching of the magnetic field is also needed.

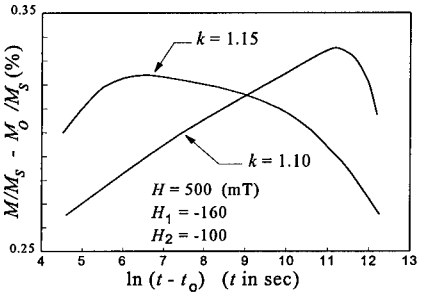

Fig. 10 Aftereffect magnetization curves for a double-field process calculated for two slightly different values of k (the ratio of the interaction and critical field standard deviations.)

CONCLUSIONS

A Preisach-Arrhenius model appears to describe many properties of the aftereffect. In particular, we have shown that such a theory can predict major features of the magnetic aftereffect behavior along a magnetization reversal curve. The model used here is a preliminary one and is based on a Preisach function with hysterons consisting of square loops. The first improvement in the model will be the incorporation of more realistic hysterons such as those used in the complete moving model [8]. Also, a distribution of fluctuation fields would be more realistic since the particles can be expected to have a distribution of volumes. The Preisach and Arrhenius functions describe a multi-parameter space for the description of all properties of the hysteresis loops, including major loop, minor loops, accommodation, and aftereffect. For any material, there is a volume in this parameter space in which all the qualitative features may be described. It is not currently known what precision is needed throughout this parameter space in order to improve the description quantitatively. The excellent qualitative agreement and the good quantitative agreement seen here justify trying to improve the parameter identification and the model.

REFERENCES

1. E. Della Torre and L.H. Bennett, "A Preisach Model for Aftereffect," *IEEE Trans. Mag.*, Sep. 1998 (in press).
2. M. LoBue, V. Basso, G. Bertotti, and K.-H. Müller, *IEEE Trans. Mag.*, **33**, 3862 (1997).
3. G. Bertotti, Phys. Rev. Lett. **76**, 1739 (1996).
4. P.D. Mitcheler, E. Dan Dahlberg, E.E. Wesseling, and R. M. Roshko, *IEEE Trans. Mag.* **32.**, 3185 (1996).
5. Y. D. Yan and E. Della Torre, *J. Appl. Phys.* **66**, 320 (1989).
6. A. Lyberatos and R.W. Chantrell, *J. Condens. Matter* **9**, 2623 (1997).
7. E. Della Torre, L.H. Bennett, and L. J. Swartzendruber, "Modeling Complex Aftereffect Behavior in Recording Materials using a Preisach-Arrhenius Approach," this conference.
8. E. Della Torre and F. Vajda, *IEEE Trans. on Mag.* **30**, 4987 (1994).
9. L.H. Bennett, L. J. Swartzendruber, F. Vajda, E. Della Torre, and J.H. Judy, *IEEE Trans. Mag.* **33**, 4173 (1997).

COMPENSATION TEMPERATURE OF A MIXED ISING FERRIMAGNETIC MODEL IN THE PRESENCE OF EXTERNAL MAGNETIC FIELDS

G. M. BUENDIA*, E. MACHADO*, M. A. NOVOTNY**

*Departamento de Física. Universidad Simón Bolívar, Apartado 89000, Caracas 1080, Venezuela.

**Supercomputer Computations Research Institute, Florida State University, Tallahassee, FL 32306-4130, USA.

ABSTRACT

The behavior of the compensation temperature of a mixed Ising ferrimagnetic system on a square lattice in which the two interpenetrating square sublattices have spins σ $(\pm 1/2)$ and spins S $(\pm 1, 0)$ has been studied with Monte Carlo methods. Our model includes nearest and next-nearest neighbor interactions, a crystal field and an external magnetic field. This model is relevant for understanding bimetallic molecular ferrimagnetic materials. We found that there is a narrow range of parameters of the Hamiltonian for which the model has compensation temperatures and that the compensation point exists only for small values of the external field.

INTRODUCTION

Ferrimagnetic ordering plays a crucial role in stable crystaline room-temperature magnets, that are currently being synthesized by several experimental groups in search for materials with technological applications [1]. In a ferrimagnet the different temperature dependence of the sublattices magnetizations raises the possibility of the appearance of compensation temperatures: temperatures below the critical point, where the total magnetization is zero [2]. The temperature dependence of the coercivity at the compensation point has important applications in the field of thermomagnetic recording [3].

Mixed Ising systems are good models to study ferrimagnetic ordering [4]. Recent results show that these models can have compensation points when their Hamiltonian includes second neighbor interactions [5]. These studies have been performed in zero magnetic field. In this work we study the effect of a constant external magnetic field on the behavior of the compensation temperature, $T_{\rm comp}$.

THE MIXED ISING MODEL

Our model consists of two interpenetrating square sublattices. One sublattice has spins σ that can take two values $\pm 1/2$, the other sublattice has spins S that can take three values, $\pm 1, 0$. Each S spin has only σ spins as nearest neighbors and vice versa.

The Hamiltonian of the model is given by,

$$H = -J_1 \sum_{\langle nn \rangle} \sigma_i S_j - J_2 \sum_{\langle nnn \rangle} \sigma_i \sigma_k - J_3 \sum_{\langle nnn \rangle} S_j S_l + D \sum_j S_j^2 - h \left(\sum_i \sigma_i + \sum_j S_j \right) \quad (1)$$

where the J's are exchange interaction parameters, D is the crystal field, and h is the external field, all in energy units. We choose $J_1 = -1$ such that the coupling between nearest neighbors is antiferromagnetic.

Mat. Res. Soc. Symp. Proc. Vol. 517 © 1998 Materials Research Society

Previous results with Monte Carlo and Transfer Matrix techniques have shown that the J_1-D model (J_2, J_3 and h are all zero) does not have a compensation temperature [6]. These previous studies showed that a compensation temperature is induced by the presence of the next-nearest neighbor (nnn) ferromagnetic interaction, J_2, between the $\pm 1/2$ spins. The minimum strength of the $J_2 > 0$ interaction for a compensation point to appear depends on the other parameters of the Hamiltonian [5]. In this work we study the effect of the external field and the J_3 parameter on the compensation temperature.

MONTE CARLO CALCULATIONS

We use standard importance sampling techniques [7] to simulate the model described by Eq. (1) on $L\times L$ square lattices with periodic boundary conditions and L=40. Data were generated with 5×10^4 Monte Carlo steps per site after discarding the first 5×10^3 steps. The error bars were taken from the standard deviation of blocks of 500 sites. We define $\beta=1/k_{\rm B}T$ and take Boltzmann's constant $k_{\rm B}$=1. Our program calculates the internal energy per site, specific heat, the sublattice magnetizations per site, M_1 and M_2 defined as,

$$M_1 = \frac{2}{L^2}\langle \sum_j S_j \rangle \quad , \quad M_2 = \frac{2}{L^2}\langle \sum_i \sigma_i \rangle \tag{2}$$

and the total magnetization per spin, $M=\frac{1}{2}(M_1 + M_2)$. The averages are taken over all the configurations, the sums over j are over all the sites with S spins and the sums over i are over all the sites with σ spins. Each sum has $L^2/2$ terms.

The compensation point, $T_{\rm comp}$, is defined as the point where the two sublattice magnetizations cancel each other such that the total magnetization is zero, i.e.,

$$|M_1(T_{\rm comp})| = |M_2(T_{\rm comp})| \tag{3}$$

and

$$sign[M_1(T_{\rm comp})] = -sign[M_2(T_{\rm comp})] \tag{4}$$

with $T_{\rm comp}<T_{\rm c}$. Note that at the compensation temperature the sublattice magnetizations are not zero, whereas at the critical temperature, $T_{\rm c}$, the total magnetization is zero and both sublattice magnetizations are also zero.

RESULTS

Previous studies on the J_1-J_2-D model showed that, for a fixed value of the parameters J_1 and D, there is a minimum value of J_2 for which the model has a compensation point. However, once this minimum value is reached, the compensation temperature remains almost independent of J_2 [5]. In this study we show that for a fixed value of J_1, D, and J_2, the compensation temperature can be changed by including the J_3 interaction (between the S spins, nnn in the lattice). The effect of the ferromagnetic J_3 parameter is to increase the value of the compensation temperature, such that as J_3 increases the compensation temperature approaches the critical temperature and eventually disappears. In Fig. 1 we show the absolute values of the sublattice magnetizations for a J_1-J_2-D model (J_3=0, h=0) and for a $J_1-J_2-J_3-D$ model (h=0). Notice that the main effect of the J_3 parameter is to keep the S sublattice ordered at higher temperatures, such that the crossing point between both sublattices [the one that satisfies Eq. (3) and Eq. (4)] occurs at higher temperatures. As J_3 becomes larger, the compensation temperature increases toward the critical point. When

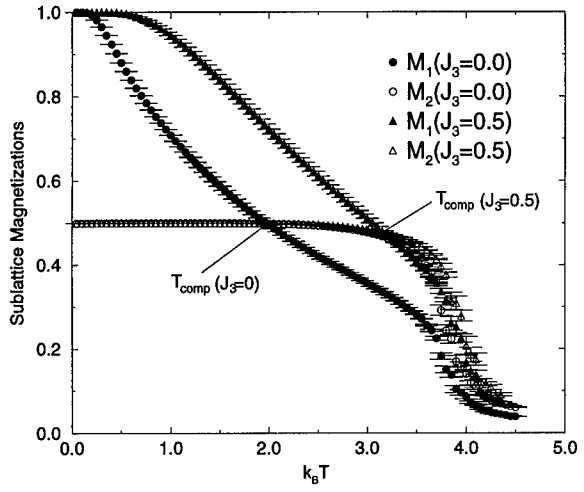

Figure 1: Dependence of the absolute values of the sublattice magnetizations with the temperature for J_3=0 (circles) and J_3=0.5 (triangles). Here J_2=6, D=1 and h=0.

both temperatures become equal we can not talk about a compensation point anymore and we only have a critical temperature.

When an external field h is added, the compensation temperature increases with the field until it disappears, i.e. becomes equal to the critical temperature, for a strong enough value of h, as shown in Fig. 2, where we plot the total magnetization vs. the temperature for several values of h. The effect of the external field on the compensation temperature is similar to that due to J_3. Notice that when h is present the system has a discontinuity in the magnetization that may signal a first order phase transition. This discontinuity seems to be due almost entirely to a discontinuity in the magnetization of the S sublattice as shown in Fig. 3.

In Fig. 4 we show the value of the compensation temperature vs. h for different values of J_3. It is interesting to note that for J_3 fixed the compensation temperature increases almost linearly with the field until it vanishes. Also the compensation temperature increases almost linearly with J_3 for a fixed value of h. As J_3 increases the compensation point only exists for a very weak or zero external field.

CONCLUSIONS

There is a strong dependence of the compensation temperature on the parameters in the Hamiltonian, and only a narrow range of parameters for which a compensation point can exist. The next-nearest neighbor interaction between the S spins and the external magnetic field tend to increase the compensation temperature until it coincides with the critical point, then we no longer have a compensation point. Since the compensation temperature

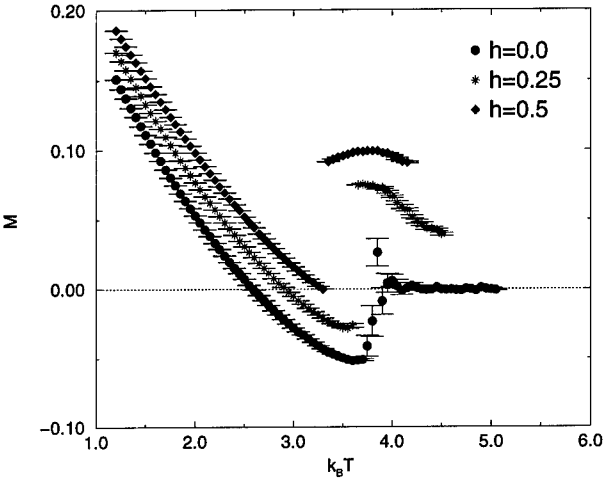

Figure 2: Total magnetizations vs. temperature for different values of h. Here J_3=0.25, J_2=6 and D=1.

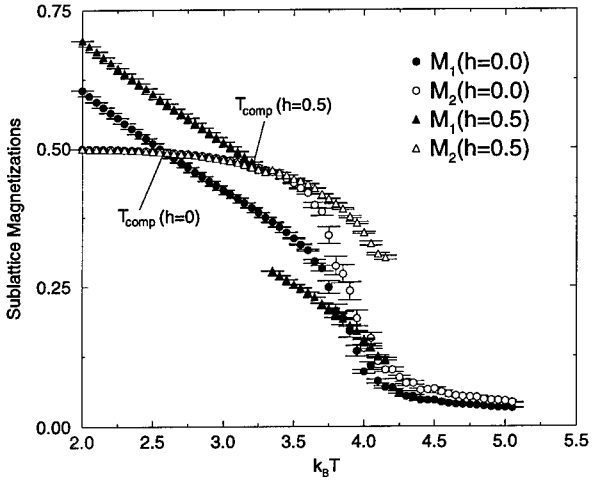

Figure 3: Dependence of the absolute values of the sublattice magnetizations with the temperature for h=0 (circles) and h=0.5 (triangles). Here J_3=0.25, J_2=6 and D=1.

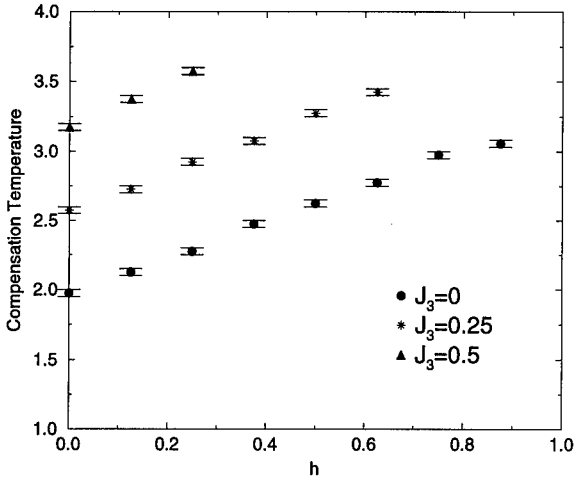

Figure 4: Dependence of the compensation temperature with the external field for different values of J_3. The last point in each curve was calculated at the highest value of h for which there is a compensation point for that particular value of J_3. Here J_2=6 and D=1.

is important in several technological applications, such as thermomagnetic recording, it is important to take into account that the external magnetic fields modify the value of the compensation temperature to higher values and that for strong fields there is no compensation temperature. Also, the presence of magnetic fields seems to induce a discontinuity in the magnetization of the S sublattice.

CONCLUSIONS

This research was supported in part by U.S. NSF Grant No. 9520325, and by the Florida State University Supercomputer Computations Research Institute (DOE Contract No. DE-FC05-85ER25000). Supercomputer access provided by the DOE at NERSC.

REFERENCES

1. T. Mallah, S. Tiebaut, M. Verdager and P. Veillet, Science **262**, 1554 (1993); H. Okawa, N. Matsumoto, H. Tamaki and M. Obba, Mol. Cryst. Liq. Cryst. **233**, 257 (1993); M. Turnbull, C. P. Landee, T. C. Soesbe and R. D. Willet, Mol. Cryst. Liq. Crys. **233**, 269 (1993).
2. L. Néel, Ann. Phys., Paris **3**, 137 (1948).
3. M. Mansuripur, J. Appl. Phys. **61**, 1580 (1987); F. Tanaka, S. Tanaka, N. Imanura, Jpn. J. Appl. Phys. **26**, 231 (1987).
4. A.F. Siqueira and I.P. Fittipaldi, J. Magn. Magn. Mater. **54**, 678 (1986); A. Bobak and M. Jascur, Phys. Rev. B **51**, 11533 (1995).

5. G.M. Buendía and M.A. Novotny, J. Phys.: Condens. Matter **9**, 5951 (1997).
6. G.M. Buendía, M.A. Novotny and J. Zhang, in Computer Simulations in Condensed Matter Physics VII, ed. D.P. Landau, K.K. Mon and H.-B. Schüttler (Springer, Berlin, 1994), p. 223; G.M. Buendía and J.A. Liendo, J. Phys.: Condens. Matter **9**, 5439 (1997).
7. K. Binder in Monte Carlo Methods in Statistical Physics, ed. K. Binder (Springer, Berlin, 1979).

Tribology, Lubrication, and Head/Disk Interface Materials

Part VIII

Nanotribology of Wear Layers for Recording Media

APPLICATION OF CATHODIC ARC DEPOSITED AMORPHOUS HARD CARBON FILMS TO THE HEAD/DISK TRIBOLOGY

SIMONE ANDERS[1], C. SINGH BHATIA[2], WALTON FONG[3], ROGER YU LO[3], AND DAVID B. BOGY[3]
[1]Lawrence Berkeley National Laboratory, 1 Cyclotron Road, Berkeley, CA 94720, SAnders@lbl.gov
[2]SSD/IBM, 5600 Cottle Road, San Jose, CA 95193
[3]Computer Mechanics Laboratory, Department of Mechanical Engineering, University of California at Berkeley, Berkeley, CA 94720

ABSTRACT

Amorphous hard carbon films deposited by filtered cathodic arc deposition exhibit very high hardness and elastic modulus, high mass density, low coefficient of friction, and the films are very smooth. All these properties are beneficial to applications of these films for the head/disk interface tribology. The properties of cathodic arc deposited amorphous carbon films are summarized, and they are compared to sputter deposited, hydrogenated (CH_x), and nitrogenated (CN_x) carbon films which are the present choice for hard disk and slider coatings. New developments in cathodic arc coaters are discussed which are of interest to the disk drive industry. Experiments on the nanotribology, mass density and hardness, corrosion behavior, and tribochemical behavior of cathodic arc films are reported. A number of applications of cathodic arc deposited films to hard disk and slider coatings are described. It is shown that their tribological performance is considerably better compared to CH_x and CN_x films.

INTRODUCTION

The continuously increasing storage density of magnetic storage devices is connected to a increasingly smaller spacing between the disk and the slider. The typical fly height for disk drives shipped today with a storage density of about 2 Gb/In^2 is about 40-50 nm, and for disk drives with a storage density of 10 Gb/In^2 which is the goal for the very near future the spacing will be about 20-30 nm. It starts to be more and more a question of semantics if this kind of recording is called near contact, pseudo-contact, or contact recording, but in any case the requirements on the tribology of the head/disk interface are harder and harder to achieve. A smaller magnetic spacing can be obtained by using a thinner protective coating on the disks. Materials such as the sputter deposited amorphous carbon overcoat CH_x which have been used successfully on disks for many years at a thickness of 12-15 nm reach their limit and fail at the smaller thickness required on future disks. A lot of research has been carried out during the last years to improve the existing material (CH_x) and to find new materials which perform adequately at the required smaller film thickness. Amorphous hard films formed by sputter deposition which contain carbon and nitrogen (CN_x), or contain carbon, nitrogen, and hydrogen (CN_xH_y) have been developed and are used for most disks and sliders today. But also these materials reach their limit at about 7-10 nm, and the search for better materials continues. One candidate is cathodic arc deposited amorphous hard carbon, which is among the amorphous, carbon based materials with the highest content of tetrahedral (sp^3) bonding which is characteristic for crystalline diamond. Other methods which yield similarly high sp^3 content are ion beam deposition [1] and laser ablation [2] for hydrogen-free films, and plasma beam deposition [3] for hydrogenated films. In the present paper we will review the deposition and film formation

Mat. Res. Soc. Symp. Proc. Vol. 517 © 1998 Materials Research Society

process of cathodic arc deposited amorphous hard carbon, describe the study of the mechanical, tribological, tribochemical, and corrosion-related properties of these films, and report on a number of applications to the head/disk interface tribology.

NEW DEVELOPMENTS IN CATHODIC ARC DEPOSITION

Cathodic arc deposition is based on the production of a plasma by a cathodic arc discharge on a graphite cathode in case of amorphous carbon deposition. The cathodic arc discharge is a high-current (typically 100-200A), low voltage (typically 20V) discharge which forms the plasma in a fast sequence of microexplosions on the cathode. The explosive character leads to a fully ionized plasma which is beneficial for the deposition since the ion energy which is the most important factor for obtaining high sp^3 content films can be easily influenced by substrate biasing. It also leads to the formation of micron-size particles (solid for graphite cathodes, liquid for metal cathodes) which can be detrimental for the film formation since the particles can be embedded in the film or cause other film defects such as pinholes. Cathodic arcs and cathodic arc deposition are described in great detail in [4].

Over the last decades research was concentrated on the optimization of the deposition conditions to form films with the highest sp^3 content and the lowest macroparticle content. It was found that the ion energy and substrate temperature are the main parameters that determine the sp^3 content with a maximum value of 85% obtained at ion energies around 100 eV [5-7] and substrates at room temperature or lower [8]. While the establishment of these parameters was relatively easy, the problem of macroparticle contamination has been severe. Attempts to filter the plasma using bent magnetic fields have been successful for applications such as the deposition of high quality titanium nitride thin films, but carbon has been a problem because the particles are solid and multiply reflected from filter walls. Straight filters [9] and filters with bending angles of 20 degrees [10], 45 degrees [11], and 90 degrees [12] were tested, and only a system consisting of two connected 90 degrees filters in the shape of an "S" could produce films which are acceptable for the application to the disk drive industry [13]. This S-filter has only a low efficiency and the larger part of the plasma produced in the source is lost, but due to the high plasma production rate of the cathodic arc discharge (the ion current is about 10% of the total arc current and therefore in the order of 10 A) and the low film thicknesses required for head/disk applications the deposition rate can be in the range of 1 nm/s and sufficient for industrial applications.

At the moment there are cathodic arc sources available on the market which are equipped with 45 degrees and 90 degrees filters, and it can be expected that sources with better filters will be available soon.

PROPERTIES OF CATHODIC ARC AMORPHOUS HARD CARBON IN COMPARISON TO OTHER AMORPHOUS CARBON FILMS

The properties of amorphous hard carbon films depend strongly on the deposition conditions. Generally, one can distinguish between hydrogen-free a-C films, CH_x, CN_x, and CH_xN_y films. Cathodic arc deposition [7,16], laser-arc deposition [17], ion beam deposition [1, 24], and pulsed laser deposition [2, 22,23] can produce a-C films which are comparable in their properties and have a high sp^3 fraction. The sp^3 fraction for high-quality films is typically between 75-85%, the hardness between 60-90 GPa, the elastic modulus around 500 GPa, the mass density about 2.7-3.3 g/cm^3, and the stress very high with 6-12 GPa. It is remarkable that it was possible to reduce the stress of pulsed-laser deposited films to very low values <0.2 GPa by annealing without

reducing the hardness of the films [2]. High compressive stress up to 10 GPa is often considered a problematic property of cathodic arc deposited films. Attempts have been made to decouple high stress and high hardness and were to some extent successful by using a carbon-carbon multilayer approach [14], or by introducing additional elements besides carbon [15]. Sputter deposited hydrogen-free a-C films have a much lower sp^3 fraction of typically 15%, a hardness of about 15 GPa, an elastic modulus of about 150 GPa, and a mass density of around 2.0 g/cm^3, but also low stress of about 0.5 GPa [18].

Among the methods to deposit CH_x films there is one which results in much more "diamond-like" films than other methods, this is plasma beam deposition [3]. These films show the highest sp^3 fraction for hydrogenated films of 75%, a hardness of 60 GPa, and a mass density of 2.9 g/cm^3. Hydrogen and nitrogen containing films deposited by other methods such as variations of the sputter technique and plasma enhanced CVD have a lower sp^3 fraction around 20-40%, a hardness of 15-35 GPa, an elastic modulus of 100-200 GPa, a mass density of 1.7-2.3 g/cm^3, and a stress of 1-3 GPa [16, 18, 19-21, 25, 26].

High sp^3 fraction is not necessarily the best optimization parameter for disk drive applications where tribochemical properties play an important role, and the whole system of slider surface, lubricant, and disk overcoat needs to be optimized under realistic wear conditions.

NANOTRIBOLOGICAL BEHAVIOR OF CATHODIC ARC AMORPHOUS CARBON FILMS

The nanowear behavior of cathodic arc deposited films has been tested in earlier experiments which showed a superior performance in comparison to other films [27, 28]. For disk coatings it is important that the films keep their excellent properties also at very low film thickness. Nanoindentation measurements showed a reduced hardness for thinner films [7], but it is very difficult to separate film properties and substrate influence for very thin, very hard films on relatively soft substrates. Therefore, nano-scratch tests were performed which probe more the properties of the film in the film plane and less perpendicular to the film as nanoindentation does. It was found before for measurements of the elastic modulus that results vary greatly for identical films if the elastic modulus is measured by a method which probes perpendicular to the film (nanoindentation, E=350-500 GPa) and a method that probes along the film (supersonic method, E=900-100 GPa) [29-32].

Scratch tests were performed on a series of cathodic arc carbon films of varying thicknesses to determine any dependence of their mechanical properties on the film thickness. Eight films were fabricated on Si substrates with the following deposition parameters: a pulsed arc current of 300 A for 5 ms with a frequency of 1 Hz, and a pulsed substrate bias of −100 V with a duty cycle of 2μs on/ 6μs off. The scratch tests were done on a Hysitron TriboScope®, which is able to scratch on the film surfaces with controlled forces. The films had thicknesses of 6.6, 10.4, 17.7, 18.2, 23.5, 44, 49, and 66 nm, respectively. The thickness values were measured with an n&k reflectance spectrometer. For films thicker than 17.7 nm, we confirmed the data with a Dektak profilometer measurement in a masked region of the sample. A diamond tip with a radius of about 100 nm was used to scratch a distance of 4 μm. Ramp scratch forces (instead of constant forces) were employed in this study to prevent initial shocks in the loading process. Before scratching each sample, a preliminary scan with 1 μN load across the test area was made to obtain a profile of the surface and to account for the possible tilt of the sample. After each test, the vertical displacement measurement is subtracted by the vertical displacement of the corresponding 1 μN scan to eliminate the errors due to sample tilting.

Figures 1-3 show the scratch depth vs. horizontal displacement (scratch curves) for the samples with film thickness 6.6, 23.5, and 66 nm, respectively.

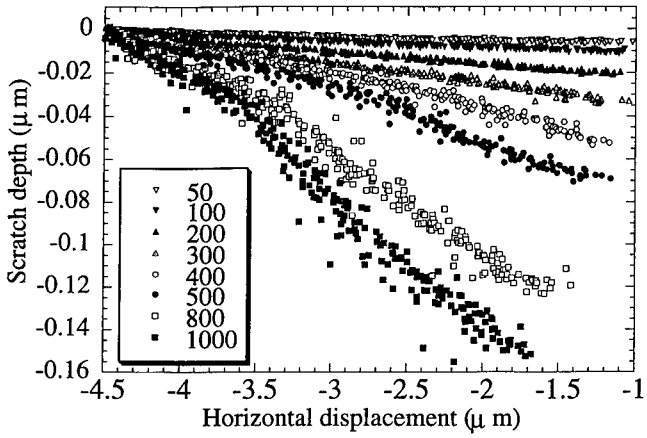

Figure 1: Scratch depth vs. horizontal displacement (scratch curves) for sample with a film thickness of 6.6 nm. The legend indicated the scratch force in μN.

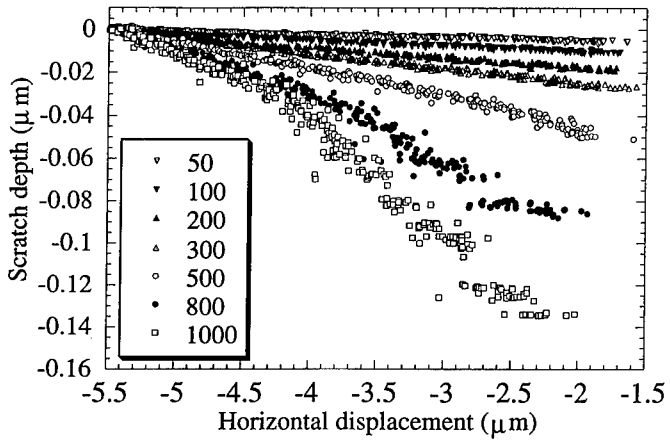

Figure 2: Scratch depth vs. horizontal displacement (scratch curves) for sample with a film thickness of 23.5 nm. The legend indicated the scratch force in μN.

When scratching with low loads, the scratch depth changes linearly with the horizontal displacement. This is due to the linear loading forces and the uniformity of film properties. With scratch forces of 400 μN or more, the sample with the 6.6 nm thick film shows two regimes on the scratch curves. The regime with the smaller slope reflects the scratch resistance of the film itself, and the regime with the larger slope is largely due to the silicon substrate. It can be seen that the cathodic arc films are more scratch resistant than the silicon substrate. Similar trends are observed for the samples with 23.5 and 66 nm thick films, also.

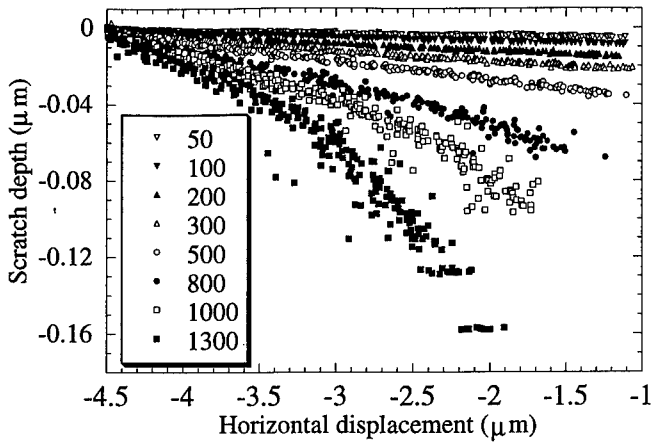

Figure 3: Scratch depth vs. horizontal displacement (scratch curves) for sample with a film thickness of 66 nm. The legend indicated the scratch force in μN.

The intersection of the two slopes could be related, but not limited, to the breakage of the film. For samples with film thicknesses of 6.6, 23.5, and 66 nm this point is at about 25 nm, 25 nm, and 55 nm, respectively. Thus, only the point for the sample with a film thickness of 23.5 nm agrees well with its thickness. For thinner films, the turning point is deeper than the film thickness. For thicker films, the turning point is shallower than the film thickness.

The scratch curves for each sample under a scratch force of 50 μN are plotted together in order to compare the scratch resistances of the eight films (figure 4). No significant difference can be noted from these curves. Figure 5 shows the scratch curves for each sample with a scratch force of 100 μN.

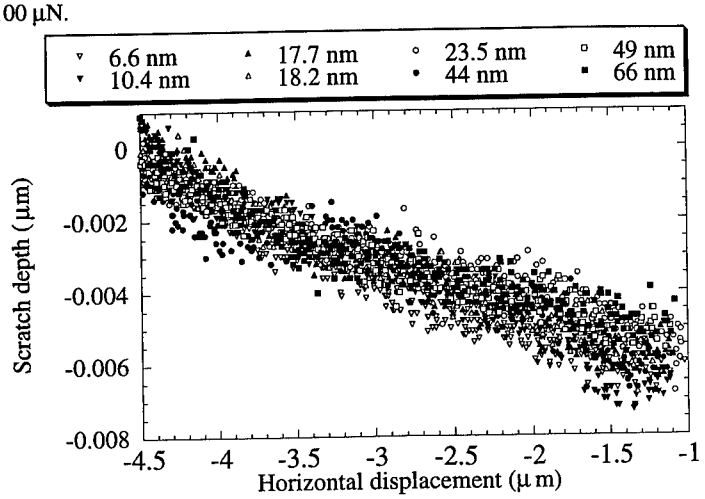

Figure 4: Scratch curves for all 8 samples under a scratch force of 50 μN.

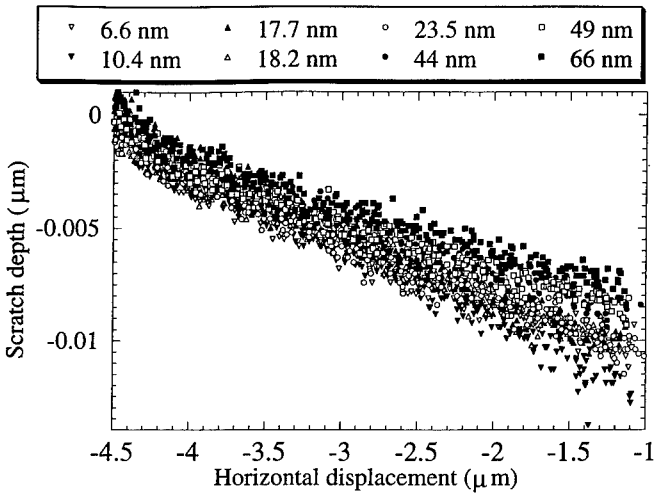

Figure 5: Scratch curves for all 8 samples under a scratch force of 100 μN.

The curves for the 6.6 nm and 10 nm thick films have slightly larger scratch depths at the end of the test due to the substrate effect on the thinner films. Excluding that, no appreciable difference was noted in these curves either. For larger scratch forces, thicker films show relatively small scratch depths, because the substrate is not influencing the measurements. We find that thin cathodic arc carbon films (6.6 nm) show the same scratch resistance as thick ones (66 nm). No thickness dependence of the mechanical properties of these films is observed as measured by the scratch tests.

MASS DENSITY AND HARDNESS OF CATHODIC ARC AMORPHOUS CARBON FILMS

We investigated two material properties, film hardness and density, of cathodic-arc deposited amorphous carbon films as a function of substrate-bias during deposition. It is described in the literature that the ion energy during deposition affects the ratio of sp^2/sp^3 bonding in carbon films, which in turn correlates to material properties such as hardness and elastic modulus [6, 7, 33]. Earlier work has been done to study the hardness and density of similar films, but the density measurements were taken often indirectly from Electron Energy Loss Spectroscopy (EELS) spectra [7].

Three films were deposited on low-resistivity Si wafers at substrate biases of -100, -500, and -1000V. An S-shaped filter for macroparticle reduction was applied, and the following deposition parameters were used: a pulsed arc current of 300A, 5 ms arc duration at a frequency of 1 Hz, and a pulsed substrate bias with a duty cycle of 2μs on/ 6μs off. The film thicknesses of the -100, -500, and -1000V bias samples were 71.5, 122.5, and 98.5 nm determined using a Dektak profilometer.

Film hardness was measured with a commercially-available Hysitron TriboScope® system. We defined hardness as the maximum indentation force divided by the contact area during indentation. All measurements were done with a tip of radius 60 nm and limited to indentations with residual depths less than 20% of the total film thickness.

Film density measurements were taken with a high-precision scale with 10^{-7} gram accuracy. The weights of each wafer were taken before and after each deposition. The film thickness was

determined using a Dektak profilometer. Density values were then calculated directly from the weight difference and film volume as determined by the thickness measurement.

Figure 6 is a plot of the film hardness and mass density versus substrate bias during deposition.

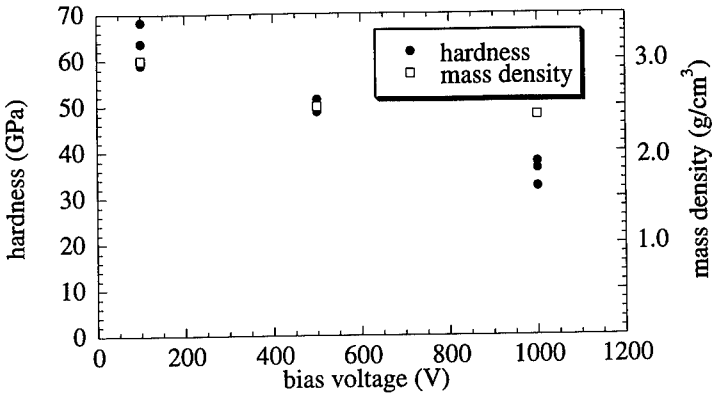

Figure 6: Film hardness and mass density versus pulsed substrate bias of cathodic arc deposited films.

From Fig. 6 it can be seen that the highest hardness (68 GPa) and density (3 g/cm^3) values belonged to the sample deposited at -100V bias, which corresponded to an ion energy of about 120 eV. With increased substrate bias, these values decreased due to increased graphitization of the film.

In summary, the most diamond-like (in hardness and density) cathodic-arc amorphous carbon films were produced at a pulsed substrate bias of -100V. The film hardness from these studies was consistent with earlier published work on similar films, and our direct measurements of film density confirmed the estimated mass density based on EELS measurements.

CORROSION STUDIES

The corrosion-resistance of cathodic-arc amorphous carbon films was studied in a series of samples with film thicknesses ranging from 2 nm to 40 nm. These films were deposited on low-resistivity Si wafers that were previously coated with a layer of 100 nm permalloy (80% Ni / 20% Fe). We applied an S-shaped filter for macroparticle removal and used the following deposition parameters: a pulsed arc current of 300A, 5 ms arc durations at a frequency of 1 Hz, and a pulsed substrate bias of –100V with a duty cycle of 2μs on/ 6μs off. Thickness measurements of the films were conducted with an n&k Analyzer 1100 reflectance spectrometer.

The corrosion comparison was based on a simple, yet effective decoration technique -- a NaCl dip test. Samples were immersed for 24 hours in a pre-mixed solution consisting of 0.5 mol NaCl, 0.5 mol $(NH_4)H_2PO_4$, 1 gram Liquinox, and 1000 grams of H_2O. Upon removal, the specimen were rinsed in deionized water and dried with a N_2 air gun. Inspection of the surface was done under an optical microscope, where an image analysis system counted the defect density (number of defects per unit area) and defect size (percent area occupied by defects).

Figure 7 is a plot of the pinhole count (number of defects per 0.8 x 1mm^2 area) per sample versus film thickness.

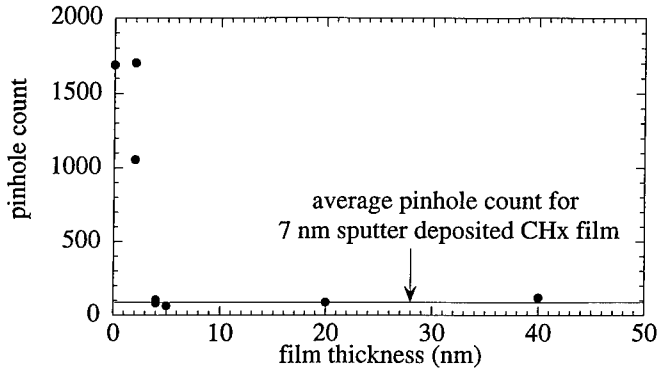

Figure 7: Pinhole count versus film thickness of cathodic arc deposited films in comparison to 7 nm thick sputter deposited film.

Higher pinhole counts infer poorer corrosion-resistance of the film. No significant difference in corrosion performance was noted for film thicknesses between 4 and 40 nm, which indicated a continuous film on the sample surface even at 4 nm. However, below 4 nm, the pinhole count rose an order of magnitude, which coincided with the values for an uncoated sample, indicating a breakdown of the film continuity/coverage. As a relative comparison, a 7 nm, RF-sputtered, hydrogenated amorphous carbon film (CH_x) was also subjected to the test. This film thickness was chosen because it corresponds to the current overcoat thickness used in today's advanced media products. Its pinhole count was 100.

Based on these results, we demonstrated that cathodic-arc amorphous carbon films provide acceptable levels of corrosion-resistance with film thicknesses as thin as 4 nm. The corrosion performance of a 4 nm cathodic-arc carbon film is comparable to that of a 7 nm sputtered CH_x film.

TRIBOCHEMICAL STUDIES

For the application of the cathodic-arc deposition technique in the area of disk drive technology tribochemical properties of the films are of great importance. In these studies, we examine the tribo-chemistry of cathodic arc deposited films during drag tests in an ultra-high vacuum (UHV) tribochamber.

The UHV tribochamber consists of a disk spindle, a slider actuator, a substrate heater, and a high-resolution quadrupole mass spectrometer (QMS) in a vacuum chamber with a base pressure $< 10^{-6}$ Pa. The QMS provides in-situ detection of gaseous products generated at the head/disk interface during drag tests. The QMS monitors 15 different atomic mass units (AMUs) simultaneously along with friction data. Further details about the system may be found

elsewhere [34]. Drag tests were conducted at a drag speed of 0.2 m/s, a load of 30 mN, and drag time of 600 seconds.

Supersmooth-textured 65 mm disks were coated with a 5 nm cathodic-arc amorphous carbon overcoat and lubricated with 0.85 nm of perfluoropolyther ZDOL lubricant. These samples were subjected to drag tests with uncoated Al_2O_3-TiC negative-pressure sliders in the UHV tribochamber. A commercial 65 mm disk with a 7 nm RF-sputtered CH_x film and 1.25 nm of ZDOL lubricant was subjected to similar tests as a comparison.

Figure 8 is a plot of the friction data versus drag time for both samples.

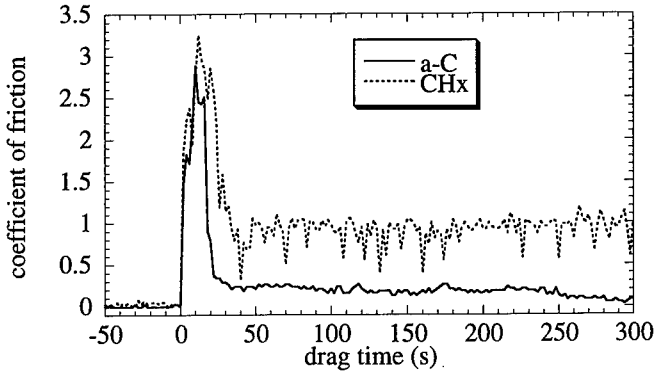

Figure 8. Friction coefficient versus drag time.

Comparable friction performance (μ = 3) was noted between the cathodic arc coated disks and CH_x coated disks before failure. Based on a visual inspection of the drag track and corresponding drops in the friction data, both overcoats had catastrophic failures after 40 seconds of dragging.

Figures 9 and 10 are plots of selected AMUs versus drag time for the cathodic arc deposited films and sputter deposited CH_x samples, respectively.

For the cathodic arc coated sample we noted a two-fold reduction in the generation of mass fragments associated with the catalytic decomposition of ZDOL (CF_3, C_2F_5) due to the Al_2O_3-TiC slider material [35]. No significant difference was observed in the mass fragments used to monitor the friction/thermal decomposition (CFO, CF_2O) between the two samples. These results indicated that the chemistry between the cathodic arc deposited films and the lubricant molecule may prevent the catalytic decomposition of ZDOL that occurs in the presence of Al_2O_3-TiC material. Further studies of the surface chemistry of cathodic arc films versus sputter deposited CH_x films are in progress to explain this phenomenon.

APPLICATION OF CATHODIC ARC AMORPHOUS CARBON FILMS TO SLIDER AND DISK SURFACES

The applications of cathodic arc deposited films to sliders and disks are still relatively scarce. A few studies have been performed and are published elsewhere in detail [33, 36,37]. Here, we summarize briefly the main results.

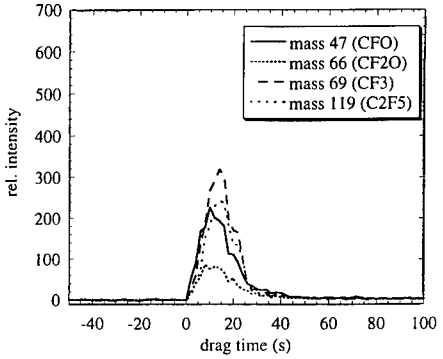

Figure 9: Mass spectrum for cathodic arc coated disk sample.

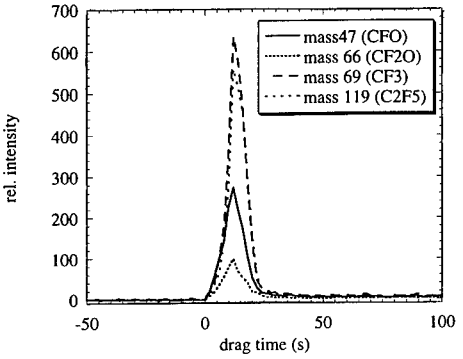

Figure 10: Mass spectrum for CHx sample.

Cathodic arc surface modification using pulsed bias can be performed in two ways - as a thin film deposition and as a low-energy ion implantation/deposition process. First tests showed that both methods can lead to drastic improvements of the slider performance.

In case of a thin film deposition typically a high bias of 1-2 kV is applied for the first 10% of the deposition process to ensure good film adhesion, and a bias of -100V is applied for the rest of the deposition for maximum film hardness. While uncoated sliders failed in a Contact Start Stop testing after 7500 cycles, the sliders coated with 2 nm cathodic arc carbon did not fail even after 100,000 cycles when the test was interrupted [36,37]. In case of a low energy (2-4 keV) ion implantation/deposition process sliders were modified with C, Ag, and Ti ions at a low dose of $2x10^{16}$ cm^{-2} [33]. This fast and easy surface treatment led to a reduction of the coefficient of friction by a factor of about 5-6 in a continuous sliding test in comparison to untreated sliders.

The coating of disks with 10 nm cathodic arc carbon led to the reduction of the worn volume on the face of the slider by almost a factor of 20 in a continuous sliding test in contact [36, 37]. Even though more systematic studies are necessary to fully explore the capabilities of cathodic arc amorphous carbon films for disk and slider coatings, first results are very promising.

CONCLUSIONS

Cathodic arc deposited amorphous hard carbon films have properties which are desirable for the application as disk and slider hard overcoats. The hardness and mass density are very high for films formed at optimum deposition conditions. Nano-scratch tests show that the films remain their high scratch resistance also at very low film thickness of 6.6 nm. Corrosion measurements demonstrate that continuous films with corrosion rates comparable to 7 nm sputter deposited films can be obtained at a film thickness of 4 nm. Cathodic arc deposited films reduce the catalytic erosion products formed during wear in comparison to sputter deposited films. A number of experiments applying cathodic arc deposited films to slider and disk surfaces show a

considerably improved performance. More systematic studies are required for the optimization of the films for disk drive applications.

The problem of macroparticle contamination of the films which has been a problem for the last two decades has been overcome by sophisticated filtering techniques. These filtering techniques have a reduced deposition rates as a consequence, but the rate is still reasonably high for hard disk and slider coating. New developments in cathodic arc deposition equipment manufacturing will make filtered arc sources available in the very near future which will facilitate a wide-range systematic testing of these films for the disk drive industry.

ACKNOWLEDGMENTS

The authors wish to acknowledge the National Storage Industry Consortium (NSIC) for its support of this work. Part of this work was supported by the Computer Mechanics Laboratory, University of California at Berkeley. Another portion of this work was supported by the U.S. Department of Energy, Division of Advanced Energy Projects, under contract No. DE-AC03-76SF00098.

REFERENCES

1. J. Koskinen, J. Appl. Phys. **63**, pp. 2094-2097 (1988).
2. T. A. Friedmann, J. P. Sullivan, J. A. Knapp, D. R. Tallant, D. M. Follstaedt, D. L. Medlin, and P. B. Mirkarimi, Appl. Phys. Lett. **71**, pp. 3820-3822 (1997).
3. M. Weiler, S. Sattel, T. Giessen, K. Jung, H. Ehrhardt, V. S. Veerasamy, and J. Robertson, Phys. Rev. B **53**, pp. 1594-1608 (1996).
4. R. L. Boxman, P. J. Martin, and D. M. Sanders, Editors, Handbook of Vacuum Arc Science and Technology, Noyes Publications, Park Ridge, 1995.
5. J. J. Cuomo, D. L. Pappas, J. Bruley, J. P. Doyle, and K. L. Saenger, K. L., J. Appl. Phys. **70**, pp. 1706-1711 (1991).
6. P. J. Fallon, V. S. Veerasamy, C. A. Davis, J. Robertson, G. A. J. Amaratunga, W. I. Milne, and J. Koskinen, Phys. Rev. B **48**, pp. 4777-4782 (1993).
7. G. M. Pharr, D. L. Callahan, S. D. McAdams, T. Y. Tsui, S. Anders, A. Anders, J. W. Ager III, I. G. Brown, C. S. Bhatia, S. R. P. Silva, and J. Robertson, J. Appl. Phys. Lett. **68**, pp. 779-781 (1996).
8. J. J. Cuomo, J. P. Doyle, J. Bruley, and J. C. Liu, J. C. J. Vac. Sci. Technol. A **9**, pp. 2210-2215 (1991).
9. B. F. Coll, P. Sathrum, R. Aharonov, and M. A. Tamor, Thin Solid Films **209**, pp. 165-173 (1992).
10. R. Lossy, D. L. Pappas, R. A. Roy, J. J. Cuomo, and V. M. Sura, Appl. Phys. Lett. **61**, pp. 171-171 (1992).
11. S. Falabella and D. M. Sanders, J. Vac. Sci. Technol. A **10**, pp. 394-397 (1992).
12. I. I. Aksenov, S. I. Vakula, V. G. Padalka, V. E. Strel'nitskii, and V. M. Khoroshikh, Sov. Phys. Tech. Phys. **25**, pp. 1164-1166 (1980).
13. S. Anders, A. Anders, M. R. Dickinson, R. A. MacGill, and I. G. Brown, IEEE Trans. Plasma Sci. **25**, pp. 670-674 (1997).
14. S. Anders, A. Anders, J. W. Ager III, Z. Wan, G. M. Pharr, T. Y. Tsui, I. G. Brown, and C. S. Bhatia, Mat Res. Soc. Proc. **383**, pp. 453-458 (1995).
15. O. R. Monteiro, M.-P. Delplancke-Ogletree, R. Y. Lo, R. Winand, and I. G. Brown, Surf. Coat. Technol. **94/95**, pp. 220-225 (1997).

16. B. K. Gupta and B. Bhushan, Thin Solid Films **270**, pp. 391-398 (1995).
17. H.-J. Scheibe and B. Schultrich, Thin Solid Films **246**, pp. 92-102 (1994).
18. N.-H. Cho, K. M. Krishnan, D. K. Veirs, M. D. Rubin, C. B. Hopper, B. Bhushan, and D. B. Bogy, J. Mater. Res. **5**, pp. 2543-2554 (1990).
19. E. C. Cutiongco, D. Li, Y.-W. Chung, and C. S. Bhatia, J. Tribology **118**, pp. 543-548 (1996).
20. B. Bhushan, A. J. Kellock, N.-H. Cho, and J. W. Ager III, J. Mater. Res. **7**, pp. 404-410 (1992).
21. Y. Wang, H. Chen, R. W. Hoffman, and J. C. Angus, J. Mater. Res. **5**, pp. 2378-23-86 (1990).
22. A. A. Puretzky, D. B. Geohegan, G. E. Jellison, and M. M. McGibbon, Appl. Surf. Sci. **96-98**, pp. 859-865 (1996).
23. D. L. Pappas, K. L. Saenger, J. J. Cuomo, and R. W. Dreyfus, J. Appl. Phys. **72**, pp. 3966-3970.
24. Y. Lifshitz, G. D. Lempert, E. Grossman, I. Avigal, C. Uzan-Saguy, R. Kalish, J. Kulik, D. Marton, and J. W. Rablais, Diamond Relat. Mater. **4**, pp. 318-323 (1995).
25. F. Rossi, B. Andre, A. van Veen, P. E. Mijnarends, H. Schut, F. Labohm, H. Dunlup, M.-P. Delplancke, and K. Hubbard, J. Mater. Res. **9**, pp. 2440-2449 (1994).
26. D. F. Francheschini, C. A. Achete, and F. L. Freire, Jr., Appl. Phys. Lett. **60**, pp. 3229-3231 (1992).
27. B. K. Gupta and B. Bhushan, B., Thin Solid Films **270**, pp. 391-398 (1995).
28. T. Y. Tsui, G. M. Pharr, W. C. Oliver, C. S. Bhatia, R. L. White, S. Anders, A. Anders, and I. G. Brown, Mat. Res. Soc. Symp. Proc. **383**, pp. 447-452 (1995).
29. D. Schneider, T. Schwarz, and B. Schultrich, Thin Solid Films **219**, pp. 92-102 (1992).
30. D. Schneider, H.-J. Scheibe, Th. Schwarz, and P. Hess, Diamond Relat. Mater. **2**, pp. 1396-1401 (1993).
31. B. Schultrich, H.-J. Scheibe, G. Grandremy, D. Schneider, D., and P. Siemroth, Thin Solid Films **253**, pp. 125-129 (1994).
32. S. Anders, A. Anders, C. S. Bhatia, S. Raoux, D. Schneider, J. W. Ager III, and I. G. Brown, Proc. Applications of Diamond Films and Related Materials: Third Int. Conf., NIST Special Publication **885**, pp. 809-812 (1995).
33. S. Anders, A. Anders, I. G. Brown, B. Wei, K. Komvopoulos, J. W. Ager III, and K. M. Yu, Surf. Coat. Technol. **68/69**, pp. 388-393 (1994).
34. X. H. Yun, D. B. Bogy, C. S. Bhatia, IEEE Transaction on Magnetics **32** (1996) pp. 3669 (1996).
35. P. H. Kasai, W. T. Tang, and P. Wheeler, Appl. Surf. Sci. **51**, pp. 201 (1991).
36. C. S. Bhatia, S. Anders, K. Bobb, R. Hsiao, D. B. Bogy, and I. G. Brown, J. Tribology, to be published.
37. S. Anders, C. S. Bhatia, D. B. Bogy, and I. G. Brown, Data Storage, pp. 31-38 (1997).

CHARACTERIZATION OF THIN DLC FILMS USING FILM STRESS AND RAMAN TECHNIQUES

J. E. Turlo*, Danny Gan*, Niranjan Gopinathan**
*KLA-Tencor Corporation, One Technology Dr., Milpitas, CA 95035
**Read-Rite Corporation, 44100 Osgood Rd., Fremont, CA 94539

ABSTRACT

Diamond like carbon (DLC) films are deposited on thin film heads in the magnetic recording industry to reduce friction and "stiction" and to provide a durable, abrasion resistant coating. The films are a mixture of graphitic phases with sp^2 bonding and diamond phases with sp^3 bonding. The present work provides the results of thin film stress measurements and Raman tests performed on 10 nm DLC films deposited on 75 mm silicon test wafers using standard optical lever techniques. Stress is measured after deposition and in-situ during thermal cycling. Isothermal relaxation data is also obtained. Raman is performed before and after annealing.

The deposited stress of 10 nm films was over 2000 MPa. The stress relaxed entirely to zero during thermal cycling to 500 °C. Isothermal relaxation at 300 °C also resulted in complete relaxation of an initial 1500 MPa stress to zero in less than 24 hours. The Raman data is consistent with prior results in the literature. The position of the G band shifts from 1513 to 1581 cm^{-1} during annealing, and the intensity ratio of the D band to the G band rises from 0.201 to 0.814 during annealing.

The decrease of the film stress to zero during thermal processing implies that the entire thickness of the film is undergoing a structural change while the stress relaxation data implies that the stress is relaxing by a fast diffusive process. The Raman data implies that the film is becoming more graphitic and the crystallites are growing in number and size during thermal processing. We suggest that the structure of the extremely thin carbon film is modified by a surface diffusion mechanism.

INTRODUCTION

Diamond-like-carbon (DLC) or amorphous carbon films are deposited on thin film heads in the magnetic recording industry as protective overcoats because of their high hardness, low friction, chemical inertness, and wear resistance. The durability of these amorphous carbon films is becoming more important as the overcoat thickness (currently 7 to 10 nm) is decreased to reduce the magnetic spacing and increase the read back signal amplitude. The thinner overcoats (< 7 nm) should have good protection against corrosion and also provide good tribological properties at the head-disk interface.

The carbon overcoats used are typically amorphous in nature and consist of a mixture of diamond (tetrahedral sp^3) and graphitic (trigonal sp^2) bonding structures. Due to the extremely large volumes of thin film heads produced, it is necessary to have fast and easy means of monitoring the quality and properties of the carbon overcoat. In this work, we have looked at residual film stress and Raman spectroscopy as monitoring tools for carbon overcoats.

Mat. Res. Soc. Symp. Proc. Vol. 517 ©1998 Materials Research Society

EXPERIMENT

This study focused on identifying the structural change in the DLC bonding phases during thermal annealing using analytical means like residual stress measurement and Raman spectroscopy. The purpose of the work was to understand the mechanism of structural evolution that led to significant changes in the film stress and Raman spectra of the DLC films resulting from thermal anneal.

Five substrates were deposited with a DLC film by an ion beam CVD process using methane gas. Deposition rates of approximately 1.5 nm / minute were measured in this process. The targeted total thickness of the overcoat was 10 nm consisting of 2 nm of a silicon interlayer and 8 nm of DLC. The film thickness was measured on silicon coupons that were coated along with the samples in an n&k optical analyzer. The DLC coated substrates in this experiment were 75 mm [100] silicon wafers.

The Raman spectroscopy was performed by backscattering from the sample using a Renishaw spectrometer with an argon ion laser (514 nm) operating at 20 mW to avoid sample degradation. The spectra were collected with a laser spot size of approximately 1 to 2 μ.

The DLC film stress was measured with a KLA-Tencor FLX-2320 film stress tool. The wafer curvature before and after DLC deposition was measured, and the change in curvature caused by the deposition was used to automatically calculate the film stress at room temperature. The FLX-2320 also allows sample heating to 500 °C while continuously monitoring the wafer curvature, so the film stress as a function of temperature during the thermal anneal can be obtained.

The room temperature film stress was measured on all 5 samples. Two samples were thermally cycled up to 500 °C at 5 degrees / minute then down to 80 °C at -5 degrees / minute. Five scfh of nitrogen is flushed through the small slot furnace of the FLX-2320 to reduce the influence of oxygen and moisture. One wafer was heated to 300 °C at 10 degrees / minute and held for 72 hours to monitor the relaxation of the film stress over time.

RESULTS

Film Stress Measurement

The room temperature stress measured on the 5 wafers of the study is shown in Table I where each value is the average of 2 measurements. The average stress of the entire data set is -2.24 GPa, and the standard deviation is 0.12 GPa. The minimum expected standard deviation of the stress measurement tool for a 10 nm film on a 375 μ substrate is about 0.05 GPa, so the numbers show reasonably typical scatter, and the deposition process was stable and uniform.

Table I. Room temperature stress measurements from 5 DLC films

Wafer	DLC Thickness (nm)	Stress (GPa)
RT101	9.7	-2.27
RT102	9.6	-2.39
RT103	9.9	-2.11
RT104	9.8	-2.12
RT105	9.8	-2.29

The stress behavior of wafer RT103, monitored during a thermal cycle to 500 °C, is shown in Figure 1. While heating below 100 °C, no change in stress is seen. At about 100 °C the high compressive stress begins to quickly relax towards zero, reaching zero stress near the end of the heating phase at 500 °C. The total heating time was 96 minutes.

The stress during the entire cooling phase remains zero implying that the thermal expansion coefficients of the film and the silicon substrate are equal. After thermal cycling, the film consists of a mix of sp^2 and sp^3 bonded carbon with thermal expansion coefficients of 6.0×10^{-6} / degree and 1.2×10^{-6} / degree respectively[1], so the thermal expansion coefficient of the mixed film will fall some where between those numbers. Since silicon has a thermal expansion coefficient of about 3×10^{-6} / degree, the flat cooling curve is sensible.

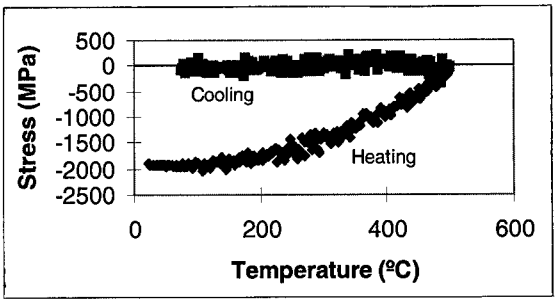

Figure 1. The first thermal cycle after deposition of a 9.9 nm DLC film

The stress relaxation behavior of wafer RT104 heated to 300 °C is shown in Figure 2. The 300 °C relaxation temperature is reached in 40 minutes during which the stress relaxes to roughly -1.5 GPa which is consistent with the thermal cycle of wafer RT103. The stress relaxes completely to zero in about 24 hours. No further changes take place over the remaining 2 days of the test.

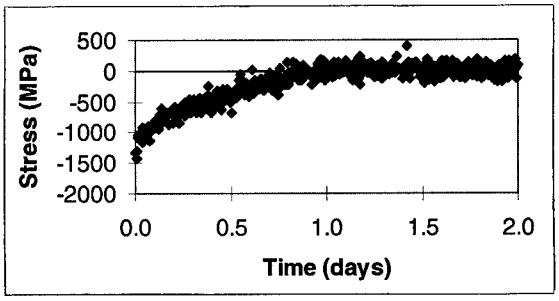

Figure 2. Stress relaxation at 300 ° C of a 9.8 nm DLC film

A log plot stress versus time is shown in Figure 3. Despite increasing noise of the data after 12 hours, the trend is linear implying an exponential relaxation of the stress over time. The film

stress is relaxing primarily by diffusion of carbon atoms to create a softer, more graphitic structure. Hydrogen may also be evolving, but evolution of a low concentration of the small hydrogen atoms from the amorphous carbon film would not be able to reduce the film stress entirely to zero.

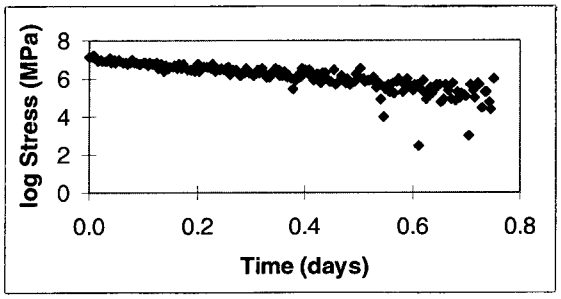

Figure 3. Log plot of the stress relaxation at 300 ° C for a 9.8 nm DLC film

Raman Spectroscopy

The Raman spectrum of the as-deposited DLC film is shown in Figure 4. The G peak occurs at 1513 cm^{-1}, the D peak occurs at 1311 cm^{-1}, and the I(D)/I(G) ratio is 0.201. The results are the averages of two separate films and are consistent with published literature on carbon films[2,3].

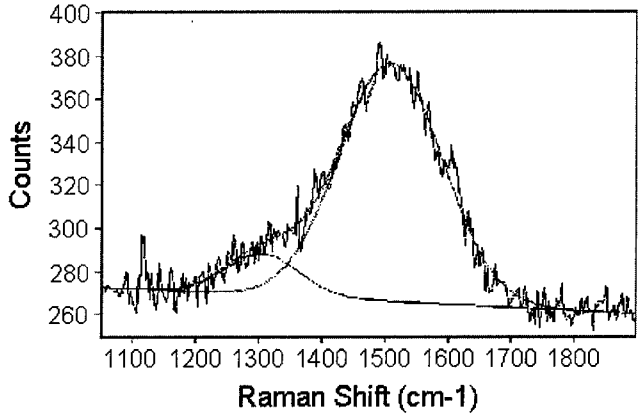

Figure 4. Raman spectrum of an as-deposited 9.8 nm DLC film.

The Raman spectrum of a 10 nm DLC film annealed to 500 °C is shown in Figure 5. The G peak has shifted to 1581 cm^{-1}, the D peak has shifted to 1413 cm^{-1}, and the I(D)/I(G) ratio has risen to 0.814. The G peak is also narrower than the G peak in the as-deposited film which

suggests that the graphite crystallites have grown. The results are again the averages of two separate films.

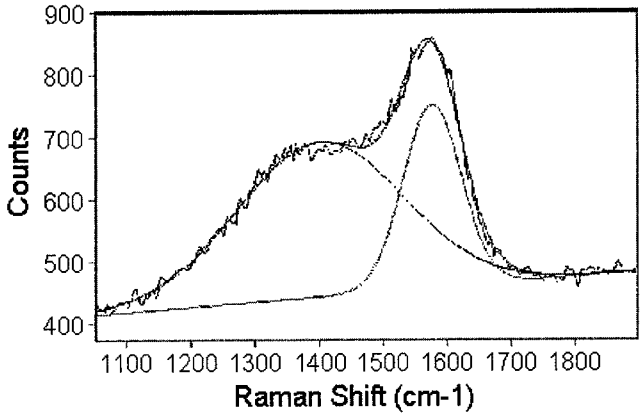

Figure 5. Raman spectrum of a 9.9 nm DLC film annealed to 500 °C.

CONCLUSIONS

Dillon[2] has described a computer model by Beeman that describes the shift in the G peak downward from the nominal value of 1581 cm^{-1} as the result of a bond angle disorder from the ideal value of 120°. Dillon reports that an average bond angle of 117.7° would shift the G peak down to 1528 cm^{-1}.

As an order of magnitude check of the stress required to cause such a change in the bond angle, consider a hexagonal cell with sides of length 2L shown in Figure 6a. Compress the cell in the vertical direction from a height of $2\sqrt{3}L$ to a height of $2\sqrt{3}L(1-\varepsilon)$ where ε is the strain, but assume that total bond lengths remain constant for this simple analysis as shown in Figure 6b. The angle, α, between the sides and the main axis is given by

$$\sin(\alpha) = \frac{\sqrt{3}(1-\varepsilon)}{2}.$$

Taking the measured average film stress of 2.24 GPa and a Young's modulus of about 150 GPa for a graphite-diamond film, the strain is 0.015, and the included angle in the strained hexagon, 2α, becomes 117.1°. Although the model presumes an sp^2 structure rather than the mixed sp^2, sp^3 DLC film structure, the compressive stress measured in the as-deposited film correlates well with the bond angle disorder used to explain the Raman shift in the G peak.

The Raman spectra of the annealed film show that the structural changes that occur during a thermal cycle to 500 °C leads to a strain-free graphite crystal structure with 120° bond angles corroborated by stress relaxation to zero. The stress is relaxing as the graphite crystallites grow in size, so the post anneal Raman spectrum shows the large D peak and a G peak location

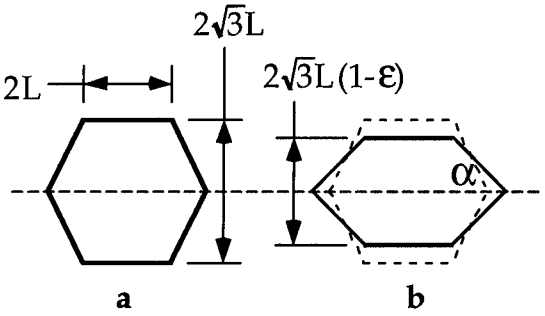

Figure 6. A simple strain model for bond angle disorder in DLC

representative of an ordered bond angle of 120°. The annealed G peak is narrower, and the annealed I(D)/I(G) ratio of 0.814 is consistent with Dillon's plot of I(D)/I(G) ratio versus anneal temperature.

The exponential stress relaxation curve in Figure 2 which relaxes entirely to zero implies a thermally activated, stress driven diffusion process. By comparison, stress relaxation tests of thicker, polycrystalline aluminum films suggest that relaxation due to dislocation motion, grain boundary diffusion or diffusion within the film plane will cease below a threshold stress[4]. Diffusive activity on grain boundaries or in the volume of the film is insufficient to completely relax the film stress, and surface diffusion effects do not penetrate deeply enough to relax the entire film. As mentioned earlier, the presence of hydrogen could not result in the high compressive stresses measured, so hydrogen evolution will also not result in a zero stress.

The DLC films are thin enough that surface diffusion can completely relieve the stress. However, relaxation tests on increasingly thick DLC films are expected to show a threshold stress above a certain thickness. Additionally, isothermal relaxation tests at various temperatures will allow the extraction of an activation energy for comparison to lattice or grain boundary diffusion energies.

ACKNOWLEDGMENTS

We gratefully acknowledge Carolyn Robinson for providing the samples used in this work.

REFERENCES

1. Perry's Chemical Engineer's Handbook, Sixth Edition, (McGraw-Hill, New York, 1984), p. 23-62.
2. R. O. Dillon, J. A. Woollam, V. Katkanant, Phys. Rev. B **29**, p. 3482 (1984).
3. D. E. Muller, E. Li, V. S. Veerasamy, J. Birkmeyer, J. Ward, J. Weiss, Thin Solid Films **236**, p. 59 (1996).
4. J. E. Turlo, Deformation Behavior of Thin Aluminum Films on Silicon Substrates, Ph. D. Dissertation, Stanford University Materials Science Department, September 1992.

OBSERVATIONS OF DEPTH-SENSING RECIPROCATING SCRATCH TESTS OF DLC AND NITROGENATED-DLC OVERCOATS ON MAGNETIC DISKS

T.W. Scharf, R.D. Ott, D. Yang, and J.A. Barnard

Department of Metallurgical and Materials Engineering and The Center for Materials for Information Technology, The University of Alabama, Tuscaloosa AL 35487-0202.

ABSTRACT

In this investigation, the wear durability of existing and candidate protective overcoats and substrates was examined. Specifically, 5 nm thick diamond-like carbon (DLC) and nitrogenated diamond-like carbon (N-DLC) overcoats were deposited by sputtering onto glass, glass-ceramic, and NiP/AlMg substrates. The magnetic medium was a 15 nm thick layer of CoCrPt deposited on a 50 nm thick underlayer of CrV. The wear resistance of the hard disks was determined by a recently developed depth sensing reciprocating scratch test using the Nano Indenter® II. During the scratch tests, a constant normal load of 30 μN was maintained at an indenter velocity of 2μm/sec. It was found the N-DLC/CoCrPt/CrV/glass disk exhibited the most wear resistance and least amount of plastic deformation after the last wear event. Conversely, the N-DLC/CoCrPt/CrV/NiP/AlMg disk displayed the least wear resistance even though the magnitude of the elastic recovery was the greatest. This amount of recovery was influenced by the high elastic modulus of the NiP/AlMg substrate. Consequently, the scratch test failed to isolate the intrinsic properties of the overcoat, however it provided a very powerful means of quantitatively assessing the overall response of the whole magnetic disk. This is more relevant since it simulates the response the disks see in performance. In addition, a discrete amount of nitrogen up to 14 atomic % incorporated into the amorphous network resulted in an increase in overcoat durability compared to the DLC overcoat. This was attributed to an increase in the XPS determined number of N-sp^3 C bonded sites in a predominantly N-sp^2 C bonded matrix. However, with increasing nitrogen concentrations ≥18%, the film structure was weakened due to the micro-Raman spectroscopy determined formation of terminated sites in the amorphous carbon network since nitrogen failed to connect the sp^2 domains within the network.

INTRODUCTION

The characterization of ultrathin tribologically hard protective overcoats is an important concern for the future requirements in magnetic disk drives. Increasing the areal recording density dictates the need for thinner protective overcoats (≈5 nm thick), which must possess high wear resistance, low friction coefficient, low surface roughness, and adherence to the magnetic media. These properties are crucial since near contact (<2 nm head-disk interface spacing) recording is on the horizon. Currently the overcoats used in production contain some form of carbon; for example, amorphous hydrogenated diamond-like carbon (DLC) on the order of 20 nm thick is being used [1,2]. However, the switch to nitrogen substitutionally-doped carbon overcoats is starting to occur in hopes of achieving improved properties [3,4]. Apart from the conventional problems associated with residual stresses, adhesion, and morphology, there still exists several unanswered questions regarding the microstructure and bonding of DLC and N-DLC films.

EXPERIMENTAL METHODS

The overcoats were produced by DC magnetron sputtering from a high purity graphite target in either a pure Ar (DLC) or Ar/N_2 (N-DLC) gas atmospheres (pressure=2.1 mTorr). Sputtering was also utilized to deposit the magnetic media CoCrPt (H_c≈1700 Oe) and underlayer CrV in pure Ar atmospheres (p=5 mTorr). Figure 1 illustrates the sequence of these layers and their respective thicknesses. The only variable in the processing of the hard disks, outside of the nitriding of the overcoat, was the substrate used. Commercial NiP/AlMg (still the substrate of choice in the hard disk industry), alumino-silicate glass, and chain silicate glass-ceramic (Canasite, 90% crystalline) substrates were studied. Only the glass-ceramic needed to be polished and lapped with an Al_2O_3 abrasive slurry due to its high intrinsic AFM determined surface roughness.

Mat. Res. Soc. Symp. Proc. Vol. 517 © 1998 Materials Research Society

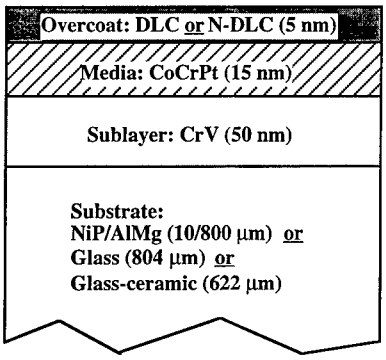

Fig.1. Schematic of different hard disk configurations with layer thicknesses.

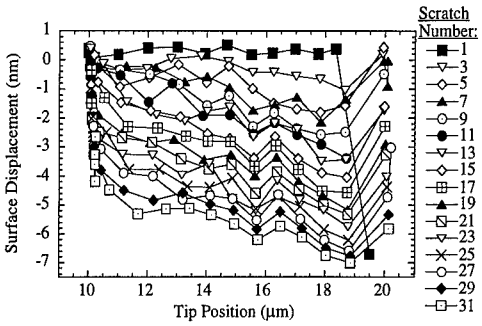

Fig. 2. Typical reciprocating scratch test showing surface displacements for indenter face orientation.

The carbon and nitrogen bonding configurations and chemical compositions were determined by XPS, while micro-Raman spectroscopy provided information on the overcoat structure. The XPS measurements were performed using a Kratos AXIS 165 surface analysis instrument with a monochromatic Al K_α x-ray source. Micro-Raman measurements were made using a modified Raman/fluorescence spectrometer. Excitation was provided by the 514.5-nm line of an argon-ion laser. For all the Raman spectra shown the laser power at the film was 100 mW and the acquisition time was 300 seconds.

A Nano Indenter® II mechanical properties microprobe (Nano Instruments, Oak Ridge TN) equipped with a nanoscratch attachment was used to characterize the multiple sliding depth sensing tribological experiments. A trigonal diamond Berkovich indenter (tip radius ≡ 150 nm) was utilized to produce a series of sliding wear tracks for each hard disk assembly. The indenter velocity for the scratch segments was 2 μm/sec. An important criteria for scratch testing of this nature is indenter tip wear. Possible blunting of the tip was monitored by examining the load vs. displacement data on a fused silica standard. The displacements only varied by 3-7 nm up to loads of 3 mN, suggesting the tip was not affected since blunting would result in a decreasing trend in displacement at a particular load. In addition, cleaning of the tip by indenting into a soft Al standard was also performed between experiments as outlined by another group [5].

The following explanation of the wear process serves as a model for all the tests performed. First the indenter contacts the film at an extremely low load of 20 μN in order to keep the indenter on the film surface. Once this contact is established, a pre-wear surface profile of 30 μm in length is traced along the film surface (indenter in a point forward direction) by moving the x-y stage beneath the stationary indenter. Next the stage, with the indenter under the same load in a face backward motion, retraces 10 μm, i.e. from 30 μm to 20 μm. The normal load is then increased to 30 μN resulting in the indenter penetrating ≈ 7 nm into the film as depicted in Figure 2. This displacement includes any elastic/plastic contributions from both film and substrate. Furthermore, the indenter elastically recoils a very small displacement due to lateral forces as the first wear scan is initiated. This first scan slides in the indenter face backward direction a total of 10 μm as shown in Figure 2. For scan two, the indenter slides with the point oriented forwards 10 μm under the same fixed normal load. The accumulated wear damage process continues with scans 3 to 31. The data from the first and last 2 μm of the wear track were disregarded because of both pile-up of material at the ends of the wear track and the plastic deformation from the initial indenter penetration.

After the final scan is completed the normal load is reduced again to 20 μN, and another 10 μm scan (10 to 0 μm) is performed. A final residual post-scan 30 μm in length is traced along the damaged film surface, which assesses the wear damage and any elastic/plastic deformation to the film and/or underlying materials. This continuous depth-sensing multiple sliding process accurately details the wear depth profiles for each scan leading to a clearer image of the evolution

of overcoat wear. This makes the technique unique with respect to other current tribological procedures for thin film analysis, e.g. AFM/FFM methods.

Critical analysis of this scratch process has been previously described, in which a discontinuity in the surface displacements for the two different sliding alignments of the Berkovich indenter, *i.e.* face (odd scans) and point (even scans) [6]. There is a negligible amount of surface displacement for the point orientation, since the face ploughs more material. Subsequently, the present results were processed separately (e.g., Figure 2) as in the case of other researchers using nanoindentation and AFM/FFM methods [7,8].

RESULTS AND DISCUSSION

X-ray Photoelectron and Raman Spectroscopies

Figure 3 shows the C 1*s* and N 1*s* XPS spectra for the DLC and N-DLC overcoats after a 1 minute sputter cleaning process. The atomic concentration of nitrogen in the N-DLC overcoats was 14%. A small amount of oxygen (<2%) was present in both overcoats even after the 1 minute sputter cleaning process. The best Gaussian fits to the XPS lines resulted in three different characteristic peaks for the C 1*s* electrons and four peaks for the N 1*s* electrons. Table I lists the binding energies and full width at half maximum for the DLC and N-DLC overcoats. For the deconvoluted carbon spectra for both overcoats, the peaks at the binding energy of 284.6 eV are attributed to C-C single bonds. This chemical state of carbon probably contains a mixture of graphite (284.2 eV) and amorphous carbon (283.7 eV). The highest binding energies listed in Table I can be assigned to C-O bonds, which likely originated when adventitious surface carbon reacted with O_2.

The other possible chemical state of carbon shifted to a higher binding energy (285.9 eV) with the incorporation of nitrogen into the overcoat, which along with the corresponding N 1*s* peak at 400.1 eV, is assigned to a C=N (imine) bond [9]. Furthermore, it has been determined that increasing the nitrogen flow resulted in even higher shifts in binding energies as well as peak broadening due to the increased frequency of C=N bonds [10]. The other major Gaussian peak at 398.4 eV has been attributed to C-N bonding [11,12], which contradicts other reports that assign this energy to C≡N (nitrile) bonds [13,14]. Raman spectra in Figure 4 for similar films revealed no C≡N bonding at this atomic percentage of nitrogen, however a broad peak at 2209 cm^{-1} (C≡N bonding) was detectable at nitrogen concentrations ≥18 at%, suggesting the chemical state at 398.4 eV is ascribed to C-N bonding for this overcoat. Excessive N_2 (≥18at% in this case) incorporated into the network resulted in the formation of dangling bonds (terminated defect sites) as evident with -C≡N conjugated to aromatic rings as illustrated in the inset of Fig.4(b).

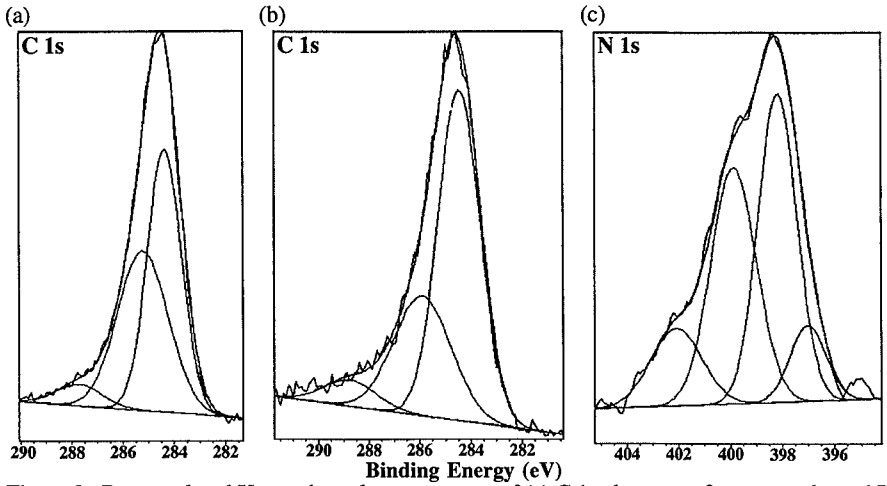

Figure 3. Deconvoluted X-ray photoelectron spectra of (a) C 1*s* electrons of a sputter cleaned DLC overcoat, (b) C 1*s* electrons and (c) N 1*s* electrons of a sputter cleaned N-DLC overcoat.

Furthermore, it may be postulated that the percentage of C-N bonds is greater than the C=N bonds based on the peak intensities. In addition, these two different N_2 binding configurations have been assigned to nitrogen bonded to sp^3 tetrahedral carbon (398.4 eV) and sp^2 trigonal carbon (400.3 eV) based on similar shifts, which is in good agreement with these results [15]. Thus a discrete amount of substitutional nitrogen (up to 14 atomic %) incorporated into the amorphous carbon network resulted in an increase in the number of N-sp^3 C bonded sites in a predominantly N-sp^2 C bonded matrix. Lastly, the minor peaks at 397.2 eV and 402.3 eV are attributed to free nitrogen atoms and N-O bonds, respectively.

Table I. XPS binding energy values of the C1s and N1s photoelectrons of C and CN overcoats obtained from the deconvolution of the spectra in Fig.3.

%N in chamber	Atomic %N	Photo-electron	Binding Energies, eV (FWHM)
0	0	C1s	284.6 (1.6), 285.4 (2.3), 287.9 (2.1)
3	14	C1s N1s	284.6 (1.9), 285.9 (2.6), 288.8 (2.4) 397.2 (1.6), 398.4 (1.7), 400.1 (2.1), 402.3 (2.3)

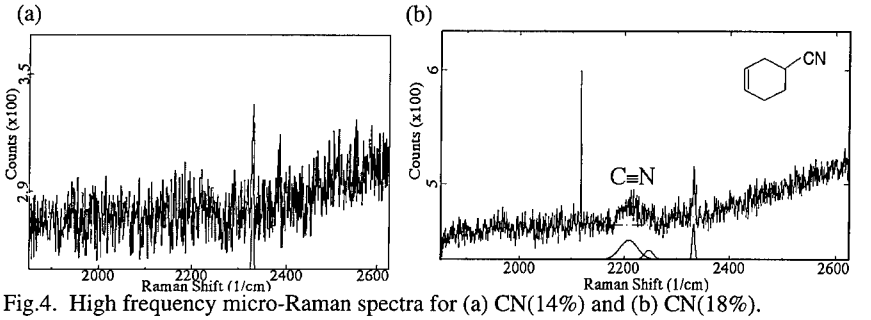

Fig.4. High frequency micro-Raman spectra for (a) CN(14%) and (b) CN(18%).

Wear Tests

Typical raw data collected during the reciprocating scratch test includes normal load, normal displacement, lateral deflection of the indenter, table position (x and y-directions), and time. Due to the large magnitude of raw data collected during scratch, an ANOVA (95% confidence) was performed on the surface displacement and residual depth profile for each scratch segment. Figure 5 shows the surface displacement as a function of the number of scratches (31, 61, and 101) for all the hard disk configurations. The N-DLC/CoCrPt/CrV/glass hard disk exhibited the least amount of surface displacement up to 31, 61 and 101 sliding scans, while the N-DLC/CoCrPt/CrV/NiP/AlMg disk displayed the most displacement up to these scan numbers. The reason for this wear behavior is due to the higher intrinsic hardness of the glass substrate. Unfortunately, the displacement data from the N-DLC/CoCrPt/CrV/glass-ceramic disk exhibited the most variation in surface displacement due to the still present high AFM determined surface roughness of the glass-ceramic substrate. In addition, the N-DLC overcoat slightly displayed improved wear resistance in comparison with the DLC overcoat on glass substrates. The reason may be a result of the substitutional nitrogen causing an increase in the number of XPS determined N-sp^3 C bonded sites in a predominantly N-sp^2 C bonded matrix. Ten scratches were performed on each hard disk and the final displacements never varied by more than four nanometers, except for the glass ceramic disk or on rare occasions when either debris, defects, etc. affected the results.

The residual depth profiles in Figure 6 provided a quantitative means of assessing the amount of permanent deformation that occurred to the disks after the final scan. Interestingly, the N-DLC/CoCrPt/CrV/NiP/AlMg disk exhibited the most amount of elastic recovery even after displacements up to 20 nm, however there was still damage to the overcoat. Although the surface displacements for the glass disks were not as high as the NiP/AlMg disk, the N-DLC/glass disk exhibited more elastic recovery than the N-DLC/NiP/AlMg and DLC/glass disks. The N-DLC/glass-ceramic disk again displayed high standard deviations in residual depths. These results clearly indicate the substrates are affecting the wear behavior.

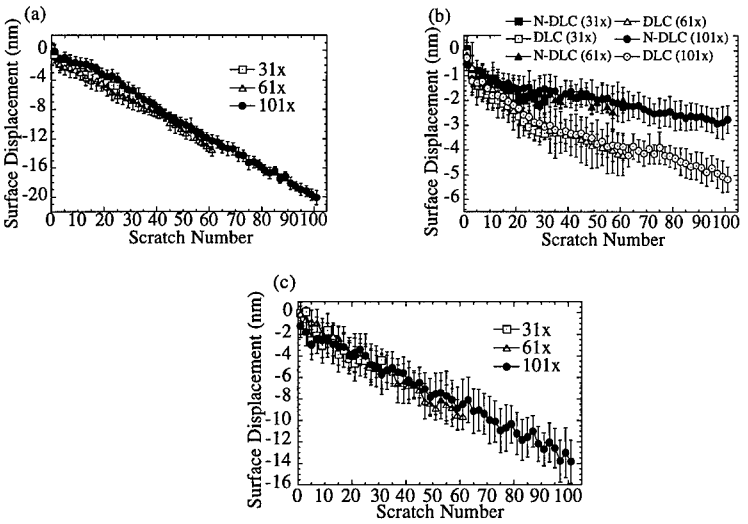

Figure 5. Surface displacement profiles for up to 31, 61, and 101 scratches on (a) NiP/AlMg, (b) glass, and (c) glass-ceramic substrates.

Concomitantly, the elastic modulus of the three substrates were measured using nanoindentation. A strong correlation was found between the elastic modulus of the substrate and the amount of elastic recovery from the wear test. The NiP/AlMg, glass, and glass-ceramic substrates possessed elastic modulus values of ≈135 GPa, 75 GPa, and 110 GPa, respectively.

To check the validity of the residual depth profiles, AFM measurements were performed on the wear tracks for the three N-DLC disks as shown in Figure 7. Indeed there was a strong correlation between the wear test and the AFM measurements. Although the glass-ceramic residual depths are fairly close with both methods, the surface topography was not ideal.

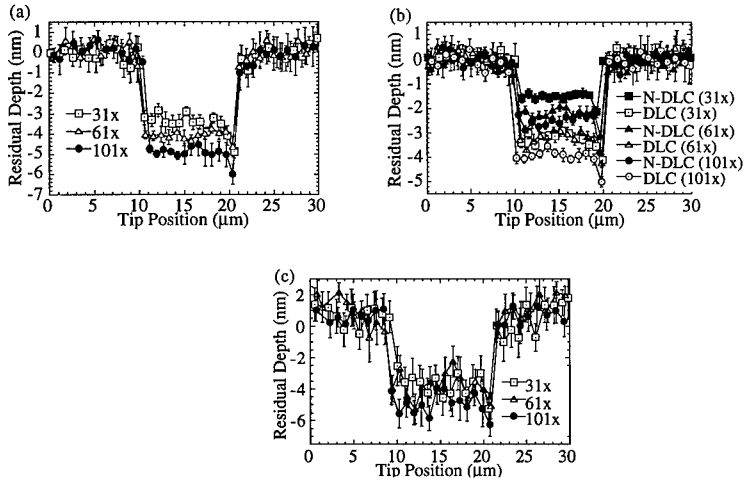

Figure 6. Residual depth profiles for up to 31, 61, and 101 scratches on (a) NiP/AlMg, (b) glass, and (c) glass-ceramic substrates.

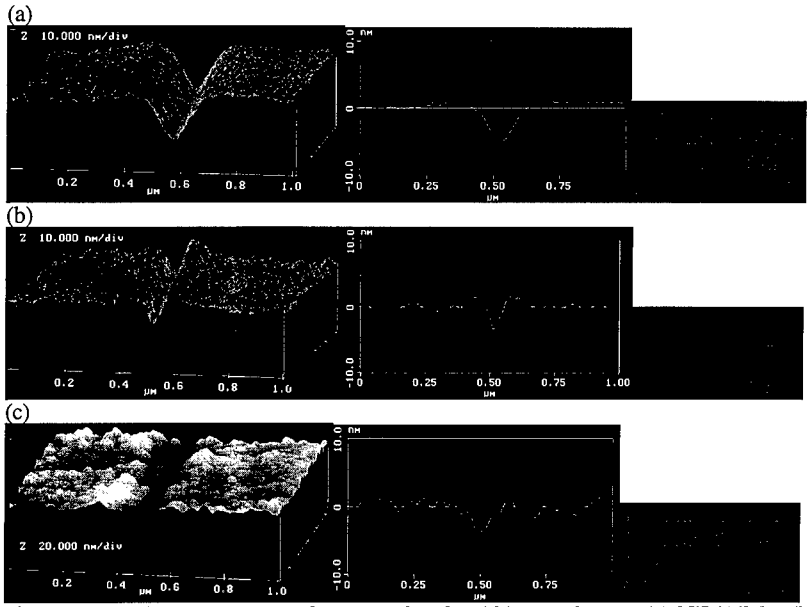

Figure 7. AFM measurements of wear tracks after 101 scratches on (a) NiP/AlMg, (b) glass, and (c) glass-ceramic substrates.

CONCLUSIONS

The N-DLC/CoCrPt/CrV/glass disk exhibited the most wear resistance and least amount of plastic deformation of the three disks. The higher hardness of the glass substrate influenced this wear behavior. The improvement with nitriding the overcoat was due to the increase in N-sp^3 C bonded sites over N-sp^2 C bonded sites. However, excessive N_2 (≥18at%) incorporated into the amorphous network resulted in terminated cyano (-C≡N) groups conjugated to aromatic rings.

ACKNOWLEDGMENTS

This work was supported by the MRSEC Program of the NSF under Award No. DMR-9400399 and NASA-EPSCoR.

REFERENCES

1) B. Marchon, J. Gui, K. Grannen, G.C. Rauch, J. Ager, S.Silva, J.Robertson, IEEETrans.Magn.,**33**,3148,(1997).
2) R. Wang, V. Raman, P. Baumgart, A. Spool, and V. Deline, IEEE Trans. Magn., **33**, 3184, (1997).
3) M.M. Yang, J.L. Chao, and M.A. Russak, IEEE Trans. Magn., **33**, 3145, (1997).
4) B. Zhang, B. Wei, D.J.D. Sullivan, and H.E. Gotts, IEEE Trans. Magn., **33**, 3109, (1997).
5) J.L. Hay, R.L. White, B.N. Lucas, and W.C. Oliver, to appear in Mat. Res. Soc. Symp. Proc. **505**
6) T.W. Scharf and J.A. Barnard, Thin Solid Films, **308-309**, 340 (1997).
7) S.D. McAdams, T.Y. Tsui, W.C. Oliver and G.M. Pharr, Mat.Res.Soc.Symp.Proc., **356**, 809 (1995).
8) B. Bhushan (ed.), *Handbook of Micro/Nano Tribology*, CRC Press, Florida, 1995.
9) M. Tabbal, P. Merel, S. Moisa, M. Chaker, A. Ricard, and M. Moisan, Appl. Phy. Lett. **69**(1698 (1996).
10) R. D. Ott, T.W. Scharf, D. Yang, and J.A. Barnard, accepted IEEE Trans. Magn., (1998).
11) D. Marton, K.J. Boyd, A.H. Al-Bayati,, S.S. Todorov, and J.W. Rabalais, Phys. Rev. Lett., **73** 118 (1994).
12) I.F. Husein, Y. Zhou, F. Li, R. C. Allen, C. Chan, J. I. Kleiman, Y. Gudimenko, and C. Cooper, Mat. Sci. and Eng. **A209**, 10, (1996).
13) F. Rossi, B. Andre, A. vanVeen, P.E. Mijnarends, H. Schut, F. Labohm, M.P. Delplancke, H. Dunlop, and E. Anger, Thin Solid Films **253**, 85 (1994).
14) S.Kobayashi,K.Miyazaki,S.Nozaki,H.Morisaki,S.Fukui,andS.Masaki, J.Vac.Sci.Technol. **A14**(3), 777 (1996).
15) H. Sjostrom, L. Hultman, J.-E. Sundgren, S.V. Hainsworth, T.F. Page, and G.S.A.M. Theunissen, J. Vac. Sci. Technol. **A14** (1), 56 (1996).

AFM NANOINDENTATION AS A METHOD TO DETERMINE MICROHARDNESS OF HARD THIN FILMS

T. BAO*, P. W. MORRISON, JR.*, and W. WOYCZYNSKI**
*Department of Chemical Engineering **Department of Statistics
Case Western Reserve University, Cleveland, OH 44106

ABSTRACT

This paper presents experimental and analytical studies of AFM nanoindentation as a method to determine microhardness of hard thin films. Indentations are performed on Au, Si, and DLC using triangular pyramidal diamond probes to determine microhardness. We examined the effects of indentation force and three different methods to measure the indentation area (direct area measurement for a triangular indentation, size analysis of an inverted AFM image of the indentation, and prediction of area from indentation depth based on a tip shape function). The responses are indentation depth, projection area, and microhardness. Relationship of responses with indentation force is examined. At a low depth range, microhardness based on pyramidal shape function is erroneously higher than the other two methods. However, all three methods generally agree with each other when indentation force exceeds 16μN. Size analysis of inverted images gives more consistent microhardness with the least variability over the whole force (4~30μN) or depth (0.5~70 nm) range. Tip shape models are developed to predict microhardness. The ellipsoidal tip model is a good approximation at low depth ranges, while the pyramidal model works better for deeper indentations. The force vs area curves are also significantly nonlinear which can distort the hardness measurements.

INTRODUCTION

Hardness of a material is defined as the resistance to a local indentation on the surface by a standardized indenter and is often expressed as a ratio of indentation load (F) to projection area (A) [1]. It is an important mechanical property and must be quantified. There is an increasing interest for characterizing microhardness of thin films where the maximal indentation depth must be not exceed 1/10~1/5 of the film thickness [2,3] in order to avoid influence of the substrate. As a result, microhardness and nanoindentation are expected to be different from traditional hardness tests on bulk materials [4-6]. Microhardness test is now possible using atomic force microscope (AFM) where a special probe replaces regular the AFM tip to accomplish both nanoindentation and *in-situ* imaging [7-10]. Presently, there is little discussion of quantitative microhardness determination and the stochastic variability of this method [11].

We have investigated AFM nanoindentation by an experimental approach to establish its capacities and limitations. The objective is to understand better the quantitative measurements of AFM nanoindentation of thin films using statistical analysis. Three different methods of area determination under various loads are evaluated.

EXPERIMENT

AFM [12,13] has been developed as an imaging tool to reproduce topographical features of a sample surface by precisely scanning a probe over the surface. Nanoindentation is an add-on option on AFM using a probe with a diamond tipped cantilever to replace the regular imaging probe. The diamond tip is three-sided symmetric pyramid with a nominal radius of ~10nm. The tip is attached to a cantilever of metal foil with a high spring constant (~100N/m) which applies indentation force ranging from 2 to 100μN. For nanoindentation, the diamond tip is engaged on a sample surface in a tapping mode [14] and starts imaging. When the indent mode is selected, the computer stops the tapping, applies a certain force to indent the surface, and then retracts the tip before switching back to imaging. Thus, the same tip images the indented surface immediately

Mat. Res. Soc. Symp. Proc. Vol. 517 © 1998 Materials Research Society

after the indentation.

In this work, a Nanoscope® III Multimode AFM by Digital Instruments (Model MMAFM-1) is used for nanoindentation. The AFM is operated in air at room temperature. Digital Instruments has supplied two diamond tips with calibrated cantilever spring constant of 147N/m. The tip apex angle is 60°. By AFM nanoindentation, indentation and *in situ* high-resolution imaging of small indentations can be achieved. Surface conditions can also be observed prior to indentation by AFM. A minimum indentation force of ~2μN over a depth range of ~0.1nm can be achieved. Consequently, AFM nanoindentation is an appropriate microhardness test for thin films.

A simple two-factor experiment [15] is performed with 3 repeated AFM measurements at each condition shown in Table I. Multiple level indentation force is applied to gold, silicon, and DLC. Indentations are possible on relatively soft Au over a wide force and depth range, while Si and DLC are more representative of hard materials. The measured responses include indentation depth (D) and projection area (A). The general formula for hardness [16], H = F/A, is used for quantifying the AFM nanoindentation; H is microhardness in units of pressure, F is indentation load, and A is area.

Table I Conditions for Nanoindentation Experiments

Material	AFM tip	Force (μN)	Response		
			Depth (nm)	Area (nm^2)	Hardness (GPa)
Au	I	8 levels (4~27)	0.8~70	3,000~20,000	H = F/A
Si	II	7 levels (4~15)	0.9~18	1,000~12,000	
DLCa	I	2 levels (17.1, 21.7)	0.5~0.9	3,000	
DLCb	I	2 levels (16.6, 20.1)	0.6~1.5	~7,000	

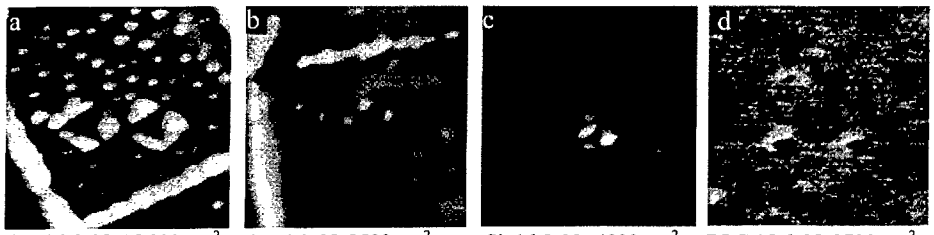

Au 16.5μN 15,000 nm^2 Au 4.1μN 2500 nm^2 Si 16.5μN 4000 nm^2 DLC 15.6μN 2700 nm^2

Fig. 1 AFM images of nanoindentation (1×1μm size; material and load indicated above)

A deep indentation should have a triangular area that is easy to measure on an AFM image (Fig. 1a). However, a low force on a soft material or a high force on a hard material like diamondlike carbon (DLC) produces very shallow indentations which may not have clear boundaries with a regular triangular area (Fig. 1b,c,d), especially at a low load (Fig. 1b). Measurement of small indentation areas is difficult and could have large errors. The source of variations may include the following: sink-in and pileup of extruded materials; irregular tip shape due to blunting and/or manufacture variation. In addition, the indentation may rebound vertically and/or contract diagonally due to the elastic recovery after removing the tip [17,18]. AFM microhardness not only depends on the nature of materials, but also on the material, shape, and condition of the tip, and many other variables. The stochastic nature and variability of microhardness measurements should be assessed in a statistically significant manner.

Three different methods are proposed to determine areas. $A_{pyramidal}$ predicts areas from indentation depth (D) based on the known tip geometry [19]. A simple geometric derivation for a

triangular pyramidal tip gives $A_{pyramidal} = kD^2$ where k is a constant. $A_{triangle}$ directly measures a side of the triangular indentation. In this way, it has a similar measurement procedure to a macrohardness measurement like Vickers hardness [5,6]. Fig. 1a shows the AFM image of a triangular indentation. The $A_{triangle}$ method is limited, however, because $A_{triangle}$ is not available for hard materials where the indentation shape is irregular. The third method ($A_{inverted}$) is obtained first by inverting the indentation image such that it becomes like an elevated grain (Fig. 1d). Then software for grain size analysis (supplied by Digital Instruments) is applied to calculate the size of the grain above a height threshold (determined by the software).

RESULTS

For a soft material like Au, the three area measurements tend to converge at high loads (Fig. 2a). When F exceeds ~16μN, $A_{pyramidal}$, $A_{triangle}$, and $A_{inverted}$ tend to agree with each other at a given force. In fact, $A_{triangle}$ is highly correlated with $A_{inverted}$ following the model $A_{triangle} = 1.22A_{inverted}$ with $R^2_{adj} = 94\%$. (R^2 is the percentage of data variation explained by the model; R^2_{adj} is an adjusted version of R^2 that allows comparison of models with different number of parameters). For Si and DLC, however, the $A_{triangle}$ method is not available, so Fig. 2b compares just $A_{inverted}$ and $A_{pyramidal}$. The data show that $A_{pyramidal}$ diverges strongly from $A_{inverted}$ at low loads, indicating $A_{pyramidal}$ is completely incorrect. Considering that H = F/A, microhardness can be grossly distorted if the wrong area is used.

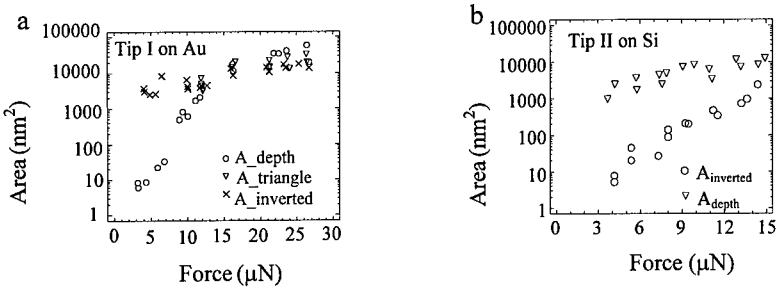

Fig 2 Comparison of three area measurements: A_{depth}, $A_{triangle}$, and $A_{inverted}$

The significant departure from ideality occurs mainly due to two reasons: deviations from the ideal pyramidal tip shape and indentation elastic recovery. The pyramidal model assumes a pyramidal tip, but other tip shapes are possible including cylindrical, spherical, ellipsoidal, or a combination of any of the above. The occurrence of a cylindrical shape would be very undesirable since the measured area would be independent of tip load, and thus the hardness would be proportional to the applied force. In the case of inelastic recovery after a shallow indentation, most materials experience a diagonal contraction that is negligible [17,18] while the vertical rebound part is dominant. Therefore, one could expect $A_{pyramidal}$ to be much smaller than $A_{inverted}$ (or $A_{triangle}$), while $A_{triangle}$ and $A_{inverted}$ would be similar to each other. For deep indentations, the vertical rebound and the tip imperfection all become insignificant, and all three methods give roughly equivalent areas.

The force-area plots for the three materials appear in Fig. 3a. In this figure, the Au and DLC measurements were performed using a blunt tip (Tip I) while Si is indented with a sharp tip (Tip II). A conventional hardness calculation for these data corresponds to taking the ratio of the applied load F to the measured area $A_{inverted}$; this corresponds to the slope of the line connecting a measured point to the origin. The results of such calculations appear in Fig. 3b. As expected, the hardness of the DLC films is much greater than Si or Au, but the Au and Si are roughly

equivalent. This equivalence occurs because the tips used in the four sets of nanoindentation experiments are not the same; a measurement of Si with Tip I correctly orders the materials. The data also seem to show that the hardness measurements have a significant amount of variability. In the case of silicon, the hardness seems to increase at smaller forces. In an attempt to determine whether this result is real, we have taken a closer look at the data using statistical model building.

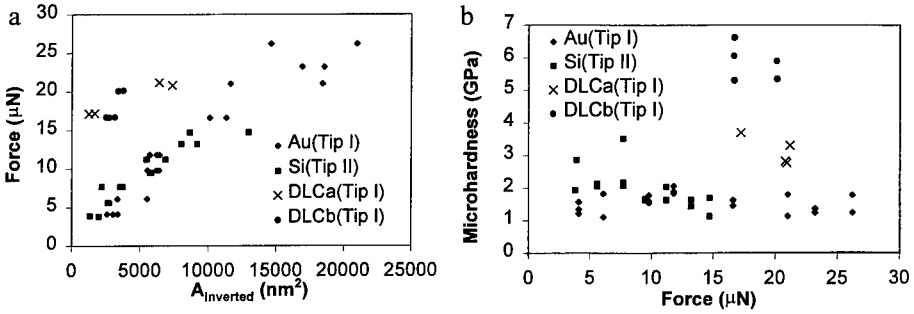

Fig. 3 Results of nanoindentation of Au (Tip I), Si (Tip II), and DLC (Tip I) a) Force-$A_{inverted}$ plot; b) Microhardness calculated from the data in (a).

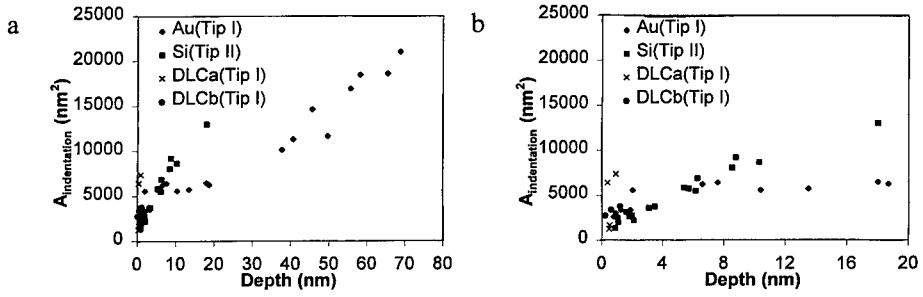

Fig. 4 Scatter plots of the measured indentation area $A_{inverted}$ and the measured indentation depths for Au, Si, and DLC. a) $A_{inverted}$ corresponding to depth between 0 – 80 nm; b) $A_{inverted}$ corresponding to depth between 0 – 20 nm

The first step in this process is to examine the additional data available in the AFM depth measurement. Fig. 4 contains the scatter plot of the measured area $A_{inverted}$ and the depth of the corresponding indentation. We have built models for the area-depth data using a polynomial function containing terms up to second order in D. The physical justification for this model function is contained in Table II. If the tip has a cylindrical shape, the area has no dependence on D while if the tip is pyramidal, the area has only a positive quadratic dependence on D. In the case of spherical or ellipsoidal tips, however, the area would show a positive linear and a negative quadratic dependence on D but no constant term. Table III summarizes the results of regressing the data in Fig. 3. As one can see, Tip I behaves as if it is a combination of a cylindrical + ellipsoidal shape at low D ($\alpha \neq 0$ and $\gamma < 0$) while at larger D, the tip behaves as if it has some pyramidal character ($\gamma > 0$). Tip II, on the other hand, behaves as if it is ellipsoidal over the whole range of depths. Keep in mind that cylindrical tips are very undesirable because the indentation area is independent of load, and thus the measured hardness would be proportional to

the load force. Thus, the use of Tip I on a harder material like DLC where the penetration depth is small (D < 5 nm) can be very misleading.

Table II Various geometrical models for the AFM tips

Tip shape	Geometry	Model equation
Cylindrical		$A_{cyl} = \pi R^2$
Spherical		$A_{sph} = 2\pi RD - \pi D^2$
Ellipsoidal	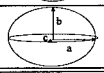	$A_{Ellips} = \frac{2\pi ac}{b}D - \frac{\pi ac}{b^2}D^2$
Pyramidal	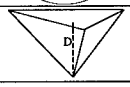	$A_{pyramidal} = cD^2$

Table III Results of regressing the data in Fig. 4 to the function $A_{inverted} = \alpha + \beta D + \gamma D^2$

	Tip	D range (nm)	α (nm²)	β (nm)	γ	R^2_{adj}	Comment
Au	Tip I	0.8~20	2907.22	544.6	-20.81	66%	Cylindrical + Ellipsoidal
Au	Tip I	0.8~80	3855.9	117.25	1.86	96%	Pyramidal dominant
Si	Tip II	0.9~18	0*	1053.3	-20.17	98%	Ellipsoidal

*statistically insignificant at 5%.

Table IV Results of regressing the data in Fig. 3 to the function $F = a + bA_{inverted} + cA^2_{inverted}$.

	Tip	F range(μN)	a (μN)	b (μN/nm²)	c (μN/nm⁴)	R^2_{adj}
Au	Tip I	4.1~30	2.43	0.00122±0.00010	0 (forced)	89%
Au	Tip I	4.1~30	-3.3*	0.00266±0.00039	-6.33E-8	93%
Si	Tip II	3.8~15	3.62	0.00104±0.00011	0 (forced)	86%
Si	Tip II	3.8~15	1.19*	0.00210±0.00033	-7.63E-8	92%

*statistically insignificant at 5%.

The data in Fig. 3 can also be tested for internal consistency. The hardness analysis described above assumes that the hardness is independent of A; that is, the applied force is proportional to the measured area. We can test this assumption by regressing the data of Fig. 3 against the model $F = a + b\,A_{inverted} + c\,A^2_{inverted}$. The constant *a* is interpreted as the threshold force corresponding to the tip touching down on the surface with a finite force but without producing an indentation; this is equivalent to assuming the material has an infinite hardness at low forces. The linear term *b* corresponds to the hardness while the quadratic term *c* can account for flow of the material at higher indentation forces. Flow would produce higher areas than expected for a given force; the coefficient *c* should be negative in these situations. The regression results appear in Table IV. In all cases, the models with just the threshold and hardness terms (*a*

and *b*) are statistically poorer in quality than the full quadratic model (*a*, *b*, and *c*). Furthermore, the quadratic fits have a statistically insignificant threshold parameter *a* (at the 95% confidence level), and the flow parameter *c* is in fact negative. Thus the data indicate that the higher forces required to indent hard materials may produce hardness measurements with significant nonlinear effects in them.

CONCLUSIONS

In this work, experimental and statistical studies are conducted systematically to address the stochastic nature of measurement of the microhardness of hard thin films by AFM nanoindentation. For hard films, it is difficult to measure indentation areas, and special attention is needed to interpret the data. We tested three area measurement techniques: $A_{triangle}$, $A_{pyramidal}$, and $A_{inverted}$. All three are roughly equivalent at deeper indentations. $A_{triangle}$ is not applicable at low depth or for harder materials because the indentation area is irregular. $A_{inverted}$ is applicable for any size indentation and is a preferred method for measuring areas. Tip shape models have been constructed and have been fitted to $A_{inverted}$ versus D scatter plots. The ellipsoidal tip model approximates the behavior of a sharp diamond tip, but a combination of a cylindrical, ellipsoidal, and pyramidal shape are required to fit a dulled tip; the pyramidal tip model tends to dominate at large indentation depths. The force versus area is significantly nonlinear indicating that the most reliable measurements of nanoindentation should be made at low loads (< 10-20 μN).

ACKNOWLEDGEMENT

This work is financially supported by National Science Foundation. The authors are indebted to Prof. John Angus for use of his AFM equipment. The technical discussion with Jeff Elings from Digital Instruments is also acknowledged.

REFERENCES

1. D. Tabor, Phil. Mag. **74**(5), 1207 (1996).
2. K. Matsuda and M. Kaneta, Phil. Mag. **74**(5), 1171 (1996).
3. D. Tabor, *The hardness of metals* (At the Clarendon Press, Oxford, UK, 1951).
4. Y. V. Ezhov, Journal of Testing and Evaluation **24**(5), 320 (1996).
5. H. Boyer (ed.), *Hardness testing* (ASM International, Metals Park, OH, 1987).
6. V. E. Lysaght and A. DeBellis, *Hardness Testing Handbook* (American Chain & Cable Co., INc., USA, 1969-74).
7. N. Burnham and R. Colton, J. Vac. Sci. Technol. A **7**(4,Jul/Aug), 290 (1989).
8. B. Bhushan and V. Koinkar, Appl. Phys. Lett. **64**(13), 1653 (1994).
9. B. Bhushan and A. Kulkarni, Phil. Mag. **74**(5), 1117 (1996).
10. D. Scholl, M. Everson, and R. Jaklevic, J. Mater. Res. **10**(10), 2503 (1995).
11. W. Vanlandingham *et al.*, J. Mat. Sci. Lett. **16**, 117 (1997).
12. G. Binnig, C. F. Quate, and C. Gerber, Phys. Rev. Lett. **56**, 930 (1986).
13. G. Binnig, H. Rohrer, C. Gerber, and E. Wiebel, Appl. Phys. Lett. **40**, 178 (1982).
14. A. Ikai, Surf. Sci. Rep. **26**, 261 (1996).
15. D. Montgomery, *Design and Analysis of Experiments*, third ed. (John Wiley & sons,, 1991).
16. J. Gubicza, A. Juhász, and J. Lendvai, J. Mater. Res. **11**(12), 2964 (1996).
17. M. Doerner and W. Nix, J. Mater. Res. **1**, 601 (1986).
18. M. Petzold, J. Landgraf, *et al.*, Thin Solid Films **264**(2), 153 (1995).
19. AFM staff, *Support Note for Nanoindentation and Nanoscratching by SPMs*, No. 225, Rev. C (Digital Insruments, Santa Barbara, CA, 1996).

KEY WORDS: AFM nanoindentation, microhardness, projection area, and statistical analysis

Part IX

Tribology, Lubricants, and Corrosion

Structure of Molecularly -Thin Perfluoropolyether Films on Amorphous Carbon Surfaces

G.W. TYNDALL*and R.J. WALTMAN**
*IBM, Almaden Research Center, 650 Harry Road, San Jose, CA 95120
**IBM, Storage Systems Division, 5600 Cottle Road, San Jose, CA 95193

ABSTRACT

Surface energies of molecularly-thin, perfluoropolyether (PFPE)-lubricated, amorphous carbon surfaces are presented as a function of the applied PFPE structure and thickness. A framework is developed to aid in the interpretation of the surface energy data. Information regarding the structure of these PFPE films adsorbed on CHx at the monolayer thickness levels is elucidated. Evidence for ordering in these polymer films is presented and interpreted to result from a combination of both, lateral cohesive interactions within the plane of the monolayer, and adhesive interactions between the PFPE monolayer and the underlying substrate.

INTRODUCTION

The hard-disk drive industry is a highly competitive $50B/year industry. Timely introduction of new products with ever-increasing magnetic recording densities is required of successful companies in this industry sector. The historic 60% compound yearly growth rate in storage densities has placed unprecedented demand on many of the materials used in the drive. In the past few years, a number of advances have been made in the magnetic films employed in both the magnetic recording heads and the magnetic recording disks. In the case of the magnetic recording head, the substituition of magneto-resitstive (MR) heads for thin-film inductive heads, and more recently the replacement of MR heads with giant magneto-resistive (GMR) heads have dramatically increased the detection sensitivity of the sensor, and hence have led to subtantial increases in the storage density. In the case of the magnetic recording media (disk), grain size reduction requirements coupled with media noise considerations, have led to the development of quartenary alloys to replace the traditional ternary alloys. In addition to advances in the magnetic films, increased recording densities can be achieved via decreasing the physical separation between the active elements. Decreasing the fly height of the magnetic recording head relative to the magnetic recording disk however, induces more frequent mechanical contact between these two surfaces, which places more stringent demands on the tribological properties of the protective, wear-resistent films employed at the head-disk interface (HDI). Future increases in magnetic recording densities will therefore require an increased focus on the materials employed at the HDI in addition to continued advancement in the magnetic materials.

The magnetic recording industry universally employs a hard, amorphous-carbon overcoat to protect the magnetic film of the disk. A similar carbon overcoat is typically used on the magnetic recording head. Perfluoropolyether (PFPE) films are then topically applied to the carbon overcoat of the disk to provide lubrication during head-disk contacts. In current hard-disk drives, nominally 100$\AA$ of amorphous carbon is used on both the head and the disk, and sub-monolayer PFPE films are used as lubricants. The materials utilized at the HDI are typically evaluated mechanically either on a component test stand or within the disk-drive environment. While mechanical testing of the HDI is simple and is universally utilized by the magnetic recording

Mat. Res. Soc. Symp. Proc. Vol. 517 © 1998 Materials Research Society

industry, it has a number of short-comings. The major difficulty in assessing the tribological merits of the materials employed at the HDI is that the mechanical performance is strongly dependent on a number of tightly coupled parameters, many of which are not directly related to the protective films under evaluation. Materials selection can be further complicated by the fact that the lubricant/carbon systems utilized are not thermodynamically stable under disk-drive operating conditions.[1-3] The results of the mechanical testing can therefore be extremely difficult to interpret. In order to meet the stingent tribological demands of future disk-drives, it is imperative that a more fundamental understanding of the HDI materials interactions, and the relationship between these interactions and the resulting tribology, be established.

In this paper we concentrate on the magnetic recording disk and the interaction forces that develop between the monomolecular PFPE lubricant films and the amorphous carbon surfaces typically employed as protective coatings. In particular, we investigate the effect of changing the chemical composition of the carbon surface, and the identity of the PFPE lubricant on the resulting interactions between these two films. We find that the forces acting on the PFPE lubricant polymers result from a combination of adhesive interactions with the surface, and lateral cohesive interactions between adjacent polymers. Since the forces operating at the lubricant-carbon interface will dictate the adhesion of the lubricant to the disk, the mobility of the lubricant on the disk, and the structure of the lubricant at the surface, the results reported here provide a framework from which the design of future protective films might be realized.

EXPERIMENT/THEORY

Two types of amorphous carbons were employed in this work, nitrogenated carbon (CNx) and hyrdogenated carbon (CHx). Both carbons were sputter deposited onto 95 mm dia. thin film disk substrates using standard disk manufacturing sputter systems. The RMS roughness of the carbon overcoats was nominally $< 10\ \mathring{A}$ for both CHx and CNx. The composition of the carbons studied in this work were determined from RBS, and grazing incidence XPS measurements and are shown in Table I.

The PFPE lubricants employed in this work were based on either the Fomblin Z, or the Demnum backbones. The structure of the PFPE lubricants studied in this work are summarized in Table II. These lubricants were applied to the carbon-overcoated, magnetic recording disk by using the dip-coat method from solutions of the PFPE's in perfluorohexane. Lubricant thicknesses were controlled via the rate at which the substrate was pulled from the PFPE/perfluorohexane solution, or the concentration of the PFPE in the solution, or both. Thickness measurements were conducted utilizing FTIR absorption measurements which have been calibrated using X-ray reflectivity.

Table I. Composition of the amorphous carbon surfaces employed in this work.

Carbon Type	Carbon (at. %)	Hydrogen (at.%)	Oxygen (at.%)	Nitrogen (at. %)
CHx	52	35 ± 3	13 ± 3	< 2
CNx	85	< 2	4 ± 2	11

Table II. Structures of the PFPE lubricants studied in this work.

Fomblin Z : $X\text{-}(CF_2O)_x(CF_2CF_2O)_yCF_2\text{-}X$

Trade Name	End-Group	MW
Z-15	- CF_3	15,000
Zdol (2000)	- CH_2OH	2,000
Zdol (4000)	- CH_2OH	4,000
Zdiac	- CH_2COOH	2,000
AM3001	- phenyl ester	3,000

Demnum : $CF_3CF_2CF_2 - (CF_2CF_2CF_2O)_m\text{-}CF_2CF_2\text{-}X$

Trade Name	End-Group	MW
Demnum SA	- CH_2OH	3600
Demnum SP	- phenyl ester	3600

The surface energies, γ, of the PFPE lubricated disks were determined as a function of lubricant thickness for a variety of lubricant backbone structures, carbon compositions, and lubricant end-groups from contact angle measurements. When a low surface energy liquid, such as the perfluoropolyethers, is applied to a higher energy solid surface, e.g. amorphous carbon, the liquid will wet the surface with the wetting being driven by the resultant decrease in Gibbs free energy of the solid, i.e. $\Delta G < 0$. Since the surface energy is defined as the Gibbs free energy per unit area,[4] the magnitude of the surface energy changes with addition of lubricant to the disk surface will, in the case of molecularly thin films, reflect the interactions that develop at the solid-liquid interface.

The forces acting on the PFPE liquid in the monolayer thickness regime can result from a variety of sources including London dispersion forces, and polar interaction forces. The London dispersion forces acting between the PFPE lubricant and the carbon surface can be probed by measurement of the "dispersive" surface energy, γ^d. The dispersive surface energy is readily obtained by measurement of the contact angle made with the surface using a reference liquid capable of interaction with the surface via dispersion forces alone, and using the Girafalco, Good, Fowkes, Young equation.[4] For the present work we have utilized a series of saturated alkanes as the reference liquids.

In addition to the dispersion forces acting between the lubricant and the carbon, specific "polar" interactions can occur between the liquid and the solid. The strongest of these polar interactions would result from formation of a chemical bond between reactive entities in the liquid and on the surface of the solid. Other strong polar interactions such as formation of acid-base adducts, and hydrogen-bonding can also occur if appropriate interaction pairs exist. The polar surface energy is obtained from measurement of the contact angle made with the surface using a polar reference liquid. In all the work presented here, water was used as the polar reference

liquid. Since water is capable of interacting as either a weak acid or weak base, both acidic and basic functionalities that may exist on the PFPE-lubricated carbon surface are detectable.[5]

RESULTS

A. Dispersive Surface Energies

In Fig. 1a we present dispersive surface energy data for a series of end-functionalized Fomblin Z and Demnum lubricants, and the non-functionalized Fomblin Z15 lubricant on CHx. For the functionalized Fomblin Z lubricants, the data reported in Fig. 1a is compiled from measurements conducted on Zdol (2000, 4000), annealed Zdol (2000) and Zdiac. In all cases, the surface energy decreases with applied lubricant thickness, asymptotically approaching that of the bulk lubricants. The lubricant thickness at which the disk surface energy becomes equivalent to the bulk is defined as full surface coverage and is designated h_0 in the following. It is apparent from Fig. 1a that the largest dispersive surface energy differences result from changing the number of functionalized end-groups in the PFPE lubricant. The functionalized Fomblin Z lubricants having two polar end-groups (see above) are the most efficient at covering the CHx surface. Complete coverage of the CHx surface by the functionalized Fomblin Z's occurs at a nominal lubricant thickness of $h_0 = 14 \pm 2$ Å independent of the identity of the polar end-groups studied, or the molecular weight (MW) employed. The Demnum SA and SP lubricants, containing only one functionalized end-group, are less efficient than the functionalized Fomblin Z lubricants at covering the carbon surface. Full surface coverage for these functionalized Demnum lubricants occurs at a nominal thickness of 30 ± 4 Å. Complete coverage of the CHx surface by the non-functionalized Fomblin Z - 15 was not obtained over the thickness regime studied. While we define h_0 as that lubricant thickness required for complete surface coverage, we note that owing to the heterogeneity of the carbon surface and the possible selective adsorption of the functionalized lubricants at specific adsorption sites, complete physical coverage determined from these measurements may occur at a quite different thickness than monolayer coverage of the carbon active adsorption sites.

In Fig.1b the dispersive surface energies for Fomblin Zdol on CNx are shown. Again very little difference is measured in the dispersive surface energies with changes to the molecular weight (Zdol 4000 vs Zdol 2000), or whether the surface is annealed after lubricant application. All systems asymptotically approach the dispersive surface energy of bulk Fomblin Z at nominally $h_0 = 21 \pm 2$ Å. Complete surface coverage for these lubricants on the CNx surface thus requires application of substantially more lubricant compared to that required on CHx.

Ab-initio calculations conducted on model carbon surfaces with model lubricants have been reported previously.[6] In the following, a brief description of the results are given to facilitate the interpretation of results presented above. The calculations employed the fluorinated, hydroxyl-terminated ether, $CF_3OCF_2CH_2OH$, as the model lubricant with structural features similar to the Zdol and Demnum SA lubricants. The results of these calculations indicate that strongly attractive, adhesive interactions develop between the hydroxyl end-group of $CF_3OCF_2CH_2OH$ and the active adsorption sites on CHx and CNx surfaces. The strength of theseinteractions (on the order of 5 - 10 kcal-mole^{-1}) are substantially greater than the typical van der Waals interaction strengths (on the order of 0.1 - 1 kcal-mole^{-1}) characteristic of the PFPE backbone interactions with the surface.

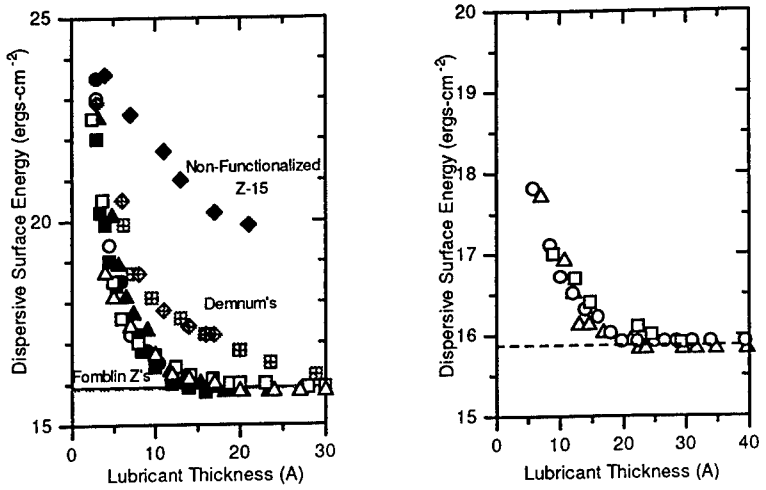

Figure 1. (a) Dispersive surface energies for a series of Fomblin Z and Demnum lubricants on CHx. (b) Dispersive surface energies of Zdol 2000 and Zdol 4000 and annealed Zdol 4000 on CNx. The value of the dispersive surface energy for bulk Fomblin Z (15.8 ergs-cm^{-2}) is designated by the dotted line.

These results suggest that interaction of the polar end-groups with the carbon overcoat should dominate the adsorption, and hence structure, of the functionalized PFPE lubricants on the disk. The dispersive surface energy data presented in Figure 1a can thus be rationalized in the following manner. The absence of functionalized end-groups in the lubricant structure, e.g. Fomblin Z15, results in adhesive interactions between the lubricant and the surface that are solely due to van der Waals forces. Since the adsorption enthalpy is relatively small, the structure of the lubricant on the disk will resemble the random structuring inherent to the bulk liquid. Incorporation of a single functionalized end-group into the PFPE structure (functionalized Demnum) will impart a certain degree of order to the lubricant structure on the surface as the attractive polar interaction of the end-group with the surface serves to effectively anchor one end of the chain to the surface. The favorable enthalpy term associated with the end-group adsorption more than compensates for the decrease in entropy that results from forming the more ordered structure (compared to the non-functionalized PFPE's) on the carbon surface. In the case of the functionalized Fomblin Z lubricants, the presence of the two functional end-groups can serve to anchor both polymer chain ends to the surface. The resulting structure is characterized by preferential orientation of the perfluoropolyether backbone parallel to the surface. Parallel orientation of the PFPE backbone with respect to the carbon surface is the optimum geometry for obtaining maximal surface for a given applied thickness. For the lubricants studied in this work, the specific identity of the polar end-group(s) does not strongly effect the measured dispersive surface energy. This result implies that each of the end-groups studied interact with the surface via polar interactions that are substantially stronger than the van der Waals interactions of the backbone with the surface, and hence dominate the adsorption.

Ab-initio calculations performed on $CF_3OCF_2CH_2OH$ with a model CNx surface reveals that the interactions between the perfluorinated lubricant backbone and CNx surface are less favorable than those that develop on the CHx surface.[3] Repulsion between the electron-rich nitrogen surface sites and the electron rich fluorine atoms of the polymer backbone tends to force the backbone off the surface. The reduction in the degree of parallel orientation of the PFPE backbone with respect to the CNx surface results in the observed shift to slightly greater Zdol thicknesses required to obtain complete coverage on the CNx vs CHx surface.

B. Polar Surface Energies

In order to explain the dispersive surface energy results, we proposed that polar interactions between the PFPE end-groups and the polar active sites on the carbon surface dominate the adsorption and structure of the functionalized PFPE lubricants. Evidence of these polar adhesive forces should therefore become apparent by measurement of the polar surface energies. In the following, we limit our discussion to the functionalized Fomblin Z lubricants.

Measurement of the lubricant thickness dependence of the polar surface energies yields information concerning the structure of molecularly-thin, end-functionalized PFPE lubricants on carbon surfaces that is difficult to obtain via more sophisticated techniques. While the experimental methodology required to determine the surface energies is straightforward, interpretation of the data can be ambiguous. We therefore begin our discussion by presenting a qualitative framework useful in extracting information concerning the interactions between the lubricant film and the carbon surface. The polar surface energy measured in this work, γ_{ml}, can be expressed as:

$$\gamma_{ml}(h) = \gamma_i(h) + \gamma_j(h) - (\xi_{ij}(h) + \xi_{jj}(h)) \qquad (1)$$

where γ_i is the surface energy of the substrate, γ_j is the surface energy of the non-interacting polar end-groups of the jth lubricant monolayer. We define ξ_{ij} as the adhesive interaction energy density between the jth lubricant layer and the underlying ith monolayer. We also define ξ_{jj} as the in-plane, lateral, cohesive interaction density between lubricant end-groups in the jth monolayer. Since attractive interactions between polar entities will result in a drop in the measured surface energy, the sign of both ξ_{ij} and ξ_{jj} as defined in equation (1) will be positive for attractive interactions. As explicitely noted, all terms in equation (1) are lubricant thickness, h, dependent. In the case of formation of the first lubricant monolayer ($h < h_0$), j = 1, and the substrate corresponds to the bare carbon surface, i.e., i = 0. In the thickness range relevant to the second monolayer formation, j = 2 and i = 1. In the multilayer thickness regime, the substrate is treated as being the carbon surface coated with i monolayers of lubricant. Thus, ξ_{ij} represents the interlayer interactions between Zdol in the ith and jth monolayers.

The concepts outlined above can be applied to the thickness dependent polar surface energies measured for a series of end-functionalized Fomblin Z based lubricants on both CNx and CHx surfaces. In Figure 2, we present the polar surface energy of Zdol (2000) on the CNx surface described in Table I. Two data sets, corresponding to the surface energy measured 1 week following Zdol application, and 6 weeks after Zdol application, are compared in Fig.2. The results of the surface energy measurements collected one week after lubricant application show the adhesive and cohesive interactions of Zdol are only very weak, i.e. ξ_{ij} and $\xi_{jj} \rightarrow 0$. The

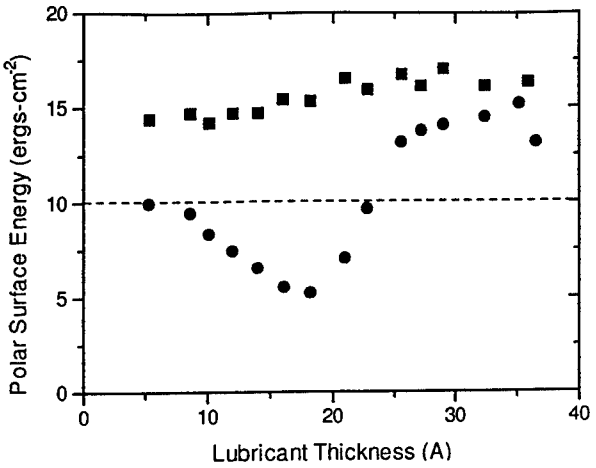

Figure 2. Comparison of the polar surface energy of Zdol 2000 on CNx 1 week after lubricant application (■), and 6 weeks after lubricant application (●). The polar surface energy of bulk Zdol 2000 is shown as the dotted line.

measured surface energy is thus dominated by the sum of the polar active sites on the carbon, and the polar end groups on the lubricant, i.e.,

$$\gamma_m(h) = \gamma_i(h) + \gamma_j(h). \qquad (2)$$

In the sub-monolayer/monolayer thickness regime ($h < 21$ Å for Zdol on CNx), the contribution of the bare carbon surface γ_i to the measured surface energy will decrease, and that of the lubricant γ_j will increase as the lubricant thickness is increased. At $h > h_0$, the contribution of the polar carbon sites to γ_m will vanish as these sites become physically covered by the applied lubricant. In this thickness regime, γ_m becomes independent of the Zdol thickness up to the highest thickness studied of 36 Å. The average value of γ_m = 17 ergs-cm^{-2} obtained at Zdol thicknesses of 21 - 36Å is interpreted, via equation (2), to be a measure of the surface energy of a monolayer of non-interacting Zdol polymers. This value can be compared with the polarity of bulk Zdol (nominally 10 ergs-cm^{-2}), and the difference of 7 ergs-cm^{-2} attributed to the cohesive, hydrogen-bonding present in the bulk. Following storage for an additional 5 weeks at room temperature and ambient humidity (nominally 40 ± 10%), the Zdol/CNx system has evolved dramatically. While the nature of this time dependence will be treated in detail elsewhere, the observed decrease in the surface energy demonstrates that attractive, polar interactions have developed in this system. As is discussed in more detail below, the observed surface energy minimum at nominally 18 Å results from the formation of both cohesive hydrogen-bonding interactions within the 1st Zdol monolayer, $\xi_{1,1} > 0$, and attractive adhesive interactions between the 1st monolayer and the CNx substrate, $\xi_{0,1} > 0$.

The polar surface energies vs applied Zdol lubricant thickness were also studied on the CHx surface. These results are compared in Figure 3 with the surface energies measured for

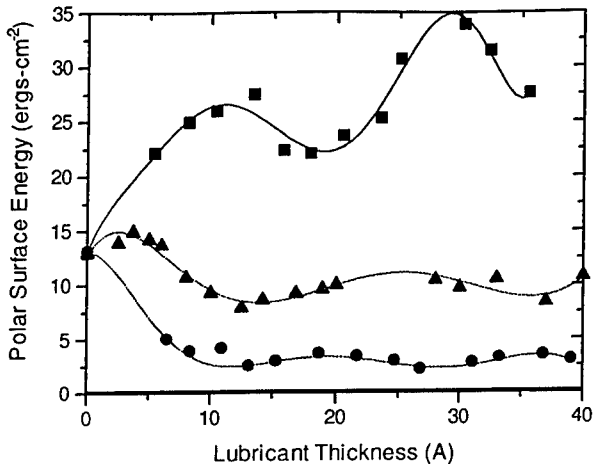

Figure 3. Polar surface energies vs. lubricant thickness for Zdiac (■), Zdol (▲), and AM3001 (●) on CHx.

Zdiac, and AM3001 on CHx. In all three examples, a complex oscillatory structure is found in the magnitude of the polar surface energy vs lubricant thickness. The relative ordering of the different Fomblin Z lubricants in terms of the magnitude of the surface energy reflects the relative polarity of the end-groups. The carboxylic end-groups of Zdiac being more polar than either the hydroxyl end-groups of Zdol, or the aromatic end-groups of AM3001, results in the highest observed surface energy at all lubricant thicknesses.

We now concentrate on the oscillatory structure observed in Figure 3. Addition of very thin films of either Zdol or Zdiac to the CHx surface results in an increase in the measured surface energy. At nominally 4Å for Zdol and 10Å for Zdiac, the polar surface energy then decreases with increasing lubricant thickness. A local maximum in the surface energy thereby results which we interpret in terms of a 2D gas → 2D liquid transition. At low lubricant thicknesses, the density of polymer chains is such that very little lateral interaction between chains is realized. We refer to the isolated lubricant chains in this thickness regime as the 2-dimensional polymer gas. Since $\xi_{1,1} \rightarrow 0$ for the 2D gas, the measured surface energy reflects the sum of the remaining three terms in equation 1, i.e. $\gamma_m(h)= \gamma_0(h) +\gamma_1(h) -\xi_{0,1}(h)$. As the surface coverage increases, those polymer end-groups not interacting strongly with the surface begin to interact cohesively with adjacent polymer end-groups and a coalescence into 2D liquid islands occurs. These lateral cohesive interactions being attractive, $\xi_{1,1} > 0$, contributes to the observed decrease in the surface energy with increasing coverage. As the amount of lubricant added to the surface increases, the average size of the liquid islands would increase. At coverages in excess of 50% (nominally 7 - 8 Å for Zdol 2000 on CHx), the surface of the PFPE lubricated disk would appear more like a series of lubricant voids (or alternatively a series of bare carbon islands) as compared to discrete lubricant islands. The nature of the cohesive interactions leading to the observed lubricant coalescence are most likely due to hydrogen-bonding between the end-groups of neighboring

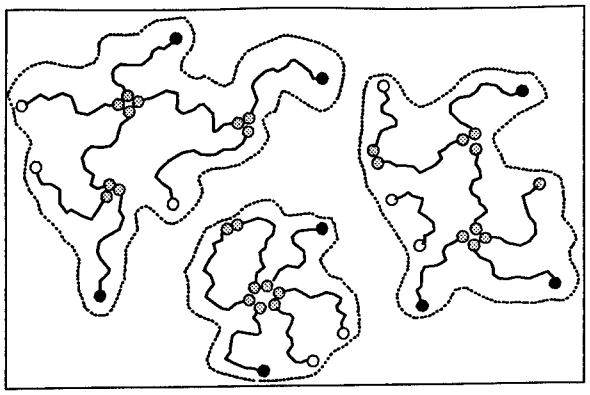

Figure 4. Proposed structure for the functionalized Fomblin Z domains on CHx. (⊙) Lubricant end-groups interacting via cohesive hydrogen-bonding, (●) end-goups interacting with the CHx surface active sites, and (○) non-interacting end-groups.

lubricant polymers. A schematic representation of the proposed structure of the lubricant domains on CHx is shown in Figure 4 for the case of Zdiac. Analogous structuring driven by hydrogen-bonding interactions have been observed in bulk Zdiac,[7,8] and in thin films of fluorinated carboxylic acids.[9] In regards to the AM3001 lubricant, a similar local maximum corresponding to the 2D gas - 2D liquid transition was not observed. We note, however, that the relatively low polarity of the AM3001 end-groups makes observation of this 2D Gas - 2D liquid transition difficult to ascertain in our measurements.

In addition to the lateral, in-plane, cohesive interactions between lubricant end-groups, attractive adhesive interactions between the end-groups and the active adsorption sites on the CHx surface, $\xi_{0,1} > 0$, could also contribute to the observed decrease in the surface energy with increasing lubricant thickness in the monolayer thickness regime. The adhesion between the lubricant end-groups and the carbon surface could result from hydrogen-bonding interactions. In the specific case of Zdol on CHx, hydrogen-bonding between the -OH end-group and the hydroxyl/carboxyl surface sites is possible. Since the interaction strength of the Zdol -OH end-group with the carbon hydroxyl active site would be comparable to the cohesive hydrogen-bonding between hydroxyl end-groups of neighboring polymer chains, it is not clear that these interactions would lead to the observed surface energy minimum. We believe the dominant interactions likely involve adhesive interactions between the Zdol end-groups and carboxyl active sites on the carbon surface. Previously published work on CHx surfaces comparable to those utilized in this work report the density of carboxyl groups on the carbon surface to be at least twice that of the hydroxyl groups.[10,11] This together with the fact that the interaction strength of the hydroxyl/carboxyl hydrogen bond is typically much greater than that of the hydroxyl/hydroxyl hydrogen bond strongly suggests that the adhesive interactions of Zdol with CHx involve the surface carboxyl moieties.

Evidence supporting the assertion that the carboxyl surface sites are responsible for the strong adhesion is obtained from annealing the Zdol + carbon surface. Upon exposing either the Zdol/CHx or the Zdol/CNx system to elevated temperature, 100% of the lubricant applied at

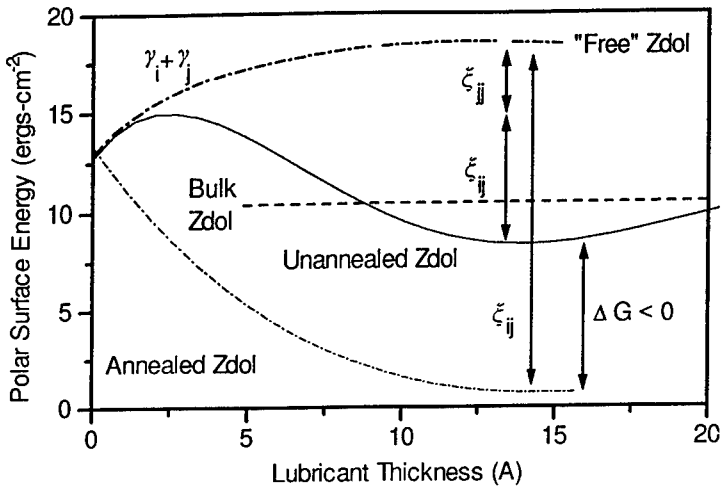

Figure 5. Adsorption energetics appropriate for the first monolayer of Zdol 2000 on CHx.

sub-monolayer coverages can be bonded to the disk surface. In Fig. 5, we compare the surface energies for the annealed vs unannealed Zdol 2000 on CHx,[6] and the qualitative estimate of $\gamma_i + \gamma_j$ based on the data of Fig. 2. Annealing the Zdol/CHx system results in a dramatic decrease in the surface energy. We intrepret the surface energy decrease to be reflective of an increase in the adhesive interaction strength between the lubricant end-groups and the active adsorption sites on the CHx surface. The relatively apolar nature of the annealed Zdol/CHx interface implies that both hydroxyl end-groups of Zdol interact strongly with the carbon surface. Finally, we note that the minimum in the unannealed case is correlated quantitatively (within 1 - 2 Å) with the maximum thickness of Zdol that can be bonded to the surface. We thus interpret the appearance of the 1st local minimum in the Zdol 2000/CHx surface energy vs Zdol thickness at nominally 13 ± 2 Å to result from a fraction of hydroxyl end-groupsbonding to the surface active sites. The fact that at room temperature only 35 - 40 % of the first monolyaer interacts strongly with the surface active sites results from the presence of an activation energy barrier to the formation of these strongly-attractive interactions. The activation energy determined for formation of these Zdol/CHx interactions is 4.3 ± 0.5 kcal-mole^{-1} independent of the Zdol MW employed.[1,2] On the CNx surface a similar activation energy of 5.0 ± 0.5 kcal-mole^{-1} was found.[3] These values are consistent with our hypothesis that at room temperature the lubricant film on the surface consists of a hydrogen-bonded network and breaking of the hydrogen-bonding is required prior to formation of the stronger adhesive interactions with the surface. We note that the hydrogen-bonded lubricant network will become increasingly unstable at elevated temperatures since formation of the adhesive bond to the carbon surface is stronger than the cohesive hydrogen-bonding within the layer, and hence thermodynamically favored.

Upon examination of Fig. 3, the position of the first surface energy minimum for Zdiac (18 ±2 Å) occurs at a greater thickness than that for Zdol (13 ± 2 Å) for comparable molecular weights. We believe this reflects the ability of Zdiac to adhere strongly to polar sites on the CHx surface which are inaccessible to Zdol. In particular, interaction of Zdiac with the hydroxyl sites

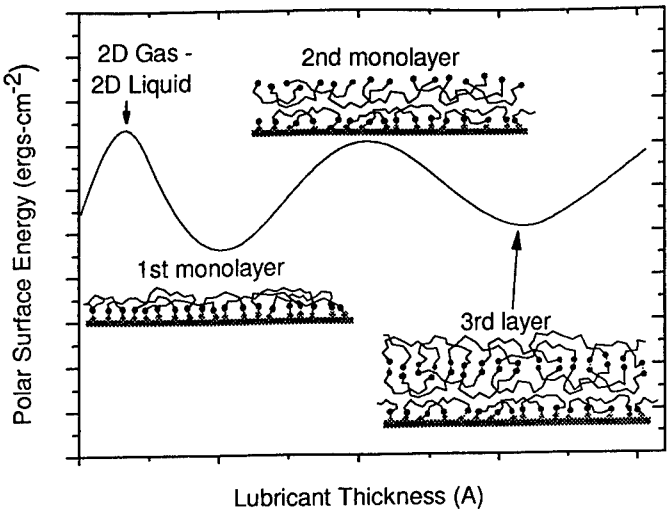

Figure 6. Idealized structures and corresponding surface energies of the Functionalized Fomblin Z lubricants vs applied lubricant thickness in the multilayer thickness regime.

on CHx is possible. However, since the hydrogen-bonding interaction between Zdiac end-groups would be energetically favored over the hydrogen-bonding of the Zdiac end-group to a hydroxyl surface site, our results suggest that chemisorption of Zdiac on CHx occurs via an esterification reaction. The shift in the 1st surface energy minimum of Zdiac compared to Zdol of nominally 5 - 6$\AA$ is then consistent with the ratio of carboxyl to hydroxyl content on the surface of approximately 2:1 as previously reported.[10,11] On the basis of the arguments given above, we propose that the 1st monolayer of Zdol and Zdiac on CHx is characterized by a fraction of the end-groups chemisorbed to the surface with cohesive hydrogen-bonding interactions occuring between many of the remaining end-groups.

Addition of lubricant to the carbon overcoated disk in excess of one monolayer initially results in an increase in the measured surface energy. Since the carbon surface is now inaccessible to lubricant end-groups, the strongly-attractive, adhesive interations with the surface responsible for the first surface energy minimum ($\xi_{0,1}$) are no longer possible. Intuitively one might expect the magnitude of the surface energy to approach that of the bulk lubricant once the CHx surface was completely covered. However, we observe the surface energy to increase to levels greater than that of the bulk lubricant. This is shown in Fig. 2 for the case of Zdol on CNx, and in Fig. 3 for Zdol and Zdiac on CHx. Figure 6 is representative of the thickness dependence of the polar surface energies measured in the multilayer thickness regime for the functionalized Fomblin Z lubricants. Included in Figure 6 are schematic depictions of the multilayer structures proposed to account for the corresponding surface energy maxima and minima. The oscillatory surface energies imply that the magnitude of $\xi_{jj} + \xi_{ij}$ is monolayer dependent, first decreasing in the 2nd monolayer (increasing surface energy) and then increasing again in the 3rd monolayer. While the in-plane cohesive interactions in the 2nd and 3rd monolayers may not differ substantially from that characteristic of the 1st monolayer, the magnitude of the interlayer interaction density, ξ_{ij}, is

dependent on the microscopic structure of the individual monolayers. In the first lubricant monolayer, 35 - 40 % of the end-groups are interacting strongly with the carbon surface via adhesive interactions.[1,2] These end-groups are therefore unavailable to interact with the lubricant end-groups of the 2nd monolayer. As a consequence of the preferential ordering of the end-groups of the 1st PFPE monolayer towards the CHx surface, a degree of ordering is imparted to the second monolayer, where a relative excess in the number of "free" hydroxyl groups at the lubricant-air interface results. The relatively high density of non-interacting hydroxyl groups in the second monolayer results in the increased surface energy associated with the 2nd monolayer. Finally, addition of the 3rd lubricant monolayer again leads to a decrease in the surface energy. The second local minimum in the surface energy is attributable to an increase in the density of attractive, interlayer interactions between the excess lubricant end-groups of the 2nd monolayer with the end groups of the third monolayer. Consequently, the structure of these functionalized Fomblin Z films orthogonal to the surface plane are also ordered.

CONCLUSIONS

Surface energy measurements are reported for a number of PFPE lubricant/carbon combinations as a function of applied lubricant thickness. The dispersive surface energy measurements are shown to be useful in determining the extent of lubricant coverage of the underlying substrate. Lubricant thicknesses corresponding to full surface coverage are strongly dependent on the number of functional end-groups in the PFPE structure. The polar surface energy measurements provide evidence for the formation of 2D structures during the formation of the first monolayer. Formation of layered structures in the z-dimension are obseved for Zdiac on CHx, and Zdol on both CHx and CNx. Both ordering phenomena are thermodynamically driven by the decrease in surface energy that results from the attractive interactions that characterize these structures.

ACKNOWLEDGMENTS

We gratefully acknowledge J. Castenada for lubricating the disks studied in this work.

REFERENCES

1. R.J. Waltman, and G.W. Tyndall, *J. Phys. Chem.*, submitted (1998).
2. R.J. Waltman, and G.W. Tyndall, *J. Phys. Chem.*, submitted (1998).
3. G.W. Tyndall, R.J. Waltman, and D. Pocker, Langmuir, *submitted* (1998).
4. A.W. Adamson, Physical Chemistry of Surfaces, 5th ed., John Wiley and Sons, NY, (1990).
5. R.J. Good, M.K. Chaudhury, and C.J. van Oss, Fundamentals of Adhesion, ed. L.-H Lee, Plenum Press, New York (1991) pg. 153.
6. R.J. Waltman, D.J. Pocker, and G.W. Tyndall, *Trib. Lett.*, accepted (1998).
7. P. H. Kasai, *J. Appl. Polym. Sci.*, **57**, 797 (1995).
8. V. Doan, R. Koppe, and P. H. Kasai, *J. Am. Chem. Soc.*, **119**, 9810 (1997).
9. T. Kato, M. Kameyama, M. Ehara, and K. Iimura, Langmuir, 14, 1786 (1998).
10. J. Ruhe, G. Blackman, V.J. Novotny, T. Clarke, G.B. Street, and S. Kuan, *J. Appl. Polym. Sci.*, **53**, 825 (1994).
11.R.-H. Wang, R.L. White, S.W. Meeks, B.G. Min, A. Kellock, A. Homola, and D. Yoon, *IEEE Trans. Magn.*, **32**, 3777 (1996).

STUDY OF HARD DISK AND SLIDER SURFACES USING X-RAY PHOTOEMISSION ELECTRON MICROSCOPY AND NEAR EDGE X-RAY ABSORPTION FINE STRUCTURE SPECTROSCOPY

SIMONE ANDERS[1], THOMAS STAMMLER[1], C. SINGH BHATIA[2], JOACHIM STÖHR[3], WALTON FONG[4], CHAO-YUAN CHEN[4], and DAVID B. BOGY[4]
[1]Lawrence Berkeley National Laboratory, 1 Cyclotron Road, Berkeley, CA 94720, SAnders@lbl.gov
[2]SSD/IBM, 5600 Cottle Road, San Jose, CA 95193
[3]IBM Research Division, Almaden Research Center, 650 Harry Road, San Jose, CA 95120
[4]Computer Mechanics Laboratory, Dept. of Mechanical Engineering, University of California at Berkeley, Berkeley, CA 94720

ABSTRACT

X-ray Photo Emission Electron Microscopy (X-PEEM) and Near Edge X-ray Absorption Fine Structure (NEXAFS) spectroscopy were applied to study the properties of amorphous hard carbon overcoats on disks and sliders, and the properties of the lubricant. The modification of lubricants after performing thermal desorption studies was measured by NEXAFS, and the results are compared to thermal desorption data. The study of lubricant degradation in wear tracks is described. Sliders were investigated before and after wear test, and the modification of the slider coating as well as the transfer of lubricant to the slider was studied. The studies show that the lubricant is altered chemically during the wear. Fluorine is removed and carboxyl groups are formed.

INTRODUCTION

X-ray Photo Emission Electron Microscopy (X-PEEM) and Near Edge X-ray Absorption Fine Structure (NEXAFS) spectroscopy are two modern analysis methods based on the availability of tunable X-ray radiation produced by a synchrotron. X-PEEM combines high spatial resolution with the ability to obtain local NEXAFS spectra. NEXAFS yields information about the elemental composition and bonding structure of the elements in the sample, and orientation of molecules (if a preferred orientation is present). All this information is obtained in a PEEM with submicron resolution, in addition to topological contrast which is present in a PEEM also. NEXAFS as measured by electron yield detection is surface sensitive, the probing depth is 2-10 nm depending on the material. But due to its elemental specificity, PEEM can also study buried layers of different materials if the top layer is not thicker than the electron escape depth.

Both methods have been applied to study the tribological behavior of the head/disk interface of magnetic storage devices. For storage devices with increasingly smaller spacing between slider and disk, approaching pseudo-contact and contact-recording, the tribochemical properties of the system consisting of the carbon overcoat of the disk, the lubricant, and the slider surface (carbon coated or uncoated) become more and more important. PEEM is a suitable tool to study these processes due to the sensitivity of NEXAFS to chemical changes. In this paper we describe the investigation of disk and slider surfaces before and after thermal desorption tests and wear tests using PEEM and NEXAFS.

Mat. Res. Soc. Symp. Proc. Vol. 517 © 1998 Materials Research Society

EXPERIMENTAL

Experiments have been performed at the undulator beamline 8.0 of the synchrotron radiation facility Advanced Light Source (ALS) in Berkeley. This beamline is equipped with a monochromator with three different gratings covering the energy range of 200-1500 eV with a spectral resolving power $\Delta E/E$ of about 5000 for the present study. The monochromatized X-rays are focused by a Kirkpatrick-Baez pair of mirrors into a 200 μm diameter spot on the sample. The PEEM working principle is based on the electron emission caused by the X-ray illumination of the sample which is proportional to the X-ray absorption. The absorption is a function of the elemental and chemical state of the sample and the X-ray wavelength. An electron optical column forms an image of the emitted electrons. It is possible to obtain locally resolved NEXAFS spectra with a resolution given by the resolution of the electron optics by tuning the X-rays through the absorption edge of the element of interest and taking images at incrementally increased photon energy. The resolution of the electron optics is about 200 nm for the experiments described in this paper. The microscope is a two-lens system operating at a nominal voltage of 10 kV, and it is described in detail elsewhere [1]. For the present studies we used the microscope without an energy filter.

RESULTS AND DISCUSSION

Studies of hard disks exposed to thermal desorption experiments

Samples from disks which were coated with 7.5 nm sputter deposited, nitrogenated amorphous hard carbon (CN_x) and lubricated with 0.85 nm perfluoropolyether (Z-dol) were exposed to a thermal desorption experiment. They were heated in UHV (base pressure $<10^{-6}$ Pa) up to 425°C in 10 min. The desorbed gaseous products were measured using a quadrupole mass spectrometer to determine the processes leading to the degradation of the lubricant due to thermal effects. These results will be published in a separate paper. We have studied the disks before and after the thermal desorption experiments using (not spatially resolved) NEXAFS spectroscopy in the total electron yield detection mode.

Figures 1, 2 and 3 show the carbon K edge, fluorine K edge, and nitrogen K edge spectra before and after heating of the disk samples. The spectra were normalized to the incident X-ray flux so that their relative intensity reflects the relative amount of the corresponding element on the surface of the disk. The probing depth of total yield NEXAFS is given by the electron escape depth, which is about 10 nm for carbon [2]. It can be seen in Figure 1 that the peaks which are characteristic for C=C π^* bonds at 285eV and σ bonds (broad peak around 300 eV) as well as the C=N peak around 286.2eV [3] and the C=O peak around 288.1eV [2] are not influenced by the heat treatment.

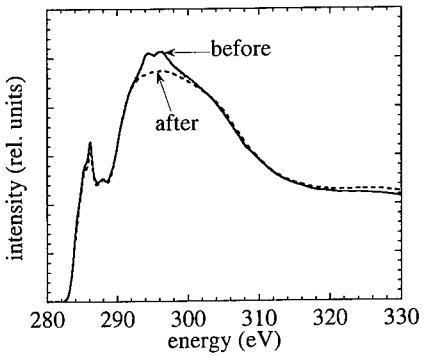

Figure 1: Carbon K edge NEXAFS spectrum of hard disks before and after thermal desorption experiments.

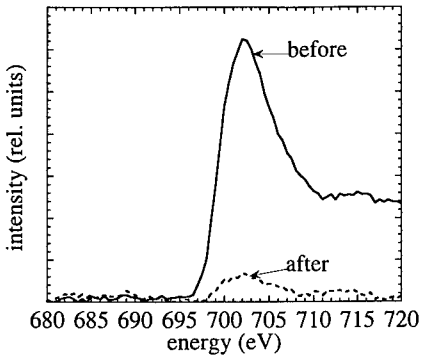

Figure 2: Fluorine K edge NEXAFS spectrum of hard disks before and after thermal desorption experiments.

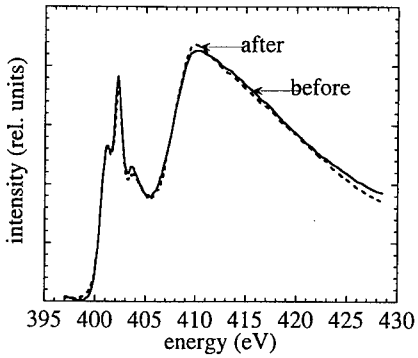

Figure 3: Nitrogen K edge NEXAFS spectrum of hard disks before and after thermal desorption experiments.

The peaks at 294.5eV and 296.3eV, which are C-F bonds [4, 5], practically disappear after the heating. The nitrogen spectra (Fig. 3) show no significant difference within the accuracy of the measurements, but the fluorine signal (Fig. 2) is reduced to 10% of its original value by the heating. The data indicate that the CNx film is not modified in structure and composition by the heating, but 90% of the fluorine from the lubricant has been removed. This is in good agreement to FTIR measurements that were performed before and after the heating to determine the thickness of the lubricant, which showed a thickness of 0.85 nm before and 0.08 nm after heating.

Study of wear tracks on disks

Supersmooth disks were coated with 5 nm cathodic arc deposited amorphous hard carbon and lubricated with 0.85 nm perfluoropolyether (Z-dol). They were used in a tribochamber wear test. The tribochamber is equipped with a spindle in UHV (base pressure $< 10^{-6}$ Pa) and a quadrupole mass spectrometer to measure the erosion products during the wear test. The disks were worn in a continuous drag test with 50% negative-pressure sliders at a speed of 0.2 m/s and a load of 30 mN. Two kinds of sliders were used: uncoated sliders (Al_2O_3/TiC) and sliders coated with sputter deposited CH_x. After the wear test the disks were studied using the PEEM microscope.

Fig. 4a shows a PEEM image of the edge of the wear track. The scratch is caused by one of the rails of the slider. The image was taken at a photon energy of 280 eV which is below the carbon K edge, therefore the image contrast is mainly topological. Local NEXAFS spectra were taken in the undamaged area of the disk, at the edge of the wear track caused by the rail, and in the area between the rails. Fig. 4b shows the carbon K edge spectra and Fig. 4c the fluorine K edge spectra.

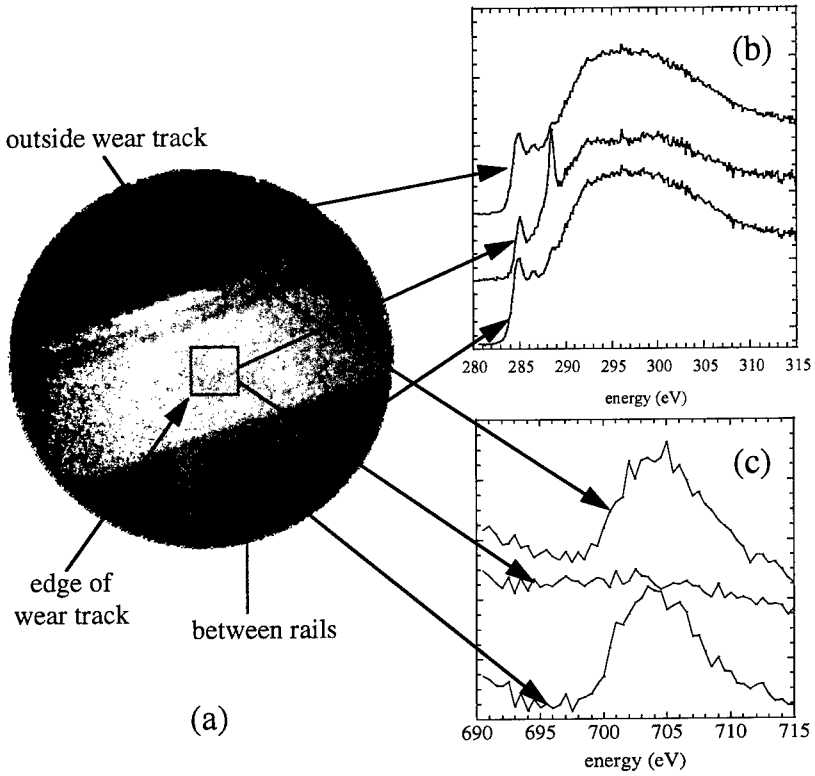

Figure 4: (a) PEEM image of the edge of a wear track taken at a photon energy of 280 eV. The field of view is 150 μm. (b) Local carbon K edge NEXAFS spectra of indicated areas. (c) Local fluorine K edge NEXAFS spectra of indicated areas.

The spectra show that the carbon overcoat/lubricant are identical in the undamaged area and between the rails. At the edge of the wear track in the scratch caused by one of the rails the fluorine is almost completely removed and the carbon spectrum shows a new peak at 288.5eV which can be attributed to the formation of carboxylic bonds [2]. The formation of these bonds was not observed for an analogue experiment using an unlubricated disks. In this case we found that the carbon overcoat thickness was reduced but the structure of the overcoat was not modified. A comparison of the tracks created by the coated and uncoated sliders showed that the modification of the lubricant and the formation of carboxyl bonds is stronger for the uncoated slider than for the coated slider. This is in agreement with the fact that the Al_2O_3/TiC material of the uncoated slider surface leads to catalytic reactions which decompose the lubricant faster than interactions which occur at the interface between the lubricant and the carbon coated slider [6].

Study of slider surfaces

The sliders which were used to wear the disks in the tribochamber for the experiments described above were also investigated using the PEEM microscope. Figure 5 shows the PEEM image of a scratch found on one of the rails of an uncoated slider after the wear test. The image is taken at 280 eV below the carbon K edge and shows therefore mainly topological contrast. Figures 6-8 show the local NEXAFS spectra at the carbon K edge, the oxygen K edge, and the titanium $L_{2,3}$ edge taken in the scratch and outside the scratch.

Figure 5: PEEM image of a scratch on one of the rails on the uncoated slider. Image taken at 280 eV, field of view 150 µm.

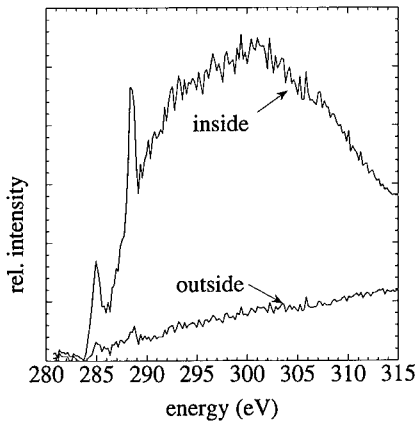

Figure 6: Local carbon K edge NEXAFS spectra inside and outside the scratch.

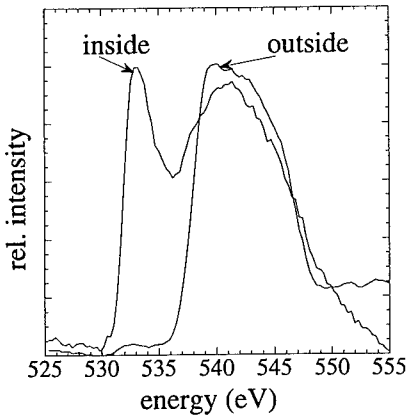

Figure 7: Local oxygen K edge NEXAFS spectra inside and outside the scratch.

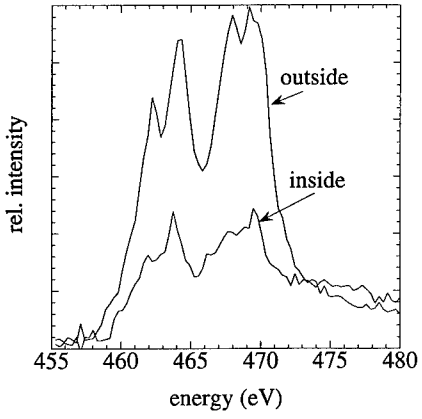

Figure 8: Local titanium $L_{2,3}$ edge NEXAFS spectra inside and outside the scratch.

The carbon spectra show basically no carbon on the undisturbed slider surface but a strong signal in the scratch. The spectrum is very similar to the one observed at the edge of the wear track on the disk (Fig. 4b). The oxygen spectrum outside the scratch shows one peak probably connected to the Al_2O_3 of the slider material, but a strong, sharp additional peak around 539 eV appears inside the scratch that can be correlated to the presence of carboxyl bonds [2]. The titanium signal is much weaker in the scratch indicating that some material has been deposited on the surface. All these data led us to conclude that material has been transferred from the disk to the slider, and this material is the same as the material at the edge of the wear track. It is probably some form of degraded lubricant which is formed during the drag test.

On the coated slider we found undamaged CH_x in most of the areas. We observed the same kind of carbon K edge spectrum with the additional peak around 288.5eV in scratches of the uncoated and coated sliders, and at the edges of the wear tracks of the disks.

CONCLUSIONS

The experiments which are presented here demonstrate that NEXAFS and PEEM are useful tools in studying the head/disk interface. Due to the elemental and bonding specificity it is possible to detect changes in the elemental composition and bonding structure of disk and slider surfaces with a high spatial resolution.

The heating of disks lubricated with perfluoropolyether (Z-dol) up to 425°C in 10 min. does not change the CN_x structure and elemental composition, but 90% of the lubricant is removed during this process.

Wear of disks lubricated with perfluoropolyether leads to a strong reduction of the fluorine content in the worn areas and to the formation of new carboxyl bonds. The formation of these bonds is not observed on unlubricated disks. Degraded lubricant showing the carboxyl peak in the carbon K edge spectrum was transferred from the disk to the sliders and accumulated in scratches of coated and uncoated sliders.

ACKNOWLEDGMENTS

The authors wish to acknowledge the National Storage Industry Consortium (NSIC) for its support of this work. Part of this work was supported by the Computer Mechanics Laboratory, University of California at Berkeley. Another portion of this work was supported by the U.S. Department of Energy, Division of Advanced Energy Projects, under contract No. DE-AC03-76SF00098.

REFERENCES

[1] B. P. Tonner, D. Dunham, T. Droubay, and M. Pauli, J. Electron Spectrosc. Relat. Phenom. **84** (1997) 211.
[2] J. Stöhr, NEXAFS Spectroscopy, Springer Verlag, New York, 1992.
[3] B. Holloway, Thesis, 1997.
[4] Ch. Ziegler, Th. Schedel-Niedrig, G. Beamson, D. T. Clark, W. R. Salaneck, H. Sotobayashi, and A. M. Bradshaw, Langmuir **10** (1994) 4399.
[5] T. Ohta, K. Seki, T. Yokoyama, I. Morisada, and K. Edamatsu, Physica Scripta **41** (1990) 150.
[6] J. Wei, W. Fong, D. B. Bogy, and C. S. Bhatia, J. Tribology, submitted for publication.

CORROSION PROTECTION OF Cu, Fe, Mn AND Co SURFACES

J.E.E. BAGLIN, A.J. KELLOCK, T.T. BARDIN, T. KARIS and D. KECK
IBM Almaden Research Center, 650 Harry Rd., San Jose, CA 95120

ABSTRACT

The mechanisms and effectiveness of corrosion protection provided by thin ion-beam carbon coatings on Cu, Fe, Mn and Co are discussed. A thin (~ 10 Å) layer of protective carbon is produced on metal surfaces by ion-beam dissociation of adventitious or intentional hydrocarbon adsorbates. Below 200°C, oxidation is strongly inhibited, as is corrosion in a humid, sulphurous ambient. Above 200°C, the carbon layer may itself be destroyed by oxidation, due to catalytic action of the metal surface. Thicker PVD carbon (up to 60 Å) was not an effective corrosion barrier, even after ion irradiation. A technique for producing high integrity ion-beam carbon layers of high stability and durability is discussed.

INTRODUCTION

With the adoption of ever thinner carbon overcoats for higher magnetic density recording, the reliability of the overcoat for corrosion protection gains new importance. Also, in many other device applications, a dependable corrosion protection treatment for Cu, Fe, Mn, Co and other metals is needed.

We have previously described [1,2] the ability of ion-beam carbon to inhibit oxidation of Cu surfaces. The thin layer in question is formed by irradiation (e.g. 2×10^{16} He^+/cm^2 at ~ 2 MeV) of the metal surface following its exposure to room air. The energetic beam evidently serves two functions: (a) The ions dissociate C-H bonds in the adventitious adsorbate hydrocarbon layer, leaving about a monolayer of carbon on the metal surface. (b) The ions provide sufficient kinetic energy to mobilize the carbon, which seeks minimum energy sites on the Cu surface (in the case of Cu(111), the threefold hollow sites). It seems likely that the carbon then serves to block chemisorption of O_2 on the surface, thus inhibiting corrosion, as discussed in detail by van Kooten et al. [3]

In this paper, the technique is extended to protection against corrosion in a humid, sulphurous atmosphere, and to protection of the metals Fe, Mn and Co. The criteria for thermal stability of the carbon coating above 200°C in air are explored, and we discuss the future use of selected hydrocarbon precursors for creating more robust ion-beam carbon layers.

EXPERIMENTS

Fig. 1. shows RBS spectra from a sample of Cu (4000 Å) deposited by e-beam evaporation on a substrate of glassy carbon. The sample was air-exposed prior to a "standard" irradiation (2×10^{16} He^+/cm^2, 1.5 MeV, on one half of the area), and then oxidized in air at 170°C for 18 h. The spectrum shows a clean Cu surface profile for the region that was irradiated prior to heating in air, but growth of about 1800 Å of CuO_x in the unirradiated oxidized area.

Fig. 2 shows the results of a similar experiment in which the samples were exposed to an atmosphere of humid air over sulphur at 50°C for 2 weeks. While the irradiated sample showed no copper corrosion, the unirradiated surface (which had become black and rough) showed extensive attack by both sulphur and oxygen. The oxygen profile is clear in the RBS spectrum

Mat. Res. Soc. Symp. Proc. Vol. 517 © 1998 Materials Research Society

(Fig. 2(a)), while the sulphur profile would be mixed with the RBS signals from a Cr layer that was used for substrate adhesion. However, the sulphur contribution is clearly seen in the PIXE spectrum from the same sample (Fig. 2(b)).

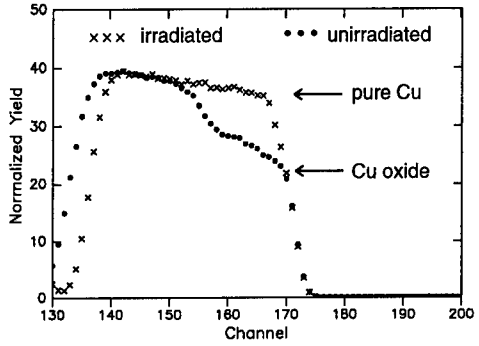

Fig.1: Protection of Cu against surface oxidation in air (170°C, 18 h). The RBS profile of Cu is abrupt, indicating little oxide for the irradiated region, while the untreated surface profile shows growth of 1800 Å of CuO_x.

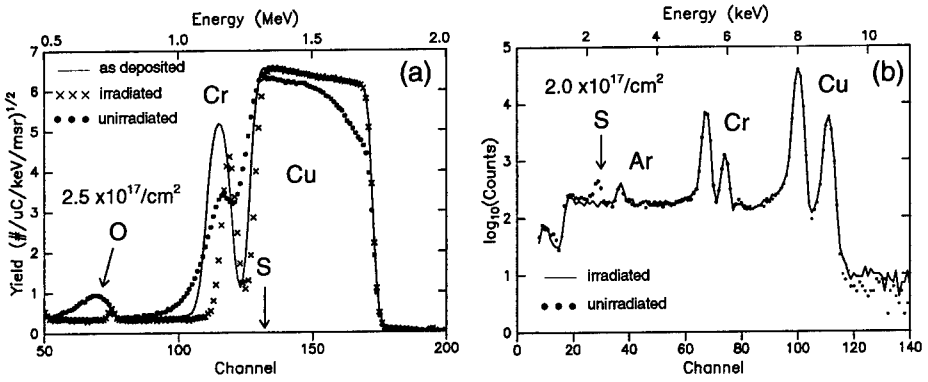

Fig.2: Corrosion protection of Cu exposed to an ambient of humid air over sulphur at 50°C for 2 weeks. Fig.2(a) compares RBS profiles for Cu (4000 Å)/Cr/glassy-carbon samples, as-deposited, and after heat treatment, for both irradiated and unirradiated areas. Extensive CuOx growth is indicated for the unirradiated surface. Fig.2(b) shows PIXE spectra from the same samples, where the sulphur peak appears exclusively for the unirradiated sample. (The corresponding sulphur signal is not separable in the RBS spectra.)

In order to develop substantial air oxidation for testing the protection of Fe, Mn and Co surfaces, these metals were exposed at 250°C for 18 - 24 h. (c.f. 170°C, 18 h for Cu). Again, half of each sample was irradiated with 2×10^{16} He^+/cm^2 at 2.3 MeV prior to oxidation. The results of these experiments are displayed in Fig. 3. We note that, in contrast to the case of Cu, the oxidation for these metals was substantially inhibited, but not totally stopped.

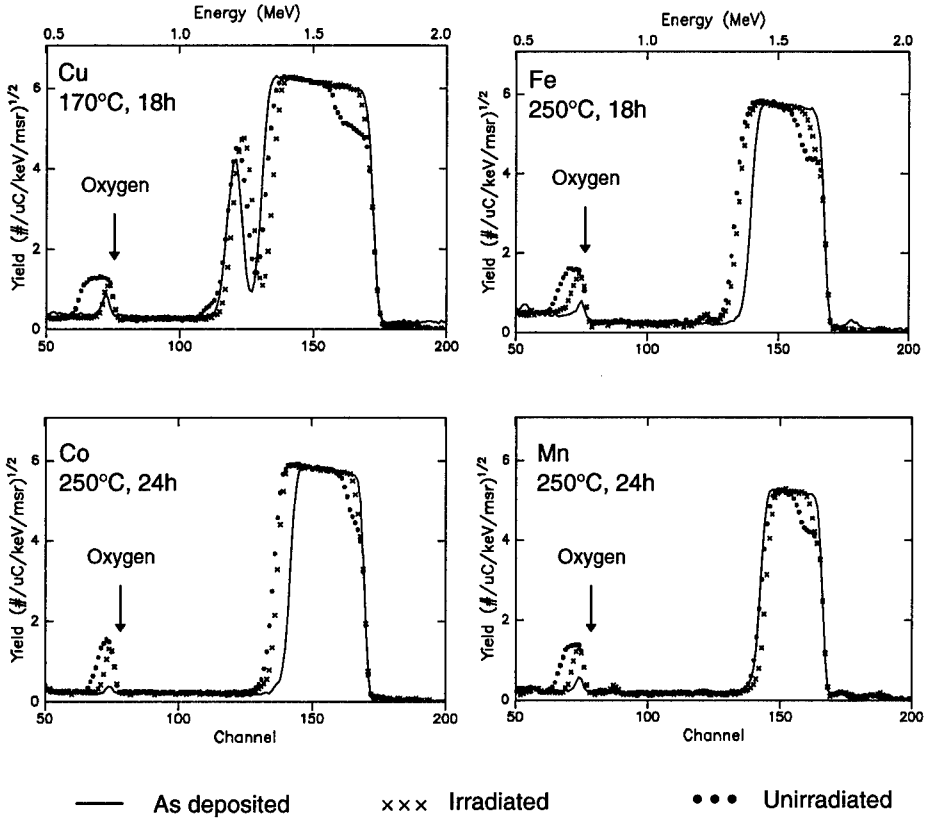

Fig. 3: Oxidation inhibition for Cu (170°C) and Fe, Mn and Co (250°C). RBS spectra show both metal and oxygen profiles, for samples (as-deposited), (irradiated + heated), and (unirradiated + heated).

The role of carbon added by the ion beam irradiation has been established [1] in a series of UHV experiments on Cu. It is further supported by the correlation of added carbon with observed corrosion protection for each of the cases Cu, Fe, Mn and Co, as shown in Fig. 4, in which the $^{12}C(p,p)$ resonance at 1.73 MeV was used to quantify the carbon on each surface before and after irradiation. In each case, a new layer of a few Å of carbon was found, in addition to carbon originating from the adventitious hydrocarbon adsorbate resident on all samples after air exposure. However, similar carbon analyses on the Fe, Mn and Co samples after oxidation at 250°C showed that the protective carbon itself had vanished. A subsequent consideration of the conclusions of ref. 4 leads us to infer that for temperatures over 200°C, blocking of the metal oxidation is not sufficient; total coverage must exclude O_2 from access to catalytic sites at the metal surface that will enable loss of the protective carbon layer itself due to oxidation.

In order to test whether carbon prepared by Physical Vapor Deposition (PVD) would provide an effective substitute for that formed by ion beam irradiation, a series of samples were prepared by deposition of Cu (2000 Å), followed in-situ by e-beam coating with amorphous carbon at

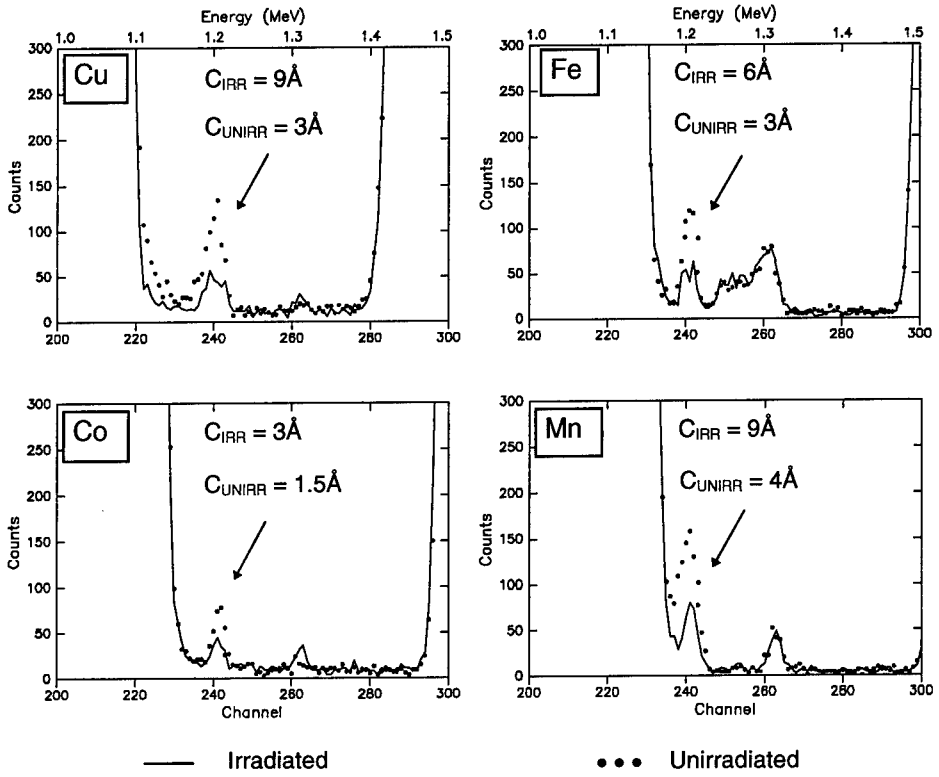

Fig. 4: Ion beam treatment adds surface carbon. Proton scattering spectra at 1.7 MeV show the resonance peak used to quantify surface carbon. The total carbon thickness is shown for samples before heat treatment. It includes, in all cases, the adventitious hydrocarbon adsorbate contribution.

various thicknesses. Half of each sample was then ion-irradiated, and all were oxidized in air at 170°C for 18 h. The amount of oxygen within each layer (an indication of the extent of corrosion) was then plotted as a function of the total thickness of carbon at the surface, as shown in Fig. 5.

From Fig. 5, it is evident that (a) irradiation of PVD amorphous carbon having no hydrocarbon precursor has made no improvement in its passivating ability; and (b) the deposited carbon layer becomes effective for preventing oxidation only for thicknesses exceeding 60 Å. By contrast, identical protection is achieved by < 9 Å of ion-beam carbon, as displayed by the single point on the Figure.

The precise nature of the bonding for ion-beam carbon is difficult to determine with certainty. Some indication of a good degree of order, possibly with a substantial sp^3 component, is provided by the comparison of Raman scattering spectra obtained for ion-beam carbon coatings of thickness 11 Å and 48 Å, with the spectra from a standard carbon (CH_x) overcoat in commercial

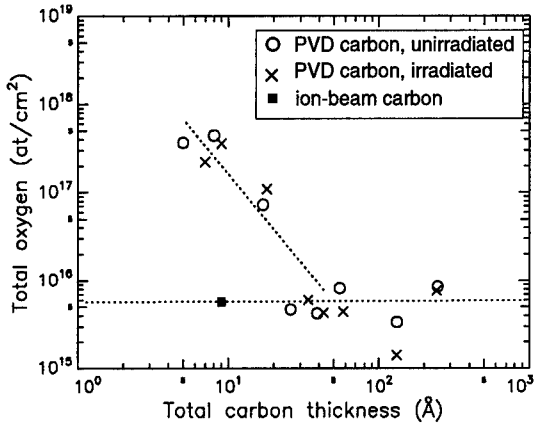

Fig. 5: Comparison of oxidation protection provided for Cu (170°C) by ion-beam carbon and PVD carbon, both with and without ion irradiation. 60 Å of PVD carbon is needed to match the performance of < 9 Å of ion-beam carbon.

use for head-disk assemblies, and with spectra from PVD carbon coats before and after irradiation. These are displayed in Fig. 6.

The thin (11Å) ion-beam carbon shows a dominant G ("graphitic") order peak, which is characteristically depleted relative to the D ("disorder") peak when the layer is thicker (48 Å). Both have G/D ratios and G-band wavenumbers very similar to those for the "hard" carbon disk overcoat. In contrast, the e-beam carbon has a low G/D ratio, that hardly changes after irradiation.

DISCUSSION

It has been reported by D. H. Lee et al.[5-7] that ion irradiation of amorphous carbon films, either at low temperatures (-100°C) or at very high beam current densities, can produce diamond-like carbon having very high hardness and wear performance. These conditions remain to be tested for the present experiment. However, it is tempting to speculate that the creation of ordered bonding in the ion-beam carbon layers may arise partly in consequence of the presence of hydrogen at dissociation sites where displaced carbon atoms are mobile and new bond configurations may be formed. With this in mind, we now plan to extend the process of ion-beam carbon film growth to include the use of selected specific precursor hydrocarbon adsorbates (e.g. pentene) that will provide a fully controllable process (independent of adventitious layers), and allow construction of ion-beam carbon coatings of arbitrary thickness, sufficient not only to effect site-blocking at the metal surface, but also to assure the stability of the carbon layer itself at temperatures above 200°C.

ACKNOWLEDGEMENTS

The authors wish to thank Wade Tang for his Raman scattering measurements and helpful discussions.

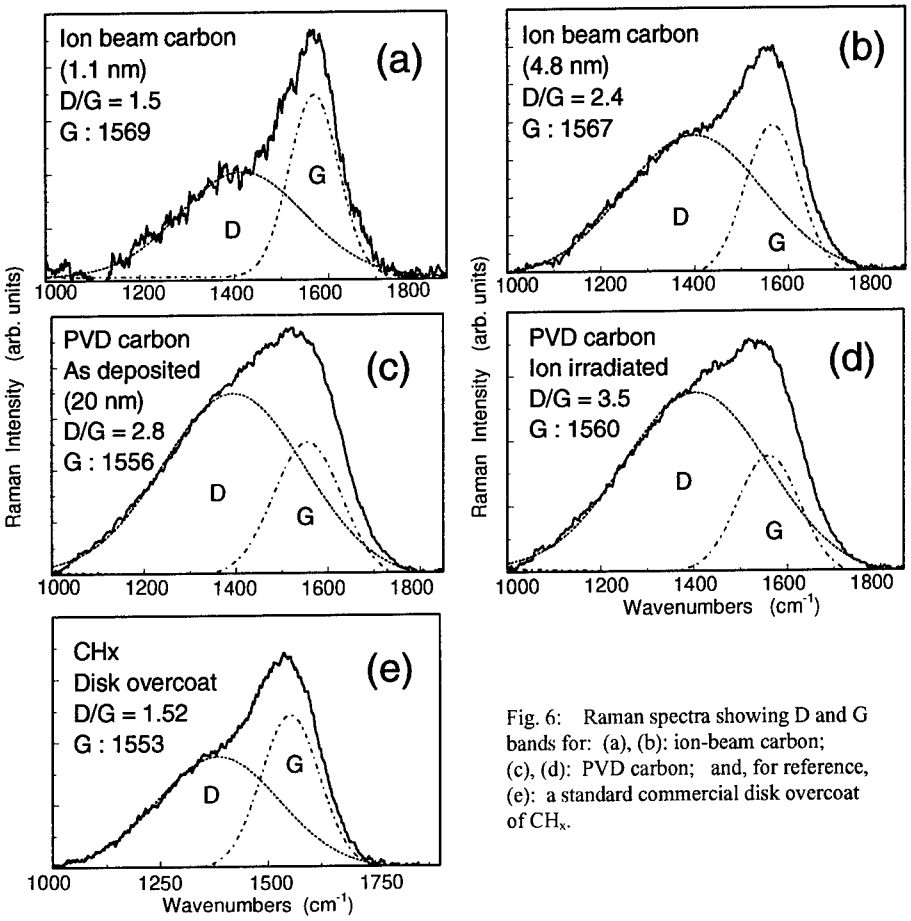

Fig. 6: Raman spectra showing D and G bands for: (a), (b): ion-beam carbon; (c), (d): PVD carbon; and, for reference, (e): a standard commercial disk overcoat of CH_x.

REFERENCES

1. A.J. Kellock, M.H. Tabacniks, J.E.E. Baglin, N.S. Somcio, T.T. Bardin and D.C. Miller, Nucl. Instrum. and Methods **B127/128,** 742 (1997).
2. J.E.E. Baglin, M.H. Tabacniks, A.J. Kellock, N.S. Somcio and T.T. Bardin, Mater. Sci. Forum **248-249**, 155 (1997), (Trans Tech Publishers, Zurich).
3. W.E.J. van Kooten, O.L.J. Gijzeman and J.W. Geus, Surf. Sci. **303,** 16 (1994).
4. W.E.J. van Kooten, D.D. Kragten, O.L.J. Gijzeman and J.W. Geus, Surf. Sci. **290,** 302 (1993).
5. D.H. Lee, B. Park, D.B. Poker, L. Riester, Z.C. Feng and J.E.E. Baglin, J. Appl. Phys. **80,** 1480 (1996).
6. D.H. Lee, H.J. Lee and B. Park, J. Mater. Res. **12**, 2057 (1997).
7. Lee, H.J. Lee, B. Park, D.B. Poker and L. Riester, Appl. Phys. Lett. **70**, 3104 (1997).

A METHOD FOR LASER ZONE TEXTURING OF GLASS BASED MAGNETIC MEDIA USING Nd:YAG LASERS

M. P. Rosenblum *, C. A. Ross **
* Komag Inc., 1704 Automation Parkway, San Jose, CA 95131
** Massachusetts Institute of Technology, Department of Materials Science and Engineering, Cambridge, MA 02139

ABSTRACT

Laser zone texturing of nickel-plated, aluminum based magnetic media has become a preferred method of providing a precisely controlled head landing zone. The Nd:YAG lasers used for this process are not suitable for directly texturing glass substrates. A novel method has been developed which allows the use of the existing Nd:YAG laser systems to zone texture glass based magnetic media.

An amorphous sputtered film of a non-magnetic Ni alloy provides a texturing layer which absorbs the laser pulse and controllably forms regular, small protrusions. Optimization of the alloy composition results in small cone-shaped bumps. Laser power sensitivity exhibits a region of invariance for a range of film thickness. This behavior provides a wide margin for manufacture by reducing the effect of thickness variation on laser bump height.

Disks fabricated using this form of laser zone texture exhibit excellent tribology performance. TEM images show the Ni alloy to be amorphous and featureless. The sputtered film does not influence the properties of the subsequently sputter deposited isotropic magnetic films.

INTRODUCTION

In a magnetic hard disk drive during normal operation the read/write transducer, or head, flies above the rotating disk on an air bearing. The head, which is mounted on a suspension connected to an actuator, moves radially across the disk to locate one of a group of concentric recording tracks.

In the start-up and shut-down processes of the disk drive, the head comes into contact with the disk. When the rotation speed is below the level necessary to create an air bearing with sufficient stiffness, the head will slide along the surface of the disk. If the two contacting surfaces of the disk and head are smooth, a large frictional force will develop. In addition, once the head remains, for a period of time, in stationary contact with the disk, a significant static friction, or stiction, force may arise.

To reduce friction and stiction to acceptable levels in a disk drive, one solution is to controllably roughen, that is texture, the surface of the disk [1]. Initially, mechanical texturing using an abrasive was applied across the entire disk surface. Eventually, the requirements for a smoother surface at high recording densities caused the texturing to be limited to a restricted area or zone at the inner diameter of the disk. The head is restricted to land and take-off from within this zone.

Within the past several years, a new method for zone texturing hard disk media has become widely used [2, 3]. The technique, known as laser zone texturing, produces an array of

Mat. Res. Soc. Symp. Proc. Vol. 517 © 1998 Materials Research Society

consistent "bumps" in a precisely controlled location on the Ni-P plated aluminum substrate. The most common lasers in production use are high-repetition-rate Q-switched infrared lasers (Nd:YAG, Nd:YLF or Nd:YVO_4). These lasers provide stable pulses at high repetition rates. The results are production systems with good process control and high throughput.

These infrared lasers ($\lambda = 1064$ nm) are not suitable for direct use with glass or glass-ceramic substrates. A novel method was developed which allows the use of existing laser systems with alternate substrates such as glass and glass-ceramic. A sputtered film that coats the surface of the substrate provides a texturing layer that absorbs the laser pulse and controllably forms regular, small bumps. Disks fabricated using this form of zone texture exhibit low friction and stiction values, even after many tens of thousands of continuous start-stop (CSS) cycles.

EXPERIMENT

Alloys of nickel and niobium were chosen for investigation because they form non-magnetic amorphous films over a broad composition range when sputter deposited [4]. In addition, the amorphous films have reported glass transition temperatures above 400°C, which make them suitable for the subsequent sputtering of magnetic films at elevated process temperatures.

Films are deposited by dc magnetron sputtering onto polished alumino-silicate or boro-silicate glass substrates. The cathode power is kept constant at a level that results in a deposition rate of 40 Å per second. Thickness is controlled by sputter time. The argon gas pressure is 6.5 mTorr. (0.86 Pa).

Texturing is performed using Nd:YVO_4 lasers with pulse widths of 14 ns or 65 ns and spot sizes of 11 µm and 10 µm, respectively. Bump heights are measured using an optical interferometer microscope, MicroXam, manufactured by Phase Shift Inc.

The measurement of bump height as a function of laser power and its associated slope, the bump height sensitivity, is made by texturing individual tracks of bumps, each at a fixed laser power.

Continuous start-stop (CSS) testing is performed by configuring a spindle, a head and suspension assembly with a strain-gauge. The test sequence is to spin-up to operating speed, in this case 7200 rpm, maintain this speed for a short period, about 2 seconds, and then spin-down to a complete stop. The cycle is then repeated. For each cycle, the maximum static or dynamic friction is determined. The CSS graph is the plot of the maximum value for each cycle.

The time at which the head remains in static contact with the disk surface is a few seconds. However, at every 5,000th cycle (or at least four times during the test) the time of static contact is increased to 2 hours to assess the static friction after an extended parking duration.

RESULTS

When irradiated with suitable laser pulses, thin films of Ni-Nb on glass produce reproducible and uniform bumps. The shape of the bump is primarily conical. This compares with the crater (or ridge) and sombrero shapes that are formed on plated NiP/Al substrates. Cross-sections from optical interferometric imaging of the three shapes are shown in Figure 1.

The bump on Ni-Nb/glass does not conserve volume unlike the crater and sombrero bumps on NiP/Al. There may be some contribution to the bump height from the glass substrate

as a result of indirect heating. Laser bumps formed directly on glass using CO_2 laser pulses are also conical in shape and do not conserve volume [5]. The chemical resistance of the film prevented its selective etching (i.e., without also etching the glass substrate).

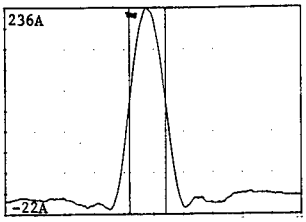

Figure 1a. Laser bump on $Ni_{50}Nb_{50}$ on glass. Peak height 236Å. FWHM 4.25 μm

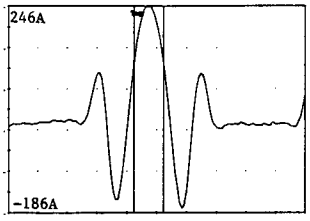

Figure 1b. Laser bump on NiP/Al. 14 ns pulse. Peak height 246Å. FWHM 3.5 μm

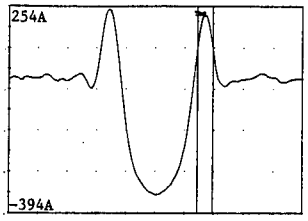

Figure 1c. Laser bump on NiP/Al. 65 ns pulse. Peak height 254Å. FWHM 1.9 μm

Bump heights for a 1300 Å film of $Ni_{50}Nb_{50}$ as a function of normalized laser pulse energy for pulse widths of 14 ns and 65 ns are shown in Figures 2 and 3, respectively.

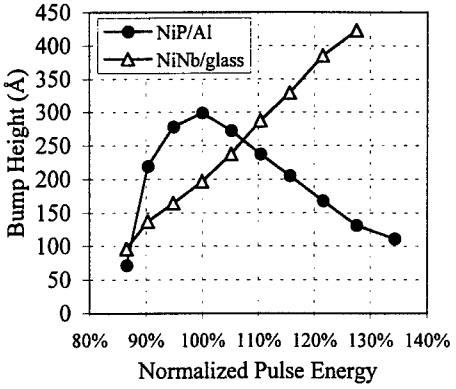

Figure 2. Power series for polished plated NiP/aluminum disk and 1300Å $Ni_{50}Nb_{50}$ on a glass disk. Laser pulse width is 14 ns. Spot size is 11 μm. 100% pulse energies are 1.34μJ and 0.67μJ for the NiP/Al and $Ni_{50}Nb_{50}$, respectively.

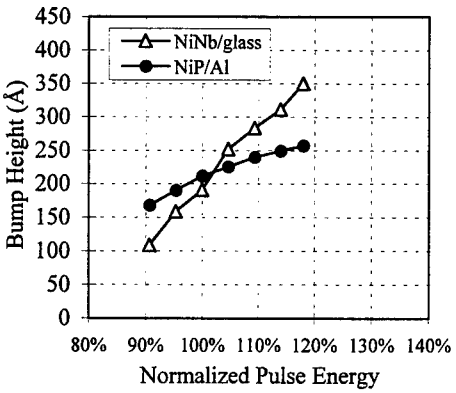

Figure 3. Power series for polished plated NiP/aluminum disk and 1300Å $Ni_{50}Nb_{50}$ on a glass disk. Laser pulse width is 65 ns. Spot size is 10 μm. 100% pulse energies are 1.2μJ and 0.96μJ for the NiP/Al and $Ni_{50}Nb_{50}$, respectively.

Bump heights for plated NiP/Al are shown for comparison. The shapes of the bumps on Ni-Nb are conical for both conditions, whereas the bumps on NiP/Al are sombrero shape for 14 ns pulses and crater shape at 65 ns. Formation of a central peak feature in Ni-Nb may result from forces other than chemicapillary, which has been proposed [6] for NiP/Al.

For practical application, the bump height sensitivity to laser power should be small enough so that fluctuations in the laser pulse energy do not result in unacceptable bump height

variation. In order to maintain an acceptable manufacturing tolerance, the bump height sensitivity should have a weak dependence on film thickness.

Both of these criteria are met with a $Ni_{50}Nb_{50}$ film thickness of 1300 Å. Bump height sensitivity is less than 10 Å for a one percent change in laser power. There is little variation in bump height sensitivity with film thickness as indicated in Table 1. Bump height sensitivity rises to greater than 20 Å for a one percent change in laser power for film thicknesses greater than 2000 Å.

Table 1. Bump height sensitivity at 150 to 200 Å bump height as a function of $Ni_{50}Nb_{50}$ film thickness. Laser pulse width is 65 ns.

Thickness (Å)	Sensitivity (Å / % laser power)
1000	3.4
1100	5.1
1200	6.5
1300	7.3
1500	6.6

To determine the uniformity of bump heights on a disk surface, 96 bumps on 12 tracks (two bumps in each of the four quadrants per track) were measured. The average bump height for this disk is 247 Å. The maximum and minimum bump heights are 263 Å and 214 Å. The standard deviation is 8.5 Å. These results are similar to those obtained on NiP/Al using the same laser tool.

To minimize stiction, it is desirable to reduce the bump diameter. Different compositions of Ni-Nb films were investigated. Alloy compositions with niobium content ranging from 16 to 60 atomic percent were studied. A plot of the bump width at the base of the bump as a function of niobium content is shown in Figure 4. There is a significant reduction in bump diameter for lower niobium content.

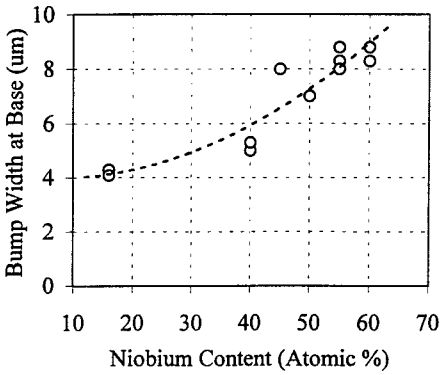

Figure 4. Bump width at base as a function of alloy composition. Bump heights are 400Å to 440Å for Nb content up to 50%. Maximum bump height is 245Å and 180Å for 55 at.% and 60 at.% Nb, respectively.

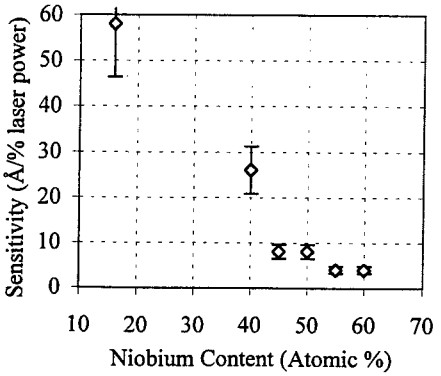

Figure 5. Bump height sensitivity as a function of alloy composition. Ni-Nb film thickness is 1300 Å. The slope of the bump height versus laser power curve is taken at a bump height of 150 - 200 Å. Laser pulse width is 65 ns.

The bump height sensitivity is also affected by niobium content. The plot in Figure 5 shows that the bump height sensitivity increases to unacceptable levels for niobium concentrations below 45 atomic percent.

Tribological performance of disks fabricated with laser texture of Ni-Nb on glass substrates is excellent. The result of 50,000 cycles of continuous start-stop testing using a conventional negative pressure slider is shown in Figure 6. Lube thickness is 36Å. Stiction values remain consistently low throughout.

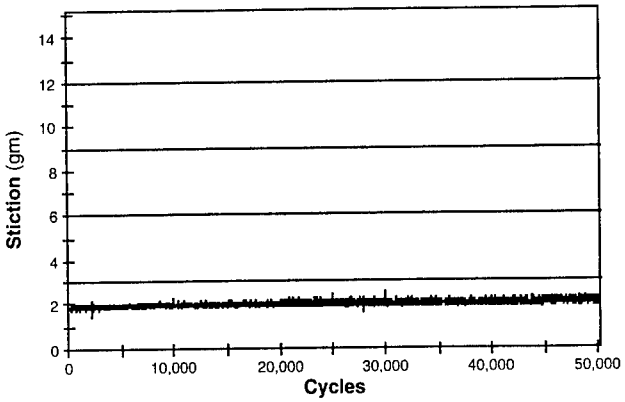

Figure 6. Continuous start-stop (CSS) test of finished disk with laser texture of $Ni_{50}Nb_{50}$ sputtered film. Bump height average is 170Å. Bump spacing is 60 μm circumferential and 30 μm radial.

Cross-section TEM, Figure 7, shows the Ni-Nb film to be smooth and featureless (no voids or columnar structure), consistent with a dense, amorphous film. The Ni-Nb film does not influence the properties or magnetic performance of the subsequently deposited CoCrPt film.

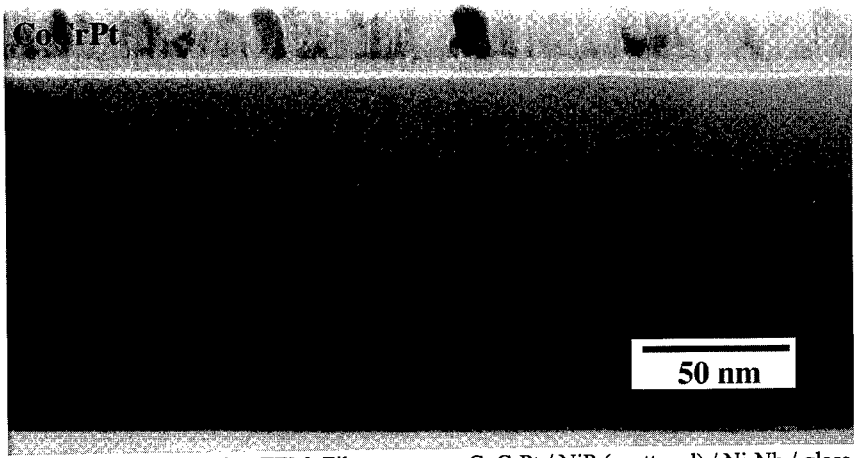

Figure 7. Cross-section TEM. Film structure: CoCrPt / NiP (sputtered) / Ni-Nb / glass

The exposure to atmosphere of the Ni-Nb layer for laser texture requires the use of a thin sputtered NiP layer deposited in-situ just prior to the CoCrPt. This provides for a fresh surface for improved nucleation of the magnetic layer.

CONCLUSION

A method has been developed which allows the use of conventional Q-switched infrared lasers to texture glass substrates. A sputtered thin film of nickel-niobium provides an absorption layer that generates regular, small conical shaped protrusions. Bump height sensitivity is in a range suitable for practical application, generating a narrow distribution of bump heights. Finished disks using this texture method exhibit excellent tribological performance. The texture layer has no influence on the subsequent deposition of the magnetic recording layer.

REFERENCES

1. B. Bhushan, Adv. Info. Storage Syst. **5**, 175 (1993).

2. R. Y. Ranjan, D. N. Lambeth, M. Tromel, P. Goglia, and Y. Li, J. Appl. Phys. **69**, 5745 (1991).

3. P. Baumgart, D. Krajnovich, T. Nguyen, and A. C. Tam, Data Storage **3**, (3), 21-27 (1996).

4. T. W. Barbee, Jr., W. H. Holmes, D. L. Keith and M. K. Pyzyna, Thin Solid Films **45**, 591 (1977).

5. E. Teng, W. Goh and A. Eltoukhy, IEEE Transactions on Magnetics **32**, 3759 (1996).

6. T. D. Bennett, D. J. Krajnovich, C. P. Grigoropoulos, P. Baumgart and A. C. Tam, ASME Proceedings of the 31st National Heat Transfer Conference, HTD-**323**, 159-169 (1996).

THE 1280 CM^{-1} ABSORPTION LINE IN AMORPHOUS HYDROGENATED BORON CARBIDE

SHU-HAN LIN and BERNARD J. FELDMAN
Department of Physics and the Center for Molecular Electronics, University of Missouri, St. Louis, MO 63121, C4840@jinx.umsl.edu

ABSTRACT

We report infrared absorption measurements that provide evidence for the presence of boron carbide icosahedra in amorphous hydrogenated boron carbide thin films. The infrared absorption spectra is dominated by an intense line at 1280 cm^{-1} with a FWHM of $\simeq$320 cm^{-1}. Similar lines have been previously reported in polycrystalline boron carbide, where boron carbide icosahedra make up the unit cell. In both systems, the linewidth narrows and the peak position shifts to higher energy with increasing carbon concentrations. From annealing studies of amorphous hydrogenated boron carbide, hydrogen plays a very small role in the 1280 cm^{-1} line. Finally, the integrated intensity of the 1280 cm^{-1} line is a sublinear function of the boron concentration, providing further evidence that the carbon concentration in these icosahedra increases as the carbon concentration of the film increases.

INTRODUCTION

Thin films of amorphous hydrogenated carbon (a-C:H) are now used in a large variety of applications, including hard disks, sun glasses, scanning panels, and machine tools [1]. Depending on the application, the following properties are important: hardness, adhesion, transparency, chemical inertness, and structural stability. We have recently discovered that the addition of boron to a-C:H dramatically improves the hardness, adhesion, and transparency of these films [2]. For example, the hardness of a-C:H that contains 50 at. % hydrogen is 0.8 GPA; the hardness of a-B:C:H that contains 50 at. % hydrogen is 9 GPa. Given that hydrogen is one of the poorest elements to use to construct a rigid lattice because it does not crosslink, it is remarkable that an amorphous material that is half hydrogen has a hardness comparable to that of single-crystal silicon. We suggested that the major reason for this dramatic improvement in hardness is the tendency of the boron to form boron carbide icosahedra.

Amorphous hydrogenated boron carbide (a-B:C:H) was first studied by Veprek as a fusion reactor inner wall coating [3]; this work led to the discovery that a-B:C:H thin films had a large hardness and good adhesion to underlying substrates [4]. These a-B:C:H films have been studied as a wear-resistant coating for mechanical systems [5], as a diode material [6], and as an ultralow friction coating [7]. The compositional, structural, electrical and optical properties of a-B:C:H thin films have been reported [8-12]. In our previous work, we reported infrared absorption and nuclear magnetic resonance results on a-B:C:H that were very similar to those in polycrystalline boron carbide, where boron carbide make up the unit cell [13]. In this paper, we report the variation of the infrared absorption spectra of a-B:C:H as a function of boron concentration and annealing temperature.

Mat. Res. Soc. Symp. Proc. Vol. 517 © 1998 Materials Research Society

EXPERIMENTAL PROCEDURES

We grew a-B:C:H thin films from a feedstock of methane (CH_4), diborane (B_2H_6), and hydrogen (H_2) in a capacitively coupled rf plasma reactor. Samples with varying boron concentrations were grown by varying the ratio, r, of the 5% diborane in hydrogen partial pressure to the methane partial pressure from 1/10 to 10/1, while keeping the total pressure constant at 130 mT, the substrate temperature constant at 60 C, and the rf power constant at 23 W All samples were grown on the cathode, using aluminum foil or silicon substrates. The films grown on silicon substrates were inserted in a Perkin-Elmer model 1610 Fourier transform infrared spectrophotometer. The thicknesses of these films were measured on an Alpha-step profilometer, so that absorption coefficients could be calculated. The films grown on the aluminum foil were immersed in dilute HCl, dissolving the aluminum. The free standing films were sent to Galbraith Laboratories for chemical analysis. Some of the films grown on silicon were evacuated in a pyrex tube and annealed for 1 hour at various temperatures. Hardness measurements were made on a Nano Indenter II.

EXPERIMENTAL RESULTS

The chemical analysis of three of our films provided the following results: the r=10/1 sample contained 42 at. % B, 10 at. % C and 48 at. % H; the r=1/1 sample contained 8 at. % B, 57 at. % C and 35 at. % H; and the r=1/10 sample contained 2.5 at.% B, 63.5 at. % C, and 34 at. % H. A plot of the B at. % as a function of the partial pressure ratio, r, is shown in Figure 1. The infrared absorption spectra of the r=1/1 a-B:C:H film is shown in Figure 2a; the spectrum is dominated by one intense, broad peak at 1280 cm^{-1}. The integrated intensity (the sum of the absorption coefficients) of the 1280 cm^{-1} line as a function of r is shown in Figure 1. The peak position and linewidth of the 1280 cm^{-1} line as a function of r are plotted in Figure 3. Figure 2b displays the infrared absorption spectra of the same r=1/1 sample used in Figure 2a, but after being annealed in vacuum for one hour at 300 C. Figure 4 shows the hardness of a r=5/1 a-B:C:H film before and after a 300 C anneal for one hour.

DISCUSSION

Stein, et al. reported a broad, intense absorption line at 1200 cm^{-1} with a FWHM of 150 cm^{-1} in polycrystalline boron carbide, with the unit cell consisting of boron carbide icosahedra [14]. This line shifted to higher frequencies and its linewidth narrowed with increased carbon concentrations. They associated this line with motion of both boron and carbon in these icosahedra. In contrast, Shirai, et al reported an intense line around 1100 cm^{-1} in a-B:C:H grown by electron cyclotron resonance plasma deposition [12]. They interpreted this line as the stretching mode of an isolated carbon-boron bond, where the carbon atom is an impurity and not part of the boron network.

The infrared absorption spectra of our a-B:C:H films are dominated by a broad peak around 1280 cm^{-1}. We propose that this line has the same origin as the 1200 cm^{-1} line observed in polycrystalline boron carbide, namely boron carbide icosahedra, and that the carbon concentration in

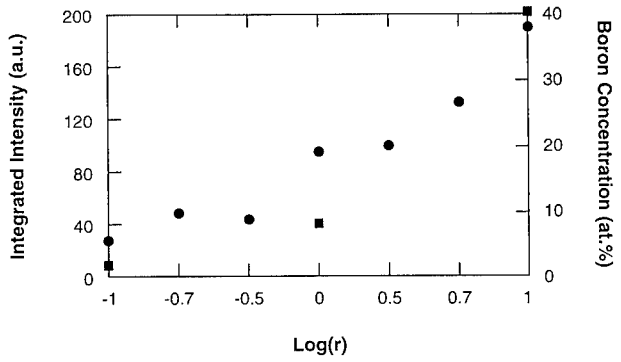

Fig. 1. The integrated intensity of the 1280 cm^{-1} line (solid circles) and the boron concentration in the film (solid squares) as a function of the diborane/methane feedstock ratio, r.

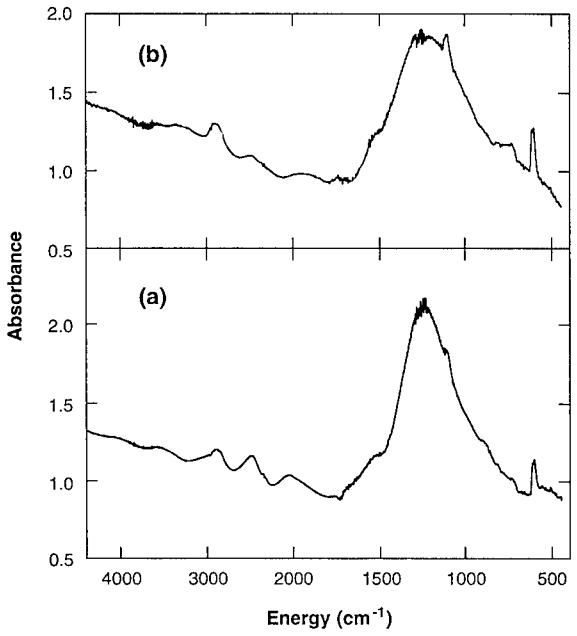

Fig. 2. The infrared absorption spectra of (a) the as-grown, r=1/1 amorphous hydrogenated boron carbide film and (b) the same film after a one hour, 300 C vacuum anneal.

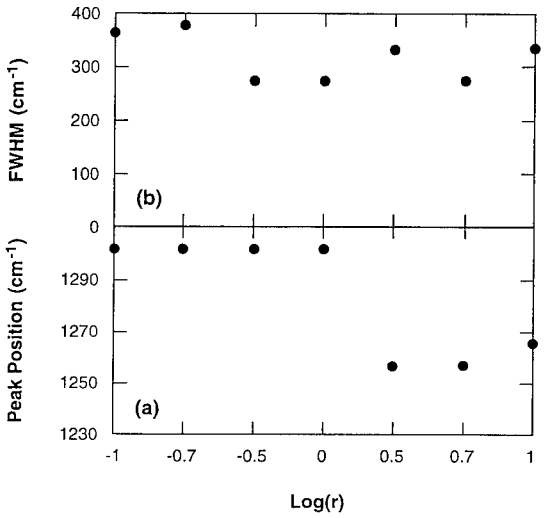

Fig. 3. The peak position and linewidth of the 1280 cm^{-1} line as a function of the diborane/methane feedstock ratio, r. The abrupt change in peak position between r=0 and r=0.5 is not understood.

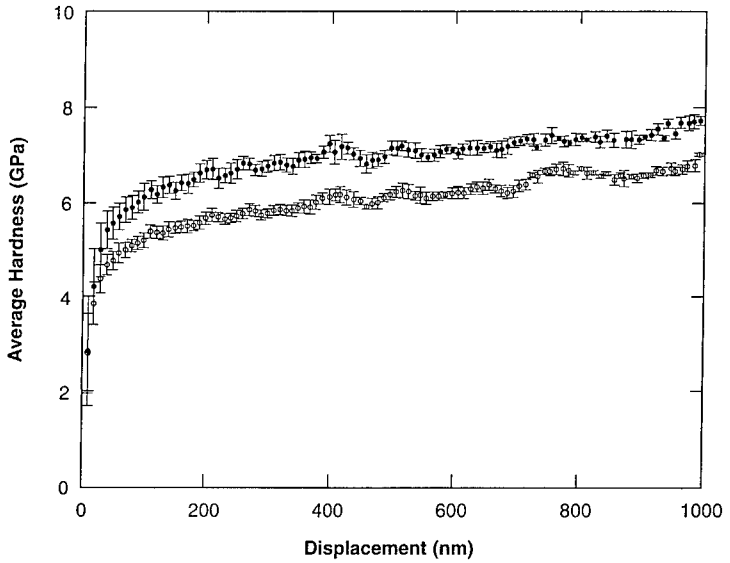

Fig. 4. Nano Indenter II displacement as a function of force for an r=5/1 a-B:C:H thin film. The open circles data was taken before the anneal; the solid circles data was taken after a 4 hour anneal at 300 C.

these icosahedra is greater in low r, carbon-rich films than in high r, carbon-poor films. The evidence is the following: The coordinated motion of all 12 atoms strongly bound in an icosahedra structure would give rise to a strong oscillator strength and consequently an intense line. Notice in Figure 2 how the 1280 cm^{-1} line is so much more intense than the C-H and B-H stretching modes at 2900 cm^{-1} and 2300 cm^{-1} respectively [12]. Second, the integrated intensity of the 1280 cm^{-1} line is zero in samples that contain no boron and it increases monotonically in samples with increasing boron concentrations (larger r), as seen in Figure 1. Third, after the a-B:C:H film is annealed, the B-H stretching mode is almost gone while the 1280 cm^{-1} line is approximately unchanged, as seen in Figure 2; this is strong evidence that the B-H bonds play a very small role in the 1280 cm^{-1} line.

The observed increased linewidths and peak position blue shifts reported in polycrystalline boron carbide are due to increased carbon concentrations in its icosahedra; the same trends observed in Figure 3 in a-B:C:H films with decreasing r are strong evidence for increased carbon concentrations in its icosahedra. Second, the integrated intensity of the 1280 cm^{-1} line increases at a sublinear function of the boron concentration in the a-B:C:H films, as seen in Figure 1. As r varies from 1/10 to 10/1, the boron concentration increases by a factor of 17 while the integrated intensity only increases by a factor of 6. Assuming that the 1280 cm^{-1} line integrated intensity is independent of the icosahedra's carbon concentration, at low r less boron is needed for each icosahedra and for a fixed amount of integrated intensity; as r is increased, more boron is needed for each icosahedra and for a fixed amount of integrated intensity. However, the observed small changes in linewidths and peak positions in the 1280 cm^{-1} line in a-B:C:H films suggest that this is only a partial explanation for this sublinear behavior; with increasing r, larger fractions of the boron are not being bound into icosahedra, but into the amorphous matrix surrounding the icosahedra.

There are a number of changes in the infrared absorption spectra of amorphous hydrodenated boron carbide due to annealing, as seen in Figure 2. Besides the decrease in intensity of the B-H stretching mode, the 1280 cm^{-1} line broadens. When the films are annealed at 400 C, there are more dramatic changes; the C-H stretching mode decreases in intensity and the 1280 cm^{-1} lineshape is dramatically changed. We suggest that annealing primarily breaks the weak B-H and C-H bonds, but many of these carbon and boron atoms that lose a hydrogen atom are part of icosahedra. Consequently, the icosahedra change shape and the 1280 cm^{-1} lineshape changes also.

The hardness of a-B:C:H thin films did not appreciably change due to annealing at 300 C for four hours, as seen in Figure 4. Even though the annealed film had significantly less hydrogen than the unannealed film, its hardness was only slightly increased. (For another a-B:C:H film, the hardness actually decreased after the anneal.) How is this result consistent with previous results [2] that show a strong correlation between hardness and hydrogen concentration. We suggest that a film that is grown with large hydrogen concentrations will be soft, because hydrogen does not crosslink; however, removing the hydrogen after growth does not enhance hardness, because the underlying boron-carbon structure is largely unchanged by the anneal.

Finally, a comment is needed in regard to the work of Shirai, et al [12]. The fact that their absorption peak is at 1100 cm^{-1} and ours is at

1280 cm^{-1} suggests that the two lines have different origins, possibly because of very different atomic structures due to different growth techniques used. Their interpretation of the 1100 cm^{-1} line as the stretching mode of localized B-C bonds is not applicable to our 1280 cm^{-1} line. It cannot explain the large intensity of the 1280 cm^{-1} line, its shift with increasing carbon concentration, or its intensity being proportional to the film's boron concentration. In contrast, the intensity of the 1100 cm^{-1} line is inversely proportional to their film's boron concentration [12].

CONCLUSIONS

We have presented infrared absorption data that provide convincing evidence for the intense line at 1280 cm^{-1} originates in boron carbide icosahedra and that the carbon content of these icosahedra increases in boron-poor, low r a-B:C:H films. The annealing studies of these films are consistent with the above conclusions, demonstrating that B-H bonds play a very small role in the 1280 cm^{-1} line.

ACKNOWLEDGMENTTS

We want to thank Mike O'Hern at Nano Instruments for the hardness measurements. This work was partly supported by a University of Missouri Center for Molecular Electronics grant.

REFERENCES

1. D. W. Brown, B. K. Daniels, F. W. Kimoch, B. J. Knapp and R. H. Petrmichl, 1995 Spring Materials Research Society Meeting Abstracts, p. 191.
2. S.-H. Lin, B. J. Feldman and D. Li, Appl. Phys. Lett. 69, 2373 (1996).
3. S. Veprek, Plasma Chemistry and Plasma Processing 12, 219 (1992).
4. S. Veprek and M. Jurik-Rajman, in Proc. 7th Int. Symp. on Plasma Chemistry, (Eindhoven, 1985) p. 90.
5. J. Onate, A. Garcia, V. Bellido and J. Viviente, Surf. Coat. Technol. 49, 548 (1991).
6. S. Lee and P. A. Dowben, Appl. Phys. A 58, 223 (1994).
7. A. Erdemir, C. Bindal and G. R. Fenske, Appl. Phys. Lett. 68, 1637 (1996).
8. S. Lee, J. Mazurowski, G. Ramsmeyer and P. A. Dowben, J. Appl. Phys. 72, 4925 (1992).
9. B. M. Way, J. R. Dahn, T. Tiedje, K. Myrtle, and M. Kasrai, Phys. Rev. B 46, 1697 (1992).
10. B. Sylvester, S.-H. Lin and B. J. Feldman, Solid State Comm. 93, 969 (1995).
11. V. Wagner, E. H. A. Dekempeneer, J. Geurts, L. J. van IJzendoorn, R. Sporken and R. Caudano, in Thin Films: Stresess and Mechanical Properties VI, (Mater. Res. Soc. Proc. 436, Pittsburgh, PA, 1997) p. 183.
12. K. Shirai, S. Emura, S. Gonda and Y. Kumashiro, J. Appl. Phys. 78, 3392 (1995).
13. J. Braddock-Wilking, S.-H. Lin and Bernard J. Feldman, Tribology Letters, in press.
14. H. Stein, T. Aselage and D. Emin, in Boron-Rich Solids, Proceedings of the 10th International Conference on Boron, Borides and Related Compounds, (AIP Conf. Proc. 231, New York, NY, 1991) p. 322.

The Application of Amine - Quinone Polymers in High Density Recording Media for Improved Corrosion Protection

Rahul Sharma*, G. W. Warren*, D. Nikles**, Y. Hu**, and S. Street**

* The University of Alabama, Department of Metallurgical and Materials Engineering
** The University of Alabama, Department of Chemistry
Tuscaloosa, AL 35487

ABSTRACT

High density, metal particle recording media consists of micron-sized iron particles in a polyurethane based polymer binder. In order to improve the corrosion resistance of the particles, two new amine-quinone (AQ) polymers, AQPU15 and AQPU100, have been investigated. Electrochemical impedance spectroscopy (EIS) was used to evaluate the corrosion behavior of iron substrates coated with two different thicknesses of each polymer. Results showed that the AQ polymers provide better protection compared with commercial polyurethane. The nature of the interaction at the polymer/metal interface has been investigated by FTIR-RA and XPS, which indicate that bonding probably occurs through the π system of the AQ functional group and the nitrogen of the soft segment, and through the quinone carbonyl functional group.

INTRODUCTION

The ability to record data on flexible magnetic media is principally responsible for the widespread, relatively inexpensive use of recorded sound and video images.[1] The media typically consists of two layers of materials, a relatively thin top layer (~ 2 to 4 μm) consisting of magnetic particles in a polymer binder painted on a substrate (~10 μm thick), usually polyethylene terepthalate (PET).[2] Current research for increasing the storage capacity per unit volume of the tape has emphasized two approaches: (a) development of smaller particles with higher magnetization and (b) the use of thinner substrates. Metal (iron) particles are desirable over other particulate materials (e.g., γ-Fe_2O_3) due to higher saturation magnetization (M_s) and coercivity (H_c) but they are also more susceptible to corrosion.[3,4] In addition, as particle size decreases, the impact of corrosion is magnified, since even a tiny amount of corrosion can cause loss of data. Amine Quinone (AQ) polymers are a candidate material for use in metal particle tape binders due to their improved corrosion protection. In this study, the corrosion protection properties of two different AQ polymers namely, AQPU15 and AQPU100 have been examined by Electrochemical Impedance Spectroscopy (EIS). Reflectance-FTIR and XPS experiments on iron substrates coated with AQPU100 polymer and a model monomer (AQM14A) have also been performed to determine the nature of the interaction at the polymer/metal interface.

Mat. Res. Soc. Symp. Proc. Vol. 517 © 1998 Materials Research Society

EXPERIMENTAL

EIS

The polymer formulation and preparation is provided elsewhere.[5] The structures of the AQPU100 polymer, and the AQM14A model monomer are shown in Figure 1.

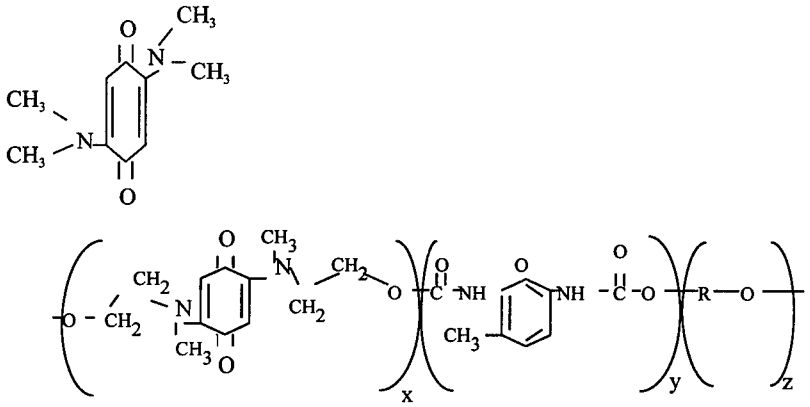

Figure 1: AQM14A monomer and AQPU15 polymer.

The difference between AQPU100 and AQPU15 is the amount of AQM1. AQPU100 contains 1% AQM1 and AQPU15 contains 40% AQM1. The iron substrates (5 x 5 x 0.16 cm) used in this study were prepared by polishing with 600, 800 and 1200 grit SiC papers followed by 1, 0.3 and 0.05 μm Al_2O_3 slurries, ultrasonically cleaned in isopropanol for several minutes, dried in air, and stored in a vacuum desiccator. The desired polymer coatings were applied by spin-coating in a class 100 clean room and cured at 65°C for 24 hours. Samples with polymer thicknesses of both 9 and 15 μm were prepared from each polymer. All coatings were applied in two layers to minimize the possibility of pinholes and to improve reproducibility. EIS measurements on the polymer coated iron substrates were performed with the experimental arrangement shown in Figure 2, using a Schlumberger Solartron 1255 frequency response analyzer (FRA), a 1286 potentiostat and appropriate software.

The electrochemical cell, Figure 2, consisted of a plexiglass cylinder held in place on top of the coated substrate by an aluminum cage and filled with 0.1 M NaCl electrolyte. A three electrode arrangement was used with the coated iron substrate as the working electrode, a platinum screen counter electrode, and an Ag/AgCl reference electrode. EIS behavior of each sample was monitored as a function of time of exposure (total elapsed time at the end of the measurement) to the 0.1 M NaCl electrolyte. The impedance data was modeled using the equivalent circuits shown in Figure 3, where the choice depends on the stage of coating degradation.[6,7,8] In early stages of exposure the

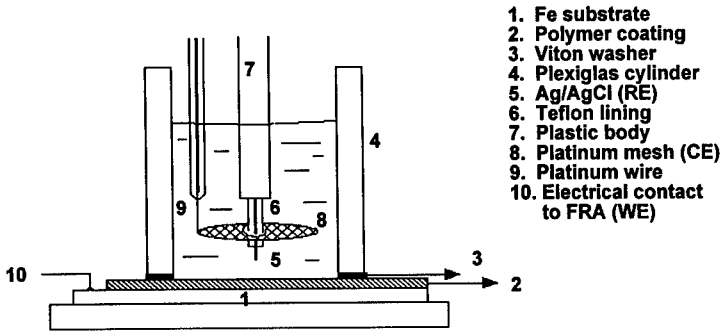

Figure 2: Experimental Set-Up

coating behaves as a pure capacitor and the equivalent circuit in Figure 3 (a) is used. As ionic species diffuse into the coating with exposure time, a coating resistance, R_{coat}, representing ionic conduction through the organic coating appears at low frequencies which is in parallel combination with the C_{coat} (Figure 3 (b)). The experimental impedance data were fitted to approximate equivalent circuit models using the complex non-linear least squares (CNLS) fitting program developed by MacDonald et al.[9]

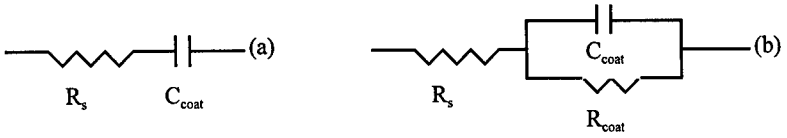

Figure 3: Equivalent circuits.

FTIR

The AQPU100 polymer was adsorbed onto an iron substrate by immersing it in a 2% solution of the polymer in cyclohexanone. The iron substrates were prepared as described above. Once immersed, the substrates were ultrasonicated for two minutes and allowed to equilibrate for 24 hours. Samples were then briefly rinsed in fresh cyclohexanone and blown dry with nitrogen. FTIR-RA was carried out using a Digilab FTS-40 spectrometer equipped with a room temperature thermal DTGS detector and a single reflection RA accessory (Harrick Scientific) at 70^0 angle of incidence. FTIR-RA spectra of a polished iron surface without polymer served as the background spectra. The number of scans was 4000 using a resolution of 16 cm^{-1}. The transmission spectra of a free standing AQPU100 polymer film was also obtained.

XPS

Since XPS spectra of the polymers are quite complex, experiments were performed using the model monomer AQM14A. XPS data was collected for the bulk

monomer and for a very thin layer again produced by dipping the substrates in a 2% solution of the monomer in cyclohexanone. A polished iron surface with no coating was used as a control sample. XPS spectra were obtained using a Kratos Analytical Inc. Axis 165 Scanning Auger / X-ray Photoelectron Spectrometer with monochromatized Al Kα radiation (1486.6 eV). Spectrometer resolution was approximately 0.2 eV. Where necessary, the spectra were fit using a proprietary program which applies Lorentzian-Gaussian peak shapes and instrument specific curve fitting parameters.

RESULTS AND DISCUSSION

EIS

The AQPU15 (15 μm) polymer has previously been shown to offer better corrosion protection compared with the same thickness of a standard polyurethane.[5] EIS results for 9 μm layers of AQPU15 and AQPU100, are shown in Figures 4 (a) and (b), respectively, for 5 minutes and 79 days of exposure to 0.1 M NaCl solution. Both polymers showed a pure capacitive behavior (-90^0 phase angle) after a few minutes of exposure. After 79 days exposure the resistance of the AQPU15 polymer decreases significantly (from 8 x 10^6 Ω cm^2 to 9 x 10^4 Ω cm^2), whereas the resistance of the AQPU100 decreases only slightly (from 4 x 10^7 Ω cm^2 to 3 x 10^6 Ω cm^2), indicating a much improved corrosion protection by the AQPU100 polymer compared to AQPU15. In addition the phase angle plot for the AQPU15 polymer shows the presence of a second time constant (at ~ 4 Hz) after 79 days of exposure resulting from the creation of a metal/electrolyte interface and the failure of the coating. Thus, the AQPU15 polymer coating failed much earlier than the AQPU100 polymer coating, which did not show a second time constant for the same time of exposure.

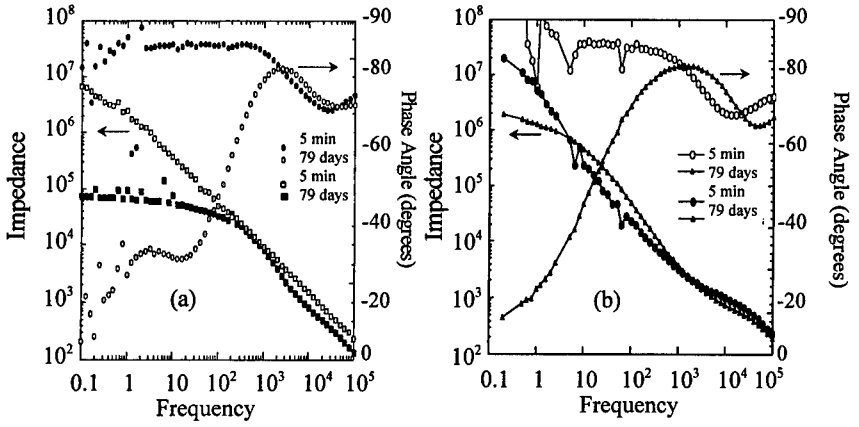

Figure 4: Bode plots for (a) AQPU15 and (b) AQPU100 polymer.

FTIR

Figure 5 shows the FTIR spectrum for the AQPU100 polymer film. Figure 5 (a) shows the FTIR-RA spectrum of AQPU100 adsorbed on an iron substrate from 2% solution and Figure 5 (b) shows the transmission spectrum of a thin AQPU100 free standing film. Two spectral shifts were observed in this case. The peak due to N-H bond in the hard segment of the polymer shifts from 3333 cm^{-1} to 3378 cm^{-1}, a shift of 45 cm^{-1}. A small shift of 13 cm^{-1} was also observed for the quinone carbonyl stretching frequency in the AQ polymer film which shifted from 1721 cm^{-1} to 1734 cm^{-1}. The 45 cm^{-1} shift and the 13 cm^{-1} shift indicates that the polymer is adsorbed to the iron surface in such a way that perturbs nitrogen and the quinone carbonyl functional groups.

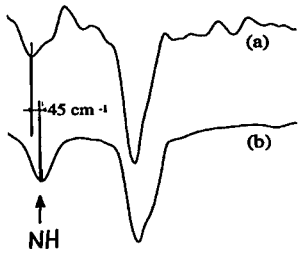

Figure 5: FTIR spectra for (a) thin film of AQPU100 on Fe and (b) bulk AQPU100.

XPS

The XPS results are summarized in the Table 1. Results show significant shifts: 0.4 eV toward lower binding energy for the Fe (2p3/2) peak; 2.2 eV toward higher binding energy for the N (1s) peak; 1.6 eV toward higher binding energy for the O (1s) peak. These results are consistent with reduction of the iron and oxidation of the oxygen and nitrogen in the monomer.

Table I : XPS data for pure Fe and a thin layer of AQM14A on Fe.

Specimen	Binding Energy (eV) of peaks for		
	Fe (2p3/2)	O (1s)	N (1s)
Pure Fe	710.8, 707.6	-	-
Bulk monomer	-	528.8	398.0
AQM14A thin layer on Fe	710.4, 707.2	530.4	400.2

Proposed Model for Interaction of AQM14A with Fe

Based on the FTIR and XPS data, a model for the interaction between the model monomer and the Fe surface can be proposed where the AQM14A monomer lies parallel to the iron surface and donation of electrons from the π system of the ring into the iron

oxide surface. The proposed structure of the bulk AQM14A and the mechanism of interaction between AQM14A and the iron surface is shown in Figure 6.[10] The electrons of the π system are delocalized over the ring, resulting in the formation of a negative dipole on oxygen, and a positive dipole on nitrogen. Donation of electrons from the π system to the iron oxide surface takes place after adsorbing the AQM14A monomer onto the iron surface. This model is consistent with the shifts in binding energies observed by XPS.

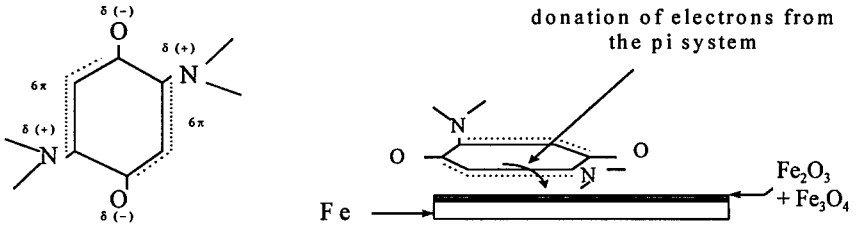

Figure 6: AQM14A monomer (in bulk state) and the proposed model for interaction

CONCLUSIONS

The following conclusions can be drawn from this study:

1. AQ films can significantly improve corrosion resistance by preventing the creation of metal/electrolyte interface as compared to the standard polyurethane binder.
2. The AQPU100 polymer offers much better corrosion protection properties as compared to AQPU15.
3. Corrosion protection is attributed to a chemical interaction between nitrogen from the polymer and the iron oxide surface. XPS studies indicate that the AQM14A monomer interacts with the iron surface through the π system.

REFERENCES

1. M. P. Sharrock, IEEE Trans. Magn., **25**, 4374, (1989).
2. R.M. White, IEEE press, New York, (1984).
3. G. Akashi, in Ferrites, p. 548, Proceedings Int'l Conference, Japan, (1980).
4. P. Williams, IEEE Trans. on Magn., **24**, 1876, (1988).
5. J.C. Arroyo, G.W. Warren, D.E. Nikles, NIST-IR 5960, Proceedings 6th Int'l Workshop on Moisture in Microelectronics, Gaithersburg, MD (1996).
6. M. Kendig, F. Mansfield and S. Tsai, Corrosion Sci., **23**, 317 (1983).
7. L.Baunier, I.Epelboin, J.C.Lestrade and H.Takenouti, Surf. Tech., **4**, p137 (1976).
8. G. W. Walter, Corrosion Sci., **26**, 681 (1986).
9. J.R.MacDonald, J.Schoonman and A.Lehnen, J.Electroanal. Chem., **131**, p.77 (1982).
10. S. Berger, P. Hertl and A. Rieker, Physical and Chemical Analysis of Quinones, J. Wiley & Sons, NY, 1974, pp. 35-79.

Symposium M

Integrated Magneto-Optics—Materials and Devices

Part I

Garnet Materials for Integrated Photonics: Fabrication and Processing

Metalorganic Chemical Vapor Deposition of Magneto-Optical Ce:YIG Thin Films

Yi-Qun Li, Mondher Cherif, Jankang Huang, Wayne Liu, and Qiushui Chen
NZ Applied Technology, 8-A Gill Street, Woburn, MA 01801

Abstract

The deposition technologies of rare-earth substituted yttrium iron garnet (RE:YIG) thin films with a large Faraday rotation and their applications are briefly overviewed. Highly cerium substituted YIG films were successfully deposited on (111) GGG, (211) GGG, (100) MgO, and MgO buffered GaAs and InP substrates by single-liquid-source metalorganic chemical vapor deposition. Ce-YIG thin films can be epitaxially grown on lattice matched GGG substrates at a temperature as low as 600°C. They have excellent optical and magnetic properties along with high Faraday rotations. The films deposited on single crystal (100) MgO substrates are polycrystalline and have good magnetic properties. Sputter deposited MgO buffer layer was demonstrated for preventing the decomposition and chemical reaction of GaAs and InP substrates resulting in successful deposition of YIG films on GaAs and InP substrates at a substrate temperature of 550°C. The films grown on MgO buffered GaAs substrates possessed good magnetic properties.

INTRODUCTION

Photonics appears to be the emerging technology capable of meeting the ever increasing demand for communication and information processing at higher data rates and larger bandwidths. Optical technology fully utilizes the characteristics of light to transmit and process information with very high bandwidth (THz) at extremely high speeds in a massively parallel fashion. The prospects for widespread applications of optical technologies depend on the performance and cost effectiveness of optical components. One of the key components in optical communication systems is the optical isolator, which allows light to pass through it in only one direction. These devices operate on the basis of non-reciprocal Faraday rotation in magneto-optical crystals. Optical isolators are critical for (1) reducing reflection-induced noise in laser diodes, (2) preventing multiple beam reflection inside fibers, and (3) improving the performance of optical fiber amplifiers. The increasing demand in the telecommunication market for affordable optical communication systems, such as for optical local area networks and fiber-to-home applications, the need for low-cost optical isolator is acute.

To realize the low-cost, compact size, and high performance required of next generation isolators, a low cost manufacturing process with the potential for monolithic fabrication of magneto-optic isolators is very desirable. Metalorganic chemical vapor deposition (MOCVD) is an ideal choice because of its compatibility with semiconductor device process. MOCVD permits the formation of high quality films with higher rare-earth substitution concentration than other growth techniques for higher device efficiency. MOCVD is also possible at lower temperatures, an advantage that is potentially critical for low cost monolithic integration with semiconductor lasers. In the present study we have demonstrated these advantages by producing large Faraday rotation in YIG films with high cerium substitution and by growing YIG films directly on semiconductor laser substrates of GaAs and InP with buffer layer technology at much lower substrate temperatures.

Mat. Res. Soc. Symp. Proc. Vol. 517 © 1998 Materials Research Society

The advantages of thin film isolators integrated with lasers are: (1) light from a laser can remain in a guided mode as it passes through the thin film, eliminating the need for collimating lenses and complex alignment procedures typically required of nonintegrated approaches; (2) films need only be a few microns thick in the planar waveguide configuration, rather than over 200 microns required of conventional isolators in which the light passes transversely through the thick film, (3) the magnetic field required to saturate a planar magnetic thin film is much smaller than that required to saturate a bulk crystal, which allows the use of thin film permanent magnets; and (4) these waveguides can act as building blocks for other integrated optic devices such as circulators, switches, modulators, polarization controllers and magnetic field sensors.

APPLICATIONS OF MAGNETO-OPTICAL GARNET THIN FILMS

A. Waveguide Isolators

Many early development works on YIG thin film waveguide isolators were done by Ray Wolf's group at AT & T Bell Laboratories (1-4) and H. Dammann et. al. in Germany (5-6). The details of these works was reviewed by Wolf in Reference 7. Fig. 1 shows a prototype waveguide isolator which consist of three LPE YIG layers on GGG substrates to promote a high-quality single-mode waveguiding. By rotating the input and the output polarizer 22.5° in opposite direction as shown in the Fig. 1, excellent isolator performance can be achieved even if the linear birefringence is not zero. The isolation spectrum of such a waveguide isolator is shown in Fig. 2, isolation ratios of more than 32 dB have been achieved over a broad band of wavelengths of 1.43-1.59 μm.

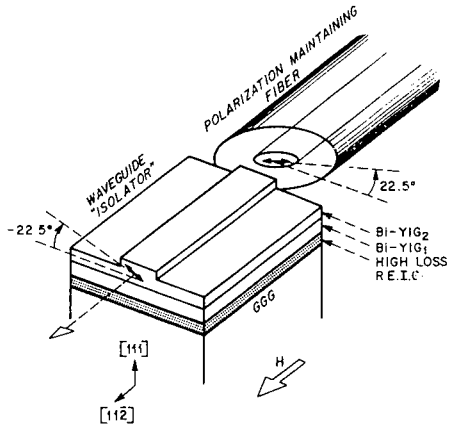

Fig. 1 Magneto-optical waveguide isolator: REIG, rare earth iron garnet. A triple film of magnetic garnet provide a single mode waveguiding and rotates the plane of polarization by 45°. Input and output polarization rotate 22.5° in opposite direction.

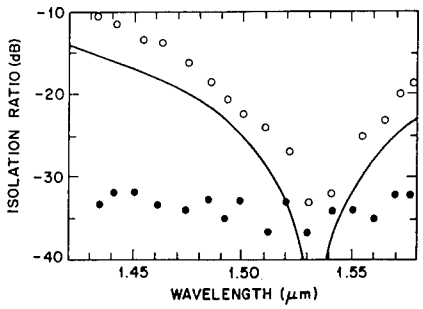

Fig. 2. Isolation ratio vs wavelength using the arrangement in Fig. 1: • experimental results for reverse isolation; ° forward results, corresponding to slight extra loss; theoretical fit to the results with the input polarization parallel to the film plane.

B. Magneto-optical recording

Bi substituted yttrium iron garnet is an attractive candidate for magneto-optic recording media because of its large carrier-to-noise ratio (CNR). The work utilizing in-situe crystallization of BiYIG thin films showed large mark CNR of 58 dB at 488 nm onto a grooved gadolinium gallium garnet (GGG) disk (8). The readout signal for BiYIG is compared with other material such as (Co/Pt) and TbFeCo in Fig. 3 (9). The drawback with Bi-garnet is that high-temperature crystallization (~ 650°C) is needed. This limits the choice of substrate materials, which may prevent the development of low-cost media.

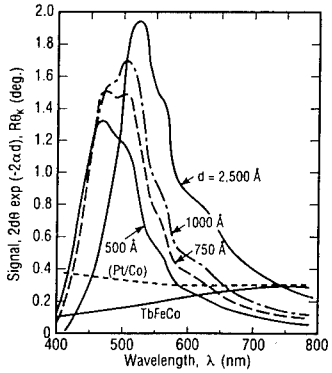

Fig. 3. Readout signal for garnet films with thickness d, compared with (Co/Pt) and TbFeCo.

C. Magneto-optical indicator film imaging

The magneto-optical indicator film (MOIF) technique was initially developed for magnetic flux visualization in superconductors (10, 11), and recently applied to the real-time

imaging of magnetic domain structure in magnetic thin film wafers. This method is expected to become a standard quality control imaging technique for the next generation of magnetic materials for sensors and storage devices. The basic apparatus for MOIF is a polarizing microscope with high-quality Bi-substituted YIG films placed on the testing magnetic materials. This technique is much simpler than the competitive method such as atomic force microscopy and scanning electron microscopy (AFM) with polarization analyses (SEMPA). Fig. 4 is a recent result using MOIF to study the magnetization reversal processes in nonsymmetric spin valve (12).

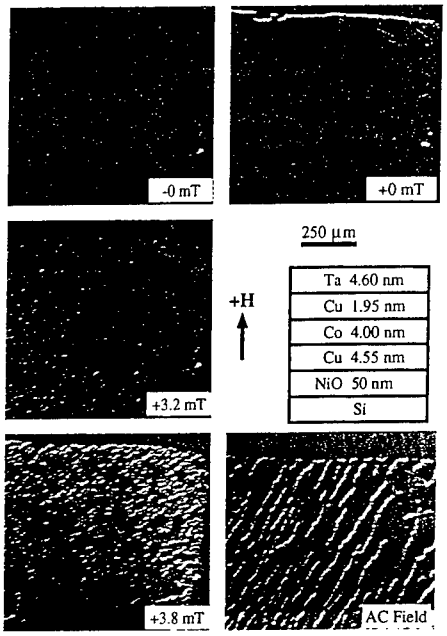

Fig. 4. Schematic profile of the structure of a single cobalt layer sample, otherwise similar to the nonsysmetric spin-valve sample. The three MOIF images on the left and the top right image represent the process of remagnetization. The image on the bottom right is the result of a 30 Hz ac field.

DEPOSITION TECHNOLOGIES FOR YTTRIUM IRON GARNET FILMS

Liquid phase epitaxial has been a dominant process to produce rare-earth substituted YIG films, in particularly for thick films (>200μm) used in the commercial optical isolators. This process requires a growth temperature over 900°C and on a limited size of GGG substrates, and it is not compatible with semiconductor process. Sputtering deposition technique is commonly be used to produce rare-earth substituted YIG films over a large area of substrates at a relative low substrate temperature. $Y_2Ce_1Fe_5O_{12}$ thin films with a giant Faraday rotation at 1.55 μm wavelength have been successfully deposited by RF diode sputtering under a typical condition listed in Table 1 (13, 14). Reactive ion-beam sputtering (RIBS) was also used, in particularly, for fully Bi-substituted YIG films: $Bi_3Fe_5O_{12}$ (15, 16). Fig. 5 and Fig. 6 show Faraday rotation hysteresis loop of $Y_2Ce_1Fe_5O_{12}$ film by RF sputtering and the Faraday rotation spectra of BIG films by RIBS, respectively.

Table 1

Power	5.6 W/cm^2
Growth Rate	6 nm/min
Substrate Temperature	500 - 700°C
Sputtering gas	Argon
Substrate	GGG

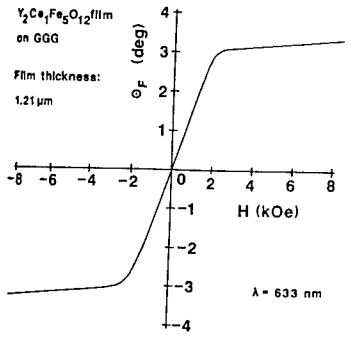

Fig. 5. Faraday rotation hysteresis loop of a $Y_2Ce_1Fe_5O_{12}$ film deposited by sputtering measured at λ=633 nm and room temperature.

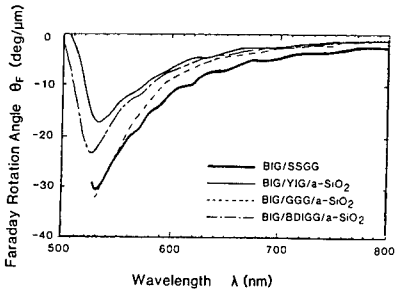

Fig. 6. Faraday rotation spectra of p-BIG layers grown on p-YIG, p-GGG, and p-BDIGG layers formed on a-SiO_2 substrates. Spectrum of single-crystalline BIG grown onto SSGG substrate is also shown. Measurement were done at room temperature and at 398 kA/m.

There is also some effort in using Laser ablation technique to deposit rare-earth substitute YIG films. An enhancement of Faraday rotation was found in an epitaxial $Y_3Fe_5O_{12}/Bi_3Fe_5O_{12}$ and $Y_5Fe_3O_{12}/Eu_1Bi_2Fe_5)_{12}$ heterostructures grown by Laser ablation by a group of researchers from Univ. California at Berkeley, Bellcore, IBM, and U.S. Army (17). A typical deposition condition is listed in Table II. Magnetic properties of the films are strongly dependent on the oxygen pressure during laser deposition as shown in Fig. 7. The Faraday rotation hysteresis loops of the multilayers of (EuBi)IG/YIG with different thickness ratio is shown in Fig. 8.

Table 2

Lasers	A248 nm KrF excimer laser
Power	3.3 J/cm^2, 10 Hz
Oxygen pressure	100 - 700 mTorr
Substrate Temperature	660°C

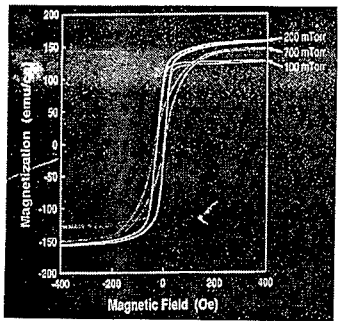

Fi.g. 7. Magnetic hysteresis loops of three different films grown at three different oxygen pressures.

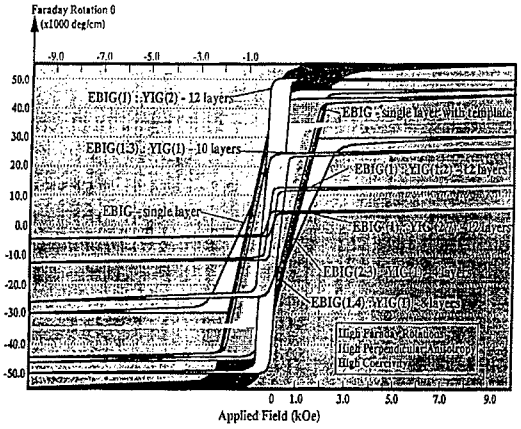

Fig. 8. A multilayer of (EuBi)IG/YIG can be optimized for high Faraday rotation, high perpendicular anisotropy, and high coercive field for applications of magneto-optical recording by varying the thickness ratio of EBIG to YIG.

METALORGANIC CHEMICAL VAPOR DEPOSITION OF CE:YIG FILMS

Metalorganic chemical vapor deposition (MOCVD) is the workhorse of the semiconductor industry and also has been proved for epitaxially growing complex oxides thin films such as superconducting $YBa_2Cu_3O_{7-x}$ and high-dielectric $BaSrTiO_3$ thin films. However, so far there is only few effort on the deposition of RE-YIG films by MOCVD. In the present study we have successfully demonstrated the feasibility of MOCVD for depositions of Ce substituted YIG films on GGG, MgO, and MgO buffered GaAs and InP substrates.

Experimental

Y(thd), Ce(thd), and Fe(thd) were purchased from Strem Chemical Inc. and used as precursors for Y, Ce, and Fe, respectively. These requisite metalorganic precursors are mixed and dissolved in an organic solvent. The solution is then injected by a liquid pump into a heated stainless steel vaporizer and carried immediately into the reactor chamber by a inert carrier gas as

shown in Fig. 9. With this new technique, the film composition is controlled by varying the molar ratio of the constituents in the solution. It allows an accurately control of film stoichiometry, which is necessary condition for forming a low loss RE-YIG film with a high Faraday rotation. It also significantly improves the deposition repeatability as compared to conventional CVD processes. The composition of the deposited films from each run was measured by energy dispersive x-ray analysis (EDX), and the result was used to compare relative compositions of the films to within 1% accuracy. But the absolute composition of a film was determined by calibrating Rutherford Backscattering Spectroscopy (RBS) result with the EDX result on the same sample.

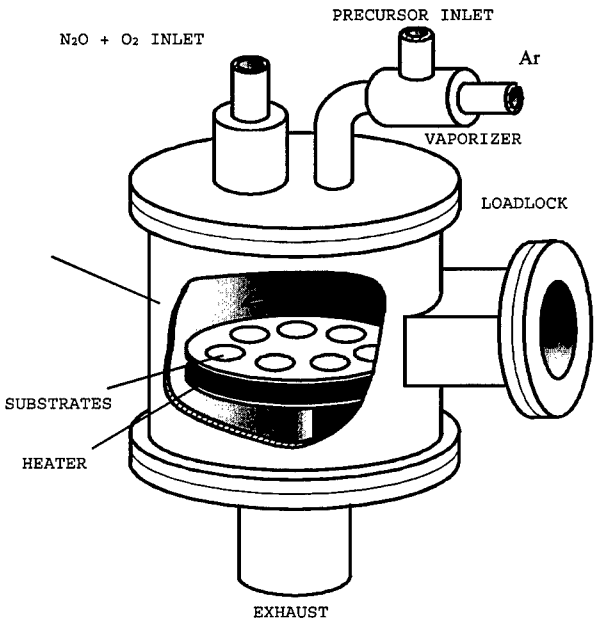

Fig. 9. Rotating-disk reactor of single-liquid-source MOCVD system for growth of complex-oxide thin films.

The RE-YIG films were deposited in a commercial stainless steel reactor with a high-speed rotating disk as shown in Fig. 9. Viscous drag forces between the disk's surface (rotating at a high speed) and the gas stream create a centrifugal "pumping" action, which results in the uniform growth of films over a large area. (The success of this design has been demonstrated by its adoption to the manufacture of semiconductor devices.) A mixture of N_2O and oxygen were used as the reactant oxidizer. A 5-inch resistance heater made of Inconel allows the substrate to be heated to any temperature up to 1000°C. A typical deposition condition of Ce-YIG thin films by MOCVD is listed in Table 3. Substrate temperature and oxygen partial pressure were the two parameters used to optimize the crystallinity and magnetic properties of the films.

Table 3

Substrate Temperature	600-700°C
Reactor Pressure	2 to 5 Torr
Oxygen Flow Rate	300 -700 sccm
Nitrous Oxide Flow Rate	0-500 sccm
Argon Flow Rate	50 sccm
Vaporizer Temperature	230°C
Solution Flow Rate	5 ml/hr
Substrate	Si, InP, GaAs, GGG, MgO

X-ray diffraction measurements were performed by Rigaku D3000 diffracotometer. The magnetic properties of the films were measured by vibrating sample magnetometer. The Faraday rotation was measured by a technique similar to the one described by Marinelli *et al* (18).

Result and Discussion

Lattice matching films to substrates is the most important factor in epitaxial growth. In this program we used proviskite $LaAlO_3$, cubic MgO, and garnet $Ga_3Gd_5O_{12}$ as substrates to optimize the MOCVD processing condition for epitaxial growth of YIG films at a low temperature. The YIG has a complex garnet structure with a lattice parameter of 12.38Å. The lattice mismatches for the three substrates mentioned above are listed in Table 4. All of the films were deposited under the conditions listed in Table 1. Stoichiometric YIG thin films deposited on $LaAlO_3$ at a substrate temperature up to 650°C were amorphous while the films grown on MgO substrates showed polycrystalline structure as indicated by x-ray θ-2θ scans in Fig. 10a. The x-ray θ-2θ diffraction pattern of YIG films grown on (111)GGG and (211)GGG substrates are totally overlapped with substrates, and the diffraction peaks shifted to lower angles (lattice parameter increase) as yttrium was substituted by Ce as shown in Fig.10b and 10c. These x-ray diffraction results of the YIG films on different substrates indicate a good correlation with the values of their lattice mismatches with YIG films as listed in Table 4.

Table 4

Materials	Crystal structure	Lattice Parameter	TEC ($^oC^{-1}x10^{-6}$)	Lattice Mismatch
$LaAlO_3$	Proviskite	a=3.792Å	12	8.1%
MgO	Cubic	a=4.213Å	13.5	2.1%
GGG	Garnet	a=12.393Å		0.1%

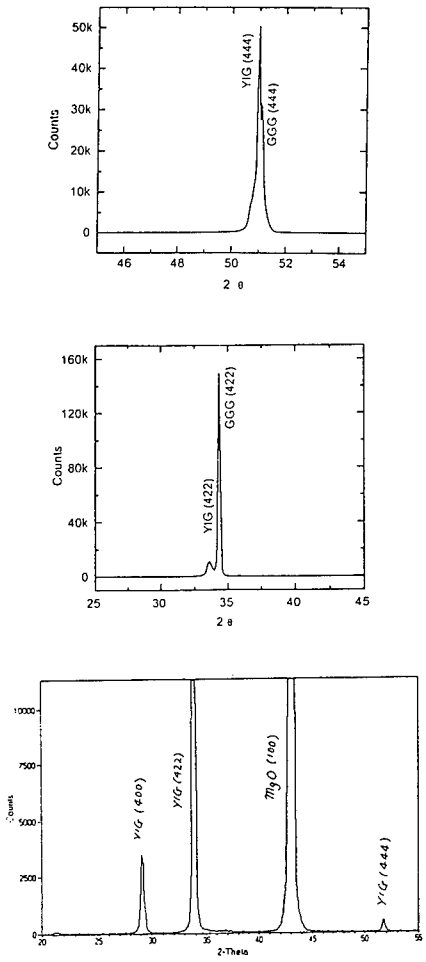

Fig. 10. X-ray θ-2θ diffraction patterns of Ce-YIG thin films deposited by MOCVD on (a) (100) MgO, (b) (111) GGG, and (c) (211) GGG substrates.

It is interesting that the dominant orientations in the films on InP differed from that in the films on GaAs although both substrates had MgO buffer layers. This result can be explained by the fact that the crystallinity of sputtered MgO on InP is much worse than that on GaAs as indicated by the x-ray diffraction intensity shown in Fig. 11a and 11b. It is clear that high crystallinity of the sputtered MgO buffer layer is required to obtain the high quality YIG thin films.

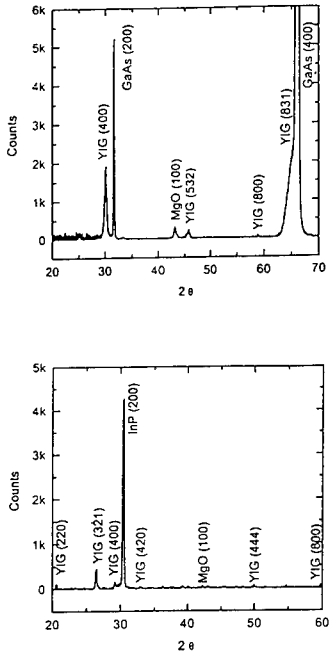

Fig. 11. X-ray θ-2θ diffraction patterns of Ce-YIG thin films deposited by MOCVD on (a) MgO buffered (100) InP, and b) MgO buffered (100) GaAs substrates.

Fig. 12 shows the magnetic hysteresis loops of a Ce-YIG film on a (111) GGG substrate prepared by MOCVD, (a) measured with a magnetic field in the plane of the film and (b) measured with a magnetic filed perpendicular to the surface of the film. It is clearly seen that the easy axis of magnetization was in the plane of the film. The value of coercive field Hc was 33 Oe, which is higher than that (<10Oe) of the YIG films prepared by Liquid-Phase-Epitaxy (LPE). But it is one of the lowest Hc reported to date for the YIG films deposited by any means of vapor deposition. The saturation field of about 500 Oe for this YIG film is quite high because the field required to rotate the magnetic moment from the easy magnetization direction <112> in (111) plane to the direction of the applied magnetic field is too high. The saturation field would be significantly reduced if the magnetic field is applied along the <112> because the saturation could be achieved primarily by domain wall movement which requires only a small magnetic field.

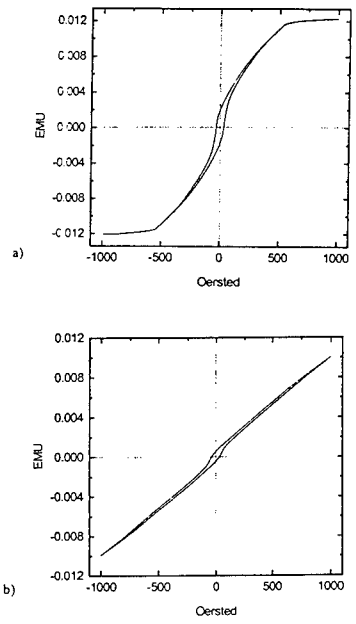

Fig.12. Magnetic hysteresis loops of a Ce-YIG film on a (111) GGG substrate prepared by MOCVD, (a) measured with an applied magnetic field in the plane of the film and (b) measured with an applied magnetic filed perpendicular to the surface of the film.

For the first time we have demonstrated a Ce-YIG film deposited on a MgO buffered GaAs substrate with good magnetic properties as shown in Fig.13. The film had isotropic magnetic properties as indicated by identical in plane and out of plane magnetic hysteresis loops. The coercive field of about 10 Oe was extremely low compared with that of films grown on GGG substrates shown in Fig. 12. The relatively low saturation magnetization of this film could be caused by nonmagnetic phases which may exists in the film particularly at the interface between the film and the substrate. Unfortunately the films grown on MgO buffered InP did not have strong magnetic properties due to the bad quality of MgO layer which might result in chemical interactions between InP and YIG film during the deposition. It is, however, very likely that we can improve the quality of MgO layer and thus improve the magnetic properties of YIG films on InP substrates by the end of this Phase I program.

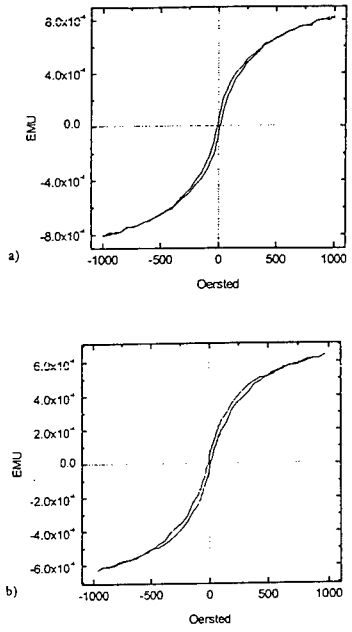

Fig. 13. Magnetic hysteresis loops of a Ce-YIG film on a MgO buffered GaAs substrate prepared by MOCVD, (a) measured with an applied magnetic field in the plane of the film and (b) measured with an applied magnetic filed perpendicular to the surface of the film.

The Faraday rotation of the Ce:YIG films grown on (111)GGG and (211)GGG were measured by the method described in the last section. The measured results of Faraday rotation are plotted as a function of the wavelength in Fig. 14. The Faraday rotation showed a rapid decrease as the wavelength increased from the visible to the infrared, as shown in Fig. 14. The rotation result is more than double of that measured for LPE grown Bi-YIG thick films, and is comparable with the highest value reported for Ce-YIG films prepared by sputtering method. However, in our Faraday rotation measurements the maximum magnetic field (500 Oe) applied perpendicular to the surface of the films is not high enough to saturate the films with a planar magnetization. Higher Faraday rotations should be obtained when the film is saturated in magnetization. The measurement of Faraday rotation of the films deposited on GaAs substrates were not successful because of the problem of rough interface of MgO buffer layers.

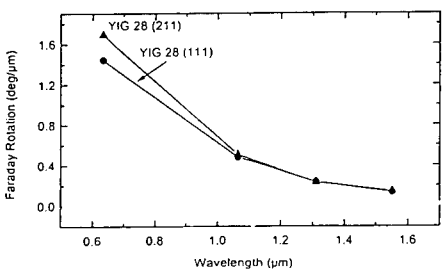

Fig. 14. Faraday rotation as a function of the wavelength for $(Y_{0.6}Ce_{0.4})_3Fe_{6.7}O_{12}$ thin films grown on (111) and (211) GGG substrates prepared by MOCVD.

CONCLUSIONS

In conclusion we have successfully developed a low-cost MOCVD process for magnetic-optic RE-YIG films at low deposition temperatures. Stoichiometric YIG films with high Ce concentration in substitution of Y were obtained by novel single-liquid-source delivery technique. Epitaxial Ce-YIG thin films on lattice matched GGG substrates showed a large Faraday rotation. MgO buffer layer was demonstrated for preventing the decomposition and chemical reaction of GaAs and InP substrates resulting in successful deposition of YIG films on GaAs, InP, and Si substrates.

ACKNOWLEDGMENTS

I would like to thank Dr. Beth Stadler at University of Minnesota for the characterization of magneto-optical properties, and Dr. Robert O'Handley at MIT for the measurement of magnetic properties by VSM. This research is supported by the U. S. Air Force under contract No. F30602-96-C-0121.

REFERENCES

1. R. Wolf, J. Hegarty, L. C. Luther, and D. L. Wood, Appl. Phys. Lett. 48 (1986) 508.
2. R. Wolf, V. J. Fratello, and McGlashan-Powell, Appl. Phys. Lett. 51 (1987) 1221.
3. R. Wolf, R. A. Lieberman, V. J. Fratello, R. E. Scotti, and N. Kopylov, 56 (1990) 426.
4. R. Wolf, J. F. Dillon, Jr., R. A. Lieberman, and V. J. Fratello, Appl. Phys. Lett. 57 (1990) 960.
5. E. Pross, W. Tolksdorf, and H. Dammann, Appl. Phys. Lett. 52 (1988) 682.
6. H. Dammann, E. Pross, G. Rabe, and W. Tolksdorf, Appl. Phys. Lett. 56 (1990) 1302.
7. R. Wolf, Thin Solid Films, 216 (1992) 184.
8. T. Suzuki, MRS Bulletin, September, 1996, p43.
9. T. Suzuki, F. Sequeda, H. Do, T. C. Huang, and G. Gorman, J. Appl. Phys. 69 (1991) p4756.
10. C. A. Duran, P. L. Gammel, R. Wolf, V. J. Fratello, D. J. Bishop, J. P. Rice and D. M. Ginsberg, Nature, 357 (1992) 474.
11. L. A. Dorosinskii, M. V. Indenbom, V. I. Nikitenko, Yu. A. Ossip'yan, A. A. Polyanski, and V. K. Vlasko-Vlasov, Physica C 203 (1992) 149.
12. V. S. Gornakov and V. I. Nikitenko, L. H. Bennett, H. J. Brown, M. J. Donahue, W. F. Egelhoff, R. D. McMichael, and A. J. Shapiro, J. Appl. Phys. 81 (1997) 5215.
13. M. Gomi, H. Furuyama and M. Abe, Jap. J. Appl. Phys. 29 (1990) L99.
14. T. Shintaku, T. Uno, and M. Kobayashi, J. Appl. Phys. 74 (1993) 4877.
15. T. Okuda, N. Koshizuka, K. Hayashi, T. Takahashi, H. Kotani, and H. Yamamoto, IEEE Trans. Magn. MAG-23 (1987) 3491.
16. T. Okuda, T. Katayama, K. Satoh, and H. Yamamoto, J. Appl. Phys. 69 (1991) 4580.
17. B. M. Simion, R. Ramesh, V. G. Keramidas, G. Thomas, E. Marinero, R. L. Pfeffer, J. Appl. Phys. 76 (1994) 6287.
18. J. Manifacier, J. Gasito, J. Fillard, J. Physics E, 9 (1976) 1002.

OPTIMIZED NONRECIPROCAL RIB WAVEGUIDES FOR INTEGRATED MAGNETO-OPTIC ISOLATORS

M. Wallenhorst, V. Backherms, A. Josef, N. Bahlmann, M. Lohmeyer, H. Dötsch, P. Hertel
University of Osnabrück, 49069 Osnabrück, Germany

ABSTRACT

Garnet films of composition $(Lu,Bi)_3(Fe,Ga,Al)_5O_{12}$ and $(Tm,Bi)_3(Fe,Ga)_5O_{12}$ are grown by liquid-phase epitaxy on [111]-oriented substrates of gadolinium gallium garnet. Ferrimagnetic films with positive or negative Faraday-rotation as well as paramagnetic films with negligible Faraday-rotation are produced by variations of the rare earth ion substitutions. The temperature dependence of Faraday-rotation is fitted with a molecular field model. Optical rib waveguides in single and double layer garnet films with different Faraday-rotations are realized. The nonreciprocal phase shift of the TM_0-Mode is studied both theoretically and experimentally at a wavelength of 1.3 μm. Results show that the maximum nonreciprocal effect at room temperature of double layer films with opposite Faraday-rotation is 1.6 times as large as that of comparable single layer waveguides. But, because of the large temperature dependence of the Faraday-rotation of the positive rotating films, these waveguides show a large temperature dependence of the nonreciprocal phase shift. This problem can be avoided if the positive rotating layer is replaced by a paramagnetic layer. Agreement between calculations and measurements is excellent.

INTRODUCTION

Magneto-optic isolators play an important role in optical communication technique. They are used to protect the semiconductor lasers from reflected light. At present only bulk isolators are available. To realize cheap integrated optical isolators, magnetic garnet films can be used. They combine low absorption with high Faraday-rotation in the near infrared. The Faraday-rotation, which is the basis of the nonreciprocal effects, can be enhanced by bismuth substitution. Various kinds of optical isolators have been proposed [1, 2, 3, 4, 5, 6, 7, 8, 9, 10]. Some promising concepts of integrated optical isolators and circulators rely on the nonreciprocal phase shift of TM modes [11, 12], which is the difference $\Delta\beta = \beta_{fw} - \beta_{bw}$ between the forward and backward propagation constants β_{fw} and β_{bw} of TM modes, respectively. The device length of such isolators is inversely proportional to this effect so that an enhancement is desirable. For this purpose double layer garnet films with opposite Faraday-rotation are suitable [13]. In this paper it is shown, how the temperature dependence and the absolute value of $\Delta\beta$ can be optimized by choosing a proper geometry of the waveguides.

NONRECIPROCAL RIB WAVEGUIDES

The following analysis is performed for the basic rib geometry sketched in Fig. 1. Mode propagation is assumed along the z axis and the magnetization $\boldsymbol{M}$ is adjusted in the film plane transversely to the propagation direction. Neglecting optical damping, the dielectric tensor of the magneto-optic films can be written as

$$\hat{\epsilon} = \begin{pmatrix} n^2 & 0 & \mathrm{i}\xi \\ 0 & n^2 & 0 \\ -\mathrm{i}\xi & 0 & n^2 \end{pmatrix}. \qquad (1)$$

Mat. Res. Soc. Symp. Proc. Vol. 517 © 1998 Materials Research Society

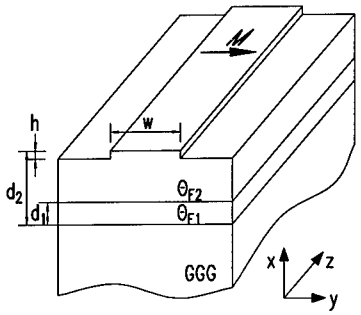

Figure 1: Basic geometry of the rib waveguide.

n is the isotropic refractive index and ξ represents the magneto-optic effect. It is related to the Faraday-rotation Θ_F by

$$\xi \approx 2n\Theta_F/k_0, \tag{2}$$

where k_0 is the vacuum wave number.

Using Maxwell's equations, one can derive the following partial differential equations describing quasi TE and quasi TM modes, respectively [14] :

$$(-\partial_x^2 - \partial_y^2 + \beta^2)E_y = \epsilon k_0^2 E_y \ , \tag{3}$$

$$(-\epsilon\partial_x\epsilon^{-1}\partial_x - \partial_y^2 + \beta^2 - \epsilon\beta(\partial_x\frac{\xi}{\epsilon^2}))H_y = \epsilon k_0^2 H_y \tag{4}$$

with $\epsilon = n^2$. The TM mode equation contains a term linear in β which causes the nonreciprocal effect. TE modes behave reciprocal.

These equations can be solved using a finite difference [14] or a finite element method [15] . Since the term $\epsilon\beta(\partial_x\xi/\epsilon^2)$ can be regarded as a small perturbation, we first solve the unperturbed mode equation utilizing a finite element method [16] . Then perturbation theory yields

$$\Delta\beta = \frac{\iint |H_y|^2(\partial_x\frac{\xi}{\epsilon^2})dxdy}{\iint \epsilon^{-1}|H_y|^2 dxdy} \tag{5}$$

for the nonreciprocal phase shift [17] .

To achieve a large $|\Delta\beta|$, double layer garnet films with opposite Faraday-rotation are prepared where the boundary between layers is located close to the maximum of $|H_y|^2$ [13]. Double layer waveguides with a positive rotating bottom layer and a negative rotating top layer show the highest differential nonreciprocal phase shift [18]. To reverse the sign of the Faraday-rotation from negative to positive, gallium is substituted onto the tetrahedral sites of the garnet until the magnetization of the octahedral sites dominates. Thus a compensation wall is established separating the layers with $\Theta_F^- < 0$ and $\Theta_F^+ > 0$. This procedure always results in $|\Theta_F^-| > |\Theta_F^+|$, see Ref. [13].

The temperature dependence of the Faraday-rotation of the garnet films investigated is displayed in Fig. 2. The composition and the material parameters of both samples are given in Table 1. Due to the large temperature dependence of the positive Faraday-rotation such films are not suitable for the realization of a device. Therefore, we use a paramagnetic bottom layer (0.18 μm) with negligible Faraday-rotation. .

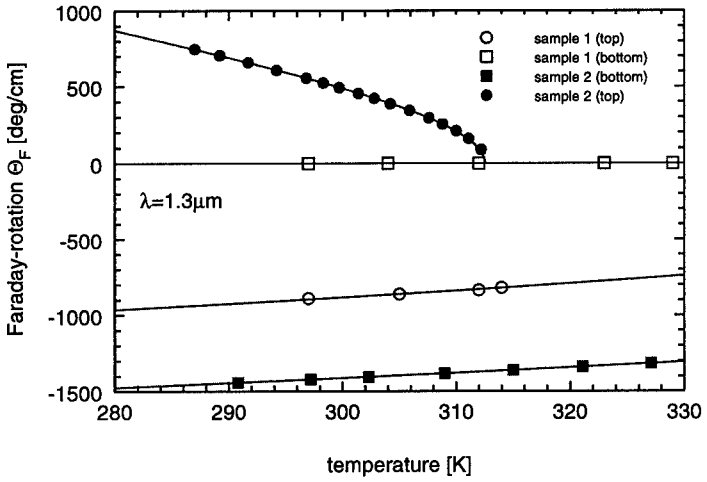

Figure 2: Measured temperature dependence of the Faraday-rotation Θ_F fitted to molecular field theory [19]. The composition and the material parameters of both samples are given in Table 1.

Table 1: Material parameters of the investigated films ($\lambda = 1.3$ μm, $T = 295K$).

sample	composition	x (f.u.)	y (f.u.)	z (f.u.)	d (μm)	Θ_F (deg/cm)	n
1 bottom	$Tm_{3-x}Bi_xFe_{5-y}Ga_yO_{12}$	0.71	1.71	0	0.20	0	2.20
1 top	$Lu_{3-x}Bi_xFe_{5-y-z}Ga_yAl_zO_{12}$	-	-	-	0.40	-900	2.27
2 bottom	$Lu_{3-x}Bi_xFe_{5-y}Ga_yO_{12}$	1.08	0.45	0	0.35	-1450	2.33
2 top	$Lu_{3-x}Bi_xFe_{5-y}Ga_yO_{12}$	1.38	1.63	0	0.35	350	2.27

In Fig. 3 three different geometries are presented together with the calculation of $\Delta\beta$ for single and double layer rib waveguides. The parameters are typical for the films investigated in this paper. It turns out that the double layer with the opposite Faraday-rotation show the highest nonreciprocal phase shift. But also in the case of paramagnetic bottom layer the maximum $\Delta\beta$ is 1.4 times larger as compared to the single layer geometry.

POLARIZATION MEASUREMENT

The nonreciprocal effect of planar waveguides has been measured by Mizumoto et al. [20] using interference technique and by Gerhardt et al. [21] and Wallenhorst et al. [13] using optical mode spectroscopy. For magneto-optic rib waveguides the nonreciprocal phase shift has been determined by Okamura et al. [22] applying an optical polarization technique. Shintaku et al. [23] applied an improved polarization technique which takes the superposition of TM and TE modes with different mode profiles into account.

To determine the waveguide parameters we used another polarization method presented in ref.[18]. This method, in addition, allows to detect depolarizing effects caused by scattering

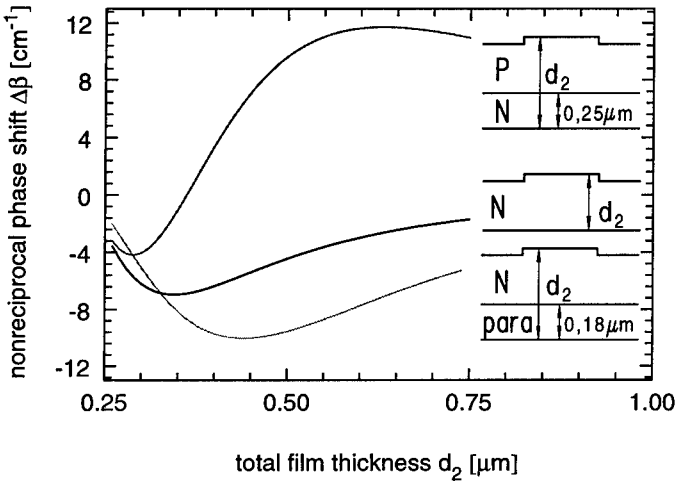

Figure 3: Calculated nonreciprocal phase shift $\Delta\beta$ of the TM_{00}-Mode for different waveguide structures at $\lambda = 1.3\ \mu$m. The waveguide parameters of the layer denoted with N are $n = 2.33$ and $\Theta_F = -1450°/\text{cm}$ and for P: $n = 2.27$ and $\Theta_F = +350°/\text{cm}$. The refractive index of the paramagnetic layer is n=2.2 . The rib width w and the rib height h are 2.0 μm and 0.04 μm and the refractive indices of the substrate and cover are 1.95 and 1, respectively. The thickness of the bottom layer is chosen to yield a maximum for the nonreciprocal phase shift $|\Delta\beta|$.

at defects at the end faces and waveguide flanks and by excitation of higher order modes. Furthermore, we are able to measure the TE/TM modecoupling. For the measurement we couple light of different linear polarizations into the waveguide and determine the polarization of the output light. Then we fit the waveguide parameters to the measured changes of polarization induced by the waveguide. For this purpose we apply the Jones formalism to the modes of the waveguide.

RESULTS AND DISCUSSION

The calculations displayed in Fig. 3 show that one can enhance $\Delta\beta$ by using double layers. The waveguides with a positive rotating top layer and a negative rotating bottom layer show the highest differential nonreciprocal phase shift [18]. However, the positive rotating film causes a large temperature dependence of $\Delta\beta$. To reduce this effect, the positive rotating film is replaced by a paramagnetic one with negligible Faraday-rotation. In Fig. 4 the temperature dependence of $\Delta\beta$ of two double layer films is displayed. To calculate $\Delta\beta(T)$ of these samples one can use Eq. 5 in the following form:

$$\Delta\beta(T) = \frac{\iint |H_y|^2 k_0 / 2n(\partial_x \frac{\Theta_i(T)}{\epsilon^2}) dxdy}{\iint \epsilon^{-1} |H_y|^2 dxdy} \quad mit \quad i = s, F_1, F_2, c. \tag{6}$$

The functions $\Theta_{F1}(T)$ and $\Theta_{F2}(T)$ are given from measured temperature dependence of

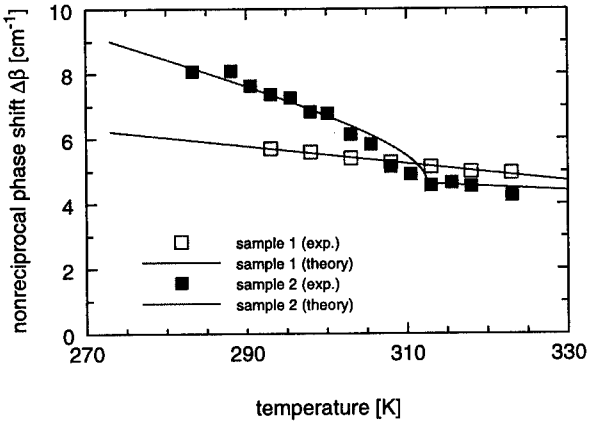

Figure 4: Measured temperature dependence of the nonreciprocal phase shift $\Delta\beta$ as compared with calculations. The composition and the material parameters of both samples are given in Table 1.

Faraday-rotation of the single layers by fitting with a molecular field theory (Fig. 2). The nonreciprocal phase shift $\Delta\beta(T)$ of sample 2 is mainly influenced by the top layer with Curie temperature: $T_C = 313$ K . The small $\Delta\beta$ of sample 1 is caused by the low Faraday-rotation $\Theta_{F2} = -900$ deg/cm. However, the temperature dependence is much better as compared to that of sample 2.

CONCLUSIONS

Double layer rib waveguides are a good choice to realize nonreciprocal devices. The temperature dependence of the nonreciprocal phase shift $\Delta\beta$ decreases by using double layers with a paramagnetic film instead of a film with positive Faraday-rotation. The further aim is to compensate $\Theta_F(T)$ of the negative rotating top layer by using a positive rotating bottom layer with opposite temperature dependence of Θ_F in the range between 270 K and 350 K.

ACKNOWLEDGEMENTS

We gratefully acknowledge financial support by Deutsche Forschungsgemeinschaft, Sonderforschungsbereich 225.

REFERENCES

[1] R. Wolfe, J.F. Dillon Jr., R. A. Lieberman, and V. J. Fratello, *Applied Physics Letters*, **57**, (10), pp. 960, 1990.

[2] M. Levy, I. Ilic, R. Scarmozzino, R. M. Osgood Jr., R. Wolfe, C. I. Guiterrez, and G. A. Prinz, *IEEE Photonics Technology Letters*, **5**, (2), pp. 198–200, 1993.

[3] M. Levy, R. M. Osgood Jr., H. Hegde, F. J. Cadieu, R. Wolfe, and V. J. Fratello, *IEEE Photonics Technology Letters*, **8**, (7), pp. 903–905, 1996.

[4] K. Ando, T. Okoshi, and N. Koshizuka, *Applied Physics Letters*, **53**, (1), pp. 4–6, 1988.

[5] T. Mizumoto, Y. Kawaoka, and Y. Naito, *The Transactions of the IECE of Japan*, **E 69**, (9), pp. 968–972, 1986.

[6] H. Hemme, H. Dötsch, and P. Hertel, *Applied Optics*, **29**, (18), pp. 2741–2744, 1990.

[7] S. Yamamoto, Y. Okamura, and T. Makimoto, *IEEE Journal of Quantum Electronics*, **QE-12**, (12), pp. 764–770, 1976.

[8] T. Shintaku, *Applied Physics Letters*, **66**, (21), pp. 2789–2791, 1995.

[9] A. Erdmann, P. Hertel, and H. Dötsch, *Optical and Quantum Electronics*, **26**, pp. 949–955, 1994.

[10] M. Lohmeyer, M. Shamonin, and P. Hertel, *Optical Engineering*, **36**, (3), pp. 889–895, 1997.

[11] F. Auracher and H.H. Witte, *Optics Communications*, **13**, (4), pp. 435–438, 1975.

[12] Y. Okamura, T. Negami, and S. Yamamoto, *Applied Optics*, **23**, (11), pp. 1886–1889, 1984.

[13] M. Wallenhorst, M. Niemöller, H. Dötsch, P. Hertel, R. Gerhardt, and B. Gather, *Journal of Applied Physics*, **77**, (7), pp. 2902–2905, 1995.

[14] A. Erdmann, M. Shamonin, P. Hertel, and H. Dötsch, *Optics Communications*, **102**, (1,2), pp. 25–30, 1993.

[15] M. Koshiba and X.P. Zhuang, *Journal of Lightwave Technology*, **11**, (9), pp. 1453–1458, 1993.

[16] N. Mabaya, P.E. Lagasse, and P. Vandenbulcke, *IEEE Transactions on Microwave Theory and Techniques*, **MTT-29**, (6), pp. 600–605, 1981.

[17] M. Shamonin and P. Hertel, *Applied Optics*, **33**, (27), pp. 6415–6421, 1994.

[18] N. Bahlmann, V. Chandrasekhara, A. Erdmann, R. Gerhardt, P. Hertel, R. Lehmann, D. Salz, F. Schröteler, M. Wallenhorst, and H. Dötsch, *Journal of Lightwave Technology*, **to be published in May 1998**, 1998.

[19] G. Winkler, *Magnetic garnets*, 1981.

[20] T. Mizumoto, O. Kiyoshi, T. Harada, and Y. Naito, *Journal of Lightwave Technology*, **LT-4**, (3), pp. 347–352, 1986.

[21] R. Gerhardt, S. Sure, H. Dötsch, T. Linkewitz, and W. Tolksdorf, *Optics Communications*, **102**, (1,2), pp. 31–35, 1993.

[22] Y. Okamura, H. Inuzuka, T. Kikuchi, and S. Yamamoto, *Journal of Lightwave Technology*, **LT-4**, (7), pp. 711–714, 1986.

[23] T. Shintaku, T. Uno, and M. Kobayashi, *Journal of Applied Physics*, **74**, (8), pp. 4877–4881, 1993.

INTEGRATED OPTICAL ISOLATOR EMPLOYING NONRECIPROCAL PHASE SHIFT BY WAFER DIRECT BONDING

H. YOKOI, T. MIZUMOTO
Department of Physical Electronics, Tokyo Institute of Technology, Tokyo, JAPAN,
hyokoi@o.cc.titech.ac.jp

ABSTRACT

A novel configuration of an integrated optical isolator employing a nonreciprocal phase shift is proposed. The isolator is equipped with a cladding layer of magnetic garnets by means of wafer direct bonding technique. This device has a semiconductor guiding layer, so high compatibility in integrating with other semiconductor optical devices is expected.

INTRODUCTION

An optical isolator is indispensable to protect optical active devices from unwanted reflected lights. The waveguide optical isolator employing a nonreciprocal phase shift is desirable because it does not need phase matching between the modes concerned and complicated magnetization control [1,2]. The nonreciprocal phase shift is experienced by TM modes traveling in a magnetooptic waveguide where the magnetization is aligned transversely to light propagation direction in the film plane. Figure 1 shows the optical isolator employing the nonreciprocal phase shift we have investigated in the past years. An optical interferometer is composed of two tapered couplers, nonreciprocal phase shifters in two arms and a reciprocal phase shifter in one of the arm. The reciprocal phase shift is achieved by an optical path difference between the two arms. The tapered coupler is composed of three coupled waveguides. The interferometer is designed so that the phase difference between the light waves propagating in the two arms becomes 0 and 180° for forward and backward traveling waves, respectively. This can be accomplished by 90° nonreciprocal phase shift and 90° reciprocal one. This device has a magnetic garnet guiding layer, a $Gd_3Ga_5O_{12}$ (GGG) substrate and a SiO_2 upper cladding layer.

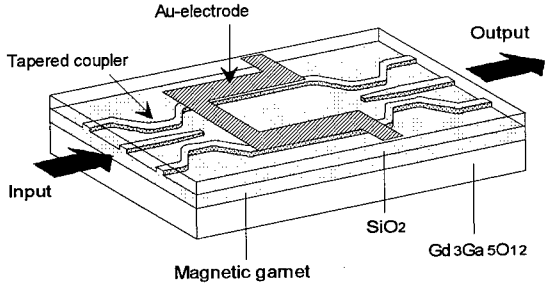

Fig. 1 Waveguide optical isolator employing a nonreciprocal phase shift composed of a magnetooptic guiding layer.

Mat. Res. Soc. Symp. Proc. Vol. 517 © 1998 Materials Research Society

Wafer direct bonding is an attractive technique for the integration of materials having dissimilar physical properties without any adhesives. Direct bonding has been used with silicon-on-insulator (SOI) [3,4], III-V compound semiconductors [5,6], and other materials [7]. We have applied this technique to the bonding between semiconductors and magnetooptic materials with the aim of integrating a semiconductor laser diode and an optical isolator [8]. Up to now, we have reported the bonding between InP and several kinds of garnet crystals. The direct bonding is achieved by chemical treatment of the wafer surfaces and subsequent heat treatment.

This technique enables us to realize novel device configurations. In this paper, we present an integrated optical isolator, employing a nonreciprocal phase shift, fabricated by the wafer direct bonding technique.

DEVICE STRUCTURE

Figure 2 shows schematic illustration of an integrated optical isolator, employing the nonreciprocal phase shift, fabricated by the wafer direct bonding technique. A magnetic garnet cladding layer is contacted to a GaInAsP guiding layer with no materials in between by the direct bonding technique. The structure is the same as the conventional isolator shown in Fig. 1 except that magnetic garnets are not used as a guiding layer but as an upper cladding layer. The waveguide has the semiconductor guiding layer that is transparent at the operating wavelength. Moreover, this device has high compatibility in integrating with other semiconductor optical devices.

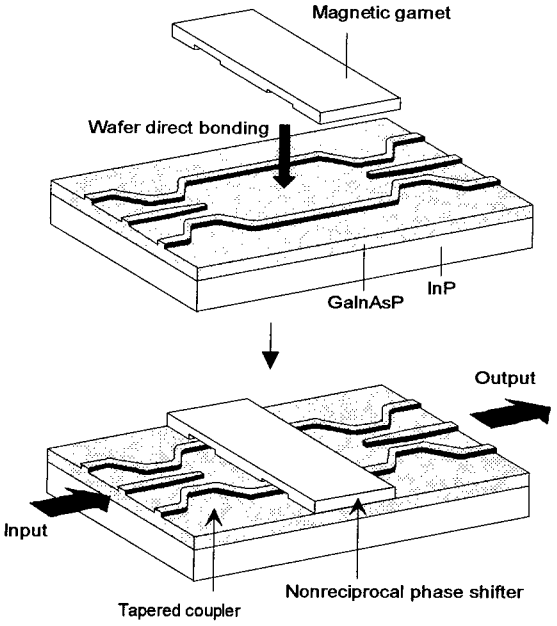

Fig. 2 Waveguide optical isolator fabricated by wafer direct bonding technique. A magnetic garnet cladding layer is contacted to a GaInAsP guiding layer by the bonding technique.

A nonreciprocal phase shift was calculated to estimate the propagation distance required for a 90° nonreciprocal phase shift. The rib waveguide with 0.1 μm rib height and 2.0 μm wide was assumed, as shown in Fig. 3. Figure 4 shows the calculated nonreciprocal phase shift experienced by light waves (λ = 1.55μm) traveling in the waveguide with a magnetic garnet / GaInAsP / InP structure. The abscissa indicates the thickness of a GaInAsP (λ_g = 1.25μm) guiding layer and the ordinate indicates the calculated nonreciprocal phase shift. $(LuNdBi)_3(FeAl)_5O_{12}$ (LNB), which has a Faraday rotation coefficient of -500 deg/cm at 1.55 μm, is used as the guiding layer of the isolator shown in Fig. 1. When LNB is used as a cladding layer of the isolator shown in Fig. 2, the required distance is approximately 50 mm for a 0.37μm-thick guiding layer. Magnetic garnets with large magnetooptic effect are requested to reduce the length of the nonreciprocal phase shifter. Ce-substituted yttrium iron garnet (Ce:YIG) is known to have a large Faraday rotation coefficient of -4500 deg/cm at 1.55 μm and in-plane magnetization [9,10]. When Ce:YIG is used as a cladding layer instead of LNB, the length can be reduced to 6.2 mm.

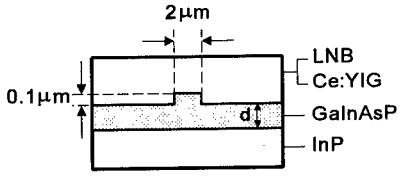

(d : GaInAsP film thickness)

LNB : $(LuNdBi)_3(FeAl)_5O_{12}$
Ce:YIG : $(CeY)_3Fe_5O_{12}$

Fig. 3 Design of a rib waveguide for calculating the nonreciprocal phase shift.

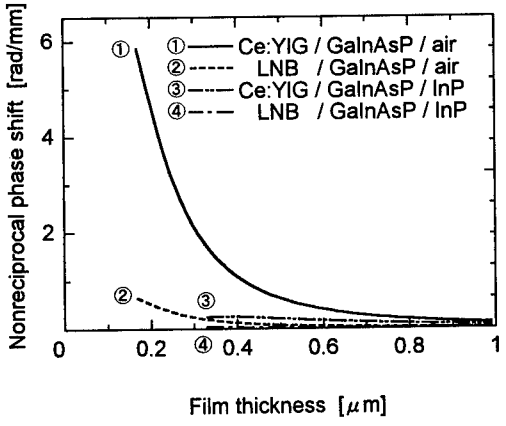

Fig. 4 Calculated nonreciprocal phase shift experienced by light waves at 1.55μm.

In the magnetic garnet / GaInAsP / InP structure, the contribution of the magnetic garnet to the nonreciprocal phase shift is weak, since only a small fraction of the guided light wave penetrates to the magnetic garnet due to its small refractive index compared with an InP substrate. Consider materials with refractive indices lower than magnetic garnets. For example, by etching an InP substrate, a lower cladding layer becomes air with refractive index 1.0. In Fig. 4, the calculated nonreciprocal phase shift was also shown for a structure of magnetic garnet / GaInAsP/ air. The maximum nonreciprocal phase shift is more than twenty times larger than that of magnetic garnet / GaInAsP / InP structure for both magnetic garnets. When LNB or Ce:YIG is used as a cladding layer, the required propagation distance is reduced to be 2.4 mm or 270 μm, respectively. The latter is of the same order as the cavity length of a semiconductor laser diode.

The optical isolator shown in Fig. 2 utilizes a push-pull nonreciprocal phase shift. Therefore, an external magnetic field is required to be applied in anti-parallel direction at respective arms. If there is one magnetooptic waveguide in the interferometer, the unidirectional magnetic field can be applied throughout the device. In this case, although the required propagation distance is twice as long as that for the push-pull type isolator, magnetization control becomes very easy.

EXPERIMENT

Wafer direct bonding between GaInAsP and magnetic garnets must be realized to construct the integrated optical isolator shown in Fig. 2. Low temperature wafer direct bonding between GaInAsP and GGG was studied. The wafers were cut to an appropriate size (5×5 mm^2), and then chemically treated to activate their surfaces. GaInAsP was treated with $HCl:H_3PO_4$ (1:3). GGG was slightly etched by H_3PO_4. The two wafers were contacted at room temperature and loaded into an annealing furnace for heat treatment. Taking into consideration that magnetic garnets were deteriorated by heat treatment in H_2 ambient at temperatures > 330℃ [8,11], heat treatment was performed in H_2 ambient at temperatures between 110 and 330℃. The bonded samples were subjected to the following device fabrication processes in order to investigate the bonding durability: baking, wet etching in a mixture of HCl and H_3PO_4, Ar sputter etching and thermal annealing at 600℃. Ar sputter etching was employed as a representative dry process in a plasma atmosphere.

Table I shows the results of the bonding between GaInAsP and GGG depending on the heat treatment temperature. Open circles indicate that the direct bonding was successful; i.e., samples remained bonded for longer than 24 hours. The bonding occurred at temperatures between 110 and 330℃. However, the bond strength was very weak for the samples bonded by the heat treatment at 330℃, so some samples separated into two wafers by handling with tweezers. It is suggested that the weakness of the bonded samples may be attributed to the thermal stress in the cooling stage after the heat treatment. The durability of the samples was also listed in Table I. The samples with heat treatment at 110 and 220℃ survived all processes intact. The bonded samples were also durable against high temperature test (150℃, > 500 hours).

Low temperature wafer direct bonding between GaInAsP and GGG was confirmed. The bonding between a planar InP wafer and a LNB rib waveguide was already achieved in our previous experiments. It is expected that the bonding between a GaInAsP rib waveguide and a magnetic garnet film will succeed.

Table I Results of the bonding between GaInAsP and GGG depending on the heat treatment temperature.

Temperature [℃]	110	220	330
Bonding	○	○	○
1. Baking	○	○	—
2. Wet etching	○	○	—
3. Ar sputter etching	○	○	×
4. Thermal annealing	○	○	—

1. Baking at 200℃ for 30 min.
2. Wet etching in the mixture of $HCl:H_3PO_4$ (3:1) for 1 min.
3. Ar sputter etching for 10 min.
4. Thermal annealing at 600℃ in H_2 ambient for 30 min.

CONCLUSIONS

A novel configuration of an integrated optical isolator employing a nonreciprocal phase shift was proposed. The magnetooptic waveguide with magnetic garnet / GaInAsP / InP (or air) structure can be fabricated by a wafer direct bonding technique. When Ce-substituted yttrium iron garnet is used as a cladding layer of the nonreciprocal phase shifter, the propagation distance required for a 90° nonreciprocal phase shift is almost same as the cavity length of a semiconductor laser diode. Since the device has a semiconductor guiding layer, high compatibility in integrating with other semiconductor optical devices is expected.

ACKNOWLEDGMENTS

The authors would like to acknowledge Dr. Y. Naito, a professor emeritus, for fruitful discussions. This work was partially supported by Exploratory Research on Novel Artificial Materials and Substances for Next-Generation Industries, Research for the Future from Japan Society for the Promotion of Science (JSPS-RFTF97P00103).

REFERENCES

[1] F. Auracher and H. H. Witte, Optics Commun. **13**, p.435 (1975).
[2] T. Mizumoto, S. Mashimo, T. Ida and Y. Naito, IEEE Trans. Magn., **29**, p.3417 (1993).
[3] J. B. Lasky, Appl. Phys. Lett., **48**, p.78 (1986).
[4] M. Shimbo, K. Furukawa, K. Fukuda and K. Tanzawa, J. Appl. Phys., **60**, p.2987 (1986).
[5] Y. H. Lo, R. Bhat, D. M. Hwang, M. A. Koza and T. P. Lee, Appl. Phys. Lett., **58**, p.1961 (1991).
[6] H. Wada, Y. Ogawa and T. Kamijoh, Appl. Phys. Lett., **62**, p.738 (1993).
[7] Y. Tomita, M. Sugimoto, K. Eda and T. Okano, Jpn. J. Appl. Phys., **33**, p.L1542 (1994).
[8] H. Yokoi, T. Mizumoto, K. Maru and Y. Naito, Jpn. J. Appl. Phys., **36**, p.2784 (1997).
[9] M. Gomi, S. Satoh and M. Abe, Jpn. J. Appl. Phys., **27**, p.L1536 (1988).
[10] T. Shintaku and T. Uno, J. Appl. Phys., **76**, p.8155 (1994).
[11] Y. Yokoyama, N. Koshizuka and N. Takeda, J. Magn. Soc. Jpn., **12**, p.175 (1988) [in Japanese].

CRYSTAL ION-SLICING OF MAGNETIC AND FERROELECTRIC OXIDE FILMS

M. LEVY *, R.M.OSGOOD, Jr. *, A. KUMAR **, H. BAKHRU **, R. LIU ***,
E. CROSS ***
*Department of Applied Physics, Columbia University, Street, New York, NY; 10027
**Department of Physics, State University of New York at Albany, Albany, NY,
***Materials Research Laboratory, Pennsylvania State University, University Park, PA 16802

ABSTRACT

The epitaxial separation of single-crystal magnetic and ferroelectric oxide films is presented. Ion implantation is used to create a buried damage layer beneath the surface. The high etch-selectivity of this sacrificial layer makes it possible to detach high quality single-crystal films from bulk samples. Magnetic and electrical properties of the films are discussed.

INTRODUCTION

Bismuth-substituted yttrium iron garnet (Bi-YIG) and lithium niobate ($LiNbO_3$) constitute particularly important materials for integrated-photonic device fabrication, because of their strong magneto-optic (Bi-YIG) and electro-optic response ($LiNbO_3$) characteristics. Magnetic garnets (Bi-YIG) are needed for on-chip thin film optical isolators, while $LiNbO_3$ is used to fabricate highly efficient electro-optic modulators. However, it has been heretofore impossible to integrate devices of these oxide systems on semiconductor platforms because of the complex high-temperature chemistry, as well as the usual problems of lattice matching, inherent in the growth of mixed oxides on single-crystal semiconductor surfaces. We describe here a novel technique to detach thin films of these oxides from their growth substrates and bond them onto semiconductor platforms.

EXPERIMENT

Samples

The crystal samples used in this study are obtained from epitaxial thin film growth (YIG) and from homogeneous bulk crystals ($LiNbO_3$). In the case of the former, the samples are obtained from 9μm-thick single-crystal films of yttrium iron garnet grown by liquid-phase epitaxy on a (111)-oriented gadolinium gallium garnet (GGG). These epitaxial films have a formula unit of $Y_3Fe_5O_{12}$, with small amounts of lanthanum to improve lattice matching to the GGG substrate. The magnetization in the yttrium iron garnet is quasi-planar, with striped domains visible under Faraday-contrast microscopy. Three-μm-thick Bi-YIG epitaxial films on GGG are also used to study the effect of ion implantation below the epilayer/substrate interface. The uniaxial growth anisotropy in these samples, typical of bismuth-substituted YIG films, results in the formation of magnetic domains with the magnetization directed normal to the sample surface. The bismuth-substituted epilayers have a formula unit of $Bi_{0.6}Y_{2.4}F_5O_{12}$, with trace amounts of gallium. The $LiNbO_3$ samples are z-cut bulk single-crystal wafers, poled along the c-axis. They are fabricated by the Czochralski technique.

Mat. Res. Soc. Symp. Proc. Vol. 517 © 1998 Materials Research Society

Processing

Singly-charged helium ions at 3.8 MeV of energy are implanted several microns below the top surface with little residual damage to the near-surface region. The implant dose on all samples is 5 X 10^{16} ions/cm^2. The samples are mounted on a 2 in.-diameter water-cooled target holder to ensure that the temperature of the substrate is below 400 °C. The uniformity of the implantation is checked by four Faraday cups outside the target holder. Helium is chosen as the implantation species because of its light weight, yielding a deeply buried damage layer, as depicted schematically in Fig. 1.

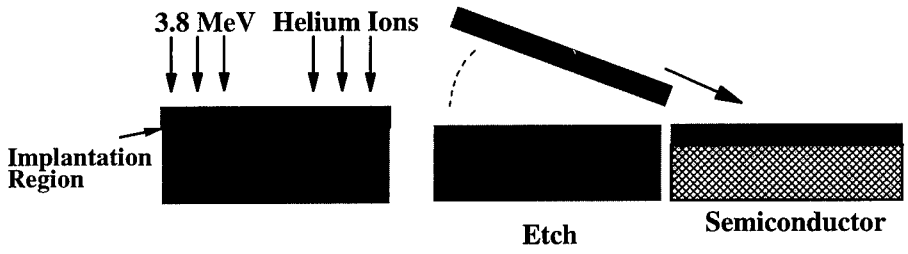

Fig. 1. Steps in crystal ion-slicing process.

Lattice defects are introduced by the transfer of energy to the target nuclei, and form mostly near the end of the ionic trajectories. Two dominant mechanisms for energy loss determine the implantation profile and the distribution of lattice damage in the crystal [1]. The energy loss per unit trajectory length, known as the stopping power, is dominated by electronic scattering at high ionic energies. This process generates very little lattice damage. At low energies the stopping power is primarily due to Rutherford scattering with the host nuclei., and generates atomic dislocations.

Transport-of-ions-in-matter [2] calculations for helium implanted at 3.8 MeV of energy into YIG, Bi-YIG, GGG, and $LiNbO_3$, show that the implantation profile is rather narrow and concentrated 8 to 10 μm below the top surface in all cases. The damage generated by the implantation induces a large etch selectivity between the sacrificial layer and the growth substrate [1].

The YIG and Bi-YIG samples are etched in commercial 85%-dilution orthophosphoric acid, an etchant reported previously for lateral patterning of ion-implant waveguides in YIG [3]. The $LiNbO_3$ samples are etched in a 10%-dilution of commercial 49%-dilution hydrofluoric acid. In all cases, a deep undercut forms after several hours in the etchant. The location of the undercut is in good agreement with the calculated implantation profile.

If unprotected during etching, the top surface of the sample is roughened by exposure to the acid. This roughening is due to residual lattice damage near the top generated by the ion implantation. The roughening process has been studied under several preparation conditions for

the YIG samples using a surface profilometer. After six hours exposure under typical etching conditions, the average roughness was measured to be 20 nm. Rapid thermal annealing (RTA) before etching but after implantation repairs this residual damage without compromising the efficiency of the subsequent wet etching of the buried layer. Specifically, tests show that, for the YIG samples, a 40s anneal (RTA) at 710 °C in forming gas (5% hydrogen, 95% nitrogen) results in a smooth surface. In this case, little difference in surface roughness is detected between etched and unetched films. On the other hand, doing the same RTA at temperatures above 800 °C, makes a significant impact on the etch rate of the buried layer by annealing out damage in this layer.

An important concern in the earlier stages of this work was whether the YIG/GGG interface would itself exhibit selective etching, or perhaps cause a more subtle influence on ion energy deposition due to ionic back-scattering during the implant process. Subsequent measurements showed that the substrate/epilayer interface plays no role in the formation of the sacrificial-layer undercut. Specifically, tests carried out on unimplanted samples show that no undercut forms in this case and that the thickness of the detached film is determined solely by the effect of material density and structure on the implantation profile, independently of epilayer thickness.

To fully detach a section of film of square-millimeter area from the substrate, the sample must be in the etchant for 24h to 48h. But contrary to the case of III-V materials, it is not necessary to rely on the stress created by any protective cover to allow the flow of reaction products away from the etching zone [4]. The films are then bonded to silicon or GaAs either by hydrophilic bonding or with an adhesive.

Yttrium iron garnet films are quite brittle and must be handled carefully to avoid developing microfractures during the processing. We have been able to produce fracture-free films routinely, but have found that some protective encapsulation or pre-patterning is needed to prevent cracks from developing. X-ray crystallographic analysis comparing implanted and unimplanted samples shows no evidence of crystal plane deformations in the epitaxial layer resulting from the implantation process itself. On the other hand, the fact that cracks develop only at the corners of the sample or in regions where oppositely directed acid flows meet, suggests that fracture formation is due to stress from bowing of the epilayer during the etching process. No equivalent cracking is found in the $LiNbO_3$ films, although they do exhibit shallow (100nm-deep) linear formations of trigonal symmetry on the underside. We are presently investigating the origin of these patterns.

Etchless Delamination of Bi-YIG Films

It is also possible to induce the separation of Bi-YIG films from their growth substrate solely by annealing, without etching, as depicted schematically in Fig. 2. This splitting occurs at the sacrificial layer. In order for the process to work, the implantation must be done across the YIG/GGG interface and into the GGG substrate. We have not found a condition for etchless delamination if the peak of the implantation profile resides in the YIG or Bi-YIG film. A rapid thermal anneal of 40 s at 810 °C is sufficient to detach the film above the implantation layer. However, it is necessary to provide rigid support to the film in order to maintain its integrity during the rapid thermal annealing. We are presently investigating the direct wafer bonding of Bi-YIG samples to semiconductor substrates for this purpose, using the technique described in Ref. [5].

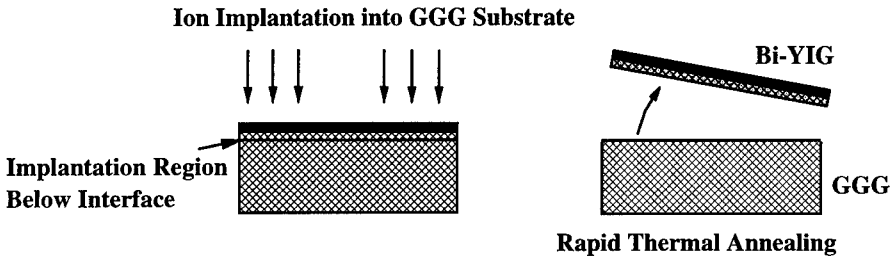

Fig. 2. Etchless delamination by rapid thermal annealing.

RESULTS

Magnetic and Electrical Properties

The domain structure in YIG and Bi-YIG films after crystal ion-slicing (CIS) was studied by Faraday contrast microscopy. The YIG samples used are (111) films with quasi planar anisotropy and some residual cubic anisotropy. These films have a lattice constant a = 12.378 Å and are therefore in tension on the GGG substrate (a = 12.383 Å). No change in the character of the anisotropy occurred as a result of the ion implantation and crystal slicing procedure, although some regions of the detached film exhibited fully lying-down domains (no residual vertical magnetization). A reduction in the measured in-plane saturation magnetic field was observed for the free-standing CIS films relative to the original unimplanted material, as described in Table I. Since these 9μm-thick YIG films are completely detached from their growth substrate, it is possible that some stress relaxation from the lattice mismatch might have occurred, thus affecting the saturation field. We are presently investigating this question.

Table I. Measured Saturation Magnetic Field for YIG Films

	(oersted)	
Crystallographic Direction	$<11\bar{2}>$	$<1\bar{1}0>$
Free-Standing CIS Film	34	75
Original Unimplanted Material	75	140

The Bi-YIG films studied have uniaxial anisotropy and maze-type domains. No change in the character of the anisotropy or domain structure occurred as a result of the crystal ion-slicing process. This contrasts with the effect of energetic heavy-ion implantation in garnets,

where damage-generated changes in the domain structure are found [6]. Electronic-dominated scattering is responsible for the stopping power in the YIG and Bi-YIG epilayers, generating very little damage except in and around the sacrificial layer [1]. Comparison between the saturation magnetic field in the Bi-YIG crystal before and after implantation and liftoff shows no change within experimental uncertainty. The measured saturation field is 250 Oe. Optical insertion loss measurements in Bi-YIG waveguide films before and after ion implantation below the epilayer/substrate interface are discussed in Ref. [7].

The poled single-crystal samples of $LiNbO_3$ maintain their polarization in the crystal ion-slicing process, indicating that the ion implantation and liftoff does not cause the film to break up into ferroelectric domains. Capacitive measurements of the low-frequency dielectric response in the $LiNbO_3$ CIS films show that the detached films have the same dielectric constant as the bulk single-crystal material to within experimental uncertainty. The measured value of the dielectric constant is 30.88. The films also exhibited a strong pyroelectric response. These results will be published elsewhere.

CONCLUSIONS

Single-crystal films of yttrium iron garnet and lithium niobate are fabricated by crystal ion-slicing. No change in anisotropic character or domain structure is observed in films with uniaxial and quasi planar magnetization. Moreover, no domain pinning or increase in magnetic coercivity is detected in the YIG and Bi-YIG films. The $LiNbO_3$ films exhibit the same low-frequency dielectric constant as single-crystal bulk material.

ACKNOWLEDGMENTS

We thank P.-C. Wang for the X-ray crystallography on YIG samples, and G.S. Cargill, III, for illuminating discussions. M.L. and R.M.O. acknowledge support by MURI/DARPA under contract #F49620-96-1-0111.

REFERENCES

1. M. Levy, R. M. Osgood, Jr., A. Kumar, H. Bakhru, Appl. Phys. Lett. **71**, 2617 (1997).

2. J. P. Biersack and L. G. Haggermark, Nucl. Instrum. Methods Phys. Res. **174**, 257 (1980).

3. W. A. Johnson, J. C. North, and R. Wolfe, J. Appl. Phys. **44**, 4753 (1973).

4. Eli Yablonovitch, T. Gmitter, J. P. Harbison, and R. Bhat, Appl. Phys. Lett. **51**, 2222 (1987).

5. H. Yokoi, T. Mizumoto, K. Maru, N. Fuke, Y. Naito, Jpn. J. Appl. Phys. **35**, 4138 (1996).

6. P. Hansen, in *Proceedings of the International School of Physics Enrico Fermi*, edited by A. Paoletti (North Holland, New York, 1978), p.61.

7. M. Levy, R. M. Osgood, Jr., A. Kumar, and H. Bakhru, J. Appl. Phys. **83**, (1998).

Integration of Yttrium Iron Garnet Films via Reactive RF Sputtering

Bethanie J. H. Stadler and Anand Gopinath

Department of Electrical and Computer Engineering, University of Minnesota, Minneapolis, MN 55126 (stadler@ece.umn.edu)

ABSTRACT

This work aims to equip integrated optical circuits with important magneto-optical devices, such as isolators, that are currently available only as discrete components. Reactive rf sputtering was used to grow cerium-doped yttrium iron garnet films onto a variety of substrates, including SiO_2-buffered Si, fused SiO_2 and MgO. MgO was used because it has proven to be a good buffer material for semiconducting substrates. Ce-doping was not effective via reactive sputtering due to a scale which formed on the Ce metal that prevented sufficient contact with the rf target. The films were amorphous as deposited. Stoichiometric $Y_3Fe_5O_{12}$ films yielded smooth, polycrystalline garnet films upon annealing. A study of the effect of fluctuations in the Y:Fe ratio revealed that oxygen content is important for the prevention of secondary phases. Therefore, a high oxygen content should be used in the sputtering gas and subsequent annealing should be performed in oxygen.

INTRODUCTION

The motivation driving this work is the integration of magneto-optical materials with semiconductor platforms. Many important applications will benefit from this integration, including photonic integrated circuits (PICs) through nonreciprocal waveguide devices such as isolators, and high resolution magneto-optic screens through spatial light modulators. Currently the choice materials for commercial magneto-optical devices are iron garnets, such as yttrium iron garnet (YIG), that are grown by liquid phase epitaxy. This technique involves very high temperatures, but more importantly, it requires garnet substrates. Therefore, integration with semiconductor platforms is only possible through hybrid techniques, such as ion slicing [1] and thermal bonding [2].

This work investigated a new fabrication technique, reactive rf sputtering, for growing iron garnets directly onto buffered semiconductor substrates. Sputtering produces more adherent, dense films than other vacuum phase techniques, and a variety of substrates can be used. The potential monolithic integration of magneto-optical components with semiconductor electro-optics promises to decrease the size, weight and cost, and increase the speed and reliability of photonic integrated circuits (PICs) and other advanced devices. Although other MO materials, such as dilute magnetic semiconductors and transition metal- and rare earth-doped III-V semiconductors, are easier to integrate with semiconductor platforms, YIG has orders of magnitude greater Faraday rotation.

Sputtering can also be used to deposit oxide buffer layers onto semiconductor substrates to protect their surfaces from decomposition and chemical reactions during garnet deposition. These same buffer layers can act as claddings for integrated magneto-optical devices which will function as waveguides. This work focused on using a variety of substrates including themally oxidized Si, and SiO_2 and MgO which have proven successful as buffer layers for use with MOCVD-grown Ce:YIG films.[3] Future work will involve sputtering buffer layers onto GaAs, InP and Si substrates prior to YIG deposition.

Mat. Res. Soc. Symp. Proc. Vol. 517 © 1998 Materials Research Society

EXPERIMENTAL

Fabrication of Ce:YIG. Reactive rf sputtering of 8" metallic targets was used to fabricate the films in this work. The targets were pure Y and Fe from Pure Tech Inc. An O_2 flux was added to the Ar sputtering gas in order to grow oxide films. Unfortunately, given the configuration of the system (the gases were fed in together), the targets were also oxidized so the deposition rate was slow. The target oxidation could be seen from the bias volages which were 500-1000V and 950-1550V for the Y and Fe targets, respectively, at rf powers of 3.1-6.2 W/cm^2. These bias voltages were almost doubled when the targets were cleaned in pure Ar such that the oxide suface layer was sputtered off. Between 20 and 35% O_2 was used in the sputtering gas and the pressure was maintained at 10 mTorr. The substrates used in this work included thermally oxidized Si, double polished Si, fused SiO_2 and MgO. The substrates were rotated under the Y and Fe targets at a rate to ensure no more that one atomic layer per rotation. The deposition rate was 10 Å/min which is comparable to films made via rf sputtering of oxide targets.[4,5] In the future, we hope to configure a system such that the targets can be sputtered as metals for faster deposition rates while O_2 by the substrates will allow the films to grow as oxides.[5] The films were annealed up to 1000°C in air for 3 hours in order to study the effects of fluctuations in the Y:Fe ratio on the resulting crystal structure.

Ce-doping was performed by adhering pieces of Ce foil to the surface of the Y target. The authors have used this method in doping Al_2O_3 waveguides with Er to make waveguide amplifiers. In the latter case, graphite tape has been a sufficient adhesive, and it is easy to remove and reapply. However, for several reasons this method was not appropriate here. Mostly, the level of dopant required was much higher (up to 50% would be acceptable) and the graphite was conductive enough to allow this level of sputtering. Therefore, a silver epoxy was used in later films in order to improve contact. In both cases, a severe scale on the Ce foil prevented optimal contact. This scale was removed using a razor blade, but some oxide was always present and a sufficient contact could not be achieved.

Characterization of Ce-YIG. These films were analyzed by a scanning electron microscope that was equipped with energy dispersive spectroscopy (EDS) for compositional analysis. An accelerating voltage of 10 keV was used in order to decrease the signal from the substrate. Some typical spectra are shown in Fig. 1 with the elemental peaks labelled. For a few of the samples, X-ray photoelectron spectroscopy was also used to verify composition. X-ray diffraction in a conventional θ-2θ configuration was used for analysis of crystal structure. Optical microscopy and electron microscopy were used to view the microstructure of the films.

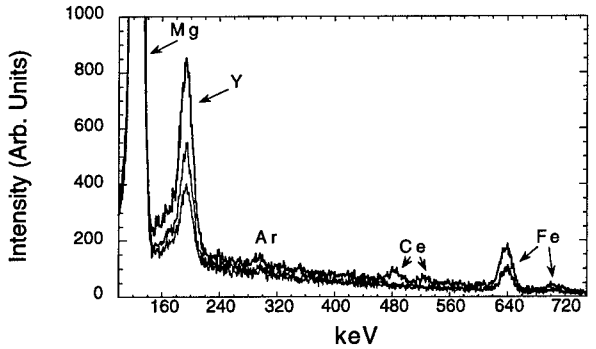

Fig. 1- Typical EDS spectra.

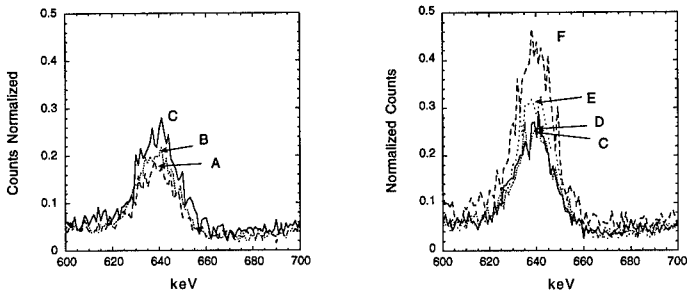

Fig. 2- Fe peak of normalized EDS spectra. Film C had the ideal stoichiometry of Y:Fe = 3:5. a) Fe-deficient films b) Fe-rich films.

RESULTS AND DISCUSSION

Composition of Ce-YIG. The EDS spectra of the Ce-YIG films were normalized using the Y peak so that compositions could be compared. This was necessary to account for effects due to variations in thickness and also due to the substrate (MgO). The samples were lettered for this paper using increasing Fe ratios with Sample C exhibiting the ideal garnet Y:Fe ratio of 3:5 according to EDS, XPS and XRD. As shown in Fig. 2, the Y:Fe ratio could be altered in a controlled fashion in order to provide samples with deficiencies or excesses of Fe. The effects of annealing on these samples is discussed below.

As was mentioned in the previous section, Ce doping was difficult due to poor conductivity between the Y target and the Ce foil that was adhered to it. Graphite tape was used as an adhesive for films D and E, but its conductivity did not appear sufficient to allow efficient Ce doping. However, when silver epoxy was used instead, it yielded a only a slightly higher dopant concentration. The Ce foil occupied 12% of the surface area of the Y target for films B and D, but the maximum Ce content (in film B) was only 1.6% Ce, as determined by XPS. The problem most likely stemmed from a scale which readily formed on the surface of the Ce foil. This scale was removed with a razor blade several times, but Ce has too high an affinity for oxygen to remain clean. In future studies, a new dopant will be selected.

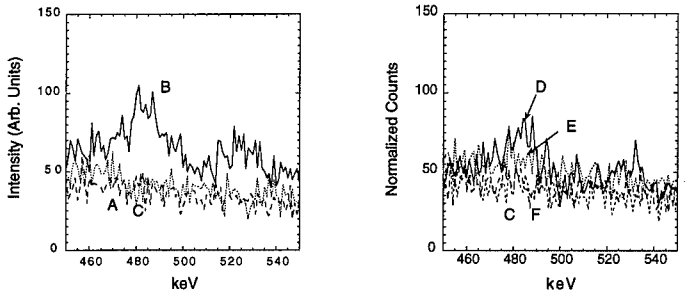

Fig. 3- Ce peak of normalized EDS spectra. For films D and E, Ce foil was adhered to to the Y target with graphite tape; for film B, it was adhered with Ag epoxy.

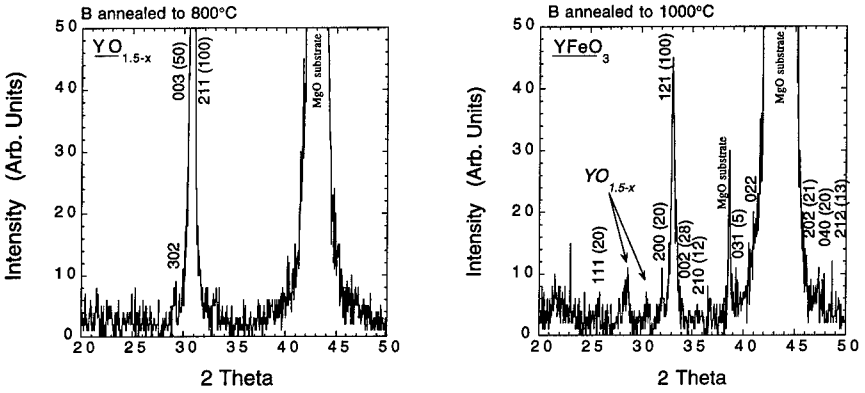

Fig. 4- XRD curves of Fe-deficient film annealed to 800 and 1000°C.

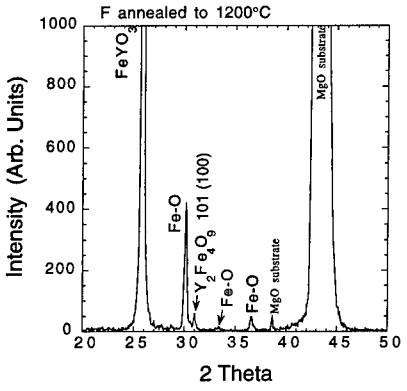

Fig. 5- XRD curves of very Fe-deficient films annealed to 1000°C.

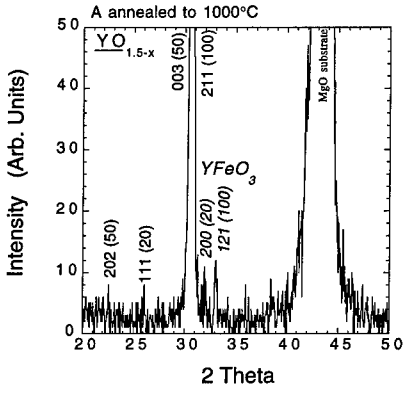

Fig. 6- XRD curves of Fe-excess films annealed to 1200°C.

Crystal structure of films. The films were all amorphous as-deposited and they remained amorphous with anneals up to 700°C. $YO_{1.5-x}$ was observed in iron deficient films that were annealed at 800°C, and the perovskite $YFeO_3$ was observed with 1000°C anneals, Fig. 4. Films that were very iron deficient yielded a corresponding mix of $YO_{1.5-x}$ and $YFeO_3$ at 1000°C, Fig. 5. Excess iron led films to crystallize into $FeYO_3$, along with iron oxides and the orthorhombic $Y_2Fe_4O_9$ at 1000°C, Fig.6. Fortunately, however, films composed of the ideal Y:Fe ratio of 3:5 yielded the garnet structure at both 800°C and 1000°C, Fig. 7. These films were also made with higher $\%O_2$ in the sputtering gas. In addition, unlike the other films, the garnet films had microstructures that were very smooth by optical and electron microscopy.

These microstructural results can be explained using the Y-Fe-O ternary phase diagram, Fig. 8. The compositions of the iron-deficient films lay within the compatibility triangle labelled A. As expected the Y-oxide and the perovskite were present at 1000°C. A small amount of the orthorhombic phase may have been present also, but the peak would have been obscured by the 003 peak of the Y-oxide. The compositions of the iron-excess films were within the compatibility triangle labelled B. In this case, $FeYO_3$, Fe-oxide, and $Y_2Fe_4O_9$ were all present. This result gives a clear glimpse of a possible solution to fabricating better films, namely they should have been annealed in oxygen or made with a higher oxygen content in the sputtering gas. As the composition of the films nears the Fe apex (away from the Y_2O_3-Fe_2O_3 binary), the oxygen content decreases. In particular, the films within the "B" compatibility triange must have been fairly deficient of oxygen. Therefore, it may be possible to accomodate fluctuations in the Y:Fe ratio by using high $\%\ O_2$ in the sputtering gas and/or by annealing in O_2.

CONCLUSIONS

It was relatively easy to tailor composition using reactive co-sputtering of Y and Fe metallic targets. However, a Ce scale prevented efficient doping to make Ce:YIG films so other dopants will be used in future work. When annealed, stoichiometric films yielded smooth polycrystalline YIG which has potential for magneto-optical applications since its isotropic index promises low scattering losses at grain boundaries. The effect of Y:Fe compositional fluctuations was studied. Fe-deficient films yielded $YFeO_3$ and Y-oxide upon annealing, and Fe-rich films were in the $Y_2Fe_4O_9$-$YFeO_3$-FeO compatibility triangle. These results indicate that using excess O_2 in the sputtering gas and/or annealing in O_2 may compensate for fluctuations in the Y:Fe ratio which may occur with upscaling this process.

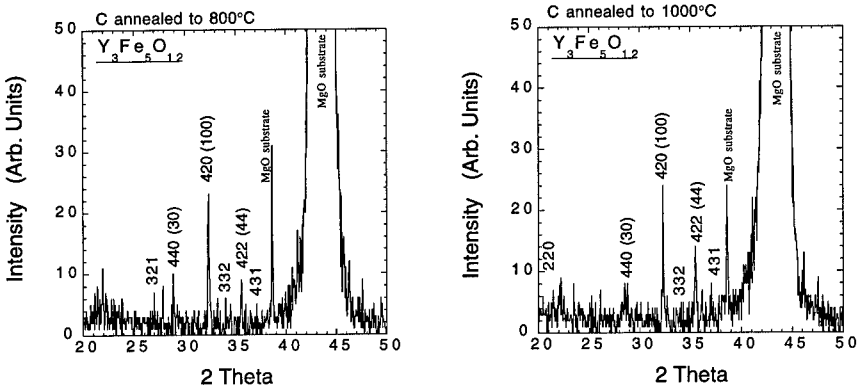

Fig. 7- XRD curves of films with the ideal garnet Y:Fe ratio of 3:5 crystallized into YIG.

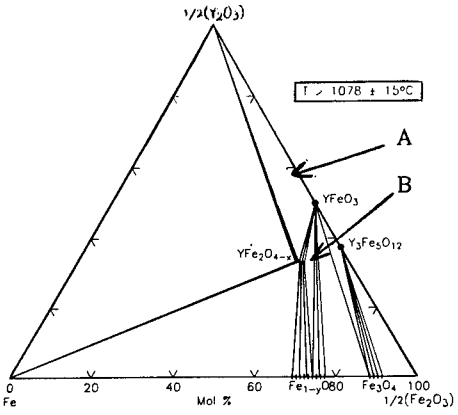

Fig. 8- Fe-Y_2O_3-Fe_2O_3 Phase Diagram. [7]

ACKNOWLEDGEMENTS

The authors would like to thank Joe Lorenzo's group at the Air Force Research Laboratory for their help in this work and also Mark Fisher, Keven Roberts and the University of Minnesota's Microtechnology Laboratory for equipment assistance.

REFERENCES

[1] M. Levy, R. Osgood, A. Kumar, H. Bakhru, R. Liu, and E. Cross, "Crystal Ion Slicing of Magnetic and Ferroelectric Oxide Films," *MRS Proceedings: High Density Recording and Integrated Magneto-Optics: Materials and Devices.* To be published (1998).

[2] H. Yokoi and T. Mizumoto, "Integrated Optical Isolator Employing Nonreciprocal Phase Shift by Wafer Direct Bonding," *MRS Proceedings: High Density Recording and Integrated Magneto-Optics: Materials and Devices.* To be published (1998).

[3] B. Stadler, Y. Li, M. Cherif, K. Vaccaro, and J. Lorenzo, "Doped Yttrium Iron Garnet Thin Films for Integrated Magneto-Opitcal Applications," *MRS Proceedings **446**: Amorphous and Crystalline Insulating Thin Films- 1996*, pp. 389-394.

[4] M. Gomi, H. Furuyama, and M. Abe, "Strong Magneto-Optical Enhancement in Highly Ce-Substituted Iron Garnet Films Prepared by Sputtering," *J. Appl. Phys.* **70** [11] (1990) p.7065-7

[5] Y. Okamura and S. Yamamoto, "Patterned Garnet Films on Substrates with Ion-Beam Bombarded Micropatterns,' *MRS Proceedings: High Density Recording and Integrated Magneto-Optics: Materials and Devices.* To be published (1998).

[6] B. Stadler, M. Oliveria, and L. Bouthillette, "Alumina Thin Films as Optical Waveguides," *Journal of the American Ceramic Society* **78** [12] 3336-44 (1995).

[7] Phase Diagrams for Ceramists VI. Eds R. Roth, J. Dennis, H. McMurdie. The American Ceramic Society, Westerville, OH (1987) p. 57.

PATTERNED GARNET FILMS ON SUBSTRATES WITH ION-BEAM BOMBARDED MICROPATTERNS

Yasuyuki Okamura*, Sadahiko Yamamoto
Osaka University, Graduate School of Engineering Science, Division of Advanced Electronics and Optical Science, 1-3 Machikaneyama-cho, Toyonaka, Osaka 560-8531 Japan,
okamura@ee.es.osaka-u.ac.jp
* Also with Wakayama University, Faculty of Systems Engineering, Department of Optomechatronics, 930 Sakaedani, Wakayama, Wakayama 640-8510 Japan

ABSTRACT

We report the selected-area epitaxy of rare-earth iron garnet crystalline and amorphous straight ridge patterns, from 4μm to 8μm in width, deposited on $Gd_3Ga_5O_{12}$ single crystal substrates. These samples were fabricated via a sputter epitaxial method on substrates that were partially etched by ion-beam bombardment. The strip pattern direction has given the considerable influence on the crystal-graphic formation of the sidewall of the grown ridge. The ridge shapes were similar to results that have been reported for the dissolution forms of garnet crystals in phosphoric acid and the facet of garnet crystals grown from flux. Furthermore, we have successfully grown both an epitaxial garnet film onto an amorphous film and an amorphous straight ridge with a triangular shape surrounded by crystal.

1.INTRODUCTION

Since cerium ion substitution in rare-earth iron garnets, in particular prepared by a sputtering, was discovered to play an important role in enhancing of Faraday rotation [1], there have been many reports concerning this material. Gomi et al. pointed out the important role of charge transfer transition from Ce^{+3} to Fe^{+3} for enhancement of the magneto-optic effect by measuring optical absorption.[2] Mino et al. investigated the structure and lattice deformation in cerium substituted yttrium iron garnet (Ce:YIG) in detail.[3] Shintaku et al. demonstrated a preliminary optical isolator using an optical channel waveguide fabricated with a Ce:YIG film.[4] Rf-diode sputtering has been conventionally used to prepare this class of iron garnet films. This technique allows us to grow nonequivalent component crystalline films, large lattice mismatched films, and disordered garnet films. Large amounts of cerium ion substitution into the rare-earth iron garnet phase is especially important.[5] The employed substrates have been gadolinium gallium garnet (GGG), magnesium doped zirconium gadolinium gallium garnet (GGCMZ), and neodymium gallium garnet (NGG). The surface of these substrates is usually polished chemically with no other surface treatment. Krumme et al. discovered that the onset temperature of single crystal bismuth substituted rare-earth iron garnet films grown on substrates whose surfaces were modified by rf-sputtering, was higher than that of films grown on unmodified substrates, and suggested selected-area epitaxy (SAE) of such films.[6]

Recently the authors discovered that etching the garnet substrate by ion-beam bombardment gave an essential influence on the crystal formation of the Ce:YIG film and revealed the deposition condition: high ion-beam energy leads to the amorphous film formation.[7] In this paper the same selected-area sputter epitaxy deposition technique was applied to the formation of amorphous and crystalline ridge strip patterns on garnet substrates. We present a method for fabricating patterned films with a micrometer width, a measured result with an XRD technique, crystal-graphic consideration of the interface between the crystalline and the amorphous regions, and observed results with a conventional optical microscope and a scanning electron microscope.

2.EXPERIMENT

2.1.Surface modification of substrate by ion-beam etching

Krumme et al. used an rf-sputtering technique to modify the surface state of a substrate. The

Mat. Res. Soc. Symp. Proc. Vol. 517 © 1998 Materials Research Society

plasma energy employed was 0.2keV, suggesting that even such small energy (compared to other ion beam bombardment methods) can affect the conditions for growing single crystal films of bismuth substituted YIG.[6] However, the plasma yielded by conventional sputtering exhibited nonuniformity, which led to irregularity of the substrate surface. Therefore, the method is not appropriate for controlled surface modification, although no detailed observation of the surface state was performed. We employed an ion-beam etching technique for the surface modification of a gadolinium gallium garnet (GGG) substrate instead of rf-sputtering. Ion-beam etching can remove atoms from the surface of a solid by bombardment with a collimated beam of ions. Since ion-beam etching takes place external to the ion discharge chamber, substrates are not subjected to a plasma environment. In addition, ion energy and ion flux density may be independently controlled, and substrate orientation to the ion beam may be varied. Disordered bonding atoms exist on the surface of the substrate and residual damage exists in the surface depth. We calculated the damaged layer depth on the order of few angstroms to tens angstroms into the GGG substrate irradiated by 0.2keV argon ion bombardment using transport-of-ions-in-matter (TRIM) simulator.[8] Furthermore, the residual damage inside of the layer near the surface can be removed by heating when growing the film. We used a Kauffman type ion-beam mil with a 3cm-diameter ion gun and Ar as the bombardment ion. The etching was performed at 2.6×10^{-2} Pa. The ion-beam bombardment energy and current were varied from 0.2 to 1keV and from 10 to 25mA (current density ranging from 1.4 to 3.5mA/cm^2), respectively.

2.2. Film deposition of cerium substituted yttrium iron garnet by magnetron sputtering

The apparatus for growing in-situ epitaxial films influences various properties of the films. Here we employed rf-magnetron sputtering in an ultrahigh vacuum (UHV) chamber originally designed for the molecular beam epitaxy.[9] Energetic particle bombardment of the growing film from an rf-magnetron plasma is negligible by comparison with an rf-diode plasma. In rf-diode sputtering a growing film is exposed to ion bombardment even at floating potential. Film perfection is impaired by particles arising from disintegration of target surface. The background vacuum in the chamber was two-orders of magnitude lower than conventionally used in sputtering: 10^{-6}Pa. A sintered ceramic target was used with the stoichiometric composition of $Ce_1Y_2Fe_5O_{12}$. However, the oxygen content in the deposited film was probably decreased due to the instability of the cerium trivalent ion. A lamp heater was employed to heat the substrate instead of a resistive heater to avoid contamination. The deposition was carried out under the following conditions: argon atmosphere mixed with oxygen of 2.6×10^{-2}Pa, an rf power density of 2.5W/cm^2, an oxygen flow rate of 0.5ccm, a substrate-to-target distance of 6cm, and substrate temperatures ranging from 680 to 750°C. Here we focused on the ion-beam energy dependence of the growth of a single crystal. In these films we did not need after annealing to achieve the crystalline state unlike other fabrication methods and materials such as a diode sputtering and bismuth substituted YIG.[10] All films were deposited on the (111)plane surfaces of the GGG substrates which were cut into 5x15mm rectangles.

2.3. Sputter deposition onto the substrate with micropattern

Figure 1 shows the process for fabricating the Ce:YIG films onto the substrates with magnetron sputtering after a strip portion of the substrate surface was etched with ion-beam bombardment. First, photoresist with 0.1μm thickness was coated on the GGG substrate with a spinner. Following the required straight patterns, a set of parallel strips equally separated or a single strip, were formed into the photoresist by conventional photolithography. The unfurnished part was etched with ion-beam etching to a depth of 0.15μm. Finally the remain photoresist was removed, and the Ce:YIG film was deposited onto the surface modified GGG substrate.

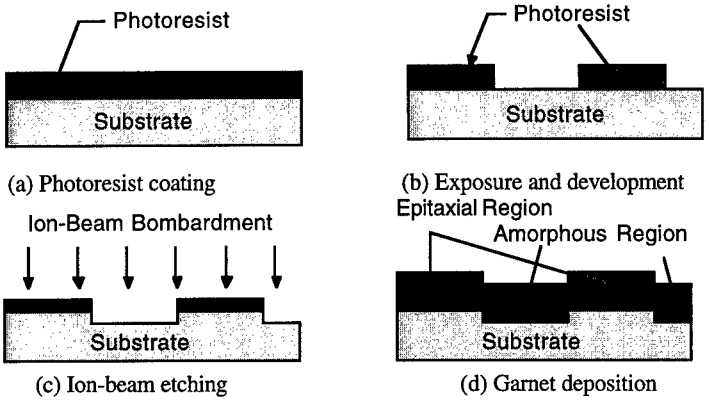

Fig.1 Process for fabricating a microstructure pattern

3. RESULT AND DISCUSSION

Films deposited on any substrates at temperatures less than 690°C showed no X-ray diffraction (XRD) peak and had a transparent brownish color, which implies the deposited films were amorphous. However, the films prepared on unmodified substrates at substrate temperatures greater than 690°C exhibited the XRD patterns as shown by a dotted curve in Fig.2 and had a transparent yellow greenish color. In this figure, the diffraction patterns of the films prepared on the substrates modified by the ion-beam energies of 0.2keV and 1keV also shown. All peaks indicate the (444)-plane diffraction. The brownish color films showed no magnetic characteristics. On the other hand, the yellow greenish films exhibited a magneto-optic effect. We concluded that the yellow

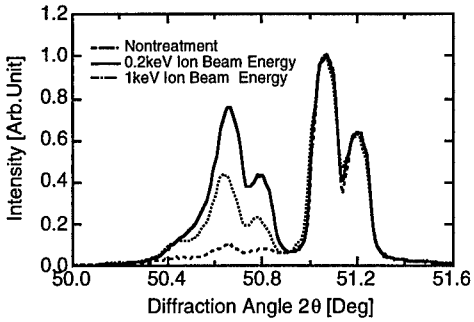

Fig.2 X-ray diffraction patterns for cerium substituted yttrium iron garnet films in-situ grown on surface modified and unmodified GGG substrates. Substrate temperature: 710°C, argon atmosphere mixed with oxygen: 2.6×10^{-2}Pa, oxygen gas flow rate: 0.5ccm.

(a) (b)

Fig.3 Optical mircrographs of (a) the overview and (b) cross section of the selected-area sputter epitaxy.

Table I Measured and predicted inclination angles of the face between amorphous and crystal regions.

Direction of line pattern	Angle from (110) plane (Degree)	Measured angle (degree)	Anticipated plane of the face	Predicted angle (Degree)
[$\bar{1}$10]	0	35.5	(110)	35.2
		37	(115)	38.9
[$\bar{4}5\bar{1}$]	10	47	(711)	43.3
		48	($\bar{1}$23)	51.9
[$\bar{2}3\bar{1}$]	19	44	(013)	43.1
		46	(52$\bar{1}$)	46.9
[$\bar{1}2\bar{1}$]	30	38	(201)	39.2
		40	(021)	39.2

greenish and brownish films were crystalline and amorphous, respectively. The color of the deposited films was thereafter used to determine the state of the films.

Figure 3(a) shows micrographs of an overview and a cross section of a Ce:YIG film deposited for 10 hours on a GGG substrate whose surface was etched in a set of parallel equal (8μm) strips. The thickness of the deposited film was 4μm. The color of the dark region is brown, and that of the light parts is yellow green. Consequently that indicates that crystalline and amorphous films were deposited simultaneously on the same substrate; we call this selected-area sputter epitaxy. The boundary between the crystalline and the amorphous regions was rather smooth. The triangular shape which formed was an amorphous region surrounded by a crystalline region.

Here the straight strip pattern was parallel to the [112] direction of the substrate. Consequently the cross section corresponds to the (112) plane. According to a stereographic projection of a (111) garnet substrate as shown in Fig.4, the slanted sidewalls indicates the (210) face. In order to confirm the facet growth of this kind we investigated various strip directions measured from the [110] direction of the substrate. Table I shows the measured and the predicted facet angles with respect to the substrate surface plane. During the sputter epitaxial deposition, {110}, {115}, {150}, {130}, and {120} facets can be noticed. The same behavior is reported for the garnet crystals grown from flux by Heimann and Tolksdorf[11].

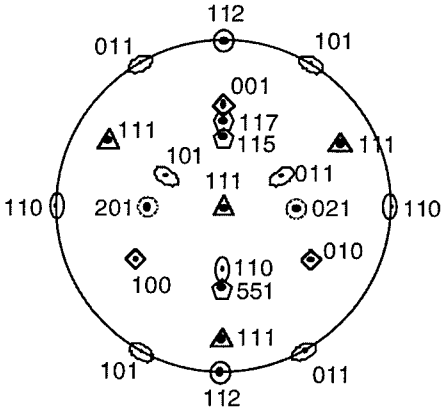

Fig.4 Stereographic projection of the (111) garnet substrate with some possible crystal faces.

Next we investigated amorphous deposition onto the selected-area sputter epitaxial film whose cross sectional profile was trapezoidal. The deposition temperature was lowered to the condition for amorphous state: 650°C. Figure 5 shows a SEM photograph of the cross section of the deposited film. Due to insufficiently lowered temperature, crystalline films were deposited on the crystalline and some part of the amorphous regions.

Even at temperature sufficient for growing the crystal, the cross section of the film was similar to that of Fig.5. This means an irregularly deposited surface is similar to the

high energy ion-beam bombardment of the bare substrate. In order to overcome this irregularity the surface of the selected-area epitaxial film was slightly etched with ion-beam etching. Figure 6(a) and (b) show optical micrographs of the overview and the cross section of the film on the selected-area epitaxial film deposited for 3-hours after ion-beam etching. A smooth film was grown on the amorphous region. The strip pattern was parallel to the [110] direction of the substrate. The inclined angles of the sidewalls were 35° and 41°, which correspond to (110) and (115) facets.

We developed this technique to grow the epitaxial films on larger amorphous areas. First we performed the selected-area epitaxy on a substrate etched by ion-beam except for a straight strip with 3μm width. Following that, epitaxial growth was performed on the deposited film after ion-beam etching. Figure 7(a) shows an optical micrograph of the overview of the deposited film. Figure 7(b) shows a SEM photograph of the cross section corresponding to three bright regions. The epitaxial growth extends to the surface of the amorphous region as well as the reversed trapezoidal region. We also confirmed the film to be crystalline using the XRD technique. The strip pattern parallel to the [110] direction leads to the asymmetric profile also seen in figure.

Furthermore, we formed a narrow amorphous strip surrounded by a crystalline region using the above mentioned technique. First a straight strip region with 3μm width was etched by ion-beam, following that, the selected-area epitaxy was performed. Figure 8(a) shows an optical micrograph of the overview and Fig. 8(b) shows a SEM photograph of the cross-section of the film. The amorphous region was shaped triangularly. Thus we can simultaneously fabricate an embedded ridge combining the selected-area sputter epitaxy and the ion-beam etching techniques. The refractive index of the amorphous film was measured to be larger than that of the crystalline film using a thin-film interference method[12], which means that the obtained straight ridge can be employed as an optical waveguide.

4. CONCLUSION

The simultaneous formation of rare-earth iron garnet crystalline and amorphous straight strips with micrometer widths has been investigated using selected-area epitaxy and ion-beam etching techniques. Clear sidewalls in the grown ridge appeared, the (hk0) and (hhl) faces, the result of which was similar to the dissolution forms of garnet crystals in phosphoric acid and the facet of garnet crystals grown from flux. Simultaneous formation of the embedded ridge is useful for optical waveguide fabrication.

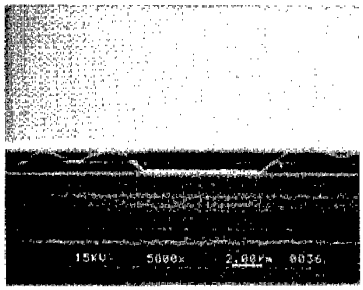

Fig.5 SEM photograph of the cross section of the film deposited on the as grown SAE film below at the on-set temperature.

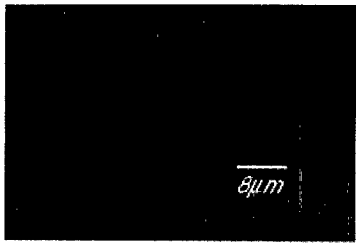

Fig.6(a) Microphotograph of the cross section of the film deposited on the SAE after ion-beam etching

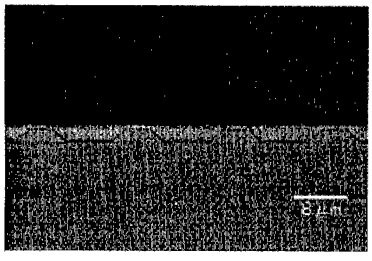

Fig.6(b) Microphotograph of the cross section of the film deposited on the SAE after ion-beam etching

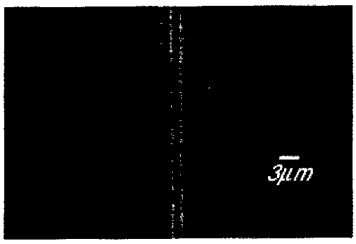

Fig.7(a) Microphotograph of the overview of the film deposited on the amorphous region.

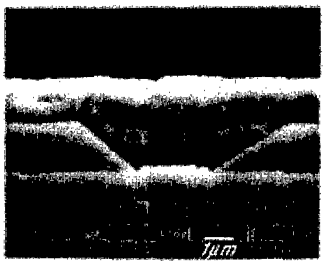

Fig.7(b) SEM photograph of the cross section of the film as Fig.7(a).

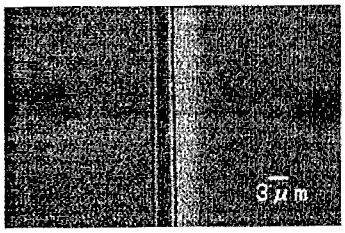

Fig.8(a) Microphotograph of the overview of the film deposited on the amorphous region.

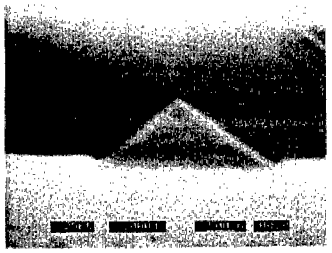

Fig.8(b) SEM photograph of the cross section of the film as Fig.8.

ACKNOWLEDGMENTS

The authors gratefully thank S.Motomura and H.Okano for their helpful assistance of experiment and measurement.

REFERENCES

[1] M.Gomi, K.Satoh, and M.Abe, Jpn.J.Appl.Phys. 27, L1536 (1988).
[2] M.Gomi, H.Furuyama, and M.Abe, J.Appl.Phys. 70, 7065 (1991).
[3] S.Mino, A.Tate, T.Uno, T.Shintaku, and A.Shibukawa, Jpn.J.Appl.Phys. 32, 3154 (1993).
[4] T.Shintaku and T.Uno, J.Appl.Phys. 76, 8155 (1994).
[5] C.Leycuras, H.Le Gall , J.M.Desvigness, M.Guillot and A.Marchand, IEEE Trans. Magn., MAG-21, 1660 (1985).
[6] J.-P.Krumme, V.Doormann, B.Strocka, and P.Willich, J.Appl.Phys. 60, 2065 (1986).
[7] S.Motomura, S.Yamamoto, and Y.Okamura, 1996 Autum Natl. Conv. Rec. IEICE Japan, C-131 (1996) .
[8] J.P.Biersack and L.G.Haggermark, Nucl.Instr.Meth.Phys.Rev., 174, 257 (1980)
[9] Y.Okamura, J.Kubota, and S.Yamamoto, IEEE Trans. Magn. 31, 3289 (1993)
[10] J.-P.Krumme, V.Doormann, and R.Eckart, IEEE Trans. Magn. MAG-20, 983 (1984).
[11] R.B.Heinmann and W.Tolksdorf, J.Crystal Growth, 62, 75 (1983).
[12] R.Swanepoel, J.Phys.E: Sci. Instrum., 17, 896 (1984).

MAGNETO-OPTICAL PROPERTIES OF Co DOPED $Bi_3Fe_5O_{12}$ GARNET FILM

T.Okuda, T.Mima, K.Ando*, N.Ohmori, N.Adachi, and H.Ohsato
Nagoya Inst. of Tech., Nagoya, 466-8555 Japan, okudatks@mse.nitech.ac.jp
*Electrotechnical Laboratory, Tsukuba-shi 305- Japan

ABSTRACT

Co-doped $Bi_3Fe_5O_{12}$ garnet (BIG) films were prepared on $Gd_3(ScGa)_5O_{12}$ (GSGG) substrates using two types of ion-beam-sputtering (IBS) technique. In the films deposited by sputtering the Co and the BIG source targets alternately with short periodicity, the interface exchange coupling of BIG and Co-spinel ferrite was characteristically observed in the Faraday hysteresis loop. The magnetic and the Faraday hysteresis loops were found to have different coercivity. In the films deposited by conventional IBS method using the BIG target doubly substituted by Co and Ge, Co^{2+} ions were highly replaced up to 0.7 atoms/formula unit for Fe^{3+} in BIG. The specific Faraday rotation angle (θ_F) at a wavelength of 1.5 μ m was 1.1 deg/μ m/Co atom. The magnetic easy direction was normal to the film plane.

INTRODUCTION

Doping of Co ions into garnet ferrite is interesting subject from the point of magnetooptical applications, since Co^{2+} ions enter the tetrahedral (d) site cause optical absorption bands centered at the wavelengths of 0.6 and 1.2 μ m [1] and magnetooptical effects at about 0.7 and 1.5 μ m [2,3] and those enter the octahedral [a] site induce magnetic anisotropy. BIG shows giant θ_F for visible light and soft, magnetic characteristics [4]. We have examined Co-doping into BIG by a reactive, alternating IBS (RAIBS) adopting the ceramic targets of composition of CoO and BIG, and have found the enhancement of magnetization and coercivity and the anomalies in magnetic and Faraday hysteresis loops, but no evidence of Co-substitution for Fe in BIG [5-7]. We will report Co-concerned magnetooptical properties of the films prepared by RAIBS using $CoFe_2O_4$ and BIG targets and by the conventional reactive IBS (CRIBS) using $Bi_3Fe_{5-2X}Co_XGe_XO_{12}$ (BICGG) target.

EXPERIMENT

BIG, which is an artificial material, is only obtainable as a film state by direct epitaxial growth from vapor phase onto a template with garnet structure [4]. The films were deposited onto (100) plane of GSGG substrates kept at 500C in

Mat. Res. Soc. Symp. Proc. Vol. 517 © 1998 Materials Research Society

oxidizing atmosphere. For RAIBS, two ceramic targets T_A (=BIG=$3Bi_2O_3 \cdot 5Fe_2O_3$) and T_B (=$CoFe_2O_4$) were sputtered alternately using Ar ion beam. Sputtering time ratio, $R = t_A/(t_A+t_B)$, was varied from 0 to 1, where t_A and t_B were sputtering time in one period for the respective targets. t_B was fixed at 60 sec excepting for $R = 0$ and $R = 1$ which corresponded to single layers of $CoFe_2O_4$ and BIG, respectively.

As cobalt ions are usually present as Co^{2+} in garnet [8], for making sure of Co-substitution into BIG lattice, Co^{2+} should be electrostatically compensated with tetravalent ions. Therefore, the ceramic targets, $3Bi_2O_3$ (5-2X)Fe_2O_3 2XCoO 2XGeO_2 (X = 1 and 2) were prepared for the film deposition by CRIBS.

The films were characterized at room temperature using X-ray diffractometry (XRD), vibrating sample magnetometry, and Faraday rotation (FR) spectrometry in visible and infrared regions.

RESULTS AND DISCUSSION

Co-doping by RAIBS Spinel (S) phase was identified by XRD in the range of $0 \leqq R \leqq 0.6$. S-phase was polycrystalline and had no preferential orientation. The lattice constant was independent of R and the values were 8.383-8.390 Å. From these results, S-phase was identified as $CoFe_2O_4$ (a = 8.383 Å). In the range of $0.5 \leqq R \leqq 1$, formation and epitaxial growth of garnet (G) phase were found by XRD. The lattice constant was independent of R and the observed values which were ranging from 12.616 to 12.630 Å were close to that of BIG (a = 12.624 Å). From these results, G-phase was identified as BIG. Formation of BIG can be inspected by the large, negative θ_F at around 500-600 nm associated with Fe^{3+}- O^{2-} charge transfer transition which is characteristic of BIG. In contrast with BIG,

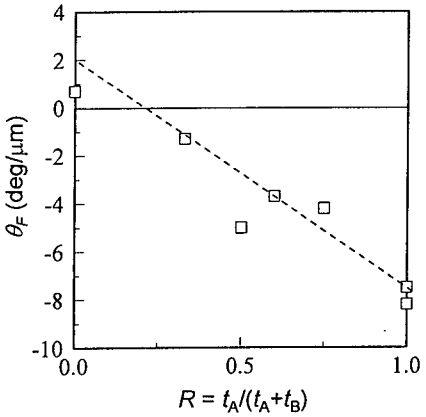

Fig.1 θ_F (λ=630 nm) of RAIBS films vs. R

θ_F: specific Faraday rotation angle

RAIBS films : films deposited by reactive alternating ion-beam-sputtering.
$R \equiv t_A/(t_A+t_B)$.
t_A and t_B: respective sputtering time in one period for $Bi_3Fe_5O_{12}$ and $CoFe_2O_4$ targets. t_B is fix ed at 60 sec.

in the same wavelength region, $CoFe_2O_4$ causes positive θ_F associated with the crystal field transition ($^4A_2 \rightarrow {}^4T_1(^4P)$) in Co^{2+} in the tetrahedral site. R dependence of θ_F measured at 630 nm is shown in Fig.1, from which one can deduce the presence of G phase at $R = 0.33$, though BIG is not observed by XRD. In Fig.2, it seems that θ_F is given as the sum of the θ_F of Co-spinel and BIG and that θ_F are proportional to the volume fractions of respective phases in the film. The saturation magnetization, $4\pi M_S$, is shown in Fig.2 as a function of R. $4\pi M_S$ decreases linearly as R increases for $0 \leqq R \leqq 0.5$ and is a maximum at $R = 0.75$ for $0.5 < R \leqq 1$. $4\pi M_S$ of 4000 G at $R = 0$ is much smaller than that of bulk $CoFe_2O_4$ (5300 G), which means that the film composition may be given by $Co_XFe_{3-X}O_4$ with $X > 1$, though the lattice constant is close to that of $CoFe_2O_4$. The fact that the $4\pi M_S$ for $0.5 < R < 1$ are larger than those expected from straightforward mixing of Co- rich $CoFe_2O_4$ (which is denoted below as Co-spinel) and BIG suggests that Co-spinel are easy to form in BIG matrix even though they are not observed by XRD at $R = 0.75$ where $4\pi M_S$ vs. R has the maximum.

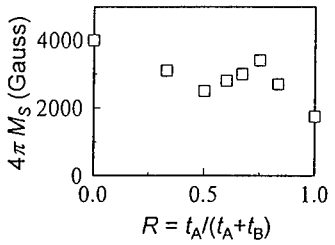

Fig.2 $4\pi M_S$ of RAIBS films vs. R
$4\pi M_S$: magnetization. (R:see Fig.1)

Faraday rotation spectra for various R shown in Fig.3 are measured in the range from 0.5 to 1.0 μ m. Large spectra due to BIG and small one due to Co-spinel are centered at the 500 and 700 nm, respectively. The spectrum for the film of $R = 0.5$ measured in the range from 0.75 to 1.6 μ m is shown in the insert of Fig.3. The absorption type spectrum with negative sign observed at around 1.5 μ m is principally ascribed to the crystal field transition ($^4A_2 \rightarrow {}^4T_1$ (^4F)) in Co^{2+} in the tetrahedral site of Co-spinel, because the same transition in garnet give rise to similar spectrum

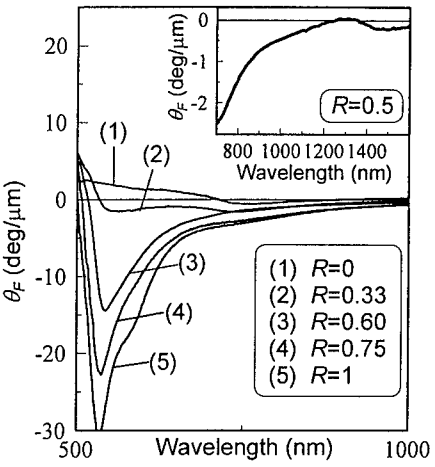

Fig.3 Faraday rotation spectra of RAIBS films. The insert is the spectrum for the film of R=0.5 measured in the range from 0.75 to 1.6 μ m (R, RAIBS films: see Fig.1)

with positive sign [2]. Therefore, Co^{2+} seems to hardly substitute in BIG lattice.

In Fig.4, Faraday hysteresis loops for $0.33 \leqq R \leqq 0.75$ are shown. All the loops are inverted. The magnetic hysteresis loop for $R = 0.85$ measured with applied magnetic field, H, perpendicular to the film plane is shown in Fig.5. Anomalous decrease of magnetization is observed as H decreases below 2.5 kOe. Coercivity obtained from the magnetic hysteresis loops, $H_{C\text{-}M}$, and those from the Faraday hysteresis loops measured at 630 nm, $H_{C\text{-}FR}$, are shown in Fig.6 as a function of R. $H_{C\text{-}M}$ becomes larger than $H_{C\text{-}FR}$, for R below 0.75 which means the films are composite of BIG with low coercivity and Co-spinel with high coercivity. The inverted Faraday hysteresis loop can be understood by considering antiferromagnetic interface-exchange-coupling between magnetically soft BIG with large, negative θ_F and magnetically hard Co-spinel with not so large, positive θ_F. The θ_F changes sign according to the direction of the net magnetic moment of Fe^{3+} in BIG which is subjected to that of Co-spinel with the coercivity much higher than that of BIG. Increase of $H_{C\text{-}FR}$ with decrease of R indicates the increase of the interface-exchange-coupling with increasing amount of Co-spinel phase.

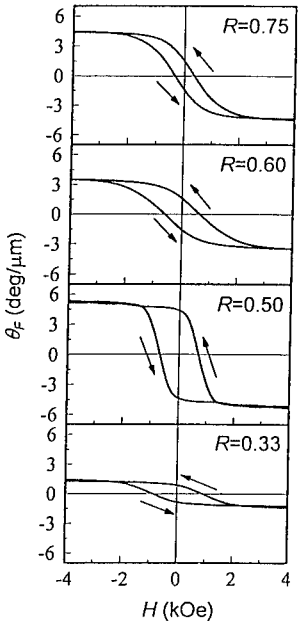

Fig.4 Faraday hysteresis loops of RAIBS films (R, RAIBS films: see Fig.1)

Co-doping by CRIBS Formation of single crystal films of BICGG were confirmed by XRD. The maximum amount of substitution of Co^{2+} attained in this experiment is X=0.7, which is much smaller than X=2.5 for $Y_3Fe_{5-2X}Co_XGe_XO_{12}$ (YICGG) [8]. The change of the $4\pi M_S$ with amount of Co is shown in Fig.7 together with the data on $Bi_2YFe_{5-2X}Co_XGe_XO_{12}$ (BYICGG)[9]. X dependence is rather close to that is calculated by Neel model assuming all Co^{2+} ions in [a] sites with 3.7 μ_B and all Ge^{4+} ions in d-sites than that all Co^{2+} ions in (d) sites with 3.4 μ_B. One can expect 80 % of Co^{2+} ions introduced into BIG may occupy [a] sites as proposed for YICGG [8], which may result in Faraday hysteresis loop of BICGG (X=0.7) with the high coercivity and squareness ratio and the magnetic easy direction normal to the film plane, as shown in Fig.8.

Faraday rotation spectra in the region from 500 nm to 1.6 μm are shown in

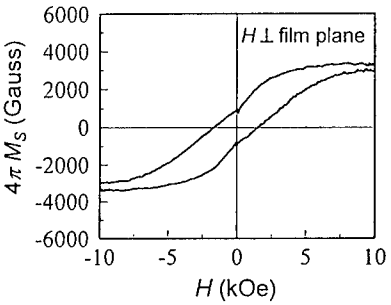

Fig.5 Magnetic hysteresis loop of RAIBS film (R=0.85)
(R, RAIBS films: see Fig.1)

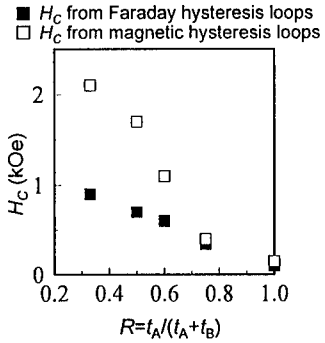

Fig.6 Coercivity obtained from magnetic and Faraday hysteresis loops of RAIBS films vs. R (R, RAIBS films: see Fig.1)

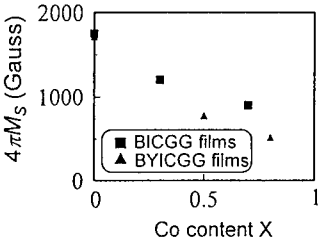

Fig.7 4 π M_S of $Bi_3Fe_{5-2X}Co_XGe_XO_{12}$ (BICGG) and $Bi_2YFe_{5-2X}Co_XGe_XO_{12}$ (BYICGG) films vs. Co content (X)

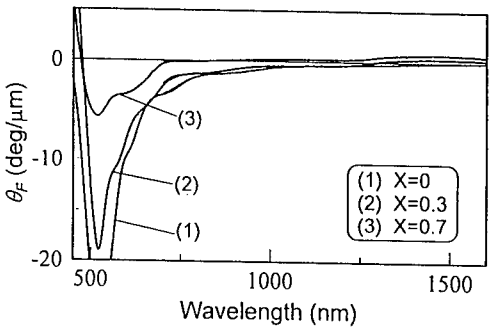

Fig.9 Faraday rotation spectra of $Bi_3Fe_{5-2X}Co_XGe_XO_{12}$ (BICGG) films

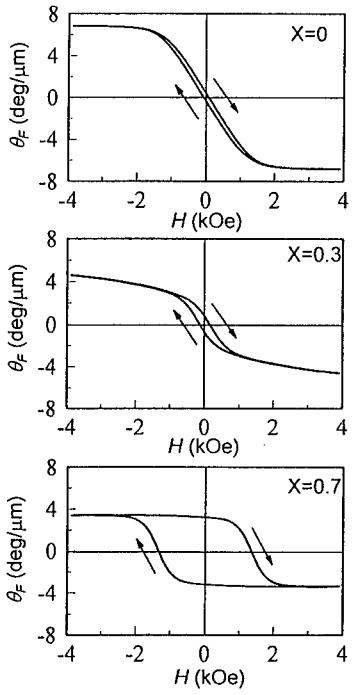

Fig.8 Faraday hysteresis loop of $Bi_3Fe_{5-2X}Co_XGe_XO_{12}$ (BICGG) films

Fig.9. θ_F at 1.455 μ m increased linearly with increasing amount of Co^{2+} at a rate of +1.10 deg/μ m/atom which is close to the rate of +1.0 deg/μ m/atom found for $Gd_3Fe_{5-2X}Co_XGe_XO_{12}$ (GICGG)[2]. θ_F at 630 nm decreased linearly with the 4 πM_S at a rate of about -6 deg/μ m/atom with increasing amount of Co^{2+}, which means that θ_F at 630 nm is mainly attributed to charge transfer transition of Fe^{3+}. θ_F due to Co^{2+} may be hidden, because its magnitude may be similar to θ_F of GICGG at 633 nm which increases at the rate of -1.0 deg/μ m/atom [2].

CONCLUSIONS

The films prepared by RAIBS using $CoFe_2O_4$ and BIG targets are the composite of magnetically hard Co-spinel and soft BIG phases. In the whole range of R, Co content of BIG is negligibly small and composition of Co-spinel is nearly constant. The interface exchange interaction couples these two phases, which is observed as the inverted Faraday hysteresis loop, and the coupling strength changes sensitively with R. The magnetic state of each phase can be monitored at the same time by magnetooptical means using the light of different wavelength.

Coupled substitution of Co^{2+} and Ge^{4+} into BIG lattice was performed by CRIBS. Dependencies of the magnetization and θ_F on Co content suggest that site distribution of Co^{2+} is similar to that in YICGG, that is, 80% of Co^{2+} in BIG may occupy [a] sites.

REFERENCES

1. D.L.Wood and J.P.Remeika, J.Chem.Phys.46, 3595(1967).
2. K.Egashira and T.Manabe, IEEE Trans. Magn. MAG-8,646(1972).
3. R.K.Ahrenkiel, T.H.Lee, S.L.Lyu, and F.Moser, Solid State Comm.12, 1113 (1973).
4. T.Okuda, T.Katayama, H.Kobayashi, N.Kobayashi, K.Satoh, and H.Yamamoto, J. Appl. Phys.67, 4944(1990).
5. T.Okuda, Y.Katoh, H.Ohsato, N.Adachi, K.Ando, T.Abe and H.Yamamoto, J. Magnetism and Magnetic Mat. 148,275(1995).
6. T.Okuda, N.Adachi, H.Ohsato, Y.Katoh and T.Mima, *J.PHYS. IV FRANCE* 7, Colloque C1, Suppl. au J.Phys.III, C1-711(1997).
7. T.Mima, T.Okuda, N.Adachi and H.Ohsato, accepted to J. Magnetics Soc. Jpn. (1998).
8. S.Geller, H.J.Williams, G.P.Espinosa, and R.C.Sherwood, Phys. Rev.136, A1650 (1964).
9. M.Gomi and M.Abe, J.Magn.Soc.Jpn.11,Suppl.No.S1, 309 (1989).

Part II

Garnet Materials: Devices for Integrated Photonics

INTEGRATED NONRECIPROCAL DEVICES FOR APPLICATION IN OPTICAL COMMUNICATION SYSTEMS

T. Shintaku, N. Sugimoto, A. Tate, E. Kubota, H. Kozawaguchi and Y. Katoh
NTT Opto-electronics Laboratories, Tokai, Ibaraki, 319-1193 JAPAN,
shintaku@iba.iecl.ntt.co.jp

ABSTRACT

We describe our recently developed integrated isolators. Their structure is simple, in that it consists solely of a single-mode channel magneto-optic waveguide. The operating principle is that a backward fundamental TM mode wave is converted to higher-order or radiation TE modes while a forward fundamental TM mode wave propagates with no mode conversion. These isolators are realized using a single-mode rib channel waveguide in Ce-substituted yttrium iron garnet which has a very large Faraday rotation. We obtain 13-27 dB isolation around a wavelength of 1.55 μm. We also review our recent study on a hybrid-integrated polarization-independent optical circulator based on a nonreciprocal Mach-Zehnder interferometer which does not need a polarization-beam splitter. We obtain 14.1-23.7 dB isolation at λ = 1.55 μm.

INTRODUCTION

The development of integrated optic components for optical communication systems has intensified the need for integrated nonreciprocal devices such as isolators and circulators. The advantages of these nonreciprocal devices include their compatibility with waveguide optics, low magnetic field requirements, and low cost. There is a difficulty, however, in that the input and output light of the waveguide must be in either the TE or TM mode. Although several waveguide nonreciprocal devices have been proposed and demonstrated, no practical device has yet been achieved.[1-7] This is mainly because they require complicated structures.

In this paper we review our recently developed integrated isolators.[8-10] Their structure is simple, in that it consists solely of a single-mode channel magneto-optic waveguide. The operating principle is that a backward fundamental TM mode wave is converted to higher-order or radiation TE modes while a forward fundamental TM mode wave propagates with no mode conversion. Operation is achieved by combining a nonreciprocal phase shift and TM-TE mode conversion. The very large Faraday rotation of Ce-substituted yttrium iron garnet (Ce:YIG) magneto-optic (MO) film enables us to realize these integrated isolators.[11-14] The principle, fabrication and optical characteristics are addressed. We also review our recent study on a hybrid-integrated polarization-independent optical circulator based on a nonreciprocal Mach-Zehnder interferometer.[15]

PRINCIPLE OF INTEGRATED ISOLATOR

Isolator structure and phase matching

The basic structure of our proposed integrated isolator is shown in Fig. 1. A single-mode rib MO waveguide is constructed on a garnet substrate. The z-axis is the propagation direction and the x-axis is perpendicular to the substrate plane. An external magnetic field is applied to the MO waveguide in-plane at an angle of θ to the y-axis. The operating principle of this isolator is that a backward fundamental TM mode wave is converted to a higher-order TE mode or TE radiation

Mat. Res. Soc. Symp. Proc. Vol. 517 © 1998 Materials Research Society

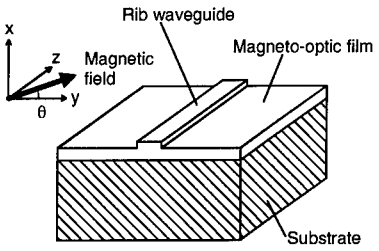

FIG. 1. Isolator structure.

mode while a forward TM mode wave propagates with no mode conversion. A previously reported waveguide isolator requires precise adjustment of phase matching between the fundamental TE and TM modes.[7] However, in general, the propagation constant of the TE mode is larger than that of the TM mode in the slab waveguide because of the geometrical birefringence. Therefore, it is easy to achieve a condition where the fundamental TM mode phase-matches the higher-order TE mode or TE radiation mode in the rib waveguide instead of the fundamental TE mode.

These phase matching conditions are illustrated by using the effective index method as shown in Fig. 2. Here Marcatili's notation is used, that is, E^y_{pq} and E^x_{pq} modes represent TE-like and TM-like modes, respectively.[16] The subscripts p and q indicate the mode numbers which correspond to the number of peaks in the field distributions in the x and y directions, respectively. Figure 2(a) shows a cross-section of the rib waveguide. w is the rib width, t_a is the core film thickness, and t_c is the cladding film thickness which is related to rib height h by the relation $t_c=t_a-h$. Figure 2(b) shows the propagation constants of the TE and TM modes in a slab waveguide. t_a determines the TE mode propagation constant β^y_a and the TM mode propagation constant β^x_a. t_c determines the E^y_{11} mode cutoff β^y_c and the E^x_{11} mode cutoff β^x_c. Therefore, the respective propagation constants of β^y_{11}, β^y_{12} and β^y_{13} for E^y_{11}, E^y_{12} and E^y_{13} modes are between β^y_a and β^y_c as shown in Fig. 2(c). The propagation constant of β^x_{11} is also between β^x_a and β^x_c. Consequently, it is possible that the E^x_{11} mode phase-matches the TE radiation modes in $w < w_1$, the

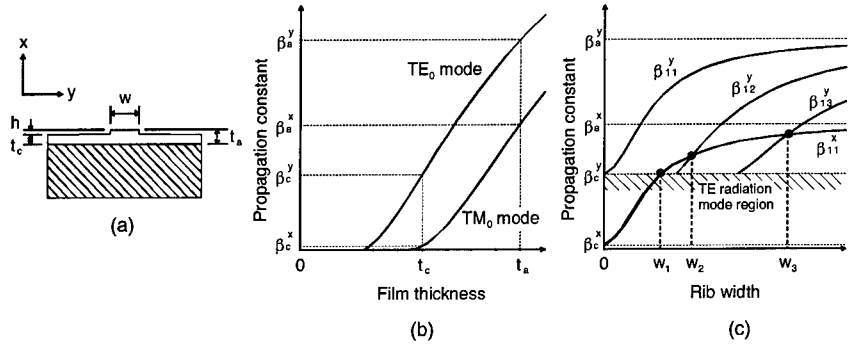

FIG. 2. Propagation constant curves: (a) A cross-section of the rib waveguide; (b) Propagation constants in a slab waveguide; (c) Propagation constants in a rib waveguide.

TE mode cutoff at $w = w_1$, the E_{12}^y mode at $w = w_2$, and the E_{13}^y mode at $w = w_3$. Using these phase matching conditions, we can achieve three types of isolator as described in detail below.

Higher-order-mode converted isolator

We proposed a higher-order-mode converted isolator whose structure is shown in Fig. 1.[9] The operating principle of this isolator is that a backward fundamental TM mode wave is converted to a higher-order TE mode while a forward TM mode wave propagates with no mode conversion. Figure 3 shows the relationship required between the propagation constants for isolator operation. The upper part of the figure shows the propagation constants of the TE mode, the lower part those of the TM mode. β_{11}^y and β_{12}^y are the propagation constants of the fundamental E_{11}^y mode and higher-order E_{12}^y mode, respectively. β_{11F}^x and β_{11B}^x are the forward and backward propagation constants of the fundamental E_{11}^x mode, respectively. These are not identical because the nonreciprocal phase shift in the TM mode is caused by the y-axis component of magnetization in the asymmetric layer MO waveguide.[17] In the rib waveguide, the E_{11}^x mode phase-matches the E_{12}^y mode as shown in Fig. 2(c). Therefore, the phase-matching condition $\beta_{11B}^x = \beta_{12}^y$ can be satisfied by adjusting the film thickness, rib height, and rib width. A coupling coefficient K couples the E_{11}^x mode to the E_{12}^y mode. K can be caused by stress-induced or magnetic anisotropy. With this propagation-constant relationship, the power conversion ratio from the E_{11}^x mode to the E_{12}^y mode is given by the coupled-mode theory[18] as

$$P_{12} = [|K|^2/(\Delta^2 + |K|^2)]\sin^2(\sqrt{\Delta^2 + |K|^2}\,L) \qquad (1)$$

where, $\Delta = |\beta_{12}^y - \beta_{11F}^x|/2 = |\beta_{11B}^x - \beta_{11F}^x|/2 = \Delta_N$ and $K = K_F$ for the forward propagation, $\Delta = |\beta_{12}^y - \beta_{11B}^x|/2 = 0$ and $K = K_B$ for the backward propagation, and L is waveguide length. Here, $2\Delta_N$ is the nonreciprocal phase shift. To achieve isolator operation, there must be no mode conversion ($P_{12} = 0$) for the forward propagation and complete mode conversion ($P_{12} = 1$) for the backward propagation. This requires the following conditions

$$\sqrt{\Delta_N^2 + |K_F|^2}\,L = \pi + m\pi \qquad (m = 0,1,2,\cdots) \qquad (2)$$

$$|K_B|L = \pi/2 + n\pi \qquad (n = 0,1,2,\cdots) \qquad (3)$$

With these conditions, the forward E_{11}^x mode of β_{11F}^x propagates without conversion to the E_{12}^y mode due to the phase mismatch $\beta_{11F}^x \neq \beta_{12}^y$. By contrast, the backward E_{11}^x mode of β_{11B}^x is coupled to the E_{12}^y mode of β_{12}^y by the coupling coefficient K_B and phase matching $\beta_{11B}^x = \beta_{12}^y$. Thus this structure acts as an isolator for a TM mode wave.

It is well known that the mode conversion between fundamental TE and TM modes is mainly caused by the xy component of the dielectric tensor.[18] However, the xy component cannot contribute to the mode conversion between the E_{11}^x and E_{12}^y modes because the E_{12}^y mode is an odd mode. By contrast, the coupling coefficient K can also be induced by the xz component of the dielectric tensor.[8] In the MO waveguide, therefore, the y-axis component of magnetization can lead to K because it forms the xz component of the dielectric tensor.

In a similar way, we can achieve an even higher-order-converted isolator so that the backward E_{11}^x mode of β_{11B}^x is coupled to the E_{13}^y mode of β_{13}^y due to the phase matching

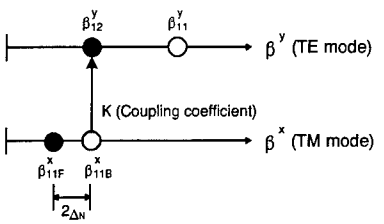

FIG. 3. Propagation constant condition for operation of higher-order-mode-converted isolator.

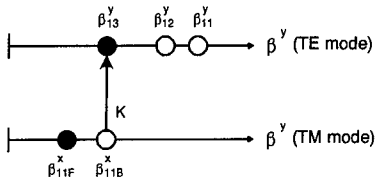

FIG. 4. Propagation constant condition for E_{13}^{y}-mode-converted isolator operation.

$\beta_{11B}^{x} = \beta_{13}^{y}$ while the forward E_{11}^{x} mode of β_{11F}^{x} propagates without conversion to the E_{13}^{y} mode due to the phase mismatch $\beta_{11F}^{x} \neq \beta_{13}^{y}$ as shown in Fig. 4.

Radiation-mode-converted isolator: Type 1

We proposed a radiation-mode-converted isolator: Type 1.[8] The structure is also shown in Fig. 1. The operating principle of this isolator is that a backward TM mode wave is converted to a TE radiation mode while a forward TM mode wave propagates with no mode conversion. Figure 5 shows the propagation constant relationship required to achieve isolator operation. The upper part of the figure shows the propagation constants of the TE mode, the lower part those of the TM mode. The forward and backward propagation constants β_{11F}^{x} and β_{11B}^{x}, respectively, of the fundamental E_{11}^{x} mode are also not identical due to the nonreciprocal phase shift caused by the y-axis component of magnetization. β_c^{y} and β_c^{x} are the cutoffs for the E_{11}^{y} and E_{11}^{x} modes, respectively. In the rib waveguide, the E_{11}^{x} mode can phase-match the TE mode cutoff as shown in Fig. 2. Therefore, the condition $\beta_{11B}^{x} < \beta_c^{y} < \beta_{11F}^{x}$ can be satisfied by adjusting the film thickness, rib height, and rib width. The coupling coefficient K couples the E_{11}^{x} mode to the TE radiation mode when β_{11B}^{x} equals the propagation constant β_R^{y} of the radiation mode. K can also be caused by magnetic anisotropy or stress-induced anisotropy. With these propagation constant configurations, the forward guided TM wave of β_{11F}^{x} propagates without conversion to the TE radiation mode due to the phase mismatch $\beta_{11F}^{x} > \beta_c^{y}$. By contrast, the backward guided TM wave of β_{11B}^{x} is coupled to the TE radiation mode of β_R^{y} by the coupling coefficient K and phase matching $\beta_{11B}^{x} = \beta_R^{y}$. The resulting radiation escapes into the slab out of the rib channel.

Here, the power flow $P(z)$ for the E_{11}^{x} mode of propagation after radiation mode conversion is approximately given by

$$P(z) \approx P(0)\exp[-2\pi|K|^2] \tag{4}$$

where $K = 0$ for the forward wave because of the phase mismatch, and $K \neq 0$ for the backward wave because of the phase matching. This means that the backward propagating wave decays with a power attenuation $2\pi|K|^2$, while the forward wave propagates with no power attenuation. Thus, this structure acts as an isolator for a TM mode wave.

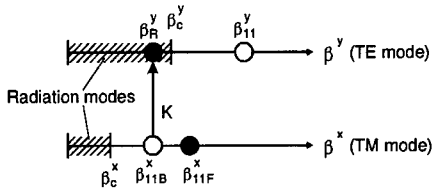

FIG. 5. Propagation constant condition for operation of radiation-mode-converted isolator: Type 1.

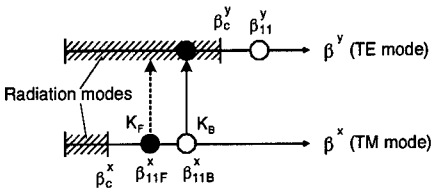

FIG. 6. Propagation constant condition for operation of radiation-mode-converted isolator: Type 2.

Radiation-mode-converted isolator: Type 2

We proposed a radiation-mode-converted isolator: Type 2.[10] The structure is also that shown in Fig. 1. The isolator operation is based on efficient nonreciprocal conversion from a fundamental TM mode to a deep TE radiation mode away from the cutoff. Figure 6 shows the relationship between the propagation constants required to achieve isolator operation. The upper part of the figure shows the propagation constants of the TE mode, the lower part those of the TM mode. Compared with Type 1, the conditions $\beta_{11F}^{x} < \beta_{c}^{y}$ and $\beta_{11B}^{x} < \beta_{c}^{y}$ are satisfied. Therefore, both the forward and backward E_{11}^{x} modes always phase-match the deep TE radiation modes. This condition is achieved because of the low rib height or narrow rib width as shown in Fig. 2. Coupling coefficients K_F and K_B couple the forward and backward E_{11}^{x} modes, respectively, to the TE radiation modes. With these phase-matching conditions, the power flow $P(z)$ for the E_{11}^{x} mode of propagation after radiation-mode conversion is also given by Eq. (4) where $K = K_F$ for the forward wave and $K = K_B$ for the backward wave. To achieve isolator operation, we must have $|K_F| \approx 0$ for the forward wave and $|K_B| >> 0$ for the backward wave. Coupling coefficients are functions of a propagation constants. If only the MO effect due to the magnetization in the y-axis direction ($\theta = 0$) is present as an optical anisotropy in the waveguide, we can obtain the coupling coefficients $|K_F| = |K(\beta_{11F}^{x})|$ and $|K_B| = |K(\beta_{11B}^{x})|$ using the same function. Then, we can choose a condition where β_{11F}^{x} can be set such that $|K_F| = |K(\beta_{11F}^{x})| = 0$ by adjusting the rib height and rib width. By contrast, we can obtain the condition $|K_B| = |K(\beta_{11B}^{x})| \neq 0$ because β_{11B}^{x} is separated from β_{11F}^{x} by the nonreciprocal phase shift. Thus these conditions achieve isolator operation for a TM mode wave. Therefore, a larger MO effect provides a higher isolation. If stress-induced and magnetic anisotropy occur simultaneously, the reciprocal and nonreciprocal conversions can be canceled out for the forward wave and can be superposed for the backward wave.

EXPERIMENT ON WAVEGUIDE ISOLATORS

MO waveguide fabrication and waveguiding method

We fabricated single-mode MO channel waveguides in Ce:YIG as shown in Fig. 1.[14] In the first step of the fabrication procedure, a Ce:YIG ($CeY_2Fe_5O_{12}$) film was grown on a (111)-oriented cation (Ca,Mg,Zr) doped gadolinium gallium garnet (GGG) substrate by rf sputter epitaxy.[12,13] The film had a large Faraday rotation of -4500 °/cm at λ = 1.55 μm and in-plane magnetization. The film thickness was ~0.5 μm which is needed to obtain maximum nonreciprocal phase shift. The

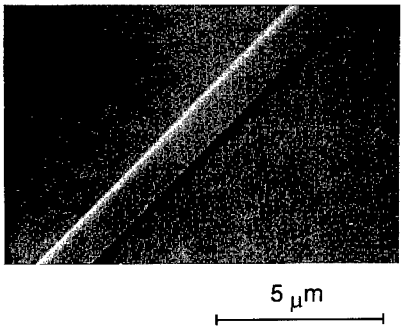

FIG. 7. Photograph of rib waveguide in Ce:YIG.

refractive index measured by m-line spectroscopy was 2.22 and the propagation loss in the slab waveguide measured with the two-prism loss measurement method was 14 dB/cm in the TM mode at λ = 1.55 μm. In the next step, ribs were etched into the garnet film. For that purpose, a Cr mask was structured on the surface using a standard photolithographic lift-off process. Then, the Ce:YIG film was etched by reactive ion etching using BCl_3 gas at a gas pressure of 1.3 Pa and an rf power of 300 W. The etching rates for the Ce:YIG and the Cr mask were in the ratio 1.4 : 1. This method allows the rib width and height to be precisely formed. The rib height and rib width were 0.11-0.17 μm, and 1.9-2.2 μm, respectively. A scanning electron microscope (SEM) photograph of the rib waveguide is shown in Fig. 7. The edges of these ribs were smooth. For our waveguiding experiments, samples were cut perpendicular to the ribs and both edge endfaces were polished.

In the waveguiding experiments, TM polarized light from an infrared tunable laser diode was end-fire coupled into the waveguide using a lensed polarization-maintaining single-mode fiber with a laminated polarizer (Lamipol)[14] at its input end.[8] An external magnetic field was applied to the MO waveguide in-plane in the y-axis direction (θ = 0°). Instead of reversing the direction of the light propagation, the direction of the magnetic field was reversed. The output endface of the waveguide was viewed by using an infrared television camera through a microscope objective.

Experiment on higher-order-mode-converted isolator

We fabricated the higher-order-mode-converted isolator shown in Fig. 7. The Ce:YIG film thickness was 0.46 μm, the rib height was 0.17 μm, the rib width was 1.9 μm and the waveguide length was 3.2 mm. Figure 8 shows the near field patterns at the output end at λ = 1550 nm. Figure 8(a) shows the fundamental E_{11}^{x} mode with a magnetic field of -50 Oe at θ = 0° which is equivalent to a forward propagating wave. A magnetic field of 50 Oe is sufficient to saturate the magnetization of Ce:YIG film. The light is well confined in the channel. Figure 8(b) shows the higher-order E_{12}^{y} mode with a magnetic field of 50 Oe at θ = 0° which is equivalent to a backward propagating wave. We confirmed that the light was TE polarized by using a TE analyzer.

To measure the isolation value, the output light from the waveguide was coupled to a lensed PM single-mode fiber with a Lamipol and the TM-polarized component was detected at a photo-diode. External magnetic fields of -50 Oe and +50 Oe were applied at an angle of θ to the y-axis and the output power ratio under these fields was taken as the isolation of the waveguide isolator. Figure 9 shows the isolation as a function of wavelength from 1548 to 1552 nm. The

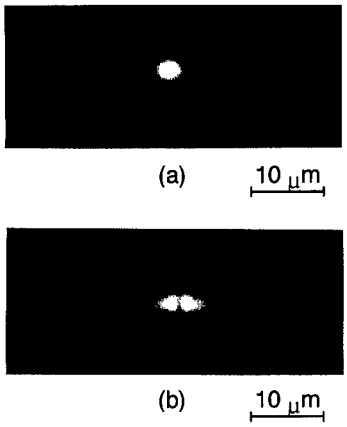

FIG. 8. Near field patterns for higher-order-mode-converted isolator. (a) -50 Oe; (b) +50 Oe.

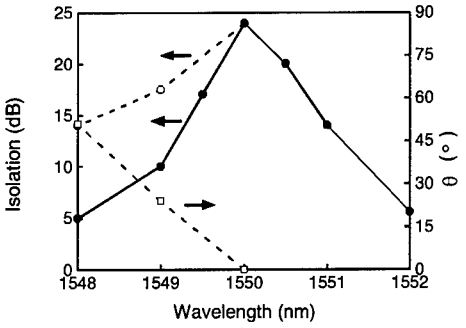

FIG. 9 Isolation spectra of higher-order-mode-converted isolator.

solid circles show the isolation at a magnetic field angle θ = 0°. The peak isolation was 24 dB measured at 1550 nm. However, the isolation value was sensitive to the wavelength. The additional loss due to unwanted conversion was 0.2 dB at the forward wave. It was possible to improve the isolation at shorter wavelengths to some extent by adjusting the magnetic field angle. The open circles show the improved isolation when the magnetic field angle θ is optimized to obtain the maximum isolation value. The angles are indicated by the open squares. The improvement is thought to result from the improvement in the phase matching condition caused by the change in the nonreciprocal phase shift. The same experimental results were obtained when the light launching edge of the waveguide was changed. It was, however, unclear whether the origin of the coupling coefficient was magnetic anisotropy or stress-induced anisotropy.

In addition, we observed a nonreciprocal conversion from the fundamental E_{11}^{x} mode to the higher-order E_{13}^{y} mode at a wider rib width of 4.0 mm. Figure 10 shows the near field patterns at the output end at λ=1550 nm. Figure 10(a) shows the E_{11}^{x} mode with 50 Oe at θ = 50°. Figure 10(b) shows the E_{13}^{y} mode with 50 Oe at θ = -130°, where we used a TE polarizer to eliminate E_{11}^{x} mode because the conversion efficiency was only 10 %.

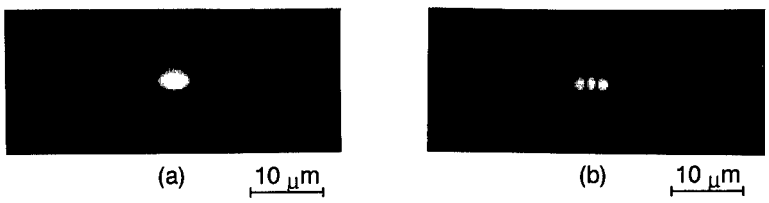

FIG. 10. Near field patterns for E_{13}^{y}-mode-converted isolator. (a) 50°; (b) -130°.

Experiment on radiation-mode-converted isolator: Type 1

We fabricated the radiation-mode-converted isolator: Type 1 shown in Fig. 7. The Ce:YIG film thickness was 0.49 μm, the rib height was 0.16 μm, the rib width was 2.0 μm and the waveguide length was 4.5 mm. Figure 11 shows the near field patterns at the output end at λ = 1536 nm. Figure 11(a) shows the guided E_{11}^{x} mode at a magnetic field of 50 Oe at θ = 0° which is equivalent to a forward propagating wave. The light is well confined in the channel. Figure 11(b) shows TE radiation modes at a magnetic field of -50 Oe at θ = 0° which is equivalent to a backward propagating wave. The light is radiated into the slab out of the channel. We confirmed that the radiated light was TE polarized by using a TE analyzer.

To measure the isolation value, the output light from the waveguide was coupled to a lensed normal single-mode fiber and then detected at a photo-diode. The radiation modes were eliminated by the single-mode fiber coupling. Figure 12 shows isolation as a function of wavelength from 1530 to 1546 nm. The solid circles show isolation at θ = 0°. The peak isolation was 13.3 dB measured at 1536 nm. At shorter wavelengths, β_{11B}^{x} becomes larger than cutoff β_{c}^{y}, so the forward and backward TM waves cannot be converted to the TE radiation modes. At the longer wavelengths, by contrast, β_{11F}^{x} becomes smaller than cutoff β_{c}^{y}, so the forward and backward TM waves are converted to TE radiation modes. It was possible to improve the isolation at shorter wavelengths to some extent by adjusting the magnetic field angle. The open circles show the improved isolation when the magnetic field angle θ is optimized to obtain the maximum isolation value. The angles are indicated by the open squares. The improvement is thought to result from the fact that the coupling coefficient increases when the z-axis component of magnetization is increased. We also obtained the same experimental results when changed the light launching edge of the waveguide. It was, however, also unclear whether the origin of the coupling coefficient K was magnetic anisotropy or stress-induced anisotropy.

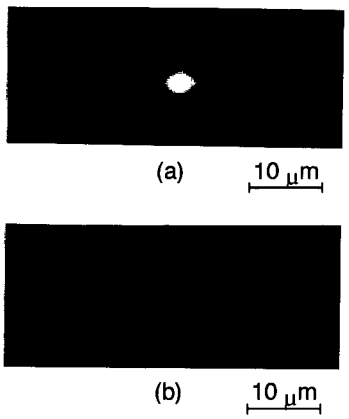

FIG. 11. Near field patterns for radiation-mode-converted isolator: Type 1. (a) +50 Oe; (b) -50 Oe.

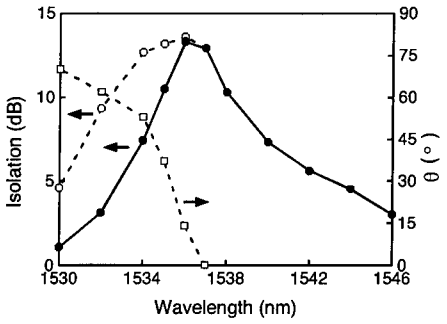

FIG. 12. Isolation spectra of radiation-mode-converted isolator: Type 1.

Experiment on radiation-mode-converted isolator: Type 2

We fabricated the radiation-mode converted isolator: Type 2 shown in Fig. 7. The Ce:YIG film thickness was 0.47 μm, the rib height was 0.11 μm, the rib width were 2.2 μm and the waveguide length was 4.1 mm. A low rib height was chosen so that both β_{11F}^{x} and β_{11B}^{x} are smaller than β_{c}^{y}. Figure 13 shows the near field patterns at the output end λ = 1535 nm. Figure 13(a) shows the fundamental E_{11}^{x} mode with a magnetic field of -50 Oe at θ = 0° which is equivalent to a forward propagating wave. The light was well confined in the channel. Figure 13(b) shows the TE radiation modes with a magnetic field of +50 Oe at θ = 0° which is equivalent to a backward propagating wave. The E_{11}^{x} mode was strongly damped by coupling it to radiation modes and it escaped out of the rib channel into the slab. We confirmed that the radiated light was TE polarized by using a TE analyzer. The magnetic-field direction in which Type 2 was operated was opposite to that for Type 1.

Figure 14 shows the isolation as a function of wavelength from 1510 to 1560 nm. The solid circles show the isolation at θ = 0°. The peak isolation was 25.6 dB measured at 1535 nm. It was possible to improve the isolation at longer wavelengths by adjusting the magnetic field angle. The open circles show the improved isolation when the magnetic field angle θ is optimized to obtain the maximum isolation value. The angles are indicated by the open squares. The highest isolation value of 27 dB was obtained at θ = 4.6° and λ = 1535 nm. The improvement is thought to result from the fact that the coupling coefficient increases when the z-axis component of magnetization is increased. The same experimental results were obtained when the light launching edge of the waveguide was changed. It was, however, also unclear whether the origin of the coupling coefficient K was magnetic anisotropy or stress-induced anisotropy.

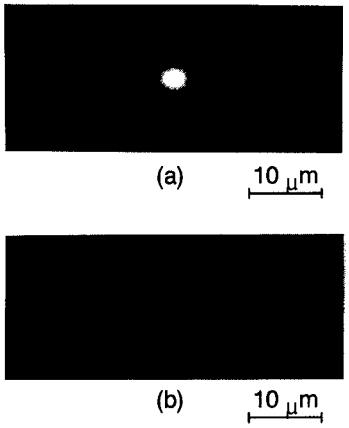

FIG. 13. Near field patterns for radiation-mode-converted isolator: Type 2. (a) -50 Oe; (b) +50 Oe.

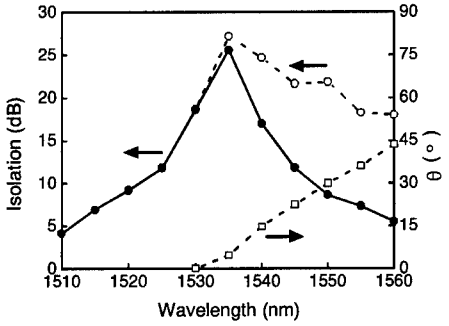

FIG. 14. Isolation spectra of radiation-mode-converted isolator: Type 2.

HYBRID INTEGRATED CIRCULATOR

We proposed and realized a new polarization-independent optical circulator using a Mach-Zehnder interferometer (MZI) which does not need a polarization-beam splitter. Figure 15 shows the schematic configuration of the proposed circulator. It is assumed that light propagates along the z direction and that the x-y plane is transverse. We can combine two waveguide 45° Faraday rotators and two half-wave plates with an MZI structure which consists of two 3-dB couplers. We set the slow axes of the upper and lower half-wave plates at respective angles of -22.5° and 22.5° in relation to the x axis in the transverse plane. If the upper and lower lights with the same polarization in phase enter the Faraday rotators and half-wave plates in the positive z direction, these lights still have the same polarization in phase after traveling through them in spite of polarization-direction rotation. By contrast, If these lights travel through the Faraday rotators and half-wave plates in the negative z direction, they have opposite polarization directions as a result of nonreciprocal rotation and their phases differ by 180°. 3-dB couplers split and combine waves with a phase difference of 90°. Therefore, by combining these Faraday rotators and half-wave plates with two 3-dB couplers, we can build a nonreciprocal MZI. This acts as a circulator, i.e., a wave travels from port 1 to port 2, port 2 to port 3, port 3 to port 4, or port 4 to port 1. We can also derive general conditions: $\theta_{F1} + \theta_{F2} = \pm 90° + 360n°$ and $\theta_{S1} - \theta_{S2} = \pm 45°$. Here, θ_{F1} and θ_{F2} are the respective Faraday rotation angles of the upper and lower Faraday rotation, n is an integer, and θ_{S1} and θ_{S2} are the respective slow-axis angles of the upper and lower half-wave plates.

We fabricated a circulator which comprises an MO waveguide array with two waveguide Faraday rotators, two silica-based 3-dB couplers, two thin half-wave plates and a permanent magnet. We prepared lanthanum- and gallium-substituted YIG buried channel MO waveguides on a GGG substrate by liquid phase epitaxy and ion-beam etching.[20] The core size was 4 μm x 4 μm. These waveguides were arrayed with a pitch of 250 μm. The MO array was cut to a length of 3.0 mm to provide 45° Faraday rotation. Both endfaces were polished and anti-reflection coated. The 3-dB wavelength-insensitive couplers were fabricated in planar lightwave circuits (PLC) on silicon substrates.[21] The core size was 8 μm x 8 μm and the length of the PLC was 22 mm. The 16-μm thick polyimide half-wave plates were then inserted in 20-μm wide grooves formed on the PLC's.[22] Next, we aligned all the components and fixed them in position with adhesive. The MO waveguides were covered with a compact Sm-Co permanent magnet to provide a sufficient magnetic field of 180 Oe.

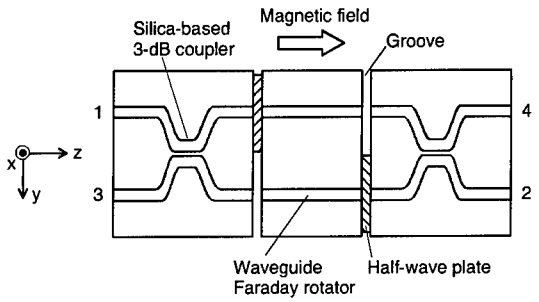

FIG. 15. Circulator structure.

Table I shows the attenuation from a numbered input port to a numbered output port. The insertion loss was 3.0-3.3 dB with a polarization dependent loss of 0.2 dB, the extinction ratio was 13.8-23.9 dB, and the isolation was 14.1-23.7 dB. The return loss was also measured and found to be 26.3-27.9 dB. The reflection came mainly from the endfaces of the MO waveguides, and this can be reduced by using beveled interfaces. We assume that the difference between the isolation in the forward and backward directions arises from deviation in the setting of the Faraday rotation angles and half-wave plate slow-axis angles. The adoption of a technique for assembly on a PLC platform will enable us to fabricate this waveguide circulator easily and to obtain good performance.[20]

TABLE I. Attenuation from a numbered input port to a numbered output port at λ = 1.55 μm.

(dB)

In \ Out	1	2	3	4
1		3.2		17.2
2	26.4		3.0	
3		17.1		3.3
4	3.1		27.0	

CONCLUSIONS

We have proposed and realized new integrated isolators based on nonreciprocal conversion from a fundamental TM mode to a higher-order TE mode or a TE radiation mode. These isolators are successfully realized using a simple single-mode rib channel waveguide in Ce-substituted YIG which has a very large Faraday rotation. 13-27 dB isolation was obtained around λ = ~1.55 μm. Further, we have proposed and realized a new hybrid-integrated waveguide polarization-independent optical circulator based on a nonreciprocal Mach-Zehnder interferometer. 14.1-23.7 dB isolation was obtained at λ = 1.55 μm. These nonreciprocal devices offer a new possibility for developing nonreciprocal devices in the field of integrated optics.

ACKNOWLEDGEMENTS

The authors thank T. Uno, M. Kobayashi, T. Miya, , N. Takato, M. Shimokozono, M. Ishii, Y. Inoue and H. Terui for their helpful advice and circulator preparation.

REFERENCES

1. J. P. Castéra and G. Hepner, Appl. Opt. **16**, 2031 (1977).
2. S. T. Kirsch, W. A. Biolsi, S. L. Blank, P. K. Tien, R. J. Martin, P. M. Bridenbaugh, and P. Grabbe, J. Appl. Phys. **52**, 3190 (1981).
3. Y. Okamura, H. Inuzuka, T. Kikuchi and S. Yamamoto, IEEE J. Lightwave Tech. **4**, 711 (1986).
4. K. Taki and Y. Miyazaki, Trans. IECE Jpn. **E71**, 161 (1988).
5. K. Ando, T. Okoshi, and N. Koshizuka, Appl. Phys. Lett. **53**, 4 (1988).

6. T. Mizumoto, H. Chihara, N. Tokui, and Y. Naito, Third Optoelectronics Conference (OEC'90) Technical Digest, Makuhari Messe, Japan, 13B4-5 (1990).
7. K. Ando, Proc. SPIE **1126**, 58 (1989).
8. T. Shintaku and T. Uno, J. Appl. Phys. **76**, 8155 (1994).
9. T. Shintaku, Appl. Phys. Lett. **66**, 2789 (1995).
10. T. Shintaku, to appear in Appl. Phys. Lett.
11. M. Gomi, K. Satoh, and M. Abe, Jpn. J. Appl. Phys. **27**, L1536 (1988).
12. T. Shintaku and T. Uno, Jpn. J. Appl. Phys. **35**, 4689 (1996).
13. T. Shintaku, A Tate, and S. Mino, Appl. Phys. Lett. **71**, 1640 (1997).
14. T. Shintaku, T. Uno, and M. Kobayashi, J. Appl. Phys. **74**, 4877 (1993).
15. T. Shintaku, N. Sugimoto, M. Shimokozono, A. Tate, E. Kubota, H. Kozawaguchi, M. Ishii and Y. Inoue, Proc. IOOC/ECOC'97 **5**, 57 (1997).
16. E. A. J. Marcatili, Bell Syst. Tech. J. **48**, 2071 (1969).
17. S. Yamamoto and T. Makimoto, J. Appl. Phys. **45**, 882 (1974).
18. S. Yamamoto, Y Koyamada, and T. Makimoto, J. Appl. Phys. **43**, 5090 (1972).
19. S. Kawakami, Appl. Opt. **22**, 2426 (1983).
20. H. Terui, A. Tate, Y. Yamada, N. Sugimoto, Y. Katoh, A. Sugita, A. Shibukawa and Y. Inoue, S. Ando and T.Sawada, Proc. ECOC '94, Firenze, 213 (1994).
21. K. Jinguji, N. Takato, Y.Hida, T. Kitoh and M. Kawachi, J. Lightwave. Technol. **14**, 2301 (1996).
22. S. Ando, T. Sawada and Y. Inoue, Electron Lett. **22**, 2143 (1993).

A COMPARISON OF AN IMPROVED DESIGN FOR TWO INTEGRATED OPTICAL ISOLATORS BASED ON NONRECIPROCAL MACH-ZEHNDER INTERFEROMETRY

N. Bahlmann, M. Lohmeyer, M. Wallenhorst, H. Dötsch, P. Hertel
University of Osnabrück, 49069 Osnabrück, Germany

ABSTRACT

Nonreciprocal rib waveguide structures can be used to realize integrated optical isolators. The nonreciprocal phase shift is the difference between the forward and backward propagation constants of TM modes in magneto-optic waveguides. It can be optimized with respect to absolute value and temperature dependence if double layer waveguides with different magnetic and nonmagnetic layers are prepared. In this paper we propose an improved design for two different Mach-Zehnder interferometer isolators the nonreciprocal parts of which are formed by such double layer waveguides. One concept utilizes a nonreciprocal and a reciprocal arm. In the other case both arms are nonreciprocal but with opposite sign of the nonreciprocal phase shift. A particular property of both concepts is that the lengths of the nonreciprocal arms are well defined. The rest of the interferometer is made by reciprocal rib waveguides. Therefore, the nonreciprocal phase shift is well known. The concepts are compared with regard to isolation ratio, forward losses and fabrication tolerances. Moreover, we simulate the entire isolator by a finite difference beam propagation calculation.

INTRODUCTION

Nonreciprocal magneto-optic devices, such as isolators or circulators, play an important role in optical technology. As they distinguish between forward and backward propagating light, they are used to protect optical components, especially lasers, from reflected light. Bulk or microoptic isolators are commercially available. Magnetic garnet films are the best choice for the realization of integrated isolators, because of their high Faraday rotation and low absorption in the near infrared.

Various kinds of optical isolators have been proposed by a number of researchers [1, 2, 3, 4, 5, 6, 7]. The most promising concepts of integrated optical isolators rely on nonreciprocal Mach-Zehnder interferometry [8, 9]. The distinction between forward and backward propagation is achieved by the differential nonreciprocal phase shift $\Delta\beta$, the difference between the forward and backward propagation constants $\Delta\beta = \beta^{\mathrm{TM}}_{\mathrm{forw}} - \beta^{\mathrm{TM}}_{\mathrm{back}}$ of TM modes in magneto-optic waveguides [10]. In forward direction, waves propagating along both arms of the Mach-Zehnder interferometer are in phase, in backward direction a phase shift of π occurs. In this paper we present a comparison of different detailed design and fabrication considerations for the realization of such isolators. The required fabrication tolerances are estimated and beam propagation calculations are used to demonstrate how the isolators work.

THEORY

Nonreciprocal Waveguides

For the basic rib geometry sketched in Fig. 1 the propagation constants of TE and TM modes propagating along the z-axis can be calculated using a finite element [11] or a finite difference method [12]. If the magnetization $\boldsymbol{M}$ is adjusted in the film plane perpendicular to the propagation direction, a nonreciprocal phase shift $\Delta\beta$ shows up for TM modes.

Mat. Res. Soc. Symp. Proc. Vol. 517 © 1998 Materials Research Society

Perturbation theory yields

$$\Delta\beta = \frac{\iint |H_y|^2(\partial_x \xi/\epsilon^2)dxdy}{\iint \epsilon^{-1}|H_y|^2 dxdy} \tag{1}$$

for the differential nonreciprocal phase shift [13]. H_y is the field distributiuon of the unperturbed TM mode, ϵ the permittivity, and ξ is related to the Faraday rotation Θ_F by $\xi \approx 2n\Theta_F/k_0$ where k_0 is the vacuum wave number.

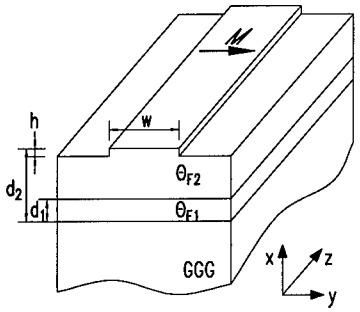

Figure 1: Basic geometry of the rib waveguide.

To achieve a large $|\Delta\beta|$, double layer garnet films with opposite Faraday rotation are prepared where the boundary between layers is located close to the maximum of $|H_y|^2$ [14]. Double layer waveguides with a positive rotating bottom layer and a negative rotating top layer show the highest differential nonreciprocal phase shift [15]. Due to the large temperature dependence of the positive Faraday-rotation such films are not suitable for the realization of a device [14]. Therefore, we use a paramagnetic bottom layer (0.18 μm thick) with negligible Faraday-rotation. The maximum nonreciprocal phase shift of 10.05 cm^{-1} is achieved at a total waveguide thickness of 0.504 μm. The refractive index and the Faraday-rotation of the films are (n=2.2, $\Theta_F = 0°/cm$) and (n=2.33, $\Theta_F = -1450°/cm$), respectively.

Nonreciprocal Mach-Zehnder Interferometer

The double layer rib waveguides described above can be used to realize the nonreciprocal part of an integrated Mach-Zehnder interferometer. Different proposals for a Mach-Zehnder type isolator have been put forward by many researchers [8, 9, 16]. Because the couplers are made by magneto-optic waveguides as well, the lengths of the nonreciprocal phase shifters are not well defined. To avoid this problem, Yokoi proposed, in ref. [17], a new design employing wafer-direct bonding.

Our concept to get rid of this problem is to replace the magnetic layer by a dielectric film for the reciprocal part. After masking the nonreciprocal waveguide sections the magnetic garnet film must be removed by ion beam etching. Afterwards this region is refilled with a dielectric layer of the same refractive index like titanium dioxide [18]. The thickness of this new layer must be well chosen in order to have equal propagation constants in the reciprocal and nonreciprocal parts. Then no reflections will occur. In this paper we propose two different isolators build with this technique. The first utilizes just one nonreciprocal interferometer arm. The rest of the Mach-Zehnder is reciprocal. For the second isolator both arms are nonreciprocal but with opposite sign of the magnetization. Therefore, the nonreciprocal effects add up (see Fig. 2).

The main advantage of the design with one nonreciprocal arm is that the whole device must be magnetized in just one direction. It is sufficient to magnetize the isolator by an

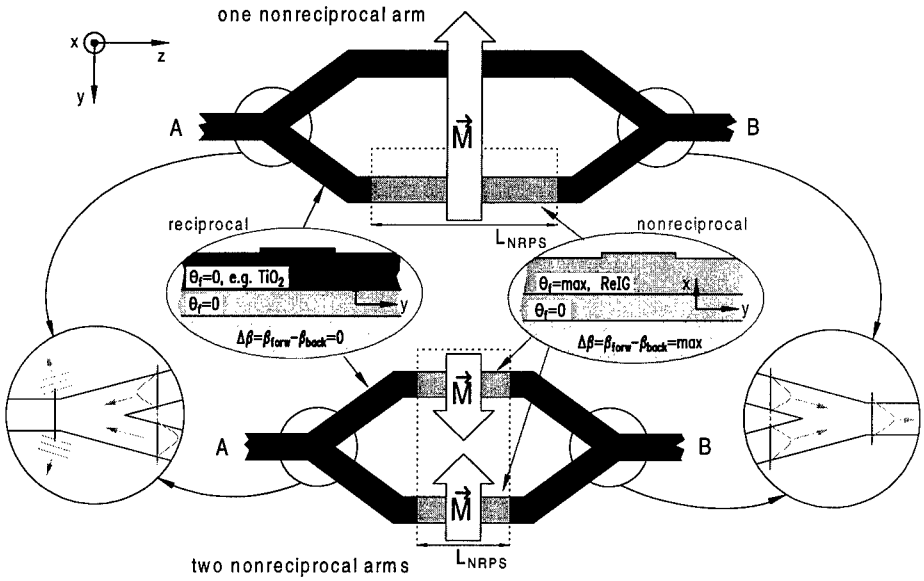

Figure 2: Basic geometry of two nonreciprocal Mach-Zehnder interferometers. The upper isolator has one nonreciprocal arm. The second one utilizes two nonreciprocal arms with opposite magnetization.

external bias magnetic field. To realize the interferometer with two nonreciprocal branches, we have to adjust the magnetization separately in each waveguide. Permanent magnets or dc electric current flowing along an electrode above the waveguides yield magnetic field opposite in the two arms. Levy et al. [2] used sputtered thin film magnets for this purpose. Thus it is possible, but it requires some additional difficult fabrication steps. The length of the well defined nonreciprocal part for the first design becomes $L_{\mathrm{NRPS}} = \pi/\Delta\beta = 0.312$ cm. This is twice as long as the reciprocal arms of the interferometer with two arms. Because of that, the losses of the device can be reduced by the second design (the losses of the y-couplers are equal in both cases). For the first design another problem occurs if the reciprocal and the nonreciprocal arms have different losses. The use of asymmetric y-splitters solves this complication but leads to unnecessary efforts.

Fabrication Tolerances

Three parameters have the strongest influence on the isolation ratio of the interferometer. The intrinsic phase difference between the arms in forward direction must vanish, whereas the total nonreciprocal phase shift in backward direction must be π. The third important factor is the splitting ratio $\bar{\alpha}$ of the y-junctions.

The intrinsic phase depends strongly on the waveguide geometry and the refractive indices. It is impossible to structure the interferometer in one step with the required accuracy. But it can be tuned in a postfabrication process by local laser annealing or stepwise reduction of the waveguide thickness in one arm. Furthermore, this is necessary to achieve an additional reciprocal phase shift of $\pi/2$ in one arm.

We estimate the isolation ratio $P_{\text{out,forw}}/P_{\text{out,back}}$ by the following expression [19]:

$$P_{\text{out}} = \frac{P_{\text{in}}}{2} K \mathrm{e}^{-\alpha L_{\text{dev}}} (1 + 2\sqrt{\bar{\alpha}(1-\bar{\alpha})} \cos \Phi). \tag{2}$$

P_{in} and P_{out} denote the input and output power, respectively. The damping of the waveguides is α and the total device length is L_{dev}. K describes additional losses which are caused e. g. by the y-couplers. The splitting ratio of the y-couplers is described by $\bar{\alpha}$ (1/2 for ideal couplers). Φ is the phase difference between the arms. To achieve an isolation of 30 dB, the splitting ratio $\bar{\alpha}$ should range from 0.48 to 0.52 if the phase difference $\Phi_{\text{forw}} - \Phi_{\text{back}}$, which is the total nonreciprocal phase shift if Φ_{forw} is assumed to be 0, lies between 177° and 183° (see Fig. 3). This requires a thickness and length variation of the nonreciprocal waveguides smaller than ± 0.03 μm and ± 5 μm, respectively. For the design with two nonreciprocal arms each length must be adjusted with double precision. Otherwise the fabrication tolerances are equal in both cases, as the intrinsic phase must be tuned in a postfabrication step.

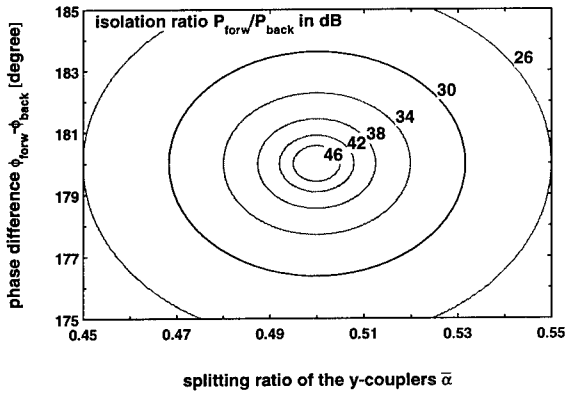

Figure 3: Calculated isolation ratio $P_{\text{forw}}/P_{\text{back}}$ for a nonreciprocal Mach-Zehnder interferometer. The intrinsic phase Φ_{forw} is assumed to be zero.

Finite Difference Beam Propagation

In order to simulate the behaviour of nonreciprocal devices like Mach-Zehnder interferometers, we employ a finite difference beam propagation method for nonreciprocal three dimensional structures (two dimensional cross section, one propagation dimension). Different beam propagation techniques for reciprocal waveguides were introduced by a number of researchers [20]. Erdmann et. al [21] introduced a BPM method for planar magneto-optic waveguides.

The following calculations are performed with effective indices. In the magneto-optic waveguides we have different indices for forward and backward direction. Therefore, we have to carry out the BPM calculation twice. In paraxial approximation one obtains the Fresnel equation [20]

$$2\mathrm{i}k_0 n_{\text{ref}} \frac{\partial E_x}{\partial z} = \frac{\partial^2 E_x}{\partial y^2} + k_0^2 [n_{\text{eff}}^2(y) - n_{\text{ref}}^2] E_x \tag{3}$$

for the dominating electric field component E_x of the TM mode. The reference index n_{ref} is supplied by a calculation without magneto-optic effect. The Fresnel equation is solved with a finite difference Crank-Nicolson procedure. In order to suppress reflections from the boundaries, transparent boundary conditions are implemented [22].

Fig. 4 shows the calculated fields for the forward and backward direction. The geometry parameters of the Mach-Zehnder interferometer with one nonreciprocal arm are given in the figure caption. Almost 97 % of the input light passes the isolator in forward direction, but less than 0.1 % in backward direction, the rest leaving the device in lateral direction. This amounts to an isolation exceeding 30 dB. Calculations for the device with two nonreciprocal arms yield analogous results. Because of the space restrictions in this paper, they are not shown here.

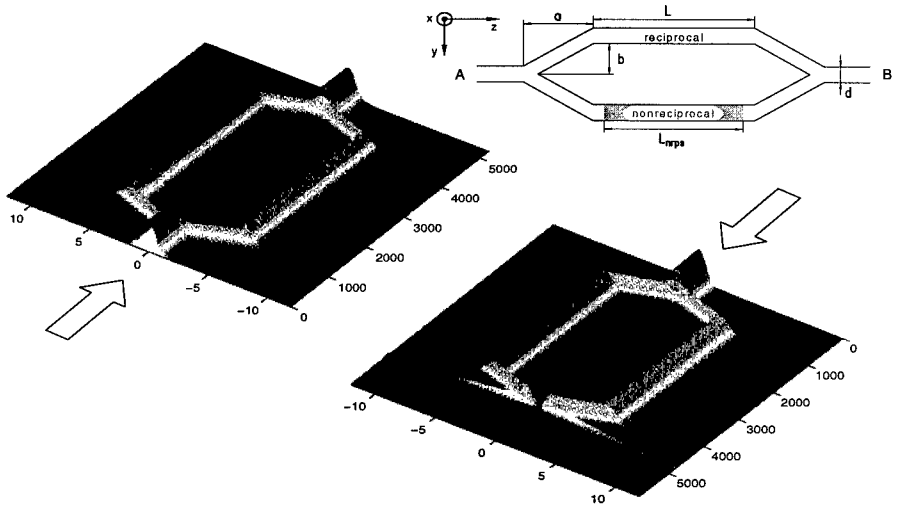

Figure 4: BPM simulation of the Mach-Zehnder interferometer. For the nonreciprocal part we use the double layer waveguide with $\Delta\beta = 10.05$ cm^{-1}. ($a = 400$ μm, $b = 4$ μm, $d = 1.5$ μm, $L = 3250$ μm, $L_{\mathrm{NRPS}} = 3123$ μm).

CONCLUSIONS

Double layer rib waveguides with one paramagnetic and one magneto-optic layer are a good choice to realize nonreciprocal devices. We propose two improved designs for a nonreciprocal Mach-Zehnder interferometer isolator. An outstanding feature of the concept is that the nonreciprocal parts of the interferometers are well defined. This leads to a well known nonreciprocal phase shift. If the intrinsic phase is tuned in a postfabrication process the fabrication tolerances are almost identical for both designs. The advantage of the design with two nonreciprocal arms is the lower forward loss due to reduced length. But a reversal of the magnetization requires additional technical efforts. Therefore it seems to be wise to make first experiments with one nonreciprocal arm. Simple BPM calculations with different effective refractive indices for forward and backward direction work well to simulate the propagation of light in the device.

ACKNOWLEDGEMENTS

We gratefully acknowledge financial support by Deutsche Forschungsgemeinschaft, Sonderforschungsbereich 225.

REFERENCES

[1] R. Wolfe, J.F. Dillon Jr., R. A. Lieberman, and V. J. Fratello, *Applied Physics Letters*, **57**, (10), pp. 960, 1990.

[2] M. Levy, R. M. Osgood Jr., H. Hegde, F. J. Cadieu, R. Wolfe, and V. J. Fratello, *IEEE Photonics Technology Letters*, **8**, (7), pp. 903–905, 1996.

[3] K. Ando, T. Okoshi, and N. Koshizuka, *Applied Physics Letters*, **53**, (1), pp. 4–6, 1988.

[4] T. Mizumoto, Y. Kawaoka, and Y. Naito, *The Transactions of the IECE of Japan*, **E 69**, (9), pp. 968–972, 1986.

[5] H. Hemme, H. Dötsch, and P. Hertel, *Applied Optics*, **29**, (18), pp. 2741–2744, 1990.

[6] S. Yamamoto, Y. Okamura, and T. Makimoto, *IEEE Journal of Quantum Electronics*, **QE-12**, (12), pp. 764–770, 1976.

[7] T. Shintaku, *Applied Physics Letters*, **66**, (21), pp. 2789–2791, 1995.

[8] F. Auracher and H.H. Witte, *Optics Communications*, **13**, (4), pp. 435–438, 1975.

[9] Y. Okamura, T. Negami, and S. Yamamoto, *Applied Optics*, **23**, (11), pp. 1886–1889, 1984.

[10] S. Yamamoto and T. Makimoto, *Journal of Applied Optics*, **45**, (2), pp. 882–888, 1974.

[11] M. Koshiba and X.P. Zhuang, *Journal of Lightwave Technology*, **11**, (9), pp. 1453–1458, 1993.

[12] A. Erdmann, M. Shamonin, P. Hertel, and H. Dötsch, *Optics Communications*, **102**, (1,2), pp. 25–30, 1993.

[13] M. Shamonin and P. Hertel, *Applied Optics*, **33**, (27), pp. 6415–6421, 1994.

[14] M. Wallenhorst, M. Niemöller, H. Dötsch, P. Hertel, R. Gerhardt, and B. Gather, *Journal of Applied Physics*, **77**, (7), pp. 2902–2905, 1995.

[15] N. Bahlmann, V. Chandrasekhara, A. Erdmann, R. Gerhardt, P. Hertel, R. Lehmann, D. Salz, F. Schröteler, M. Wallenhorst, and H. Dötsch, *Journal of Lightwave Technology*, to be published in May 1998.

[16] T. Mizumoto, S. Mashimo, T. Ida, and Y. Naito, *IEEE Transactions on Magnetics*, **29**, (6), pp. 3417–3419, 1993.

[17] H. Yokoi and T. Mizumoto, *Electronics Letters*, **33**, (21), pp. 1787–1788, 1997.

[18] P. Löbl, M. Huppertz, and D. Mergel, *Thin Solid Films*, **251**, pp. 72–79, 1994.

[19] W. Karthe and R. Müller, *Integrierte Optik*, Akademische Verlagsgesellschaft Geest & Portig, Leipzig, 1991.

[20] Y. Chung and N. Dagli, *IEEE Journal of Quantum Electronics*, **26**, (8), pp. 1335–1339, 1990.

[21] A. Erdmann and P. Hertel, *IEEE Journal of Quantum Electronics*, **31**, (8), pp. 1510–1516, 1995.

[22] G. R. Hadley, *Optics Letters*, **16**, (9), pp. 624–626, 1991.

RADIATIVELY COUPLED WAVEGUIDE CONCEPT FOR AN INTEGRATED MAGNETO-OPTIC CIRCULATOR

M. Lohmeyer, M. Shamonin, N. Bahlmann, P. Hertel, H. Dötsch
Department of Physics, University of Osnabrück, 49069 Osnabrück, Germany

ABSTRACT

Three-guide couplers with multimode central waveguides allow for remote coupling between optical channels. A simple three mode approximation turns out to be sufficient for the description of the main features of the power transfer behavior. The specific form of the relevant modes suggests the design of integrated optical isolators and circulators based on magnetic garnet materials. These novel devices are superior to conventional nonreciprocal couplers with respect to the total length and admissible fabrication tolerances. We characterize the isolation performance and the transmission loss for the proposed devices by propagating mode simulations and estimate the influence of geometry parameter deviations.

INTRODUCTION

The majority of integrated optical isolator proposals comprises two waveguide ports, which are connected for light propagation in the direction of transmission. In the opposite direction the power is either damped by a polarizer or radiated into the surrounding. In contrast the concept of the nonreciprocal coupler [1, 2] is suitable for the realization of circulator devices, since the blocked power remains well confined in its own output waveguide. For current magneto-optic materials with undesirably high optical losses, the conventional X-coupler has the drawback of large total length and prohibitively strict fabrication tolerances. In this paper we show how this can be overcome by insertion of a third multimode rib, for both planar and rib waveguide devices .

RADIATIVELY COUPLED WAVEGUIDES

Fig. 1 depicts the three waveguide couplers discussed in this paper. For numerical modeling we regard the entire structure between $z = 0$ and $z = L$ as a single lossless multimode waveguide. Interference of its supermodes determines the power transfer between the outer waveguides.

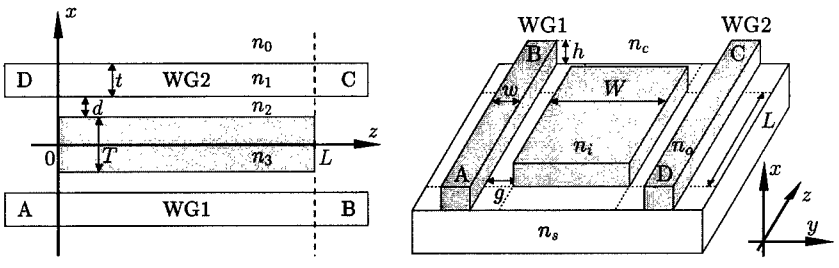

Figure 1: Geometries of the planar (left) and rib waveguide devices (right). The central layer or the central rib, resp., couples two identical outer waveguides WG1 and WG2. The structures are to be considered four port devices with input and output channels A to D.

We start with a look at the dispersion characteristics, focusing on planar devices first. For given vacuum wavelength $\lambda = 2\pi/k$ and polarization state, each outer waveguide supports one mode with a propagation constant denoted β_*. To achieve remote coupling, the isolated central waveguide must support modes with propagation constants beyond this level. Then the effective

Mat. Res. Soc. Symp. Proc. Vol. 517 © 1998 Materials Research Society

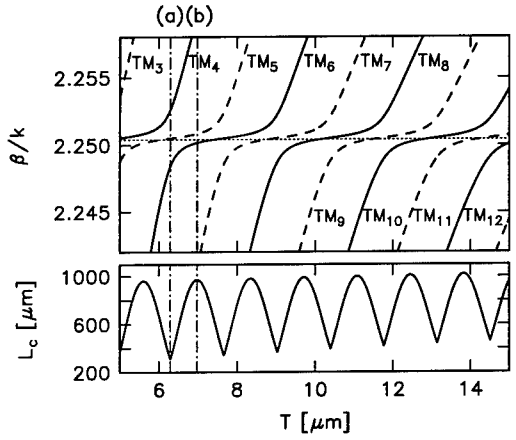

Figure 2: Effective indices β/k (top) and the corresponding coupling length L_c (bottom) for TM-polarized modes versus the thickness T of the central layer in a planar structure. The dotted line indicates the level $\beta_*/k = 2.25041$ of the single outer waveguide's TM mode. Only a small fraction of the region allowed for modal indices is displayed. Parameters are: $\lambda = 1.3\,\mu$m, $t = 0.8\,\mu$m, $d = 0.8\,\mu$m, $n_0 = n_2 = 2.18$, $n_1 = n_3 = 2.30$.

mode indices of the entire structure typically exhibit a dependence on the coupling layer thickness T as depicted in Fig. 2.

For each thickness T there are either two or three propagation constants close to β_*. The corresponding modes show large field amplitudes in the outer guiding regions (see Fig. 3), thus carrying most of the power if the structure is excited by the mode of one outer waveguide. For the parameters given for Fig. 2 and T up to 15 μm this amount is larger than 90% for the three modes with propagation constants next to β_*. Therefore we focus at first on the interference between only these three most excited modes.

The two of them with the smaller difference between their propagation constants β_s, β_a, define a characteristic length $L_c = \pi/|\beta_s - \beta_a|$. L_c can be regarded a coupling length if either the power carried by the third mode is negligible, or if the propagation constant of the third mode fits properly to enable complete power transfer. We have found that points T with the relevant propagation constants properly spaced occur frequently to justify calling L_c the coupling length for all T. This is further elaborated in [3].

Due to the harmonic dependence of the modes on the transverse coordinate x in the coupling region, L_c shows a nearly periodic dependence on T as well. Around the minima of $L_c(T)$, three modes determine the coupling behaviour, next to the maxima only two modes have to be considered. We call these regions the three- and two-mode regime, respectively. Two examples have been marked in Fig. 2, Fig. 3 shows the relevant mode field profiles.

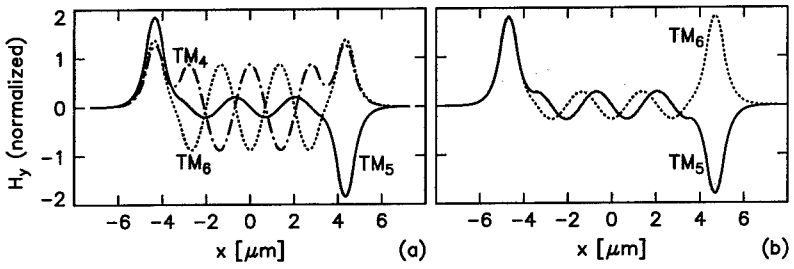

Figure 3: Mode field profiles for coupling layer thicknesses $T = 6.29\,\mu$m (a) and $T = 6.98\,\mu$m (b), corresponding to the three- (a) and two-mode regimes (b) marked in Fig. 2.

In a realistic simulation all normalized modes ψ_j of the entire structure have to be considered. Denote by β_j the corresponding propagation constants and by ϕ_1, ϕ_2 the normalized modes of

WG1 and WG2. Suppose ϕ_1 is launched into the coupling region at $z = 0$. Neglecting reflections at input and output, the relative power transmitted to waveguide k at $z = L$ is given by $P_k(L) = |\sum_j \langle\phi_k, \psi_j\rangle \langle\psi_j, \phi_1\rangle \exp(-\mathrm{i}\beta_j L)|^2$. $\langle .,. \rangle$ denotes the appropriate scalar product. It is a very good approximation to restrict the sum to guided modes. At least for the planar structures in this paper we have found $P_1(0) \geq 0.999$, thus these devices show only low radiation losses at input and output. Reflections should be of the same order of magnitude, i.e. negligible. Note that waveguide bends as needed for the conventional coupler can be completely avoided.

MAGNETO-OPTIC LAYERS

We will now assume that some layers have a linear magneto-optic effect with the static magnetization adjusted in the y direction (see Fig. 1). In these regions the permittivity tensor $\hat{\epsilon}$ reads

$$\hat{\epsilon} = \begin{pmatrix} n^2 & 0 & -\mathrm{i}\xi \\ 0 & n^2 & 0 \\ \mathrm{i}\xi & 0 & n^2 \end{pmatrix}, \tag{1}$$

where the small off-diagonal elements are related to the specific Faraday rotation Θ_F and refractive index n by $\xi = n\lambda\Theta_\mathrm{F}/\pi$. ξ enters via a perturbational expression [4]. While TE-like modes are not affected in first order, the propagation constants of TM modes are shifted by an amount $\delta\beta$. For a two-dimensional piecewise constant profile with discontinuity lines in $x = x_j$, $y_{j,0} < y < y_{j,1}$ separating permittivities $n_{j,-}$, $\xi_{j,-}$ below and $n_{j,+}$, $\xi_{j,+}$ above, the nonreciprocal phase shift can be written

$$\delta\beta = \frac{1}{2}\sum_j \int_{y_{j,0}}^{y_{j,1}} \left(\frac{\xi_{j,+}}{n_{j,+}^2} - \frac{\xi_{j,-}}{n_{j,-}^2} \right) |H_y(x_j, y)|^2 \mathrm{d}y \,, \tag{2}$$

where $H_y(x, y)$ denotes the transverse magnetic field component of the TM mode in the corresponding isotropic waveguide, normalized to $\iint n^{-2}|H_y|^2 \mathrm{d}x\,\mathrm{d}y = 1$. We refer to the semivectorial approximation, neglecting the normal component H_x. In the case of planar waveguides, the second argument y and the corresponding integration must be removed.

Reversing the direction of propagation while the static magnetization remains changes the sign of ξ, thus the propagation constants for forward and backward direction differ by $2\delta\beta$. Usually the coupling lengths L_c^f and L_c^b for forward and backward propagation are different as well. An isolator results if the device length can be adjusted such that $L = lL_\mathrm{c}^\mathrm{f} = (l \pm 1)L_\mathrm{c}^\mathrm{b}$ holds for an integer number l.

Indicating by subscripts s and a the most relevant supermodes of our coupler structures, the smallest possible isolator length can be shown to be

$$L_\mathrm{is} = \frac{\pi}{2|\delta\beta_\mathrm{s} - \delta\beta_\mathrm{a}|}. \tag{3}$$

To realize a short device, not only a large phase shift is required, but also the *difference* between the nonreciprocal phase shifts of the two modes must be as large as possible.

Note that this is the weak point of the conventional coupler: its two squared supermodes appear very similar, thus the difference in the nonreciprocal phase shifts remains small.

PLANAR DEVICES

As an example, Fig. 4 shows the squared amplitudes of the relevant supermodes in the three mode regime. The largest differences occurr in the center of the outer waveguides and periodically in the central waveguide. Obviously the shortest isolating device results if the guiding regions can be manufactured from layers with opposite Faraday rotation, such that the ξ profile changes exactly at these points. This is illustrated in the bottom inset of Fig. 4.

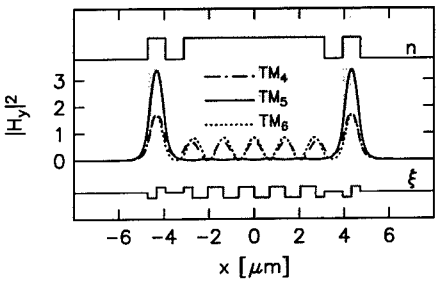

Figure 4: Field intensity for the modes of Fig. 3(a). The insets outline the corresponding refractive index profile (top) and an optimum choice for the profile of the Faraday rotation (bottom).

For such multilayer configurations, Eq. 3 evaluates to the curves of Fig. 5. Clearly, the shortest devices can be expected in the regions of the three mode regime, for periodically occurring values T. Note that Fig. 5 gives a rough estimate of the realistic device length only, since merely two modes enter Eq. 3. However, the exact numerical calculations show that close to the values indicated by Eq. 3 sets of parameters for well performing devices can be found [3].

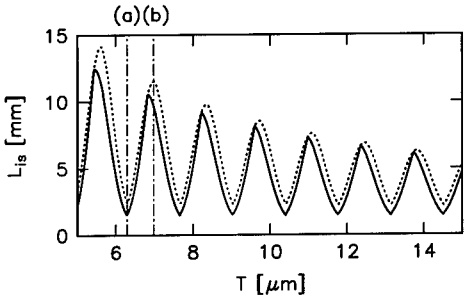

Figure 5: Isolator device length L_{is} versus the thickness T of the coupling layer. For the dotted curve, only the central layer has been modeled as a magnetic grating with alternating Faraday rotation, while for the continuous curve the outer waveguides are assumed to be double layer waveguides with opposite Faraday rotation as well. Parameters are as given for Fig. 2, $\xi = \pm 0.005$.

Fig. 6 illustrates the light propagation in one of these devices. With outer waveguides formed as double layers, each of thickness $t/2$, with opposite sign of Θ_F, and the coupling region made up of 10 layers of alternating Faraday rotation, the device achieves an isolation $10\log_{10} P_1^f/P_1^b$ of 38 dB and a forward transmission loss $-10\log_{10} P_1^f$ of 0.15 dB. The tolerances given in the figure caption guarantee isolation better than 20 dB and losses below 0.5 dB, where losses due to material absorption must be added.

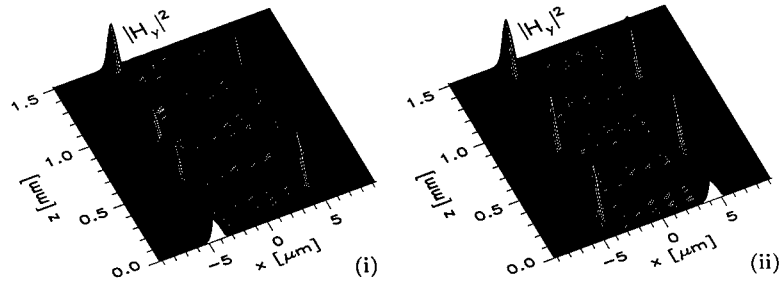

Figure 6: TM-field propagation along the planar isolator device corresponding to mark (a) in Figs. 2,3,5. (i): propagation in the direction of transmission, the mode of one outer waveguide is inserted at $z = 0$ and the power remains in the input waveguide (A to B in Fig. 1). (ii): propagation in the blocking direction, the structure is excited in $z = 1.5$ mm and the power is transferred to the opposite waveguide (transmission B to D). Parameters are as given for Fig. 2, $T = 6.261\,\mu$m, $L = 1512\,\mu$m, $\xi = \pm 0.005$. Tolerances: $\Delta T = \pm 5$ nm, $\Delta L = \pm 35\,\mu$m, $\Delta t = \pm 3$ nm, $\Delta d = \pm 16$ nm.

For comparable conventional nonreciprocal couplers ($T = 0$ in Fig. 1) the total length must be larger than 2.8 mm ($2d = 0$) or 10.5 mm ($2d = 0.8\,\mu$m), with a maximum tolerance of 0.7 μm ($2d = 0$). The gap width 0.8 μm has to be maintained with a tolerance of ± 0.4 nm.

RIB WAVEGUIDE DEVICES

In somewhat more realistic 3-D structures analogous mode patterns appear. Fig. 7 illustrates the supermodes of a rib coupler in the three mode regime, generated by means of a recently proposed semivectorial mode solver [5]. The three most relevant modes corresponding to the planar profiles in Fig. 3(a) can be clearly identified.

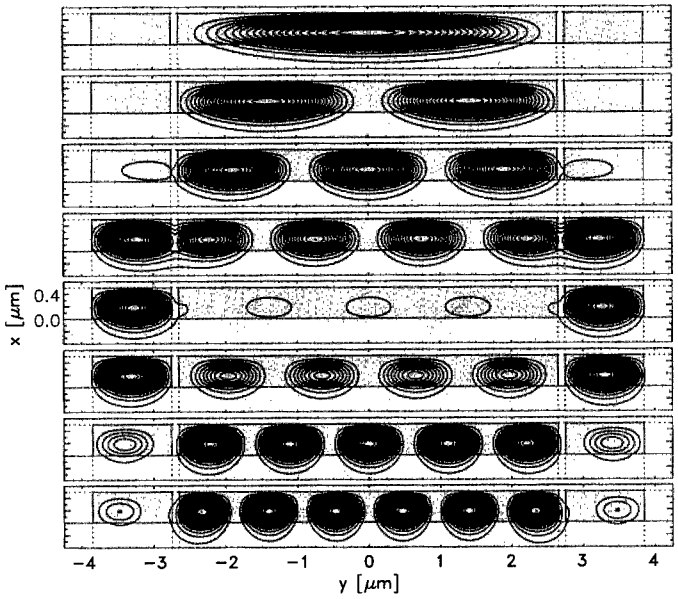

Figure 7: Mode intensity profiles for the eight TM polarized modes of a radiatively coupled waveguide structure given by the following parameters: $W = 5.3\,\mu$m, $w = 1.1\,\mu$m, $g = 0.1\,\mu$m, $h = 0.5\,\mu$m, $n_i = n_o = 2.3$, $n_s = 1.95$, $n_c = 1.0$, $\lambda = 1.3\,\mu$m (cf. Fig. 1). The contours correspond to the squared dominant magnetic field component $|H_y|^2$.

The mode shape inspires an isolator configuration as shown in Fig. 8. It does not exploit the opposite symmetry, but the strongly differing amplitudes of the relevant modes. The nonreciprocal phase shifts of the central and the surrounding mode must be as unequal as possible, therefore contrarily directed jumps in the Faraday rotation should be manufactured along the lines of the corresponding field maxima.

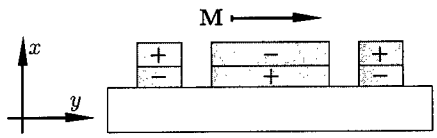

Figure 8: Concept for an TM–isolator/circulator based on radiatively coupled rib waveguides. The boundary between layers with opposite Faraday rotation (signs) should be adjusted to the maximum field amplitude.

With the central layer thickness T replaced by the width W of the central rib, the dispersion characteristic of the 3-D devices is similar to the planar case, as confirmed by Fig. 9. According to the bottom inset, evaluation of Eqs. 2,3 yields an estimate for the minimum achievable device length of 1.02 mm. This is one order of magnitude smaller than the value of 10 mm given in [2] for a conventional two-waveguide nonreciprocal coupler comprising comparable materials and geometry.

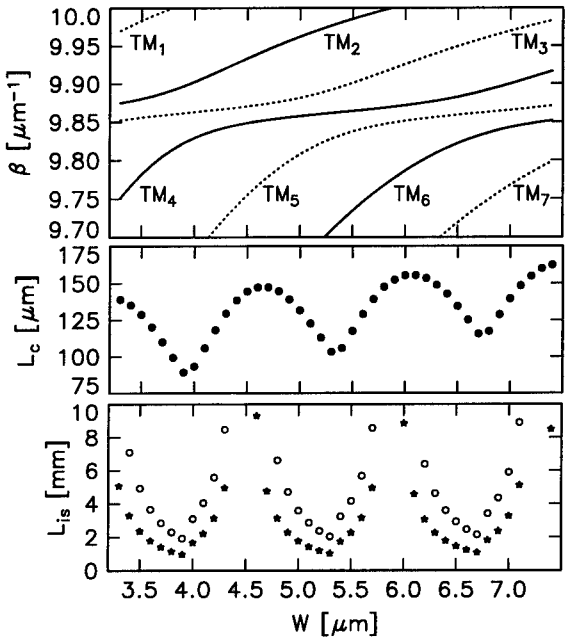

Figure 9: Propagation constants β (top), coupling length L_c (center), and the estimated isolator device length L_{is} (bottom) for TM-polarized light versus the central rib width W of the three rib waveguide coupler. Only part of the region allowed for propagation constants is displayed. Other parameters are as given for Fig. 7, with an off-diagonal permittivity element $\xi = \pm 0.005$. Circles in the bottom chart correspond to a device with isotropic outer guides but a double layer magneto-optic central waveguide, while the stars indicate the total length for a device with both central and outer waveguides made of magneto-optic material as sketched in Fig. 8, with a thickness of the bottom magneto-optic layers of 0.18 μm.

CONCLUSIONS

For a nonreciprocal three waveguide rib coupler consisting of magneto-optic garnet materials, the proposed design enables standard isolating performance with a total length of about 1 mm. This is achieved by exploiting the specific shape of the relevant mode fields. As in the planar case, strict but manageable tolerance requirements can be expected. Within the complete simulation of the 3-D devices, the numerically involving part of accurately calculating the guided supermodes is by now finished, while the implementation of the propagating mode analysis procedures for the rib waveguide structures is under way.

ACKNOWLEDGMENT

We gratefully acknowledge financial support by Deutsche Forschungsgemeinschaft, Sonderforschungsbereich 225.

REFERENCES

[1] T. Mizumoto, K. Oochi, T. Harada, and Y. Naito, *Journal of Lightwave Technology*, **4**, (3), pp. 347–352, 1986.

[2] A. Erdmann, P. Hertel, and H. Dötsch, *Optical and Quantum Electronics*, **26**, pp. 949–955, 1994.

[3] M. Lohmeyer, M. Shamonin, and P. Hertel, *Optical Engineering*, **36**, (3), pp. 889–895, 1997.

[4] S. Yamamoto and T. Makimoto, *Journal of Applied Physics*, **45**, pp. 882, 1974.

[5] M. Lohmeyer, *Optical and Quantum Electronics*, **29**, pp. 907–922, 1997.

RECENT ADVANCES IN MAGNETOSTATIC WAVES-BASED INTEGRATED MAGNETOOPTIC BRAGG CELL MODULATORS IN YIG-GGG WAVEGUIDES*†

Chen S. Tsai

Department of Electrical and Computer Engineering and Institute for Surface and Interface Sciences
University of California, Irvine, CA 92697

ABSTRACT

The most recent advances in the integration architecture and diffraction efficiency of magnetostatic wave (MSW)-based guided-wave magnetooptic (MO) Bragg cell modulators in yttrium iron garnet-gadolinium gallium garnet (YIG-GGG) waveguides are reported. A curved ion-milled hybrid waveguide lens pair has been integrated with a MO Bragg cell modulator in a taper waveguide with dimensions of 6.0x16.0mm^2 to facilitate the collimation and focusing functions. An enhancement in the Bragg diffraction efficiency by two-to six-fold has been accomplished using a non-uniform bias magnetic field. An oscillator-based MO Bragg cell modulator has also been constructed and has provided a Bragg diffraction efficiency which is higher by a factor of two to four than that of a conventional delayline-based modulator.

INTRODUCTION

Magnetooptic (MO) Bragg interactions between guided-optical waves and magnetostatic waves (MSWs) and resulting devices [1] in a suitable magnetic substrate such as the yttrium iron garnet-gadolinium gallium garnet (YIG-GGG) waveguides [2] have continued to be a subject of considerable interest. MSWs can be readily and efficiently generated by applying a microwave signal to a microstrip line transducer, deposited directly on or laid upon the YIG-GGG waveguide substrate. The carrier frequency of the MSWs can be tuned, typically from 0.5 to around 25 GHz, by simply varying an external bias magnetic field in synchronism with the carrier frequency of the microwave signal. MO Bragg diffraction results from the moving optical gratings induced by the MSW through the Faraday and Cotton-Mouton effects in a manner similar to guided-wave acoustooptic (AO) Bragg diffraction in which the surface acoustic waves (SAW) induce moving optical gratings through the photoelastic effects [3]. In analogy with the AO Bragg cell modulators, the resulting MO modulators such as the one shown in Fig. 1, which utilizes magnetostatic forward volume waves (MSFVW), are called the MO Bragg cell modulators. A guided-light beam incident upon the MSFVW at Bragg angle θ_B is diffracted at an angle of $2\theta_B$ from the undiffracted light. The relative power and scan angle of the Bragg-diffracted light are proportional to the drive power and the carrier frequency of the

* This work was supported by the ONR.

† Invited Paper

Mat. Res. Soc. Symp. Proc. Vol. 517 © 1998 Materials Research Society

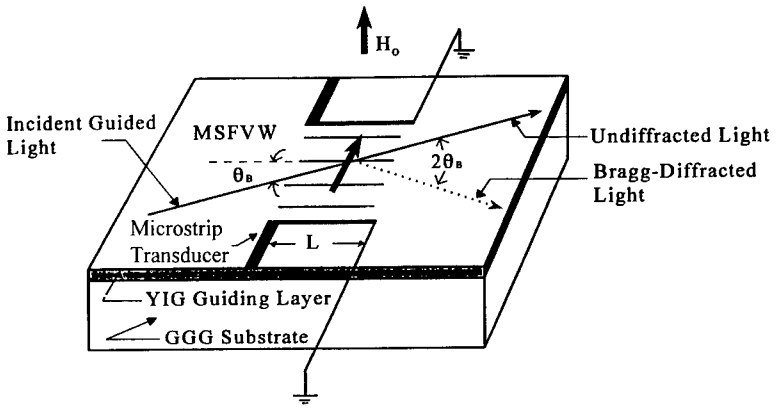

Fig. 1 Guided-Wave Magnetooptic Bragg Cell Modulator Using Magnetostatic Forward Volume Wave (MSFVW)

MSW, respectively. Such MSW-based MO Bragg cell modulators have demonstrated a number of unique advantages in comparison to their AO counterparts such as tunable and much higher carrier frequency, much faster modulation and switching speeds, and simplicity in transducer design and fabrication. Consequently, such MO Bragg cell modulators possess the potential for applications in wide-band real-time RF signal processing, high-speed multiport optical deflection/switching, and high-speed wideband optical frequency shifting, and should therefore compliment the now prevalent AO Bragg cell modulators.

In this paper, the most recent advances in terms of architectural integration and diffraction efficiency of the MO Bragg cell modulators are reported.

INTEGRATION OF MO BRAGG CELL MODULATOR WITH WAVEGUIDE LENSES

As in integrated AO Bragg cell device modules, it is essential to incorporate a collimation-focusing waveguide lens pair in a common YIG-GGG waveguide substrate to form an integrated MO Bragg cell device module. For this purpose, a curved hybrid ion-milled lens pair of parabolic contour was integrated with the MO modulator in a taper waveguide as shown in Fig. 2(a). The curved hybrid lenses have provided larger angular field of view and lower level of coma in comparison to those of straight contour. Fig. 2(b) shows the detailed architecture and dimensions of the integrated MO Bragg cell device module that has been constructed [4].

The initial layer thickness of the Bi-substituted YIG waveguide sample used, 6.0 X 16.0 mm^2 in size, was 3.25 μm. The two end regions of the taper waveguide were ion-milled down to 2.68 μm in several steps in order to produce a gradual transition, and thus ensure a high transmission for the light beam. A pair of curved hybrid lenses of 4.0 mm focal length and 0.8 mm aperture were then fabricated in the two end regions (each 5.0 mm in length) using the ion-milling technique [4]. The measured focal spot profiles obtained at 1.31 μm wavelength from the curved hybrid lenses show low level of coma with sidelobe levels lower than 12.3 dB from the main lobe for the incident angle up to ± 3.5 degrees from the lens axis.

An MO Bragg cell modulator was subsequently constructed by incorporating a microstrip line transducer in the central region of the taper waveguide. A compact magnetic circuit was used to provide the required bias magnetic field for excitation and tuning of the carrier frequency

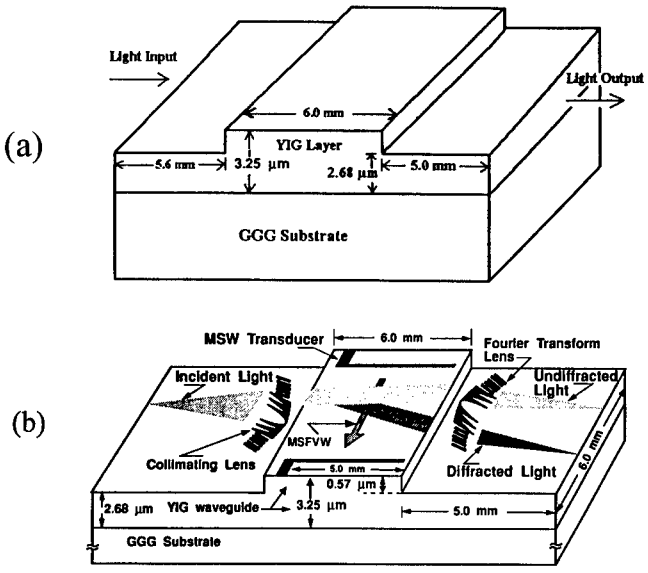

Fig. 2 (a) A YIG-GGG Taper Waveguide Structure
(b) An Integrated Magnetooptic Bragg Cell Modulator in YIG-GGG Taper Waveguide Structure

of the MSFVWs ranging from 2 to 12 GHz. Typical performance figures such as a bandwidth of 260 MHz at the center carrier frequency of 10.0 GHz, a diffraction efficiency of 2.0% at one watt RF drive power, and a dynamic range of 30dB were measured with the resulting integrated MO Bragg cell modulator module. The modulator module was used to successfully demonstrate light beam scanning and switching, and RF spectral analysis at X-band carrier frequencies [4].

BRAGG DIFFRACTION EFFICIENCY ENHANCEMENT USING NON-UNIFORM BIAS MAGNETIC FIELD

In terms of practical applications it is desirable to realize MO Bragg cell modulators that provide as high a diffraction efficiency at as low an RF drive power as possible. For this purpose a technique for significant enhancement of the diffraction efficiency using a non-uniform bias magnetic field was explored recently [5]. Specifically, a non-uniform bias magnetic field was employed to reduce the angular spreading of the magnetostatic forward volume wave (MSFVW) involved. Since for certain range of the carrier frequency the velocity of propagation of the MSFVW, V_{MSFVW}, increases with the bias magnetic field H_0, a bias magnetic field of linear distribution $H_0(x)$ across the transducer aperture such as the one shown in Fig. 3(a) will modify the wavefront of the resulting MSFVW. In other words, this specific distribution of bias

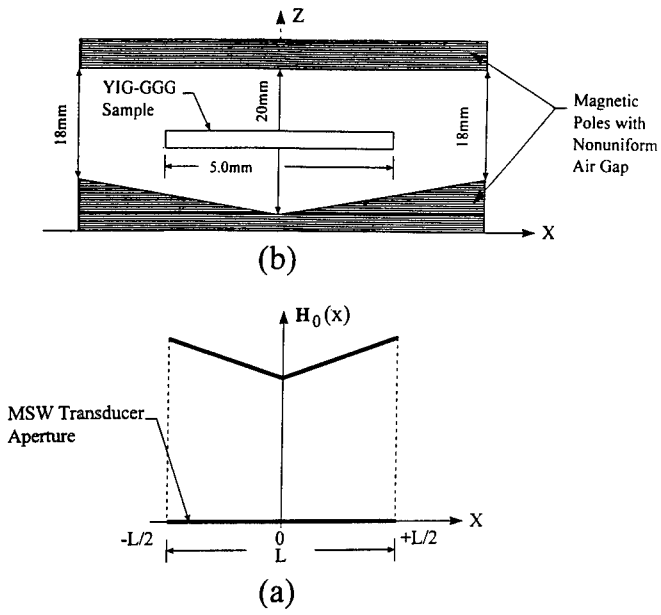

Fig. 3 Focusing of MSFVW Using a Nonuniform Bias Magnetic Field:
(a) A Bias Magnetic Field of Linear Distribution $H_0(x)$ Across the Transducer Aperture;
(b) Cross-Section View of Magnetic Pole Pieces and YIG-GGG Waveguide Sample.

magnetic field creates a focusing effect upon the MSFVW, and corresponding reduction in its angular beam spread, and thus enhances the MO Bragg diffraction efficiency.

In this work the aperture of the microstrip line transducer or the MO interaction length involved was 5.0mm and the non-uniform bias magnetic field was facilitated by using an air gap of linear variation as depicted in Fig. 3(b) in a compact Sm-Co magnetic circuit [6]. Note that this particular air gap distribution between the two pole pieces in the magnetic circuit was used to create a bias magnetic field distribution similar to Fig. 3(a), namely, increasing linearly from the center of the air gap to the two edges. Measurement of the resulting bias magnetic field for an air gap setting of 21 mm at the center and 18 mm at the two edges has shown that such magnetic field distribution can be readily facilitated. The bismuth-substituted YIG-GGG sample used has a 6 μm YIG guiding layer and the dimensions of 7.0x8.0 mm^2. The corresponding velocity profile of the MSFVW at the carrier frequency of 3.17GHz, deduced using the experimental data, suggests focusing of the resulting MSFVW. Note that for establishment of a uniform bias magnetic field, flat surfaces were used for the two pole pieces, so that there was no spatial variation in the air gap.

Measurement of the Bragg diffraction efficiency and the bandwidth of the resulting MO Bragg cell modulator was carried out at the carrier frequency range of 2.0 to 3.5GHz and the

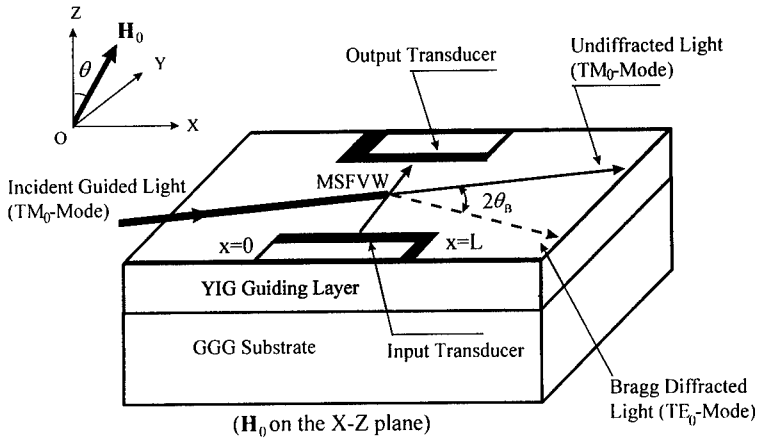

Fig.4 Guided-Wave Magnetooptic Bragg Diffraction Under Tilted Bias Magnetic Field

optical wavelength of 1.31μm in free-space using the established technique [1]. The carrier center frequency was readily tuned by changing the bias magnetic field which was in turn tuned by changing the air gap through a micrometer. The measured Bragg diffraction efficiencies for the cases with uniform and non-uniform bias magnetic fields has demonstrated a diffraction efficiency enhancement by a factor of two to six. At a carrier frequency of 3.17GHz, a diffraction efficiency as high as 70% has been measured at an RF drive power of 2.7watts. Thus, when compared to the earlier performance figure of 12% at 2.0 watt RF drive power and 5.0mm interaction length obtained using a uniform bias magnetic field [1], an increase in the figure of merit in terms of diffraction efficiency per RF drive power by a factor of four has been accomplished.

MO BRAGG DIFFRACTION UNDER A TILTED BIAS MAGNETIC FIELD

As another attempt for enhancement of MO Bragg diffraction efficiency a theoretical treatment on the propagation characteristics of MSWs and related guided-wave MO Bragg diffraction in a YIG-GGG waveguide under a tilted bias magnetic field is being carried out [7,8]. Fig. 4 shows the interaction geometry involved. Note that the bias magnetic field is in the *X-Z* plane. The *Z*-component of the bias magnetic field will facilitate excitation and propagation of the MSFVW, while the *X*-component will do the same for magnetostatic surface wave (MSSW). Hence, the interactions between the guided-light wave and the magnetostatic waves (MSWs) becomes much more complicated.

Employing the coupled-mode method [1] the MO Bragg diffraction efficiency η involving the $TM_0 \rightarrow TE_0$ mode conversion is determined as follows:

$$\eta^{\pm} = \frac{(\kappa_1 \mp \kappa_2)^2}{\left(\frac{\Delta}{2}\right)^2 + (\kappa_1 \mp \kappa_2)^2} \sin^2\left\{\sqrt{\left(\frac{\Delta}{2}\right)^2 + (\kappa_1 + \kappa_2)^2}\, L\right\}$$

where

L = interaction length

$$\kappa_1 = \frac{k_0}{4\sqrt{\varepsilon_r}} f_1 \, | \, m_x^{(0)} \, |$$

$$\kappa_2 = \frac{k_0 M_0}{4\sqrt{\varepsilon_r}} \left[2 f_{44} \cos\theta + \frac{1}{3} \Delta f \, (2\cos\theta + \sqrt{2}\sin\theta) \right] | \, m_y^{(0)} \, |$$

$$\vec{\Delta} = \vec{\beta}_{TE_0} - \vec{\beta}_{TM_0} \mp \vec{K} \, .$$

in which M_0 is the magnitude of saturation magnetization in YIG film; $m_x^{(0)}$, $m_y^{(0)}$ are the components of RF magnetization; $\vec{\beta}_{TE_0}, \vec{\beta}_{TM_0}, \vec{K}$ are, respectively, wave vectors of the guided optical modes and the MSW. Also, f_1 is the circular or first-order magnetic birefringence (Faraday effect), and is approximately equal to $2\sqrt{\varepsilon_r}\phi_r / (k_0 M_0)$ in which ε_r and ϕ_r are, respectively, the relative permittivity and the Faraday rotation of the YIG film, and $k_0 = 2\pi / \lambda_0$ is the wavenumber of the light beam with free-space wavelength λ_0; $\Delta f \equiv f_{11} - f_{12} - 2 f_{44}$ where f_{11} , f_{12} , and f_{44} are the three independent components of the linear or second-order magnetic birefringence(Cotton-Mouton effect). Finally, "+" and "–" designate the situations for anti-Stokes (with frequency upshifted diffracted light) and Stokes (with frequency downshifted diffracted light) interaction, respectively. Since the quantities $m_x^{(0)}$, $m_y^{(0)}$ are functions of the tilt angle θ, the MO Bragg diffraction efficiency is a complicated function of θ.

The analytical results obtained shows that the resulting MO Bragg diffraction is a complicated function of the tilt angle of the magnetic field θ and many other physical parameters. Further theoretical analysis and experimental studies are in progress.

MSW OSCILLATOR-BASED INTEGRATED MO BRAGG CELL MODULATOR

As further effort toward ultimate integration of the modulator and enhancement of Bragg diffraction efficiency, a feedback loop was most recently incorporated in the conventional MO Bragg cell modulator which simply utilizes the MSW as a delayline [9]. Specifically a feedback loop having proper loop gain and phases was incorporated in a MSFVW delayline to facilitate oscillations. The frequency of oscillation was readily tuned by varying the bias magnetic field. The resulting MSW oscillator-based MO Bragg cell modulator has provided a significantly higher diffraction efficiency per RF drive power than the MSW delayline-based counterpart.

Fig. 5 shows such oscillator-based MO Bragg cell modulator. The MSFVW oscillator consists of a 9.0 μm-thick and 6.0 mm-wide Bi:YIG film and a pair of identical microstrip line

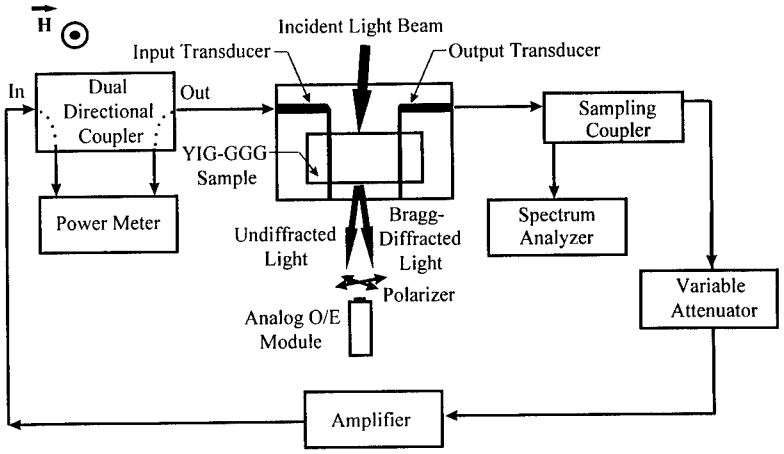

Fig. 5 MSFVW Oscillator-Based Magnetooptic Bragg Cell Modulator

transducers at a separation of 5.0 mm. In the feedback loop, a microwave solid state amplifier is connected to the input transducer via a dual directional coupler. The output transducer of the delay line is fed into the amplifier through a sampling coupler. The fed power is in turn controlled using a variable attenuator. The transmission and reflection characteristics of the delay line as well as the oscillating frequencies are measured at the output ports of the sampling coupler. A compact magnetic circuit provides an adjustable magnetic field to the oscillator to create necessary values of phases required for oscillation. Accordingly, the carrier frequency of the RF signals for MO Bragg interaction is readily tuned. A linear dependence of the oscillating frequency from 2.112 to 3.274 GHz has been measured as the external magnetic field increases from 2350 to 2900 Oe.

Measurements of the Bragg diffraction efficiency for both oscillator-and delayline-based MO Bragg cell modulators were again carried out at the optical wavelengths of 1.31 μm. The measurement for the latter was done by connecting the input of the amplifier directly to a sweep generator which supplies the drive signals in the same frequencies as the measured oscillating frequencies under the corresponding bias magnetic fields. An enhancement in Bragg diffraction efficiency by two-to four-fold has been measured with the oscillator-based MO modulator. This enhancement of diffraction efficiency in the oscillator-based modulator can be attributed to the drastic reduction in the insertion losses of the MSFVW oscillator. We have found that the insertion losses versus the carrier frequency for the delay line depend strongly on the bias magnetic field. However, for the oscillator, the insertion losses incur only minor changes even though the oscillation frequency varies linearly with the bias magnetic field. Specifically, the measured insertion loss of the MSFVW oscillator ranges from -14 to -11dB.

CONCLUSIONS

A new class of optical devices called MO Bragg cell modulators which are capable of providing desirable features similar to that of the now prevalent AO Bragg cell modulators, but

with superior performance characteristics in terms of much higher carrier frequency and its electronic tunability, have been devised. This MO modulator has paved the way for realization of a variety of MSW-based hybrid integrated MO device modules, such as high-speed optical scanners, optical space switches, tunable carrier frequency band RF spectrum analyzers and correlators, and tunable wideband optical frequency shifters and modulators [4,10].

It is well recognized that the SAW-based devices in the VHF to UHF region (100 to 2000MHz) have little competition as broadband RF signal processors. Meanwhile, the MSW-based devices, when fully developed, will have no competition in the frequency region higher than 2000 MHz. Thus, the integrated MO device modules should compliment the AO counterparts in the field of real time wideband RF signal processing at carrier frequencies far beyond 2000 MHz.

In order to expedite realization of the aforementioned hybrid integrated MO device modules and their various applications, further advances such as development of robust coupling techniques between the YIG-GGG waveguide and the laser and/or the photodetector, and development of packaging technology for the integrated MO device modules are needed. As to further enhancement of the Bragg diffraction efficiency and the device optical throughput preparation and characterization of YIG-GGG waveguides with substitution of other elements and their combinations will be of great interest. Finally, R and D efforts aimed at realization of laser sources in Er-doped YIG-GGG substrates are essential toward ultimate realization of monolithic MO device modules.

REFERENCES

[1] See, for example, the many references cited in C. S. Tsai and D. Young, "Magnetostatic Forward Volume Wave-Based Guided-Wave Magnetooptic Bragg Cells and Applications to Communication and Signal Processing," IEEE Trans. on MTT, **38**, 560-70 (1990)

[2] P. K. Tien, R. J. Martin, R. Wolfe, R. C. LeCraw, and S. L. Bank, "Optical Waveguides of Crystal Garnet Films," Appl. Phys. Lett., **21**, 207-209 (1972)

[3] See, for example, the many references cited in C. S. Tsai, "Integrated Acoustooptic Circuits and Applications," IEEE Trans. on UFFC, **39**, 529-553 (1992)

[4] C. L. Wang and C. S. Tsai, "Integrated Magnetooptic Bragg Cell Modulator in YIG-GGG Taper Waveguide and Applications," IEEE J. Lightwave Tech., **15**, 1708-1715 (1997)

[5] C. S. Tsai, Y. S. Lin, J. Su, and S. R. Calciu, "High Efficiency Guided-Wave Magnetooptic Bragg Cell Modulator using Non-uniform Bias Magnetic Field," Appl. Phys. Lett., **71**, 3715-3717 (1997).

[6] C. L. Wang, Y. Pu, and C. S. Tsai, "Permanent Magnet-Based Guided-Wave Magnetooptic Bragg Cell Modules," IEEE J. Lightwave Tech., **10**, 644-648 (1992)

[7] O. V. Kolokoltsev, Y. A. Gaidai, and V. I. Zaets, "Diffraction of Optical Guided Waves by Magnetostatic Waves in Inclined Magnetic Field", Proc. of 1995 European Integrated Optics Conference pp. 221-223, Delft, Netherlands, April 3-6.

[8] W. Zuo, J. Su, G. Q. Liu and C. S. Tsai, "Guided-Wave Magnetooptic Bragg Diffraction in YIG-GGG Waveguide under tilted and Non-uniform Bias Magnetic Field," Proc. of 1997 IEEE Ultrasonics Symp., 757-760, IEEE Cat # 97CH36118.

[9] J. Su and C. S. Tsai, "Magnetostatic Wave Oscillator-Based Integrated Magnetooptic Bragg Cell Modulator," (To be presented at 1998 MRS Spring Meeting, April 13-17, San Francisco, CA).

[10] Y. Pu and C. S. Tsai, "Wideband Electronically Tunable Integrated Magneto-Optic Frequency Shifter at X-Band," Appl. Phys. Lett., **62**, 3420-3422 (1993)

MAGNETO-STATIC WAVE OSCILLATOR-BASED INTEGRATED MAGNETO-OPTIC BRAGG CELL MODULATOR*

Jun Su and Chen S. Tsai
Department of Electrical and Computer Engineering and Institute for Surface and Interface Sciences, University of California, Irvine, CA 92697

ABSTRACT

A novel magnetooptic (MO) Bragg cell modulator that utilizes a magnetostatic forward volume wave (MSFVW) oscillator is presented. The carrier frequency of the MSFVW signals involved in the MO interaction is tuned linearly from 2.112 to 3.274 GHz by increasing an external bias magnetic field from 2350 to 2900 Oe. Compared with a conventional magnetostatic wave (MSW) delay line-based MO Bragg cell modulator, the proposed modulator can provide significantly higher diffraction efficiency owing to reduction of insertion losses in the MSFVW oscillator. Furthermore, the oscillator-type MO modulator can be more easily integrated with other MMIC devices.

INTRODUCTION

Magnetooptic (MO) Bragg interactions between guided optical waves and magnetostatic waves (MSW) in yttrium iron garnet (YIG)-gadolinium gallium garnet (GGG) waveguides have demonstrated considerable potential toward realization of integrated MO devices for wideband real-time RF signal processing and optical communications[1]. MO Bragg diffraction possesses characteristics similar to guided-wave acoustooptic (AO) Bragg diffraction[2]. However, the advantages of the resulting MO Bragg devices over their AO counterparts are distinct. Firstly, the MO Bragg devices can perform signal processing directly at microwave frequencies, a frequency range where surface acoustic wave (SAW) devices do not operate; secondly, the modulation/switching speeds of the MO Bragg devices are much higher; and finally, the microstrip technique for MSW excitation in the MO Bragg devices is much simpler. Until now, various MO devices based on the Bragg interactions such as modulators, scanner, frequency shifters, spectrum analyzers, etc., have been proposed and demonstrated[3-6].

A typical MO Bragg cell modulator consists of a magnetic garnet film waveguide of good magnetic and optical characteristics and an MSW delay line that is fabricated upon the waveguide. When an RF signal is fed into the delay line through a microstrip transducer, the MSW excited will perturb the optical waveguide to form the moving optical gratings through the Faraday and Cotton-Mouton effects[1, 3]. Thus, guided-wave MO Bragg diffraction can be facilitated. Obviously, the transduction efficiency of MSW excitation in an MO waveguide is of crucial importance in MO Bragg diffraction. As is well known, the MSW power required for the MSW propagation in a magnetic film can be supplied either by an external RF signal generator or by a well-designed oscillation loop. Both device architectures have applications in microwave signal processing. Furthermore, it is envisioned that the size of a planar MO Bragg cell modulator can be greatly reduced by employing an MSW oscillator because the oscillator is apt to be embedded into an MMIC chip[7-9].

* This work was supported by the ONR

Mat. Res. Soc. Symp. Proc. Vol. 517 © 1998 Materials Research Society

In this paper we present, for the first time, an MO Bragg cell modulator that incorporates an MSFVW oscillator through a feedback loop. In the oscillator the oscillations occur at frequencies where the gain of the loop consisting of the MSFVW delay line, a solid-state amplifier and a directional coupler exceeds unity, and the phase shifts around the loop satisfy the following condition[10]

$$\phi_{MSFVW}+\phi_A+\phi_C=2n\pi \tag{1}$$

where ϕ_{MSFVW}, ϕ_A, and ϕ_C are the phase shifts corresponding to the MSFVW delay line, the amplifier, and the other external components, respectively, and n is an integer. The microwave frequency involved in the MO interaction can be selected by magnetically tuning the oscillations in the loop.

MSFVW OSCILLATOR-BASED MO BRAGG CELL MODULATOR

MSFVW Oscillator

Fig. 1 shows an MO Bragg cell modulator that utilizes an MSFVW delay line to realize an oscillator via a feedback loop. The MSFVW oscillator consists of a 6.0 μm-thick and 7.0 mm-wide Bismuth-substituted yttrium iron garnet (Bi:YIG) film and a pair of identical microstrip line transducers at a separation of 5.0 mm. In the feedback loop, a microwave solid state amplifier is connected to the input transducer via a dual directional coupler. The output transducer of the delay line is fed into the amplifier through a sampling coupler. The fed power is in turn controlled using a variable attenuator. The transmission and reflection characteristics of the delay line as well as the oscillating frequencies are measured at the output ports of the directional coupler.

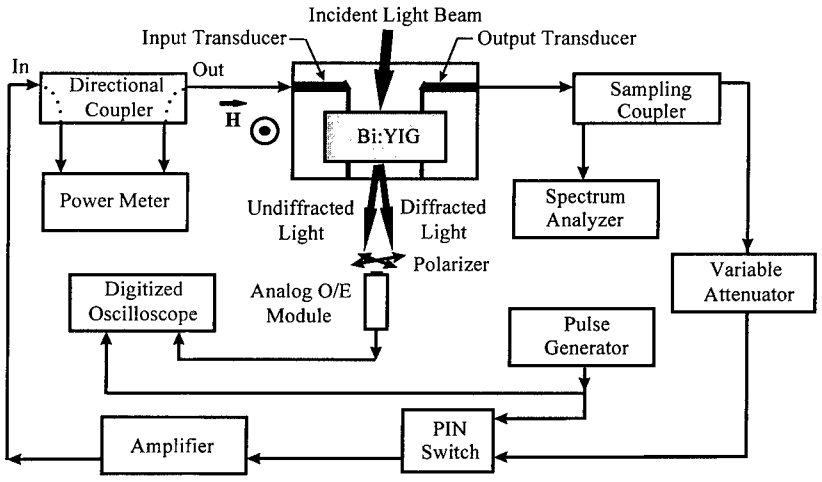

Fig. 1 MSFVW Oscillator-Based Magnetooptic Bragg Cell Modulator

Oscillator-Based MO Bragg Cell Modulator

As shown in Fig. 1, an optical beam of 1.313 μm in wavelength is edge-coupled into the YIG waveguide in a direction nearly perpendicular to that of the MSFVW propagation. The intensities of the Bragg-diffracted and undiffracted lights are measured by means of an analog optoelectronic module. A compact magnetic circuit provides an adjustable magnetic field to the oscillator to create necessary values of ϕ_{MSFVW} required by Eq. (1). Therefore, the carrier frequency of the RF signals for MO Bragg interaction can be readily tuned.

Results and Discussions

As discussed above, tuning the bias magnetic field can control the carrier frequency of the MSFVW that is involved in the MO interaction in the proposed modulator. Fig.2 shows a linear dependence of the oscillating frequency (from 2.112 to 3.274 GHz) as the external magnetic field increases (from 2350 to 2900 Oe).

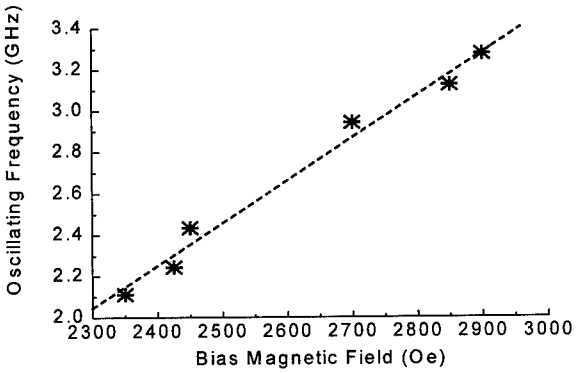

Fig. 2 Oscillating Frequency as a Function of External Bias Magnetic Field. The Stars are the Experimental Data.

In order to compare such oscillator-based MO Bragg cell modulator with the conventional MO Bragg cell modulator, namely, the one just involving an MSFVW delay line, we have also measured the MO Bragg diffraction efficiencies by disconnecting the feedback loop and connecting the input of the amplifier directly to a sweep generator which supplies the signals in the same frequencies as the measured oscillating frequencies under the corresponding bias magnetic fields.

We see from Table 1 that the oscillator-based MO modulator is considerably more efficient than the one based on the delay line. We have found experimentally that the efficiency enhancement of MO Bragg diffraction in the oscillator-based modulator can be attributed to the drastic reduction in the insertion losses of the oscillator. Figs. 3(a) to 3(c) show the measured insertion losses of the oscillator at the frequencies listed in Table 1 and of the delay line at the identical frequencies at the bias magnetic field of 2425, 2450 and 2850 Oe, respectively.

As shown in Fig. 3, the insertion loss versus the carrier frequency for the delay line strongly depends on the bias magnetic field. However, for the oscillator, the insertion loss incurs only

minor changes even though the oscillation frequency varies linearly with the bias magnetic field. In our experiments, the measured insertion loss of the oscillator ranges from -14 to -11 dB.

Table 1 Comparison of Measured MO Bragg Diffraction Efficiencies Using MSFVW Delay Line and Oscillator

f(GHz)	H (Oe)	$\eta_{\text{delay line}}$ (%)	$\eta_{\text{oscillator}}$ (%)
2.112	2350	9.4	17.8
2.244	2425	2.0	8.3
2.435	2450	17.4	33.3
2.941	2700	9.6	27.6
3.124	2850	7.0	12.3
3.274	2900	2.8	9.1

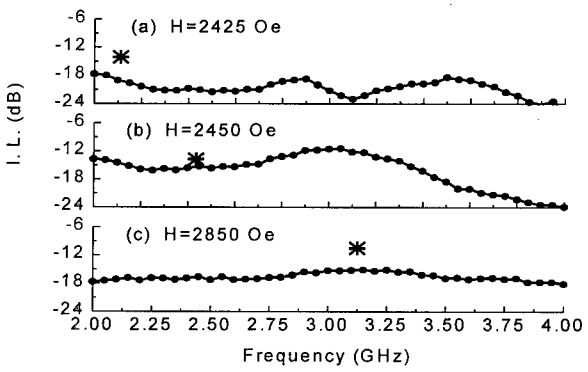

Fig. 3 Insertion Loss of MSFVW Delay Line versus the Carrier Frequency under Different Magnetic Biasing Conditions: (a) H=2425 Oe; (b) H=2450 Oe; (c) H=2850 Oe. The Stars Correspond to the Insertion Losses of the Oscillator.

According to the MSW theory[11, 12], for a given MSW operation frequency, the propagation loss can be modeled by setting the wave number K as a complex number. Thus, if the MSFVW propagation is characterized by exp(iKy) where y-axis is the propagation direction, the wave amplitude will decay in the factor of $exp[Im(\mathrm{K})y]$. $Im(\mathrm{K})$ is associated with the full ferromagnetic resonance linewidth, ΔH, and the MSFVW group velocity, v_g. Since ΔH and v_g as well as the first-order magnetic birefringence (Faraday effect) and the second-order magnetic birefringence are identical under a specific frequency for MO Bragg diffraction in an MSFVW delay line and the oscillator constructed by the very same delay line, the difference in diffraction efficiency between the MO Bragg cell modulators using an MSFVW delay line and the MSFVW delay line-based oscillator can only be attributed to the energy conversion mechanisms for the delay line and the oscillator. Now, of particular interest to us is how the conversion between the RF drive power and the MSFVW power inside an MO film waveguide affects the MO Bragg diffraction. Based on the MSW-optical interaction theory[13] and our previous analysis, we

simplify the diffraction efficiency η as a function of the insertion loss of a delay line, IL, and the RF drive power, P_0, e. g.,

$$\eta = \sin^2[C\exp(0.115\,\mathrm{IL})\sqrt{P_0}] \tag{2}$$

where C is a constant that is associated with the magnetic and MO parameters.

With P_0 as a parameter, Fig. 4 shows the relationship between η and IL. As shown, once the insertion loss of an MSFVW delay line is reduced to, say, less than -15dB, the MO Bragg diffraction efficiency can be improved dramatically. Meanwhile, it is obvious that a higher input RF power can result in a higher diffraction efficiency. In our measurements, it is also found that the return loss of the MSFVW delay line is higher than that of the oscillator. Therefore, the input RF power to the proposed MO modulator is enhanced. Fig. 3 and the data listed in Tab. 1 indicate that as the oscillator has much lower insertion losses compared with the delay line, the oscillator-based MO Bragg cell modulator functions much more efficiently.

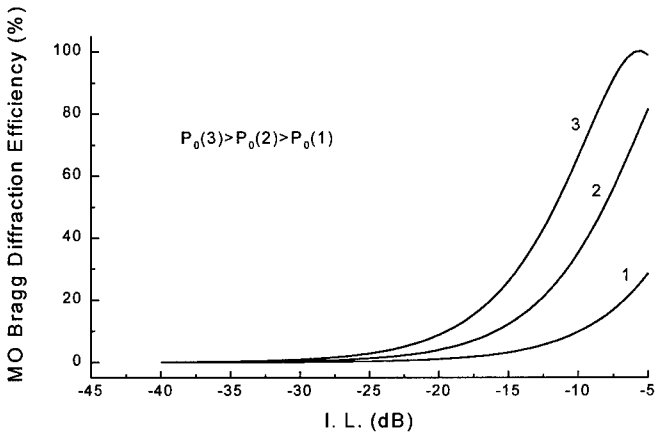

Fig. 4 MO Diffraction Efficiency versus the Insertion Loss of an MSFVW Delay Line.

CONCLUSIONS

MSFVW oscillator-based guided wave MO Bragg diffraction in YIG-GGG has been realized. The MSFVW signal involved in the MO interaction is generated when the oscillation condition in the feedback loop is satisfied. The RF carrier frequency involved is tuned simply by an external bias magnetic field. Since the insertion loss of the MSFVW delay line in the oscillator architecture is greatly reduced, the resulting MO Bragg diffraction efficiency is significantly enhanced.

ACKNOWLEDGEMENTS

The authors gratefully acknowledge the support by the ONR.

REFERENCES

1. C. S. Tsai, Magnetostatic Waves-Based Integrated Magnetooptic Bragg Cell Devices and Applications, IEEE Transactions on Magnetics, 32, 4118(1996)
2. C. S. Tsai (Ed.), Guided-Wave Acousto-optics, *Interaction, Devices and Applications*, Springer-Verlag Berlin Heidelberg, 1990
3. C. S. Tsai and D. Young, Magnetostatic Forward Volume Wave-Based Guided-Wave Magnetooptic Brag Cells and Applications to Communication and Signal Processing, IEEE Trans. on Microwave Theory and Techniques, 38, 560(1990)
4. Y. Pu and C. S. Tsai, Wideband Electronically Tunable Integrated Magnetooptic Frequency Shifter at X-Band, Appl. Phys. Lett., 62, 3420(1993)
5. C. S. Tsai, Integrated Acoustooptic and Magnetooptic Devices for Optical Information Processing, Proceedings of the IEEE, 84, 853(1996)
6. C. S.Tsai, Y. S. Lin, J. Su; S. R. Calciu, High Efficiency Guided-Wave Magnetooptic Bragg Cell Modulator Using Nonuniform Bias Magnetic Field, Appl. Phys. Lett., 71, 3715(1997)
7. Kinoshita, A. Nakagoshi, S. Takeda, and S. Kubota, Magnetostatic Wave Chip Resonator and Tunable Integrated Oscillator, IEEE 1987 Ultrasonics Symposium Proceedings, 1, 213(1987)
8. C. L. Chen, A. Chu, L. J. Mahoney, W. E. Courtney, R. A. Murphy, and J. C. Sethares, Oscillators Using Magnetostatic-Wave Active Tapped Delay Lines, IEEE Trans. on Microwave Theory and Techniques, 37, 239(1989)
9. C. L. Chen, L. J. Mahoney, Tunable Magnetostatic-Wave Oscillator Employing a Single GaAs MMIC Chip, Electronics Letters, 25, 196(1989)
10. W. S. Ishak, Magnetostatic Wave Technology: A Review, Proceedings of the IEEE, 76, 171(1988)
11. C. Vittoria and N. D. Wilsey, Magnetostatic Wave Propagation Losses in an Anisotropic Isolator, J. Appl. Phys., 45, 414(1974)
12. D. D. Stancil, Theory of Magnetostatic Waves, New York, Springer-Verlag, 1993
13. Y. Pu and C. S. Tsai, RF Magnetization of Magnetostatic Forward Volume Wave in a YIG-GGG Layered Structure with Application to Design of High-Performance Guided-Wave Magnetooptic Bragg Cells, Intern'l J. High Speed Electronics, **2**, 185(1991)

FARADAY EFFECT DEVICES, OPTICAL ISOLATORS

Author: Donald K. Wilson, President
OFR, Inc.
Box 82
Caldwell, NJ 07006

973-228-4480
FAX -0915

dwilson@ofr.com

ABSTRACT

Although discovered over 150 years ago, it was not until the 1970's that materials were developed that enabled magneto-optic (Faraday) effect devices of practical sizes. These developments are: magneto-optic materials with high Verdet constants, and the rare-earth magnet materials, capable of extremely high magnetic fields.

The magneto-optic effect has enabled development of equipment used in diverse laser applications, from industrial use to fiber-optic telecommunications.

The principle of operation of optical isolators and circulators is described herein, as well as descriptions of critical components in such equipment, such as the polarizers and the magnets.

BACKGROUND

In 1845, Michael Faraday discovered that the plane of polarized light rotates while passing through glass that is contained in a magnetic field. The amount of rotation is dependent upon the component of the magnetic field parallel to the direction of light propagation, the path length in the optical material, and the ability of the magneto-optic material to rotate the polarization plane as expressed by the Verdet constant.

Since Faraday's time, many materials having magneto-optic rotation have been discovered, including some whose Verdet constants are exceedingly high. These materials make possible a device of practical dimensions for the control of one of the most important problems in laser applications: optical feedback, or reflections of the laser's own energy back into itself.

The effects of feedback are well known: amplitude fluctuations, frequency shifts, limitation of modulation bandwidth, noise, and even damage. Feedback may, indeed, be the ultimately limiting factor in the performance of all lasers. An important application of Faraday rotation is its use in a device called the optical isolator. The device avoids the deleterious effects of optical feedback by limiting light propagation to one direction only.

THE MAGNETO-OPTIC EFFECT

When a magnetic field is introduced into an atomic system, a split occurs in the quantum energy levels describing that system. Macroscopically, this splitting causes circular magnetic birefringence, or unequal indices of refraction of right-handed and left-handed circularly polarized light. The result is rotation of polarization.

The sign of the birefringence is independent of the direction of light propagation; this is what makes the Faraday effect unique and the optical isolator possible.

An optical isolator in its simplest form consists of a rod of Faraday rotator material with its end polished flat and parallel. The rod is contained in a magnet configured so that the lines of flux are along the axis of the rod and, thus, parallel to the direction of the light. Plane-polarized light

Mat. Res. Soc. Symp. Proc. Vol. 517 © 1998 Materials Research Society

enters the rod and, by virtue of the Faraday effect, the plane of polarization rotates as the light propagates.

Assuming no deteriorating effects are present, the light emerges from the opposite end of the rod with its plane of polarization rotated by an amount

$$\theta = VHL$$

where θ is the amount of rotation in minutes, V is the Verdet constant in minutes/Gauss-centimeter, H is the magnetic field strength in Gauss, and L is the length of the rod in centimeters.

It is important to emphasize the nonreciprocal nature of the Faraday effect. The direction of rotation is dependent only upon the direction of the magnetic field and the sign of the Verdet constant, not on the direction of light propagation. This is exactly opposite to the case of rotation in optically active materials such as crystalline quartz or sugar solutions in which the rotation depends upon the direction of light propagation.

FARADAY ROTATING MATERIALS

Rotating materials generally fall into three categories: the paramagnetics, the diamagnetics, and the ferromagnetics. Paramagnetics have a negative Verdet constant that varies inversely as the absolute temperature, and varies approximately as the inverse square of the wavelength.

Diamagnetics have a positive Verdet constant that is essentially unaffected by temperature and, like paramagnetics, varies approximately as the inverse square of the wavelength.

Ferromagnetics have a positive Verdet constant that is affected by temperature according to the specific material. As with paramagnetics and diamagnetics, it varies approximately as the inverse square of the wavelength. It is important to note that extreme deviations from these simple relationships are possible.

THE PARAMAGNETICS

Among the most commonly available paramagnetic materials is terbium-doped borosilicate glass. Although the base glass is diamagnetic, it is the paramagnetic ion of terbium that causes the Verdet constant to be much higher than in any of the high-index glasses (such as the heavy flints).

However, because the Verdet constant of the paramagnetics is inversely proportional to the absolute temperature, relatively low rotations at room or elevated equipment temperatures can be a determining factor in the choice of this material. This, along with thermally induced strain birefringence caused by a high-power laser, can degrade polarization purity, thus reducing isolation. Additionally, the terbium absorption band at 470-490 nm renders this glass useless at the blue line of the argon-ion laser (488 nm), though not at 500 nm and longer wavelengths.

Another significant paramagnetic material is terbium-gallium-garnet (TGG). Its Verdet constant is 50% to 80% greater than the terbium glass described above. The very low absorption of this water-clear crystal makes it an excellent candidate for isolation of wavelengths in the visible and near-IR regions. TGG is one of the most commonly used materials in optical isolators. It is capable of withstanding very high laser power, and is used with high power YAG lasers.

THE DIAMAGNETICS

Many glasses fall into this category, and all have a comparatively weak Verdet constant. However, unlike the Faraday rotation of paramagnetics, the rotation of diamagnetic materials is not specifically affected by specific temperature change. In some applications this may be of overriding importance.

Some common diamagnetics are the chalcogenide materials (those containing II-VI elements such as sulphur, selenium and tellurium). One such Faraday rotating material is zinc selenide,

which has a Verdet constant 30% higher than terbium-doped glass. However, the method of growing this crystal (chemical vapor deposition) produces grain boundaries that contribute to a scattering loss at visible and near-IR wavelengths.

THE FERROMAGNETICS

Among the ferromagnetic materials are certain rare-earth garnets possessing a high degree of magneto-optic rotation. They are primarily limited to the 1100 to 5000 nm spectrum. A characteristic of the ferromagnetics is that their Faraday rotation saturates at a specific magnetic field strength. This implies that rotation in an aperture can be constant, provided that the entire aperture is contained in this minimum field.

Thus, one would expect full-aperture isolation to be superior using a ferromagnetic rotator because variations in the magnetic field will not cause variations in rotation, as is the case with both paramagnetics and diamagnetics.

A newly available ferromagnetic crystal, epitaxially grown bismuth substituted garnet, has an extremely high Faraday rotation, and magnetic saturation occurs in a small field. These materials have made possible very small isolators.

THE OPTICAL ISOLATOR

An optical isolator permits the forward transmission of light while simultaneously preventing reverse transmission with a high degree of extinction. It consists of a Faraday rotator, two polarizers, and a body to house the parts.

The Faraday rotator consists of a magnet in which is contained the magneto-optically active optical material.

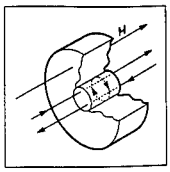

FIGURE 1. In a Faraday rotator, plane-polarized light passes through a rod of magneto-optical material contained in a magnet, with lines of flux parallel to the direction of light propagation.

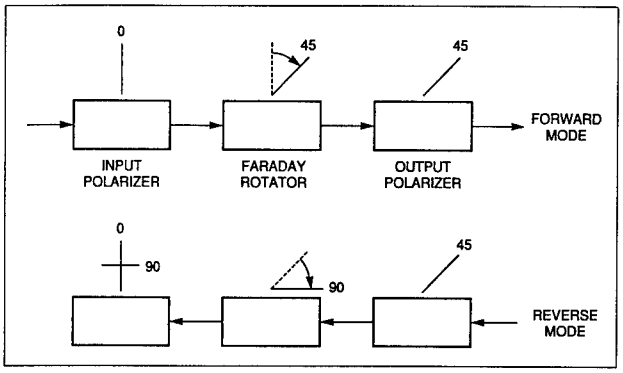

FIGURE 2. Principle of Operation of an Optical Isolator

In the forward mode (top), light entering the Input polarizer, becomes linearly polarized in the vertical plane at 0°. This vertically polarized light then enters the Faraday rotator, which rotates the plane of polarization clockwise by 45°. The light polarized at 45° then passes through the output polarizer whose transmission axis is also at 45°, thus permitting the light to exit with no diminution.

The light then goes farther into the system or experiment where reflections occur; any of this reflected light that now travels back into the laser constitutes optical feedback.

In reverse mode (bottom), the retropropagating light becomes polarized at 45° upon passing backward through the output polarizer. The light then passes through the Faraday rotator, which produces another 45° of rotation, still in a clockwise direction.

The light is now polarized at 90°, or horizontally, and will be extinguished by the Input polarizer, still at 0°. The reflected light cannot get back into the laser.

We can classify optical isolators into two groups: those larger models utilizing relatively long rotator rods with weak Verdet constants, requiring large and often complex magnets, and the smaller units that use short rotators with very strong Verdet constants and a small magnet. The wavelength of operation is the usual determinant.

THE MAGNETS become monumentally important in an isolator using a rotator with a weak Verdet constant. The development of magnets of 8,000 Gauss and above can be challenging. However, development of rare-earth magnets continues. Samarium cobalt is a commonly used high strength material. Another is neodymium-iron-boron, and we achieve more than 10,000 Gauss in magnets now in production.

Magnetic field variations are both longitudinal and radial within the cylindrical volume in which the rotator is positioned. Radial variations can limit isolation. Affected are the paramagnetic and diamagnetic rotators, but not the saturating ferromagnetics.

THE POLARIZERS

In general, the final isolation of the optical isolator seems to be equally dependent upon the Faraday rotator and the polarizers; high extinction depends upon both. Polarizers in calcite crystal, either the classical Glan air-spaced type or variations thereof, are routinely capable of 100,000: 1 (50 dB) extinction and beyond, which is absolutely necessary for reverse isolations of 30 dB and more. Whereas classical calcite polarizers are quite lossy because of internal reflections, it is possible to make these so that transmittance reaches 99%. Thus, with carefully selected materials and antireflection coatings, complete isolators with total insertion loss of 5% are easily achievable.

Other polarizers, such as dielectric Brewster's angle plates, are now available with performance equaling that of the calcite crystal types, although optical bandwidths are much less.

A class of dichroic polarizers is uniquely manufactured by Corning. These are the Polarcor polarizers. Thin glass plates with a layer of microscopic, metallic elongated spheroids, easily extinguish better than 50 dB, and transmit to 99%.

MINIATURIZED ISOLATORS FOR DIODE LASERS AND FIBEROPTICS

The availability of the garnet films and the dichroic polarizers has enabled the development of very small, high performance lasers for use in fiber-optic telecommunications systems. In fact, very small, highly efficient isolators have permitted important advancement of the industry.

The next step in evolution might be a waveguide isolator, a small device that is "optically hard-wired," or optically continuous, without air gaps. An ideal isolator will fit into the laser can, thus allowing easy encapsulation. Clearly, packaging technology now becomes the limiting factor.

ISOLATOR CHARACTERISTICS

Design requirements of an isolator depend upon its application, physical location, and local environment. Extremes of outdoor temperature and humidity demand different design considerations than more-moderate indoor locations where the environment is controllable. If polarization insensitivity is needed, the design becomes more complex, due to the number of additional components and increased optical path length, which make alignment stability difficult.

SIGNIFICANCE OF WAVELENGTH

Certainly the controlling element in the isolator is the optical material, a specific glass or crystal, whose Verdet constant at the wavelength of interest determines one very important feature of the device, its size. A rotator material of high Verdet constant permits the use of a small magnet, resulting in a small device.

Wavelength is the most important determinant of the magneto-optic material to be used. This is because of the Verdet constant at that wavelength. Clearly, if size of the isolator is always a consideration, then one needs to use a material with high Verdet constant. But another factor, optical absorption, is equally important. This is especially true if the laser is high power (absorption can result in damage to the crystal), or the application demands extremely low loss (typical in telecommunications).

VERDET CONSTANTS OF SEVERAL MATERIALS (min/cm-Oe)

	Diamagnetic			Paramagnetic		Ferromagnetic
Wavelength	ZnS	ZnSe	CdZnTe*	Te_glass	TGG	
488 nm	+0.30					
633 nm	+0.18	+0.40				
800 nm		+0.25		-0.20	-0.30	
980 nm		+0.15	+0.34	-0.12	-0.19	
1064 nm		+0.13	+0.28	-0.10	-0.16	
1550 nm						+600

*Patent pending to OFR for use in optical isolators.

ISOLATION LIMITATIONS

The factors that limit isolation are found in both the polarizers and the Faraday-rotator material. Intrinsic strain, inclusions, and surface reflections contribute to reducing the purity of polarization, and this affects isolation. About -40 dB is the average for today's materials in a single-isolator stage. If two isolators are cascaded in tandem, it is possible to double the isolation value.

FUTURE ISOLATORS

Until a laser is developed that is immune to the effects of optical feedback, Faraday rotation seems to be the only way to achieve optical isolation. Isolators for fiber-optic tele-communications are becoming smaller and smaller, but are still "bulk" devices. Whereas "waveguide" isolators have been made in the laboratory, they have not yet become production items.

OPTICAL CIRCULATORS

In the isolator, it is seen that the returned energy (which is considered to be undesirable), is either rejected out the side face of the polarizer, or it is absorbed. On the other hand, some applications require further use of the returned energy. For these applications, an optical circulator is used. In Figure 3, it is seen that the returned signal is usable. It is noted that the most common use of an optical circulator is in fiber-optic applications.

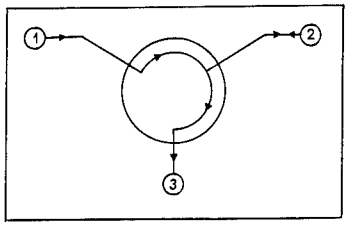

FIGURE 3 Schematic Principle of Operation of an Optical Circulator

The signal is input into Port 1, thus passing into what is effectively an optical isolator. It exits from Port 2, and on to its application. However, for whatever reason, a return signal propagates in reverse, back into Port 2. This is the basic operation of an optical isolator, except in this case, rather than simply being rejected into space, the returned signal is coupled into an optical fiber through Port 3.

SPECIAL NOTICE

Permission has been granted by the following publications for use of material in this article which had originally appeared in articles in said publications as written by the Author:

LASER FOCUS WORLD, PENWELL PUBLISHING CO.
Vol. 24, No. 12, p. 103; Vol. 27, No. 4, p. 175

PHOTONICS SPECTRA, LAURIN PUBLISHING CO.
Jan. '92, p. 81

REFERENCES

D. J. Dentz et al, AIP, 19th Annual Conf. proceedings (1973)
J. K. Furdyna et al, Proceedings CLEO Conf. San Francisco (1986)
R. M. Jopson et al, Electron Lett, 21, 18, 783-784
M. J. Weber, SPIE 30th Ann. Intl Tech Symp Proceed (july 1986)
J. A. Wunderlich et al, Appl. Opt, p 1584, June, 1977

A LENS-FREE AND MIRROR-FREE FIBER INTEGRATED OPTICAL MAGNETIC FIELD SENSOR USING Bi-SUBSTITUTED GARNET

H. Minemoto, N. Itoh, D. Ishiko, and S. Ishizuka
Multimedia Systems Research Laboratory. Matsushita Electric Industrial Co., Ltd.
3-1-1, Yagumo-nakamachi, Moriguchi, Osaka 570 Japan, minemoto@bn.ctmo.mei.co.jp

ABSTRACT

We have developed a novel lens-free and mirror-free fiber integrated optical magnetic field sensor. The use of a bent optical fiber and chip optical components allows easy assembly with no alignment. The linearity error and temperature dependence of the sensitivity of this sensor were less than ±1% and +2%, respectively.

INTRODUCTION

Many types of optical current transformers (OCTs) have been developed [1-5]. In particular, OCTs utilizing sensors with Bi-substituted rare earth iron garnet ((BiR)IG) have high sensitivity, and good temperature characteristics [4-6].

We have already developed optical magnetic field sensors using (BiR)IG for power distribution systems. Recent requirements for such sensors are high accuracy [7, 8] and high productivity. Figure 1(a) shows the schematic configuration of an OCT in a power distribution system. For easy setting of the sensor head in an air gap of the magnetic core, the sensor head's input and output optical fibers should be parallel to each other and perpendicular to the magnetic field. Figure 1(b) shows a conventional magnetic field sensor structure with the optimal arrangement of optical fibers. In principle, only a polarizer, an analyzer, a garnet crystal, and optical fibers are needed for a magnetic field sensor. However, actual sensors use many other components such as lenses, lens holders and mirrors.

In this paper, we propose a new type of optical magnetic field sensor for electric power distribution systems. The sensor does not require any lens or mirror. The sensor has a very simple fabrication process without the need for alignment of optical fibers or components.

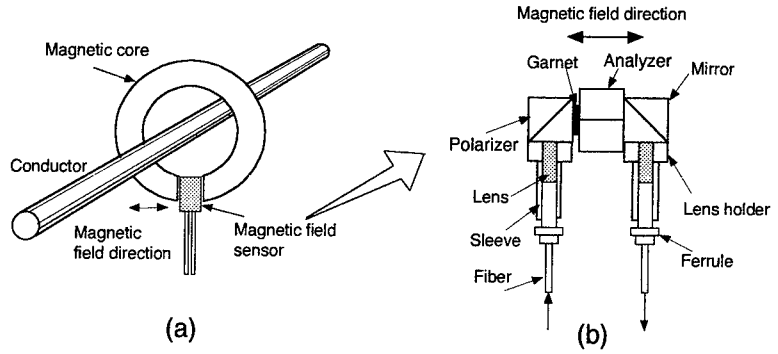

Fig.1 (a) Schematic configuration of an OCT in a power distribution system.
(b) Conventional magnetic field sensor structure.

NEW TYPE OF MAGNETIC FIELD SENSOR

There have been many attempts to reduce the number of optical components in not only

Mat. Res. Soc. Symp. Proc. Vol. 517 © 1998 Materials Research Society

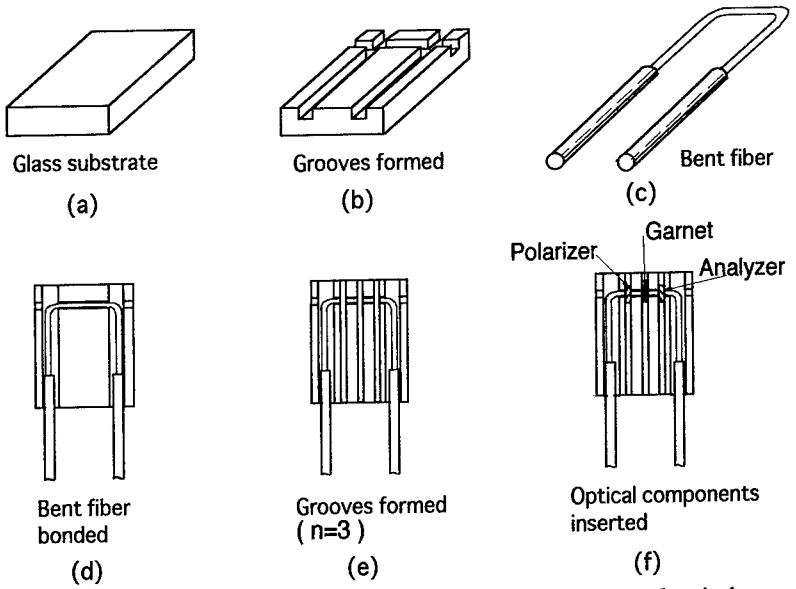

Fig.2 Fabrication process of a lens-free and mirror-free fiber integrated optical magnetic field sensor.

optical fiber sensors but also in devices for optical telecommunication [9, 10]. However, since these devices are long and straight, it is difficult to use them in the small air gap of a magnetic core. We adopt a bent optical fiber for a small sensor in the magnetic field direction which can be easily set in the air gap. We also use direct coupling of the optical path without any lens or alignment of optical components. Figure 2 shows the fabrication process of the optical magnetic field sensor. Figure 2(a) shows the substrate for the sensor. Three grooves were formed with a precise rotating blade saw (Fig. 2(b)). A bent optical fiber with an inverted U shape (Fig. 2(c)) was made from a multimode optical fiber by heat treatment. This bent fiber was bonded in the grooves with epoxy resin (Fig. 2(d)). Then, other grooves (n=3) were formed and the fiber was simultaneously cut to insert the optical components such as the polarizer, the analyzer, and

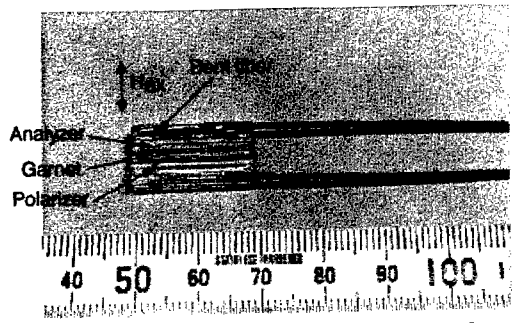

Fig. 3 Photograph of fabricated lens-free and mirror-free optical magnetic field sensor.

the Faraday rotator (Fig. 2(e)). We used a garnet crystal ($(BiGdLaY)_3(FeGa)_5O_{12}$) and two glass polarizing plates whose dimensions ware all $1x1x0.5mm^3$. These chip optical components were inserted in the grooves and bonded with epoxy resin (Fig. 2(f)).

Figure 3 shows the fabricated fiber integrated optical magnetic field sensor. The width parallel to the sensor's applied magnetic field direction was 10 mm. This sensor was fabricated without any alignment of the bent fiber or the optical components.

SENSOR CHARACTERISTICS

The optical loss of the fabricated sensors were 22-24 dB. Figure 4 shows the magnetic field dependence of the linearity error calculated by the following formula,

$$\text{Linearity error (\%)} = \frac{\text{Sensor input signal-Output signal}}{\text{Sensor input signal}}$$

The output fiber of the conventional sensor which adopted the collimated beam system can detect only the zeroth-order diffracted beam by the garnet domain structure. As a result, the linearity error of this sensor is grater than that of fiber integrated sensor. The linearity error of the fiber integrated sensor was less than ±1.0% between 10 and 300 Oe. The sensitivity of this sensor was 0.16%/Oe.

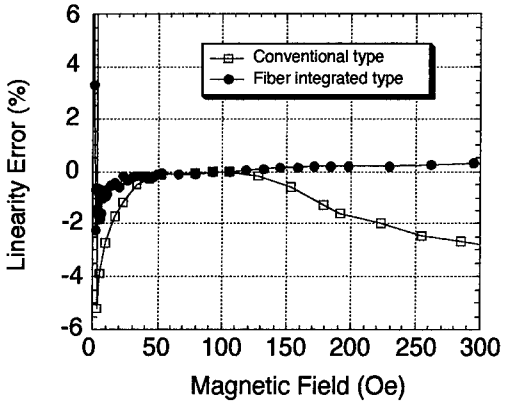

Fig.4 Magnetic field dependence of linearity error. The fabricated fiber integrated sensor have good linear characteristics. Linearity error of conventional sensor in Fig. 1(b) is shown in open square plots.

Figure 5 shows the temperature dependence of sensor output error. The sensor output error was less than +2% from -20 to +80°C . These good results for linearity and temperature characteristic nearly match the performance of our recent magnetic field sensors[6,7]. More recently, we have developed a sensor using more thin garnet crystal and polarizing plates whose thickness are all 0.2 mm. The components were bonded together for a sensor chip. In this case, only one 0.6-mm-wide grove for a sensor chip was made in Fig.2(e). This chip was inserted and bonded in the groove. The optical loss of this type of sensors was 17-18 dB. Furthermore, the sensitivity, the linearity error and the temperature dependence of the output error are almost equal to those in Fig. 4 and Fig. 5.

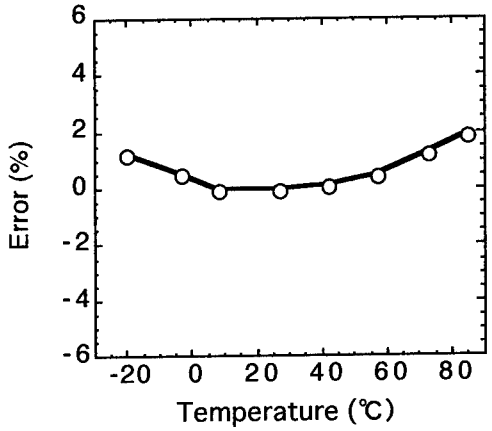

Fig.5 Temperature dependence of sensor output error in fabricated sensor.

DISCUSSION

To achieve good linearity, higher diffracted beams by domain structure of garnets have to be detected[7, 8]. We used a Bi-substituted garnet film with domain pitch of 15.8 μm. Figure 6 shows a simple analysis of diffracted beams by the domains. The third-order diffracted angle of the beam in the fiber core is 6.2 deg which is much smaller than the critical angle of 19.5 deg for a bent fiber. Most diffracted beams for the incident beam parallel to the fiber are detected by the output fiber. Most inclined incident beam from the input fiber to the output fiber is the critical angle of 19.5 deg. This incident beam power is much small than that of parallel one. Furthermore, for this incident beam, only the diffracted beams to the outer direction cannot be detected by the output fiber. Consequently, the total detected power of the higher-order diffracted beams by the output fiber would be much greater than that of total undetected beam power. As a result, the fiber integrated sensors show good linearity. This sensor structure of direct coupling of the optical path is effective to achieve good linearity.

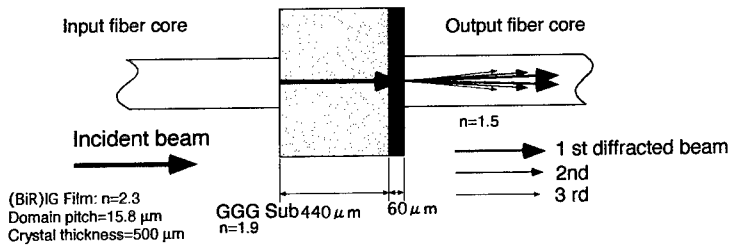

Fig.6 Simple analysis of diffracted beams by the domain structure of a garnet film. Third-order diffracted beam angle in the fiber core is 6.2 deg. Higher-order diffracted beams would be detected by the output fiber.

CONCLUSION

We have developed a novel lens-free and mirror-free fiber integrated optical magnetic

field sensor. This sensor was assembled without any alignment of optical fibers or components. The linearity error and temperature dependence of the sensitivity of this sensor were less than ±1% and +2%, respectively. The optical loss of 17-18 dB in the sensors was achieved with a 0.6-mm-thick sensor chip.

The good linearity of the sensor would result from the detection of higher-order diffracted beams by the garnet domains. The sensor structure of direct coupling of the optical path is effective to achieve good linearity.

REFERENCE

[1] Emerging technologies working group, and Fiber optic sensor working group, IEEE Trans. Pwr. Delivery , **9**, 1778 (1994).

[2] K. B. Rochford, A. H. Rose, and G. W. Day, IEEE Trans. Magn. **27**, 4113 (1996).

[3] K. Kurosawa, Y. Yoshida, and K.Sakamoto, J. Lightwave Tech., **13**, 1378 (1995).

[4]K. B. Rochford, A. H. Rose, M. N. Deeter, and G. W. Day, Opt. Lett. **19**, 1903 (1994).

[5] A. H. Rose, M. N. Deeter, and G. W. Day, Opt. Lett. **18**, 1471(1993).

[6] O. Kamada, H. Minemoto, and N. Itoh, J. Appl. Phys.**75**, 6801 (1994).

[7] N. Itoh, H. Minemoto, D. Ishiko, and S. Ishizuka, IEEE Trans. Magn., **31**, 3191 (1995).

[8] T. Numata, M. Yao, S. Inokuchi, and Y. Sakurai, IEEE Trans. Magn., **27**, 5393 (1991).

[9] D. M. Gualtieri, S. M. Emo, and T. R. Kinney, J. Appl. Phys., **69**, 5978 (1991)

[10] K. Shiraishi, T. Chuzenji, and S. Kawakami, J. Lightwave Tech., **10**, 1839 (1992).

Part III

Magneto-Optic Recording Media: Materials and Devices

AMORPHOUS RARE EARTH-TRANSITION METAL ALLOYS FOR MAGNETO-OPTICAL STORAGE

RICHARD J. GAMBINO
Department of Materials Science and Engineering
State University of New York at Stony Brook
Stony Brook, NY 11794-2275, RGAMBINO@ccmail.sunysb.edu

ABSTRACT

Amorphous alloys of the heavy rare earth elements with cobalt and iron have magnetic and optical properties that make them ideally suited for magneto-optical mass storage media. These materials are used in all commercial erasable (MO) optical disk systems and in optically assisted magnetic storage such as the recordable music minidisk. The important properties of these materials for this application are: 1/ ferrimagnetic exchange with a magnetic compensation point near room temperature, 2/ perpendicular easy axis anisotropy when prepared under suitable conditions as thin films, 3/ low media noise as compared to polycrystalline films, 4/ low processing temperatures compatible with polymer substrates and 5/ thermally stable when cycled repeatedly to the Curie temperature. The magneto-optical Kerr effect that is used to read the information off the disk is large at the 800 nm wavelength used in current devices but low at 400 nm. Since the areal storage density is set by the diffraction limit, improvements in shorter wavelength device performance are needed.

INTRODUCTION

Amorphous rare earth - transition metal alloys are at the present time the only commercially used magneto-optical storage medium. At the time of the discovery of perpendicular anisotropy in these amorphous alloys [1] there was intense interest in new materials for magneto-optical storage media. As we approach the next millennium, there is a similar search for the erasable optical storage medium of the future.

The rare earth transition metal amorphous alloys have a combination of useful properties which make them viable candidates for future storage products. Some of these properties arise from the fact that they are ferrimagnets. This gives them low saturation magnetization but at the same time they have a large magneto-optic Kerr rotation. They are amorphous so that they do not produce grain noise, yet, in spite of their amorphous nature, they can be produced with uniaxial anisotropy under certain deposition conditions. Because they are ferrimagnets it is possible to find compositions with compensation points. The high coercivity in the vicinity of a compensation point can be used in thermomagnetic writing. Present media alloys use a combination of compensation point and Curie point writing. The conditions which produce good media properties are also compatible with deposition on polymer substrates. This feature makes it possible to use low cost injection molded substrates with tracking grooves molded into the surface. The amorphous nature of the material makes it possible to substitute most of the elements in the periodic table in the alloy and retain the same structural features.

Materials with higher magneto-optical (MO) Kerr effect at short wavelengths are needed. Controlling the local field at the RE site can produce materials such as EuS with large MO effects in fairly narrow bands. In amorphous alloys in contrast the local field varies from site to site so the MO effects occur in broad bands. Macroscopic ferrimagnets consist of nanocrystals of EuS embedded in an amorphous metallic alloy matrix to which the EuS is exchange coupled. These two phase systems offer some of the same advantages of RE-TM amorphous alloys while providing a favorable crystal field for strong MO effects from divalent europium [2]. However, it

Mat. Res. Soc. Symp. Proc. Vol. 517 © 1998 Materials Research Society

is also important that composition fluctuations in a MO medium be small compared to the size of the written spots. Retaining the desired crystal field may not be compatible with reducing the size of the EuS nanocrystals sufficiently to avoid fluctuations in the size of the written bits.

Ferrimagnetism

In some of the rare earth - transition metal (RE-TM) intermetallic compounds and amorphous alloys the RE and the TM sublattices (subnetworks) have their magnetic moments antiparallel. The net magnetization thus reflects the difference of the RE and TM magnetic moments rather than the sum. This ferrimagnetic behavior is only observed in the compounds and alloys of the heavy rare earths (Gd to Lu).

In the case of similar RE-TM compounds and alloys of the light rare earths (Ce to Eu), ferromagnetic behavior is generally observed. The difference in behavior between the light rare earths and the heavy rare earths is a consequence of the nature of the RE-TM exchange interaction combined with Hund's rule. The light rare earths have a less than half filled 4f shell, Gd has 7 4f electrons so the heavy rare earths have a more than half filled 4f shell. For shells less than half filled, states with lower J values are lower in energy. So for the light rare earths J = L - S. Following Hund's rule, states with higher J are lower in energy for the heavy rare earths, J = L + S. In the light rare earths L is typically greater than S so J is antiparallel to S but the rare earth spin, S, is antiparallel to the TM moment which means the net moments of the RE and TM are parallel. The interatomic RE-TM exchange is the same, negative, for all the rare earths but because of Hund's rule the light rare earths couple parallel. As to the reason for the negative exchange between the rare earths and the transition metals, it is likely that the rare earth exchange mainly involves the 6s and 5d electrons which have much greater radial extent than the 4f electrons. The rare earth 5d and the transition metal 3d interatomic exchange is probably positive (ferromagnetic) but the 5d - 4f rare earth intra-atomic exchange is strongly negative. Since most of the rare earth magnetic moment is associated with the 4f electrons the net result is a antiferromagnetic RE-TM exchange.

Mean field analysis has been helpful in predicting the temperature dependence of magnetization in a limited composition range. It has also been shown that the exchange constants in Gd-Co systems are, in the order of their magnitudes:

$$J_{CoCo} > J_{GdCo} > J_{GdGd}$$

The order is quite different in, for example, the Gd-Fe amorphous alloys where the Gd-Fe exchange is comparable in strength to the Fe-Fe exchange.

When Co is replaced by Fe in the amorphous alloy the spins in the Fe subnetwork are not parallel but rather are somewhat fanned out. This type of fanning was postulated to explain the lower than expected magnetization of Tb-Fe alloys. In that system it was suggested that the single ion anisotropy of the Tb causes the fanning. Each Tb site in the amorphous alloy has a crystal field which acts on the Tb atom creating a random local anisotropy field. In the absence of an external field or an exchange field, the Tb spins will be dispersed over all possible directions, a spin structure called spheromagnetic by Coey [3]. In a small applied field, one direction along the local axis will be favored over the other so the spherical distribution will become a hemisphere. As the applied field is increased, the fanning angle decreases. In an alloy with Co or Fe the exchange coupling with the transition metal plays the role of the applied field. The competition between the local random anisotropy and the exchange field determines the fanning angle. In the case of Fe alloys the Fe-Fe exchange is relatively weak so even the Fe subnetwork is somewhat

fanned out. With amorphous Dy-Co the Co subnetwork is collinear but the Dy subnetwork is fanned.

Returning to the Gd-Fe system, the local random anisotropy model certainly does not apply and yet there is magnetization evidence that the Fe subnetwork is fanned out somewhat. In amorphous Y-Fe and Zr-Fe alloys there is evidence of a spin glass like state [4,5]. There is no reason to expect strong local random anisotropy effects in these Fe alloys so exchange frustration is suggested as the mechanism of the spin glass state.

In the binary system Fe-Co there is a maximum in transition metal moment [6]. Amorphous ternary systems such as Gd-Fe-Co or Nd-Fe-Co [7,8] show a maximum in the transition metal moment as well. The TM-TM exchange also appears to be somewhat enhanced in the region of enhanced moment. Because of the stronger exchange, there is also less fanning of the TM subnetwork. All of these factors tend to make for larger magneto-optical Kerr effect but also tend to increase the Curie temperature. Thus practical compositions tend to be Tb-Fe with some Co addition.

TERNARY SYSTEMS

A number of ternary amorphous ferrimagnetic systems have been studied. It is useful to plot magnetization at a fixed temperature, usually room temperature, as a function of composition. By connecting compositions of equal saturation magnetization, M_s, a kind of contour plot is obtained. The contours with $M_s = 0$ are of particular significance. One such contour is the Curie line connecting all compositions with the Curie temperature equal to the fixed temperature for the diagram, usually room temperature. In a ferrimagnetic system there may be another contour with $M_s = 0$, that is a compensation line, compositions with room temperature compensation. In the vicinity of the compensation line the coercivity is high as shown in figure 1 for the pseudoternary system Gd-Nd-FeCo. The change in sign of the Kerr effect, Faraday effect and the Hall effect can be used to help locate the compensation line.

Another type of pseudo ternary system is shown in Fig. 2 [9]. In this system, the Tb, a heavy rare earth couples antiferromagnetically to the transition metal (FeCo) subnetwork whereas the Nd, a light rare earth couples ferromagnetically. The compensation line thus separates Tb dominated regions from regions where the Nd and transition metal combined are dominate. In this system the largest MO effects occur outside of the composition range with perpendicular anisotropy.

MACROSCOPIC FERRIMAGNETS

In 1993, Gambino, Ruf and Bojarczuk reported compensation temperatures in thin films consisting of an amorphous Co matrix containing 10 nm crystallites of EuS [10]. It was proposed that the negative exchange between Co and EuS at the phase boundary was coupling the EuS magnetization antiparallel to the Co matrix. Subsequent magneto-optical studies have shown that the EuS retains many of the features of its magneto-optical spectrum including the crystal field split main peak [2]. However, in Co dominated samples the sign of the rotation is opposite that of EuS showing that the EuS magnetization is opposite to the Co magnetization. The change in sign of the Kerr effect occurs at compensation as in an atomic ferrimagnet. At low temperatures the EuS dominates and the sign of the Kerr loop is negative as is EuS at a photon energy of 2.15 eV. As the temperature is increased the sign of the loop reverses at 20 K. In this system and at this photon energy, the Co and the EuS have opposite signs of Kerr rotation. This can lead to

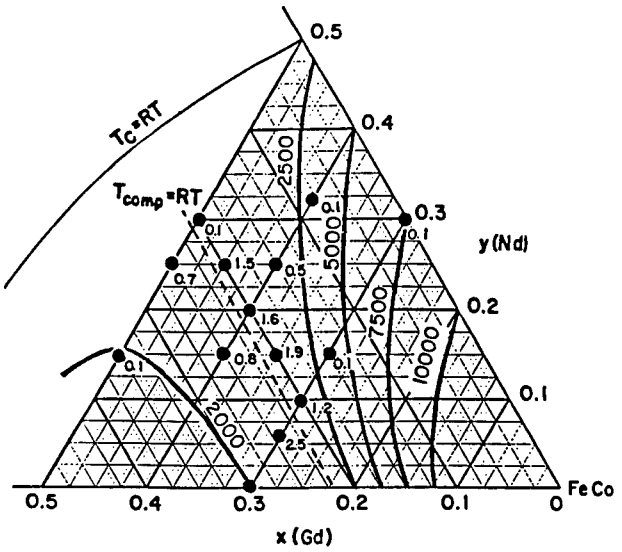

1/ Gd-Nd-FeCo system. Contour lines of equal saturation magnetization are shown. The coercive field, in kOe, of selected compositions (data points) is also shown.

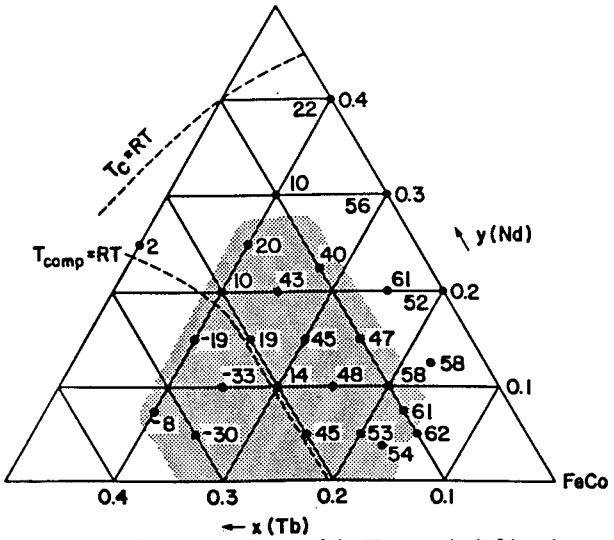

2/ Nd-Tb-FeCo system. Composition dependence of the Kerr angle (2θ in minutes of arc) at 633 nm wavelength is shown, The shaded area shows compositions with perpendicular anisotropy when deposited by e-beam evaporation.

magneto-optical compensation where the two sublattices have equal and opposite Kerr effects so the net Kerr effect gradually decreases, passes through zero, then gradually increases with opposite sign. Similar evidence of ferrimagnetic behavior has been reported in the system EuO/Tb-Fe-Co where the EuO precipitates out of an amorphous Tb-Fe-Co alloy [11]. In this system there are two types of ferrimagnet interactions: macroscopic ferrimagnetism between the FeCo in the amorphous alloy matrix and the EuO particles and microscopic (atomic) ferrimagnetism between the Tb and the FeCo in the amorphous alloy. These more complex systems including Tb-Co-EuS have the advantage from the practical point of view of perpendicular anisotropy at room temperature and even square loops in some cases. In the simpler Co-EuS system, the transition, as a function of field, to ferromagnetic alignment is actively being studied. The change from antiparallel to parallel Co and EuS magnetizations is accompanied by a large change in electrical resistance [12]. At 5 K the magnetization is not saturated even at 35 kOe. The high field susceptibility observed may be caused by spins which are being rotated into the field direction against the exchange.

Lastly, the amorphous magneto-optic medium can be deposited on polymer substrates typically by magnetron sputtering. This is a major economic advantage but polymer substrates limit the upper processing temperature to about 80 C. Higher temperature substrate materials, such as high temperature glass, can be used and in fact are required for such materials as the iron garnets. However, the higher costs of glass substrates seems to outweigh any performance advantages that higher processing temperatures might produce.

MAGNETIC ANISOTROPY

Spin orbit coupling is usually the dominant mechanism of anisotropy in the alloys and compounds of the non-S-state rare earth elements. These elements have non-spherical 4f electron density distributions, that is, an orbital magnetic moment and strong spin orbit coupling. The charge distribution of the RE interacts electrostatically with the charge distribution of the RE site in the solid, the local field. The effect of a given crystal field will depend on the shape of the rare earth 4f charge density distribution which can usually be described as a prolate (cigar shaped) or oblate (disk shaped) ellipsoid.

The magnetic anisotropy can be induced by stress through the inverse magnetostriction effect [13]. The magnetostriction, like the single ion anisotropy is a consequence of the spin orbit coupling. Among the rare earths, the elements with 4f charge density distributions which are the most aspherical have the largest magnetostriction.

In discussing magnetic anisotropy it is essential to understand the structural origins as well as the microscopic mechanism. In the case of amorphous magnetic materials the anisotropic structural features which produce magnetic anisotropy are formed during preparation of the material. A crystalline material with an anisotropic crystal structure has intrinsic magnetic anisotropy known as magnetocrystalline anisotropy. Cubic materials, such as the rare earth iron garnets, have cubic anisotropy but their crystal structure does not produce a uniaxial anisotropy. However, garnets are known to have growth induced uniaxial anisotropy, a structural feature produced during growth which produces magnetic anisotropy through one of the microscopic mechanisms outlined above. In the case of amorphous materials the cubic anisotropy is absent but as in the cubic materials, growth induced uniaxial anisotropy is possible.

We can exclude magnetocrystalline anisotropy in the amorphous case because there is no long range order. It is possible to prepare amorphous films with columnar microstructure and if the exchange coupling between the columns is broken and the columns have a high aspect ratio we can expect, as an upper limit, an anisotropy field $H_K = 4\pi M_s$. A columnar microstructure is

apparently the main cause of anisotropy in electrodeposited amorphous films of Co-P and NiCo-P [14]. Small angle x-ray diffraction of electrodeposited Co-P revealed the presence of oriented, acicular voids with their long axis oriented perpendicular to the film plane [15]. However, shape anisotropy is not the main cause of anisotropy in amorphous RE-TM films used as magneto-optical media. In the latter case, anisotropy fields many times $4\pi M_s$ have been observed and this is not possible with the simple shape model. Secondly, Cargill and Mizoguchi showed that in the Gd-Co amorphous alloys, films with the highest density and no evidence of voids had the highest anisotropy [16]. One of the mechanisms of anisotropy in crystalline alloy solid solutions is pair ordering. The theory of pair ordering has been developed by Nèel [17] and Taniguchi [18]. Pair ordering is certainly possible in an amorphous alloy because it does not involve long range ordering. However, more complex forms of short range ordering are also possible in amorphous materials. In fact, pair ordering can be treated as a limiting case of Compositional Directional Short Range Ordering (CDSRO). Instead of considering the distribution of pairs, in CDSRO we characterize the angular distribution of nearest neighbors of a given element around a central atom. For example, in a close packed f.c.c. alloy like NiFe each Fe has 12 nearest neighbors (nn). In a random solid solution, the average number of Fe having an Fe nearest neighbor, nn_{FeFe}, is the product of the coordination number (CN) and the Fe atomic fraction (X_{Fe}), that is:

$$nn_{FeFe} = CN_{Fe}(X_{Fe}) \qquad (16)$$

The probability of Fe having an Fe nn is the average over the total number of nn atoms:

$$P_{FeFe} = nn_{FeFe}/CN_{Fe} = CN_{Fe}(X_{Fe})/CN_{Fe} = X_{Fe} \qquad (17)$$

Chemical short range ordering is a deviation from this statistical distribution. For example in amorphous Cu-Zr alloys Mizuguchi has shown that Zr has more Cu nearest neighbors than would be expected on the basis of a random statistical distribution [19].

In directional short range ordering, CDSRO, the deviation from a random distribution depends on the direction. If the probability is represented by the distance from the origin, when it is the same in all directions in the xy plane, the probability distribution is a circle. When the center atom only has one type of neighbor in the x direction and the neighbors in the y direction have an equal probability of being RE or TM the distribution can be represented by a distorted ellipse which extends out to the unit circle, representing a probability of one, in the x direction and to 0.5 in the y direction. The chemical short range ordering has not changed, what has changed is the probability of finding a given type of neighbor in a particular direction. In crystalline material the distribution of atomic positions in space is dictated by the lattice and the structural parameters. By contrast, in an amorphous dense random packing all directions have an equal probability of being occupied so the geometric figure would be an undistorted ellipse. Figure 3 shows a two dimensional representation of CDSRO.

Another type of directional ordering has been proposed to explain the anisotropy that develops in amorphous materials after plastic deformation followed by annealing. The anisotropy comes about because the bond distances are different in different directions in the material. This structural anisotropy has been called Bond Directional Short Range Order (BDSRO). In addition to the deformation/anneal route to this type of anisotropy, the authors have suggested that BDSRO might develop during the deposition of amorphous RE-TM alloys [20].

Harris et al[21] using EXAFS have recently detected an anisotropic CDSRO in Tb-Fe. They used linearly polarized synchrotron radiation at normal incidence and at glancing incidence to

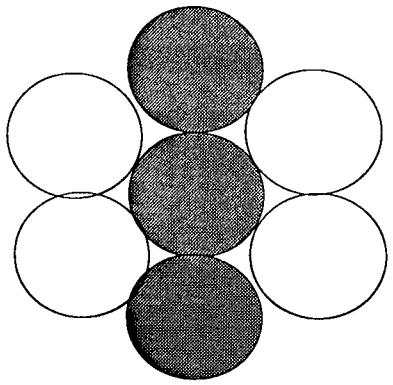

Chemical Directional Ordering

"Pair Ordering"

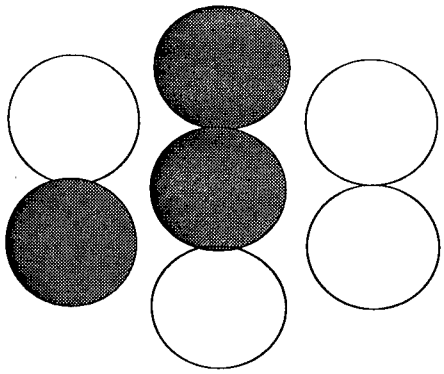

Bond Directional Ordering

"Bond Orientational Anisotropy"

3/ Example of chemical directional short range ordering (CDSRO) and bond directional short range ordering (BDSRO) in two dimensions. Both are anisotropic distributions about a hatched central circle. The near neighbor atoms of 1/3 cross hatched and 2/3 open circles is shown with chemical directional ordering in the upper figure. The lower figure shows a random distribution with respect to the probability of an open circle in all directions. The structural anisotropy shown is in the bond lengths, bond directional ordering.

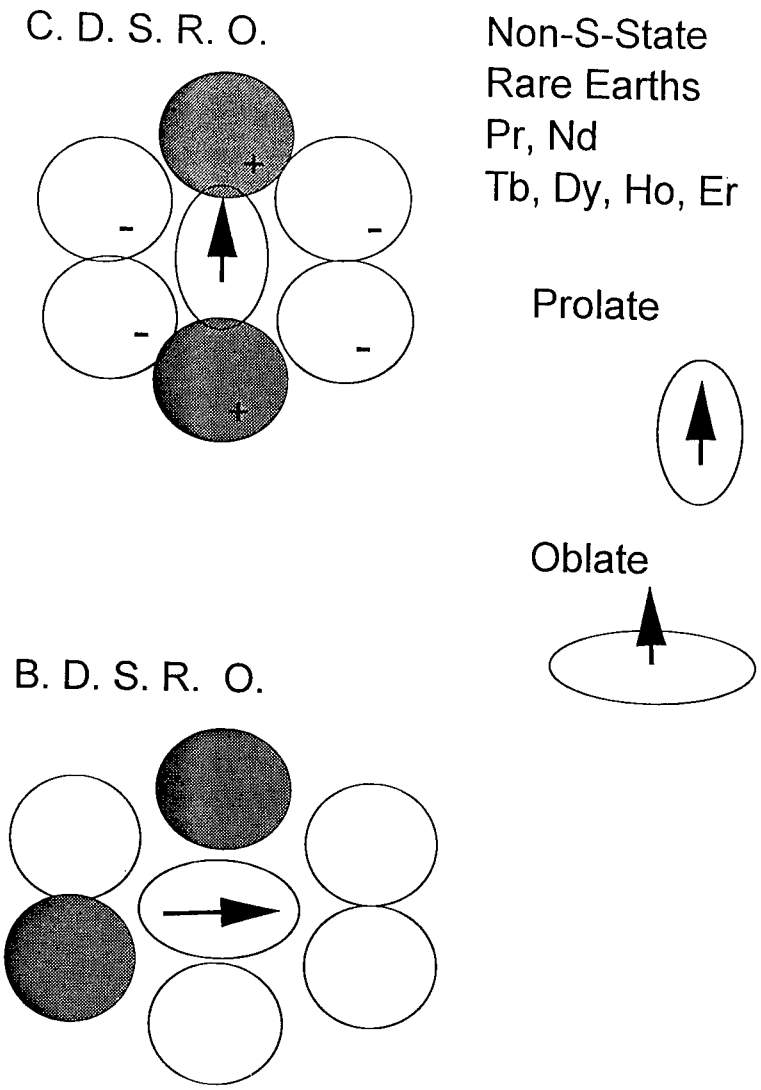

4/ Interaction of a non-S-state rare earth with the anisotropic local electric fields of sites with short range chemical ordering (upper) and bond ordering (lower). The orientation of the easy axis depends both on the crystal field and the 4f electron probability density distribution, usually approximated by a prolate or oblate ellipsoid.

probe the structure in the plane of the film and perpendicular to the plane of the film. They find clear evidence of structural anisotropy in films with a large magnetic anisotropy. When the anisotropy of the film is decreased by annealing the structural anisotropy is decreased. Moreover, Harris et al show that there is a significant difference in relative number of Fe and Tb nearest neighbors in the plane vs. out of the plane. This EXAFS method has provided the first clear evidence of structural anisotropy and of CDSRO. It is possible that BDSRO is also present however the compositional anisotropy probably makes a very strongly anisotropic crystal field causing a large single ion anisotropy.

Even more recently, Hufnagel et al have used x-ray scattering to show that the pair distribution in sputtered amorphous Tb-Fe is anisotropic [26]. They find a larger number of Tb-Fe pairs in the out of plane direction than in the plane. The structure anisotropy was detectable in a comparison of the reduced radial distribution functions (RDF) obtained from out-of-plane (reflection) and in-plane (transmission) scattering experiments. The observations were confirmed by the Tb-edge differential distribution function (DDF) from anomalous dispersion data.

The mechanisms which produce an anisotropic structure in an amorphous phase have been discussed in the literature since the discovery of anisotropy in Gd-Co [1]. The anisotropy depends on deposition conditions, for example, Tb-Fe produced by high rate sputtering is not anisotropic [23] whereas amorphous Tb-Fe deposited at more normal rates is anisotropic. However, the random anisotropy of amorphous $TbFe_2$ causes the observed decreased Curie point and magnetization in accord with the theory of Harris, Plischke and Zuckermann [24]. Therefore, the microscopic mechanism of anisotropy which is active is single ion anisotropy caused by the non-S-state Tb in an anisotropic crystal field. Yet there is no anisotropy with respect to the film growth direction in high rate sputtered films because the easy axis of each site is randomly oriented

It is also clear that thermal annealing and ion implantation damage both destroy anisotropy [25,26,27,28,29]. Both of these processes are associated with randomization so these effects are evidence that there is an ordering mechanism during deposition.

References:

[1] P. Chaudhari, J. J. Cuomo and R. J. Gambino, "Amorphous Metallic Films for Beam Addressable Applications," Applied Phys. Lett. 22, 337 (1973). P. Chaudhari, J. J. Cuomo and R. J. Gambino, "Amorphous Metallic Films for Bubble Domain Applications," IBM Journ. of Res. and Devel. 17, 66 (1973).

[2] R. J. Gambino and P. Fumagalli, "Magneto-Optic Properties of Macroscopic Ferrimagnets," IEEE Trans. Mag. 30, 4461 (1994)

[3] J. M. D. Coey and P. W. Readman, Nature, 246, 476 (1973); K. Moorjani and J.. D. Coey, Magnetic Glasses, Elsevier, Amsterdam, 1984

[4] S. J. Pickart, J. J. Rhyne and H. A. Alperin, Phys. Rev. Lett. 33, 424 (1974)

[5] H. Hiroyoshi and K. Fukamichi, J. Appl. Phys. 53, 2226 (1982)

[6] Slater - Pauling Curves, see R. M. Bozorth, Ferromagnetism, IEEE Press Classic Reissue, 1993

[7] R. J. Gambino and T. R. McGuire, "Magneto-Optic Properties of Nd-Fe-Co Amorphous Alloys," J. Appl. Phys. 57, 3906 (1985).

[8] R. J. Gambino and T. R. McGuire, "Enhanced Magneto-Optic Properties of Light Rare Earth-Transition Metal Amorphous Alloys," J. Mag. Magn. Mat. 54-57, 1365 (1986).

[9] W. Reim, R. J. Gambino, R. R. Ruf and T. S. Plaskett, "$Tb_xNd_y(FeCo)_{1-x-y}$: Promising

Materials for Magneto-Optical Storage?", J. Appl. Phys. 61, 3349 (1987).
[10] R. J. Gambino, R. R. Ruf and N. A. Bojarczuk, "Macroscopic Ferrimagnets as Magneto-Optic Media", J. Appl. Phys. (abstract only) 75, 6871 (1994)
N. A. Bojarczuk, R. J. Gambino and R. R. Ruf, U.S. Patent 5612131: Composite magneto-optic memory and media.
[11] R. J. Gambino, "EuO/Tb-Fe-Co Exchange Coupled Films," J. Magn. Soc. Japan 19 (Supplement No. S1), 17 (1995).
[12] R. J. Gambino, J. Wang and T. R. McGuire, "Magnetoresistance of Co-EuS Macroscopic Ferrimagnets", IEEE Trans. Mag. 31, 3915 (1995)
[13] S. Chikazumi, Physics of Magnetism, John Wiley, New York, 1964
[14] G. S. Cargill, III, R. J. Gambino and J. J. Cuomo, IEEE Trans. Mag. 10,804 (1974)
[15] G. S. Cargill, III, and R. W. Cochrane in Amorphous Magnetism, H. O. Hooper and A. M. de Graaf, Editors, Plenum,New York, 1972, pp. 313-320
[16] G. S. Cargill, III and T. Mizoguchi, J. Appl. Phys. 49, 1753 (1978), J. Appl. Phys. 50, 3570 (1979)
[17] L. Nèel, J. Phys. Radium, 15, 225 (1954)
[18] S. Taniguchi, Sci. Rep. Res. Inst. Tohoku Univ. A7, 269(1955)
[19] T. Mizoguchi, in Diffraction Studies on Non-Crystalline Substances, I. Hargittai and W. J. Orville-Thomas, Elsevier, Amsterdam, 1981
[20] X. Yan, M. Hirscher, T. Egami and E. E. Marinero, Phys. Rev. B., 43, 9300 (1991)
[21] V. G. Harris, K. D. Aylesworth, B. N. Das. W. T. Elam and N. C.Koon, Phys. Rev. Letters, 69, 1939 (1992), V. G. Harris, K. D. Aylesworth, B. N. Das, W. T. Elam and N. C. Koon, IEEE Trans. Mag. 28, 2958 (1992)
[22] T. C. Hufnagel, S. Brennan, P. Zschack, and B. M. Clemens, paper AD-02, Intermag Conf., Seattle, Washington, 1996
[23] J. J. Rhyne, S. J. Pickart and H. A. Alperin, Phys. Rev. Lett. 29, 1562 (1972)
[24] R. Harris, M. Plischke and M. J. Zuckermann, "New Model for Amorphous Magnetism", Phys. Rev. Lett. 31, 160 (1973)
[25] R. Hasegawa, R. J. Gambino, J. J. Cuomo and J. F. Ziegler, "Effect of Thermal Annealing and Ion Radiation on the Coercivity of Amorphous GdCo Films," J. App. Phys. 45, 4036 (1974).
[26 R. J. Gambino, J. Ziegler and J. J. Cuomo, "Effects of Ion Radiation Damage on the Magnetic Domain Structure of Amorphous Gd-Co Alloys," Appl. Phys. Lett. 24, 99 (1974).
[27] T. Mizoguchi, R. J. Gambino, W. N. Hammer and J. J. Cuomo, Effects of Ion Implantation Damage on the Magnetic Properties of Amorphous GdCoMo Films," IEEE Trans. Magnetics, MAG-13, 1618, (1977).
[28] T. Katayama, K. Hasegawa, K. Kawanishi and T. Tsushima," Annealing Effects on Magnetic Properties of Amorphous GdCo, GdFe and GdCoMo Films", J. Appl. Phys. 49, 1759 (1978)
[29] F. E. Luborsky, "Kinetics for Changes in Anisotropy Coercivity and Argon Content of Transition Metal - Rare Earth Films", J. Appl. Phys. 57, 3592 (1985)

Characterizing the Magneto-optic Properties of Amorphous Rare Earth - Transition Metal Thin Films

W. A. CHALLENER
Imation Corp., Advanced Technology Center, 1 Imation Place, Oakdale, MN 55128

ABSTRACT

The amorphous rare earth - transition metal (RE-TM) thin film alloys and nanolayered materials exhibit numerous properties advantageous for optical recording, including perpendicular anisotropy, high coercivity and low magnetization at room temperature, low noise, and easily adjustable Curie and compensation points. As a result these materials have been employed in all commercial magneto-optic (MO) media. On the other hand, the MO effect of these materials is relatively small and tends to decrease with decreasing wavelength. It is important to understand the useful limits of these materials in MO media, and to determine if their MO figure of merit can be substantially increased through appropriate doping or nanolayering. In this paper we discuss experimental techniques for measuring MO properties, a theoretical approach for analyzing the data and designing optical thin film stacks, and results for a variety of RE-TM thin film materials.

INTRODUCTION

The RE-TM alloys, first discovered about twenty-five years ago,[1] have a unique set of characteristics which make them highly suitable for MO recording media. In particular, their perpendicular anisotropy allows use of the polar MO Kerr effect for readout, their ferrimagnetism allows large coercivity at room temperature for data stability, they have easily adjustable Curie points for optimizing recording sensitivity, and their amorphous structure leads to low recording noise.[2] The MO-active material in commercial rewritable MO media is generally an alloy of TbFeCo, perhaps with additional rare earths to adjust magnetic parameters like anisotropy, coercivity, and Curie point, and small amounts of additional transition metals primarily for corrosion resistance[3-8] or improved recording sensitivity.[6,9,10] MO media are currently designed for operation at specific wavelengths between the red (635 nm) and near infrared (830 nm) depending on data storage capacity. In this wavelength range the polar Kerr effect is not large, but provides adequate SNR for readback, and the dominant contribution to the MO effect is due to the transition metal component.[11] The 4f bands of the heavy rare earths lie too far from the Fermi surface to contribute substantially to the MO effect for visible wavelengths. Small and low cost semiconductor or frequency-doubled lasers with wavelengths in the 405 to 430 nm range will soon be commercially available. New MO media designs will make use of these lasers for large increases in storage capacity. Unfortunately, the MO effect of the RE-TM alloys decreases significantly towards the short wavelength end of the visible spectrum, so it becomes more important to understand the effects of composition and nanolayering on the maximum MO signal available from these materials at the shorter wavelengths.

This report begins with a brief review of the Lissberger-Mansuripur figure of merit (LM FOM) for characterizing the MO effect of different materials. It then presents a simpler and more rapid means for acquiring much, but not all, of the LM FOM information, and applies this

Mat. Res. Soc. Symp. Proc. Vol. 517 © 1998 Materials Research Society

to TbFe alloys doped with a wide variety of other elements. Results for nanolayered TbFeCoBi are also presented.

A variety of different parameters have been used as FOM's for comparing MO materials for use in data storage media.[12] The ideal FOM would only depend upon the physical properties of the MO layer and would correlate directly with the bit error rate (BER) of the finished media. Obviously this is not possible because there are many other factors in media design (such as encoding scheme, substrate birefringence, laser noise, electronic noise, and depolarization noise from substrate grooves) affecting background noise levels and BER which are unrelated to or only marginally related to the physical properties of the MO layer[13].

Although in this sense an ideal FOM does not exist, the LM FOM,[14,15] which is a function of the optical properties of the MO material as given by Eq. (1), is a very good starting point.

$$(\text{LM FOM}) = \frac{1}{2}(1-R)\sqrt{\left(\frac{1}{n^2}+\frac{1}{K^2}\right)\left(\Delta n^2+\Delta K^2\right)} \geq \sqrt{R}\cdot\sqrt{\theta_K^2+\varepsilon_K^2} \qquad (1)$$

In Eq. (1) the index of refraction of the MO material for right and left circular polarizations is

$$N_{\pm} = (n \pm \Delta n) + i(K \pm \Delta K), \qquad (2)$$

R is the reflectance of the film stack, θ_K is the Kerr rotation, ε_K is the Kerr ellipticity, and all parameters are for normal incidence (the angles are in radians). For a fully optimized thin film stack at normal incidence, the LM FOM can predict several parameters, including the maximum Kerr rotation, the maximum MO signal (Kerr rotation times reflectance), and the maximum shot-noise limited SNR.[14-17]

The derivation of the LM FOM also determines the optimum thin film stack design. The MO layer must be thin compared to its skin depth, and be placed upon a perfect reflector, with or without intervening perfectly transparent dielectric layers for adjusting the ratio of Kerr rotation to Kerr ellipticity in the reflected light,[17] and with any number of perfectly transparent dielectric layers above the MO layer for adjusting the film stack reflectance. The optimum film stack reflectance is determined by the dominant noise source.[18] Any absorption of light in the dielectric layers or reflector layer degrades the MO properties of the film stack, but with some effort it is possible to realize Kerr rotation values ≥97% of the LM FOM prediction.[19]

If both Kerr rotation and Kerr ellipticity are measured for the light reflected from an optically thick (opaque) MO film, then a parameter called the "maximum Kerr rotation"[20] can be calculated,

$$\theta_{max} \equiv \sqrt{\theta_K^2+\varepsilon_K^2} = \frac{2\sqrt{\Delta n^2+\Delta K^2}}{\sqrt{\left(n^2-K^2-1\right)^2+(2nK)^2}}. \qquad (3)$$

Maximum Kerr rotation is also the MO rotation measured when a phase retardation plate is employed to eliminate the Kerr ellipticity (essentially converting it into additional Kerr rotation). The functional dependence of θ_{max} upon Δn and ΔK is identical to that of the LM FOM, although the dependence upon n and K is different. Hence, *maximum* Kerr rotation (not to be

confused with Kerr rotation alone) can be used as a FOM if one is comparing materials with essentially the same n and K indices of refraction.[21] In particular, as a small amount of dopant is added to a specific alloy there is a much larger change in Δn and ΔK than in n and K, so the maximum Kerr rotation should be proportional to the LM FOM for small dopant concentrations. When n and K change substantially, however, as occurs at two widely separated wavelengths for RE-TM alloys, then the maximum Kerr rotation will no longer be proportional to the LM FOM. In other words, maximum Kerr rotation is a useful FOM when comparing substantially similar materials at a single wavelength, but is not useful for comparing different materials or the same material at two different wavelengths. For doing this, the LM FOM must be used. However, in experiments when maximum Kerr rotation is an appropriate FOM, it has the advantage of being much simpler to measure than the LM FOM. Only Kerr rotation and Kerr ellipticity measurements are required to determine the maximum Kerr rotation, while a determination of the complete index of refraction of the MO material is necessary to compute the LM FOM.

RE-TM alloys must be protected from oxidation for accurate optical measurements. This generally means overcoating the MO film by a dielectric. Hence, rotation and ellipticity measurements are either made through the dielectric thin film overcoat or through a transparent substrate. Substrate measurements are complicated by surface cleanliness requirements and the inevitable thin surface layer of water and outgassing which react with the MO film during deposition, so it is generally safer to measure magneto-optical properties of the RE-TM alloys through a thin dielectric overcoat than a glass substrate. However, Eq. (3) is not applicable to measurements of rotation and ellipticity through a dielectric layer, although it is straightforward to determine the functional dependence of the maximum Kerr rotation for this case. For any multilayer film stack the complex reflectance amplitude is a function of the refractive indices and thicknesses of each layer, the refractive index above and below the film stack, and the wavelength,

$$r = f(N_0, N_1, N_2, \ldots, N_m, N_{m+1}, t_1, t_2, t_3, \ldots, t_m, \lambda). \tag{4}$$

The maximum Kerr rotation for such a film stack is[14]

$$\theta_{max} = \left|\frac{r_+ - r_-}{2r_{ave}}\right| = \left\{\frac{1}{|r|}\cdot\left|\frac{\partial r}{\partial N_{MO}}\right|\right\}\cdot\sqrt{\Delta n^2 + \Delta K^2}\,. \tag{5}$$

The factor within curly brackets is a function of the nonmagnetic indices of refraction and layer thicknesses, but not Δn and ΔK. Hence, the maximum Kerr rotation of a multilayer stack has the same functional dependence on Δn and ΔK as that of an optically opaque MO film and the LM FOM. As long as the thickness and refractive index of the dielectric overcoat do not change from sample to sample, the magneto-optic properties measured through this layer will also be proportional to the LM FOM and the maximum Kerr rotation measured on an optically opaque, nonoxidized MO film.

EXPERIMENT

RE-TM thin film samples for measurement of maximum Kerr rotation were prepared in the following way. Standard glass microscope slides were precleaned in an ultrasonic bath with Liqui-Nox™, rinsed in distilled water, and blown dry. The slides and polished Si wafers were

then coated in a magnetron sputtering system with multiple source targets and a base pressure of $< 3 \times 10^{-7}$ Torr. The MO films were produced by cosputtering from elemental targets of Tb, Fe, and other dopants at 2 mTorr of Ar, while the samples were rotated past each sputtering gun at a rate sufficient to guarantee submonolayer deposition (except in the case of TbFeCoBi films to be discussed later). The MO film was optically opaque with a thickness of 150 to 200 nm. A 10 nm protective dielectric overcoat of YO_x was deposited over the MO film. X-ray fluorescence spectroscopy (XRF) or inductively coupled plasma spectroscopy (ICP) were used to analyze the sample compositions. For each different dopant at least four runs were made with varying dopant levels, while maintaining the ratio of Tb to Fe at about the room temperature compensation composition, $Tb_{0.22}Fe_{0.78}$. The composition of each sample could, therefore, be expressed in the form

$$\text{composition} = (Tb_{0.22+\Delta}Fe_{0.78-\Delta})_{1-x}R_x \qquad (6)$$

where x typically varied from 0 to 10%, and Δ was small and constant within each dopant sample set.

An MO hysteresigraph with a monochromator light source was used to measure coercivity, and Kerr rotation and ellipticity from the YO_x side of the film stack as a function of wavelength from 400 nm to 900 nm at room temperature. The sample temperature could be varied while it was situated between the pole pieces of the magnet. Although the magnet could apply fields up to 19 kG across the sample, in many cases for sample compositions near the compensation point it was necessary to magnetically saturate the sample at elevated temperatures. For some samples the anisotropy was not sufficiently large to hold the magnetic moment perpendicular at zero applied field. For those samples Kerr rotation and ellipticity were measured at two different applied fields sufficient to saturate the sample and a linear extrapolation was made to zero field.

RESULTS

TbFe is a sperimagnetic alloy. The amorphous structure gives rise to random local fields and anisotropy, and variation in the exchange interaction, causing a dispersion in the direction of the Tb and Fe atomic moments.[22,23] Maximum Kerr rotation was computed and plotted vs. concentration of the dopant, ["x" in Eq. (6)] at each wavelength, and a least squares linear fit to the data points was also computed. At each wavelength the slope of the linear fit was normalized by the y-axis intercept to obtain a single number describing the effect of the dopant upon the maximum Kerr rotation and LM FOM, and the results are given in Fig. 1.

The only dopant with a positive FOM slope is Co. The addition of Co increases the Curie point, the magnetization of the TM subnetwork, and the perpendicular anisotropy of the alloy. The maximum FOM occurs for $Fe_{0.5}Co_{0.5}$, as shown in Fig. 2, while the maximum magnetization of FeCo alloys occurs for $Fe_{0.7}Co_{0.3}$ according to the Slater-Pauling curve. The dominant effect on the FOM is the TM magnetization, but the shift of the peak in the FOM curve towards the Co-rich side is due to the higher Curie point enhancing the FOM at room temperature.

Mg -0.28 -0.53 +0.2	Normalized slopes for $\lambda = \begin{bmatrix} 900 \\ 650 \\ 400 \end{bmatrix}$ nm										Al -1.4 -1.7 -1	Si
Ca	Sc	Ti	V -2.7 -3.0 -3	Cr -4.7 -4.9 -5	Mn -7.6 -7.6 -8	Fe -0.62 -0.74 -0.8	Co +1.8 +1.7 +1	Ni -0.66 -0.47 -0.3	Cu -1.3 -1.5 -2	Zn	Ga	Ge
Sr	Y	Zr -4.7 -4.7 -5	Nb -6.2 -6.6 -7	Mo -40 -39 -40	Tc	Ru	Rh	Pd	Ag -1.3 -1.3 -1	Cd	In	Sn -0.99 -1.1 -2
Ba	La	Hf -2.5 -2.9 -4	Ta -5.1 -5.3 -6	W -12 -12 -10	Re	Os	Ir	Pt -0.20 -0.01 -0.2	Au -0.84 -0.85 -1	Hg	Tl	Pb

La	Ce	Pr	Nd -0.86 -1.3 -1	Pm	Sm	Eu	Gd -0.16 -0.72 -2	Tb -0.92 -0.99 -0.4	Dy -3.0 -3.0 -4	Ho	Er	Tm

Fig. 1: Change in FOM slopes vs. dopant concentration at 900 nm, 650 nm, and 400 nm.

The dopants studied to the right of Co on the periodic table have a small negative effect upon the FOM. A simple nonmagnetic dilutant should have a FOM slope of -1, so for TbFe alloys it appears that Cu, Ag, Au, and Sn behave like nonmagnetic dilutants. Indeed, the FOM slope remains constant for Cu, Ag, and Au to dopant levels approaching 30 at. %, perhaps indicating that these materials are not appreciably soluble in the TbFeCo alloy. On the other hand, the FOM slopes for Fe, Ni, and Pt are greater than -1 indicating some contribution to the MO effect from these elements.

In general the dopants to the left of Fe on the periodic table, with the exception of Mg, exhibit fairly large degradation of the FOM. The elements closer to the Fe column are worse, due primarily to their effect upon the Curie point.[10] For instance, adding 2 at. % Mo to $Tb_{0.2}Fe_{0.8}$ is nearly sufficient to reduce the Curie point to room temperature.

The rare earth dopants do not in general have as large an effect upon the FOM as the transition metal dopants. This is most likely due to a smaller effect upon the Curie point of the alloy. Gd-TM alloys have a higher Curie point than other RE-TM alloys, and at 900 nm Gd doping exhibits the smallest reduction of the FOM. However, there is no contribution to the MO effect at shorter wavelengths from Gd.

Nd is a light rare earth which aligns ferromagnetically with Fe. There is general agreement in the literature that the 4f bands of Nd are closer to the Fermi surface than those of the heavy rare earths, and hence able to contribute to the MO effect in the visible,[24-27] although the exact energy spacing is somewhat controversial, ranging from 2 eV to 4.5 eV.[28-30] The relatively small reduction in FOM for Nd compared to other dopants, in spite of the reduction in Curie point, may be due to a contribution to the MO effect from the Nd. However, no enhancement with Nd

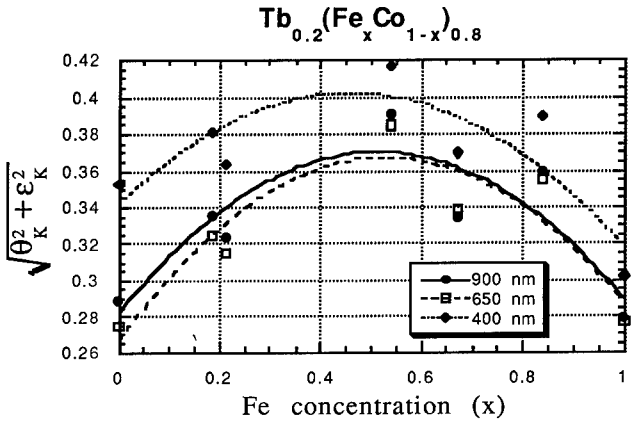

Fig. 2: θ_{max} vs. Fe/Co ratio

doping in TbFe is found, in contrast to many reports of Kerr rotation enhancement with NdFeCo alloys. The presence of Co may have an important effect on the alignment of the Nd atomic moments.

The heavy rare earth dopant Dy does exhibit a relatively large negative FOM slope, indicating that the decrease in Curie point with this dopant significantly reduces the MO effect at room temperature.[31]

The FOM slope for the addition of *both* Tb and Fe in small amounts to $Tb_{0.22}Fe_{0.78}$ is *negative*. This means that the MO effect in TbFe is maximized at the compensation composition.[22,32] In fact, the Tb concentration at which the maximum Kerr rotation occurs shifts with temperature in the same manner as the compensation point as shown in Fig. 3. As the Tb concentration increases, the Curie point drops until the alloy is no longer ferrimagnetic at room

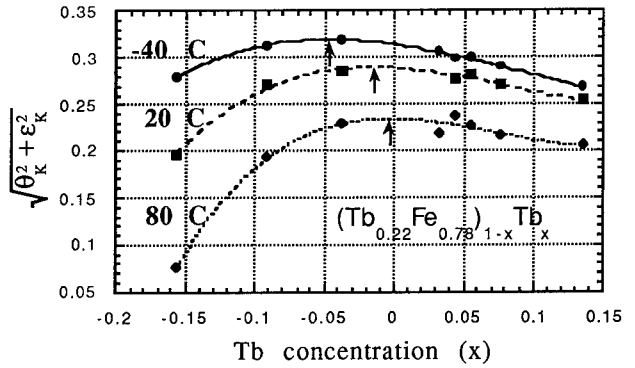

Fig. 3: θ_{max}(λ = 650 nm) vs. Tb concentration in TbFe at different temperatures

temperature. Likewise, as the composition of the alloy approaches pure amorphous Fe, the Curie point drops. The range of x for the Tb concentration for which the Curie point is above room temperature is about -0.19 to +0.49, and the maximum Curie point occurs for $x \approx +0.13$.[32] Therefore, a maximum in the FOM must occur for some composition between pure Fe and pure Tb. The fact that the maximum FOM occurs at the compensation composition rather than the composition corresponding to maximum Curie point indicates that the internal demagnetizing field of the MO layer may partially overcome the perpendicular anisotropy tending to align the individual Fe atomic moments, thereby reducing their contribution to the polar MO effect. At the compensation composition the internal magnetic field is zero (on average), allowing the perpendicular anisotropy to achieve its maximum effect in aligning the Fe spins for contributing to the polar MO effect. Mossbauer spectroscopy of Fe^{57} in TbFe alloys also indicates the smallest dispersion in Fe atomic moments occurs at the compensation point.[33]

When TbFe is doped with Co, the Curie point no longer approaches zero as the Tb concentration is reduced as a result of the stronger exchange coupling between Co-Co and Co-Fe atoms. The perpendicular anistropy also increases substantially. Likewise, when the maximum Kerr rotation is plotted vs. Tb concentration for TbFeCo, a maximum in the FOM is *not* found at the compensation composition, but instead the maximum Kerr rotation increases monotonically as the Tb concentration is reduced.

The Kerr rotation of GdFe alloy films has been reported to increase by 50% at 633 nm by doping with Bi.[34] Tb/($Fe_{0.67}Co_{0.33}$)/Bi exchange-coupled nanolayers have also been reported to exhibit maximum Kerr rotations at least 50% larger than alloyed $Tb_{0.21}(Fe_{0.86}Co_{0.14})_{0.79}$ at visible wavelengths.[20] About 20% of the reported enhancement of the MO effect in the Bi nanolayered film can be attributed to the additional Co in the film stack. Another 10% of the enhancement can be attributed to a reduction in the Tb concentration (the reported Tb layer thickness was 2.8 Å/layer which corresponds approximately to 17 atomic % Tb in the MO nanolayer). The remaining enhancement must be due to the presence of Bi.

There are three topologically inequivalent sequences for the four elements in a TbFeCoBi nanolayered film stack. All three sequences were investigated. The sputtering rates and revolution speed of the substrate planetary mount were adjusted to obtain TbFeCoBi nanolayered films with approximate layer thicknesses of 3.6 Å Tb / 3.8 Å Fe / 2.2 Å Co / x Å Bi, where x varied from 0 to 5. Due to the large surface roughness of the Bi films when deposited separately for film thickness measurements by a profilometer, the actual value of x in the nanolayered films is probably only reliable to within 50%. The compositions for each sequence of samples were $Fe_{0.50}Co_{0.31}Tb_{0.19}Bi_x$, $Fe_{0.47}Co_{0.29}Bi_xTb_{0.24}$, and $Fe_{0.47}Tb_{0.25}Co_{0.27}Bi_x$. The compensation point, coercivity, and perpendicular anisotropy all dropped steadily with the addition of Bi.

The sequence of the layers makes a critical difference in the FOM. As shown in Fig. 4, the maximum Kerr rotation is enhanced by about 10% for a Bi layer thickness of about 2.5Å in the two sequences in which Bi is deposited adjacent to Tb. On the other hand, if the Bi layer is separated from the Tb layer by Fe and Co layers then there is no enhancement of the maximum Kerr rotation by nanolayering. Even in this case, however, a considerable amount of Bi can be included in the TbFeCo film stack without a reduction in the maximum Kerr rotation.

Adding Bi to the TbFeCo nanolayer can have a significant effect upon the average indices of refraction of the MO film, and so maximum Kerr rotation can be a misleading FOM. To

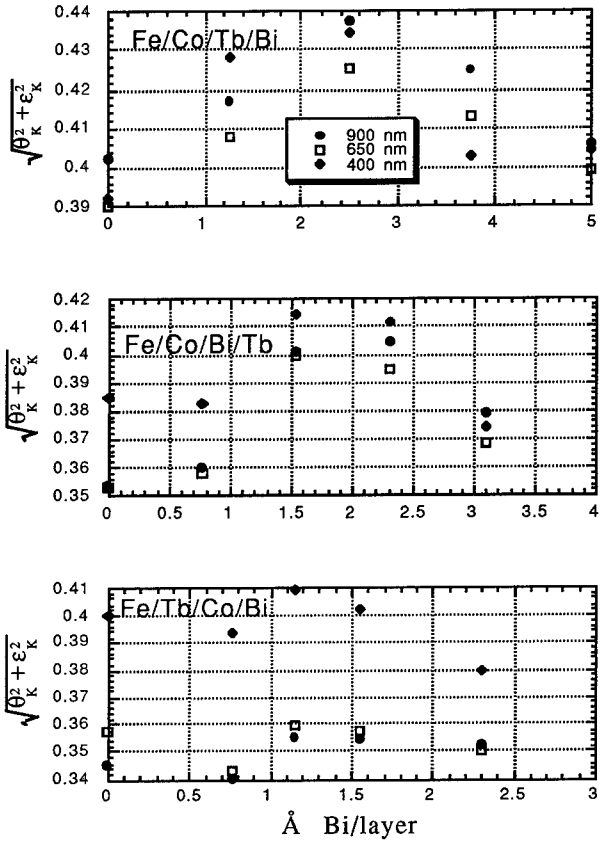

Fig. 4: θ_{max} vs. Bi layer thickness in nanolayered TbFeCoBi

investigate this, two samples were deposited for determination of the indices of refraction, one with the Bi/Fe/Co/Tb structure with the largest maximum Kerr rotation, and a second with the same structure minus the Bi. These samples were trilayers with 15 nm of SiC on either side of a 15-17 nm MO nanolayer deposited onto glass microscope slides. Measurements of the thin film reflectance, transmittance, and polar Kerr rotation and ellipticity were used to compute the refractive indices.[35] At a wavelength of 400 nm an index of refraction of (4.110±0.0173) + i(4.486±0.0336) was measured for TbFeCo, and (4.052±0.0232) + i(3.886±0.0316) for TbFeCoBi. The maximum Kerr rotation for an opaque film according to Eq. (3) is 23% larger for the nanolayer with Bi. However, the LM FOM, according to Eq. (1), is only 12% larger for the nanolayer with Bi, and predicts a maximum Kerr rotation of 0.72° for a fully optimized thin film stack with a 20% reflectance. In Fig. 5 the LM FOM is graphed for both samples as a function

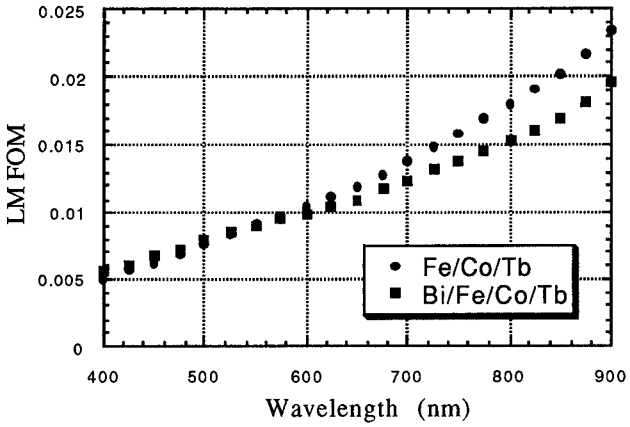

Fig. 5: LM FOM vs. wavelength for TbFeCo and TbFeCoBi

of wavelength for a film stack with a 20% reflectance. The maximum Kerr rotation overstates the actual improvement in FOM that can be obtained with a Bi/Fe/Co/Tb nanolayer, but nevertheless the LM FOM is enhanced with the addition of Bi for wavelengths shorter than about 525 nm.

CONCLUSIONS

When comparing the MO properties of different materials or a single material at different wavelengths, the Lissberger-Mansuripur figure of merit is useful both as an indicator of potential MO signal and for guidance in designing an optimized thin film stack. The only drawback of this FOM is the extra effort required to completely characterize the MO index of refraction of the material being studied. If one is interested only in the effect on the MO properties of small changes in the MO alloy due to the addition of dopants in quantities sufficiently small that they have no substantial effect on the nonmagnetic part of the index of refraction, then a measurement of maximum Kerr rotation, $\theta_{max} = \sqrt{\theta_K^2 + \varepsilon_K^2}$, is also a suitable FOM. Maximum Kerr rotation may be used as a FOM for any MO thin film stack, and in particular for an opaque MO film with a thin dielectric overcoat, if the film stack design remains constant over the series of samples of different dopant concentrations.

Measurements of maximum Kerr rotation for a variety of TbFe samples doped with small amounts of other elements give a direct measurement of the effect of these dopants upon the MO signal at a specific wavelength. Three factors are found to influence the FOM, the effect of the dopant on Curie point, on the TM subnetwork magnetization, and on the perpendicular anisotropy. Of the dopants studied, only Co was found to actually increase the FOM, both through its effect on the subnetwork magnetization and on the increase in Curie point. Cu, Ag, Au, and Sn dopants act as simple dilutants, while Fe, Ni, and Pt contribute somewhat to the MO effect. The rare earths, particularly Nd, Gd, and Tb, have only a small negative effect on the FOM. The effect of perpendicular anisotropy is seen most clearly as Tb concentration is varied

in TbFe, leading to a peak in the FOM at the compensation composition when there are no internal fields opposing perpendicular alignment of the Fe spins. This effect disappears with the addition of Co. As a result, it is possible that substantially different values for the FOM slopes will be found for these same dopants in TbFeCo alloys.

The addition of the correct Bi layer thickness to a nanolayer of Tb, Fe, and Co in the correct sequential order increases the maximum Kerr rotation at all visible wavelengths. However, the LM FOM based upon a complete determination of the index of refraction indicates a smaller enhancement of the MO effect, and only for wavelengths shorter than about 525 nm. The difference between maximum Kerr rotation and the LM FOM is a result of changes in the nonmagnetic index of refraction with the addition of Bi, and is an example of why maximum Kerr rotation should be used with caution as a FOM. Nevertheless, a predicted Kerr rotation of 0.72° with a film stack reflectance of 20% at a wavelength of 400 nm for the optimum Bi/Fe/Co/Tb nanolayer is a remarkable result for these RE-TM materials, and may be sufficient for device applications.

ACKNOWLEDGMENTS

The author would like to acknowledge the privilege he has felt to be a part of the MO media development effort, first at 3M and then Imation. The contributions of many different people in the lab, in vacuum equipment design and operation, materials characterization under various deposition conditions, and simple willingness to listen to new ideas, have been essential for the progress of this work. I would especially like to acknowledge the support of Bill Mitchell over the years, who has encouraged me to also share these results with a wider audience.

REFERENCES

1. P. Chaudhari, J. J. Cuomo, and R. J. Gambino, Appl. Phys. Lett. **22,** 337 (1973).
2. J. Daval and B. Bechevet, J. Magn. Magn. Mater. **129**, 98 (1994).
3. S. J. Zhang, X. L. Li, X. Y. Yang, and F. P. Zhang, J. Appl. Phys. **69,** 5994 (1991).
4. K. Aratani, T. Kobayashi, T. Tsunashima, and S. Uchiyama, J. Appl. Phys. **57**, 3903 (1985).
5. T. Iijima and I. Hatakeyama, IEEE Trans. Magn. **MAG-23**, 2626 (1987).
6. F. Kirino, N. Ohta, and N. Ogihara, J. Electrochem. Soc. **139**, 187 (1992).
7. F. Kirino, N. Ogihara, and N. Ohta, J. Electrochem. Soc. **138**, 2259 (1991).
8. G. G. Zheng, T. Iijima, and K. V. Rao,J. Magn. Soc. Jpn. **15** Supp. S1, 193 (1991).
9. T. K. Hatwar and D. G. Stinson, J. Appl. Phys. **69**, 4963 (1991).
10. N. Horiai, T. Ohashi, S. Yoshida, M. Miura, T. Tokushima, and T. Fujii, J. Appl. Phys. **69**, 4764 (1991).
11. D. K. Hairston, and M. H. Kryder, J. Appl. Phys. **63**, 3621 (1988).
12. W. A. Challener, J. Phys. Chem. Solids **56**, 1499 (1995).
13. C. Peng and M. Mansuripur, Appl. Opt. **37**, 921 (1998).
14. R. Gamble, P. H. Lissberger, and M. R. Parker, IEEE Trans. Mag. **MAG-21**, 1651 (1985).
15. M. Mansuripur, Appl. Phys. Lett. **49**, 19 (1986).
16. W. A. Challener, SPIE Proc. **3109**, 52 (1997).
17. R. Atkinson, I. W. Salter, and J. Xu, J. Magn. Magn. Mater. **102**, 357 (1991).
18. R. Atkinson, J. Magn. Magn. Mater. **124**, 178 (1993).

19. R. Atkinson, I. W. Salter, and J. Xu, J. Magn. Magn. Mater. **104-107**, 1013 (1992).
20. R. H. Victora, C. F. Brucker, T. K. Hatwar, J. E. Hurst, B. Uryson, and D. Karns, J. Appl. Phys. **81**, 3833 (1997).
21. R. H. Victora, private communication.
22. T. R. McGuire, R. J. Gambino, A. E. Bell, and G. J. Sprokel, J. Magn. Magn. Mater. **54-57**, 1387 (1986).
23. G. A. N. Connell, J. Magn. Magn. Mater. **54-57**, 1561 (1986).
24. T. Suzuki and T. Katayama, IEEE Trans. Magn. **MAG-22**, 1230 (1986).
25. S. Honda and M. Yoshiyama, Jpn. J. Appl. Phys. **27**, 1687 (1988).
26. P. Hansen, D. Raasch, and D. Mergel, J. Appl. Phys. **75**, 5267 (1994).
27. S. Tsunashima, T. Otani, X. Y. Yu, and S. Uchiyama, J. Magn. Magn. Mater. **104-107**, 1021 (1992).
28. R. J. Gambino and T. R. McGuire, J. Magn. Magn. Mater. **54-57**, 1365 (1986).
29. D. Weller, and W. Reim, MRS Symp. Proc. **150**, 33 (1989).
30. H. Tanaka and S. Takayama, J. Appl. Phys. **67**, 5334 (1990).
31. M. Akihiro, T. Satoh, J. Tada, and T. Satoh, IEEE Trans. Magn. **MAG-22**, 928 (1986).
32. P. Hansen, C. Clausen, G. Much, M. Rosenkranz, and K. Witter, J. Appl. Phys. **66**, 756 (1989).
33. V. S. Rusakov, B. S. Vvedensky, E. T. Voropaeva, and E. N. Nikolaev, IEEE Trans. Magn. **28** 2524 (1992).
34. M. Urner-Wille, J. Magn. Magn. Mater. **15-18**, 1339 (1980).
35. W. A. Challener and S. L. Grove, Appl. Opt. **29**, 3040 (1990).

MAGNETIC AND MAGNETO-OPTICAL PROPERTIES OF Al SUBSTITUTED Bi-RIG PARTICLES DISPERSED IN A PLASTIC BINDER

T. Hirano*, K. Yoshida*, Y. Yamazaki**, T. Namikawa** and M. Kishi**
*Material Research Laboratory, Toppan Printing, Co., Ltd. TRI, Saitama, 345-8508 Japan
**Tokyo Inst. Tech., Yokohama, 226-8502 Japan

ABSTRACT

Nano-size $R_2BiAl_xFe_{5-x}O_{12}$ (R: Dy, Gd, Tb) particles were prepared with a coprecipitation and annealing method. The coating films of the particles were prepared with a coating technique. The magnetic and magneto-optical properties of the particles and films were investigated. The coercive force H_C of the particles and films was increased and saturation magnetization M_S dropped with the Al content x. The H_C of the coating films was about 200 Oe at the compositions of dispersed particles for which the M_S was almost zero. These results suggest that the increase was made with magnetic compensation. The $BiTb_2Al_{0.6}Fe_{4.4}O_{12}$ coating film shows Faraday rotation spectra. The figure of merit of the film is about 0.5 at 520 nm. The coating $BiTb_2Al_{0.6}Fe_{4.4}O_{12}$ film is one of the candidate materials for a new economical magneto-optical storage medium.

INTRODUCTION

We have been studying the preparation process and applications of coating magneto-optical films [1][2]. Nano size particles of Bi-YIG have been dispersed in plastic binders on base films. The increase in the coercive force of the particles has been one of the major tasks in order to apply the films to recording media. The fine particles of garnet, however, require more effort to increase the coercive force than the thin films because of their low internal stresses [3][4].

Some high coercive force films have been prepared by dry processes [5][6] with a substrate temperature of more than about 500°C. Inexpensive plastic sheets can not be used as substrates. We can solve this thermal problem by employing the coating technique in film preparation processes.

In this paper, the magnetic and magneto-optical properties of Bi-RAlIG ($R_2BiAl_xFe_{5-x}O_{12}$ (R: Dy, Gd, Tb ; $0.0 \leq x \leq 1.5$)) particles and its coating films were investigated to develop high coercive force films.

EXPERIMENT

Preparation of the Bi-RIG particles

Bi-RAlIG particles were prepared by co-precipitation and annealing processes [7]. Fig.1 shows the preparation process of the particles. Aqueous solutions of nitrates of Bi, Dy, Gd, Tb, Al and Fe were mixed in order for the ratio of the cations to correspond to the composition of $R_2BiAl_xFe_{5-x}O_{12}$ (R: Dy, Gd, Tb ; $0.0 \leq x \leq 1.5$). The solution was mixed with a NaOH solution with stirring at room temperature. After the coprecipitation reaction, the pH of the solution was 12 ~ 13. The obtained slurry was washed, filtered and dried at 300°C for 1.5h. Then the coprecipitate was heated in air at 700°C for 4h. The crystal phases of

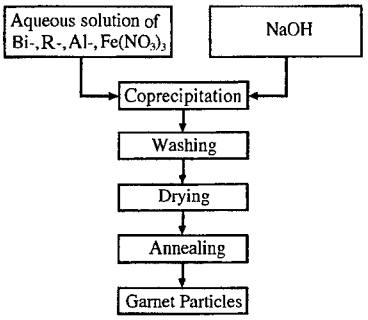

Fig.1 The preparing process of the particles.

Mat. Res. Soc. Symp. Proc. Vol. 517 © 1998 Materials Research Society

the particles were examined by x-ray diffraction analysis.

Preparation of the coating films

The particles were mixed with an epoxy binder (Epo-tek 396 ; Epoxytechnology), dissolved in a cyclohexanone and milled with a planetary milling machine (Pulverisette 7 ; Fritsch) for 30h. They were then coated by a spin coater on Corning 7059 glass. The thickness of the films was about 2μm. It was controlled by the viscosity of the ink and the rotation speed of the spin coater. The films were dried at 80°C for 1h in an oven. The volume content of the particles in the coating films was about 0.2.

The magnetic properties of the films were measured with a vibrating sample magnetometer (VSM) Faraday rotation θ_F was measured by the polarization modulation method. The absorption coefficient α was measured with a spectrophotometer.

RESULTS

Magnetic properties of the particles

Figure 2 shows the relations between the lattice constants of the Bi-RAlIG particles and Al contents of the coprecipitates. The relations show straight lines to Al content of the coprecipitates. The slopes of the relations are the same. These results suggest that the Al substitutions to the garnet crystal are proportional to x in these regions.

Figure 3 and 4 show the saturation magnetization M_S and coercive force H_C of the Bi-RAlIG particles. The M_S of the particles decreased with x. The M_S was less than 1 emu/g at the compositions of $0.8 < x < 1.0$ (R:Dy), $0.6 < x < 0.8$ (R:Tb) and $0.4 < x < 0.6$ (R:Gd). The Bi-RAlIG

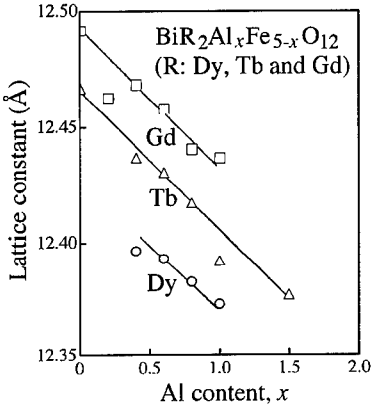

Fig.2 The relation between the lattice constant and the composition on the particles.

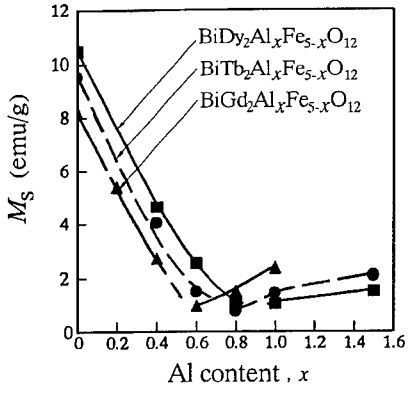

Fig.3 The relation between the M_S and Al content x of the Bi-RAlIG particles.

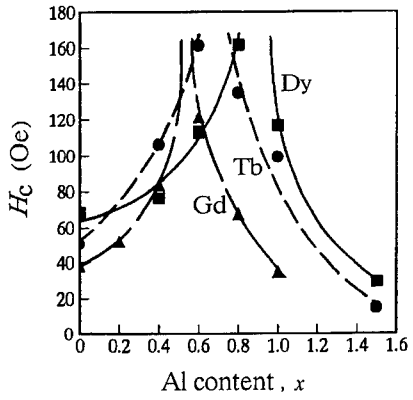

Fig.4 The relation between the H_C and Al content x of the Bi-RAlIG particles.

particles have magnetic compensation at these compositions x. The H_C of the particles was increased at those compositions. The H_C for the composition of $BiDy_2Al_{0.8}Fe_{4.2}O_{12}$ and $BiTb_2Al_{0.6}Fe_{4.4}O_{12}$ is about 160 Oe. Those values are about 5 times larger than that of the Bi-YIG particles[1].

Magnetic properties of the coating films

Figures 5, 6 and 7 show the *M-H* loops of the Bi-RAlIG coating films. The Figures (a) show the *M-H* loops of the Bi-RIG coating films which have no Al substitution. The H_C of the Bi-RIG coating films is about 30 ~ 50 Oe which is the same value as that of the particles. The Figures (b) show the *M-H* loops of the Bi-RAlIG which have x = 0.8 (R:Dy), 0.6 (R:Tb) and 0.6 (R:Gd). The H_C of the Bi-RAlIG coating films have about 200 Oe.

As indicated in these figures, we measured the difference between the in-plane M_S and perpendicular M_S. The reason is not clear but we measured the difference in all measurements. We presume that the difference belongs to the films which are dispersed materials.

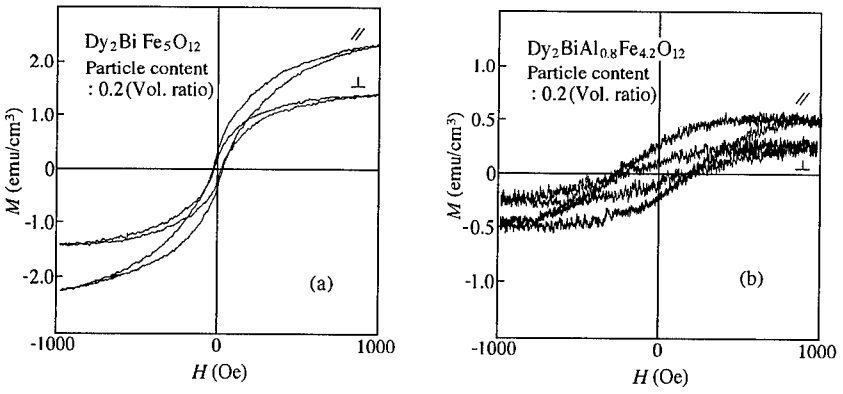

Fig. 5 The *M-H* loops of the Bi-DyAlIG coating films.

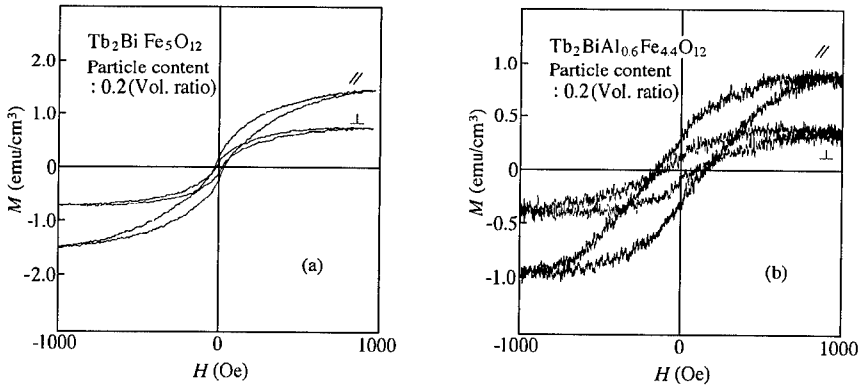

Fig. 6 The *M-H* loops of the Bi-TbAlIG coating films.

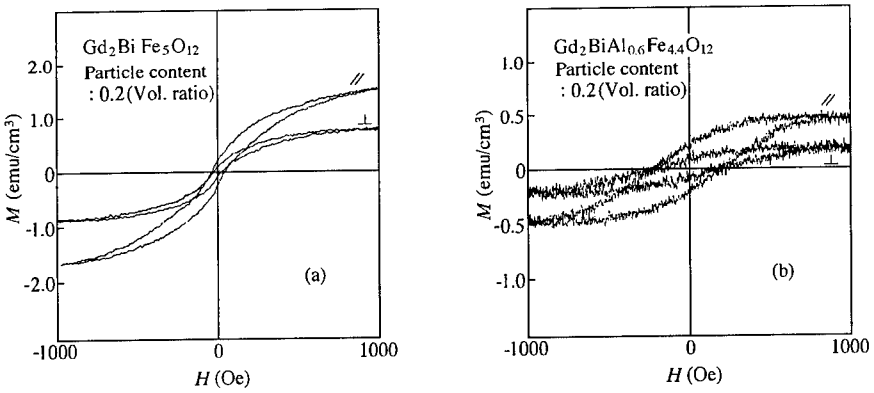

Fig. 7 The *M-H* loops of the Bi-GdAlIG coating films.

Magneto-optical properties of the coating films

Figure 8 shows the Faraday rotation spectra and absorption spectra of the Bi-RIG coating films. In the figures, we show the figure of merit θ_F/α of the films at 520 nm. The figures of merit are about 0.5 ~ 1 (degree). We can expect that the figures of merit will be 2~3 times larger than those of these films, because the volume ratios of the particles in the films are only about 0.2. However, increasing the volume ratio is not difficult.

Figure 9 shows the Faraday rotation spectrum and absorption spectrum of the $BiTb_2Al_{0.6}Fe_{4.4}O_{12}$ coating film. Although the film has Faraday rotation, it has small M_S. The figure of merit θ_F/α of the film at 520 nm is about 0.5. These results indicate that the coating films have the potential to develop into a new economical magneto-optical recording medium.

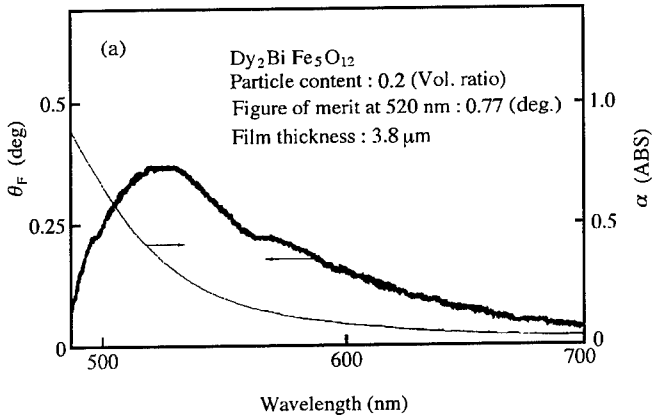

Fig.8(a) Faraday rotation spectrum and absorption spectrum of the Bi-DyIG coating film.

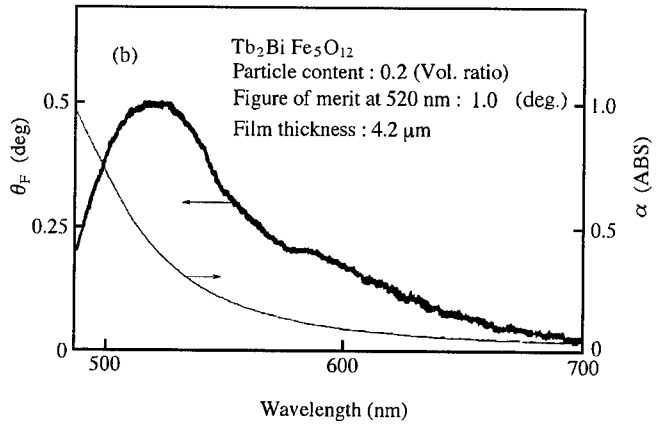

Fig.8(b) Faraday rotation spectrum and absorption spectrum of the Bi-TbIG coating film.

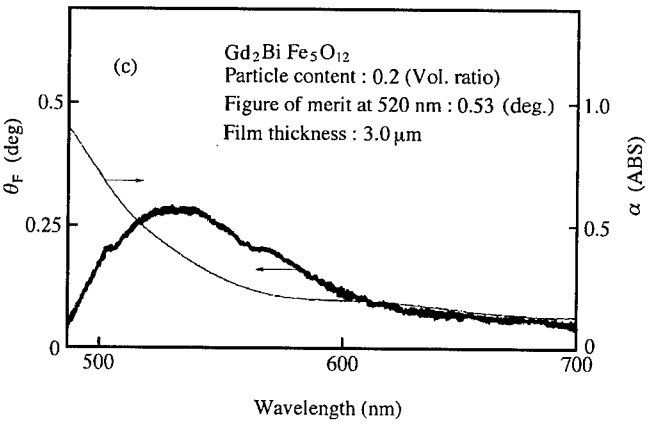

Fig.8(c) Faraday rotation spectrum and absorption spectrum of the Bi-GdIG coating film.

IV. CONCLUSIONS

Nano-size Bi-RAlIG particles were synthesized by coprecipitation and annealing processes. Thin films of the particles were prepared by coating methods with the ink made by a milling process. The magnetic and magneto-optical properties of the particles and films were measured.

The H_C of the Bi-RAlIG particles increased with decreasing M_S of the particles. The H_C of the particles were about 160 Oe when the M_S were almost zero.

The Faraday rotation θ_F of the Bi-RIG and Bi-RAlIG (R = Dy, Tb and Gd) films were measured. The figure of merit θ_F/α of the $BiTb_2Al_{0.6}Fe_{4.4}O_{12}$ coating film is about 0.5 at 520 nm. These results show that the coating $BiTb_2Al_{0.6}Fe_{4.4}O_{12}$ film is one of the candidate materials for a new, economical magneto-optical storage medium.

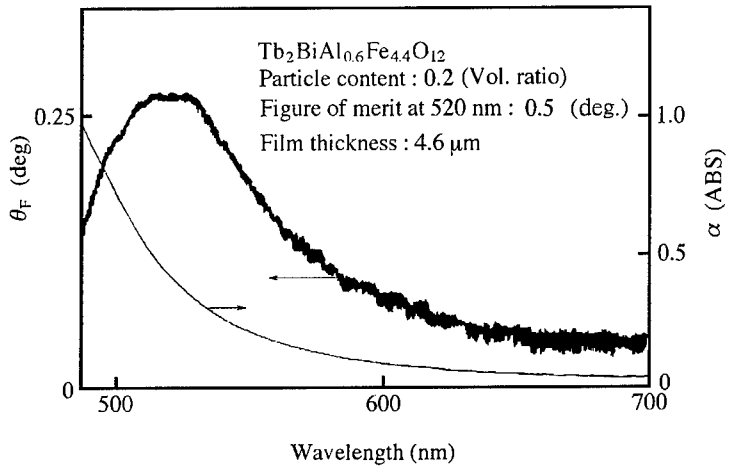

Fig.9 Faraday rotation spectrum and absorption spectrum of the $Tb_2BiAl_{0.6}Fe_{4.4}O_{12}$ coating film.

REFERENCES

[1] T. Hirano, T. Namikawa and Y. Yamazaki, *Denki Kagaku*, **64**, p. 307 (1996).

[2] Y. Yamazaki, T. Namikawa, T. Hirano and K. Yoshida, *J. Phys. IV France*, **7**, p. C1-543 (1997).

[3] T. Fujimoto, Y. Kumura, M. Gomi and M. Abe, Digest of 14th Annual Conf. Magn. Soc. Jpn., p. 209 (1990).

[4] Y. Kumura, T. Fujimoto, M. Gomi and M. Abe, Digest of 14th Annual Conf. Magn. Soc. Jpn, p. 210-211 (1990).

[5] K. Shono, S. Kuroda, M. Alex and S. Ogawa, *J. Magn. Magn. Materials.*, **88**, p. 205 (1990).

[6] Hyeon Soo Kim, Young Hee Lee and Sang Soo Lee, *Jpn. J. Appl. Phys.*, **32** (Part2,12B), p. L1804 (1993).

[7] T. Hirano, T. Namikawa and Y. Yamazaki, *IEEE Trans. Magn.*, **31**, p. 3280 (1995).

COLLOIDAL PARTICLES: SPHERICAL YTTRIUM IRON GARNET

R.H.M.GODOI*, M.JAFELICCI JR, R.F.C.MARQUES and L.C.VARANDA.
Universidade Estadual Paulista – Unesp, Departamento de Físico-Química, Araraquara, SP, Brasil.* e-mail: godoi@iq.unesp.br

ABSTRACT

The purpose of this work is to obtain spherical particles YIG from micrometric to nanometric scales. The spherical particles were obtained from cation hydrolysis in acid medium by adding urea or ammonia in order to carry out a homogeneous nucleation process up to 90°C. Different composition and morphology were achieved by changing reactant concentrations, precipitation agent and stabilizing agent. X-ray diffractometry, electrophoretic mobility, transmission and scanning electron microscopies were carried out on these particles to investigate the phase identification, mobility, morphology and particle size. Crystalline YIG, with spherical characteristics, was obtained. The surface potential presented different characteristics for different dispersion media.

INTRODUCTION

Magnetic colloidal particles, yttrium iron garnet (YIG), exhibit different physical and chemical properties in relation to the classical coprecipitation reaction carried out. Properties of magnetic colloidal particles often depend strongly on the morphology and on the various physical characteristics of the dispersed matter, as well as on its chemical composition[1]. The motivation of YIG preparation as colloidal dispersion with both uniform size and shape is related to the preparative chemistry of special materials[2]. Moreover, the preparation of yttrium iron garnet with nanometric size is very important for academic reasons and for industrial applications as magnetic dye, magnetooptic devices, microwave absorption and magnetic fluids. Colloidal behavior of particles can be regarded as a function of surface features with outstanding technological consequences. Magnetic particles[3] covered with another inorganic phase gives rise to multiphase and multicomponente composite system. The shape is especially important to provide the mechanism of heterocoagulation as well as to assure the reproducibility of the systems[1, 4]. YIG has been mentioned in the literature and obtained by different techniques[5, 6] such as pyrolysis, coprecipitation, microemulsion and sol-gel process. The accurate control of the precipitation process of precursors for magnetic materials is crucial and shows advantages in relation to high purity, homogeneous phase and low temperature processes. Although homogeneous precipitation conditions usually provides spherical habit to colloidal particles the agglomeration process takes place yielding different shape aggregates. This paper reports on the spherical YIG colloids in different size scales, from precursor element salts precipitation.

EXPERIMENT

Yttrium chloride [$Y(Cl)_3.6H_2O$, 99,9%], iron chloride [$FeCl_3$ anhydrous, 97%], urea p.a, ammonium hydroxide [28-30% NH_3], ammonium iron (III) sulfate [$NH_4Fe(SO_4)_2$ $12H_2O$, p.a] and poly(vinylpyrrolidone) (PVP, mol wt: 360,000) were all reagents used without further purification. All stock solutions were prepared with doubly distilled water and filtered through 0.1μm pore size Nuclepore membranes. YIG amorphous particles were obtained by hydrolysis of metal chloride. The starting solution is a mixture of iron chloride and yttrium chloride in chloridic acid 0.01 mol L^{-1}. These two solutions were mixed, so that the ratio of Fe to Y is 5:3, and preheated up to 90°C.

Mat. Res. Soc. Symp. Proc. Vol. 517 © 1998 Materials Research Society

Afterwards, urea or ammonia was added in different concentrations for increasing pH and improving hydrolysis process. In some cases, it was added poly(vinylpyrrolidone) and ammonium iron (III) sulfate [$NH_4Fe(SO_4)_2$ $12H_2O$ in w% to avoid aggregation[7]. The hydrolysis reaction (1) is:

$$5Fe(Cl)_3 + 3Y(Cl)_3 + 24H_2O \rightarrow \{x[Fe_5Y_3O_{12}] + (1\text{-}x)[5Fe(OH)_3]\ [3Y(OH)_3]\} \quad (1)$$

After keeping the solution at the temperature of 90°C for 3 hours the resulting dispersion was filtered through 0.1μm pore size Nucleopre membrane. The powder was then dried in a desiccator under vacuum. The scheme of preparation of YIG particles is shown in figure 1.

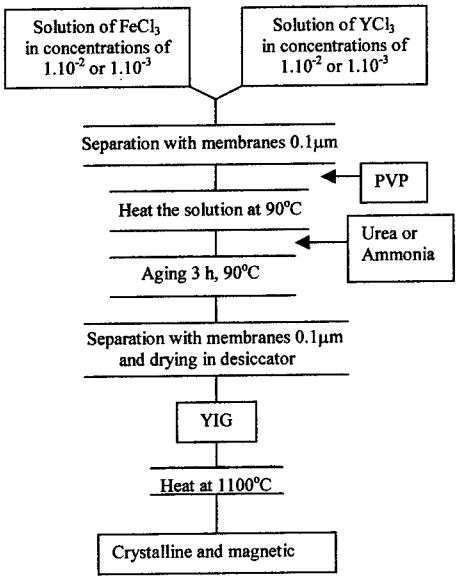

Figure 1. Scheme of the process

Table I: Experimental conditions for YIG sample preparations.

Samples	Precipitation agent ($mol.L^{-1}$)	Concentration of iron chloride ($mol.L^{-1}$)	Addition of PVP (% w/w)	Addition of $NH_4Fe(SO_4)_2$ (% w/w)
P1	Urea (1)	10^{-2}	-	-
P2	Urea (2)	10^{-2}	-	-
P3	Urea (1)	10^{-3}	-	-
P4	Urea (2)	10^{-3}	1.7	-
P5	NH_3 (2)	10^{-2}	-	-
P6	NH_3 (2)	10^{-3}	-	-
P7	NH_3 (2)	10^{-3}	1.7	-
P8	Urea (0.5)	10^{-3}	-	-
P9	Urea (0.25)	10^{-3}	-	50%
P10	Urea (0.5)	10^{-3}	-	50%
P11	Urea (0.5)	10^{-3}	1	50%

RESULTS

Precipitates were calcinated at 1100^{0}C for 4 hours and yield, cubic YIG particles. The surface charge behavior was investigated by dispersing the precipitate in different solvents. Figure 2 demonstrates that there are variations in electrophoretic mobility in different alcohols depending on the added ammonium hydroxide volume.

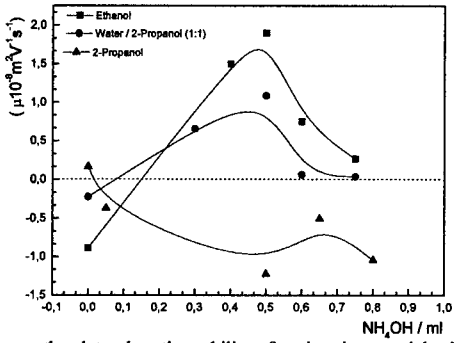

Figure 2. Dependence on the eletrophoretic mobility of yttrium iron particles in different alcohols, (▲)ethanol, (■) 2-propanol and (●) water/2-propanol 1:1 mixed, for sample P3 at a constant ionic strength (0.001 mol L^{-1} KNO_3), depending on NH_4OH volume. The sample P3 was treated at 1100^{0}C for 4 hours before the dispersion.

Organic solvents are used as dispersion medium for silica[3] heterocoagulation in low dielectric constant media. The behavior of used alcohols demonstrated that ethanol is better solvent than other alcohols because the particle surface charge is more positive than that in 2-propanol/water mixture. Despite the low dielectric constant of the solvent, the results in figure 2 demonstrate that ammonium hydroxide exhibits strong basic property in alcoholic medium. The pH was evaluated by addition of phenolphthalein in these alcohols in which it changes color characteristic after small addition of ammonium hydroxide. Yttrium iron garnet samples obtained from different routes, showed in scheme of Table I, and calcinated were dispersed in ethanol. Figure 3 shows the behavior of variables such as concentration of urea, PVP and $NH_4Fe(SO_4)_2$, in relation to the electrophoretic mobility.

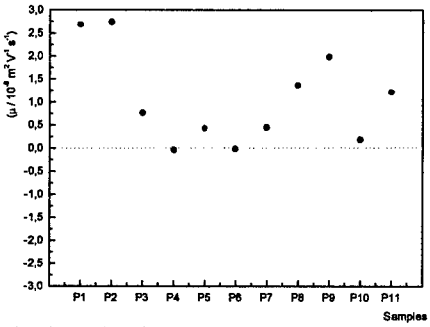

Figure 3. Dependence on the electrophoretic mobility for different samples of yttrium iron garnet particles in ethanol with 0.75 ml of NH_4OH and constant ionic strength (0.001 mol L^{-1} KNO_3). The samples were treated at 1100^{0}C for 4 hours before the dispersion.

Electrokinetic mobility may be related to different effects in the yttrium iron garnet which is obtained by variable parameters in the precipitation. These parameters, such as the

presence of urea or ammonia as well as PVP and/or ammonium iron sulfate in different concentrations, affect the surface potential of the particle and, therefore, the colloidal particles migration. In figure 4 the phase transition is shown in the X-ray diffractograms of amorphous and crystallized YIG samples. Each sample was heated for 4 hours at the temperatures of 700, 800, 900, 1000, 1100 and 1200°C , respectively. Crystallization begins at 800°C according to the Figure 4 in which the orthorhombic structure changes to a cubic one at 1100°C.

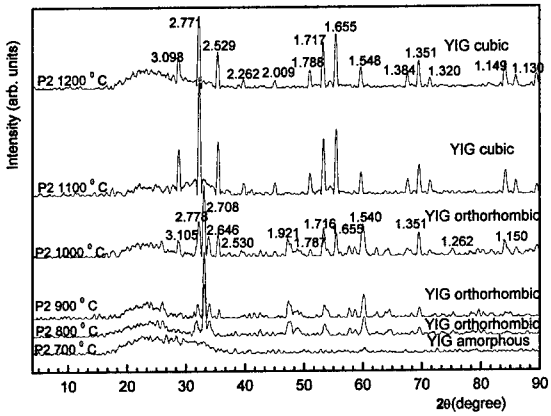

Figure 4. X-ray diffraction patterns (XRD) of the sample P2, heated for 4h. Crystallization begins around 800°C and the orthorhombic to cubic phase transformation takes place at 1100°C.

Figure 5 shows the X-ray powder diffraction of different samples calcined at 1200°C.

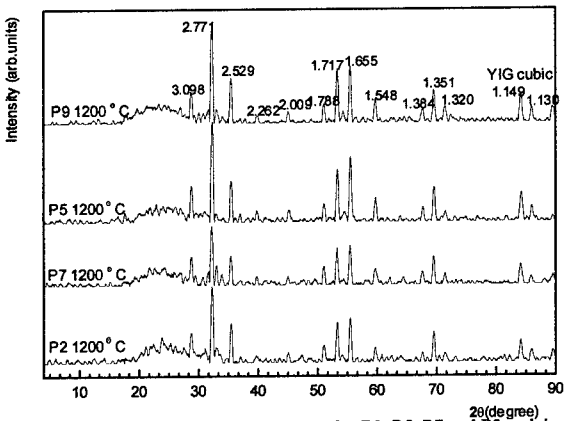

Figure 5. X-ray diffraction patterns (XRDP) of the samples P9, P5, P7 and P2, calcined for 4h.

Figures 4 and 5 show that in all routes of precipitation the same crystalline phase is obtained and suggest the formation of cubic YIG in dissimilar samples.

Figure 6 indicates the transmission electron microscopy results of amorphous YIG obtained from both urea and ammonium media and it illustrates the effect of coprecipitation medium on particles formation. The influence of urea or ammonium hydroxide on the

precipitate characteristics is presented in Figures 6a and 6b. The presence of ammonium in the precipitation medium induces higher particles agglomeration than in presence of urea at the same concentration. The particles shape and size apparently do not suffer drastic changes for the precipitation agents variation.

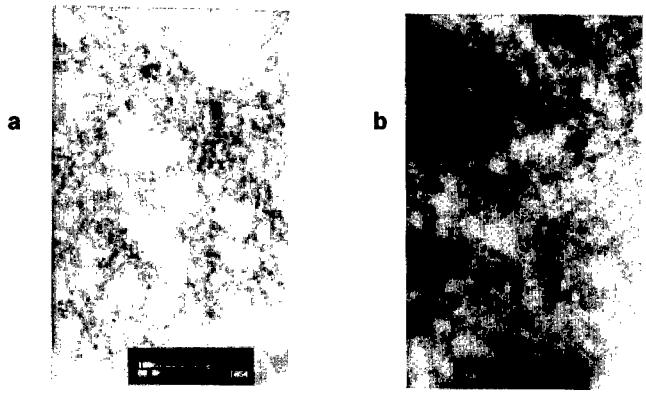

Figure 6 TEM micrographs of YIG dispersed in water: **a** - sample P2, Fe=1.10^{-3} mol.L^{-1} , Urea=2.0 mol.L^{-1} ; **b**-sample P6, Fe= 1.10^{-3} mol.L^{-1}, NH_3=2.0 mol.L^{-1},

Polyvinylpyrrolidone (PVP) was added to the system at 1.7% (w/w) in order to avoid aggregation of YIG particles. Figure 7 shows PVP which arbitrarily involves the YIG particles.

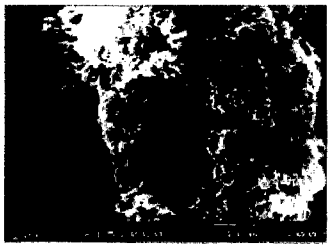

Figure 7: SEM micrograph of sample P4, [Fe]=1.10^{-3} mol.L^{-1}, [Urea]=2.0 mol.L^{-1}, 1.7% PVP.

Figures 8 a, b, c and d have demonstrated that the morphology of yttrium iron garnet particles are influenced by the addition of PVP and/or $NH_4Fe(SO_4)_2$. These stabilization agents showed a satisfactory behavior in the dispersion of ethanol and they not affected the spherical particles. The addition of PVP and or $NH_4Fe(SO_4)_2$ in specific amounts leads to smaller and more dispersed particles due to stabilization properties[7].

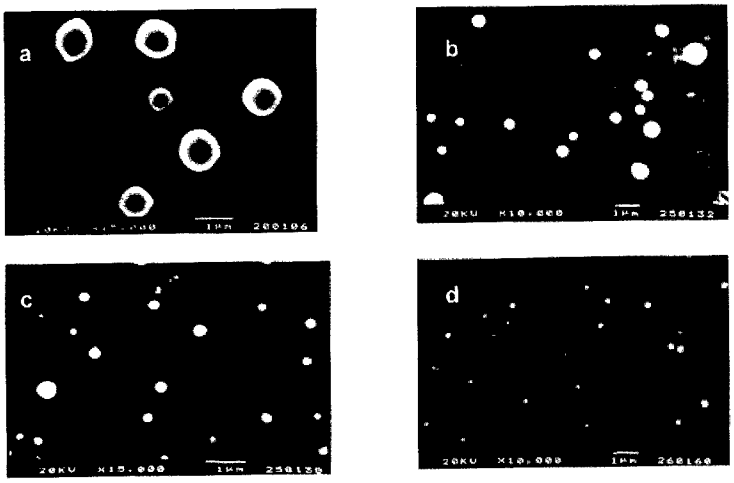

Figure 8: SEM micrographs of YIG dispersed in ethanol: **a**-sample P3, [Fe]=1.10^{-3} mol.L^{-1}, [Urea]=1 mol.L^{-1}; **b**- sample P8, [Fe]=1.10^{-3} mol.L^{-1}, [Urea]=0.5 mol.L^{-1}, **c**- sample P10, [Fe]=1.10^{-3} mol.L^{-1}, [Urea]=0.5 mol.L^{-1} 50% $NH_4Fe(SO_4)_2$, **d**- sample P11, [Fe]=1.10^{-3} mol.L^{-1}, [Urea]=0.5 mol.L^{-1}, 50% $NH_4Fe(SO_4)_2$, 1% PVP.

CONCLUSIONS

Spherical yttrium iron garnet was obtained by coprecipitation of a mixture of yttrium chloride and iron chloride in acid medium changing from micrometric to nanometric scales. Increasing yttrium and iron ion concentrations in the starting solution apparently resulted in most homogeneous particles. Phase transition temperature from amorphous to crystalline YIG is around 800°C and the transition from orthorhombic to cubic phases occurs at 1100°C. The transmission electron microscopy revealed that amorphous YIG particles of 20nm were obtained. The samples precipitated with urea indicated better morphology than samples precipitated with ammonia. The scanning electron microscopy showed that the addition of PVP promotes particles linkage. However, after the calcination process of these samples the PVP under these circumstances worked as an agent of stabilization.

REFERENCES

1 – E. Matijevic, Chemtech, **March**, p.176-181, (1991).

2 – E. Matijevic, Langmuir, **10**, p.8-16, (1994).

3 – E. Matijevic and M. Ohmori, Colloids and Surfaces, **150(2)**, p.594-598, (1992).

4 – R. J. Hunter. in Zeta Potencial in Colloid Science, ed. by Academic Press, London, 1981.

5 – S. Taketomi, K. Kawasaki, Y. Osaki and S. Yuasa, J. Am. Ceram Soc, **77** p 1787-1792, (1994).

6 – D. Segal, J. Mater. Chem, **7(8)**, p.1297-1305, (1997).

7 – E. Matijevic, W. P. Hsu and G. Wang, Colloids and Surfaces, **61**, p.255-267, (1991).

ACKNOWLEDGEMENTS

We acknowledge financial support from FAPESP.

HIGH DENSITY RECORDING ON CONVENTIONALLY STRUCTURED MAGNETO-OPTICAL DISK BY MAGNETIC FIELD MODULATION

M. KANEKO , A. FUKUMOTO
Advanced Development Laboratories, Sony Corporation
6-7-35 Kitashinagawa, Shinagawaku, Tokyo 141-0001, Japan

ABSTRACT

Two recent topics on high density recording are reviewed in this paper on conventionally structured MO disk by magnetic field modulation. One topic is the MO disk with a capacity of 650 MB/ ϕ 64 mm. Using a light wavelength of 650 nm and an numerical aperture of an objective lens of 0.52, a track pitch of 0.95 μm and a bit length of 0.34 μm for (1,7) RLL coding has been applied to achieve 650 MB within a size of a Mini Disc(MD). Groove conditions such as the depth and groove duty in a 1.2-mm thick polycarbonate substrate are optimized to reduce the cross-talk from adjacent tracks. As a result, the recording power margin of $\pm$ 20% is obtained. The disk tilt margin is $\pm$ 0.82 deg and $\pm$ 0.63 deg in the radial and tangential direction, respectively.

The other topics is land/groove recording using an optical phase shifter. A maximum carrier level and a minimum cross-talk are achieved simultaneously when an optical phase shifter is inserted into the optical path before an analyzer. The optimum phase shift is 40 deg for recording on land and -40 deg for recording in groove. Recording on 0.5 μm land/0.5 μm groove with 1.2-mm thick substrate is investigated with a bit length of 0.35 μm for (1,7) RLL code using a light wavelength of 693 nm and a numerical aperture of 0.55. MO recording using an optical phase shifter is promising for an areal density of 3.7 Gb/in^2. Furthermore, when an optical phase shifter is applied to recording on 0.36 μm land/0.36 μm groove with a bit length of 0.258 μm, light wavelength of 642 nm, and NA of 0.7, a capability of 7.0 Gb/in^2 using conventionally structured MO disk is shown.

INTRODUCTION

Magneto-optical disk are expected to achieve removable storage devices with a huge capacity and high reliability. Especially, the magneto-optical recording by magnetic field modulation enables higher linear density than that by light intensity modulation, because a minute mark edge is not limited by an irradiated light profile but precisely determined by the switching of a magnetic field.

Magnetic layers in magneto-optical disks can be roughly divided into two categories; conventionally structured layers and magnetically induced superresolution (MSR) layers[1,2]. New technologies such as magnetic amplifying magneto-optical system (MAMMOS) [3] and domain wall displacement detection (DWDD)[4] have been recently reported. They are considered to belong to MSR family, but have their own advantages in increasing the carrier level even for 0.1-μm mark. Conventionally structured MO can be compared to the conventional in-plane recording in hard disk drive technology. In contrast, the MSR family may be compared to per-

Mat. Res. Soc. Symp. Proc. Vol. 517 © 1998 Materials Research Society

pendicular recording. The MSR family has a great possibility in increasing areal density due to its higher resolving power than optical limit and due to crosstalk canceling effect. But it is not yet commercially available partly because of the complicated multilayer structure and partly because the laser power must be precisely controlled during readout. In contrast, conventionally structured magneto-optical disks are well established massproduction. We believe that conventionally structured MO disk will continue to play an important role in the growth of MO disk market, before the MSR family will be finally introduced.

In this paper we describe two topics of conventionally structured MO disk technology. One is the MO disk with a capacity of 650 MB/ ϕ 64 mm. The other topics is land and groove recording using an optical phase shifter for achieving 7 Gb/in^2.

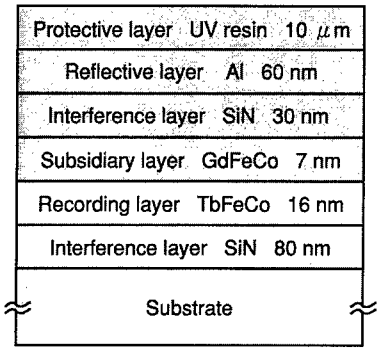

Fig. 1 Layer structure of magneto-optical disk in this paper. The magnetic single layer in conventional disk is replaced by magnetic double layers for reducing a magnetic field required for recording by magnetic field modulation. Typical thickness is shown for each layer.

Table I Specifications of MD DATA2 in comparison with MD DATA.

	MD DATA2	MD DATA
Memory Capacity (MB)	650	140
Disk Diameter (mm)	64	64
Disk Thickness (mm)	1.2	1.2
Laser Wavelength (nm)	650	780
Lens Numerical Aperture	0.52	0.45
Track Pitch (μm)	0.95	1.60
Bit Length (μm)	0.34	0.55
Linear Velocity (m/s)	2.0	1.2
Signal Encoding Method	(1,7) RLL	EFM
Data Transfer Rate (kB/s)	576	133
Recording Method	MFM with pulse irradiation	MFM with cw irradiation
Addressing Method	Interlaced wobble	Continuous wobble
Recording Area	On land	In groove

DISK STRUCTURE WITH MAGNETIC DOUBLE LAYER FILM

We adopted double layers GdFeCo/TbFeCo for magnetic layers in MO disks for both topics[5]. Since double layers are strongly coupled by exchange interaction between them, they act magnetically like an single layer. Magnetic double layers are sandwiched by SiN dielectric layers to protect from corrosion and to enhance the Kerr rotation angle of reflected light from the Al reflective layer. The disk structure shown in Fig. 1 is similar to commercially available MO disks in which single magnetic layer is commonly used. The main role of the GdFeCo layer is to reduce a magnetic field required for recording by magnetic field modulation. The GdFeCo layer contributes in some extent to increase the Kerr rotation angle because GdFeCo has an higher magneto-optical effect than TbFeCo.

MO DISK WITH A CAPACITY OF 650 MB/ ϕ 64 mm

Specifications for MD DATA2

Since the introduction of MiniDisc(MD) into the market in 1992 for digital audio and in 1993 for data storage[6], the market is now growing for digital audio and for digital still camera. But a higher capacity is demanded for multimedia applications. We have been investigating the perfomance of conventionally structured MO disks to establish a physical format for MD DATA2[7]. The major specifications are listed in Table I in comparison with MD DATA. A capacity of 650 MB/ ϕ 64 mm for MD DATA2 is 4.6 times higher than 140 MB for MD DATA. The technical contributions to increase the capacity are divided into factors as follows:
(1) The laser spot size is proportional to λ/NA, where λ and NA are the light wavelength and the numerical aperture of objective lens, respectively. A factor of $(NA/\lambda)^2$ for increasing areal density is 1.9 times higher for MD DATA2 than that for MD DATA.
(2) The data efficiency is 80% for MD DATA2, while 54% for MD DATA. Thus, a factor of 1.5 is gained.

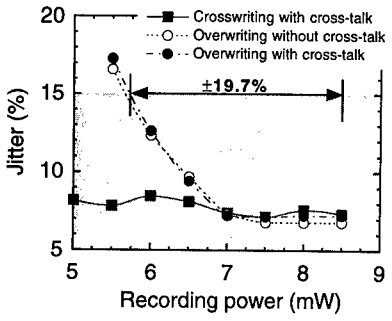

Fig. 2 Recording power dependence of jitter for recording of random data by (1,7) RLL with a track pitch of 0.95 μm and a bit length of 0.34 μm. Polycarbonate substrate was used in the experiment. The highest power was limited by the power available in the system. The power margin was evaluated by three curves; ○ :Overwriting one track with decreasing power, ● : Overwriting main track by decreasing power after adjacent tracks were recorded with the highest power, ■ : Crosswriting adjacent tracks by an increasing power after recording the main track with the same power.

(3) A factor of 1.6 is contributed from improvements of media and drive technology, resulting in cumulated capacity increase of 4.6. These improvements include recording by magnetic field modulation with pulse irradiation for wider power margin, optimization of groove geometory for minimum crosstalk, and new interlaced wobble addressing method for ensureing good address signal quality against crosstalk.

Optimization and characteristics of MO media

Magnetic field modulation with pulse irradiation has been adopted for a track pitch of 0.95 μm and a bit length of 0.34 μm using (1,7) RLL code, while dc irradiation was used for MD DATA. Pulse irradiation with a width of 53 ns per one channel clock of 113 ns was effective to get a wide recording power margin of ± 20%, as shown in Fig. 2. The jitter is evaluated by its standard deviation for random data. In our evaluation of various margins, criterion of the jitter we use is 15% of channel clock. When dc irradiation was used for the same track pitch and bit length, the upper limit of the power was affected by crosswrite from adjacent tracks.

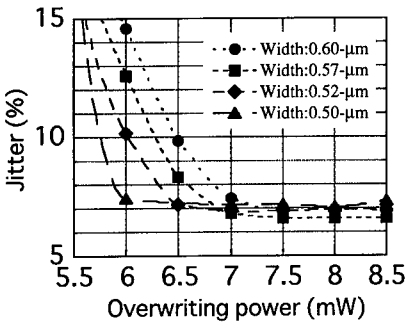

Fig. 3 The jitter as a function of decreasing overwriting power with land width as the parameter. Glass 2P substrate with a fixed track pitch of 0.95 μm was used for recording of 0.34-μm bit with (1,7) RLL. Date written by 8.5 mW was overwritten by decreasing power without written data on adjacent tracks.

Groove depth and width was carefully optimized considering the balance between overwritability, crosstalk, and crosswrite characteristics. The groove depth was adjusted to 70 nm so as to minimize crosstalk from adjacent tracks[5]. Figure 3 shows jitter vs. overwriting power with the land width as the parameter. The land width corresponds to the mark width which is recorded on land. With an increase in land width for a fixed track pitch of 0.95 μm, or equivalently with decrease in groove width, jitter for low overwriting power increases. The jitter with crosstalk and crosswrite took the minimum value for a land width of 0.57 μm. As a result, a land width of 0.52 to 0.57 μm were chosen as the balanced width.

The interlaced wobble addressing shown in Fig. 4 was adopted for a track pitch of 0.95 μm. The period of wobbled groove is 1.9 μm, and period of straight groove is also 1.9 μm. A wide groove wobbling has been used for MD with a 1.6-μm track. If the same wobbling is used for a 0.95-μm track, address information can not be read out because of serious crosstalk from adjacent wobble signals. Address information in wobbled groove is read out by a subspot using three spots tracking method, and is shared by track A and B as shown in the figure.

A practical system must be robust against disk tilt as well as against mechanical and optical tilt of the pick up. Our target tilt margin was ± 0.70 deg in the radial direction and ± 0.55 deg in the tangential direction. Figure 5 shows the jitter for random data vs. tilt angle. A radial tilt margin of ± 0.82 deg and a tangential tilt margin of ± 0.63 deg are obtained, where the margin is defined as the region with a jitter of less than 15% of channel clock. Thus, satisfactory tilt margins as well as wide recording power margin of ± 20% have been achieved at an areal density of 2.0 Gb/in^2, which corresponds to 650 MB for a ϕ 64 mm disk.

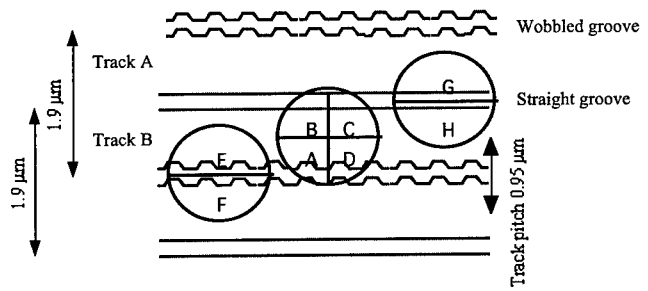

Fig.4 Interlaced wobble addressing method introduced for MD DATA2. Period between wobbled grooves as well as between straight grooves is 1.9 μm. The MO signal is recorded on land. Address information from modulated wobble signal is shared between track A and track B.

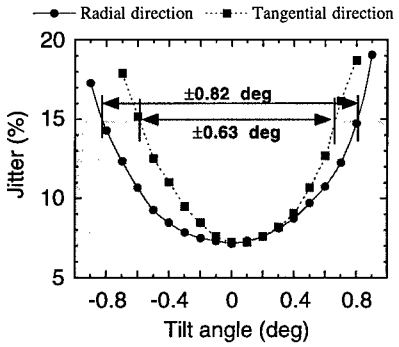

Fig. 5 Tilt angle dependence of the jitter for recording with 0.95-μm track and 0.34-μm bit. The disk with polycarbonate substrate was tilted only during readout in radial and tangential direction.

that non zero Kerr ellipticity can be compensated by an optical phase shifter with a relation

$$\tan \phi = -(\varepsilon_k/\theta_k) \quad (1)$$

where ϕ is the optical phase shift angle, ε_k is the Kerr ellipticity, and θ_k is the Kerr rotation angle. Figure 6 shows the experimental result and a simulation of the crosstalk canceling effect[9]. When an optical phase shifter is not used, the crosstalk is reduced at different groove depths for recording on land from that for recording in groove. The phase shift angle is calculated as 30 deg from (1) using θ_k=1.26 deg and ε_k=-0.73 deg. When a wave plate with a phase shift of 30 deg is inserted before the analyzer, the

LAND AND GROOVE RECORDING USING AN OPTICAL PHASE SHIFTER

Phase shifter with common values for land and groove

Land and groove recording on the phase change disk with crosstalk cancellation was reported as a promising technique for increasing track density[8]. In order to minimize crosstalk from land to groove and crosstalk from groove to land at the same time, an optimum groove depth around λ/6 and optical design of almost zero reflectivity from amorphous phase are required. For the magneto-optical disks a crosstalk cancellation similar to phase change disks is possible by choosing an optimal groove depth around λ/6 and almost zero Kerr ellipticity[9]. The advantage in the MO disk case is

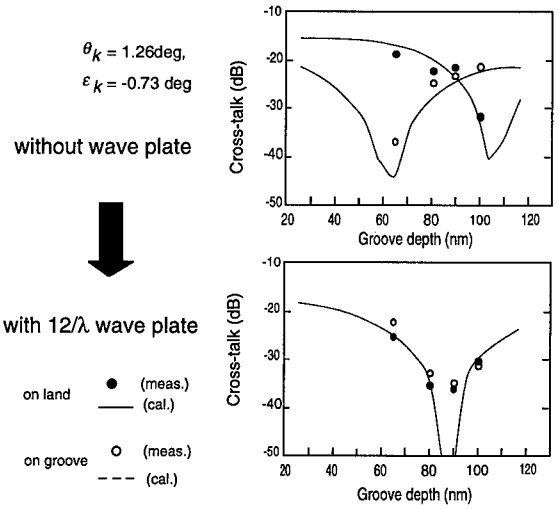

Fig. 6 Groove depth dependence of the crosstalk for optical phase shift of 0 deg and 30 deg. MO disk with Kerr rotation θ_k of 1.26 deg and Kerr ellipticity ε_k of -0.73 deg was used in the experiment. The simulation for land (solid curve) and for groove (dashed curve) is compared with the experiment for land (solid circle) and for groove (open circle).

Table II. System margins obtained under crosstalk canceling condition. λ=690 nm, NA=0.55, groove depth=76 nm (=λ/6), θk=0.95 deg, εk=-0.06 deg.

areal density		2.63 Gbit/in^2	2.02 Gbit/in^2
bit length		0.35 μm	0.40 μm
track pitch		0.7 μm	0.8 μm
tangential disk tilt	L	± 0.45 deg	± 0.61 deg
	G	± 0.44 deg	± 0.56 deg
radial disk tilt	L	± 0.42 deg	± 0.70 deg
	G	± 0.40 deg	± 0.59 deg
defocus	L	———	± 1.4 μm
	G	———	± 1.2 μm
recording power margin	L	± 8 %	± 10 %
	G	± 9 %	± 11 %

crosstalk can be canceled at the same groove depth for recording on land and in groove. The experimental results well coincide with the simulation. Under the crosstalk canceling condition, land/groove recording on conventionally structured MO disks with magnetic double layers was investigaged to get the results tabulated in Table II[10]. The results indicate the possibility of an areal density of 2.63 Gb/in^2 at a track pitch of 0.7 μm.

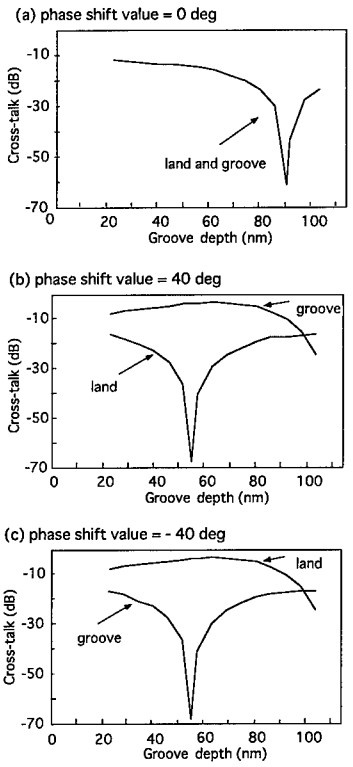

Fig. 7 Crosstalk as a function of groove depth calculated for three phase shift values, (a) 0 deg, (b) 40 deg, and (c) -40 deg.

Analysis of independent phase compensation for land and groove

A further increase in track density based on the technology described above, however, can not be expected, because the S/N ratio is decreased and the minimum crosstalk realized in the above conditions is seriously affected by various perturbations such as disk tilt and defocusing. Then a new approach must be introduced to further increase track density. The basic idea to introduce an independent phase compensation for land and groove to achieve a maximum carrier level and minimum crosstalk level at a groove depth of λ/8 for track pitches of 0.7 μm and 0.6 μm was reported[11].

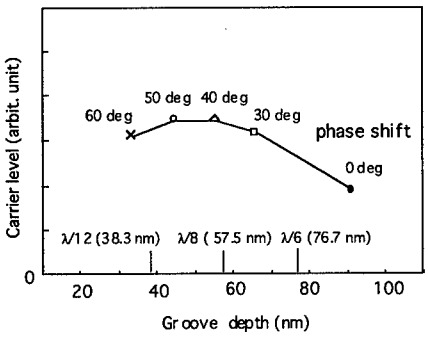

Fig. 8. Carrier level as a function of the optimum groove depth calculated for various phase shift values. The maximum carrier level obtained for phase shift of 45 deg and groove depth of 50 nm is 6 dB higher than that for zero phase shift.

We investigated in detail the feasibility of an independent phase shifter for a very narrow track pitch of 0.5 μm and 0.36 μm using a numerical aperture NA of 0.55 and 0.7, respectively[12]. Figure 7 shows the crosstalk as a function of groove depth calculated for the readout of a rectangular 1.88-μm mark for land and groove with a track pitch of 0.5 μm. The Kerr ellipticity was assumed to be zero in this calculation. In contrast to case (a) with a phase shift of 0 deg, in case (b) with a phase shift of 40 deg, the crosstalk on land is canceled at a groove depth of 56 nm, while the crosstalk in groove is quite large. The situation is reversed for case (c) with a phase shift of -40 deg. Then crosstalk can be canceled for a groove depth of 56 nm by inserting a 40 deg phase shifter for readout on land and a -40 deg phase shifter for readout in groove. Besides, the carrier level is increased by 6 dB compared to zero phase shift case, as is calculated in Fig. 8 . Increase in carrier level is caused by the shallower groove depth. The calculation concludes that the maximum improvement in carrier level and complete cancellation of crosstalk can be achieved simultaneously with a phase shift of 40 deg for readout on land and -40 deg for readout in groove.

In addition to the carrier level, the independent phase shifter improves the tolerance against optical errors such as defocus and disk tilt. Figure 9 shows crosstalk vs. radial disk tilt calculated for various phase shift values. Taking a phase shifter of 40 deg as an example, the carrier level on land is 10 dB higher than that in groove for an optimized groove depth of 56 nm. This difference corresponds to the suppression of crosstalk by 10 dB, which results in a wider radial tilt margin than that for a zero phase shift.

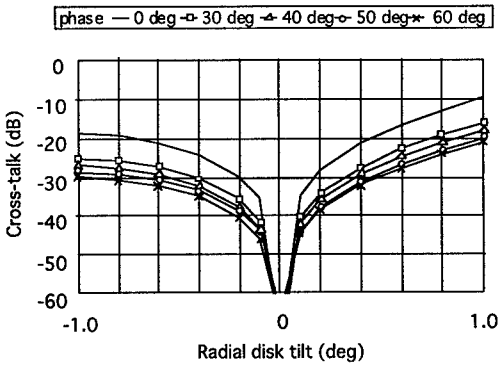

Fig. 9 Crosstalk vs. radial disk tilt calculated for various phase shift values. The crosstalk at tilt of 1.0 deg is supressed by 10 dB for a phase shift of 40 deg compared to zero phase shift.

Experiment using independent phase shifter

Two types of experiments, Experiment 1 and Experiment 2, were made using an independent phase shifter for land and groove recording. Experimental conditions and results are tabulated in Table III. The disk

structure was the same as in Fig. 1, but each layer thickness was designed so as to get almost zero Kerr ellipticity. Phase shift value was changed by rotating a half wave plate between a pair of fixed quarter wave plates. Optimum phase shift values in Experiment 1 were 47 deg for land and -37 deg for groove. The asymmetry observed can be ascribed to the phase offset of -5 in other optical parts. Figure 10 shows jitter as functions of radial disk tilt and tangential disk tilt in Experiment 1. A fairly wide margin is obtained for radial disk tilt considering the substrate thickness d of 1.2 mm. The experimental result is well explained by the calculation in Fig. 9. Figure 11 shows the eye pattern of random data recording for Experiment 2. As shown in the figure, the jitter is worse for groove than for land. The worse jitter was caused by 2 dB higher disk noise level in groove than on land. Since the coma aberration is proportional to dNA^3/λ, a factor of 0.90 is expected for the ratio of radial tilt margin in Experiment 2 to that in Experiment 1. The tilt margin is smaller than expected, this might be caused by degraded S/N ratio of the system, especially by the disk noise induced by the narrow track pitch.

Table III. Experimental conditions and results of independent phase shift for land and groove.

	Experiment 1	Experiment 2
Light wavelength (nm)	693	642
Numerical Aperture	0.55	0.7
A/W (tangential)	0.60	0.62
A/W (radial)	0.75	0.82
Kerr rotation (deg)	1.1	
Kerr ellipticity (deg)	-0.01	
Groove depth (nm)	60	49
Groove duty (%)	52	50
Substrate thickness (mm)	1.2	0.6
Track pitch (μm)	0.50	0.36
Bit length (μm)	0.35	0.258
Modulation code	(1,7)RLL	(1,7)RLL
Areal density (Gb/in²)	3.69	6.95
Channel clock frequency (MHz)	18	18
Linear velocity (m/s)	4.2	3.1
Recording laser power (mW)	9.6	5.4
Readout laser power (mW)	1.1	0.8
Jitter (%)/ Land	7.4	7.1
Groove	7.4	9.2
Tangential tilt margin (deg)/ Land	± 0.55	± 0.40
Groove	± 0.56	± 0.40
Radial tilt margin (deg)/ Land	± 0.73	± 0.52
Groove	± 0.64	± 0.44
Defocus margin (μm)/ Land	± 2.2	
Groove	± 1.7	
Detrack margin (μm)/ Land	± 0.1	
Groove	± 0.1	

CONCLUSION

High areal densities have been achieved in conventionally structured magneto-optical disks by magnetic field modulation with laser pulse irradiation. A density of 2 Gb/in^2 enabled a capac-

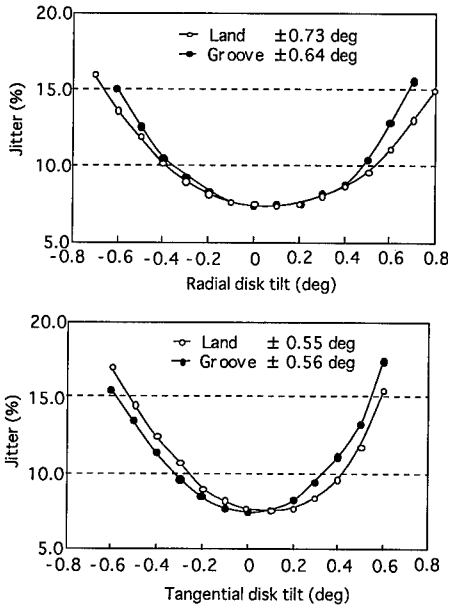

Fig. 10 Jitter as a function of radial disk tilt and tangential disk tilt in Experiment 1.

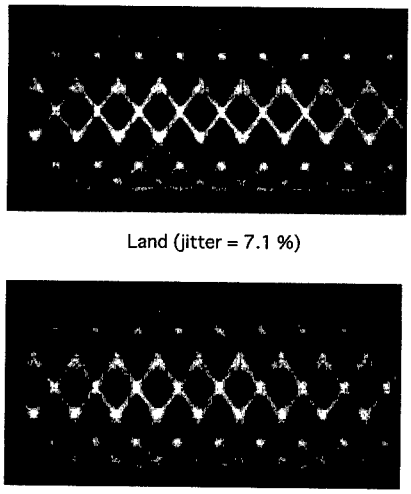

Fig. 11 Eye pattern of random data recorded for Experiment 2.

ity of 650 MB per 64 mm disk diameter for the next version of Mini Disc. A system with a capacity of 650 MB has been devoloped with acceptable margins for recording power and disk tilts in radial and tangential direction. Recording on land of 1.2 mm thick substrate conforms to current MD system.

A higher areal density has been confirmed by adopting an optical phase shifter for land and groove recording. Since the improvement of the carrier level and crosstalk cancellation is possible simultaneously, wide radial tilt margin of $\pm$ 0.73 deg for 0.5-μm land and $\pm$ 0.64 deg for 0.5-μm groove is obtained to get 3.7 Gb/in^2 even using 1.2 mm thick substrate. When an numerical aperture of 0.7 was used, substrate thickness was decreased to 0.6 mm to relax the coma aberration due to the disk tilt. The feasibility of 7.0 Gb/in^2 density is shown with a radial tilt margin of $\pm$ 0.52 deg for 0.36-μm land and $\pm$ 0.44 deg for 0.36-μm groove. A problem of land and groove recording is the rather small recording power margin. It can be improved by introducing deep groove technology in land/groove recording[13]. There is a condition in which the deep groove is optically equivalent to shallow groove adopted in this paper. Besides, further improvement of S/N ratio of MO media will allow 7.0 Gb/in^2 to be achieved in a practical system.

REFERENCE

[1] M. Kaneko, K. Aratani, and M. Ohta, Jpn. J. Appl. Phys., vol. 31, Part 1, No. 2B, pp. 568-575 (1992).
[2] Y. Murakami, N. Iketani, A. Takahashi, K. Ohta, and T. Ishikawa, Magn. Soc. Japan, vol. 17, Suppl. S1, p.201 (1993).
[3] H. Awano, H. Shirai, H. Watanabe, K. Shimazaki, M. Yoshihiro, and N. Ohta, Dig. Joint MORIS/ISOM, Yamagata 1997, Th-Q-33.
[4] T. Shiratori, E. Fujii, Y. Miyaoka, and Y. Hozumi, Dig. Joint MORIS/ISOM, Yamagata 1997, Tu-E-04.
[5] K. Aratani, T. Narahara, A. Fukumoto, S. Masuhara, N. Arakawa, Y. Takemoto, and Y. Takeshita, Jpn. J. Appl. Phys., vol. 35, pp. 433-436 (1996).
[6] T. Yoshida, Proc. IEEE, vol. 82, pp. 1492-1500 (1994).
[7] M. Shinoda, M. Kanno, S. Masuhara, M. Hattori, and M. Kaneko, Dig. Joint MORIS/ISOM, Yamagata 1997, Th-K-02.
[8] N. Miyagawa, Y. Gotoh, E. Ohno, K. Nishiuchi, and N. Akahira, Jpn. J. Appl. Phys. vol. 32, pp. 5324-5328 (1993).
[9] A. Fukumoto, S. Masuhara, and K. Aratani, Dig. Symp. on Optical Memory, Tokyo 1994, pp. 41-42.
[10] A. Fukumoto, S. Masuhara, and K. Aratani, Proc. SPIE vol. 2514, Optical Data Storage, San Diego 1995, pp. 374-382.
[11] N. Aoyama, Y. Morimoto, and T. Miyahara, J. Magn. Soc. Japan, vol. 20, Suppl. S1, pp. 233-238 (1996).
[12] A. Fukumoto, S. Kai, S. Masuhara, and K. Aratani, Dig. Joint MORIS/ISOM, Yamagata 1997, We-I-02.
[13] S. Morita, M. Nishiyama, and T. Ueda, Jpn. J. Appl. Phys., vol. 36, pp. 444-449 (1997).

NEAR-FIELD MAGNETO-OPTIC FIBER PROBE

M.A. Seigler, D.N. Lambeth
ECE Department, Carnegie Mellon University, Pittsburgh, PA 15213

ABSTRACT

A novel near-field magneto-optic fiber probe (NF-MOFP) for readback of ultra high density magnetic recording, or high resolution imaging of magnetic domains is described. This NF-MOFP consists of a partially metalized tapered fiber, as used in conventional near-field scanning optical microscopy (NSOM), with the subwavelength sized aperture coated with a reflective magneto-optic (MO) film. This device is then used in a manner similar to conventional NSOM. The properties of the MO film deposited on the fiber tip, the NF-MOFP's response to applied fields, and images of magnetic domains taken with the device are described.

INTRODUCTION

The areal density of magnetic recording has been increasing at about 60% a year since the early 1990's. While the areal density of state of the art commercial products is around 4 Gb/in^2, IBM recently announced an 11 Gb/in^2 laboratory demonstration [1]. In order for the 60% per year areal density increase to continue, 100 Gb/in^2 will need to be demonstrated by the year 2003. If conventional recording media continues to be used, it has been proposed by Charap et al. that serious thermal decay due to superparamagnetic grain sizes will be seen before this density is reached [2]. One proposed solution is to eliminate the grain structure by using magneto-optic (MO) recording where a continuously exchanged coupled media such as CoPt is employed. It has been proposed that CoPt, as made in the laboratory today, should support small enough domains for recording densities well in excess of 100 Gb/in^2 [3]. Hence, the areal density limit would not be set by the continuously exchange coupled media, but by the diffraction limited spot size of the writing

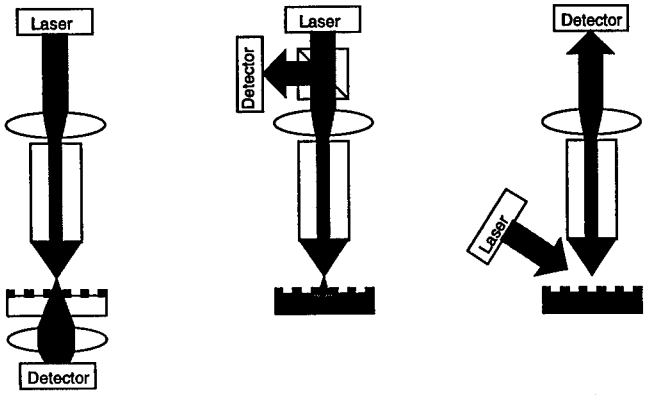

(a) (b) (c)

Figure 1: Some common NSOM setups: (a) illumination, (b) illumination/collection, (c) collection

Mat. Res. Soc. Symp. Proc. Vol. 517 © 1998 Materials Research Society

and reading light. Some researchers have proposed methods to extend the diffraction limit by using special multilayered media and recording techniques, such as MSR (magnetic super resolution) and MAMOS (magnetic amplifying magneto-optical system) [4,5]. Even when using these techniques the light that is writing and reading the magnetic domains is diffraction limited, and is the limiting factor in the areal storage density of the recording. This is where the benefits of near-field optics may help to increase the areal storage density.

Examples of combining common NSOM configurations, as shown in figure 1 [6], and conventional data storage methods using a rotating magnetic media, may be to either mount a coated tapered fiber onto a slider [3], or to fabricate a tapered channel waveguide on the backside of a slider [7]. Even, if one of these approaches is attempted, there may still be significant restraints on the type of overcoat, magnetic media, and disk substrate that could be used. Configuration 1(a) is limited to transparent samples while configurations 1(b & c) are constrained to imaging the first reflective surface. In addition, 1(a) would need detection optics on the opposite side of the disk that would have to remain aligned with the near-field probe at all times. Despite its limitations, the optical alignment of 1(b) is very attractive since both the illumination and detection are performed by the near-field aperture. This configuration suffers, however, from a low signal-to-noise ratio since the light not only has to pass through the subwavelength aperture to illuminate the sample, but after scattering off the sample, the light must be recollected by that same small aperture.

The new near-field magneto-optic fiber probe (NF-MOFP) that we propose is illustrated in figure 2. Our probe is very similar to the probe shown in figure 1(b), but with a soft magnetic film covering the subwavelength aperture. The light that would normally illuminate the media through the aperture now reflects off the MO film on the probe tip, and this reflected light then travels back up the fiber to the detection optics. The light never actually exits the near-field aperture. The magnetic state of the MO film on the fiber-tip, and thus the polarization state of the light reflecting off the MO film, is modulated by the fringing fields from the magnetic media passing in close proximity to the NF-MOFP. The modulated polarization state of the light is then used to form a readback signal for data storage, or to

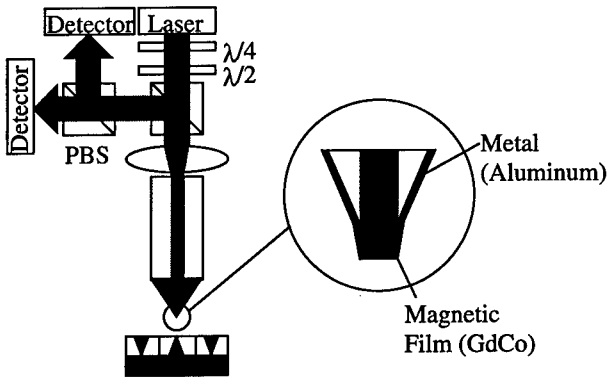

Figure 2: The proposed NF-MOFP. The exploded portion shows the magnetic film coating the subwavelength aperture where the light would normally exit.

form an image of the magnetic state of the media. Since the light never exits the aperture to interact with the media, the signal from this NF-MOFP would not be affected by the optical properties of the media, but by the magnetic fringe fields from the media. This may allow our probe to image magnetic samples that conventional NSOM may not, such as conventional longitudinal magnetic recording media. Obviously, if this type of probe were to be used in a storage device a separate recording transducer may be needed for writing.

EXPERIMENT

An ideal MO film for this probe should have a low coercivity, perpendicular magnetic orientation, large Kerr rotation, high Curie temperature, good corrosion resistance, and be able to be deposited on glass (optical fiber). GdCo seems to be a good compromise for these requirements, and its magnetic properties are well documented from its use as a bubble material [8]. GdCo can be deposited on glass with a perpendicular magnetic orientation, with a reasonable coercivity, Kerr rotation and curie temperature, but its corrosion resistance is limited (see the next section or Ref. 8 for more information on these characteristics). In order to characterize GdCo, it was RF sputtered onto Corning 7059 glass substrates using a target made by bonding Gd pieces to a pure Co sputtering target. A bias voltage was applied to the substrate to control the film composition and anisotropy. Since GdCo quickly oxidizes, and looses its perpendicular anisotropy, all GdCo films were capped with a thin layer (40nm) of sputtered AlTi. The MO properties of the GdCo were measured using an MO loop tracer using 633 nm light. While the behavior of GdCo films on glass substrates can be fully characterized, it is not known how the magnetic film is going to behave when deposited on the end of a partially metalized tapered fiber. The film's behavior when deposited on the fiber tip may be effected by the shape and roughness of the tip, roughness of the metal forming the subwavelength aperture, and the elevated, but not accurately known, temperature of the tip during operation.

Tapered optical fibers were fabricated by etching a standard single mode optical fiber in the meniscus formed by a 40% HF solution and silicon oil [9,10]. The sides of the tapered fibers were then coated with copper using deposition by laser ablation leaving an uncoated aperture at the tip of the fiber. The highly directional deposition using laser ablation is ideal for fabricating partially metalized tapered fibers which depend on shadowing of the tip to form the aperture at the tip.

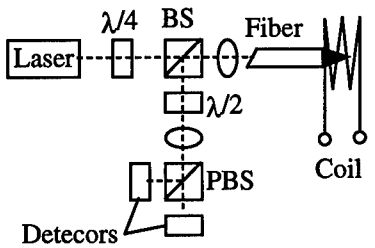

Figure 3. (a) The test setup used for testing cleaved MOFP and NF-MOFP. When taking an image with the cleaved fiber probe the fiber was scanned above the sample using stepper motors with no tip-sample spacing feedback control.

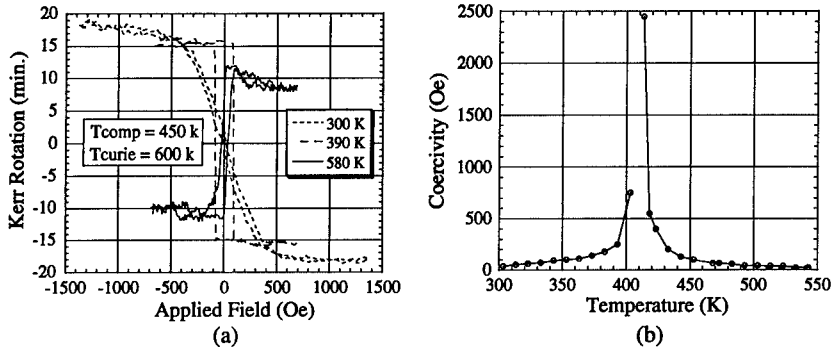

Figure 4. (a) MO loops at different temperatures for a typical GdCo film. (b) Coercivity versus temperature for a typical GdCo film.

GdCo was deposited on the end of a cleaved (not tapered) fiber as a starting point and tested using an MO loop tracer, as sketched in figure 3, using 488 nm light. MO loops were taken to verify that the GdCo film still had good magnetic and optical properties when deposited on the end of the cleaved fiber, and that its Kerr rotation could be detected. The aperture of a partially metalized tapered fiber was then coated with GdCo, and MO loops were taken.

RESULTS

Stahelin et al. have shown that the tip of a partially metalized fiber fabricated by locally melting and pulling can reach temperatures of 500 K with 3.3 mW of optical power coupled into the fiber. Chemically etched fibers have a shorter tapered region, allowing for better heat conduction away from the tip and into the bulk fiber, and less light absorption by the side walls of the tapered region. Hence for a given input power the tip should be cooler than it would for a pulled fiber geometry [11,12]. MO loops of a typical GdCo film deposited on a glass substrate are shown in figure 4(a) for three different temperatures. This figure shows

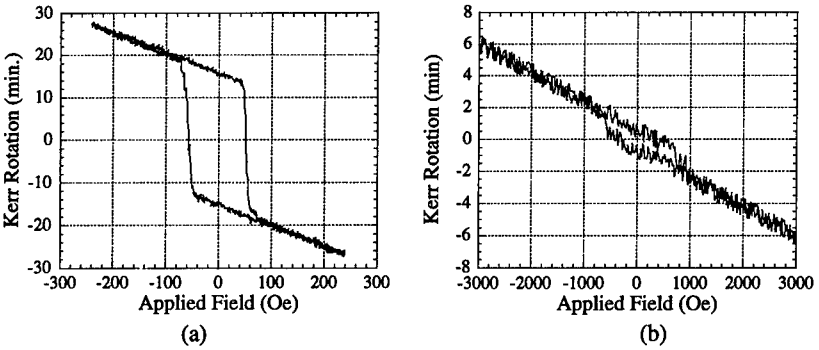

Figure 5. (a) A typical MO loop of a cleaved MOFP. The magnetic field was applied using a simple coil. (b) An MO loop of a NF-MOFP. The magnetic field was applied using a c-core magnet driven by a coil in order to achieve the relatively large fields.

that GdCo can have good magnetic and optical properties at high temperatures. Figure 4(b) shows the coercivity as a function of temperature for a typical film. As can be seen from this graph, the coercivity can be made to be constant over a wide range of temperatures, but it is desirable to have an even lower coercivity than has been achieved here.

Once GdCo had been deposited on glass substrates with good magnetic and optical properties, it was deposited on the ends of cleaved optical fibers. Figure 5(a) shows a typical MO loop of a cleaved MOFP, taken using the setup shown in figure 3.

Partially metalized tapered fibers were fabricated as described above, and the polarization extinction ratio of the transmitted light was measured for each fiber. Tapered fibers with extinction ratios of over 300 have been fabricated while ratios of 50-100 are more common. The reason for some partially metalized tapered fibers having better extinction ratios than others is being investigated at this time. The fibers with good extinction ratios, above 100, were then used, metalized as shown in figure 2, to produce NF-MOFPs. These tips were tested using the setup shown in figure 3, and the resulting MO hysteresis loop of one of our probes is shown in figure 5(b). The partially metalized tapered fiber used to fabricate this NF-MOFP had an extinction ratio of about 200:1 and the subwavelength aperture had a diameter of about 200nm.

A perpendicularly oriented CoCr sample, representative of magnetic recording media, was saturated in one direction, and then a large domain was written on it using a bar magnet. The cleaved fiber probe was then used to image the magnetic transition in the CoCr sample. Due to the high coercivity of the GdCo film on the fiber tip, there was hysteresis in the image when scanning back and forth over the transition. An AC magnetic field, with a magnitude just below the cleaved MOFP's coercivity, was applied to the fiber tip to remove this hysteresis. Figure 6(a) shows minor MO hysteresis loops of the cleaved MOFP used for this imaging, and figure 6(b) shows the image taken of the CoCr sample. Because of the approximately 800 Oe coercivity of the GdCo film of the NF-MOFP a sample could not be imaged with this probe.

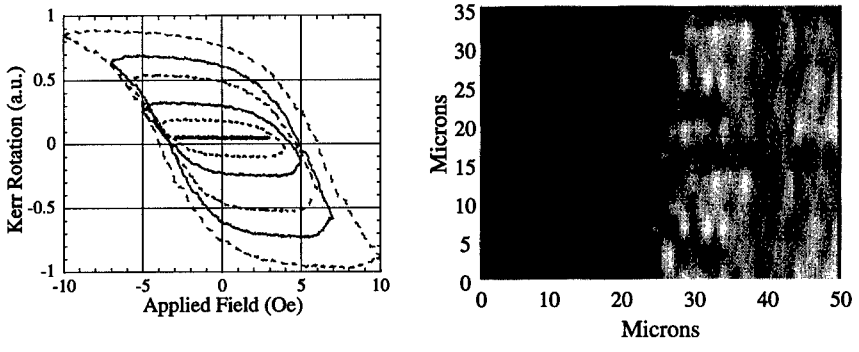

(a) (b)

Figure 6. (a) Minor loops of a GdCo film on a cleaved MOFP with an AC magnetic field applied. (b) Image of a magnetic transition in a perpendicularly oriented CoCr sample taken with the cleaved MOFP.

CONCLUSIONS

GdCo films were deposited on the end of cleaved optical fibers and partially metalized tapered optical fibers, and MO loops of these devices were taken. The coercivity of both the cleaved MOFP and NF-MOFP were higher than desired, but applying an AC bias field to the cleaved MOFP successfully increased its sensitivity to an applied field. The cleaved MOFP, with an AC bias applied, was used to successfully image a perpendicularly oriented CoCr sample. We are currently working on decreasing the coercivity of the NF-MOFP by varying sputtering conditions, and we are investigating the use of other materials instead of GdCo.

ACKNOWLEDGMENTS

I would like to thank Hen Gong for supplying me with the CoCr sample and Dan Razum for his early work in developing our near-field scanning optical microscope. This work was supported in part by the National Science Foundation under grant #ECD-8907068.

REFERENCES

[1] Dave Thompson, seminar given at Carnegie Mellon University
[2 Pu-Ling Lu and S.H. Charap, IEEE Trans. Mag. **30** (6), 4230-4232 (1994)
[3] M.H. Kryder, Optoelectronics-Dev. and Tech. **10** (3), 297-302 (1995)
[4] K. Aratani, K. Fukumoto, M. Ohta, M. Kaneko, and K. Watanabe, Proc. SPIE **1499**, 209-215 (1991)
[5] H. Awano, S. Ohnuki, H. Shirai, N. Ohta, A. Yamaguchi, S. Sumi, and K. Torazawa, Appl. Phys. Lett. **69** (27), 4257-4259 (1996)
[6] Michael Paesler and Patrick Moyer, Near-Field Optics: Theory, Instrumentation, and Applications, (John Wiley & Sons, Inc., 1996), pp.14
[7] Bernard W. Bell, U.S. Patent No. 5 199 090 (3 March 1993)
[8] A.H. Eschenfelder, Ferromagnetic Materials, Vol. 2, (North-Holland Publishing Company, 1980), pp.345-380
[9] K. Takahashi, J. Colloid Interface Sci. **134** (1), 181-187 (1990)
[10] S. Mononobe, M. Ohtsu, J. Lightwave Tech. **14** (10), 2231-2235 (1996)
[11] M.Stahelin, M.A. Bopp, G. Tarrach, A.J. Meixner, and Zschokke-Granacher, Appl. Phys. Lett. **68** (19), 2603-2605 (1996)
[12] B.I. Yakobson, A. Larosa, H.D. Hallen, M.A. Paesler, Ultramicroscopy **61**, 179-185 (1995)

READOUT OF MAGNETIC FILM-BASED MEMORIES BY NONLINEAR-OPTICAL MAGNETIC KERR EFFECT

T.V. MURZINA, N.V. DIDENKO, A.A. FEDYANIN, A.V. MELNIKOV, T.V. MISURYAEV, O.A. AKTSIPETROV
Physics Department, Moscow State University, Vorobyovi Gori, 119899 Moscow, Russia, aktsip@astral.ilc.msu.su

ABSTRACT

Magnetic field induced second harmonic generation (MSHG) is suggested as a nonlinear-optical readout for magnetic film-based memories: Systematic studies of the nonlinear-optical magnetic Kerr effect and MSHG interferometry are carried out for (i) magnetic rare-earth iron garnet films, (ii) Gd-containing Langmuir-Blodgett films and (iii) Co_xCu_{1-x} granular films. The magneto-induced nonlinear-optical properties of thin films being used for recording the information can be easily distinguished by the MSHG nondestructive probe. An estimation of the signal-to-noise ratio (readout error) shows an acceptable value of the magnetic contrast for this potential readout.

INTRODUCTION

The development of optical storage technology has given rise recently to the search for new magnetic materials for high density memories. Apart from the traditional magneto-optical materials, e.g., magnetic rare-earth iron garnet films, a number of new magnetic nanostructures and composite materials have been developed, such as magnetic multilayers and granular films with magnetic nanocrystals. At the same time, the potential use of new memories leads to the search for effective nondestructive readout techniques. In the present paper magneto-induced second harmonic generation (MSHG) is suggested as a readout for magnetic memories. The choice of the MSHG probe as a readout is motivated by the high sensitivity of the quadratic response to the magnetic properties of nanostructures and low-dimensional systems [1]. Therefore, the wavelength of readout fundamental radiation can be chosen far from electronic resonances of the film, which makes this probe nondestructive, while the wavelength of the SHG radiation can be resonant and thus provide an effective SHG output.

In the present paper the potential of the SHG readout of magnetic memories is demonstrated with the examples of (i) Bi-containing iron garnet films, (ii) thin Co-Cu granular films and (iii) organo-metallic Langmuir-Blodgett (LB) films containing monolayers of Gd ions. The last two systems are of special interest, as the size of the storage unit can be less than 60 nm for the case of Co nanocrystals in granular films and is about 5 nm for a single period of Gd-containing structure in LB films

The SHG readout discussed is based on the nonlinear-optical magnetic Kerr effect (NOMOKE), i.e., magneto-induced changes in the SHG intensity and rotation of polarization of the second harmonic (SH) wave. This is a consequence of the general property of changing the nonlinear susceptibility of a material as a result of information recording. The NOMOKE effect has been studied for thin metallic films and multilayers both experimentally [1,2] and theoretically [3,4]. As compared with the magneto-optical Kerr effect (MOKE), a large magneto-induced alteration of the SHG intensity, magneto-induced phase shift and polarization rotation of the SH wave were obtained. For the case of the (210)-oriented Bi-containing iron-garnet films, sufficient magnetization induced changes of the SHG intensity were demonstrated for off-resonant and near-resonant fundamental radiation [2,5]. The SHG readout has already been suggested for the photochromic films and iron garnet films in [6].

Mat. Res. Soc. Symp. Proc. Vol. 517 © 1998 Materials Research Society

EXPERIMENT AND RESULTS

The output of a Q-switched YAG:Nd^{3+} laser at 1064 nm, a pulse duration of 15 ns and a repetition rate of 12.5 Hz is used as the fundamental radiation in the nonlinear-optical experiments. The SHG signal from the films is selected by bandpass filters and detected by a photomultiplier tube (PMT) and gated electronics. To improve the signal-to-noise ratio in nonlinear-optical measurements, the reference SHG channel is used for normalizing the SHG signal reflected from the sample to the square of the input laser pulse intensity. The pump pulse intensity is about 1 MW/cm^2 for a laser spot diameter of about 1 mm. The DC-magnetic field parallel to the film surface is applied by mounting the samples between the poles of the electromagnet in the transversal and longitudinal NOMOKE configurations [2].

The magneto-induced phase shift of the SH wave [7] is measured in the NOMOKE experiments by the use of a thin SnO_2 film as a source of the reference SH wave. The phase shift between the SH waves reflected from the sample and generated by the reference sample is changed using the different dispersions in air at the fundamental and SH frequencies. It is varied by changing the distance between the reference and the sample.

For the quantitative characterization of the magnetoinduced changes of the reflected SHG intensity the magnetic contrast $\rho_{2\omega}=(I_{2\omega}^{M+}-I_{2\omega}^{M-})/(I_{2\omega}^{M+}+I_{2\omega}^{M-})$ is introduced, where $I_{2\omega}^{M+/-}$ is the SHG intensity for the opposite directions of the magnetization. The magneto-induced rotation of the SH wave polarization is measured by the rotation of the analyzer as DC-magnetic field is applied to the sample.

Iron-garnet films

The samples studied are Bi containing noncentrosymmetric iron garnet films grown by a liquid phase epitaxy technique from a $PbO\text{-}Bi_2O_3\text{-}B_2O_3$ flux melt on nonmagnetic (Ga,Gd) garnet (111) substrate. The magnetization easy axis is oriented in the plane of the film. The thickness of the films is about 5 μm. Figure 1 shows the dependence of the SHG intensity on the external magnetic field strength for the geometry of the transversal NOMOKE. A p-polarized fundamental radiation is used. Odd in magnetization variations of the MSHG intensity are observed for an 50^0 angle of incidence of the fundamental radiation. NOMOKE magnetic contrast is about $\rho_{2\omega}=(3\pm1)\times10^{-2}$ for the saturating value of the DC-magnetic field of 0.6 kOe. This is enough for distinguishing the magneto-induced states of the iron garnet film by means of the MSHG. It is worth noting that the IR radiation being off-resonant does not disturb the information recorded, allowing use of the SHG probe as an effective readout for memories based on these films.

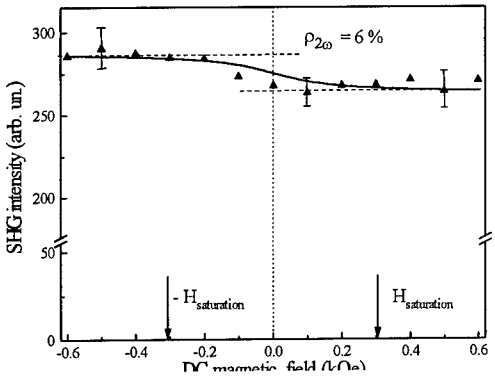

Fig. 1. Transversal nonlinear-optical magnetic Kerr effect for rare-earth iron garnet film.

Co-Cu granular films

The samples studied are granular Co_xCu_{1-x} films comprised by Co nanocrystals in a Cu matrix. Films 200 nm thick are prepared using a *e*-beam co-deposition system and annealed for 10 min at 850 K. The STM studies indicate that the granules of about 60-100 nm size are present in the film structure. It was shown [8] that a system containing nanoparticles could reveal bulk electrodipole susceptibility that arises from the breakdown of the inversion symmetry of the system on the fundamental wavelength scale due to the noncentrosymmetric shape of the nanoparticles and their chaotic distribution.

Figure 2 shows the MSHG intensity as a function of analyzer rotation angle (the SHG polarization diagrams) studied for the transversal NOMOKE geometry. The SHG polarization diagrams are measured for the p-polarized fundamental radiation and for the opposite directions of the DC-magnetic field of 1 kOe applied. The magnetic contrast is found to be $\rho_{2\omega}=(4\pm1)\times10^{-2}$ at an angle of incidence of 50°. The magnetic contrast measured in the linear MOKE experiments at the SH wavelength is $\approx0.1\times10^{-2}$.

As in the case of the iron-garnet films, the presence of *the linear* (*odd*) in magnetization M effect in magnetoinduced SHG intensity is obtained. Thus two states of the film corresponding to the opposite directions of the external magnetic field offer potential for developing magneto-optical memories.

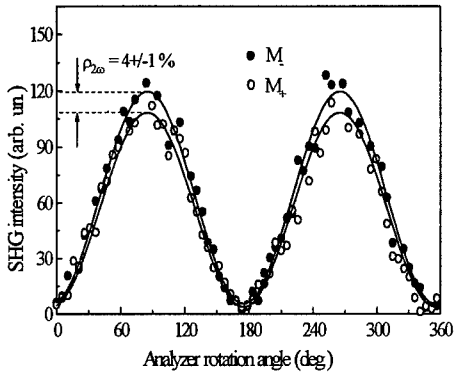

Fig. 2: Polarization diagrams of the transversal NOMOKE in $Co_{0.48}Cu_{0.52}$ granular film for the opposite directions of magnetization $M_{+/-}$ (φ=0 corresponds to the p-polarized SH wave).

Organo-metallic Gd-containing Langmuir-Blodgett films

The films are prepared by the Langmuir-Blodgett technique from a solution of stearic acid in chloroform (2×10^{-4} M) spread on the water-subphase containing 5×10^{-4} M Gd^{3+}. A fused quartz substrate is used. The SHG from the quartz substrate and the LB films of pure stearic acid are found to be negligibly small compared with the SHG signal from the Gd containing LB films. A period of the Gd-containing LB film consists of the monolayer of Gd ions surrounded by two monolayers of stearic acid. The thickness of the period is about 5 nm. The area per Gd ion in the monolayer is about 10 $Å^2$. The electron paramagnetic resonance (EPR) studies carried out indicate the existence of magnetic ordering in these films at room temperature, the saturating magnetic field being about 0.7 kOe [9].

The SHG output is found to be highly isotropic and depolarized. Figure 3 shows the SHG polarization diagrams measured in the configuration of the longitudinal NOMOKE for the opposite directions of the DC-magnetic field. The s-polarized fundamental radiation is used. The magneto-induced rotation of the SH wave is about 12^0. This effect is accompanied by the reversible in magnetization changes in the intensity of the reflected SHG. The magnetic contrast corresponding to the saturation of the magnetization is found to be $\rho_{2\omega}=$

$(3\pm1)\times10^{-2}$, which sufficiently exceeds the linear optical analogue measured for the case of the pure Gd surface and can be easily distinguished by means of the MSHG.

Figure 4 shows the interference pattern of the SHG intensity measured for the configuration of the longitudinal NOMOKE. The s-polarized fundamental radiation is used. The magneto-induced change in the SH wave phase is about $115^0\pm10^0$.

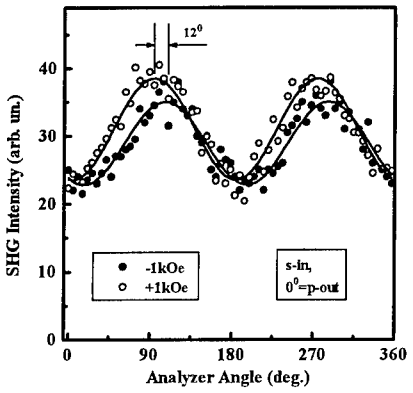

Fig. 3. Polarization diagrams of the s-polarized SHG intensity measured for the opposite directions of the magnetic field in the geometry of the transversal NOMOKE.

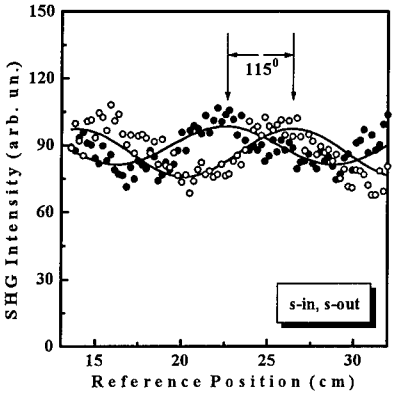

Fig. 4. MSHG phase measurements for the longitudinal NOMOKE in 40-periods' Gd-containing LB film.

DISCUSSION

The experimental results described above testify that the magneto-induced states of the materials studied can be clearly distinguished by the MSHG readout. The readout parameters can be the SHG intensity or the polarization and/or phase of the SH wave. It should be noted that for novel magnetic systems such as LB films, containing monolayers of magnetic ions, and granular magnetic films, this technique is nondestructive. This stems from the reversible character of the dependence of the SHG intensity on the input power.

The number of misreading (readout error (RE)) is the key parameter for the characterization of the optical readout. In our case it can be determined as follows: $\eta=(1-erf(\rho_{2\omega}/2\Delta\rho_{2\omega}))/2$, where $erf(x)=2/\sqrt{\pi}\int_0^x\exp(-y^2)dy$ is the error function [10]. For the magnetic granular and organo-metallic LB films the value of the magnetic contrast can be assumed to be $\rho_{2\omega}=(4\pm1)\times10^{-2}$. Thus the η value can be estimated to be less than 10^{-3}. This seems promising from the point of view of developing a novel readout method.

RE for the magneto-induced SHG interferometry is much less than for the case of the MSHG intensity changes, while this nonlinear-optical technique is more complicated from the experimental point of view.

It should be noted that the value of the magnetic contrast $\rho_{2\omega}$ can be increased, and consequently the error in distinguishing between the magneto-induced can be diminished. Actually, the magnetic contrast $\rho_{2\omega}$ in the first approximation is proportional to the ratio of

the magneto-induced nonlinear susceptibility $\chi^{(2)}_{mag}$ to the nonmagnetic (crystallographic) one $\chi^{(2)}_{cryst}$. Thus the value of $\rho_{2\omega}$ can be increased by using a near-resonant fundamental or SHG radiation. It has been already shown that for the case of the iron-garnet films the magneto-induced rotation of the SH wave polarization for the nonlinear-optical Faraday effect can be dozens of degrees as the near-resonant fundamental radiation is used [11].

CONCLUSIONS

In conclusion, magnetic field induced optical second harmonic generation is suggested as a readout for magnetic films-based memories. Systematic studies of MSHG are carried out for magnetic rare-earth iron garnet films, Gd-containing Langmuir-Blodgett films and Co-Cu granular films. The magneto-induced states of the films being used for recording can be distinguished by the MSHG nondestructive probe. An estimate of the readout error shows an acceptable value of the magnetic contrast for the MSHG readout.
Thin film systems studied in this paper serve the illustration of the novel readout which is based on *the general property of changing the nonlinear-optical properties of any material as a result of any information recording*. Apart from thin magnetic films studied, this method can be potentially used for a wide variety of storage systems, e.g. ferroelectric and photochromic memories.

ACKNOWLEDGMENTS

This work was supported by INTAS-93 grant 370 (ext), the Russian Foundation of Basic Research (RFBR) grant for Russian Leading Scientific Schools 96-15-96420, RFBR grants 97-02-17919, 97-02-17923, RFBR-DFG grant 98-02-04092, Federal Integration Program "Center of Fundamental Optics and Spectroscopy", Program of Russian Ministry of Education "Universities of Russia" and Programs of Russian Ministry of Science "Physics of Solid State Nanostructures" and "Fundamental Metrology".

REFERENCES

[1] J.Reif, C.Rau, E.Matthias. Phys. Rev. Lett. **71,** p. 1931,1934 (1993).

[2] Th. Rasing, J. Magn. Magn. Mater. **165**, p. 35 (1997).

[3] U. Pustogowa, T.A. Luce, W. Hübner, K.H. Bennemann. J. Appl. Phys. **79**, p. 6177,6180. (1996).

[4] U. Pustogowa, W. Hübner, K.H. Bennemann. J. Magn. Magn. Mater. **148**, p. 269,272 (1995).

[5] O.A. Aktsipetrov, V.A. Aleshkevich, A.V. Melnikov, T.V. Misuryaev, T.V. Murzina, V.V. Randoshkin. J. Magn. Magn. Mater. **165**, p. 421 (1997).

[6] O.A. Aktsipetrov, A.A. Fedyanin, A.V. Melnikov, E.D. Mishina, and T.V. Murzina, Jpn. J. Appl. Phys. **36**, p. 48 (1998).

[7] R.Stolle, K.J.Veenstra, F.Manders, Th.Rasing, H. van den Berg, N.Persat. Phys. Rev. B, **55**, p. R4925, R4927 (1997).

[8] O.A. Aktsipetrov, P.V. Elyutin, A.A. Fedyanin, A.A. Nikulin, and A.N. Rubtsov, Surf. Sci. **325**, p. 343 (1995).

[9] A.M. Tishin, Yu. A. Koksharov, J. Bohr, G.B. Khomutov, Phys. Rev. B, **55,** p. 17 (1996).

[10] G.A. Korn, Th. M. Korn, Mathematical Handbook, McGraw-Hill Book Company, New York, 1968, p. 514.

[11] V.V.Pavlov, R.V.Pisarev, A.Kirilyuk, Th.Rasing J. Appl. Phys. **81**, p. 4631,4633 (1997).

Part IV

Diluted Magnetic Semiconductors and Other Materials

DILUTED MAGNETIC SEMICONDUCTOR THIN FILMS AND MULTILAYERS

J. K. FURDYNA
Department of Physics, University of Notre Dame, Notre Dame, IN 46556
furdyna @ nd.edu

ABSTRACT

We review the properties of diluted magnetic semiconductor (DMS) thin films and multilayers, with special attention to their usefulness in magneto-optical device applications. We begin with the most widely studied DMS family, i.e., alloys of II-VI semiconductors involving Mn ions. Prospects and challenges are discussed for achieving $II_{1-x}Mn_xVI$-based non-reciprocal devices; and for devices operating in the far infrared. We also consider the unique advantages which DMSs offer for probing the properties of semiconductor heterostructures. We then discuss *ferromagnetic* DMSs, including those based on the III-V semiconductor family. And we briefly review the status of hybrid ferromagnetic-semiconductor structures achieved through recent advances in epitaxy of new materials.

INTRODUCTION

Diluted magnetic semiconductors (DMSs) are semiconducting alloys in which part of the lattice has been replaced by substitutional magnetic ions. II-VI semiconductors in which the group-II element is replaced by a transition metal ion (e.g., $Cd_{1-x}Mn_xTe$, $Zn_{1-x}Mn_xSe$) are the best-known examples of such systems. Many such DMS alloys (e.g., cubic $Cd_{1-x}Mn_xSe$, and *all* cubic $II_{1-x}Mn_xVI$ alloys with a high Mn content, including their x = 1 end points) can *only* be fabricated in thin film form, making them natural candidates for incorporation in thin film geometries, which constitute the subject of this paper.

The rich physics of DMS materials [1] (e.g., enormous Zeeman splittings of electronic levels, giant Faraday rotation, formation of magnetic polarons, etc.), when combined with the new degrees of freedom that characterize semiconductor multilayers (quantum confinement, superlattices, modulation doping, etc.) hold promise of unprecedented opportunities both for fundamental studies and for possible magneto-optical applications. To illustrate these opportunities and their relevance to integrated optics, we will use many of the results obtained on thin film structures of the most widely studied group of DMSs, the $II_{1-x}Mn_xVI$ alloys. However, a number of new materials are now emerging beyond this "traditional" DMS family (most notably $III_{1-x}Mn_xV$ alloys, II-VI-based *ferromagnetic* systems, and multilayers involving Mn-based magnetic thin films [2]), and much of this paper will be devoted to reviewing the status and future prospects of these new materials systems. Since developments in this area are relatively recent, an attempt will be made to provide, if not a complete, at least a representative set of references for the convenience of the interested reader.

Finally, we note that the objective of this paper is to discuss those novel phenomena displayed by the DMS films which may be of interest in the context of integrated magneto-optics. Thus we will not discuss issues of strictly magnetic interest, such as 2D magnetism, antiferromagnetic long range order in thin films and multilayers, etc. Rather, we will focus primarily on the interaction between band electrons and localized magnetic ions (the so-called "sp-d interaction"), which leads to enormous Zeeman splittings of electronic eigenstates when a magnetic field is applied. This results

Mat. Res. Soc. Symp. Proc. Vol. 517 © 1998 Materials Research Society

in significant field-induced modifications of the band structure, that can be harnessed to produce striking magnetooptical phenomena -- especially so in multilayers.

THE sp-d EXCHANGE AND BAND-OFFSET TUNING

As has been remarked, one of the most interesting mechanisms characteristic of DMSs is the sp-d exchange interaction of band electrons with localized magnetic moments (e.g., those associated with Mn^{++} ions). As a consequence of this sp-d exchange the spin-up and spin-down states of electronic levels (e.g., band edge energies, shallow impurity states, etc.) experience enormous Zeeman splittings when a magnetic field is applied, that can achieve values of as much as 100 meV at low temperatures in relatively modest magnetic fields. We will not discuss the underlying physics of this sp-d exchange, since it has been extensively presented in the literature [1], but rather will focus on its effect on thin film structures involving DMSs. It is important to appreciate, however, that the above interaction is inherently a spin phenomenon. The electronic spin -- which in the context of semiconductor physics has traditionally been only of academic interest -- is now playing a central role.

One of the most interesting magnetooptic manifestations of the above exchange phenomena arises in thin film systems comprised of alternating DMS and non-DMS layers. Since the band edges of the DMS material experience a large Zeeman shift, while the corresponding splitting in the non-magnetic layers is negligible by comparison, we can use this splitting to "tune" the valence and conduction band offsets simply by applying an external magnetic field -- thus tuning the properties of the multilayer as a whole. Furthermore, since such tuning is spin-selective (electrons with one spin orientation in the DMS layers experience a large upward shift of the band edge, while those with the opposite spin experience a comparable downward shift), this band-offset tuning also results in *spin segregation:* electrons with opposite spin orientation can be separated into different layers of the multilayer structure.

This phenomenon has been used to form "spin superlattices" [3,4]; to convert type-II band alignment into type-I, and vice versa [5]; to control the coupling between double quantum wells separated by a DMS barrier [6]; etc. Although these effects are extremely interesting, their impact has been primarily on basic studies, because the Zeeman splitting which underlies the above effects is large only at low temperatures (typically below 10K). Even with this limitation, however, one aspect of band-offset tuning has already had a major -- albeit indirect -- practical application, in the form of "mapping" of electron probability distributions in various semiconductor heterostructures [7]. For example, this DMS property has been used to determine that states at energies above the barriers are -- perhaps counter-intuitively -- localized *in the barrier layers* [8]. It has also been used to show that even a *single barrier* can quasi-localize states from the above-barrier continuum [9]. And band-offset tuning was instrumental in demonstrating that direct (type-I-like) excitons dominate excitonic absorption in type-II superlattices [10]. We emphasize that all these phenomena are universal; the DMS-based heterostructures were only used as a tool for observing them, thus increasing our understanding of semiconductor heterostructures generally.

DMS-BASED NON-RECIPROCAL DEVICES

One of the most spectacular and most widely known phenomena exhibited by II-VI-based DMSs is an enormous Faraday rotation. For example, at liquid helium temperatures $Cd_{1-x}Mn_xTe$ displays rotations of the order of 1000° in a 1 mm length and a field of 1 kG with relatively little loss [11]. This feature immediately suggests the suitability of DMSs for applications as optical isolators, modulators, and phase shifters. Although the large Faraday rotation in DMS media falls off rapidly with increasing

temperature, non-reciprocal devices referred to above typically require rotations of "only" 45° or 90°. Since rotations of this magnitude can readily be attained at room temperature [12], the possibility of fabricating a DMS-based optical isolator has long been of interest [13], particularly for protecting lasers which serve as relay-sources in optical fiber communications in the important wavelength region of 1.3 to 1.6 μm from accidental surges of reflected signal. We will therefore discuss the options for Faraday rotation devices in the context of thin films and their integration.

As has been remarked, to construct an optical isolator one requires a rotation of 45°. Faraday rotation in a DMS material can be conveniently expressed in the form [14]

$$\theta = \frac{\sqrt{F_0}}{4\hbar c}\,\frac{(\beta - \alpha)}{\mu_B}\,M\,\frac{\hbar^2\omega^2}{(E_g^2 - \hbar^2\omega^2)^{3/2}}\,d\,, \qquad (1)$$

where M is the magnetization, E_g is the energy gap of the DMS material, α and β are the s-d and p-d exchange constants, μ_B is the Bohr magneton, d is the thickness of the sample, ω the operating frequency of light, and F_o is a constant involving parameters such as the interband matrix element, as defined in Bartholomew *et al.*, Ref. [14]. From Eq. (1) we see that θ is proportional to the magnetization of the magnetic sublattice of the DMS, the length of the optical path, and the proximity of the wavelength of interest to the energy gap of the DMS material. Optimization of one or more of these parameters (M,d, or E_g) can be used to increase the effect, but each of these approaches has its own limitations. The behavior of magnetization M in traditional (i.e., $II_{1-x}Mn_xVI$) DMSs is the primary stumbling block, since M decreases rapidly as a function of increasing temperature. We can increase θ by using materials with an energy gap close to the desired frequency, but then we face the trade-off with increasing losses, since the near-band-edge absorption also increases as $\hbar\omega \rightarrow E_g$.

With the advent of DMSs in layer form, however, new opportunities become available, that should be considered in the present context. Although the films are thin (typically limited to 5 μm or less), the quality of the film material is generally superior to its bulk counterpart. The thickness issue constitutes an obvious limitation, but it may be possible to circumvent this in one of two ways.

Enhancement of Faraday rotation by multiple reflections

The first of these applies to the geometry where both light propagation and magnetic field are normal to the film. The obvious limitation of this geometry is the small thickness of the film. However, here one can increase the Faraday rotation by using multiple reflections. It is a characteristic of non-reciprocal propagation phenomena that the rotation in a slab increases as the transmitted beam is reflected back and forth between the interfaces of the sample, simply as the number of reflections. Thus, if a DMS medium is placed in a high-Q cavity, the rotation will increase essentially by the Q of the cavity. The last several years have seen enormous advances in semiconductor microcavities at optical wavelengths, in connection with work on vertical-cavity surface emitting lasers. Such cavities typically involve distributed Bragg reflectors (DBRs) that are grown epitaxially by MBE or MOCVD, in the same process as the fabrication of the active layer, and have reflectivities reaching 99.9%.

This technology can be readily tapped to achieve enhanced Faraday rotation in epitaxially-grown DMS layers. With good quality DBRs (i.e., with $Q \approx 1000$) one should

then achieve rotations enhanced by three orders of magnitude. A 1 μm layer of CdMnTe would then manifest, in such a cavity, a rotation comparable to single-passage rotation observed in 1 mm of bulk material.

Faraday rotation in planar DMS waveguides

An area that has so far been conspicuously neglected in DMS films is the issue of non-reciprocal *guided wave propagation* in the layer plane, where one can easily achieve optical path lengths of 1 cm or so in high-quality materials. Although such guided wave propagation in DMSs in the presence of an external magnetic field has not been explored, there exists a vast literature on guided wave propagation in other gyrotropic media, that can be extended to DMS layers. The basic problem is that guided wave propagation in an epitaxial layer is of its nature linearly birefringent. When a magnetic field is applied, this birefringence reduces the Faraday rotation [15], thus acting against the desired figure of merit. However, the birefringence of the guided waves (which depends on the thickness of the film) can be counteracted by introducing a new birefringence of opposite sign, arising from strain (achieved through lattice mismatch), in a manner similar to that used in guided wave propagation in rare-earth iron garnets [16]. By choosing an appropriate combination of thickness and strain, it may be possible to balance out the two effects, thus achieving an essentially isotropic medium. Light propagating in the layer plane of the DMS film, along an applied magnetic field, would then exhibit Faraday rotation characteristic of bulk DMSs -- enabling the use of such films for non-reciprocal devices, that can be integrated with other semiconductor-based opto-electronic structures.

Enhancement of magnetization

It is clear from Eq. (1) that Faraday rotation is proportional to magnetization M, and can therefore be increased by devising schemes for increasing M. Here one should note that the well-known II-VI-based DMS materials involving Mn exhibit antiferromagnetic interactions between the Mn ions. That is, the magnetization increases with Mn concentration x for small x (up to $x \approx 0.10$ or so), but then saturates -- and actually *decreases* with further increase of x, vanishing for $x = 1.0$, as should be the case for a true long-range antiferromagnet. This is because the contribution of a given Mn ion to the magnetization tends to be partially cancelled (even in alloys) by the opposite contributions of its antiferromagnetically-oriented nearest neighbors. This is clearly illustrated in Fig. 1, which plots magnetization (in the form of an *effective* Mn concentration $\bar{x}$) as a function of the true Mn concentration x [17].

Various schemes have been proposed to reduce this undesirable fall-off of magnetization which occurs with increasing x, by designing structures that contain a maximum number of Mn ions with a minimum number of nearest neighbors. In bulk media this is possible by growing DMS materials in specific crystallographic forms, in which Mn atoms are ordered in such a way that they have fewer Mn nearest neighbors than they would in a random alloy. For example, in the tetrahedrally-coordinated crystal such as Cu_2MnGeS_4 which crystallizes in the stannite structure [18], Mn constitutes 25% of all atoms, but no Mn atom has a Mn nearest neighbor, resulting in a much greater magnetization than the maximum magnetization achievable in a random alloy with the *same* average Mn concentration of $x = 0.25$.

Epitaxy offers additional opportunities to also decrease the number of nearest neighbors, thus increasing the contribution *per Mn ion* to the overall magnetization. Consider $Cd_{1-x}Mn_xTe$ with $x = 0.50$. If, instead of growing a 1 μm thick layer of such alloy, we "interrupt" this alloy, say, every 30Å by a 10Å layer of CdTe, the Mn ions at

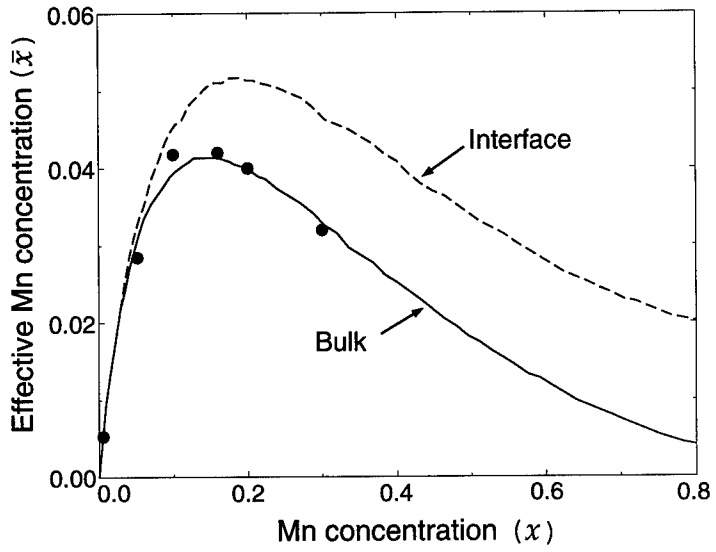
0.06
0.04
0.02
0.00
0.0
0.2
0.4
0.6
0.8
Effective Mn concentration ($\bar{x}$)
Mn concentration (x)
Interface
Bulk

Fig. 1

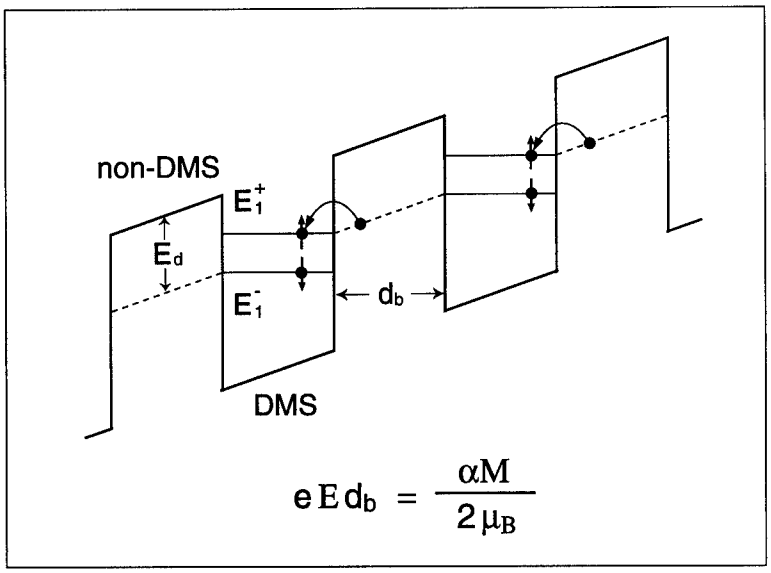
non-DMS
E_1^+
E_d
E_1^-
d_b
DMS
$eEd_b = \frac{\alpha M}{2\mu_B}$

Fig. 2

the interfaces see fewer Mn nearest neighbors than they would otherwise, resulting in a much greater contribution *of those interfacial ions* to the magnetization. What are the ideal dimensions (thicknesses of DMS and non-DMS layers), and which materials are to be used, is yet to be explored. For example, it is yet to be determined whether it is desirable -- or irrelevant -- that the non-DMS layers constitute barriers of such a superlattice for the purpose of maximizing the magneto-optical effects. That is, what is the importance of electron *localization* in the phenomena under consideration. But the general idea is to explore the effect of reducing the number of nearest Mn neighbors, so as to achieve a larger magnetization, thus enhancing the Faraday rotation -- as well as other effects that depend on Zeeman splitting within the DMS medium.

DMS-BASED FAR-INFRARED CASCADE LASER

Zeeman splittings of energy levels which occur in DMSs in "ordinary" magnetic fields of one Tesla or so typically correspond to the energies of far infrared photons in the wavelength range of 50 μm or longer. It is therefore natural to think of DMSs as potential candidates for detectors and/or sources for this very difficult region of the spectrum.

As an example of such application, consider the arrangement shown in Fig. 2. This was actually proposed some years ago [19], but has now become much closer to reality because of advances made in doping (and especially in modulation doping) of wide-gap II-VI-based DMSs [20]. The figure represents the conduction band of a superlattice consisting of DMS wells (e.g., ZnCdMnSe) and non-DMS barriers (e.g., ZnSe). E_1 is the ground state in the well. This state can be populated either by doping the wells directly, or by modulation doping. When a magnetic field is applied, the ground state splits into E_1^+ (spin-up) and E_1^- (spin-down) states. Applying an electric bias along the growth direction, one can make the E_1^- level in the right-hand well *resonant* with the E_1^+ state in the left-hand well when the following relation is satisfied:

$$eEd_b = \frac{1}{2}\frac{\alpha M}{\mu_B}, \qquad (2)$$

where E is the applied electric field, e the electronic charge, d_b the width of the barriers, and $\alpha M/2\mu_B$ gives the spin splitting energy $E_1^+ - E_1^-$. The electron in the E_1^- state in the right-hand well will then tunnel to the left with a spin-flip process, where it will go to the E_1^- state, returning to its original spin state as it emits a photon with an energy $E_1^+ - E_1^- = \alpha M/2\mu_B$.

Having a superlattice of the system depicted in Fig. 2, one would then attain sequential tunneling, similar to that originally demonstated in non-magnetic superlattices for the case involving resonance of the ground state E_1 and the first excited state E_2 in successive wells [21]. In other words, one would have a *far infrared cascade laser.* It is interesting to point out that, while in the non-magnetic cascade laser the photon energy is *fixed* by the dimension of the well, and the states E_1 and E_2 are brought into resonance by the electric bias, in the DMS case illustrated above the photon energy is *tunable* by the appropriate combination of magnetic and electric fields. The laser would, furthermore, emit *circularly polarized* photons, as determined by the selection rules for the $E_1^+ \rightarrow E_1^-$ transition. Such a laser is expected to be of primary interest in the laboratory, and hence the requirement of low temperature operation is not as restrictive as it would be in the case of devices of more widespread commercial use.

FERROMAGNETISM IN II-VI-BASED DMS ALLOYS

The attractive magnetooptical properties of DMS materials described above all arise from the large Zeeman splitting of electronic levels. Although these splittings -- and the effects arising from them -- are typically quite large at cryogenic temperatures, they diminish rapidly as the temperature increases, to the point where they may not be sufficient for practical use in magneto-optical devices at room temperature. As has been already pointed out, the size of all these effects (Zeeman shift of the band edges, Faraday rotation, etc.) is determined by the magnetization M, which in Mn-based systems is limited by the fact that as a rule Mn-Mn interactions are *antiferromagnetic*. We had already discussed the possibility of enhancing the magnetization by reducing the number of nearest neighbors in an ordered fashion, to reduce the effect of this interaction. But clearly one would make much greater strides toward increasing magnetization -- and thus enhancing the magnetooptical effects -- by fabricating materials where interactions between magnetic ions are *ferromagnetic*. Indeed, recent advances in materials do indicate the possibility of ferromagnetic inter-ion interactions in II-VI-based systems, and we outline these below as a promising step toward significant enhancement of magnetooptical effects in DMSs.

Ferromagnetic interactions in p-type $II_{1-x}Mn_xVI$ alloys

Recently it has been predicted [22] and confirmed experimentally [23] that the two-dimensional hole gas in modulation-doped $Cd_{1-x}Mn_xTe$ quantum wells produces, via the RKKY interaction, a ferromagnetic interaction between Mn spins. This RKKY interaction due to the presence of holes overcompensates the antiferromagnetic coupling mediated by superexchange, resulting in effect in a $II_{1-x}Mn_xVI$ ferromagnet. This seminal work thus demonstrates that the well-established techniques of modulation doping can be put to use to tailor *magnetic* properties of DMS-based heterostructures. As a consequence, in the experimental work cited above a colossal enhancement of Zeeman splitting (as observed by inter-band magnetooptical transitions) has been achieved. In addition to the promise that such ferromagnetic inter-ion coupling in DMSs holds in store for magnetooptical device applications, it also provides important information on critical phenomena in disordered magnetic systems of reduced dimensionality. In particular, it shows how long-range spin-spin interactions can stabilize an ordered phase and make fluctuations of magnetization irrelevant. This itself is a milestone in our understanding of layered DMS structures, introducing yet another mechanism for harnessing their magnetic and magnetooptical properties as we design new systems involving DMS films.

Ferromagnetic interactions in $II_{1-x}Cr_xVI$ alloys

Another method of obtaining ferromagnetic DMS alloys is to choose magnetic ions for which the net inter-ion superexchange interaction is ferromagnetic. A clear suggestion of this possibility emerges from the extensive investigation of $II_{1-x}Cr_xVI$ alloys by Twardowski and his colleagues [24], who observe that the sign of the p-d interactions between Cr^{++} ions and valence electrons is ferromagnetic, which in turn suggests that Cr-Cr d-d interactions are also ferromagnetic. This inference is indeed also supported by theoretical tight binding model calculations of Blinowski *et al.* [25]. The experimental status of this issue in bulk crystals is hampered at this time by the rather low solubility of Cr in the II-VI matrix (less than 1%), so that -- to the author's knowledge -- no experimental verification of ferromagnetic Cr-Cr interactions is yet available. However -- as is the case with many ternary alloys -- the Cr solubility in the II-VI lattice can be greatly increased by using non-equilibrium growth methods such as MBE, as

indeed has been done in the case of $Cd_{1-x}Cr_xTe$ [26]. Thus $II_{1-x}Cr_xVI$ may yet prove to be a valuable ferromagnetic DMS material for magnetooptical thin film applications.

III-V-BASED DILUTED MAGNETIC SEMICONDUCTORS

II-VI-based DMSs (and particularly those involving Mn) have been explored the most extensively, and have paved the way for our understanding of the interplay of semiconductor physics and magnetism described in the preceding sections. However, recently very significant strides have also been made in the area of III-V-based DMSs (and, again, the alloys involving Mn are leading the way). This work, which was begun with the pioneering success of Munekata and co-workers in growing $In_{1-x}Mn_xAs$ films by MBE [27], is important for several reasons. First, it holds out the promise of integrating DMSs with III-V-based electronics and opto-electronics in a natural way; and second, the work on the $III_{1-x}Mn_xV$ alloys already carried out suggests that they are ferromagnetic. It is possible that the Mn ions (which have a strong preference for the divalent state) act both as the localized magnetic moments and as acceptors, so that ferromagnetic coupling mediated by holes (as already discussed in the preceding section in connection with $Cd_{1-x}Mn_xTe$) may also dominate in these systems. The $III_{1-x}Mn_xV$ systems fit naturally in the discussion of magnetic thin films not only because of the possibility of integration with III-V-based heterostructures, but also because -- owing to the low equilibrium (i.e., bulk) solubility of Mn in the III-V matrix -- they can only be grown in thin film form by one of the non-equilibrium epitaxial methods, such as MBE or MOCVD.

While the field of III-V-based DMSs is considerably less developed than that of their established II-VI-based counterparts, it is rapidly expanding [28-31], owing perhaps to the more recent successes with the fabrication of $Ga_{1-x}Mn_xAs$ and its heterostructures. We therefore present here a brief and admittedly superficial discussion of $III_{1-x}Mn_xV$ systems, primarily in the hope of calling the reader's attention to this very new but rapidly accelerating and potentially very important area of DMS films.

The prevalence of GaAs-based devices, from high-speed transistors to light emitting diodes and diode lasers, needs no introduction. Bringing in a magnetic component into the picture (especially if it is ferromagnetic, and may eventually retain significant magnetization above cryogenic temperatures) is therefore of obvious interest, with a view of achieving in GaAs-based heterostructures the kind of band-offset tuning discussed in connection with $II_{1-x}Mn_xVI$ DMSs in an earlier section. But there are other devices, not involving GaAs, that should be mentioned here because of their potentially even greater sensitivity to such tuning. Consider, for example, the lattice-matched type-II heterostructure GaSb/InAs. This system is unique in that the top of the valence band of GaSb lies *above* the bottom of the InAs conduction band [32]. Such band alignment makes this system a semimetal, i.e., electrons from the GaSb valence band automatically spill over to the InAs conduction band near the interface, so that this region is populated with free electrons. A superlattice consisting of GaSb and InAs quantum wells can either remain a true semimetal (where quantum wells in the conduction band of InAs are *always* populated, as described above, even at 0 K) or semiconducting, where states in the InAs quantum wells are *pushed* by quantum confinement *above* the top occupied states in the GaSb valence band. If one of the constituent materials is now made magnetic by introducing Mn (i.e., either $In_{1-x}Mn_xAs$ or $Ga_{1-x}Mn_xSb$), we should be able to move the system between a semiconductor and a semimetal state by magnetic band-offset tuning. This may likely result, for example, in enormous effects on magnetoresistance, in tuning the transitions possible in this system in the infrared, or in tuning states in adjacent layers so as to result in resonant tunneling. All these situations have broad applications, and hence a system of this sort deserves considerable attention. It is to be hoped that the momentum in the field of III-V-based DMSs evident today may eventually make some of these and similar speculations a practical reality.

HYBRID SEMICONDUCTOR-FERROMAGNETIC THIN FILM STRUCTURES

As has been repeatedly emphasized, harnessing the impressive magnetooptical phenomena in DMSs for device applications is contingent on achieving sufficiently high magnetization within the DMS medium. We have thus far emphasized modifications of the DMS medium itself to achieve this goal in some practical applied magnetic field. One can follow an alternate route, that of enhancing the applied magnetic field in the medium. In this section we will briefly review the various schemes which exist for epitaxially growing ferro- or ferri-magnetic films on semiconductors -- and particularly on DMSs -- with the view of using fields from such films for the purpose of locally increasing magnetic flux -- and hence magnetization -- within the DMS material. It should be appreciated, however, that the physics and application of such films is also of interest in its own right. The latter is outside the intended scope of the present paper, but provides yet another interesting illustration of the fruitful marriage of semiconductor physics and magnetism.

It has now been firmly established that Fe films of very high quality can be grown epitaxially on GaAs, AlAs, and ZnSe, as well as on some of their alloys [33]. The ability to integrate ferromagnetic Fe films with, e.g., ZnMnSe thus contains the promise of using such films in order to achieve local magnetic fields in the Tesla range within the DMS medium, using external applied fields in the range of only Oersteds. So far this extremely promising situation has escaped device applications because the field is "locked" within the film. The easy axis of magnetization for Fe (a soft cubic ferromagnet) is in the plane of the film; and, furthermore, external fields applied normal to the layer do not result in any beneficial enhancement of magnetization in the adjacent semiconductor region because of total demagnetization within the film. When the magnetization is in the plane of the film, however, one can exploit fringing field to achieve significant magnetization in the DMS region immediately outside the Fe layer, by using *lithographically patterned* Fe films [33]. Then indeed one can, by applying fields on the scale of Oersteds, achieve significant fringing fields at the edges of the lithographically treated Fe layer. Such fields can be as large as 2 Tesla at distances from the Fe film edge that are smaller than the film thickness. By patterning the Fe film lithographically one can thus achieve *patterned magnetization* in the adjacent semiconductor medium, that can be put to imaginative use.

Since the pioneering work of Prinz and co-workers on the Fe films, there has been impressive progress in the fabrication of a variety of new ferromagnetic and ferrimagnetic films that can be grown epitaxially on III-V and II-VI semiconductor surfaces. These include the ferromagnetic MnAs [34], MnSb [35], MnAl [36], and MnGa [37] layers, and the ferrimagnetic Mn_2Sb [38], all of which can be grown by MBE with atomic coherence on semiconductor substrates of various orientations, thus holding promise of integration with both III-V and II-VI semiconductor systems. Furthermore, the easy magnetization axes of these systems can be in the plane of the layer, at some angle to the plane, or normal to the plane. These features, together with the various anisotropies exhibited by the magnetic films, utilization of substrates of different orientations, and imaginative patterning of the films by lithographic techniques, can be put to use toward the goal of extracting the fringing-fields for magnetizing the DMS medium with which the magnetic film is integrated. For an illustration of such imaginative schemes used to extract the fringing fields into the surrounding medium, the reader is referred to, e.g., the excellent work of Van Roy *et al.* [39].

A related -- and possibly very promising -- area is that of magnetic inclusions in a semiconductor matrix. It has been shown, for example, that MnAs can form self-organized magnetic precipitates within a III-V matrix such as GaAs [40]. Such formation is very similar to the well established phenomenon of As precipitation in GaAs grown at low temperatures (the so-called LT-GaAs) [41]. In the case of magnetic inclusions, the fringing fields from such precipitates can create a pattern of strong

mesoscopic internal fields, that may be of interest in the present context. For example, one can imagine such fields localized on MnAs precipitates immersed in a DMS medium to form magnetic-field-induced quantum-dot-like pockets of lower potential just around the inclusion. We emphasize that the precipitates are likely to be single ferromagnetic domains, and (because they are finite in all three dimensions) the demagnetizing fields will not be sufficient to cancel the fields emanating from them into the surrounding material. Such fields will correspond to a significant fraction of the MnAs magnetization, so that the potential "pockets" created by the Zeeman splitting in the DMS medium immediately outside the precipitates are expected to be sufficient for achieving spin-selective carrier and/or exciton localization in those regions.

CONCLUDING REMARKS

The rich spectrum of physical phenomena which occur in DMSs arises because of the interplay of two disciplines, semiconductor physics and magnetism, resulting in a host of novel and often spectacular effects. With the advance of epitaxial fabrication, enabling the growth of DMS-based multilayers, one can harness this spectrum of characteristic DMS effects into the equally rich context of quantum wells, superlattices, and also structures of lower dimension, such as quantum dots and wires.

In this paper we have attempted to review the status of DMS films, with primary attention to the possible uses they may have in magneto-optical devices. We have discussed not only those phenomena which can be directly applied in devices (like Faraday rotation), but also those which have an *indirect* usefulness, allowing the scientist to gain a better understanding of the physics of semiconductor heterostructures generally (like the pinpointing of electron probability distribution by using magnetic band offset tuning). We gave considerable space to the challenges that need to be overcome to further increase the desired magnetooptical effects (like the fabrication of *ferromagnetic* DMSs); and to the emerging field of III-V-based DMSs, which holds great promise of introducing spin-based physics into the well developed field of III-V heterostructures. Finally, we briefly noted the advances in ferromagnetic films that can be epitaxially grown on III-V (and certainly also on II-VI) semiconductors, to form hybrid semiconductor-ferromagnetic thin film structures. As usual, the true excitement lies at the interfaces -- the physical ones, and especially the metaphoric interfaces between the different areas of physics that together make up the field of magnetic semiconductor thin films and multilayers.

ACKNOWLEDGMENTS

The author wishes to acknowledge illuminating discussions with J. Kossut, A. Twardowski, and W. Van Roy. This work was supported by NSF Grant DMR95-10241 and DMR97-05064.

REFERENCES

1. See, e.g., Diluted Magnetic Semiconductors, ed. by J. K. Furdyna and J. Kossut as Vol. 25 of the series Semiconductors and Semimetals, ed. by R. K. Willardson and A. C. Beer (Academic, Boston, 1988); also T. Dietl, in Handbook on Semiconductors, ed. by T. S. Moss (North Holland, Amsterdam, 1994), Vol. 3b, p. 1251.

2. See, e.g., J. De Boeck, W. Van Roy, C. Bruynseraede, A. Van Esch, H. Bender, and G. Borghs, Microelectronics Journal **27**, 383 (1996).

3. W. C. Chou, A. Petrou, J. Warnock, and B. T. Jonker, Phys. Rev. Lett. **67**, 3820 (1991).

4. N. Dai, H. Luo, F. Zhang, N. Samarth, M. Dobrowolska, and J. K. Furdyna, Phys. Rev. Letters **67**, 3824 (1991).

5. X. Liu, A. Petrou, J. Warnock, B. T. Jonker, G. A. Prinz, and J. J. Krebs, Phys. Rev. Lett. **63**, 2280 (1989); also E. Deleporte, J. M. Barroir, G. Bastard, C. Delalande, J. M. Hong, and L. L. Chang, Phys. Rev. B **42**, 5891 (1990).

6. S. Lee, M. Dobrowolska, J. K. Furdyna, and L. R. Ram-Mohan, Phys. Rev. B **54**, 16939 (1996).

7. See, e.g., J. K. Furdyna, Solid-State Electronics **37**, 1065 (1994); also M. Dobrowolska, H. Luo, and J. K. Furdyna, Acta Phys. Polonica A **87**, 95 (1995).

8. F. C. Zhang, N. Dai, H. Luo, N. Samarth, M. Dobrowolska, J. K. Furdyna, and L. R. Ram-Mohan, Phys. Rev. Letters **68**, 3220 (1992).

9. H. Luo, N. Dai, F. C. Zhang, N. Samarth, M. Dobrowolska, J. K. Furdyna, C. Parks, and A. K. Ramdas, Phys. Rev. Letters **70**, 1307 (1993).

10. F. C. Zhang, H. Luo, N. Dai, N. Samarth, M. Dobrowolska, and J. K. Furdyna, Phys. Rev. B **47**, 3806 (1993).

11. See, e.g., J. A. Gaj, R. R. Galazka, and M. Nawrocki, Solid State Commun. **25**, 193 (1978); also Eunsoon Oh, A. K. Ramdas, and J. K. Furdyna, Journal of Luminescence **52**, 183 (1992).

12. N. Kullendorf and B. Hök, Appl. Phys. Lett. **46**, 1016 (1985); also J. F. Dillon, Jr., J. K. Furdyna, U. Debska, and A. Mycielski, J. Appl. Phys. **G7**, 4917 (1990).

13. A. E. Turner, R. L. Gunshor, and S. Datta, Applied Optics **22**, 3152 (1983); see also Diluted Magnetic Semiconductors, Report of Solid State Sciences Committee, National Research Council (National Academy Press, Washington, DC, 1991).

14. D. U. Bartholomew, J. K. Furdyna, and A. K. Ramdas, Phys. Rev. B **34**, 6943 (1986); see also Eq. (38) and its discussion in J. K. Furdyna, J. Appl. Phys. **64**, R29 (1988)

15. See, e.g., Eunsoon Oh, D. U. Bartholomew, A. K. Ramdas, J. K. Furdyna, and U. Debska, Phys. Rev. B **42**, 5201 (1990).

16. R. Wolfe, R. A. Lieberman, V. J. Fratello, R. E. Scotti, and N. Kopylov, Appl. Phys. Lett. **56**, 426 (1990); also R. Wolfe, Thin Solid Films **216**, 184 (1992) and references therein.

17. See, e.g., Ref. 6 for detailed discussion of the effective concentration parameter $\bar{x}$ and its relation to the magnetization of the Mn sublattice.

18. Y. Shapira, E. J. McNiff, Jr., N. F. Oliveira, Jr., E. D. Honig, K. Dwight, and A. Wold, Phys. Rev. B **37**, 411 (1988).

19. J. Kossut and J. K. Furdyna, Acta Phys. Polonica A**73**, 851 (1988).

20. S. Scholl, H. Schafer, A. Waag, K. von Sckierstedt, B. Kuhn-Heinrich, and G. Landwehr, Appl. Phys. Lett. **62**, 3010 (1993); also I. Smorchkova and N. Samarth, Appl. Phys. Lett. **69**, 1640 (1996).

21. F. Capasso, K. Mohammed, and A. Y. Chao, Appl. Phys. Lett. **48**, 478 (1986).

22. T. Dietl, A. Haury, and Y. Merle d'Aubigné, Phys. Rev. B **55**, R3347 (1997).

23. A. Haury, A. Wasiela, A. Arnoult, J. Cibert, S. Tatarenko, T. Dietl, and Y. Merle d'Aubigné, Phys. Rev. Lett. **79**, 511 (1997).

24. W. Mac, A. Twardowski and M. Demianiuk, Phys. Rev. B **54**, 5528 (1996).

25. J. Blinowski, P. Kacman, and J. A. Majewski, Phys. Rev. B **53**, 9524 (1996).

26. T. Wojtowicz, G. Karczewski, and J. Kossut, Thin Solid Films **306**, 271 (1997).

27. H. Munekata, H. Ohno, S. von Molnar, A. Segmuller, and L.L. Chang, Phys. Rev. Lett. **63**, 1849 (1989); also H. Ohno, H. Munekata, T. Penny, S. von Molnar, and L.L. Chang, Phys. Rev. Lett. **68**, 2664 (1992).

28. H. Ohno, A. Shen, F. Matsukura, A. Oiwa, A. Endo, S. Katsumoto, and Y. Iye, Appl. Phys. Lett. **69**, 363 (1996).

29. T. Hayashi, M. Tanaka, K. Seto, T. Nishinaga, and K. Ando, Appl. Phys. Lett. **71**, 1825 (1997).

30. S. Koshihara, A. Oiwa, M. Hirasawa, S. Katsumoto, Y. Iye, C. Urano, H. Takagi, and H. Munekata, Phys. Rev. Lett. **78**, 4617 (1997).

31. F. Matsukura, H. Ohno, A. Shen, and Y. Sugawara, Phys. Rev. B **57**, R2037 (1998).

32. See, e.g., J. R. Meyer, C. A. Hoffman, F. J. Bartoli, and L. R. Ram-Mohan, Phys. Rev. B **49**, 2197 (1994); and Appl. Phys. Lett. **67**, 757 (1995).

33. See, e.g., G. A. Prinz, Science **250**, 1092 (1990).

34. See, e.g., M. Tanaka, J. P. Harbison, M. C. Park, Y. S. Park, T. Shin, and G. Tothberg, J. Appl. Phys. **76**, 6278 (1994).

35. See, e.g., H. Akinaga, K. T. Tanaka, K. Ando, and T. Katayama, J. Crystal Growth **150**, 1144 (1995); H. Akinaga, S. Miyanishi, W. Van Roy, and L. H. Kuo, Appl. Phys. Lett. **70**, 2472 (1997); and S. Miyanishi, H. Akinaga, and K. Tanaka, Physika B **237-238**, 281 (1997).

36. See, e.g., T. Sands, J. P. Harbison, M. L. Leadbeater, S. J. Allen, Jr., G. W. Hull, R. Ramesh, and V. G. Keramidas, Appl. Phys. Lett. **57**, 2609 (1990); also W. Van Roy, J. De Boeck, H. Bender, C. Bruynseraede, A. Van Esch, and G. Borghs, J. Appl. Phys. **78**, 398 (1995).

37. See, e.g., M. Tanaka, J. P. Harbison, J. De Boeck, T. Sands, B. Philips, T. L. Cheeks, and V. G. Keramidas, Appl. Phys. Lett. **62**, 1565 (1993); also W. Van Roy, H. Akinaga, S. Miyanishi, and A. Asamitsu, Appl. Phys. Lett. **71**, 971 (1997).

38. S. Miyanishi, H. Akinaga, W. Van Roy, and K. Tanaka, Appl. Phys. Lett. **70**, 2046 (1997).

39. W. Van Roy, J. De Boeck, and G. Borghs, Appl. Phys. Lett. **61**, 3056 (1992); also W. Van Roy, E. L. Carpi, M. Van Hove, A. Van Esch, R. Bogaerts, J. De Boeck, and G. Borghs, J. Magn. Magn. Mat. **121**, 197 (1993).

40. J. De Boeck, R. Oesterholt, A. Van Esch, H. Bender, C. Bruynseraede, C. Van Hoof, and G. Borghs, Appl. Phys. Lett. **68**, 2744 (1996).

41. See, e.g., M. R. Melloch, D. D. Nolte, J.C.P. Chang, D. B. Janes, and E. S. Harmon, Critical Reviews in Solid State and Materials Sciences **21**, 189 (1996).

DILUTED MAGNETIC SEMICONDUCTOR MAGNETO-OPTIC WAVEGUIDES FOR MONOLITHIC-INTEGRATION WITH SEMICONDUCTOR OPTIC DEVICES

K.ANDO, W. ZAETS* and K.WATANABE**

Electrotechnical Laboratory, Tsukuba, Ibaraki 305-8568, Japan, ando@etl.go.jp

ABSTRACT

We propose to use a paramagnetic diluted magnetic semiconductor $Cd_{1-x}Mn_xTe$ for magneto-optic waveguides, which can be integrated with semiconductor optic devices. Single crystal $Cd_{1-x}Mn_xTe$ films are epitaxially grown on GaAs substrates by molecular beam epitaxy method. A good optical confinement is obtained in the waveguide by using a $Cd_{1-y}Mn_yTe$ clad layer with Mn concentration higher than that of the waveguide core layer.

INTRODUCTION

An integrated optic circuit [1] originally means a circuit that contains all sort of optic devices such as laser, amplifier, switch, modulator, coupler, and electronic package. Such integrated optic circuit has not been achieved. Simpler optic circuits have been sufficient for practical purposes. But in future, demands for more reliable and more functional optic devices will require an integrated optic circuit in the original meaning. Magneto-optic waveguide devices, *i.e.*, optical isolators and circulators, are indispensable components for the integrated optic circuits [2]. Up to now, the magnetic garnet films have been used for the magneto-optic waveguide [3]. But these oxide films can not be grown on the semiconductor substrates. Recently, some attempts to integrate magneto-optic waveguides with semiconductor have been reported. Yokoi *et al.*[4] and Levy *et al.*[5] propose a direct bonding of magnetic garnet films onto semiconductor substrates. Hammer *et al.* [6] proposes a polycrystalline-metal-ferromagnetic optical waveguide isolator in which a semiconductor optical waveguide amplifier is combined with a ferromagnetic iron film. We propose to use epitaxial films of diluted magnetic semiconductors on semiconductor substrates as magneto-optic waveguide [7].

Diluted magnetic semiconductors (DMSs) [8] are semiconductors which contain large amounts of transition metal ions as substitutional elements. $Cd_{1-x}Mn_xTe$ ($0 \le x \le 1$) is a typical DMS with a zinc-blende crystal structure. The *d*-orbitals of the transition metals strongly mix with the *p*-orbitals of the host semiconductors. The valence band of DMS is composed of both of the *p*- and *d*-orbitals. Due to this *p-d* mixing, the Zeeman splitting of the valence band is strongly enhanced, typically two order of magnitude larger than the Zeeman splitting of non-magnetic semiconductors. Although DMSs are paramagnetic at room temperature, they show a huge Faraday effect under moderate magnetic field strengths. Figure 1 shows a typical wavelength dependence of the Faraday effect observed in a $Cd_{1-x}Mn_xTe$ film. The Faraday effect becomes larger as the wavelength approaches the band gap. The absorption edge is determined by the band gap of $Cd_{1-x}Mn_xTe$ for low Mn concentration, *i.e.*, $x<0.4$, and by the d-d^* intra-ionic optical transition at 2.1eV for higher Mn concentration[9]. The absorption edge varies from 1.4eV to 2.1eV. This makes the $Cd_{1-x}Mn_xTe$ crystals compatible with AlGaInP:GaAs

Mat. Res. Soc. Symp. Proc. Vol. 517 © 1998 Materials Research Society

optoelectronics devices operating at wavelengths of 600-800 nm. For longer wavelength devices (λ=800-1500 nm) $Cd_{1-x-y}Mn_xHg_yTe$ can be used. By choosing appropriate compositions of DMSs, one can utilize the huge Faraday effect of DMS for both visible and infrared wavelength regions. The optical absorption also becomes larger as the wavelength approaches the band gap. But DMSs still show high figure-of-merit [10-12] (Fig.2). Bulk optical isolators [13] using $Cd_{1-x}Mn_xTe$ and $Cd_{1-x-y}Mn_xHg_yTe$ are now commercially available.

DMSs have an another good point for the integration of magneto-optic waveguide onto semiconductor substrates. Because most DMSs are zinc-blende type semiconductors, films of DMSs can be epitaxially grown on semiconductor substrates by using a molecular beam epitaxy (MBE) method. This paper reports the growth of $Cd_{1-x}Mn_xTe$ films on GaAs substrates [7] and their waveguiding properties.

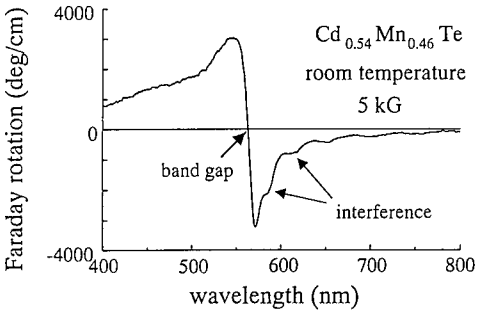

Fig. 1 : Faraday rotation of a (Cd,Mn)Te film as a function of wavelength.

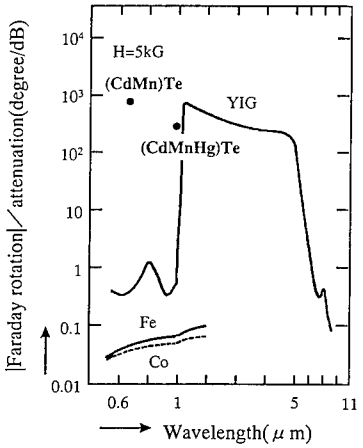

Fig. 2 : Magneto-optic figure-of-merit of (Cd,Mn)Te and (Cd,Mn,Hg)Te bulk crystals (●) estimated for H=5kG using data in Refs. 10 and 11. The data of YIG, Fe, and Co are from Ref.12.

EXPERIMENT

$Cd_{1-x}Mn_xTe$ and ZnTe single crystal films have been grown on GaAs(001) and sapphire (0001) substrates by the MBE method using solid sources of CdTe, MnTe, and ZnTe. The typical growth temperature is 300℃.

The waveguiding property has been investigated by the method of *m-line* spectroscopy. Figure 3 shows a setup of the one-prism *m-line* spectroscopy experiment. The light is reflected from the film through the prism. Because the refractive index of the GaP prism (n_{GaP}=3.09~3.30 at λ=600~1150 nm) is higher than refractive index of the film (n_{CdMnTe}=2.6~3.0 at λ=600~1150 nm), the light propagation constant inside the prism can be equal to the propagation constant of the waveguide mode. In this case, the light is coupled from the prism to the optical waveguide. A short-focus lens(f=5 mm) produced a wide

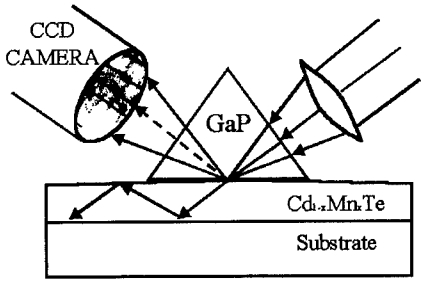

Fig. 3 : One-prism *m-line* spectroscopy.

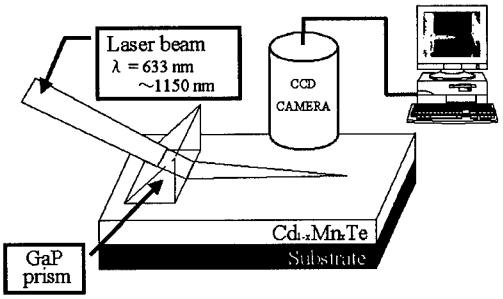

Fig. 4 : Experimental scheme to measure the optical propagation loss of $Cd_{1-x}Mn_xTe$ waveguide.

range of the incidence angle. At the angles where the propagation constant inside the prism coincides with the propagation constant of the waveguide, the light is efficiently coupled into the film and is not reflected. This causes the dark lines (*m-lines*) in reflected light. From the output angles of these lines we deduce the propagation constants of the waveguide modes, from which the film parameters, *i.e,* refractive index and film thickness, are calculated. The precision of the refractive index is estimated to be 0.001.

The optical propagation loss has been estimated by detecting the scattered light from the waveguide with TV-camera (Fig.4).

WAVEGUIDE MODES IN $Cd_{1-x}Mn_xTe$ FILMS AND THEIR REFRACTIVE INDEX

Figure 5 shows the refractive index of $Cd_{1-x}Mn_xTe$ as a function of Mn-concentration at the wavelength of 1150, 784 and 670 nm [7]. The refractive index of $Cd_{1-x}Mn_xTe$ rapidly decreases with increasing Mn-concentration. For all investigated wavelengths this change is about 0.03-0.05 per 0.1 change of Mn-concentration.

Fig. 5 : The refractive index of $Cd_{1-x}Mn_xTe$.

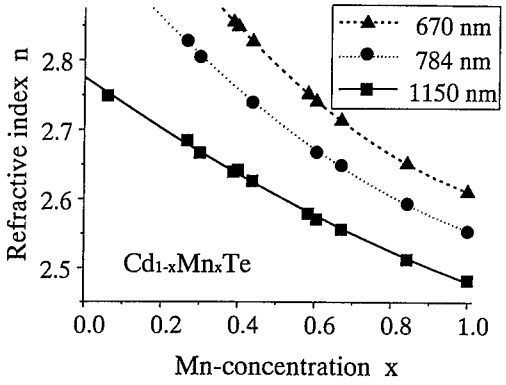

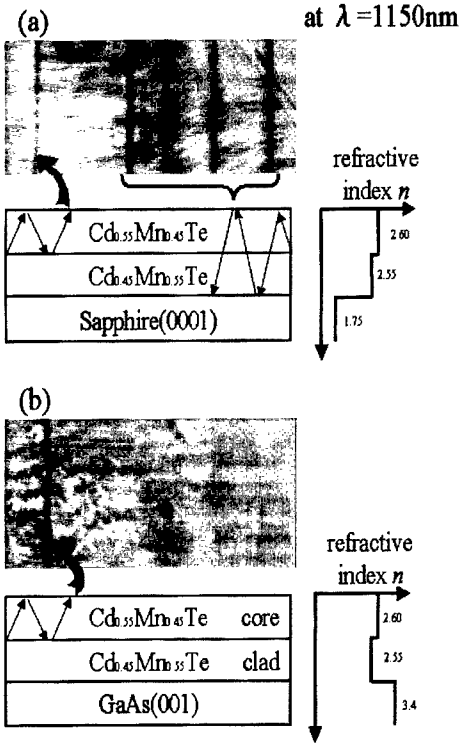

Fig. 6 : (a) Double-layer $Cd_{1-x}Mn_xTe$ waveguide on sapphire substrate, and its *m-lines*. (b) Double-layer $Cd_{1-x}Mn_xTe$ waveguide on GaAs substrate, and its *m-line*.

The double-layer waveguide have been grown on sapphire and GaAs substrates at the same time. The 1.5 μ m thick $Cd_{0.45}Mn_{0.55}Te$ is a clad layer and 1.5 μ m thick $Cd_{0.55}Mn_{0.45}Te$ is a core layer. Figure 6 (a) shows the *m-lines* from the waveguide on the sapphire substrate. Several *m-lines* appeared. They can be classified into two group, *i.e.* four right-side *m-lines* and one left - side *m-line*. The distance between the adjacent four right-side *m-lines* systematically decreases. This behavior of the *m-lines* is typical for the multi mode single layer waveguides. Because the refractive index step between two $Cd_{1-x}Mn_xTe$ layers is small, these *m-lines* correspond to the waveguiding propagation between the air and the sapphire substrate (See Fig.6(a)). The other separated *m-line* corresponds to the waveguiding propagation only in the upper $Cd_{0.55}Mn_{0.45}Te$ layer. On the contrary, the waveguide on GaAs substrate showed only one *m-line* (Fig.6(b)). The position of this *m-line* corresponds to the 'separated' *m-line* of Fig.6(a). In the waveguide on the GaAs substrate the light can propagate only in the upper layer, because of higher refractive index and larger optical absorption of GaAs. The same position of *m-line* from waveguide on GaAs and on sapphire shows the achievement of the good optical confinement in the $Cd_{1-x}Mn_xTe$ waveguide.

PROPAGATION LOSS OF $Cd_{1-x}Mn_xTe$ WAVEGUIDE

Figure 7 shows an example of light propagation in a $Cd_{1-x}Mn_xTe$ film. The light intensity decreases with the propagation distance. The estimated propagation loss of the waveguide on GaAs substrate is 70dB/cm at λ =1150nm. Because the waveguide on the sapphire substrate showed a very small loss, *i.e.*, ~0.3dB/cm at the same wavelength, the observed high optical loss is not intrinsic to $Cd_{1-x}Mn_xTe$ waveguides. The mismatch of lattice constants between $Cd_{1-x}Mn_xTe$ and GaAs is about 12%, which is much larger than that of 4% between the sapphire substrate and (111) oriented $Cd_{1-x}Mn_xTe$ film. Observations with an optical microscope have revealed rough surfaces of the films grown on GaAs substrates while the surfaces of the films grown on sapphire substrates are smooth.

In order to improve the film quality, a 1 μ m thick CdTe has been grown as a buffer layer after depositing 2nm thick ZnTe on GaAs. The 1.5 μ m thick $Cd_{0.5}Mn_{0.5}Te$ is a core layer and 3 μ m thick $Cd_{0.2}Mn_{0.8}Te$ is a clad layer. Although streaky RHEED patterns are observed for the waveguides both with and without the buffer layers, the RHEED pattern becomes clearer and brighter when the buffer layers are used (Fig.8). The width of the X-ray diffraction peaks and the surface roughness are also reduced. These results imply the improved crystalline quality for films

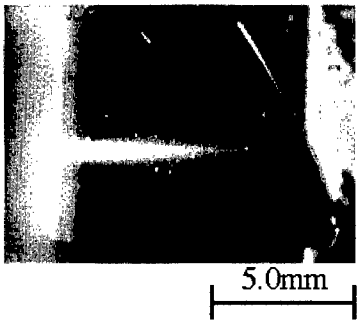

at λ =780nm

Fig. 7 : A streak of a guided mode in $Cd_{1-x}Mn_xTe$ waveguide

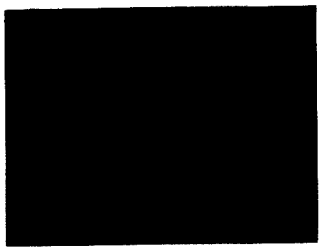

without CdTe/ZnTe buffer layers

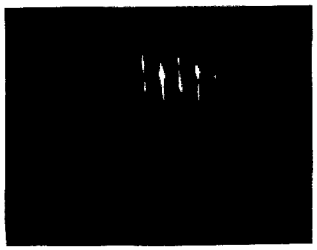

with CdTe/ZnTe buffer layers

Fig. 8 : RHEED patterns of $Cd_{0.5}Mn_{0.5}Te$ core layers observed along <110> direction (a) without and (b) with the ZnTe/CdTe buffer layers.

Table 1 : Effect of CdTe/ZnTe buffer layers on optical propagation loss

CdTe/ZnTe buffer layers	Optical loss(dB/cm)		
	λ=1150nm	λ=784nm	λ=633nm
—	$70_{\pm 5}$	$\gg 250$	$\gg 250$
○	$16_{\pm 5}$	$33_{\pm 5}$	$144_{\pm 10}$

with the buffer layers. Correspondingly the optical loss has been strongly reduced by the use of buffer layers (Table 1). For further reduction of the optical loss, a third $Cd_{1-z}Mn_zTe$ layer is inserted between the $Cd_{0.2}Mn_{0.8}Te$ clad layer and the $Cd_{0.5}Mn_{0.5}Te$ core layer. The Mn concentration z gradually changes from 0.8 at the clad layer side to 0.5 at the core layer side. The thickness of the graded layer is 0.8 μ m. The surface roughness has been further improved by using the graded layer, although it is still rougher than the film surface on a sapphire substrate. The optical loss is reduced as shown in Table 2.

The obtained magneto-optic figure-of-merit is 9deg/dB at λ =633nm under a magnetic field of 5kG. This value of figure-of-merit is smaller than that of $Cd_{1-x}Mn_xTe$ bulk crystals. By

Table 2 : Effect of Mn-graded layer on optical propagation loss.

Mn-graded layer	Optical loss(dB/cm)		
	λ=1150nm	λ=784nm	λ=633nm
—	16±5	33±5	144±10
○	11±5	26±5	88±10

adjusting the growth condition, we must further improve the film quality to obtain higher figures-of-merit.

CONCLUSIONS

We have shown that the magneto-optic $Cd_{1-x}Mn_xTe$ waveguide can be monolithically integrated on a GaAs substrate. The optical propagation loss of the waveguide can be reduced by inserting ZnTe and CdTe buffer layers and smoothing layers between the clad and core layers.

REFERENCES

* Permanent address : Kiev Univ..
** On leave from Kyushu Inst. Tech.
1. P.K.Tien, Rev.Mod.Phys. **49**, 361(1977).
2. K.Ando, SPIE **1126**, 58(1989).
3. K.Ando, T.Okoshi, and N.Koshizuka, Appl.Phys.Lett. **53**, 4 (1988)
4. H.Yokoi, T.Mizumoto, K.Maru, Y.Naito, Electron. Lett. **31**, 1612(1995)
5. M.Levy, R.M.Osgood, A.Kumar, H.Bakhru, Appl. Phys. Lett. **71**, 2617(1997)
6. J.M.Hammer, J.H.Abeles, and D.J.Channin, IEEE Photon.Technol.Lett. **9**, 631(1997).
7. W.Zaets, K.Watanabe, and K.Ando, Appl.Phys.Lett. 70, 2508(1997).
8. J.K.Furdyna, J.Appl.Phys. **64**, R29(1988).
9. Y.R.Lee and A.K.Ramdas, Solid State Commun. **51**, 861(1984).
10. A.E.Turner, R.L.Gunshor, and S.Datta, Appl.Opt.**22**, 3152(1983).
11. K.Onodera and H.Ohba, Cryst.Res.Technol. **31**, 29(1996).
12 P.F.Bongers, IEEE Trans. Magn. **MAG-5**, 472(1969).
13. K.Onodera, T.Masumoto, and M.Kimura, Electron.Lett. **30**, 1954(1994).

MAGNETIZATION PROCESS IN CR SUBSTITUTED DILUTED MAGNETIC SEMICONDUCTOR FILMS

N. Adachi, J. Hirano, T. Yamazaki, T. Okuda, H. Kitazawa*, G. Kido*
Department of Materials Science and Engineering, Nagoya Institute of Technology,
Gokiso-cho, Showa-ku, Nagoya 466, Japan, nadachi@mse.nitech.ac.jp
* National Institute for Metals (NRIM), Physical Properties Division,
1-2-1 Sengen, Tsukuba, Ibaraki 305, Japan

ABSTRACT

Cr substituted dilute magnetic semiconductor $Cd_{1-x}Cr_xSe$ films were grown onto fused silica and sapphire (00 • 1) substrates by vapor deposition technique. The films with wurtzite structure were obtained at composition of $0 \leqq x \leqq 0.66$. Saturation magnetization and magnetic susceptibility increased as x increased. In comparison with Mn-DMS system, the initial magnetization curves saturate easily. This tendency is different from most DMS materials in which magnetic ions interact with each other antiferromagnetically. It is possible that ferromagnetic interactions exist in $Cd_{1-x}Cr_xSe$.

INTRODUCTION

Diluted magnetic semiconductors (DMS) exhibit novel magneto-optical phenomena such as a Faraday effect or a Zeeman splitting of electronic (band and impurity) levels. They arise from exchange interactions between magnetic ions and conduction- or valence- band electrons (*sp-d* exchange interaction) [1]. Since the first report in the end of 1970's [2], many studies have been done especially on the Mn-based DMS family. With developments in the crystal growth of thin film by MBE etc., interest is recently attracted to quantum effects in superlattices [3]. The magneto-optical effects of DMS have also attracted much attention for their application to optoelectric materials. Onodera et. al. first practically applied $Cd_{1-x}Mn_xTe$ to optical isolators [4]. In most DMS families such as $Cd_{1-x}T_xTe$ or $Cd_{1-x}T_xSe$ (T : Mn, Fe, Co), the exchange interaction between valence band *p*-type electrons and *d*-electrons of magnetic ions is antiferromagnetic, which leads to antiferromagnetic *d-d* interactions. As the concentration of magnetic ion increases, higher external magnetic fields are required to saturate the magnetization.

Recently, the ferromagnetic phase was first discovered in III-V based DMSs, $Ga_{1-x}Mn_xAs$ and $In_{1-x}Mn_xAs$ [5]. For II-VI based DMS systems, Cr substituted DMSs have been expected, since *p-d* interactions in $Zn_{1-x}Cr_xSe$ are ferromagnetic [6]. The d^4 electronic configuration of the Cr ion makes both spin-down and spin-up electrons from the valance band jump onto the *d*-level, which is attributed to ferromagnetic *p-d* coupling. However, reports are limited to those about specimens with low concentrations ($x<0.01$), because attempts to grow bulk crystals with large x resulted in precipitation of Cr_xSe_y. For precise investigations of magnetic properties, the difficulty lies in preparation of a sample with a large amount of Cr. Deposition techniques have made it possible to grow a variety of materials at thermally non-equilibrium. We report on the crystal growth of $Cd_{1-x}Cr_xSe$ film by co-deposition. The preparation process and the magnetic properties will be described here.

Mat. Res. Soc. Symp. Proc. Vol. 517 © 1998 Materials Research Society

EXPERIMENT

$Cd_{1-x}Cr_xSe$ films about 3000 to 8000Å in thickness were prepared by co-deposition. We used CdSe (5N) source and CrSe (3N) source contained in a high quality carbon crucibles. The crucibles were 40 cm away from the substrate in a vacuum chamber. The base pressure of the chamber was 1×10^{-6} Torr, which was obtained with a diffusion pump. CrSe was heated by electron bombardment and CdSe was heated by radiation from a tungsten filament. The deposition rates of CdSe and CrSe were monitored by an oscillation thickness monitor (XTC). We used fused silica and <00 • 1>-, <11 • 0>- and <01 • 2>- oriented sapphire as substrates. The substrates were etched by a mixed acid solution composed of H_2SO_4 and H_3PO_4 (1:3 mole ratio) at 90 ℃ for 5 minutes. They were placed onto a silicon plate resistance heater. After thermal cleaning at 400 ℃ for 10 minutes, the temperature of the substrates was lowered to the growth temperature and monitored during deposition.

The crystal structure was analyzed by X-ray diffraction (XRD) method using a Rigaku X-ray diffractometer equipped with a Cu target. The chemical compositions of the deposited films were determined by X-ray dispersive energy analysis (EDX). The surface morphology of the film was observed by atomic force microscopy (Seiko SPI 3600). Magnetizations were measured using a Quantum Design superconducting quantum interference device (SQUID) magnetometer. The magnetic field was applied parallel to the substrate plane.

RESULTS AND DISCUSSIONS

Substrate temperatures above 300°C caused a remarkable decrease of the deposition rate, while the temperature below 200 ℃ caused exfoliation of the film. Fig. 1 shows XRD patterns of $Cd_{1-x}Cr_xSe$ films of x=0 and 0.15 deposited on fused silica at the substrate temperature of 300 ℃ . The strongest line is assigned to be 00 • 2 reflection of the wurtzite structure. According to powder XRD patterns of CdSe, the strongest line is the 10 • 0 reflection and second is the 11 • 0 reflection. The XRD patterns show the preferential orientation along the c-axis in the deposited films. The preferential orientation along the c-axis is also recognized for the deposited film on sapphire substrates.

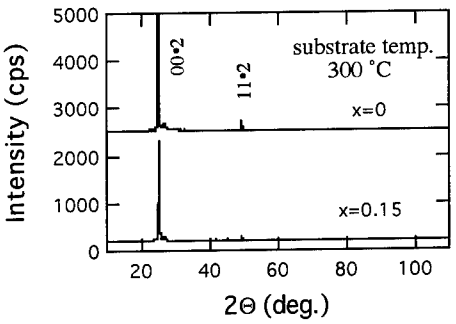

Fig.1 X-ray diffraction patterns of $Cd_{1-x}Cr_xSe$ films with x=0 and 0.15 deposited on fused silica at 300℃. The preferential orientation to the c-axis is seen.

Fig. 2 shows XRD patterns of $Cd_{1-x}Cr_xSe$ on sapphire (00 • 1), (11 • 0) and (01 • 2) substrates. No diffraction peaks, except for 00 • 2 peak, are found in the film deposited on (00 • 1) substrate. In the films deposited on (11 • 0) and (01 • 2) substrates, 11 • 0 and 11 • 2 peaks were observed except for 00 • 2 peak. Wurtzite type 00 • 2 peak is dominant in the composition x from 0 to 0.6. The 20 • 1 peak appears in the film with x=0.66. Attempts to

grow films with x>0.7 results in synthesis of CrSe with the hexagonal structure of NiAs type compounds.

The lattice constant of deposited CdSe film on sapphire (00 • 1) is evaluated to be a_0=4.31Å, which is a little larger than that of bulk crystal (a_0=4.298Å). In the x range from 0 to 0.6, the wurtzite 00 • 2 peak shows no shift. This is in contrast with the case of $Cd_{1-x}Mn_xSe$. One of the reasons for the small change of lattice constant in $Cd_{1-x}Cr_xSe$ may be the difference in ionic radius between Cr^{2+} and Mn^{2+}. According to Shannon, the ionic radius of Cr ion is larger than that of Mn ion with the same coordination number [7].

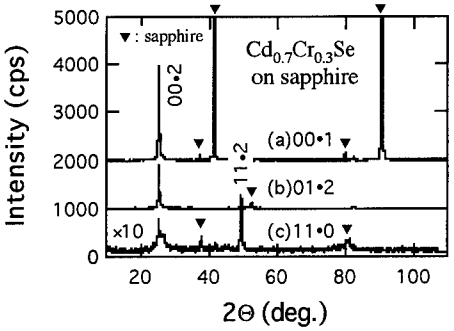

Fig.2 X-ray diffraction patterns of $Cd_{1-x}Cr_xSe$ films on sapphire (11 • 0) and (01 • 2). The easy orientation to the c-axis is also seen for the deposited film. The peak labeled " ▼" is due to sapphire substrate.

Table I The composition of $Cd_{1-x}Cr_xSe$ films analyzed by EDX. The label " W" means a wurtzite structure, and the label " N" means a structure of NiAs type compounds. The x(XTC) and x(EDX) are the values estimated by XTC and EDX, respectively.

$Cd_{1-x}Cr_xSe$	x(XTC)	x(EDX)	Cr(mol %)	Cd(mol %)	Se(mol %)
W*	0	-	-	-	-
W	0.01	0.01	0.58	57.42	42
W	0.11	0.07	4.06	53.94	42
W	0.29	0.17	9.35	45.65	45
W	0.30	0.27	14.58	39.42	46
W	0.42	0.34	17	33	50
W	0.51	0.58	28.42	20.58	51
W	0.60	0.66	32.34	16.66	51
(a) N*	0.52	1	47	0	53
(b) N	0.73	1	37	0	63
(c) N	0.85	1	40	0	60
(d) N	0.91	1	50	0	50
N	1	-	-	-	-

Composition of the $Cd_{1-x}Cr_xSe$ films are listed in Table I. The specimens with $0 < x(XTC) < 0.6$ show wurtzite sturucture. The specimens with $x(XTC) \geqq 0.7$ show hexagonal structure of NiAs type compounds, and they are CrSe films with different composition ratios. The structure of the film seem to change from wurzite type into NiAs type at about x(XTC)=0.6. For the films with wurtzite structure, total amounts of cation of tend to be stoichiometrically larger than those of anion. It is possible that lattice vacancies at the anion sites give rise to the deviation. For the films with NiAs type structure, the amount of Cd in the films is zero althogh XTC does not indicate zero. It may be difficult to substitute Cd ions for Cr ions in CrSe compounds.

Fig 3 shows the AFM image of $Cd_{1-x}Cr_xSe$ film. The average grain size is about 200 to 300nm. A hexagonal symmetry is seen for the grain which grows along the c-axis.

Fig. 4 shows the magnetic field dependence of the magnetization of $Cd_{1-x}Cr_xSe$. The magnetization almost saturates above 1 T for compositions ranging from x = 0.07 to 0.66. The saturation magnetization increases approximately in proportion to the amount of Cr ion. The magnetizations of the films with x=0.58 and 0.66 seem to increase gradually even in the high magnetic field region around 5 T. In comparison with $Cd_{1-x}Mn_xSe$ or $Cd_{1-x}Co_xSe$,

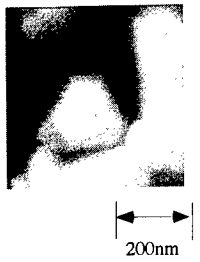

Fig3. AFM image of $Cd_{0.99}Cr_{0.01}Se$ film. The grain average size is about 200 ~ 300 nm. A hexagonal morphology is observed.

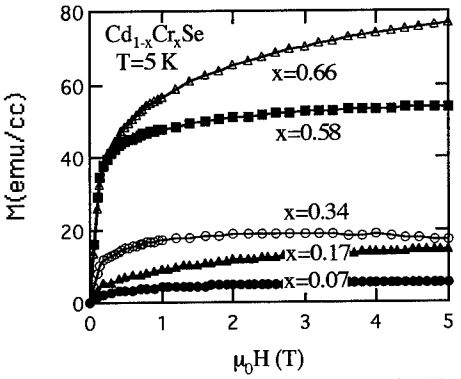

Fig. 4. Magnetization of $Cd_{1-x}Cr_xSe$ at 5K for H parallel to the substrate plane. The magnetizations almost saturate up to 1T. Saturation magnetizations is approximately in pro-portion to the composition x.

initial magnetization curves saturate easily in $Cd_{1-x}Cr_xSe$. At the temperature 4.2 K, the magnetic field requires more than 5 T to saturate the magnetiztion of $Cd_{0.98}Mn_{0.02}Se$ or $Cd_{0.99}Co_{0.01}Se$, and the magnetic susceptibility decrease as the concentration of magnetic ion increases [8][9].

The magnetic susceptibility of $Cd_{1-x}Cr_xSe$ obviously increases as the Cr concentration increases. These magnetization processes are caused by ferromagnetic interactions between Cr ions. In order to analyze the magnetization curve, the data are fitted to the modified Brillouin function written as

$$M = xM_0\langle S_z\rangle + \chi_0 H,$$

where, $M_0 = \frac{g_{Co^{2+}}\mu_B N_0}{W}$, $\langle S_z\rangle = SB_S(\varsigma)$, $B_S(\varsigma)$ is the Brillouin function for the spin S=2, and $\varsigma = \frac{g_{Co^{2+}}\mu_B SH}{k_B(T+T_0)}$. T_0 and x are fitting parameters introduced by Gaj [10]. The second term represents the diamagnetic contribution of the CdSe matrix and the diamagnetic susceptibility, and χ_0 is about 3.3×10^{-7} emu/g for CdSe. We assume the g factor for H⊥c-axis to be 2.0, taking into account that the g-values of Cr^{2+} in other II-VI crystals are approximately 2.0 [11]. We also estimate the density of $Cd_{1-x}Cr_xSe$ as $(191.37-60.41x)\times2.96\times10^{-2}(g/cm^3)$, assuming that Cr ion is substituted for Cd ion with no change of lattice constant.

Fig. 5 shows magnetization of $Cd_{0.93}Cr_{0.07}Se$ and its fitting curves. The parameters are calculated to be x=0.01 and $T_0=-2.0$ K by least square procedure. The calculated curve does not fit the data well below μ_0H=2.0 T. Usually, complete fits by the modified Brillouin function is only possible at low concentrations of magnetic ions, because the formation of clusters may effect the magnetization curve. However, two general comments can be made about the parameters. First, the value of T_0 is negative, which suggests the possibility of ferromagnetic interaction between magnetic ions. In the DMSs such as $Cd_{1-x}T_xSe$ (T : Mn or Co), T_0 shows always positive value which is contributed to the antiferromagnetic *d-d* interaction. Secondly, the value of parameter x associated with the concentration of magnetic ions is much smaller than the estimated value by EDX analysis.

The magnetic moment of free Cr^{2+} ion is considered to be about 3.7 μ_B instead of 4 μ_B owing to the contribution of orbital momentum [12]. If the full magnetic moments of Cr^{2+} ions are ordered parallel to the external magnetic field, the saturation magnetization would be about ten times as large as the experimental result. The net magnetic moment per Cr atom estimated from experimental data at 5 T is shown in table II. These values are close with each other, and the average value is 0.5 μ_B. In order to explain ferromagnetic susceptibility

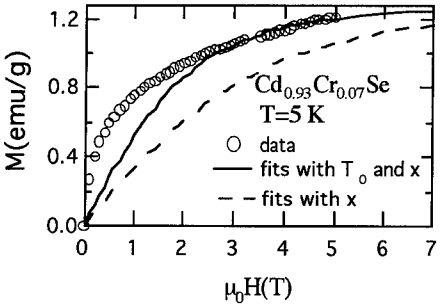

Fig. 5. Magnetization of $Cd_{0.93}Cr_{0.07}Se$ and fitting curve at 5K. The solid line indicates fitting curve using modified Brillouin function(T_0=-2.0K, x=0.010). The dashed line is the curve using Brillouin function withx=0.01.

Table II Net magnetic moment per Cr atom estimated at 5 T. The average value is 0.50 μ_B.

composition x	0.07	0.17	0.34	0.58	0.66
magnetic moment (μ_B/Cr)	0.58	0.57	0.33	0.48	0.56

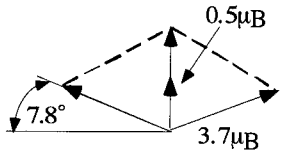

Fig. 6. A schematic representation of the configuration of spin(solid arrows), where each spin is canted 7.8° to antiparallel direction.

and reduced magnetic moment of Cr ion, we propose a canted antiferromagnetic order schematically as shown in Fig 6. In this situation, each spin of Cr ion is canted about 8 degrees to an antiparallel configuration. As a result, a weak ferromagnetic component appears. At the present stage, it is difficult to determine the magnetic structure, however, the following magnetization data can give a hint of the possibility of weak ferromagnetic interaction between Cr ions.

Fig. 7 shows the field dependence of magnetization of Cr_xSe_y film at 5 K with different composition ratios. It is evident that ferromagnetic hysteresis loop is seen in the $Cr_{4.7}Se_{5.3}$ film, and the coercive force is about 0.3 T. The magnetization curve of Cr_5Se_5 and Cr_4Se_6 films show antiferromagnetic behavior and their susceptibilities are

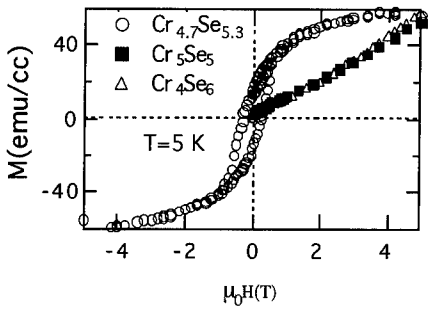

Fig. 7 Magnetization of Cr_xSe_y films. The magnetization curves of the Cr_5Se_5 and Cr_4Se_6 films are antiferromagnetic and magnetic susceptibilities are almost same order of the value by Ref.[13]. The ferromagnetic hysteresis loop is observed in the $Cr_{4.7}Se_{5.3}$ and the coercive force is as large as 0.3 T.

consistent with previous reports [13][14]. The magnetizations of the these films are the same order. If the full magnetic moments of Cr ions are ordered in the magnetic field, the saturation magnetization must be much larger than that at 5 T. Besides, the magnetization seems to increases in proportion to the external magnetic field above 2 T. It can be considered that spins of Cr ions are canted with antiferromagnetic ordering in the applied magnetic field, then they gradually align themselves as the magnetic field.
In previous references, all of Cr_xSe_y bulk system show antiferromagnetism. The origin of ferromagnetic phase is not clear at the present experimental stage.

CONCLUSION

We successfully prepared wurtzite $Cd_{1-x}Cr_xSe$ films with composition x ranging from x=0 to 0.6 by co-evaporating CdSe and CrSe. The deposited films show preferential orientation along the c-axis. The net magnetic moment of Cr ion is much less than the full magnetic moment of the free ion, however, the initial magnetization curve of the films behaves like a ferromagnet. It was shown that a ferromagnetic phase exists in Cr_xSe_y system.

ACKNOWLEDGMENTS

The authors wish to thank M. Sakai and staff members of the Institute for Molecular Science. This work was supported by Grant-in-Aid for Scientific Research from the Ministry of Education, Science and Culture, the Okura Kazuchika Finance Foundation and Chubu Electric Power Basic Technical Laboratory Foundation.

REFERENCES

1. J. K. Furdyna, J. Appl. Phys. **64** , R29 (1988).
2. R. R. Galazka, Proc. XIV Intern. Conf. Phys. Semi cond., Edinbourgh, p.133 (1978).
3. Y. Oka, Proc. 4th Japan-Korea Joint Symposium (Cheju island, korea 1994) 26.
4. R. Oikawa, K. Onodera, Y. Honda: Tokin Tech. Rev.,**19**, 32 (1993).
5. T. Hayashi, M. Tanaka, T. Nishinaga and H. Shimada, J. Appl. Phys. **81**, p. 4865 (1997).
6. W.Mac, N.T. Khoi, A. Twardowski, J. A. Gaji and M. Demianiuk, Phys.Rev. Lett. **71**, p.2327 (1993).
7. R. D. Shannon, Acta Crystallographica **A32**, p.751 (1976).
8. J. R. Anderson, G. Kido, Y. Nakagawa, Y. Nishina, M. Gorska, L. Kowalcyk and Z. Golacki, Phys. Rev. **B41**, p.1014 (1990).
9. N. Adachi, M. Inoue, I. Mogi and G. Kido, J. Phys. Soc. Japan **64**, p.1378 (1995).
10. J. A. Gaj; Acta PhtsicaPonica **73**, p.463 (1988).
11. J. T. Vallin and G. D. Watkins, Phys. Rev. **B9** , p.2051(1974).
12. W.Mac, A. Twardowski, P. J. T. EGGENKAMP, J. M. Swagten, Y. Shapira and M. Demianiuk, Phys.Rev. **B50**, p.14144 (1994) .
13. I. Tsubokawa, J. Phys. Soc. Japan **15**, p.2243 (1960).
14. M. Yuzuri, Y. Adachi, T. Kaneko, Y. Yoshida and S. Abe, J. Magn. Magn. Mat. **140-144**, p.151 (1995) .

SOLUTION FLOW SYSTEM FOR HYDROTHERMAL-ELECTROCHEMICAL SYNTHESIS: NEW OPPORTUNITIES FOR MULTILAYERED OXIDE FILMS

W. SUCHANEK, T. WATANABE, B. SAKURAI, M. YOSHIMURA
Center for Materials Design, Materials and Structures Laboratory,
Tokyo Institute of Technology, 4259 Nagatsuta, Midori-ku, Yokohama 226 Japan

ABSTRACT

A solution flow system for hydrothermal-electrochemical synthesis has been constructed in our laboratory. This equipment can operate at 20°-200°C, under the pressure of 1-50 atm., at flow rate of 1-50 cm^3/min. Applicability of the flow system for low-temperature, hydrothermal-electrochemical synthesis of single-layer and multilayered thin films has been demonstrated using the $BaTiO_3$-$SrTiO_3$ system as an example. Single phase thin films as well as double layers have been deposited at 150°C, current density of 1 mA/cm^2, and flow rates of 1-50 cm^3/min. The flow rate is an important parameter allowing additional control of the films' morphology by affecting the growth rate. The multilayers can be prepared in only one experiment by simply changing the flowing solution. Processing using the solution flow cell may serve as an inexpensive and environmentally friendly way of fabricating any multilayered thin films, including magneto-optic films.

INTRODUCTION

Processing of thin films has been dominated by chemical vapor deposition [1], physical vapor deposition [1], and sol gel techniques [2,3]. However, it is possible to fabricate thin films directly from solution, without subsequent heat treatments, by hydrothermal and/or electrochemical methods [4]. These techniques give similar results as any other process using fluids (such as vapor, gas, plasma) and/or beam/vacuum processing. The total energy consumption among all these processing routes should be the lowest in aqueous solution systems because a much larger excess of energy is necessary to create melts, vapor, gas or plasma than to form aqueous solutions at the same temperatures [4,5]. Solution processing is located in the temperature-pressure range characteristic for conditions of living on earth. The other processing routes which are connected with increasing temperature and/or increasing (or decreasing) pressure, are environmentally stressed, energy consuming, and expensive [5].

Surprisingly, researchers investigating hydrothermal and hydrothermal-electrochemical synthesis of thin films have been focused only on film preparation in closed autoclaves and/or beakers. However, fabrication of thin films in a continuous process under solution flow is essential for possible future application of this technique for integration with advanced device technology. Advantages of thin film fabrication in a solution flow system are: possibility of the recycled (i.e. closed) flow, possibility of fabrication of multilayered materials in only one run, and additional control (improvement) of the film microstructure by changing conditions of the solution flow [6]. The best suited equipment for this purpose seems to be a solution flow cell for hydrothermal-electrochemical synthesis. Such equipment has been recently constructed in our laboratory. Generally speaking, its design is similar to other flow-cells used in geological studies [7] or in materials engineering (ferrite plating) [8].

We have demonstrated applicability of our solution flow system for synthesis of multilayered $BaTiO_3$-$SrTiO_3$ thin films. These materials have recently attracted attention of researchers

Mat. Res. Soc. Symp. Proc. Vol. 517 © 1998 Materials Research Society

because demands to miniaturize and/or upgrade the DRAM capacitors necessitate fabrication of multilayered microstructures in order to reduced the leakage current several orders of magnitude, while keeping the high dielectric constant [9]. Another interesting application of the multilayered films in the $BaTiO_3$-$SrTiO_3$ system are functionally graded materials having different chemical compositions across the film thickness, resulting in a desired gradient of the dielectric constant across the material. Such materials can find applications as tunable multilayer capacitors, waveguide phase shifters, filters etc. [9]. Previously prepared $BaTiO_3$-$SrTiO_3$ multilayerd structures were fabricated by tape-casting, dip-coating, or r.f. magnetron sputtering which required additional heat treatments in the range of 500°-700°C and/or vacuum [9]. The heat treatments often result in cracking and/or peeling of the deposited layers, reaction of the film with the substrate, and they are energy-consuming.

The purpose of the research presented in this paper was demonstration of applicability of the flow cell for hydrothermal-electrochemical synthesis for preparation of single-phase thin films and multilayers in the $BaTiO_3$-$SrTiO_3$ system, investigation of the processing conditions and the mechanism of growth of the $BaTiO_3$-$SrTiO_3$ multilayers. Most of our observation related to film fabrication in the flowing solution have a very general character, and thus may be applied to synthesis of other materials including magneto-optics. Possible applications of the solution flow cell particularly for synthesis of the magneto-optic materials are pointed out in a separate section at the end of the paper.

EXPERIMENT

Solution Flow System for Hydrothermal-Electrochemical Synthesis

All the experiments have been accomplished in the flow cell (designed by the authors) for hydrothermal-electrochemical synthesis. A general schematic of the equipment is shown in Fig. 1. A solution is pumped from the container to the autoclave (flow cell) with the flow rate of 1-50 cm^3/min. which corresponds to Reynolds numbers of about 46-2300, i.e. in the range of the laminar flow. Our flow system can operate up to 200°C which is a maximum temperature for industrial applications of the hydrothermal synthesis. Temperature is controlled by a chromel-alumel thermocouple just below the substrate. Electrochemical conditions can be controlled in a range determined by our potentiostat/galvanostat equipment (Kikusai Electronics Corp., Japan).

Fabrication of $BaTiO_3$, $SrTiO_3$, and $Ba_xSr_{1-x}TiO_3$ Single-Phase Thin Films

Reagent grade $Ba(CH_3COO)_2$ (Wako Pure Chemical Industries Ltd., Japan), $Sr(CH_3COO)_2{\cdot}0.5H_2O$ (Wako Pure Chemical Industries Ltd., Japan), and polished titanium sheets (roughness 1-2 nm, purity 99.5%, Nilaco Corp., Japan) were used as sources of barium, strontium and titanium, respectively. Appropriate quantities of the acetates were dissolved in distilled and degassed water to yield 0.25 M solutions. The pH of each solution was adjusted to the value of 13 by 1.0 M-NaOH solution (Wako Pure Chemical Industries Ltd., Japan). During the experiments, the acetate solutions were constantly bubbled with argon gas. Experiments have been carried out for 1 hour at the temperature of 150°C. In all cases galvanostatic conditions with constant current densities of 1 or 20 mA/cm^2 were applied. The titanium substrate served as positive electrode (anode). The synthesis was carried out under open or closed (recycled) flow. Solution flow rates were in the range of 1-50 cm^3/min.

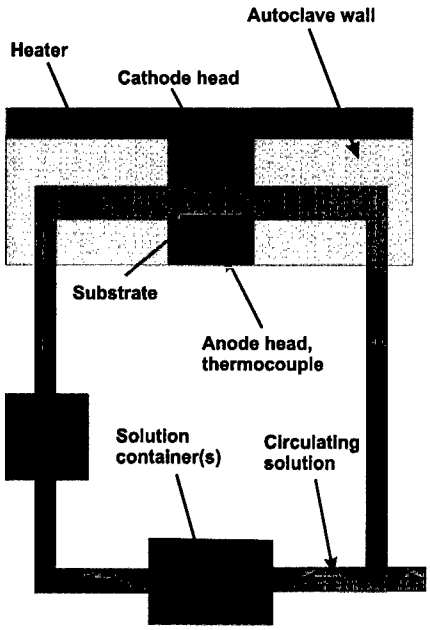

Fig. 1. General schematic of the solution flow system for hydrothermal-electrochemical synthesis.

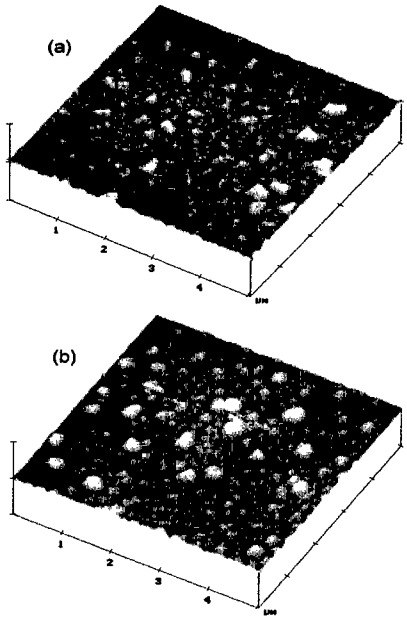

Fig. 2. AFM images of the $SrTiO_3$ thin films prepared at 150°C (1 h, 1 mA/cm^2) at the flow rate of 10 cm^3/min. in the open flow system (a) and closed (recycled) flow (b).

Fabrication of $BaTiO_3$-$SrTiO_3$ Double Layers

Starting solutions were the same as those described in the previous section. The synthesis was carried out in open flow. Solution flow rate was kept constant at 10 cm^3/min. Synthesis was carried out in two 1 hour-long steps, at 150°C, under galvanostatic conditions (constant current of 1 mA/cm^2). In the case of $BaTiO_3/SrTiO_3$ double layers (sequence of the layers: $BaTiO_3/SrTiO_3/Ti_{substrate}$), Sr-acetate solution was used in Step 1; in the following Step 2 Ba-acetate solution was used. Transition from Step 1 to Step 2 occurred without cooling, just by changing the flowing solution. In the case of $SrTiO_3/BaTiO_3$ double layers (sequence of the layers: $SrTiO_3/BaTiO_3/Ti_{substrate}$), Ba-acetate solution was used in Step 1, in the following Step 2, Sr-acetate solution was used. Transition from Step 1 to Step 2 occurred without cooling, but with (or without) a 30 min.-long surface treatment of the $BaTiO_3$ layer using distilled and degassed water (pH=7).

Characterization of the Materials

The phase compositions of the prepared films were characterized by X-ray diffraction (XRD, 40 kV-40 mA, CuKα, MAC Science Co. Ltd., Tokyo, Japan). The surface morphologies of the films were observed using atomic force microscopy (AFM, PicoSPM, model MS300, Molecular

Imaging/Digital Instruments, USA). The depth profiles of the Sr, Ba, Ti, and O were obtained by X-ray photoelectron spectroscopy (XPS, ESCA-3200, Shimazu Co. Ltd., Tokyo, Japan). Raman spectra were obtained using a laser Raman spectrometer (T64000 Atago-Jobin Yvon, France-Japan) working in a "micro" mode. An Ar laser with a wavelength of 514.5 nm was used for excitation. The laser beam was focused to produce 1-2 μm diameter spot. The double-layered films were characterized after each step of their fabrication.

RESULTS AND DISCUSSION

$BaTiO_3$, $SrTiO_3$, and $Ba_xSr_{1-x}TiO_3$ Single-Phase Thin Films

Results of synthesis carried out in the open and closed (recycled) flow were almost the same (Fig. 2). Under the investigated conditions, only single phase $BaTiO_3$, $SrTiO_3$ or $Ba_xSr_{1-x}TiO_3$ have been prepared, if the current density did not exceed 1 mA/cm^2 (Fig. 3). Carbonates and/or titanium oxides were not detected in any case. When the current density was 20 mA/cm^2 large amounts of Ba- or Sr-carbonates were formed. Under the experimental conditions, formation of $BaCO_3$ or $SrCO_3$ together with the corresponding titanates is favorable when carbonate ions are present in the solution [10]. Presence of the carbonate ions in the solutions was high probably due to electrochemical decomposition of the acetate ions on the anode, since acetate ions have been known to be metastable under hydrothermal conditions in the investigated temperature range [11].

Effects of the flow rate on the grain size of the single-phase $BaTiO_3$, $SrTiO_3$ or $Ba_xSr_{1-x}TiO_3$ thin films are shown in Fig. 4. The grain size increases almost linearly with increasing flow rate, reaching plateau at approximately 20 cm^3/min. Effects of the flow rate in our experiments are in

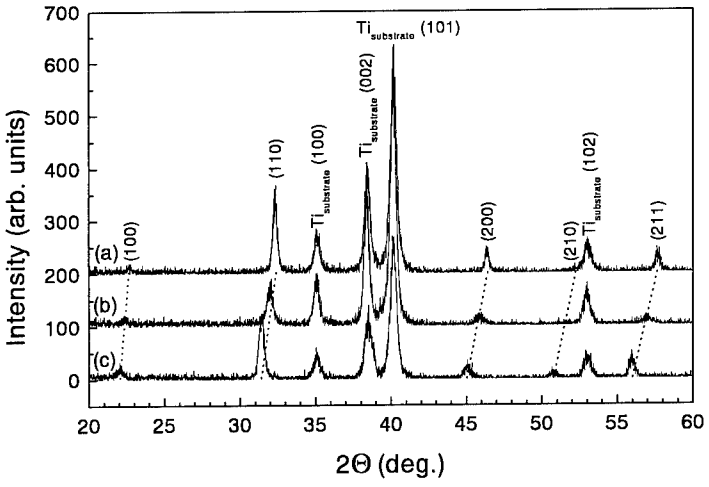

Fig. 3. X-ray diffraction patterns of: (a) $SrTiO_3$, (b) $Ba_xSr_{1-x}TiO_3$ (x= 0.75 in the starting solution), and (c) $BaTiO_3$ single-phase thin films. Temperature of 150°C, current density of 1 mA/cm^2, synthesis time of 1 h, and flow rate of 1 cm^3/min. were applied in all cases.

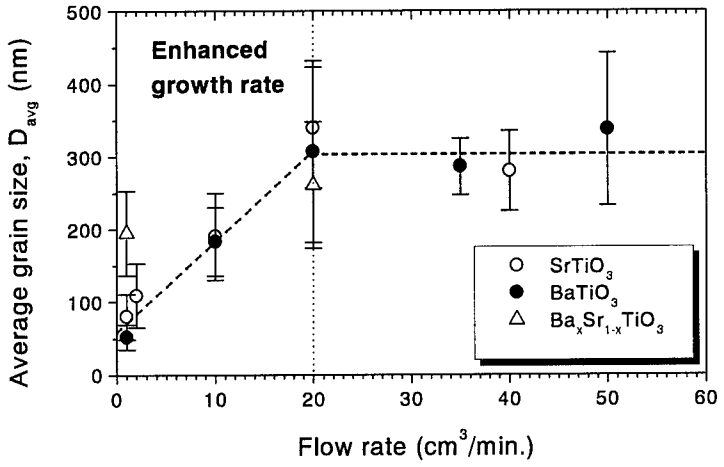

Fig. 4. Average grain size of the $BaTiO_3$, $SrTiO_3$, and $Ba_xSr_{1-x}TiO_3$ single-phase thin films as a function of flow rate at constant temperature of 150°C. Error bars denote standard deviations for the average values.

fact similar to the effects of stirring applied in growth of crystals from solutions or melts. Usually, they lead to reduction of supersaturation inhomogenities and increase of the growth rate [12]. In has been known, that growth rate of crystals increases with increasing solution flow rate until limiting rate is reached when the growth rate becomes controlled by the interfacial kinetic process [12]. Our experimental results suggest that the microstructure of the films at various flow rates is controlled by the growth rate, which initially increases, and then remains unchanged from the flow rate of 20 cm^3/min.

$BaTiO_3$-$SrTiO_3$ Double Layers

$BaTiO_3/SrTiO_3$ and $SrTiO_3/BaTiO_3$ double layers have been fabricated in our flow cell in only one experiment, without cooling, just by changing the flowing solution. XRD patterns of the double layers show distinct peaks derived from $SrTiO_3$ and $BaTiO_3$ layers. Presence of $Ba_xSr_{1-x}TiO_3$ solid solutions has not been detected by XRD, but we cannot preclude dissolution of small quantities of Ba in the $SrTiO_3$ layers or Sr in the $BaTiO_3$ layers. XPS data confirm presence of the Ba- or Sr-rich layers on the surface and respectively Sr- or Ba-rich layers, below (Fig. 5). XPS data suggest also presence of Ti-oxide layer (not detected by XRD) between the Ti-substrate and the titanate layers (Fig. 5). These data demonstrate that initially formed $SrTiO_3$ and $BaTiO_3$ layers have been covered by layers of $BaTiO_3$ and $SrTiO_3$, respectively.

The $BaTiO_3$ could be easily deposited on the $SrTiO_3$ layer to form the $BaTiO_3/SrTiO_3$ double layer. However, an additional surface treatment of the $BaTiO_3$ using pure water was necessary to deposit $SrTiO_3$ on $BaTiO_3$ to fabricate the $SrTiO_3/BaTiO_3$ double layer. The initially formed $BaTiO_3$ layer remained almost unchanged when the synthesis was carried out without the intermediate (between Steps 1 and 2) water treatment. It was covered with $SrTiO_3$ crystals if the

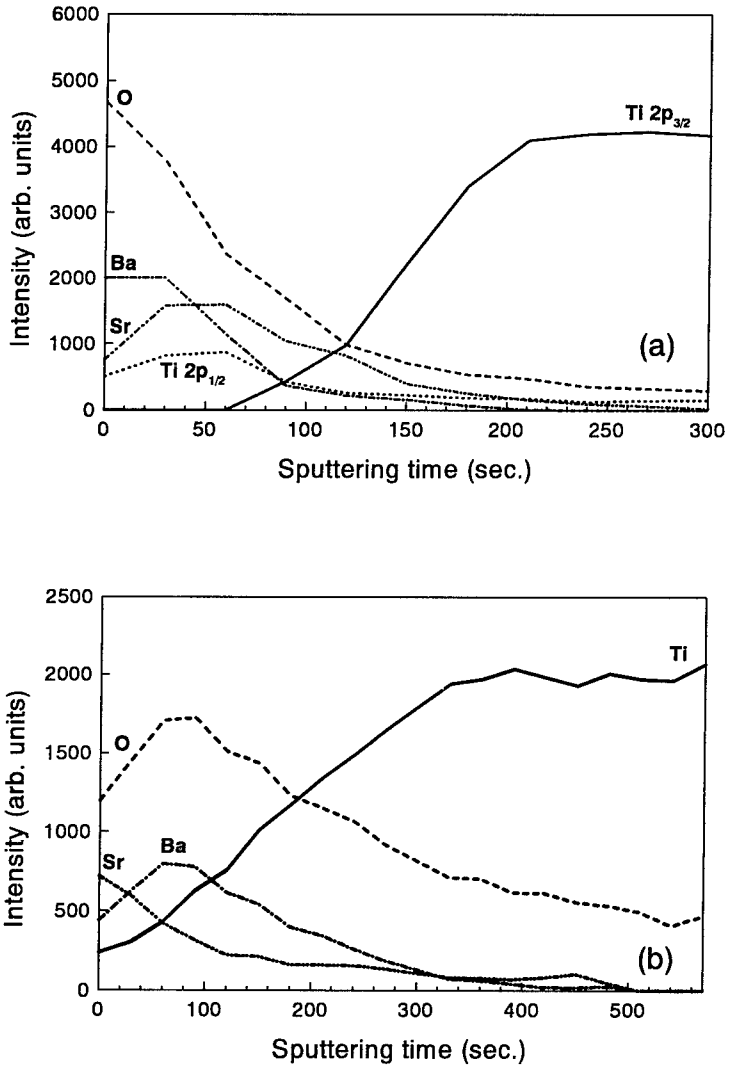

Fig. 5. X-ray photoelectron spectroscopy depth profiles of Sr (3d), Ba (3d), Ti (2p), and O (1s) for (a) $BaTiO_3/SrTiO_3$ double layer thin film; (b) $SrTiO_3/BaTiO_3$ double layer thin film.

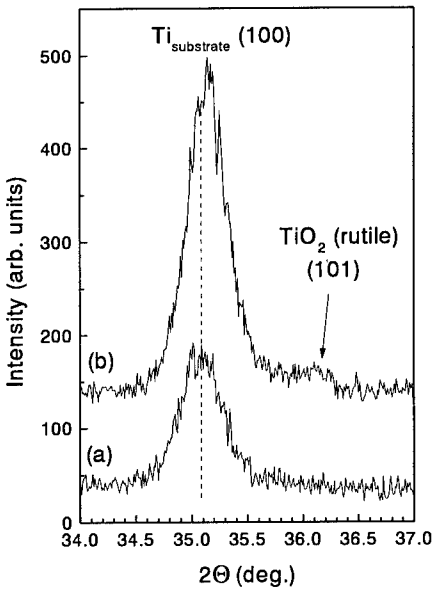

Fig. 6. X-ray diffraction patterns of a $BaTiO_3$ layer prepared in Step 1 (temperature of 150°C, current density of 1 mA/cm^2, synthesis time of 1 h, and flow rate of 10 cm^3/min); (a) before and (b) after the treatment in H_2O at 150°C for 30 min.

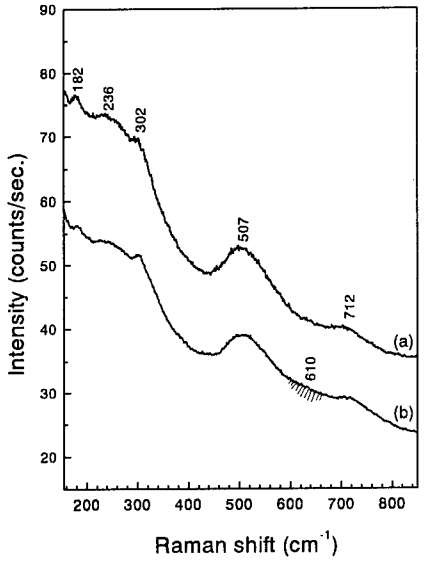

Fig. 7. Raman spectra of a $BaTiO_3$ layer prepared in Step 1 (temperature of 150°C, current density of 1 mA/cm^2, synthesis time of 1 h, and flow rate of 10 cm^3/min) (a) before and (b) after the treatment in H_2O at 150°C for 30 min. The shadowed area in (b) corresponds to the TiO_2 (rutile)-derived band.

intermediate water treatment was applied. The positive effect of the water treatment of the $BaTiO_3$ layer seems to be due to the formation of TiO_2 (rutile) on the surface of $BaTiO_3$ after this intermediate step. The presence of rutile has been detected both by XRD (Fig. 6) and Raman spectroscopy (Fig. 7). The TiO_2 has already been reported to be formed on the surface of $BaTiO_3$ under quite similar experimental conditions [13]. The rutile layer seems to be responsible for easier deposition of $SrTiO_3$ crystals onto $BaTiO_3$ during the Step 2.

Potential Applications of the Solution Flow System in Magneto-Optics

In spite of the fact that most thin films are prepared by chemical or physical vapor deposition or by sol-gel techniques, multiple thin films have been fabricated using low-temperature hydrothermal-electrochemical techniques. Examples include ceramics, such as $Ba_xSr_{1-x}TiO_3$, $SrTiO_3$, $BaTiO_3$, $PbTiO_3$, $LiNbO_3$, PZT, TiO_2, ZnO, PbS, CdSe, etc. [14], Co_3O_4 [15], ferrites [16,17], variety of metals and alloys [18]. The microstructure and chemical composition of these materials can be controlled in a wide range at temperatures of 20°-200°C. Recent demands to miniaturize and/or upgrade electronic devices require fabrication of nanometer-scale structures [19]. Fortunately, also epitaxial layers [20,21], monomolecular layers [20], nanometric-size

metallic [22] or ceramic [23,24] multilayers, and even ceramic superlatices [25,26] can be fabricated by the hydrothermal and/or electrochemical techniques.

There are variety of materials in the field of magneto-optics, including metals and ceramics in the form of single-phase films or multilayers [27]. The solution flow cell seems to be well suited for synthesis of magneto-optic materials, particularly for the multilayers, if only the desired compound can be synthesized under hydrothermal-electrochemical conditions. Examples of magneto-optic materials which have already been synthesized by hydrothermal-electrochemical technique include: epitaxial iron garnets by hydrothermal method at T>500°C and p>1 kbar [28], electrodeposited metallic multilayers such as $(Co/Pt)_n$ [29], $(Co/Cu)_n$ [30], electrodeposited thin films such as Co-Pt [31], Fe-Co [32], ZnS [33], GaAs [34], and powders of $CoFe_2O_4$ (135°-173°C) [35], $BaFe_{12}O_{19}$ (95°-900°C) [36,37], $BaFe_{12-2x}Co_xTi_xO_{19}$ (300°-500°C) [38] by the hydrothermal method.

We can consider the solution flow cell for hydrothermal-electrochemical synthesis as applicable for synthesis of single layers of metals, alloys, and ceramics. It allows synthesis of magnetooptic multilayers of metals, alloys, and/or ceramics in only one experiment, providing that appropriate solution precursors can be found. Non-aqueous solutions can be applied in order to increase number of possible to (co)deposit elements [39]. Finally we can think about hydrothermal epitaxy of magneto-optic materials at reduced temperature. In a recent few years, the synthesis temperature of epitaxial $BaTiO_3$ on $SrTiO_3$ has been reduced from 400°-800°C [40] to 90°C [41,42]. We should start to think seriously about methods to integrate the hydrothermal/electrochemical methods with magneto-optic device technology. From this point of view, fabrication of ceramic thin films in the solution flow, in the recycled system, below 200°C is very important. Some processing for fabrication of integrated circuits already includes chemical solution processing (etching, sol-gel), in addition to chemical and physical vapor deposition [43]. In some cases, the (electro)chemical routes are considered as alternatives for the presently used vapor techniques (for example copper deposition) [44]. For these reasons the technique using the solution flow under hydrothermal-electrochemical conditions is an important step in integration of solution processing with advanced device technology including magneto-optics.

CONCLUSIONS

A newly constructed solution flow cell has been used to synthesize single and double layers in the $BaTiO_3$-$SrTiO_3$ system under hydrothermal-electrochemical conditions at 150°C using Ti-sheets, Ba-acetate, and Sr-acetate as sources of Ti, Ba, and Sr, respectively. Purity and uniformity of the single-phase films were confirmed by XRD and micro-Raman spectroscopy. The $BaTiO_3/SrTiO_3$ and $SrTiO_3/BaTiO_3$ double layers have been characterized by XRD, XPS, AFM and Raman spectroscopy after all preparation stages. $BaTiO_3$ layers could be easily deposited on $SrTiO_3$ layers at 150°C (1 h, 1 mA/cm^2). To deposit $SrTiO_3$ layers on $BaTiO_3$ layers, water leaching of the $BaTiO_3$ surface (150°C, 30 min) with subsequent formation of TiO_2 (rutile) was necessary. This processing route may serve as an inexpensive and environmentally friendly way of fabricating functionally graded materials in the $SrTiO_3$-$BaTiO_3$ system as well as other multilayered materials. There is a great potential in using the solution flow system for fabrication of magneto-optical films. A variety of magneto-optic materials have been already prepared by hydrothermal methods or by electrodeposition. Thus the solution flow system seems to be well suited for fabrication of multilayered magneto-optics at low temperatures, low cost, under environmentally benign conditions.

ACKNOWLEDGMENTS

This research was supported by the "Research for the Future" Program No. 96R06901 of the Japanese Society for the Promotion of Science (JSPS). The authors are greatly indebted to Prof. M. Kakihana, Prof. M. Yashima, Prof. M. Abe, Dr. J. Frantti, and Dr. K-S. Han (all Tokyo Institute of Technology, Japan) for stimulating discussions and to Mr. N. Kumagai for experimental assistance.

REFERENCES

1. M. Ohring, The Materials Science of Thin Films, Academic Press, 1992.

2. L. Klein (editor), Sol-Gel Technology for Thin Films, Fibers, Preforms, Electronics, and Specialty Shapes, Noyes Publ., 1988.

3. L. Klein (editor), Sol-Gel Optics. Processing and Applications, Kluwer Academic Publishers, Boston/Dordrecht/London, 1994.

4. M. Yoshimura and W. Suchanek, Solid State Ionics, **98**, 197 (1997).

5. M. Yoshimura, J. Mater. Res., **13**, 796 (1998).

6. M. Yoshimura, W. Suchanek, T. Watanabe, B. Sakurai and M. Abe, J. Mater. Res., **13**, 875 (1998).

7. J. M. Porter, D. C. Pohl and J. D. Rimstid in Hydrothermal Experimental Techniques, edited by G. C. Ulmer and H. L. Barnes (John Willey & Sons, New York, 1987), pp. 240-60.

8. M. Abe, Y. Tamaura, Y. Goto, N. Kitamura and M. Gomi, J. Appl. Phys., **61**, 3211 (1987).

9. see the introductory section of ref. [6].

10. M. Lencka and R. E. Riman, Ferroelectrics, **151**, 159 (1994).

11. J. S. Seewald and W. E. Seyfried Jr., Geochimica et Cosmochimica Acta, **55**, 659 (1991).

12. D. Elwell and H. J. Scheel, Crystal Growth from High-Temperature Solutions, Academic Press, 1975.

13. H. W. Nesbitt, G. M. Bancroft, W. S. Fyfe, S. N. Karkhanis, A. Nishijima and S. Shin, Nature, **289**, 358 (1981).

14. for list of references see ref. [4] and [5]

15. M. Koinuma, T. Hirae and Y. Matsumoto, J. Mater. Res., **13**, 837 (1998).

16. Y. Kitamoto, S. Kantake and M. Abe, J. Magnet. Soc. Jpn., **21**, 81 (1997).

17. M. Abe, Y. Kitamoto, K. Matsumoto, M. Zhang and P. Li, IEEE Trans. Magn., **33**, 3649 (1997).

18. B. L. McKinney and C. L. Faust, J. Electrochem. Soc., **124**, 379C (1977).

19. N. Yokoyama, S. Muto, K. Imamura, M. Takatsu, T. Mori, Y. Sugiyama, Y. Sakuma, H. Nakao and T. Adachihara, Solid-State Electronics, **40**, 505 (1996).

20. J. H. Fendler and F. C. Meldrum, Adv. Mater., **7**, 607 (1995).

21. F. F. Lange, Science, **273**, 903 (1996).

22. C. A. Ross, Annu. Rev. Mater. Sci., **24**, 159 (1994).

23. M. Abe, T. Miki and Y. Kitamoto, J. Phys IV France, **7**, C1-597 (1997).

24. M. Abe, J. Phys IV France, **7**, C1-467 (1997).

25. J. A. Switzer, C. J. Hung, B. E. Breyfogle, M. G. Shumsky, R. Vanleeuwen and T. D. Golden, Science, **264**, 1573 (1994).

26. J. A. Switzer, C. J. Hung, L. Y. Huang, F. C. Miller, Y. Zhou, E. R. Raub, M. G. Shumsky and E. W. Bohannan, J. Mater. Res., **13**, 909 (1998).

27. A. K. Zvezdin and V. A. Kotov, Modern Magnetooptics and Magnetooptical Materials, Intitute of Physics Publ., London, 1997.

28. M. J. G. Van Hout, J. C. Verplanke and J. M. Robertson, Mater. Res. Bull. **10**, 125 (1975).

29. V. Georgescu, V. Mazur and O. Chelogu, J. Magnet. Magnet. Mater. **156**, 27 (1996).

30. Y. Jyoko, S. Kashiwabara and Y. Hayashi, J. Electrochem. Soc., **144**, L5 (1997).

31. L. Callegaro, E. Puppin, P. L. Cavallotti, N. Lecis and G. Zangari, J. Appl. Phys., **78**, 457 (1995).

32. V. G. Shadrov, T. M. Tkachenko, A. V. Boltushkin and A. V. Semeshko, Phys. Stat. Sol. A, **141**, K51 (1994).

33. C. D. Lokhande, M. S. Jadhav and S. H. Pawar, J. Electrochem. Soc., **136**, 2756 (1989).

34. M-C. Yang, U. Landau and J. C. Angus, J. Electrochem. Soc., **139**, 3480 (1992).

35. T. Pannaparayil, R. Marande, S. Komarneni and S. G. Sankar, J. Appl. Phys., **64**, 5641 (1998).

36. F. Dogan, S. O'Rourke, M-X. Qian and M. Sarikaya, Mater. Res. Soc. Symp. Proc., **457**, 69 (1997).

37. M. A. Hadj Farhat and J. C. Joubert, J. Magnet. Magnet. Mater., **62**, 353 (1986).

38. M. V. Cabañas, J. M. Gonzales-Calbet and M. Vallet-Regi, J. Solid State Chem. **115**, 347 (1995).

39. E. W. Brooman, Plat. Surf. Fin., 1985, 142.

40. K. Kajiyoshi, N. Ishizawa and M. Yoshimura, Jpn. J. Appl. Phys., **30**, L120 (1991).

41. A. T. Chien, J. S. Speck, F. F. Lange, A. C. Daykin and C. G. Levi, J. Mater. Res. **10,** 1784 (1995).

42. A. T. Chien, L. Zhao, M. Colic, J. S. Speck and F. F. Lange, J. Mater. Res. **13,** 649 (1998).

43. H. L. Tuller, Ceram. Trans., **68**, 97 (1996).

44. R. J. Gutmann, T. P. Chow, S. Lakshminarayanan, D. T. Price, J. M. Steigerwald, L. You and S. P. Murarka, Thin Solid Films, **270**, 472 (1995).

MAGNETIC SECOND HARMONIC GENERATION STUDIES OF Co-Cu GRANULAR FILMS

T.V. MISURYAEV, T.V. MURZINA, E.A. GANSHINA, V.S. GUSHIN,
D.V. KAZANTSEV, O.A. AKTSIPETROV
Physics Department, Moscow State University, Vorobyovi Gori, 119899 Moscow, Russia,
aktsip@astral.ilc.msu.su

ABSTRACT

Magneto-induced optical second harmonic generation (MSHG) is used to study the structural and magnetic properties of Co-Cu granular films. Azimuthal anisotropy of the SHG response reveals an existence of the regular structure of Co nanocrystals. The nonlinear magneto-optical Kerr effect (NOMOKE) is observed for the longitudinal and transverse configurations. The coherence of the SH responses from the nonmagnetic and magnetic subsystems of the Co-Cu granular films is demonstrated by the MSHG phase measurements (the MSHG interferometry).

INTRODUCTION

Nanostructures of magnetic materials have attracted a lot of attention recently because of their specific properties. New magnetic phenomena are observed in these materials such as the giant magnetoresistance and the oscillatory coupling through the nonmagnetic spacers [1,2]. Apart from such magnetic effects these compound materials reveal new magneto-induced nonlinear-optical effects, e.g. the nonlinear magneto-optical Kerr effect (NOMOKE) [3].

Second harmonic generation (SHG) is known as a probe of buried interfaces [4] and low-dimensional systems [5]. The unusual sensitivity of the SHG probe to the properties of nanostructures arises from the break down of the structural inversion symmetry of the centrosymmetric material at the interfaces. Another segment of nonlinear optics of low-dimensional systems appears as the break down of the structural inversion symmetry is combined with the break down of time reversal symmetry due to the magnetization in a magnetic material. In this paper the (MSHG) effects are studied in Co nanocrystals imbedded to Cu matrix. Magnetic noncentrosymmetric nanocrystals possess surface and bulk nonmagnetic structural (crystallographic) susceptibilities and surface and bulk magnetic susceptibilities. As the corresponding surface and bulk nonmagnetic and magneto-induced nonlinear polarizations are excited simultaneously, their interference enhances the appearance of the magnetic nonlinear optical effects. Such interference effects are discussed in [6,7] for rare-earth iron garnet films.

The motivation for the studies of the thin magnetic granular films is two-fold: on the one hand, to study their intrinsic nonlinear magneto-optical properties and, on the other hand, to develop a nonlinear-optical probe of their technological characterization and a nonlinear-optical readout of these potential high-density magnetic memories based on their giant magnetoresistance [8].

EXPERIMENT

The samples of granular films were prepared by co-deposition from *e*- beam sources with further annealing for 10 min at 850 K. The films are about 200 nm thick. The mean size of Co granules estimated from the STM scans is about 60-100 nm for the $Co_{0.42}Cu_{0.48}$ film. Figure 1

Mat. Res. Soc. Symp. Proc. Vol. 517 © 1998 Materials Research Society

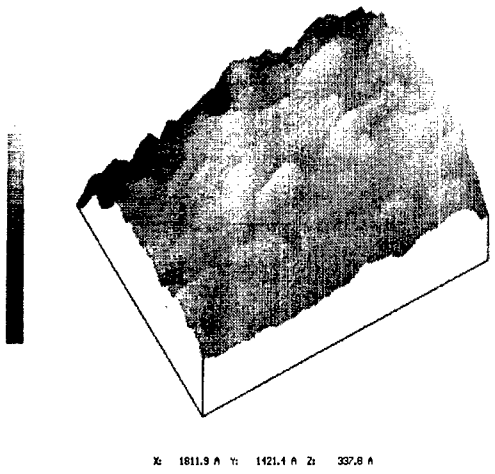

Fig.1. The STM pattern for the $Co_{0.42}Cu_{0.58}$ granular film.

shows the STM pattern for such a film.

To study the nonlinear-optical properties of Co-Cu granular films the azimuthal anisotropy of the SHG intensity is studied using the output of a Q-switched YAG:Nd^{+3} laser at a wavelength of 1064 nm, with a pulse duration of 15 ns and an intensity of 2 MW/cm^2. In the NOMOKE studies a DC-magnetic field up to 1 kOe is applied. The longitudinal NOMOKE is studied and compared with the results of the spectroscopic MOKE studies.

RESULTS

Figure 2 shows the azimuthal angular dependence of the SHG intensity from the $Co_{0.42}Cu_{0.58}$ film for three combinations of polarization of the fundamental and second harmonic (SH) wave. The clear two-fold and four-fold symmetry is found for the s-in, s-out and p-in, s-out combinations, respectively. The four-fold symmetry combined with a strong one-fold pattern is observed for p-in, p-out combination.

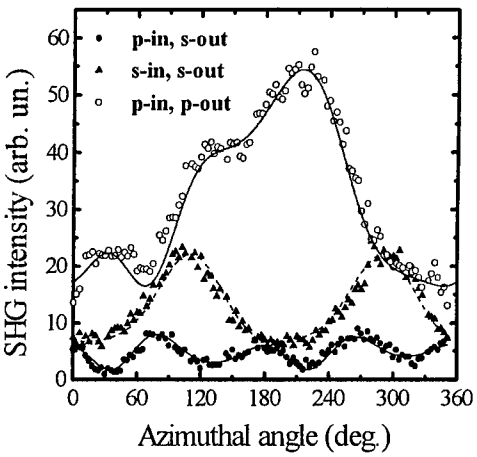

Fig.2. The azimuthal angular dependence of the SHG intensity from the CoCu film.

Figure 3 shows the dependence of the SHG intensity on the analyzer rotation angle in the $Co_{0.42}Cu_{0.58}$ film for two opposite directions of the magnetic field applied in the transversal geometry. NOMOKE is characterized quantitatively by the magnetic contrast $\rho_{2\omega}=(I_{M+}(2\omega)-I_{M-}(2\omega))/(I_{M+}(2\omega)+I_{M-}(2\omega))$, where $I_{M+/-}(2\omega)$ is the MSHG intensity for opposite directions of the magnetization M. The magnetic contrast $\rho_{2\omega}$ measured at a 50° angle of incidence is about 4×10^{-2}, while the linear MOKE contrast measured at the wavelengths 532 nm 1064 nm is about 10^{-3}. Thus, NOMOKE exceed the linear analog by more than an order of magnitude.

The magneto-induced phase shift of the SH wave [9] is in granular films with a thin SnO_2 film as a reference. Figure 4 shows the dependence of the MSHG intensity on the reference position (the SHG interference pattern) for the $Co_{0.42}Cu_{0.58}$ film. The contrast of the SHG interference pattern depends on a coherence of the SH wave generated from the array of the Co nanocrystals and on a mutual coherence of the nonmagnetic and magnetic contributions to the total SH field. The magneto-induced shift of the interference pattern is about 0.5 cm which corresponds to ~ 8^0 in the phase shift domain.

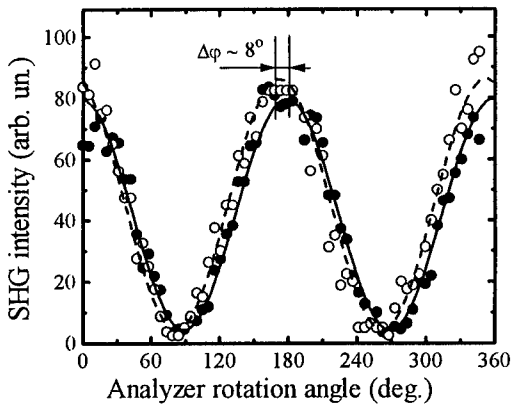

Fig.3. The longitudinal NOMOKE.

The analysis of the MSHG data allows to consider the enhancement of the magneto-induced effects in terms of the phenomenological models of the MSHG discussed in [6,7]. According to [6], the odd in magnetization M surface-bulk cross-terms ($\chi^{(2)B}\chi^{(2)SM}M$) and ($\chi^{(2)S}\chi^{(2)BM}M$) should enhance the appearance of magneto-induced alterations in the SHG intensity from noncentrosymmetric magnetic films due to the interference of the SH fields originating from the nonmagnetic bulk and surface dipole contributions and from the surface and bulk magneto-induced contributions

The central point of these models is the simultaneous breaking down of the time reversal symmetry and the inversion symmetry of the material. The former occurs in Co nanocrystals due to their magnetic ordering. On the other hand, there are two mechanisms which are responsible for the appearance of dipole $\chi^{(2)}$ in metal nanocrystals. The first is the mechanism of the surface dipole $\chi^{(2)S}$ which stems from the lack of inversion symmetry at interfaces [4]. The second mechanism of the bulk dipole $\chi^{(2)B}$ in metallic nanocrystals has been discussed recently [5,11] and occurs from breaking down of the centrosymmetry in particles with noncentrosymmetric shape. A deviation of particle shape from centrosymmetric breaks down the forbiddance on dipole $\chi^{(2)B}$ in nanocrystals of centrosymmetric materials [11].

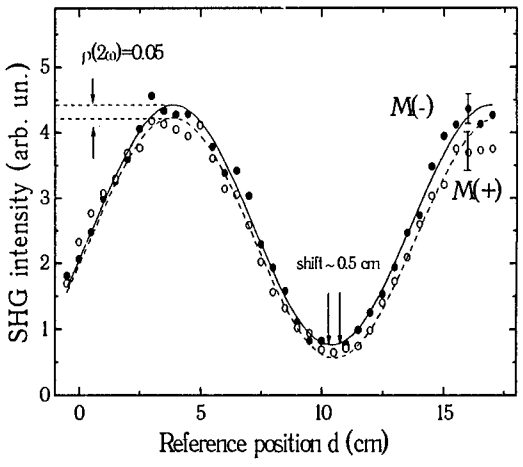

Both these mechanisms are of importance in the case of Co nanocrystals. The sufficient

one-fold Fourier component of Fig. 4. MSHG interference patterns measured for the the anisotropic SHG intensity transversal NOMOKE.
for the p-in, p-out polarization combination can be attributed to the polar axis in the film structure, which is tilted to the normal to the film surface. A regular deviation of the particle shape from centrosymmetric and, as a consequence, the appearance of the polar axis in the topmost array of Co nanoctystals probed by SHG can be caused by a predominant regular asymmetry of the film-vacuum interface. Noncentrosymmetric shape of Co nanocrystals in granular films has been observed in [12] as well.

The mutual coherence of the nonlinear contributions from the nonmagnetic and magnetic sub-systems of the metallic Co nanocrystals obtained by the MSHG interferometry probably indicates the existence of the regular $\chi^{(2)B}$ in Co-Cu granular films.

Thus, the surface-bulk interference cross-terms ($\chi^{(2)B}\chi^{(2)SM}M$) and ($\chi^{(2)S}\chi^{(2)BM}M$) and the bulk-bulk interference cross-terms like ($\chi^{(2)B}\chi^{(2)BM}M$) can be significant in MSHG from Co-Cu granular films due to the appearance of $\chi^{(2)S}$ and $\chi^{(2)B}$ in metal nanocrystals.

CONCLUSION

The significant NOMOKE is observed in magnetic Co-Cu granular films. The structure of the films is studied by STM and anisotropic MSHG. The analysis of the symmetry of the azimuthal SHG anisotropy shows the existence of a regular bulk dipole contribution to the quadratic polarization. The mutual coherence of the SH waves generated by the nonmagnetic and magnetic sub-systems of the Co-Cu granular films is observed by the MSHG interferometry. The role of bulk-bulk and surface-bulk interference in the appearance of the MSHG effects is discussed.

ACKNOWLEDGEMENT

This work was supported by INTAS-93 grant 370 (ext), special RFBR grant for Russian Leading Scientific Schools 96-15-96420, RFBR grants 97-02-17919, 97-02-17923, Integration Program "Center of fundamental optics and spectroscopy" and Programs of Russian Ministry of Science "Physics of Solid State Nanostructures", "Fundamental metrology" and "Fullerenes and nanoclusters".

REFERENCES

1. S.S.P. Parkin, N. More, and K.P. Roche, Phys. Rev. Lett. **64**, p. 2304 (1990).

2. M. Baibich, J. Broto, and A. Fert, Phys. Rev. Lett. **61**, p. 2472 (1988).

3. Th. Rasing, J. Magn. Magn. Mater. **165**, p. 35 (1997).

4. T.F. Heinz, in Nonlinear Surface Electromagnetic Phenomena, H.-E. Ponath and G.I. Stegeman, eds. (North Holland, 1991), 355.

5. O.A. Aktsipetrov, P.V. Elyutin, A.A. Fedyanin, A.A. Nikulin, and A.N. Rubtsov, Surf. Sci. **325**, p. 343 (1995).

6. O.A. Aktsipetrov, A.A. Fedyanin, A.V. Melnikov, E.D. Mishina, and T.V. Murzina, Jpn. J. Appl. Phys. **36**, p. 48 (1998).

7. V.V. Pavlov, R.V. Pisarev, A. Kirilyuk, and Th. Rasing, Phys. Rev. Lett. **78**, p. 2004 (1997).

8. J.Q. Xiao, J.S. Jiang, and C.L. Chien, Phys. Rev. Lett. **68**, p. 3749 (1992).

9. R. Stolle, K.J. Veenstra, F. Manders, Th. Rasing, H. van den Berg, and N. Persat, Phys. Rev. B **55**, p. R4925 (1997).

10. R. Stolle, G. Marowsky, and G. Berkovic, Appl. Phys. B **63**, p. 491 (1996).

11. O.A. Aktsipetrov, P.V. Elyutin, A.A. Nikulin, and E.A. Ostrovskaya, Phys. Rev. B **51**, p. 17591 (1995).

12. S. Mitani, H. Fujimori, and S. Ohnuma, J. Magn. Magn. Mater. **165**, p. 141 (1997).

NONLINEAR MAGNETO-OPTICAL KERR EFFECT IN Gd-CONTAINING LANGMUIR-BLODGETT FILMS

N.V. DIDENKO, A.A. FEDYANIN, G.B. KHOMUTOV, T.V. MURZINA, O.A. AKTSIPETROV
Physics Department, Moscow State University, Vorobyovi Gori, 119899 Moscow, Russia, aktsip@astral.ilc.msu.su

ABSTRACT

Magnetization induced second harmonic generation (MSHG) is observed in Gd-containing Langmuir-Blodgett (LB) films. The nonlinear optical studies reveal significant alterations in the second harmonic generation (SHG) intensity and in the polarization and phase of the second harmonic (SH) wave induced by application of DC magnetic field. The violation of polarization selection rules and the diffusenes of the MSHG intensity indicates the inhomogeneity of LB structure and the hyper-Rayleigh scattering mechanism of MSHG. The latter proofs the existence of 2D-islands of Gd ions in the structural unit of the LB films which is composed by monolayer of rare-earth ions compressed between two layers of stearic acid molecules.

INTRODUCTION

The properties of magnetic nanostructures have attracted a lot of attention recently because of observation of new magnetic effects, e.g. giant magnetoresistance in nanogranular films [1], interlayer coupling through nonmagnetic spacer in layered magnetic/nonmagnetic metal nanostructures [2], *etc.* One of the burning issues in this area is the magnetic properties of atomic monolayers of magnetic materials. Apart from magnetic epilayers, the organometallic Langmuir-Blodgett (LB) films containing monolayers of magnetic ions are potential nanostructers for basic studies and applications as a high density magnetic and magneto-optical storage. In the aspect of the basic studies, these LB films are of interest as a model of the 2D magnetic systems. Magnetic properties of such LB films composed by monolayers of Gd^{3+} ions are studied in [3] by the EPR technique. In the aspect of the further potential application of this material as a magneto-optical storage, the development of nonlinear optical readout from these memories looks very promising [4].

Even-order nonlinear-optical processes, such as second harmonic generation, have been demonstrated to be extremely sensitive to the structural, electronic, magnetic etc. properties of thin films and nanostructures [5-7]. In principle, information about the magnetization state of a magnetic system can be obtained by magneto-optical Kerr effect (MOKE). At the same time, the sensitivity of this technique is restricted to the amount of the magnetic material in the system. That limits the applications of MOKE to the characterization of magnetic properties of thin films and nanostructures. The nonlinear-optical analogue of the MOKE, so called nonlinear magneto-optical Kerr effect (NOMOKE), manifests itself in the magnetization induced changes of the SHG intensity and polarization, and the phase of the SH wave. The magnetic contrast of NOMOKE has been shown to exceed sufficiently the magnetic contrast of MOKE [8].

In the present paper, NOMOKE is used to study the nonlinear-optical magnetic properties and structural features of the organo-metallic LB films containing monolayers of Gd ions.

Mat. Res. Soc. Symp. Proc. Vol. 517 © 1998 Materials Research Society

EXPERIMENT

The organo-metallic LB films are prepared by the Langmuir-Blodgett technique on fused quartz substrates from a solution of stearic acid in chloroform spread on the water subphase. Gd^{3+} ions are dissolved in water from Gd acetate of 5×10^{-4} M concentration and are adsorbed at the floating stearic acid monolayer. This allows for the creation of two-dimensional areas of magnetic ions binded to the solid organic monolayers. The structural unit of periodic LB film 5 nm thick consists of the monolayer of Gd^{3+} ions surrounded by two monolayers of stearic acid. The films composed of 40 structural units are studied. The area per Gd ion in the monolayer is ~10 $Å^2$ and the distance between Gd^{3+} ions in monolayer is about 3.3 $Å$. SHG from the quartz substrate and the LB films of pure stearic acid are found to be negligibly small as compared with the SHG signal from the Gd containing LB films.

The NOMOKE is studied for the longitudinal magnetization of the film. The output of a Q-switched YAG:Nd^{3+} laser at the wavelength of 1064 nm, a pulse duration of 15 ns and a repetition rate of 12.5 Hz is used as a fundamental radiation. The SHG signal generated from LB film is selected by bandpass filters and detected by a PMT and gated electronics. The fundamental pulse intensity is about 1 MW/cm^2 for the laser spot diameter of about 1 mm.

The magneto-induced phase shift of the SH wave, i.e. magnetoinduced SHG interferometry [9], is studied by the use of a thin SnO_2 as the sourse of a reference SH wave. The phase shift between the SH waves generated by the sample and by the reference is varied as the distance d between the reference and the sample is changed [10].

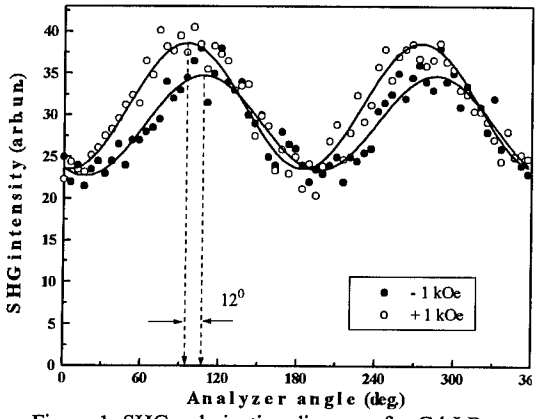

Figure 1. SHG polarization diagrams for Gd-LB films measured for the longitudinal NOMOKE; the fundamental radiation is s-polarized, φ=0 corresponds to the p-polarized SHG.

Azimuthal angular anisotropy of the SHG intensity testifies that the films are isotropic.

Magnetoinduced changes in the SH response from Gd-containing LB films are studied by measuring the SH wave polarisation diagrams, i.e. dependences of the SHG intensity on the rotation angle of the analyzer φ, for the geometry of the longitudinal NOMOKE. The magnetoinduced rotation of the SHG polarisation, measured for the saturating magnetic fields of the opposite signes and for the s-polarised fundamental radiation, is found to be about 12^0 (Fig. 1).

The MSHG interferometry pattern for the longitudinal NOMOKE measured in *s*-in, *s*-out geometry indicates the 130^0 shift of the phase of the SH wave for the opposite directions of magnetic fields ±1 kOe (Figure 2, a). For the p-in, p-out SHG the similar dependences reveal no differences within the experimental accuracy (Figure 2, b).

DISCUSSION

Consider first the polarisation of the SHG radiation reflected from Gd-LB films. It can be seen from both the NOMOKE and SHG interferometry experiments that the s-in, s-out SHG response exists. It is well known that this component of the SHG intensity is forbidden for an isotropic homogeneous media. In this case $\langle\chi^{(2)}\rangle=0$ and $\left\langle\left|\chi^{(2)}-\langle\chi^{(2)}\rangle\right|^2\right\rangle=0$, $\chi^{(2)}$ being the quadratic susceptibility of the LB film and the brackets denote the averaging over all the realizations. Thin films can be described by the electro-dipole susceptibility $\chi^{(2)}$.

At the same time, s-to-s SHG component can be observed for a randomly inhomogeneous films with average dimensions of the homogeneous areas small as compared with the fundamental wavelength. In the latter case $\langle\chi^{(2)}\rangle=0$ while $\left\langle\left|\chi^{(2)}-\langle\chi^{(2)}\rangle\right|^2\right\rangle\neq0$. The s-to-s component of the SHG intensity can be given by [11]:

$$I_{2\omega}^{s-s}(cryst)\sim 1/2\pi\int\Delta\chi^{(2)}d\psi= \\ =1/2\pi\int\left\langle\left|\chi^{(2)}-\langle\chi^{(2)}\rangle\right|^2\right\rangle\Delta\chi^{(2)}d\psi \quad (1)$$

Probably this mechanism of the nonlinear response plays the key role in the case of the Gd-LB films studied.

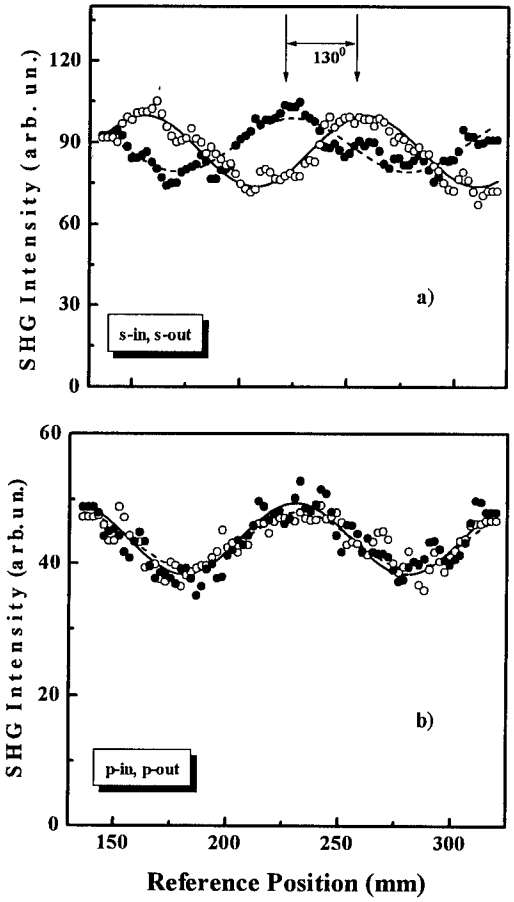

Figure 2. Magnetoinduced SHG interferometry for Gd-LB films measured for the longitudinal NOMOKE; the fundamental radiation is s-polarized (a) and p-polarized (b).

Let us now turn to the discussion of the MSHG interferometry. It was shown in Ref [9] that for a magnetized sample the SHG intensity of the interfering waves depends on magnetization M and reference position d and can be given by:

$$I_{2\omega}(d,M)\propto\left|E_{2\omega}^{sam}(M)+E_{2\omega}^{ref}\right|^2=I_{2\omega}^{sam}(M)+I_{2\omega}^{ref}+2\alpha\sqrt{I_{2\omega}^{sam}(M)I_{2\omega}^{ref}}\cdot\cos\Delta\Phi(d,M), \quad (2)$$

where $I_{2\omega}^{sam}(M)$ is the MSHG intensity from the sample, $I_{2\omega}^{ref}$ is the SHG intensity from the SnO_2 reference, α is the mutual coherence of the interfering SH waves ($0<\alpha<1$),

$\Delta\Phi(d,M)=(\Phi_{sam}(M)+\Phi_{PSU}(d))-\Phi_{ref}$ is the phase difference in the far-field-region between the SH waves generated by the reference (Φ_{ref}) and the sample. The latter is determined by the phase shift $\Phi_{sam}(M)$ of the SH wave, generated in the sample, regarding to the phase of the fundamental wave, and the phase shift $\Phi_{PSU}(d)$ of the fundamental wave in the phase shifting unit (PSU). In our experiments Φ_{ref} is constant for a fixed fundamental wavelength, $\Phi_{sam}(M)$ is magnetization dependent, $\Phi_{PSU}=\frac{2n_{2\omega}-n_{\omega}}{\lambda}x$, where n_{ω} and $n_{2\omega}$ are refractive indices of air at fundamental and SH wavelengths, and the period of the interference pattern is $L=2\pi\Delta k^{-1}=2\pi(k_{2\omega}-k_{\omega})^{-1}\approx 13$ cm, where $k_{2\omega}$ and k_{ω} are the wave vectors of the fundamental and SHG waves in air.

It can be seen from Fig. 2 that the application of the dc magnetic field results in the appearance of the modulation of the $I_{2\omega}(d)$ dependence, d being the position of the reference SHG source. This modulation can be attributed to the appearance of a *regular magnetoinduced* contribution to the SHG intensity. For s-to-s geometry odd in magnetization changes of the MSHG interference patterns are obtained, while for the p-to-p geometry there is no magneto-induced variations in the SHG interference pattern.

This is consistent with the analysis of the symmetry of the magneto-induced electro-dipole susceptibility for an isotropic media. It can be shown [9] that for the s-polarized fundamental radiation two magneto-induced components of $\chi^{(2)}$ can appear: χ_{zyy} and χ_{yyy}. The first one is even in M and contributes to the p-polarized SHG, thus there should be no differences in the SHG interference patterns under the inversion of the magnetization of the film. The second magneto-induced component is odd in M and contributes to the s-polarized SHG. At the same time, one can expect magneto-induced phase shift of the $I_{2\omega}^{s-s}(d)$ dependence being equal to π, while in our experiments this value is about 130^0, that is not quite clear for now.

While discussing the results of the longitudinal NOMOKE for the s-polarized input radiation, one should point out, first, that in the absence of the magnetization the polarization patterns $I_{2\omega}^{s-s}(\varphi)$ dependence is two-fold. This results probably from the different Fresnel coefficients for the p- and s-polarized SHG components for the s-polarized fundamental beam.

Describing the nonmagnetic contribution to the SHG by (1) and taking into account that it does not interfere with the magneto-induced contributions, the polarization MSHG dependences $I_{2\omega}(\varphi)$ for the s-polarized fundamental radiation take the following form:

$$\begin{aligned} I_{2\omega}(\varphi) &= I_{2\omega}(M=0)+I_{2\omega}(M)= \\ &= I_{2\omega}(M=0)+\left\{(A\chi_{zyy}^{even}(M)+B\chi_{yyy}^{odd}(M))E_{\omega}E_{\omega}\right\}^2= \\ &= I_{2\omega}(M=0)+(A\chi_{zyy}^{even}(M)E_{\omega}E_{\omega})^2+\left(B\chi_{yyy}^{odd}(M)E_{\omega}E_{\omega}\right)^2\pm \\ &\quad \pm AB\chi_{zyy}^{even}(M)\chi_{yyy}^{odd}(M)E_{\omega}{}^4 \end{aligned} \tag{3}$$

where $\pm$ correspond to the opposite directions of the magnetic field. The results of the corresponding approximation are shown in Fig. 1 by solid lines.

Basing on the experimental data of both the MSHG interferometry and NOMOKE it is possible to make an estimation of the relative value of the magneto-induced SHG intensity with respect to the nonmagnetic SHG contribution: $I_{2\omega}(M)/I_{2\omega}(M=0)\approx 0.1$. This means that the relative value of the magneto-induced susceptibility of the Gd-LB film with respect to the hyper-Rayleigh susceptibility of the film, that is determined by the *fluctuations* of the $\chi^{(2)}$ in the Gd-LB film, is $\chi^{(2)}(M)/\Delta\chi^{(2)}(M=0)\approx 0.3$. At the same time, the magnetoinduced correction to the second-order susceptibility $\chi^{(2)}(M)/\chi^{(2)}(M=0)$ can be much smaller.

CONCLUSIONS

In conclusion, magnetization induced second harmonic generation and nonlinear magneto-optical Kerr effect is observed in Gd-containing Langmuir-Blodgett films. The nonlinear optical studies performed for the geometry of the longitudinal NOMOKE reveal significant alterations in the SHG intensity and in the polarization and phase of the SH wave induced by DC magnetic field. The violation of polarization selection rules and the diffusenes of the SHG intensity indicates the incoherence of the MSHG phenomenon and can be attributed to the inhomogeneity of LB structure and to the hyper-Rayleigh scattering mechanism of MSHG. The magneto-induced effects in the hyper-Rayleigh scattering proof the existence of 2D-islands of Gd ions in the structure of the LB films.

ACKNOWLEDGEMENTS

This work was supported by INTAS-93 grant 370 (ext), special RFBR grant for Russian Leading Scientific Schools 96-15-96420, RFBR grants 97-02-17919, 97-02-17923, Integration Program "Center of Fundamental Optics and Spectroscopy" and Programs of Russian Ministry of Science "Physics of Solid State Nanostructures" and "Fundamental Metrology", program "Universities of Russia".

REFERENCES

[1] J.Q. Xiao, J.S. Jiang, and C.L. Chien, Phys. Rev. Lett. **68**, 3749 (1992).

[2] S.S.P. Parkin, N. More, and K.P. Roche, Phys. Rev. Lett. **64**, 2304 (1990).

[3] A.M. Tishin, Yu. A. Koksharov, J. Bohr, G.B. Khomutov, Phys. Rev. B, **55,** p. 17 (1996).

[4] O.A. Aktsipetrov, A.A. Fedyanin, A.V. Melnikov, E.D. Mishina, and T.V. Murzina, Jpn. J. Appl. Phys. **36**, p. 48 (1998).

[5] T.F. Heinz, in Nonlinear Surface Electromagnetic Phenomena, H.-E. Ponath and G.I. Stegeman, eds. (North Holland, 1991), 355.

[6] J. Reif, C.Rau, E. Matthias. Phys. Rev. Lett. **71,** p. 1931,1934 (1993).

[7] U. Pustogowa, T.A. Luce, W. Hübner, K.H. Bennemann. J. Appl. Phys. **79**, p. 6177,6180. (1996).

[8] Th. Rasing, J. Magn. Magn. Mater. **165**, p. 35 (1997).

[9] R. Stolle, K.J. Veenstra, F. Manders, Th. Rasing, H. van den Berg, N. Persat. Phys. Rev. B, **55**, p. R4925,R4927 (1997).

[10] R. Stolle, G. Marowsky, and G. Berkovic, Appl. Phys. B **63**, 491 (1996).

[11] O.A. Aktsipetrov, A.A. Fedyanin, D.A. Klimkin, A.A. Nikulin et al. Ferroelectrics, **186**, p. 215 (1996).

AUTHOR INDEX

Abarra, E.N., 255
Adachi, N., 493, 633
Adekor, B.T., 193
Aktsipetrov, O.A., 605, 651, 657
Aldinger, F., 159
Allen, E.L., 13
Anders, Simone, 371, 415
Ando, K., 493, 625

Babushkina, N.A., 111
Backherms, V., 463
Baglin, J.E.E., 13, 421
Bahlmann, N., 463, 513, 519
Bakhru, H., 475
Bao, T., 395
Bardin, T.T., 421
Barnard, J.A., 349, 389
Belova, L.M., 111
Bennett, L.H., 291, 355
Bentley, J., 205, 211
Berkowitz, A.E., 9
Beyers, R., 13
Bhatia, C. Singh, 371, 415
Bogy, David B., 371, 415
Brown, G., 279
Brown, H.J., 355
Buendia, G.M., 361
Butera, A., 349

Cadeville, M-C., 325
Cadieu, F.J., 141
Celis, J.P., 331
Chaiken, A., 43
Challener, W.A., 565
Chandrasekaran, K., 147
Chang, C.A., 67
Chen, Chao-Yuan, 415
Chen, L.H., 129, 165
Chen, Li, 141
Chen, P.J., 9
Chen, Qiushui, 449
Chen, Y.C., 67
Cherif, Mondher, 449
Chiang, D.Y., 67, 73
Childress, J.R., 79, 141
Cho, H.S., 37
Choi, K.K., 135
Cross, E., 475

da Silva, M.F., 97
Dahmen, K.H., 141
Daughton, J.M., 9
Dedukh, L.M., 43
Deline, V.R., 13
Della Torre, E., 291, 355
Diamandescu, L., 337
Didenko, N.V., 605, 657
Dierickx, D.D., 331
Doerner, Mary, 261
Dorsey, P.C., 193
Dötsch, H., 463, 513, 519
Dova, P., 231

Egelhoff, Jr., W.F., 9

Farhoud, M., 193
Fedyanin, A.A., 605, 657
Feldman, Bernard J., 433
Fernandes, J., 31
Ferreira, M., 31
Fitzsimmons, M.R., 311
Folks, L., 319
Fong, Walton, 371, 415
Freitas, P.P., 31, 97
Fujiwara, H., 25, 37
Fukumoto, A., 589
Fung, K.K., 343
Furdyna, J.K., 613
Futamoto, M., 243

Galvão, T.T., 97
Gambino, Richard J., 555
Gan, Danny, 383
Ganshina, E.A., 651
Geng, Ji-bin, 55, 343
Gillman, E.S., 141
Godoi, R.H.M., 583
Goldberg, Jason, 261
Gong, Heng, 181, 223
Gopinath, Anand, 481
Gopinathan, Niranjan, 383
Gorbenko, O.Yu., 111
Gornakov, V.S., 43
Grange, W., 325
Gushin, V.S., 651
Güttler, B., 111

Harllee, Peter S., 181
Hegde, H., 49
Hellman, F., 311
Hertel, P., 463, 513, 519
Hirano, J., 633
Hirano, T., 577
Hirayama, Y., 243
Ho, C.H., 67, 73
Honda, Y., 243
Hong, J., 5
Hou, C., 25, 37
Hsi, C.S., 165
Hsu, Y-N., 199
Hu, Y., 439
Huang, D.R., 67, 73

Huang, H.H., 67
Huang, Jankang, 449
Hurst, Jr., A.T., 79

Inaba, N., 243
Ishiko, D., 547
Ishizuka, S., 547
Ito, K., 243
Itoh, N., 547

Jafelicci, Jr., M., 583
Jenson, M., 79
Johnson, D., 79
Josef, A., 463
Judy, J.H., 9, 355
Jung, K.B., 79, 141

K., Sirisha, 153
Kamijo, A., 87
Kaneko, M., 589
Karis, T., 421
Katoh, Y., 501
Kaul, A.R., 111
Kazantsev, D.V., 651
Keck, D., 421
Kellock, A.J., 13, 421
Khomutov, G.B., 657
Kido, G., 633
Kishi, H., 25
Kishi, M., 577
Kitazawa, H., 633
Klik, I., 67, 73
Kling, A., 97
Kozawaguchi, H., 501
Kryder, M.H., 19
Kubota, E., 501
Kumar, A., 475
Kumar, D., 123, 171

Laidler, H., 231
Lal, Brij B., 267
Lambeth, David N., 181, 199, 217, 223, 285, 599
Laughlin, David E., 181, 199, 217, 223
Leal, J.L., 19
Lee, C.B., 123, 171
Lee, Li-Lien, 181
Lee, S.F., 67, 73
Lee, Y.K., 273
Levy, M., 475
Li, Yi-Qun, 449
Liew, T.Y.F., 273
Lin, J.L., 129
Lin, M.T., 67, 73
Lin, Shu-Han, 433
Liou, Y., 73
Liu, R., 475
Liu, Wayne, 449
Lo, C.K., 67, 73
Lo, Roger Yu, 371
Lohmeyer, M., 463, 513, 519
Low, T.S., 273
Lu, Bin, 181

Machado, E., 361
Majewski, P., 159
Malhotra, Sudhir S., 267
Marinero, Ernesto, 261
Marques, R.F.C., 583
Martien, D., 9
Matsuda, K., 87
McMichael, R.D., 9, 61
Melnikov, A.V., 605
Mihaila-Tarabasanu, D., 337
Mima, T., 493
Minemoto, H., 547
Misuryaev, T.V., 605, 651
Mitsuzuka, T., 87
Mizumoto, T., 469
Moffat, T.P., 61
Morrison, Jr., P.W., 395
Moshchalkov, V.V., 331
Murzina, T.V., 605, 651, 657

Nagasaka, K., 25
Nakano, K., 135
Namikawa, T., 577
Narayanasamy, A., 153
Nickel, Janice H., 103
Nikitenko, V.I., 43
Nikles, D., 439
Nolan, T.P., 205, 211
Novotny, M.A., 279, 361
Novozhilov, M., 111

O'Grady, K., 231
Ohmori, N., 493
Ohsato, H., 493
Okamoto, I., 255
Okamura, Yasuyuki, 487
Okuda, T., 493, 633
Osgood, Jr., R.M., 475
Ott, R.D., 389

Parasote, V., 325
Parker, M.A., 13
Parks, D., 9
Pearton, S.J., 79, 141
Pierron-Bohnes, V., 325
Pietambaram, Srinivas V., 123, 171
Powell, C.J., 9

Qian, X.R., 141

Ramachandra Rao, M.S., 147
Rani, R., 141
Rikvold, P.A., 279
Rosen, Hal, 261
Rosenblum, M.P., 427
Ross, C.A., 193, 427
Rubin, Kurt, 261
Russak, Michael A., 267

Sakurai, B., 639
Salamanca-Riba, L., 61
Sant, S.B., 49
Schabes, Manfred, 261
Scharf, T.W., 389
Seigler, M.A., 599
Shamonin, M., 519
Shapiro, A.J., 43
Shapiro, A.L., 311
Sharifi, F., 141
Sharma, Manish, 103
Sharma, Rahul, 439
Shima, M., 61
Shimizu, Y., 25
Shintaku, T., 501
Shull, R.D., 43
Sin, K., 5
Sinclair, R., 211
Singh, Rajiv K., 123, 171
Skuja, L., 111
Smith, Henry I., 193
Soares, J.C., 97
Soares, V., 97
Sorescu, M., 337
Sousa, R.C., 97
Stadler, Bethanie J.H., 481
Stammler, Thomas, 415
Stöhr, Joachim, 415
Street, S., 439
Su, Jun, 535
Suchanek, W., 639
Sugimoto, N., 501
Sun, J.J., 97
Suzuki, Takao, 255, 299
Swartzendruber, L.J., 291, 355

Tan, L.P., 273
Tanaka, A., 25
Tate, A., 501
Thiele, J-U., 319
Toney, M.F., 319
Tsai, Chen S., 525, 535
Tsuge, H., 87
Turlo, J.E., 383
Twisselmann, D.J., 193
Tyndall, G.W., 403

Ueda, F., 37

Varadaraju, U.V., 147, 153
Varanda, L.C., 583
Veloso, A., 31
Vijayaraghavan, R., 147

Wallenhorst, M., 463, 513
Waltman, R.J., 403
Wang, J., 49
Wang, J.J., 141
Wang, J.P., 273
Wang, N., 343
Wang, Shan X., 5, 103
Warren, G.W., 439
Watanabe, K., 625
Watanabe, T., 639
Weller, D.K., 319
Westmore, T.H., 13
Wilson, Donald K., 541
Wittig, J.E., 205, 211
Wong, H.L., 273
Woyczynski, W., 395
Wu, C.Y., 67
Wu, D.H., 165

Xhie, Jie, 55
Xiao, R.F., 55

Yamada, Yoshiyasu, 299
Yamamoto, Sadahiko, 487
Yamasaki, M., 135
Yamazaki, T., 633
Yamazaki, Y., 135, 577
Yan, X., 55, 343
Yang, D., 389
Yang, Wei, 181, 223, 285
Yao, Y.D., 67, 73
Yokoi, H., 469
Yoshida, K., 577
Yoshimura, M., 639

Zaets, W., 625
Zhang, X.X., 343
Zhang, Xiao-feng, 55, 343
Zou, Jie, 181, 217

SUBJECT INDEX

activation volume, 231, 273, 349
AFM, 395
aftereffect, 355
Al_2O_3, 103
aluminum, 331
amine-quinone, 439
amorphous
  alloys, 555
  hard carbon, 371
  hydrogenated boron carbide, 433
anisotropy, 43, 141, 181, 325
  field, 285
  in-plane, 193
  magnetic, 273, 299, 319
  perpendicular, 299
annealing, 433
antiferromagnetic materials, 25, 171

Ba-doped PCMO, 171
BC, 433
bias voltage dependence, 97
$Bi_3Fe_5O_{12}$ garnet, 493
Bragg diffraction efficiency, 525, 535
buffered semiconductors, 449, 481

carbon, 383
  overcoat, 421
cathodic arc, 371
Ce-YIG, 449, 481
chemical ordering, 319
circulator, 501, 519
Cl_2-based plasma, 79
closed d-shell, 147
CoAg, 349
CoCrPt, 199, 217, 261
CoCrPtTa, 255
CoCrPtTaNb, 255
CoCrTa, 205, 211
CoCrTaPt, 193
CoCrX, 205
Co-Cu granular films, 605, 651
Co/Cu multilayers, 61
Co-doped, 493
coercivity, 37, 181, 231
colossal magnetoresistance (CMR), 111, 129, 141
compensation temperature, 361
contact resistance, 343
conventionally structured, 589
CoPt, 311, 325
Co_3Pt, 299
corrosion, 171
  protection, 421
  resistance, 31
Cr, 633
critical field, 231
CrMn, 217
crystal ion slicing, 475
Cu/Ni interface, 13
current sensor, 547
curved ion-milled hybrid waveguide lens, 525

dc bias, 273
decay coefficient, 291
delta-M, 349
diamondlike carbon (DLC), 383, 389, 395
  nitrogenated, 389
diluted magnetic semiconductor, 613, 625, 633
  dislocations, 43
dispersed particles, 577, 583
doctor-blade method, 165
domain-wall motion, 37
double barrier, 97
dynamic coercivity, 261

effective
  anisotropy, 19
  pinning field, 37
EFTEM, 211
electrochemical impedance spectroscopy, 439
electrochemistry, 331
electrodeposition, 61
elemental mapping, 205
energy filtered transmission electron microscopy, 205, 211
epitaxy, 181
etch
  rates, 141
  yield, 79
etching, 331
exchange
  bias, 25, 43
  coupling, 25, 49
  interactions, 285
  layers, 31

Faraday
  effect devices, 535, 541, 547
  rotation, 463
FeN, 5
FePt, 319
ferroelectric oxide films, 475
ferromagnet/antiferromagnet systems, 37
ferromagnetic
  insulator, 153
  interaction, 633
  order, 311
  transition temperature, 147
fiber
  probe, 599
  sensor, 547
fourfold symmetry, 61
FTIR, 439

GaAs, 449
garnet particles, 577, 583
giant magnetoresistance (GMR), 9, 19, 49, 61, 73, 153
glass-based magnetic media, 427
grain
  boundary, 135
  isolation, 181
  size, 267
granular exchange coupling, 217
grooves, 193

hard-disk
  drive, 403
  interface, 403
hardness, 433
head-disk interface (HDI), 403
  tribology, 371
heat dissipation, 55
high
  moment materials, 5
  resolution transmission electron microscopy (HRTEM), 49, 211
hole-doped manganites, 171
hybrid ferromagnetic-semiconductor structures, 613
hydrothermal(-)
  electrochemical synthesis, 639
  method, 337
hyper-Rayleigh scattering, 657
hysteresis loop, 337
  shift of, 37

icosahedra, 433
inductively-coupled plasma (ICP), 79
InP, 449
insulating, 171
insulator-to-metal transition, 123
integrated
  magneto-optic Bragg Cell modulators, 525, 535
  nonreciprocal device, 501
  optical isolator, 501, 513, 519
interactions
  intergranular, 285
  interparticle, 349
interdiffusion kinetics, 13
interfacial junction contamination, 343
interferometric lithography, 193
intergranular coupling, 181, 267
interlayer diffusion, 217
internal chemical pressure, 123
ion(-)
  beam bombardment, 487
  density, 141
  etching, 343
ir absorption, 433
irreversible susceptibility, 349
Ising ferrimagnetic, 361

Kerr effect, 555, 565, 605, 651, 657

$L1_0$, 319, 325
LaCaMnO, 129, 141, 147
$LaMnO_3$, 159
LaNdCaMnO, 129
Langevin micromagnetic calculations, 279
Langmuir-Blodgett films, 605, 657
lanthanum manganite thin films, 123
laser zone texture, 427
LaSrMnO, 135
LaYCa, 129
liquid-phase epitaxy, 463
lubricant degradation, 415
lubrication, 403

Mach-Zehnder interferometer, 513
magnetic(-)
  disks, 389
  domains, 319
  field modulation, 589
  force microscopy (MFM), 255, 319
  garnets, 469, 547
  media, 181, 217, 427
  oxide films, 475
  polarization, 311
  random access memory (MRAM), 67, 97
  tunnel junction, 87
  viscosity, 349
magnetites, 337
magnetization(-), 43
  density, 311
  induced second harmonic generation, 605, 651, 657
  process, 37
  reversal, 231
magnetocrystalline anisotropy constants, 243
magneto-optic, 43
  isolators, 463, 469, 501, 541
magneto-optical
  properties, 493
  storage, 555, 589
magnetoresistance (MR), 55, 87, 97, 123, 129, 135, 165, 171
  polar, 67
magnetoresistive heads, 343
magneto-static waves, 525, 535
manganites, 111
media noise, 181, 267
microhardness, 395
microstructure, 165
mini disc (MD), 589
Mn-based magnetic thin-film multilayers, 613
MOCVD, 449
monolithic integration, 481, 625
Mössbauer spectroscopy, 337
multilayered thin films, 639
multilayers, 73

nanodots, 331
nanoindentation, 395
nanolayered, 565
nanoprobe, 211

nanostructures, 331
natural oxidation, 87
near-field scanning optical microscopy
(NSOM), 599
NEXAFS, 415
Ni pillars, 279
NiAl, 199, 217
Ni/Cu interdiffusion, 13
NiFe, 79
NiFeCo, 79
$Ni_{80}Fe_{20}$/Cu interface, 13
nonlinear optical readout, 605
nonreciprocal
magneto-optic waveguides, 513, 625
phase shift, 463, 469

optical phase shifters, 589
ordered
epitaxial phase, 319
phase, 299
oscillator, 535
overcoat diffusion, 181
oxidation
of Cu, Fe, Mn,,and Co, 421
process, 181
oxygen isotope effects, 111

partially filled d-shell, 147
patterned garnet films, 487
perfluoropolyether (PFPE), 403
permalloy, 73
perovskite, 153
phase diagrams, 159
photoresist, 343
polarized neutrons, 311
pole tip, 5
polymer, 171
PrBaCaMnO, 171
PrCaMnO, 147
Preisach-Arrhenius,291, 355
protective overcoats, 389
pulsed laser deposition, 123

radiatively-coupled waveguide, 519
Raman, 383
phonon scattering, 111
rare-earth-transition-metal alloys, 555, 565
read heads, 19, 31
recording
high density, 31
longitudinal, 67, 243
media
longitudinal, 211, 255
magnetic, 205
particulate, 355
perpendicular, 243
relaxation process, 291
resistance, 87
rotation mechanism, 37

scratch, 389
segregation, 205
selected-area epitaxy, 487
self-organization, 331
semiconductor guide, 469
silicon, single crystal, 181
single-domain ferromagnetic particles, 279
SmCo, 141
solution flow system, 639
spin(-)
dependent tunneling (SDT), 103
valve, 9, 19
heads, 25, 31
thermal stability, 13
sputter epitaxial method, 487
sputtering, 135, 141
reactive, 481
SQUID magnetometer, 123, 171, 325
stiction, 383
Stoner-Wohlfarth, 231, 261
stress, 43, 383
substitutions, 337
superparamagnetic, 61
surface energy, 403
sweep-rate dependence, 231
switching volume, magnetic, 267
synthetic antiferromagnet, 19

Ta_2O_5, 103
taper waveguide, 525
texture, 199
thermal
decay, 261
stability, 181, 243, 255, 261
switching, 279
thermomagnetic recording, 361
thick films, 165
thin-film media, 181
three-guide coupler, 519
$II_{1-x}Mn_xVI$ alloys, 613
$III_{1-x}Mn_xV$ alloys, 613
time decay of remnant magnetization, 273
topographically-induced magnetic
anisotropy, 193
transverse, 67
tribology, 371, 383
tunnel
barrier, 87
junctions, 97

wafer direct bonding, 469
waveguide isolator, 501
write head, 5

X-PEEM, 415
XPS, 439

YIG-GGG waveguides, 525

Zener double exchange interaction, 147